NUREG/CP-0060

Proceedings of the U.S. Nuclear Regulatory Commission

The First International Workshop on Fundamental Aspects of Post-Dryout Heat Transfer

Held at
Salt Lake City, Utah
April 2-4, 1984

U.S. Nuclear Regulatory Commission

Office of Nuclear Regulatory Research

Compiled by R. Lee

Available from

GPO Sales Program
Division of Technical Information and Document Control
U.S. Nuclear Regulatory Commission
Washington, D.C. 20555

Printed copy price: $12.00

and

National Technical Information Service
Springfield, VA 22161

NUREG/CP-0060

Proceedings of the U.S. Nuclear Regulatory Commission

The First International Workshop on Fundamental Aspects of Post-Dryout Heat Transfer

Held at
Salt Lake City, Utah
April 2-4, 1984

Manuscript Completed: November 1984
Date Published: December 1984

Compiled by: R. Lee

Division of Accident Evaluation
Office of Nuclear Regulatory Research
U.S. Nuclear Regulatory Commission
Washington, D.C. 20555

Preface

The purpose of the First International Workshop on Fundamental Aspects of Post-Dryout Heat Transfer was to review recent developments and the state of art in the field of post-dryout heat transfer. The workshop centered on interchanging ideas, reviewing current research results, and defining future research needs. The following five sessions dealing with the fundamental aspects of post-dryout heat transfer were held.

Computer Code Modeling and Flow Phenomena: flow regimes, drop size, drop formation and behavior, interfacial area, interfacial drag, computer modeling. Session Chairman: Dr. R. Duruaz, Service des Transferts Thermiques, Centre d'Etudes Nucleaires de Grenoble, Grenoble, France.

Quenching Phenomena: nature of rewetting, maximum wetting temperature, Leidenfrost phenomenon, heat transfer in the vicinity of quench front. Session Chairman: Mr. M. W. Young, USNRC, MS 1130SS, Washington, D.C., 20555, USA.

Low-Void Heat Transfer: inverted annular-flow heat transfer, inverted slug-flow heat transfer, thermal non-equilibrium, computer modeling. Session Chairman: Dr. Y. Murao, Japan Atomic Energy Research Institute, Division of Reactor Safety, Tokai-Mura Naka Gun, Ibaraki Kev, Japan 319-11.

Dispersed-Flow Heat Transfer: drop interfacial heat transfer, vapor convection, thermal non-equilibrium, correlations and models. Session Chairman: Dr. G. F. Hewitt, Head of Engineering Sciences Division, Building 392, AERE Harwell, England OX11 ORA.

Effects of Grids and Blockages: interaction with continous-phase fluid, interaction with dispersed-phase fluid, downstream effects, computer modeling. Session Chairman: Professor Y. Y. Hsu, Department of Chemical and Nuclear Engineering, University of Maryland, College Park, Maryland 20742, U.S.A.

The papers are published according to the five sessions along with a summary by individual session chairman.

Workshop Organizing Committee:

Prof. J. Chen (Lehigh University)
Dr. G. Costigan (AERE)
Dr. M. Cumo (CNEN)
Dr. D. Groenveld (AECL)
Dr. G. Hewitt (AERE)
Prof. Y. Hsu (Univ. of Maryland)
Prof. U. Muller (KfK)
Dr. Y. Murao (JAERI)
Mr. M. Young (USNRC)
Dr. R. Lee (USNRC)
Dr. R. A. Nelson (LANL), Chairman

TABLE OF CONTENTS

Preface iii

Acknowledgements xi

I. Computer Code Modeling and Flow Phenomena 1

1. "Visualization of the Reflooding of a Vertical Tube by Dynamic Neutron Radiography," by G. Costigan and C. D. Wade, AERE Harwell, United Kingdom. 2

2. "Investigation of Dispersed Flow Heat Transfer using Different Computer Codes and Heat Transfer Correlations," by I. Vojtek, GRS, FRG. 14

3. "Reflood Analysis Code: REFLA," by Y. Murao, Japan Atomic Energy Research Institute, Japan. 56

4. "RELAP5/MOD2 Post-CHF Heat and Mass Transfer Models," J. C. Lin, C.C. Tsia, V. H. Ranson and G. W. Johnsen, EG&G Idaho, Inc. USA. 68

5. "TRAC-BD1/MOD1 Post-Dryout Wall Heat Transfer," by R. W. Shumway, EG&G Idaho, Inc. USA. 79

Chairman's Summary by R. Deruaz, CEN, France. 94

II. Quenching Phenomena 102

1. "Quench Front Movement during Reflood Phase," 103
by Y. Murao, Japan Atomic Energy Research Institute, Japan.

2. "Maximum Wetting Temperature up to Critical 118
Pressure," by D. Hein, V. Kefer and H. Liebert, KWU, FRG.

3. "Minimum Heat Flux Conditions in Boiling 137
Heat Transfer," by S. Nishio, Univ. of Tokyo, Japan.

4. "Quenching of Rod Bundles with Fuel Rod Simulators of 171
Different Desisn," by P. Ihle, K. Rust and F. Erbacher,
KfK, FRG.

5. "A Study of Interfacial and Wall Heat Transfer 179
downstream of a Quench Front," by D. Juhel,
CEN, France.

6. "Numerical Simulation of the Rewetting of a 205
Horizontal Tube using a Two-Fluid Model,
by C. B. So and K. H. Ardron, AECL, Canada.

7. "Prediction of Transition Boiling Heat Transfer 231
in Annular Flow via the Moving Front Model," by
J. Weisman and Y. K. Kao, Univ. of Cincinnati, USA.

8. "COBRA-TF Analysis of Westinghouse Upper Head 245
Injection ECCS Heat Transfer Tests," by
J. M. Kelly/PNL and B. A. McIntyre/Westinghouse, USA.

Chairman's Summary by M. W. Young, USNRC, USA. 265

III. Low-Void Heat Transfer 269

1. "A Correlation of Low Flow, Low Pressure, and 270
Low-to-Moderate Quality Post-CHF Data," by
J. C. Chen/Lehigh Univ., C. D. Morgan/B&W and
R. K. Sundaram/Yankee Atomic Electric Company, USA.

2. "Inverted Annular Film Boiling and the Bromley 303
Model," by M. K. Denham, UKAEA, United Kingdom.

3. "Transition Boiling on Surfaces of Different Surface 315
Energy," by S. K. R. Chowdhury and R. J. S. Winterton,
Univ. of Birmingham, United Kingdom.

4. "Post-CHF Low-Void Heat Transfer of Water: Measurements 331
in the Complete Transition Boiling Region at Atmosphere
Pressure," by K. Johannsen and W. Meinen, Tech. Univ.
of Berlin, FRG.

Chairman's Summary by Y. Murao, JAERI, Japan. 351

IV. Dispersed-Flow Heat Trasfer 357

1. "A Simple-to-Use Post-Dryout Heat Transfer Model 358
Accounting for Thermal Non-Equilibrium," by
D. Hein and W. Kohler, KWU, FRG.

2. "Droplet Dynamics and Heat Transfer in Dispersed 373
Two-Phase Flow," by A. J. Clare and S. A. Fairbairn,
CEGB, United Kingdom.

3. "An Experiment Study of Heat Transfer Enhancement 397
in Dispersed Flow in Rod Bundles," by H. Kianjah,
V. K. Dhir/UCLA and A. Singh/EPRI, USA.

4. "Forced Convective, Non-equilibrium Post-CHF Heat 417
Transfer Experiment: Description, Data Analysis and
Correlation Comparison," by K. G. Condie et. al.

5. "Post-Dryout Heat Transfer Prediction," by..... 457
A. F. Varone, Jr. and W. M. Rohsenow, MIT, USA.

6. "A Two-Region Vapor Generation Rate Model for 485
Convective Film Boiling," by S. W. Webb/SANL and
J. C. Chen/Lehigh University, USA.

7. "Post-Dryout Heat Transfer on a Vertical Straight 509
Tube of a Steam Generator," by K. Roko and
M. Shiraha, Kawaski Heavy Industries, Ltd. Japan.

8. "Numerical Fluid Dynamics Calculations of Non- 538
Equilibrium Steam-Water Flows with Entrained
Droplets," by K. A. Williams, LANL, USA.

9. "Dispersed Flow Reflood Heat Transfer in Rod Bundles of Different Fuel Rod Simulator Design," by P. Ihle, K. Rust and F. Erbacher, KfK, USA. 575

Chairman's Summary by G. E. Hewitt, AERE Harwell, United Kingdom. 583

V. Effects of Grids and Blockages 589

1. "Droplet Breakup and Entrainment at P. W. R. Spacer Grids," by J. E. Adams and A. J. Clare, CEGB, United Kingdom. 590

2. "Premature Quenching by Balloned and Burst Fuel Rod Claddings in a LOCA," by F. Erbacher and K. Wiehr, KfK, FRG. 615

3. "Measurement of Droplet Dynamics Across Grid Spacer in Mist Cooling of Subchannel of PWR," by S. L. Lee, et. al., SUNY Stony Brook, USA. 619

4. "Reflood Heat Transfer in Severely Blocked Fuel Assemblies," by K. G. Pearson and C. A. Cooper, UKAEA, United Kingdom. 643

5. "Grid Spacer Effects in Reflood Experiments Using Rod Bundles of Different Fuel Rod Simulator Design," by P. Ihle, K. Rust and F. Erbacher, KfK, FRG. 673

Chairman's Summary by Y. Y. Hsu, Univ. of Maryland, USA. 683

VI. Attendence List 693

Acknowledgements

The Organization Committee would like to ackrowledge the work done by the meeting secretary/treasurer, Dr. Keith Condie, and the work done by Dr. Harold Sullivan in making meeting arrangements. Thanks are also extended to the EG&G Idaho, Inc. and the Los Alamos National Laboratory for their support in these organizing efforts.

Finally, the committee would like to thank the session chairmen. The work done by R. Duruaz, Y. Murao, G. F. Hewitt, M. W. Young and Y. Y. Hsu on the organization and chairing of their sessions was fundamental in making this meeting a success.

I. Computer Code Modeling and Flow Phenomena

International Workshop on Post-dryout Heat Transfer,
Salt Lake City, Utah
April 1-4 1984

VISUALISATION OF THE REFLOODING OF A VERTICAL TUBE BY DYNAMIC NEUTRON RADIOGRAPHY

by

G. Costigan,* C.D. Wade*

Abstract

Steady state, low quality, post-dryout data taken recently at Harwell in both upflow and downflow suggest that flow regime changes may be affecting the results. In addition, the degeneration of inverted annular flow to dispersed droplet flow ahead of a quench front is relatively poorly understood. To elucidate these phenomena, preliminary flow visualisation experiments have been performed. A stainless steel tube (12.2 mm O.D., 9.25 mm I.D., 600 mm long) was mounted in a low energy neutron beam from the Harwell materials testing reactor DIDO. The tube was heated to 600°C and quenched by water introduced from the bottom or the top of the tube as required. The neutron imaging system provided a dynamic visual record of the quenching process at various positions along the tube. The results confirm that different flow patterns occur in upflow and downflow and provide valuable insight into the quenching phenomena. The usefulness of the technique for examining other important problems such as the effects of blockages and grids is clearly demonstrated.

*Engineering Sciences Division,
A.E.R.E. Harwell,
Oxfordshire, England.

NOMENCLATURE

D_j	jet diameter
h	heat transfer coefficient
k_v	vapour thermal conductivity
T_s	saturation temperature
T_w	wall temperature
u_{rel}	velocity of vapour relative to liquid
Z	distance from quench front
Δh_v	enthalpy of vaporisation
α	void fraction
η_v	vapour viscosity
ρ_L	liquid density
ρ_v	vapour density
σ	surface tension

1. INTRODUCTION

Studies of the consequences of a variety of loss of coolant accidents (LOCA) in water cooled reactors have stimulated research into the mechanisms of heat transfer in the vicinity of a quench front. In the blowdown and reflood phases of a large break LOCA in a pressurised water reactor (PWR), post-dryout heat transfer with low fluid quality is of particular interest, since it precedes the arrival of the quench front and influences the rate at which the quench front progresses. Low quality post-dryout data at pressures of about 70 bar and over a wide range of mass fluxes (up to about 3000 kg/m^2s) are relevant to the blowdown phase of a LOCA, whereas the reflood phase is typified by pressures up to 4 bar and mass fluxes usually much less than 300 kg/m^2s. In both of these cases the flow may oscillate and the possibility of flow reversal occurring indicates the need for data taken in downflow as well as upflow. Until comparatively recently such data did not exist. This deficiency is being gradually remedied, but there is still a need for more information to aid our understanding of the physics of the rewetting process.

At Harwell a number of experiments have been performed in the low pressure, low flow regimes of post-dryout heat transfer which are typical of the reflood phase of a LOCA. The present study was undertaken in an attempt to explain the results of these experiments more fully.

2. BACKGROUND

Low quality, post-dryout heat transfer data have been obtained from a variety of test section types, such as thick walled cylinders or long thin walled tubes, which are preheated and then quenched by the introduction of water. To avoid the problems associated with such transient experiments, Groeneveld [1] suggested a technique for obtaining steady state post-dryout data with low inlet qualities. These suggestions have been adopted by a number of researchers [2-5].

Barnard [6] obtained data from composite thick walled copper blocks for a wide range of inlet conditions in upflow and downflow. These data indicate that a sharp deterioration in post-dryout heat transfer occurs at low mass fluxes (less than 200 kg/m^2s) in both upflow and downflow. Similar trends were observed in quenching experiments performed on thick walled nickel cylinders [7].

More recent steady state post-dryout data taken at Harwell on a "hot-patch" type test section [5] support the observations concerning the effects of reductions in flow rate (Figures 1 and 2). Data showing the effect of varying the tube power at constant inlet conditions are presented in Figures 3 and 4. Higher rates of heat transfer over the first 30 cm of tube are observable in both upflow and downflow, in accordance with the predictions of laminar film boiling models of the Bromley type [8]. Figures 5 and 6 show comparisons of measured data with the local heat transfer coefficients predicted by such a model viz

$$h = 0.5 \left[\frac{k_v^3 \rho_v (\rho_L - \rho_v) \Delta h_v}{\eta_v (T_w - T_s) Z} \right]^{\frac{1}{4}} \quad \ldots\ldots (1)$$

A radiation component based on a tube wall emissivity of 0.3 and a water emissivity of 1.0 was added to the above equation to obtain the predictions shown.

This model predicts a monotonic decrease in heat transfer coefficient with increasing tube length. The upflow data exhibit an initial decrease and then either become constant or increase. This behaviour has been attributed to improved convective heat transfer as more vapour is generated along the tube [2].

The inverted annular flow pattern must eventually break down to form dispersed droplet flow and since no evidence of a sudden change in the rate of heat transfer along the tube was obtained in any test, it must be concluded that the transition is a gradual process.

The Bromley model was not able to predict the effect of varying the tube power. In downflow the measured heat transfer coefficients were frequently less than half the predicted values and no explanation could be found for the wall temperature variations shown in Figure 4 -- these variations were found to decrease with flowrate (Figure 2).

The present study was undertaken in an attempt to obtain an insight into the mechanisms of heat transfer in the vicinity of a travelling quench front under reflood conditions.

3. EXPERIMENT

3.1 Principle of the technique

Visualisation of the internal reflooding of a hot stainless steel tube by water is made possible by taking advantage of the fact that a beam of low energy neutrons (3 milli eV) is strongly attenuated by water (or any hydrogenous material), whilst most metals are relatively transparent to neutrons at these energies. Thus by placing a neutron absorbing fluorescent screen behind the object being viewed a neutron shadow can be produced. With sufficient contrast a dynamic record can be made by using an image intensifier and camera.

The technique requires a high intensity source of neutrons and the present study was carried out inside the reactor building of the Harwell materials testing reactor DIDO at a point where the neutron flux was about $10^5 n/cm^2 s$. The available headroom limited the overall length of test section to 600 mm. A diagram of the experimental arrangement is given in Figure 7.

The diameter of the neutron beam at the point of measurement was about 12 cm; therefore to view the reflooding process from different axial positions along the tube, it was necessary to move the tube up or down relative to the horizontal centreline of the neutron beam. This was achieved by mounting the tube on a photographic pillar stand equipped with a rack and pinion.

Water was supplied to the test section via a flexible hose from a portable water supply consisting of: a preheated five gallon tank, a small centrifugal pump, throttle valve and flowmeter. The exhaust from the test section returned through another flexible hose to the tank which operated at atmospheric pressure. Valved quick release couplings on the flexible hoses made it possible to supply water to the top or bottom of the tube as required.

The tube was of type 316 stainless steel 12.2 mm O.D., 9.25 mm I.D.. Eight 1 mm diameter sheathed NiCr-NiAl thermocouples were brazed into 1 mm deep holes in the tube wall at 2 cm from the tube inlet and then at every 8 cm. Inlet and exit temperatures were measured by similar thermocouples and their outputs were recorded on a Rikadenki 10 channel pen recorder. A portable a.c. power supply (0-4 volts, 0-1000 amps) was used to preheat the tube.

3.2 Operating procedure

The flow was set to give a nominal reflooding velocity of either 2.5 cm/s or 7.5 cm/s as water was circulated through a bypass hose. A temperature controller connected to an immersion heater in the tank maintained a constant preset temperature measured just after the flow-meter. The tube was heated to a temperature of 600°C. The low voltage a.c. power supply was then switched off and the water flow was diverted into the tube. At the same time the neutron beam and the video camera were switched on.

When the tube had quenched completely the flow was diverted through the bypass and the tube was drained. It was then repositioned relative to the beam centre line and another run at the same inlet conditions was carried out. A total of seven runs were performed to cover the complete length of the tube at a given inlet condition.

4. RESULTS

A typical set of temperature versus time traces are shown in Figure 8, for a reflooding rate of 7.5 cm/s in upflow with a nominal water inlet temperature of 80°C. The inlet water temperature can be seen to have risen gradually to the desired level during the test, due to the comparatively long inlet pipe and low flow rate.

As the liquid progressed into the tube an increase in the cooling rate became apparent after about 10 seconds. This corresponded with a sudden rise in temperature at the exit thermocouple location and signified the arrival of a dispersed steam-water flow generated during the quenching of the tube inlet. The quench front proceeded into the test section at about 5.5 mm/s, its speed gradually increasing with time to 8 mm/s at the centre of the tube.

Shortly after the second tube wall thermocouple indicated quenching, a slow quench was recorded by the thermocouple nearest the exit. This was due to a falling film of water extending downwards from the relatively cool exit flange. The lower velocity upflow runs exhibited similar behaviour to that described above with variations in the speed of the quench front.

Downflow temperature-time traces indicated that a quench front progressed down the tube at a speed between 5 mm/s and 7 mm/s depending upon the flooding velocity. The thermocouple temperature nearest the exit from the tube fell gradually during a run rather than quenching suddenly. At the lower flooding rates oscillations in the inlet and outlet temperatures were noticeable; whilst at higher flooding rates, tube wall temperatures often fell in a number of small steps, rather than in the smooth manner observed in the upflow tests.

The reflooding process was recorded on video tape by a JVC low light video camera. The real-time images thus obtained were sufficiently clear to allow a number of observations to be made.

At an upflow reflooding velocity of 2.5 cm/s with an inlet temperature of 35°C the progression of the quench front was quite distinct. The water filled the tube and appeared black up to a point on the wall at which vigorous nucleate boiling took place. Nucleate boiling extended about 4 mm axially along the tube wall and formed a distinct "neck" on the thin central column of liquid which flowed past the quench front. Under these conditions there was no evidence of any vapour being generated below the quench front by stored energy from the re-wetted part of the tube.

Ahead of the quench front a central liquid filament was in violent motion and rarely reached an axial length of more than 10 cm before it broke down. Breakdown was either due to varicose or sinuous instabilities (see Figures 9 and 10). Occasionally the vapour formed in the "neck" at the base of the liquid core would separate the core completely from the quench front. The progression of the quench front up the tube wall was quite uniform.

The liquid core either broke down into droplets (varicose instability) or ligaments (sinuous instability) which were then levitated by the vapour. The chaotic flow pattern which was formed higher in the tube was characterised by large diameter (approximately 6.0 mm) elongated drops preceded and followed by satellite drops of one or two millimetres diameter. These larger drops travelled quite slowly and often fell back down the tube. They became larger by collisions with other drops, before they were propelled forward again by the vapour generated below them. Near the exit end of the tube there was a larger population of smaller droplets but their velocities were still quite low.

A turbulent falling film was observed to quench the uppermost 10 cm of the tube. The film appeared to absorb the large droplets rising in the tube and thus progressed downwards until it met the rising quench front. For the 2.5 cm/s injection rate the void fraction shortly above the quench front was high - typically above 60%.

At a reflooding rate of 7.5 cm/s more water flowed past the quench front to form a flow pattern more akin to the conventional model of inverted annular flow (Figure 11). A much greater concentration of droplets above the liquid core was evident at the higher reflooding rate. These droplets appeared to have considerably higher velocities than in the low flooding rate case. The incidence of stagnant or falling droplets was much lower, and near the tube exit more smaller diameter higher velocity droplets were observed.

Both downflow runs showed that quenching was occuring due to a falling film of liquid on the tube wall. The bouyancy of the vapour formed a core of steam which preheated the liquid film by condensation - the tube wall temperature did not fall below 100°C until the whole of the tube was completely quenched, despite an inlet water temperature of about 35°C. The film which formed near the tube exit in the upflow runs was circumferentially uniform and was augmented by droplets rising from below. In the downflow runs, however, the quench front was usually asymmetrical: excess water reaching the quench front ran around the tube to a point on the film where the surface tension was lowest. At this point the water was thrown off the wall in the form of a jet which fell at an angle to the tube axis (Figure 12) and was deflected from a point diametrically opposite on the tube wall some distance lower down. The length of the jet depended upon the flooding rate. At 2.5 cm/s the jet was short and occasionally was reduced to only a few drops, whereas at 7.5 cm/s it was continuous and often fell down the tube in a zig-zag fashion, rebounding from opposite sides of the tube.

5. DISCUSSION

These observations throw considerable light on the quenching of small bore thin walled tubes and are of assistance in interpreting the results mentioned earlier.

It is immediately apparent from the video recordings that post CHF heat transfer models which envisage a thin laminar film of vapour separating a central liquid core from a hot tube wall are not appropriate to the lowest velocity (about 2.5 cm/s) reflooding rates. At higher liquid velocities (above 7.5 cm/s) in

upflow this model appears to be a better physical description of events. However in both cases the amount of vapour which is generated at the quench front is important in establishing the subsequent hydrodynamic and heat transfer behaviour.

Calculations made for the 2.5 cm/s upflow runs indicate that the quench front velocity can be estimated by performing a one dimensional heat balance on a short axial length of tube. The region of vigorous nucleate boiling at the quench front is taken to be 5.0 mm long. The heat flux over this length is assumed to vary linearly from zero to the critical pool boiling heat flux corresponding to the local water temperature. This fixes the rate of removal of stored energy and hence the time taken to quench the 5 mm length. If all of this heat produces steam without reducing the subcooling of the bulk of the liquid, a value of 3.0 m/s is obtained for the superficial velocity of the steam formed.

The actual velocity of the steam will depend upon the local void fraction. Ishii [9] presents a criterion for the transition from varicose to sinuous breakup of liquid jets as

$$\left[\frac{\rho_v u^2_{rel} D_j}{\sigma}\right]_{\alpha^2} = 1.73 \qquad \ldots\ldots (2)$$

Since both types of jet breakup were observed in this run equation (2) was considered to apply and a value of void fraction of 38.6% was calculated, suggesting that the actual steam velocity was of the order of 7.8 m/s. Assuming that a frozen quality model of the type used by Robershotte [10] for low velocity downflow comparisons applies in upflow, a heat transfer coefficient of 42.6 W/m²K can be calculated. This is much closer to the values observed at these low flow conditions than the predictions of inverted annular models.

Despite the fact that the above calculations are approximate they result in improved heat transfer predictions using a reasonable physical description of events near the quench front. Attempts to calculate steady state post CHF heat transfer rates at higher reflooding velocities, using an idealised model of the observed flow patterns, suggest that some form of liquid-wall interaction is augmenting the heat transfer rate.

At higher flooding rates the amount of vapour generated at the quench front appears to be inadequate to entrain all of the liquid passing the front. Hence an inverted annular core is formed which will remain stable until the vapour in the film reaches a critical relative velocity. At this point the core will break down to form dispersed droplet flow.

Downflow heat transfer predictions can also be made by a frozen quality model [10] and a minimum value typical of natural convection to steam is expected to occur at a water velocity which is just sufficient to bring a rising slug of steam to rest.

The observations of a liquid jet falling down the tube and impingeing on the tube wall at various points below the quench front, provide an explanation of the tube wall at temperature variations observed in Figures 2 and 4. The fact that the magnitude of the temperature variations increased with water flow rate, is consistent with the flow pattern observations. These downflow results were taken from a hot patch test section, the tube of which was subsequently found to have deformed due to differential thermal expansion at these positions.

The neutron radiography technique in its present form is capable of giving a good first order physical picture of two phase flow events in low void fraction

flows. Work is continuing to improve the resolution of the images obtained. The technique could be used to examine the behaviour of other components such as grids or blockages under more realistic conditions than are possible with most simulation experiments.

6. CONCLUSIONS

1. Dynamic neutron radiography of the reflooding of a hot vertical tube has provided video recordings of the flow patterns which occur.

2. At low reflooding velocities in upflow the post-dryout flow pattern consists of a liquid filament which rapidly breaks down into large droplets which move slowly in a low velocity steam flow.

3. A simple frozen quality model gives more satisfactory heat transfer coefficient predictions under low reflood conditions than a laminar film boiling model.

4. At higher upflow reflooding rates a pattern more akin to the inverted annular flow pattern is observed.

5. For the downflow velocities investigated a falling film/liquid jet flow pattern was observed.

6. The neutron radiography technique has the potential for revealing the pre-quench flow patterns in a number of other geometries of interest in reactor safety studies.

REFERENCES

1. Groeneveld, D.C., Gardiner, S.R.M. "A method of obtaining flow film boiling data for subcooled water". Int. J. Heat Mass Transfer v21 (1978) pp 17-26.

2. Fung, K.K., Gardiner, S.R.M., Groeneveld, D.C. "Subcooled and low quality flow film boiling of water at atmospheric pressure". Nucl. Eng. Des. 55 (1979)

3. Nijhawan, S., et al. "Measurement of vapour superheat in post critical heat flux boiling". ASME Symp. on Non Equilibrium Transport Processes. Eds. Chen and Bankoff (1979).

4. Gottula, R.C. et al. "Forced convective non equilibrium post CHF heat transfer experiments in a vertical tube". ASME-JSME Thermal Engineering Joint Conference (1983).

5. Costigan, G., Holmes, A.W., Ralph, J.C. "Steady state post dryout heat transfer in a vertical tube with low inlet quality". Submitted to 1st U.K. National Heat Transfer Conference, Leeds (1984).

6. Barnard, D.A., Glastonbury, A.G., Ward, J.A. "The measurement of post-dryout heat transfer at low pressure and mass quality under steady state conditions", European Two Phase Flow Group, Grenoble, (1977).

7. Costigan, G. "The quenching of thick-walled nickel test sections". 2nd Int. Topical Meeting on Nuclear Reactor Thermalhydraulics (1983) St. Barbara.

8. Andersen, J.G.M. "Low flow film boiling heat transfer on vertical surfaces, Part 1: theoretical model". AiChE Symp. Series v73 no. 164 pp 2-6.

9. Ishii, M., De Jarlais, G. "Inverted annular two-phase flow experiments and modelling". 11th Water Reactor Information meeting, Gaithesburg (1983).

10. Robershotte, P., Griffith, P. "Downflow post-critical heat flux heat transfer to low pressure water". Nucl. Technol. v56 no. 1 pp 134-140. (1982).

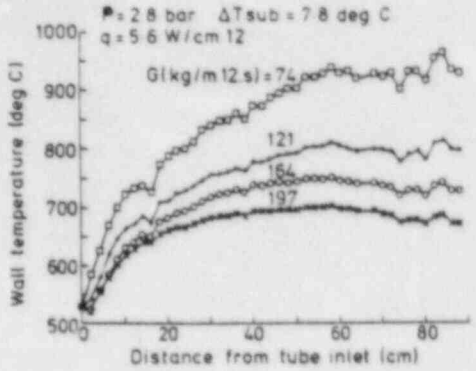

FIG 1. EFFECT OF FLOW RATE IN UPFLOW

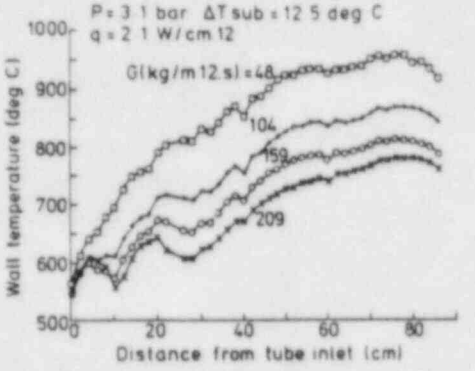

FIG 2. EFFECT OF FLOW RATE IN DOWNFLOW

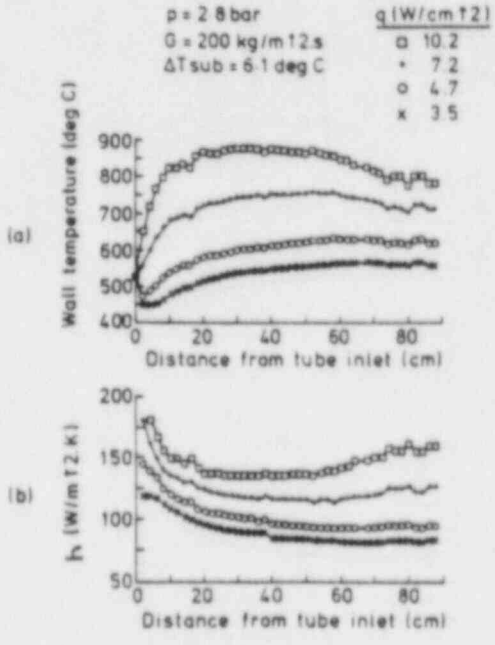

FIG 3. VARIATION OF TUBE POWER IN UPFLOW

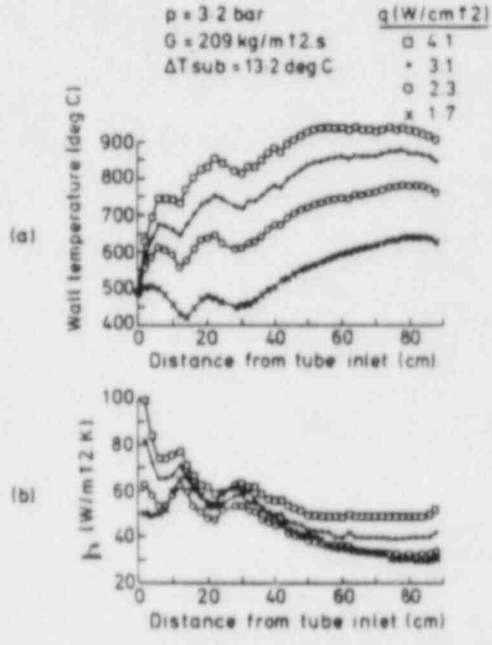

FIG 4. VARIATION OF TUBE POWER IN DOWNFLOW

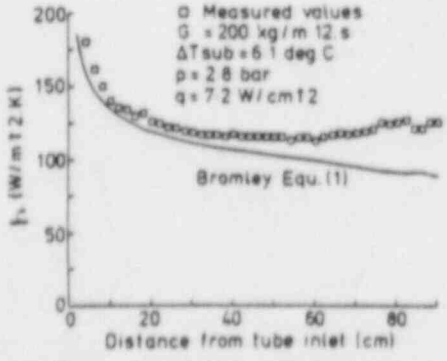

FIG 5 HEAT TRANSFER COEFFICIENTS - UPFLOW

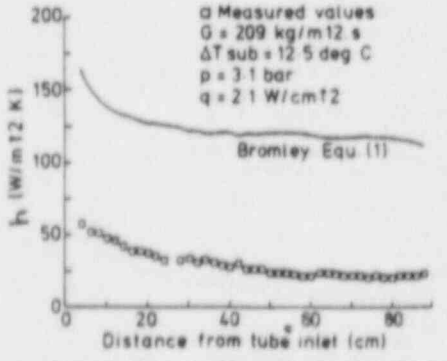

FIG 6 HEAT TRANSFER COEFFICIENTS - DOWNFLOW

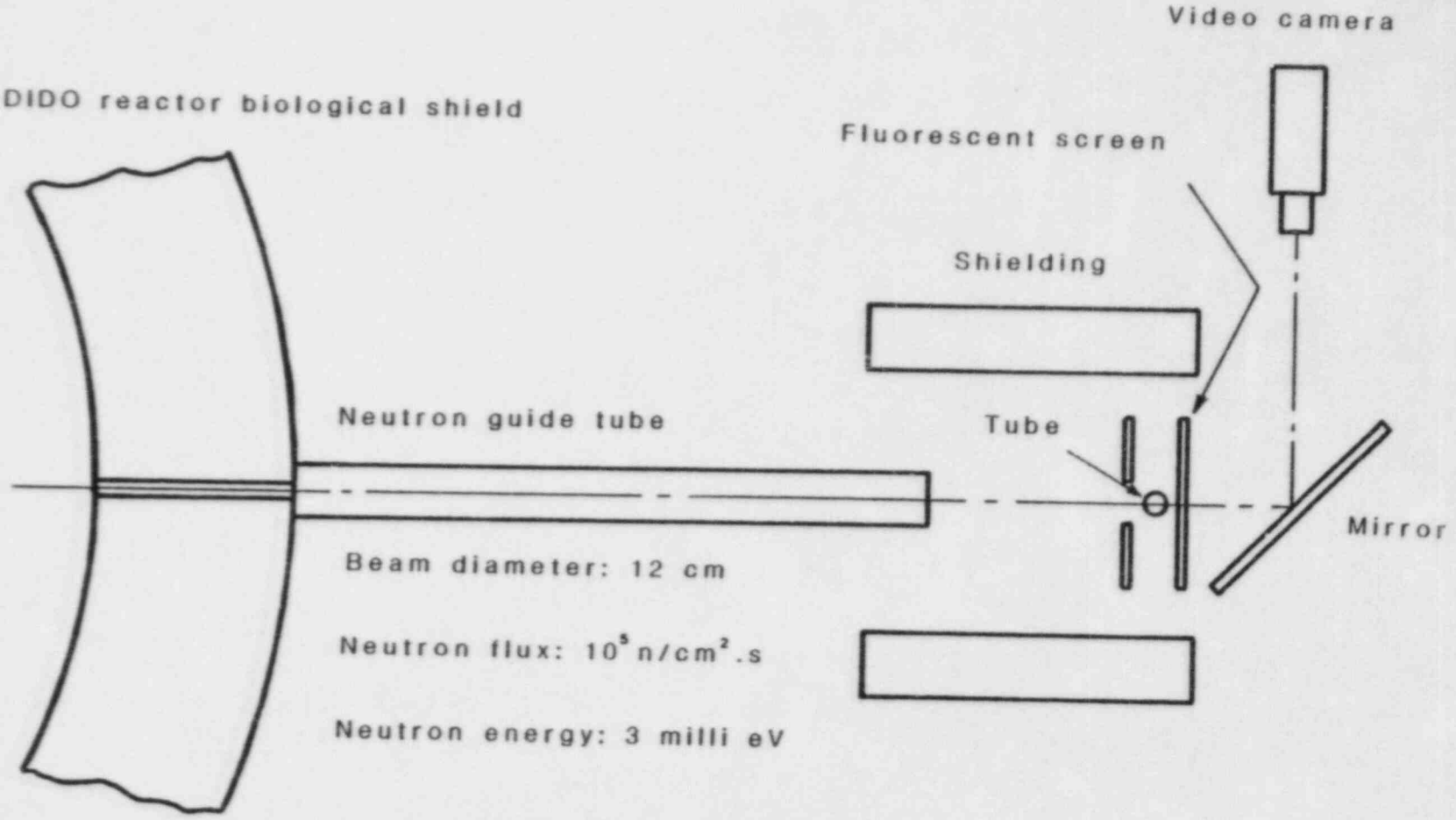

Fig 7 Neutron radiography arrangement in DIDO reactor

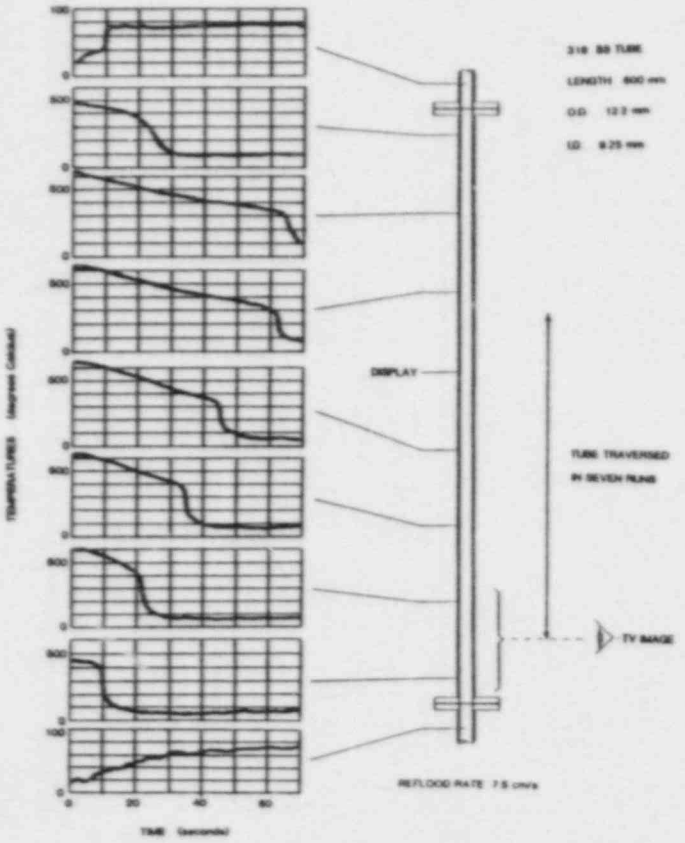

Fig 8 Temperatures vs. time

Fig. 9 Varicose instability at 2.5 cm/s

Fig. 10 Sinuous instability at 2.5 cm/s

Fig. 11 Inverted annular flow at 7.5 cm/s

Fig. 12 Falling film and jet at 7.5 cm/s

INVESTIGATION OF DISPERSED FLOW HEAT TRANSFER USING DIFFERENT COMPUTER CODES AND HEAT TRANSFER CORRELATIONS

I. VOJTEK*

Gesellschaft Fuer Reaktorsicherheit, Garching, FRG

ABSTRACT

As a part of German safety program, transient heat transfer experiments have been performed at the blowdown heat transfer test facility by the Kraftwerk Union company in Karlstein. The purpose of these experiments was to investigate the transient critical heat flux phenomena and the forced convective film boiling heat transfer. The first part of the post experimental analysis has been performed by the Gesellschaft Fuer Reaktorsicherheit using the computer Code BRUDI-VA a modified version of the German homogeneous equilibrium blowdown code BRUCH-D. The purpose of this part of this investigation was the calculation of local thermal hydraulic parameters and the evaluation of different correlations used in the analysis of reactor safety problems for the calculation of maximum critical heat flux (CHF) and post-CHF heat transfer coefficients. Using the results of this analysis a new method for the calculation of the dispersed flow heat transfer components has been developed. The next part of the post-experimental analysis is presently being performed by the author at Los Alamos National Laboratory using the nonequilibrium two-fluid computer code TRAC-PF1/MOD1. Different correlations and models has been applied for the calculation of wall-droplet and wall-vapor heat flux component in the post-CHF region of described experiments. The results of this investigation have shown that different combinations of available correlations can be used with sufficient confidence for the prediction of wall-fluid heat flux in the high pressure wall to dispersed flow heat transfer regime.

---

*Presently working as a resident engineer at Los Alamos National Laboratory Los Alamos, NM.

1. INTRODUCTION

The experimental and analytical investigation of transient critical heat flux and boiling heat transfer is important for the fundamental understanding of forced convection boiling heat transfer which would occur in a nuclear reactor during a loss of coolant accident.

A substantial amount of data concerning steady state critical heat flux (CHF) phenomena and film boiling heat transfer, which were obtained in simple geometries, is available in the literature and has been used by many investigators for the development and evaluation of CHF and film boiling heat transfer correlations.

There has been very little transient CHF and film boiling heat transfer experimental data obtained in complex and large geometries - similar to the actual construction of water cooled nuclear reactor cores.

Blowdown heat transfer experiments were performed with a 25 rod bundle by the Kraftwerk Union AG (KWU) at the KWU heat transfer test facility as a part of the German reactor safety program. The main purpose of the experiments was to generate additional data for the analytical investigation of transient CHF phenomena and film boiling heat transfer and for the evaluation of correlations which are commonly used in the analysis of reactor safety problems associated with loss of coolant accidents.

2. TEST FACILITY DESCRIPTION

The KWU blowdown heat transfer test facility is a nonnuclear experimental apparatus with a test section that contains a 5x5 bundle of electrically heated rods. This facility was designed for a pressure of up to 17 MPa and maximum power of 5 MW. The test section is schematically shown in Fig. 1. It consists of a pressure vessel and inlet and outlet control valve stations. A detailed description of the test facility can be found in /1/.

The heater rod design and geometry is shown in Fig. 2. The stepwise variation of the heater wall thickness resulted in a nonuniform axial power distribution which is similar to a PWR profile and is shown in Figure 2. All 25 rods were uniformly heated which produced a flat radial power profile in the bundle. The following important parameters have been measured during each test:

- Inlet and outlet pressure
- Differential pressure between inlet and outlet
- Inlet and outlet fluid temperature

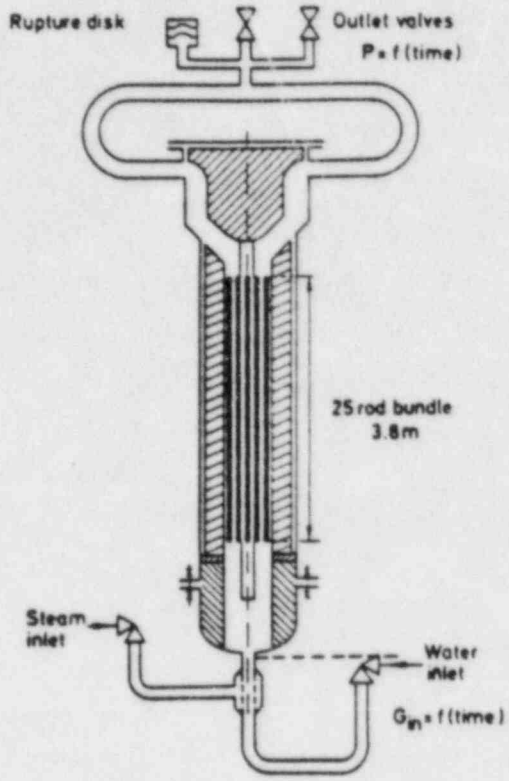

Fig. 1 Schematic of the test section

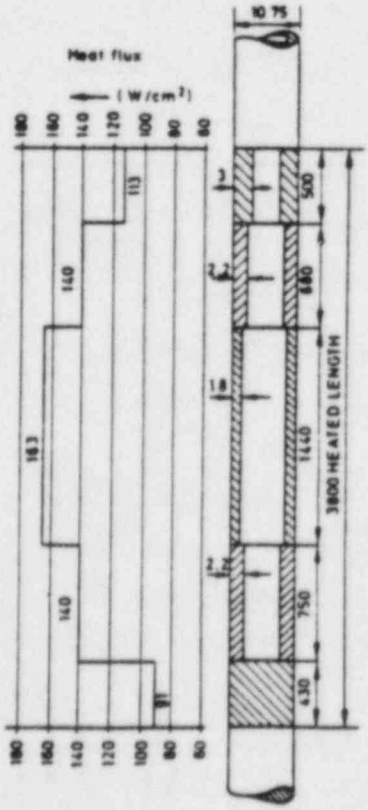

Fig. 2 Heater rod geometry

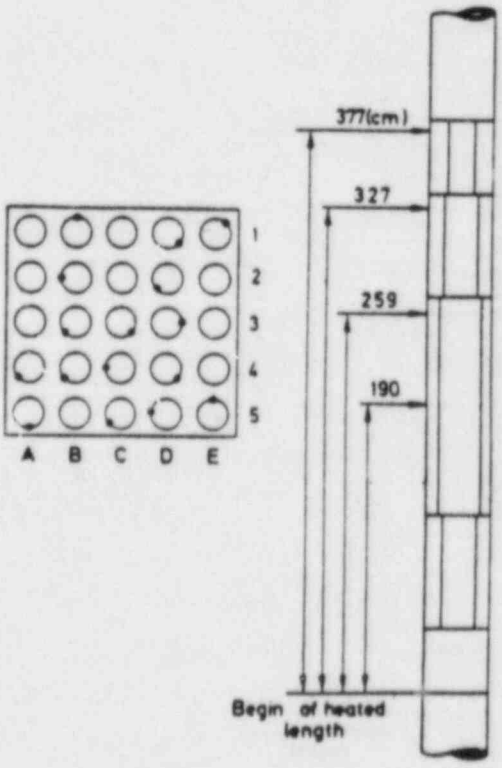

Fig. 3 Location of thermocouples

- Inlet single phase mass flow rates
- Electrical power
- Test-section wall temperature
- 80 heater wall temperatures (Fig. 3)

3. EXPERIMENTAL PROGRAM

The experimental program has been divided into two groups of experiments called "DNB" and "Post DNB" tests.

3.1 DNB-Experiments.

The variation of the test parameters for the specified 11 tests can be seen in Table 1. The typical time histories of pressure and inlet flow are shown in Fig. 4.

Table 1: Variation of test parameters - DNB tests

TEST NUMBER	INITIAL MASS FLOW RATE [KG/M²·S]	REDUCED MASS FLOW IN POST-CHF REGION [KG/M²·S]	INLET ENTHALPY [KJ/KG]
DNB-1	3300.	1419.	1284.
DNB-2	3300.	957.	1284.
DNB-3	3300.	660.	1284.
DNB-4	3300.	1450.	1233.
DNB-5	3300.	990.	1233.
DNB-6	3300.	660.	1233.
DNB-7	3828.	1378.	1284.
DNB-8	3828.	957.	1284.
DNB-9	3828.	689.	1284.
DNB-10	3300.	660.	1233.
DNB-11	3300.	660.	1233.

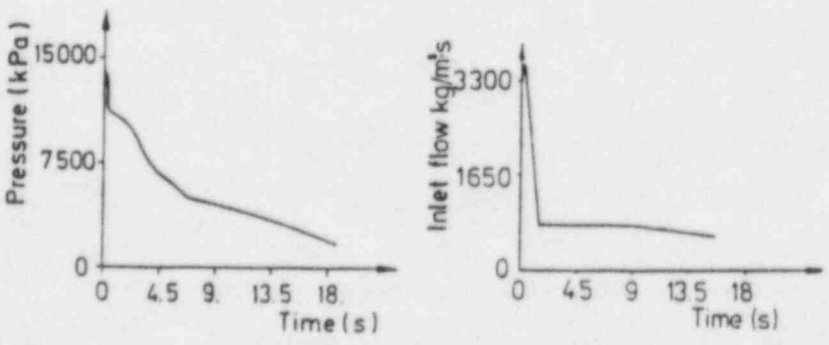

Fig. 4 Typical pressure and inlet flow time histories

3.2 Post-DNB Experiments.

The specified test parameters for these 9 tests can be seen in Table 2. The typical pressure and power histories are shown in Fig. 5. A detailed description of the experimental results can be found in /2/.

Table 2: Variation of test parameters - Post-DNB tests

TEST NUMBER	INLET ENTHALPY	INLET MASS FLOW RATE	MAXIMAL HEAT FLUX	TIME OF DEPRESSURIZATION
	[KJ/KG]	[KG/M² S]	[W/CM²]	[S]
PD 1	1247.	1254.	162.	21.
PD 3	1086.	248.	113.	23.7
PD 5	1238.	858.	121.	29.
PD 7	1086.	248.	113.	29.
PD 8	1519.	157.	74.	35.
PD 9	1519.	165.	78.	29.
PD 10	1466.	91.	74.	32.5
PD 11	1295.	319.	112.	51.
PD 14	1461.	91.	74.	150.

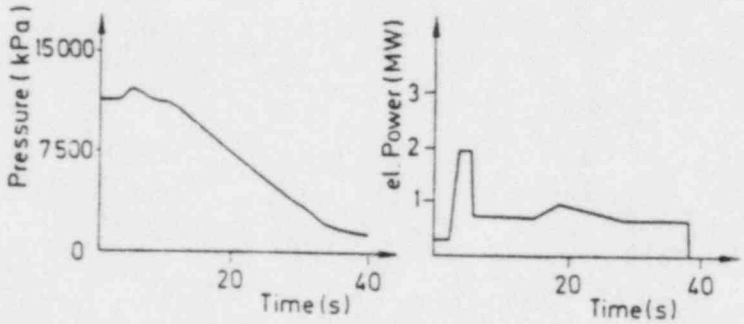

Fig. 5 Typical pressure and power time histories

4. CALCULATIONS OF HEAT TRANSFER COEFFICIENTS

The calculations of film boiling heat transfer coefficients was performed by KWU using computer code "NOTK-25" /3/. This computer code is based on the "inverse" solution of the transient heat conduction problem. The heat transfer coefficients was defined and calculated as:

$$h_M = \frac{q_M}{T_W - T_{SAT}} \qquad (1)$$

The detailed description of the calculation procedure and results can be found in /3/.

5. POST EXPERIMENTAL ANALYSIS USING COMPUTER CODE BRUDI-VA.

The first and main part of the post-experimental analysis has been performed by the Gesellschaft fur Reaktorsicherheit using computer code BRUDI-VA a modified version of the German blowdown code, BRUCH-D /4,5/. The computer code BRUDI-VA /7/ is based on the homogeneous equilibrium model of the two-phase fluid flow and the lumped parameter technique was used for the nodal representation of the test section. The basic set of the differential equations of BRUDI-VA is shown in Table 3.

Table 3. Basic differential equations of computer code BRUDI-VA.

$$\dot{p} = \frac{-\dot{M}\cdot(h + \frac{v}{\varepsilon_h}) - (G\cdot h)_A + (G\cdot h)_E + Q}{M(\frac{\varepsilon_p}{\varepsilon_h} + v)}$$

$$\dot{h} = \frac{v\cdot\dot{M} - \varepsilon_p\cdot\dot{p}\cdot M}{M\cdot\varepsilon_h}$$

$$\varepsilon_p = (\frac{\partial v}{\partial p})_h \qquad \varepsilon_h = (\frac{\partial v}{\partial h})_p$$

$$\dot{G} = \frac{1}{\int_i^{i+1}\cdot\frac{dz}{F}}\cdot\left[p_i - p_{i+1} - g\cdot\varsigma(H_{i+1} - H_i) - K\cdot G\cdot/G/\right]$$

The heater-wall-temperatures and the heat generation in the wall of electrically heated rods have been calculated using one-dimensional transient heat conduction model with internal heat sources.

5.1 Evaluation of correlations for calculation of maximum critical heat flux.

Since the reasonable prediction of the beginning of the transition boiling is one of the most important boundary condition by the calculation of wall-temperatures in post-CHF heat transfer region a different correlation for the calculation of maximum CHF have been evaluated in the study. The time to the beginning of transition boiling heat transfer regime for selected DNB tests is given in Table 4. The calculations showed that the average local equilibrium quality at the transition from nucleate to film boiling varied between 0.08 to 0.14 - dependent on the local surface heat flux. This type of nucleate to film boiling transition is usually related to the departure of nucleate boiling (DNB) and this name will be used in this study. The following correlations have been applied for the calculation of maximum critical heat flux:

- modified Zuber correlation /7/
- W3-Tong correlation /8/
- Transient Hench-Levy correlation /9/
- Israel Casterline Matzner correlation /9/
- Biasi correlation /15/.

The calculated times to CHF, using these correlations as obtained by the post experimental analysis of different DNB tests, are shown in Table 4.

Table 4: Time to DNB - Corr. Comparison

TEST	TE Elev. (cm)	Time to DNB (s)					
		Data	Mod. Zuber	W-3	Sli-fer	Israel	Biasi
DNB-1	135	No DNB	2.6	-	-	-	-
	190	No DNB	0.7	0.65	-	-	-
	259	0.7	0.6	0.45	-	-	0.9
	327	0.4	0.5	0.2	1.1	1.1	0.6
	377	0.7	0.5	0.1	1.15	1.15	0.6
DNB-3	135	No DNB	0.8	0.7	1.5	1.5	1.4
	190	No DNB	0.65	0.5	1.2	1.2	1.0
	259	0.45	0.5	0.35	1.0	1.0	0.7
	327	0.2	0.4	0.15	0.85	0.85	0.46
	377	0.5	0.4	0.1	0.8	0.8	0.5
DNB-9	135	No DNB	0.9	0.85	-	-	-
	190	No DNB	0.75	0.65	1.3	1.3	0.8
	259	0.7	0.65	0.5	1.1	1.1	0.5
	327	0.5	0.55	0.4	1.0	1.0	0.4
	377	0.6	0.6	0.45	1.0	1.0	0.4

It can be seen that only modified Zuber correlation predicted time to CHF realistically at the upper elevation, but it predicted DNB also in the lower

part of the test section where no DNB occurred during the tests. The W3-correlation did not predict DNB when it was used in the given validity range. When using it outside of the validity range, it predicted DNB too early and also predicted it in the lower part of the test section where it did not occur. The critical heat flux, calculated using the other two correlations, was too high and they predicted the transition from nucleate to film boiling too late and at higher qualities.

5.2 Evaluation of Post-CHF heat transfer correlation.

The heat transfer coefficients have been determined over the following ranges of test parameters:

- Pressure	2	to 12 MPa
- Mass Flux	100	to 1400 kg/m^2s
- Quality	0.3	to 1.0
- Rod surface temperature	300	to 700 ^oC

The analysis of experimental results showed that the mass flux, quality, and temperature difference between wall and fluid significally influenced the values of heat transfer coefficients in the film boiling heat transfer regime.

The following correlations have been used for the calculation of heat transfer coefficients in the film boiling regime.

Equilibrium correlations:

- Modified Dougall-Rohsenow /8/
- Groeneveld 5.7 /10/
- Condie-Bengston IV /11/

Nonequilibrium correlations:

- Groeneveld-Delorme /12/
- Chen, Ozkaynak, Sundaram /13/

The wall-vapor heat transfer coefficients predicted with the nonequilibrium correlations have been compared to those predicted by the vapor Dittus-Boelter correlation.

The time histories of wall temperatures and heat transfer coefficients which were obtained using equilibrium correlations, are shown in Figs. 6 through 9. The calculated wall temperatures as obtained from the analysis of test DNB-3 are compared with experimentally determined values. Heat transfer coefficients computed using correlations are compared with those calculated directly from the measurements.

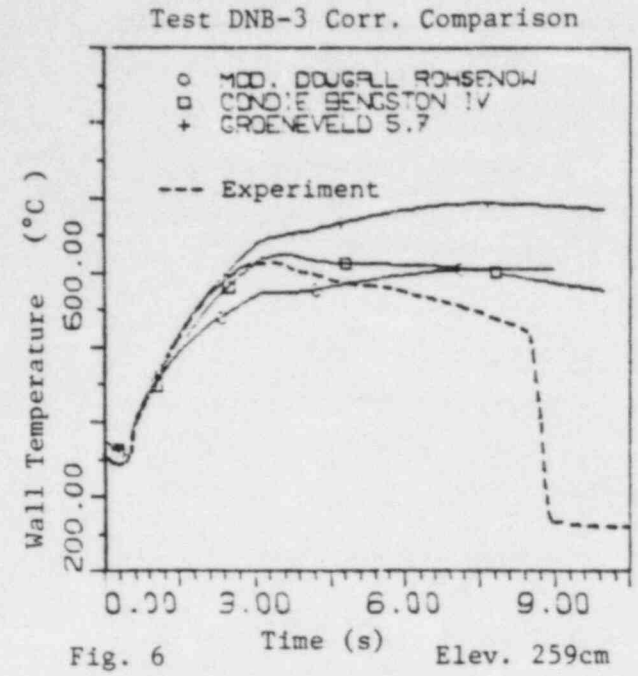

Fig. 6 Elev. 259cm

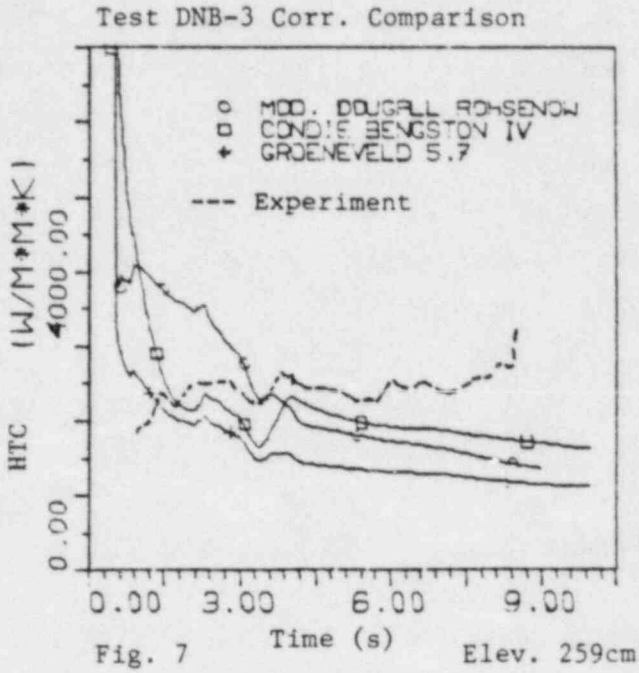

Fig. 7 Elev. 259cm

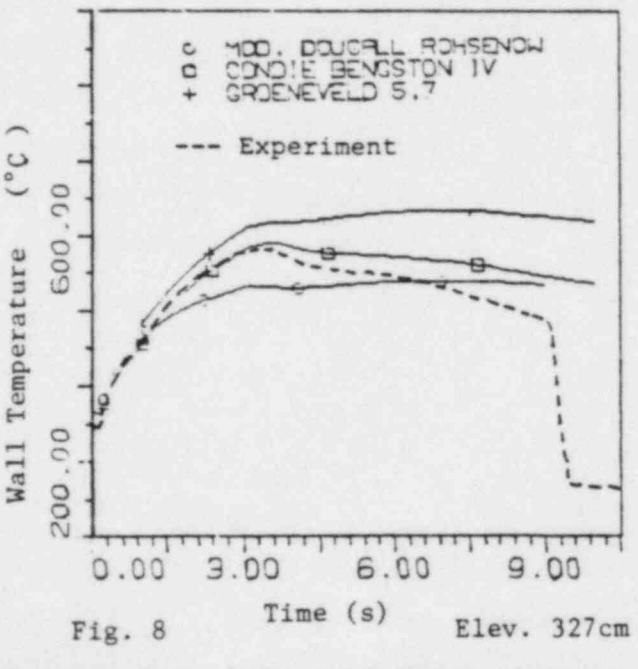

Fig. 8 Elev. 327cm

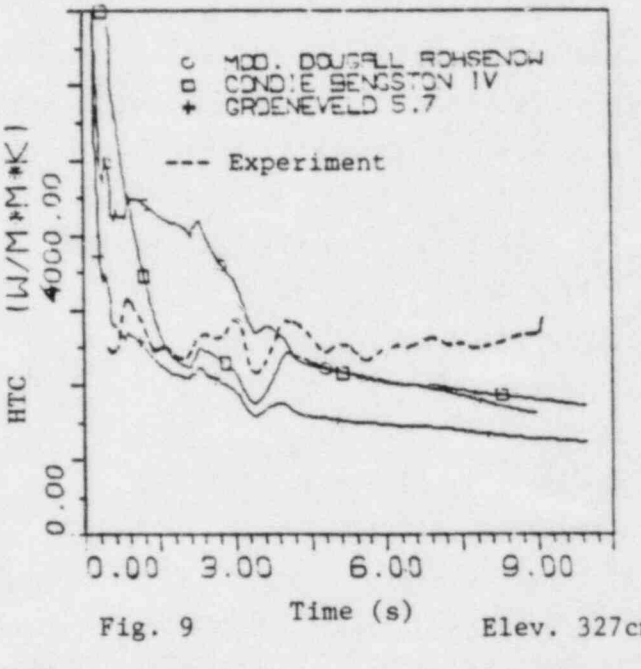

Fig. 9 Elev. 327cm

The results of the evaluation of nonequilibrium correlations are shown in Figs. 10 through 12. The time histories of heat flux were used for this comparison rather then effective values of heat transfer coefficients. Additional comparison of calculated vapor temperatures can be also found in these figures.

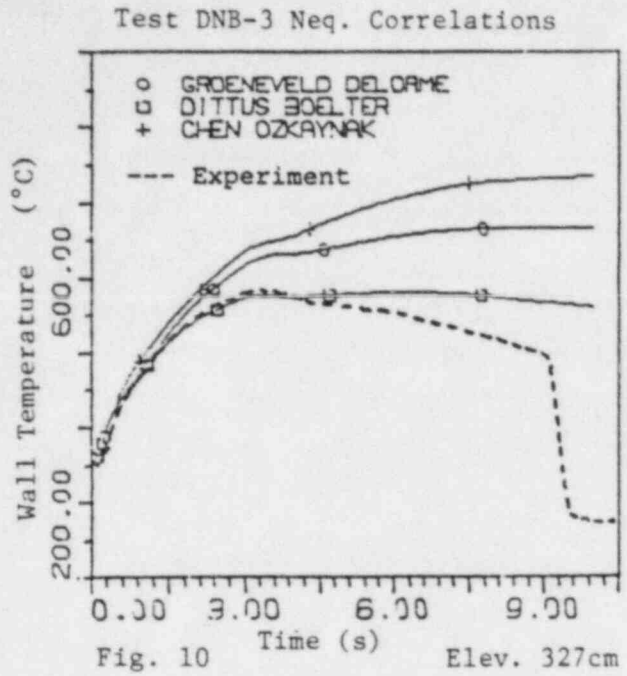

Fig. 10 Elev. 327cm

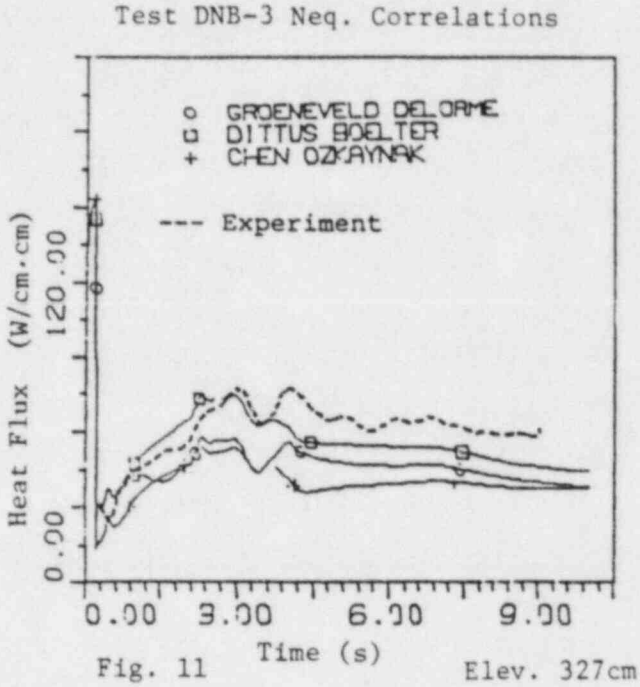

Fig. 11 Elev. 327cm

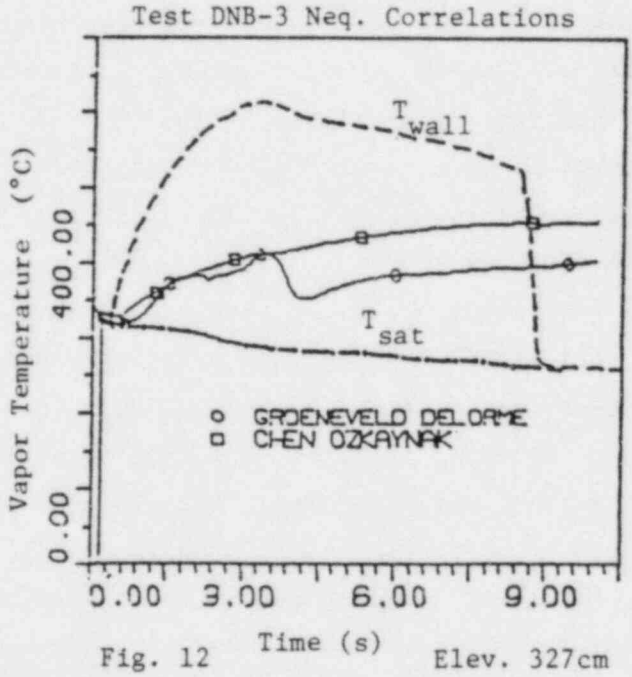

Fig. 12 Elev. 327cm

These results were found to be representative for all DNB experiments and also for Post-DNB experiments with higher mass flow rates - i.e., for experiments where the equilibrium quality varied in the range between 0.3 to 1.0. A comprehensive overview of results obtained by the analysis of all experiments using equilibrium correlations can be found in /6/.

The comparison of calculated and measured results has shown that the modified Dougall-Rohsenow correlation overpredicts the values of heat transfer coefficient in the early post-CHF region but underpredicts the heat transfer coefficients in the later part of the transient. The Groeneveld 5.7 correlation seems to underpredict the value of heat transfer coefficients in the entire range of test parameters. The Condie-Bengston IV correlation follows the data trend but still underpredicts the values of heat transfer coefficients. The comparison of measured data to the results of calculation where the vapor Dittus-Boelter correlation was used pointed out that the reduction of wall-vapor heat flux, because of reduction of effective temperature difference ($T_{WALL} - T_{VAPOR}$, where $T_{VAPOR} > T_{SAT}$), leads to larger discrepancy between measured and calculated values. This trend could be observed by comparison of measured and calculated wall temperatures when the nonequilibrium correlations were used for the calculation of wall-coolant heat flux.

5.3 Detailed Investigation of Dispersed Flow Heat Transfer Process.

The results of evaluation of different heat transfer correlations have shown that none of the applied correlations predicted heat transfer coefficients with sufficient accuracy in the entire post-CHF region of these experiments. It was found that the largest disagreement between measurements and correlaltions predicted results exists in the high-flow, intermediate- quality region in the later part of tests. Therefore, the main emphasis of the further analysis with the computer code BRUDI-VA has been focused on the investigation of the individual dispersed flow heat transfer processes i.e., wall-vapor, wall-droplet and vapor-droplets heat transfer. The results of this investigation are described in detail in /16/ and the representative results can be found in /17/. The results of the investigation of individual heat transfer processes indicated the need for nonequilibrium and nonhomogeneous description of the dispersed flow, which was shown to be important for the appropriate modeling of interfacial and direct wall-droplet heat transfer. Therefore, the next part of the analysis which is now in progress is performed using the nonequilibrium two-fluid code -TRAC-PF1/MOD1.

6. POST EXPERIMENTAL ANALYSIS USING COMPUTER CODE TRAC-PF1/MOD1.

The main purpose of this part of analysis which is presently being performed by the author at Los Alamos National Laboratory is the comparison of results calculated with homogeneous equilibrium and two fluid nonequilibrium computer codes and the assessement of the TRAC-PF1/MOD1 heat transfer model.

6.1 Brief description of TRAC-PF1/MOD1.

The Los Alamos National Laboratory in developing a best-estimate computer code for the PWR accidents analysis which is known as the Transient Reactor Analysis Code - TRAC. The TRAC code is based on the full two-fluid nonequilibrium thermal and fluid dynamic model with a flow-regime dependent constitutive equations treatment and the rewet capability for both bottom flood and falling film quench fronts. The TRAC-PF1/MOD1 incorporates detailed heat transfer analysis of the vessel and the loop components. Included is also two-dimensional (r,z) treatment of fuel rod heat conduction. The heat transfer from the fuel rods and other system structures is calculated using flow-regime dependent selection of correlations for the calculation of heat transfer coefficients. Because of the purpose of this investigation, only the TRAC-PF1/MOD1 calculation of heat transfer coefficients in transition and film boiling regime will be described in this paper. The detailed description of all TRAC-PF1/MOD1 heat transfer regimes can be found in /18/. The change from nucleate to the transition boiling occurs in the TRAC- calculation if the wall temperature exceeds the so called CHF-temperature. The CHF-temperature (T_{CHF} is calculated using a Newton-Raphson iteration to determine the intersection of the heat flux found by using the nucleate boiling heat transfer coefficient and the value of critical heat flux which is calculated by the Biasi correlation /15/. The total wall-to-fluid heat flux in the transition boiling regime is obtained from a quadratic interpolation between the Biasi CHF and the minimum stable film-boiling heat flux which is calculated using the value of minimum stable film boiling temperature (T_{MIN}) from the homogeneous nucleation temperature correlation. The wall-to-fluid heat flux in this heat transfer regime is then given by:

$$q_{TRANS} = \delta \cdot q_{CHF} + (1 - \delta) \cdot q_{MIN} \qquad (2)$$

where

$$\delta = \left(\frac{T_W - T_{MIN}}{T_{CHF} - T_{MIN}}\right)^2 \qquad (3)$$

In the film boiling heat transfer regime ($T_W > T_{MIN}$) the wall-vapor and wall-liquid heat transfer are treated separately using the following calculational scheme. The wall-liquid heat transfer coefficient is assumed to be the sum of three components:

$$h_{\ell} = (h_{RAD} + h_{PFB}) \cdot \left(\frac{T_W - T_{SAT}}{T_W - T_{\ell}}\right) + h_{DF} \qquad (4)$$

where h_{RAD} is a radiative HTC, h_{PFB} is a pool boiling HTC, and h_{DF} is a dispersed flow HTC. The pool boiling h_{PFB} is decreasing from its actual value to zero in the void fraction range between $0.5<\alpha<.75$ and in the same void fraction range the dispersed flow h_{DF} is increased from zero to its actual value. If the value of actual h_{PFB} is smaller then h_{DF} than h_{PFB} is taken for the calculation of wall-liquid HTC. The wall-vapor heat transfer coefficient in this heat transfer regime is calculated using the Dougall-Rohsenow correlation and the turbulent natural convection correlation. The greater value predicted with these two correlations is taken for the calculation of wall-vapor heat flux:

$$q_{WV} = \text{MAX}\,(h_{DR}, h_{NC}) \cdot (T_W - T_V) \qquad (5)$$

and

$$q_{W\ell} = h_{\ell} \cdot (T_W - T_{\ell}) \qquad (6)$$

6.2 TRAC-PF1/MOD1 model of the test facility and important input for the analysis of test DNB-3.

The TRAC-PF1 model of the test section of the KWU heat transfer test facility is shown in Fig. 13. Five one-dimensional-core components are representing the five different axial power regions of the test section. The measured single phase mass flow at the test section inlet has been prescribed as a input time function in the fill component which is connected to the inlet of the first core component. The measured pressure at the test section outlet has also been input as a second boundary parameter in the break component. The power generation for each power region has been calculated separately using the temperature-dependent resistivity and measured electrical current and was also input as a time function for each of the core components.

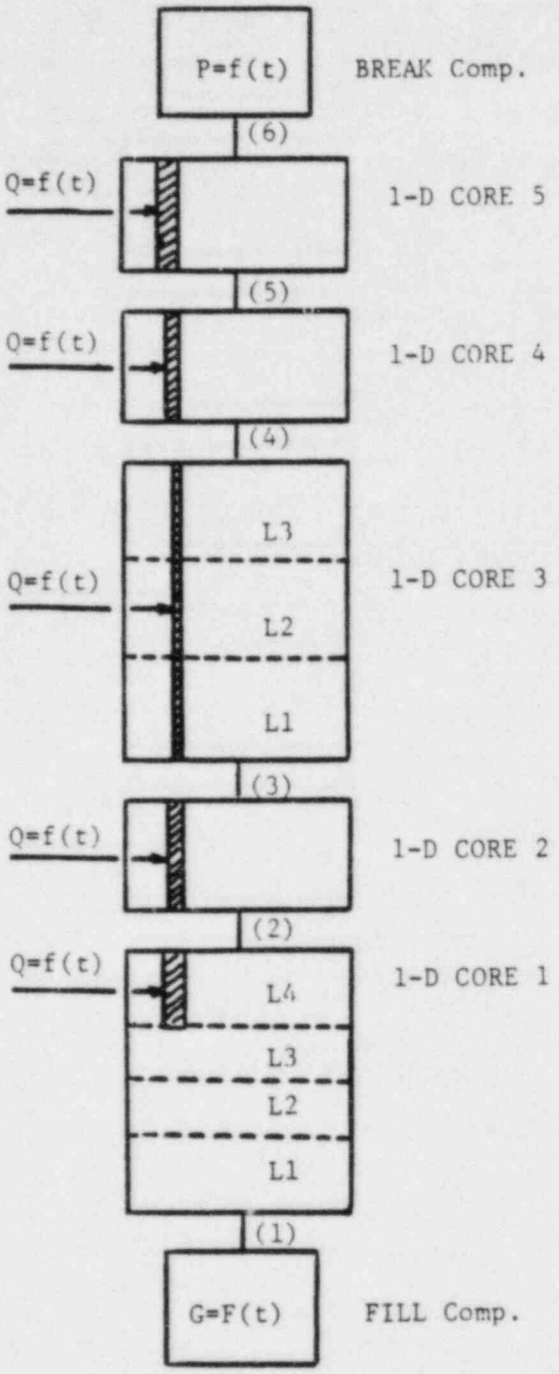

Fig. 13 TRAC-PF1/MOD1 Model of the test section

6.3 Calculation of the test DNB-3 using different correlations for the calculation of POST-CHF heat transfer coefficients.

The first computer run has been performed using the original set of TRAC-PF1/MOD1 post-CHF heat transfer correlations i.e.,:

Wall-vapor: Dougall-Rohsenow

$$h_{FC} = 0.023 \cdot \frac{\lambda v}{D_{eq}} \cdot \left\{\frac{\varrho[\alpha \cdot U_v + (1-\alpha)\, U_\ell\ ]}{\eta_v} \cdot D_{eq}\right\}^{0.8} \cdot Pr_v^{\ 0.4} \qquad (7)$$

Wall-liquid: Mod. Bromley

$$h_{PFB} = 0.61 \cdot \left[\frac{\lambda_{vf}^{\ 3} \cdot g_c \cdot \rho_v \cdot (\rho_\ell - \rho_v) \cdot \Delta\alpha^*}{\eta_{vf} \cdot (T_w - T_{SAT}) \cdot a}\right]^{0.25} \qquad (8)$$

$$a = \left(\frac{\sigma}{g(\rho_\ell - \rho_u)}\right)^{0.5}$$

Radiation

$$h_{RAD} = (1 - \alpha) \cdot \sigma \cdot \varepsilon \cdot \left(\frac{T_w^{\ 4} - T_{SAT}^{\ 4}}{T_w - T_{SAT}}\right) \qquad (9)$$

Vapor-droplets: Lee-Riley

$$h_{vd} = \frac{\lambda_v}{d_D} \cdot \left[2 + 0.74 \cdot Re_D^{\ 1/2} \cdot Pr^{1/3}\right] \qquad (10)$$

$$R_{eD} = \frac{(U_v - U_\ell) \cdot \rho_v \cdot d_D}{\eta_v}$$

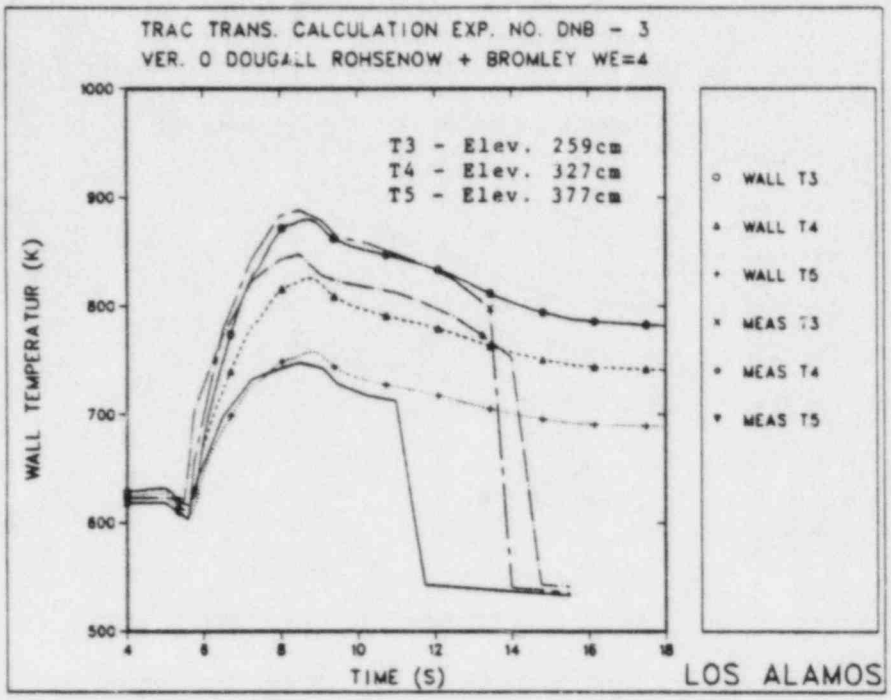

Fig. 14 Comparison of calculated and measured wall temperatures

The results of this calculation are shown in Figs. 14 through 16. The comparison of calculated and measured wall temperatures shows a good agreement. The time to CHF has been predicted well at the elevations 259 cm and 377 cm in the bundle. At the elevation 327 cm, where the DNB occurred 0.2 s after the beginning of the experiment, TRAC-PF1/MOD1 predicted it with a 0.45 s delay. This late change in the heat transfer regime resulted in too low wall temperature prediction at this particular elevation. Since there is no possibility in the present version of TRAC to prescribe the time to CHF as an input value, this partial disagreement will be observed throughout this investigation.

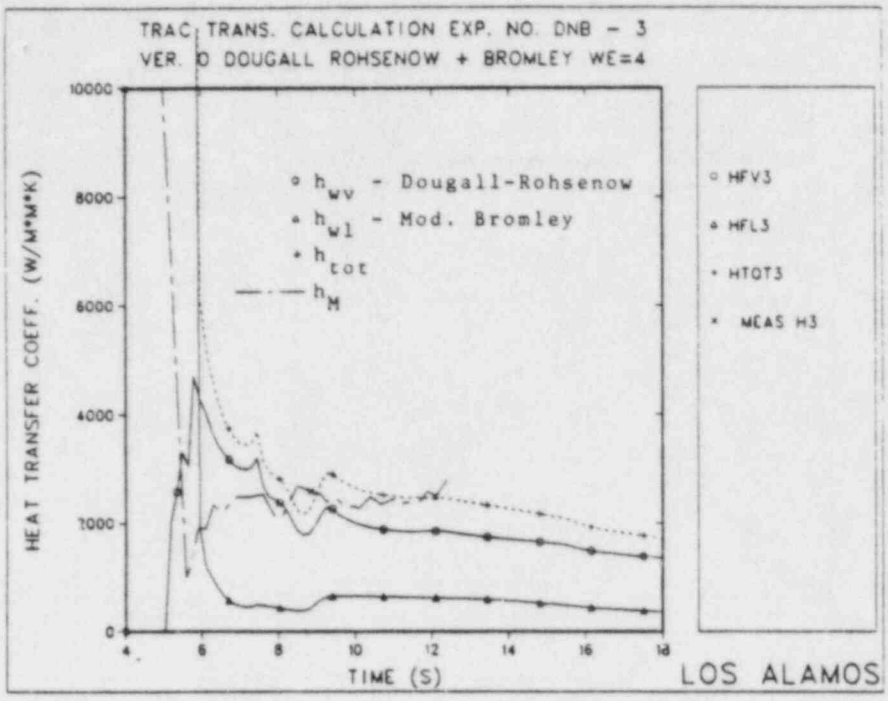

Fig. 15 Comparison of experimental and calculated HTCs (Elev. 259 cm)

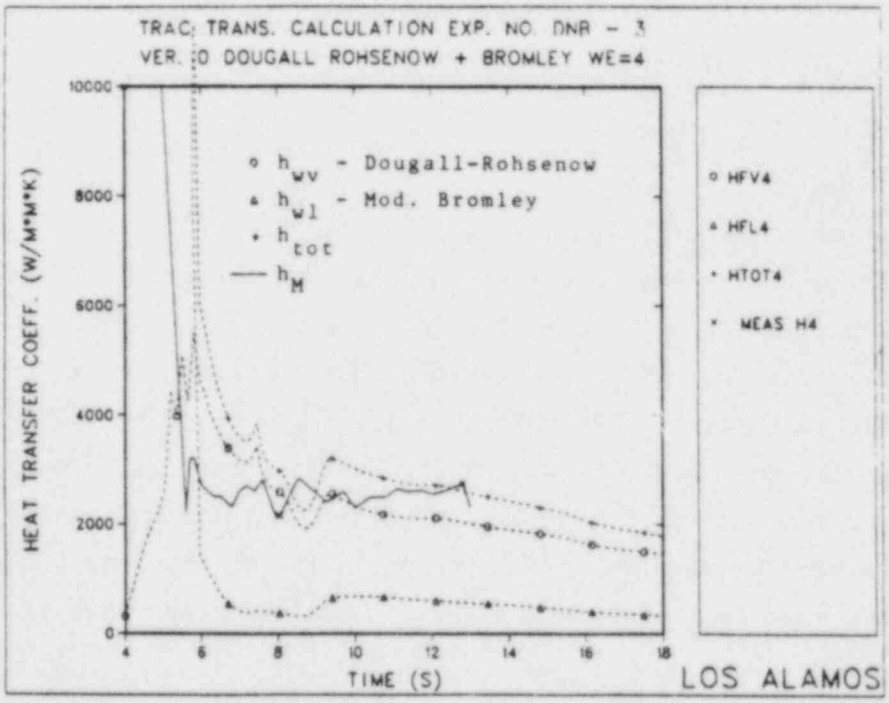

Fig. 16 Comparison of experimental and calculated HTCs (Elev. 327 cm)

Although the agreement of this calculation with the data is good it is questionable if the Dougall-Rohsenow correlation can be used for the calculation of the pure wall-vapor forced convection heat transfer coefficients. On the other hand, in the first part of this study, the pool film boiling treatment of the wall-droplet dispersed flow heat transfer component was shown to underpredict the wall-droplet heat flux. Therefore, for the next calculation, the Dougall- Rohsenow correlation has been replaced with Dittus-Boelter correlation and the Forslund-Rohsenow correlation was applied for the prediction of the wall-droplet heat flux component in the high void region ($0.8 \leq \alpha \leq 0.99$) in the post CHF part of the test.

Dittus-Boelter correlation.

$$h_{vc} = 0.023 \cdot \frac{\lambda_{vf}}{D_{eq}} \cdot Re_v^{0.8} \cdot Pr_v^{0.4} \qquad (11)$$

Forslund-Rohsenow correlation

$$h_{DF} = K_1 \cdot 1.276 \cdot (1-\alpha)^{2/3} \cdot BRAC^{1/4} \cdot \frac{T_w - T_{SAT}}{T_w - T_\ell} \qquad (12)$$

$$BRAC = \frac{\lambda_{vf}^3 \cdot g_c \cdot \rho_\ell \cdot \rho_v \cdot \Delta h^*}{(T_w - T_{SAT}) \cdot \eta_{vf} \cdot d_D}$$

$K_1 = 1.5$ for water

The results of this calculation are shown in Figs. 17 through 19. The comparison of calculated and measured wall temperatures shows again good agreement. The comparison of the heat transfer coefficients, vapor temperatures and velocities from these two calculations shows that the splitting of total wall-fluid heat flux (Dougall-Rohsenow q_{wv} > Dittus-Boelter q_{wv} and Bromley $q_{w\ell}$ < Forslund-Rohsenow $q_{w\ell}$) has no significant influence on the vapor superheat and vapor velocities (Figs. 20 through 23).

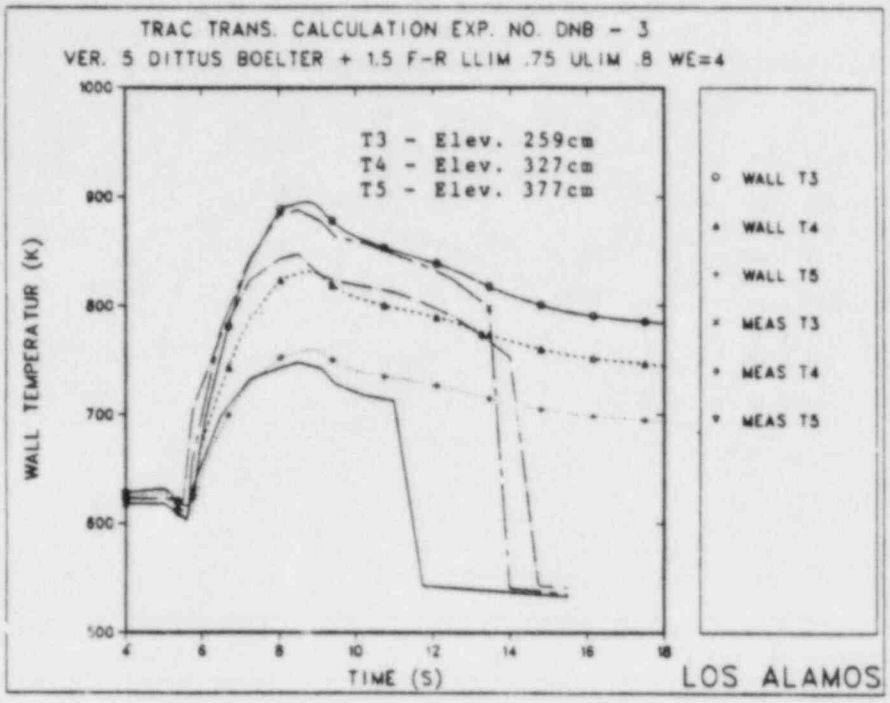

Fig. 17 Comparison of calculated and measured wall temperatures

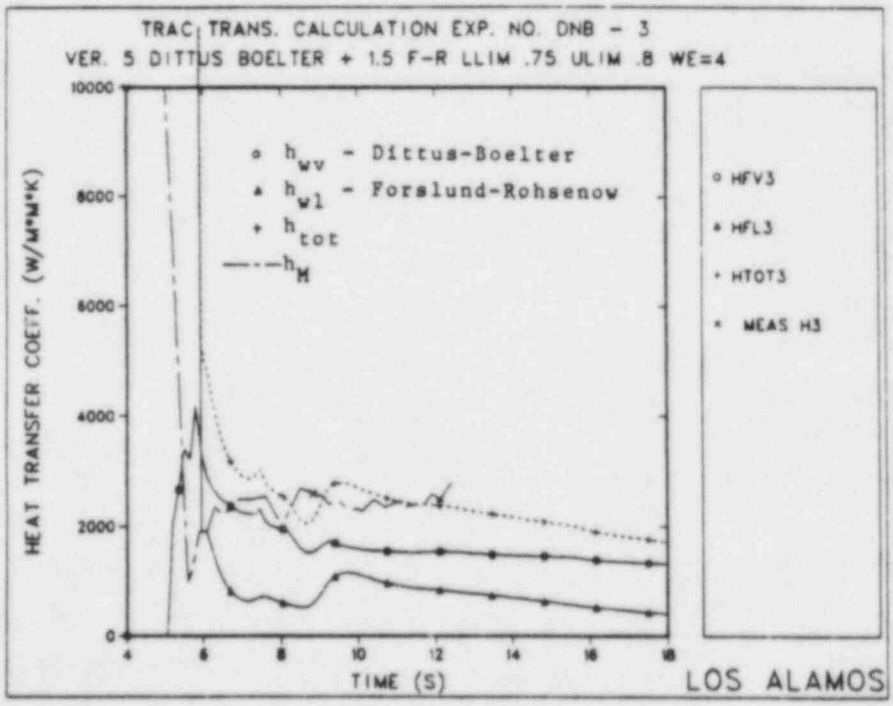

Fig. 18 Comparison of calculated and experimental HTCs (Elev. 259 cm)

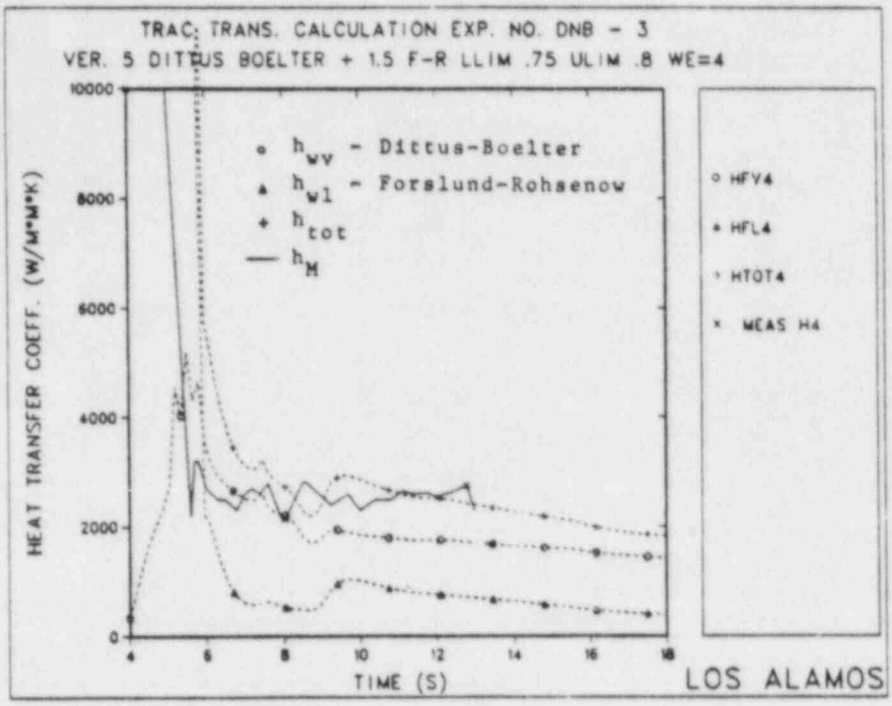

Fig. 19 Comparison of calculated and experimental HTCs (Elev. 327 cm)

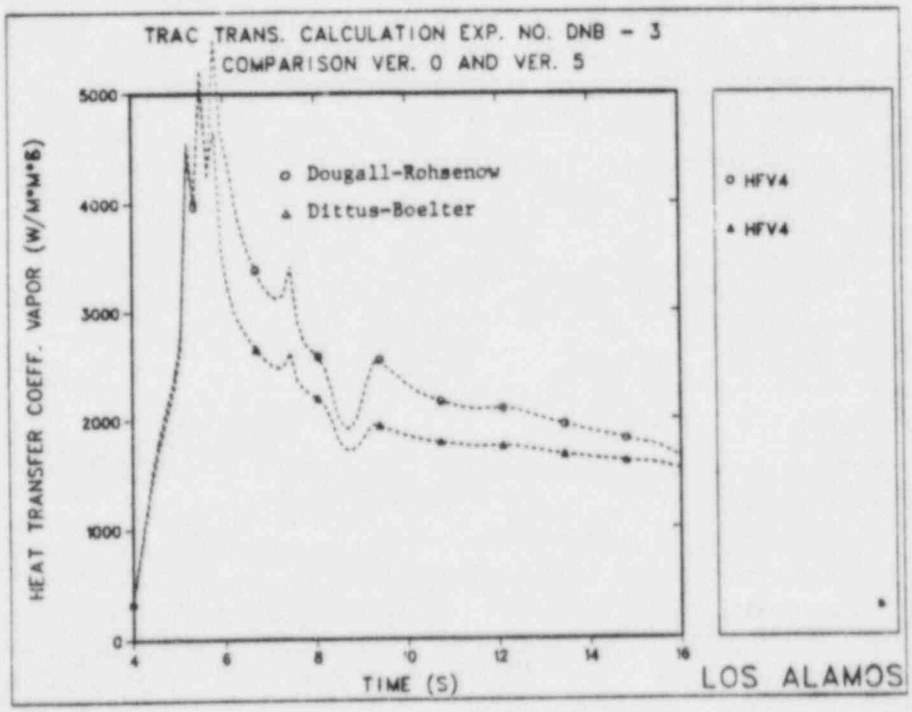

Fig. 20 Comparison of calculated wall-vapor HTCs

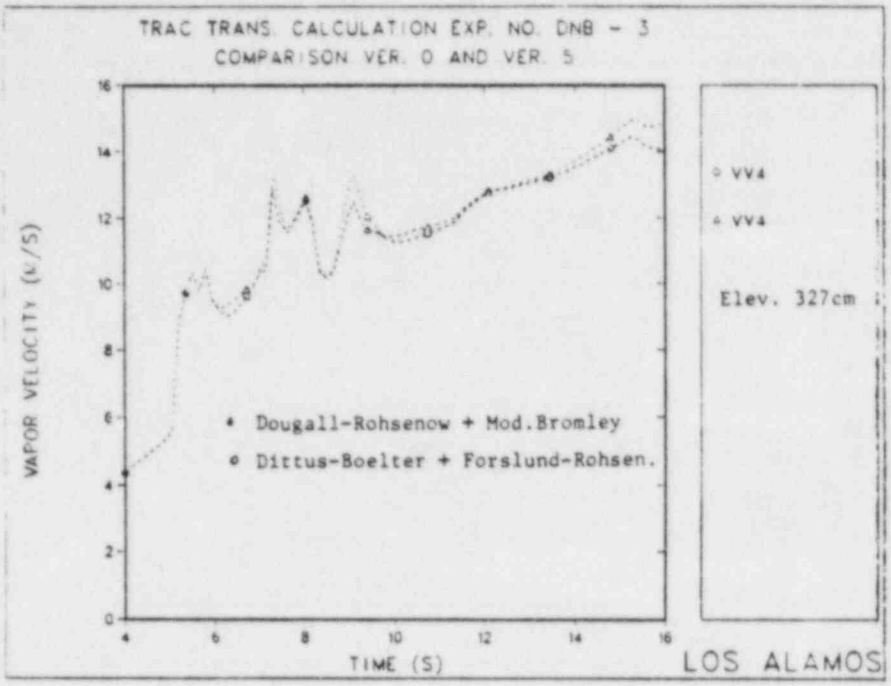

Fig. 21 Comparison of calculated vapor velocities

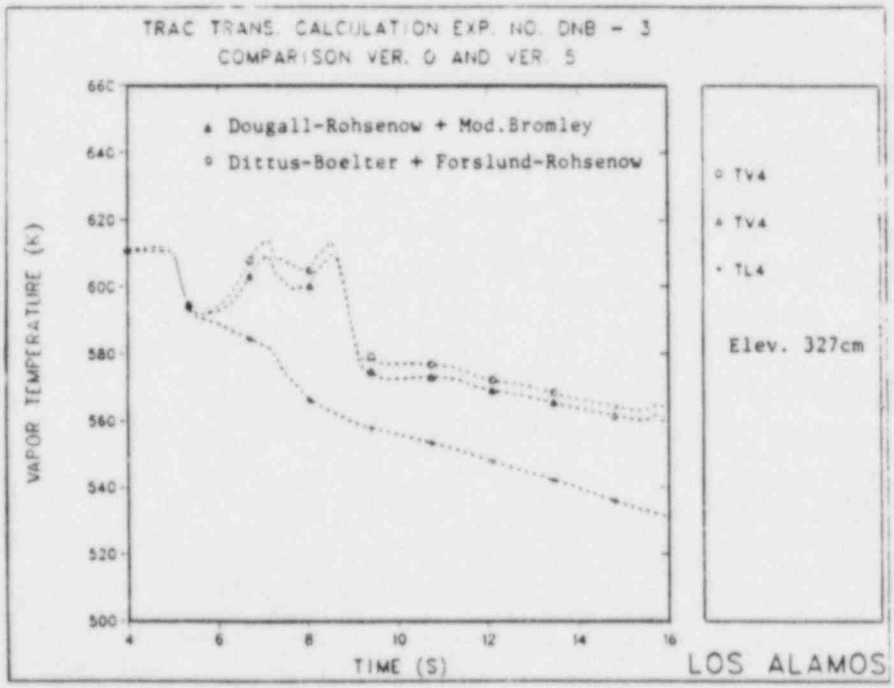

Fig. 22 Comparison of calculated vapor temperatures

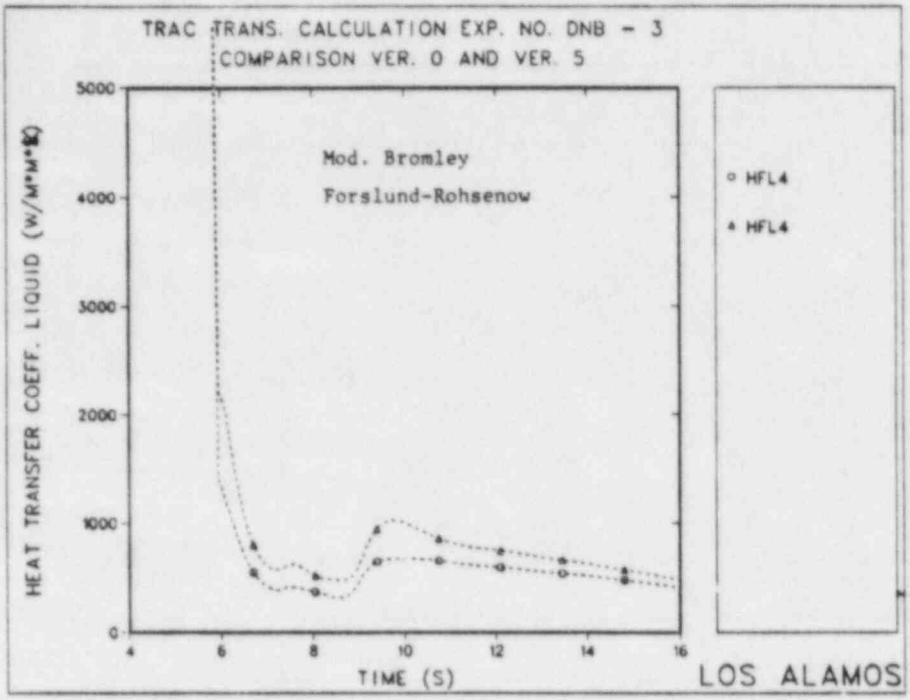

Fig. 23 Comparison of calculated wall-liquid HTCs

6.4 Influence of critical Weber number.

Since there is not much agreement about the appropriate value of critical Weber number (values between 0.1 to 13 can be found in the literature), three computer runs were performed to investigate the influence of We_{CRI} on the calculated results. The value of the We_{CRI} = 1, 4 and 7.5 was used in these calculations. Also, the limits of droplet diameter $10^{-4}<d_D<3.10^{-3}$ which are presently used in TRAC-PF1/MOD1 were changed to $10^{-5}<d_D<10^{-2}$ for these calculations. The calculated time histories of wall and vapor temperatures, heat transfer coefficients and void fractions are shown in Figs. 24 through 29. The comparison of calculated and measured wall temperatures shows that the presently used value of We_{CRI} = 4 gives the best results when it is used together with other correlations and correlation constants.

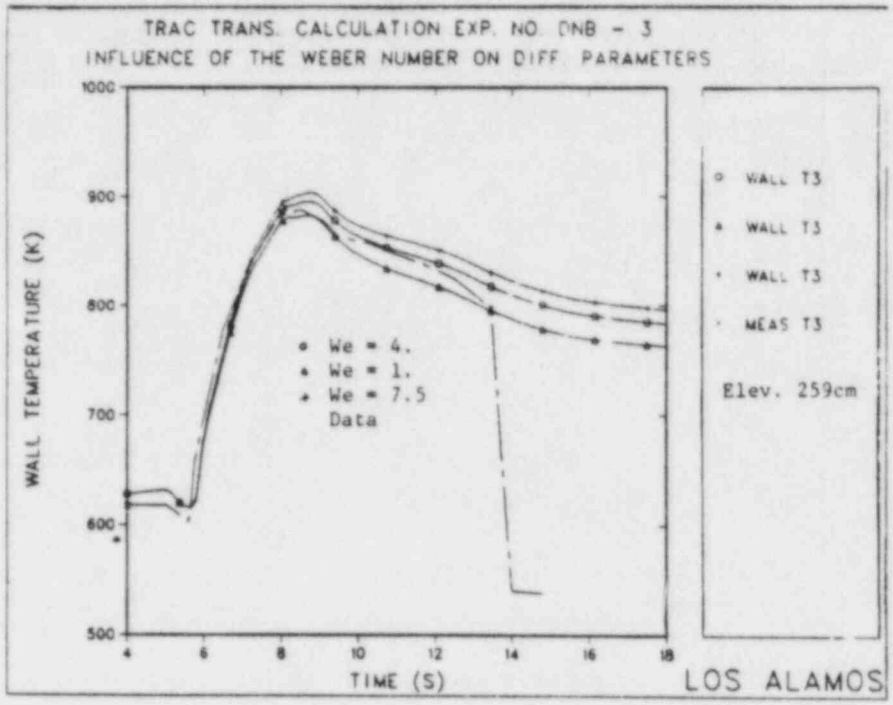

Fig. 24 Influence of Weber number on calculated wall temperatures

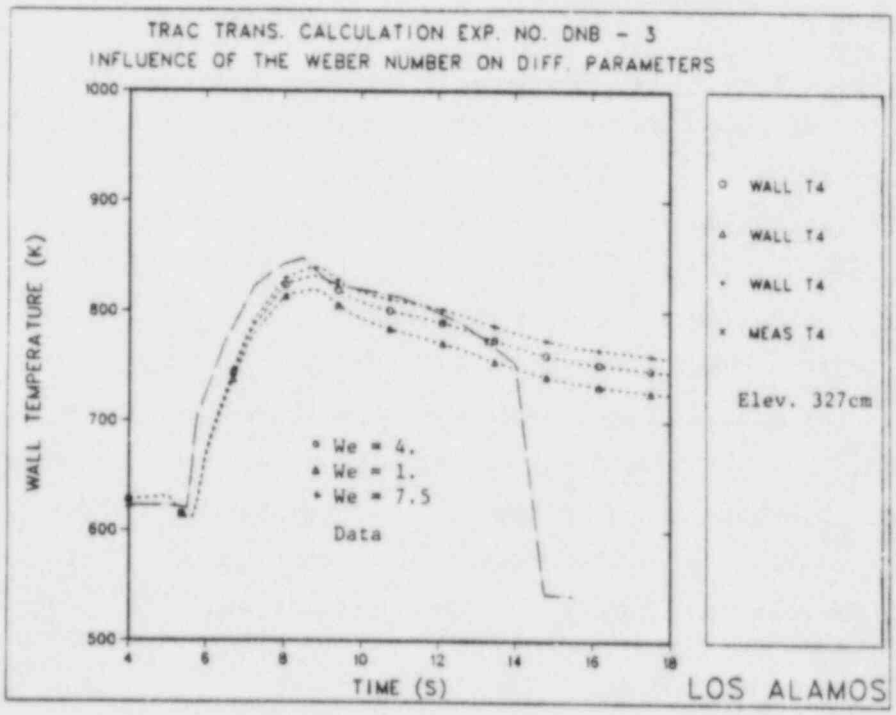

Fig. 25 Influence of Weber number on calculated wall temperatures

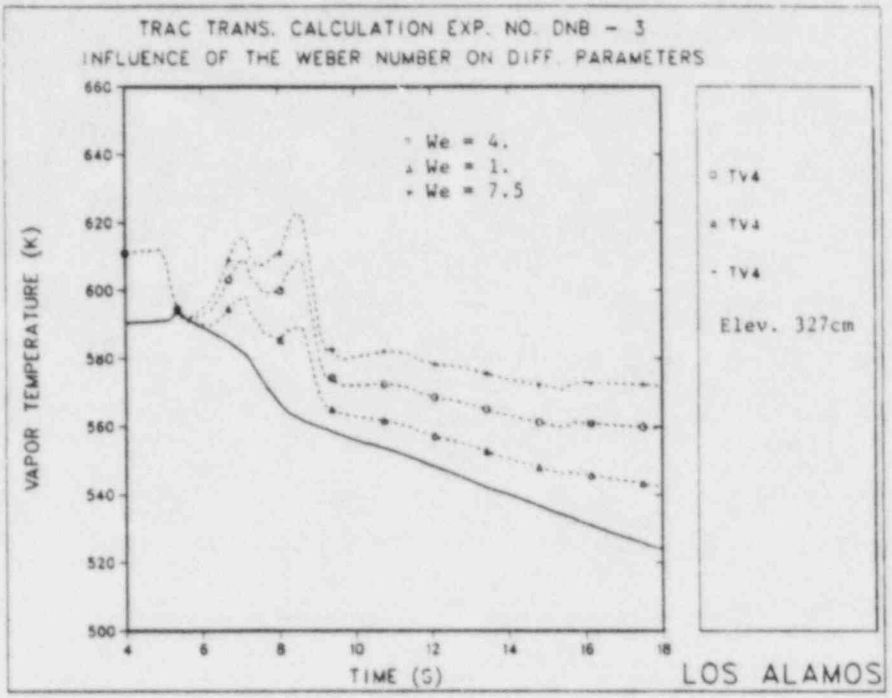

Fig. 26 Influence of Weber number on calculated vapor temperatures

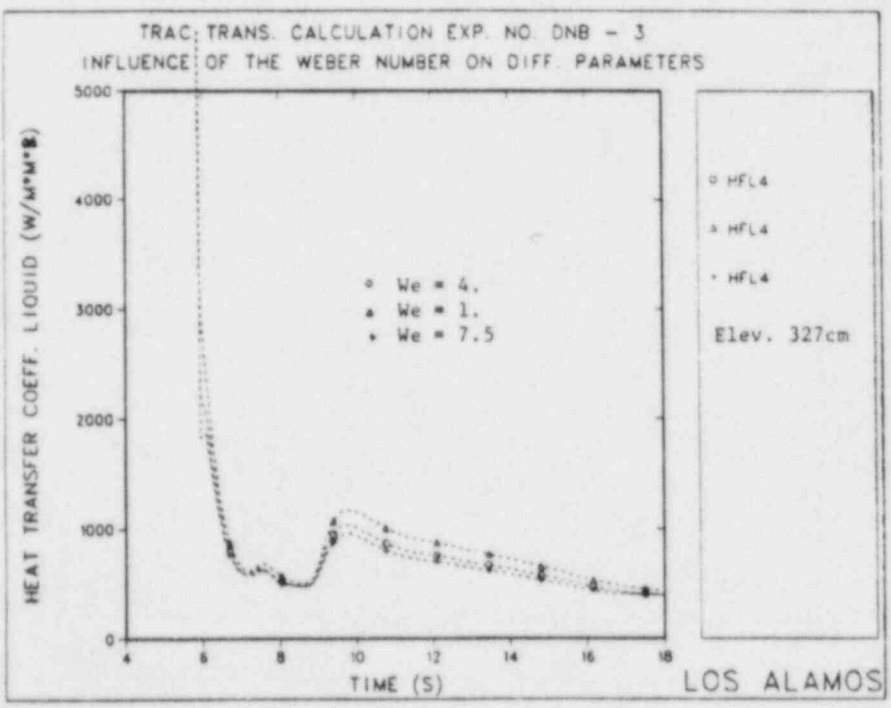

Fig. 27 Influence of Weber number on calculated wall-liquid HTCs

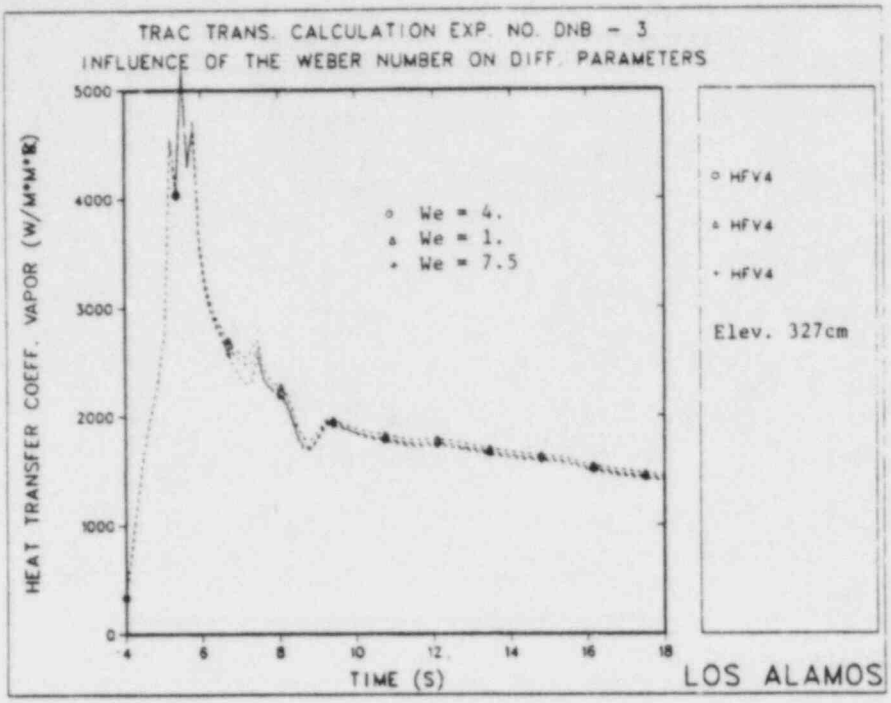

Fig. 28 Influence of Weber number on calculated wall-vapor HTCs

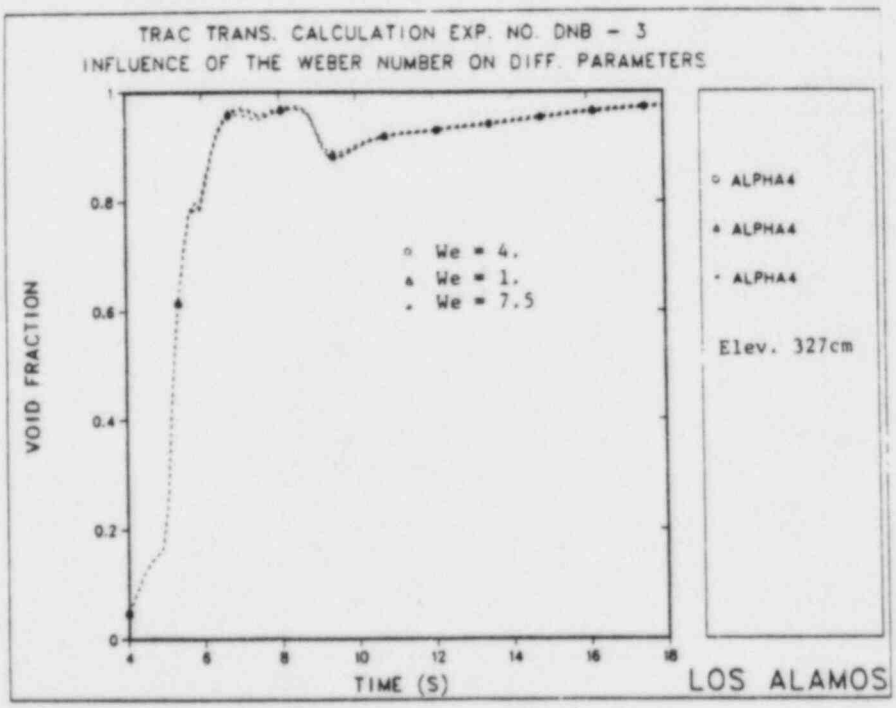

Fig. 29 Influence of Weber number on calculated void fractions

6.5 Influence of wall-vapor heat transfer correlations.

To investigate the influence of wall-vapor component on the wall to dispersed flow heat transfer process, three different correlations have been applied for the calculation of wall-vapor heat transfer coefficients.

a) Dittus-Boelter correlation (Eq. 11)

b) McEligot correlation /16/

$$h_{vc} = 0.021 \cdot \frac{\lambda_{vf}}{D_{eq}} \cdot Re_v^{0.8} \cdot Pr_v^{0.4} \cdot \left(\frac{T_v}{T_w}\right)^{0.5} \qquad (13)$$

c) Chen correlation /13/

$$h_{vc} = \frac{f}{2} \cdot G_v \cdot Cp_{vf} \cdot Pr_{vf}^{-2/3}$$

with $f = 0.037 \cdot (Re)^{-0.17}$ and

$$Re = \frac{D_{eq} \cdot \rho_v \cdot \langle j \rangle}{\eta_v}; \quad \langle j \rangle = \frac{G_v}{\rho_v} + \frac{G_{TOT} - G_v}{\rho_\ell} \qquad (14)$$

The wall-liquid component of heat flux was calculated using the Forslund-Rohsenow correlation (Eq. 12) for direct wall-droplet heat transfer and the radiative component was added to the wall-liquid heat flux. The results of these calculations are shown in Figs. 30 through 35. The comparison of calculated and measured wall temperatures shows that the Dittus-Boelter correlation seems to be the most suitable for the calculation of wall-vapor heat transfer coefficients when it is combined with the proposed form of Forslund-Rohsenow correlation.

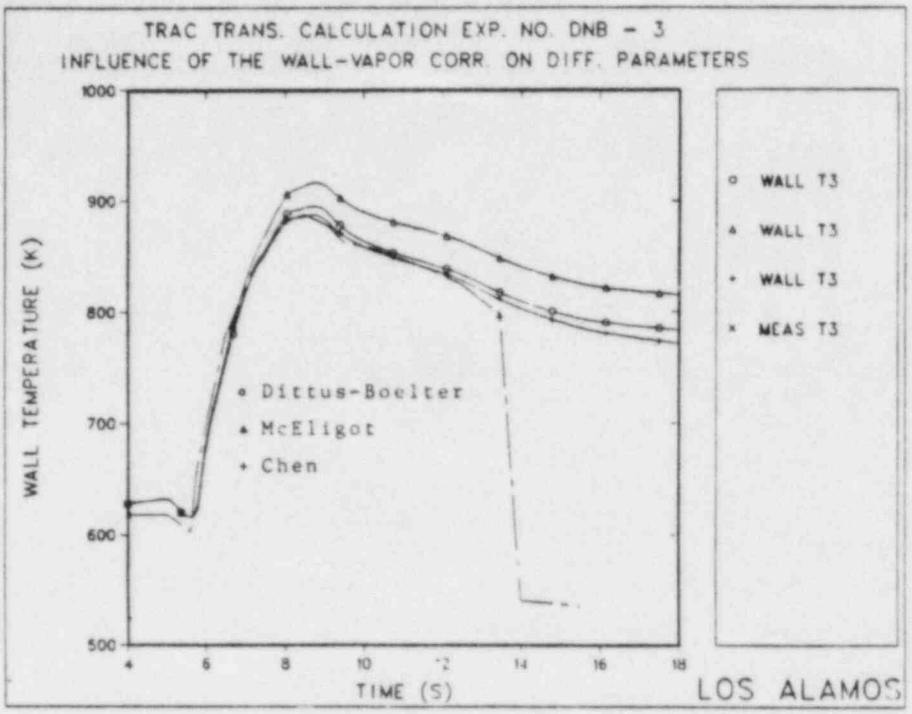

Fig. 30 Comparison of calculated wall temperatures using different wall-vapor correlations

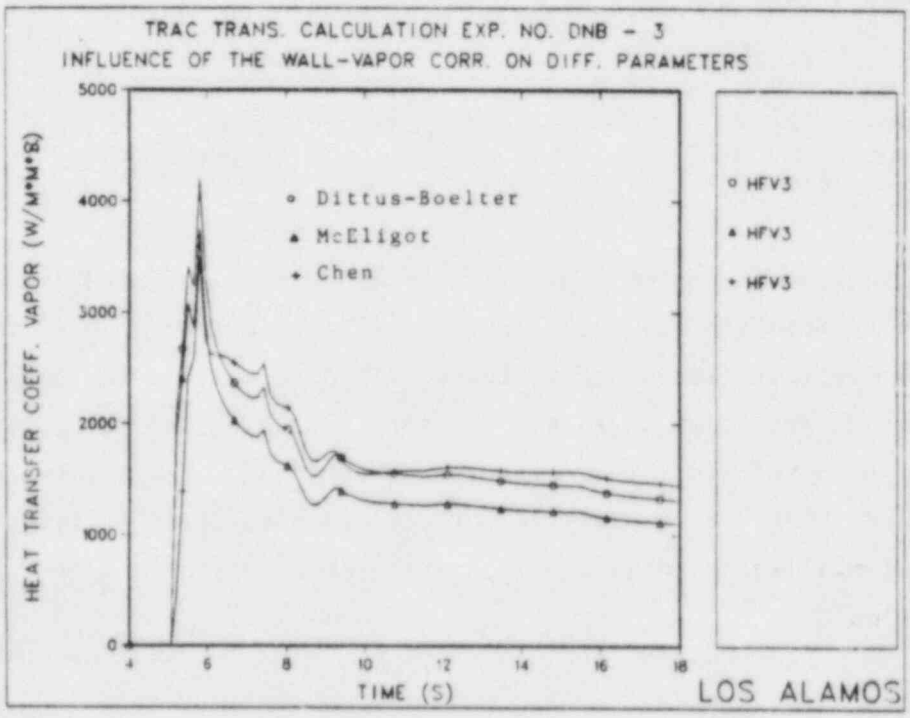

Fig. 31 Comparison of wall-vapor HTCs calculated with different correlations

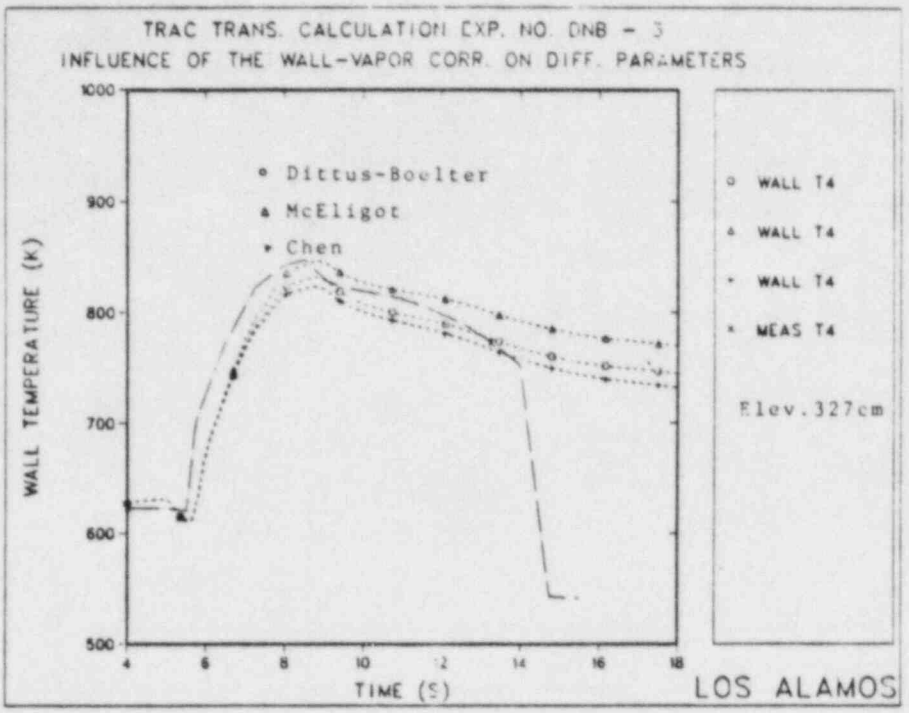

Fig. 32 Comparison of calculated and measured wall temperatures using different wall-vapor correlations

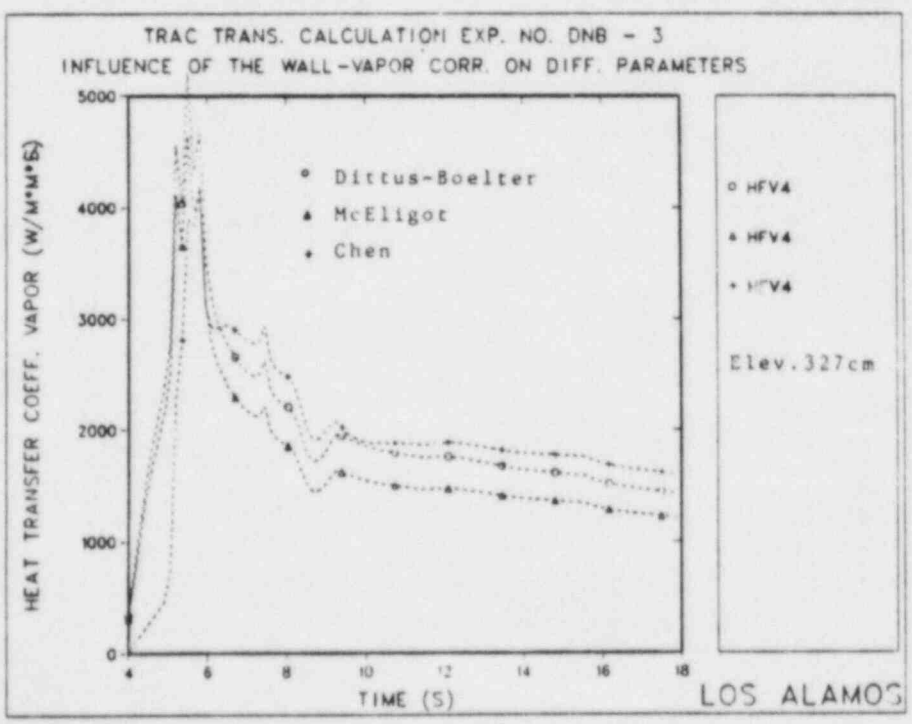

Fig. 33 Comparison of wall-vapor HTCs calculated with different correlations

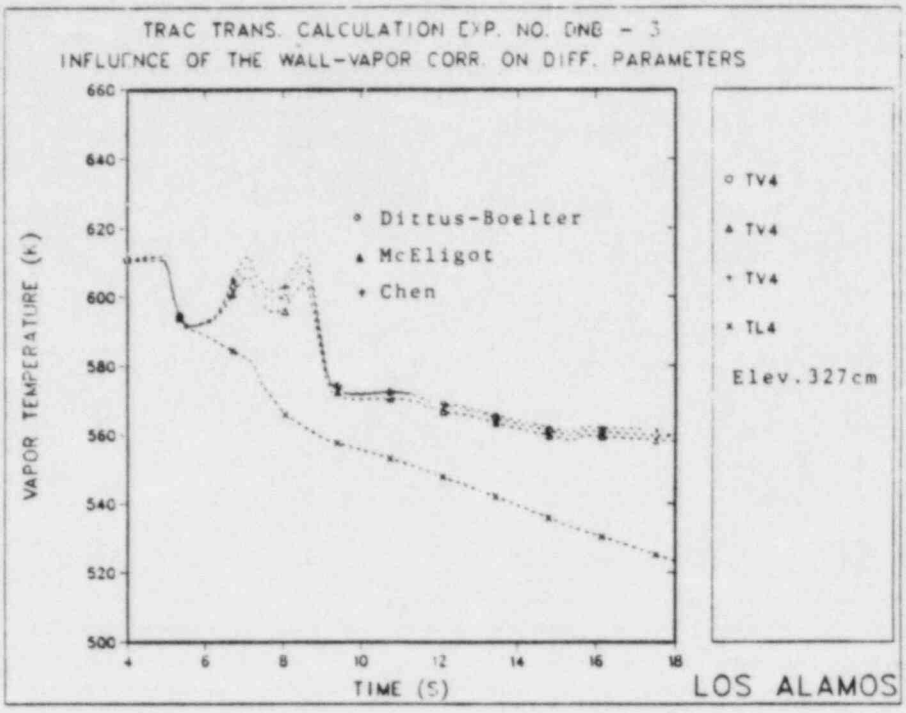

Fig. 34 Comparison of calculated vapor temperatures using different wall-vapor correlations

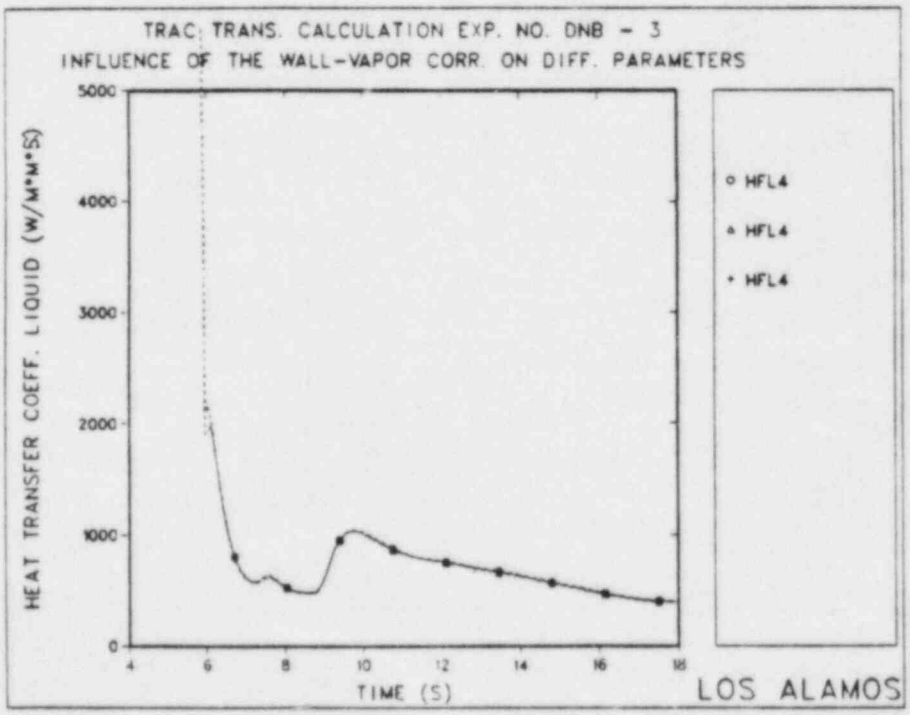

Fig. 35 Wall-liquid HTCs calculated with Forslund-Rohsenow correlation

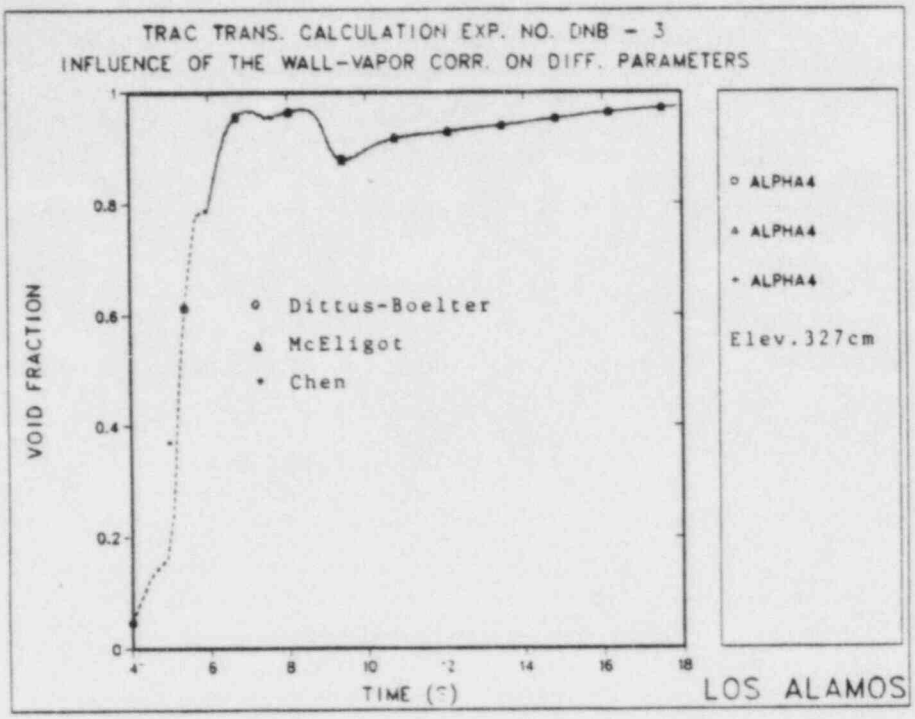

Fig. 36 Comparison of calculated void fractions using different wall-vapor correlations

6.6 Influence of wall-liquid heat transfer component.

Four different methods have been applied for the calculation of wall-liquid heat transfer component in this study:

a) Berenson pool film boiling correlation /14/

$$h_{PFB} = 0.425 \cdot \left[\frac{\lambda_{vf}^3 \cdot g_c \cdot \rho_v \cdot (\rho_\ell - \rho_v) \cdot \Delta h^*}{\eta_{vf} \cdot (T_w - T_{SAT}) \cdot a}\right]^{0.25} \qquad (15)$$

$$a = \left[\frac{\sigma}{g \cdot (\rho_\ell - \rho_v)}\right]^{0.5}$$

b) Forslund-Rohsenow correlation

$$h_{DF} = K_1 \cdot 1.276 \cdot (1 - \alpha)^{2/3} \cdot BRAC^{1/4} \cdot \frac{T_w - T_{SAT}}{T_w - T_\ell} \qquad (16)$$

$$BRAC = \frac{\lambda_{vf}^3 \cdot g_c \cdot \rho_\ell \cdot \rho_v \cdot \Delta h^*}{(T_w - T_{SAT}) \cdot \eta_{vf} \cdot d_D}; \; K_1 = 1.5 \text{ for water}$$

c) Droplets mass flux treatment of wall-liquid heat transfer component which was proposed by Vojtek /16/.

The total heat flux from the wall to fluid was written as:

$$q_{TOT} = q_{wv} \cdot \alpha + \Delta h \cdot N_D^{2/3} \cdot \frac{\pi \cdot d_D^3}{6} \cdot U_\ell \cdot \rho_\ell \qquad (17)$$

d) Modified version of Eq. (17) to eliminate the influence of droplet diameter:

$$q_{TOT} = q_{wv} \cdot \alpha + K \cdot \Delta h \cdot G_\ell \cdot (1-\alpha) \qquad (18)$$

with $K = 2.5 \cdot 10^{-4}$

All these calculations were performed using the Dittus-Boelter correlation for the prediction of wall-vapor heat transfer component and the radiative component has been added to the wall-liquid heat flux. The results are shown in Fig. 36 through 40. Also this comparison shows that there is no significant influence of method used for the calculation of wall-liquid heat transfer with a exception of the results obtained using Berenson pool film boiling correlation.

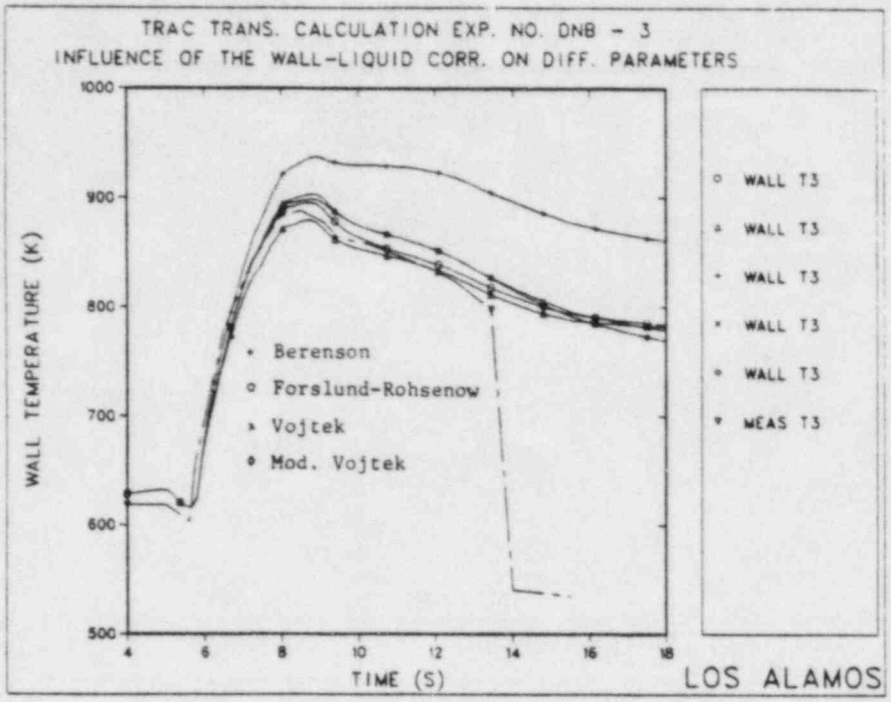

Fig. 37 Comparison of calculated and measured wall temperatures using different wall-liquid correlations

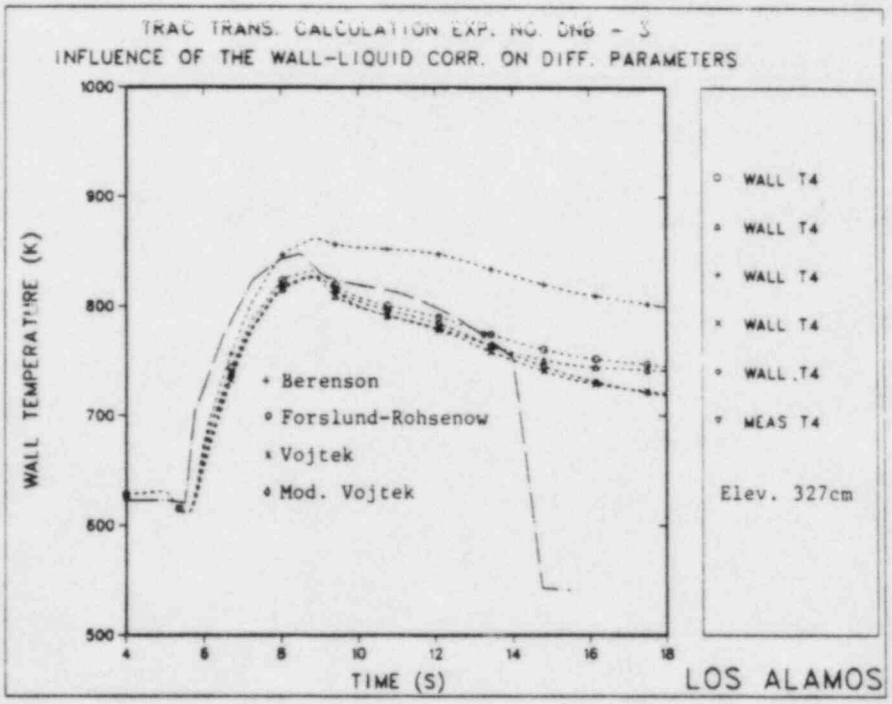

Fig. 38 Comparison of calculated and measured wall temperatures using different wall-liquid correlations

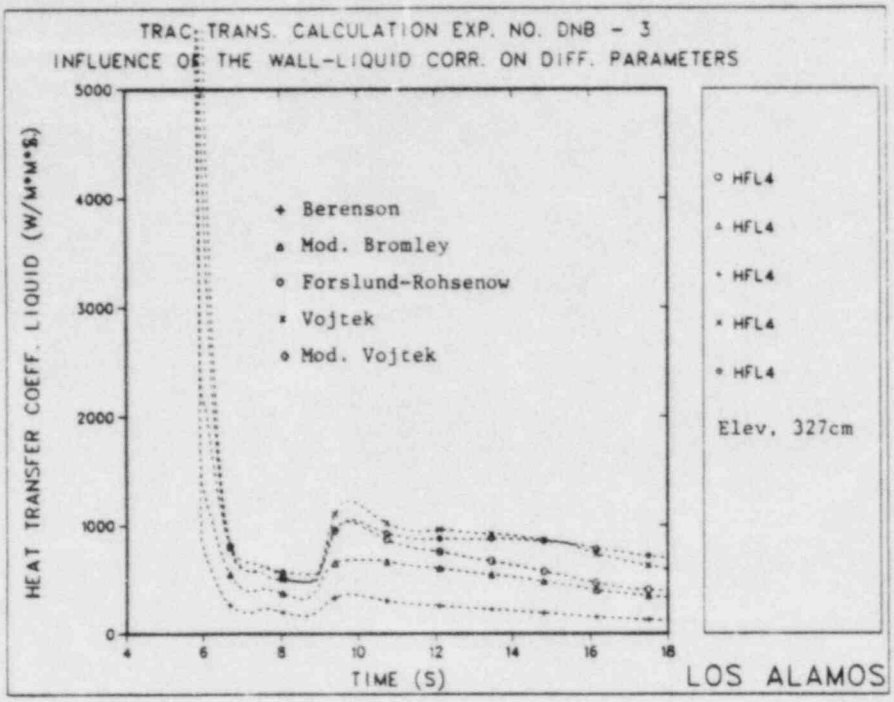

Fig. 39 Comparison of effective wall-liquid HTCs calculated with different correlations

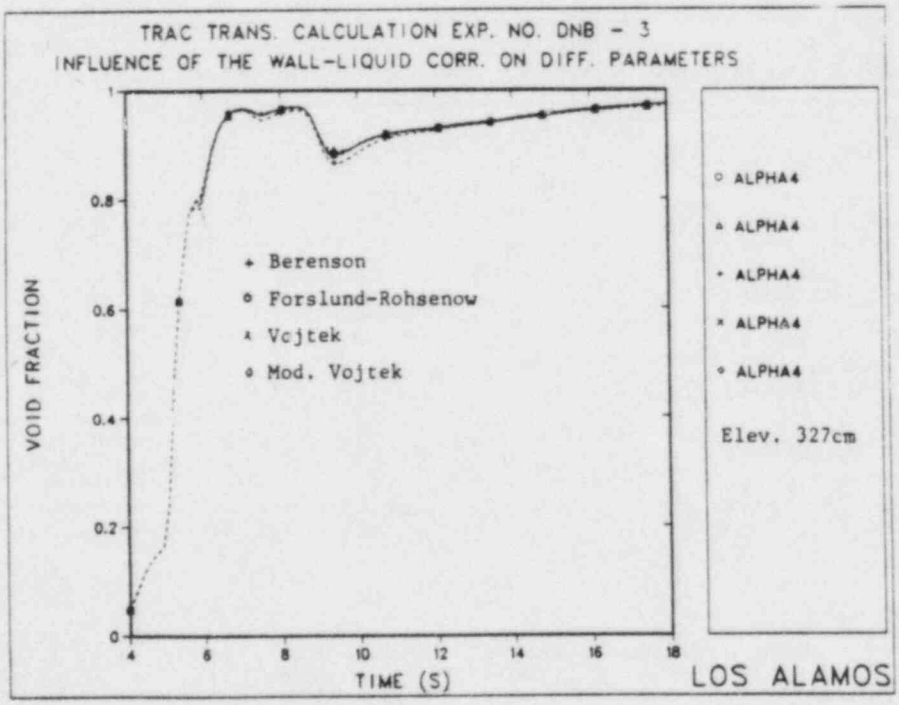

Fig. 40 Comparison of calculated void fractions using different wall-liquid heat transfer correlations

6.7 Evaluation of correlations for the calculation of minimum film boiling temperatures.

Two different correlations have been used for the calculation of minimum film boiling temperatures:

a) Present TRAC-PF1/MOD1 correlation

$$T_{MIN} = T_{NH} + (T_{NH} - T_{\ell}) \cdot R^{0.5} \qquad (19)$$

$$R = \frac{(\rho \cdot C_p \cdot \lambda)_{\ell}}{(\rho \cdot c_p \cdot \lambda)_w}$$

$$T_{NH} = 705.44 - (4.722 \cdot 10^{-2}) \cdot DP + (2.3907.10^{-5}) \cdot DP^2 - (5.8193 \cdot 10^{-9}) \cdot DP^3$$

$$DP = 3203.6 - P$$

The pressure P is in psia and T_{NH} in degrees Fahrenheit.

b) Groeneveld correlation for pressure ≤ 9MPa and no liquid subcooling

$$T_{MIN} = 284.7 + 0.0441.P - 3.72 \cdot 10^{-6} \cdot P^2; \text{ P is in kPa} \qquad (20)$$

The comparison of calculated and measured wall temperatures have shown that none of these two correlations predicted the return to nucleate boiling (RNB) in the first 13s of DNB-3 experiment. The measured wall temperatures show that RNB occurs at about 6s in the upper part and approximately 9s after test initiation in the middle part of the test bundle.

6.8 The selection of best fit set of correlations for the calculation - of test DNB-3.

The results of investigation of the different wall-vapor correlation have shown that only the HTC's which were calculated with the Chen correlation did not decrease in the late part of the transient. Because a similar trend was also observed by the analysis of experimental data this correlation and the Vojtek method of calculation of wall-liquid heat flux which shows the similar behavior were chosen for the final calculation of test DNB-3. The results of this calculation are shown in Figs. 41 through 44. The comparison of calculated and measured resutls shows again very good agreement at the elevation 259 cm and 377 cm in the test bundle. The agreement in the later part of the transient was

even slightly improved in the comparison to the results of previous calculations (Figs. 14 through 19).

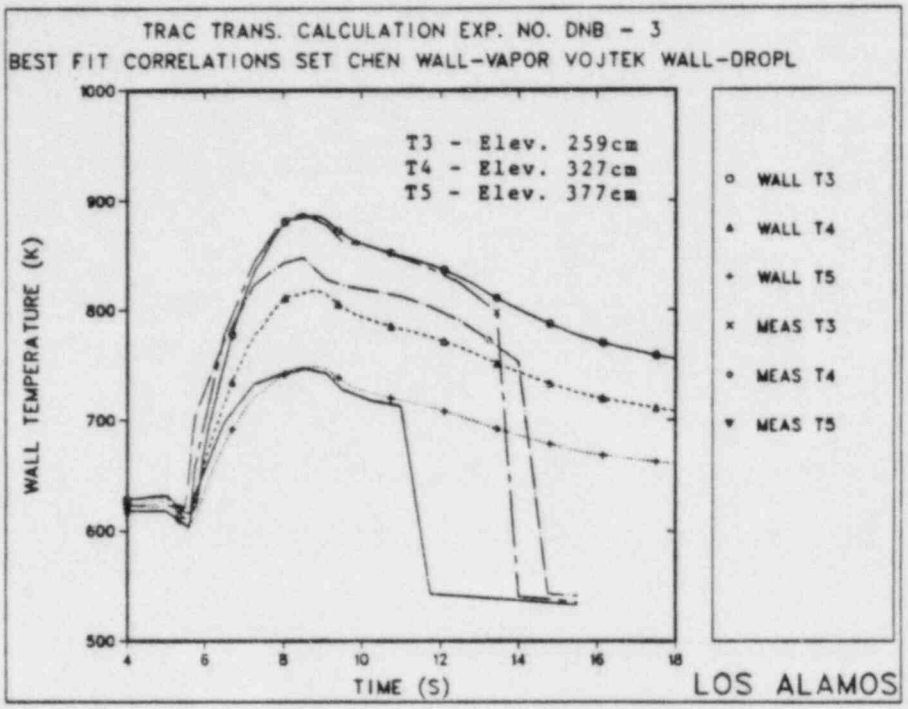

Fig. 41 Comparison of calculated and measured wall temperatures

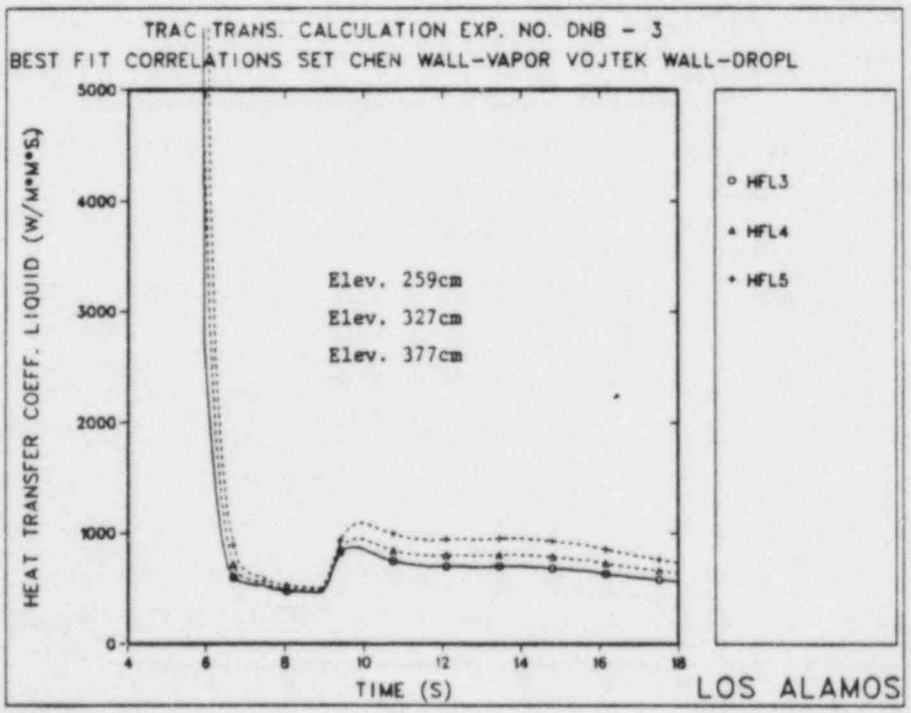

Fig. 42 Wall-liquid HTCs calculated at different elevations

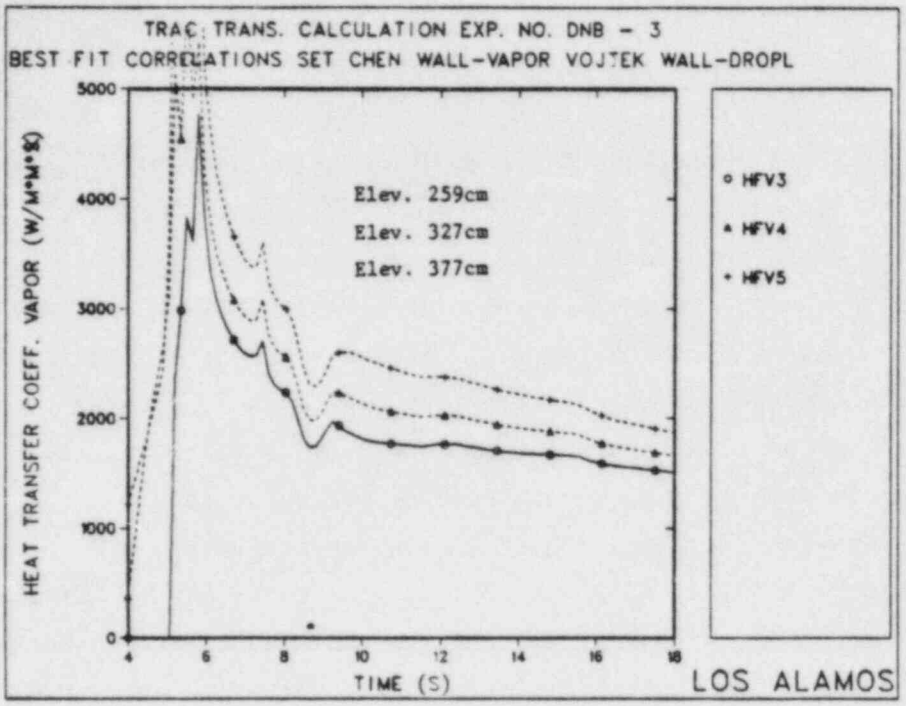

Fig. 43 Wall-vapor HTCs calculated at different elevations

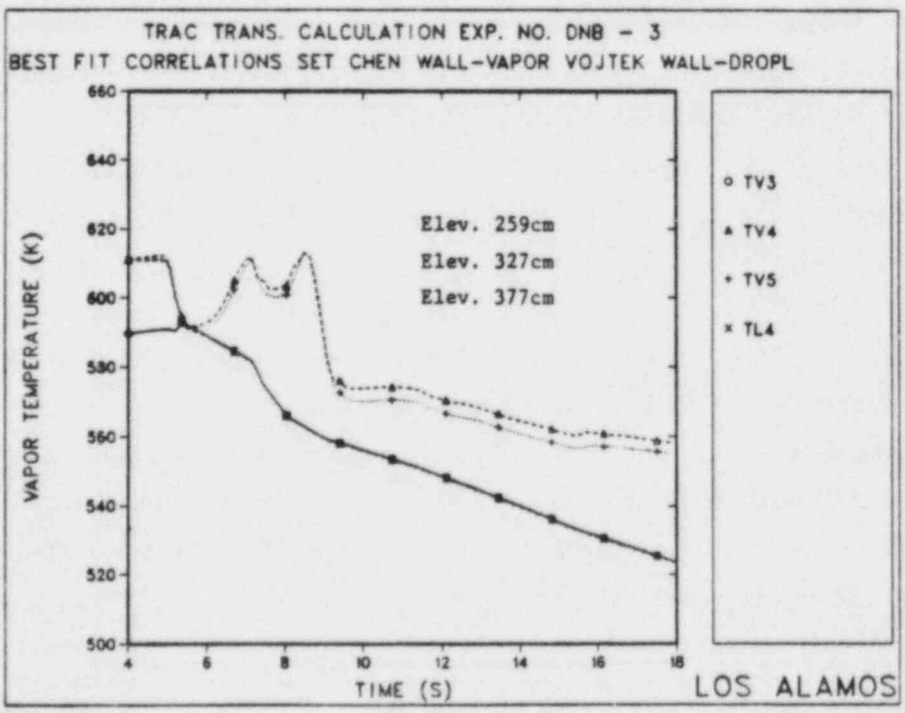

Fig. 44 Vapor temperature calculated at different elevations

CONCLUSIONS AND FINAL REMARKS

1. Valuable data for the investigation of transient critical heat flux phenomena and forced convective film boiling heat transfer were obtained in the experiments described in this paper.

2. The evaluation of correlations for the prediction of maximum critical heat flux and film boiling heat transfer coefficients which are used or developed for the analysis of loss of coolant accidents in nuclear reactors showed that significant discrepancies still exist among different correlations and between correlations and experimental data. It was shown that none of applied overall film boiling heat transfer correlations can be used with sufficient confidence during the entire post-CHF portion of the blowdown phase of the LOCA. The analysis of experimental and calculated results has shown that in the post-CHF portion of transient experiments for the approximately same values of independant parameters (G, X, P, T_W and T_{SAT}) two significantly different values of HTC can exist. This effect of flow regimes on the wall-fluid heat transfer cannot be reproduced by the heat transfer correlations which were developed and assessed using steady state conditions data.

3. The results of this investigation showed that the presence of water droplets significantly improves the wall-to-dispersed flow heat transfer. Therefore, by the further investigation of wall to dispersed flow heat transfer processes attention should be paid not only to the modeling of interfacial heat transfer which is decreasing the vapor superheat, but also to the disturbing effect of vapor flow boundary layer caused by droplets and to the direct wall-droplet heat transfer.

4. The results of TRAC-PF1/MOD1 post-experimental analysis of test DNB-3 have shown that the splitting of total wall-fluid heat flux into the wall-vapor and wall-liquid components has no significant influence on the calculated thermal hydraulic parameters such as vapor temperature and vapor and liquid velocity unless the total heat flux using different combinations of correlations is under- or over-predicted. The TRAC PF1/MOD1 calculations indicated that there is no high thermal nonequilibrium in the high pressure intermediate quality dispersed flow.

5. The droplets mass flux method which was proposed by the author has been shown to be applicable for the calculation of the wall-liquid heat transfer

component in the nonequilibrium two-fluid code TRAC-PF1/MOD1. However the present form of this correlation should be considered only as a boundary equation for the further detailed investigation of the heat and mass transfer processes which are taking place in the boundary layer of the vapor flow.

6. Both applied correlations for the calculation of minimum stable film boiling temperature did not predict the return to nucleate boiling which was observed in experiment. These results indicated the need for the further experimental and analytical investigations of the RNB phenomena in the high pressure region of LOCA.

NOMENCLATURE

A	area, cross section	m^2
c_p	specific heat capacity	$J/(K \cdot kg)$
d	diameter	m
d_{equ}	equivalent diameter	m
G	mass flux	$kg/(m^2 \cdot s)$
g	acceleration of free fall	m/s^2
h	specific enthalpy	J/kg
Δh	latent heat of vaporization	J/kg
l	length	m
m	mass	kg
N_D	number of droplets	$1/m^3$
p	pressure	N/m^2
Q	heat per unit of area	W/m^2
q	heat flux density	W/m^2
r	radius	m
T	temperature	$k(^0C)$
U	velocity	m/s
X	equilibrium quality	

Greek letters

α	void fraction	
η	dynamic viscosity	$kg/(s \cdot m)$
λ	thermal conductivity	$W/(K \cdot m)$
ρ	mass density	kg/m^3
σ	surface tension	N/m

Dimensionless parameters

$Pr = \frac{\upsilon}{a}$ Prandtl number

$Re = \frac{ul}{\upsilon}$ Reynolds number

Subscripts

D	droplet
E	equilibrium
f	film
ℓ	liquid
M	measurement
MAX	maximum
MIN	minimum
SAT	saturation
TOT	total
V	vapor
W	wall

REFERENCES

/ 1/ Agemar, Brand, Emmerling, Flittner, Köhler, Loser, Abschlußbericht über die Inbetriebnahme des Versuchsstandes für gesteuerte Bundelmessungen und uber die ersten Versuche mit einem DWR-25-Stab-Bundel, Technischer Bericht KWU R52-3015.

/ 2/ Agemar, Brand, Emmerling, DWR Hauptversuche mit einem 25 Stabbündel, Teil 1: Experimentelle Durchfuhrung and Dokumentation der Meßergebnisse, KWU-RE23/012/77.

/ 3/ Emmerling, DWR-Hauptversuche mit einem 25 Stabbündel, Teil 2: Berechnung der Warmeubergangskoeffizienten, KWU- RE23/029/77.

/ 4/ Karwat, H., Wolfert, K , BRUCH-D A Digital Program for PWR- Blowdown Investigations, Nucl. Eng. Des. 11 (1970), p 241-254.

/ 5/ Liesch, K.J., Steinhoff, F., Vojtek, I., Wolfert, K., BRUCH-D -Q2 Ein Rechenprogramm zur Analyse der fluid- und thermodynamischen Vorgange im Primarkreis von Druckwasserreaktoren bei schweren Kuhlmittelverlustunfallen MRR-P-3, Laboratorium fur Reaktorregelung und Anlagensicherung, Garching.

/ 6/ Vojtek, I., Auswertung der 25 Stabbündel-Versuche mit dem Rechenprogramm BRUDI-VA, GRS-A-208, September 1978.

/ 7/ Smith, R.A., Griffith, P., A simple model for estimating time to CHF in PWR LOCA, Trans. of American Society of Mechanical Engineering, paper no. 76-HT-9, 1976.

/ 8/ Liesch, K.J., Raemhild, G., Hofmann, K., Zur Bestimmung des Warmeuberganges und der kritischen Heizflachenbelastung im Hinblick auf besondere Verhaltnisse in den Kuhlkanalen eines DWR bei schweren Kuhlmittelverluststorfallen, MRR 150, Laboratorium fur Reaktorregelung und Anlagensicherung, Garching, 1975.

/ 9/ Steinhoff, F., Vergleich theoretischer und experimenteller Ergebnisse der SWR-Notkuhlversuche mit einem Vierstabbundel, MRR-I-37, Laboratorium fur Reaktorregelung und Anlagensicherung, Garching, 1975.

/10/ Groeneveld, D.C., An investigation of heat transfer in the liquid deficient regime, AECL-3281, 1969.

/11/ Condie, K.G., Bengston, S.J., Richlen, S.L., Post-CHF heat transfer data-analysis, comparison and correlation, EG&G, Idaho, Idaho Falls.

/12/ Groeneveld, D.C., Delorme, G.G.J., Prediction of thermal nonequilibrium in the post-dryout regime, Nucl. Eng. Des. 36 (1976) 17-26.

/13/ Chen, J.C., Ozkaynak, F.T., Sundaram, R.K., Vapor heat transfer in post-CHF region including the effect of therodynamic nonequilibrium Nucl. Eng. Des 51 (1979) 143-155.

/14/ Berenson, P.J., Trans. ASME J. Heat transfer, 83, 351 (1961).

/15/ Biasi, L. et al., Studies on Burnout, Part 3 Energia Nucleare, Vol. 14, No. 9, Sept. 1967.

/16/ Vojtek, I., Untersuchung der Wärmeübertragungsverhältnisse in der Hochdruckphase eines Kuhlmittelverluststorfalls mit mittlerem und grossem Bruchquerschnitt GRS-A-709, Gesellschaft fur Reaktorslcherheit, Marz 1982.

/17/ Vojtek. I., Investigation of transient heat flux phenomena and forced convection film boiling heat transfer, 7th International heat transfer conference, Munich, FRG, September 1982.

/18/ TRAC-PF1/MOD1 User Manual, to be published.

REFLOOD ANALYSIS CODE "REFLA"

Yoshio MURAO

Japan Atomic Energy Research Institute

Tokai-mura, Ibaraki-ken,319-11,Japan

Abstract

This paper contains a short description of the reflood analysis code "REFLA", which was developed to calculate the thermo-hydro-dynamics of a nuclear core durind a reflood transient in which ECC water is introduced into the bottom of the core.

The description emphasizes the following items:

1. Heat transfer model.
2. Quench front propagation model.
3. Core water accumulation phenomena.

1. Introduction

In the safety analysis on the Loss-of-Coolant Accident (LOCA) of light water reactros, it is very important to evaluate the temperature history of the fuel rod calddings during the reflood phase, which is governing the integrity of the first enclosure of the fission product. In the safety evaluation of the reflood phase of a PWR, the empirical correlations on the reflood heat transfer and the carry-over rate fraction have been used. The latter is used for calculating the core inlet flooding rate in the system analysis. For obtaining the flexibility of application for safety analysis, we are developing a computer code REFLA for the reflood phase based on the physical understanding of the phenomena.

2. Code development

The one-dimensional core code, REFLA-1D (core), calculates steam/water velocities in the core, void fractions, differential pressures, cladding temperatures, temperatures of the steam/water at the exit of the core. The boundary conditions are the system pressure, and the velocity and temperature of the water at the inlet of the core. The small scale reflood test results and the FLECHT/FLECHT-SET data [3] in the USA are used in the modeling of REFLA-1D (core) as well as the basic experimental knowledge, for example,flow patterns shown in Fig.1.

The latest version of the code is REFLA-1D/MODE 3.[4] This version includes some new improvements in the core thermo-hydrodynamic models, which were developed using the experimental data of the small scale reflood facilities, such as, the JAERI small scale reflood test facility and the FLECHT facilities. The scaling ratios of the core flow area of these facilities to a 1000 MWe class PWR are 1/2500 and 1/370 for the JAERI and the FLECHT facilities, respectively.

In the region above the quench front, two types of hydrodynamic models, i.e. Case 1 and Case 2, are introduced as shown in Fig. 2. In both cases, a water accumulation region is assumed to exist above the quench front. The length of this region is now set to 0.3 m. Above the water accumulation region, there exists a normal dispersed

flow region in Case 1, whereas amother water accumulation region in Case 2. In the water accumulation region, the void fraction has a value between the values corresponding to the slug flow and the dispersed flow due to the integration of dispersed droplets. The heat transfer coefficient and the void fraction in the water accumulation region for Case 2 is calculated by interpolating the values for the dispersed flow and the slug flow. The correlations of the void fraction and heat transfer coefficient for the slug flow[5],[6] are indicated in Appendix 1. The void fraction of the dispersed flow is calculated based on the slip velocity corresponding to the critical Weber number Wec. The heat transfer coefficient for the dispersed flow is calculated based on the model of the solid spherical water drop moving in the steam.

The quench velocity correlation was improved in order to extend the applicability of the correlation to the lower quench temperature than the maximum liquid superheat temperature and to the lower and higher system pressures than 0.4 MPa. The correlation is described in Appendix 2.

3. Calculational results

In Figs. 3 to 12, indicated are the results of some simulation calculations[4] with the REFLA-1D (core) code. Inputted values for the simulation calculations of the test runs are tabulated in Table 1. In the calculations for FLECHT tests, results without showing case number were obtained by the calculation with Case 1. Although improvements of models are necessary, practically good agreements are obtained in either Case 1 or 2 for many one-dimensional reflood tests.

The difference of the thermal responses between Cases 1 and 2 seems to be small. The hydrodynamic responses of Cases 1 and 2 are clearly different from each other as shown in Fig. 13. In Case 1, the local void fraction is almost unity until the quench front arrives near the concerning region, while in Case 2, the local void fractions at every location begin to decrease just after steam flow is developed and they become noticeably smaller value than unity. The Case 1 appeared at the flooding rate less than 4 cm/s in FLECHT low flooding and FLECHT

SEASET tests. On the contrary, the Case 2 appeared as shown in Fig. 14 and 15 for CCTF tests and JAERI small scale reflood tests, even when the flooding rate was about 2 cm/s. These differences can be attributed to the multi-dimensional effect, i.e. as shown in Fig. 16 the water, which is entrained by steam flow and separated at the top of the core, can reflux into the core if the core is wide enough or has cold structures which allow the separated water to form the falling liquid film. Accordingly, the REFLA code with Case 2 model is expected to be applied to reflood phenomena in a wide core.

4. Summary

The status of the reflood code development is described. Although some improvements are necessary, practically this one-dimensional reflood model is expected to be used for prediction of reflood phenomena in wide cores.

References

(1) Murao Y.: Correlation of quench phenomena for bottom flooding during loss-of-coolant accidents, J. Nucl. Sci. Tehcnol., 15 [12], pp. 875 ∿ 885, (1978).

(2) Murao Y., et al.: REFLA-1D/MODE1: A computer program for reflood thermo-hydrodynamic analysis during PWR-LOCA, user's manual, JAERI-M 9286 (1981).

(3) For instance, Rosal E.R., et al.: FLECHT low flooding rate cosine test series data report, WCAP-8651 (1975).

(4) Murao Y.: Study of the thermo-hydrodynamic penomena in the nuclear core during reflood phase (in Japanese), JAERI-M 83-032 (1983).

(5) Murao Y., et al.: Experimental modeling of core hydrodynamics during reflood phase of LOCA, J. Nucl. Sci. Tech., 19 [8] pp. 613 ∿ 627 (1982).

(6) Murao Y., et al.: Correlation of heat transfer coefficient for saturated film boiling during reflood phase prior to quenching, J. Nucl. Sci. Tech. 18 [4], pp. 275 ∿ 284 (1981).

Table 1 Test runs used for simulation calculation and inputted values

Test run	System pressure (MPa)	Maximum linear power density (kW/m)	Peak clad temp. at reflood initiation (K)	Initial clad surface temp. (K)	Flooding rate (cm/s)	Core inlet fluid temp. (K)	Power decay curve
FLECHT low flooding 2833	0.28	2.92	1143	Measured values at reflood initiation	2.03	325	ANS×1.2 (30S after shutdown)
PWR-FLECHT Group 162							
0408	0.41	4.07	1143	416	25.4	350	B**
3541					15.0		B**
4321					9.91		B**
4225					4.83		B**
6948					2.54		B**
7057					2.03		A***
6749					1.52		A***
FLECHT SEASET 31504	0.28	2.30	1093	403	2.4	324	ANS×1.2 (30S)
FLECHT skewed power 13404	0.28	2.30	997*	403	2.54	326	ANS×1.2 (30S)
Semiscale S032	0.41	2.26	996	427	2.29	350	ANS×1.2 (30S)

* Peak clad temperature at midplane at reflood initiation.

** Normalized function = $0.42e^{-0.0283t} + 0.58 - 3.92\times10^{-4}\ t$

*** Normalized function = $0.4518e^{-0.0283t} + 0.5482 - 4.922\times10^{-4}\ t$

where t is time after reflood initiation.

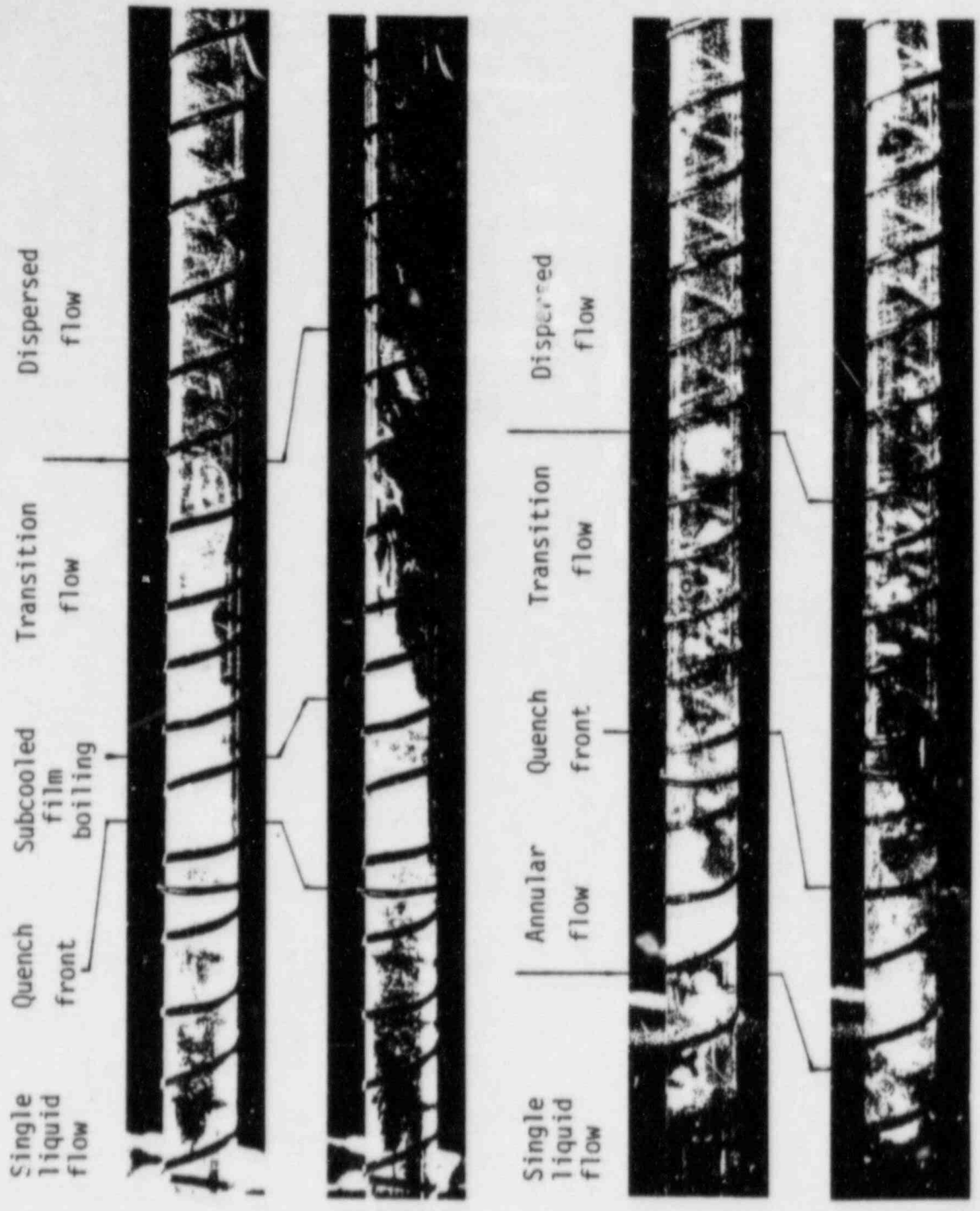

Flow inlet

(a) $\Delta T_{sub} \simeq 90$ K

$u_{lin} \simeq 15$ cm/s

Flow inlet

(b) $\Delta T_{sub} \simeq 5$ K

$u_{lin} \simeq 2$ cm/s

Fig.1 Flow patterns observed in outside-heated quartz tube experiment

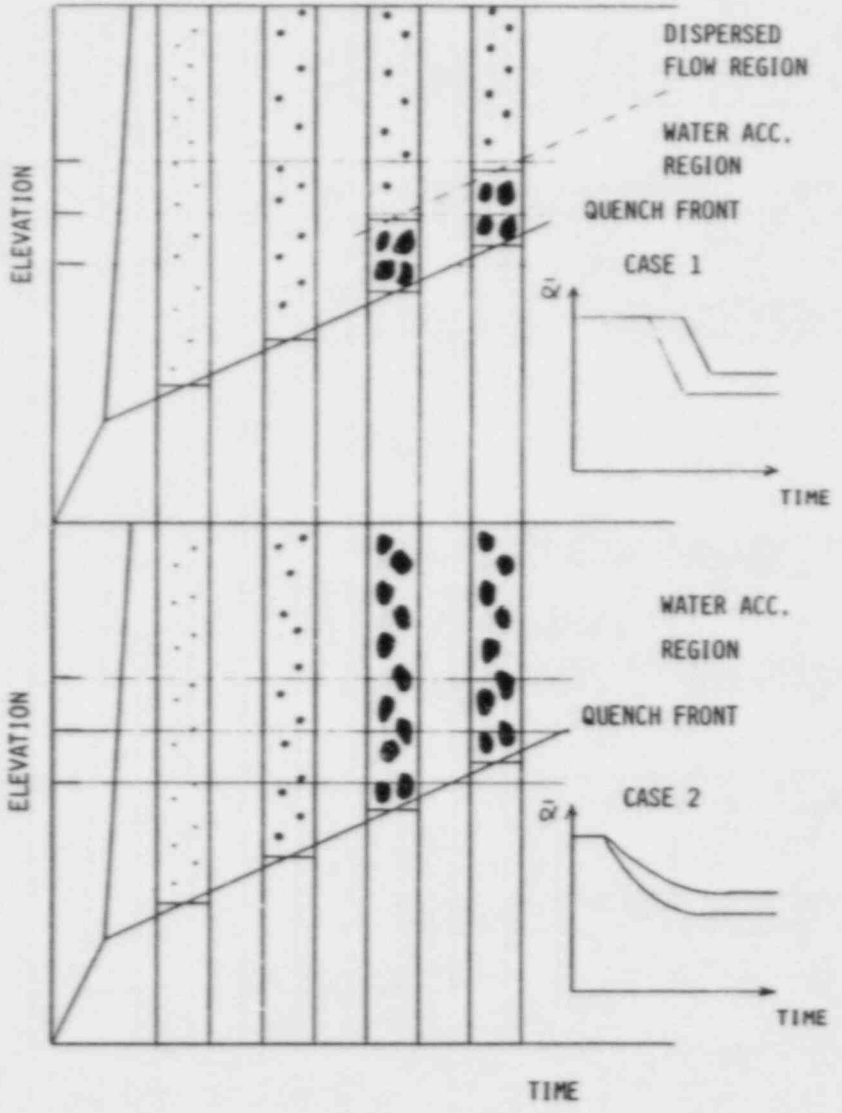

FIG. 2 HYDRODYNAMIC BEHAVIOR IN CASE 1 AND 2

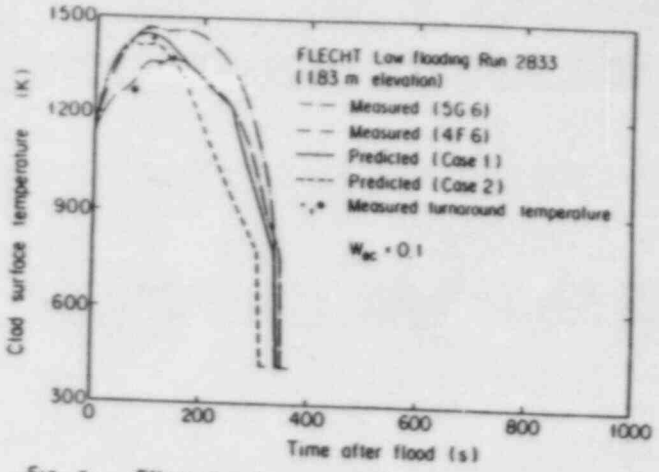

Fig. 3 Effect of water accumulation above quench front on history of clad surface temperature

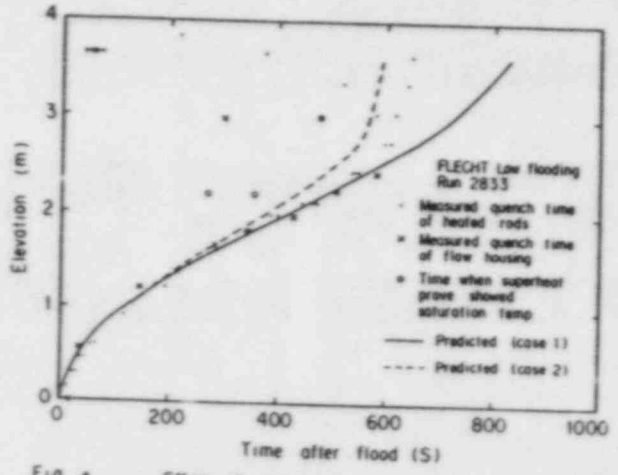

Fig. 4 Effect of water accumulation above quench front on quench envelope

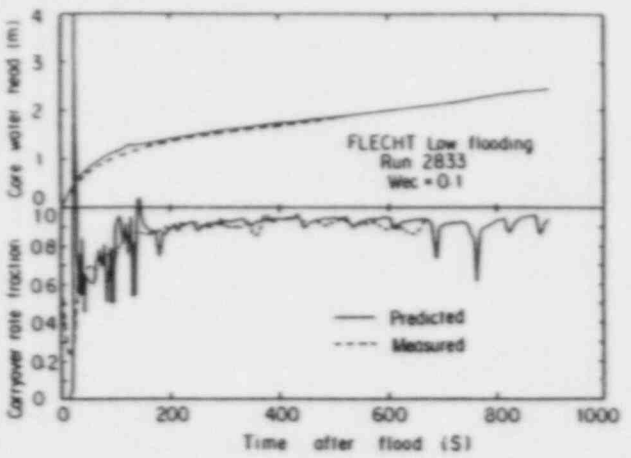

Fig. 5 Core water head and carryover rate fraction

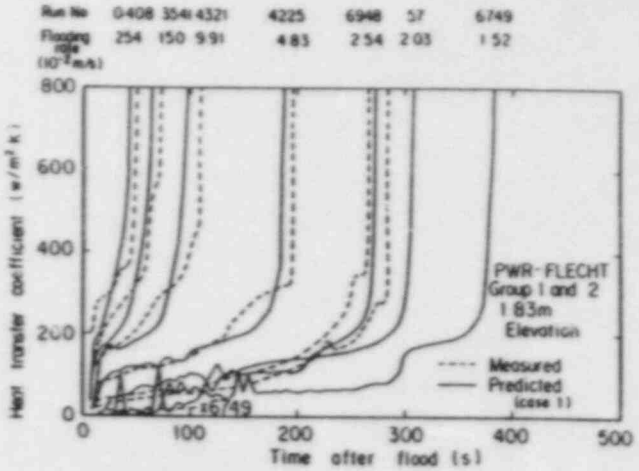

Fig. 7 Comparison of measured and predicted heat transfer coefficients

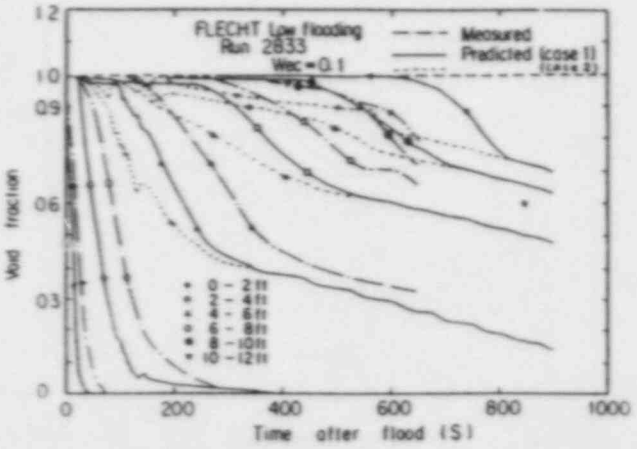

Fig. 6 Comparison of measured and predicted void fractions

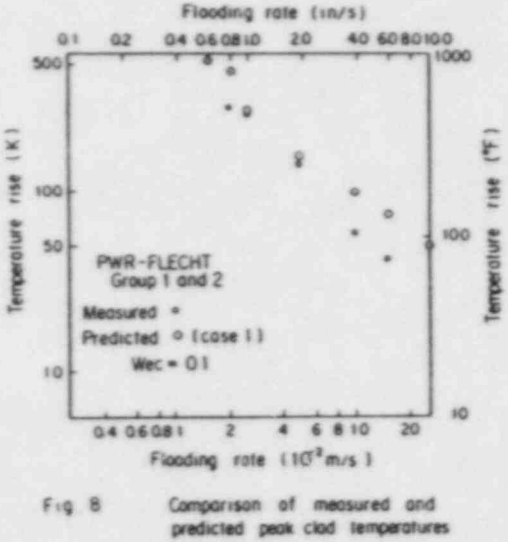

Fig. 8 Comparison of measured and predicted peak clad temperatures

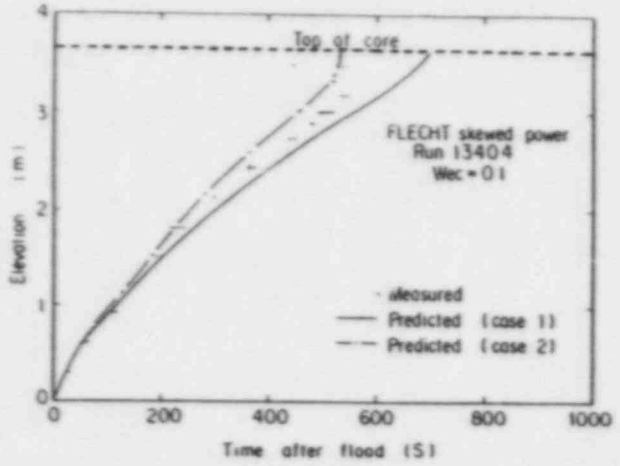

Fig. 9 Comparison of measured and predicted quench envelope for FLECHT skewed power test Run 13404

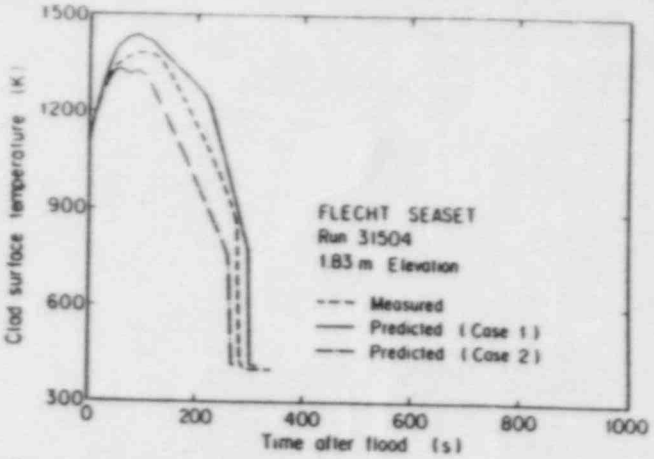

Fig. 11 Comparison of measured and predicted clad surface temperature history for FLECHT SEASET Run 31504 (1.83 m elevation)

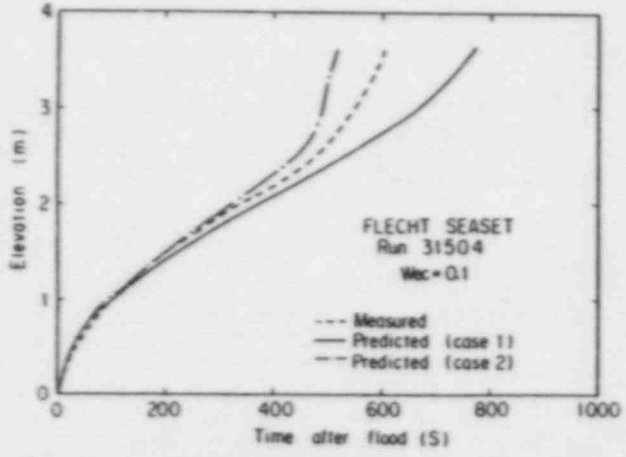

Fig. 10 Comparison of measured and predicted quench front envelope for FLECHT SEASET Run 31504

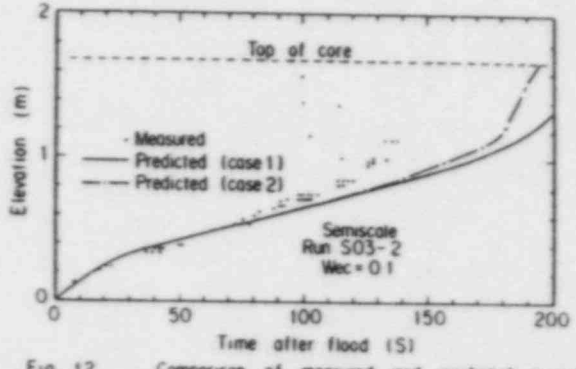

Fig. 12 Comparison of measured and predicted quench envelope for semiscale Run S03-2

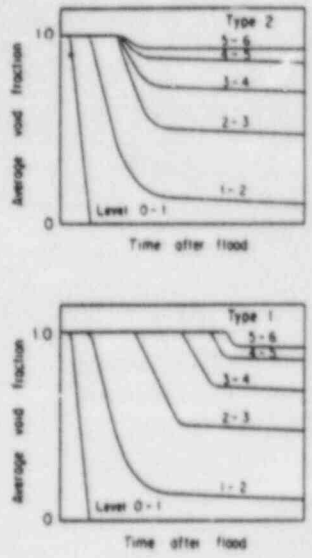

Fig. 13 Classification of core water accumulation type

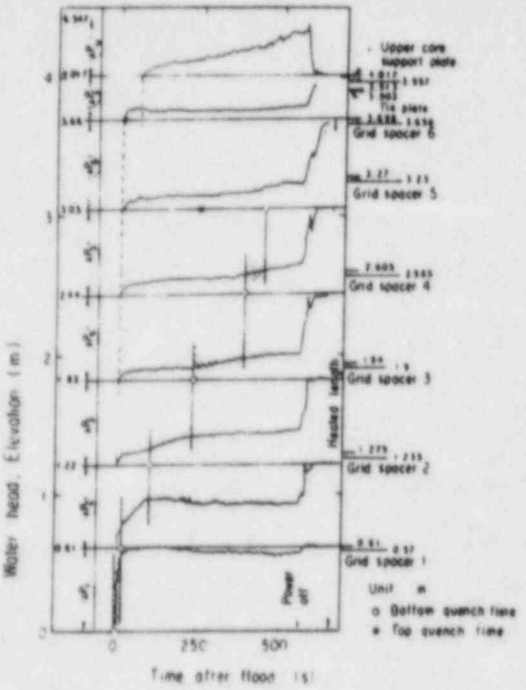

Fig. 14 Comparison of the differential pressures at whole core, end box region and upper plenum

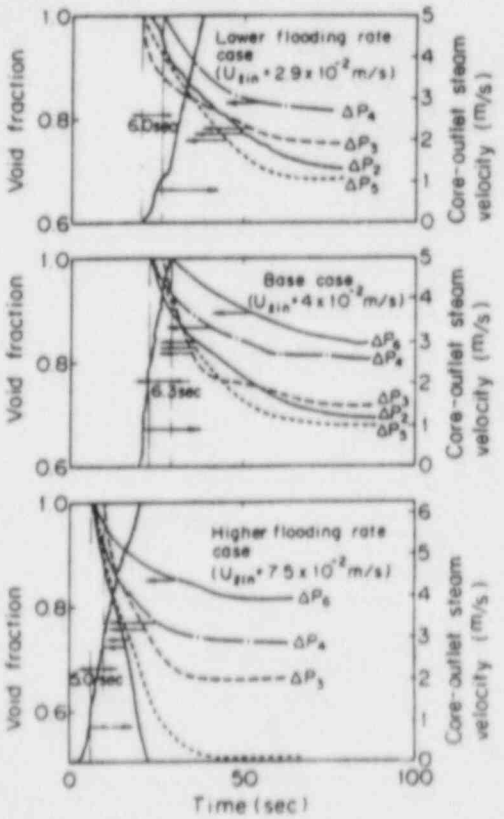

Fig. 15 Void fraction transients in core

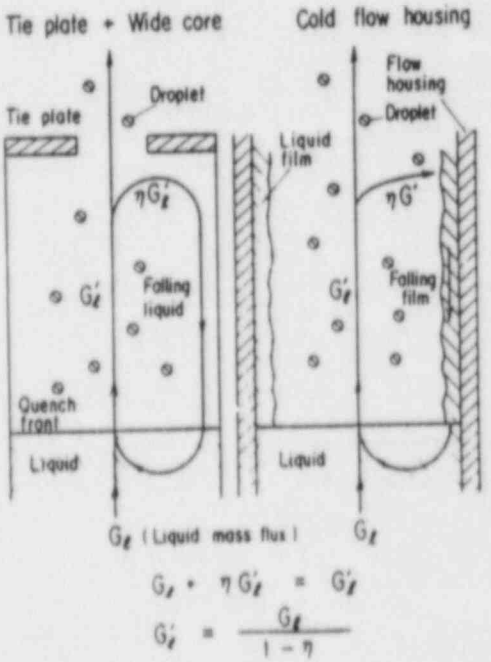

Fig. 16 Reflux model in core

APPENDIX 1

HEAT TRANSFER COEFFICIENT AND VOID FRACTION CORRELATIONS FOR SLUG FLOW

$$h_t = h_{sat} \times (1-\alpha)^{1/4} + h_R \times (1-\alpha)^{1/2}$$

$$h_{sat} = 0.94 \left(\lambda_l^3 \rho_g \rho_l H_{fg} g / L_0 \mu_l \Delta T_{sat} \right)^{1/4}$$

$$h_R = E \epsilon \left(T_w^4 - T_{sat}^4 \right) / \Delta T_{sat}$$

$$\alpha = \left\{ 1 + (U_{go} + U_{lo}) / \Delta U - \left(1 + 2 (U_{lo} - U_{go}) / \Delta U + (U_{go} + U_{lo})^2 / \Delta U^2 \right)^{1/2} \right\} / 2$$

$$\Delta U = U_{go} / \min (\alpha_{ych}, \alpha_{LM})$$

$$\alpha_{ych} = 0.925 \left(\rho_g / \rho_l \right)^{0.239} \left(U_{go} / U_{bcr} \right)^a$$

$$U_{bcr} = 1.53 \left(\sigma g / \rho_l \right)^{0.25}$$

$$a = 0.67 \ (U_{go}/U_{bcr} < 1), \quad a = 0.47 \ (U_{go}/U_{bcr} \geq 1)$$

$$\alpha_{LM}^{-1} = 1 + 3 \times 0.28 \left(U_{lo} / U_{go} \right)^{0.64} \left(\rho_l / \rho_g \right)^{0.28} \left(\mu_l / \mu_g \right)^{0.07}$$

APPENDIX 2

QUENCH MODEL

(1) $T_Q > T_{cont}$

$$U_Q^{-1} = \frac{C_p \rho \ (T_Q - T_{MT})}{Q_{eff}(1 + 0.2778 \times 10^{-4} \Delta T_{sub}{}^3)} = f(T_{MT})$$

(2) $T_{MH} < T_Q < T_{cont}$

$$U_{Q1}^{-1} = f\ (T_{MT})$$

$$U_{Q2}^{-1} = f\ (T_{MH})$$

$$U_Q^{-1} = \left(\frac{T_Q - T_{MH}}{T_{cont} - T_{MH}}\right) U_{Q1}^{-1} + \left(\frac{T_{cont} - T_Q}{T_{cont} - T_{MH}}\right) U_{Q2}^{-1}$$

(3) $T_Q < T_{MH}$

$$U_Q^{-1} = 0$$

$$Q_{eff} = Q_{eff}(p = 4\ kg/cm^2) \times (0.2209p + 0.1163)$$

$$Q_{eff}(p = 4\ kg/cm^2) = 2.19 \times 10^6\ (Kcal/m^2 \cdot hr)$$

$$T_{cont} = T_{MT} + (\lambda_1 \gamma_1 C_{p1})^{1/2} / (\lambda_c \gamma_c C_c)^{1/2} \times (T_{MT} - T_1)$$

RELAP5/MOD2 POST-CHF HEAT AND MASS TRANSFER MODELS[a]

J. C. Lin, C. C. Tsia, V. H. Ransom, G. W. Johnsen
EG&G Idaho, Inc.
Idaho Falls, Idaho 83415

ABSTRACT

RELAP5/MOD2 is a new version of RELAP5 containing improved modeling features that provide a generic pressurized water reactor transient simulation capability. In particular, the nonequilibrium modeling capability has been generalized to include post critical heat flux (CHF) conditions which occur in severe core damage accidents and large break loss-of-coolant accident. The objective of this paper is to describe the post-CHF wall heat transfer and interphase mass transfer model in RELAP5/MOD2 and to report the developmental assessment results using separate effects experiments.

The post-CHF wall heat transfer and interphase mass transfer in RELAP5/MOD2 is mechanistically modeled. The developmental assessment results show that the post-CHF wall heat transfer and the interphase mass transfer are properly modeled. For further modeling improvements, new data with local void fraction or phasic velocity measurement are needed.

NOMENCLATURE

A	Heat transfer area (m^2)
C_p	Heat capacity (kJ/kg-K)
D_e	Hydraulic diameter (m)
d	Droplet diameter (m)
H	Heat transfer coefficient time area/volume (W/m^3-K)
h_{fg}	Latent heat (kJ/kg)
h	Enthalpy (kJ/kg) or heat transfer coefficient (W/m^2-K)
k	Thermal conductivity (W/m•K)
Nu	Nusselt number
P	Pressure (MPa)
Pr	Prandtl number
Q	Heat per unit volume (W/m^3)
q	Heat flux (kW/m^2)
Re	Reynolds number

a. Work supported by the U.S. Nuclear Regulatory Commission, Office of Nuclear Regulatory Research Under DOE Contract No. DE-AC07-76ID01570.

T	Temperature (k)
ΔT	Temperature difference between the wall temperature and saturation temperature (K)
v	Velocity (m/s)
α	Void fraction
ρ	Density (kg/m^3)
σ	Surface tension (N/m) or Stefan-Boltzmann constant (W/m^2-K^4)
ε	Gray-body factor
Γ	Volumetric vapor generation rate (kg/m^3-s)
μ	Viscosity (kg/m-sec)

Subscripts

d	Droplet
f	Liquid
g	Vapor
id	Droplet side interface
if	Liquid side interface
ig	Vapor side interface
s	Saturation
sat	Saturation
w	Wall

Superscripts

*	Local condition

INTRODUCTION

RELAP5/MOD2[1] is a new version of the RELAP5 thermal hydraulic computer code[2,3] containing improved modeling features that provide a generic pressurized water reactor (PWR) transient simulation capability. In particular, the nonequilibrium modeling capability has been generalized to include the conditions which occur in severe core damage accidents and large break loss-of-coolant accidents (LOCAs). During these accidents the fuel rods in the reactor core are exposed to superheated steam and the fuel rod surface temperature is at a temperature beyond the critical heat flux (CHF) temperature limit. The objective of this paper is to present the post-CHF heat and mass transfer models in RELAP5/MOD2 and an assessment of the models using the data from

separate effects experiments, and to offer recommendations on the need for further modeling improvement.

The hydrodynamics in RELAP5/MOD2 are represented by a one-dimensional transient, two-fluid (nonhomogeneous), two energy equations, nonequilibrium model.[1] The thermal boundary of RELAP5/MOD2 is calculated using an one-dimensional transient model and is explicitly coupled with the hydrodynamic model. The wall-to-fluid heat transfer is modeled using the boiling heat transfer regime technique which consists of selecting the heat transfer regime according to the boiling curve.[4] In particular, the wall-to-fluid heat transfer regime is divided into pre-CHF, CHF, and post-CHF regimes. A detailed description of the wall-to-fluid heat transfer and the interphase mass transfer in the post-CHF regime is presented in the following sections.

POST-CHF HEAT TRANSFER MODEL

The post-CHF heat transfer regime consists of transition film boiling, film boiling, and single phase vapor convective heat transfer. The two energy formulation used in RELAP5/MOD2 requires partitioning the wall-to-fluid heat transfer into liquid and vapor components. In RELAP5/MOD2, the partitioning is mechanistically modeled according to the contacted area between the wall and each phase, that is

$$Q_{wf} = h_{wf} A_w F_L (T_w - T_f)/V \qquad (1)$$

$$Q_{wg} = h_{wg} A_w (1 - F_L)(T_w - T_g)/V \quad , \qquad (2)$$

where F_L is the fraction of the wall contacted by liquid.

In the transition heat transfer regime, a mechanistic heat transfer model developed by Tong and Young[5] is adapted in RELAP5/MOD2. The model assumes that the wall-to-fluid heat transfer is due to both transition film boiling and film boiling heat transfer. The liquid contact area is modeled using the co-relation developed by Chen[6] which is an exponential function of the square root of the temperature difference between the wall temperature and the saturation temperature corresponding to the local system pressure. The final wall to liquid and wall to vapor heat transfer is computed as:

$$Q_{wf} = \{q_{crit} A_w \exp(-\omega \Delta T_{sat}) + (1 - \alpha) A_w \sigma_f (T_w^4 - T_f^4) B\}/V \qquad (3)$$

$$Q_{wg} = \{q_{VC} A_w [1 - \exp(-\omega \Delta T_{sat})] + \alpha A_w \sigma_g (T_w^4 - T_g^4) B\}/V \qquad (4)$$

where q_{crit}, q_{VC}, and B are the critical heat flux, the convective heat flux, and the Boltzmann constant, respectively. The critical heat flux, q_{crit}, in the above equations is calculated using the Biasi CHF correlation when the mass flux is greater than 200 kg/m^2-s and a modified Zuber correlation[8] when the mass flux is less than 100 kg/m^2-s. A linear interpolation with respect to mass flux is used to evaluate the critical flux when the mass flux is between 100 and 200 kg/m^2-s. The ω in the above equations is a correlation parameter given in Reference 6. The convective heat flux, q_{VC}, is evaluated by the Dittus-Boelter[9] correlation.

In the film boiling regime, a mechanistic heat transfer model developed by Forslund and Rohsenow[10] is modified and used in RELAP5/MOD2. The model assumes that the

wall-to-fluid heat transfer consists of a film boiling heat transfer in the sublayer close to the wall, and a dispersed droplet film boiling heat transfer in the bulk fluid. The wall heat transfer area contacted by the liquid is a linear function of the local void fraction. The resulting wall to liquid and wall to vapor heat transfer are

$$Q_{wf} = (1 - \alpha)[A_w h_{Bromley\text{-}Pomeranz}(T_w - T_s) + A_w \epsilon_{wf}(T_w^4 - T_s^4)B]/V \quad (5)$$

$$Q_{wg} = \alpha[A_w h_{Dittus\text{-}Boelter}(T_w - T_g) + A_w \epsilon_{wg}(T_w^4 - T_g^4)B]/V \quad (6)$$

where $h_{Bromley\text{-}Pomeranz}$ and $h_{Dittus\text{-}Boelter}$ are the heat transfer correlation developed by Bromley and Pomeranz given in Reference 11 and by Dittus and Boelter,[9] respectively and where ϵ_{wf} and ϵ_{wg} are the liquid and vapor gray-body factor calculated using the model developed by Sun[12] for droplet radiation in superheated vapor.

MASS TRANSFER MODEL

In the post-CHF regime, the interphase mass transfer in RELAP5/MOD2 is modeled in accordance with the physical process, heat transfer process, and flow regime. After the physical and heat transfer process is decided, a flow regime map based on the work of Taitel and Dukler[13] is used for selecting the interfacial area correlation developed by Ishii.[14]

The basic model in RELAP5/MOD2 assumes that the interphase mass transfer occurs both at the wall and in the bulk fluid, that is

$$\Gamma = \Gamma_{wall} + \Gamma_{bulk} \quad (7)$$

In the post-CHF regime, the interphase mass transfer at the wall is calculated from the wall to liquid heat transfer. It is assumed that the wall to liquid heat transfer is used to vaporize the liquid in the sublayer close to the wall and to superheat the vapor. The final mass transfer at the wall is

$$\Gamma_{wall} = \frac{Q_{wf}}{h_{fg}(1 + 0.5\, C_{p_g} \Delta T_{sat}/h_{fg})} \quad (8)$$

where Q_{wf} is calculated from the wall to liquid heat transfer given by Equation (3) or Equation (5).

The interphase mass transfer in the bulk fluid is modeled according to the heat transfer mechanism at the interface and using the energy balance at the interface to evaluate the net mass transfer. The resulting formulation is

$$\Gamma_{bulk} = \frac{Q_{if} + Q_{ig}}{h_g^* - h_f^*} \quad (9)$$

where Q_{1f} and Q_{1g} are the liquid to interface and the vapor to interface heat transfer respectively, and where h_f^* and h_g^* are the local liquid and vapor enthalpies. The local enthalpy is used in Equation (9) to satisfy the second law of thermodynamics.

In the post-CHF regime, the liquid to interface heat transfer is modeled as:

$$Q_{1f} = H_{1f}(T_s - T_f) \tag{10}$$

where

$$H_{1f} = \frac{6\ (1 - \alpha)}{d_d^2}\ k_f\ Nu_{1d} \tag{11}$$

$$Nu_{1d} = 10^5 \tag{12}$$

and where Nu_{1d} is the Nusselt number for the droplet. In the post-CHF regime, it was determined by Chen[6] that the droplet temperature is at saturation temperature corresponding to the local pressure. Therefore, a large Nusselt number is used in Equation (10) to drive the liquid temperature toward the saturation temperature. The vapor to interface heat transfer consists of the convective heat transfer to the liquid droplet in the superheated vapor and the convective heat transfer at the sublayer near to wall. The convective heat transfer to the liquid droplet in superheated vapor developed by Lee and Reley[15] is adapted in RELAP5/MOD2. Therefore, the vapor to interface heat transfer for the bulk fluid can be written as:

$$Q_{1g} = H_{1g}(T_s - T_g) \tag{13}$$

where

$$H_{1g} = \frac{6(1 - \alpha)}{d_d^2}\ k_g(2.0 + 0.74\ Re_d^{0.5}\ Pr_g^{0.33})$$

$$+ 0.023\ Re_g^{0.8}\ k_g\ \frac{\alpha^{0.5}}{D_e^2} \tag{14}$$

$$Re_d = \frac{\rho_g d_d |v_g - v_f|}{\mu_g} \tag{15}$$

and where Re_d is the Reynolds number for the droplet. It should be noted that the interfacial area for the droplet in the sublayer near to the wall proportional to the square root of the local void fraction as suggested by Ishii.[14]

DEVELOPMENTAL ASSESSMENT RESULTS

Data from the experiments conducted by Bennett,[16] Chen,[17] and Gottula,[18] were used to assess the post-CHF heat transfer and interphase mass transfer modeling. The Bennett experiment also provided data needed for assessing the CHF modeling in RELAP5/MOD2.

The Bennett heat tube experiment were conducted using a vertical 1.26 cm diameter tube that was electrically heated. Water at a pressure of 6.9 MPa flowed upward in the tube. The Bennett experiments were simulated by using a pipe having 32 vertical volumes 31 junctions and two time dependent volumes to provide the inlet and outlet boundary conditions. The heat generated by electric power in the test section was modeled using 32 heat slabs and the initial and boundary conditions were input to RELAP5/MOD2.

A comparison of the calculated wall temperature and the Bennett post-CHF data for the low flow and low power test is shown in Figure 1. A similar comparison is shown in Figure 2 for the high flow and high power test. In general, the RELAP5/MOD2 calculated wall temperature profile and CHF location are in very good agreement with the data for both the high flow, high power and low flow, low power cases.

Since there were no vapor temperature measurements made in the Bennett experiments, the Chen experiments were used to assess the mass transfer modeling in RELAP5/MOD2. The Chen post-CHF experiments were conducted using the Lehigh University facility. The test section consisted of a vertical tube with a 1.41 cm inside diameter and 150 cm in length. The tube was heated by passing an electric current through it. The wall temperatures were measured at various elevations and the vapor temperature was measured by aspirating steam probe located close to the exit of the tube. The RELAP5/MOD2 model for the Chen heated tube experiment consisted of a pipe having 15 vertical volumes and 14 junctions for the test section, a pipe of six vertical volumes and five junctions for the heat bank, and a pipe of four vertical volumes and three junctions for the riser. The heat bank and riser were in parallel and were connected at the bottom. The riser was located immediately below the test section and the outlet of the riser was connected to the inlet of test section. The reason of simulating the heat bank and riser was to obtain a stable flow condition at the inlet of the test section. The heat generated by the electric power in the test section was modeled by 15 heat slabs. The test initial and boundary conditions were input to the RELAP5/MOD2 code.

Comparison of calculated wall and steam temperatures with measured data are shown in Figures 3 and 4 for low inlet equilibrium quality (X_e = 0.066) and high inlet equilibrium quality (X_e = 0.58) tests, respectively. In both cases, the calculated wall temperatures are higher than the measured data at lower elevations of the test section.

For the high inlet quality test, the calculated steam temperature is a little bigger than the 60 K uncertainty of the test data. For the low inlet quality tests, the calculated steam temperature is about 150 K lower than the data. This underprediction in steam temperature indicates that the vapor generation rate in the post-CHF regime may be too large. However, in Reference 19, Chen indicated that the post-CHF steam temperature data may not be accurate for low quality tests and suggested that the new data presented in Reference 19 should be used. Further assessment of the post-CHF interfacial mass transfer in RELAP5/MOD2 is underway using the new data.

The experiments of Gottula et. al. were conducted at the Idaho National Engineering Laboratory (INEL). The test section consisted of a vertical Inconnel-625 tube with a 15.39 mm inside diameter, 1.83 mm wall thickness and 213.36 cm in length. The tube was heated by passing an electric current through it. The wall temperatures were measured

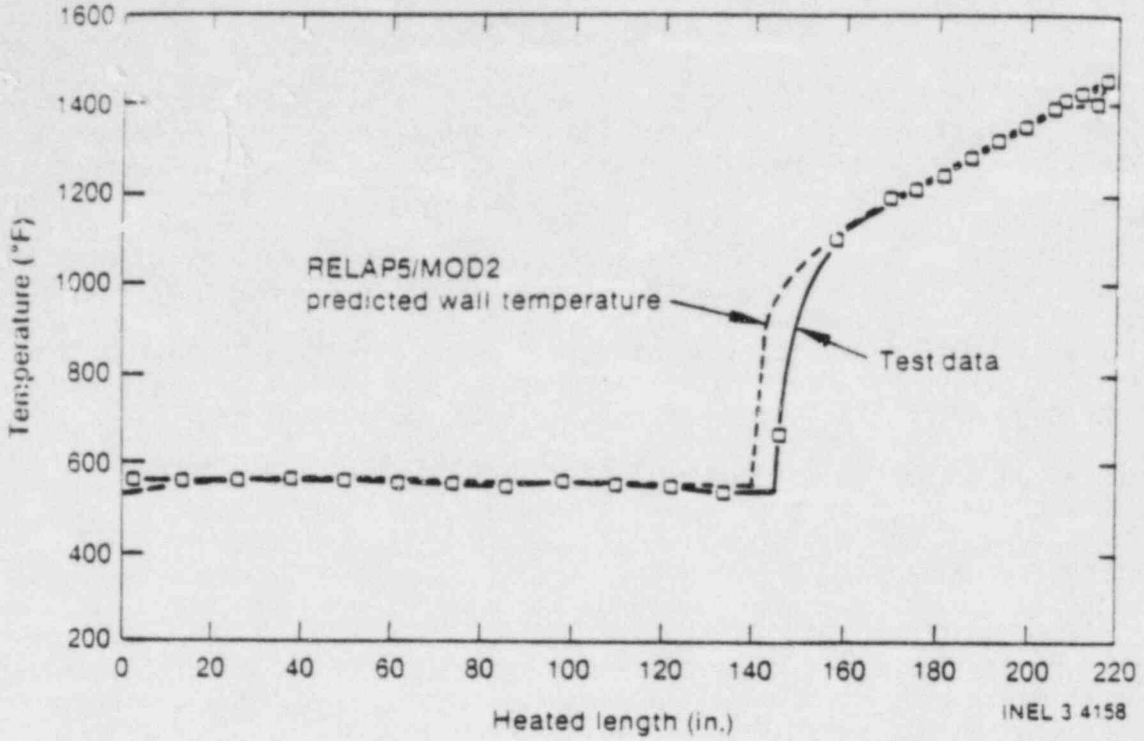

Fig. 1 Comparison of measured and calculated axial wall temperature profiles (Bennett's experiment Test Run 5358).

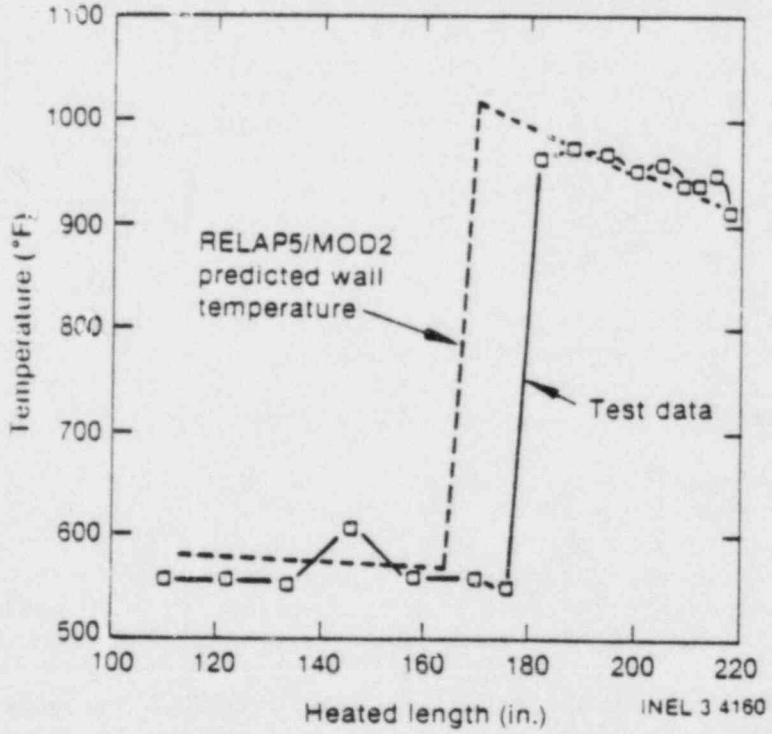

Fig. 2 Comparison of measured and calculated axial wall temperature profiles (Bennett's experiment Test Run 5394).

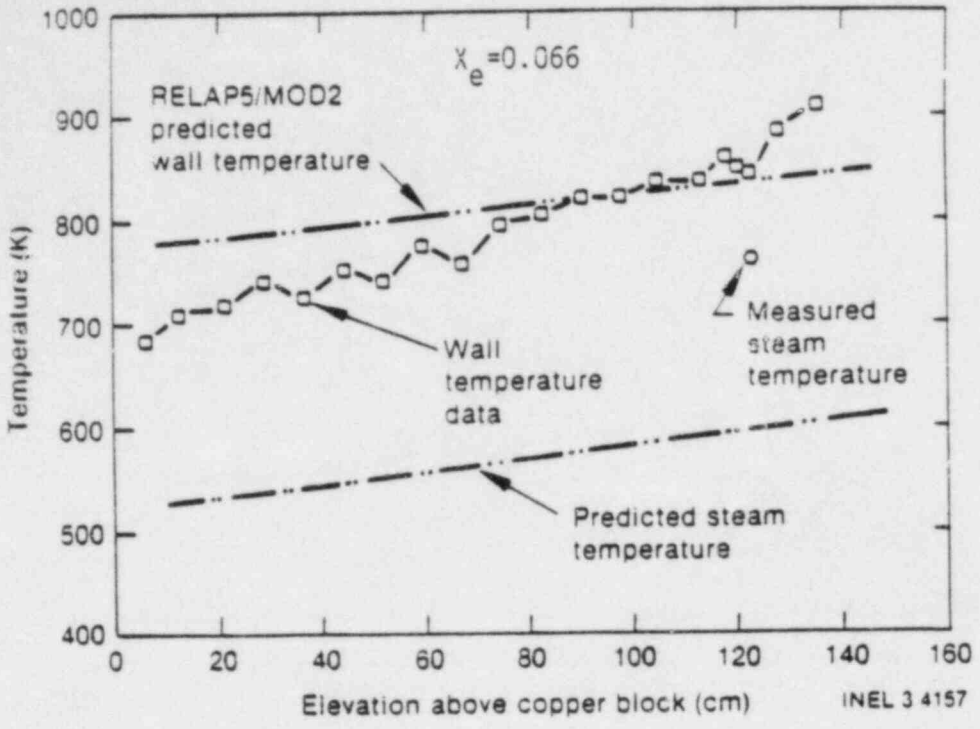

Fig. 3 Comparison of measured and calculated wall and steam temperatures (Chen's experiment Test Run 174-93).

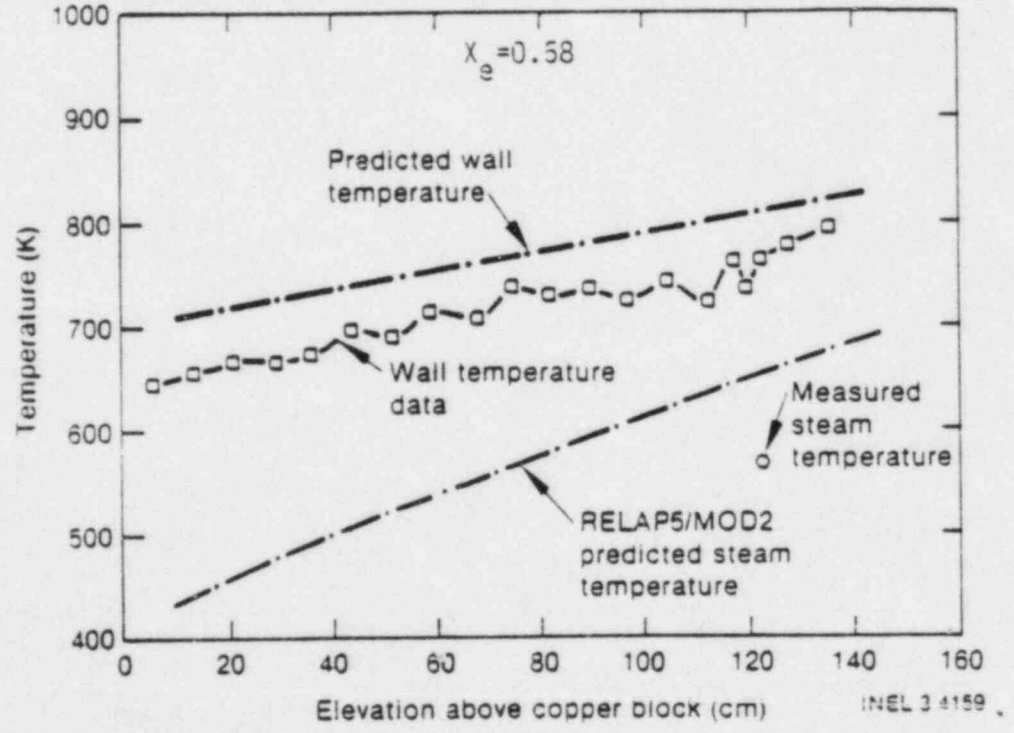

Fig. 4 Comparison of measured and calculated wall and steam temperatures (Chen's experiment Test Run 318-84).

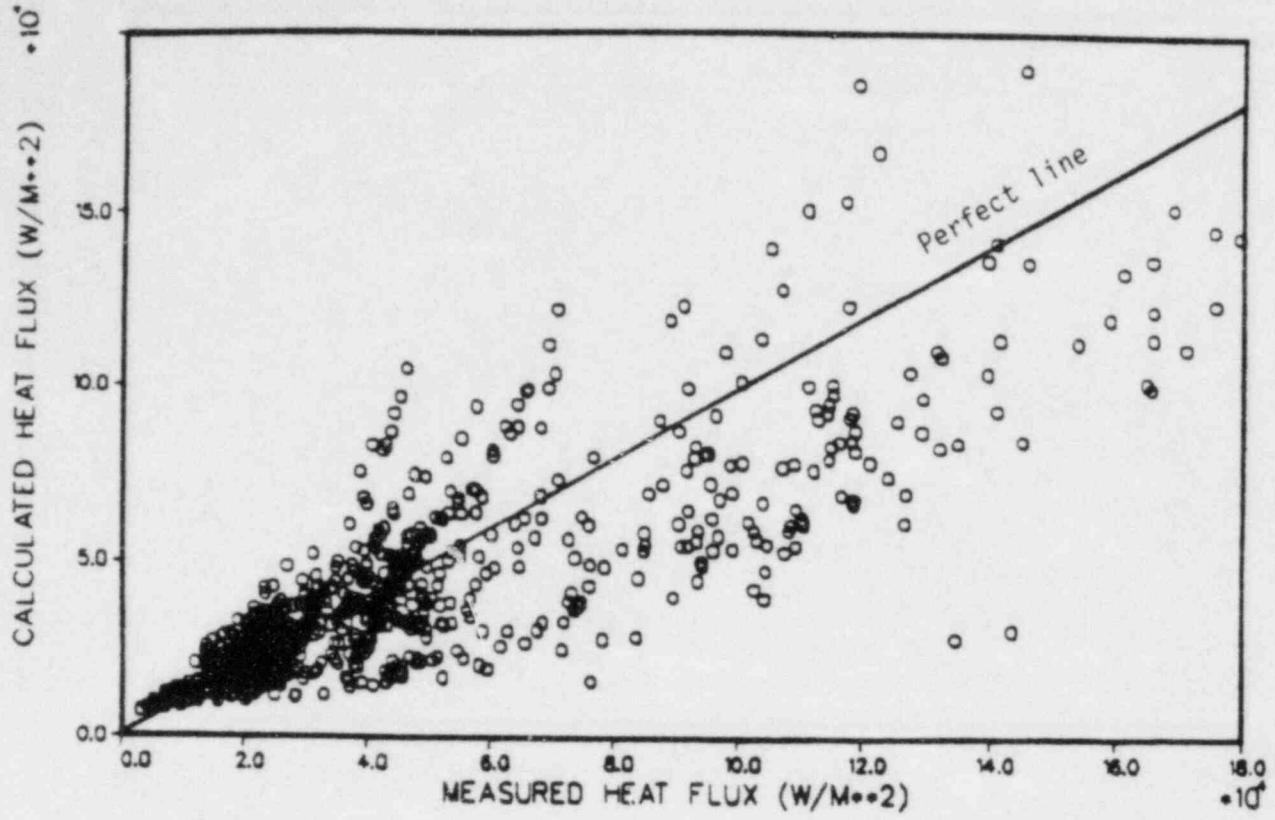

Fig. 5 Comparison of measured and calculated heat flux (INEL experiment).

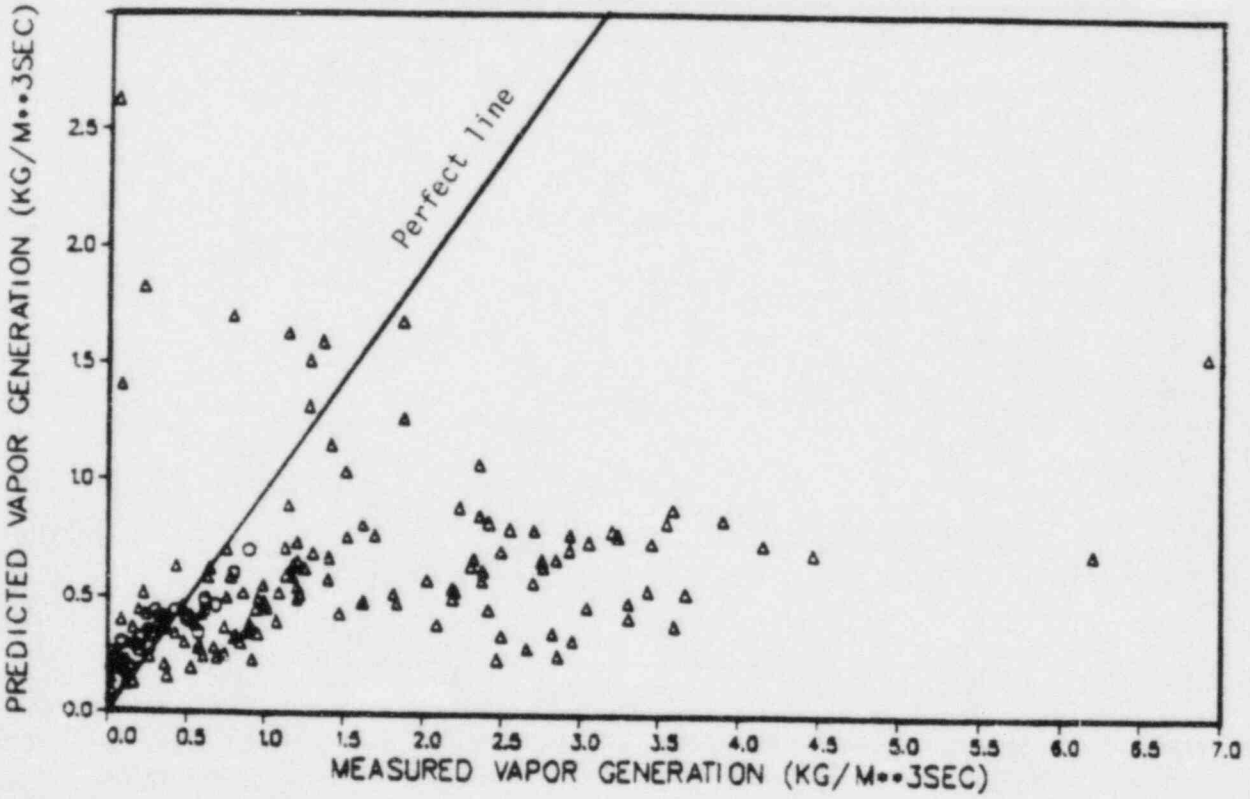

Fig. 6 Comparison of measured and calculated vapor generation rate (INEL experiment).

at various axial elevations and the vapor temperature was measured by aspirating steam probes located at the 122.92 cm, 152.4 cm, and 182.88 cm elevations. System pressure was measured at the inlet and outlet of the test section and mass flow rate was measured by an orifice located at the pipeline connecting to the test section inlet. Over seven hundred data points at high pressure and low mass flux were taken during the tests.

Since the parameters required in the RELAP5/MOD2 post-CHF heat transfer and mass transfer correlations were measured in the INEL post-CHF experiment, a driving program (using the measured data as input and the RELAP5/MOD2 post-CHF heat and mass transfer package as a subroutine) was developed to calculate the wall-to-fluid heat transfer and interphase mass transfer. Figure 5 shows a comparison of the calculated wall heat flux with the measured data. The agreement between the calculated wall heat flux and the measured data is reasonably good. However, the standard deviation from the mean value is rather large (about 34%). This large deviation resulted from the large uncertainty in data (about 25%) and from the homogeneous flow assumption for the void fraction calculation during the data reduction. For the low flow quality condition, the slip ratio (the ratio of liquid velocity to vapor velocity) calculated by RELAP5/MOD2 for the Chen experiment, which is similar to this experiment, ranges from 2 to 5. Therefore, the homogeneous flow assumption for the void fraction calculation is very questionable. Figure 6 shows the comparison of the calculated vapor generation rate with the measured data. Again, the calculation vapor generation rate is in reasonably good agreement with data but the standard deviation is large.

CONCLUSIONS

In conclusion, the post-CHF wall heat transfer and interphase mass transfer in RELAP5/MOD2 are mechanistically modeled to accommodate the two energy formulation, which is required for accurately simulating the behavior of highly nonequilibrium PWR LOCAs involving post-CHF heat transfer with highly void systems. The developmental assessment using separate effects experiments shows that the post-CHF wall heat transfer and interphase mass transfer are properly modeled for the range of conditions tested. The comparison of the calculated wall heat flux and the measured data from the INEL experiment shows that the standard deviation from the mean is large (34%). The large standard deviation resulted from the large data uncertainty and the homogeneous flow assumption for the void fraction calculation during the data reduction. This is considered a poor assumption for the low flow quality conditions.

The steam temperature measurement in the Chen and INEL experiments provided data for modeling the nonequilibrium behavior in the post-CHF regime. However, the local void fraction or phasic velocity need for modeling the nonhomogeneous behavior in the post-CHF regime was not measured. For further modeling improvement, new data with local void fraction or phasic velocity measurement are needed.

REFERENCES

1. V. H. Ransom et al., RELAP5/MOD2 Code Manual, EGG-SAAM-6377, September 1983.

2. V. H. Ransom et al., RELAP5/MOD0 Code Description, CDAP-TR-0957, Idaho National Engineering Laboratory, May 1978.

3. V. H. Ransom et al., RELAP5/MOD1 Code Manual, NUREG/CR-1826, EGG-2070, March 1982.

4. F. Kreith, Principles of Heat Transfer, Intext Press Inc., 1973.

5. L. S. Tong, and J. D. Young, "A Phenomenological Transition and Film Boiling Correlations," Proceedings of the 5th International Heat Transfer Conference, Vol. IV, B 3.9, Tokyo, 1974.

6. J. C. Chen et al., A Phenomenological Correlation for Post-CHF Heat Transfer, TS-774, Dept. of M. E., Lehigh University, April 1977.

7. J. G. Collier, Convection Boiling and Condensation, London: McGraw-Hill Book Company, Inc., 1972.

8. R. A. Smith and P. Griffith, "A Simple Model for Estimating Time to CHF in a PWR LOCA," Transactions of American Society of Mechanical Engineers, Paper No. 76-HT-9, 1976.

9. F. W. Dittus, and L. M. K. Boelter, "Heat Transfer in Automobile Radiators of the Tubular Type," Publications in Engineering, University of California, Berkeley, 2, pp. 443-461, 1930.

10. R. P. Forslund and W. M. Rohsenow "Dispersed Flow Film Boiling," ASME Paper Number 68-HT-44, Journal of Heat Transfer, November 1968.

11. M. L. Pomeranz, "Film Boiling on a Horizontal Tube in Increased Gravity Fields," J. of Heat Transfer, 86, 213-219, 1964.

12. K. H. Sun, J. M. Gonzalez-Santelo, and C. L. Tien, "Calculations of Combined Radiation and Convective Heat Transfer in Rod Bundles under Emergency Cooling Conditions," J. of Heat Transfer, 98, pp. 414-420, 1976.

13. Y. Taitel and A. E. Dukler, "Modeling Flow Pattern Transitions for Steady Upward Gas-Liquid Flow in Vertical Tubes," AICHE J., Vol. 26, pp. 345-354, 1980.

14. M. Ishii and K. Mishma, Study of Two-Fluid Model and Interfacial Area, NUREG/CR-1873, ANL-80-111, 1980.

15. K. Lee and D. J. Ryley, "The Evaporation of Water Droplets in Superheated Steam," Journal of Heat Transfer, November 1968.

16. A. W. Bennett, "Heat Transfer to Steam-Water Mixtures Flowing in Uniformly Heated Tubes in which the Critical Heat Flux Has Been Exceeded," AERE-R-5373, UKAEA, Harwell, 1967.

17. J. C. Chen et al., Investigation of Nonequilibrium Effects in Post-CHF Heat Transfer in a Vertical Tube, Lehigh University Report, TS-816, April 1981.

18. R. C. Gottula et al., Forced Convective, Nonequilibrium, Post-CHF Heat Transfer Experimental Data and Analysis Report, NUREG/CR-3193, February 1984.

19. D. G. Evans, S. W. Webb, J. C. Chen, Measurement of Axially Varying Nonequilibrium in Post-Critical-Heat-Flux Boiling in a Vertical Tube, NUREG/CR-3363, TS-831-1, Vols. 1 and 2, June 1983.

TRAC-BD1/MOD1 POST-DRYOUT WALL HEAT TRANSFER

by

R. W. Shumway
Idaho National Engineering Laboratory
EG&G Idaho, Inc.

1. INTRODUCTION

Recently there has become available a large amount of post-CHF data[1,2,3] which has an improved steam temperature measurement. Gottula, et al.[4] show that commonly used film boiling correlations do not predict this data well. Since the film boiling heat transfer regime strongly influence the core heatup results calculated for postulated reactor loss-of-coolant accidents, comparison of the data with reactor safety calculation techniques is important. Reference 1 compared the data with the TRAC-PD2[4] code heat transfer package calculations and this report compares the data with TRAC-BD1/MOD1[5]. PD2 is used for pressurized water reactor safety calculations and BD1 is used for boiling water reactors.

Calculation of the energy exchange rate between steam and liquid drops in the TRAC-BD1 code is performed by the Webb-Chen-Sundaram[6] correlation discussed and compared with data in Reference 1. This report, therefore, concentrates on wall heat transfer comparisons using the measured steam temperatures. A sample of a test where the steam temperature is calculated is presented at the end of the report.

Figure 1 is an example from Reference 1 which shows that the wall heat flux calculated from a commonly used correlation (Dittus-Boelter[7]) underpredicts the majority of the INEL post-CHF data. TRAC-BD1 uses a combination of correlations depending on the flow conditions and therefore has the potential to compare better with all the data than any individual correlation compared with all the data as is done in Figure 1.

2. DESCRIPTION OF TRAC-BD1 WALL HEAT TRANSFER LOGIC

TRAC-BD1 uses a combination of five correlations for predicting post-CHF wall heat flux. The total flux is:

$$q'' = h_\ell (T_w - T_\ell) + h_v (T_w - T_v) \quad (1)$$

where

q'' = wall heat flux

h_ℓ = heat transfer coefficient between wall and liquid

h_v = heat transfer coefficient between wall and vapor

T_w = wall temperature

T_v = vapor temperature

T_ℓ = liquid temperature.

The liquid heat transfer coefficient is:

$$h_\ell = (1 - \alpha)h_{BROM} \quad (2)$$

where

α = vapor void fraction

h_{BROM} = Bromley[8] coefficient.

The importance of the liquid heat transfer coefficient in this situation is increased by the fact that the driving force is $(T_w - T_\ell)$ and the liquid temperature is generally close to the saturation temperature.

The vapor heat transfer coefficient is the maximum of the Rosenhow-Choi[9] laminar flow equation:

$$h_v = 4\ k_v/D \quad (3)$$

the Dougall-Rosenhow[10] turbulent flow equation:

$$h_v = 0.023 K_v Re^{.8}\ P_r^{.33}/D \quad (4)$$

and the McAdams[11] natural convection equation:

$$h_v = 0.13\ K_v\ (G_r \cdot P_r)^{1/3}/D \quad (5)$$

where

K_v = vapor conductivity based on film temperature

D = hydraulic diameter

$$R_e = \rho_v(\alpha V_v + (1 - \alpha)V_\ell)\ D/\mu_v \quad (6)$$

ρ_v = vapor density

V_v = vapor velocity

V_ℓ = liquid velocity

μ_v = vapor viscosity

$P_r = \mu_v c_{p_v}/K_v$

C_{p_v} = vapor specific heat

The Grashof number is also based on the hydraulic diameter:

$$G_r = \rho_v^2 \, g_c \, (T_w - T_v) \, D^3/\mu_v^2 \, T_v) \qquad (7)$$

where

g_c = gravitational constant.

If the equilibrium quality is greater than one or the void fraction is greater than 0.999, the liquid velocity term is no longer used in the Reynolds number and Equation (4) is the Dittus-Boelter equation except that Dittus-Boelter used a power of 0.4 on the Prandtl number.

3. COMPARISONS WITH DATA

The average error of the Dittus-Boelter comparison shown in Figure 1 is 28% for the 766 INEL data points. The average error of the TRAC-BD1 heat transfer package is 2% for the same data set. Even though data scatter is significant, TRAC predicts through the middle of the data. There are several reasons for this improvement. Figure 3, which shows the flux error versus gas Reynolds number, reveals a considerable amount of data close to the laminar-turbulent transition. For forty-three data points, TRAC calculated that the natural convection h was larger than the forced convection h. Figure 4 illustrates the data in various TRAC heat transfer regimes. Mode 4.0, 4.1, and 4.2 are the natural convection, laminar and forced convection regimes respectively. The laminar convection h's were never larger than the other two h's. Mode 4.2 had 687 points and mode 5.8 (Dittus-Boelter equation for quality greater than 1.0 or void fraction greater than 0.999) had 31 points. Without the use of natural convection correlation, the average error rises to 3%. The big factor is the use of a vapor conductivity based on the film temperature. If TRAC correlations used a conductivity based on the bulk temperature, the overall average flux error would rise to 21%. Figure 5 shows the TRAC heat flux error versus measured vapor temperature. There is a tendency for TRAC to overpredict flux at low temperatures and underpredict at high temperatures. This skew trend is not evident when error is plotted against other parameters such as pressure, mass flux, void fraction, quality and distance from the quench front. Figure 6 shows the error versus pressure.

Void fraction was calculated by:

$$\alpha = \frac{1}{1 + \frac{\rho_v}{\rho_\ell} \frac{S(1 - Xa)}{Xa}} \qquad (8)$$

where

S = V_v/V_ℓ, slip

Xa = actual flow quality given by the experimenters

ρ_v = vapor density

ρ_ℓ = liquid density.

Figure 7 shows the flux error versus void fraction assuming a slip of one. All the previously given informatin is also for a slip of one. Figure 7 makes the point that this data is all very high void fraction data. If a slip of two is assumed, the points in Figure 7 shift to the left. The amount of shift is 7% for the points on the left edge and negligible for the points on the right edge of Figure 7. The average TRAC heat flux error increases to 9% when a slip of two is assumed. Based on previous TRAC calculations, the slip is believed to be somewhere between 1.5 and 2.0 for these types of tests.

A complete hot tube test system calculation is shown in Figure 8 for Lehigh University Test SN-99[2]. The test is modeled by injecting saturated water into the bottom of four TRAC cells which represent the experiment test section preheaters. Enough power is added to achieve the equilibrium quality reported by the experimenters at the test section inlet. Fourteen cells each 0.1m long represent the test section which has a specified wall heat flux boundary condition. TRAC over predicts the one steam temperature measurement and most of the wall temperature measurements. If interfacial heat transfer were larger, both the wall temperature and steam temperature would agree better with the data.

The point has already been made that void fraction influences calculated results and void measurements need to be made. Accurate high void fraction measurements are difficult but film boiling can also occur at low void fraction in rod bundles prior to rod quenching as discussed in Reference 12. An example is shown in Figure 9. The void fraction measured using gamma densitometers is shown at three bundle elevations with the corresponding measured heat transfer coefficients. Bundle inlet flow oscillations were causing void oscillations between 0.8 and 0.1 at the 115 cm elevation for many seconds prior to quenching at about 58 seconds. This would be excellent data for correlation assessment except there was considerable uncertainty in bundle inlet flow.

Another area where data is needed to help code development is the experimental conditions which result in pulsating flow. TRAC-BD1 has alternating periods of counter-current flow and co-current flow on many tests where no oscillations were observed by experimenters. The TRAC calculations for the test shown in Figure 8 was not completely stable. TRAC's calculated interfacial drag cannot be arbitrarily increased to prevent counter-current flow because it must accurately predict counter-current flow in many applications.

4. SUMMARY

A comparison of TRAC-BWR heat transfer package with 766 data points is presented. On the average, TRAC-BWR provides a better prediction of the data compared to any single correlation although there is still a large scatter in TRAC-BWR prediction. Regarding any potential changes in the TRAC-BD1/MOD1 wall heat transfer package, it is concluded that no significant improvement in the film boiling area can be made until data with better measurements are obtained and analyzed. Specifically, data is needed which has a wide range of accurately measured void fractions. Heated tube data is also needed which addresses the counter-current flow transition conditions.

REFERENCES

1. R. C. Gottula, et.al.; "Forced Convective, Nonequilibrium, Post-CHF Heat Transfer Experiment Data and Correlation Comparison Report Draft," NUREG/CR-3193, EGG-2245, January 1984.

2. R. K. Sundaram, S. M. Nijhawan, J. C. Chen; "Parametric Trends in Vapor Nonequilibrium in Post-Dryout Steam Water Flow," Institute of Thermo-Fluid Engineering & Science, Lehigh University, TS-815, August 1981.

3. D. G. Evans, S. W. Webb, J. C. Chen, "Measurement of Axially Varying Nonequilibrium in Post-Critical-Heat-Flux Boiling in a Vertical Tube," NUREG/CR-3363, TS-831-1, June 1983.

4. Los Alamos National Laboratory, "TRAC-PD2: An Advanced Best Estimate Computer Program for Pressurized Water Reactor Loss-of-Coolant Accident Analysis," LA-8709-MS, February 1981.

5. Idaho National Engineering Laboratory," TRAC-BD1/MOD1 An Advanced Best Estimate Computer Program for Boiling Water Reactor Transient Analysis," NUREG/CR-3633, EGG-2294, January 1984.

6. S. W. Webb, J. C. Chen, R. K. Sundaram, "Vapor Generation Rate in Nonequilibrium Convective Film Boiling," Proceedings of the 7th International Heat Transfer Conference. Munich, Germany, Vol. 4, p. 437.

7. F. W. Dittus, L. K. Boelter, "Heat Transfer in Automobile Radiators of Tubular Type," Publications in Engineering, U of C, Berkeley, pp. 443-461, 1930.

8. L. A. Bromley, "Heat Transfer in Stable Film Boiling," Chemical Engineering Progress, 46, May 1950, pp. 221-227.

9. W. M. Rohsenow and H. Y. Choi, Heat, Mass, and Momentum Transfer, Englewood Cliffs: Prentice-Hall, Inc., 1961.

10. R. S. Dougall and W. M. Rohsenow, Film Boiling on the Inside of Vertical Tubes with Upward Flow of the Fluid at Low Qualities, Massachusetts Institute of Technology, Mechanical Engineering, 9079-26, 1963.

11. W. H. McAdams, Heat Transmission, 3rd Ed., New York: McGraw-Hill Book Co. Inc. 1954.

12. G. G. Loomis and R. W. Shumway," Low Pressure Transient Flow Film Boiling in Vertically Oriented Rod Bundles," Nuclear Technology, Vol. 63, No. 1, October 1983, p. 151.

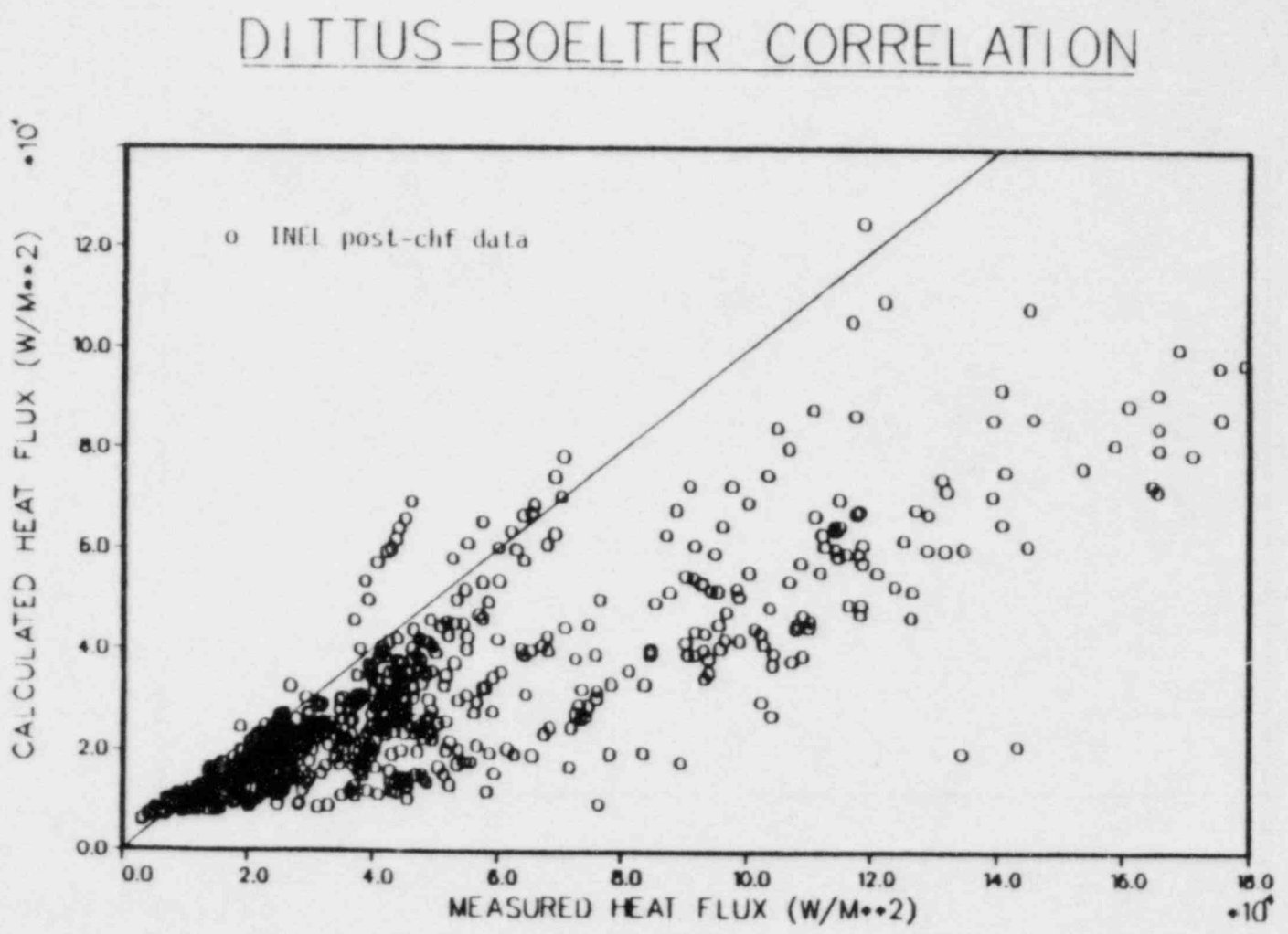

Figure 1. Dittus-Boelter heat flux versus data.

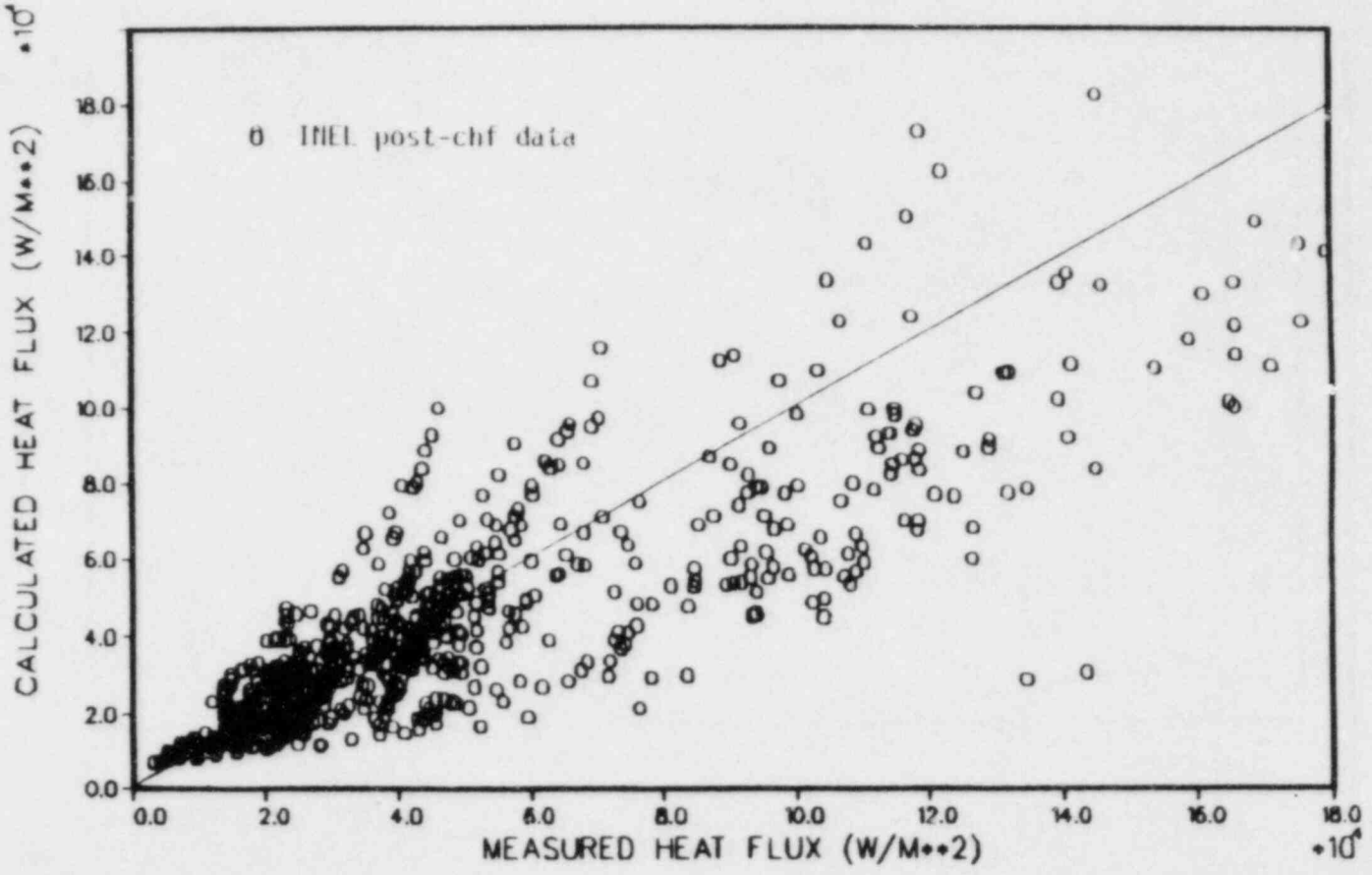

Figure 2. TRAC-BD1 heat flux versus data.

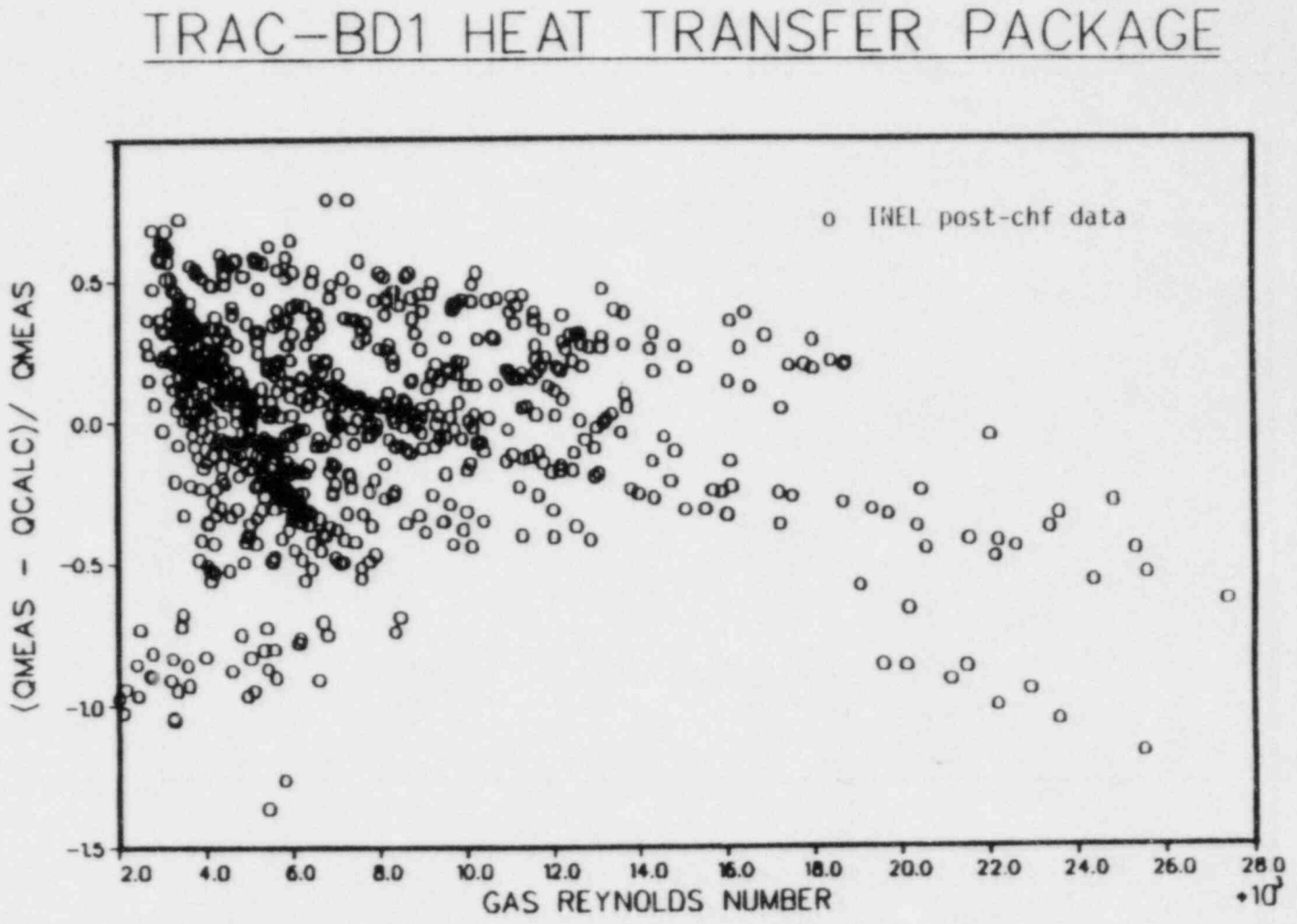

Figure 3. TRAC flux error versus gas Reynolds number.

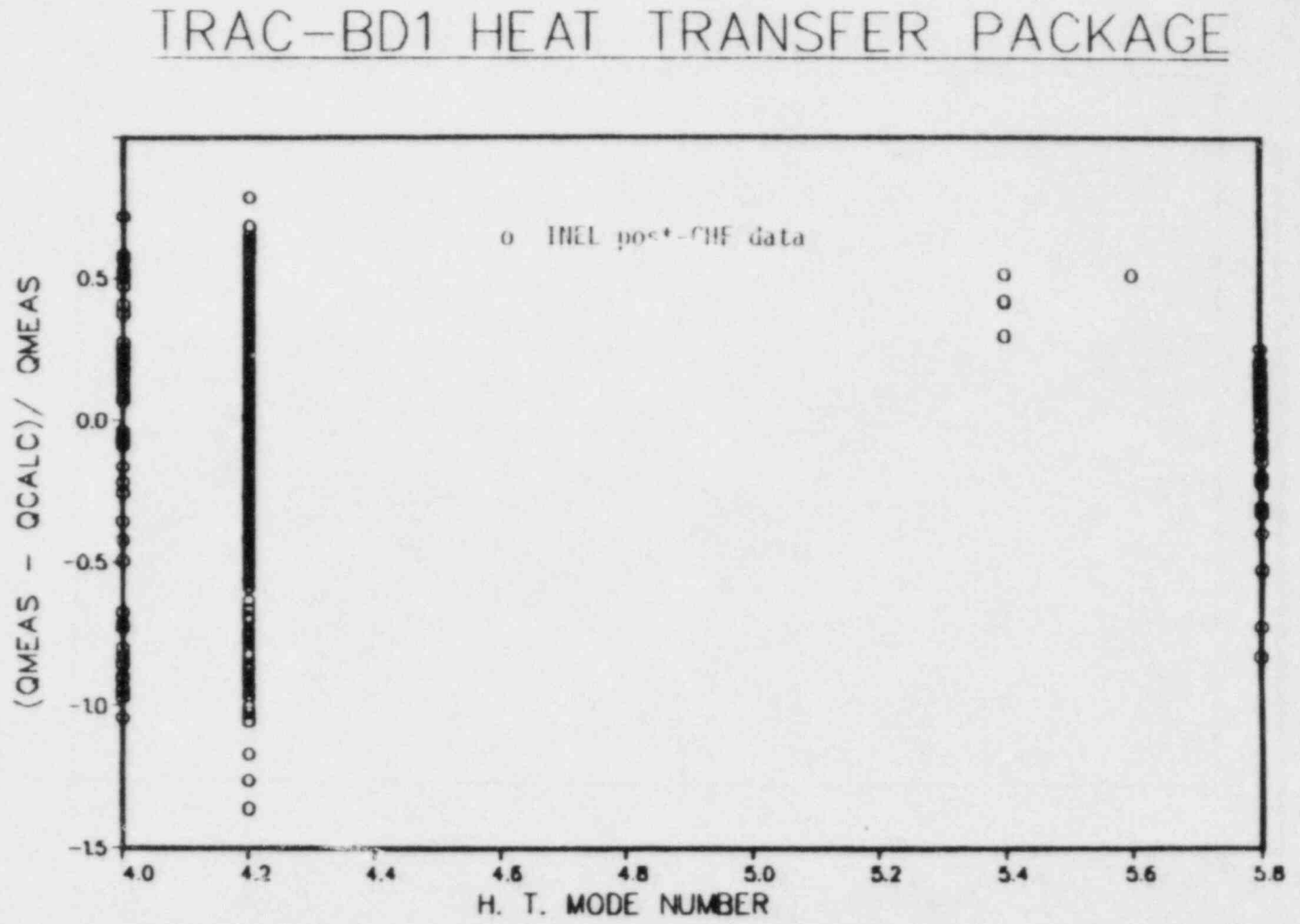

Figure 4. TRAC flux error versus heat transfer regime.

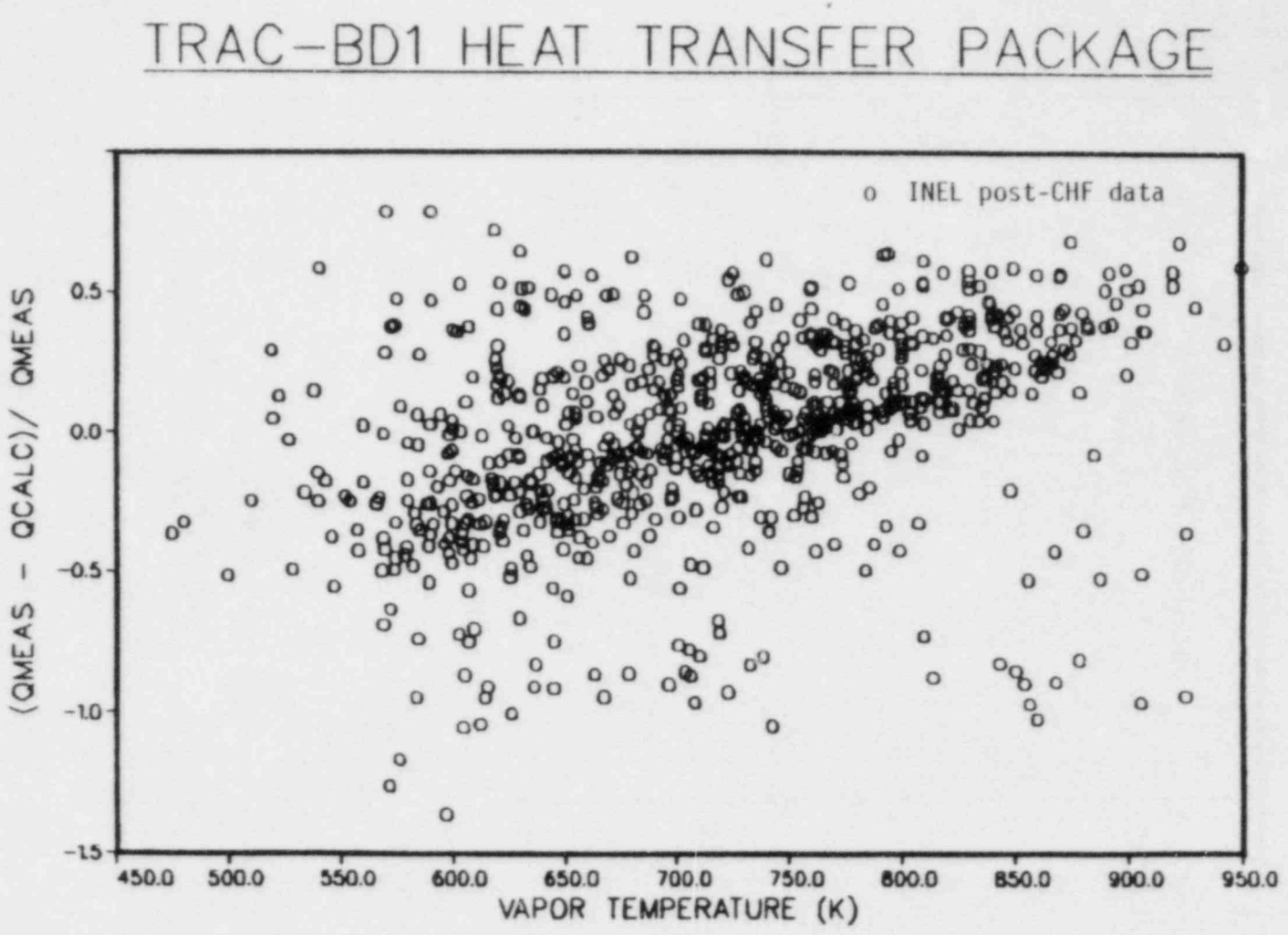

Figure 5. TRAC flux error versus measured vapor temperature.

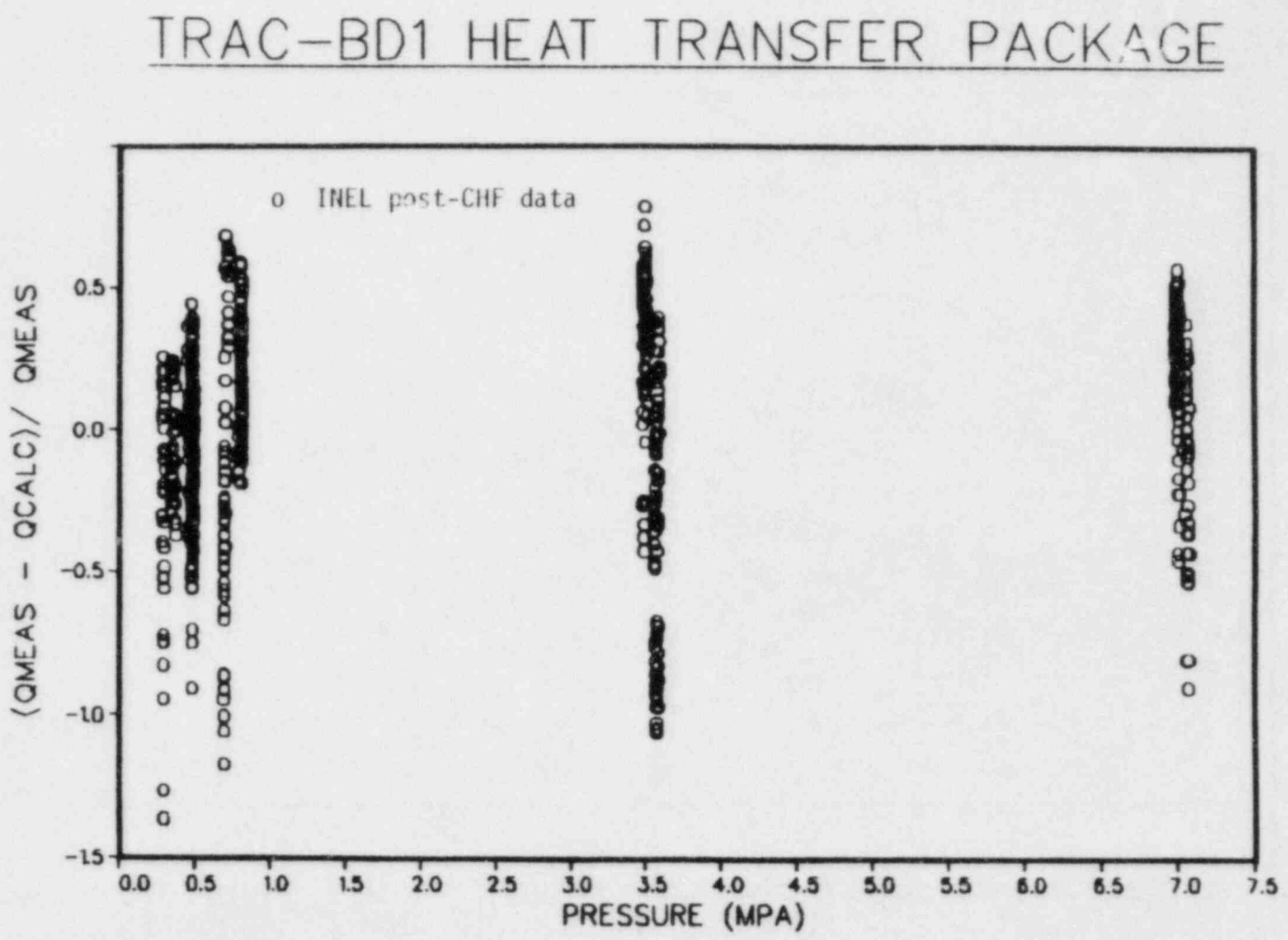

Figure 6. TRAC flux error versus pressure.

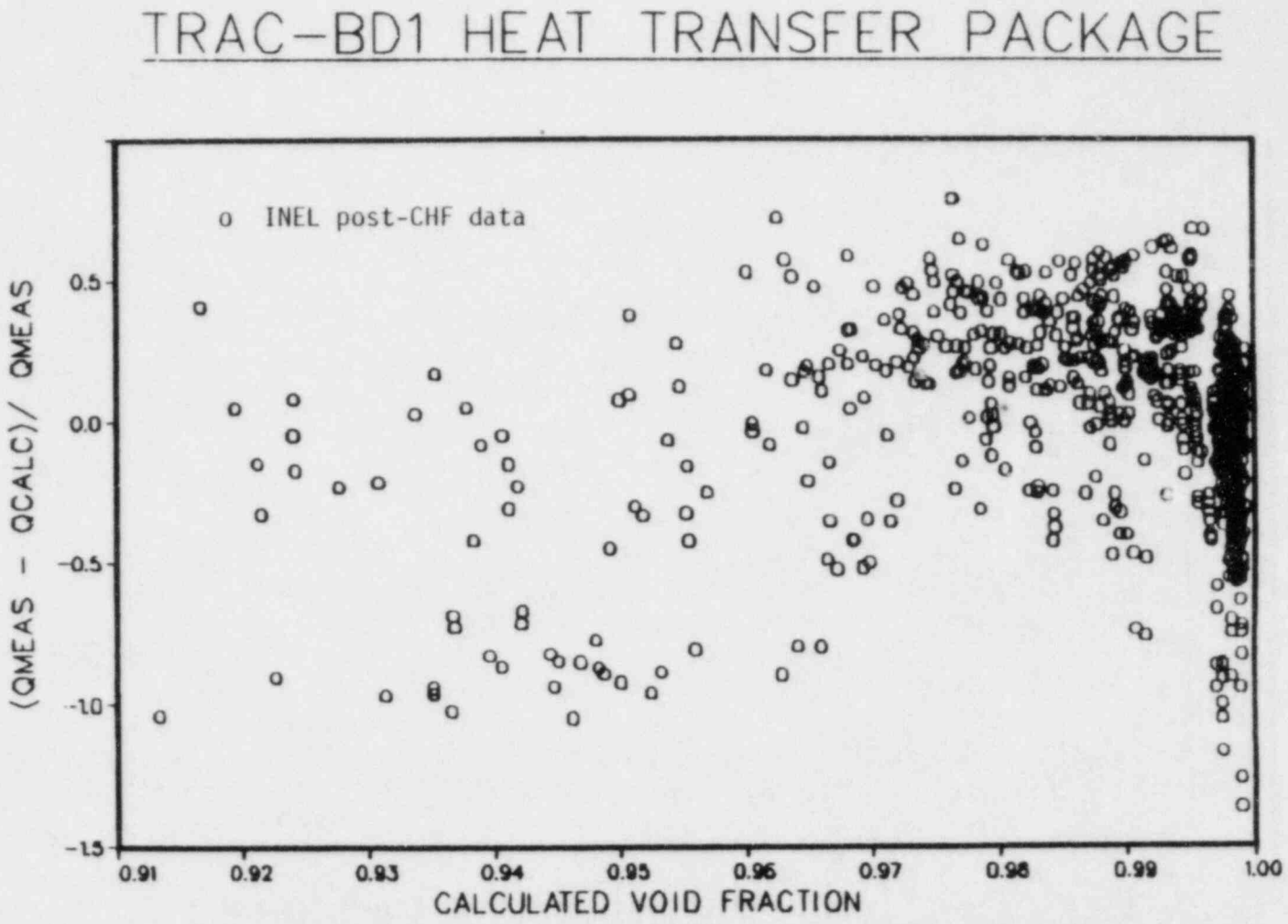

Figure 7. TRAC flux error versus void fraction.

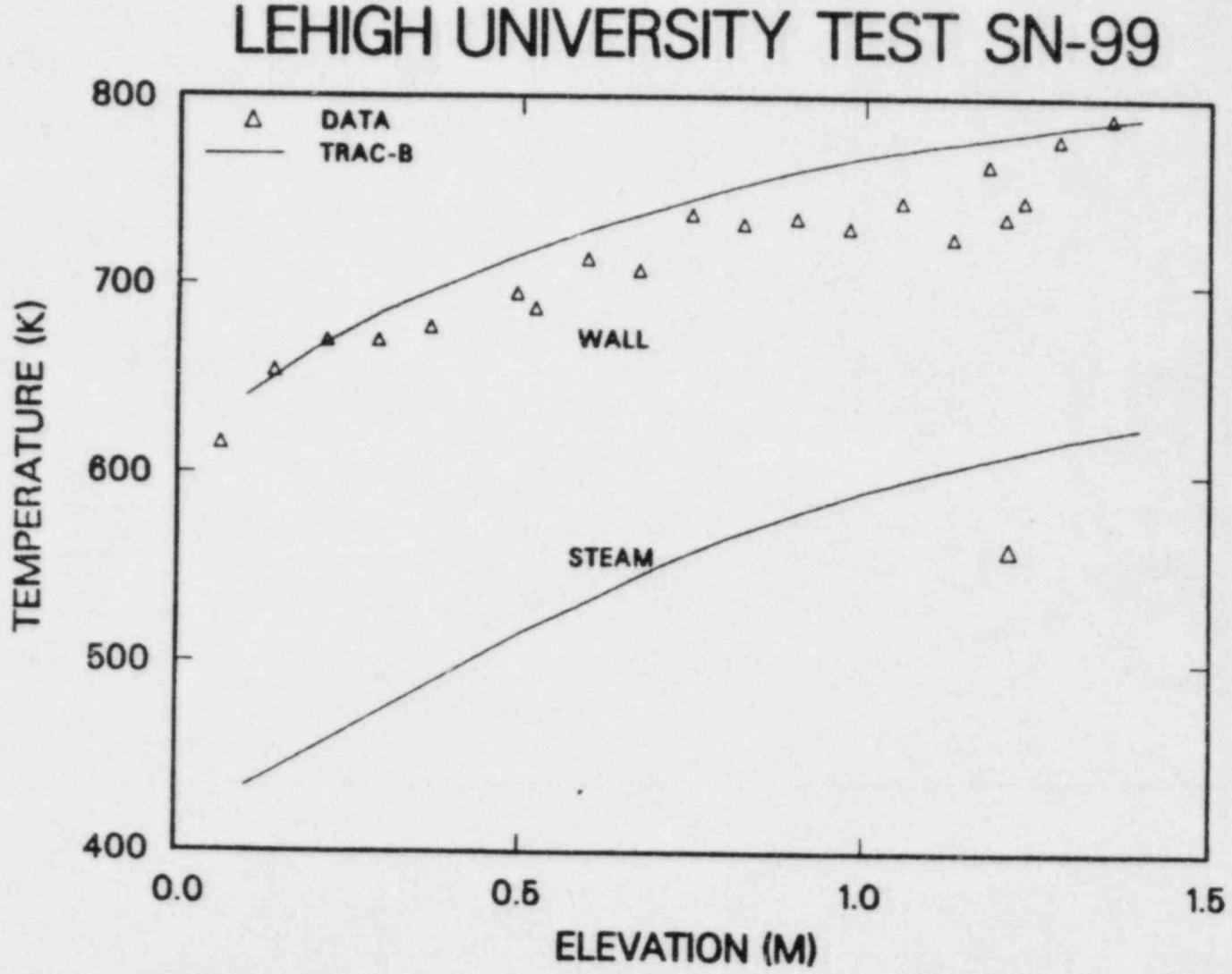

Figure 8. Lehigh University data versus TRAC-BD1.

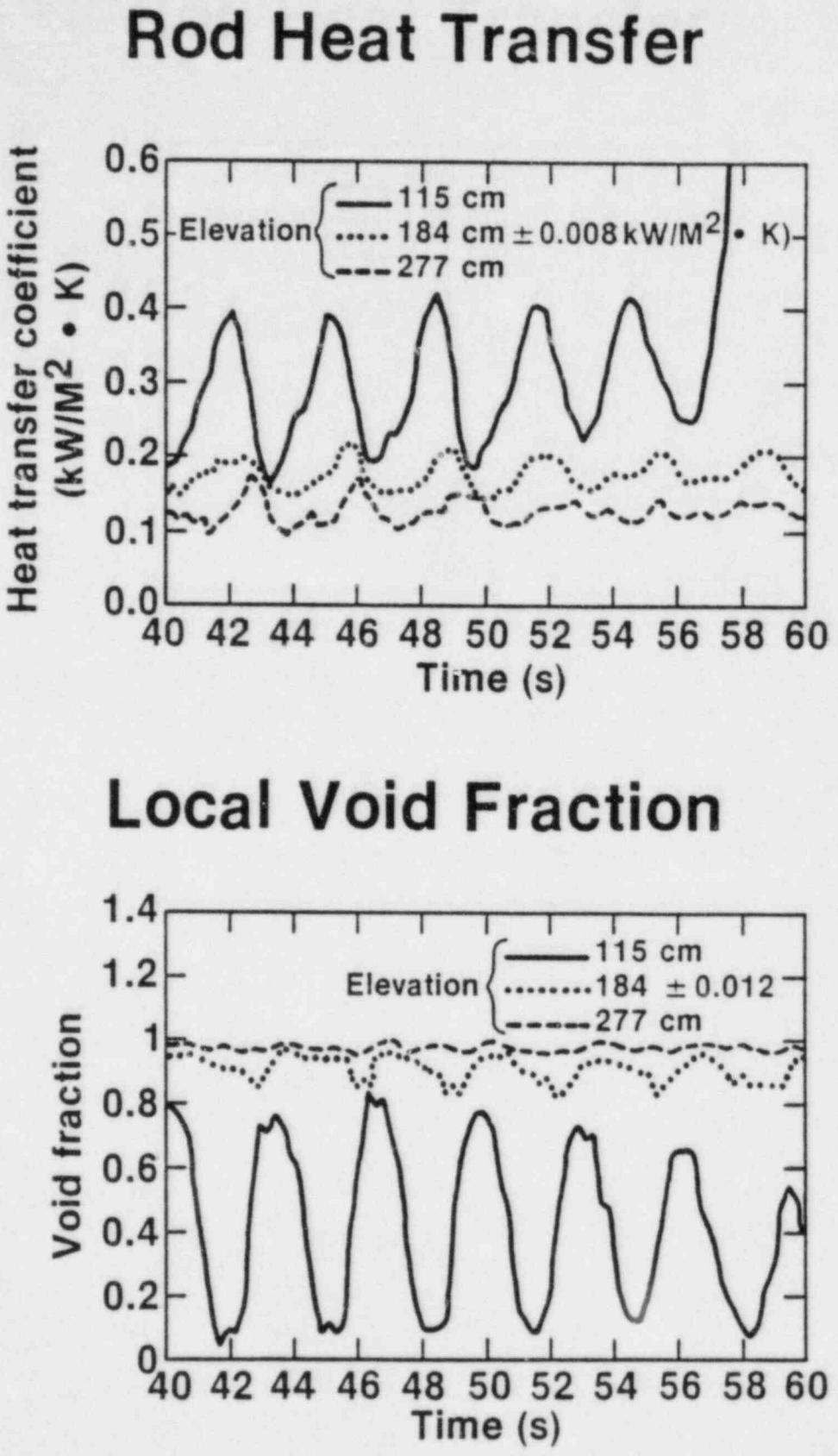

Figure 9. Semiscale measured void fractions and rod heat transfer coefficients.

Summary of Discussion in the Computer Code Modeling and Flow Phenomena Session

R. Deruaz

Service des Transferts Thermingues

Centre d'Etudes Nucleaires de Grenoble

85X 3804 Grenoble CEDEX France

Summary of the session

"COMPUTER CODE MODELING AND FLOW PHENOMENA"

and following discussion

Among the six papers included in this session, five were indeed directly related to computer code modeling and one was dealing with basic aspects of two-phase flow during reflooding.

A table is given as an attempt to present the main aspects of the works (objectives, experimental basis and computer code used by the authors as well as their main conclusions) and the main content of the discussions, both during the poster session and the plenary discussion, is summarized.

I. SUMMARY OF WORKS

Title - Author(s)	Objectives	Code(s)	Experimental basis	Main conclusions
1 - Visualisation of the reflooding of a vertical tube by dynamic radiography G. Costigan C.D. Wade	Get an insight into flow regimes and HT mechanisms in the vicinity-downstream of the quench front		600 mm long SS tube (up and downflow)	. Low reflooding velocities : liquid filament → large droplets . High reflooding velocities : flow close to the classical "inverted annular flow" picture . Downflow : liquid jet impinging the wall at various points → wall temperature oscillations . Potentiality of the technique to investigate flow patterns in the vicinity of grids and blockages
2 - Investigation of dispersed flow HT using different computer codes and HT correlations I. Vojtek	Evaluation of : - available overall correlations for prediction of : . CHF . film boiling HT - models and correlations for dispersed flow HT processes (W → L, W → V, V → L)	BRUDI-VA TRAC PF1 mod 1	25 HR bundle blowdown experiment (KWU)	. A detailed description of all HT processes is necessary (non equilibrium and nonhomogeneous description) . Partition $W \rightleftarrows {}^{L}_{V}$ is found to have no significant effect on T_W, T_V, . Chen-Vojtek is recommended for W → L . Additional work is needed for Return to Nucleate Boiling

Title - Author(s)	Objectives	Code(s)	Experimental basis	Main conclusions
3 - Reflood Analysis code REFLA Y. Murao	Description of Refla code for thermalhydraulics of a nuclear core during a reflood transient - bottom injection - . HT . quench front progression . core water accumulation (dry region)	REFLA 1D Mod 3	. CCTF . Jaeri small scale facility . Flecht (W)	Some separation of water from steam occurs in the dry region if the core is wide enough or/and cold structures are present. The new version of Refla takes into account this phenomenon through simple models and shows a more significant effect on quench front progression than on the turnaround temperatures.
4 - Relap 5 mod 2 Post CHF Heat and Mass Transfer J.C. Lin et al.	- Description of H and MT models - Developmental assessment	RELAP 5 Mod 2 (generalized non equilibrium capability of RELAP 5)	Separate effect tests on tubes: 1. Harwell 2. Lehigh university 3. Inel	. 1. Good agreement for T_W 2. T_W over estimated, T_V^W over or under estimated depending on quality 3. Reasonable agreement, but rather large standard deviations regarding - heat flux - vapour generation . Need for experiments with local void fraction measurements for any further improvements of the codes for post CHF

Title - Author(s)	Objectives	Code(s)	Experimental basis	Main conclusions
5 - Trac BD1 mod 1 Post Dry Out Wall Heat Transfer R.W. Shumway	. Description . Assessment	Trac BD1 mod 1	Separate effect tests on tubes: 1. Inel 2. Lehigh University	. Better prediction than with any single correlation but : - still large scatter - overprediction of T_W (case 2) . Improvements need : - wide range of accurately measured void fraction - countercurrent flow transition conditions
6 - Post CHF HT analysis using a two-fluid model R.K. Sundaram R.T. Fernandez	. Description . Investigation of the effect of droplet size models on post-CHF predictions	RELAP 5/YA	Separate effect tests on tubes: 1. Harwell 2. Lehigh University	. Strong interaction between the various transport processes . Good prediction of 1 with properly specified droplet size variation . Uncertainties at low flow . Need for : - mechanistic explanation of droplet size variation - assessment of the effect of droplet size distribution

2. DISCUSSION

In a (relatively) recent past, code modeling has moved from overall empirical correlations towards a detailed description of flow regimes and related heat transfer processes as soon as it appeared clearly that single correlations have really no chance to succeed in predicting the fuel thermal behaviour in a large variety of situations. Some works of this session (papers 2 and 5) confirm that point for predictions in the post-CHF regime. However problems are still raising to perform accurate predictions despite the fact that several present codes have the structure which could allow to take into account very detailed mechanisms occuring in two-phase flow. Disregarding here the classical problems of computer time and related cost which are indeed very important ones but strongly related to numerics and computer power, the discussion mainly dealt with physical aspects, according to the purpose of the meeting : with this respect, what about the needs of code developpers to improve their tool, are there experimental informations of interest which are not presently sufficiently used, what kind of studies could be performed to get lacking information...

It was agreed by most participants and demonstrated by some works presented at this meeting that needs deal with (without order of importance) :

a - Flow regime maps for which important shortcomings are remaining in codes and is asked the question of the definition of appropriate separate effect tests.

b - Droplets :
- formation and size variation which is shown to have a significant effect (paper 6), especially on vapour generation

- impact on vapour flow turbulence (see session on dispersed flow)

- size distribution for which there is still a lack of sensitivity studies : experiments leading to the knowledge of this parameter are certainly possible but is it really necessary to take it into account in codes considering the corresponding additional complexity.

- radial velocity which is known to play an important role regarding wall to liquid heat transfer but which is both quasi-impossible to determine experimentally in realistic situations and very difficult to introduce in codes.

c - Void fraction, especially in the upper range, which is of particular importance for the post-CHF regime where liquid fraction significantly influences all heat transfer processes. Existing data in dispersed flow were pointed out and used (paper 5, session 2).

Some important additional points were made with respect to experiments (already conducted or to be performed) and their use to improve computer code modeling, in particular :

- much care has to be taken defining experimental conditions regarding initial conditions for post-CHF, which are sometimes rather unrealistic and could lead to erroneous conclusions and even could explain some apparent contradictory results

- most analytical experiments, for obvious reasons of simplicity and cost, have been (are) performed in tubes and are extensively used to verify (develop) code modeling (papers 4-5-6). However the final purpose of codes is to be used for nuclear plants where significant differences occur in comparison with tubes, mainly : open and not closed geometry, external and not internal flow, presence of spacer grids which effects are known not to be only local. So there is certainly a need for well instrumented rod bundle experiments.

It was finally stated that certainly important additional knowledge was obtained in the near past regarding flow phenomena and that codes are improving their capability to take them into account. Work however is remaining to be done : sensitivity studies to define clearly where exists a lack of experimental information as well as analytical tests in the areas where the needs are already well defined.

II. Quenching Phenomena

Quench Front Movement during Reflood Phase

Yoshio MURAO

Japan Atomic Energy Research Institute

Tokai-mura, Ibaraki-ken, 319-11, Japan

Abstract

This report presents a new quench propagation model which is valid for wider pressure range than the previous model. This new model is applicable to the low temperature quench phenomena which occur at the lower temperature than the thermodynamic maximum liquid superheat and usually appear at the lower portion of the core.

For development of this model, a hydrodynamic maximum liquid superheat measured by Sakurai as a minimum film boiling temperature was introduced and an empirical correlation was derived with the PWR-FLECHT test data and so on.

This model well predicted the quench phenomena in the JAERI's small scale test.

This paper has been submitted to hte International Workshop on Post-dryout Heat Transfer, Salt Lake City, April 1-4th, 1984.

1. Introduction

The following correlation[1] has been derived for the quench front propagation velocity in the case of heat conduction controlled quench by using the PWR-FLECHT Group 1 data[2]:

$$u^{-1} = \gamma C\ (T_q - T_M)/\phi \equiv g(T_M) \quad , \tag{1}$$

where

$$\phi = 2.55 \times 10^6 (1 + 2.778 \times 10^{-5}\ \Delta T_{sub}^3)\ (W/m^2) \quad , \tag{2}$$

Tq is the apparent quench temperature, T_M is the liquid maximum superheat and ΔT_{sub} is the local coolant subcooling (K).

T_M is expressed by the following equation which was derived by approximating the thermodynamic liquid maximum superheat obtained by Groeneveld[3] using the equation of state for water:

$$T_M = 584.05 + 2.417 \times 10^{-6}\ P \tag{3}$$

The apparent quench temperature means the surface temperature at the apparent quench front explained later.

The axial power distribution in the reactor core is approximated by a chopped cosine and the clad surface temperature is lower in the lower portion of the core than that in the central portion and occasionally lower than the temperature T_M expressed in Eq. (3). In these cases Eq. (1) predicts instantaneous quench, however, sometimes film-boiling-like heat transfer appeared and an instantaneous quench did not occur. And further it must be noticed that Eq. (2) has been developed mainly based on the data taken under the pressure of 0.4 MPa.

In this paper, a correlation of quench velocity, which is valid for wide quench temperature and wide system pressure, will be derived and verified with the full-length 4 by 4 rod reflood test data.

2. Low temperature quench model

Sakurai et al.[4] studied the stable film boiling on pratinum wire and obtained the relation between the minimum film boiling temperature T_{min} and the system pressure in saturated water as shown in Fig. 1. From this figure, it is found that T_{min} approaches the thermodynamic liquid maximum superheat line (Eq. (3)) with increase of system pressure and approaches the liquid maximum superheat based on the hydrodynamic stability criteria model like Berenson's model when the system pressure approaches the atmospheric pressure. T_{min} is written as

$$T_{min} = 480 + 8 \times 10^{-5} p \quad , \tag{4}$$

where p is system pressure (Pa).

Below the thermodynamic liquid maximum superheat T_M, it is considered that the liquid occasionally contact the heating surface and generated steam ejects the liquid from the surface so that the film boiling is unstable in the range of T_M to T_{min} in the surface temperature. Accordingly the previous quench model cannot be applied to the case where the contact temperature is less than T_M. This case is termed a low temperature quench.

In this section, the low temperature quench model will be derived by analogizing from the previous quench model (termed high temperature quench). The wall temperature T_R whose contact temperature is T_M can be written as

$$T_R = T_M + \{(\lambda\gamma Cp)_\ell/(\lambda\gamma C)_c\}^{\frac{1}{2}} (T_M - T_\ell) \quad . \tag{5}$$

Since the axial temperature distribution of unqnenched region can be expressed as[1]

$$T = T_W - (T_W - T_M) \exp(-\gamma CUZ/\lambda) \quad , \qquad (6)$$

the distribution is schematically shown in Fig. 2(a) and is analogous to the temperature history of quenching on a point in axial direction. The distance and the period between appearance of dominant temperature change at the point B and the initiation of wetting on the heat transfering surface at the point A can be approximately expressed as $\lambda/(\gamma CU)$ and $\lambda/(\gamma CU^2)$ respectively. For stainless steel, it is calculated that the thermal boundary thickness is 0.42 millimeter if the quench velocity is 1 cm/second and the quench occurs in about 50 milliseconds. The wall surface temperature steelpy falls down between points B and A due to low heat conductivity and more steeply falls down between the point A and the quenched region due to rewetting. Therefore the point B is recognized as quench front experimentally. Hence the point B is defined as an apparent quench front.

In the case of high-temperature quench, the occurence of the unstable film boiling might be supposed to exist, since the surface temperature is equal to T_{min} at a point between the point A and the quenched region. However, in fact, the temperature rapidly falls down at the point A or B and the film boiling does not appear.

This can be explained in the following way: The minimum wave length of liquid-vapor interface is finite and of the order of one centimeter in the unstable film boiling, while the distance between the point B and the quenched region is of the order of one or less than one millimeter. Hence the unstable film boiling cannot exist in this case.

On the other hand, in the low temperature quench, the unstable film boiling can take place right side of the point B as illustrated

in Fig. 2(b) ①, since the wall temperature is almost same over the distance of the order of the wave length due to low heat transfer. At the point where the temperature is T_{min}, the unstable film boiling is terminated and the nucleation boiling is initiated, that is, the pcint of T_{min} is corresponding to the point of T_M (the true quench front) for the high temperature quench. Accordingly the point of T_{min} was considered to be the true quench front for the low temperature quench. Further more it was considered that another situation like the high temperature quench (illustrated in Fig. 2(b) ②) is possible, since the unstable film boiling is a probablistic phenomenon and disappear in certain probability.

Assuming that ϕ is idential as that for the high temperature quench and the probabilities that the true quench temperatures are T_M and T_{min} are $f(T_q)$ and $(1 - f(T_q))$ respectively, the following equation is derived:

$$u^{-1} = f(T_q)\, u_T^{-1} + (1 - f(T_q))u_H^{-1} \tag{7}$$

$$\left.\begin{array}{ll} \text{where} & u_T^{-1} = g(T_M) \quad , \\ \text{and} & u_H^{-1} = g(T_{min}) \quad . \end{array}\right\} \tag{8}$$

$$\left.\begin{array}{ll} \text{And} & u^{-1} = 0 \quad , \\ \text{of} & T_q \leq T_{min} \quad . \end{array}\right\} \tag{9}$$

The form of function $f(T_q)$ was assumed as

$$f(T_q) = \{(T_q - T_{min})/(T_R - T_{min})\}^{\eta} \quad , \tag{10}$$

where η is unknown variable and to be determined from experimental data.

$$\left.\begin{array}{l} \text{And} \quad f(T_q) = 1 \quad , \\ \text{for} \quad T_q \geq T_R \\ \text{and} \quad f(T_q) = 0 \quad , \\ \text{for} \quad T_q \leq T_{min} \end{array}\right\} \qquad (11)$$

Using ϕ, which was obtained from the Yamanouchi's data[5] for top-quench tests under atmospheric pressure, the quench front velocities were parametrically calculated for η as shown in Fig. 3. The appropriate value of η is in the range of 0.6 to 2.0 and $\eta = 1$ is found to be reasonable.

3. Pressure effect

From the analogy of ϕ and the maximum heat flux on a boiling curve, ϕ was assumed to be a linear function of system pressure and determined from the FLECHT low flooding test data[6] taken under the pressures of 0.137, 0.274 and 0.39 MPa, which are shown in Fig. 4. ϕ is written as

$$\phi = (5.74p + 0.297 \times 10^6)(1 + 2.778 \times 10^{-5} \Delta T_{sub}^3) \quad , \qquad (12)$$

In this procedure, the scattered points like point A in Fig. 4 were neglected.

The equation (12) was evaluated with top-quench data. The results are shown in Figs. 5 and 6, indicating good prediction up to 7 MPa.

4. Evaluation of the derived model by using data of a small scale reflood tests

Small scale reflood tests were performed with full-length PWR-simulated 4 by 4 rods bundle under the forced feed condition. Figure 7 shows the cross sectional view of test section, axial power distribution and locations of thermocouples for temperature measurement. The test runs were numbered in order of tests.

Figure 8 shows the comparison of the quench times measured at verious elevations and the quench front envelopes parametrically calculated with Eqs. (7) to (10) for n. It is found from the figure that $n = 1$ reasonable.

In order to evaluate Eq. (12) for the effect of system pressure on the quench velocity, the data measured under the pressure of 0.196 MPa and the line expressing Eq. (12) are indicated in Fig. 9. The quench velocities were evaluated from the quench times of thermocouples 4L and 4U or 3L and 3U shown in Fig. 7. The poor predictions are found for the data after Run 6039. The data marked Ⓐ and Ⓑ were taken under the idential test conditions and it is considered that the influence of the oxidation of clad surface appears in the later period of the experiment.

When the heat transfer surface is covered with an oxide layer, the surface temperature becomes remarkably lower than the measured in the clading due to high thermal resistance of the layer. Consequently the quench velocity estimated from the measured quench temperature is higher the measured.

Figure 10 shows the plots for the small scale reflood test data exclusive of the data shown in Fig. 9 and for FLECHT low flooding test data in comparison with lines expressing Eq. (12) for corresponding

system pressures.

In both figure, it is found that the effect of the system pressure on the quench velocity is able to be predicted with Eq. (12) within ±20 % error, if the influence of the surface oxidation might be neglected.

5. Conclusion

(1) The low temperature quench was modeled by considering the thermodynamic and the hydrodynamic liquid maximum superheat, T_M and T_{min} respectively. The minimum film boiling temperature obtained by Sakurai was introduced as a hydrodynamic liquid maximum superheat.

(2) The low temperature quench was found to be correlated with Eqs. (7) through (9) and Eq. (10) with $\eta = 1$.

(3) The system pressure effect was found to be predicted with Eq. (12) in the range of 0.1 MPa ~ 7 MPa in the pressure within ± 20 % error.

(4) It was found that the prediction of the quench velocity became difficult due to surface oxidation of clading with the repetition of tests.

[Nomenclature]

C, C_p : Specific heat (KJ/Kg·K)

f : Function of probability

g : Function defined in Eq. (1)

p : System pressure (Pa)

T : Temperature (K)

T_ℓ : Liquid temperature (K)

T_{min} : Hydrodynamic liquid maximum superheat (K) (Eq. (4))

T_M : Thermodynamic liquid maximum superheat (K)(Eq. (3))

T_q : Apparent quench temperature (K)

T_R : Wall temperature whose contact temperature is T_M (K) (Eq. (5))

U : Quench velocity (m/s)

Z : Axial distance from quench front (m)

γ : Specific weight (Kg/m^3)

ΔT_{sub} : Liquid subcooling (K)

η : Unknown variable in Eq. (10)

ϕ : Heat flux (W/m^2)

λ : Heat conductivity (W/m)

References

(1) Murao, Y.: Correlation of quench phenomena for bottom flooding during loss-of-coolant accidents, J. Nucl. Sci. Technol., 15[12], pp 875 ~ 885, 1978.

(2) Cermak, J.C., et al.: PWR full length emergency cooling heat transfer (FLECHT) Group 1 test report, WCAP-7435, (1970).

(3) Groeneveld, D.C.: The thermal behaviour of a heated surface at and beyond dryout, AECL-4309, (1972).

(4) Sakurai, A., et al.: Steady and unsteady film boiling heat transfer at subatmospheric and elevated pressures, presented at the 1980 ICHMT International Seminar, Nuclear Reactor Safety Heat Transfer, Dubrovnik, Yugoslavia, (1980).

(5) Yamanouchi, A.: The velocity of falling liquid film boundary on a vertical hot wall, Bulletin of J.S.M.E. (Part 2), 34 (266), pp 1756 ~ 1767, (1968)(in Japanese).

(6) Lilly, G.P., et al. PWR-FLECHT cosine low flooding rate test series evaluation report, WCAP-8838, (1977).

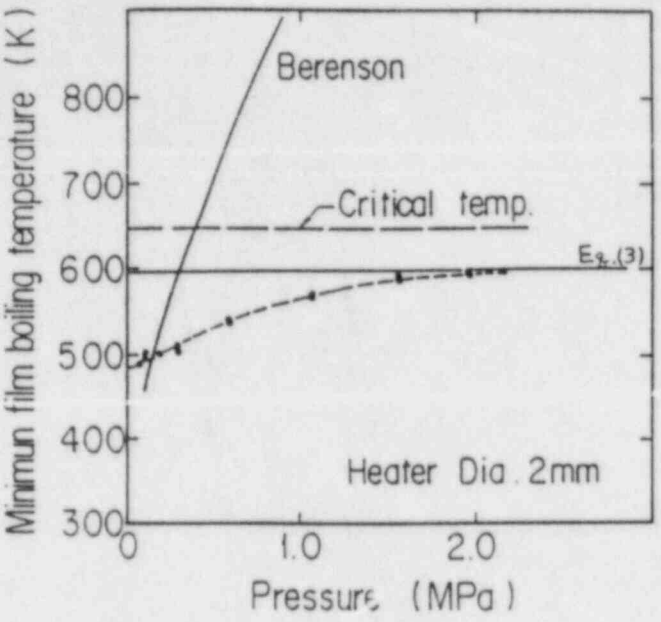

Fig. 1 Minimum film boiling temperature

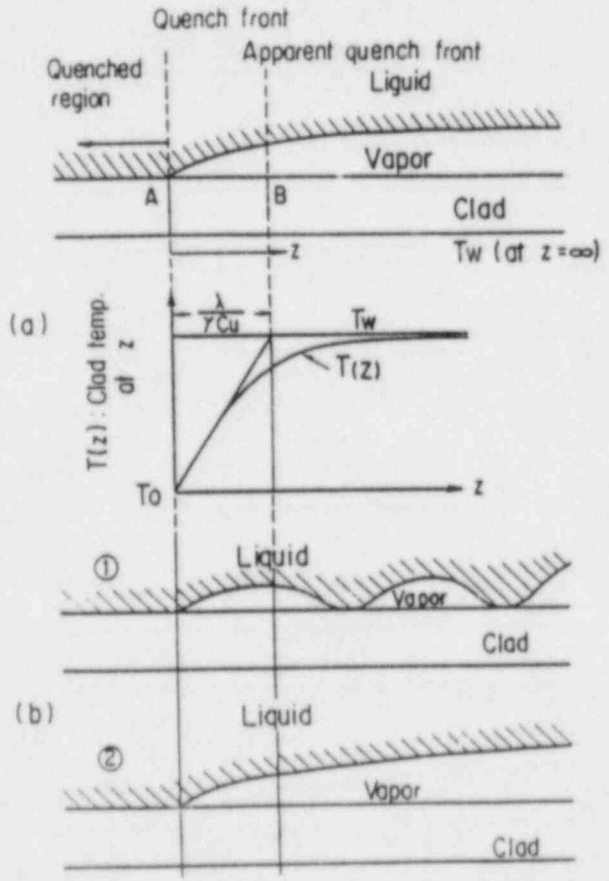

Fig. 2 Temperature distribution in unquenched region and condition of vapor film

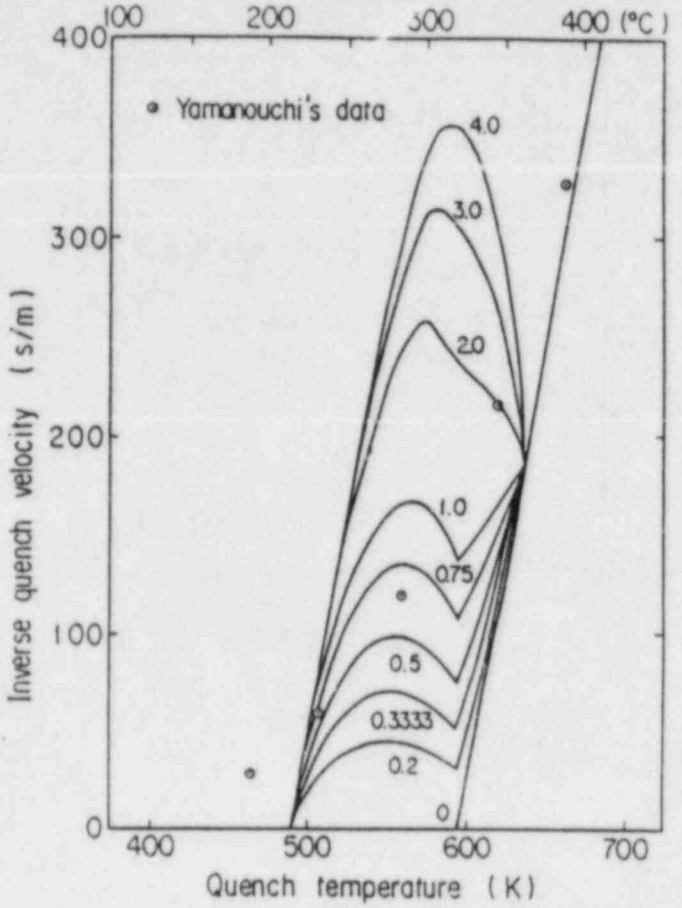

Fig. 3 Determination of η with Yamanouchi's data

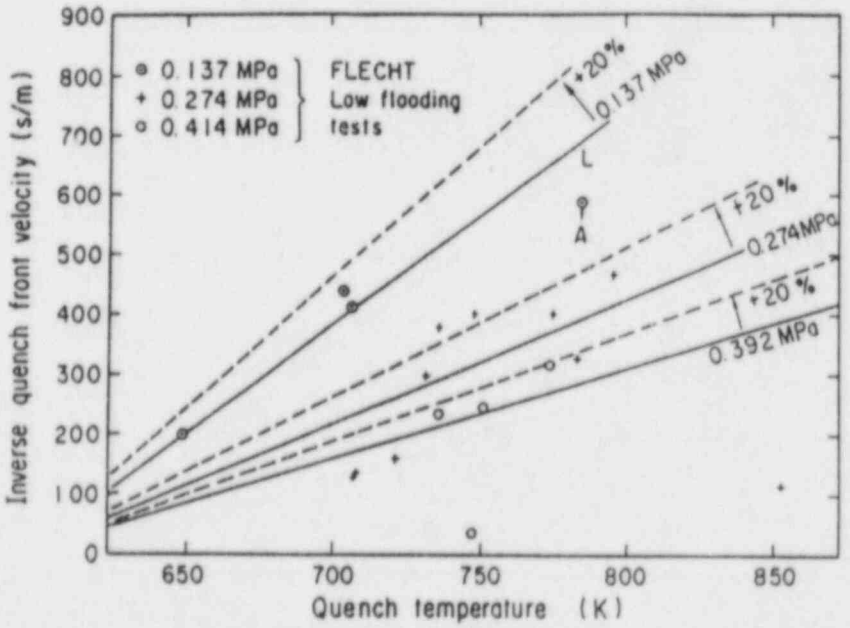

Fig. 4 Determination of Eq. (12) with FLECHT low flooding data

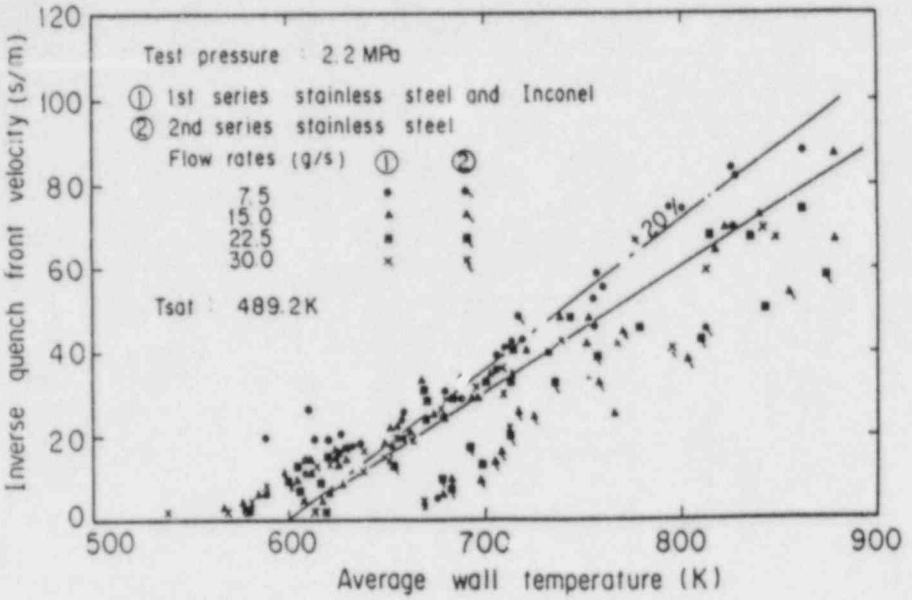

Fig. 5 Evaluation of Eq. (12) with 2.2 MPa data

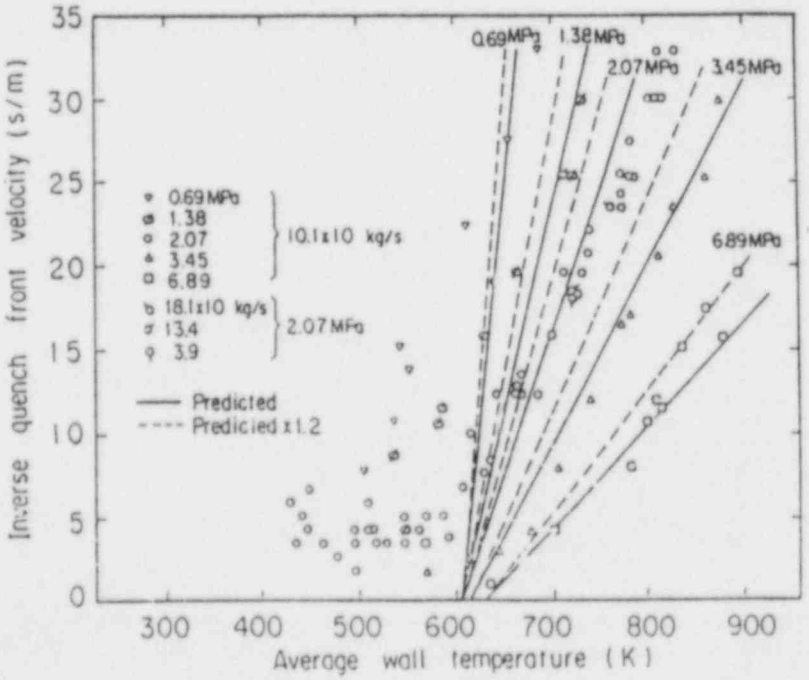

Fig. 6 Evaluation of Eq. (12) with 7 - 0.7 MPa data

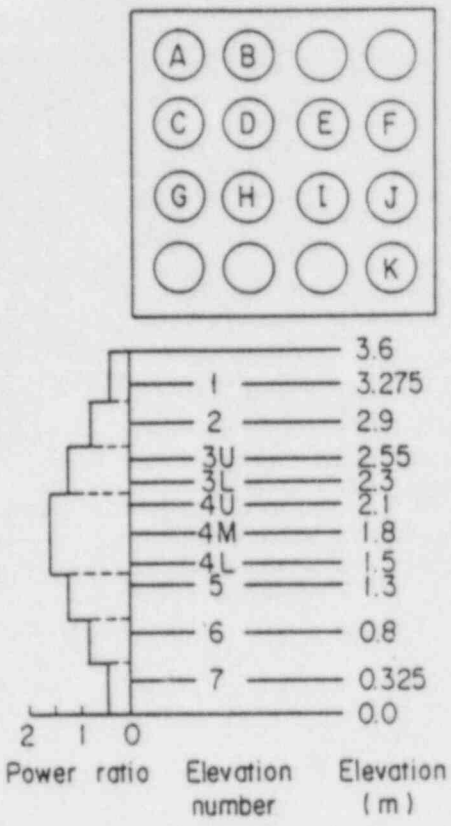

Fig. 7 Test section

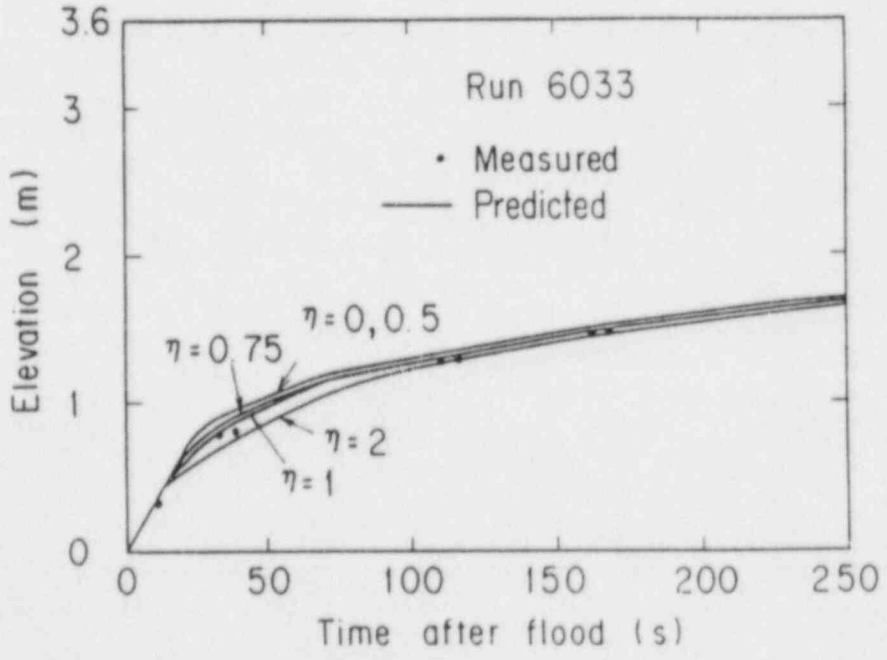

Fig. 8 Evaluation of η with small scale reflood test

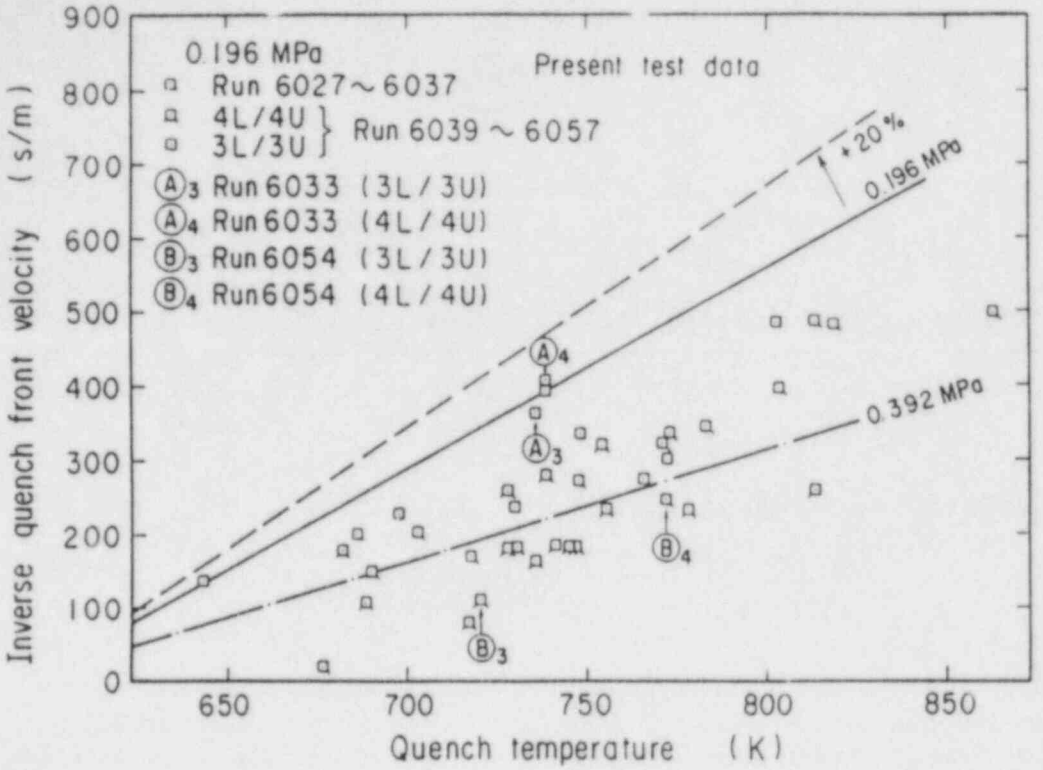

Fig. 9 Evaluation of Eq. (12) with 0.196 MPa data

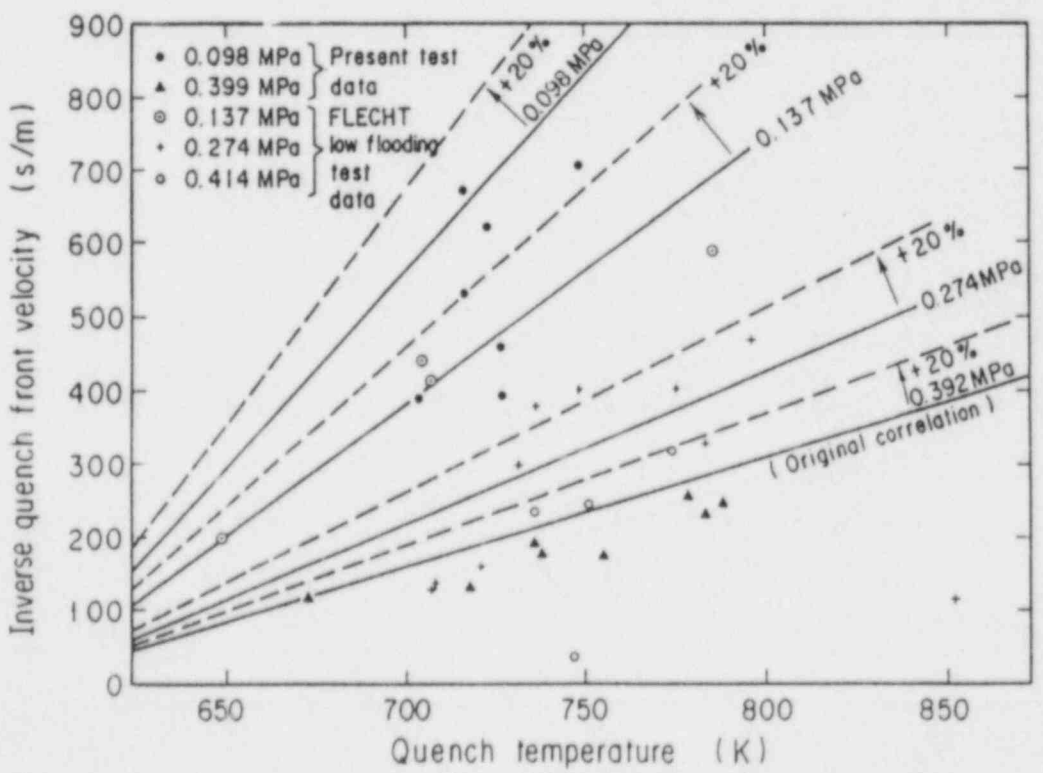

Fig. 10 Evaluation of Eq. (12) with data except for 0.196 MPa data

Maximum Wetting Temperatures Up To Critical Pressure

D. Hein, V. Kefer, H. Liebert

Kraftwerk Union AG, Erlangen, FRG

Abstract

To determine the influence of pressure on the maximum wetting temperature experiments were carried out with freon R 12 and water up to the critical pressure. An intermittently cooled probe was used. With this method of non-steady cooling of a probe the most interesting additional influences like sub-cooling or flow velocity can be easily investigated.

Two different test series were performed: one under the least disturbed conditions attainable with the fluid at saturation temperature, an initially stagnant pool and polished and cleaned surfaces, the second under forced flow conditions also with sub-cooling of the fluid and oxidized surfaces.

For the cooling of the probe in an initially stagnant pool of fluid in the low pressure region ($p/p_{cr} < 0{,}4$) the maximum wetting temperature was found to run parallel to the saturation temperature while at higher pressures a drastic reduction of the wetting temperature close to the saturation temperature was found. This drastic reduction was not observed in the test series under forced flow conditions. There a smooth reduction of the temperature difference ($\vartheta_L - \vartheta_S$) in the high pressure region ($P/Pc > 0{,}4$) was found.

1. Introduction

Leidenfrost in 1756 / 1 / was the first to establish that a drop of water in a red hot spoon did not wet the metal, but at first evaporated very slowly and later, at a lower temperature of the metal, suddenly disappeared. This temperature ϑ_L represents in the Nukiyama diagram the boundary between the region of stable film boiling and that of transition boiling. This point on the Nukiyama diagram is thus designated the "Leidenfrost point".

Because of the significance of the rewetting process in safety considerations of light water reactors, a series of treatises has been published recently. However the wetting process is also of interest, for example, in filling of lines and tanks with liquid nitrogen or oxygen or in hardening of materials, i.e. in quenching of hot workpieces by dipping them in an oil bath. While these process take place at low pressures wetting temperatures up to the critical pressure are of interest for once-through boilers.

In the process of rewetting by flooding, the level of temperature at which wetting commences is of interest. Search of the relevant literature shows that for the determination of the wetting temperature the process of droplet evaporation is mainly utilised. Measurements undertaken by this method on various materials /2 - 8/ resulted in wetting temperatures for water at a pressure of 1 bar between 155 °C and 330 °C.

Measurement methods using the cooling of wires, rods or spheres in order to determin the wetting temperature /9 - 18/ also showed at pressure of 1 bar and water at saturation temperature, wetting temperatures between 150 °C and 655 °C.

While in the low pressure region from 1 to 10 bar the dependence of the wetting temperature on pressure only can be regarded as relatively certain /10, 13, 15, 17/ data on the influence of sub-cooling are rare /10, 20, 21/.

Spiegler et. al. /18/ give for the minimum temperature at which stable film boiling still prevails the relationship

$$\vartheta_{min} = (0{,}13 \frac{p}{p_{crit}} + 0{,}84)\, \vartheta_{crit}$$

TONG /21/, on the basis of measurements of BRADFIELD /10/, gives for the influence of sub-colling on wall superheating on wetting the relationship

$$(\vartheta_w - \vartheta_s) = 6{,}15\, (\vartheta_s - \vartheta_{fl}) + 200$$

To resolve the problem at what maximum temperature a wall can be wetted and the dependence of this wetting temperature on pressure two test series were carried out:

- under as undisturbed conditions as possible, that means innitially stagnant pool, polished and cleaned surface, high purity fluid,

- under more realistic flooding conditions meaning forced flow and oxidized surface.

2. Experimental Apparatus

Determination of wetting temperature can, as illustrated in Fig. 1 be effected in 3 ways differing in principle:

a) by taking the boiling curve according to Nukiyama /22/

b) by measuring the evaporation time of droplets, and

c) by cooling of a probe.

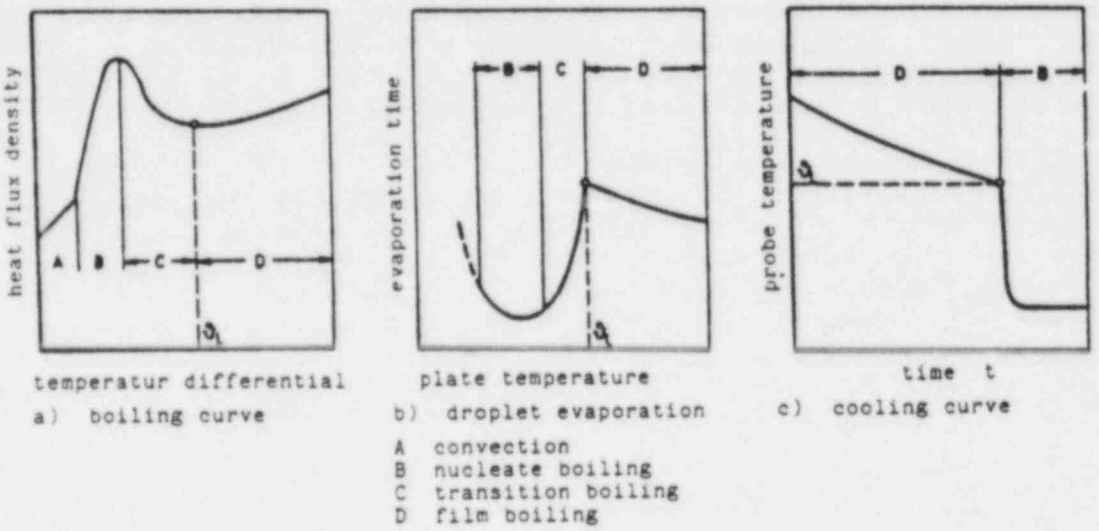

Figure 1: Method of determining wetting temperature

The shape of the boiling curve according to Nukiyama for water at atmospheric pressure is plotted in Figure 1a. The wetting temperature is that wall temperature at which the heat flux density at which stable film boiling still prevails exhibits a minimum.

With the method of droplet evaporation small drops of fluid are evaporated on a hot plate at constant temperature. For different initial plate temperatures different evaporation times result, giving a picture as shown in Figure 1b. The wetting temperature is then that temperature of the plate at which the evaporation time exhibits a maximum.

While with droplet evaporation effects occur which can strongly affect the wetting temperature and in particular investigations

with a sub-cooled fluid are not possible, in determination from the boiling curve inaccuracies occur because of the curve's flat shape in the region of the wetting temperature.

More success, including with sub-cooled fluid, is expected from a third measurement method in which a probe is cooled intermittently. Figure 1c illustrates the temperature-time curve for such a probe. In the region of film boiling the temperature at first declines only slowly. If the wetting temperature is reached, the wall temperature of the probe falls rapidly due to the transition from film boiling to nucleate boiling.

With this method of non-steady cooling of a probe, which shows the advantage that the parameters of interest are well set up and can be varied, two different series of experiments were performed. In one of these under the most ideal conditions attainable the wetting temperature for water at saturation temperature as a function of pressure in an initially still fluid was determined. In the second series of measurements the influence of sub-cooling and of flow velocity, as well as of a surface already oxidized by flooding experiments, on wetting temperature was investigated.

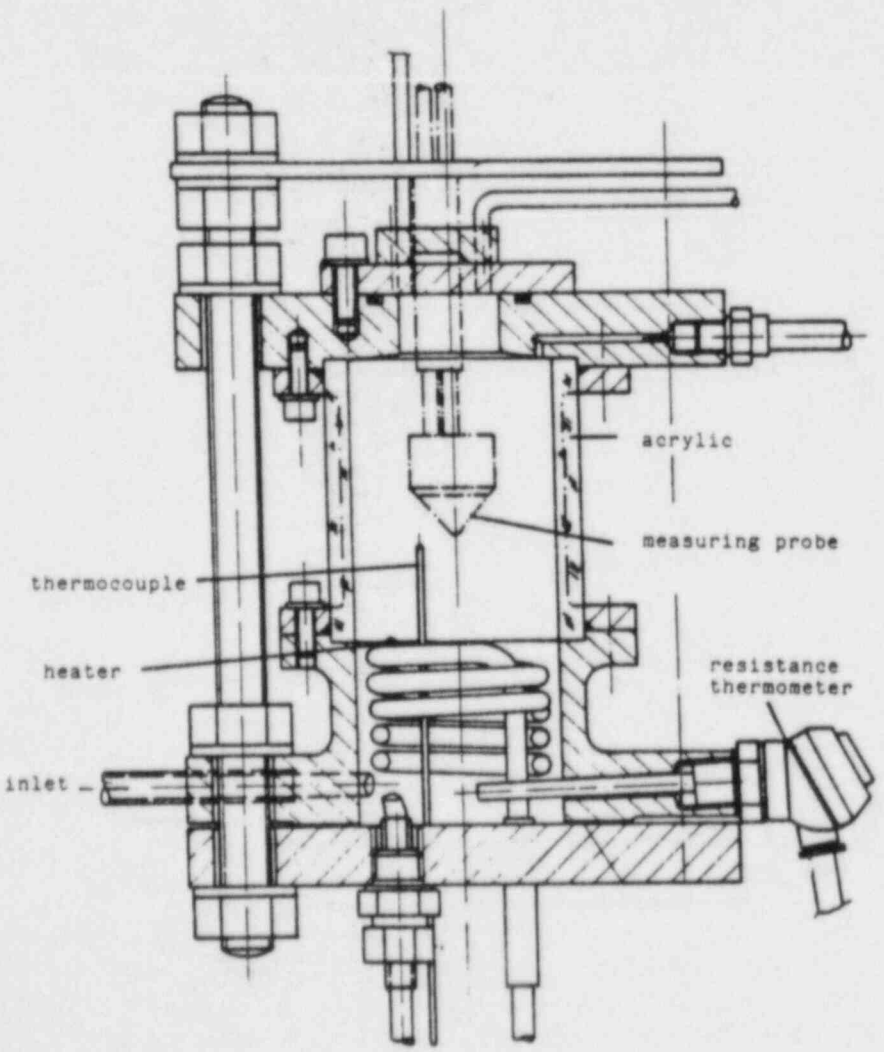

Figure 2: Experimental apparatus for determination of wetting temperature as a function of pressure

For measurement of the pressure-dependence of the wetting temperature under the most ideal conditions attainable - i.e. polished, clean surface, least possible disturbance to flow through flow turbulence - the method of non-steady cooling of a circular conical probe was used, a thermocouple at the tip indicating the onset of wetting. Figure 2 illustrates the assembly of the experimental apparatus.

This experimental rig is based on the idea that a probe, installed in a tank, is heated in a steam atmosphere and then flooded. As soon as the liquid level is above the upper edge of the probe the flooding process is interrupted so that cooling of the probe can proceed under free convection.

The probe shown in detail in Figure 3, of austenitic steel, represents the result of ideas regarding its form and material. The form of a circular cone and the thermal conductivity of austenitic steel produce in the probe a temperature field which guarantees the occurence of wetting at the probe tip.

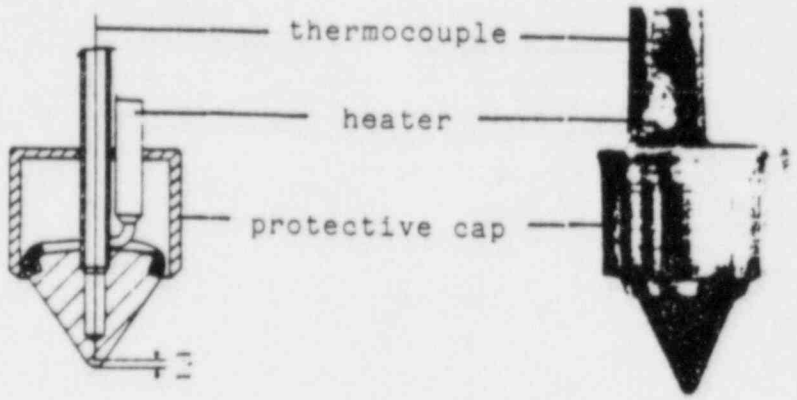

Figure 3: Circular conical probe for determination of wetting temperature

Through the low thermal capacity of the probe tip a significant drop in temperature is caused on the surface (but also inside the probe at the point at which the thermocouple is fitted) immediately after wetting.

Figure 4 shows a measured curve of the temperature at the probe tip during the course of an experiment. Recognisable are the heating process in the steam atmosphere (A), the short period of flooding (B) and the cooling process (C) with the sharp kink in the temperature-time curve at time t_L which indicates wetting of the probe tip.

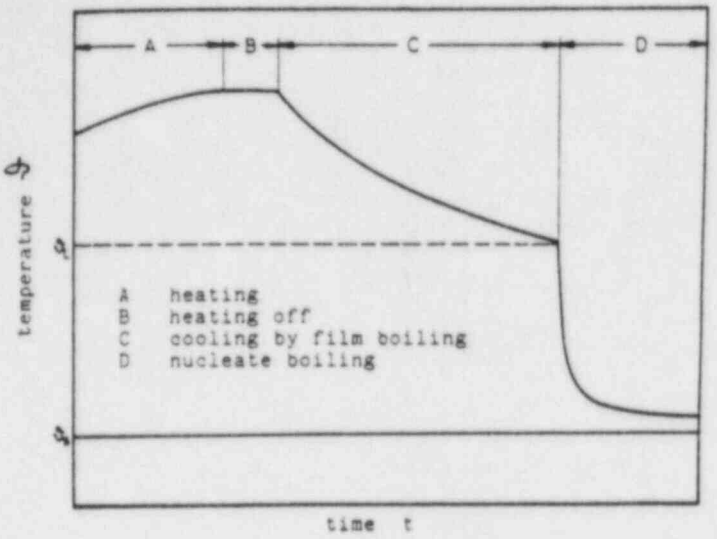

Figure 4: Time-curve of temperature at tip of probe

While with the experimental rig described above the dependence of the wetting temperature on pressure was determined under the least disturbed conditions attainable and ideal surface conditions (polished, degreased, unoxidized), for the measurements of the dependence of wetting temperature on pressure, subcooling and flow velocity two facilities have been used:

- a low pressure arrangement shown in Fig. 5, and
- a high pressure loop shown in Fig. 6.

In the low pressure experiment a rod-shaped probe was utilized in order to simulate as closely as possible the conditions on wetting of the end of a fuel rod by an experimental procedure related to actual practice. For the high pressure tests an internally cooled tube was used as test section having in mind the internally cooled once-through boiler tubes.

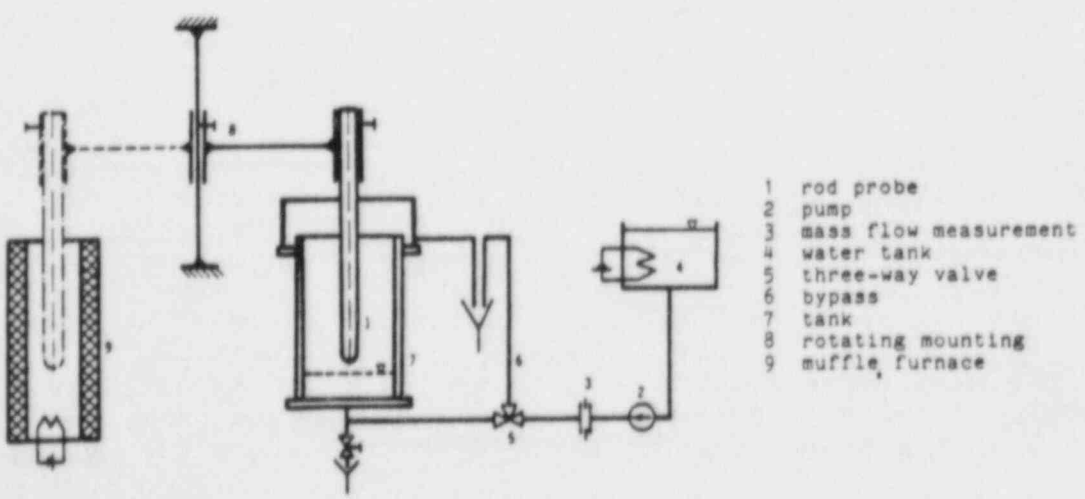

Figure 5: Experimental arrangement for determination of wetting temperature on flooding

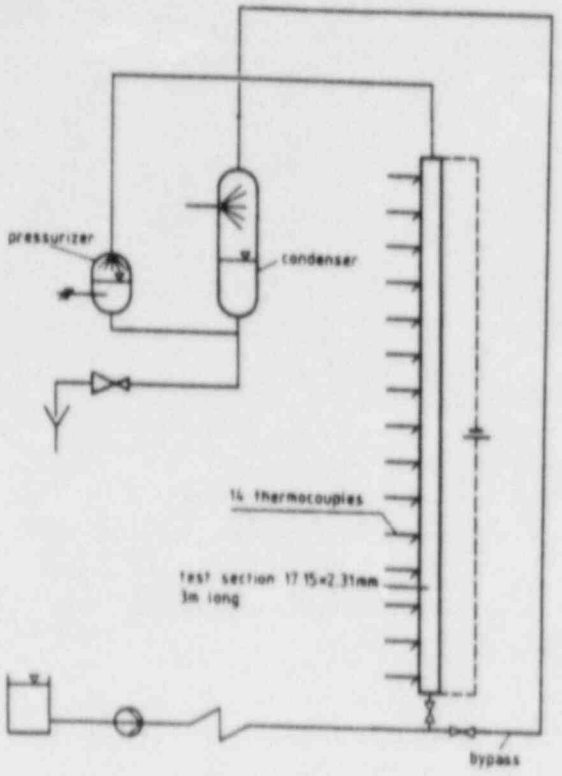

Figure 6: Test facility for high pressure tests

3. Experimental Results

3.1 Pressure Dependence of Wetting Temperature Under the Most Ideal Conditions Attainable

For determination of the pressure dependence of the wetting temperature the experimental apparatus shown in Figures 2 and 3 was used. In order to obtain this dependence in a wide pressure range, measurements were first performed with the refrigerant freon R 12.

Figure 7 shows the temperature at the probe tip for three different pressures.

In the presence of film boiling a very thin and quiescent vapour film could continually be observed on the probe, which shortly before wetting became less quiescent. Wetting occurs at the probe tip and in about 4 s travels over the whole surface of the probe.

Since in repetition of series of measurements deviations were observed from previous measurements, in spite of only slight scattering of the measurement values within one series of measurements, the conclusion must be drawn that even minor differences in the treatment of the probe surface affected the results with freon.

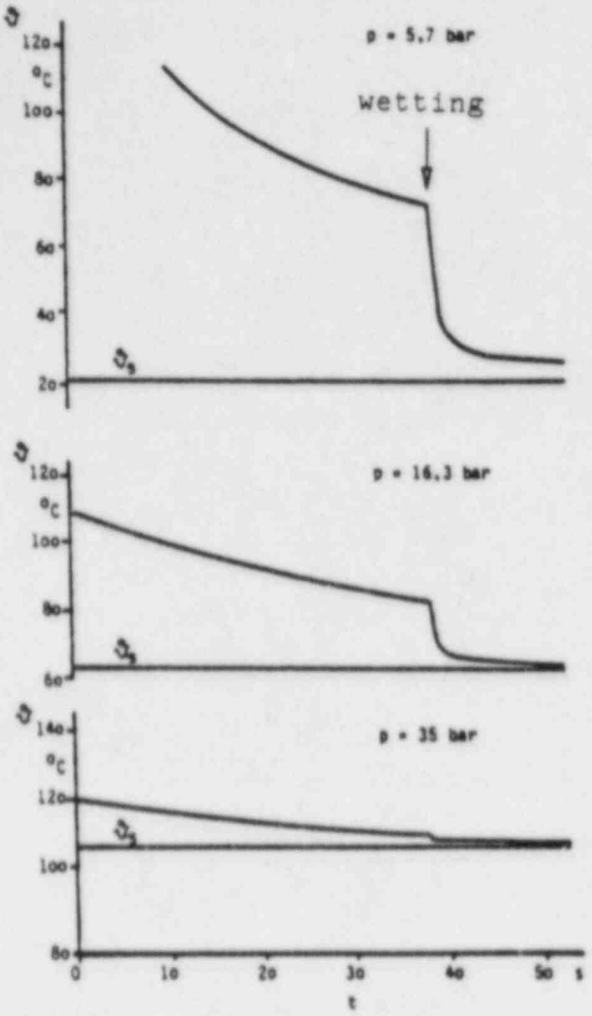

Figure 7: Curve of temperature at tip of probe at different pressures. Refrigerant: freon R 12

The result of 8 series of experiments is plotted in Figure 8 against the dimensionless pressure $\pi = p_1/p_{cr}$.

The measurements cover a range from $\pi = 0.1$ to 0.9. At still higher pressures, ie in the vincinity of critical pressure, flooding of the probe presents difficulties, since for flooding the difference in density between fluid and steam is utilised, which in this region tends to disappear.

As the diagram shows, the measurements scatter at pressures of $\pi < 0.5$ very sharply from series to series, while at pressures of $\pi > 0.5$ hardly any scatter is present. This boundary collapses with a drastic reduction of wetting temperature of $(\vartheta_1 - \vartheta_s) = 30 \div 50$ K in the lower pressure range to about 4 K in the high pressure range.

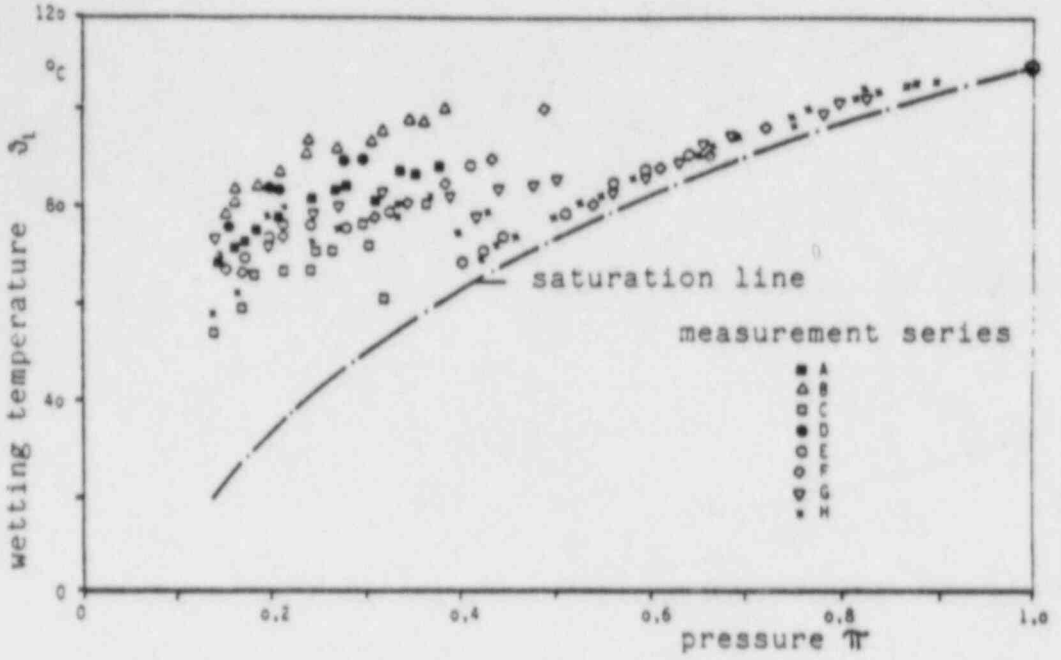

Figure 8: Dependence of wetting temperature on pressure
Fluid: freon R 12

Within series C a measurement point was determined at a pressure ratio of π = 0.33 which stood out clearly from the measurement series in the low pressure region and was only 8.5 K above the saturation temperature. Observations showed that the vapour film in this case too was very thin and quiescent shortly before wetting, so that it was hardly perceptible visually. No success was achieved in confirming this low value - which would fit a curve extrapolated from high pressure - in reproducibility experiments.

These experiments with freon R 12 showed that in the range of low and medium pressures the wetting temperature is strongly influenced by the surface finish of the probe, contamination of the freon by oil, as well as variations in the freon quality through the presence of metals (eg copper, tin, zinc, lead etc).

A corresponding series of experiments with demineralised and degassed water produced the diagram shown in Figure 9. In the low pressure region wetting temperatures were measured which scattered about a curve running at a distance of 100 K from the saturation line. Above a pressure of 40 bar the values scatter much more widely, the lowest values being only about 20 K above the corresponding saturation temperature. Pressures up to 70 bar were possible with the apparatus. It can therefore only be supposed that at still higher pressures the wetting temperature, similarly to the results with freon R 12, is only a few degrees above saturation temperature.

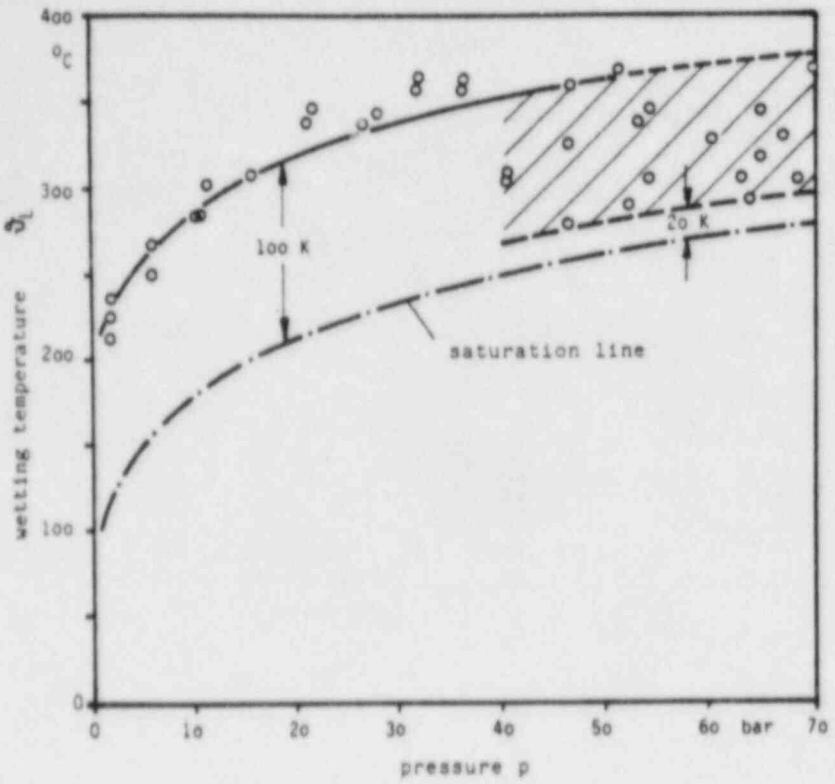

Figure 9: Dependence of wetting temperature on pressure
Fluid: water

3.2 Dependence of Wetting Temperature on Pressure under Flooding Conditions

The test series under the most ideal conditions attainable showed that the stability of the vapour film plays an important part in the rewetting process. Therefore it is to be expected that for an experimental set-up with forced turbulent flow at the point of rewetting there are different condition resulting in different rewetting temperatures as compared to the ideal case.

Fig. 10 shows selected temperature-time curves obtained in an internally flooded pipe at different pressures. These curves are directly comparable to those in Fig. 10 . One can recognize that during flooding the various heat transfer regions effect different degrees of pre-cooling prior to wall rewetting.

Further it has to be taken into account that in all cases of pipe rewetting (in the presence of axial conduction) being caused by a progressing rewetting front the latter differs slightly from the quench temperature (the sharp dip in the temperature-time curve) and has to be adjusted.

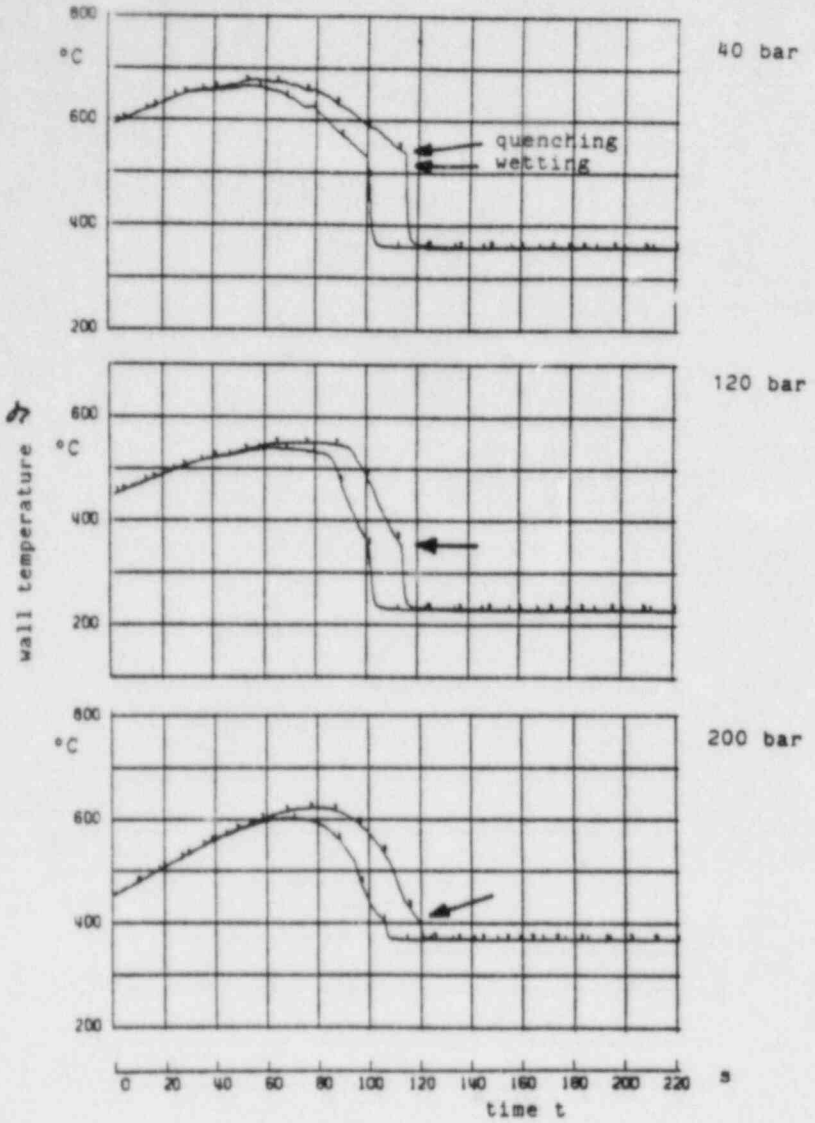

Figure 10: Wall temperatures at different pressures during flooding
Fluid: water

Results, already adjusted, of tests with internally flooded pipe for a pressure range of 5 to 210 bar are plotted in Fig. 11

While at pressures below 80 bar the wetting temperature curve is parallel to the saturation line, at high pressure the two curves approach gradually. The curves of ϑ_L and ϑ_S merge, as expected, at the critical point.

For the material Inconell 800 (1.4876) of hydraulic smooth surface with R_T = 3.5 µm slightly oxidized by repeated heat ups to ca. 600 °C the dependence of the wetting temperature on pressure can be empirically expressed as

$$\vartheta_L = \vartheta_S + 160 - f(p)$$

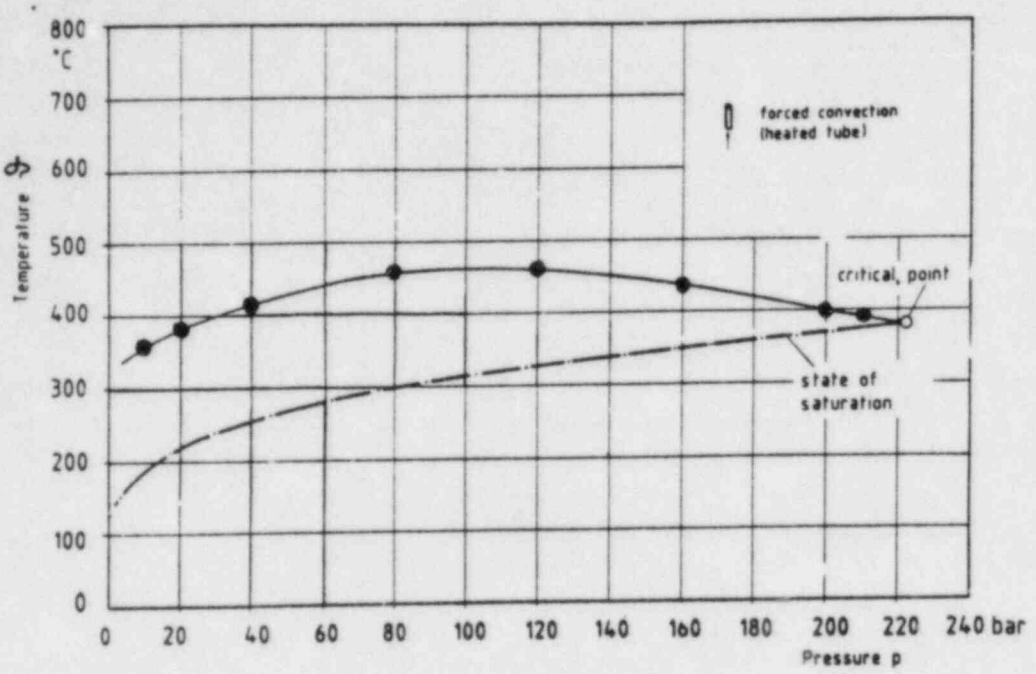

Figure 11: Dependence of wetting temperature on pressure for flooding conditions

3.3 Dependence of Wetting Temperature on Sub-Cooling of the Fluid

In order to be able to produce hypotheses as to whether the flow velocity and the sub-cooling of the fluid influence the temperature at which wetting occurs, experiments were performed with the test arrangement shown in Figure 5.

Results of the experiments showed that the wetting temperature is a function of sub-cooling, as illustrated in Figure 12. No influence by the flow velocity in the range from $0 < w < 10$ cm/s could be established.

Apparently through the oxidized surface the value for the wetting temperature is at $\Delta\vartheta = 0$, ie with water at saturation temperature at 260 °C and so 160 K above saturation temperature.

The increase in wetting temperature with rising sub-cooling can in the range covered by measurements be reproduced as a straight line with gradient 10 K/K.

A comparison with measured values by Lauer /20/ and with a relationship quoted by Tong /21/ , which were also plotted in Figure 12, shows useful agreement if the influence of sub-cooling, ie the gradient of the curves, is considered. Deviations of the absolute values can be put down to differences in the surface finish.

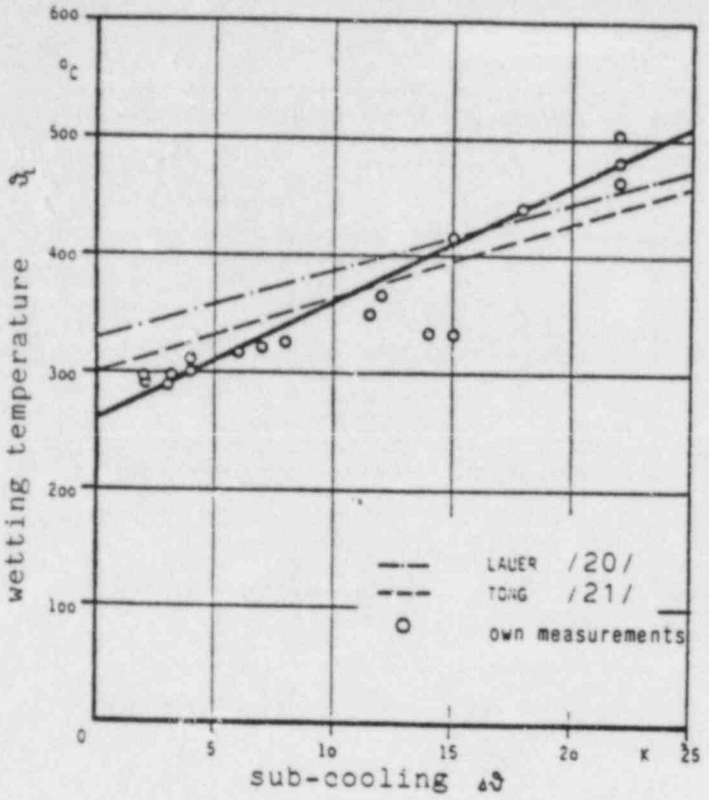

Figure 12: Dependence of wetting temperature on the sub-cooling of the fluid at a temperature of 1 bar

Thus for the calculation of flooding experiments the wetting temperature can be determined according to the following empirical equation:

$$\vartheta_L = \vartheta_S + 160 + 10\Delta\vartheta$$

Range of validity:

$1 \leq P \leq 40$ bar

$0 \leq \Delta\vartheta \leq 25$ K

Material: Inconel with oxidized surface.

4. Discussion and Conclusions

On the basis of the experimental results it can be stated that the wetting temperature can be regarded not as a property of the fluid but that it is influenced by the hydraulics, i.e. the stability of the vapour film plays an important part in the onset of wetting.

In the meantime several authors came to the same conclusions. Fröhlich and Oswald /23/ went as far as predicting the collapses of the vapour film and rewetting at saturation temperature when all external accidental disturbances could be excluded.

Komnos /24/ developed on the basis of mass and energy balances a model for the rewetting process. A permanent collapse of the vapour film is possible when

- the condensing mass flow $\dot{m}_c$ exceeds the evaporation mass flow $\dot{m}_v$
- there is no excess of energy so that the wall temperature decreases.

The mass and energy curves behave according to Komnos /24/ as shown in Figure 13. Exact calculations are only possible by assuming a value of heat transfer coefficient α from the fluid surface into the water which depends on the degree of turbulence.

According to Figure 13 wetting can take place when the condensing mass flow exceeds the evaporating mass flow ($\dot{m}_c > \dot{m}_v$) and at the same time $E \leq 0$ i.e. no excess of energy resulting fall in temperature. At point L (the Leidenfrost point) mass and energy equilibrium exists. It follows that this is the point where rewetting can start. The above mentioned diagram shows that L can merge with S (the saturation point) when

$$\alpha (\vartheta_o - \vartheta_B) = 0$$

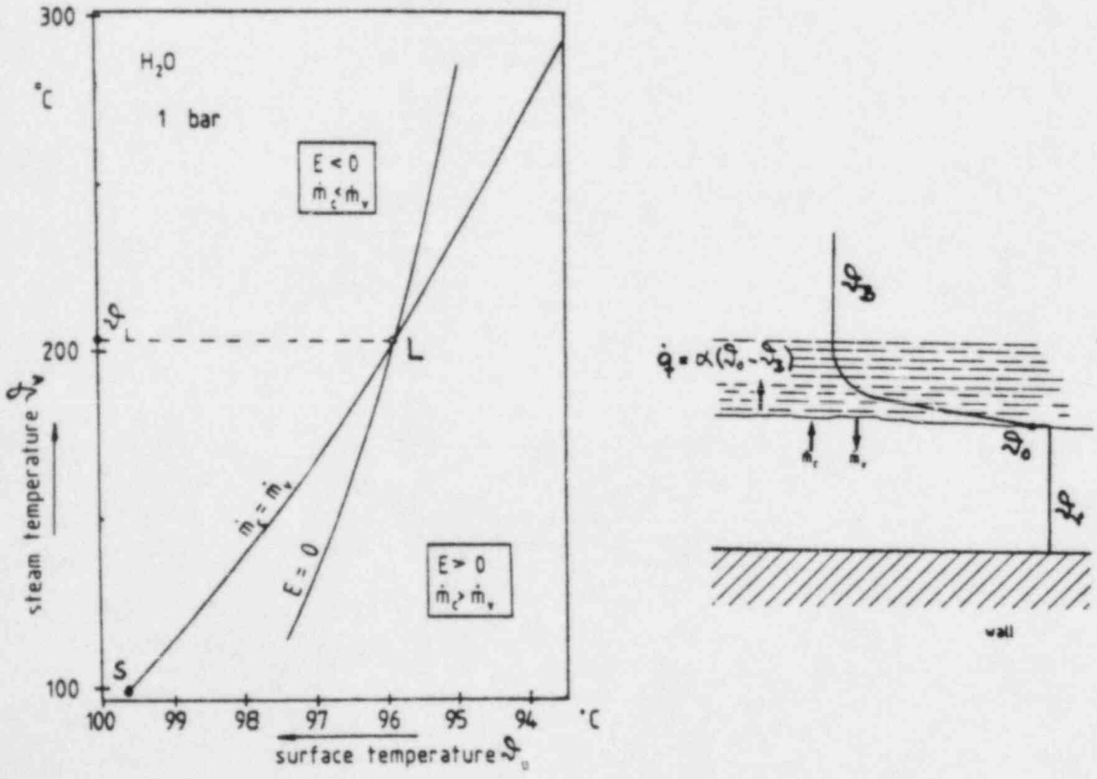

Figure 13: Determination of the wetting temperature by mass and energy ballance according to KOMNOS /24/

By increasing the above product i.e. by increasing

- the value of α meaning higher degree of turbulence in the fluid and
- the value of $(\vartheta_o - \vartheta_B)$ meaning higher degree of sub-cooling

the energy curve shifts towards right and leads to higher wetting temperatures ϑ_L.

If this proposed model is correct - the agreement about the influence of important parameters seems to confirm it - it will mean that the prediction of a wetting temperature can be made only for particular, exactly defined hydraulic conditions.

This is also the reason for the large differences in wetting temperatures reported by various authors whose experiments were carried out under seemingly identical conditions.

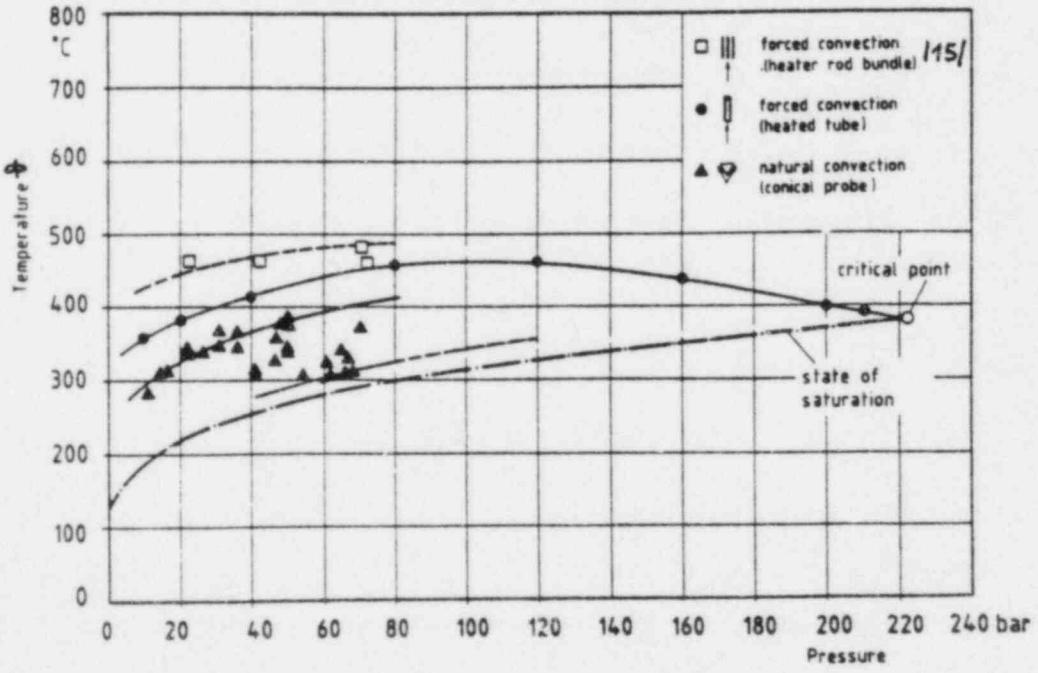

Figure 14: Wetting temperatures for different test conditions
Fluid: water

Consequently the task ahead is to determine wetting temperature classes subdivided according to different technical applications e.g.

- wetting in the case of free convection
- flooding in pipes
- flooding in bundles
- wetting by impinging water jets,etc.

as shown in Figure 14.

Future work should therefore aim in this direction. The model of Komnos /24/ may be a help to put the measurements in order.

References

/1/ Leidenfrost, J.G.
De Aqua Communis Nonnullis Quailitatibus Tractatus
Duisburg 1756 übersetzt von C. Wares in Int. J. of Heat and Mass Transfer, 9, S. 1153 - 1166 (1966)

/2/ Baumeister, K.J., Simon, F.F.
Leidenfrost temperature - Its correlation for liquid metals, cryogens, hydrocarbons and water
J. Heat Transfer 95, 166 - 173 (173)

/3/ Baumeister, K.J., Simon, F.F., Henry, R.E.
Role of the surface in the measurement of the Leidenfrost temperature
Proceedings ASME Symp.: Augmentation of Convective Heat Mass Transfer, 91 - 101, Winter Annual Meeting, New York (1970)

/4/ Borishansky, W.M.
Heat transfer to a liquid freely flowing over s surface heated to a temperature above the boiling point
Problems of heat transfer during a change of state
A collection of articles, AEC-tr-3405, 1953, U.S. Atomic Energy Commission, Washington, D.C.

/5/ Bell, K.J.
The Leidenfrost phenomenon: A survey
Chemical Engineering Progress Symposium Series, Bd. 63, Heft 79, S. 73 - 82 (1967)

/6/ Cumo, M., Farello, G.E., Ferrari, G.
Notes on droplet heat transfer
Chemical Engineering Progress Symposium Series, Band 65, Heft 92, S. 175 - 187 (1969)

/7/ Emmerson, G.S.
The effect of pressure and surface material on the Leidenfrost point of discrete drops of water
Int. Joural Heat Mass Transfer, Bd. 18, S. 381 - 386 (1975)

/8/ Gottfried, B.S., Lee, C.J., Bell, K.J.
The Leidenfrost phenomenon: Film boiling of liquid droplets on a flat plate
Int. J. Heat Mass Transfer 2, 1167 - 1187 (1966)

/9/ Bergles, A.E., Thompson, W.G.
The relationship of quench data to steady-state pool boiling data
Int. J. Heat Mass Transfer 13, 55 - 68, (1970)

/10/ Bradfield, W.S.
On the effect of subcooling on wall superheat in pool boiling
J. Heat Transfer 89, 269 - 270 (1967)

/11/ Cumo, M., Pitimado, D.
On the determination of the Leidenfrost temperatures
Termotechnica, Bd. 22, Heft 8, Aug. 1968, S. 373 - 381

/12/ Farber, E.A., Scorah, R.L.
Heat transfer to water boiling under pressure
ASME Trans. Band 70, Heft 64, S. 369 - 384 (1948)

/13/ Hosler, E.R., Westwater, J.W.
Film boiling on a horizontal plate
ARS Journal, Bd. 32, Heft 4, April 1962, S. 553 - 558

/14/ Kautzky, D.E., Westwater, J.W.
Film boiling of a mixture on a horizontal plate
Int. J. Heat Mass Transfer, Bd. 10, S. 253 - 256 (1967)

/15/ Anklam, T.M.
Small-Break LOCA heat transfer test series I: High-pressure reflood analysis
NUREG/CR-2114 (1981)

/16/ Peterson, W.C., Zaalouk, MG.
Boiling curve measurements from a controlled heat transfer process
Journal of Heat Transfer, Trans.ASME, Serie C, Bd. 93, Heft 4, Nov. 1971, S. 408 - 412

/17/ Stock, B.J.
Observations on transition boiling heat transfer phenomena
ANL-6175, Argonne National Laboratory, Argonne I 11, (1960)

/18/ Spiegler, P., Hopenfeld, J., Silberberg, M., Bumpus, Jr., C.F., Norman, A.
Onset of stable film boiling and the foam limit
Int. Journal Heat Mass Transfer, Bd. 6, S. 987 - 994 (1963)

/19/ Emmerson, G.S.
The effect of pressure and surface material on the Leidenfrost point of discrete drops of water
Int. Journal Heat Mass Transfer, Bd. 18, S. 381 - 386 (1975)

/20/ Lauer, H.
Investigation of heat transfer and rewetting in cooling of hot metal bodies
EUR 5702.d, 1976

/21/ Tong, L.S.
Heat transfer mechanism in nucleate and film boiling
Nucl. Eng. Des. 21, S. 1 - 25 (1972)

/22/ Nishikawa, K., Ito, T.
Two-phase boundary layer treatment of free convective film boiling
Int. J. Heat Mass Transfer 9, S. 103 - 115 (1966)

/23/ Fröhlich, G., Osswald, H.

Aufbau und Abbau des Leidenfrost-Phänomens in Wasser an kugelförmigen Flächen mit und ohne Störstellen

Institut f. Kernenergetik, Universität Stuttgart, Bericht Nr. 2-15 (1975)

/24/ Komnos, A.

A thermo-hydraulic model for rewetting

Thesis, Techn. University Munich, Feb. 1981

MINIMUM HEAT FLUX CONDITIONS IN BOILING HEAT TRANSFER

S. Nishio
Institute of Industrial Science
Univ. of Tokyo, Japan

ABSTRACT

This paper reviews the published information on the minimum heat flux condition in boiling heat transfer.

The first part is devoted to a survey of the subprocesses of heat transfer mechanism in the vicinity of the minimum heat flux point. Concepts and experimental results are summarized for the following subprocesses; (a)contact mode, (b)liquid-solid contact behavior and (c)liquid-vapor interface behavior.

In the second part, parametric effects on the minimum heat flux condition are summarized. System factors known to affect the minimum heat flux condition are as follows; (a)liquid-solid contact mode, (b)geometry of heating surface, (c)system pressure, (d)liquid subcooling, (e)liquid velocity, (f)acceleration in field, (g) thermal conductance of heating surface, (h)surface condition and (i)temperature transient. Experimental results and correlating equations for the effects of these factors are summarized and areas are noted where research efforts should be encouraged.

In the final part, analytical models to predict the minimum heat flux condition are reviewed. The predicted results are compared with the published data and the state-of-the-art is discussed.

1. INTRODUCTION

Boiling heat transfer is a mode of heat transfer in many modern technological apparatuses and its by order of magnitude more intensive than respective convective heat transfer for the same condition in the system. This is the main reason why boiling heat transfer is frequently used in modern equipments and installation. It even becomes more important for the equipment where safety requirements are imposed to the limited heat transfer area. For this reason, the need of a better understanding of boiling heat transfer, for many years, has been one of the main goals in the development of the heat transfer knowledge.

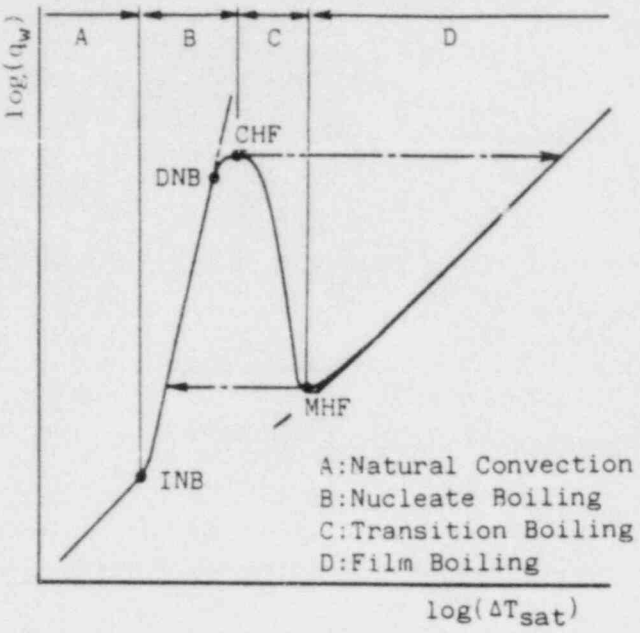

Fig.1 Pool Boiling Curve

General characteristics of boiling heat transfer are schematically shown with the boiling curve(Fig.1). On the boiling curve, there are three distinct regions-i.e., nucleate boiling, transition boiling and film boiling regions. These three sections of the boiling curve are bounded by "the critical heat flux (CHF) point" and "the minimum heat flux (MHF) point".

Even though it is desirable in most boiling heat transfer applications to operate under nucleate boiling conditions, the possibility of exceeding the critical heat flux and the practical application of liquid-quench necessitate a full understanding of the boiling phenomena. Especially, recent enlargement in application of liquid-quench calls for a thorough understanding of the minimum heat flux condition. Liquid-quench is sometimes encountered at the time of cooldown or during operational setups in many cryogenic systems and at the vapor explosion accidents. Similarly, effective quenching techniques become needed in the fields of metallurgy and reactor safety. Since the total cooldown time during quench is essentially affected by the minimum heat flux or quench condition, a better understanding of the minimum heat flux condition is indispensable to analyze such quench processes.

Unfortunately, however, the minimum heat flux condition has undergone less study in comparison with the critical heat flux, and there has been no comprehensive survey of the minimum heat flux condition appearing in the literature that seeks to put into perspective all of the work done in this area. Indeed, the only other reviews that treat the minimum heat flux condition in detail are those of Clements and Colver(1) and Grigoryev et al.(2). Thus, it is the purpose of this review to provide a comprehensive, in depth study of the minimum heat flux condition. In this paper, the published information on the minimum heat flux conditions under natural and external convective conditions is summarized. The auther believes that the information for such conditions is instructive also for the post-dryout heat transfer in channels.

2. SUBPROCESSES

The minimum heat flux point does not correspond only to the lowest surface temperature to support film boiling but also to the highest surface temperature of the transition boiling region.

First, the minimum heat flux point is considered as the lowest surface temperature in film boiling. Wachters et al.(3) and Baumeister et al.(4) reported that the lowest surface temperature sufficient to support the metastable spheroidal state of a small droplet occurred very near the saturation temperature of the liquid. However, Godleski and Bell(5), and Henry et al.(6) reported that it was impossible to support film boiling of extended drops with bubble breakthrough at such small surface superheats. These experimental results indicate that collapse of established film boiling necessitates the existence of system disturbances. In the this paper, the mode of system disturbances, which seems effective to bring about liquid-solid contacts in film boiling, is called "the liquid-solid contact mode".

Next, the minimum heat flux point is considered as the highest surface temperature of the transition boiling region. Berenson(7) has provided a concise description of the transition boiling mechanism: "Transition boiling is a combination of unstable film boiling and unstable nucleate boiling alternately existing at any given location on a heating surface. The variation in heat transfer rate with temperature is primarily a result of a change in the fraction of time each boiling regime exists at a given location." Following this description of the transition boiling mode, the total heat flux (q_w) in the transition boiling regime is thus expressed as

$$q_w = q_c F_c + q_d(1-F_c) \qquad \text{-----(1)}$$

where, F_c; spacial and time fraction of liquid-solid contact, q_c; mean heat flux at wetted area and q_d; mean heat flux at dry area.

Since liquid-solid contacts have been observed also under stable film boiling conditions (Bradfield(8), Swanson et al.(9), and Yao and Henry(10)), eq.(1) seems valid also for heat fluxes in the vicinity of the minimum heat flux point. On the other hand, following the definition, the minimum heat flux condition is expressed as

$$dq_w/d\Delta T_{sat} = 0 \ , \quad d^2q_w/d\Delta T_{sat}^2 > 0 \qquad \text{-----(2)}$$

Knowing the expressions for F_c, q_c and q_d in terms of the surface superheat, we can predict the minimum heat flux condition (T_M, q_M) with using eqs.(1) and (2). Since the minimum heat flux point does not necessarily correspond to the condition of F_c= 0, the temperature dependence of the fraction F_c, which is determined by liquid-solid contact behavior and liquid-vapor interface behavior, is important to calculate the minimum heat flux condition using eqs.(1) and (2).

Thus, in the present chapter, the published information on the following subprocesses is reviewed.

(a). liquid-solid contact mode
(b). liquid-solid contact behavior
(c). liquid-vapor interface behavior

2.1 Liquid-Solid Contact Mode

In the fully developed film boiling region where the surface superheat is suf-

ficiently high, the liquid is perfectly separated from the heating surface by vapor layer and thus there exists no direct contacts between liquid and solid. We consider, in this section, a process where liquid-solid contacts become to occur due to system disturbances as the heating surface is slowly cooled from the fully developed film boiling region under the saturated condition. In such a process, there seem to be two possible ways to induce the first contact-i.e., the liquid-rush-in mode and the liquid-creep-in mode.

(a). Liquid-Rush-in Mode (Fig.2(A))

Vapor layer thickness in film boiling is fluctuated due to the system disturbances caused by bubble departure etc.. The fluctuation in vapor thickness forces the liquid toward the heating surface. When the vapor thrust generated at the liquid-vapor interface is greater than the forces directing the liquid toward the heating surface, the liquid is turned back before it reaches the heating surface. However, when the vapor thrust is insufficient, the liquid can experience a direct contact with the heating surface. In this paper, this contact mode is called "the liquid-rush-in mode". The liquid-rush-in mode can be subdivided into the following three types according to the system disturbance directing the liquid toward the heating surface.

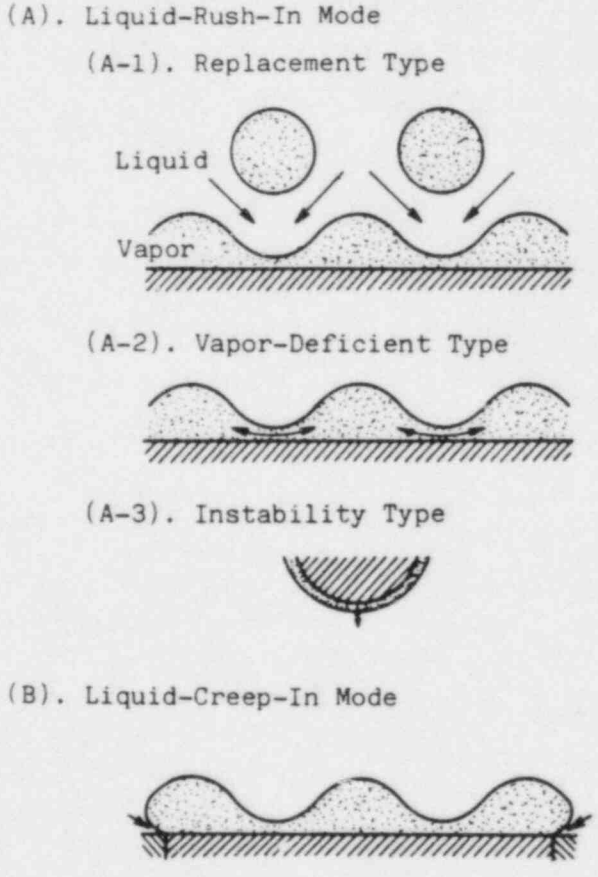

Fig.2 Liquid-Solid Contact Mode

(a-1). Replacement type (Fig.2(A-1)): Henry(11) proposed a contact mode of this type as a physical picture of heat transfer mechanism in the vicinity of the minimum heat flux point. In this kind of liquid-rush-in mode, the system disturbances caused by bubble departure are supposed effective to bring about liquid-solid contacts in film boiling. As bubbles depart from the vapor layer, the liquid rushes toward the heating surface, and it momentarily contacts the heating surface if possible. Borishanski(12) has shown that the liquid instantaneously contacts the heating surface in film boiling after a bubble breaks away from the liquid-vapor interface.

(a-2). Vapor-deficient type (Fig.2(A-2)): Lienhard and Dhir(13) proposed this kind of liquid-rush-in mode. Following their description, this kind of liquid-rush-in mode is explained as follows: The horizontal cylinder and horizontal flat plate generate vapor at a nearly constant rate and deliver it to an escapement process in the collapsing Taylor wave above the heating surface. Thus, liquid-solid contacts will occur where the constant rate of vapor production becomes insufficient to supply the instantaneous natural rate of wave motion. Namely, in this type, the system disturbances caused by bubble growth are supposed to bring about vapor deficience at the antinode of the Taylor wave and thus to result in the occurrence of liquid-solid contact in film boiling.

(a-3). Instability type (Fig.2(A-3)): Fedemski(14) proposed a stability model of the vapor layer oscillating at the stagnation point during forced convective film boiling on a sphere. His results show that there exists the lowest surface temperature to support the stable film boiling due to the system disturbances caused by unstable forces.

To the auther's knowledge, there has not been a sufficient amount of observation for the liquid-solid contact mode. Yao and Henry(10) examined the frequency and magnitude of liquid-solid contacts in the film boiling of saturated ethanol and water on horizontal flat stainless steel and copper plates with electrical conductance probes. They found that the contact frequency for water was in good agreement with the bubble departure frequency. Toda and Mori(15) studied the vapor film behavior for subcooled film boiling on a horizontal wire and a sphere with a laser beam. They found that the fluctuation in vapor film thickness was strongly affected by system pressure, subcooling and heat flux.

In this paper, the surface temperature, at which the first contact appears as the heating surface is slowly cooled down from the fully developed film boiling region, is called "the maximum contact temperature". As mentioned previously, the maximum contact temperature seems to be determined by the disturbances prepared in the boiling system. The maximum contact temperature for the liquid-rush-in mode was analyzed for a droplet approaching a heating surface by Iloeje et al.(16). They analyzed the vapor thrust force at the penetration of a truncated droplet into the thermal boundary layer on the heating surface, using a creeping flow solution for the spheroidal state. Their resulting equation for the maximum contact superheat (ΔT_{lc}) is

$$\Delta T_{lc} = (y_r)^3(\rho_v L/(\pi\mu_v k_v r^4))E/\sin^4\phi \qquad \text{-----(3)}$$

where, y_r; roughness hight of the heating surface, r; radius of droplet, E; kinetic energy at entrance to thermal boundary layer and ϕ; truncation angle of droplet. When, with decreasing the vapor layer thickness(y_v), y_v becomes to the same order of magnitude of the mean free path of a vapor molecule, a major portion of energy transfer may occur by direct passage of single molecules entirely across the vapor film, rather than by the ordinary process of thermal diffusion. Eq.(3) was

derived neglecting such a process and deformation of the interface.

Nishio(17) examined the maximum contact temeprature for a water droplet impinging on a fused quartz prism using a total reflection technique, and showed that a water droplet of 80K in subcooling could not come in contact with the fused quartz prism surface at a surface temeprature of about 850K.

(b). Liquid-Creep-in Mode

On a heating surface adjoining to thermally isolated materials (for example, a wire heater connected to electrodes submerged in liquid and a plate surface surrounded by insulator), liquid-solid contacts are induced also by this mode. That is, regardless of temperature level of the heating surface, the thermally isolated surface is always wetted by the liquid. Thus, the liquid will creep into the dry surface from the circumference under film boiling conditions. In this paper, this contact mode is called "the liquid-creep-in mode". Since wetting boundary formed by the liquid-creep-in mode always attacks the vapor film, this wetting boundary forms a weak spot for the vapor film. This kind of contact mode has been observed by Sciance and Colver(18).

2.2 Liquid-Solid Contact Behavior

As mentioned in the previous section, liquid-solid contacts become to occur due to the system disturbances as the surface temperture is decreased from the fully developed film boiling region. However, when the surface temperature is sufficiently high, such liquid-solid contacts experience an early termination as a result of dense nucleation. Such insignificant contacts have been observed by Bradfield(8) and Nishio(17). Bradfield photographically observed liquid-solid contacts beneath a water droplet and reported the existence of the liquid-solid contact coexistent with stable vapor film. That is, "contact filament migrated from point to point beneath this droplet during 155 milliseconds-; nevertheless, complete disengagement never occurred". Similar experiments were conducted by Nishio. Following the technique utilized by Bradfield, an electrode probe was setted passing through the spheroidal state of a water droplet. Then DC voltage of 60V was charged between the electrode and the surface heated at 550K. Fig.3 shows the photograph taken under such conditions. The occurrence of liquid-solid contact is clearly shown in the area indicated by the arrow, but it does not result in collapse of film boiling. Thus, in order that contacts provide a significant amount of energy transfer in comparison to the total energy transfer rate in film boiling, it is necessary that the interface conditions upon contact satisfy the so-called wetting conditions.

The wetting condition is usually termed "the maximum wetting temperature". It goes without saying that the maximum wetting temperature should be distinguished conceptually from the maximum contact temperature. Although the maximum wetting temperature is of practical importance, we have only two concepts on the maximum wetting temperature. One is called "the limit-of-liquid-superheat hypothesis" and the other "the limit-of-adsorption hypothesis"

(a). Limit-of-Liquid-Superheat Hypothesis

The theoretical and experimental aspects of the limit of liquid-superheat are excellently reviewed by Blander and Katz(19). As mentioned in their review, the limit of liquid-superheat has been analyzed with the kinetic approach (i.e., the kinetic limit of liquid-superheat T_{kls}) and also with the thermodynamic approach (i.e., the thermodynamic limit of liquid-superheat T_{tls}). In the thermodynamic approach, the limit of liquid-superheat is determined with the combination of the thermodynamical stability condition of phase and an equation of state. On the other hand, in the kinetic approach, the limit of liquid-superheat is determined by the

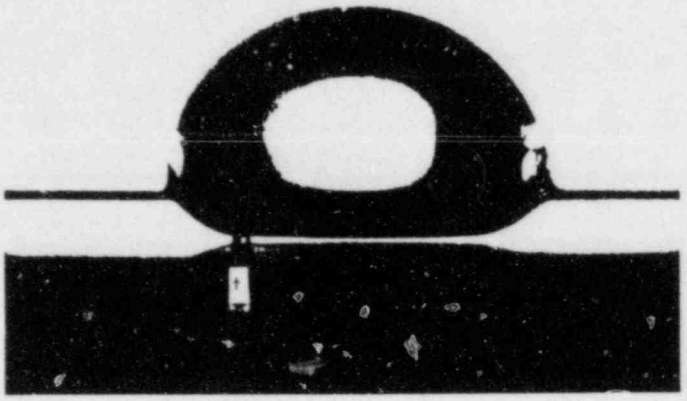

Fig.3 Insignificant Liquid-Solid Contact beneath a Water Droplet (T_w=550K, V=60V)(17)

spontaneous nucleation theories, they are, the homogeneous and heterogeneous nucleation theories. It also goes without saying that the thermodynamic limit of liquid-superheat corresponds to the highest spontaneous nucleation temperature.

Although the limit of liquid-superheat has been studied for isothermal systems, Spiegler et al.(20) supposed that the limit of liquid-superheat under non-isothermal conditions does not differ from that under the isothermal condition. The details of spontaneous nucleation mechanisms (nucleation site densities, thermal boundary layer development and bubble growth characteristics) have been analyzed for non-isothermal systems by Henry and Fauske(21). Following their paper, if the surface temperature lies above the limit of liquid-superheat (for example, the homogeneous nucleation temperature), the volumetric nucleation rate provided by density fluctuations is many orders of magnitude greater than that supplied from preferred sites. With such a dominant, high density nucleation mechanism, liquid-solid contacts should experience an early termination before wetting. This is the reason why the limit of liquid-superheat is considered as one of the wetting conditions. In this paper, the above stated concept is called "the limit-of-liquid-superheat hypothesis".

Lienhard(22) combined the Van der Waals equation of state with Maxwell's criterion and obtained the following simple equation for the thermodynamic limit of liquid-superehat.

$$(T_{tls}-T_{sat})/T_{cr} = 0.905 - (T_{sat}/T_{cr}) + 0.095(T_{sat}/T_{cr})^8 \quad \text{-----(4)}$$

Gunnerson and Cronenberg(23) and Nishio(24) have reported that the above equation provides a better estimation for non-metallic liquids. Using the expression of the interface temperature upon contact between semi-infinite slubs(25) and eq.(4), the maximum wetting temperature (T^*_{lw}) in the limit-of-liquid-superheat hypothesis is

$$T^*_{lw} = T_l + (1+\beta^{0.5})(T_{tls}-T_l) \quad \text{-----(5)}$$

where, $\beta=(k\rho c)_l/(k\rho c)_w$.

In the limit-of-liquid-superheat hypothesis, although wetting characteristics of the interface upon contact can be taken into account, dynamics in wetting process seems to be too simplified.

(b). Limit-of-Adsorption Hypothesis

The limit-of-adsorption hypothesis has been recently proposed by Segev and Bankoff(26). The concept proposed by them is summarized as follows; "wetting upon contact in a non-isothermal system is controlled by a thin liquid film that pulls some liquid to form an evaporating meniscus on the heating surface in film boiling. As long as the surface temperature allows the formation of at least one monolayer of liquid molecules on the surface, wetting is possible. When the temperature is increased above a specific value, no continuous monolayer can be formed, and initial spreading will be discontinued." Segev and Bankoff calculated the fraction of adsorption sites which were occupied,with the Langmuir monolayer adsorption model and determined the limit-of-adsorption assuming the fraction=0.9.

To the auther's knowledge, there are only a few experiments for the maximum wetting temperature. Waldram et al.(27) examined the maximum contact and wetting temepratures for small droplets allowed to fall 0-15cm onto the surface of a pool of hot silicone oil or glycerol. Stable liquid-liquid contacts were obtained if the Weber number upon impact exceeded a critical value, which depended weakly on the surface temperature, and wetting was observed if the temperature was below the homogeneous nucleation temperature of the liquid. Similar experiments have been reported in Ref.(28)(29). On the other hand, Seki et al.(30) measured the surface temperature variation upon contact with a thin-film thermometer deposited on a stainless steel surface. Their results show that the interface temperature upon contact between water and stainless steel at the Leidenfrost point is much lower than the homogeneous nucleation temperature of water.

2.3 Liquid-Vapor Interface Behavior

Since the disturbances prepared in the system are a controlling factor to induce liquid-solid contacts in film boiling, the liquid-vapor interface behavior is of importance as a subprocess of heat transfer mechanism in the vicinity of the minimum heat flux point.

The behavior of an interface separating fluids of different density was first clearly formulated by Taylor(31). The form of the interface disturbance introduced into the first order perturbation analysis is

$$y = y_o \exp(bt)\cos(mx), \quad (m=2\pi/\lambda) \qquad \text{-----(6)}$$

At the node of this disturbance wave

$$y_n = y_o \exp(bt) \qquad \text{-----(6')}$$

Assuming potential flow, the growth rate parameter of the disturbance wave is expressed as

$$b^2 = ((\rho_l-\rho_v)gm-\sigma m^3)/(\rho_l+\rho_v \coth(my_v)) \qquad \text{-----(7)}$$

where liquid layer thickness is assumed infinity. Further assuming thickness of vapor layer is also infinity, the following equations are derived for the condition of the most susceptible disturbance wave.

$$\lambda_d = (2\pi)(3\sigma/g(\rho_l-\rho_v))^{0.5} \qquad \text{-----(8)}$$

$$b_d = ((4\pi/3)(\rho_l-\rho_v)g/(\rho_l+\rho_v)\lambda_d)^{0.5} \qquad \text{-----(9)}$$

where λ_d denotes the most susceptible wavelength.

Chang(32), Zuber(33) and Berenson(34) showed how the minimum heat flux q_M could be predicted for a saturated condition on the basis of the Taylor instability on a horizontal flat plate. Their description suggests that the dominant wavelength, the bubble growth rate, the frequency of bubble departure and the diameter of departure bubble are important.

(a). Dominant Wavelength

Assuming infinite vapor-layer-thickness and one-dimensional analysis, the dominant wavelength in film boiling is determined by eq.(8). Sernas et al.(35) showed that the dominant wavelength in the film boiling on a horizontal flat plate was

$$\lambda_{d2} = \lambda_{d1} \qquad \text{-----(10)}$$

where λ_{d1} is given by eq.(8).

Shoji and Takagi(36) have recently shown that the infinite vapor-layer-thickness assumption causes a considerable error in the estimation of wave characteristics at high system pressures.

Lienhard and Wong(37) have redone the Taylor analysis for a horizontal cylinder and have derived the most susceptible wavelength and the growth rate parameter for such a configuration.

$$\lambda_{dc} = \lambda_d/(1+2/D'^2)^{0.5} \qquad \text{-----(11)}$$

$$D' = D/(\sigma/g(\rho_l-\rho_v))^{0.5} \qquad \text{-----(12)}$$

$$b_{dc} = b_d(1+2/D'^2)^{0.5}(\lambda_d/\lambda_{dc})^{0.5} \qquad \text{-----(13)}$$

The most susceptible wavelength on a horizontal flat plate predicted with eqs. (8) and (10) are in good agreement with the data for water and Freon-113(38). Similarly, eq.(11) is also in good agreement with the data for organics(37)(39) and for water(40).

(b). Bubble Growth Rate and Bubble Departure Frequency

Lewis(41) showed experimentally that Taylor's theory satisfactorily predicted the growth of the disturbance as long as the amplitude was less than $0.4\lambda_d$. Since the diameter of departure bubble (D_o) is approximately equal to $0.5\lambda_d$, the growth rate of wave motion is derived from eq.(6') as

$$dy/dt = (y_o b)\exp(bt) \qquad \text{-----(14)}$$

and the frequency of departure bubble is

$$f = b_d \ln(y_o/D_o) \qquad \text{-----(15)}$$

Assuming that the magnitude of initial disturbance (y_o) is proportional to the diameter of departure bubble, eq.(15) is rewritten as

$$f = (\text{const.})b_d \qquad \text{-----(16)}$$

However, Lienhard and Dhir(13) have pointed out for isopropanol and cyclohexane data that the exponential growth (eq.(14)) blends into a linear growth after the amplitude reaches a value of (0.12-0.25)λ_d and the growth rate in the linear region is proportional to ($b_d\lambda_d$).

$$dy/dt = (\text{const.})b_d\lambda_d \qquad \text{-----(17)}$$

The frequency of departure bubble from vapor film around a horizontal cylinder has been examined by Sakurai et al.(40). Their results show that the frequency predicted with eqs.(13) and (16) does not agree with their data of water. Their data are correlated for water at system pressures from 0.1 to 1.1MPa as

$$f = 1.49(\rho_l/\rho_v)^{0.22} \qquad \text{-----(18)}$$

(c). Diameter of Departure Bubble

The diameter of departing bubble is usually eatimated to be $0.5\lambda_d$. Hosler and Westwater(38) have reported that the average diameter of departing bubble on a horizontal flat plate is about 73% of λ_d (eq.(8)). However, Sakurai et al.(40) have reported that the ratio D_o/λ_d for cylindrical heaters is not constant but dependent on the system pressure and the diameter of the cylinder.

$$D_o = 2.0(1+7.4\times10^{-5}(\rho_l/\rho_v)^{1.15})(\sigma D/g(\rho_l-\rho_v))^{1/3} \qquad \text{-----(19)}$$

2.4 Problems to be answered

As stated above, the liquid-solid contact mode, the liquid-solid contact behavior and the liquid-vapor interface behavior are of importance as the subprocesses of heat transfer mechanism in the vicinity of the minimum heat flux point. The auther considers that the following information on the subprocesses is needed.

(a). Charateristics of liquid-vapor interface under subcooled conditions

(b). Analysis of the maximum contact temperature including the Knudsen layer problem.

(c). Novel concepts on the maximum wetting temperature accounting for dynamic characteristics of wetting

(d). Experiments for the maximum contact temperature and the maximum wetting temperature

3. PARAMETRIC EEFECTS

In this chapter, parametric effects on the minimum heat flux condition are summarized from experimental and correlational points of view. System factors known to affect the minimum heat flux condition are as follows;

(a). liquid-solid contact mode
(b). geometry of heating surface
(c). system pressure
(d). liquid subcooling
(e). liquid velocity
(f). acceleration in field
(g). thermal conductance of heating surface
(h). surface condition
(i). temperature transient

Table 1 Source of Data (HP: Horizontal Plate, HC: Horizontal Cylinder, HW: Horizontal Wire, SP: Sphere, VP: Vertical Plate, SS: Steady-State Test, TS: Transiet-State Test)

First Auther(Ref.)	Geometry (mm)	Material	Liquid	Pressure (MPa)	ΔT_{sub} (K)	Vel. (m/s)		Comments
1962,Berenson(7)	HP(50.8)	Cu,Ni,Inc.	CCl_4,C_5H_{12}	0.101	0	0	SS	(g),(h)
1962,Hosler(38)	HP(203)	Al	H_2O,R-11	0.101	0	0	SS	
1963,Lienhard(62)	HW(0.51)	Nichrome	H_2O,C_6H_{12}, C_6H_6,C_3H_7OH, CH_3OH,C_2H_6CO	0.0019-0.101	0	0	SS	(a)(c)
1964,Merte(53)	SP(25.4)	Cu	Nitrogen	0.101	0	0	TS	(b)(f)
1964,Lienhard(37)	HW(0.025-0.65)	Nichrome, W	C_6H_6,C_3H_7OH	0.101	0	0	SS	(a)(b)
1966,Kovalev(42)	HW(2-2.5)	Nichrome	H_2O	0.1-9.9	0	0	SS	(a)(c)(h)
1966,Simoneau(84)	VP	Fe,Cr,Al	Nitrogen	0.24	0	0-1	SS	(e)
1967,Merte(57)	SP(6.35-25.4)	Cu	Nitrogen	0.1-0.5	0-16	0	TS	(b)(c)(d)
1967,Bradfield(66)	SP(59.7)	Cu	H_2O	0.101	5-78	0	TS	(d)
1968,Simon(85)	VT(12.8)	Ni	Nitrogen	0.24-1.4	0	0-3.1	SS	(c)(e)
1968,Nishikawa(77)	HP(6.0)	Cu	C_2H_5OH	0.101	0-15	0	SS	(d)(h)
1969,Giventer(80)	HW(0.25)	Constantan	Nitrogen	0.101	0	0	TS	(i)
1969,Witte(86)	SP(9.04)	Ag	H_2O	0.101	5-77	0	TS	(d)
1969,Rhea(87)	SP(12.7-25.4)	Cu	Nitrogen	0.101	0	0	TS	(b)(f)
1970,Nikolayev(64)	HC(4.0)	Brass	CO_2,C_5H_{12}, C_6H_{14},SF_6	0.1-p_{cr}	0	0	SS	(c)
1970,Bergles(44)	HC,HP		H_2O,R-113, Nitrogen	0.101	0	0	TS,SS	(h)(i)
1970,Bulter(88)	VP	Cu(coated)	Helium	0.101	0	0	TS	(h)(i)

Table 1 (Cont'd)

First Auther(Ref.)	Geometry (mm)	Material	Liquid	Pressure (MPa)	ΔT_{sub} (K)	Vel. (m/s)		Comments
1970,Sciance(18)	HC(20.6)		CH_4,C_2H_6,C_3H_8 C_4H_{10}	0.1-p_{cr}	0	0	SS	(c)
1971,Nishikawa(78)	HP(8.0)	Cu	H_2O	0.101	0	0	SS	(h)
1971,Peterson(89)	HW(0.127)	Pt	H_2O	0.101	0	0	SS	
1971,Veres(50)	SP(23.8)	Cu	R-113	0.101	0	0	SS,TS	(h)(i)
1972,Tachibana(90)	HP(18,50)	Cu	R-113,C_2H_5OH	0.101	0-40	0	SS,TS	(d)(i)
1973,Berlin(71)			Nitrogen,H_2O C_2H_5OH,R-12, 13,22	0.101	0	0	TS	(g)
1973,Hesse(55)	HC(14.0)	Ni	R-12,113,114	0.1-p_{cr}	0	0	SS	(c)
1973,Stevens(91)	SP(25.4)	Ag	H_2O	0.101	23-76	1.5	TS	(d)
1974,Skripov(92)	HW		C_5H_{12}	0.1-p_{cr}	0	0	SS	(c)
1974,Sakurai(93)	HW(1.2)	Pt	H_2O	0.101	0-40	0	SS	(a)(d)
1974,Farahat(68)	SP(12.7, 25.4)	Ta	Na	0.101	6-681	0	TS	(d)
1974,Henry(6)	HP	Hg,H_2O	H_2O,C_2H_5OH, R-11,12	0.101	0	0	TS	(h)
1975,Zhukov(94)	HP(42.0)	Cu(coated)	R-113	0.101	0	0	SS	(g)
1975,Klimenko(95)	HP(8-36)	Cu	Nitrogen	0.101	0	0	SS,TS	(b)(g)
1977,Bier(56)	HC(8.0)	Cu	R-12,115,13B1 RC-318	0.4-4	0	0	SS	(c)
1978,Yao(10)	HP	Cu,S.S.	H_2O,C_2H_5OH	0.03-1.5	0	0	TS	(c)(g)
1978,Peyayopanakul(51)	HP(50.8)	Cu	Nitrogen	0.101	0	0	TS	(i)
1978,Ishigai(96)	HP(12.0)	S.S.	H_2O	0.101	0-55	0.5-3	TS	(d)(e)

Table 1 (Cont'd)

First Auther(Ref.)	Geometry (mm)	Material	Liquid	Pressure (MPa)	ΔT_{sub} (K)	Vel. (m/s)		Comments
1978,Dhir(48)	SP(19,25.4)	Cu,Ag,S.S.	H_2O	0.101	0-50	0-0.45	TS	(d)(e)
1980,Yilmaz(69)	HC(6.4)	Cu	R-113	0.101	0	0-6.8	SS	(e)
1980,Sakurai(65)	HW(1.2,2.0)	Pt	H_2O	0.02-2	0-41	0	SS,TS	(c)(d)(i)
1981,Shih(45)	SP(3.2-6.4)	Brass	R-11,113	0.101	0-20	0	TS	(b)(d)
1982,Toda(15)	HW(0.3)	Pt	H_2O	0.1-0.5	0-40	0	SS,TS	(c)(d)
1982,Lin(72)	HP(50.8)	Cu,Al,Zn, Pb,Bi	Nitrogen	0.101	0	0	TS	(g)(i)
1983,Sakurai(40)	HC(1.2-3.0)	Pt	H_2O	0.1-2	0	0	SS	(c)
1983,Nishio(43)	SP(3.2-19)	Brass	R-12,22,N_2	0.101	0	0	TS	(1)(2)
1983,Takagi(67)	SP(9.5)	S.S.	H_2O	0.101	30-80	0	TS	(d)
1983,Nishio(47)	HC(6.0)	Ag	H_2O	0.101	5-80	0	TS	(d)
1983,Nagano(49)	HP(62.0)	Cu	R-113	0.04-0.8	0	0	SS	(c)
1984,Nishio(52)	HP(22.0)	Cu	Nitrogen	0.101	0	0	SS,TS	(a)(g)(h)

Table 2 Effect of Geometry of Heating Surface

Liquid	Heater Geometry(Size)	ΔT_M K	q_M kW/m^2	Ref.
Water	Horizontal Flat Plate(50mm)	110	14	(46)
	Horizontal Cylinder(1.2mm)	117	46	(40)
	Horizontal Cylinder(2.0mm)	119	35	(40)
	Horizontal Cylinder(3.0mm)	117	25	(40)
	Horizontal Cylinder(6.0mm)	104	30	(47)
	Sphere(19mm)	101	25	(48)
	Sphere(25.4mm)	109	24	(48)
Freon-113	Horizontal Flat PLate(62mm)	53	10	(49)
	Sphere(23.8mm)	55	11	(50)
Nitrogen	Horizontal Flat Plate(50mm)	22	9	(51)
	Horizontal Flat Plate(22mm)	22	18	(52)
	Sphere(3.2mm)	26	5.7	(43)
	Sphere(19mm)	26	7.8	(43)
	Sphere(25.4mm)	25	4.6	(53)

Sources of the data are given in Table 1. The alphabets in the "comments" column correspond to the system factors stated above.

3.1 Effect of Liquid-Solid Contact Mode

Kavalev(42) and Nishio(43) examined the effect of the liquid-creep-in mode on the minimum heat flux condition. Kovalev measured the minimum heat flux on a horizontal cylinder for pressurized water and found that the liquid-creep-in mode along the electrodes increased the minimum heat flux by factors of 5-8 in comparison to that in a system having no liquid-creep-in mode. Also Nishio examined the minimum heat flux conditions on spheres (D=3.2-19.1mm) for liquid nitrogen, Freon-12 and Freon-22. The experimental results show that, with decreasing sphere diameter, the liquid-creep-in mode comes to increase T_M and q_M.

Bergles and Thompson(44) pointed out that the liquid-creep-in mode (they called the end-effects) created large axial temperature gradients during quench tests of horizontal cylinders. Thus, the wetting boundary formed by the liquid-creep-in mode always attacks the vapor film and also cools the surface with the two dimentional heat conduction along the surface.

3.2 Effect of Geometry of Heating Surface

As well known, heat transfer coefficients in film boiling (h_f) vary with geometry and size of the heating surface. Thus, if the heat transfer coefficient at the minimum heat flux point is equal to the value of $h_f(T_M-T_{sat})$, it is considered rea-

sonable that the minimum heat flux varies with geometry and size of the heating surface. Thus, in this section, we consider only the effect on the temperature condition at the minimum heat flux point.

Experiments on hot small brass spheres of 3.18-6.35mm in diameter, suddenly immersed in Freon-11 and Freon-113 were carried out by Shih and El-Wakil(45). They found that T_M was increased with decrease in sphere diameter. For example, their correlating equation for saturated Freon-11 is

$$T_M = T_{sat} + (48.5)D^{-0.276} \quad , (D:cm) \qquad \text{-----(20)}$$

Similar experiments were conducted for saturated nitrogen, Freon-12 and Freon-22 by Nishio(43). The experimental results show that the temperature condition at the minimum heat flux point is independent of sphere diameter in the range of D=3.2-19.1 mm. The published data of the minimum heat flux condition for a variety of surface geometries are compared in Table 2 for saturated water, Freon-113 and nitrogen(40)(43)(46)-(53). From this table, the temperature condition at the minimum heat flux point seems to be a unique value for a given liquid as long as the liquid-solid contact mode is not essentially changed. In this paper, such a concept is called "the temperature-control hypothesis".

3.3 Effect of System Pressure

The effect of system pressure on the minimum heat flux condition has been studied from several points of view.

Experimental data of the temperature condition at the minimum heat flux point are shown in Figs.4 and 5(10)(18)(40)(49)(54)-(57). Nishio(58) has surveyed these data and has pointed out that there are three distinct pressure regions; (a)low pressure region (the superheat at the minimum heat flux point is decreased with increasing system pressure),(b)medium pressure region (the superheat is increased or kept nearly constant with incerasing system pressure) and (c)high pressure region (the superheat is again decreased with inceasing system pressure).

As shown in Fig.5, a part of these data lies above the critical temperature the liquid. Adopting the limit-of-liquid-superheat hypothesis as the wetting criteria, the temperature at the minimum heat flux point will not exceed the temperature determined with eq.(5). Yao and Henry(10) and Sakurai et al.(40) have presented the data supporting this hypothesis. Sakuari et al. have examined the minimum heat flux conditions for saturated water at pressures from 101kPa to 2MPa on horizontal cylinders of 1.2-3mm in diameter and have pointed out that the temperature condition at the minimum heat flux point is determined by the spontaneous nucleation temperature at system pressures above 1MPa. Similar results have been reported by Yao and Henry for pressurized water and ethanol. Sakurai et al. correlated their data on a cylinder of 2mm in diameter as

$$\Delta T_M = (480 - T_{sat}) + (10)\exp(2.22p), \text{ for } p<0.94\text{MPa} \qquad \text{-----(21)}$$

$$\Delta T_M = (480 - T_{sat}) + (80)\exp(0.34(p-0.94)), \text{ for } p>0.94\text{MPa} \qquad \text{-----(22)}$$

As stated above,Nishio(58) postulated the three distinct pressure regions and proposed the following correlations of the superheat at the minimum heat flux point for the medium and high pressure regions.

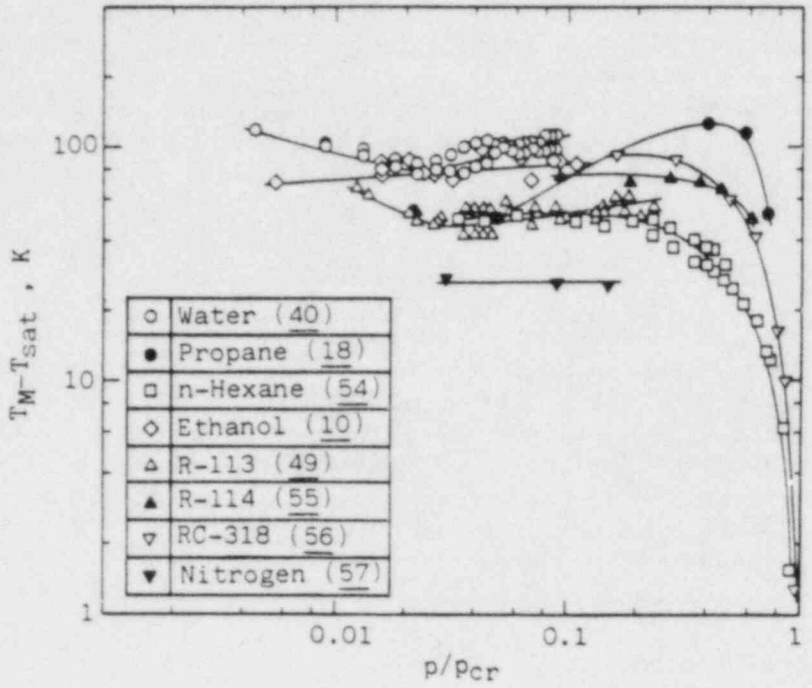

Fig.4 Effect of System Pressure(I) ($T_l=T_{sat}$)

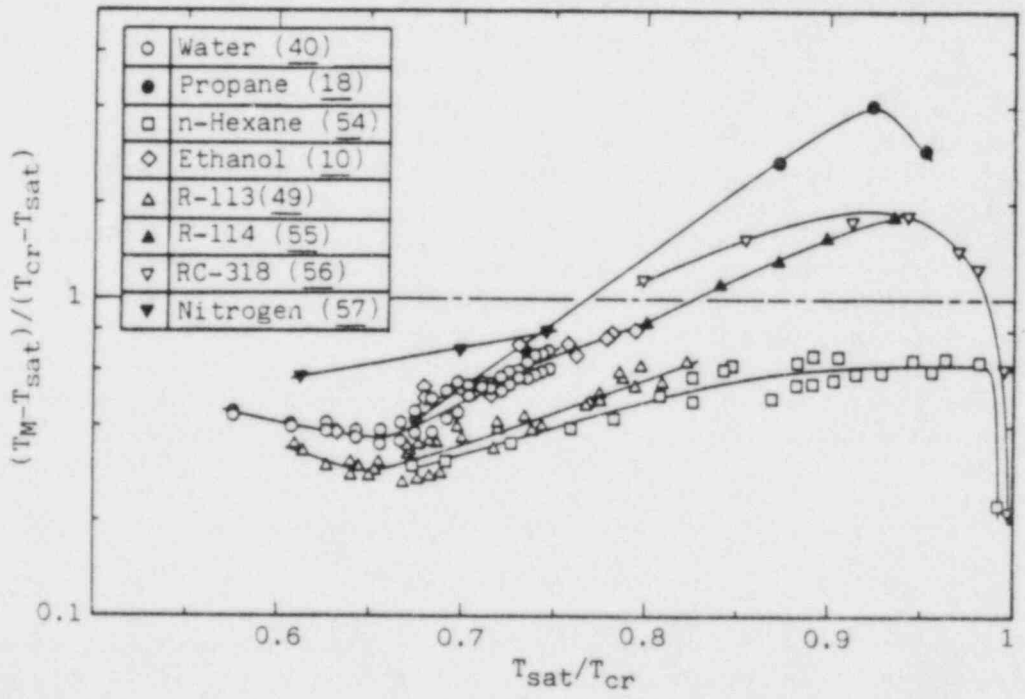

Fig.5 Effect of System Pressure(II) ($T_l=T_{sat}$)

$$T_M - T_{sat} = (3.449\times10^{-4})(T_{cr}-T_{sat})(Ja^*)^{-1}(\rho_r^*)^{0.6302} \times (Pr^*)^{1.008}(l_r^*)^{0.2056}\exp(4.94T_{sat}/T_{cr})$$

, for medium pressure region -----(23)

$$T_M - T_{sat} = T_{cr}(0.905-(T_{sat}/T_{cr})+0.095(T_{sat}/T_{cr})^8)$$

, for high pressure region -----(24)

where * denotes the value at $T_{sat}/T_{cr}=0.7$ and

$$Ja = c_l L/(T_{cr}-T_{sat}),\ \rho_r = \rho_v/\rho_l,\ Pr = \upsilon_l/\alpha_l,\ l_r = \sigma^3/g(\rho_l-\rho_v)^3\upsilon_l^4$$

As for the pressure dependence of the minimum heat flux, the experimental data for organics(18)(64) and refrigerants(56) show that the value of q_M reaches a maximum in the pressure range of $p/p_{cr}=0.2$-0.4. This pressure dependence of q_M is similar to that found for the critical heat flux q_C. From the equations of Zuber(33)(59), the following relationship for the ratio q_M/q_C is obtained:

$$q_M/q_C = (\text{const.})(\rho_v/\rho_l)^{0.5} \quad -----(25)$$

However, the existence of an approximately constant ratio between q_M and q_C has been observed by Kutateladze(60). Thus as suggested by Chang(61) and Bier et al.(56), it is better to modify eq.(25) as

$$q_M/q_C = (\text{const.}) \quad -----(26)$$

Lienhard and Schrock used the following equation for q_M(62)

$$q_M = (\text{const.})(\rho_v L)(\sigma g(\rho_l-\rho_v)/(\rho_l+\rho_v)^2)^{0.25} \quad -----(27)$$

as the starting point for a generalized correlating equation in terms of reduced pressure. The resulting equation was

$$q_M = a_M x f_1(p/p_{cr},\ \text{geometry}) \quad -----(28)$$

$$a_M = g^{0.25}p_{cr}P/M(8Mp_{cr}/3RT_{cr})^{0.75} \quad -----(29)$$

Lienhar and Watanabe(63) extended this relationship as

$$q_M = a_M x f_2(p/p_{cr}) f_3(\text{geometry}) \quad -----(30)$$

where $f_2(p/p_{cr})$ represents the pressure dependence and is the same as for a horizontal flat plate, and f_3(geometry) represents the geometry dependence. As for f_2, Nikolayev and Skripov(64) proposed the correlating equation using data of four organic liquids.

$$a_M f_2(p/p_{cr}) = 1.67q_M(p/p_{cr}=0.31)(p/p_{cr})^{0.24}(1-p/p_{cr})^{0.61} \quad -----(31)$$

$$a_M f_2(p/p_{cr}) = 4.18q_M(p/p_{cr}=0.9)(p/p_{cr})^{0.24}(1-p/p_{cr})^{0.61}$$

, for high pressures -----(31)

Bier et al.(56) confirmed this type of correlation for refrigerants.

Sanders and Colver(1) also used the corresponding states principle in proposing the relation

$$q_M = (11.2\times10^6)p^{0.468}(p/p_{cr}-(p/p_{cr})_{tp})^{0.293}(1-p/p_{cr})^{0.827}a'_M \quad --(32)$$

where $(p/p_{cr})_{tp}$ is the reduced pressure at the triple point of the fluid and

$$a'_M = p_{cr}(RT_{cr}/M)^{0.5} \quad -----(33)$$

3.4 Effect of Liquid Subcooling

The effect of liquid subcooling on the minimum heat flux condition has been studied for water in steady-state experiments(15)(65) and quenching experiments(47)(48)(66)(67). Fig.6 shows the comparison between these data at atmospheric pressure. Although these data were taken on a variety of surface geometries, they show a nearly unique subcooling dependence of the superheat at the minimum heat flux condition. Also this result seems to suggest that the minimum heat flux condition may be represented by the temperature condition.

All of the quench data (Fig.6) show a linear dependence of T_M over holl region of subcooling. For example, Dhir and Purohit(65) correlated the subcooling dependence for water as

$$T_M = 201 + 8(T_{sat}-T_l) \quad ------(34)$$

This equation shows that the temperature at the minimum heat flux point exceeds the

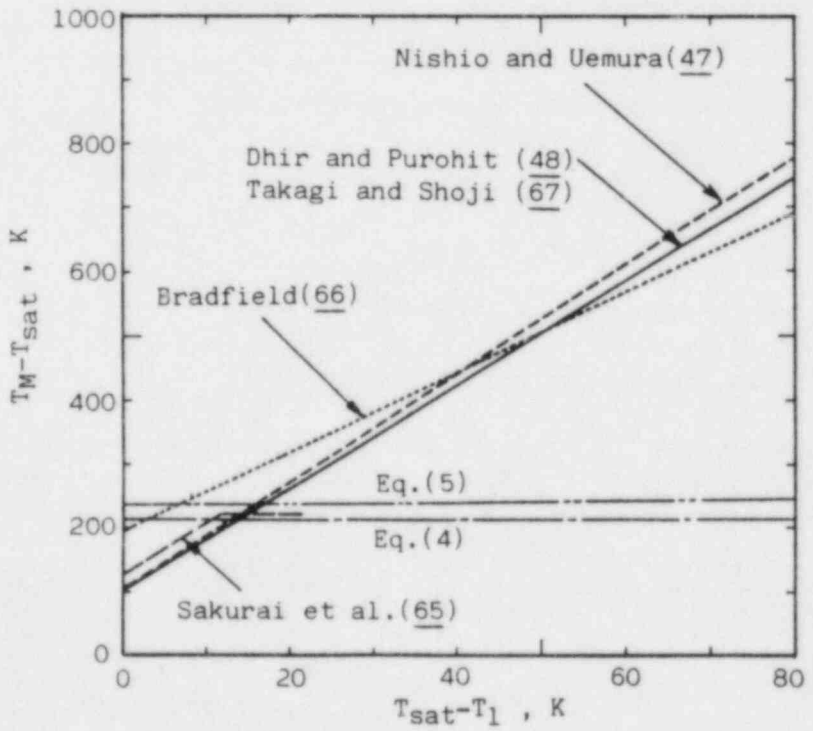

Fig.6 Effect of Liquid Subcooling (Water, p=0.1MPa)

critical temperature of water at subcoolings greater than 22K and also exceeds the limit of liquid-superheat at subcoolings greater than 14K. In Fig.6, eqs.(4) and (5) are shown for water on a platinum surface. Sakurai et al.(65) examined the effect of subcooling on the minimum heat flux condition for pressurized water in 0 to 40 K subcoolings. Their results are schematically shown in Fig.7 and summarized as follows; (a)the subcooling dependence of (T_M-T_{sat}) is almost linear for low subcoolings but it saturates at a subcooling when the linear increase of (T_M-T_{sat}) reaches the spontaneous nucleation temperature, (b)the gradient in the linear region is decreased with increasing system pressure and (c)as a result of (a) and (b), at system pressures above 1Mpa, the temperature at the minimum heat flux point is determined by the spontaneous nucleation temperature for all region of subcooling. Although a linear dependence of T_M has been reported also for sodium by Farahat et al.(68), the subcooling dependency of the temperature at the minimum heat flux point should be intensively studied. The descrepancy between quench data and steady-state data on the subcooling effect may result from the effect of the liquid-creep-in mode, because it was carefully taken away in Sakurai's experiments.

As for the effect of liquid subcooling on the minimum heat flux, Sakurai et al. (65) reported also the intersting results; (a)for small subcoolings,the subcooling dependence of q_M is relatively small and (b)for large subcoolings, q_M becomes to be determined only by liquid subcooling and to be independent of system pressure. Such tendencies were also reported by Toda and Mori(15).

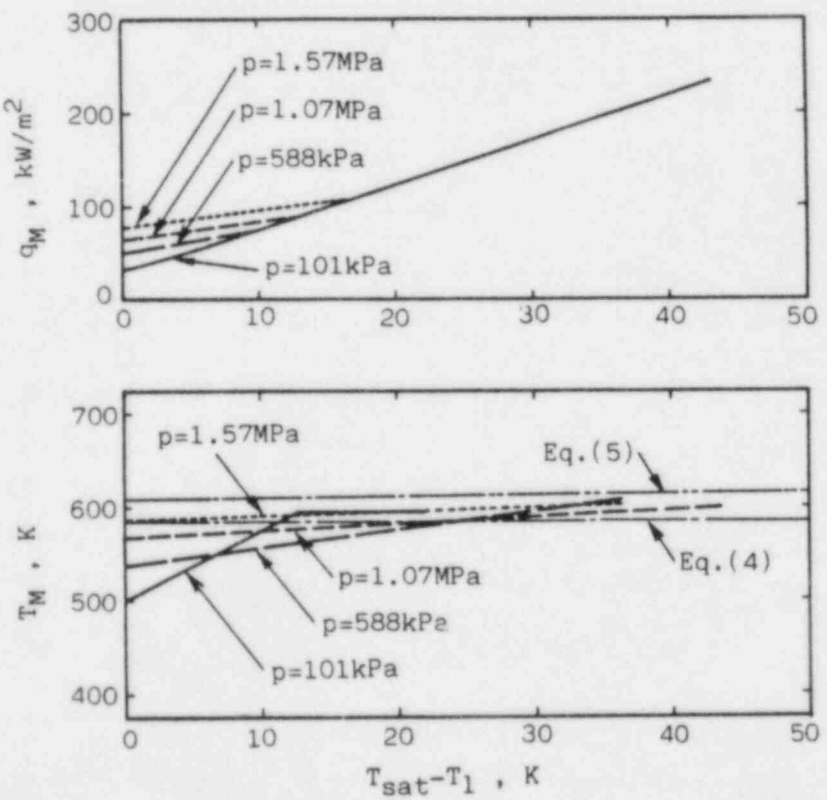

Fig.7 Effect of Liquid Subcooling(Water, Horizontal Cylinder, D=2mm)(65)

3.5 Effect of Liquid Velocity

It has been known that liquid velocity has remarkable effects on the transition boiling and film boiling characteristics. For example, Yilmaz and Westwater(69) observed for boiling of Freon-113 on a horizontal cylinder that heat fluxes in film boiling were proportional to liquid velocity to the exponent 0.56 and that transition boiling was very sensitive to liquid velocity. Thus, it seems reasonable to expect the minimum heat flux to be increased with an increase in liquid velocity.

However, Dhir and Purohit(48) reported that the temperature at the minimum heat flux point was kept constant for liquid velocities from 0 to 0.45m/s. Their results are shown in Fig.8. From this figure, it seems reasonable to expect T_M to be kept constant for low velocities.

3.6 Effect of Acceleration in Field

The effect of reduced gravity upon the minimum heat flux condition for spheres has been studied by Merte and Clark(53). They found a very approximate $g^{0.25}$ dependence for q_M. Lienhard(70) used eq.(30) to correlate their data and showed that the parameter D' (eq.(12)) represented the effect of gravity in the same way as the effect of geometry.

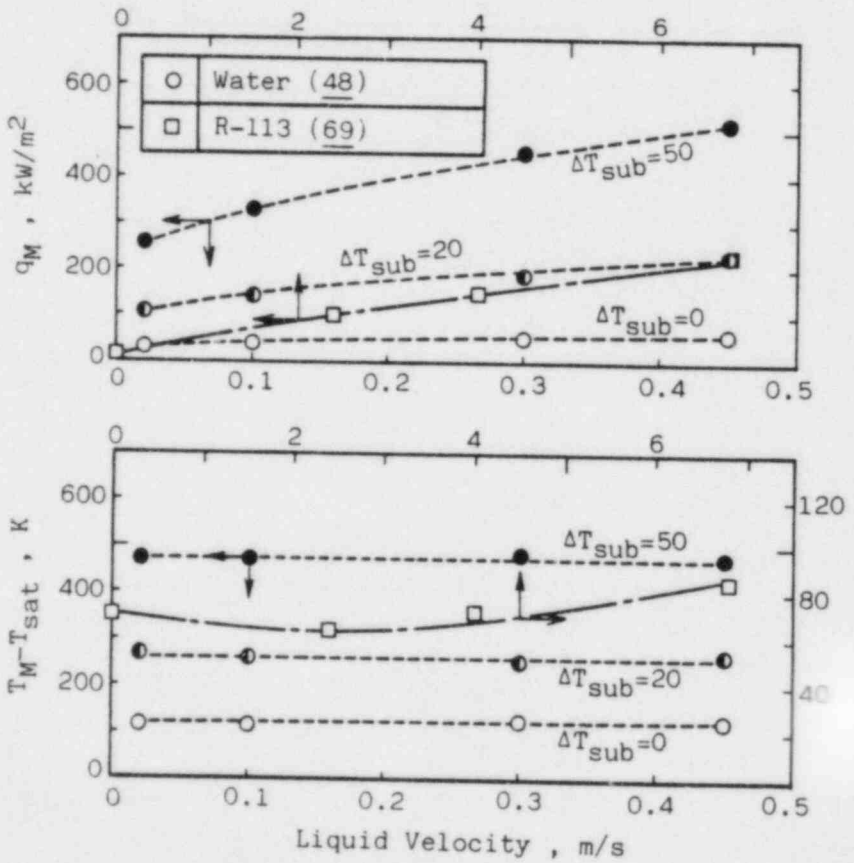

Fig.8 Effect of Liquid Velocity (p=0.1MPa)

3.7 Effect of Thermal Conductance of Surface

It has been recognized that thermal properties of the heating surface do not affect heat transfer coefficients in film boiling but they affect the Leidenfrost temperature of a droplet.

Dhir and Purohit(48) examined the effect of thermal properties of surfaces for boiling of water on spheres of steel, copper and silver. They found that thermal properties of spheres did not affect the minimum heat flux condition. On the other hand, the experiments for pentane(7) and nitrogen(52)(71)(72) show that the temperature at the minimum heat flux point is increased with decreasing thermal conductance of surfaces. These data are shown in Fig.9 together with the data for water.

There are some other data suggesting remarkable effects of thermal conductance of surfaces on the minimum heat flux condition. Cowley et al.(73) observed that thin coatings of a poor thermal conductor on metallic objects reduced a lengthy cooldown process in liquid nitrogen. Similar results have been reported for water quench by Moreaux et al.(74). Nishio(52)(75) showed that such paradoxical phenomena resulted from the effect of thermal conductance of the surface on the minimum heat flux condition. Experiments on the cooldown in liquid nitrogen of coated and uncoated copper plates were carried out and it was found that T_M was increased with increasing coating thickness (Fig.10).

The effect of thermal conductance of the heating surface on the temperature at the minimum heat flux point has been analyzed taking account of a decrease in surface temperature upon contact. In the simplest model, the decerase in surface temperature

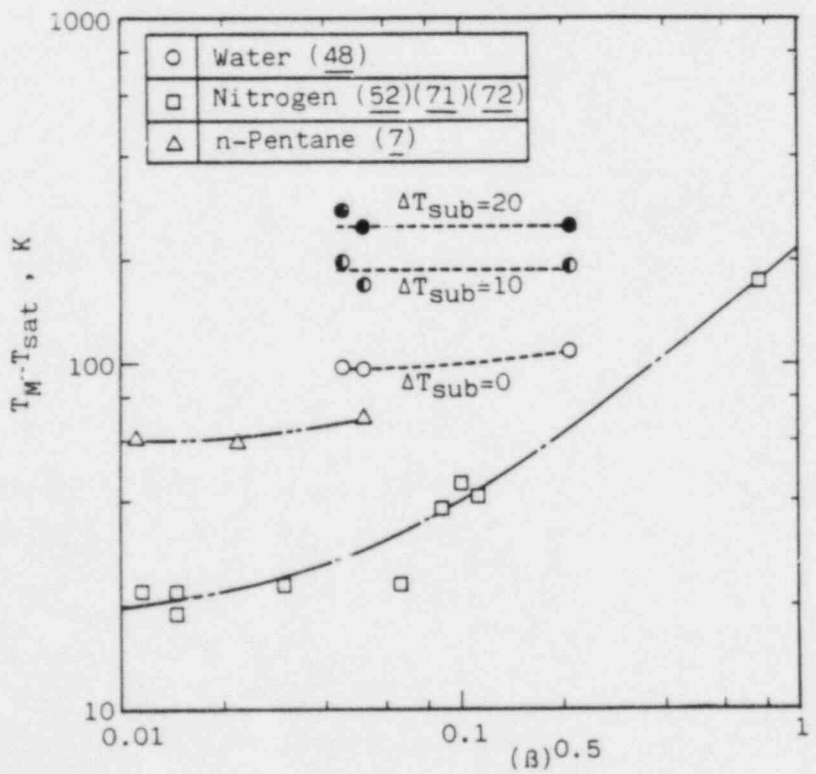

Fig.9 Effect of Thermal Properties of Surface (p=0.1MPa)

upon contact is estimated with the expression of the interface temperature upon contact between semi-infinite slubs. As stated in 2.2 Seki et al.(30) have measured the decrease in surface temperature upon contact. Their results for water droplets show that this simple expression does not agree with the measured temperature response. Manson(97) used analog computer to demonstrate the effect of a periodic heat transfer coefficient in the vicinity of the minimum heat flux point. The results show that such fluctuations cause large temporal variation in the heat transfer surface temperature. Thus Manson speculated that fluctuations in heat transfer coefficient were sufficient to produce local cold spots. Baumeister and Simon(76) proposed a prediction model for the Leidenfrost temperature considering the effect of thermal properties of the surface. In their model, the variation in surface temperature is estimated using the solution of the unsteady heat conduction problem in a semi-infinite slub with convective heat losses.

Henry(11) developed the correlating equation of the superheat at the minimum heat flux point taking account of the variation in surface temperature upon contact on the basis of Berenson's theory.

$$(T_M-T_{MI})/(T_{MI}-T_l) = (0.42)(\beta^{0.5}L/c_l(T_{MI}-T_{sat}))^{0.6} \qquad -----(35)$$

where T_{MI} is given with eq.(47). This equation has been confirmed for sodium by Farahat and Eggen(68). Berlin et al.(71) developed the following correlating equation for the effect of thermal properties of the heating surface.

$$T_M-T_{sat} = (T_{cr}-T_{sat})(0.165+2.5\beta^{0.25}+\beta) \qquad -----(36)$$

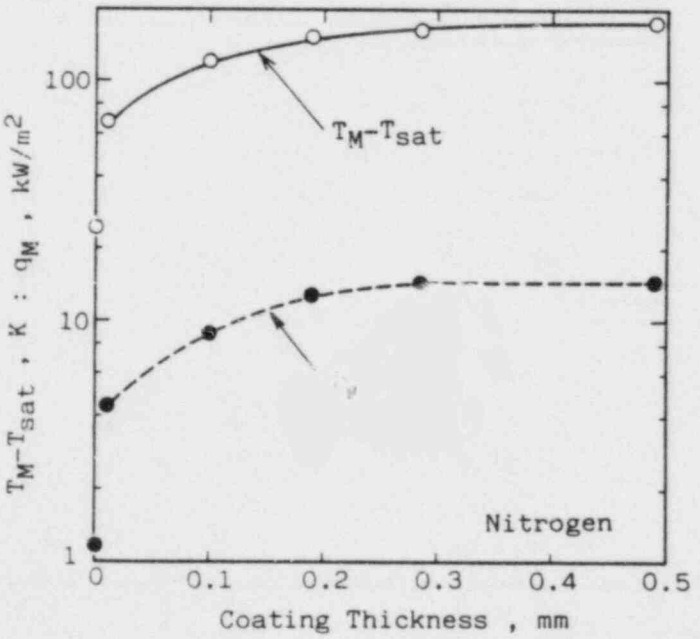

Fig.10 Effect of Thermal Conductance of Surface (p=0.1MPa, $T_l=T_{sat}$)(52)

3.8 Effect of Surface Condition

Berenson(7) studied the effect of surface roughness on transition boiling in a pool boiling system using a variety of organics. In general, commercial surface finish did not have a strong effect on T_M and q_M. Berenson's observations agree with those of Nishikawa et al.(77), although Nishikawa et al. observed a slight increase in q_M with increasing surface roughness.

The auther considers that the most effective factor in surface conditions is wetting characteristics. Nishikawa et al.(78) observed that film boiling persisted well into small surface superheats on a poor wetted sysytem (T_M-T_{sat}=30K for water) although it collapsed on a normal surface at a superheat near 100K. Such observations agree with those of Gaertner(79). As well known, the surface cleanness and oxidization of the heating surface change the wetting characteristics. In general, they markedly increase both of T_M and q_M(7)(44)(50)(77). Berenson explained the mechanism of the effect of wetting characteristics as follows: "Borishanski(12) has shown that the liquid instantaneously contacts the solid surface in film boiling after a bubble breaks away from the two-phase interface. If the liquid spreads sufficiently fast upon contacting the surface a vapor film may not reform. Therefore, under these conditions the location of the minimum would depend upon spreading rate.---The value of the minimum heat flux for dirty surfaces depends upon the rate of spreading."

As reviewed above, the effect of surface condition has been studied only qualitatively. Thus, the physical propoerties representing the dynamic characteristics of wetting snould be pointed out.

3.9 Effect of Temperature Transient

Bergles and Thompson(44) studied the pool boiling curves during quenching and steady-state conditions in several liquids. They observed an decerased q_M for the transient tests in liquid nitrogen and explained as a result of a relatively long delay time required for film collapse. Giventer and Smith(80) applied a step decrease in power to an 0.25mm in diameter constantan wire which was initially in film boiling with liquid nitrogen, and found that delays of up to 2.5msec were encountered before the nucleate boiling was established.

Veres and Florschuetz(50) studied the pool boiling curves of Freon-113 during quenching and steady-state conditions using the same copper spheres of 23.8mm in diameter. They found that the quench data for the minimum heat flux condition were in good agreement with those for the steady-state conditions as long as the surface was free from fouling and oxidization. Their results agree with those of Sakurai et al. (65) for pressurized water.

However, Peyayopanakul and Westwater(51) and Nishio(52) studied the pool boiling curves of liquid nitrogen on horizontal flat plates of various thicknesses under quenching conditions and showed that q_M was markedly decreased with decreasing plate thickness although T_M was independent of the plate thickness. Their data are shown in Fig.11.

3.10 Problems to be Answered

From the information reviewed in this chapter, the auther considers that research efforts should be encouraged in the following areas.

(a). Experimental studies on the geometry effect on the temperature condition of the minimum heat flux point.

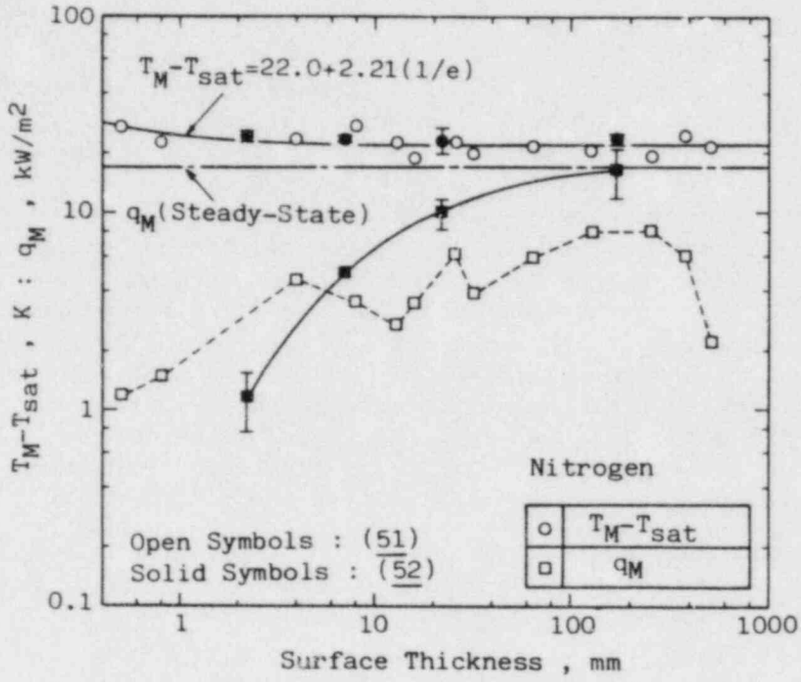

Fig.11 Effect of Temperature Transient (Horizontal Flat Plate, p=0.1MPa $T_l=T_{sat}$, e:Plate Thickness)

(b). Experimental studies on the pressure and subcooling effects on the temperature condition of the minimum heat flux point to check the possibility that it may exceed the spontaneous nucleation temperature at high pressures or subcoolings

(c). Experimental studies on the effects of surface properties and temperature transients on the minimum heat flux condition

(d). Experimental studies to check the temperature-control hypothesis for the minimum heat flux condition

(e). Experimental studies on the minimum heat flux condition for liquid metals and at low system pressures

(f). Experimental studies to find out the physical properties representing the dynamic characteristics of wetting

4. ANALYTICAL MODELS

In this chapter, analytical models to predict the minimum heat flux condition are reviewed. The analytical models are classified into the following types.

(a). temperature-control models

(b). heat-flux-control models

4.1 Temperature-Control Model

In the temperature-control models, the temperature condition of the minimum heat flux point is recognized as the controlling condition for the minimum heat flux condition, and the temperatute T_M is equated to a kind of the maximum wetting temperature. The limit-of-liquid-superheat model and the limit-of-adsorption model

are typical of them.

In this approach, q_M is calculated using a predicted value of heat transfer coefficient at the minimum heat flux point as

$$q_M = h_M x (T_M - T_{sat}) \qquad \text{------(37)}$$

(a). Limit-of-Liquid-Superheat Model

Spiegler et al.(20) proposed "the foam limit model" that the temperature at the minimum heat flux point corresponds to the limit of liquid-superheat predicted by Van de. Waals equation of state and the thermodynamical stability condition of phase. As stated in 2.2, the limit of liquid-superheat can be predicted more precisely with the kinetic and thermodynamic approaches. The kinetic limit of liquid-superheat is not a true limit and there is a true limit, the thermodynamic limit of liquid-superheat, which is the temperature at which the liquid branch of a pressure-volume diagram for a fluid is at a minimum. The spontaneous nucleation may be either homogeneous or heterogeneous depending on the transient wetting characteristics of the given system. For simplicity, well-wetted systems will be considered which mean that the nucleation is homogeneous within the liquid. Lienhard(22) has derived the simple correlating equation (eq.(4)) for the thermodynamic limit of liquid-superheat. Fig.12 shows the comparison between this equation and the published data of $(T_M - T_{sat})$. As shown in this figure, the minimum heat flux point appears to be determined by eq.(4) at high pressures . However, the data for low pressures lie well below the limit of liquid-superheat. Thus, as pointed out by Yao and Henry(10), Sakurai et al.(40) and Nishio(58), validity of the limit-of-liquid-superheat model seems to be restricted within high pressure region. Henry(11) pointed out that the liquid-metal data of Farahat et al.(68) and Paddia(81) differed greatly from the limit-of-liquid-superheat model. The auther considers that their data correspond to the low pressure region stated in 3.3 and the limit-of-liquid-superheat model is intrinsically invalid in this pressure region.

Baumeister ans Simon(76) modified the foam limit model for heated surface properties. However, Yao and Henry(10) pointed out that this prediction was unrealistic at high pressures because it was less that the saturation temperature of the liquid.

(b). Limit-of-Adsorption Model

Segev and Bankoff(26) proposed the model that the temperature at the minimum heat flux point corresponds to the temperature condition at the adsorption limit predicted with the Langmuir adsorption model. To compare this model with the published data of T_M, the data of heat of adsorption are needed. Unfortunately, however, the auther could not perform such a comparison due to a lack of available data of heat of adsoprtion.

The reasons why the temperature-control models are supported are summarized as follows: (i). There are some data indicating that the minimum heat flux point appears to be determined by the limit of liquid-superheat at high system pressures (Fig.12) and for high subcoolings (Fig.7). (ii). There are some data indicating that the temperature T_M for the given liquid is independent of geometry of the heating surface, liquid velocity and temperature transient (Table 2, Figs.8 and 11). On the other hand, these models include the following weak points: (i). Most of the data of T_M at low pressures differ greatly from these models. (ii). Most of the data of T_M for highly subcooled conditions exceed the limit of liquid-superheat (Fig.6). (iii). Eq. (5) seems not to agree with the dependency of the data on thermal conductance of the heating surface and liquid subcooling.

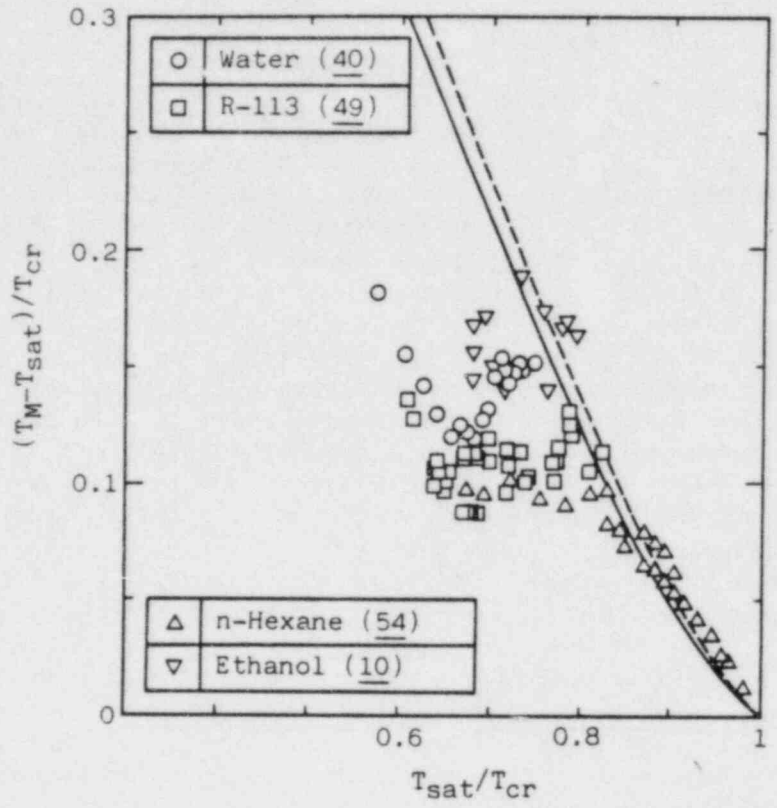

Fig.12 Comparison between Limit of Liquid-Superheat and Data of T_M under saturated conditions

4.2 Heat-Flux-Control Model

In the heat-flux-control models, the heat flux condition at the minimum heat flux point is recognized as the controlling condition for the minimum heat flux condition.

Zuber(33) showed how q_M for saturated film boiling could be predicted on the basis of the Taylor instability. Following Zuber's idea,

$$q_M = (A)(B)(C) \qquad \text{-----(38)}$$

where, (A) = (energy transfer per departing bubble)
(B) = (bubbles per unit heating area in one oscillation)
(C) = (minimum number of oscillations per unit time)

From the information reviewed in 2.3, the terms (A) and (B) are estimated as

$$(A) = (\rho_v L)(4\pi/3)(\lambda_d/4)^3 \qquad \text{-----(39)}$$

$$(B) = 2/(\lambda_d)^2, \text{ for horizontal flat plates} \qquad \text{-----(40)}$$

$$= 2/(\pi D\lambda_d), \text{ for horizontal cylinders} \qquad \text{-----(41)}$$

Berenson(34) used eqs.(9) and (16) to estimate the value of (C).

$$(C) = (\text{const.})((4\P/3)g(\rho_l-\rho_v)/((\rho_l+\rho_v)\lambda_d))^{0.5} \qquad \text{-----(42)}$$

From eqs.(38)-(42), Berenson gave the following expression of q_M on a horizontal flat plate.

$$q_M = 0.09(\rho_v L)Z^{0.25} \qquad \text{-----(43)}$$

$$Z = g\sigma(\rho_l-\rho_v)/(\rho_l+\rho_v)^2 \qquad \text{-----(44)}$$

The proportional constant 0.09 was determined experimentally. Lienhard and Wong(37) similarly derived q_M for a horizontal cyliner and their expression was modified into the following dimensionless form by Lienhard and Watanabe(63).

$$q_M=(\text{const.})(\rho_v L)Z^{0.25}(1+2/D'^2)^{0.5}(D'^{2/3}/(2+D'^2))^{3/4} \qquad \text{-----(45)}$$

The constant of proportionality in eq.(45) was also determined experimentally(37)(39). Lienhard and Dhir(13) derived analytically the proportional constants in eqs.(43) and (45) on the basis of the instantaneous natural rate of wave motion. The analytical values obtained by them are (0.078-0.104) for a horizontal flat plate and (0.051-0.068) for a horizontal cylinder. These values are in excellent agreement with the values determined experimentally.

The basic models of Zuber and Berenson consider fully developed film boiling to be a stationary process, with bubbles departing from nodes when enough vapor has been generated to make the vapor layer unstable. Ruckenstein(82) has proposed a nonstationary model in which the growth of the nodes from the initial radius to the radius at breakoff is considered. The final form proposed by Ruckenstein is

$$q_M = (\text{const.})(\rho_v L)/(\ln(D_o/D_i))xZ^{0.25} \qquad \text{-----(46)}$$

Using eqs.(37) and (43), Berenson gave the following expression for the surface superheat at the minimum heat flux point

$$T_M-T_{sat} = (0.127)(\rho_v L/k_v)(g(\rho_l-\rho_v)/(\rho_l+\rho_v))^{2/3}(\sigma/(g(\rho_l-\rho_v)))^{1/2} x(\mu_v/(\rho_l-\rho_v))^{1/3} \qquad \text{-----(47)}$$

The above reviewed models are derived for q_M of saturated liquids. Gunnerson and Cronenberg(83) presented an analytical model for spherical and horizontal flat plate surfaces in saturated and subcooled liquids. As the starting point, they modified eq.(38) as

$$q_M = (A)(B)(C) + (D) + (E) \qquad \text{-----(48)}$$

where, (D) = (heat transferred into subcooled liquid per unit area per unit time)
(E) = (heat flux due to transient liquid-solid contact)
They estimated the total heat transfer coefficient (h_t) likewise as

$$h_t = (h_f(T_f-T_{sat})/(T_M-T_{sat}))F_1+(h_c(T_c-T_{sat})/(T_M-T_{sat}))F_2 \qquad \text{---(49)}$$

where h_c is the effective, transient liquid-solid contact heat transfer coefficient. T_f and T_c are the surface temperature over which each heat transfer process is considered. The weighting factors F_1 and F_2 are included to account for the spacial and

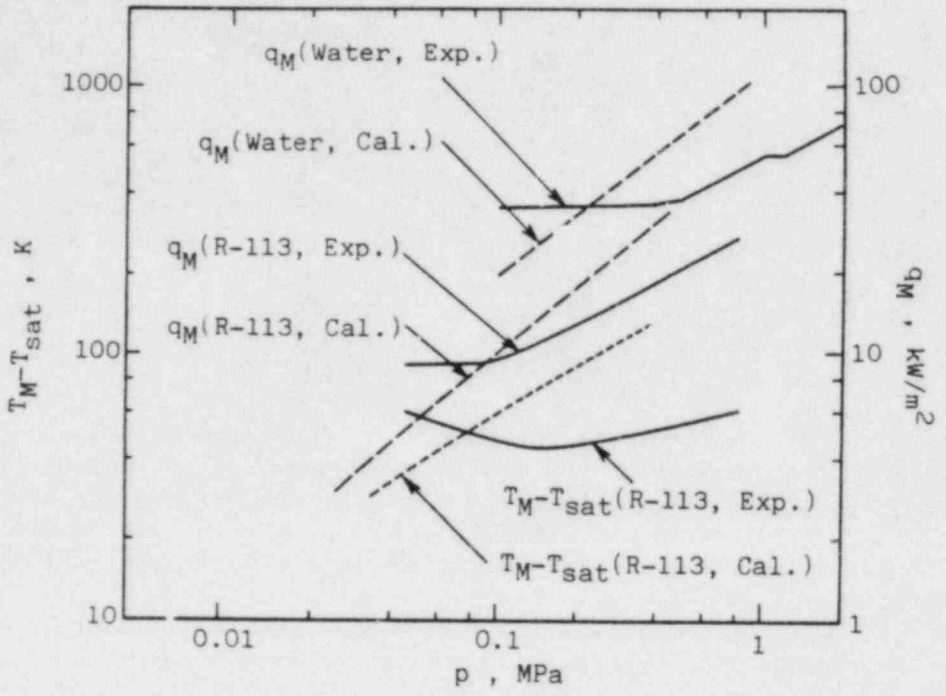

Fig.13 Comparison between Heat-Flux-Control Model and Data of q_M(40)(49)

time dependence of the heat transfer modes.

Eqs.(43) and (45) have been compared with experimental data by several researchers. The data on horizontal flat plates for organic liquids and Freon-113 at atmospheric pressure(34)(49) are in good agreement with the prediction of eq.(43). Similarly, the data on horizontal cylinders for organic liquids and water at atmospheric pressure(37)(40) agree with the prediction of eq.(45). However, Sakurai et al. (40) showed that the data of the minimum heat flux condition came to differ from the prediction of eq.(45) with increasing system pressure. Nagano and Shoji(49) also reported similar results for Freon-113 (Fig.13).

The reasons why the heat-flux-control models have been supported are summarized as follwos: (i). Data of the minimum heat flux condition for organic liquids, water and refrigerants at atmospheric pressure agree with the values predicted by these models. (ii). These models can predict at least qualitatively the pressure dependence of q_M(18)(56). However, the heat-flux-control models have the following weak points: (i). Eq.(38) can not be used under subcooled conditions. (ii). The predicted dependence of the minimum heat flux condition on system pressure doesn't agree quantitavely with the data. (iii). If the effects of contacts are neglected, these models can not predict the effects of wettability and thermal conductance of the heating surface.

4.3 State-of-the-Art

As reviewed above, both of the temperature-control and heat-flux control approaches have not secceeded to predict the parametric effects on the minimum heat flux condition. As pointed out by Yao and Henry(10), it seems reasonable to consider that the minimum heat flux condition appears to be determined either by a Taylor

instability vapor removal and by the spontaneous nucleation upon contact and that the governing mechanism is the one which is stable at the lowest surface temperature.

To develop the analytical models predicting more precisely the parametric effects on the minimum heat flux condition (especially. the effects of system pressure, liquid subcooling, and wetting characteristics), the following studies should be encouraged.

(a). Development of the temperature-control models accounting for wettability and thermal conductance of the heating surface

(b). Development of the heat-flux-control models for vertical surfaces

(c). Development of the heat-flux-control models accounting for the effects of liquid subcooling, liquid velocity, wettability and thermal conductance of the heating surface.

5. Conclusions

A state-of-the-art review is presented on the study of minimum heat flux conditions. It goes without saying that each of the above reviewed works has, more or less, made some contribution to the accumulation of valuable knowledge. However, it seems optimistic to believe that the goal will be reached in very near future, seeing that a number of obstacles have appreared on the way to the goal. Thus, it has been felt by the auther that both the deep investigations on every subprocess which composes the entire process of heat transfer in the vicinity of the minimum heat flux point and as well the synthesizing works of putting each investigation together are equally inevitable.

NOMENCLATUTE

a_M : defined by eq.(29)
a'_M : defined by eq.(33)
b : growth rate parameter of disturbance wave
b_d : growth rate parameter of most susceptible disturbance wave on horizontal flat plate
b_{dc} : growth rate parameter of most susceptible disturbance wave on horizontal cylinder
c : specific heat
D : diameter of heating surface
D' : demensionless diameter defined by eq.(12)
D_o : diameter of departure bubble
e : thickness of heating surface
F : fraction of liquid-solid contact
f : frequency of bubble departure
g : acceleration in field
h : heat transfer coefficient
Ja : Jakob number $(c_l L/(T_{cr}-T_{sat}))$
k : thermal conductivity
L : latent heat of vaporization
M : molecular weight
m : wave number
P : parachor
Pr : Prandtl number of liquid phase

p : system pressure
q : heat flux
R : universal gas constant
r : radius of droplet
T : temperature (ΔT_{sat}: superheat, ΔT_{sub}: subcooling)
t : time
V : voltage
x,y : coordinates parallel with, and normal to, liquid-vapor interface
y_r : surface roughness
y_v : thickness of vapor layer
Z : defined by eq.(44)
α : thermal conductivity
β : $(\kappa\rho c)_l/(k\rho c)_w$
μ : dynamic viscosity
λ_d : most susceptible wavelength on horizontal flat plate
λ_{dc} : most susceptible wave length on horizontal cylinder
υ : kinematic viscosity
ρ : density
ρ_r : density ratio (ρ_v/ρ_l)
σ : surface tension

Subscripts

C : critical heat flux point
c : liquid-solid contact
cr : critical property
d : dry area or most susceptible disturbance wave
f : film boiling
kls : kinetic limit of liquid-superheat
l : liquid
lc : limit of liquid-solid contact
ls : limit of liquid-superheat
lw : limit of wetting
M : minimum heat flux point
sat : saturation
tls : thermodynamic limit of liquid-superheat
v : vapor
w : heating surface

REFERENCES

(1). Clements, L.D. and Colver, C.P., I & EC, 62-9(1970), pp.26-46.
(2). Grigoryev, V.A., Klimenko, V.V., Pavlov, Yu.M. and Ametistov, Ye.V., Heat Transfer-Soviet Research, 11-6(1979), pp.84-130.
(3). Wachters, L.H.J., Bonne, H. and Van Nouhuis, H.J., Chem. Engng Sci., 21 (1966), pp.923-936.
(4). Baumeister, K.J., Hendricks, R.C. and Hamill, T.D., NASA TN D-3226(1966).
(5). Godleski, E.S. and Bell, K.J., Proc. 3rd Intern. Heat transfer Conf., (Chicago), 4(1966), pp.51-58.
(6). Henry, R.E., Quinn, D.J. and Spleha, E.A., Proc. 5th Intern. Heat Transfer Conf., (Tokyo), 4(1974), pp.101-104.
(7). Berenson, P.J., Intern. J. Heat Mass Transfer, 5(1962), pp.985-999.
(8). Bradfield, W.S., I & EC Fundamantals, 5-2(1966), pp.200-204.

(9). Swanson, J.L., Bowman, H.F. and Smith, J.L. Jr., Trans. CSME, 3(1975), pp. 131-140.
(10). Yao, S.C. and Henry, R.E., Trans. ASME, Series C, 100(1978), pp.260-267.
(11). Henry, R.E., AIChE Sym. Series, 70-138(1974), pp.81-90.
(12). Borishanski, V.M., AEC-TR-3405(1953).
(13). Lienhard, J.H. and Dhir, V.K., Trans. ASME, Series C, 102(1980), pp.457-460.
(14). Fedemski, T.R., Proc. 7th Intern. Heat Transfer Conf., (Munich), 4(1982), pp.369-374.
(15). Toda, S. and Mori, M., Proc. 7th Intern. Heat Transfer Conf., (Munich), 4 (1982), pp.173-178.
(16). Iloeje, O.C., Plummer, D.N., Rohsenow, W.M. and Griffith, P., MIT TR 72718-92(1974).
(17). Nishio, S., Report of Institute of Industrial Science, (Univ. of Tokyo), 28-6(1980).
(18). Sciance, C.T. and Colver, C.P., Trans. ASME, Series C, 92(1970), pp.659-661.
(19). Blander, M. and Katz, J.L., AIChE J., 21-5(1975), pp.833-848.
(20). Spiegler, P., Hopenfeld, J., Silberberg, M., Bumpus, C.F., Jr. and Norman, A., Intern. J. Heat Mass Transfer, 6(1963), pp.987-944.
(21). Henry, R.E. and Fauske, H.K., Proc. 3rd Specialist Meeting on Sodium/Fuel Interaction in Fast Reactors, (Tokyo), 1(1976), pp.595-622.
(22). Lienhard, J.H., Chem. Engng Sci., 31(1976), pp.847-849.
(23). Gunnerson, F.S. and Cronenberg, A.W., Trans. ASME, Series C, 100(1978), pp. 734-736.
(24). Nishio, S., Preprint of JSME, No.815-2(1981), pp.142-144.
(25). Carslaw, H.S. and Jaeger, J.C., "Conduction of Heat in Solid", (Clarendon Press), Oxford, (1959).
(26). Segev, A. and Bankoff, S.G., Intern. J. Heat Mass Transfer, 23(1980), pp. 637-642.
(27). Waldram, K.L., Fauske, H.K. and Bankoff, S.G., Can, J. Chem. Engng, 54(1976), pp.456-458.
(28). Iida, Y. and Takashima, T., Trans. JSME, Series B, 46(1980), pp.725-733.
(29). Akiyama, M., Proc. 17th National Heat Transfer Symposium of Japan, (1980), pp.217-219.
(30). Seki, M., Kawamura, H. and Sanogawa, K., Trans. ASME, Series C, 100(1978), pp.167-169.
(31). Taylor, G.I., Proc. Roy. Soc. London, Series A-201(1950), pp.192-202.
(32). Chang, Y.P., Trans. ASME, 79(1957), pp.1501-1513.
(33). Zuber, N., AEC Report No.AECU-4439, Physics and Mathematics, (1959).
(34). Berenson, P.J., Trans. ASME, Series C, 83(1961), pp.351-358.
(35). Sernas, V., Lienhard, J.H. and Dhir, V.K., Intern. J. Heat Mass Transfer, 16(1973), pp.1820-1821.
(36). Shoji, M. and Takagi, N., Trans. JSME, Series B, 48(1982), pp.2324-2334.
(37). Lienhard, J.H. and Wong, P.T.Y., Trans. ASME, Series C, 86(1964), pp.220-226.
(38). Hosler, E.R. and Westwater, J.W., ARS J., 32(1962), pp.553-558.
(39). Lienhard, J.H. and Sun, K.H., Trans. ASME, Series C, 92(1970), pp.292-298.
(40). Sakurai, A., Shiotsu, M. and Hata, K., "Thermal-Hydraulics of Nucl. Reactors", (ANS), 1(1983), pp.280-285.
(41). Lewis, D.J., Proc. Roy. Soc. London, Series A-202(1950), pp.81-92.
(42). Kovalev, S.A., Intern. J. Heat Mass Transfer, 9(1966), pp.1219-1226.
(43). Nishio, S., Trans. JSME, Series B, 49(1983), pp.1185-1194.
(44). Bergles, A.E. and Thompson, W.G., Jr., Intern. J. Heat Mass Transfer, 13

(1970), pp.55-68
(45). Shih, C. and El-Wakil, M.M., Nucl. Sci. Egngng, 77(1981), pp.470-479.
(46). Nishikawa, K., Hasegawa, S., Kitayama, N. and Sakamoto, T., Technological Reports of Kyushu Univ., (Kyushu Univ. Japan), 38-4(1966), pp.399-404.
(47). Nishio, S. and Uemura, M., J. Japan Soc. Heat Treatment, 23(1983), pp.260-265.
(48). Dhir, V.K. and Purohit, G.P., Nucl. Engng Des., 47(1978), pp.49-66.
(49). Nagano, H. and Shoji, M., Proc. 20th National Heat Transfer Symposium of Japan, (1983), pp.193-195.
(50). Veres, D.R. and Florschuetz, L.W., Trans. ASME, Series C, 93(1971), pp.229-232.
(51). Peyayopanakul, W. and Westwater, J.W., Intern. J. Heat Mass Transfer, 21 (1978), pp.1437-1445.
(52). Nishio, S., Preprint of JSME, No.840-5, (1984), pp.65-72.
(53). Merte, H. Jr. and Clark, J.A., Trans. ASME, Series C, 86(1964), pp.351-359.
(54). Nikolayev, G.P., Bychenkov, V.V. and Skripov, V.P., Heat Transfer-Soviet Research, 6-1(1974), pp.128-132.
(55). Hesse, G., Intern. J. Heat Mass Transfer, 16(1973), pp.1611-1627.
(56), Bier, K., Engelhorn, H.R. and Gorenflo, D., "Heat Transfer in Boiling", (Hemisphere Pub. Co.), New York, pp.85-97.
(57). Merte, H. Jr. and Lewis, E.W., In "Cryogenic Heat Transfer", Adv. Heat Transfer, (Academic Press), 5(1968), pp.325-517.
(58). Nishio, S., Preprint of JSME, Submitted.
(59). Zuber, N., Trans. ASME, 80(1958), pp.711-720.
(60). Kutateladze, S.S., U.S.AEC Translation 3405.
(61). Chang, Y.P., In discussion of Ref (62).
(62). Lienhard, J.H. and Schrock, V.E., Trans. ASME, Series C, 85(1963), pp.261-272.
(63). Lienhard, J.H., and Watanabe, K., Trans. ASME, Series C, 88(1966), pp.94-100.
(64). Nikolayev, G.P. and Skripov, V.P., Heat Transfer-Soviet Research, 2-3(1970), pp.122-127.
(65). Sakurai, A., Shiotsu, M. and Hata, K., Proc. 1980 ICHMT Intern. Seminar, (Dubrovnik), (1980).
(66). Bradfield, W.S., Trans. ASME, Series C, 89(1967), pp.269-270.
(67). Takagi, N. and Shoji, M., Trans. JSME, Series B, 49(1983), pp.2190-2199.
(68). Farahat, M.M.K., Eggen, D.T. and Armstrong, D.R., Nucl. Sci. Engng, 53 (1974), pp.240-253.
(69). Yilmaz, S. and Westwater, J.W., Trans. ASME, Series C, 102(1980), pp.26-31.
(70). Lienhard, J.H., Trans. ASME, Series C, 90(1968), pp.180-182.
(71). Berlin, I.I., et al., Inhz.-fiz. zhurn., 24-2(1973), pp.205-210.
(72). Lin, D.Y.T. and Westwater, J.W., Proc. 7th Intern. Heat Transfer Conf., (Munich), 4(1982), pp.155-160.
(73). Cowley, C.W., Timson, W.J. and Sawdye, J.A., I & EC Process Des. Dev., 1-2 (1962), pp.81-84.
(74). Moreaux, F., Chevries, J.C. and Beck, G., Intern. J. Multiphase Flow, 2 (1975), pp.183-190.
(75). Nishio, S., Proc. 1983 ASME-JSME Thermal Engng Joint Conf., (Hawaii), 1 (1983), pp.103-109.
(76). Baumeister, K.J. and Simon, F.F., Trans. ASME, Series C, 95(1973), pp.166-173.
(77). Nishikawa, K., Hasegawa, S., Honda, H. and Sakaguchi, S., Trans. JSME, 34

(1968), pp.134-141.
(78). Nishikawa, K. Fujii, T. and Honda, H., Trans. JSME, 37(1971), pp.1018-1025.
(79). Gaertner, R.F., Trans. ASME, Series C, 87(1965), pp.17-29.
(80). Giventer, L.L. and Smith, J.L., Jr., Adv. Cyogenic Engng, 15(1969), pp.259-270.
(81). Paddia, A., Jr., Ph.D Thesis, Univ. Michigan, (1966).
(82). Ruckenstein, E., Intern. J. Heat Mass Transfer, 10(1967), pp.911-919.
(83). Gunnerson, F.S. and Cronenberg, A.W., Trans. ASME, Series C, 102(1980), pp. 335-341.
(84). Simoneau, R.J. and Simon, F.F., NASA TN D-3354(1966).
(85). Simon, F.F., Papell, S.S. and Simoneau, R.J., NASA TN D-4307(1968).
(86). Witte, L.C., Stevens, J.W. and Henningson, P.J., Trans. Am. Nucl. Soc., 12 (1969), p.806.
(87). Rhea, L.G. and Nevins, R.G., Trans. ASME, Series C, 91(1969), pp.267-272.
(88). Bulter, A.P., James, G.B., Maddock, B.J. and Norvis, W.T., Intern. J. Heat Mass Transfer, 13(1970), pp.105-115.
(89). Peterson, W.C. and Zaalouk, M.G., Trans. ASME, Series C, 93(1971), pp.408-412.
(90). Tachibana, F. and Enya, S., Trans. JSME, 38(1972), pp.1056-1064.
(91). Stevens, J.W. and Witte, L.C., Intern. J. Heat Mass Transfer, 16(1973), pp. 669-678.
(92). Skripov, V.P., "Metastable Liquids", (John Willy & Sons), New York, (1974).
(93). Sakurai, A. and Shiotsu, M., Proc. 5th Intern. Heat Transfer Conf., (Tokyo), 4(1974), pp.81-85.
(94). Zhukov, V.M., Kazakov, G.M. and Kuzwa-Kichta, Yu.A., Heat Transfer-Soviet Research, 7-3(1975), pp.16-26.
(95). Klimenko, V.V., In Ref.(2)
(96). Ishigai, S., Nakanishi, S. and Ochi, T., Proc. 6th Intern. Heat Transfer Conf., (Toronto), 1(1978), pp.445-450.
(97). Manson, L., Trans. ASME, Series C, 89(1967), pp.111-112.

Quenching of Rod Bundles with Fuel Rod Simulators of Different Design

P. Ihle, K. Rust, F. Erbacher

Kernforschungszentrum Karlsruhe
Institut für Reaktorbauelemente
Postfach 3640, 7500 Karlsruhe
Federal Republic of Germany

Abstract

Reflood tests with 5 x 5 rod bundles consisting of electrically heated full length fuel rod simulators with Zircaloy claddings and a helium filled gap between cladding and internal Al_2O_3 pellets (REBEKA) have been performed (SEFLEX). For the tests the same facility has been used as for tests carried out previously with a 5 x 5 rod bundle consisting of rods with stainless steel claddings without gap between cladding and MgO insulation (FEBA). The reflood parameters, e.g. bundle power, system pressures, flooding velocities were the same for both types of rod bundles.

A comparison of selected data measured as well as evaluated from tests of both the bundles shows the following: Fuel rod simulators with Zircaloy claddings and a helium filled gap underneath the claddings quench significantly earlier than "gapless" fuel rod simulators with thick stainless steel claddings. Quenching is inititated from a higher level of the heat stored prior to quenching of rods with a gap.

Introduction

The reflood phase of a LOCA in a PWR is terminated when all fuel rods are quenched completely. Out-of-pile reflood experiments performed with electrically heated rods show different quench behavior depending on the design of the fuel rod simulators used. However, in-pile experiments show that quench times of nuclear fuel rods are significantly shorter than those obtained in tests using electrically heated rods without gap between cladding and internal heat source.

The objective of this investigation is to analyse the quenching in rod bundles with fuel rod simulators of different design comparing experimental and evaluated data. Emphasis is placed on the influence of the different radial thermal heat resistance of individual fuel rod simulators on the quenching behavior.

Experiments

The comparison of FEBA data /1, 2/ with REBEKA data /3/ indicated different reflood and quench behavior inspite of same outer rod dimensions, bundle size and power distribution. Direct comparison was difficult because the REBEKA tests were performed in a different test facility, under different operational procedures, and with less variation of the flooding parameters.

Therefore, the data base established with the FEBA program is being complemented by the SEFLEX program (Fuel Rod Simulator Effects in Flooding Experiments). For this program the FEBA bundle consisting of 5 x 5 "gapless" fuel

rod simulators with 1 mm stainless steel cladding (see Fig. 1) is replaced by a bundle consisting of 5 x 5 REBEKA fuel rod simulators with Zircaloy claddings and a gas filled gap between the cladding and the Al_2O_3 pellets (see Fig. 2). SEFLEX reflood tests have been performed in the FEBA facility.

In the tests performed up to now, the filling gas of the rods was helium leading to the lowest gap resistance and minimizing the "gap effect". With a real mixture of fission gases with helium, the gap influence becomes more dominant. The nominal width of the radial gap in the REBEKA rods used is 0.05 mm corresponding to nuclear fuel rods.

The initial and the boundary conditions as well as the operational procedure of most of the FEBA tests without blockages (Series I) have been repeated for close comparison of the results obtained from both bundles of different rod design.

Initial axial temperature profile, bundle power at start of the reflood phase (200 kW), decay heat transient, axial power distribution as well as power steps along the rods were the same for both test series. The design and the arrangements of the grid spacers - without mixing vanes - were the same as those of the FEBA tests. The system pressures applied for the different tests were 2 and 4 bar, the flooding velocities 3.8 and 5.8 cm/s corresponding to portions of the matrix of the FEBA tests /1, 2/. All data are recorded with a scan frequency of 10 cycles/s.

Results

Figure 3 shows cladding temperature transients measured and corresponding heat flux transients evaluated from a FEBA rod bundle and a REBEKA rod bundle. The data were obtained from thermocouples embedded in the claddings at axial level 1680 mm referenced to the top end of both bundles.

In the SEFLEX test using a bundle of 5 x 5 REBEKA fuel rod simulators, the maximum cladding temperature was lower than in the FEBA test with the "gapless" rods. The quench time (t_Q) was shorter in the SEFLEX test as well at the elevation mentioned. (SEFLEX03: t_{Q1680} = 248 s, FEBA216: t_{Q1680}= 304 s).

Comparing the shapes of both the cladding temperature transients plotted, significant differences occur during the time span about 50 s prior to quenching up to the individual quench times. The signal obtained from the thermocouple embedded in the FEBA rod cladding stays smooth because of the high heat capacity of the 1 mm thick cladding of stainless steel. The signal of the thermocouple embedded in the 0.72 mm thick Zircaloy cladding of the REBEKA rod shows spikes. The lower heat capacity of the Zircaloy cladding (about 1/4 of the FEBA rod cladding) as well as the gap between cladding and Al_2O_3 pellets enable the two-phase flow to cool down local spots of the cladding significantly. For the same time span the surface heat flux, i.e. the heat removal from the rod, is increased significantly compared with that of the FEBA test. During most of the reflood phase of both the tests, performed with a flooding velocity of 3.8 cm/s and a system pressure of 4 bar, the heat flux transients at the axial level mentioned are roughly the same.

Further evaluation of the data leads, e.g., to the maximum temperatures within the two different types of rods as well as to the corresponding heat stored instantaneously within the rods including the claddings (see Fig. 4). At initiation of reflood the maximum temperatures in the cross sections of both the rods are the same. Later in time, the maximum temperature in the

cross section of the FEBA rod is higher, and the sudden drop of the temperature (indicating the passing of the quench front) occurs later. Comparing the shapes of both the internal temperature transients, again during the time span about 50 s prior to quenching, the most significant differences occur. The drop of the temperature within the REBEKA rod (SEFLEX) is initiated from a higher level than that of the FEBA rod.

This finding is similar for the stored heat plotted in the same figure. At initiation of reflood, the stored heat of the FEBA rod is about 10 % higher than that of the REBEKA rod. Prior to quenching (t_Q = 304 s) it is lower than that of the REBEKA rod shortly prior to its quenching (t_Q = 248 s).

For a more detailed analysis of the conditions at the quench front in both types of bundles, the transients shown are plotted with an enlarged time scale. A recording window of 40 s, i.e. 20 s before through 20 s after the quench fronts passed the axial level 1680, is analyzed in the following. The quench time t_Q of the individual rod sections (t_Q = 304 s for FEBA and t_Q = 248 s for SEFLEX) is set t = 0 for a new time scale allowing a better comparison of the transients from both tests.

Figure 5 shows the cladding temperatures of both tests measured at axial level 1680 mm versus the new time scale. The data measured with a scan frequency of 10 cycles/s are identical to those plotted in Fig. 3. However, the temperature "spikes" recorded by the thermocouple embedded in the Zircaloy cladding of the REBEKA rods in SEFLEX are detected as peaks of a duration of less than 1 s and a maximum temperature variation of up to 60 K for $t < 0$. There is no thermocouple noise influencing these signals indicated by the smooth signal during the single phase cooling condition ($t > 0$) after quenching.

Figure 6 shows the surface heat flux transients (from Fig. 3) plotted again with the new time scale t as before. Downstream of the quench front ($t < 0$) the surface heat flux is significantly higher in the SEFLEX test than in the FEBA test as described above.

It has to be mentioned that the heat transfer analysis applied does not take into account the axial heat conduction within the rods and the claddings, respectively. Calculating the heat balance and the temperature distribution within the rods an axial length of 10 mm is assumed to have constant axial conditions. Therefore, the individual values within steep gradients can only be used qualitatively. However, the balance is correct and the values outside of steep gradients are accurate. Within the steep gradients of the surface heat flux shown in Fig. 6, i.e. $-6 \text{ s} < t < 6 \text{ s}$, somewhat more heat is being removed from the REBEKA bundle (SEFLEX) than from the FEBA bundle. Figure 7 shows the corresponding stored as detail from the data already presented in Fig. 4. For the reflood conditions mentioned, the stored heat within the rod with Zircaloy cladding is higher than that of the gapless FEBA rod prior to quenching. At initiation of reflood, there was an inverse situation as mentioned explaining Fig. 4.

The quench front locations versus time are plotted in Fig. 8 for both the tests discussed. The local quench front velocities can be determined using the local slope of the individual curves. At the axial level 1680 mm the quench front velocity is about 6.7 mm/s for the SEFLEX test and 6.2 mm/s for the FEBA test. A time step of 1.5 s corresponds roughly to an axial step of 10 mm.

Fluid temperatures measured near the quench front indicated saturation temperatures for the liquid as well as the vapor phase. Superheated steam leaving the hot and unwetted portions of the rod claddings was not detectable measuring the fluid temperatures with thermocouples described in /1/.

Conclusions

Fuel rod simulators with Zircaloy claddings and a helium filled gap between cladding and internals of the rods quench significantly earlier than "gapless" fuel rods with thick stainless steel claddings.

The heat removal from rods with gap is increased especially during the film boiling regime. The heat stored in the rods with gap (REBEKA) is about 10 % lower at initiation of reflood than that of the gapless rods (FEBA). However, prior to quenching, the increased heat removal starts from a higher level of the heat stored shortening the quench times by at least 20 % for helium filling in the gap.

References

/1/ Ihle, P.; Rust, K.:
"FEBA - Flooding Experiments with Blocked Arrays, Evaluation Report"
KfK 3657, March 1984

/2/ Ihle, P.; Rust, K.:
"FEBA - Flooding Experiments with Blocked Arrays, Data Report 1, Test Series I through IV"
KfK 3658, March 1984

/3/ Erbacher, F.J.; Neitzel, H.J.; Wiehr, K.:
"Effects of Thermohydraulics on Clad Ballooning, Flow Blockage and Coolability in a LOCA"
OECD-NEA-CSNI/IAEA Specialists' Meeting on Water Reactor Fuel Safety and Fission Product Release in Off-Normal and Accident Conditions, Risø National Laboratory, Denmark, May 16-20, 1983

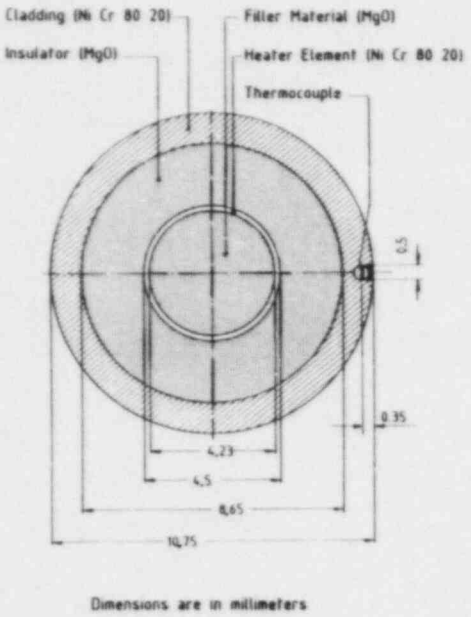

Fig. 1 FEBA fuel rod simulator

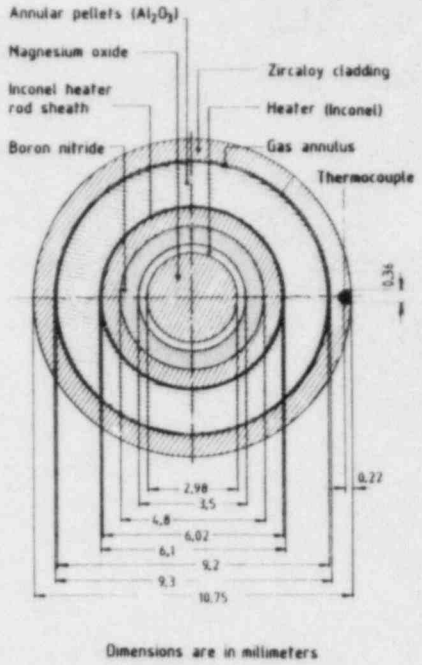

Fig. 2 REBEKA fuel rod simulator used for SEFLEX tests

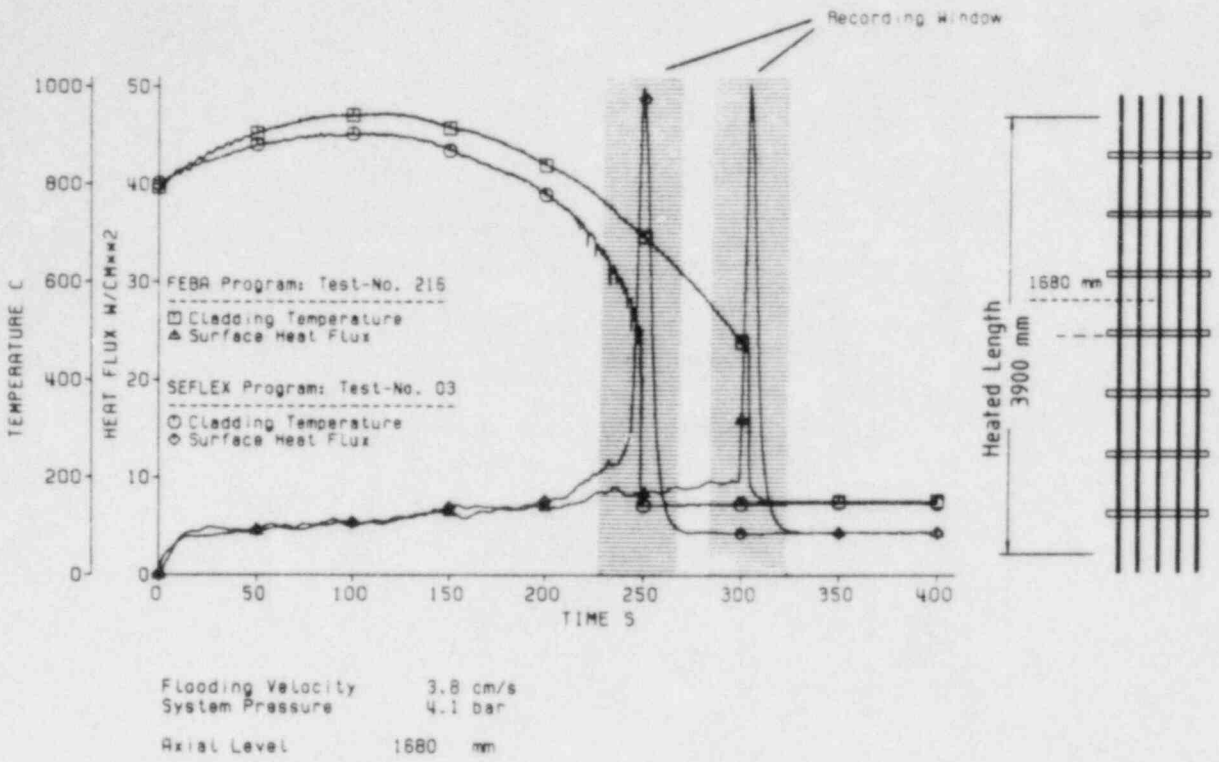

Fig. 3 Cladding temperature and surface heat flux

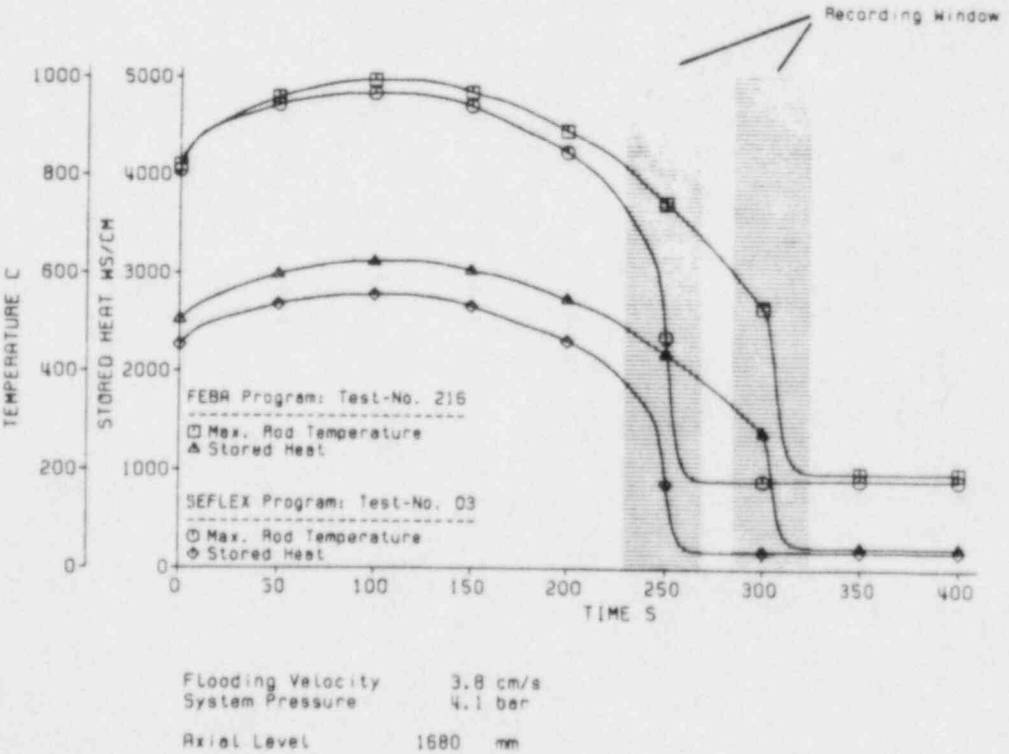

Fig. 4 Cladding temperature and surface heat flux

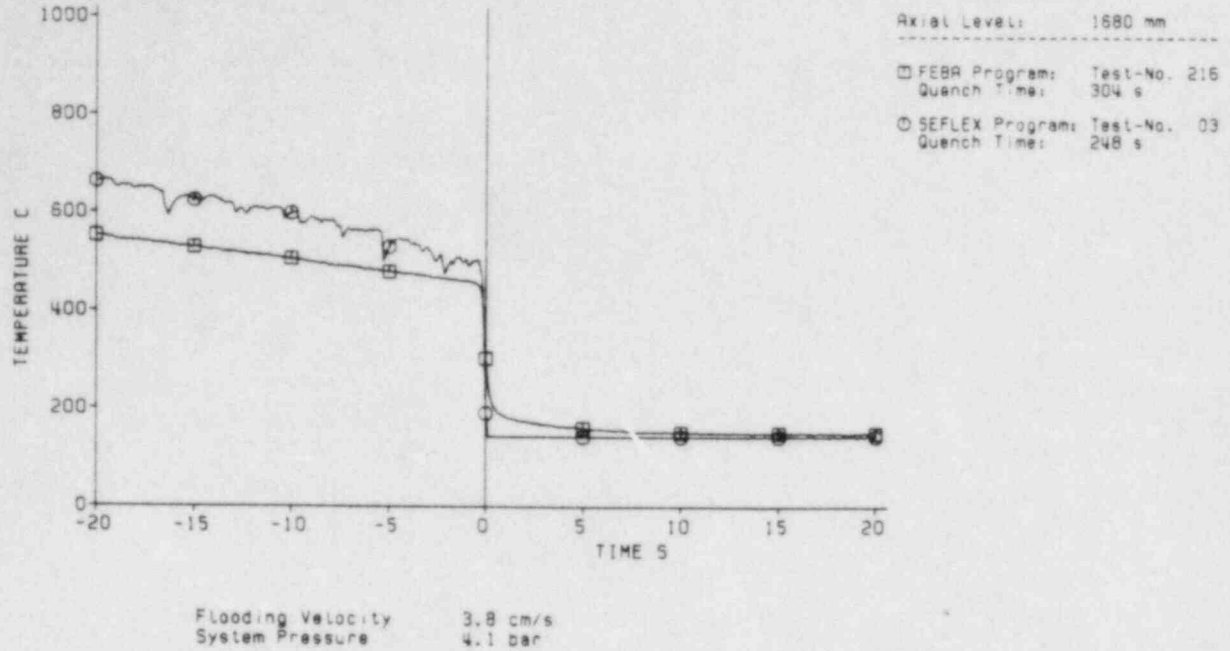

Fig. 5 Cladding temperatures versus shifted time scale

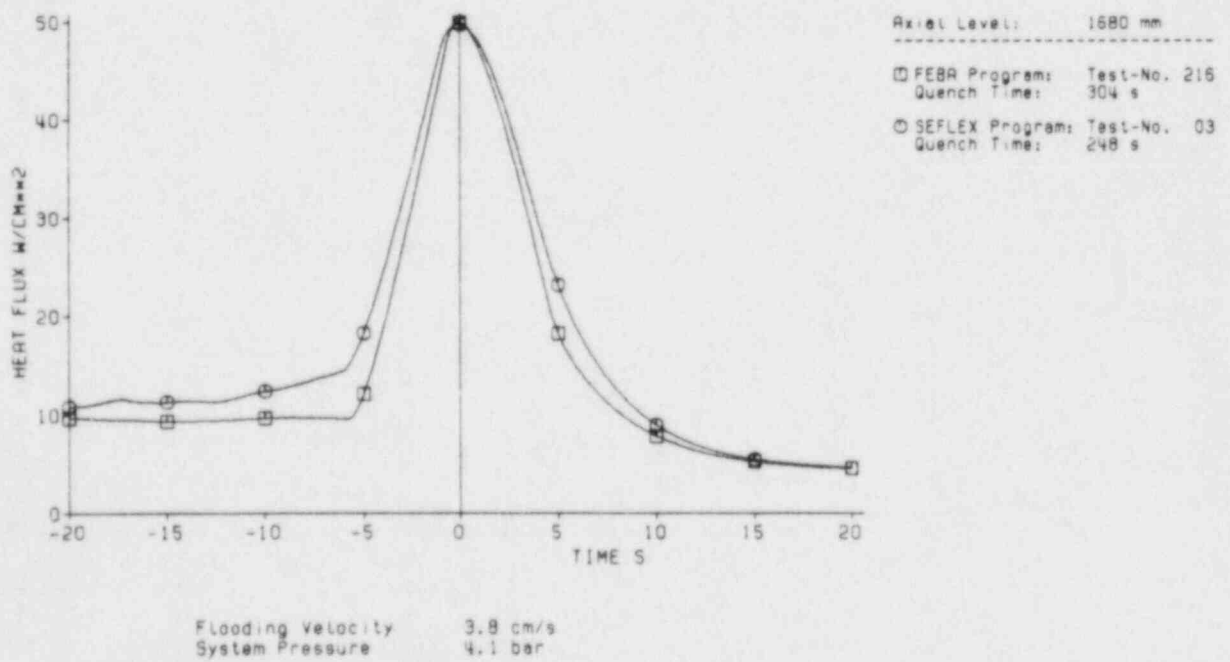

Fig. 6 Surface heat flux versus shifted time scale

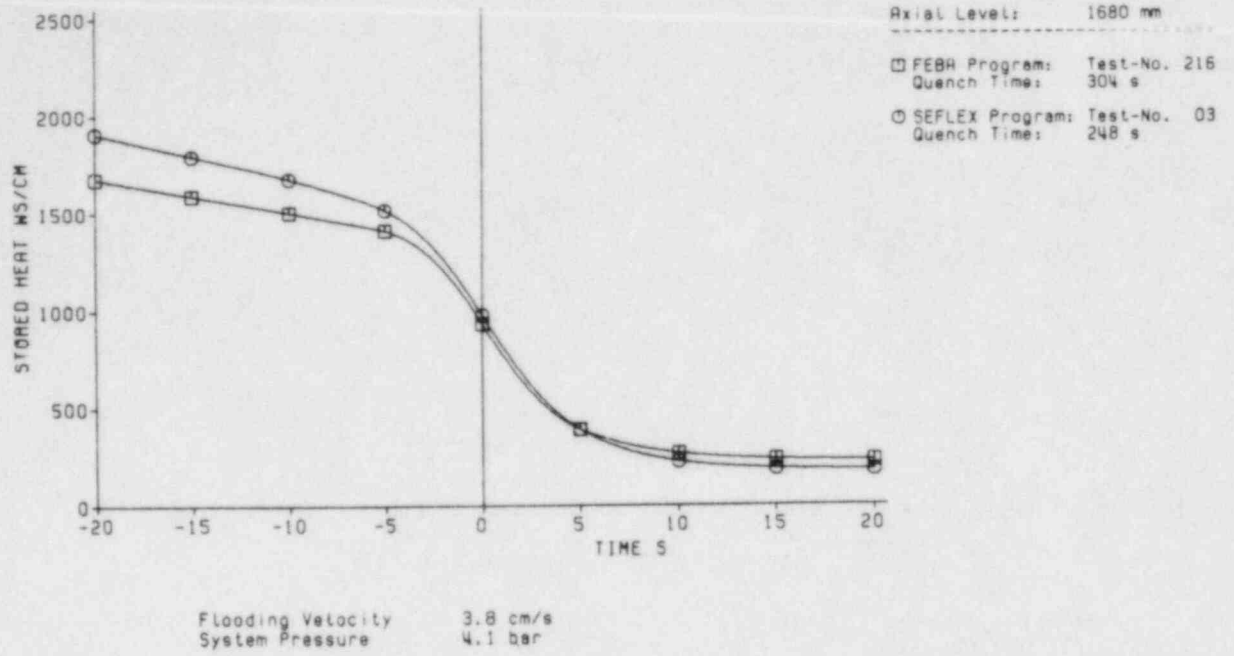

Fig. 7 Stored heat versus shifted time scale

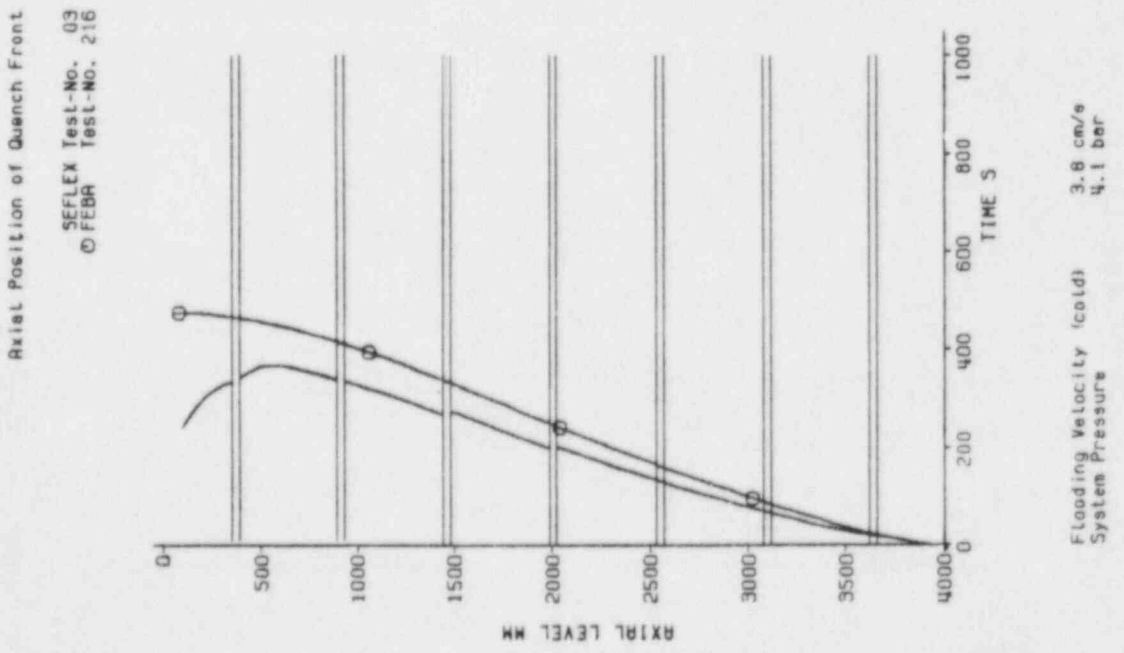

Fig. 8 Influence of heater rod design on quench front progression

A STUDY ON INTERFACIAL AND WALL HEAT TRANSFER DOWNSTREAM A QUENCH FRONT

D. JUHEL

Service des Transferts Thermiques
C.E.N. GRENOBLE
85 X
38041 GRENOBLE CEDEX

SUMMARY

Using experimental tests to investigate heat transfer in dispersed flow in tubes downstream of a quench front :

- We first check a mechanical model to evaluate $(1-\alpha)$, V_V and V_L
- Then develop a heat transfer model including :

. Heat transfer from the wall :
  * To the vapour by radiation
    by convection
  * To the liquid by radiation
    Due to the liquid rearrangement downstream of the quench front

. Heat transfer between liquid and vapour.

Two correlations are proposed, one for droplet diameter which is of importance for radiation and liquid vapour energy exchange, and the other for the special heat transfer exchange between wall and liquid downstream of a quench front.

NOMENCLATURE

Cp	Specific heat
D_H	hydraulic diameter
f	function
G	mass velocity
h	heat transfer coefficient
m	gradient of a linear function
n	number of droplets per unit of volume
Nu	Nusselt number
P	Pressure
Q_{IV}	Energy exchange between vapour and liquid per unit of volume
t	Time
V	Velocity
We	Weber number
Z	Elevation

Greek letters

α	void fraction
δ	Droplet diameter

λ	thermal conductivity
μ	viscosity
ρ	density
σ	surface tension or standard deviation
Φ_{CV}	wall-vapour convection heat flux
Φ_{qpvi}	wall-liquid heat flux due to liquid flow rearrangement downstream of the quench front
Φ_{RL}	wall-liquid radiation heat transfer
Φ_{RV}	wall-vapour radiation heat transfer

Subscripts

L	liquid
QF	quench front
sat	saturation
V	vapour
W	wall

SUMMARY

NOMENCLATURE

1) INTRODUCTION

2) DADINE TESTS ; VOID FRACTION CHECKING
   2.1) Experimental set up
   2.2) Use of results

3) ERSEC DROPLET DIAMETER DETERMINATION
   3.1) Modeling of heat transfer terms
        3.1.1) Radiation
        3.1.2) Convection
        3.1.3) Energy transfer between vapour and liquid
   3.2) Data correlation
        3.2.1) Evaporation
        3.2.2) Break up

4) ERSEC HEAT FLUX BETWEEN WALL AND LIQUID (EXCLUDING RADIATION)
   4.1) Data correlation
        4.1.1) Initial coefficient
        4.1.2) Decay of h with distance
   4.2) Comparison between correlation and data

5) RECONSTITUTION TESTS

6) CONCLUSION

REFERENCES

ANNEX A

ANNEX B

FIGURES

1) INTRODUCTION

ERSEC and DADINE experiments are reflood tests performed in the Grenoble heat transfer laboratory within the framework of a bilateral contract between the French Atomic Energy Committee and Electricité de France.

- ERSEC tube experiments are used to study heat transfer downstream of a quench front. We specially developed a modelization of heat transfer exchanges: radiation and heat transfer between liquid and vapour, in terms of droplet diameter. We also developed a modelization of the heat flux between wall and liquid in the vicinity of the quench front.

In order to correlate these terms, it is of interest to determine void fraction, vapour and liquid velocities, vapour superheat along the test section.

Flow test section calculations are performed at a given time using the six-equation model code CATHARE with the following conditions :

- Steady state for hydraulics
- Experimental hydraulic boundary conditions
- Total heat flux between wall and fluid deduced from wall temperature measurements by inverse conduction calculation including transient terms
- Heat removal due to quench front progression deduced from experimental results
- The studied parameter is adjusted on each mesh so that the computed wall temperature is equal to the experimental value.

Such an approach is questionable if $(1-\alpha)$ which is a very important and sensitive parameter is not previously checked out. For this purpose, DADINE experiments are used, where a special void fraction measurement in reflood conditions has been developed.

This presentation deals successively with :

Dadine studies
Ersec studies - drop size
- heat flux between wall and liquid

2) DADINE TESTS ; VOID FRACTION CHECK

2.1) Experimental set up [Ref. 1]

The main problems of void fraction measurements in reflood conditions are:

- Methods leading to a flow disturbance are not suitable.
- A high resolution is required for high void fraction values, which is not generally feasible with γ or X-ray attenuation techniques
- Sensitivity to radial flow distribution has to be as small as possible

Using a neutron beam one has to choose

- attenuation or scattering
- Energy of neutrons

The best results are obtained using scattering of a thermal neutron beam (see diagram). A typical result is a curve $\alpha(t, z=1.6\ m)$ for given pressure and inlet flow conditions [figure 1].

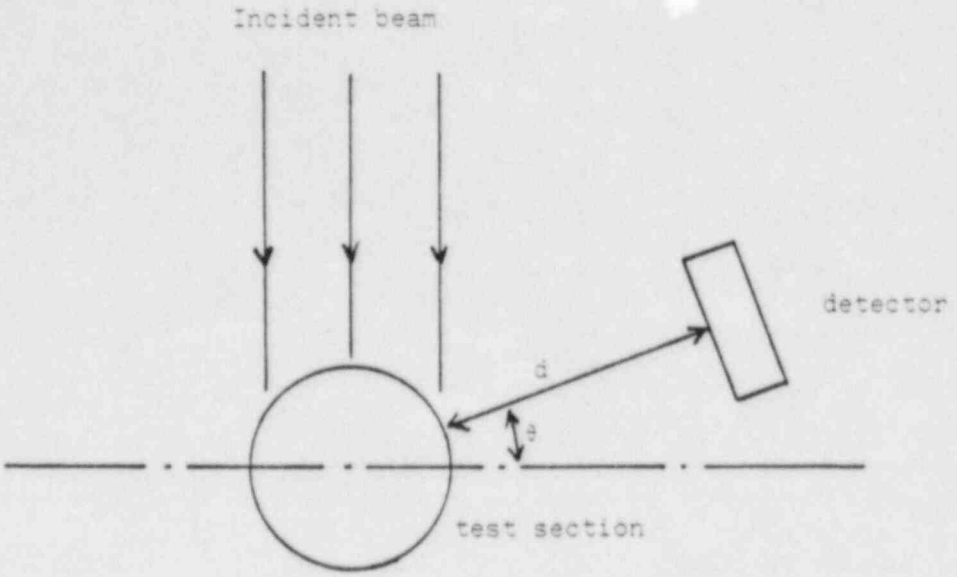

2.2) Use of results

For a given test a time is chosen such that the assumption of steady state is valid $\left[\frac{d}{dt}\ (\Delta P)_{\text{test section}}\right.$ close to zero$\left.\right]$. A calculation is performed using experimental hydraulics (P, G, T_{inlet}) and thermal ($\Phi_{(z)}$) conditions. Computed and experimental void fraction are compared, at the measurement elevation.

As a first step, using the standard CATHARE code model, a systematic error was observed. Consequently we slightly modified this model to obtain overall agreement between experimental and calculated values [figure 2].

It is this adjusted model (see annex A) that is used for ERSEC analysis.

An important remark should be made :

- In such an experiment the total mass flow rate is set
- Vapour mass flow rate at the outlet is the result of a thermal balance (the error due to the uncertainty on vapour superheat is small)

The consequences are :

- As void fraction is close to one, V_V is fairly well determined
- Liquid mass flow rate is determined (steady state) and as $(1-\alpha)$ is adjusted on the experimental value, V_L is fairly well determined too.

In conclusion, the check made on DADINE experiments means that a fairly high degree of confidence can be had in our determination of $(1-\alpha)$, V_V and V_L.

3) ERSEC DROPLET DIAMETER DETERMINATION

ERSEC experiments [Ref. 2] are performed with in an electrically heated tube 3.6 m long, 1.2 cm inner diameter, in which wall temperatures, test section pressure drop, liquid mass flow rate and vapour temperature at the outlet are measured. For these reflooding tests, inlet mass flow rate and quality are set.

In these tests, a first area is dealt with, far enough from the quench front for the most importa t phenomenon are supposed to be droplet behaviour connected with radiation and vapour-liquid energy exchange ; and convection.

3.1) Modeling of heat transfer terms

3.1.1) Radiation (see annex B)

$$\emptyset_{RL} = f(\delta, (1-\alpha), P, T_L, T_W)$$

$$\emptyset_{RV} = f(\delta, (1-\alpha), P, T_V, T_W)$$

Parameters δ and $(1-\alpha)$ are very important ; Their effects are shown in figure 3.

3.1.2) Convection

A simple correlation of the Cathare model is used.

$$\emptyset_{CV} = h(T_W - T_V)$$

$$h = .0083 \frac{\lambda_V}{D_H} \left(\frac{\alpha \rho_V V_V D_H}{\mu_V}\right)^{.877} \left(\frac{\mu_V Cp_V}{\lambda_V}\right)^{.611}$$

3.1.3) Energy transfer between vapour and liquid

Liquid is assumed to be in the form of droplets the diameter of which is uniform in any cross-section.

Energy exchange between a sphere and a continuum can be expressed as :

$$Nu = \frac{h \delta}{\lambda_V} = \left\{ 2 + .552 \left[\frac{\rho_V (V_V - V_L) \delta}{\mu_V}\right]^{.5} \left[\frac{\mu_V Cp_V}{\lambda_V}\right]^{1/3} \right\}$$

Interfacial area per unit of volume is :

$$A = \frac{6(1-\alpha)}{\delta}$$

Then

$$q_{IV} = \frac{\lambda_V}{\delta} \left\{ 2 + .5 \left(\frac{\rho_V (V_V - V_L) \delta}{\mu_V}\right)^{1/2} \left(\frac{\mu_V Cp_V}{\lambda_V}\right)^{1/3} \right\} \frac{6(1-\alpha)}{\delta} (T_V - T_{sat})$$

With the following assumptions :

- Laminar term negligible
- Prandtl number close to 1

$$q_{IV} = 3\,\lambda_V \left(\frac{\rho_V}{\mu_V}\right)^{1/2} (V_V - V_L)^{1/2} \left(\frac{1-\alpha}{\delta^{3/2}}\right) (T_V - T_{sat})$$

In this expression, δ and $(1-\alpha)$ are still important parameters. As the void fraction model has been verified, δ remains the most important term. In our calculation δ is tied to the experimental value of T_W for every mesh.

A typical result is presented in figure 4.
The calculation results constitute a data bank :

δ, $(1-\alpha)$, P, T_V, V_V, V_L

3.2) Data correlation

Of course the values of δ are not a measurement but values obtained through hypotheses and a modelization ; we nevertheless try to correlate these data according to physical processes :

- evaporation
- break-up

3.2.1) Evaporation

With the hypothesis previously mentioned : water in the form of droplets of a single diameter ; the evaporation process alone means a constant droplet flux through a cross-section :

$$n.V_L = \frac{6(1-\alpha)}{\pi\,\delta} \times V_L = \text{constant}$$

Results are shown in figure 5 where droplet flux $(n.V_L)$ is plotted versus distance to the quench front for different tests.

This flux generally increases with distance except in a few tests where it becomes stable.

This observation means that the evaporation process alone is not the main phenomenon by which droplet diameter decrease can be evaluated.

3.2.2) Break-up

Droplet break-up in a tube without spacer grids (which have a complex effect in reflood conditions) may obey a Weber criterion :

$$We = \frac{\rho_V\, V^2\, \delta}{\sigma}$$

The problem is to define the velocity which must be used : V_V or $(V_V - V_L)$. Choosing V_V means that the main turbulence source is due to the overall flow. This is probably true for high velocities. On the contrary, the choice of relative velocity means that the main turbulence source is due to interfacial shear stress. This should occur when the slip ratio is high enough (for instance low velocities and upward flow).

For each test, the average Weber number expressed with V_V and $V_V - V_L$ is set out in table 1.

The overall average value is :

$(V_V - V_L) : \bar{W}_e = .45 \quad \sigma = .09 \quad (20\%)$

$V_V \quad : \bar{W}_e = 3.0 \quad \sigma = .9 \quad (30\%)$

In figure 6 the ratio r is plotted for each test :

$$r = \frac{(\bar{W}_e)_{\text{for one test}}}{(\bar{W}_e)_{\text{for all tests}}} = f(V_V) \text{ or } f(V_V - V_L)$$

The two hypotheses V_V and $V_V - V_L$ lead to a discrepancy of the same order of magnitude ; nevertheless a remark has to be made about test 1969 :
It is the only test where experimental wall temperatures clearly indicate slug flow (little and regular oscillations for all thermocouples). The whole modelization based on dispersed flow is inadequate in such a case.

Using $(V_V - V_L)$ the mean Weber number for this test is abnormally low, whereas using V_V, this value is near the average value. Excluding this test a new overall average value is obtained :

$(V_V - V_L) : \bar{W}_e = .48 \quad \sigma = .06 \quad (12\%)$

$V_V \quad : \bar{W}_e = 3.0 \quad \sigma = .9 \quad (30\%)$

The difference between the two discrepancies is now significant especially as reconstitution calculations show that wall temperatures are very sensitive to droplet diameter parameter.

So it seems that $(V_V - V_L)$ is the best scale for velocity in the Weber number. The average value of .48 is small in relation to those determined in other studies. We have to note that this value is greatly dependent on relative velocity which has been previously checked with DADINE experiments.

In conclusion, it can be said that using our modelization, droplet diameter can be determined by a Weber criterion expressed with $V_V - V_L$.

4) ERSEC HEAT FLUX BETWE'.N WALL AND LIQUID (EXCLUDING RADIATION)

A second term is investigated in these tests ; it is a special heat flux occurring in reflood conditions, downstream of the quench front. The assumed controlling phenomenon is the intense water agitation connected with the flow rearrangement above the quench front.

Such a mechanism vanishes as distance to the quench front increases (see diagram).

The method is the same as in the first part except, that this heat flux is tied to T_W.

Modelization is also the same, and in order to minimize errors, droplet diameter is evaluated with the mean Weber value from part one, for each test.

The calculation results lead to the data bank :

Φ_{PVI}, $(z-z)$, $(1-\alpha)$, V_V, V_L ...

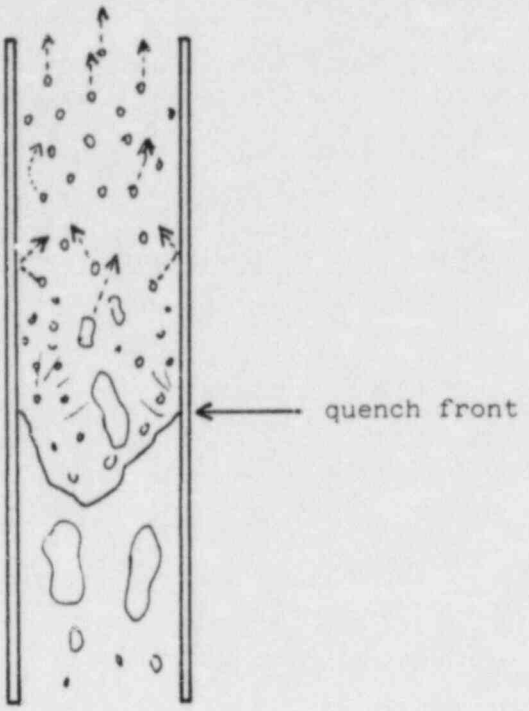

4.1) Data correlation

First, data were compared to some correlations available in literature.

- An exponential decay in $(Z-Z_{QF})$ as in the present form used in the CATHARE code [Ref. 3] is possible but dispersion is large.
- Ellion correlation [Ref. 4] in $(Z-Z_{QF})^{-1}$. The decay with the distance is too low.
- Shi Chune Yao and Sun [Ref. 5] propose a correlation in $\left[a - \frac{(Z-Z_{QF})}{b}\right]^2$ which is in poor agreement with our data.

As none of the tested forms seem to agree with our data, we tried to correlate these data.

In our tests water is always in saturated conditions ; we define the heat transfer coefficient as :

$$\Phi_{PVI} = h\,(T_W - T_{sat})$$

Our correlation research was performed in two steps :

- h for $Z=Z_{QF}$: initial coefficient
- Decay of h with distance to the quench front.

4.1.1) Initial coefficient

Among the different parameters which were tested the best agreement is obtained with $(1-\alpha)$ (figure 7).

It can be noted that :

- A straight line can reasonably be drawn through the points
- The point ($h=0$; $\alpha=1$) belongs to this straight line

This last remark is quite satisfactory because it is obvious that when no more water remains this kind of heat transfer disappears.

4.1.2) Decay of h with distance

We can easily correlate h as a linear function of $(1-\alpha)$ at different locations, for all the tests as shown in figure 8

Results are summarized as follows :

$Z = Z_{QF}$	$h = 1400\ (1-\alpha)$
$Z-Z_{QF} = .1$ m	$h = 1275\ (1-\alpha)$
.2	$h = 970\ (1-\alpha)$
.3	$h = 830\ (1-\alpha)$
.4	$h = 630\ (1-\alpha)$
.5	$h = 500\ (1-\alpha)$

In figure 8 the gradients of the preceeding linear functions $h = f(1-\alpha)$ are plotted versus distance to the quench front.

They are well correlated by a linear function :

$$\left| \begin{array}{l} h = m(1-\alpha) \\ m = 1400 - 1880\ (Z-Z_{QF}) \end{array} \right.$$

So the final correlation is :

$$\left\{ \begin{array}{l} \Phi_{QPVI} = h(T_W - T_{sat}) \\ h = \left[1400 - 1880\ (Z-Z_{QF})\right](1-\alpha) \\ h \geq 0 \end{array} \right\} \quad \begin{array}{l} \text{SI} \\ \text{units} \end{array}$$

Two remarks should be made on this correlation :

- The heat transfer coefficient drops to zero at about .75 m above the quench front whatever the flow parameters.
- All the information on the flow is concentrated in the local void fraction.

4.2) Comparison between correlation and data

Figure 9 presents a comparison between experimental and computed values of the heat transfer coefficient. Except for low values (due to inaccuracy) a good agreement is observed.

5) RECONSTITUTION TESTS

Figure 10 presents a typical comparison between experimental and computed wall temperature. Calculations were performed using the whole proposed model.

6) CONCLUSION

In tube bottom reflooding, the study of dispersed flow downstream of the quench front is of particular importance, in order to evaluate wall temperatures.

The studies based on ERSEC and DADINE experiments have led to the development of two-phase flow mechanical and thermal models, which were simultaneously established and are consequently interdependent. The mechanical model includes indissociable wall and interfacial shear stress correlations. The thermal model includes wall-liquid and wall-vapour radiation, wall-vapour convection, and liquid-vapour energy exchange.

Droplet diameter is, with the $(1-\alpha)$ parameter, the main parameter for these different heat transfers. A droplet diameter correlation is proposed.

Moreover a special heat transfer process occuring downstream of the quench front and connected with the flow rearrangement has been also correlated.

The whole results of this study, based only on tube analysis, are to be introduced in the advanced safety code CATHARE.

Future developments are now in progress. They consist of the analysis of bundle reflooding experiments, performed on the same loop ERSEC, in order to introduce spacer grid effects in such a modelization ; on the PERICLES loop to verify that the transposition to a larger scale is still valid and to evaluate radial effects.

REFERENCES

1. R.L. FREITAS, R. DERUAZ,
   Void fraction measurement in a reflooded single tube by a neutron scattering technique.
   European Two-Phase Flow Group Meeting Glasgow 1980.

2. P. CLEMENT, R. DERUAZ, M. LAMBERT, P. PIC
   Refroidissement de secours des réacteurs à eau légère. Essais de renoyage en géométrie tubulaire.
   Service des Transferts Thermiques - Rapport TT n°156. (1979)

3. CATHARE code documentation. Internal report. (1984)

4. M.E. ELLION
   A study of the mechanism of boiling heat transfer
   Jet Propulsion Laboratory, Memo 20-88 CIT (1954).

5. SHI CHUNE YAO, K.H. SUN
A dispersed flow heat transfer model for low flow bottom reflooding conditions.
Heat and Mass Transfer Seminar on Nuclear Reactor Safety. Dubrovnik 1980.

6. R. DERUAZ, B. PETITPAIN
Modeling of heat transfer by radiation during the reflooding phase of a L.W.R.
Specialist's Meeting on the behaviour of water reactor fuel elements under accident conditions. Spätind (1976).

TABLE 1

WEBER NUMBER EXPRESSED WITH V_V AND $V_V - V_L$

MEAN VALUE AND STANDARD DEVIATION FOR EACH TEST

	$V_v - V_L$		V_v	
Test ref.	$\overline{We}$	σ	$\overline{We}$	σ
1952 A	.46	.11	2.05	.78
1952 D	.53	.03	2.39	.26
1957 B	.49	.03	3.77	.75
1966 C	.45	.10	1.84	.66
1968 A	.42	.06	2.22	.30
1968 D	.43	.06	2.63	.21
1969 A	.28	.05	3.44	.33
1969 D	.25	.05	3.30	.26
2026 B	.39	.07	1.84	.28
2040 A	.54	.04	3.62	.74
2040 D	.55	.03	4.34	.27
2068 B	.51	.04	4.78	.80
2077 A	.43	.02	3.56	.84
2077 D	.42	.02	4.09	1.0
2080 A	.58	.13	2.39	.28
2080 D	.52	.10	2.28	.28

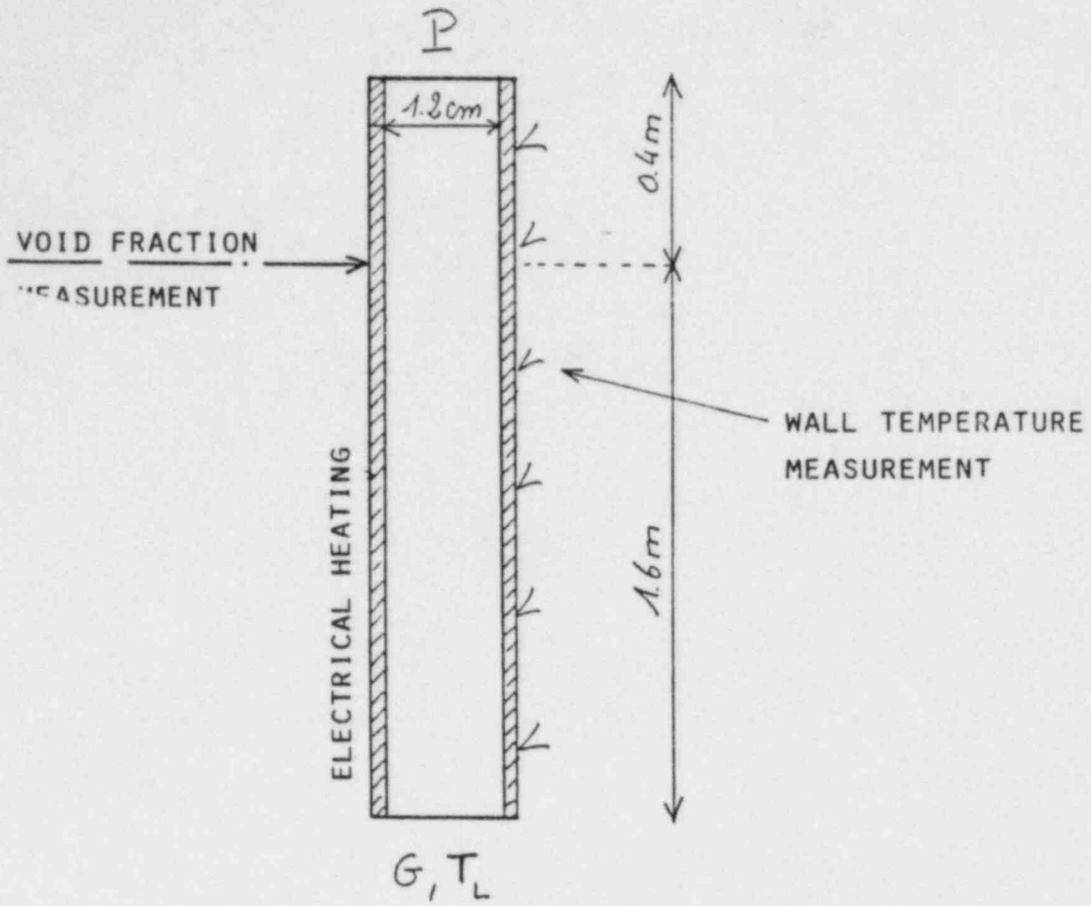

DADINE TYPICAL RESULT $\alpha(T, z = 1.6\ m)$

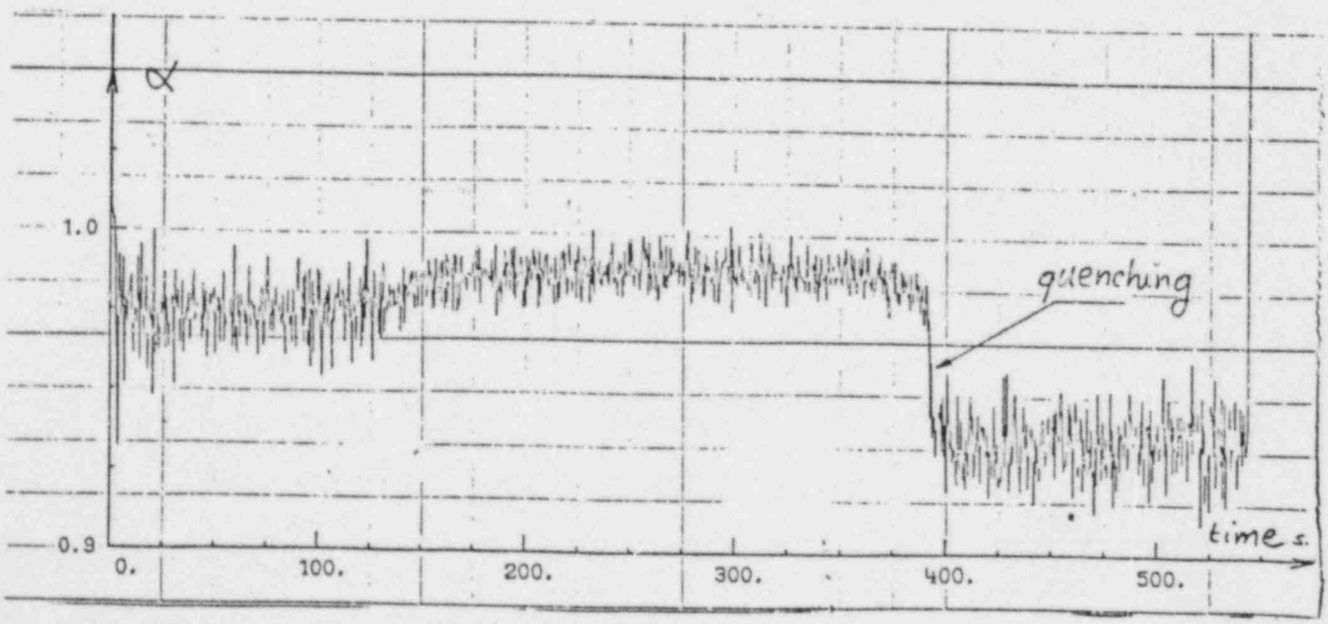

FIGURE 1

DADINE VOID FRACTION EVALUATION

COMPARISON BETWEEN COMPUTED AND EXPERIMENTAL VALUES

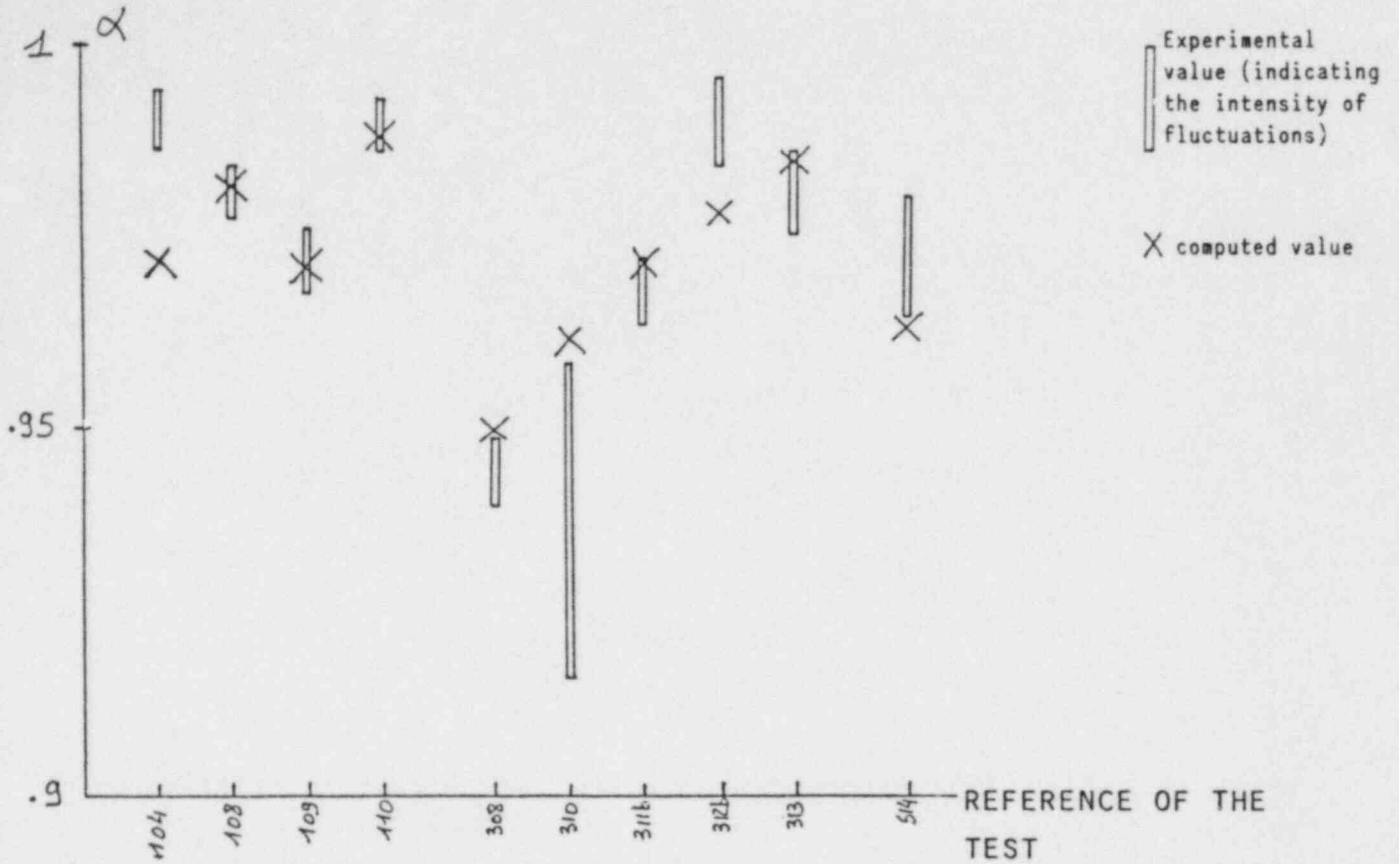

1	1	1	1		3	3	3	3	3	6	P bars
55	140	88	55		140	55	88	24	55	24	G kg/m² s
80	20	20	20		20	20	20	20	23	20	$T_{inlet} - T_{sat}$ °C
5	5	3	3		5	3	5	3	5	3	φ_o w/cm² °C *

EXPERIMENTAL CONDITIONS

* NOMINAL HEAT FLUX

FIGURE 2

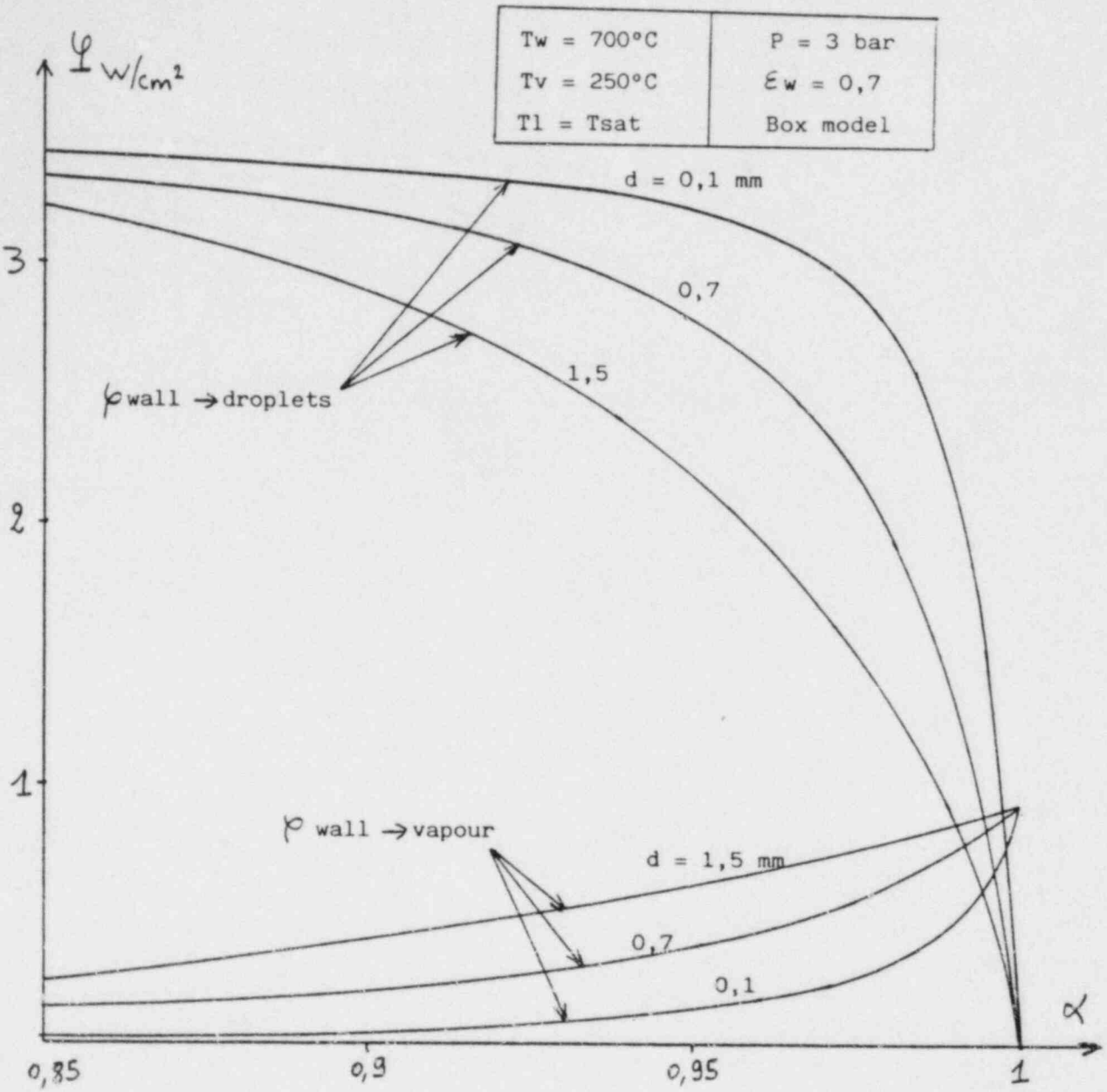

FIGURE 3

RADIATIVE HEAT FLUXES ABSORBED IN THE DRY REGION :
VOID FRACTION AND DROPLET DIAMETER EFFECT

DROPLET DIAMETER VERSUS QUENCH FRONT DISTANCE
TYPICAL RESULTS

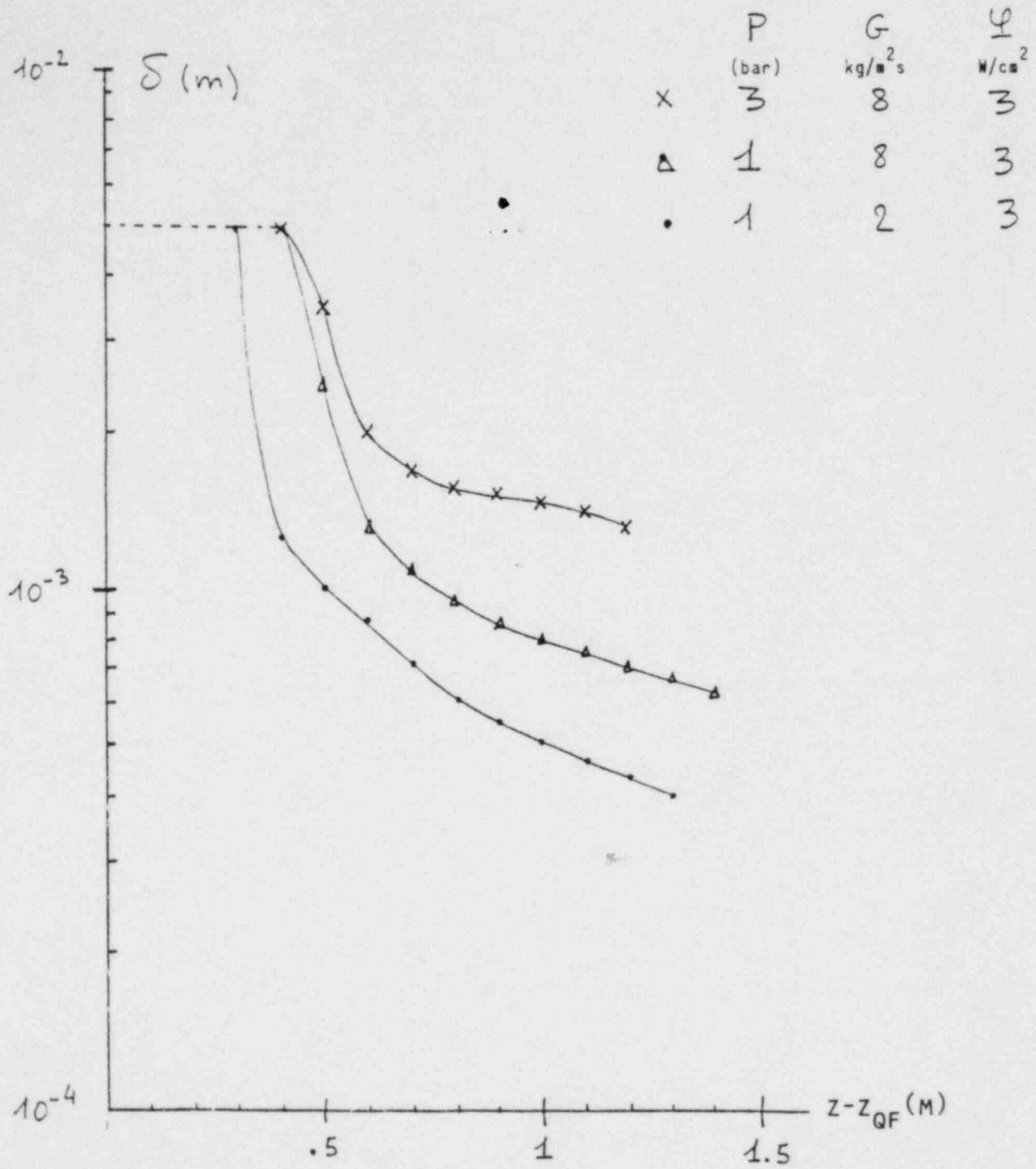

FIGURE 4

FIGURE 5

DROPLETS FLUX THROUGH A CROSS SECTION VERSUS DISTANCE TO THE QUENCH FRONT

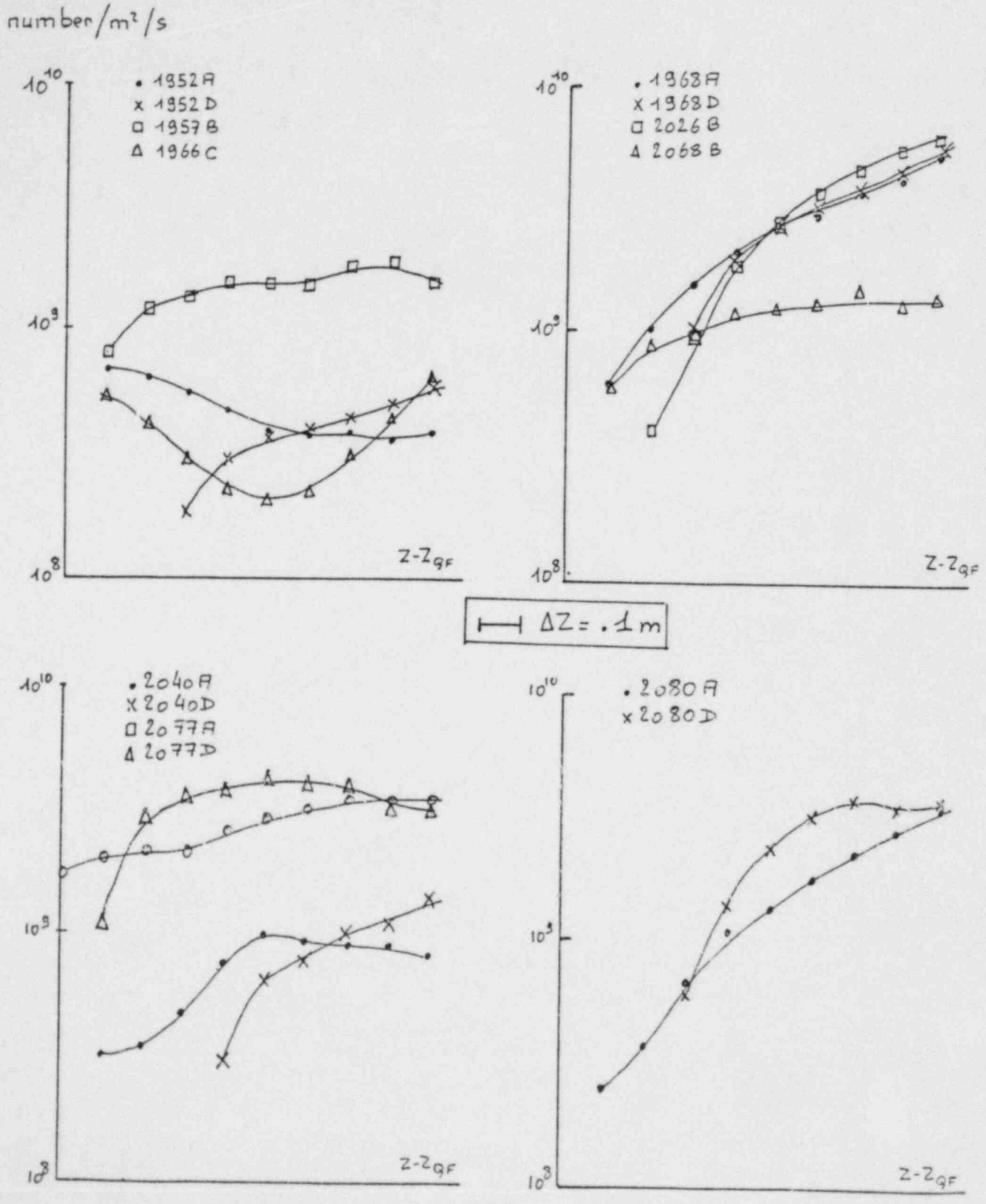

COMPARISON BETWEEN WEBER NUMBER EXPRESSED WITH V_V AND $V_V - V_L$

{ DASHED LINE : We EXPRESSED WITH $(V_V - V_L)$
{ STRAIGHT LINE: We EXPRESSED WITH V_V

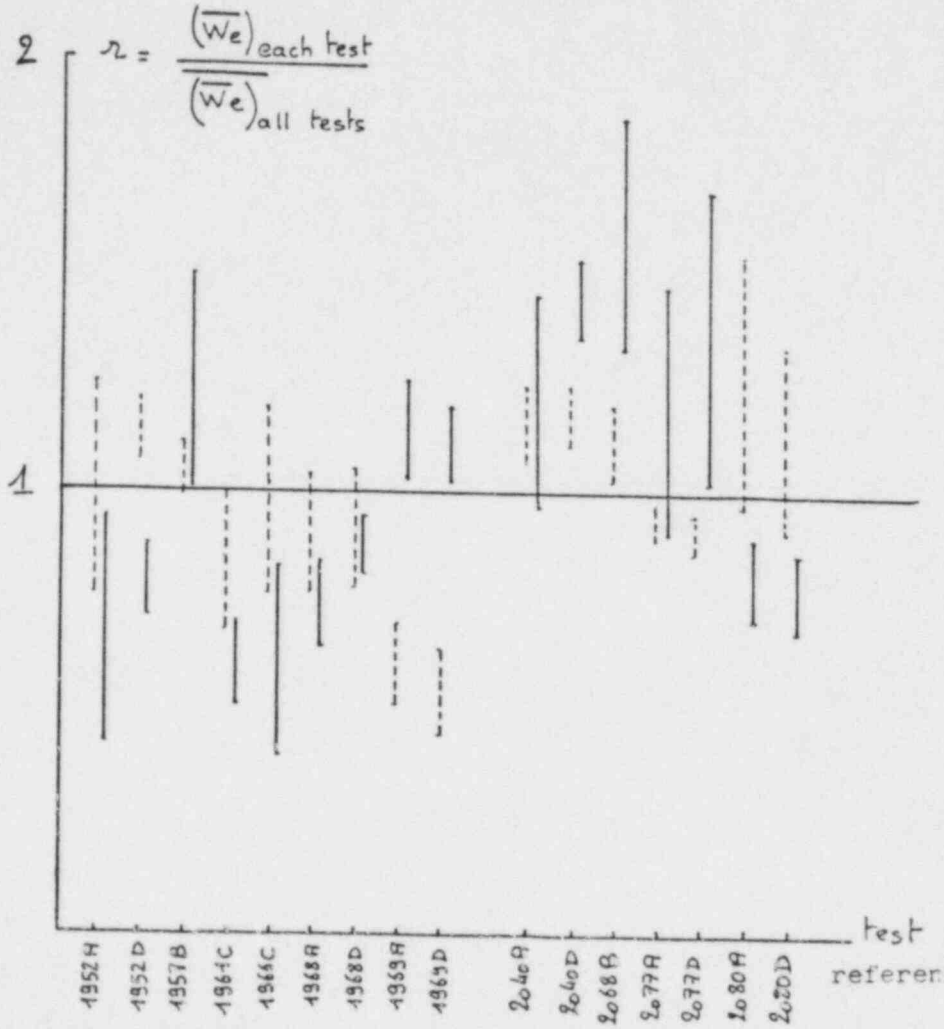

3	3	3	6	1	1		6	6	3	1	P bars
80	50	50	50	80	80		120	50	50	20	G kg/m²s
3	5	3	5	3	5		5	7	7	3	$\underline{\varphi}$ w/cm²

MAIN EXPERIMENTAL PARAMETERS

FIGURE 6

HEAT TRANSFER COEFFICIENT FUNCTION OF $(1-\alpha)$ FOR VARIED DISTANCES TO THE QUENCH FRONT

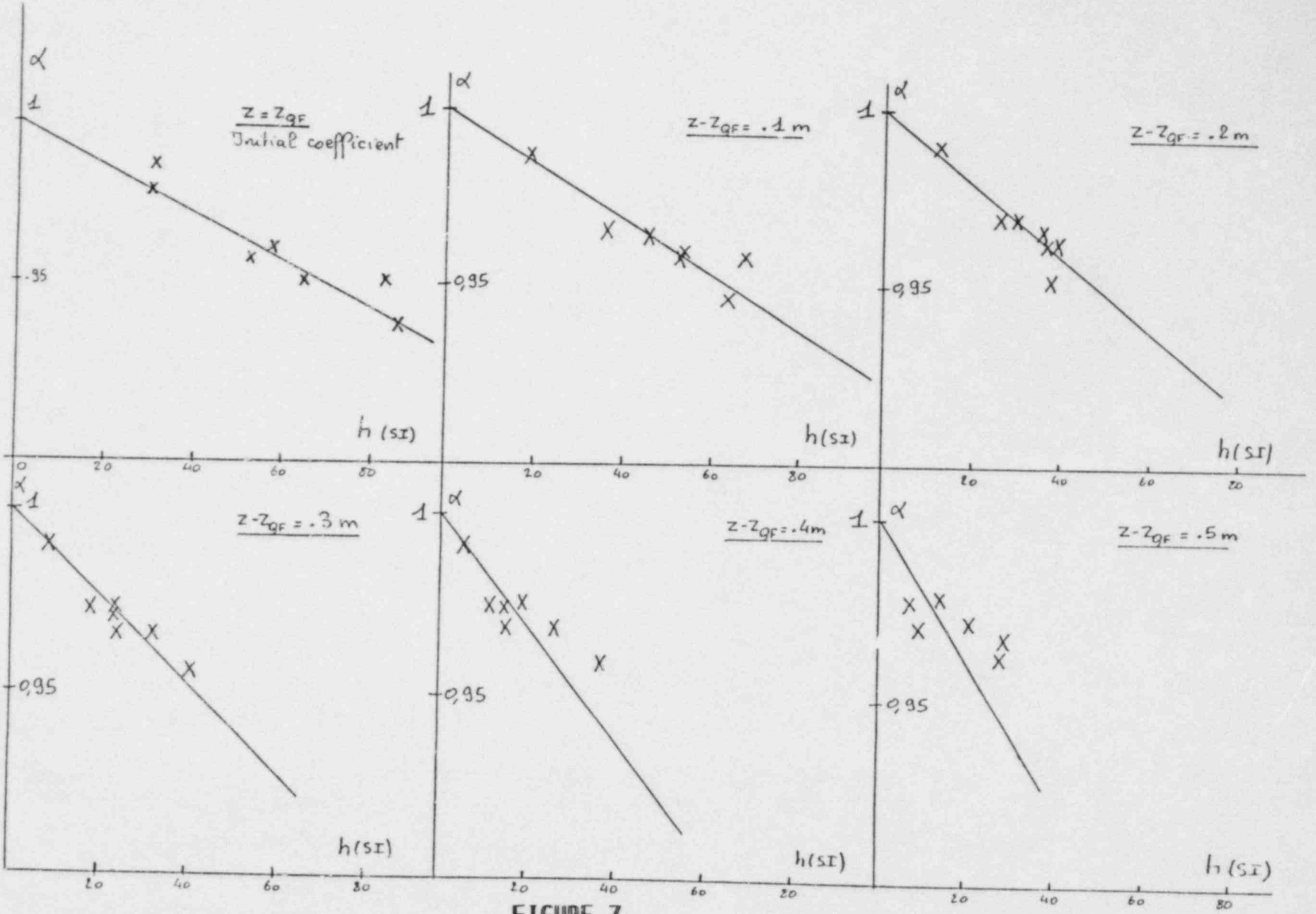

FIGURE 7

LINEAR FUNCTION H=M(1-α) GRADIENT
VERSUS QUENCH FRONT DISTANCE

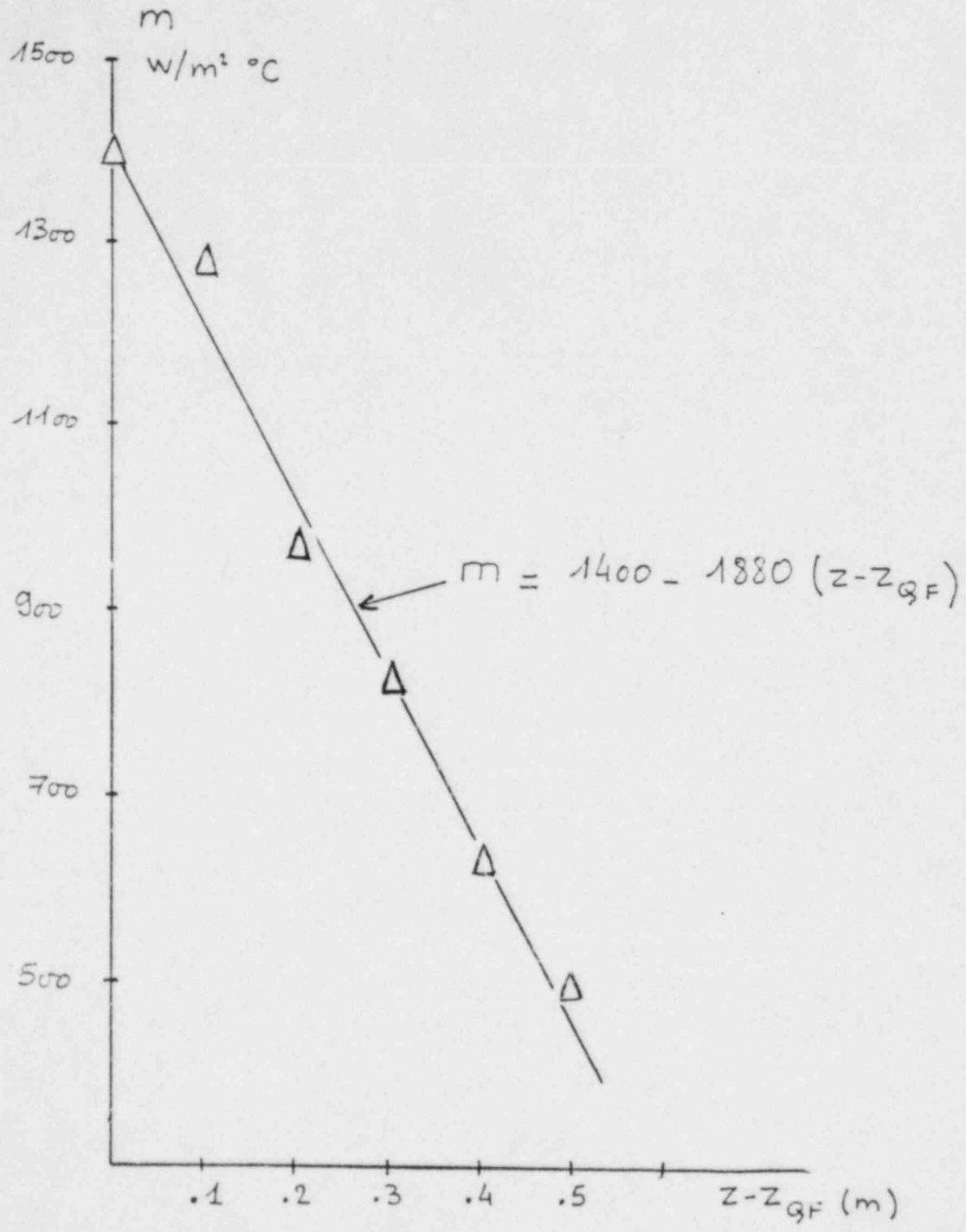

FIGURE 8

CORRELATED HEAT TRANSFER COEFFICIENT VERSUS EXPERIMENTAL
ONE FOR ALL THE TESTS

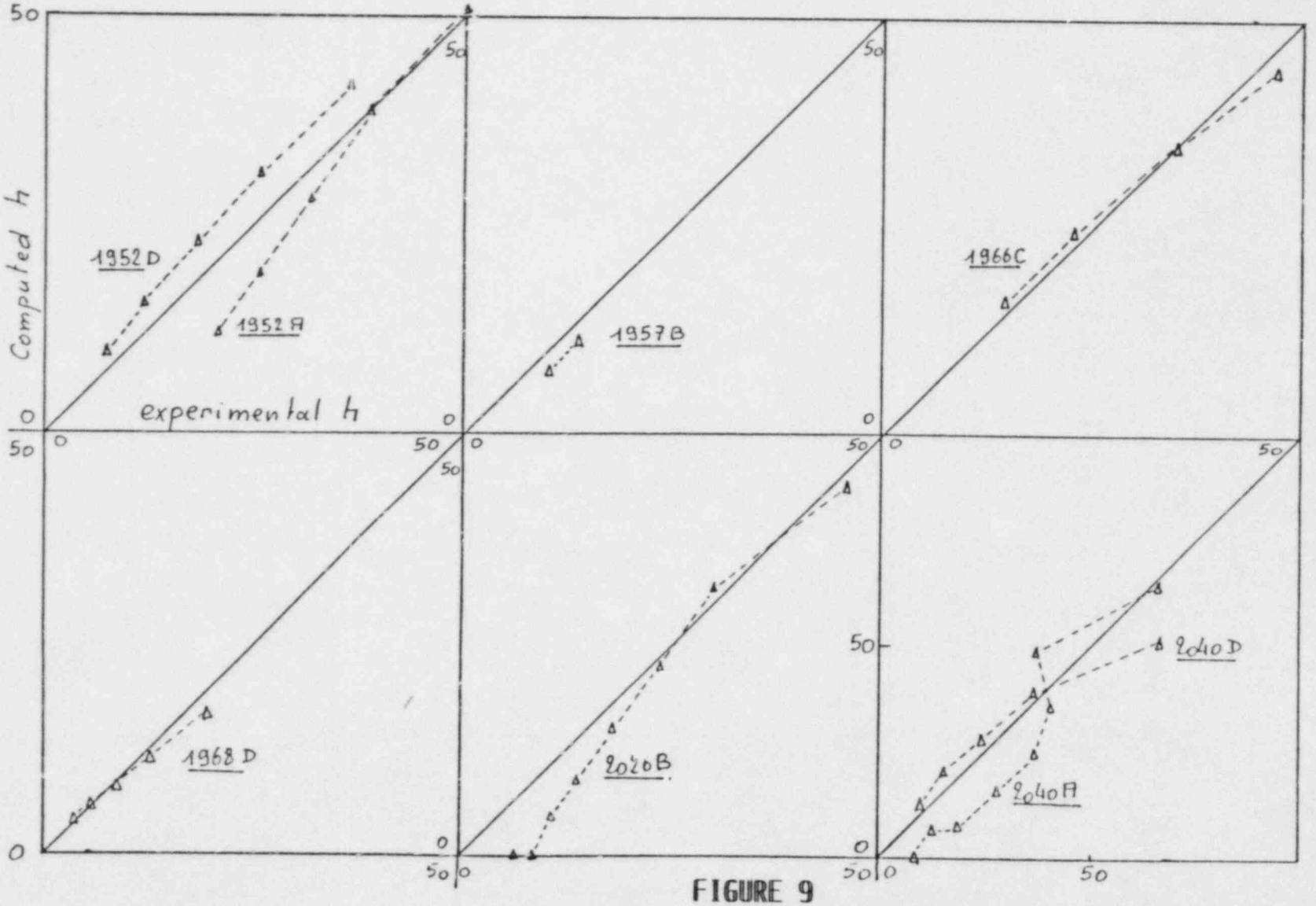

FIGURE 9

EXPERIMENTAL AND COMPUTED WALL TEMPERATURES FOR TWO TYPICAL TESTS

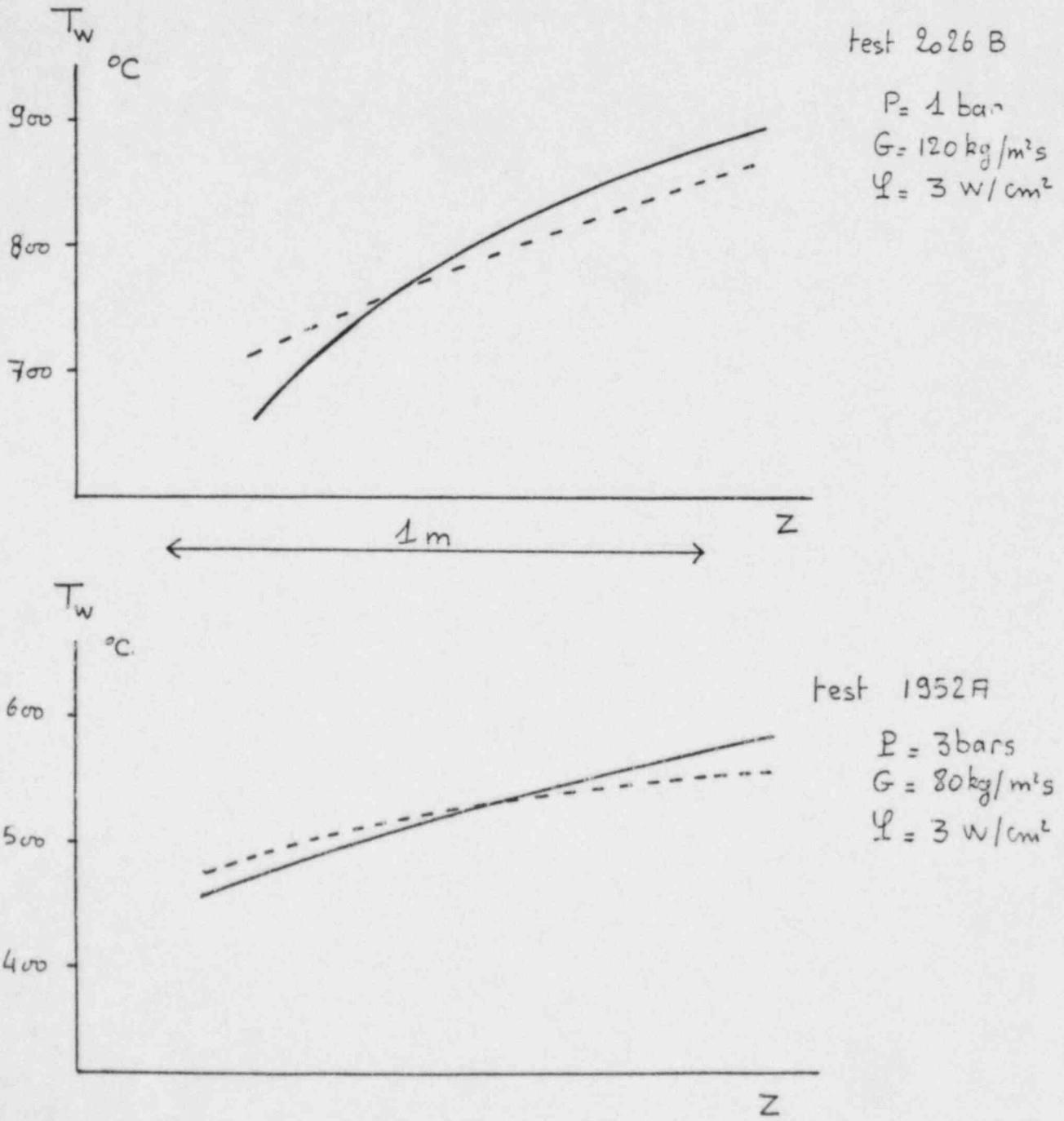

FIGURE 10

ANNEXE A

MECHANICAL MODEL

This model is issued from CATHARE model.

Impulsion equations :

$$\text{Liquid} \ldots + \frac{\partial}{\partial Z} A(1-\alpha)\rho_L V_L^2 = - \chi_L \tau_L + A \tau_i$$

$$\text{Vapour} \ldots + \frac{\partial}{\partial Z} A \alpha \rho_V V_V^2 = - \chi_V \tau_V - A \tau_i$$

Wall shear stress :

$$\chi_L \tau_L = (1-\alpha) f_L \rho_L \frac{V_L^2}{2}$$

$$\chi_V \tau_V = \alpha f_V \rho_V \frac{V_V^2}{2}$$

$$f_K = \text{Max} \left\{ \frac{16}{Re_K}, .079 Re_K^{-1/4}, 3.10^{-3} \right\} \quad K = L \text{ or } V$$

Interfacial shear stress

$$\tau_i = .75 \alpha(1-\alpha)\rho_V \frac{\rho_L C_d V_V^2}{2.3 \, 10^2 \sigma} (V_V - V_L)^2$$

$$C_d = 0.5$$

ANNEXE B

HEAT TRANSFER BY RADIATION

The CATHARE model is used it is a simplified version of Deruaz-Petitpain (Ref. 6) model.

It describes scattering and grey absorption by droplets as well as nongrey absorption by steam. We assume uniform size, temperature and spatial distribution for droplets and uniform temperature for steam.

The model is :

$$\Phi_{rpV} = \frac{\sigma(T_p^4 - T_V^4)}{B} \quad \frac{\alpha K_V^a}{K}$$

$$\Phi_{rpL} = \frac{\sigma(T_p^4 - T_L^4)}{B} \quad \frac{n_1^2(1-\alpha)K_1^a}{K}$$

with :

$$B = \frac{1}{\epsilon_p} + \frac{1}{1-2E_3(K.D)} - 1 \qquad \text{geometrie plane}$$

$\epsilon_p = 0,7$ **wall emissivity**

$$E_3(x) = \int_1^\infty \frac{e^{-XT}}{t^3}\, dt$$

$$K = n_1^2\,(1-\alpha)K_1^a + \alpha\, K_V^a$$

$$D = 0,534\, D_H$$

$$n_1^2 = 1,77$$

$$K_1^a = \frac{1,5}{\delta}\ (cm^{-1})$$

δ = **droplet diameter**

$$K_v^a = f(P,\ T_V,\ T_W,\ \lambda)$$

NUMERICAL SIMULATION OF THE REWETTING OF A HORIZONTAL TUBE USING A TWO-FLUID MODEL

by

C.B. So and K.H. Ardron

ABSTRACT

The RAMA-UVUT two-fluid computer code was used to simulate tests in which a hot horizontal tube was rewetted by a forced flow of subcooled water at atmospheric pressure. Comparisons were also made with counterpart experiments using an unheated tube.

The RAMA model underpredicted the slope of the gas-liquid interface during the refilling of the unheated tube. The reasons for the discrepancy are not understood. However, it was found that the predictions of the existing model could be made to agree with the experimental results by using an enhanced wall-friction factor in the two-phase region.

Using the enhanced wall-friction factor, the predictions of the RAMA model were in good agreement with the hot-tube rewetting data. The calculations indicated that the post-dryout heat transfer in the tube is strongly influenced by the liquid subcooling. Further horizontal-tube rewetting tests covering a range of inlet subcoolings are suggested as a means of confirming the subcooling effect.

Atomic Energy of Canada Limited
Whiteshell Nuclear Research Establishment
Pinawa, Manitoba ROE 1LO
1984 March

NOMENCLATURE

a	fraction of the wall surface immersed in water
A	wall surface area, flow area
C	specific heat at constant pressure
D	tube diameter
D_k	hydraulic diameter of the part of the tube occupied by phase k
f	friction factor
g	gravitational acceleration
h	enthalpy
K	thermal conductivity
m	mass generation rate per unit flow volume
P	pressure
Pr	Prandtl number
q	heat transfer rate per unit flow volume
q''	heat flux
Re	Reynolds number
t	time
T	temperature
T_{min}	minimum film-boiling temperature
U	velocity
w_i	interface width
y	height above bottom of pipe
$\bar{y}_k$	height of centroid of portion of pipe occupied by phase k
X	thermodynamic quality
X_{tt}	Martinelli parameter
Z	axial distance

Greek

α_k	volumetric concentration of phase k
λ	heat transfer constant
ν	kinematic viscosity
ρ	density
σ	surface tension
τ	shear force per unit flow volume
ϕ	angle subtended at pipe centre

Superscript

(n)	the n^{th} wall surface
b	bulk phase

Subscript

B	boiling
g	gas phase
i	interface
k	phase k
ℓ	liquid
w	wall
CHF	Critical Heat Flux
sat	saturation
sub	subcooling
min	quantity evaluated at T_{min}

1. INTRODUCTION

An understanding of the mechanism involved in the rewetting of hot surfaces is important for the analysis of emergency cooling system performance in water-cooled nuclear reactors. Numerous studies have described the rewetting of vertical channels by bottom flooding or top spray, and reviews are available (see, e.g., [1] and [2]); however, comparatively little work has been reported on the rewetting of horizontal channels. Experiments described in Reference [3] to [5] showed that horizontal channel rewetting is quite different from the vertical channel case. Because of gravity, flow stratification occurs in the rewetting of a horizontal channel. Thus at a given location, the bottom surface rewets before the top surface. In the experiments of Chan and Banerjee [3], using a horizontal tube, observed rewetting temperatures were up to 200°C higher than those normally found in pool-boiling experiments, or in experiments with vertical surfaces. This led Chan and Banerjee to postulate a hydrodynamic instability mechanism for rewetting in horizontal flow, in which gravity forces play an important role.

The RAMA-UVUT computer code has been used for calculating the rewetting of the horizontal fuel channels in a CANDU-PHW reactor, under certain postulated fault conditions [6]. RAMA-UVUT solves the conservation equations for one-dimensional, two-fluid flow, to calculate the phase temperatures and velocities in the channel. The distribution of liquid across the channel area is determined using a flow-regime map.

In this paper, the RAMA-UVUT model used to describe channel rewetting under stratified-flow conditions is described briefly. Code predictions are then compared with the horizontal-tube rewetting experiments described in References [3] and [4]. The hydrodynamic rewetting criterion proposed by Chan and Banerjee is discussed in the light of the new calculations.

2. RAMA-UVUT MODEL FOR HORIZONTAL-CHANNEL REWETTING

The RAMA-UVUT computer code uses a two-fluid model that treats the vapour and liquid as individual streams with different velocities, temperatures and pressures. Constitutive relationships are specified to describe the exchange of mass, momentum and energy between the phases, and to evaluate the wall-to-fluid heat transfer. Thermal conduction within solid wall elements and radiation between solid surfaces are also calculated.

The form of the conservation equations and the constitutive laws depend on the flow regime. Three flow regimes are recognized in the RAMA model:

(i) horizontal stratified flow

(ii) vertical annular film flow

(iii) dispersed flow.

The appropriate flow regime is selected by using a flow regime map. Since the present work is concerned with stratified flow in a horizontal tube, only the equations used for this regime will be described here.

2.1 Conservation Equations for Horizontal Stratified Flow

The conservation equations for horizontal stratified flow are derived by cross-section and time averaging of the local, instantaneous, phasic conservation equations [7]. The equations used are:

Mass Conservation, Phase k

$$\frac{\partial}{\partial t} A\, \alpha_k \rho_k + \frac{\partial}{\partial z} A\, \alpha_k \rho_k U_k = A\, m_{ki} \tag{1}$$

Momentum Conservation, Phase k

$$\frac{\partial}{\partial t} A\, \alpha_k \rho_k U_k + \frac{\partial}{\partial z} A\, \alpha_k \rho_k U_k^2 + \alpha_k A \frac{\partial P_k}{\partial z} + A\, \beta_k \frac{\partial \alpha_k}{\partial z} \tag{2}$$

$$= A\, m_{ki}\, U_{ki} + A\, \tau_{kw}$$

Energy Conservation, Phase k

$$\frac{\partial}{\partial t} A\, \alpha_k \rho_k H_k + \frac{\partial}{\partial z} A\, \alpha_k \rho_k U_k H_k - \alpha_k A \frac{\partial P_k}{\partial t} - A\, \beta_k \frac{\partial \alpha_k}{\partial t}$$

$$= A\, m_{ki} \left(h_{ki} + \frac{U_{ki}^2}{2}\right) - A\, q_{kw}^b \tag{3}$$

where $H = h + U^2/2$ and the function $(-1)^k$ is defined by the equations

$$(-1)^k = -1 \text{ for vapour } (k = g)$$

$$(-1)^k = 1 \text{ for liquid } (k = \ell)$$

2.2 Constitutive Relationships

The flow pattern assumed for horizontal stratified flow in a tube is shown in Figure 1. The interface is assumed to be smooth, and droplet entrainment in the vapour phase is neglected. The constitutive equations used to give the mass, momentum and energy transfer terms in Equations (1) to (3) are listed in Table 1. A complete description of the constitutive relationships for all flow regimes is given in Reference [6].

2.2.1 Wall-to-Fluid Heat Transfer

The RAMA-UVUT model is able to describe the radial temperature distribution in a large number of independent elements comprising the channel wall. These elements can represent individual fuel pins, circumferential segments of a tube wall, etc. Conductive heat transfer between wall elements is not modelled, but radiative heat transfer is included. The mean heat flux at the surface of the n^{th} wall element is given by

$$q''^{(n)} = a^{(n)}\, q_B''^{(n)} + (1 - a^{(n)})\, q_{FCV}''^{(n)}$$

where $a^{(n)}$ is the fraction of the surface immersed in water, $q_B''^{(n)}$ is the heat flux for boiling or liquid forced convection, and $q_{FCV}''^{(n)}$ is the heat flux for vapour forced convection. In stratified flow, we take $a^{(n)} = 1$ for surfaces completely below the liquid level, and $a^{(n)} = 0$ for surfaces completely above the liquid level. A value between zero and one is used for partially immersed surfaces.

In the current RAMA model, heat released in boiling is assumed to enter the bulk liquid phase. The conversion of the heat to vapour generation in saturated boiling is ensured by making the liquid-to-interface heat-transfer constant ($\lambda_{\ell i}$) arbitrarily large for $T_\ell \geq T_{sat}$, as shown in Table 1. For subcooled boiling, heat transfer from the wall is assumed to result in heating of the bulk liquid phase. Note that subcooled voiding cannot be represented with this model.

The formulations used for the surface heat flux for boiling and vapour-forced convection are given in Table 2. Figure 2 shows the boundaries between the different boiling regimes.

2.3 Numerical Solution Scheme

In the version of RAMA-UVUT employed, the conservation equations (1) to (3) were solved using a finite-difference method with a fixed spatial mesh [8]. The dependent variables of solution are α_g, P_g, U_g, U_ℓ, h_g, and h_ℓ. The solution method uses a staggered mesh technique in which the phase velocities are evaluated at cell edges and the other variables at cell centres. Stability is maintained by using differencing procedures similar to those described in Reference [17], in which viscous-type terms are introduced into the momentum equations. Also, a mass-conservation algorithm is introduced to ensure strict mass conservation. Details are given in Reference [8].

3. COMPARISON OF PREDICTIONS WITH THE HORIZONTAL-TUBE REWETTING EXPERIMENTS

Chan and Banerjee [3] performed experiments in which a hot horizontal tube was rewetted by a forced flow of subcooled water at atmospheric pressure. Their apparatus is shown schematically in Figure 3. The test section, which was uninsulated, consisted of a 2-m-long, thin-walled Zircaloy tube with an internal diameter of 18.0 mm and a wall thickness of 0.898 mm. The tube was heated electrically to a temperature close to 500°C. The electrical power was then shut off and the tube rewetted by diverting a controlled flow of subcooled water (T = 8°C) into the test section using quick-acting valves QAV2 and QAV1. The tube wall temperature was measured using thermocouples spot welded to the tube external surface at top, bottom and mid-side locations.

Chan and Banerjee also performed experiments on the refilling of an unheated Pyrex tube to provide information on the shape of the liquid front during refilling. The experimental setup is also shown in Figure 3. In the tests, the velocities of the leading and trailing edges of the refilling front were observed visually.

3.1 Unheated-Tube Experiments

To test the hydrodynamic modelling in RAMA, comparisons were first made with the results of one of the unheated-tube refilling experiments. A 13-node representation of the test section was used, as shown in Figure 4. To demonstrate numerical convergence, one calculation was repeated with a 25-node representation; no significant change in the solution was obtained.

Comparisons were made with a refilling test in which the injection flow rate was 70 g/s. Measured and predicted void profiles at t = 4 s and t = 6 s are shown in Figure 5. (The experimental profile is interpolated from the position of the leading and trailing edges of the refilling front.) Code predictions using the modelling assumptions in Section 2 are shown as the curves labelled "A". The predicted refilling front is much too flat.

Chan and Banerjee [3] modelled this test using their two-fluid code REWET. They found that reasonable agreement with data could be obtained if the smooth-tube wall-friction factor in the two-phase region was multiplied by a factor of 60. This modification was also introduced into RAMA, and the calculations repeated. The results are shown as the curves labelled "B" in Figure 5. Agreement with data is now good. In view of this, the factor of 60 was adopted for the heated-tube rewetting simulations described below. This procedure was also followed by Chan and Banerjee in their calculations [3].

It should be noted that the use of the friction multiplier has no obvious theoretical basis. It seems likely that the multiplier actually compensates for errors introduced in attempting to describe the two-dimensional flow field at the leading edge of the refilling front with a one-dimensional model. Further investigations of this are in progress.

3.2 Heated-Tube Experiments

The nodalization scheme used for the simulation of the hot-tube rewetting tests is shown in Figure 4. Again 13 nodes were used to represent the test section. For the heat transfer calculation the tube wall was subdivided into four circumferential elements, as shown in Figure 6. From symmetry considerations, segments B and D were assigned the same temperatures. Thus, three independent wall-temperature calculations were done at each axial node. Heat losses from the external surface of the tube were neglected. The modelling assumptions used were those described in Section 2, except for the use of the wall-friction multiplier of 60 in the two-phase region (see section 3.1 above).

Simulations were made of tests at injection flow rates of 47 and 84.5 g/s. Predicted and measured tube-wall temperatures for three axial stations are plotted in Figures 7 and 8. Agreement is quite good, and would clearly be improved even more if heat losses to the surroundings had been represented in the calculations.

Agreement obtained in the 84.5 g/s case is somewhat better than in the 47 g/s case. This is probably due to the use of the friction multiplier, which was selected to give good agreement with the shape of the refilling front at a flow rate of 70 g/s (see section 3.1). Use of the multiplier at a flow rate of 47 g/s appears to give a refilling front that is too steep. This is not surprising since the multiplier has no physical basis.

3.2.1 Effect of Subcooling

For the experimental conditions the RAMA model predicts values of T_{min} in the range 290 to 650°C. These high values are a consequence of using the Groeneveld-Stewart [15] correlation, which predicts very high values of T_{min} for subcooled liquid conditions. The importance of subcooling on post-dryout heat transfer has only been recently identified, mainly as a result of experiments by Groeneveld and co-workers [13].

To show the importance of the subcooling effect in the present case, the rewetting calculations described earlier were repeated with the equations for T_{min} and the film boiling heat flux in Table 2 replaced with relationships given by Berenson [18], which do not account for the effect of liquid subcooling. Figure 9 shows the results of the new calculations for some typical cases. In general, the agreement with data obtained with the Berenson equations is unsatisfactory. Errors are large in the higher flow-rate case, particularly at locations near the tube entrance, where the liquid subcooling at the quench front is the highest (see Figure 9(a)). The smallest errors occur for the low flow-rate case, at stations near the tube exit, where the calculated liquid subcooling at the quench front is small, as shown in Figure 9(b). These observations seem to confirm the importance of liquid subcooling on the rewetting behaviour in this experiment.

Chan and Banerjee [3] analyzed these experimental data using their two-fluid code REWET. They did not allow for the effect of liquid subcooling on the post-dryout heat transfer, and were thus unable to account for the high rewetting temperatures that were observed experimentally. Therefore, they postulated a hydrodynamic rewetting mechanism for horizontal-channel rewetting, which indicates that rewetting will occur essentially independently of the surface temperatures. Our interpretation, based on the RAMA calculations, is that the high rewetting temperatures observed were actually a consequence of the high liquid subcoolings used in the tests. Further horizontal-tube rewetting tests with variable inlet subcooling are required to confirm if this interpretation is correct.

4. CONCLUSIONS

1. The RAMA-UVUT two-fluid code has been used to simulate experiments in which a hot horizontal tube was rewetted by a forced flow of subcooled water. Comparisons have also been made with the results of refilling experiments on an unheated horizontal tube.

2. Comparisons indicate that the simple horizontal stratified-flow model in RAMA significantly underpredicts the slope of the gas-liquid interface during refilling of the tube. The reasons for the discrepancy are being investigated. The predictions of the existing model can be brought into agreement with the experimental data by using an enhanced wall-friction factor in the two-phase region.

3. Using the enhanced wall-friction factor, good agreement has been obtained between the predictions and the hot-tube rewetting data.

4. Calculations indicate that the levels of post-dryout heat transfer in the experiment were strongly influenced by the liquid subcooling. Further horizontal-tube rewetting tests covering a range of inlet subcoolings would be useful to confirm this inferred effect of subcooling.

REFERENCES

1. Butterworth, D. and Owen, R.G., "The Quench of Hot Surfaces by Top and Bottom Flooding - A Review", UKAEA Report. AERE-R-7992, 1975.

2. Delhaye, J.M., Giot, M., and Riethmuller, M.L., "Thermohydraulics of Two-Phase Systems for Industrial Design and Nuclear Engineering", McGraw-Hill, Washington, 1981.

3. Chan, A.M.C. and Banerjee, S., "Refilling and Rewetting of a Hot Horizontal Tube," Parts I, II, and III, J. Heat Transfer 103 281-286, 287-292, 653-659, 1981.

4. Chan, A.M.C., "Transient Two-Phase Flows: Refilling and Rewetting of a Hot Horizontal Tube," Ph.D. Thesis, Dept. of Engineering Physics, McMaster University, 1980.

5. Hancox, W.T., Rajan, V.S.V., Barclay, F.W., Hanna, B.N. and McDonald, B.H., "Refilling and Rewetting of Horizontal Fuel Channels," International Meeting on Thermal Nuclear Reactor Safety, Chicago, Illinois, August 1982.

6. Ardron, K.H., Barclay, F.W., Hanna, B.N., Mallory, J., McDonald, B.H., Scarth, D. and So, C.B., "Progress in Modelling Separated Flow Effect in the Refilling of Horizontal Heated Channels," International Conference on Numerical Methods in Nuclear Engineering, CNS/ANS, 61-70, Montreal, September 1983.

7. Hancox, W.T., Ferch, R.L., Liu, W.S. and Nieman, R.E., "One-Dimensional Models for Transient Gas-Liquid Flows in Ducts," Int. J. Multiphase Flow 6, 25-40, 1980.

8. Richards, D.J., et al., "RAMA-UVUT, An Advanced Computer Code for Transient Thermalhydraulic Analysis of Pipe Networks - Theoretical Manual," WNRE Report in preparation.

9. McAdams, W.H., "Heat Transmission," 3rd edition McGraw-Hill," New York, 1954.

10. Yuen, M.C. and Chen, L.W., "Heat-Transfer Measurements of Evaporating Liquid Droplets," J. Heat Transfer 21, 537-542, 1978.

11. Heineman, J.B. "An Experimental Investigation of Heat Transfer to Superheated Steam in Round and Rectangular Channels," ANL-6213 1960.

12. Chen, J.C., "Correlation for Boiling Heat Transfer to Saturated Fluids in Convective Flow," I and EC Process Design and Development 5 322-329, 1966.

13. Groenveld, D.C. and Rousseau, J.C., "The Advances of Two-Phase Flows and Heat Transfer," NATO Advanced Research Workshop, September 1982.

14. Bjornard, T.A. and Griffith, P., "PWR Blowdown Heat Transfer," ASME Symposium on the Thermal and Hydraulic Aspects of Nuclear Reactor Safety 1, 17-41, November 1977.

15. Groenveld, D.C. and Stewart, J.C., "The Minimum Film Boiling Temperature for Water During Film Boiling Collapse," 7th International Heat Transfer Conference, Munich 1982.

16. Biasi, L., Cherici, G.C., Garribba, S., Sala, R. and Tozzi, A., "Studies on Burnout Part 3 - A New Correlation for Round Ducts and Uniform Heating and Its Comparison With World Data," Energia Nucleare 14, 530-536, 1967.

17. Ransom, V.H. et al., "RELAP5/MOD1 Code Manual Volume 1: System Models and Numerical Methods (DRAFT)," NUREG/CR-1826, EGG-2070, EG&G Idaho Inc., 1980.

18. Berenson, P.J., "Film-Boiling Heat Transfer From a Horizontal Surface," J. Heat Transfer 83, 351-358, 1961.

TABLE 1

Constitutive Equations Used in the RAMA-UVUT Stratified-Flow Model

Constitutive Relationship	Equation Used	Notes
Interface condition	$P_{gi} = P_{\ell i}$ $U_{gi} = U_{\ell i} = U_{\ell}$ - $T_{ki} = T_{sat}(P_{ki})$	
Mass generation	$m_{ki} = (-1)^k \sum_k q^b_{ki}/h_{g\ell i}$	Interfacial heat balance [6]
Wall shear	$\tau_{kw} = -\frac{\Psi_k f_{kw}}{D} \frac{1}{2} \rho_k U_k U_k$ $\Psi_\ell = (1 - \Psi_g) = \phi/2\pi$ $f_{kw} = \begin{cases} 0.184\ Re_k^{-0.2} & Re_k > 2000 \\ 64/Re_k & Re_k \leq 2000 \end{cases}$ $Re_k = U_k D_k/\nu_k$	
Interfacial shear	$\tau_{ki} = (-1)^k \frac{w_i \rho_g f_i}{8A} (U_g - U_\ell) U_g - U_\ell$ $f_i = \begin{cases} 0.184\ Re_{ig}^{-0.2} & Re_{ig} > 2000 \\ 64/Re_{ig} & Re_{ig} \leq 2000 \end{cases}$ $Re_{ig} = (U_g - U_\ell)D_g/\nu_g$	Assumes smooth tube friction factor at interface

Phase-to-interface pressure difference	$\beta_k = P_k - P_{ki}$ $= \rho_k g(y_i - \bar{y}_k)$ y_i and $\bar{y}_k$ are expressed as functions of D and ϕ	see Reference [8]
Liquid-to-interface heat transfer	$q^b_{\ell i} + m_{\ell i}(h_\ell - h_{\ell i})$ $= \lambda_{\ell i}(h_\ell - h_{\ell i})$ $\lambda_{\ell i} = 2.10^5 \alpha_g \alpha_\ell \quad h_\ell \geq h_{\ell i}$ $\lambda_{\ell i} = 0 \quad h_\ell < h_{\ell i}$	
Vapour-to-interface heat transfer	$q^b_{gi} + m_{gi}(h_g - h_{gi})$ $= \lambda_{gi}(h_g - h_{gi})$ $\lambda_{gi} = \frac{w_i K_g}{A D_g C_g}(0.023\, Re_{ig}^{0.8}\, Pr_g^{0.4})$	Assumes usual relationship for forced convection [9] modified to allow for mass transfer as suggested in [10]
Wall-to-fluid heat transfer	$q^b_{\ell w} = -\sum_N q_B''(n) a(n) A(n)$ $q^b_{gw} = -\sum_N q''_{FCV}(n)(1 - a(n))A(n)$ Summations taken over all different heat transfer surfaces comprising the channel wall.	see below

TABLE 2 - Heat Transfer Models in RAMA

Heat Transfer Characteristic	Equation Used	Reference
Heat flux for vapour-forced convection	$q''_{FCV} = \text{Max}(x_1, x_2)$ where $x_1 = \frac{3.66\,K_g}{D}(T_w - T_g)$ $x_2 = \frac{K_g}{D} C\,Re_g^n\,Pr_g^m\,(T_w - T_g)$ $C = 0.0133$ $n = 0.84$ $m = 1/3$	Heineman [11]
Heat flux for nucleate boiling and liquid-forced convection	$q''_B = q''_{NB} + q''_{LC}$ $q''_{LC} = \text{Max}(x_3, x_4)$ where $x_3 = \frac{3.66\,K_l}{D}(T_w - T_l)$ $x_4 = 0.023\,\frac{K_l}{D}\,Re_l^{0.8}\,Pr_l^{0.4}\,F_2(T_w - T_g)$ $F_2 = \begin{cases} 1 & X_{tt}^{-1} \le 0.1 \\ 2.35(X_{tt}^{-1} + 0.213)^{0.74} & X_{tt}^{-1} > 0.1 \end{cases}$ $q''_{NB} = 0.00122 \left\{ \frac{K_l^{0.79}\,C_l^{0.45}\,\rho_l^{0.20}}{\sigma_l^{0.5}\,\mu_l^{0.29}\,h_{lg}^{0.24}\,\rho_g^{0.24}} \right\} \cdot (P_{sat}(T_w) - P_g)\,S\,(T_w - T_{sat})^{1.24}$ where $S = 1/[1 + 2.53 \times 10^{-6}\,Re_{TP}^{1.17}]$ $Re_{TP} = Re_l\,F_2^{1.25}$	Chen [12]
Heat flux for film boiling	$q''_B = 0.425 \left(\frac{K_g^3\,\rho_g\,g\,(\rho_l - \rho_g)\,h'_{lg}}{\nu_g (T_w - T_{sat})\,\rho_g \sqrt{g(\rho_l - \rho_g)/\sigma_l}} \right)^{1/4} (T_w - T_{sat})\,(1 + 0.025\,\Delta T_{sub})$ $h'_{lg} = h_{lg}\left\{1 + \frac{0.4\,C_g\,(T_w - T_{sat})^2}{h_{lg}}\right\}$	Groeneveld and Rousseau [13]

continued...

TABLE 2 (concluded)

Heat flux for transition boiling	$q''_B = \delta\, q''_{CHF} + (1-\delta)\, q''_{min}$ where $\delta = \left(\frac{T_w - T_{min}}{T_{CHF} - T_{min}}\right)^2$	Bjornard and Griffith [14]
Minimum film-boiling temperature (rewet temperature)	$T_{min} = 284.7 + 44.11 \times 10^{-6} P_f - 3.72 \times 10^{-12} P_f^2 - \frac{10^4 x}{2.819+1.219\times10^{-6} P_f}$ for $x \le 0$ and $P_f < 10^7$ Pa $T_{min} = 284.7 + 44.11 \times 10^{-6} P_f - 3.72 \times 10^{-12} P_f^2$ for $x > 0$ and $P_f < 10^7$ Pa $T_{min} = T_{sat} + \left(42.8 - \frac{10^4 x}{15.01}\right)\left(\frac{P_{crit} - P_f}{P_{crit} - 10^7}\right)$ for $P_f > 10^7$ Pa	Groeneveld and Stewart [15]
Critical heat flux	For $\alpha_g < 0.3$ $q''_{CHF} = \frac{1.883 \times 10^3}{(100\,D)^{0.6}(G/10)^{1/6}} \left\{\frac{f_1(P_f)}{(G/10)^{1/6}} - x\right\} \cdot 10^4$ where $f_1(P_f) = 0.7249 + 0.099 \left(\frac{H}{10^5}\right) \exp\{-0.032 \times 10^{-5} P_f\}$ For $\alpha_g > 0.8$ $q''_{CHF} = \frac{3.78 \times 10^3}{(100\,D)^{0.6}(G/10)^{0.6}} f_2(P_f)(1-x) \cdot 10^4$ where $f_2(P_f) = -1.159 + 0.149 \times 10^{-5} P_f \exp(-0.019 \times 10^{-5} P_f) + \frac{8.99 \times 10^{-5} P_f}{10 + 10^{-10} P_f^2}$ For $0.3 < \alpha_g < 0.8$ q''_{CHF} = linear interpolation between q''_{CHF} ($\alpha_g = 0.3$) and q''_{CHF} ($\alpha_g = 0.8$)	Biasi et al. [16]

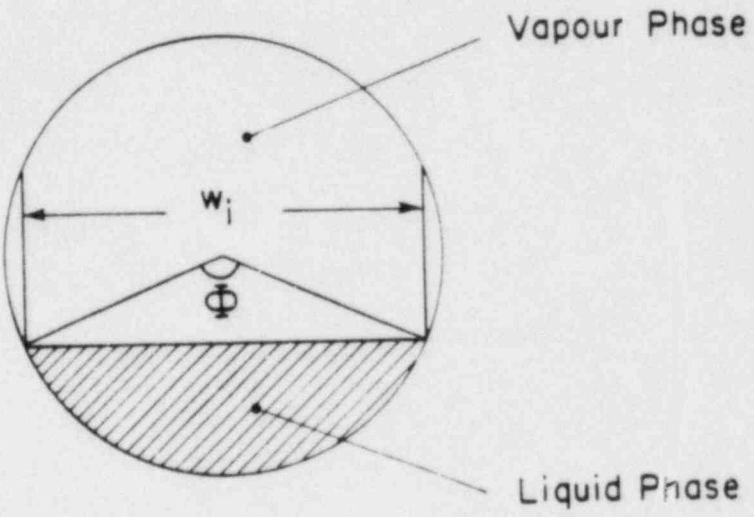

Figure 1: Stratified Flow Geometry.

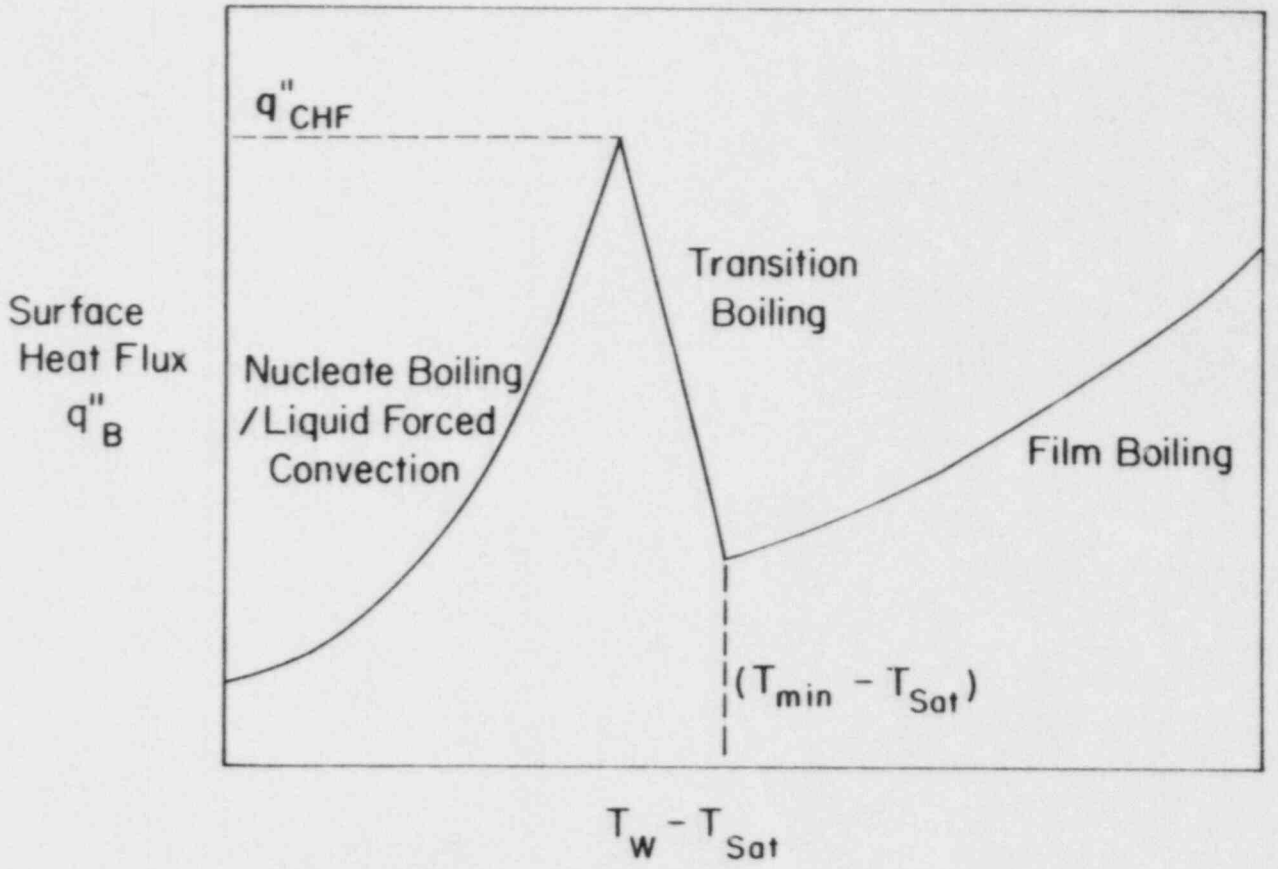

Figure 2: Boiling Heat Transfer Regions.

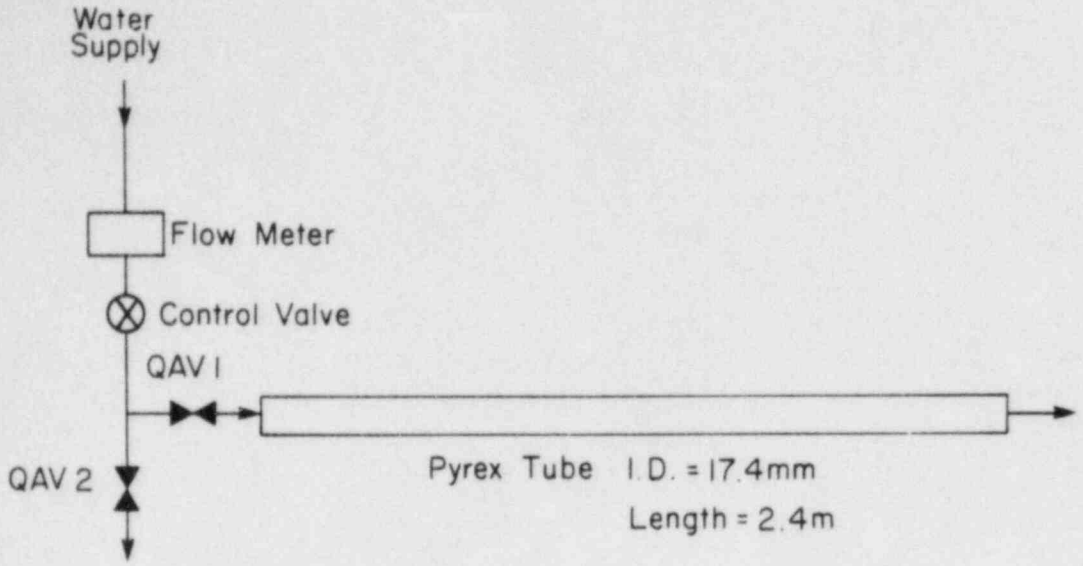

(a) Unheated Tube

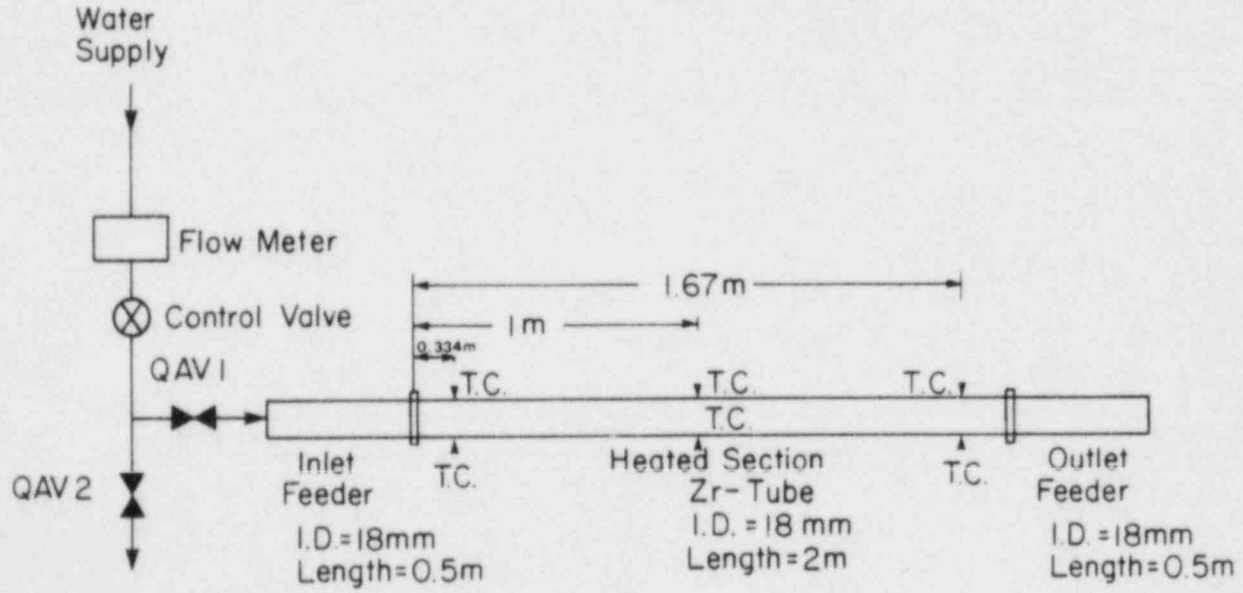

(b) Heated Tube

Figure 3: Experimental Apparatus.

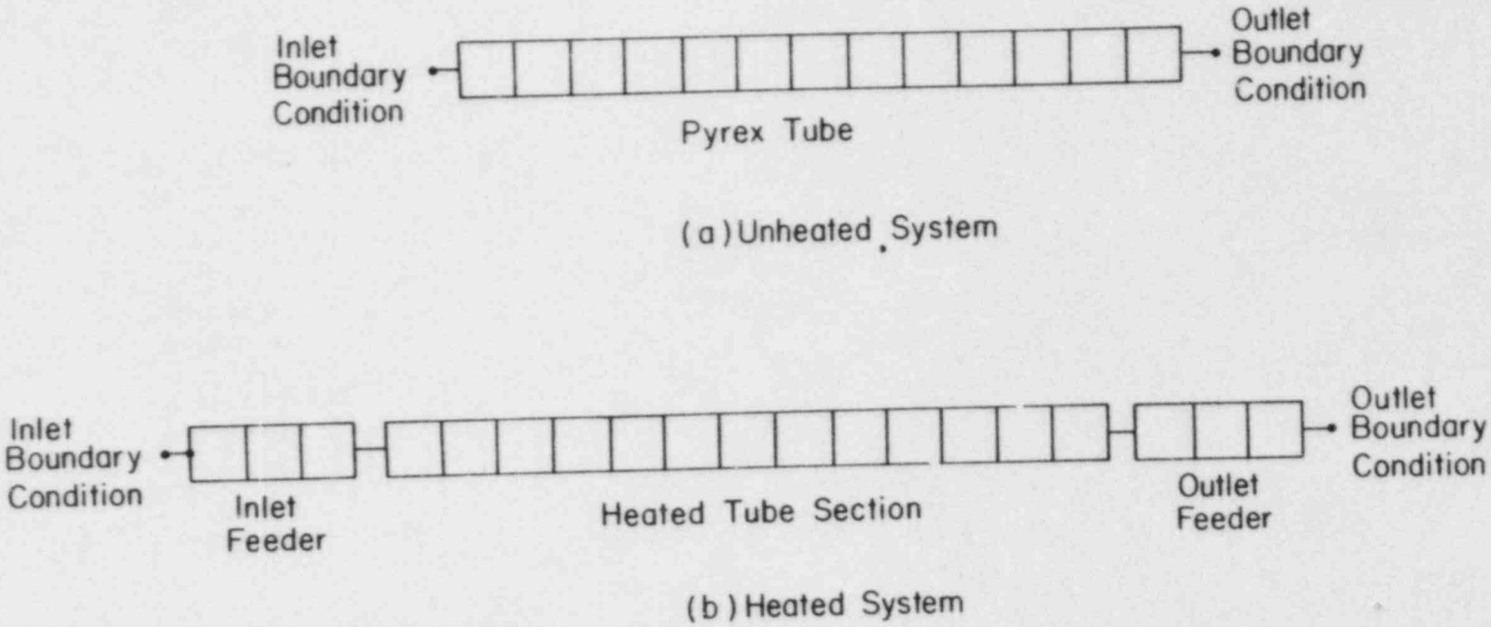

Figure 4: Noding Diagram for Numerical Calculations.

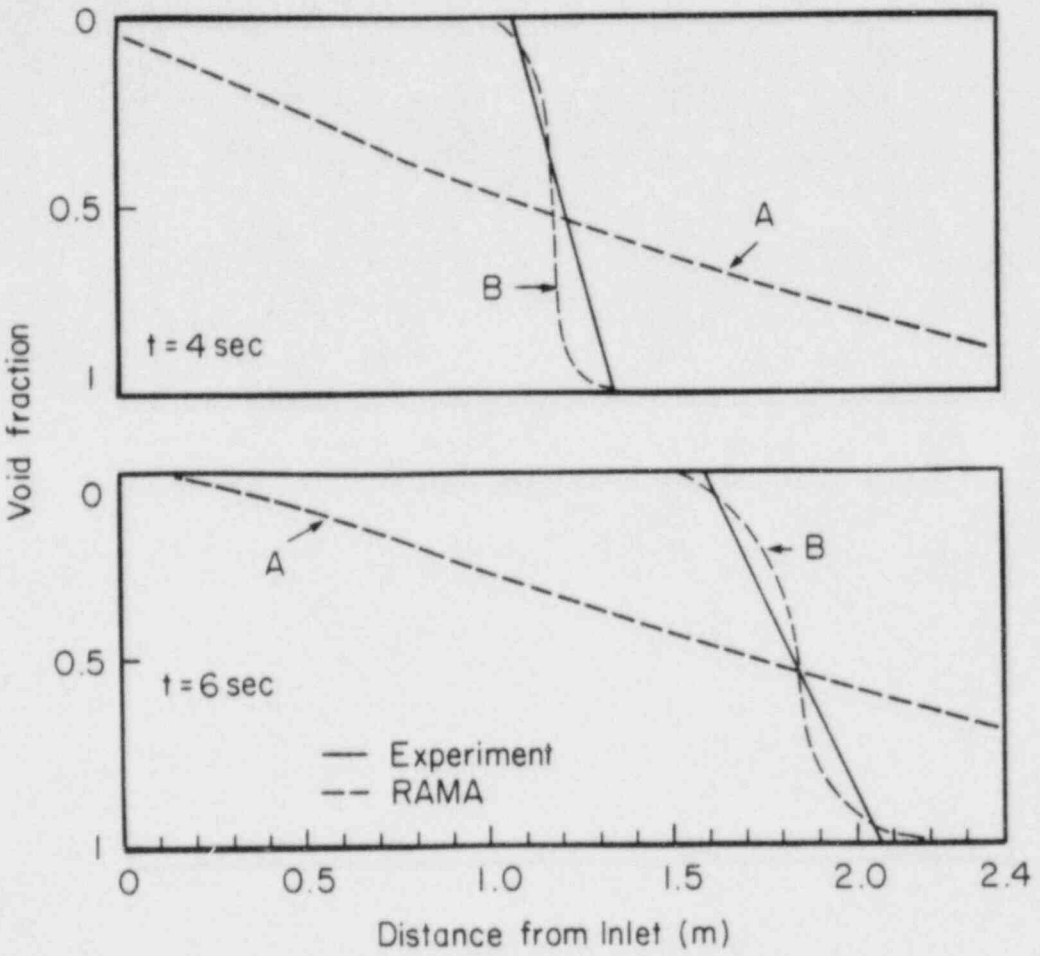

Figure 5: Liquid Front Profile in Unheated Tube Filling Test (Refilling Rate = 70 g/s).

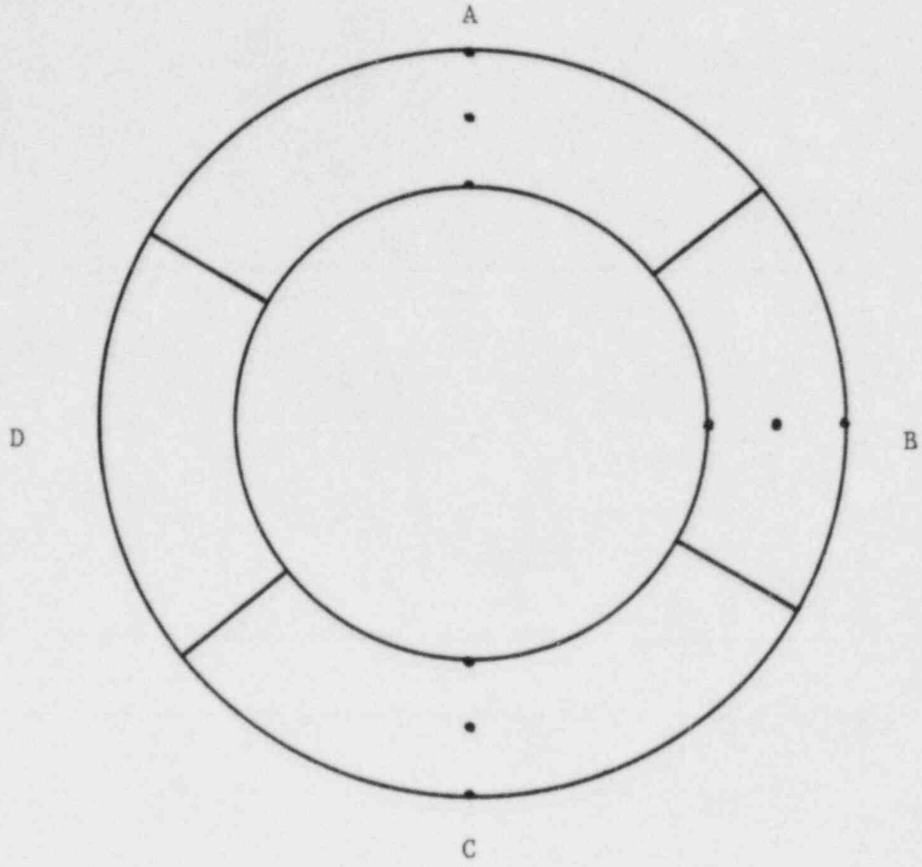

Figure 6: Wall Sectors Used for Heat Transfer Calculation.
Points Are Nodes for Wall Heat Conduction Calculation.

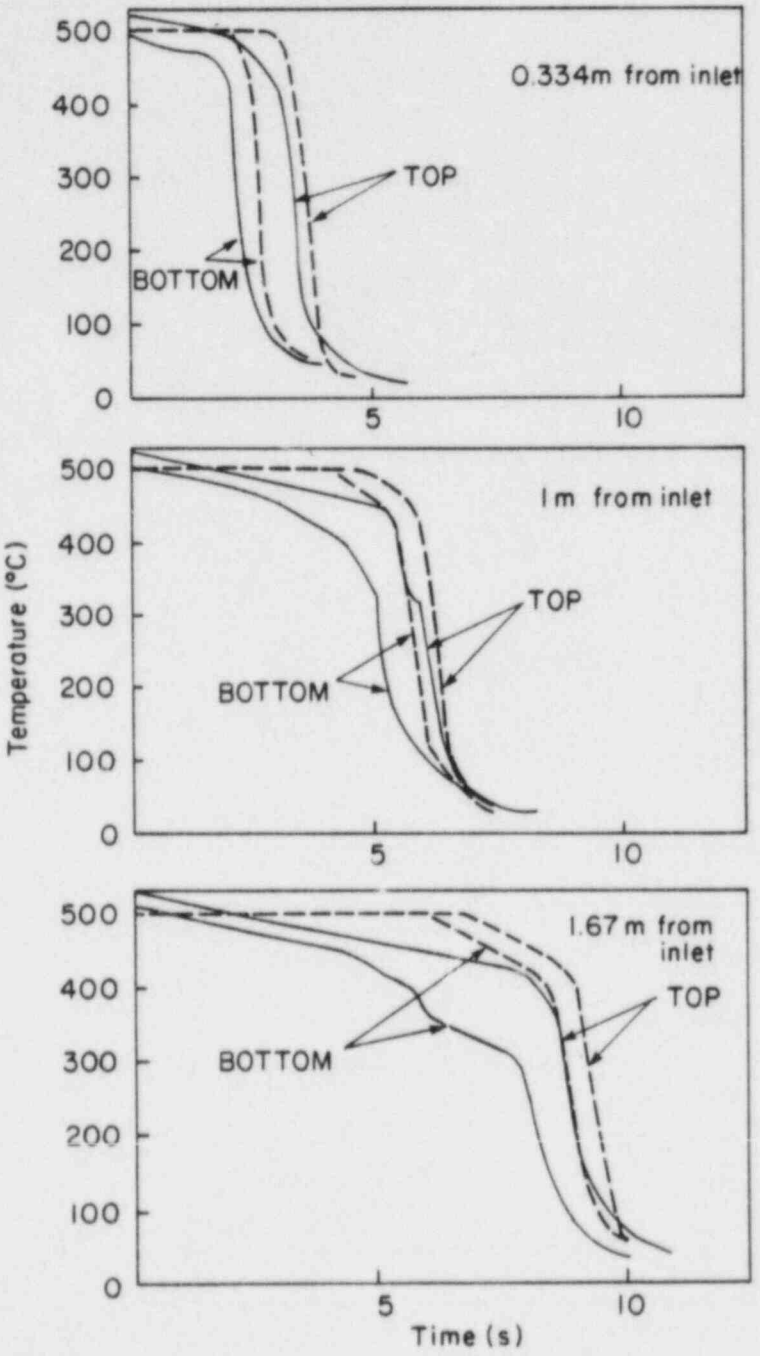

Figure 7: Comparison with Chan and Banerjee Experiment (Refilling Rate = 84.5 g/s).

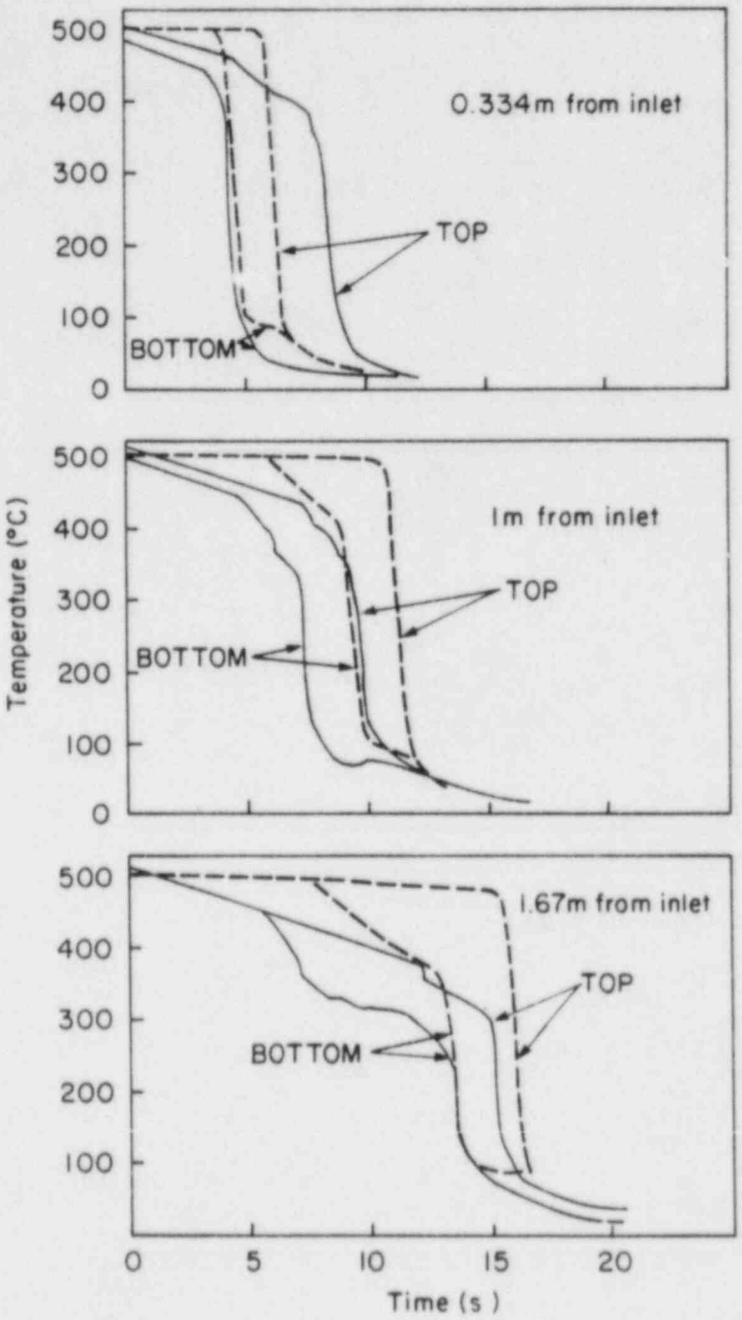

Figure 8: Comparison with Chan and Banerjees Experiment (Refilling Rate = 47 g/s).

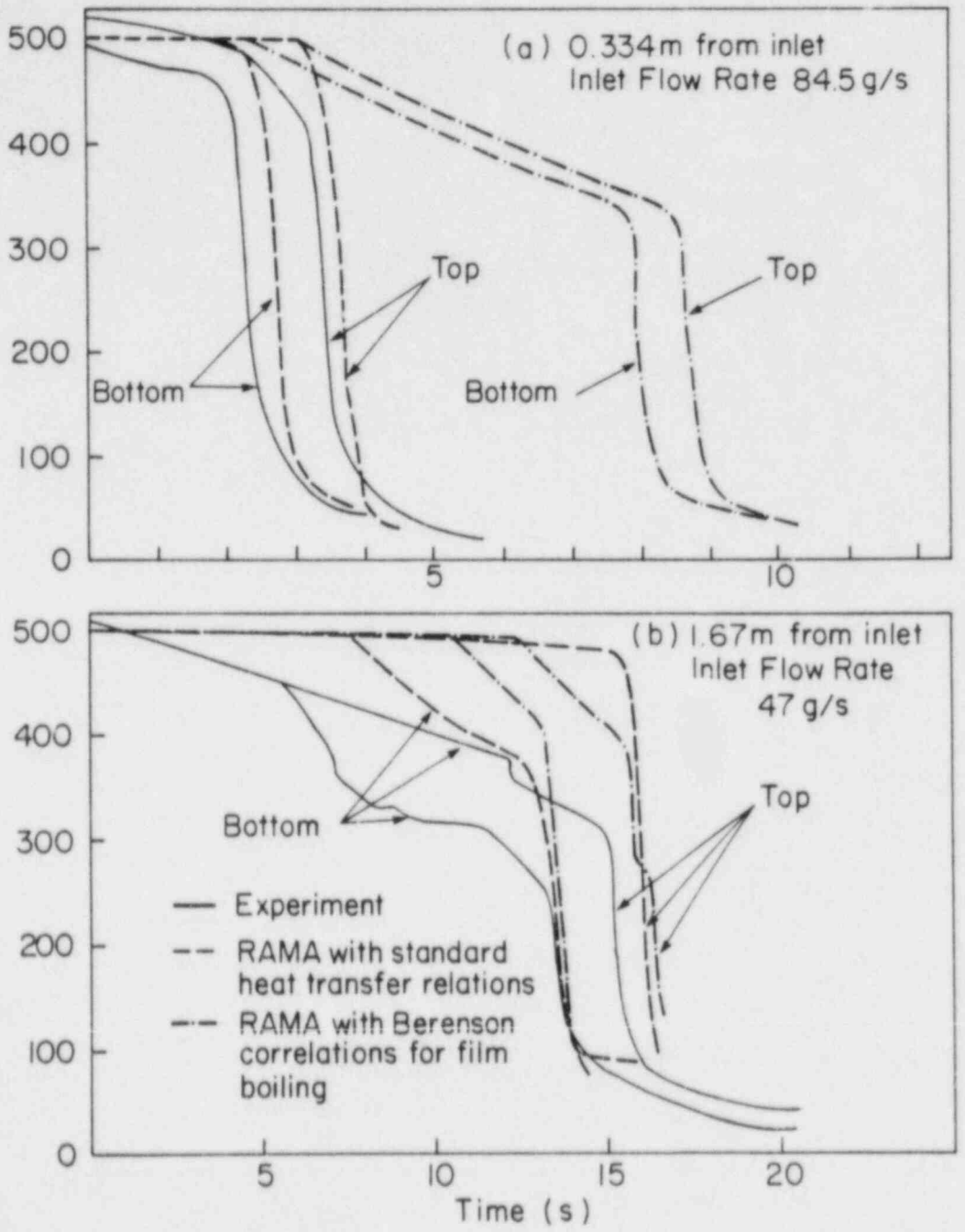

Figure 2: Effect of Using Berenson's [18] Correlations for Film Boiling Heat Transfer and Minimum Film Boiling Temperature.

Prediction of Transition Boiling Heat Transfer in Annular Flow Via The Moving Front Model

J. Weisman and Y.K. Kao
Department of Chemical & Nuclear Engineering
University of Cincinnati
Cincinnati, Ohio 45221

Abstract

In previous work[1], the authors showed that, during annular flow, steady state transition boiling temperature oscillations may be modeled by use of a vertically oscillating rewet front. In the present work, this modeling is extended to provide phenomenologically based predictions of steady-state heat transfer coefficients. Although no vertical rewet front oscillations were observed during transients, the rewet area heat fluxes estimated from steady-state data are shown to be in accord with transient observations.

Introduction

At high void fractions, annular flow is generally observed. Under these conditions, the quenching of a hot rod is determined by the advance of the thin liquid layer along the surface of the rod. The edge of the liquid layer constitutes the rewet front. The advance of this rewet front is relatively slow and rewetting rates are substantially lower than those seen during inverted annular flow.

It is generally agreed that the heat transfer in the vicinity of the rewet front is via transition boiling and that the heat transfer rate in this area can be a significant factor in determining the rate at which the front advances. A better understanding of this phenomenon is therefore clearly desirable.

Several of the more recent attempts to model transition-boiling during annular flow[2][3][4], have focused on the "rivulet model". In this model it is assumed that, as the liquid film drys out, thin rivulets form. The meanderings of these rivulets over the surface are assumed to account for the temperature fluctuations typical of steady-state transition boiling.

Some recent evidence has tended to cast doubt on the rivulet model. France et al.[5], who studied a liquid-metal heated steam generator observed temperature fluctuations during transition boiling with two thermocouples at the same elevation but different circumferential locations. They found that, at high qualities where annular flow is encountered, there was a very high degree of correlation (cross correlation coefficients up to .96) between the two temperatures. Meandering rivulets would be expected to lead to the temperature oscillations at the two locations with a very low cross correlation coefficient.

Two recent visual and photographic studies also failed to support the rivulet hypotheses. In studies at the University of Cincinnati, visual and photographic observations of the film on the surface of a rod in transition boiling did not disclose any rivulets. The slightly ragged front appeared to oscillate in the vertical direction more or less as a unit. Such a vertical oscillation would account for the high cross correlation coefficients observed by France, et al.[5]

Nakanishi et al's.[6] photographic study of the transition boiling region also failed to show numbers of meandering rivulets. At high vapor velocities an occasional rivulet was observed near dryout but the rivulet was constrained to a limited area and wall temperature oscillations were small. Under most conditions, no rivulets were seen. The general behavior can be described briefly as dry patch formation

near to edge of the front, followed by growth and aggregation of these to form a large dry area. This area is then narrowed by an advancing liquid film. The cycle is then repeated.

In view of the foregoing, the authors devised a moving front model for estimation of steady-state transition-boiling temperature fluctuations.[1] The model was compared to data from the authors' experiments with a mercury heated test section with good success. In the present paper, we extend this model to provide phenomenologically based predictions of steady-state transition boiling heat transfer coefficients. The predicted heat transfer rates to the wetted area are then used to explain the authors' transient data.

Previous Work

The experimental data to which model predictions were compared were obtained with the University of Cincinnati's heat transfer loop which uses hot mercury. The mercury is heated outside of the test section and then flows downward into the test section at a controlled temperature. Water near the saturation temperature is introduced counter-currently and is boiled by the hot mercury located in an outer annulus or central tube.

In the tests of the annular test section[7] (mercury in central tube, water in annulus) not only were heat transfer rates measured but wall temperature oscillations were recorded and visual observations made through a glass window. Both steady-state and transient tests were conducted.

The wall thermocouples were located at an effective depth of between 10 and 30 mils below the outer surface of the heater. Because of the close proximity to the water-wall interface, relatively large (e.g. 30°C) temperature oscillations could often be observed. Kao and Weisman[1] used these oscillations to determine wetted area fractions. They assumed that the surface is wet during the period when the temperature is generally dropping, or at a low value, and dry when generally rising or at a high value. They further assumed that when the surface is dry the heat transfer rate corresponds to the low rate seen at the end of the transition region. They then used the overall heat transfer rate and wetted fraction to compute the heat transfer rate while the surface is wetted, q''_{wet}. The results of these calculations are shown in Fig. 1.

Figure 1 shows that the heat transfer rate to the wetted area does not rise with rising surface temperature. Instead the rate stays at approximately the CHF value and decreases slightly as the surface temperature increases.

To analyze the temperature oscillations, Kao and Weisman[1] conducted a Fourier analysis to obtain the frequency spectrum. They observed that the peak was in the range of 0.4 to 0.6 Hz. This peak appeared to correspond to the more or less regular axial oscillations of the rewet front which were observed visually.

Kao and Weisman[1] assumed that the major cause of the observed temperature oscillations was the axial oscillation of the rewet front. The concept of a sinusoidally oscillating rewet front is in agreement with the authors visual observation, and the thermocouple measurements of France et al.[5]. It also would appear to provide an approximate representation of the observations of Nakanishi[6]. The coefficients obtained from the Fourier analysis of the authors' experimental data, for the frequencies between about 0.3 Hz and 0.8 Hz were therefore, used to reconstruct the temperature oscillations due to the simple axial motion of the wetting front. The magnitudesof the reconstructed temperature oscillations were then compared with the magnitudesof numerical calculations of the temperature variations due to a sinusoidally oscillating rewet front moving over a length of 2.5 cm. Reasonable agreement between the numerical calculations and the experimental observations were obtained for the several values of q''_{wet}.

Present Analysis of Steady State Behavior

The first step in extending the previous work was the recognition that all the numerical results obtained for temperature oscillations can be reduced to single curve. This is accomplished by multiplying the oscillation magnitudes by (q''_{std}/q''_{wet}) and plotting these normalized magnitudes against $(T_{m,in}-T_w)(q''_{std}/q''_{wet})$. This is done in Fig. 2 where the solid line represents the calculation for a thermocouple at a depth of 10 mils and the dotted line represents a thermocouple depth of 30 mils. Also shown in Fig. 2 are the experimental data with the vertical bars indicating the estimated error in the oscillation magnitude. It is seen that the predictions are in the correct range but there is considerable scatter. Over much of the range, the observations are somewhat below predictions. This is in part attributable to the fact that the predictions assume the wetted heat flux remains constant whereas in fact in drops with increasing wall temperature.

A single curve for the prediction of wetted area fraction, f, is obtained when f is plotted against $(T_{m,in}-T_{wet})(q''_{std}/q''_{wet})$. The computed curve is compared to the experimentally derived values of f in Fig. 3. The experimental data show relatively little scatter when treated in this fashion but high wetted fractions are reached at lower wall temperatures (greater values of $(T_{m,in}-T_w)$) than predicted. This is consistant with the fact (see Fig. 2) that oscillations persist at wall temperatures below those that predicted for the termination of temperature oscillations. A possible explanation for this behavior comes from the fact that the edge of the rewet front is actually highly irregular rather than the simple plane assumed in the model. While the simple edge assumed in the model probably represents the average location of the front, the wall would really not be fully wetted at the end of the assumed oscillation but at a somewhat lower elevation and hence lower temperature.

Heat Transfer Predictions

The fact that the model leads to the single curves of Figs. 2 and 3 for all of the data, suggests that the analytical model could lead to heat transfer predictions. To reduce the relationship between the predictions and the specific apparatus used to obtain the present data, it was desired to eliminate the reliance on the inlet mercury temperature, $\bar{T}_{m,in}$. For given value of $\bar{T}_{m,in}$, the analytically derived curves show that the range of wall temperatures over which significant wall temperature oscillations occur is fixed. The all wet or all dry conditions are associated with particular values of $(\bar{T}_{m,in}-\bar{T}_w)(q''_{std}/q''_{wet})$.

Now consider the difference in temperature between the conditions at which the wall is fully wetted and the average temperature at which the wetted fraction is f_i. For the wall temperature corresponding to f_i, designated as $\bar{T}_{w,i}$, the value of $(\bar{T}_{m,in}-\bar{T}_{w,i})(q''_{std}/q''_{wet})$ is fixed. Similarly, for the all wet condition, $(\bar{T}_{m,in}-\bar{T}_{w,wet})(q''_{std}/q''_{wet})$ is fixed. For any given value of $\bar{T}_{m,in}$ the difference between these quantities is

$$(\bar{T}_{m,in}-\bar{T}_{w,wet})(q''_{std}/q''_{wet}) - (\bar{T}_{m,in}-\bar{T}_{w,i})(q''_{std}/q''_{wet}) = (\bar{T}_{w,i}-\bar{T}_{w,wet})(q''_{std}/q''_{wet}) \quad (1)$$

or

$$\Delta T_{eff} = (\bar{T}_{w,i} - \bar{T}_{w,wet})(q''_{std}/q''_{wet}) \quad (2)$$

Since the same expression would be obtained for any given value of $\bar{T}_{m,in}$, a given value of f is associated with a given value of ΔT_{eff}. When $\bar{T}_{w,i}$ equals $\bar{T}_{w,wet}$, ΔT_{eff} is zero and f is zero.

To calculate $\bar{T}_{w,wet}$, it is assumed that the standard nucleate boiling heat

transfer correlations apply. We therefore use the McAdams[8] correlation for water boiling at near atmosphere pressure; that is

$$q''_{wet} = 2.25\ (\bar{T}_{w,wet} - T_{sat})^{3.86} \tag{3}$$

where q" is in w/m^2 and T is in °C. The foregoing approach is used in Fig. 4 where the wetted fraction is plotted against ΔT_{eff}. It may be seen that the data are well correlated by this procedure.

If the analytical model which has been proposed has a reasonable validity, then we would expect that the total heat flux, q''_t, should be given by

$$q''_t = fq''_{wet} + (1-f)q''_{conv} = fq''_{wet} + (1-f)h_c\ (\bar{T}_w - \bar{T}_{sat}) \tag{4}$$

and

$$h_t = q''_t/(\bar{T}_w - \bar{T}_{sat}) \tag{5}$$

To use this approach for prediction of heat transfer coefficients, a means for prediction of q''_{wet} is required. If we assume, as we did in developing the model for prediction of wall temperature oscillation, that q''_{wet} is equal to the critical heat flux, then q''_{wet} may be predicted following the approach previously used for predicting the critical heat flux. Wang, Kao and Weisman[7] have recommended that at the low flows of the present test, q''_{crit} be obtained from the curve of Griffith et al.[9] These latter investigators concluded that, at low flows, the ratio of q''_{crit} during pool boiling is directly related to the local void fraction. Fig. 5 shows this relationship.

The forced convection heat transfer coefficient for steam was also estimated following the suggestion of Wang et al.[7] They predicted h_c by means of the Quinn's[10] correlation. For annuli, Quinn suggested

$$h_c = .023\ (k_B/D)(\mu_B/\mu_w)^{0.14} Pr_B \left(\frac{GDx}{\mu_B}\right)^{0.8} \left[1 + \frac{(1-x)}{x}\frac{\rho_B}{\rho_\ell}\right]^{0.8} \tag{6}$$

This correlation tends to underestimate h_c since the effect of heat transfer to droplets striking the wall is neglected. However, the total convective heat transfer coefficient is small and its value does not substantially affect the result.

Fig. 6 shows a parity plot in which the measured heat transfer coefficients for the uppermost thermocouple are compared to the predictions via Equation (4). The value of q''_{wet} was taken as q''_{crit} obtained from Griffith et al.,[9] and h_c was obtained from Equation (6). Values of "f" were computed from Fig. 4. It may be seen that the comparison is quite reasonable although there is substantial scatter.

It is useful to compare the predictions shown in Fig. 6 with the predictions obtained from the entirely empirical correlation reported by Wang et al.[7]. To compare the two transition boiling heat transfer correlations, the ratio, R is defined as

$$R = \frac{\text{Predicted heat transfer coefficient}}{\text{Measured heat transfer coefficient}} \tag{7}$$

A statistical comparison of the points shown in Fig. 6, based on the use of the ratio R, is shown in Table 1.

TABLE 1

Comparison of Present Transition Boiling
Heat Transfer Correlation with
Previous Empirical Correlation

	$\mu(R)$	$\sigma(R)$
Present Correlation (q''_{wet} constant)	1.18	0.77
Revised Correlation (q''_{wet} decreases with T_w)	1.03	0.60
Previous Empirical Correlation of Wang et al.	1.11	0.63

It may be seen that both of the correlations tend to overpredict the data somewhat and both show very substantial scatter [high $\sigma(R)$]. However, the value of $\sigma(R)$ for the present approach is only about 25% greater than that of the strictly empirical correlation. It was believed that both the overprediction of the present correlation and the value of $\sigma(R)$ could be reduced by a more realistic treatment of the heat flux during the wetted period. It will be recalled (see Fig. 1) that the heat flux did not remain constant but declined somewhat with increasing wall temperature. If we approximate the heat flux variation by

$$q''_{wet} = q''_{crit} \exp\left[-0.89\times10^{-3}\left(\bar{T}_w - \bar{T}^{*}_{w,wet}\right)\right] \qquad (8)$$

the overprediction is largely eliminated and the standard deviation is significantly reduced (see Table 1). The revised correlation now shows less scatter than the original empirical correlation. The relatively high value of $\sigma(R)$ remaining may largely be attributed to the stochastic nature of transition boiling heat transfer.

Transient Behavior

In addition to the steady-state experiments which form the basis for the foregoing analysis, a series of transient tests were also performed. In these experiments, hot mercury again flowed through the central tube. The tube was cooled by water flowing in the outer annulus at a rate so low that only the lower portion of the tube was wetted. A step increase in flow then allowed the rewet front to move up the tube. Heat transfer coefficients and rewetting rates observed during these tests were previously reported by Wang, et al.[7]

In those runs where the entering water had little subcooling, rewetting of the upper thermocouples was relatively slow. The rewetting occurred some time after the exit quality had reached its new equilibrium value. In a typical run, calculations indicated that the exit quality had reached its new lower value in about 3 seconds while rewetting of the upper thermocouple did not occur until 12 seconds after the transient was initiated.

In some of the runs, it was possible to observe the liquid film on the surface of the hot tube. After the step change in flow rate, the liquid film slowly advanced up the tube. The arrival of the liquid film at a given thermocouple approximately coincided with a rapid temperature decrease in temperature at that point. The liquid film appeared to advance more or less steadily without the periodic vertical oscillations seen in steady state. Of course, the edge of the liquid film was not smooth and there was a small scale random oscillation of the edge. The temperature measurements confirmed the lack of substantial vertical oscillations of the front since the large size temperature oscillations seen in the steady-state runs were not observed here.

By increasing the inlet subcooling, a point was reached at which the rewetting rate increased appreciably. The sharp climb of the rewetting rate until it approximately equalled the nominal reflooding rate was in the region where annular flow gave way to intermittent flow.

Wang, et al.,[7] postulated that, during annular flow, the slow advance of the rewetting front (advance of thin water film on heated tube), was controlled by the rate at which heat is transferred to the liquid film in the rewet region. They wrote a heat balance around the rewetting front region in a manner similar to that suggested by Yadigaroglu and Arrieta[11]. Wang et al's.[8] heat balance had the form,

$$\begin{matrix}\text{Stored heat} \\ \text{released by steel}\end{matrix} + \begin{matrix}\text{Stored heat} \\ \text{released by Hg}\end{matrix} + \begin{matrix}\text{Heat transported} \\ \text{by Flowing Hg}\end{matrix} = \begin{matrix}\text{Heat transferred} \\ \text{to coolant}\end{matrix} \qquad (9)$$

The rate of heat transfer to the coolant was obtained by writing an approximate correlation of the experimentally observed transition boiling heat transfer coefficients during transients as

$$q'' = 1.6 \times 10^{6} \exp(-.014\ \Delta T_{sat}) \qquad (10)$$

and integrating this over the temperature range corresponding to the change from dry to wetted conditions. With this approach, Wang et al.[8] were able to obtain good agreement with observed rewetting rates between 0.3 and 3.5 cm/sec.

If the wetted area heat transfer rates estimated from the steady-state transition boiling data are applicable during transients, then the heat transfer rate prediction of Equation (10) would only be a rough approximation. We could expect that, at the lower values of ΔT_{sat}, the heat transfer rates would correspond to those of a fully wetted region. These high heat transfer rates should then be followed by a region of rapidly declining heat transfer corresponding to the narrow region in which the edge of the rewetting front fluctuates. At high values of ΔT_{sat}, we would expect a low rate of heat transfer corresponding to that attainable in the presence of droplet-laden steam.

The actual heat transfer rates observed during two typical transient experiments (runs 706 and 801) are plotted vs. ΔT_{sat} in Fig. 7. Also shown is a plot of Equation (10) used by Wang et al., to estimate the transient heat transfer rates in the transition region. It is obvious that Equation (10) is only an approximation of the experimental observations. The observed heat transfer rates do indeed show a region of high heat transfer followed by a narrower region of rapidly declining heat transfer.

The shaded region shown in Fig. 7 represents the wetted area heat fluxes predicted on the basis of Equation (8). It may be seen that these predictions are in moderately good agreement with the observed heat transfer rates at the lower values of ΔT_{sat}. Thus the predictions of wetted area heat transfer based on the steady-state observations appear to agree with the wetted heat transfer rates observed during the transient.

In describing the quenching of a hot rod, some authors[12][13] distinguish between the "quench" and "rewet" temperatures. They define the quench temperature as that temperature at which rapid cooling begins. The rewet temperature is defined as the temperature at which permanent contact between liquid and heater wall is reestablished. With this terminology, the beginning of heat transfer to a fully

wetted wall would correspond to the rewet temperature. Bennettet al.,[14] have suggested that the rewet temperature may be taken as (T_{sat} + 100°C). However, the data of Wang et al.,[7] would seem to indicate that (T_{crit} + 120°C) as a somewhat better approximation.

Although the full description of the heat transfer in the rewet region is complicated, a simple approximation is probably adequate for design purposes. Since the average heat transfer rate in the partly wetted region is only about 30% of that in the fully wetted region, and since the partly wetted region is small, it is suggested that the heat transfer to the liquid film be ignored in the partly wetted region. The transition boiling heat transfer would then be approximated as being equal to q''_{wet} (from Equation (8) between T_{crit} and the rewet temperature (T_{crit} + 120°C). This approximation would be conservative in that it would lead to an underestimate of the rate at which the rewet front advances. If this approximation were to be used instead of Equation (10) to predict the heat transfer rate in the rewet-velocity calculation of Wang et al.,[7] the total heat transfer rate would be about 80% of that used by Wang et al.

It should be noted that, on the dry region above the rewet front, the rate of heat transfer was significantly above that which could be attributed to convection to steam alone. Since wall temperatures were relatively low, it appears likely that there was significant heat transfer from the wall to impinging liquid droplets. Estimate of this heat transfer with the Ganic-Rohsenow[15] correlation were in the same range as the experimental observations[16].

Conclusion

It appears that the simplified vertically oscillating quench front model can explain the general features of the observed temperature oscillations during steady-state transition boiling at high void fractions. Although there are discrepancies between the quantitative predictions of the model and experimental observations, the discrepancies are of a nature which can be accounted for by the simplifications made.

By use of the results of the numerical model, the wetted area estimates could be correlated with a parameter designated as ΔT_{eff}. It was then possible to develop a reasonable prediction of observed steady-state heat transfer with this wetted area correlation. It should be noted, however, that if the vertical oscillation of the edge of this liquid film is hydrodynamically controlled, the temperature variation produced may be expected to vary with the heating element used. The relationship between the wetted fraction and ΔT_{eff} found here may not apply to other systems.

Reexamination of the transient rewetting data, indicates that transition boiling heat transfer occurs in the neighborhood of the rewet front. The rate of heat transfer over the temperature range between T_{crit} and the rewet temperature appears to be in reasonable agreement with the estimates of heat transfer to the wetted region derived on the basis of steady-state data.

Nomenclature

D	= diameter, m
f	= wetted fraction
G	= mass velocity, kg/m^{2}s
k	= thermal conductivity, w/m°C
Pr	= Prandtl No.
q''	= heat flux, w/m^2
h_{conv}	= convective heat transfer coefficient, w/m^2°C
R	= predicted value/measured value

T = temperature, °C
$\bar{T}$ = mean temperature, °C
x = quality (dimensionless)
ρ = density, kg/m^3
μ = viscosity of vapor, kg/(s m)
$\mu(R)$ = mean value of R
$\sigma(R)$ = standard deviation of R

Subscripts and Superscripts

crit = at critical heat flux conditions
m = mercury
t = total
w = wall surface
sat = saturation
m,in = mercury at the inlet to the test section
wet = wet
B = vapor at bulk conditions
ℓ = liquid
dry = dry

Acknowledgement

The authors wish to acknowledge the financial support of the Electric Power Research Institute for the experimental program from which the data were obtained.

References

1. Kao, Y.K. and J. Weisman, "A Moving Front Transition-Boiling Model," Paper presented at AIChE, Los Angeles Meeting, (Nov. 1982). Accepted for publication in AIChE Journal.

2. Chu, C.L., J.M. Robert and A.W. Dalcher, Journal of Heat Transfer, 100, 424 (1978).

3. Kao, Y.K. and J. Weisman, "An Analysis of Wall Temperature Fluctuations in Transition Boiling Heat Transfer," in Basic Mechanisms in Two-Phase Flow and Heat Transfer, R.T. Lahey, ed. ASME, New York (1980).

4. Kao, T.T., S.M. Cho, D.H. Pai, Int. J. of Heat and Mass Transfer 25, 181 (1982).

5. France, D.M., T. Chiang, R. Carlson and R. Primer, Int. J. of Heat and Mass Transfer, 25, 691 (1982).

6. Nakanishi, S., M. Ozawa, S. Ishighi and E. Mewa, "Dryout Phenomena in Shear Flow," in Heat Transfer in Nuclear Reactor Safety, S.G. Bankoff and N.H. Afgan, eds. Hemisphere Publishing Corp., Wash., D.C. (1982).

7. Wang, S., Y.K. Kao and J. Weisman, Nuc. Eng. Des., 70, 223 (1982).

8. McAdams, W.T., W.E. Kennel, C.S. Mihden, R. Carl, P. Picornell and J. Dew, Trans. Int. Chem. Eng., 41, 1945 (1949).

9. Griffith, P., C.F. Avedesian and J.P. Walkush, p. 149 of "Heat Transfer - Research and Application," AIChE Symposium Series 74, No. 174 (1978).

10. Quinn, E.P., "Forced Flow Heat Transfer to High Pressure Water Beyond the Critical Heat Flux," ASME Paper 63-HT-34 (1963).

11. Yadigaroglu, G. and Arieta, "Analytical Model for Bottom Reflooding Heat Transfer in Light Water Reactors," Electric Power Research Inst. Report NP-756 (1978).

12. Gunnerson, F.S., Trans. ANS 34, 466 (1980).

13. Kim, A.K., and Y. Lee, Letters in Heat and Mass Transfer 6, 117 (1979).

14. Bennett, A.W., G.J. Hewitt, H.A. Kearsey and R.F. Keeys, "The Wetting of Hot Surfaces by Water in a Steam Environment at High Pressures," UKAE Report AERE-R5146 (1966).

15. Ganic, E.N. and W.M. Rohsenow, "An Analysis of Dispersed Flow Heat Transfer Using a Deposition Model," in Two-Phase Transport and Reactor Safety," L.N. Veziroglu and S. Kakac, eds., Hemisphere Publishing Co., Washington, D.C. (1978)

16. Wang. S., "A Study of Transition Boiling Phenomena With Saturated Water at 1-4 Bar," Ph.D. Thesis, College of Engineering, University of Cincinnati, Cincinnati, Ohio (1981).

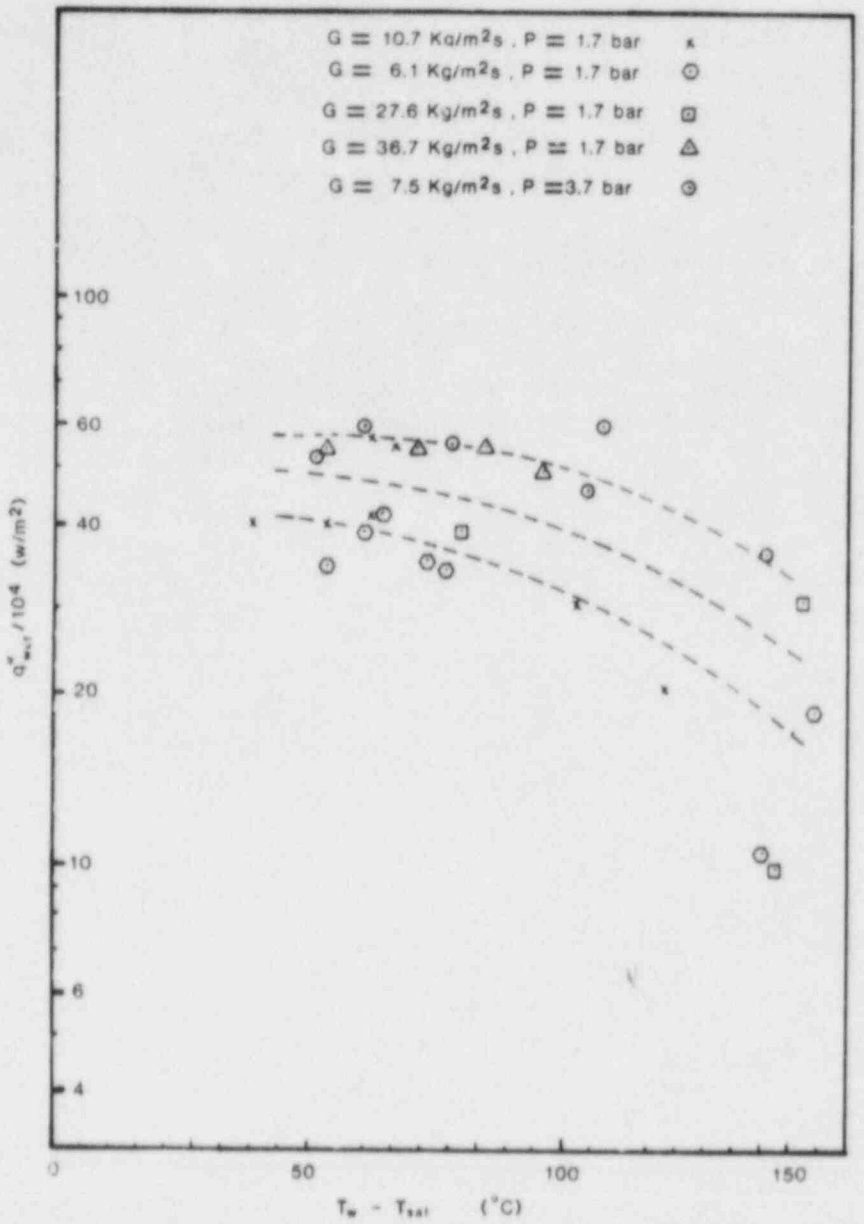

Fig. 1 - Wetted Area Heat Fluxes

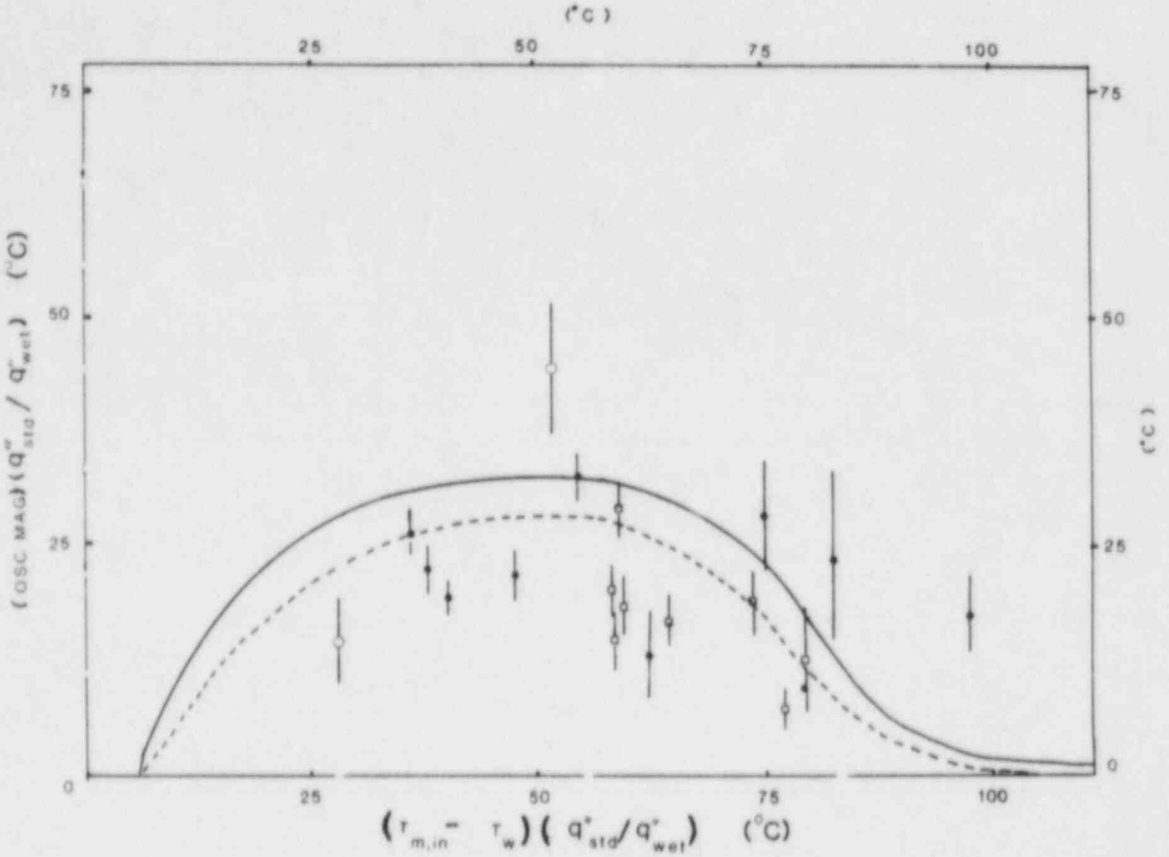

Fig. 2 - Comparison of Observed and Computed Temperature Oscillations

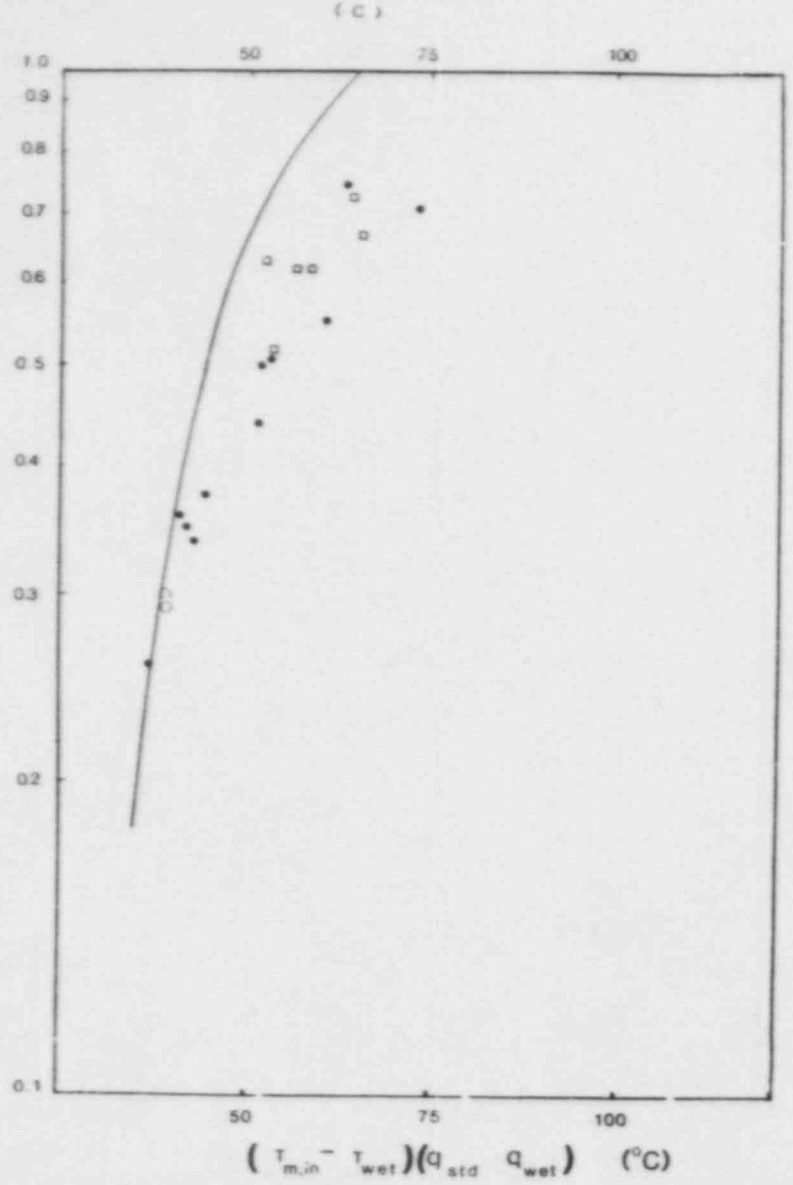

Fig. 3 - Observed and Computed Wetted Area Fractions

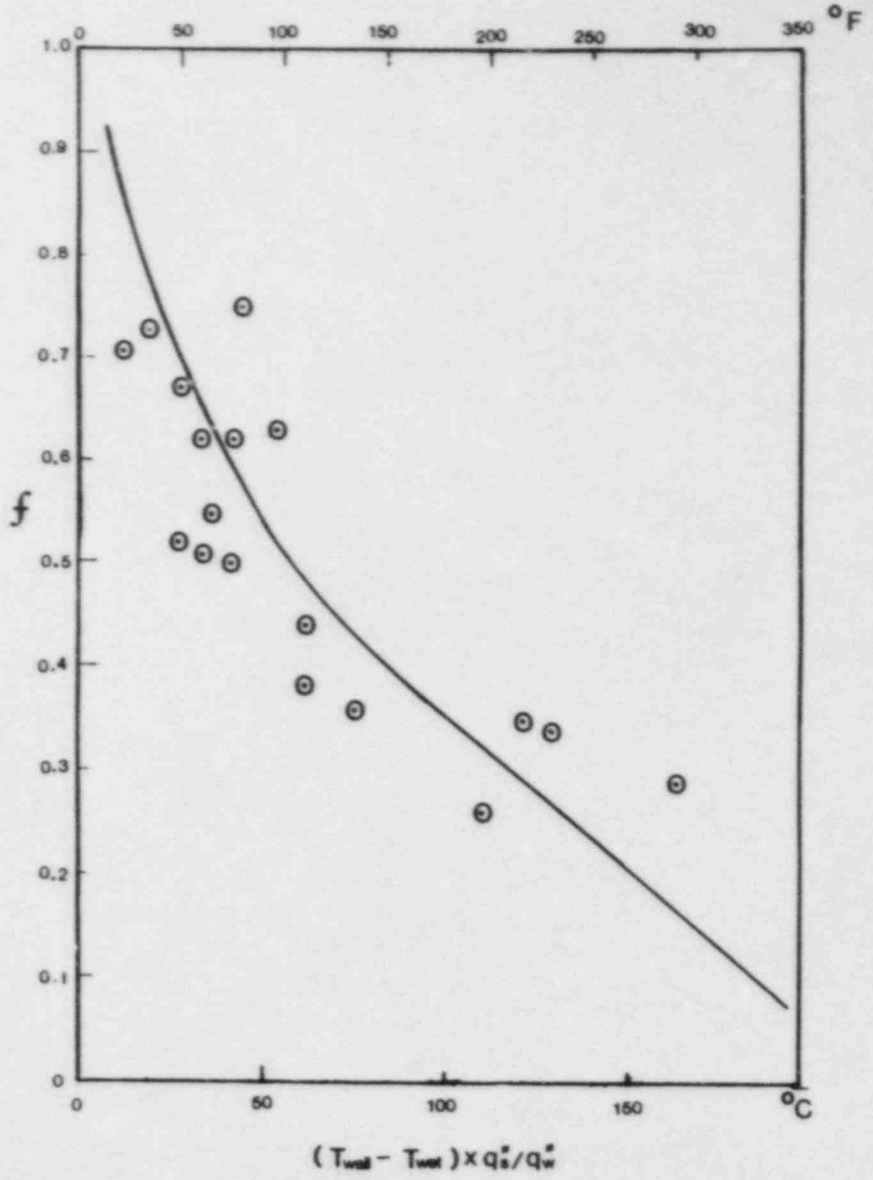

Fig. 4 - Wetted Fraction (f) Correlation

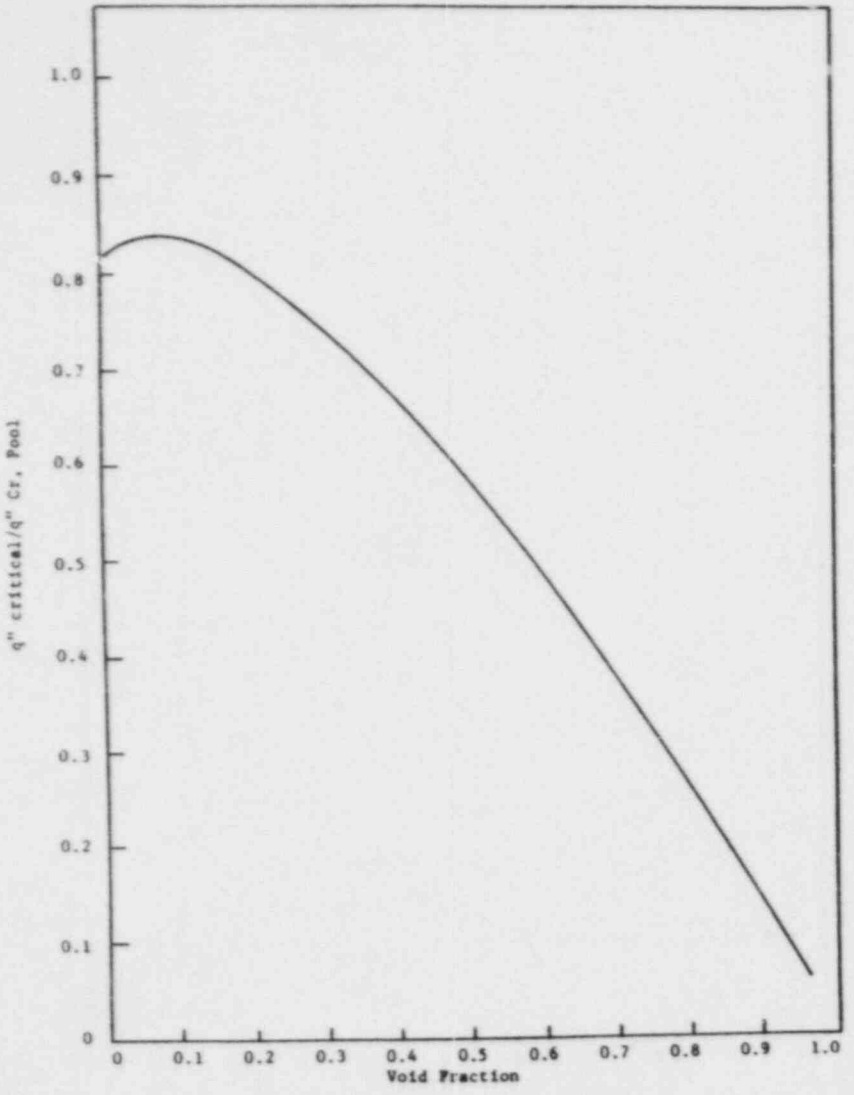

Fig. 5 - Relationship Between Critical Heat Flux and Void Fraction

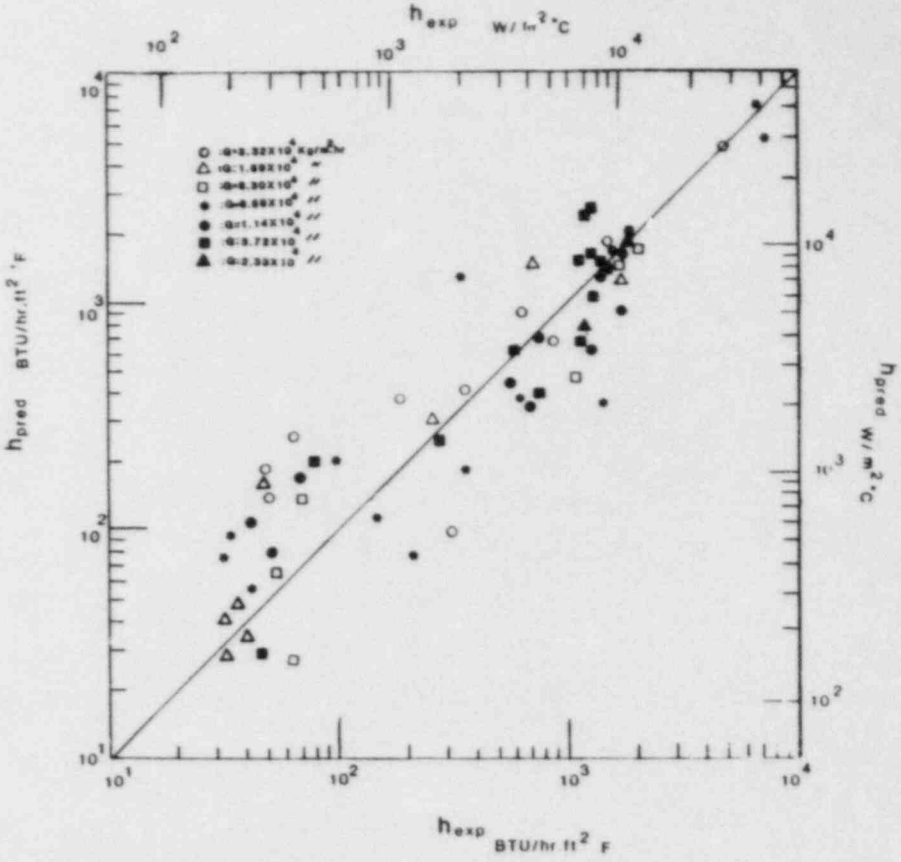

Fig. 6 - Comparison of Predicted and Measured Steady-State Heat Transfer Coefficients

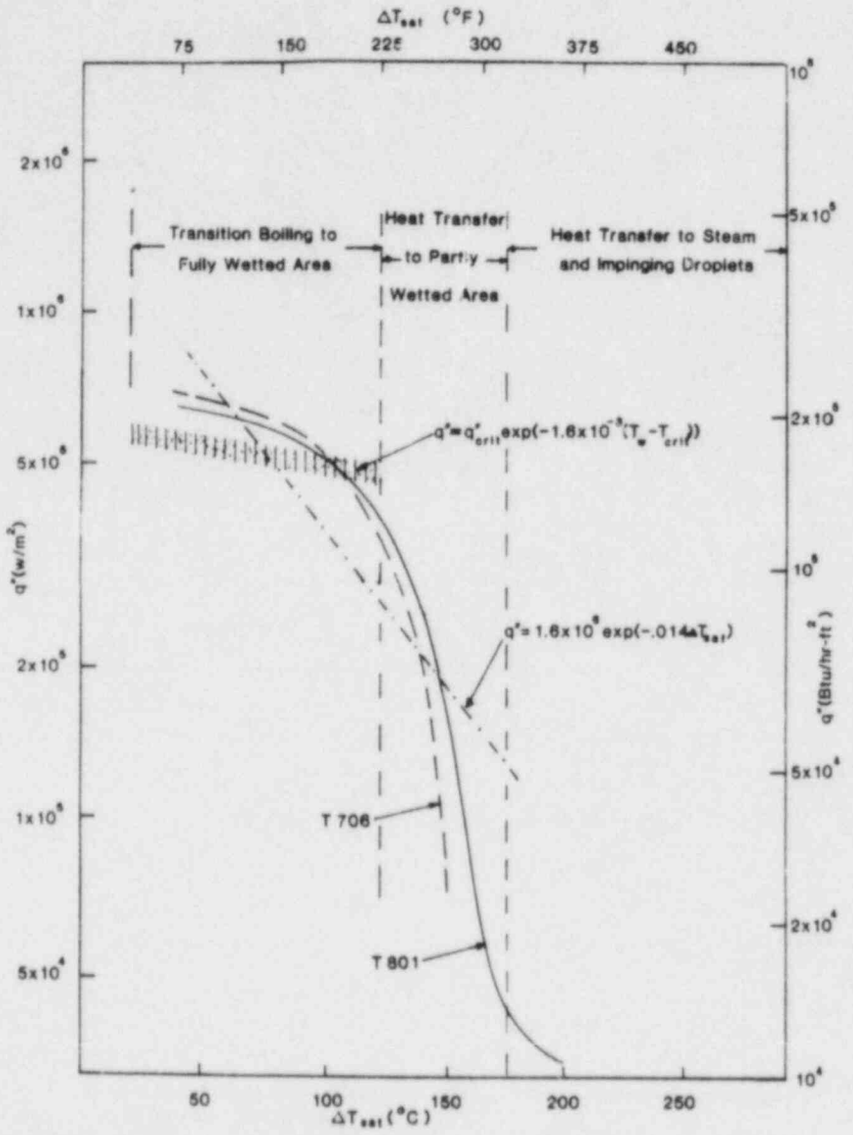

Fig. 7 - Heat Transfer Rates During Reflooding Transient

COBRA-TF ANALYSIS OF WESTINGHOUSE UPPER HEAD INJECTION ECCS HEAT TRANSFER TESTS

J. M. Kelly[1]
B. A. McIntyre[2]

ABSTRACT

The Westinghouse upper head injection ECCS heat transfer tests constituted a severe test of the COBRA-TF quench front models. Initial simulations indicated that significant modifications to the minimum film boiling temperature and transition boiling heat transfer models were necessary. COBRA-TF, with the modifications detailed in this paper, was then applied to a set of six UHI tests. Excellent predictions of bundle quench rates for constant pressure tests at 60, 100, 200, and 500 psia were realized. Quenching rates were slightly overpredicted for a 20 psia test and underpredicted for a variable pressure (800 → 20 psia) test.

The need for a minimum film boiling temperature correlation applicable to the entire pressure range (20 - 1000 psia) and an expression for transition boiling heat transfer immediately downstream of a top quench front was indicated.

INTRODUCTION

The Westinghouse upper head injection (UHI) ECCS[3] heat transfer tests constituted a severe test of the COBRA-TF[4] (ref.1) quench front models. Developmental assessment of COBRA-TF had included simulations of both falling film quenching and bottom reflood tests. However, the quenching rates observed in the UHI tests were 1 to 2 orders of magnitude greater. As expected, modifications to the quench front models were required to adequately simulate the UHI tests. This paper details the required modeling changes.

The COBRA-TF computer program was developed at the Pacific Northwest Laboratory by the U.S. Nuclear Regulatory Commission to provide best-estimate predictions of the thermal-hydraulic conditions within a light water reactor vessel. In particular, this program has two main objectives:

- develop a hot bundle analysis capability to calculate coupled thermal-hydraulic/rod deformation behavior
- develop a primary system simulation capability able to model the complex internal vessel geometry of a UHI-equipped PWR.

To achieve the latter, the one-dimensional loop components from the TRAC-PD2 code (ref. 2) were added to COBRA-TF. The resulting code is COBRA/TRAC.

---

(1) Pacific Northwest Laboratory
(2) Westinghouse Electric Corporation
(3) ECCS: Emergency Core Cooling Systems
(4) COBRA-TF: Coolant Boiling in Rod Arrays-Two Fluid

In concert with the above code development effort, an extensive developmental assessment program was conducted. Single effects tests, in which (theoretically) one thermal-hydraulic phenomena was isolated, constituted the bulk of this effort. By this means, COBRA-TF's ability to model the important phenomena anticipated to occur during postulated accidents was assessed individually. Examples of such phenomena are ECC bypass and bottom reflood. The UHI ECCS heat transfer tests were simulated to enlarge the COBRA-TF data base to include the high pressure, low void, high flow rate, reversed core flow period expected during a large-break LOCA[1] in a UHI-equipped PWR.

CODE DESCRIPTION

COBRA-TF provides a two-fluid, three-field representation of two-phase flow. Each field is treated in either a three-dimensional Cartesian coordinate system or a subchannel formulation. The three fields are comprised of a vapor, continuous liquid, and entrained liquid droplet field. The inclusion of the droplet field is essential to mechanistic modeling of two-phase phenomena having both a liquid film on surfaces within the flow field and liquid drops dispersed in the vapor phase. Countercurrent flow limiting, top and bottom reflood, and film dryout CHF are examples of such phenomena.

This treatment results in a set of eight equations. Three mass conservation equations, two energy equations (the liquid and entrained liquid are assumed to interact at a rate sufficient to nearly maintain thermal equilibrium), and three momentum equations (allowing the liquid and entrained liquid fields to flow with different velocities relative to the vapor phase) are solved.

COBRA-TF also features a flexible noding scheme which allows for modeling complex geometries encountered in reactor vessel internals, such as slotted control rod guide tubes, jet pumps, core bypass regions, etc. These geometries do not lend themselves easily to modeling in regular Cartesian or cylindrical mesh coordinates but, since they have significant impact on the thermal-hydraulic response of the system, must be modeled with reasonable accuracy.

The fuel rod heat transfer model utilizes a fine-mesh-rezoning technique (ref.3) to automatically reduce the rod heat transfer mesh size in regions of high heat flux or steep temperature gradients and increase the mesh size in regions of low heat flux. This model has proven very effective in resolving the boiling curve in the region of the quench front.

In addition, to effect closure of the eight-equation set, numerous constitutive relations (e.g., flow regime selection, interfacial friction, etc.) are necessary. Two of these relations, the minimum film boiling temperature (a cornerstone of the boiling curve) and the transition boiling heat flux were modified as a result of the UHI simulations and serve as the focus of this paper.

UHI ECCS TEST DESCRIPTION

The upper head injection system is designed to provide enhanced core cooling during the early part of a large-break LOCA transient. The UHI system is comprised

---

(1) LOCA: loss-of-coolant accident

of an additional ECCS accumulator connected to the upper head and an upper internals package containing direct flow paths from the upper head to the top of the core. Typically, UHI flow begins 2 seconds after the initiation of a large-break LOCA and continues for approximately 22 seconds. During this period, core flow is predominantly negative and the addition of subcooled UHI water results in fluid qualities much lower than encountered in a non-UHI LOCA. The UHI ECCS heat transfer tests were designed to evaluate the effectiveness of UHI and its dependence on system parameters.

The major components of the UHI test facility (ref. 4), designated the G-2 loop, are shown schematically in Figure 1. The test vessel (see Figure 2) contains an electrically heated rod bundle (336 heater rods, 25 thimbles) arranged in a 17 x 17 type configuration with a heated length of 164 in.) and is connected to a simulated external downcomer.

The test vessel receives flow from a UHI accumulator via an injection manifold and a flash chamber-inline mixer system. The UHI ECCS water is delivered from the injection manifold through 13 UHI ports directly above the tie plate. Both flow rate and subcooling of the UHI water are controlled during the transient. The reversed flow from the unbroken loop hot legs flowing into the reactor vessel upper plenum during a LOCA is simulated by the flash chamber-inline mixer system. This system delivers a two-phase mixture of prescribed flow and quality to the test vessel hot leg. System pressure is regulated via a computer-controlled valve just upstream of the steam exhaust manifold.

The boundary conditions for the UHI Blowdown test series were evaluated based on a thermal-hydraulic analysis of a double-ended cold leg guillotine break for a PWR equipped with UHI. The parameters were taken from the time of core flow reversal to the end of the blowdown period. The fluid quality, pressure, power, and UHI subcooling transients were taken from this analysis. The fluid flow rates were scaled by the ratio of the test bundle flow area to the PWR core flow area to preserve the mass velocity through the test bundle. The initial clad temperature and bundle power were determined from fuel rod calculations based on this analysis at the time of core flow reversal.

The UHI tests were run as single-parameter effects tests in that only one test parameter was varied at any one time from the nominal test conditions. The parameters studied were:

1. UHI flow rate
2. UHI flow subcooling
3. rod bundle power
4. test vessel pressure
5. initial peak clad temperature
6. upper plenum inlet flow rate
7. upper plenum inlet flow quality
8. UHI flow distribution.

The parameter values for this study were selected such that the full range of calculated PWR conditions would be evaluated. The parameter ranges tested are shown in Table 1. A total of 25 tests were run in the G-1 loop (15 x 15 configuration) and 24 tests in the G-2 loop. In addition, a second set of 42 low-pressure UHI refill tests were conducted in the G-2 loop. Comparisons between code calculations

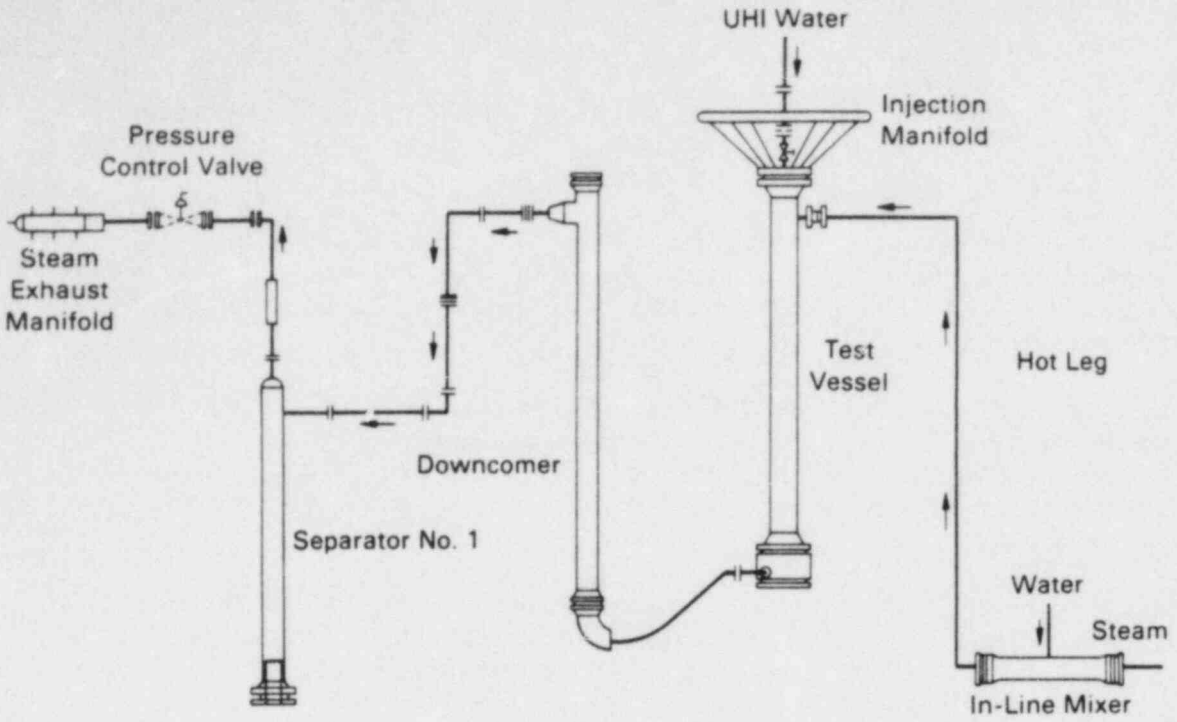

Figure 1 Schematic of Westinghouse UHI Test Loop

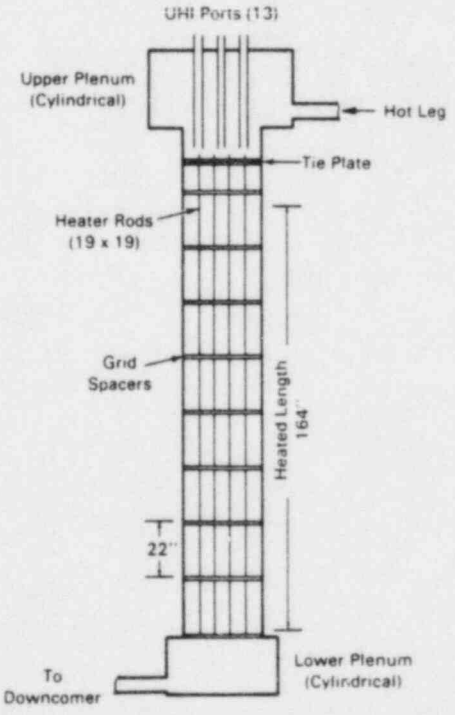

Figure 2 UHI Test Vessel

Table 1 UHI Test Parameter Ranges

	G-1	G-2
Bundle Flow Area (ft^2)	0.5885	0.3346
UHI Flow (lb/sec)	0-45	0-35
UHI Subcooling (°F)	240-340*	25-150
Unbroken Loop Flow (lb/sec)	0-20	0-20
Unbroken Loop Quality	0.05-0.25	0.10-0.30
Peak Bundle Power (kW/ft)	0.75-1.11	0.723-1.20
Clad Temperature (°F)	300-1700	300-1700
Pressure (psia)	200-800	100-800
UHI Flow Distribution	Various	Various

*Temperature rather than subcooling

and the G-2 experimental data will be made for three Blowdown and three Refill tests (see Table 2).

PRELIMINARY CALCULATIONS

The UHI test series included several test configurations, including combined injection. To narrow the focus to high pressure, low quality, top-down quenching, a set of tests was selected (Table 2) in which the flow path is unidirectional (the broken hot leg is closed). The two-phase reversed flow from the intact hot leg combines with the UHI water in the upper plenum and is swept down through the test bundle.

The COBRA-TF model was basically a one-dimensional representation of the test vessel (see Figure 2) with flow boundary conditions for the hot leg and UHI ports and a pressure boundary condition at the crossover pipe between the lower plenum and the downcomer. In the upper plenum, just above the tie plate, a two-channel model was employed to model the flow area through the tie plate and the surrounding volume above the tie plate separately. The UHI port injected water into the channel

Table 2 UHI Test Conditions

	Run	U.P. Pressure (psia)	Peak Initial Clad Temp. F	Peak Power (kW/ft)	Hot Leg Flow Rate (lbm/sec)	Hot Leg Quality	(UHI) Flow Rate (lbm/sec)	(UHI) Subcooling F
	667	800-20	1300	1.065	10	0.18	15	60
Blowdown	661	500	1300	1.065	10	0.18	15	60
	655	200	1300	1.065	10	0.18	15	60
	741	60	1000	0.915	0		10	0
Refill	738	20	1000	0.915	0		10	0
	742	100	1000	0.915	0		10	0

representing the volume above the solid part of the tie plate. The test bundle was modeled with one channel (14 in. axial nodes) and one averaged heater rod. The heat transfer effects of the housing were assumed insignificant due to the large number of active heater rods (336).

To further simplify the task of assessing the COBRA-TF top quench model under UHI conditions, a constant-pressure 500 psia test (run 661) was chosen for the first simulation. A comparison of the measured quench envelope and quench front propagation predicted by a previous version (cycle 10) of COBRA-TF is given in Figure 3. The rapid quench rates evident in the test data (the whole bundle quenched in less than 40 seconds) were grossly underpredicted by cycle 10. Two areas for model improvement were indicated:

- The 1000°F upper limit on the rewet temperature was overly restrictive.
- The heat transfer in the transition boiling region near a falling film quench front needed enhancement.

COBRA-TF MODIFICATIONS

As stated above, the top quench models in cycle 10 were inadequate. The modifications to the minimum film boiling temperature (rewet temperature) and transition boiling heat flux are described below.

MINIMUM FILM BOILING TEMPERATURE

The transition boiling regime is bounded by the critical heat flux (CHF) point (below which the wall is continuously wetted and nucleate boiling exists) and the minimum stable film boiling point (above which the liquid cannot wet the wall and film boiling exists). During quenching, the heater rod traverses the boiling curve in reverse, from film boiling, through transition boiling, to nucleate boiling. In

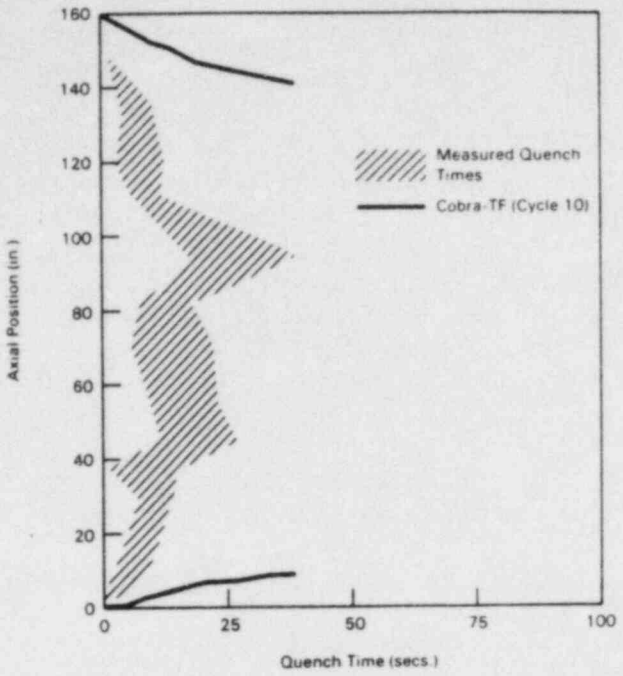

Figure 3 Comparison of Quench Envelope Data and COBRA-TF (cycle 10) Quench Rates for the Initial Simulation of the 500 psia Blowdown Test (#661)

general, once the rod surface temperature is at or below the minimum film boiling temperature (T_{MIN}), and if there is sufficient liquid present, the rod surface heat flux will rise rapidly, as liquid contact heat transfer begins, quenching the rod.

Henry's modification (ref. 5) of the Berenson correlation is employed to define T_{MIN} in COBRA-TF:

$$T_{MIN} = T_B + 0.42\,(T_B - T_\ell)\left\{\sqrt{\frac{(k\rho C_p)_\ell}{(k\rho C_p)_w}}\left[\frac{h_{fg}}{C_{pw}(T_B - T_f)}\right]\right\}^{0.6} \qquad (1)$$

where

$$T_B = T_f + 0.127\,\frac{\rho_v h_{fg}}{k_v}\left[\frac{g(\rho_f - \rho_g)}{(\rho_f + \rho_g)}\right]^{2/3}\left[\frac{g_c \sigma}{g(\rho_f - \rho_g)}\right]^{1/2}\left[\frac{\mu_v}{g(\rho_f - \rho_g)}\right]^{1/3} \qquad (2)$$

In addition, the minimum film boiling temperature was restricted to:

$$800^\circ F \leq T_{MIN} \leq 1000^\circ F$$

The above limits, based on bottom reflood test data (20-60 psia), were applied to constrain T_{MIN} within reasonable physical limits.

An examination of the UHI test data (ref. 6) suggested that an upper limit of 1200°F might be more appropriate. Figure 4 compares the envelope of bundle-average quench temperatures versus pressure and the Henry correlation with an upper limit of 1200°F. In viewing quench temperature "data", it should be recognized that the quench temperature is inferred from rod temperature data and that the reported values are usually conservatively low. This conservatism is a result of the physical nature of the quench phenomena; namely that the condition of rod surface temperature being less than the quench temperature is necessary but not sufficient for the rod to quench. There must also be a adequate amount of liquid present.

Two means exist to produce rod surface temperatures that are lower than the quench temperature before sufficient liquid is available:

- the rod temperature can be reduced by precooling due to dispersed flow film boiling
- the rod peak temperature never exceeded the quench temperature.

The latter is demonstrated by Figures 5 and 6. Quench temperatures from General Electric film boiling and rewetting tests (ref. 7) are plotted in Figure 5 along with a data point from LOFT test L2-3 (ref. 8). A spread of over 400°F is present in this data. Replotting the G.E. data, removing any points whose initial temperature (peak temperatures were not available, but little heatup occurred in these tests) was below 1200°F and denoting the initial temperature by a bar above the data point, results in Figure 6.

Taken together, the data from Figure 6 and the top of the envelope from Figure 4 present a good case for readjusting the upper limit on the correlation for T_{MIN} to 1200°F. A more satisfactory approach would be the development of a correlation suitable for the entire pressure range.

TRANSITION BOILING HEAT FLUX

At present, there is no consensus on a correlation for the transition boiling region. COBRA-TF employs a simple interpolation scheme (ref. 9) between the critical heat flux and the minimum film boiling point. This method is simple, physically based (qualitatively), and results in a continuous boiling curve.

It is assumed that the transition boiling heat transfer is composed of both nucleate boiling (wet wall) and film boiling (dry wall) heat transfer, as follows:

$$q''_{TB} = (1 - \alpha) \cdot \delta \cdot q''_{CHF} + q''_{FB} \qquad (3)$$

where

$$\delta = \left(\frac{T_{MIN} - T_w}{T_{MIN} - T_{CHF}}\right)^2 \qquad (4)$$

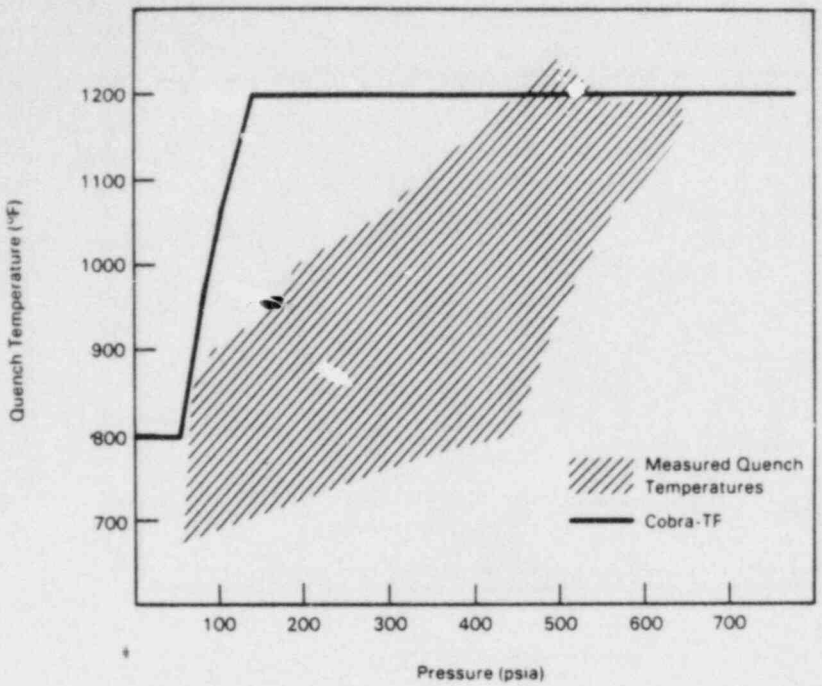

Figure 4 Bundle-Average Quench Temperatures Versus Pressure for the UHI Blowdown Tests

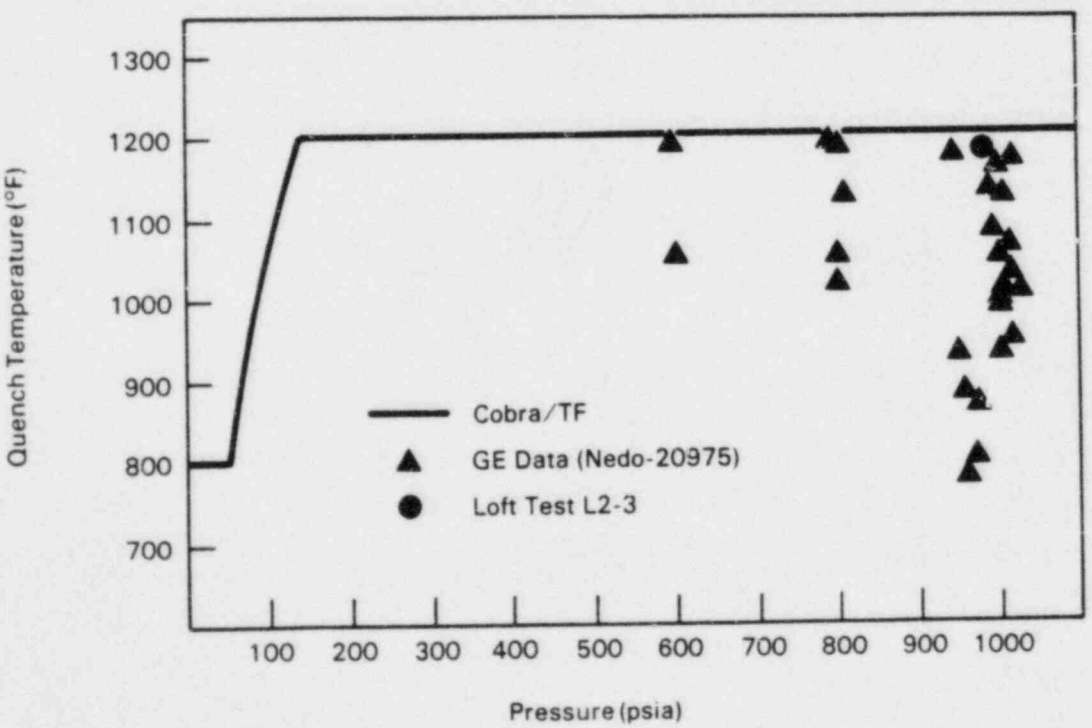

Figure 5 Quench Temperatures from the General Electric Rewet Tests

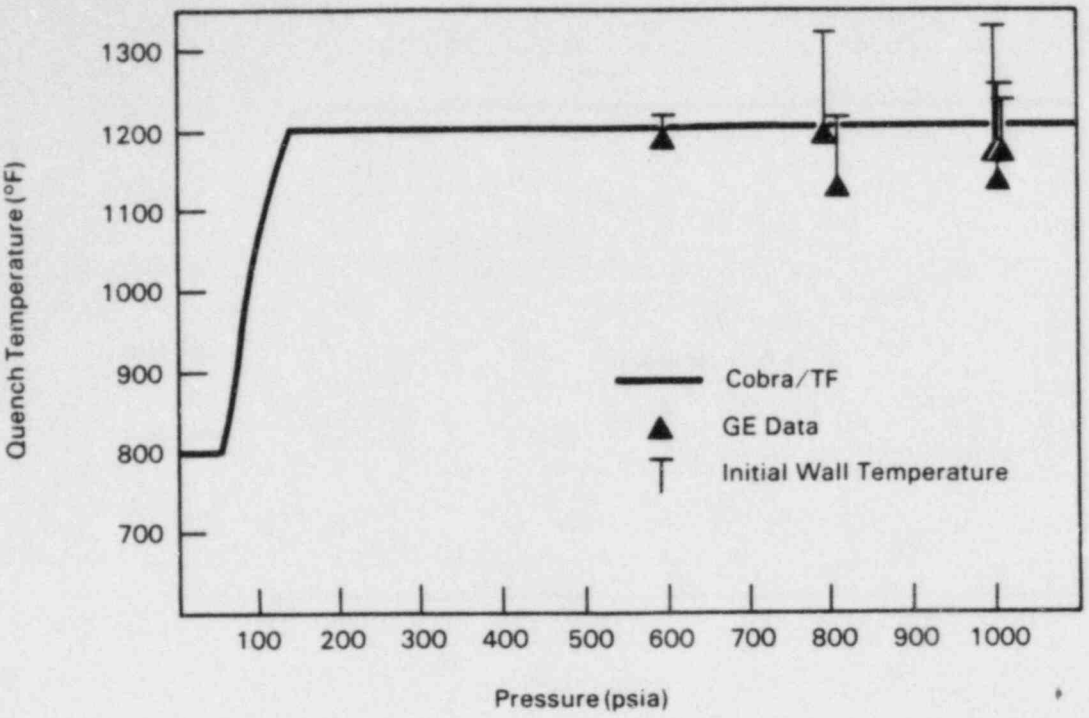

Figure 6 General Electric Quench Data Excluding Points with Initial Temperatures less than 1200°F

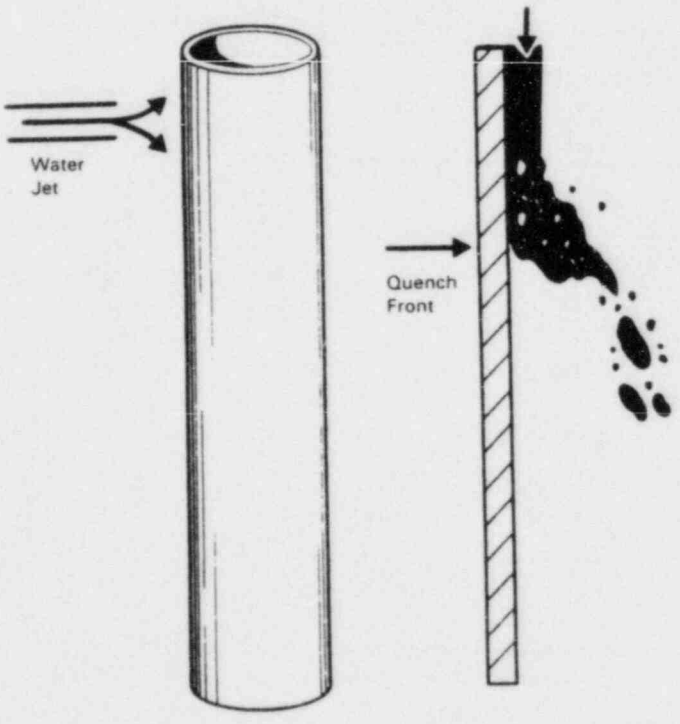

Figure 7 Illustration of Simple Falling Film Quench Test

This approach has proven adequate for the simulation of bottom reflood transients.

To assess the "fine mesh-rezoning" quench front model, the simplest type of falling film quench test was chosen. Figure 7 shows a schematic of this type of test, where a liquid film is initiated at the top of a tube which has been heated above the quench temperature. The tube is located in the open atmosphere, which results in low precooling since the liquid blown off of the tube at the "sputtering front" and the vapor generated by the quenching are not constrained to flow near the tube surface.

In the first COBRA-TF simulations, the region downstream of the quench front was assumed to be adiabatic; both the transition and film boiling heat transfer coefficients were set to zero. These results are plotted as a dashed line in Figure 8 versus the data of Duffy and Porthouse (ref. 10) and Morris et al (ref. 11). The correlation parameter, the square root of the Biot number divided by the Peclet number, is inversely proportional to the square root of the quench front velocity. Assuming that a small amount of precooling was present, the solid line in Figure 8 results in a much better prediction of the quench rate. From these tests it was concluded (incorrectly) that little transition boiling was present in top-down quenching and that Equation 3 would yield reasonable results.

However, the quenching rates observed in the UHI tests (2-6 in./sec) were much greater than those of the falling film tests (0.01 - 0.05 in./sec) and required that a significant amount of transition boiling be present immediately downstream of the quench front. The $(1-\alpha)$ modifier of Equation 3 applies too restrictive a constraint upon the transition boiling heat flux due to the high void fraction (0.95 - 0.99) present in these tests. To overcome this limitation, the $(1-\alpha)$ modifier was removed and the critical heat flux assumed to exist at the top quench front and decay exponentially downstream. The transition boiling heat flux is then:

$$q''_{TB} = \xi \cdot \delta \cdot q''_{CHF} + q''_{FB} \qquad (5)$$

where

$$\xi = \text{maximum } (1-\alpha, \beta)$$

$$\beta = \text{EXP } [-3.6\ (\Delta z - 0.1)]$$

$$\Delta z = \text{distance below a top quench front (ft)} \qquad (6)$$

The exponential decay function (Equation 6) has no empirical basis and obviously oversimplifies the problem (it should at least be a function of pressure and film flow rate). However,it has been our experience that, combined with the increased rewet temperature, this formulation leads to a reasonable prediction of the top quenching rates over a large pressure range (20 - 500 psia).

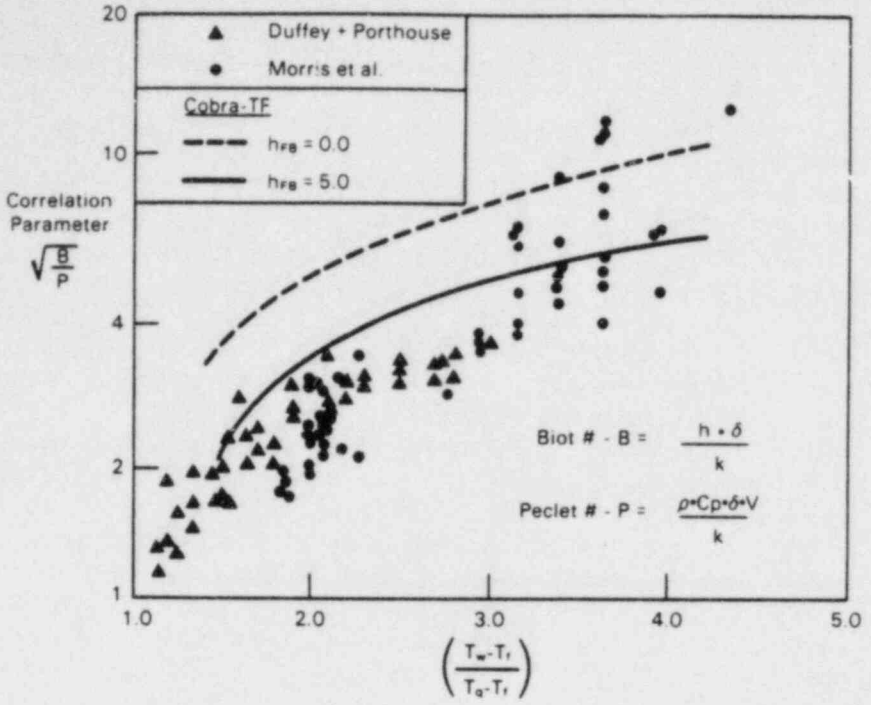

Figure 8 Comparison of Measured and Predicted Quench Front Velocity for Falling Film Test

DATA COMPARISONS

To assess the modified version of COBRA-TF (cycle 11), simulations of three UHI Blowdown and three UHI Refill tests were conducted. The results follow.

UHI BLOWDOWN TESTS

Three UHI Blowdown tests were simulated, two at constant pressure (500, 200 psia) and one variable pressure (800 → 20 psia); see Table 2. The power, hot leg and UHI flow rates, and peak clad temperature are the same for all three tests.

Figure 9 shows a comparison of predicted and measured quench times for test 661 (500 psia). The rapid top-down quenching, 100 in. in 25 sec, was well predicted. Also, the more moderate quenching, 60 in. in 25 sec, from the bottom-up due to drop deposition was predicted. The different modes for top-down and bottom-up quenching calculated by COBRA-TF for a typical blowdown test are illustrated by Figure 10. A well-developed rapidly progressing top quench front, due to a falling liquid film, is shown by the temperature profiles at 10 and 20 sec. In contrast, the bottom rewet, due to precooling and droplet deposition, progresses more slowly and has the appearance of a slowly collapsing temperature profile rather than a well-defined "quench front".

Also of interest are the points of the quench envelope at 94 and 82 in. At the 94-in. elevation, the measured quench times vary from 17 to 39 sec, with most of the thermocouples quenching between 17 and 22 sec. (COBRA-TF predicted a quench time of 20 sec.) The one thermocouple quenching late (39 sec) provides a good indication of the maximum effect of nonuniform delivery of ECC water downstream of the tie plate. Just downstream, at 82 in., the quench times vary from 7 to 18 sec (the

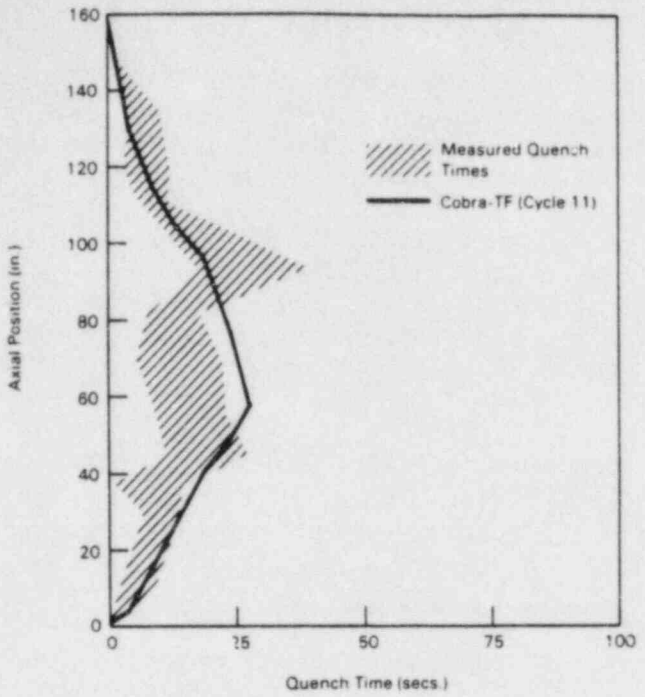

Figure 9 Comparison of Quench Envelope Data and COBRA-TF Prediction for the 500 psia Blowdown Test (#661)

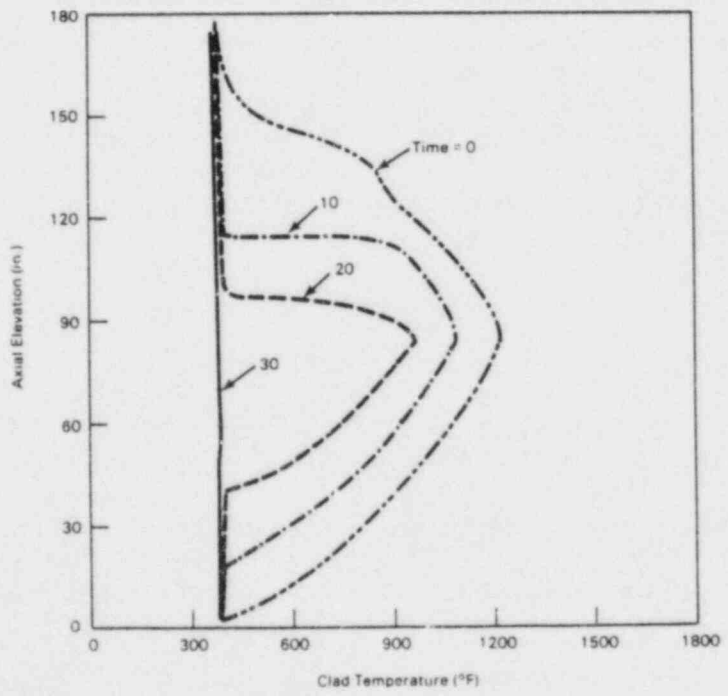

Figure 10 Calculated History of the Axial Temperature Profile for a Typical Blowdown Test

COBRA-TF value was 23 sec). These early quench times at the rod bundle peak temperature location are due to the presence of a grid spacer immediately upstream of the thermocouple. These two effects, a large spread of quench times at 94 in. and early quenching at 82 in., are evident in the entire test series.

Figure 11 compares the predicted quench times and the quench envelope for test 655 (200 psia). Very little difference between the 200 and 500 psia tests is evident in either the data or the calculation. The predicted quench times compare well with the data except for the early grid spacer induced quenching at the bundle midplane. No effort was made to model the grid heat transfer effects in these simulations.

The final UHI Blowdown test simulated, run 667, was constrained to follow the pressure transient, calculated for a LOCA from 800 psia (core flow reversal) to 20 psia (containment pressure), shown in Figure 12. Figure 13 plots the predicted and measured quench times for this test. The observed quench rates are even more rapid (the entire bundle quenches in 15 sec) than those of the constant pressure tests. COBRA-TF predicts this high quench rate well for the first 10 sec, during which the top third of the bundle is calculated to have quenched. However, as the pressure drops below 150 psia (~10 sec) to 75 psia (~15 sec), the predicted quench rate slows dramatically.

When the pressure drops below 150 psia, the minimum film boiling temperature used by the code (see Figure 4) begins to rapidly decrease from the 1200°F upper limit to about 850°F at 75 psia. This reduction in the rewet temperature is responsible for the slow quench rates calculated after 13 sec. It is tempting to conclude that the rewet temperature is simply underpredicted at lower pressures. While that may be partially true, it is inconsistent with the good quenching predictions observed in the low pressure refill tests (see below). Instead, it appears that the rapid quenching is due to precooling the bundle significantly below the rewet temperature during the initial part of the blowdown transient. During this period, the rod temperatures decreased at a rate approximately 5 to 8 times greater than that of the constant pressure tests. To more accurately predict this test, it is probably necessary to model the hot leg from the inline mixer to the upper plenum, as opposed to using a flow boundary condition with the prescribed nominal values of flow and quality.

UHI REFILL TESTS

The Refill tests, which simulate a later period of a UHI LOCA, are constant low pressure tests (20 - 100 psia) with no hot leg injection (see Table 2). The portion of the bundle quenched at the end of the test (105 sec) obtained from a thermocouple quench census will be compared to the COBRA-TF predicted axial temperature profile.

Figure 14 shows the data comparison for test 742 (100 psia). The fraction of the bundle quenched from the top (164 → 102 in.) is predicted very well. However, the bottom quench is slightly overpredicted. Also, the bundle exhibits a considerable portion of quenched thermocouples near the midplane, probably due to grid spacer effects.

The data comparison for test 741 (60 psia) is given in Figure 15. Both top and bottom quench fronts are well predicted. A pressure effect between 60 and 100 psia, though present, is relatively minor in both the data and the COBRA-TF

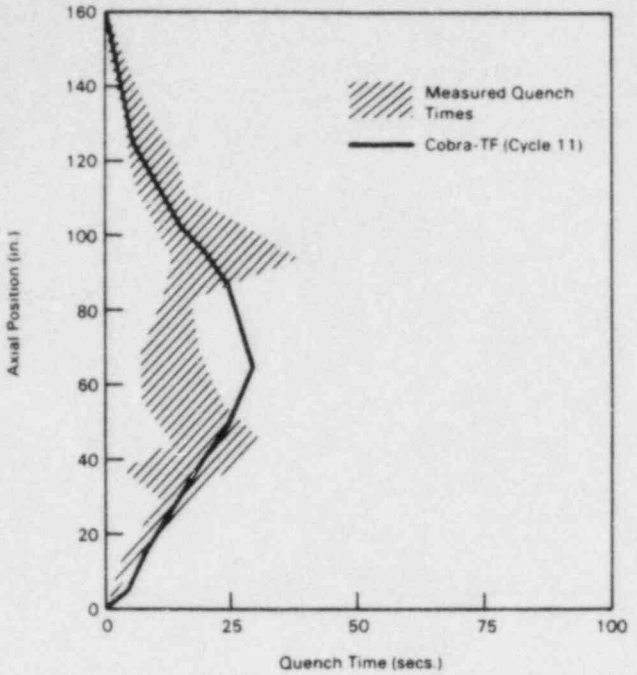

Figure 11 Comparison of Quench Envelope Data and COBRA-TF Prediction for the 200 psia Blowdown Test (#665)

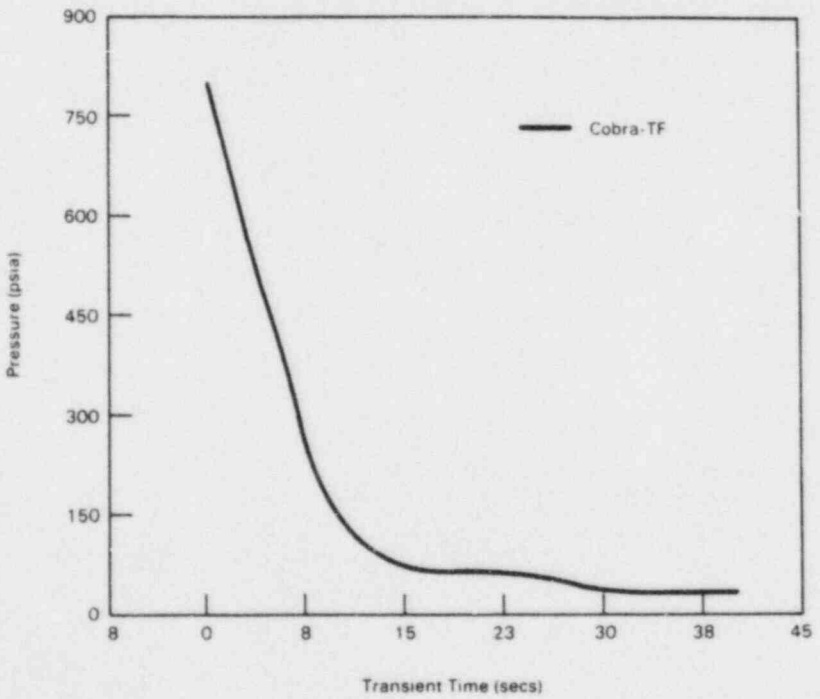

Figure 12 Pressure Transient for the Variable Pressure Blowdown Test (#667)

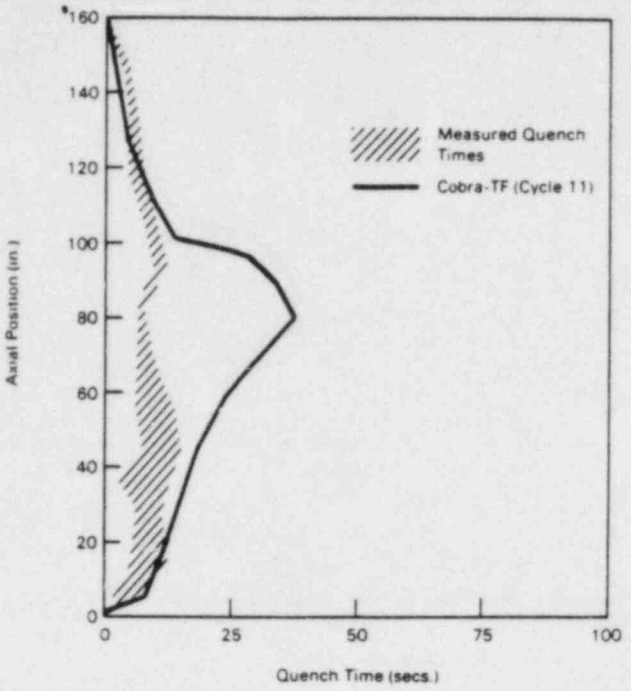

Figure 13 Comparison of Quench Envelope Data and COBRA-TF Prediction for the Variable Pressure Blowdown Test (#667)

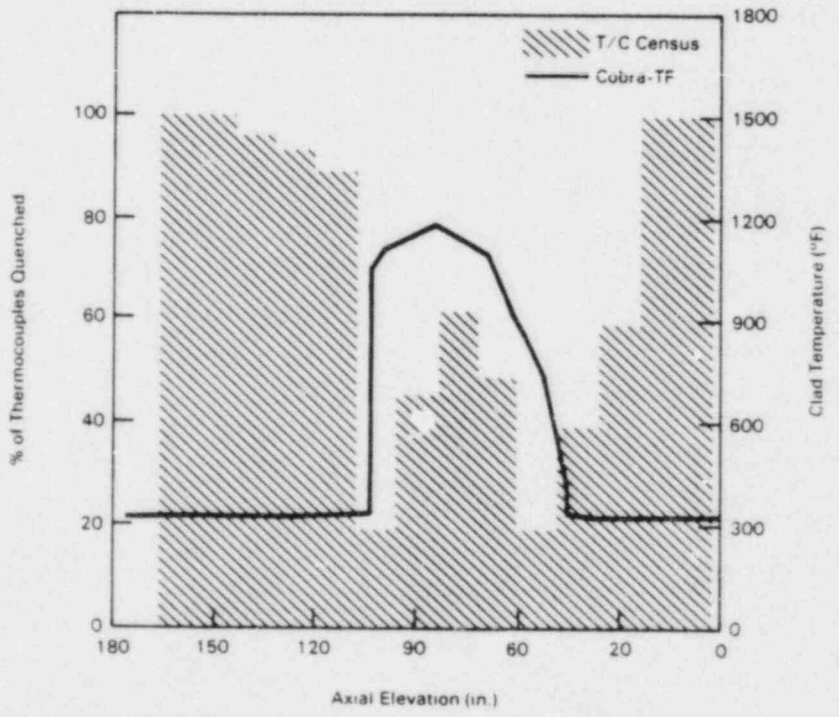

Figure 14 Comparison of Thermocouple Quench Census and COBRA-TF Temperature Profile at End of 100 psia Refill Test (#742)

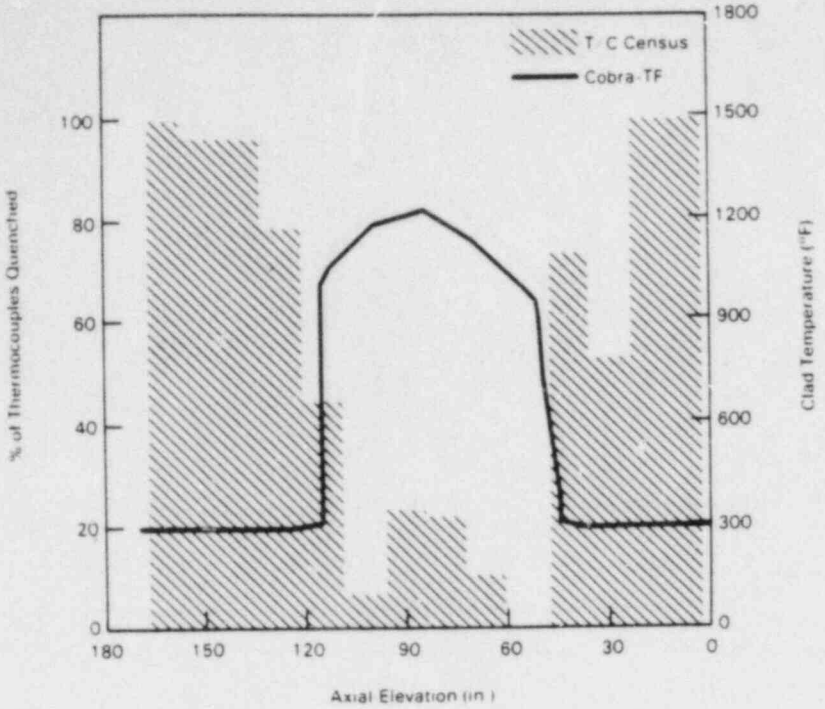

Figure 15 Comparison of Thermocouple Quench Census and COBRA-TF Temperature Profile at End of 100 psia Refill Test (#742)

calculations. Figure 16 plots the results for the 20 psia test, number 738. Both the top and bottom quench fronts are somewhat overpredicted for this test. The dependence of the quench rate upon pressure is readily apparent from the data and not strong enough in the code.

SUMMARY

The Westinghouse upper head injection ECCS heat transfer tests provided a good data base for qualifying the ability of COBRA-TF to predict top-down quenching. From initial simulations, it was determined that significant modifications to the minimum film boiling temperature and transition boiling heat transfer models were required. The upper limit on the rewet temperature was raised to 1200°F and a simple exponential decay model was substituted for the overly restrictive liquid fraction ramp in the transition boiling region.

A new version of COBRA-TF, cycle 11, incorporating these changes, was applied to six UHI tests, three from the high pressure Blowdown series and three from the low pressure Refill series. Excellent comparisons of bundle quench times were achieved for four of the tests (constant pressure, at 60, 100, 200, and 500 psia). At 20 psia, the bundle quench rates were overpredicted by about 25%. During the simulation of a variable pressure test (800 → 20 psia), the quench rates were predicted correctly for the top third of the bundles and underpredicted thereafter. The bundle precooling for this test was several times greater than that of the constant pressure tests and was significantly underpredicted. The prediction for this test may be improved by simulating the entire hot leg rather than using a flow boundary condition on the upper plenum.

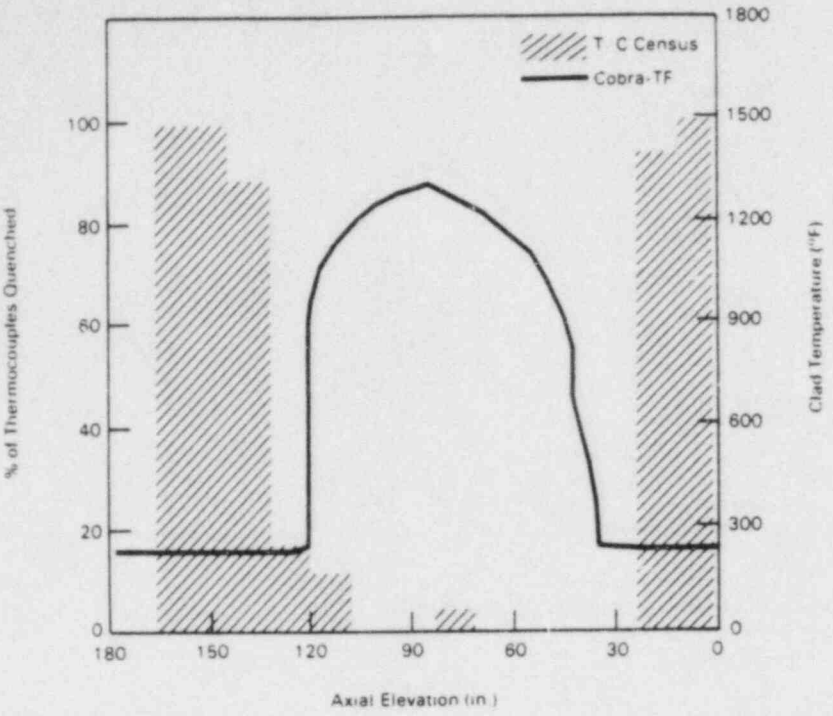

Figure 16 Comparison of Thermocouple Quench Census and COBRA-TF Temperature Profile at End of 100 psia Refill Test (#742)

The simulation of the UHI tests demonstrated the need for a minimum film boiling temperature correlation that is applicable over a wide pressure range (20 - 1000 psia). Also, a better description of the transition boiling heat transfer immediately downstream of a falling film quench front is needed.

NOMENCLATURE

C_p	specific heat (Btu/lbm-°F)
g	gravitational constant (ft/sec^2)
g_c	conversion factor (lbm-ft/lbf-sec^2)
h_{fg}	latent heat (Btu/lbm)
k	thermal conductivity (Btu/sec-ft-°F)
q"	heatflux (Btu/hr-ft^2)
T	temperature (°F)

Greek

α	void fraction
δ	fraction of wall wettable (Equation 4)
μ	viscosity (lbm/ft-sec)
ρ	density (lbm/ft^3)

Subscripts

B	Berenson correlation (Equation 2)
CHF	critical heat flux
f	saturated liquid
FB	film boiling
g	saturated vapor
ℓ	liquid
MIN	minimum film boiling
TB	transition boiling
v	vapor property at the film temperature
w	wall

REFERENCES

1. Thurgood, M. J., et al. March 1983. "COBRA/TRAC - A Thermal-Hydraulic Code for Transient Analysis of Nuclear Reactor Vessels and Primary Coolant Systems." Volumes 1-5, NUREG/CR-3046, PNL-4385.

2. D. R. Liles, et al. 1981. "TRAC-PD2, An Advanced Best-Estimate Computer Program for Pressurized Water Reactor Loss-of-Coolant Accident Analysis." USNRC Report NUREG/CR-2054.

3. J. M. Kelly. 1979. "Quench Front Modeling and Reflood Heat Transfer in COBRA-TF". Paper 79-WA/HT-63, ASME Winter Annual Meeting, New York, New York.

4. B. A. McIntyre. July 1977. "Heat Transfer Experiments with Upper Head Injection." ANS Topical Meeting on Thermal Reactor Safety. Sun Valley, Idaho.

5. R. E. Henry. 1974. "A Correlation for the Minimum Film Boiling Temperature." AIChE Symposium Series, 70 (138), pp 81-90.

6. T. S. Andreychek, et al. January 1976. "Blowdown Experiments with Upper Head Injection in G-2 17x17 Rod Array Facility." WCAP-8582.

7. E. Janssen and J. A. Kervinen. August 1975. "Film Boiling and Rewetting." NDEO-20975, General Electric Company, San Jose, California, 95125.

8. P. G. Prassinos, B. M. Galusha, and D. B. Engleman. July 1979. "Experimental Data Report for LOFT Power Ascension Experiment L2-3." NUREG/CR-1792, TREE-1326.

9. T. A. Bjornard and P. Griffith. 1977. "PWR Blowdown Heat Transfer," Thermal and Hydraulic Aspects of Nuclear Reactor Safety, American Society of Mechanical Engineers, New York, Vol. 1, pp 17-41.

10. Duffey, R. B. and D.T.C. Porthouse. August 1972. "Experiments on the Cooling of High-Temperature Surfaces by Water Jets and Drops." Report No. RD/B/N2386, Berkeley Nuclear Laboratories, England, August 1972.

11. R. H. Morris, et al. July 1977. "Top-Spray Cooling of Heated Rods Under Simulated Loss-of-Coolant Conditions." ANS Topical Meeting on Thermal Reactor Safety, Sun Valley, Idaho.

Summary of Discussion in the Quenching Phenomena

M.W. Young

Mail Stop 1130SS

U.S. NRC

Washington, DC 20555

Quench Phenomena

Following a summary by the Chairman and poster session of the eight papers presented under the Quench Phenomena session, an open discussion was convened to provide an open exchange of comments and questions on this topic. The following highlights the major discussion items.

Dr. Grenoveld questioned the physical possibility of the minimum wetting temperature exceeding the thermodynamic critical temperature as described in Dr. Murao's paper entitled, "Quench Front Movement During Reflood." It appeared though that there was no question that the apparent quench temperature was not dependent on the history of the quench front movement. Dr. Groneveld agreed that the minimum wetting temperature correlates well with the sputtering temperature based on the Chaulk River results of Dr. Juhel. Drs. Ishii and Dhir questioned the momentary liquid contact on the heated surface as described in Dr. Murao's paper. Dr. Murao explained that in a region of highly subcooled liquid and a vapor interface, momentary liquid at localized spots were observed due to oscillation of the interface. Dr. Murao referenced some earlier research provided by Dr. Toda.

Dr. Hsu questioned the vertical application of the horizontal rewet model as presented in Dr. Juhel's paper entitled, "A Study on Interfacial and Wall Heat Transfer Downstream of a Quench Front." Dr. Ardon replied that the one-dimensional model certainly does not include recirculation effects and that subcooling is decreased at the point of quench even though high subcooling is observed at the entrance of the testing appratus.

The Chairman posed to the audience the choice between (1) defining a minimum wetting temperature correlation and (2) following a boiling surface crises approach, that will provide a correct surface heat flux under a wide range of

conditions. Dr. Kelly maintained that aboiling surface curve approach was preferable; however, the wetted surface fraction, F_L, is needed during transition boiling and should also be applied to the critical heat flux. Dr. Weisman alleged that since there was no universal transition correlation to be applied over the wide range of flow conditions, this approach would be difficult to support. Dr. Vojtek maintained that a definition of the CHF point (e. g. Biasi Correlation) was not well predicted so that definition of a transition region by predicting the two boundary points (CHF and T_{min}) was not particularly accurate. Dr. Lin stated that RELAP5 utilizes a boiling surface approach and uses the Chen Correlation in transition boiling. Dr. Lin added that there was no proven T_{min} correlation; however, suggested that an encounter in the transition region is relatively short and therefore, may have little impact on the overall heat transfer from the heated wall. Dr. Murao maintained that the boiling surface approach is not a practical way to predict the quench propagation because (a) tne boiling curve is generated from steady-state correlations and (b) requires excessive computing time by the codes.

In addition, Dr. Hewitt explained that the boiling surface correlates heat flux and quality and therefore has no meaning in determining the minimum wetting temperature. The steam temperature is a function of history and cannot be predicted by the boiling curve.

Dr. Chen urged that two classes of heat transfer must be recognized and clearly distinguished; (a) wall-to-vapor heat transfer and (b) wall-to-liquid heat transfer. The heat transfer process should be broken down into mechanisms involved rather than defined by a particular regime or heat transfer label (e.g. transition boiling). The boiling curve should be understood to be a series of curves which reflects a dependence on quality and mass flux. For very low mass flux and quality, the knee of the boiling curve may not exist and hence a minimum wetting temperature or the conventionally defined transition region is nonexistent.

III. Low-Void Heat Transfer

A CORRELATION OF LOW FLOW, LOW PRESSURE, AND LOW-TO-MODERATE QUALITY POST CHF DATA

John C. Chen
Professor and Director of
the Institute of Thermo-Fluid
Engineering and Science
Lehigh University
Bethlehem, PA

Charles D. Morgan
Technical Consultant
Utility Power Generation Division
Babcock & Wilcox
P. O. Box 1260
Lynchburg, VA 24505

Ramu K. Sundaram
Senior Engineer
Yankee Atomic Electric Company
1671 Worcester Road
Framingham, MA 01701

ABSTRACT

Post CHF data in the low flow, low pressure, and low to moderate quality regime were obtained as part of Babcock & Wilcox Company reactor safety research. These data are significant since they help fill a gap in the existing data base. These data were compared to existing correlation with unsatisfactory results. Mechanistic reasons for the poor agreement were postulated and the Lehigh post CHF correlation was modified to account for these effects.

1. INTRODUCTION

As part of its Research and Development program in nuclear reactor safety, the Babcock & Wilcox Company performed a series of thermal hydraulic experiments in its boiling heat transfer facility (BHTF) at its Alliance Research Center. The series of experiments included low flow critical heat flux tests, steady state film boiling tests, and transient tests which were designed to study the influence of rapidly changing pressure on post-CHF heat transfer. The steady state tests have been reported previously.[1,2,3]

In 1979 Babcock & Wilcox became a member of Lehigh University's Industrial Liaison Program. The Institute of Thermo-Fluid Engineering Science at Lehigh University was given the data tapes from these transient experiments and was asked to determine if there were any additional data of significance on these tapes. Fortunately, it was possible to obtain post-CHF data in the low flow, low pressure, and low-to-moderate quality regime. These data help fill a gap in the existing data base which is important since these conditions may be encountered toward the end of blowdown during a loss of coolant accident.

2. DESCRIPTION OF EXPERIMENT

The boiling heat transfer facility was a closed circuit test loop consisting of a pressurizer system, a circulating pump, flow control valves, fluid heaters, and a heat removal system. Figure 1 shows a schematic drawing of this test facility. The film boiling experiments were carried out using a LOCA subloop, indicated by solid black lines in Figure 1. The subloop connected into the main loop immediately downstream of the circulating pump. The subloop consisted of a flow control valve, turbine

flow meters, capillary flow tubes, a preheater. venturi heaters, a blowdown valve, a blowdown containment tank, a gate valve, and the heat transfer test section.

The test section was a vertical stainless tube of 3/4" O.D. and 1/2" I.D. Ohmic heating of the tube was obtained by current flow through the tube wall, with an effective heated length of five feet. Voltage along the test section length was measured by voltage taps located at both ends of the test section. The test section was insulated along its length to minimize heat loss to the surroundings. Test section wall temperatures were measured by skin thermocouples mounted at one inch intervals along the axial length of the test section. These wall thermocouples were attached in a spiral pattern, with 90° offsets around the tube circumference between successive thermocouples.

The temperature of the inlet fluid to the test section was measured by two resistance temperature detectors located in the rotary valve mixing tee. The exit fluid temperature was measured by a sheathed thermocouple. Pressure transducers were used to measure the test section pressure. Fluid flow rates were measured by turbine flow meters and capillary tubes were used to cover the entire flow range of the test program.

The film boiling results analyzed in this paper were obtained in a series of depressurization blowdown experiments where feedback was provided to the flow control valve which was continually adjusted to maintain an approximately constant flowrate through the test section. The total time for blowdown ranged between 20 and 120 seconds. The data analyzed in this paper were taken toward the end of blowdown when the pressure was relatively constant. Test data were recorded with a multichannel scanner and a minicomputer, to be subsequently transcribed on magnetic tapes.

3. SELECTION OF DATA FOR ANALYSIS

For each run the reduced data consisted of the following information as a function of time in the transient:

1. Test section pressure
2. Total mass-flow flux
3. Wall heat flux
4. Internal wall temperatures as a function of axial position
5. Equilibrium vapor qualities as a function of axial position

In the process of selecting suitable data for analysis, the first step was to obtain parametric plot showing:

1. Mass flow rate (G) as a function of time.
2. The equilibrium qualities in and out of the test section as a function of time.
3. The decay of saturation temperature during blowdown, as a function of time (pressure).
4. Inside wall temperatures at various axial positions, as a function of time.
5. Axial wall superheats (above the instantaneous saturation temperature) for various times, as a function of axial elevation in the test section.

In selecting data for analysis, an attempt was made to use measurements obtained during periods of relatively slowly changing conditions. Figure 2 is a portion of the plot of heat and mass flux versus time for run 10504. The portion of the transient analyzed is indicated on the figure. This transient was the most severe as far as variations in pressure are concerned. The maximum variations for this transient was 27 psi/sec while pressure changes on the order of 1 psi/sec are representative

of most of the data. In selecting data for post-CHF heat transfer from the slowly varying regions, a criterion was that the local wall superheat exceeded a minimum value of 150°F.

With this screening procedure several hundred post-CHF data points were selected out of experimental runs 10501 through 10509. The range of test parameters encompassed by this group of data are as follows:

TABLE 1

PARAMETRIC RANGE OF POST-CHF DATA USED IN ANALYSIS

	Minimum	Maximum
Pressure, psia	25	264
Mass flux, lbm/hr ft^2	$.4 \times 10^5$	1.1×10^5
Heat flux, Btu/hr ft^2	2×10^4	6×10^4
Equilibrium quality	.04	1.20

4. DATA ANALYSIS

Since the test section was thin and the selected data points were taken from slow transient effects, the correction to the data for the transient effects are small and can be obtained from a lumped parameter analysis. From the lumped analysis:

$$\therefore \quad h = \frac{q\,(R_o^2 - R_i^2)}{2R_i(Tw - Tv)} - \frac{\rho_m C_{pm}}{q}\,\frac{dT_w}{Dt} \qquad (1)$$

where:

- h = heat transfer coefficient, Btu/hr ft^2°F volumetric
- q = heat generation rate, Btu/hr ft^3
- R_o = outside radius, ft.
- R_i = inside radius, ft.
- T_n = wall temperature
- T_w = vapor temperature
- ρ = metal density, lbm/ft^3
- Cpm = metal specific heat, Btu/lbm°F
- t = time, hr.

The equilibrium quality change over an increment of the test section can be obtained from an energy balance.

$$Xe_2 = \frac{2(Z_2 - Z_1)h(T_w - T_v)}{GH_{fg}R_i} + Xe_1 \qquad (2)$$

where:

G = mass flux, $lbm/ft^2,hr$

X_e = equilibrium quality

Z = axial location, ft.

H_{fg} = enthalpy vaporization, Btu/lbm

The screened data (Table 1) consisted of 9 experimental runs (Runs 10501 through 10509). For each run, at any particular time during the run, a "snapshot" yielded the system pressure, inlet quality, mass flux, heat flux and axial wall temperatures at 1 inch intervals. The data used in analysis consisted of all 9 runs with several "snapshots" for each run. As mentioned previously, only data obtained at relatively slow transient conditions have been used. A typical data set is shown in Figure 3.

The next step in the analysis was to compare these low pressure, low flow data to available post-CHF correlations. Table 2 lists the ten correlations that were used in this analysis with the results of the comparison. As noted in the Table, eight of these correlations are equilibrium correlations which assume the sink (vapor) temperature to be the saturation temperature. The two other correlations attempt to account for non-equilibrium effects, allowing the vapor to superheat with a corresponding deviation of the actual misture quality from the equilibrium mixture quality.

The comparison of these correlations to the data was made on the basis of calculated to measured wall heat fluxes. It was found that none of the

correlations provided entirely satisfactory comparisons. Figures 4 and 5 show two correlations which provided the best comparison. Of these, the Condie-Bengston IV correlation is an equilibrium correlation while the Lehigh correlation uses a non-equilibrium approach. The poor comparison between these data and correlations was not completely unexpected. All the correlations involve a fair amount of empiricism and have predominantly used data at higher pressures, flow rates and quality in the derivation of needed empirical constants. The above comparison only indicates that these correlations are of questionable reliability for low flow rates and low-to-moderate qualities.

The list of correlations in Table 2 do not comprise all available post-CHF correlations. In particular, they do not include non-equilibrium correlations developed relatively recently (for example Ref: 9, 10) which have focused on more detailed mechanistic modeling of phenomena in the post-CHF heat transfer regimes. The correlations listed in Table 2 are all "local" correlations, in that the location of CHF and conditions at CHF are not necessary for post-CHF calculations. This results in less lengthy calculational procedures and provides a representative sample of the correlations used currently in large thermal-hydraulic codes used for Reactor LOCA calculations.

5. PRELIMINARY CORRELATION DEVELOPMENT

The low pressure, low flow data presented here provide a valuable extension of the range of the currently available data on post-CHF heat

transfer. The poor comparison between the data and correlations indicated that there may be signifianct mechanistic differences in the heat transfer process between low flow and high flow Post-CHF conditions. The thrust of the correlation development program was mainly to highlight these differences. The emphasis was on the identification of mechanisms and predictions of correct qualitative trends.

First of all, it is recognized that at the low flow rates of the data, there would be significant thermal non-equilibrium between phases under post-CHF conditions. This has been shown in experimental measurements of the non-equilibrium vapor temperature at comparable system conditions (11, 12).

Generally, the post-CHF wall heat flux may be written (8) as:

$$Q_W = Q_{LC} \cdot F_L + Q_{VC}(1-F_L) + Q_R \qquad (3)$$

where:

Q_{LC} = Heat flux due to liquid contact

Q_{VC} = Heat flux due to vapor contact
(primarily convection)

Q_R = Heat flux due to radiation

F_L = Fraction of wall area in contact with liquid

At the system pressures and wall temperatures of the present data, Q_R is small. Since the void fractions are usually high, F_L would be expected to be small. Hence, once can approximately write:

TABLE 2

COMPARISON WITH EXISTING POST-CHF CORRELATIONS
(1351 DATA POINTS)

	Number Calculable Points	Avg. Dev.	Dev. Standard	Comments
Dougall-Rohsennow [4]	1351	50.8	55.7	Equilibrium
Modified Dougall-Rohsenow [6]	1351	61	64	Equilibrium
Groeneveld 5.5 [5]	1351	302.7	2448.8	Equilibrium
Groeneveld 5.7 [5]	239	2203.3	6867.4	Equilibrium
Groeneveld 5.9 [5]	239	988.1	092.8	Equilibrium
Groeneveld-Delorme [7]	127	94	94	Non-equilibrium
Condie-Bengston [6]	1351	665.4	721.4	Equilibrium
Condie-Bengston Film [6]	1351	595.4	647	Equilibrium
Condie-Bengston 4 [6]	1351	32.8	45.2	Equilibrium
Lehigh (Chen-Sundaram-Ozkaynak) [8]	1351	48.3	74.3	Non-equilibrium

$$Q_W = Q_{VC} = h_{VC}(T_W - T_V) \quad (4)$$

where:

h_{VC} = wall-to-vapor heat transfer coefficient and

T_V = bulk vapor temperature

Looking at Figures 4 and 5, it is seen that both the Condie-Bengston IV correlation (6) and the Lehigh (CSO) correlation (8) underestimate the wall heat fluxes. From equation (4), this implies that the heat transfer coefficient is too low or the vapor temperature is too high. The Condie-Bengston IV correlation already uses the minimum possible vapor temperature (T_{sat}). The Lehigh correlation uses a non-equilibrium model to predict the vapor temperature, but in comparing the model to vapor temperature data at comparable low flow conditions (11, 12), it was found to consistently underestimate the vapor temperature. Hence it was judged that the underestimation of wall heat flux was largely due to the underprediction of the wall-to-vapor heat transfer coefficient.

Both the Condie-Bengston IV and Lehigh (CSO) correlations have had comparable and reasonably good success in predicting a large amount of previously available data at higher flow rates and qualities. The CSO correlation further has non-equilibirum modeling capabilities. Hence, it was chosen as a candidate for further comparison with the low flow B&W data. It was judged that if there were any systematic differences between these data and previous high flow data, this comparison would bring them out for further investigation.

In comparing the data to the Lehigh (CSO) correlation, "experimental" heat transfer coefficients were first derived from the data as:

$$h_E = Q_{W,E}(T_{W,E} - T_V) \quad (5)$$

Since T_V was not measured in these tests, the CSO correlation was used to obtain estimates of T_V. It was pointed out earlier that these estimated vapor temperatures were expected to be slightly low and hence the "experimental" heat transfer coefficients are expected to be slightly, but consistently, underestimated.

The CSO correlation predicts the vapor temperature and the actual quality by simultaneous solution of the following two equations:

$$(x_a/x_e) = H_{fg}(P)/[H_V(P,T_V)-H_f(P)] \tag{6}$$

$$(X_a/x_e) = 1 - \frac{0.26}{[1.15 - (P/P_{CR})^{0.65}]} \frac{(T_V-T_{SAT})}{(T_w-T_V)} \tag{7}$$

In this correlation, the heat transfer coefficient is calculated by momentum analogy with a two-phase friction factor and is given by:

$$h_{CSO} = 1/2\ [0.037\ \frac{GD}{M_{V,f}}\ [x_a + (1-x_a)\ \frac{P_V}{P_L}]^{0.17}$$

$$o\ GX_a C_{pV,f}\ Pr_{V,f}^{-2/3}$$

In the comparison of data to the correlation, the heat transfer coefficients have been converted to Nusselt numbers:

$$Nu_E = h_E.D/k_V \tag{9}$$

$$Nu_{CSO} = h_{CSO}.D/k_V \tag{10}$$

As a first step in gaining understanding of the differences between the data and correlation, the ratio of experimental to calculated Nusselt numbers were plotted for a few selected runs as a function of the local vapor Reynolds number defined as:

$$Re_V = GDX_a/\mu_V \tag{11}$$

Figure 6 shows this comparison for five data sets from run 10502. Each data set can be distinguished by the continuous decrease of the Nusselt number ratio with increasing vapor Reynolds number, as vapor quality increased along the length of the test section.
The same comparison is shown for a number of data sets in Figure 7. In spite of the confusion of many more points on the plot, several observations can be made: (1) the experimental Nusselt numbers were consistently higher than those calculated by the existing CSO correlation, (2) Nusselt number ratios approach unity, indicating improved agreement, at the higher vapor Reynolds numbers, and (3) there is a distinctly sharp change in the Nusselt number ratio near the tube entrance.

6. ENTRY LENGTH EFFECT

From single-phase analyses, it is known that enhancement of local heat transfer coefficients occurs near the entrance region of heated channels. It is believed that the sharp increase in Nusselt number near the tube entrance is due to this thermal entry length effect. However, entry length effects are not expected to persist beyond about 20 tube diameters from the entrance (about 10 inches for these data). Hence an additional mechanism must be found to account for the rest of the enhancement seen in the experimental heat transfer coefficients.

It was hypothesized that this enhancement could be due to heat sinks provided by evaporation of liquid droplets in the vapor, especially in the near wall thermal boundary layer region. This type of mechanism has been referred to by Dix and Andersen (13) and also by Iloeje (14) who attempted to account separately for heat transfer to droplets near the hot wall (but not in contact with it) in his three-step model for post-CHF heat transfer. It was also judged that this mechanism would become more visible at low flow rates when convective heat removal mechanisms would be relatively less effective in cooling the hot channel wall. Hence modifications to the existing CSO correlations were undertaken to account for (a) thermal entry effects and (b) heat sink effects.

Thermal entry length effects can be acccounted for by defining a thermal entry length correction factor F_{th} as:

$$F_{th} = Nu_Z/Nu_{FD}$$

where:

Nu_Z = local Nusselt number

Nu_{FD} = Fully developed Nusselt number

In this analysis, it has been assumed that:

$Nu_{FD} = Nu_{CSO}$ given by equation (10)

The local Nusselt number, Nu_Z, can be calculated once the flow regime is known. For these low flow B&W data, vapor Reynolds numbers were estimated to be in the range $0.2 - 6.0 \times 10^4$. Thus, the flow regime is in transition from laminar to turbulent flow for several of the data sets. In order to ensure continuity, the local Nusselt number was approximated as:

$$Nu_Z = Nu_{T,Z} + Nu_{L,Z} \qquad (13)$$

This approximation was considered reasonable for most of the data, which were in a Reynolds number range higher than $0.6 \times 10_4$. Under these conditions, $Nu_{L,Z}$ is much smaller than $NU_{T,Z}$ and Equation (11) introduces little errror.

$Nu_{L,Z}$ was calculated by using equations described by Kays (15). $Nu_{T,Z}$ was calculated approximately by differentiating the Nusselt Equation (16) which gives average turbulent Nusselt numbers in the thermal entry region. The differentiation yields:

$$Nu_{T,Z} \quad 0.03402 \; Re_v \; 0.8 \; Pr_v^{1/3} \; (Z/D)^{-0.055} \qquad (14)$$

The thermal entry length factor was then calculated be Equation (12).

Figure 8 shows the Nusselt number ratio corrected for thermal entry length effects plotted against the vapor Reynolds number for the same data sets shown in Figure 6. It can be seen that the magnitude of the Nusselt number ratio has moved closer to unity and the steep decline of the Nusselt number near the tube entrance has been considerably reduced. It should be noted that in the context of post-CHF heat transfer, axial length is measured from the CHF location.

7. LIQUID DROPLET SINK EFFECT

In order to account for the further enhancement of the effective heat transfer coefficients due to the presence of liquid droplets near the hot channel wall, a factor F_s was defined such that:

$$Nu_c = Nu_{CSO} \cdot F_{th} \cdot (1 + F_s) \qquad (15)$$

As mentioned previously, this enhancement effect due to liquid droplets is expected to be most noticeable at low flow rates and become relatively insignificant in highly turbulent flows. On this basis, one would expect the factor F_s to decrease and approach zero as the volume fraction of the liquid $(1-\alpha)$ decreases and as the vapor flow rate increases.

To test this hypothesis, "experimental" values of F_s were calculated as:

$$F_s = Nu_e/(Nu_E/(Nu_{CSO} \cdot F_{th})-1 \qquad (16)$$

Figure 10 shows a plot of these F_s values as a function of liquid volume fraction for all the data sets. A strong power law dependence of F_s on $(1-\delta)$ is clearly evident.

The void fraction, α, has been calculated, as a first approximation, using homogeneous flow theory.

In a similar manner, it as hypothesized that the sink factor F_s should decrease with increasing vapor Reynolds number and, as a first order correlation, an attempt was made to fit the sink factor F_s by the function:

$$F_s = C(1-\alpha)^{a1} \cdot Re_v^{a2} \qquad (17)$$

where C, a_1 and a_2 are constants, regression analysis fo all the data yielded the following correlation:

$$F_s = 1.858 \times 10^5(1-\alpha)^{0.509} \cdot Re_v^{-0.9834} \qquad (18)$$

Figure 10 shows the Nusselt number ratio plotted against the vapor Reynolds number for all the data where the calculated Nusselt number was obtained from Equation (15) with Equation (12) for the thermal entry factor F_{th} and Equation (18) for the sink factor F_s. A direct comparison with Figure 7 shows that the maximum value of the Nusselt number ratio has been reduced from about 3.0 to about 2.0. While this was encouraging, there were a few data sets where the Nusselt numbers were underestimated. A further look at the data indicated that there was a second order effect due to the wall heat flux. Therefore, a second correlation was derived using the Boiling number (N_B) as an additional correlation parameter. Regression analysis of the data yielded the following correlation:

$F_S = 2238 \times 10^{10} (1-\alpha)^{11236} Re_v^{-0.2367} N_B^{2.093}$ where N_B (19)

is defined as:

$$N_B = Q_W/(G.H_{fg}) \quad (20)$$

Figure 11 shows a plot of the Nusselt number ratio against the vapor Reynolds number for all data using Equation (19) for F_S. It can be seen that this correlation provides significant improvement over the previous correlation. However, use of the Boiling number in the correlation calls for an iterative solution in calculating the wall heat flux.

The two correlations described for the sink factor F_S are both very empirical and extension of the correlation to other system conditions is questionable. It is expected that at higher mass fluxes the correlation will provide correct trends, but not necessarily at higher pressure. This is because the term $(1-\delta)$ is quite sensitive to system pressure. An attempt was made to compare the modified CSO correlation (using Equation (19) for F_S) to the higher pressure and higher flow data used in the original development of the CSO correlation (8). It was found that the effect of system pressure could be handled somewhat better if one used the vapor quality instead of the vapor void fraction in accounting for the presence of droplets. Recalculation of the functional dependence of F_S by regression analysis with the B&W data gave the following correlation:

$$F_S = 79.19 \frac{(1-x_a)}{x_a}^{0.6579} Re_v^{-0.5522}$$

Table 3 presents a summary of the comparisons of the various modifications of the original Lehigh correlation to account for the low

flow-low quality effects to data. While the sink factor given by Equation 19 has the lowest average deviation compared to the data, it would required an interative solution, thus, it would not be attractive for use in large LOCA codes. The sink factor given by Equation 12 would be recommended for LOCA code applications.

Conclusions

1. Post-CHF heat transfer data have been obtained at low mass fluxes and low-to-moderate qualities and are in a range of conditions of interest to Reactor Safety studies. Data at these conditions have not been generally available before.
2. Comparison of the data to ten different post-CHF correlations showed relatively poor agreement. This was not unexpected because the correlations have been derived from previously available data at higher mass fluxes and qualities.
3. A more detailed comparison of one of the correlations (9) with the data indicated that there could be substantial enhancement of the effective post-CHF heat transfer coefficient at the low flow rates of these tests.
4. It was found that the data could be correlated reasonably well by a simple empirical approach which accounted for two effects--thermal entry region effects and evaporative effects of liquid droplets in the near wall region.

TABLE 3

SUMMARY OF COMPARISONS WITH DATA

	Average Deviation in Percent		
Original Lehigh Correlation	F_s Given by Equation 18	F_s Given by Equation 19	F_s Given by Equation 21
48.3	28.5	14.0	28.3

References

1. Hao, B. R., Morgan, C. D., Parker, M. B., Howard, C. G., "Post-CHF Heat Transfer at Low Flow and High Quality," ANS Transactions, Vol. 22, November, 1975.

2. Hao, B. R., Parker, M. B., Howard, C. G., Low Flow Critical Heat Flux," ANS Transactions, Vol. 22, November, 1975.

3. Babcock & Wilcox Company, "Forced Convection Post-CHF Heat Transfer Test," presented at 3rd Water Reactor Safety Information Meeting, Washington, (1974).

4. Dougall, R. S. and W. M. Rohsenow, "Film Boiling on the Inside of Vertical Tubes with Upward Flow of the Fluid at Low Qualities," MIT Technical Report No. 9079-26, (1963).

5. Groeneveld, D. C., "An Investigation of Heat Transfer in the Liquid Deficient Regime," AECL-3281, (1969).

6. Richlen, S. L., and K. G. Condie, "Comparison of Post-CHF Heat Transfer Correlations to Tube Data, INFL Report No. SRD-134-76, (1976).

7. Groenevled, D. C. and G. G. J. Delorme, "Prediction of Thermal Non-equilibrium in the Post-Dryout Regime," Nuclear Engineering and Design, Vol. 36, pp. 17-26, (1976).

8. Chen, J. C., Sundaram, R. K. and Ozkaynak, F. T., "Phenomenological Correlation for Post-CHF Heat Transfer," NUREG-0237, (1977).

9. Jones, O. C. and Zuber, N., "Post-CHF Heat Transfer: A Non-equilibrium Relaxation Model," ASME Paper 77-H5-79, 17th NHTC, Salt Lake City, (1977).

10. Saha, P., "A Non-equilibirum Heat Transfer Model for Dispersed Droplet Post-Dryout Regime," Int. J. of Heat and Mass Transfer, Vol. 23, pp. 483-492, (1979).

11. Nijhawan, S., chen, J. C., Sundaram, R. K. and London, E. J., "Measurement of Vapor Superheat in Post-CHF Boiling," J. of Heat Transfer, Vol. 102, pp. 465-475, (1980).

12. Nijhawan, S., Chen, J. C. And Sundaram, R. K., "Parameteic Effects on Vapor Non-equilibrium in Post-Dryout Heat Transfer," ASME Paper 80-WA-HT-50, Winter Annual Meeting, Chicago (1980).

13. Dix, G. E. and Andersen, J. G. , "Spray Cooling Heat Transfer for a BWR Fuel Bundle."

14. Iloeje, O. C., Plummer, D. N., Rohsenow, W. M., and Griffith, P., "A Study of Wall Rewet and Heat Transfer in Disperesed Vertical Flow," Report No. 72718-92, MIT Heat Transfer Lab, (1974).

15. Kays, W. M., "Convective Heat and Mass Transfer," McGraw-Hill, (1966).

16. Nusselt, W., Forsch. Greb. Ingenieurwes., Vol. 2, P. 309, (1931).

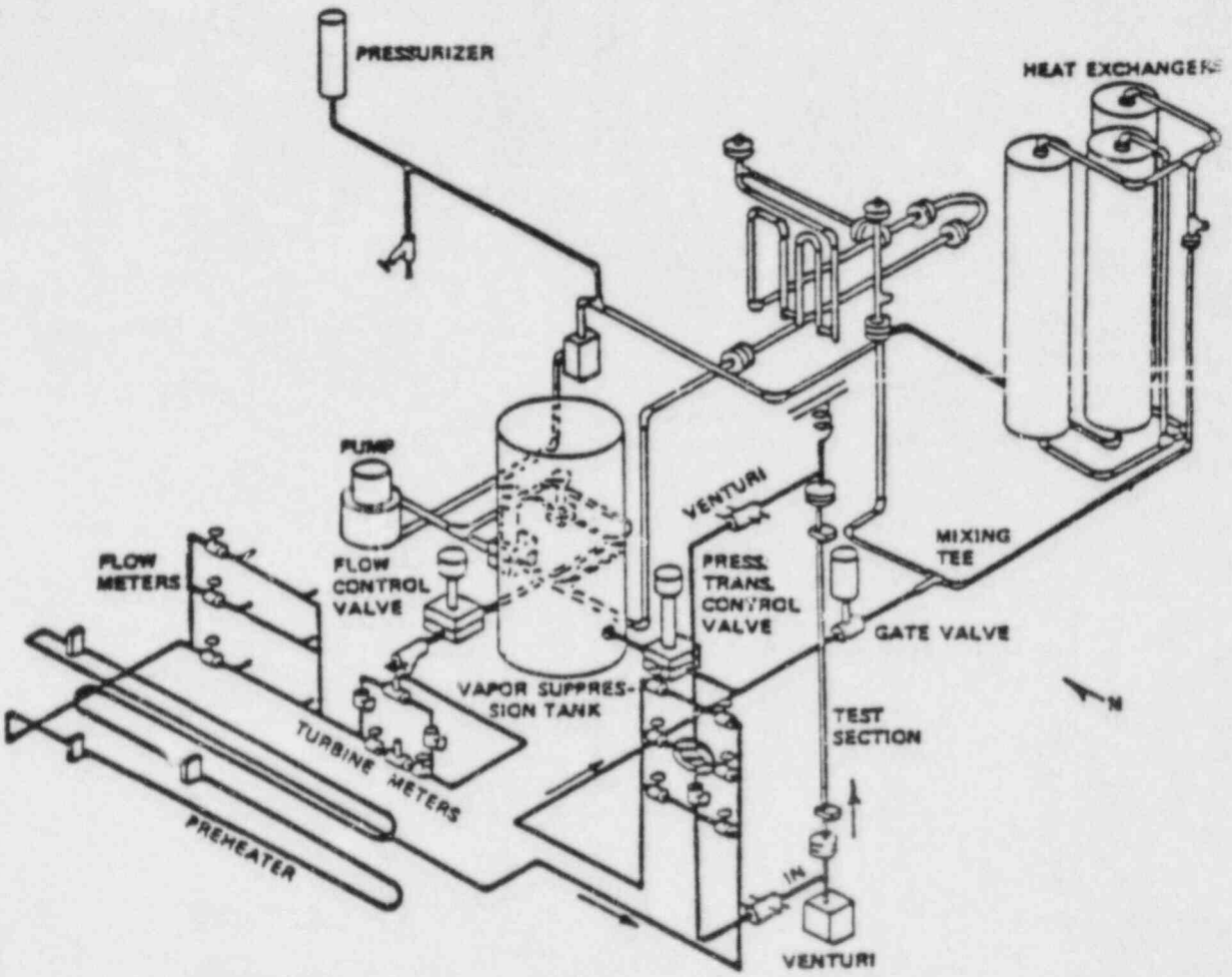

FIGURE 1 SCHEMATIC PIPING ARRANGEMENT OF BOILING HEAT TRANSFER FACILITY SHOWING POST CHF TEST

Figure 2. HEAT AND MASS FLUX VERSUS TIME FOR RUN 10504

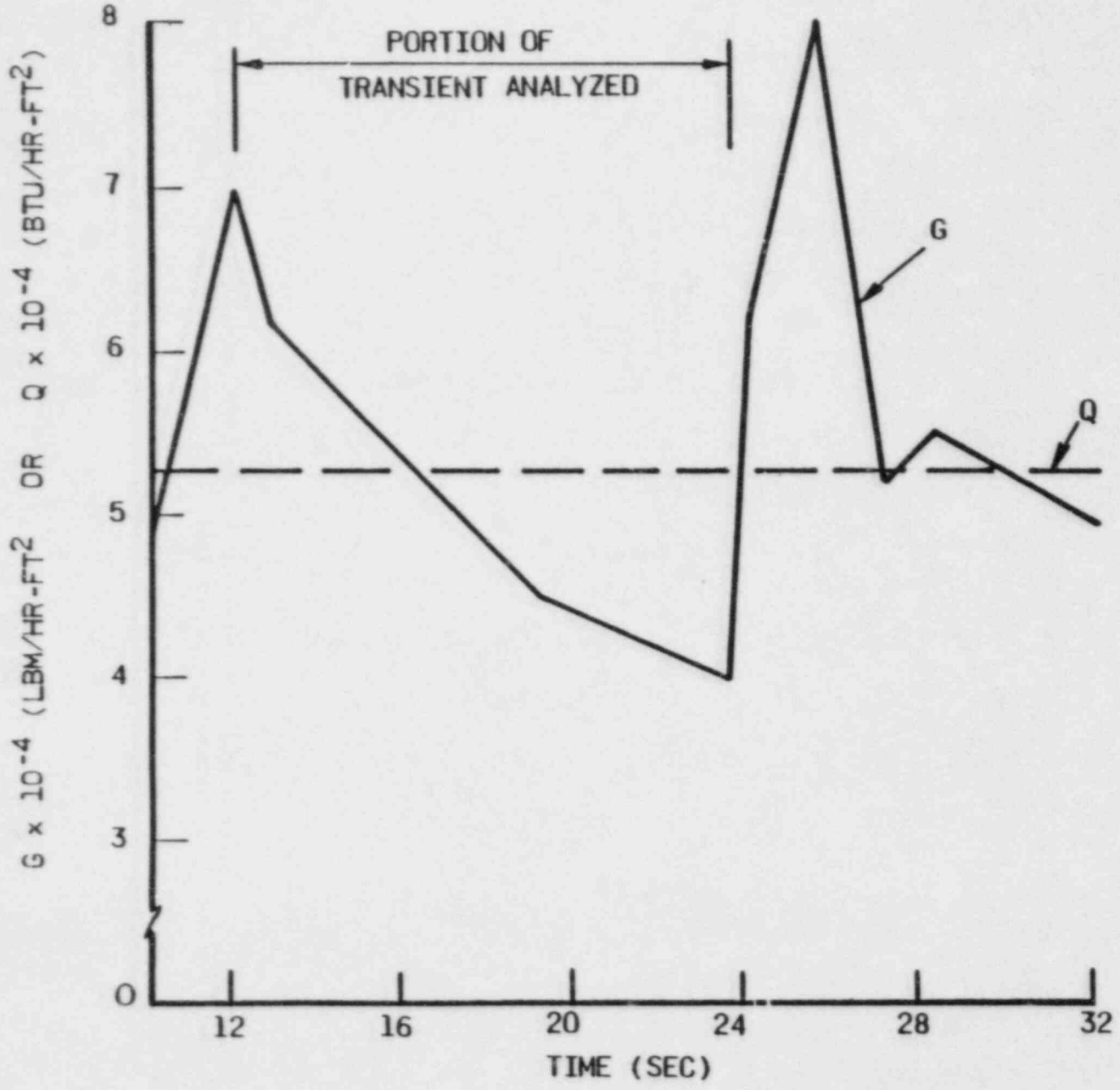

Figure 9. TYPICAL DATA USED IN ANALYSIS

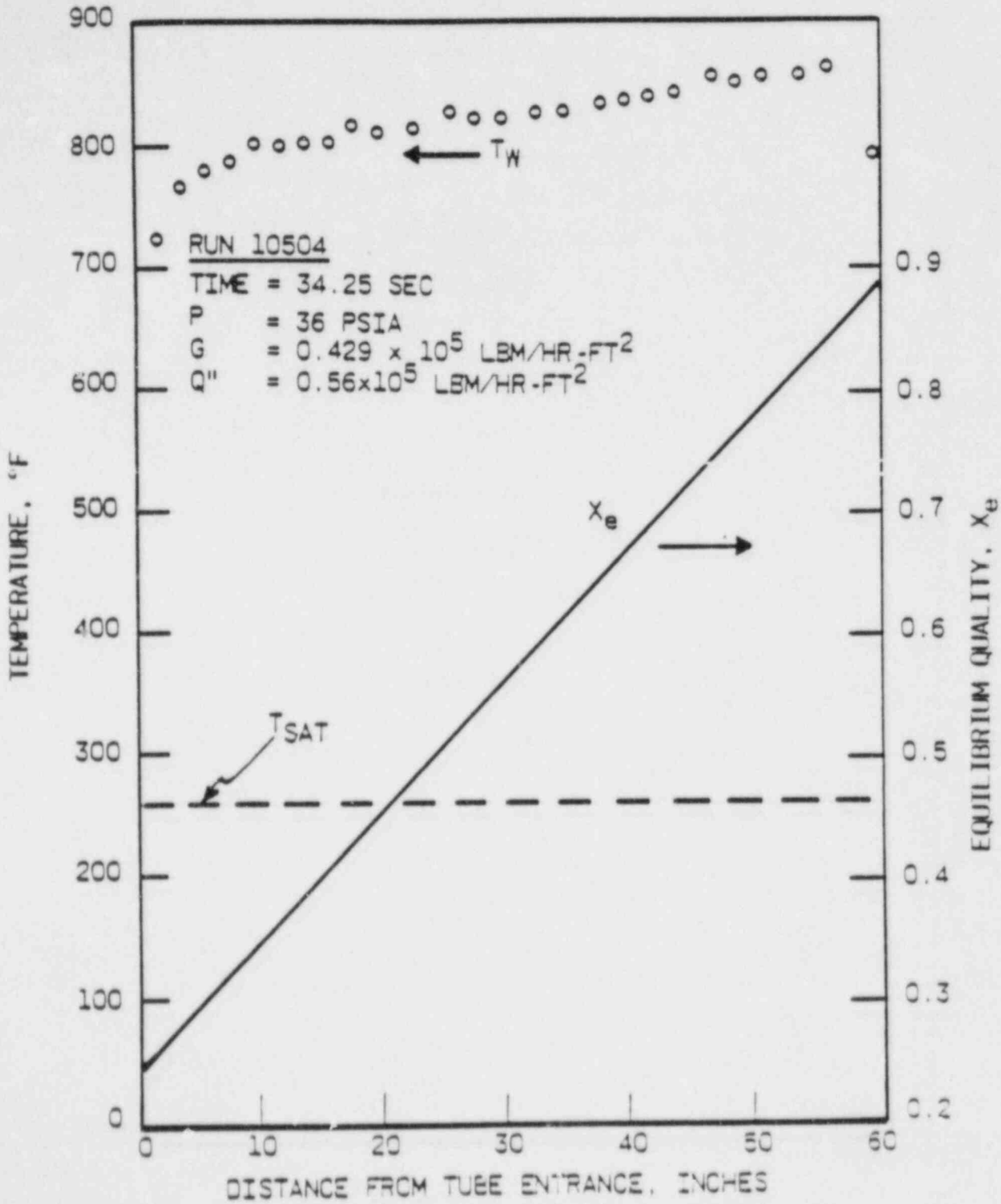

Figure 4. COMPARISON WITH CONDIE-BENSTON IV CORRELATION

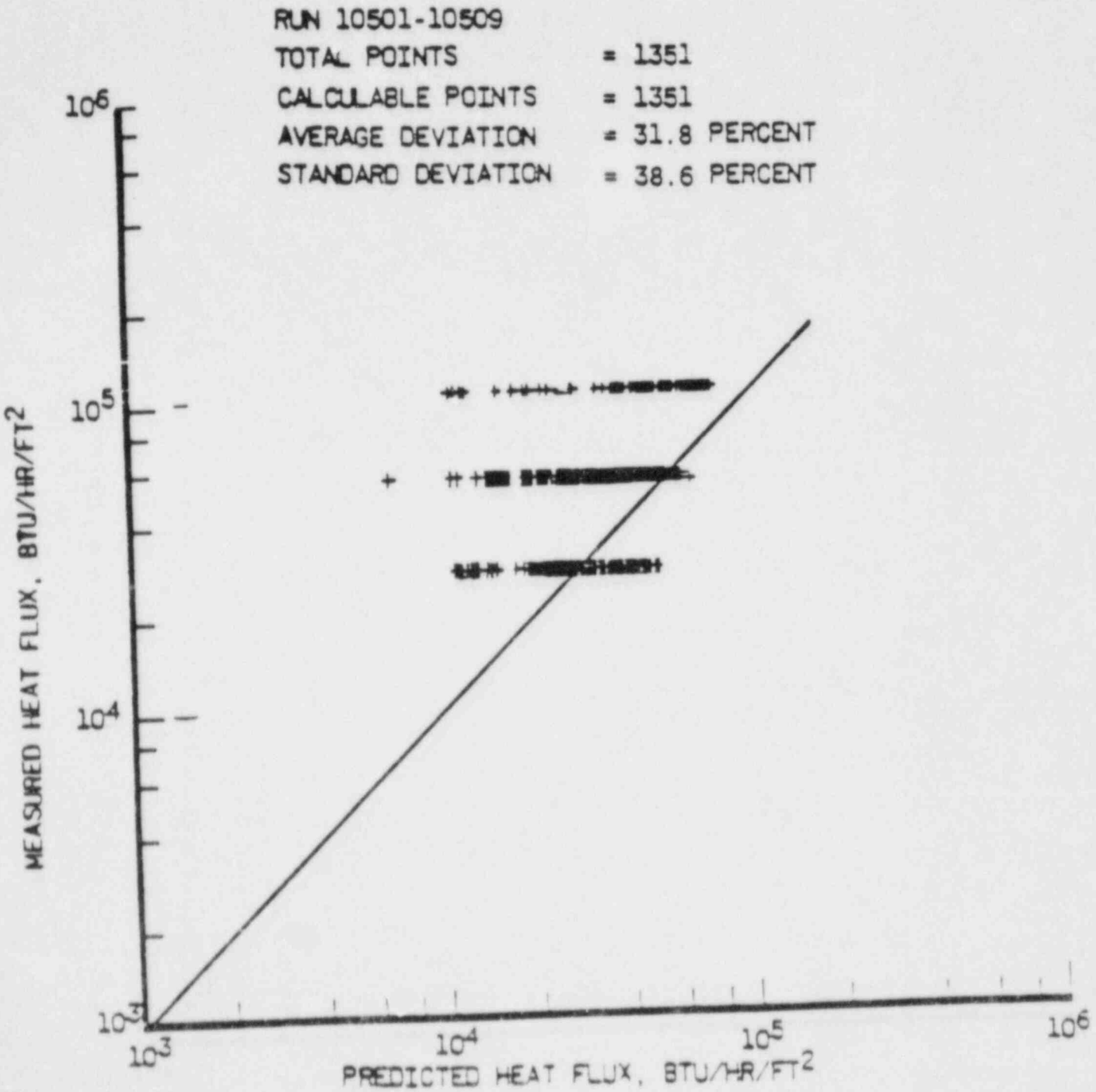

Figure 5. COMPARISON WITH LEHIGH CORRELATION

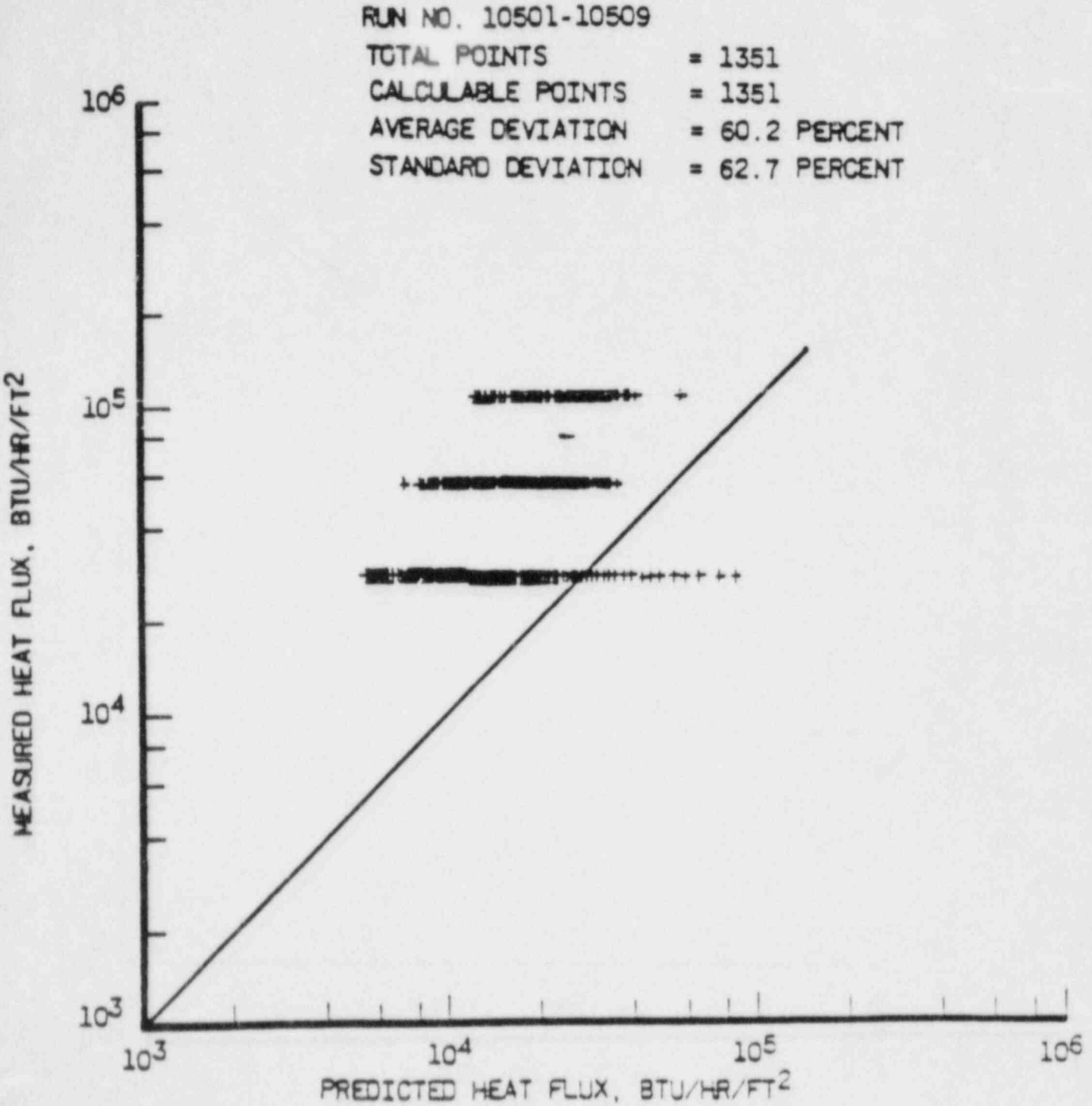

Figure 6. COMPARISON OF EXPERIMENTAL NUSSELT NUMBERS WITH NUSSELT NUMBERS CALCULATED BY EXISTING LEHIGH CORRELATION

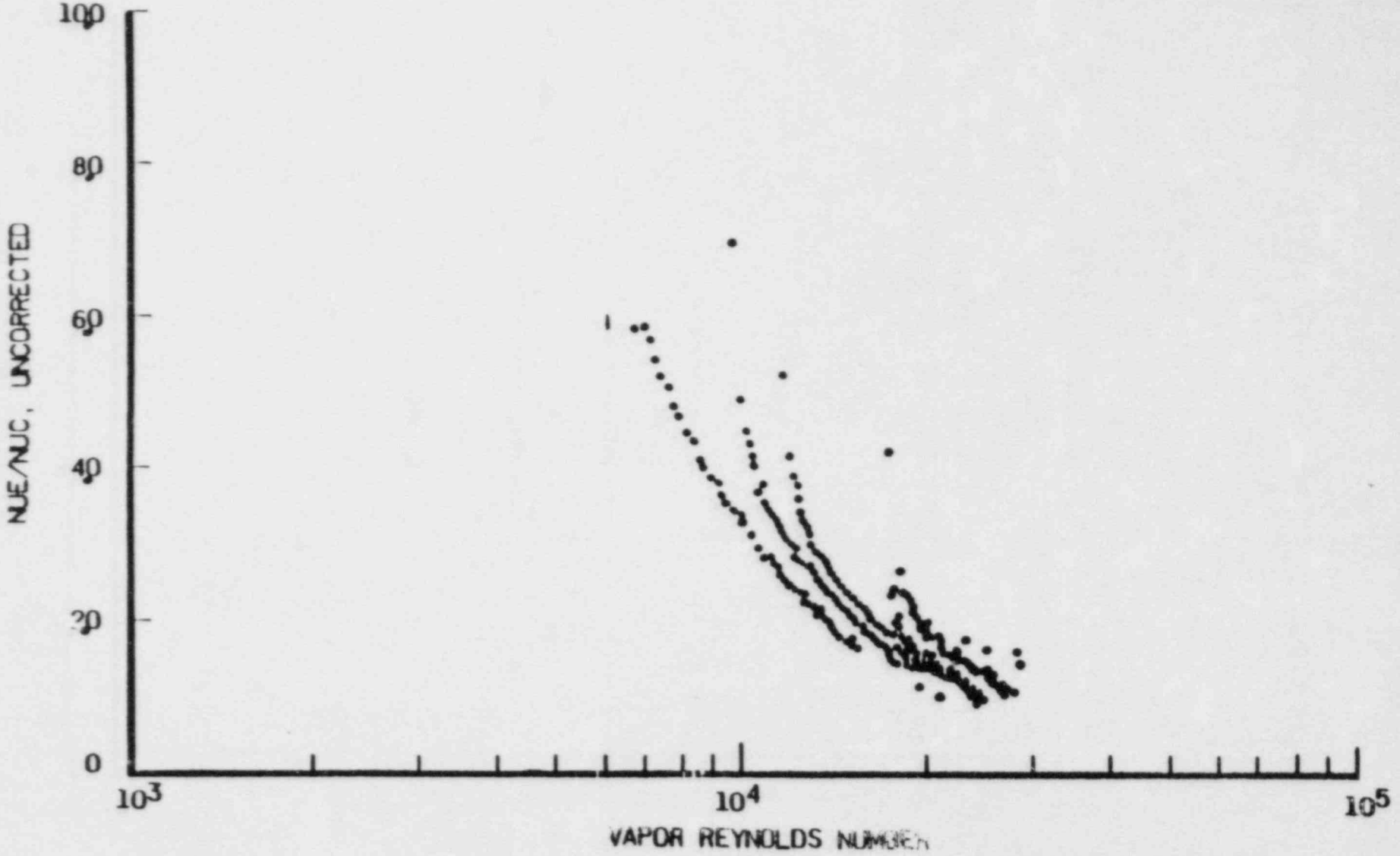

Figure 7. COMPARISON OF EXPERIMENTAL NUSSELT NUMBERS WITH NUSSELT NUMBERS CALCULATED BY EXISTING LEHIGH CORRELATION

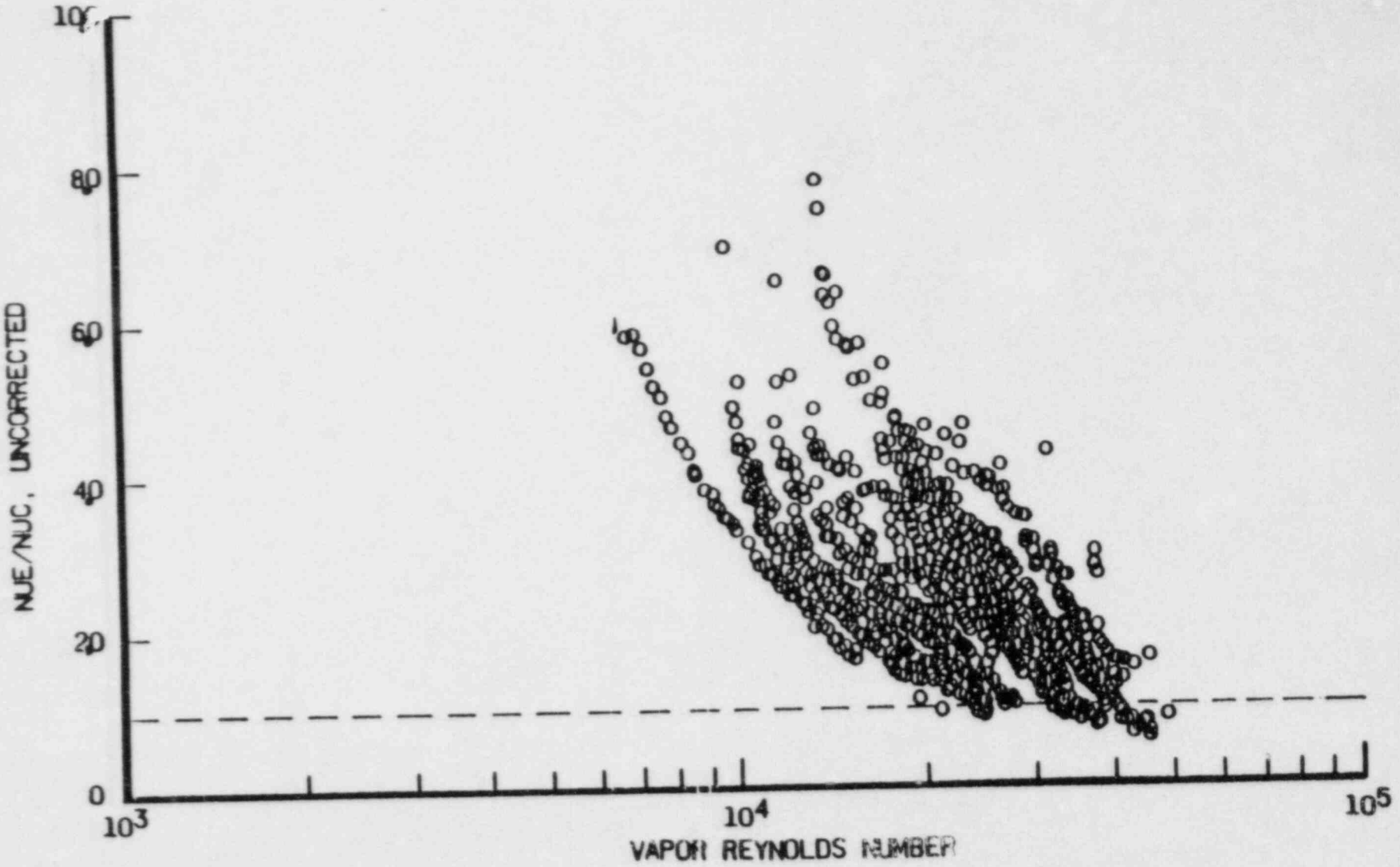

Figure 8. NUSSELT NUMBER RATIOS--
CORRECTED FOR ENTRY REGION EFFECT

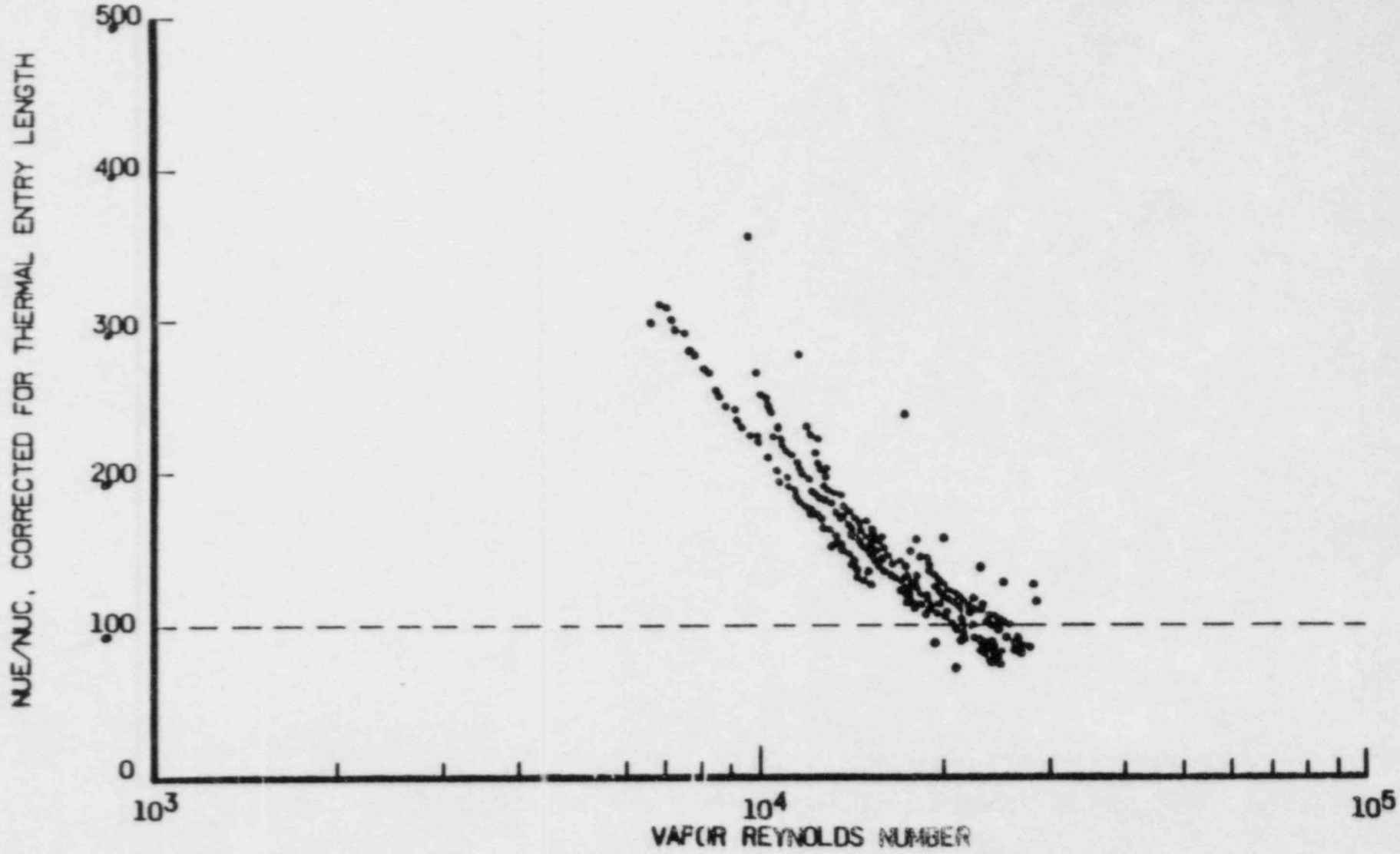

Figure 9. SINK FACTOR VERSUS LIQUID VOLUME FRACTION

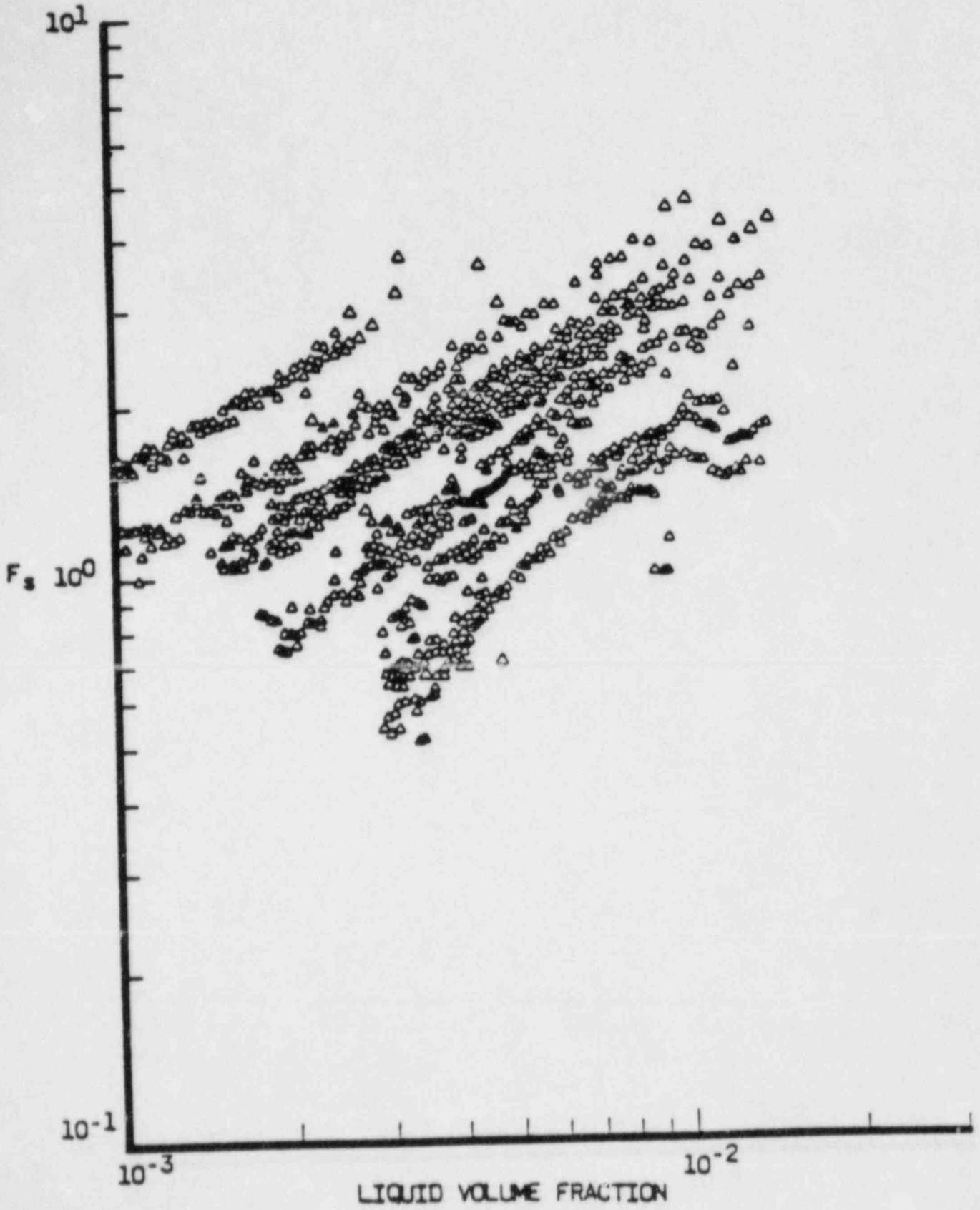

Figure 10 NUSSELT NUMBER RATIOS FOR EQUATION 18

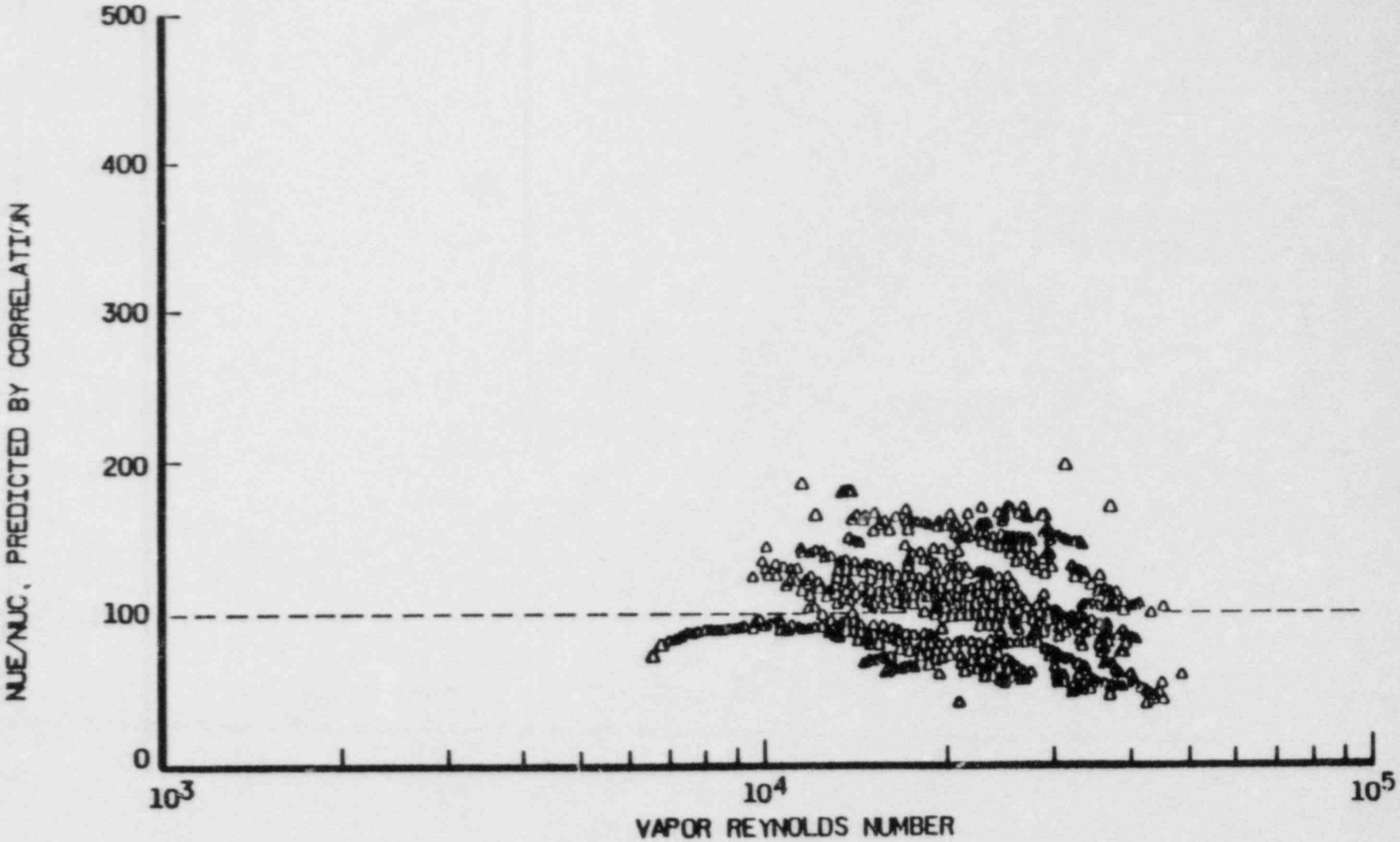

Figure 11. NUSSELT NUMBER RATIOS FOR EQUATION 19

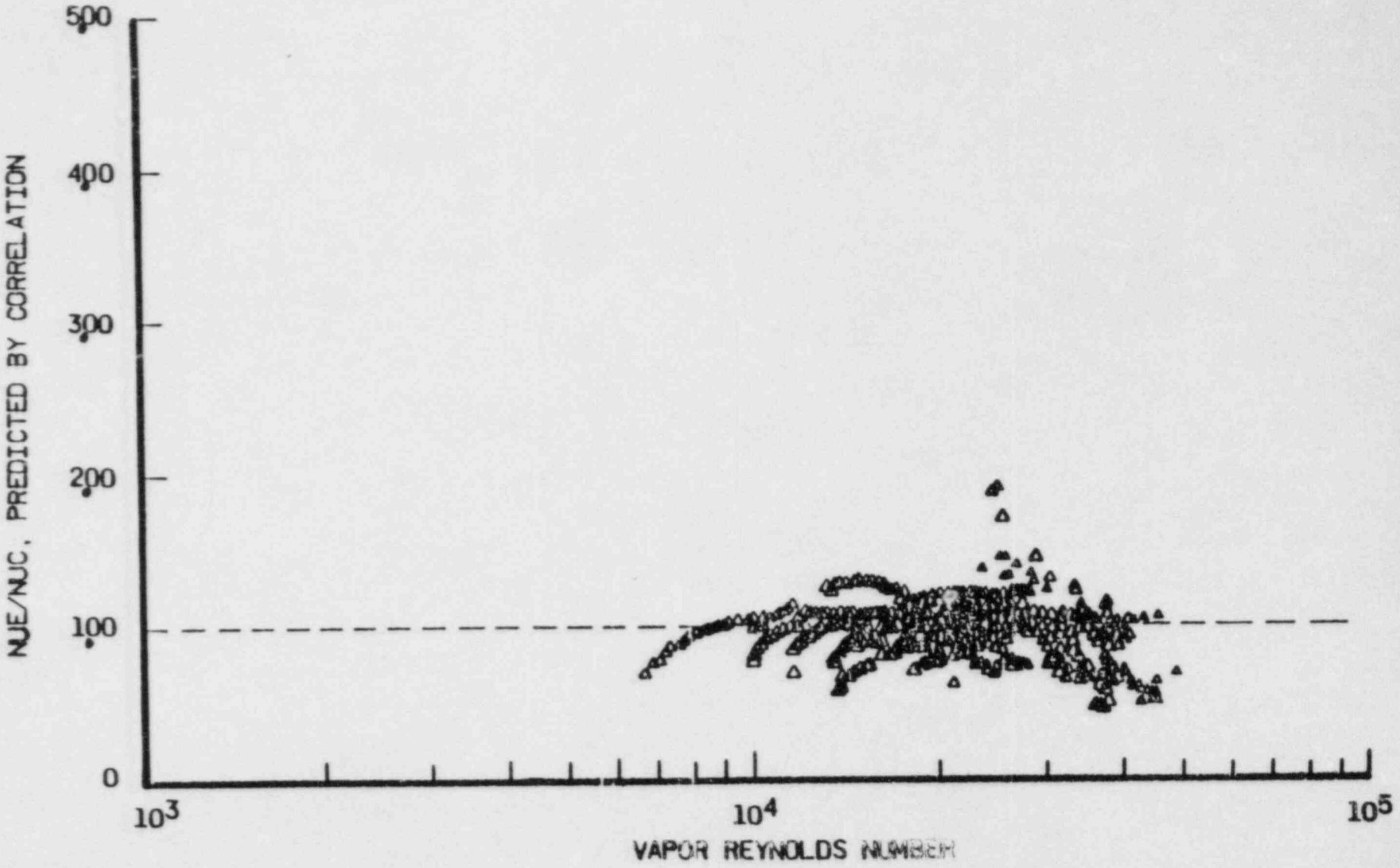

INVERTED ANNULAR FILM BOILING AND THE BROMLEY MODEL

M K Denham*

The inverted annular flow regime is one of those which occur in a boiling two-phase flow when the wall temperature is too high for the liquid to wet the wall. This paper briefly reviews the current knowledge of inverted annular flow, and goes on to consider the effect of quality and flow rate on the associated heat transfer. A new model, developed from the well known Bromley model, is compared with new data from a single tube reflooding experiment. Good agreement is demonstrated for the range of conditions appropriate to the reflooding of a PWR core following a large loss-of-coolant accident.

PREVIOUS WORK ON INVERTED ANNULAR FLOW

Physical Structure

During inverted annular flow in a tube, a central core of liquid is separated from the hot wall of the tube by an annular film of flowing vapour (Fig 1). Heat is transferred from the hot wall to the vapour, and then to the liquid. Heat is also radiated from the wall to the liquid. Some of the heat received by the liquid is conducted into the bulk of the liquid (if the liquid is subcooled) while the remainder evaporates liquid, producing more vapour. Usually such a regime starts at a quench front, a region of violent boiling separating a cool, wetted length of tube from a hot, dry length. The inverted annular regime extends on the dry side of the quench front. Eventually, at a certain distance from the quench front, the vapour flow rate becomes sufficient to disrupt the core of liquid. The core breaks up into droplets and the inverted annular flow gives way to a dispersed flow of droplets and vapour. Inverted annular flow is generally restricted to subcooled conditions (at least in low pressure water flow) because the relatively high volume of vapour present at positive quality precludes the existence of a coherent liquid core.

The description above is based mainly on the work of Dougall [1], who photographed Freon boiling in a transparent tube, but more recent work suggests that water behaves similarly at atmospheric pressure [2].

*UKAEA, AEE Winfrith, Dorchester, Dorset.

Modelling

The following brief review summarises the author's recent survey of the subject [3]. Even today, the most widely used models for film boiling are based on the well known one developed by Bromley in 1950 [4]. In Bromley's model the steam in the film rises because of buoyancy, but is held back by frictional forces exerted by the hot wall and by the liquid. The film is supposed to be in laminar flow. This balance of forces determines the steam film thickness and hence the rate of conduction of heat across the steam film to the liquid. The resulting equation for the heat flux is as follows (symbols are defined in the nomenclature):

$$q \propto \Delta T \left(\frac{k_G^{\,3}\, g\, (\rho_L - \rho_G)\, \rho_G\, \Lambda}{z\, \mu_G\, \Delta T} \right)^{1/4} \qquad (1)$$

Many film boiling experiments and analyses have subsequently shown that several, additional, interacting factors may influence heat transfer rates during film boiling. The main ones are: liquid subcooling, liquid velocity, vapour superheating, turbulence in the liquid or vapour, and instability of the vapour-liquid interface. However, these effects may not all be important in a particular situation.

Two types of experiments have been conducted to obtain information on inverted annular film boiling of water [3]. These are, firstly, transient quenching experiments using tubular or rod bundle test sections and secondly, steady-state experiments in which the quench front is held by a "hot patch". Both types of experiment have shown that the heat transfer coefficients are generally consistent with the Bromley model, both in magnitude and in the way they decrease with distance from the quench front. This lends support to the assumption of laminar vapour flow. It also suggests that interface instabilities are not important, since models based on instability, like the so-called "modified Bromley" model [5], predict a heat transfer coefficient which is independent of distance.

The same experiments have also shown that the heat transfer rate is increased if the liquid is subcooled, particularly at higher flow rates. It is generally believed that some of the heat received by the liquid is absorbed by the liquid core and does not generate steam. As a result, the vapour film is thinned and the heat transfer rate increases. Increasing the liquid flow rate increases the capacity of the liquid to absorb heat, further increasing the heat transfer rate. These effects are not included in the Bromley model, but several attempts have been made to model such processes. Chan and Yadigaroglu [6] made calculations specifically for inverted annular flow and presented a favourable comparison with limited

data. The details of their model have unfortunately not been published.

The significance of vapour superheating is uncertain. Elias and Chambre [7] have shown that it could be important if all the steam is generated at the quench front. In the present paper, it is assumed, in contrast, that the film developes gradually. Its thickness is calculated by Bromley's method but allowance is made for heat transfer into the core.

THE NEW MODEL

The thickness of the steam film, δ, is related to the mass flow rate of steam, m_G, by a force balance, as in Bromley's derivation.

$$\delta = \left(\frac{\xi \, m_G \, \mu_G}{g(\rho_C - \rho_G) \quad \rho_G} \right)^{1/3} \qquad (2)$$

The heat conducted across the steam film from the wall to the steam water interface, and the heat transferred by radiation, are given by:

$$q_{WI} = k_G \, (T_W - T_S)/\delta \, , \qquad q_R = \frac{\sigma \, (T_W^4 - T_S^4)}{\frac{D_W}{D_L} \frac{1}{\epsilon_L} + \left(\frac{1}{\epsilon_W} - 1 \right)} \qquad (3 \, , \, 4)$$

Now we extend the Bromley model to account for the heat transfer from the liquid surface into the bulk of the liquid. It is assumed that, at the quench front, the liquid core is at a uniform temperature. Then, if the core is subcooled, condensation of a small quantity of vapour will immediately bring the core surface temperature up to saturation temperature. Subsequently, heat will be conducted from the surface into the bulk of the liquid. If axial conduction is neglected, the problem is the classical one of conduction of heat into a circular cylinder, with a sudden change of surface temperature [8]. A good approximation to the heat flux at the core surface, for short times and thus suitable for the present application, is:

$$q_{IL} = -k_L \left[\frac{\partial T}{\partial r} \right]_I = k_L \frac{T_S - T_L}{\sqrt{(\pi \alpha_L t)}} \quad \frac{1}{1 + 3.75 \, Fo} \qquad (5)$$

The heat flux into the core at a certain height is obtained by substituting the time taken for the core to travel from the quench front to this height. In this way the effect of flooding rate is brought into the model.

The rate of evaporation of liquid is determined by the net heat flux to the vapour-liquid interface:

$$\frac{dm_G}{dz} = (q_{WI} + q_R - q_{IL})/\Lambda \qquad (6)$$

Equations 2 to 6 form a first order non-linear differential equation which can be integrated numerically [3], starting from the quench front and using the boundary conditions discussed below.

COMPARISON OF MODEL WITH EXPERIMENTS

Experimental Results

Experimental measurements of the heat flux and wall temperature just ahead of the quench front were obtained from single tube reflooding experiments carried out in the REFLEX Rig at Winfrith. In these experiments [9] an Inconel 600 tube 4 m long and 12 mm inside diameter, was heated electrically to 600°C and then reflooded with water from the bottom. Thermocouples spaced along the length of the tube at 150 mm intervals indicated the wall temperature. The heat fluxes to the coolant during each reflood transient were calculated from a heat balance on the tube wall at each thermocouple station. Detailed axial profiles of the temperature and heat flux near to each station could then be deduced because the quench front moved past each station in turn at a steady speed.

Boundary Conditions and Thermal Properties

Calculations were all carried out using experimentally determined wall temperature profiles. Exploratory calculations were performed [3] to investigate various plausible assumptions concerning the initial steam flow rate and the core thermal properties. As a result, it was decided to assume that the initial steam flow rate was zero and the core quality was equal to the quality just below the quench front. In other words, the heat released at the quench front was neglected. These initial calculations also indicated an optimum value of the velocity profile parameter, $\xi = 5.2$. ξ is traditionally regarded as a correlating factor, and this value is physically reasonable.

The thermal properties of the steam film were evaluated at the average of the wall and saturation temperatures. The latent heat of

evaporation included an allowance for superheating the steam, but this amounted only to a small correction. The core density was set equal to the liquid density if the core was subcooled, but if the core was saturated the homogeneous density was used instead.

The core thermal conductivity, which of course is relevant only when the core is subcooled, was at first set equal to the liquid thermal conductivity. It became apparent that this value was not large enough at the higher flow rates investigated, because the core Reynolds number was too high for laminar flow to exist. An approximate "eddy" conductivity was obtained by multiplying the molecular conductivity by the ratio of Nusselt numbers for laminar and turbulent flow in a tube. Well established expressions for the Nusselt number were used, giving ratios of up to 10 at a Reynolds number of 8 000.

The emissivities of the wall and the water were taken to be 0.8 and 0.95 respectively.

Typical Results

Figure 2 shows the experimental wall temperature and heat flux profiles for one typical run. The lower graph compares the experimental and calculated heat fluxes. It can be seen that there is good agreement for about 10 cm. After this, the experimental fluxes gradually fall below the calculated ones, probably because the inverted annular flow regime began to break down, as discussed below. The lower graph also shows the contributions to the heat balance, of radiation and of conduction into the core. Radiation is calculated to rise with distance because the wall temperature rises. Conduction into the core falls as the core temperature rises.

The upper graph in Figure 2 shows some calculated parameters of the steam film. Up to a distance of 10 cm, where the model and experimental heat fluxes diverge, the film thickness is less than 0.3 mm, and the film Reynolds number is less than 300. The transition Reynolds number for a flow in an annulus is 2 000, and so the assumption of laminar flow appears justified.

Breakdown of Inverted Annular Flow

Figure 2 also shows the behaviour of a Weber number calculated from the steam kinetic energy and the core diameter. As several authors have suggested, this may characterise the breakdown of the core, leading to dispersed flow, a less efficient heat transfer regime. We found that the Weber number was indeed correlated with the height at which the experimental and calculated heat fluxes diverged significantly, even though the decrease in the experimental heat flux was evidently a gradual process. An average critical value of 20 was determined.

Effect of Quality and Flow Rate on the Heat Transfer Rate

Heat transfer coefficients, based on the experimental wall temperature and saturation temperature, were calculated from both the model and the experimental results. Comparisons were made for a range of quench front quality, pressure, power and flow rate. It was found that the Bromley equation itself allows correctly for the effects of pressure and power. Figure 3 shows the effect of quench front quality, with the other parameters held constant. It can be seen that the new model accounts well for the effect of subcooling, by means of heat transfer into the core. It also accounts well for the effect of a positive quality by means of the homogeneous core density assumption. The dramatic decrease in heat transfer coefficient once the quench front becomes positive probably explains why the quench front invariably slows down at the same time.

Figure 4 shows the effect of flow rate. The marked increase in heat transfer coefficient with flow rate is well modelled, again because of the inclusion of heat transfer into the core.

FINAL REMARKS

It is clear from the above results that the new model accounts correctly for the effects of quality and flow rate. Figure 5 makes an overall comparison of experimental results with the calculated values. 95% of the results for which the Weber number was less than the suggested critical value of 20, agreed to within 20 $W\ m^{-2}\ K^{-1}$ + 5%. One of the widely used "modified Bromley" models [5] was much less successful, as shown by Figure 6.

It would be highly desirable to obtain detailed experimental measurements of temperature and velocity profiles in the steam film in inverted annular flow, to confirm that the new model is physically justified. In particular, the role of the heat released at the quench front, which is neglected in the present model, needs to be clarified.

NOMENCLATURE

a	radius of liquid core	α	thermal diffusivity
D	diameter	δ	vapour film thickness
Fo	Fourier number $\alpha_L t/a^2$	ΔT	$T_W - T_S$
g	acceleration due to gravity	ϵ	emissivity
k	thermal conductivity	ρ	density
m	mass flow rate	μ	dynamic viscosity

q	heat flux	Λ	latent heat
r	radial position in core	σ	Stefan's constant
t	time	ξ	velocity profile parameter
T	temperature		
z	distance from quench front		

Subscripts

C	core	R	radiation
G	vapour phase	S	saturation
I	vapour - liquid interface	T	total
L	liquid phase	W	wall

REFERENCES

1. DOUGALL, R S., and ROHSENOW, W M. Film Boiling on the Inside of Vertical Tubes with Upward Flow of the Fluid at Low Qualities. MIT-TR-9079-26. (1963)

2. GOODMAN, J., and ELIAS, E. Heat Transfer in the Inverted Annular Flow Regime During Reflooding. Trans ANS 28 397-399 (1978)

3. DENHAM, M K. Inverted Annular Film Boiling and the Bromley Model. AEEW - R 1590, (1983).

4. BROMLEY, L A. Heat Transfer in Stable Film Boiling. Chem Eng Prog 46, 221-227 (1950)

5. LEONARD, J E., SUN, K H., and DIX, G E. Low Flow Film Boiling Heat Transfer on Vertical Surfaces Part II. A I Ch E Symposium Series No 164 73, 7-13 (1977).

6. CHAN, K C., and YADIGAROGLU, G. New Formulation for Inverted Annular Film Boiling Heat Transfer. Trans ANS 33, 966-967 (1979).

7. ELIAS, E., and CHAMBRE, P. Inverted Annular Film Boiling Heat Transfer from Vertical Surfaces. Nucl Eng and Design 64, 249-257 (1981).

8. CARSLAW, H S., and JAEGER, J C. Conductionof Heat in Solids. Oxford University Press (1959)

9. DENHAM, M K., ELLIOTT, D F., and BRITTON-JONES, K A. Experimental Study of the Reflooding of a Constricted Tube in the REFLEX Rig. AEEW - R 1564 (1982).

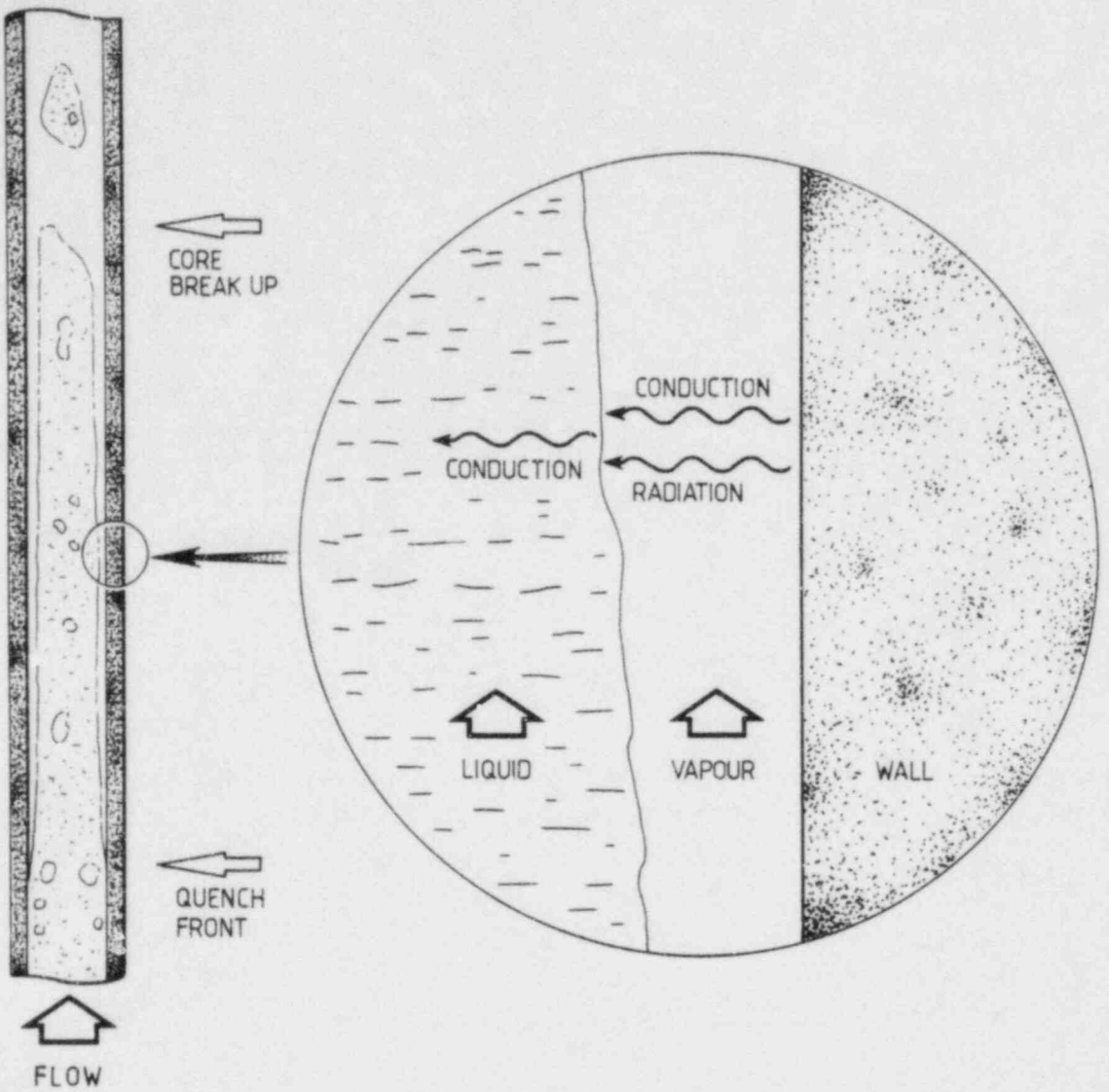

FIG.1 INVERTED ANNULAR FILM BOILING IN A TUBE

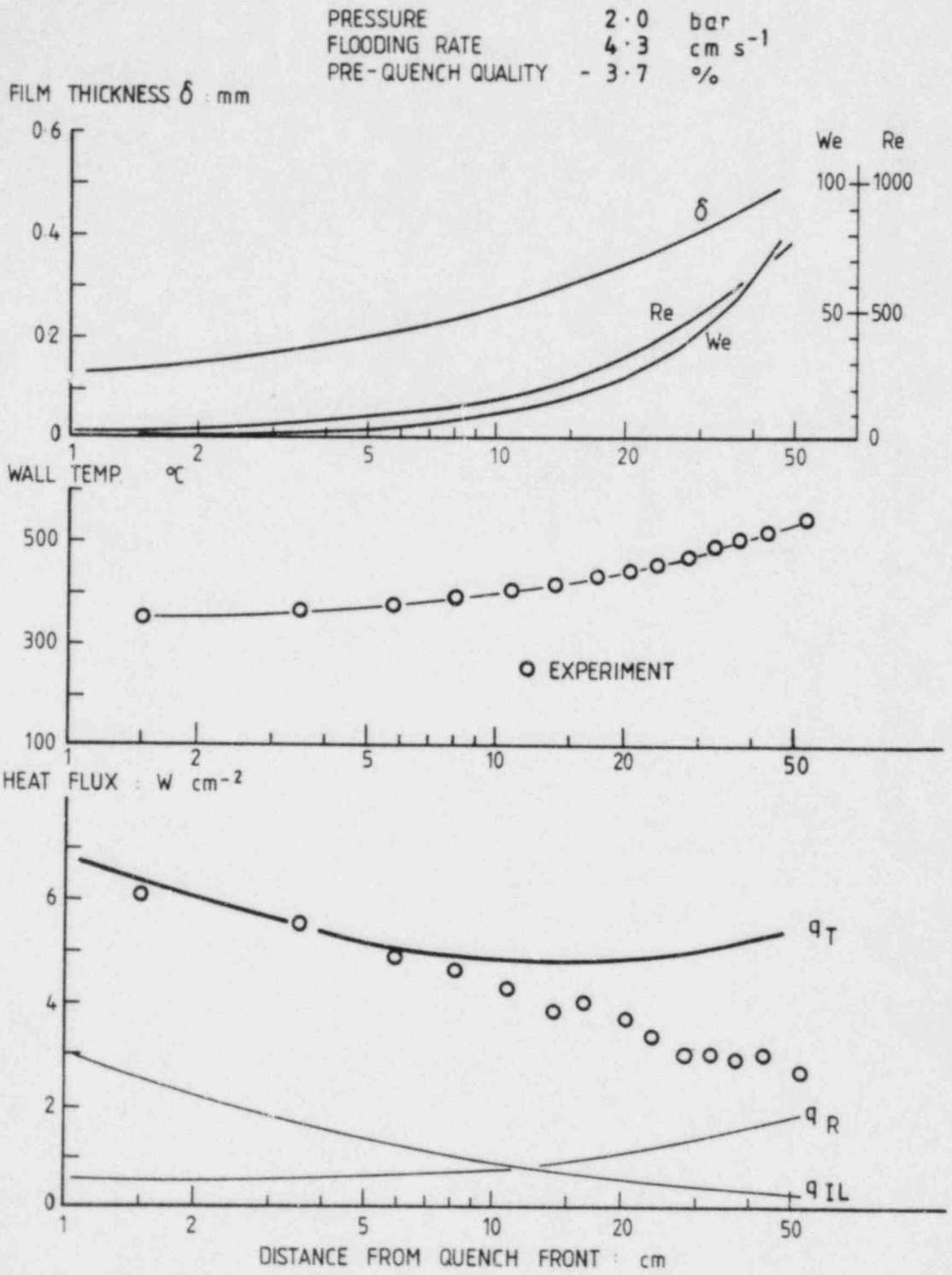

FIG. 2. HEAT FLUX, WALL TEMPERATURE, STEAM FILM PARAMETERS

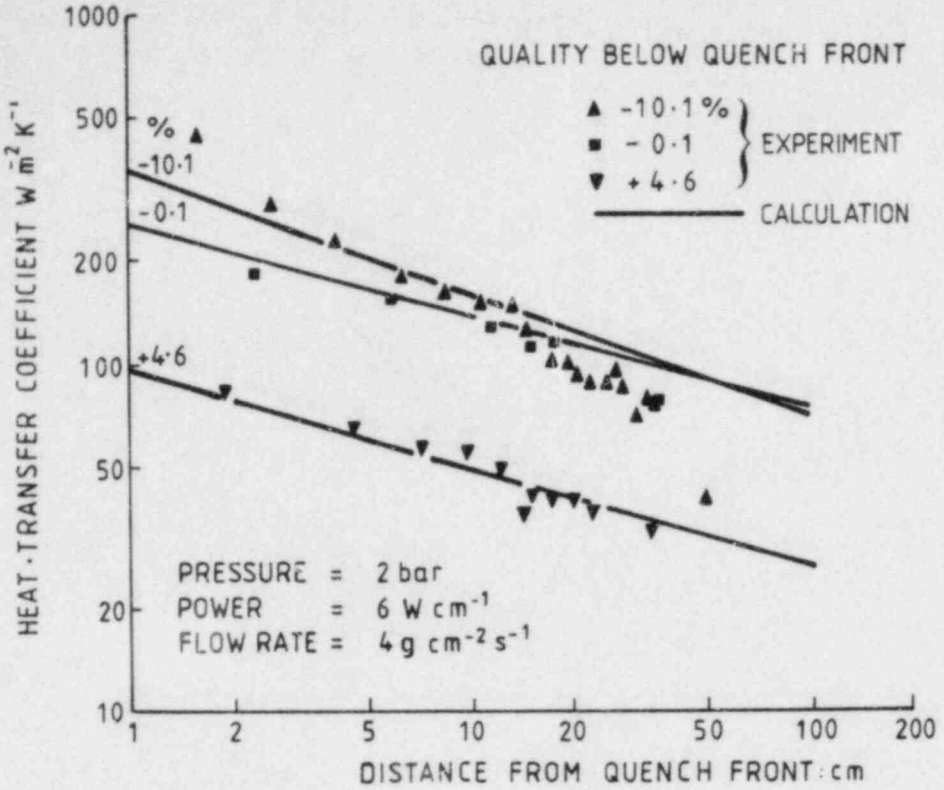

FIG. 3. EFFECT OF QUALITY

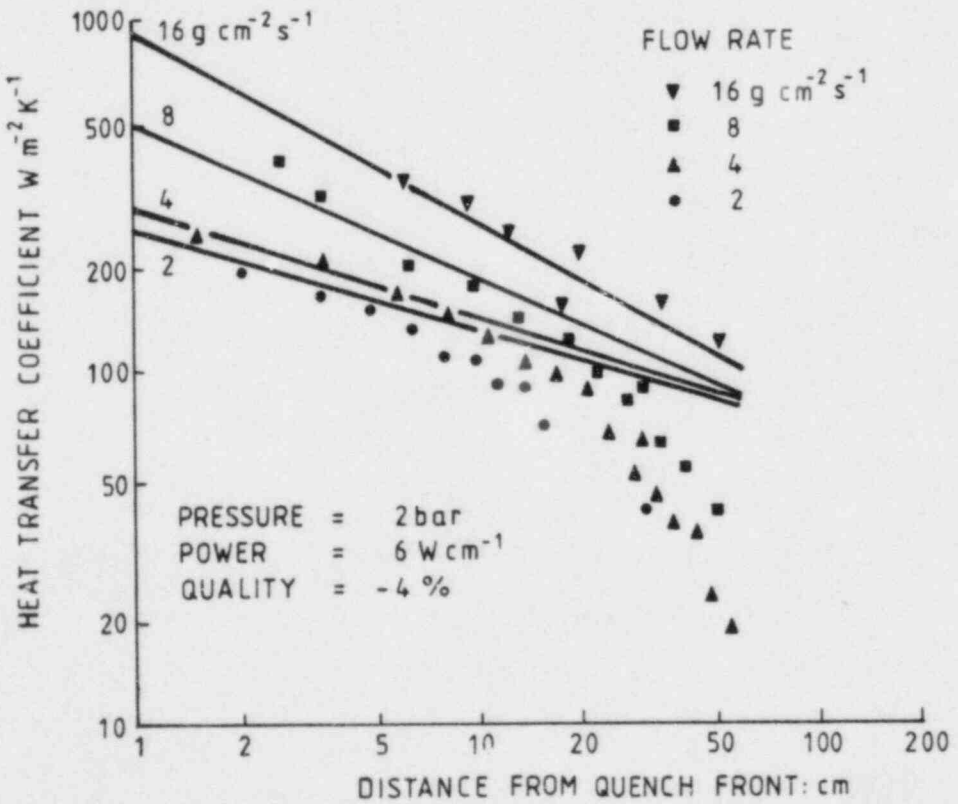

FIG. 4. EFFECT OF FLOWRATE

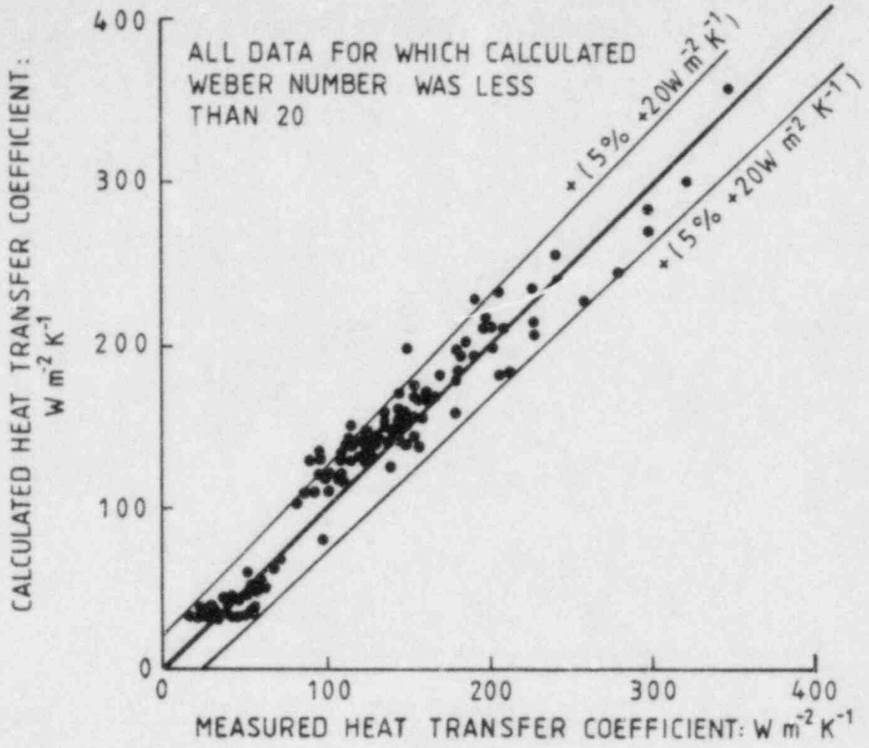

FIG.5. COMPARISON OF MEASURED AND CALCULATED HEAT TRANSFER COEFFICIENTS - PRESENT WORK

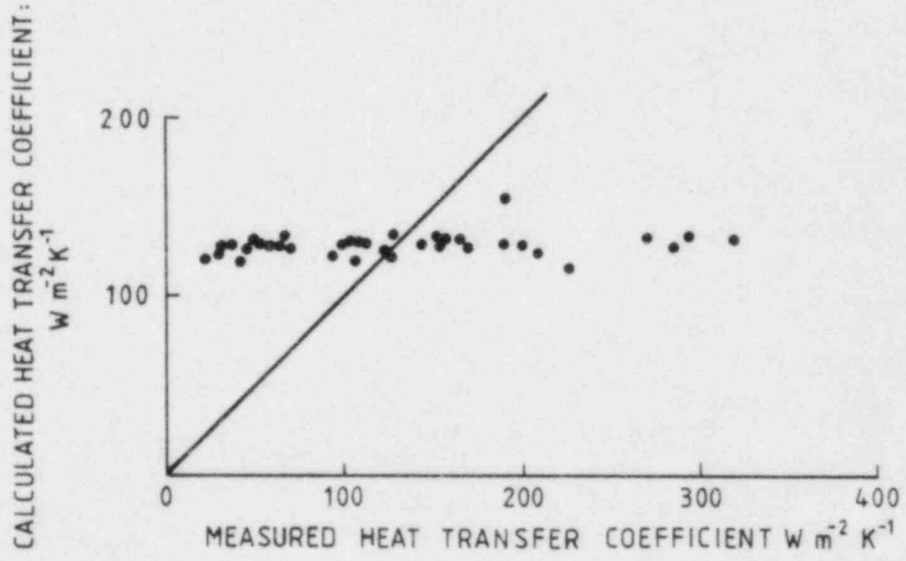

FIG.6. COMPARISON OF MEASURED HEAT TRANSFER COEFFICIENTS WITH "MODIFIED BROMLEY" MODEL

TRANSITION BOILING ON SURFACES OF DIFFERENT SURFACE ENERGY

S.K. ROY CHOWDHURY and R.H.S. WINTERTON

Department of Mechanical Engineering,
University of Birmingham,
P.O. Box 363,
Birmingham,
B15 2TT

ABSTRACT

A large number of pool boiling curves have been obtained by quenching of metal cylinders in saturated liquids. Aluminium, copper and aluminium coated with silicone rubber have been used for the cylinders and water and methanol as the boiling liquids. The liquid contact angle is taken as a measure of surface energy.

The main results relate to aluminium specimens quenched in water. Using a variety of surface treatments, a wide range of contact angle has been achieved. The entire transition boiling region, including the critical heat flux and the minimum film boiling heat flux, is shown to be strongly influenced by the contact angle.

INTRODUCTION

There is good evidence now that a number of parameters have a systematic effect on transition boiling heat transfer. The largest single body of evidence has been provided by the workers at the University of Ottowa (e.g. [1],[2]), but as detailed in a review by one of the present authors [3] most of these effects have been substantiated by other workers. In relation to forced convection transition boiling, it is found that the heat flux increases for a given surface temperature with increases in mass velocity or subcooling, and the heat flux decreases with increase in the kpc parameter. The main purpose of this paper is to present evidence that there may be another parameter to be taken into account, and that is the surface energy. So far the information available appears to be confined to pool boiling, but it is hoped that the work described in this paper will shortly be extended to flow boiling.

The project at Birmingham involves looking in a quite general way at the influence of surface parameters on all parts of the boiling curve. It is considered that the relevant surface parameters are the surface roughness, the surface energy and the thermal properties of the immediate surface layer. So far, the influence of the thermal properties has not been studied in a systematic way, but the other effects have.

The effect of surface roughness appears to be confined to nucleate boiling. Many workers have in the past measured the effect of surface roughness on nucleate boiling heat transfer (e.g. [4, 5, 6]). Generally, it has been found that rougher surfaces give better heat transfer at a given superheat, though there are a number of exceptions. In the present project, the rougher surfaces (as measured by the c.l.a.) have fairly consistently given better heat transfer, with the exception of aluminium surfaces that have been anodised after roughening. The anodising does not significantly affect the measured roughness, but it does produce a surface in which a high heat flux in nucleate boiling is obtained independent of roughness (over the c.l.a. range of 1.2 to over 5 μm). This is attributed to the anodising producing a large number of nucleation sites. Certainly scanning electron microscope pictures of the surfaces reveal a much larger number of potential sites of roughly the correct dimensions on the anodised surface [7]. The conclusion from this aspect of the work is that it is the number of nucleation sites and the cavity geometry that determine the nucleate boiling heat transfer rather than surface roughness alone.

The second surface parameter that has been studied, and the subject of this paper, is the effect of surface energy. Just as the liquid-vapour or liquid-gas interface has a surface energy σ_l which is numerically equal to the surface tension, equally there is an energy per unit area associated with the solid-vapour interface, σ_s, and an energy associated with the solid-liquid interface σ_{sl}. These energies are related to the contact angle that the liquid displays on the surface by Young's equation:-

$$\sigma_l \cos\theta = \sigma_s - \sigma_{sl} \qquad (1)$$

This equation would result in fact if all the σ values were simply considered as tensions, and a force balance conducted parallel to the solid surface at the line of three phase contact. To measure the surface energies themselves is difficult; in this paper the contact angle is taken as a measure of surface energy.

With a high energy solid surface, it can be energetically favourable for the liquid to spread over the surface and the observed contact angle is zero. With a low energy solid surface there is no spreading tendency resulting from the surface forces (though other forces, such as gravity, may cause spreading on a macroscopic scale), and the contact angle is greater than 90°.

Although Berenson [5] showed some time ago that contact angle has a pronounced effect in transition boiling (in pool boiling of n-pentane), there has been little discussion of this in work on post-dryout heat transfer. Recently both Witte and Lienhard [8] and Winterton [3] have suggested that the effect of contact angle should be included. Some striking evidence for the effects of extreme changes in contact angle in pool boiling heat transfer of water (Winterton [9]) are shown in Figure 1. The water results are taken from Nishikawa et al [10]. Details of the non-wetted surface are not given but almost certainly the contact angle would have been over 90°. The mercury results are taken from Lyon et al [11]. Again contact angles were not measured, but it is usual for mercury to display a large contact angle on the steel surface used, and the effect of adding 0.1% of sodium as a wetting agent would be to give small contact angles. For the mercury system, which was heat flux controlled, it was not possible to obtain transition boiling results, but the evidence for film boiling persisting over the entire range of superheats is remarkable.

In addition, Nishikawa, Hasegawa and Honda [12] found changes in transition boiling heat transfer which they attributed to contamination of the surface by a "soft organic scale" and these changes were associated with differing values of the contact angle. A low contact angle gave better heat transfer. In view of the gross contamination found it is not clear that contact angle by itself could be considered responsible for the change in the boiling curve.

The evidence available in the literature, while impressive, is not completely convincing. In the majority of cases either the contact angles were not measured or there was evidence of other changes in the surface in addition to the changed contact angle.

EXPERIMENTAL

Apparatus

A schematic view of the apparatus is shown in Figure 2. The apparatus essentially consists of a heating chamber and a quenching bath. The heating chamber comprises a cast-iron cylinder with a central hole for the specimen and three concentric cartridge heaters, 240V, each 300W. The chamber is connected to an argon cylinder so that the specimens may be heated in an inert atmosphere to avoid severe oxidation at high temperatures. The quenching bath is basically a thermostatic bath fitted with a stirrer and a condenser. The coverplate separating the heating chamber and the quenching bath is provided with a specimen entrance which is closed with a freely rotating lid during heating so that the heating chamber is free from water vapour.

The cylindrical specimens are normally of 18 mm diameter and 40 mm long. Both aluminium and copper specimens with various surface preparations have been used. These are heated to around 200°C - 450°C, depending on their minimum film boiling temperatures, and then quenched vertically in saturated deionised water or methanol. Basically transient tests are conducted and the central temperature is continuously measured by a Comark - 6100 fixed programme microprocessor thermometer via a

centrally located thermocouple. The thermometer has a resolution of 0.1°C up to 700°C and gives a digital display along with an analogue output of ± 1v for 500°C in its middle range.

Data Processing and Measurements

Considering the very short term (~30 sec.) required by the whole quenching process and even shorter time period by the transition zone, a micro-computer is used tc record and reduce the data. The analogue output from the thermometer is fed into a 6502 CPU, 32k micro-computer via an A-D converter. The data is initially just stored in arrays to avoid lengthy programming, which may increase the sampling interval, and then processed at the end of the test to give sequencial temperatures and corresponding heat fluxes. The data reduction is based on the assumption that the aluminium and copper specimens can be thermally lumped for their high thermal conductivities and the heat flux may be calculated from:-

$$q = \frac{MC}{A} \frac{\Delta T}{\Delta t} \qquad (2)$$

There is a small error in this thermally lumped approach, particularly near the critical heat flux. The heat flux may vary over the surface and there is a difference between the centre temperature and surface temperature. Neither effect can invalidate the trends seen as the surface properties are varied.

The micro-computer system used is capable of scanning the central temperature at a time interval between 10 to 100 ms depending on the length of the program in basic. At this time interval, however, considerable scatter is observed. It has proved necessary to average the temperature gradient over a time of around 1 s (see [7] for details).

The cylindrical specimens are normally given various degrees of surface finish and then, depending on the test requirements, they are degreased by acetone, etched in NaOH or anodised. Contact angles through a liquid drop over the experimental surface are measured by a horizontal-projection-microscope before and after the tests. Essentially it is the advancing contact angle that is measured. Surface roughnesses are measured by a Talysurf-10 profilometer in terms of CLA values. Where the profilometer traces are insensitive, for example anodised surfaces containing fine pores, SEM micrographs at a high magnification are taken. The anodising procedure uses 15% by volume sulphuric acid and a current density of 130 amp m^{-2}. The voltage is increased from an initial value of 20V to around 30V to maintain this desired current density. The process takes about 20 minutes.

RESULTS

The first point to make about the measurements is that it does appear to be possible to obtain reproducible quenching results. This may be done by ageing the surface; starting with either polished or etched aluminium specimens, after a series of heating and quenching runs, the surface settles down and shows very little change in subsequent runs. This ageing procedure is similar to that required for the standard (Inconel) test probe used in the comparative test of quenching oils [13]. Alternatively, if the aluminium specimen is anodised, reproducible results are obtained from the beginning.

Contact angle variations are obtained either during this ageing process on a single specimen; or are found from one metal cylinder to another with nominally identical

specimen preparation. Larger variations appear when slightly different methods are used to prepare the specimens. The second striking feature of the results is that in every single case so far tested, a reduction in contact angle is associated with an improvement in transition boiling heat transfer (higher heat flux at a given surface temperature). It is worth listing the separate tests that have been performed:-

a) Aluminium cylinders as received from machining, possibly contaminated with oil.

b) Aluminium etched with NaOH (ageing of single specimen, see Figure 3).

c) Etched aluminium, different specimens.

d) Polished aiuminium (ageing of single specimen, see Figure 3).

e) Anodised aluminium, different specimens.

f) Polished copper, ageing of single specimen.

g) Copper, different specimens, boiling of methanol (all other runs conducted with water). This run was slightly different in that all specimens gave the same contact angle (zero) and all gave the same transition boiling curve.

h) More recent tests, much as (d), but with the cylinders heated up to 450°C instead of 300°C before quenching and duralumin used in place of commercially pure aluminium.

Where a number of specimens have been used in a test, they have normally had different surface roughness, but otherwise identical preparation. There is no evidence that the roughness itself affects the transition boiling.

If the results of different tests are compared then the influence of contact angle is not quite so clear cut, but still impressive. Figure 4 shows all the runs on pure aluminium specimens, excluding only the preliminary results (Test (a)) where degreasing of the surface with acetone was omitted and tap water was used instead of deionised water. Over the contact angle range 0 to 100, it is clear that transition boiling heat transfer correlates very well with contact angle. At certain surface temperatures the extreme values of contact angle correspond to an order of magnitude change in heat flux.

In fact, the preliminary results with the contaminated surface and the copper/water run also fit in with the others but it was not thought reasonable to include them without further evidence. The common features then for the runs in Figure 4 are that the specimens were all cleaned with acetone, followed in some cases by more severe cleaning, all must have had an oxide layer present on the surface since the specimens were exposed to air and the maximum temperature reached was below 300°C.

More recently, in order to elucidate the influence of contact angle on the minimum film boiling point, quenching has been conducted with a higher starting temperature (around 450°C) and duralumin cylinders. These results (Figure 5) do not completely superimpose on the earlier ones (Figure 4) so it seems that there are other properties of the surface that must be taken into account in addition to contact angle.

Figure 5 shows that the influence of the contact angle value does extend as far as the minimum film boiling point. This in itself throws some doubt on the homogeneous nucleation theory of the minimum film boiling point but the predictions of this theory are included in the Figure for comparison.

The minimum film boiling temperature is often considered to occur when the temperature of the liquid on contact with the surface equals the homogeneous nucleation temperature, T_{hn}. For water at atmospheric pressure, the homogeneous nucleation temperature is about 307°C (e.g. [3]). The temperature on contact is not the same as the wall temperature since the momentary contact of liquid with the wall cools it. A simple analysis based on purely conduction heat transfer after contact gives:-

$$T_{mfb} = T_{hn} + (T_{hn} - T_l) \left(K_l \rho_l c_l / K_s \rho_s c_s\right)^{1/2} \qquad (3)$$

l = liquid, s = solid

For the estimates in Figure 5, T_l is the liquid saturation temperature, and the solid properties are calculated for both pure aluminium and for alumina. The minimum film boiling temperatures work out at 321°C and 341°C respectively.

Even the curves for the large contact angles in Figures 4 and 5 do not quite show the extreme behaviour of the large contact angle, non-wetted surfaces in Figure 1, and it was considered of interest to try and reproduce this type of behaviour by coating an aluminium specimen with a thin layer of silicone rubber sealant, to see if even larger contact angles could be achieved. In fact, the measured value was 113°. The quenching behaviour (Figure 6) is more like that of the non-wetted surfaces in Figure 1.

Comparison of the results in Figure 6 for the normal specimen in addition to the silicone coated specimen shows that the measurements coincide in the film boiling region. It is widely considered that in film boiling there should be no influence of surface properties because the liquid does not touch the surface. The silicone rubber layer displayed weak interference colours, suggesting that its thickness was a few μm. In an attempt to measure the coating thickness, a small region was removed with acetone and a Talysurf trace taken across the surface. Any step in going from the clean to the coated surface was concealed by the surface roughness (0.4 μm), so the coating thickness must be a few μm at most. The temperature drop through a layer of this thickness would be less than 1°C.

DISCUSSION

The correlation of transition boiling heat transfer with contact angle, as shown in Figure 4, is as good as could reasonably be expected, bearing in mind that there are probably errors of a couple of degrees in measuring the contact angles and that these measurements were made at room temperature, not during the boiling process. Also, some of the runs were performed with the end surfaces of the cylinder sealed, to confine boiling to the vertical, curved, surface. These runs systematically displayed a lower heat flux. If this effect is taken into account, then the correlation of heat flux with contact angle improves.

There are known hydrodynamic limits on the maximum possible value of the critical heat flux [14, 15] and on the minimum possible film boiling heat flux [15, 16]. There is little evidence in these results that the critical heat

flux limit has been reached, since the value appears to change continuously with contact angle over the whole range. In fact, the highest heat flux measured (Figure 4) is some 70% below the Kutateladze limit. However, the lowest film boiling heat fluxes (Figure 4) are close to the Berenson limit (although strictly this relates to a horizontal, upward facing surface).

The extreme type of heat transfer behaviour previously noted on some non-wetted surfaces, with film boiling covering all or nearly all of the boiling temperature range, has not completely been reproduced, but with very large contact angles the nucleate boiling region is greatly reduced in extent and the critical heat flux is much lower.

CONCLUSIONS

A key parameter in determining the level of transition boiling heat transfer is the liquid contact angle.

Heat transfer improves with decrease in the contact angle.

Although, so far, the effect has only been demonstrated in pool boiling, it is likely that it will also appear in forced convection.

ACKNOWLEDGEMENT

We thank the Science and Engineering Research Council for supporting this work.

REFERENCES

1. RAGHEB, H.S., CHENG, S.C. and GROENEVELD, D.C. "Measurement of transition boiling boundaries in forced convection flow", Int. J. Heat Mass Transfer 24, 1981, 1127-1137.

2. CHENG, S.C., POON, K.T., NG W.W.L. and HENG, K.T. "Transition boiling heat transfer in forced vertical flow", Final Report 1979-1981, Argonne Contract No. 31-109-38-3564, 1981.

3. WINTERTON, R.H.S. "Transition boiling", U.K. Atomic Energy Authority Report AEEW-R1567, 1982.

4. CORTY, C. and FOUST, A.S. "Surface variables in nucleate boiling", Chemical Engineering Progress Symposium Series, Vol. 51 No. 17, 1955, pp. 1-12.

5. BERENSON, P.J. "Experiments on pool boiling heat transfer", International Journal of Heat and Mass Transfer, Vol. 5, 1962, pp. 985-999.

6. HSU, S.T. and SCHMIDT, F.W. "Measured variations in local surface temperatures in pool boiling of water", Journal of Heat Transfer, Trans. ASME, Series C, Vol. 3, 1961, pp. 254-260.

7. ROY CHOWDHURY, S.K. and WINTERTON, R.H.S. "Surface effects in quenching of hot solids", First U.K. National Heat Transfer Conference, Leeds, July 1984, to be published.

8. WITTE, L.C. and LIENHARD, J.H. "On the existence of two 'transition' boiling curves", Int. J. Heat Mass Transfer 25, 1982, 771-779.

9. WINTERTON, R.H.S. "Comments on 'On the existence of two "transition" boiling curves'", Int. J. Heat Mass Transfer 26, 1983, 1103-1104.

10. NISHIKAWA, K., FUJII, T. and HONDA, H. "Experimental study on the mechanism of transition boiling heat transfer", Bull, JSME 15, 1972, 93-103.

11. LYON, R.E., FOUST, A.S. and KATZ, D.L. "Boiling heat transfer with liquid metals", Chem. Engng. Prog. Symp. Ser. 51 (No. 17), 1955, 41-47.

12. NISHIKAWA, K., HASEGAWA, S. and HONDA, H. "Studies on boiling characteristic curve", Memoirs of the Faculty of Engineering, Kyushu University, Vol. 27, 1967, pp. 133-154.

13. WOLFSON HEAT TREATMENT CENTRE, UNIVERSITY OF ASTON. "Laboratory test for assessing the cooling characteristics of industrial quenching media", 1982.

14. KUTATELADZE, S.S. "Heat transfer in condensing and boiling", U.S. Atomic Energy Commission Report No. AEC - tr - 3770, 1952.

15. ZUBER, N. "On the stability of boiling heat transfer", Journal of Heat Transfer, Trans. ASME, Vol. 80, 1958, p. 711.

16. BERENSON, P.J. "Film boiling heat transfer from a horizontal surface", Trans. ASME J. Heat Transfer 83, 1961, 351-358.

FIGURE CAPTIONS

1. Data reported in the literature for pool boiling of water on wetted and non-wetted surfaces (no contact angle values given).

2. Schematic diagram of the apparatus.

3. Effect of ag ing on etched and unetched surfaces.

4. Effect of contact angle on boiling curves.

5. Effect of contact angle on minimum film boiling point.

6. Effect of silicone rubber coating on the boiling curve.

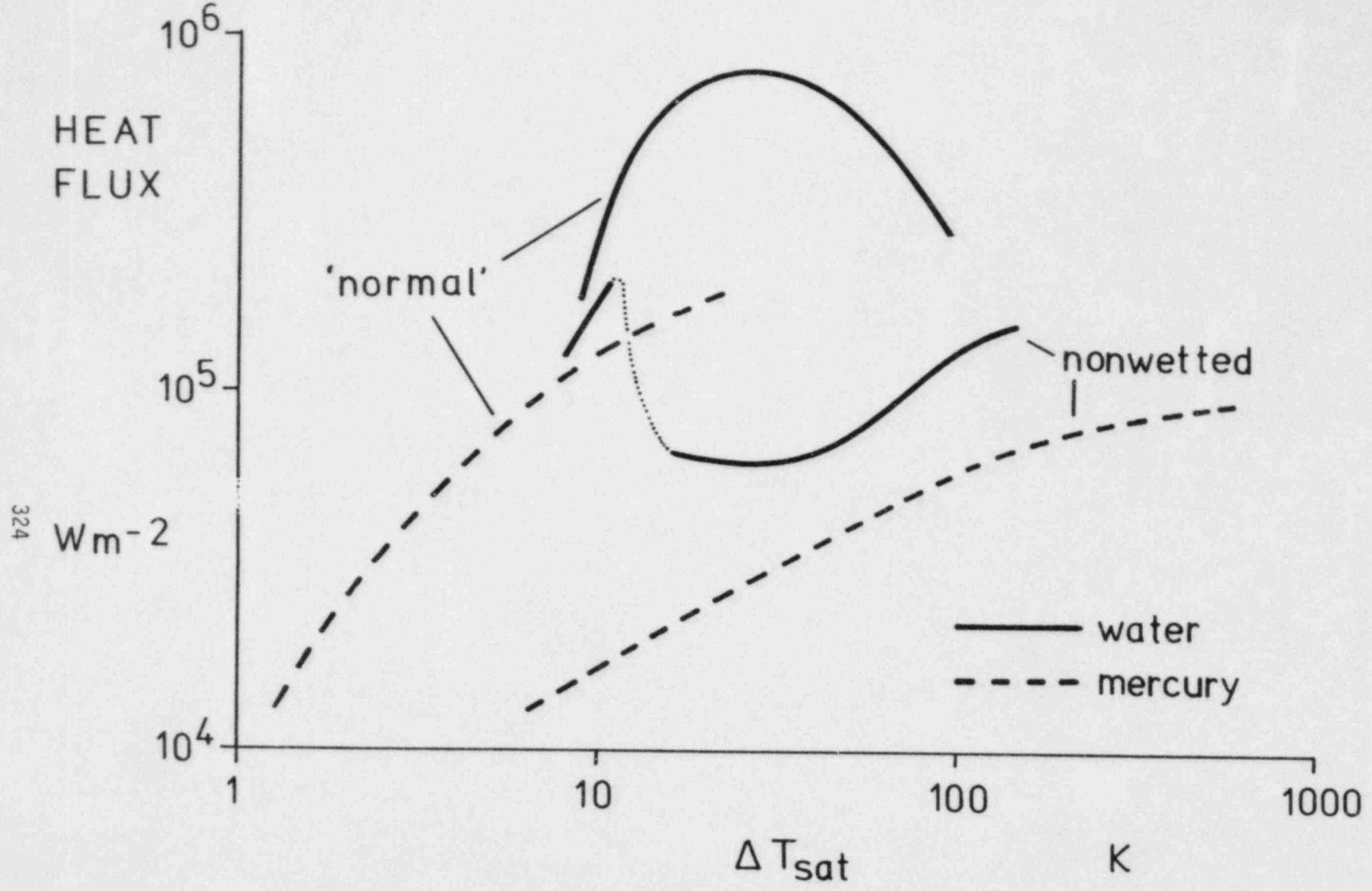
HEAT
FLUX
10^6
10^5
10^4
Wm^{-2}
'normal'
nonwetted
water
mercury
1
10
100
1000
ΔT_{sat}
K

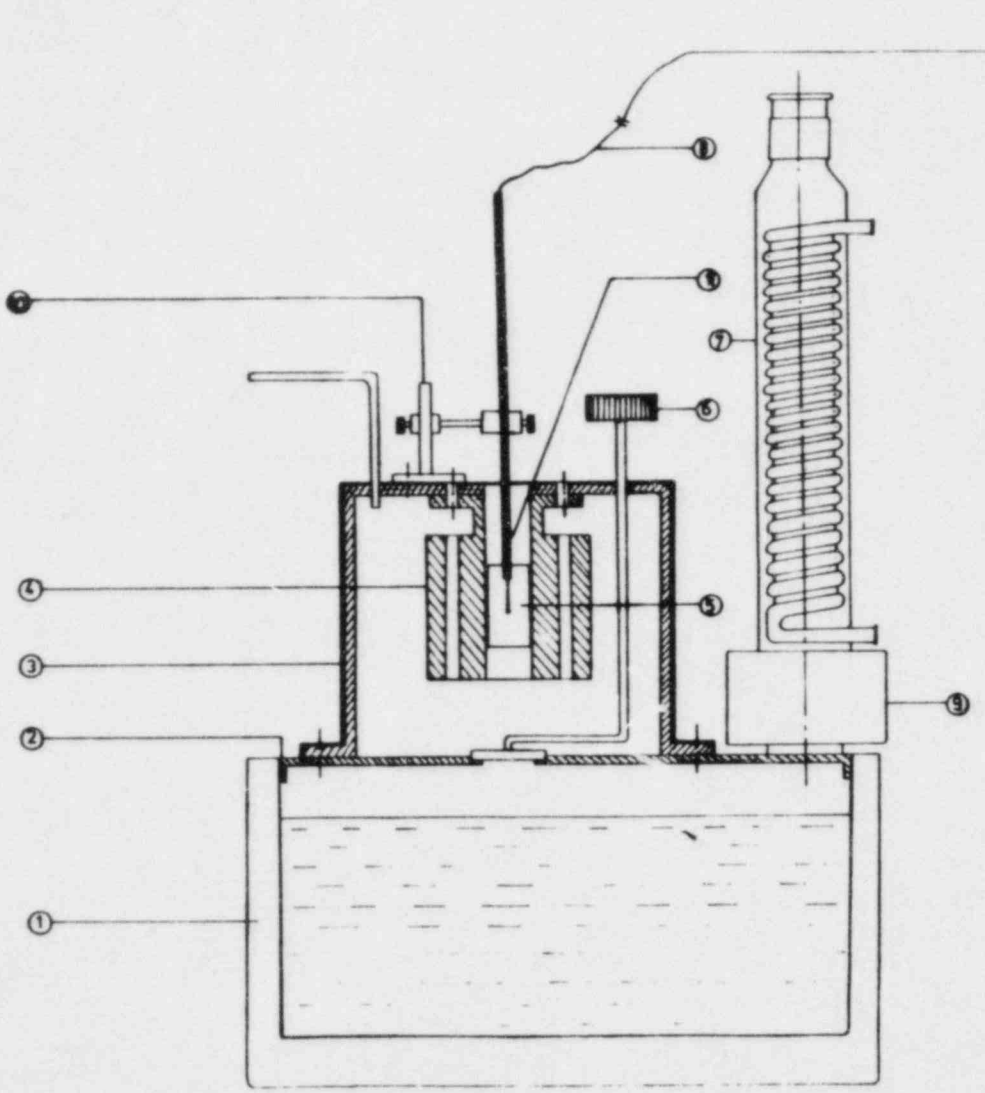

ITEM NO.	DESCRIPTION
1	QUENCHING LIQUID TANK
2	COVER B
3	LAGGING
4	HEATER ASSEMBLY
5	SPECIMEN
6	SPECIMEN ENTRANCE COVER
7	CONDENSER
8	THERMOCOUPLE
9	THERMOSTIRRER
10	SPECIMEN HOLDER ASSEMBLY
11	THERMOCOUPLE & SPECIMEN HOLDER
12	COMARK 6100 THERMOMETER
13	MICROCOMPUTER

FIG. 2

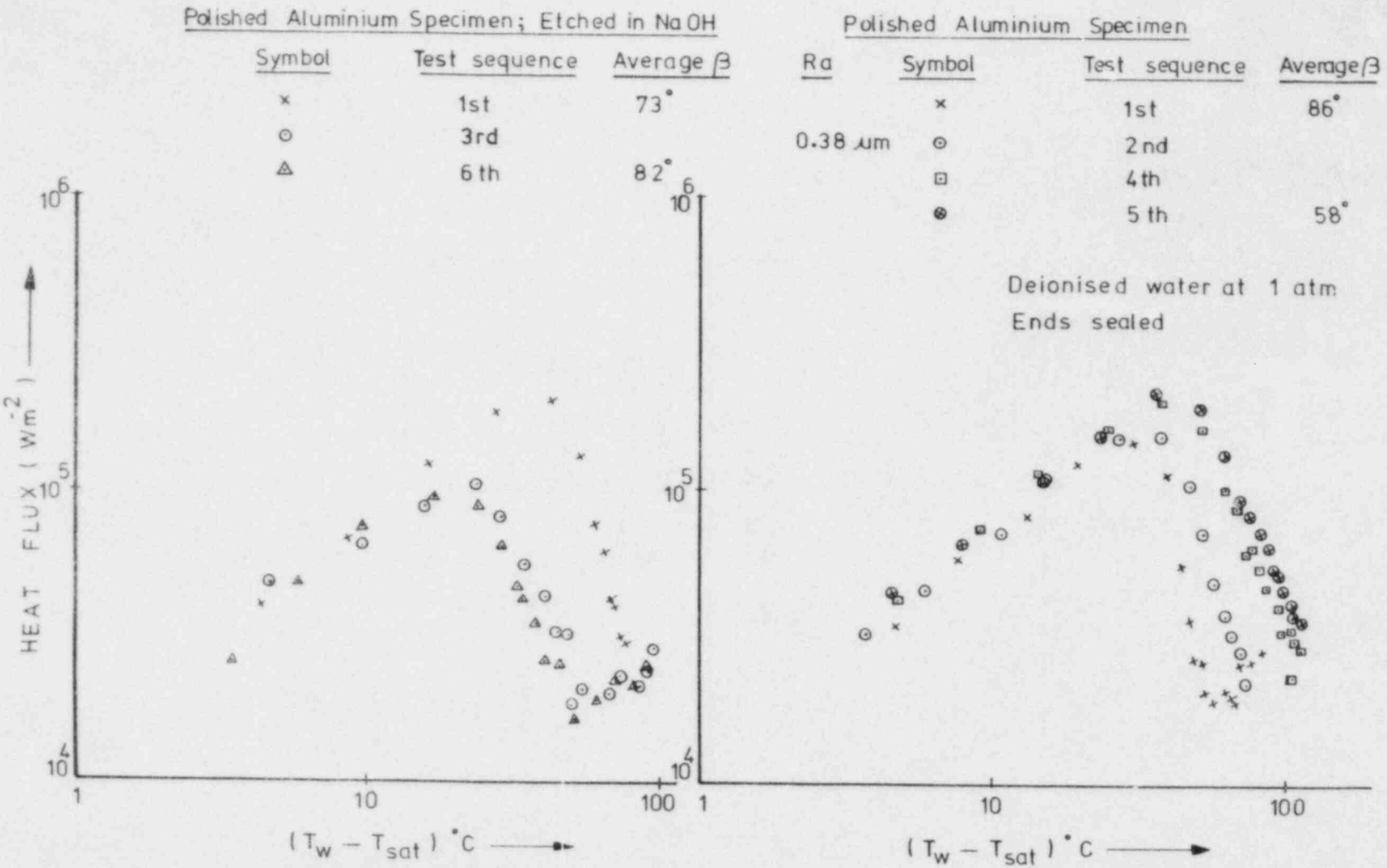
Polished Aluminium Specimen; Etched in NaOH
Symbol
Test sequence
Average β
×
1st
73°
⊙
3rd
△
6th
82°
Polished Aluminium Specimen
Ra
Symbol
Test sequence
Average β
×
1st
86°
0.38 μm
⊙
2nd
⊡
4th
⊛
5th
58°
Deionised water at 1 atm
Ends sealed
HEAT FLUX (W/m-2)
10^6
10^5
10^4
1
10
100
(Tw − Tsat) °C

FIGURE – 3

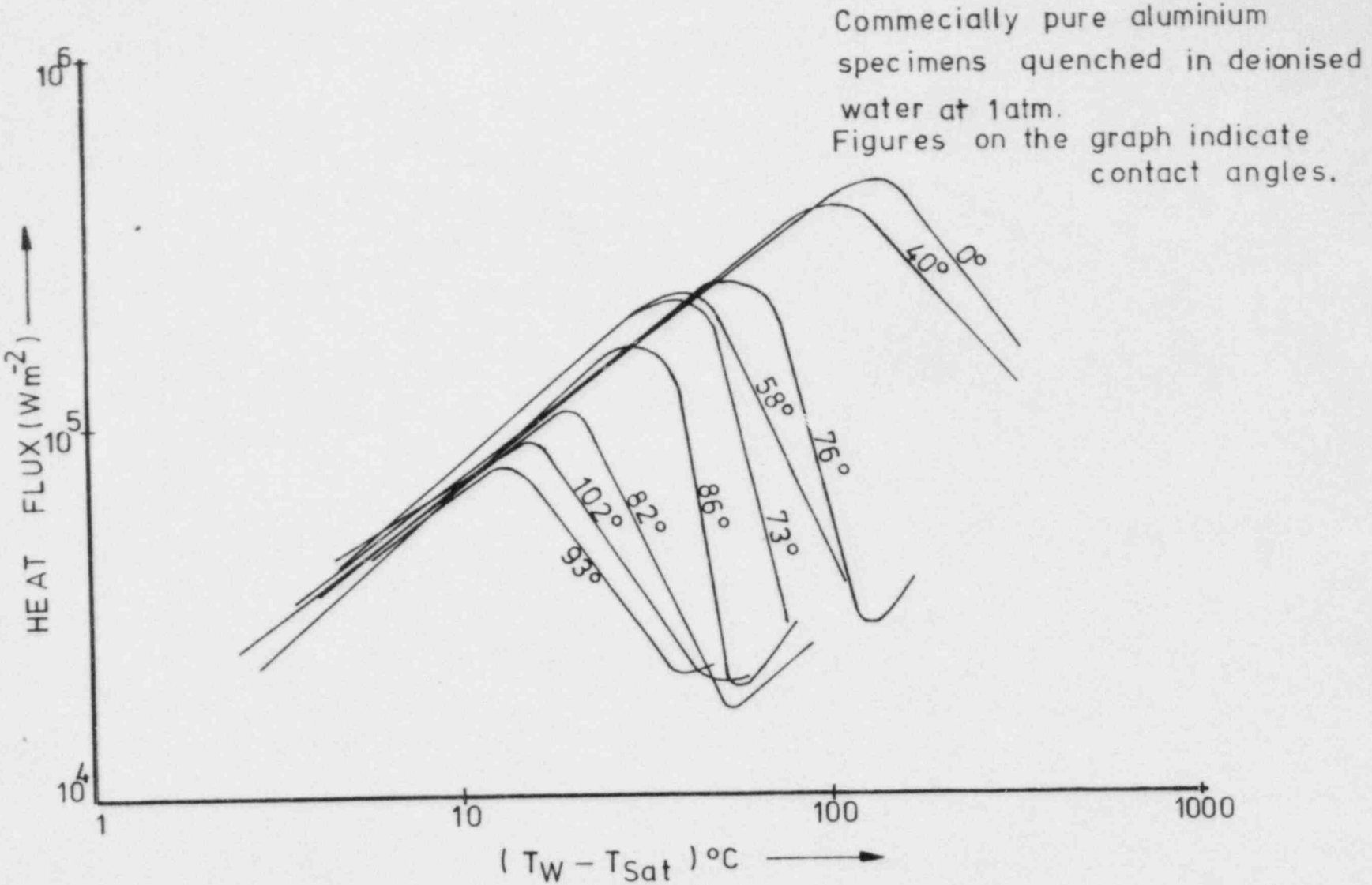
Commecially pure aluminium specimens quenched in deionised water at 1atm.
Figures on the graph indicate contact angles.
HEAT FLUX (Wm^{-2})
10^6
10^5
10^4
0°
40°
58°
76°
73°
86°
82°
102°
93°
1
10
100
1000
$(T_W - T_{Sat})$ °C

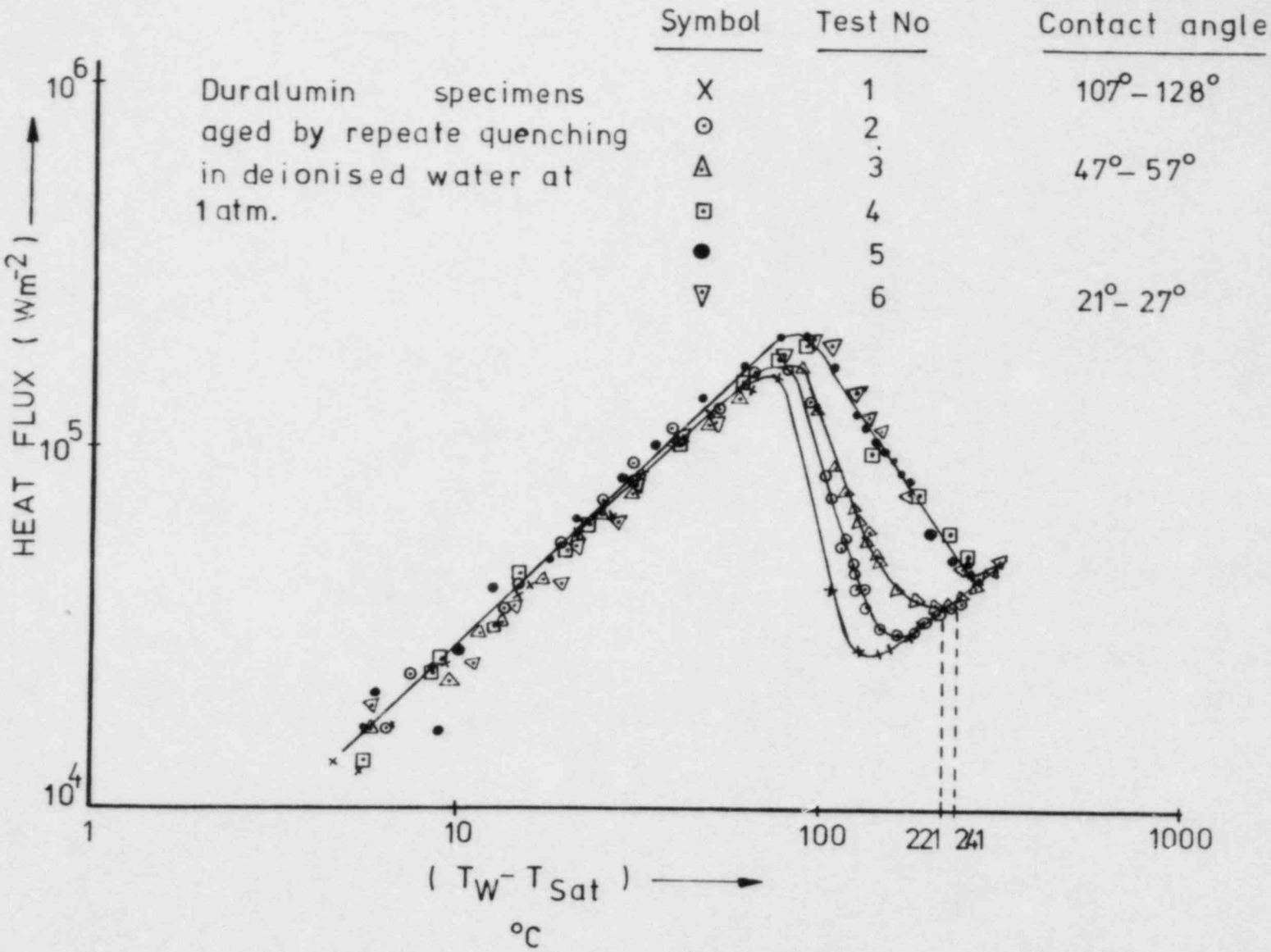
Symbol
Test No
Contact angle
Duralumin specimens aged by repeate quenching in deionised water at 1 atm.
X 1 107°–128°
⊙ 2
△ 3 47°–57°
⊡ 4
● 5
▽ 6 21°–27°
HEAT FLUX (Wm⁻²)
10⁶
10⁵
10⁴
1
10
100
221
241
1000
(Tw – Tsat)
°C

Symbol	Description	β
X	Polished	71°-74°
⊙	Smeared with silicone rubber	105°-121°

Duralumin specimens quenched in deionised water at 1 atm.

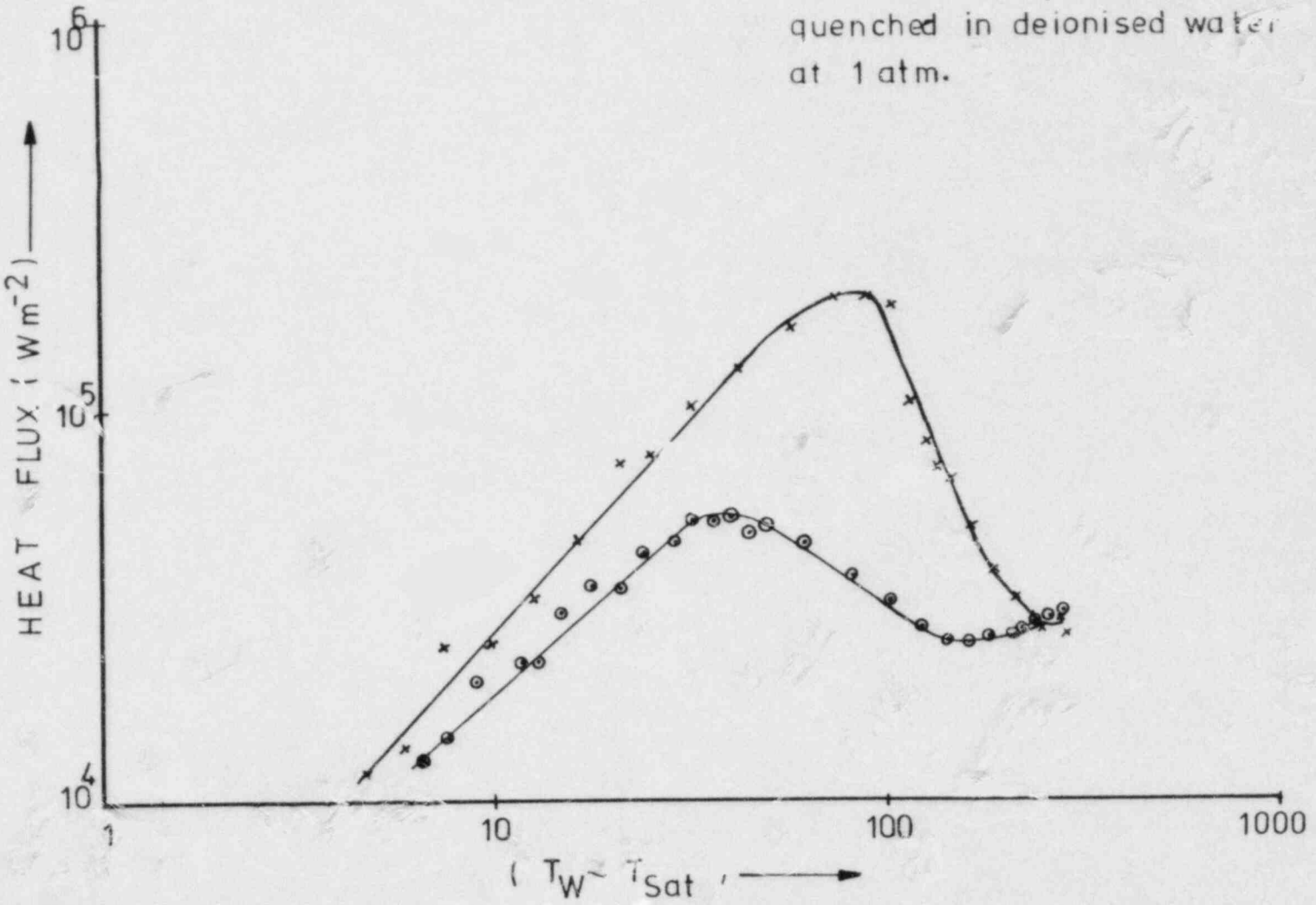

POST-CHF LOW-VOID HEAT TRANSFER OF WATER: MEASUREMENTS IN THE COMPLETE TRANSITION BOILING REGION AT ATMOSPHERIC PRESSURE

K. Johannsen and W. Meinen
Institut für Kerntechnik
Technische Universität Berlin
Marchstraße 18, 1000 Berlin 10
Federal Republic of Germany

ABSTRACT

An experimental investigation of low-void heat transfer of water has been performed in the range of CHF and the minimum stable film boiling temperature. The heat transfer system used consists of a vertically mounted copper tube of 1 cm I.D. and 5 cm length with surface-temperature controlled, indirect Joule heating. Results are presented for upflowing water at inverted annular flow conditions in the inlet subcooling range of 2.5 - 40 °C and mass flux range of 137 - 600 kg/m^{2}s in terms of boiling curves and heat transfer coefficients versus wall temperature. Heat transfer in the stationary rewetting front, which occurs within the test section during operation in the transition boiling mode, is also dealt with. At high mass flux, occurence of an "inverse rewetting front" has been observed. It is also noted that, at fixed location, minimum heat flux observed is usually not associated with the minimum stable film boiling temperature.

1. INTRODUCTION

In a great number of engineering applications, including steam generators, jets or rockets, nuclear reactors, and cryogenic systems, forced convection boiling at and beyond critical heat flux (CHF) is encountered during normal operation or may be found in the event of certain postulated accidents. In recent years, the loss-of-coolant accident (LOCA) which has been established as the design-basis accident for light-water reactors has promoted a worldwide effort for a better empirical knowledge and an adequate analytical description of the heat transfer phenomena taking place in the reactor core during the reflooding phase where the boiling curve is traversed in reverse. In spite of this research effort, the exact mechanisms for post-CHF heat transfer are still poorly understood, and reliable CHF and post-CHF correlations are not yet available for low flows, void fractions, and pressures /1/.

Traditionally, post-CHF flow boiling is subdivided into the regimes of film boiling and transition boiling. This latter section of the boiling curve is bounded by the critical heat flux and the minimum heat flux and is characterized by a negative slope, i.e., the heat

flux decreases with an increase in surface temperature. Due to this rather unique heat transfer behavior, experimental investigation of this boiling mode requires a temperature-controlled system which is difficult to realize, especially, at the high heat flux rates encountered in water boiling at low values of pressure and mass quality (and high mass flow rates).

Hence, transient techniques have usually been applied to generate low pressure data of subcooled water (e.g., /2,3/). These measurements as well as others, performed by use of the stabilizing fluid technique /4 to 6/, have not been extended up to wall temperatures high enough as to include the minimum film boiling temperature. This temperature terminates stable flow film boiling, when the boiling curve is investigated traversing it in reverse /7 to 9/ by use of a directly heated tube with an upstream hot patch to stop propagation of a rewetting front /10/. Thus, one may state that there still exists a gap of information even relative to the behavior of boiling curve of water between transition boiling at low heat flux and the minimum film boiling temperature, when pressure and quality are low. Consequently, the physical mechanisms that prevail in this range are not well understood yet. To date, it also does not seem clearly established, which temperature the minimum heat flux of the flow boiling curve at these conditions is associated with.

Despite of the recent experimental efforts cited above, one has to agree with Groeneveld's critical statements issued in his recent review on prediction methods for post-CHF heat transfer /1/, namely, that the scarce amount of available transition boiling data "is not considered sufficiently accurate and plentiful to serve as a basis for deriving a correlation. Correlations for the low-quality or subcooled film boiling region should be suspected because of the lack of a reliable data base and the difficulty in accounting for the various physical mechanisms in a single correlation".

To extend the scarce and rather unreliable data base as well as to improve understanding of the governing physical mechanisms, it seems most promising to perform better temperature-controlled, steady-state experiments that also include the lower portion of the stable film boiling region. Such experiments may be accomplished using a heat transfer system of high thermal conductance with temperature-controlled, indirect Joule heating as demonstrated previously /11, 12/. In the present paper, post-CHF heat transfer data of water at atmospheric pressure up to wall temperatures of about 500 ^{o}C will be presented that have been acquired by this experimental setup. The data cover a mass flux range of 137 - 600 kg/m^{2}s and an inlet subcooling range of 2.5 - 40 ^{o}C.

2. EXPERIMENT

The tests were conducted on a vertically mounted test section connected into a low-pressure boiling water rig /11/. A slightly simplified drawing of the test section is shown in Fig. 1. The section consists of a copper tube of 5 cm length and 32 mm O.D. (10 mm I.D.)

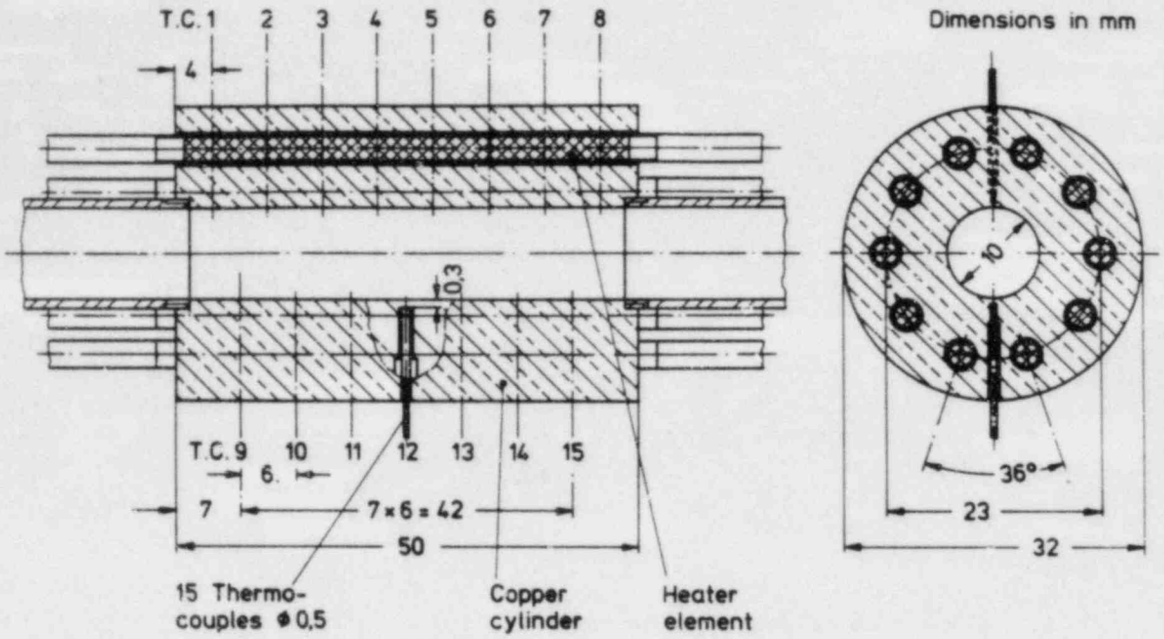

Fig. 1. Test section for post-CHF boiling studies

which is heated by ten cylindrical heating elements of 3 mm O.D. that are located on a circle of radius 11.5 mm. Since cartridge heaters of required specific power as well as dimensions have not been found available, we used stainless steel tubes of 0.33 mm wall thickness which are electrically insulated from the copper cylinder by a high-temperature cement. The heaters were carefully manufactured and selected such that the maximum deviation of their electrical resistance was well within 1 percent of the average value. For early detection of possible heater failures, their individual electrical resistances are continuously measured and recorded during operation. The test section has successfully been operated yet up to an average heat flux of 700 W/cm^2 at the inner heat transfer surface.

Since fast oxidation of the copper surface has been found to occur during operation in transient boiling mode, a nickel coating ($\sim$ 50 µm thick) has been brought up on the heat transfer surface by galvanization to diminish variation of surface conditions during a test run. Note that in previous tests /12/, a gold coating was used.

For purpose of axial temperature measurement within the test section, fifteen stainless-steel sheathed Ni-CrNi thermocouples (T.C.) of 0.05 cm O.D. were installed close to the surface of the central flow channel. The position of the junction of each individual thermocouple relative to the outer tip of the sheath was determined from X-ray photographs. After calibration, the thermocouples were press fitted into thermocouple holes (0.06 cm diameter with a reduction to 0.05 cm in T.C. tip region) and then fixed by individual clamps. Axial location of the thermocouples is shown in Fig. 1;

junction of the thermocouples was about 0.1 cm apart from flow channel surface.

Further measurements relevant to the present experiments were water flow (turbine flowmeter), inlet pressure and test section power (current and voltage measurements). Temperatures of the degassed and destilled water (electrical conductivity less than 2 µS/cm) used were measured by NiCrNi thermocouples at the flowmeter and at test section entrance and exit. Saturation temperature was calculated from the measured pressure.

In the measurements, the heater power is controlled by feedback control in dependence of surface temperature using a weighted average of the signals sensed by three of the thermocouples within the test section (T.C. no. 2, 4, and 6; cf. Fig. 1) to secure stable operation of test section within the transition boiling region including its bounds DNB and minimum film boiling temperature. The criteria applied in design of the temperature-control circuit, the design itself, and the compensation function finally selected have been described in a previous paper /12/.

The physical realization of the compensation function, i.e., a PID-controller with 4th order filtering, was performed by analog computer components and a Krohn-Hite filter. A simplified block diagram of the control loop is presented in Fig. 2. Temperature signals from the thermocouples within the test section are fed into a signal conditioner which evaluates a suitably weighted average signal. In a comparator, this voltage signal is compared with a control point voltage equivalent to a set point or reference temperature which establishes the process operating point. The difference of both signals is then amplified, passed through a 4th order low-pass filter, and fed

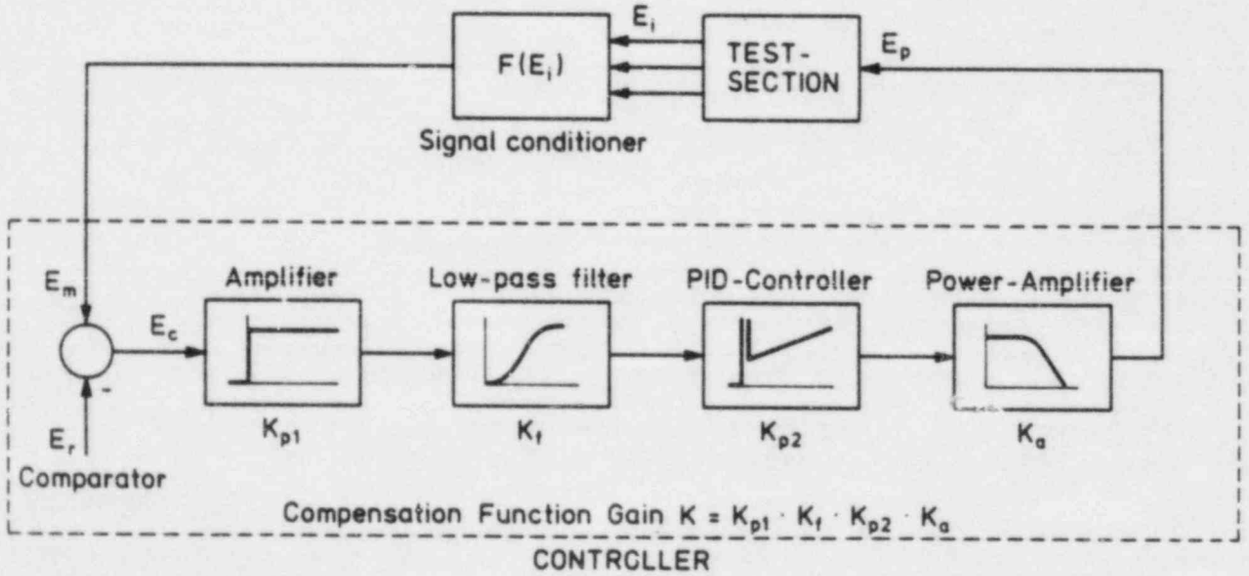

Fig. 2. Simplified block diagram of control system

forward to the PID-controller. The controller which performs amplifying and compensating functions, finally produces the input signal to the power amplifier. The output of the DC power supply unit (max. current 2,500 A at 15 V) establishes the heater power level and also introduces low frequency variations in power in accordance with the base input voltage delivered by the controller. It may be noted that the measured Bode diagram of the power supply component reveals a corner frequency of approximately 200 Hz; up to about 500 Hz, its transfer function is almost invariant to variations in power amplitude. Therefore, the power supply system could safely be considered to contain no significant dynamics in view of the low-frequency control.

The characteristics of the control circuit have been investigated measuring frequency transfer functions in closed loop operation of the test section, when it experienced the situations of critical heat flux as well as transition boiling, that in open loop operation would be unstable /12/. The corresponding Bode diagrams revealed that the damping characteristics of the control loop were satisfactory in both cases. Temperature variations at frequencies less than about 0.5 Hz are well controlled, while fluctuations above 1.0 Hz are compensated by less than about 10 percent, and thus may be considered to be only slightly affected by the controller. In case of transition boiling, measurements indicated a resonance peak to occur at a frequency of roughly 1.5 Hz. Presumably, this frequency corresponds to the characteristic rewetting frequency at the given operating point of the test section, however, systematic studies using signals from single thermocouples are required to substantiate this conclusion.

The experimental procedure applied in the measurements was as follows: During each test run, pressure, flow rate, and water temperature at test section inlet were fixed, while set-point wall temperature versus average wall heat flux was traversed from nucleate to film boiling (max. wall temperature about 500 ^{o} C). Small incremental changes of set-point temperature were chosen in those regions of the boiling curve where large variations of its gradient occur. After each change, steady-state conditions were established prior to data collection. The test section power and all wall thermocouple signals were scanned in 1 second intervals for 20 seconds, stored, and then averaged by a data processing unit (Hewlett-Packard, HP 3054/85A). Steady-state conditions were considered to be established when averaged data of consecutive collections in 1 minute intervals did not reveal any changes but statistical variations around constant mean values. Flow parameters that were practically invariant with time were only collected once during each scanning interval applying 100 ms integration time per value. Data averages of usually several scannings for each operating point were carefully processed in the on-line computer, i.e. corrected for calibration errors etc., converted to engineering units, and recorded for further evaluation. In evaluating the power transfered to the fluid via the inner heat transfer surface, heat loss through the outer insulated walls as found from heat loss calibration runs was considered.

For data reduction, a two-dimensional, steady-state, multi-regional heat conduction analysis of the test section has been performed to determine axial distributions of temperature and heat flux at the heat transfer surface. Assuming that circumferential variations of temperature induced by the arrangement of heating elements are negligible close to heat transfer surface, the heating elements were represented by a middle annular region of same thickness as the diameter of the heating element, with a weighted average of its thermal conductivity. The specific heat generation rate in this zone was determined from the measured average power reduced by the heat losses. Thus, the outer walls could be considered adiabatic which seemed permissible in view of both the small percentage of the actual heat losses and resulting simplicity. Further details of the calculational procedure may be found in reference 12.

3. EXPERIMENTAL RESULTS

The present results have been obtained almost as byproducts during the process of improving the test section relative to admissable maximum power and temperature during longtime operation as well as accuracy of measurement. Thus experiments have been performed at rather high mass fluxes (max. 1000 kg/m^{2}s) and subcoolings up to 40 ^{o}C. Further tests to be conducted in the immediate future will preferably cover the low mass flow range at high entrance subcoolings.

In this paper, we will emphasize on the principal functional dependence of post-CHF heat transfer in the range of CHF and minimum stable film boiling temperature on the relevant parameters and some special phenomena observed.

3.1. Boiling Curve of Test Section

The "boiling curve of the test section" may be constructed plotting average wall heat flux versus average wall temperature for each experimental point. In Fig. 3, such a plot is shown for a fixed value mass flux (600 kg/m^{2}s) and subcooling (2.5 ^{o}C). Numbers at the symbols indicate those experimental points, for which the associated axial wall temperature distributions are shown in Fig. 4.

Though the preset reference wall temperature during this experimental run was increased by small increments only, Fig. 3 reveals that rather large discontinuities occur in the heat flux within the transition boiling portion of the boiling curve. This behavior has to be attributed to the fact that, by the feedback control, stable operation can only be secured for a given average of wall temperature rather than an axially constant wall temperature. At the observed discontinuities of heat flux, the character of axial wall temperature distributions drastically changes due to either increasing local variations in heat transfer conditions imposed by the fluid flow at the surface that cannot be compensated by axial conduction anymore, or due to the opposite effect.

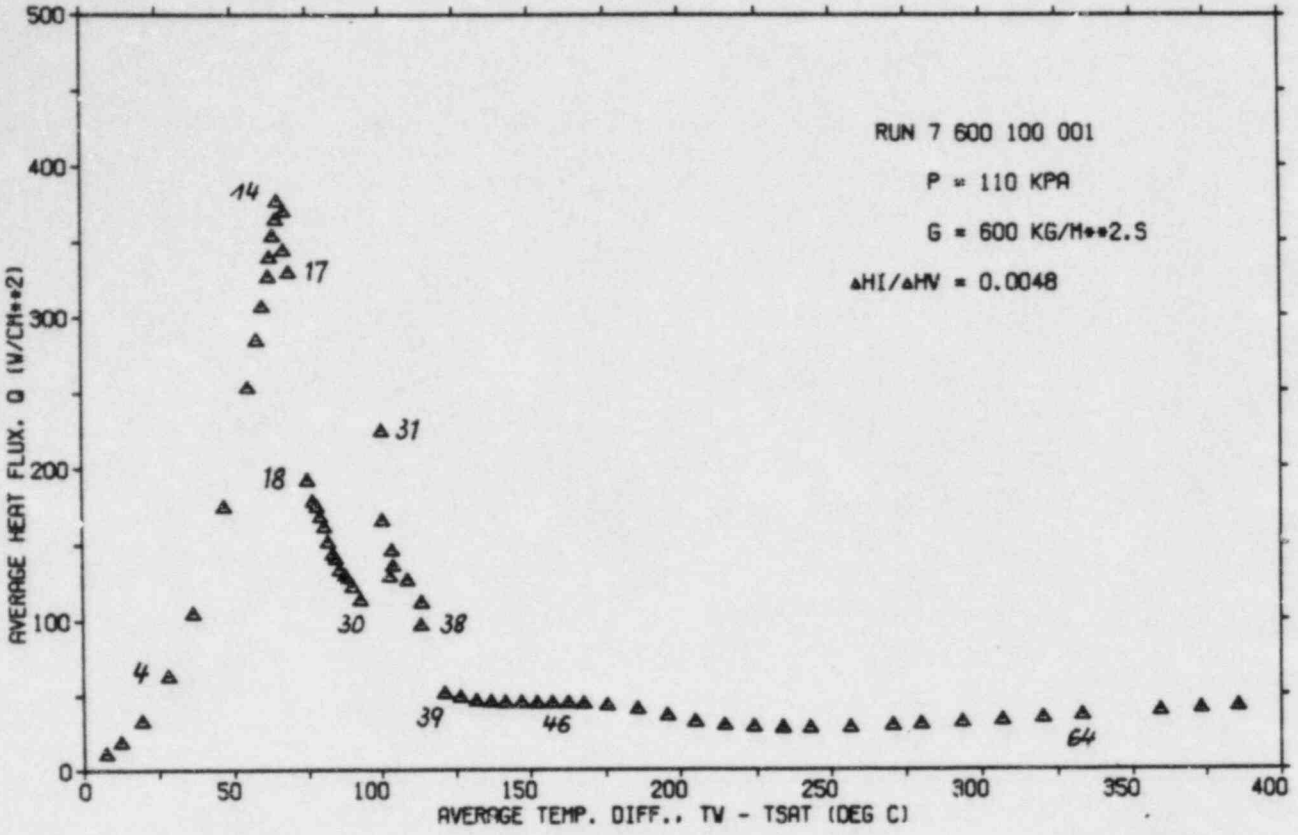

Fig. 3. Sample for boiling curve of test section (ΔT_{SUB} = 2.5 °C)

3.2. Axial Wall Temperature Distributions

For example, Fig. 4 a shows the axial temperature distributions corresponding to the experimental points (E.P.) 4, 14 and 17 the latter of which are close to or at maximum average heat flux. At E.P. no. 4, the entire surface is in developed nucleate boiling, while at E.P. Nr. 14 maximum heat flux is just locally reached at the position z ≈ 2.2 ($q"_{CHF}$ = 395 W/cm^2). The curve for E.P. no. 17, average maximum heat flux has been exceeded, shows that the position of maximum wall temperature and critical heat flux has shifted upstream. CHF occurs very close to the beginning of heated length, followed by a region which is in the transition boiling mode. At the downstream end of heated length, nucleate boiling still prevails. Note, that axial variations of wall temperature are rather small, since imposed differences in local heat transfer and, subsequently, heat flux in the radial direction may still be sufficiently compensated by axial conduction within the copper cylinder. Now, with a further slight increase of reference temperature, CHF location has reached the beginning of heated length which results in a further increase of axial heat flux in the upstream direction;

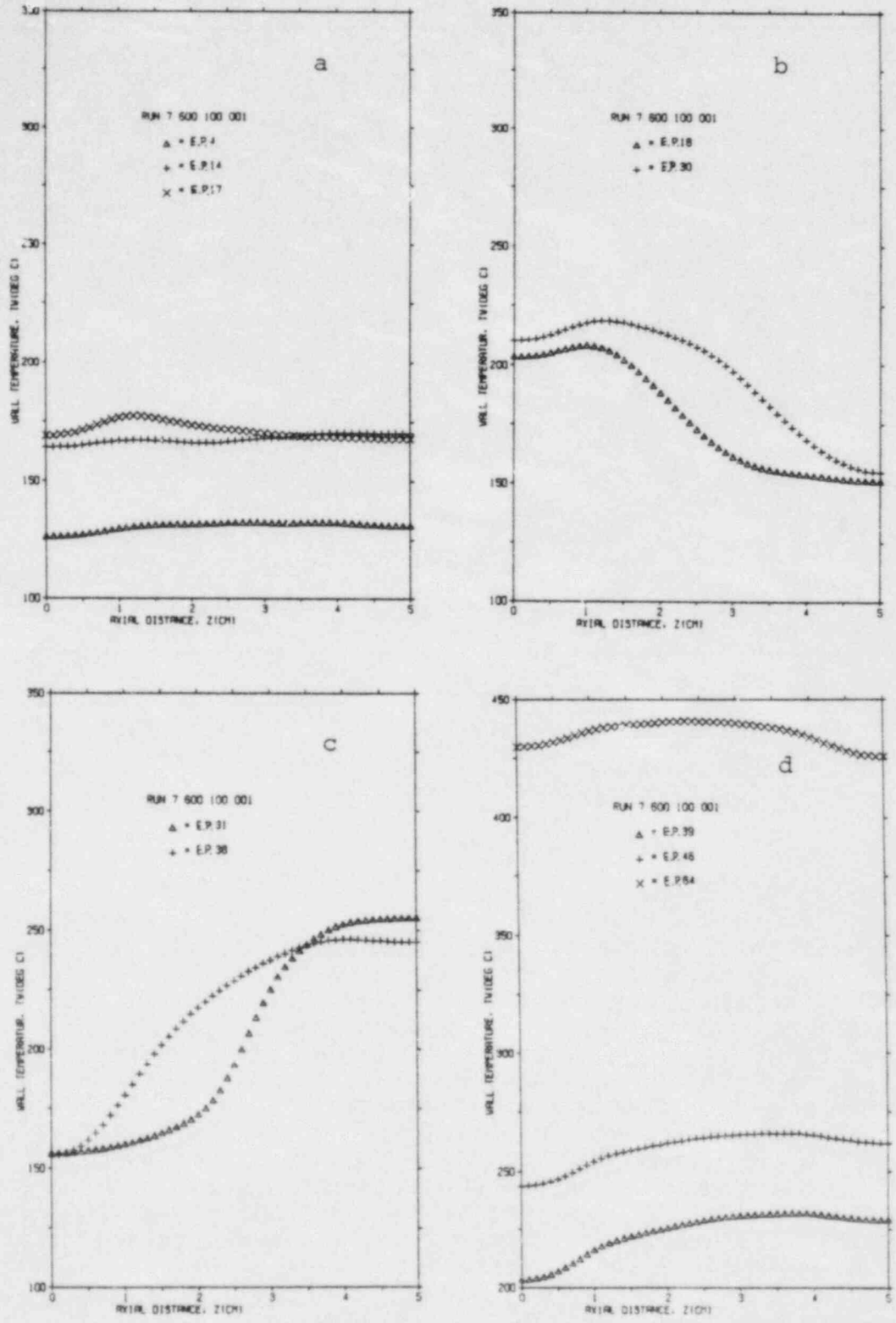

Fig. 4. Axial temperature distributions at difference measurement points of Fig. 3 case

thus, the region of heated length which experiences transition boiling also further extends: A thermally unstable situation within the test section develops. Finally, a different, again rather stable temperature profile is reached as shown in Fig. 4b (E.P. no. 18), which does not change much in character with further increase in reference temperature until E.P. no. 30.

The situation shown in Fig. 4b is rather unique inasmuch an upstream CHF occurs which is followed by strongly increasing transition boiling heat transfer in flow direction (inverse rewetting front). At the end of heated length, wall temperature is less than CHF temperature and nucleate boiling exists. This special situation has only been observed in such a characteristic development in the runs with high mass fluxes (600 kg/m^{2}s). With lower mass fluxes, the temperature distribution of Fig. 4a was directly followed by that shown in Fig. 4c, as one would expect. It usually occurs, when CHF has (also) been exceeded at the downstream end (cf. discussion in ref. /12/).

Fig. 4c represents the situation of typical rewetting fronts with zero propagation velocity at different average heat fluxes. Due to the high thermal conductance of the test section, the axial temperature variation is rather gradual, and thus accessible to comparably accurate measurement as intended by the design. This temperature distribution changes again to an axially rather smooth one (Fig. 4d), once the (weighted average) reference temperature has been set such that CHF temperature is also exceeded at upstream end of heated length.

3.3. Axial Heat Flux Distributions

In Figs. 5 and 6, heat flux at the heat transfer surface in both the radial and axial directions is plotted as a function of axial coordinate for the experimental points 18 ("inverse rewetting front") and 31 (regular rewetting front), respectively, of the run shown in Fig. 3. Note that axial heat conduction is of comparable order of magnitude as radial conduction, due to the high thermal conductivity and wall thickness of the test section. In both cases, surface heat transfer coefficient changes by one order of magnitude along the heated length, absolute values being about 25 percent less in the inverse rewetting front case, since the presence of a vapor blanket upstream of transition boiling reduces downstream heat transfer considerably. The value of maximum radial heat flux (DNB heat flux) is roughly a third less, though the local equilibrium mass quality is reduced from 0.017 to 0.009, thus constituting a strong example, where the local conditions do not exclusively determine CHF in low quality flow boiling.

3.4. Local Boiling Curves

Having once evaluated wall heat flux and temperature as a function of axial coordinate, boiling curves may be constructed for any fixed value of relative distance from the entrance, z/D. As an example, the resultant boiling curve at the midplane of the test section (z/D = 2.5)

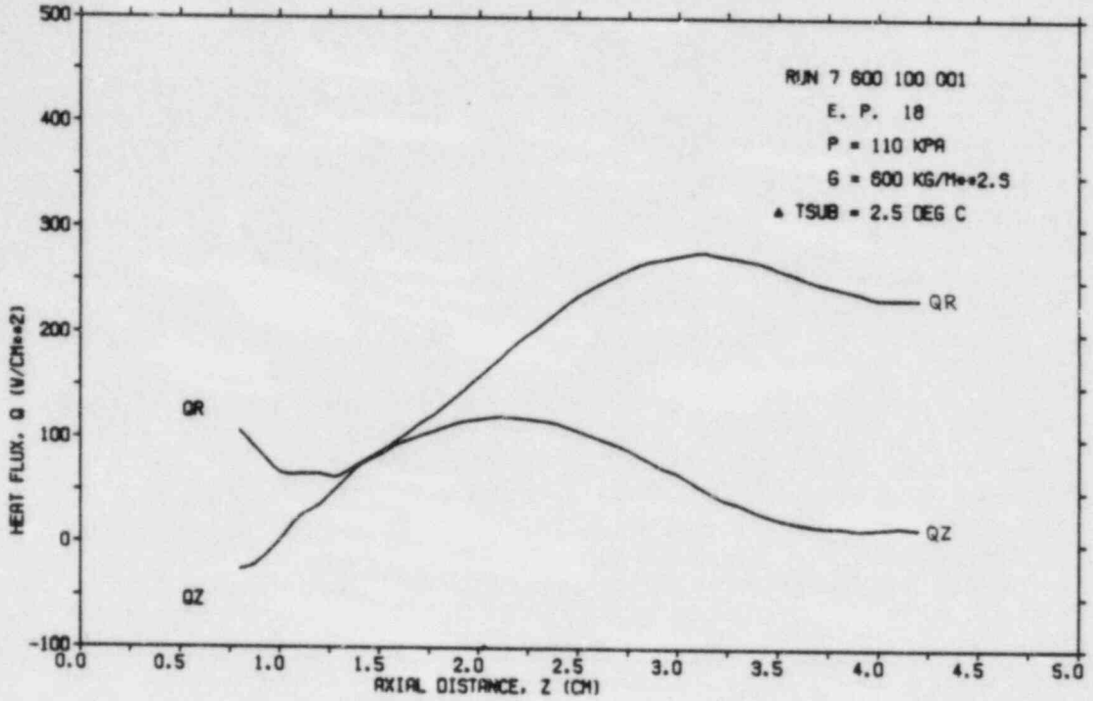

Fig. 5. Axial and radial heat flux components at heat transfer surface in an "inverse rewetting front" (positive values when directed against coordinate direction)

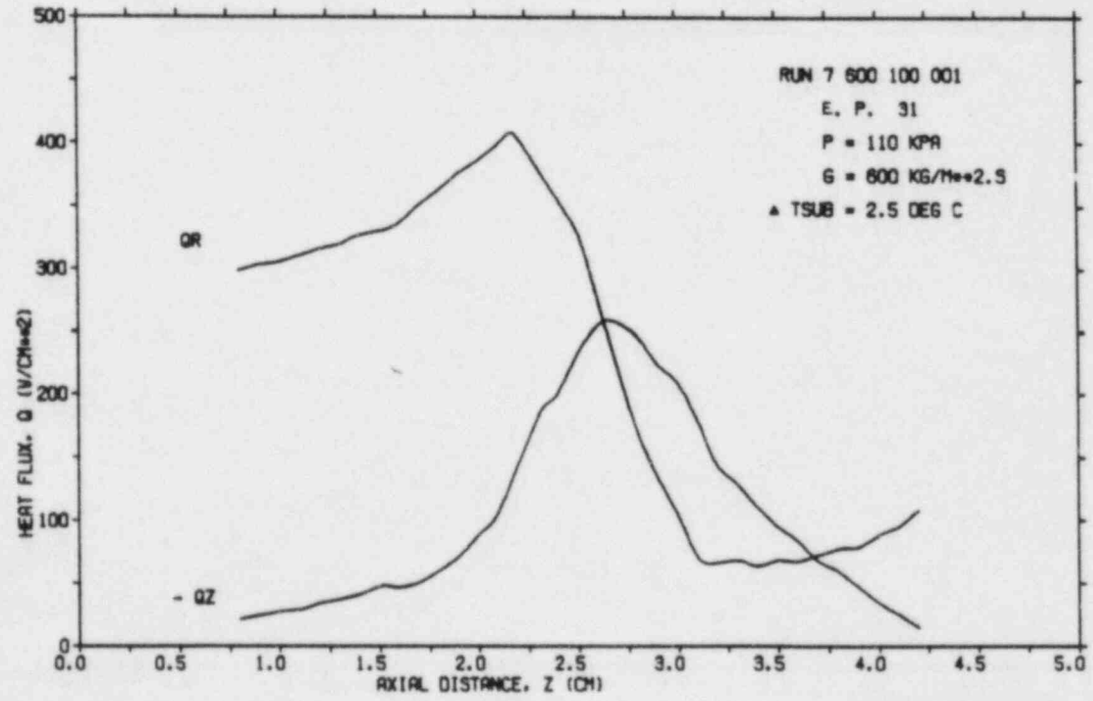

Fig. 6. Axial and radial heat flux components at heat transfer surface in a rewetting front (positive values when directed against coordinate direction)

is presented for the case discussed above (Fig. 3) in Fig. 7. It may be noted that a distinct minimum of boiling curve in the post-CHF region cannot be identified.

Effect of Inlet Subcooling. The effect of inlet subcooling for a fixed mass flux of 200 kg/m^{2}s may be deduced from Fig. 8, where boiling curves at fixed z/D = 2.5 for inlet flow subcooling varying from 2.5 ^{o}C to 40 ^{o}C are shown. In line with expectations and results of previous investigations /3,12/, the transition boiling heat flux increases with an increase in subcooling.

Though the difference beween wall temperature and saturation temperature has been extended up to 400 degree C in these investigations, none of the curves reveals any notable increase of heat flux even at the highest wall temperatures yet, which typically is associated with the occurence of stable film boiling.

Effect of Mass Flux. The effect of a change in mass flux may be infered from Fig. 9, where (mid-plane) boiling curves are plotted for mass fluxes of 137 and 600 kg/m^{2}s, respectively. In the nucleate boiling region, the heat flux decreases at a fixed temperature difference with an increase in mass flux. Interpreting transition boiling

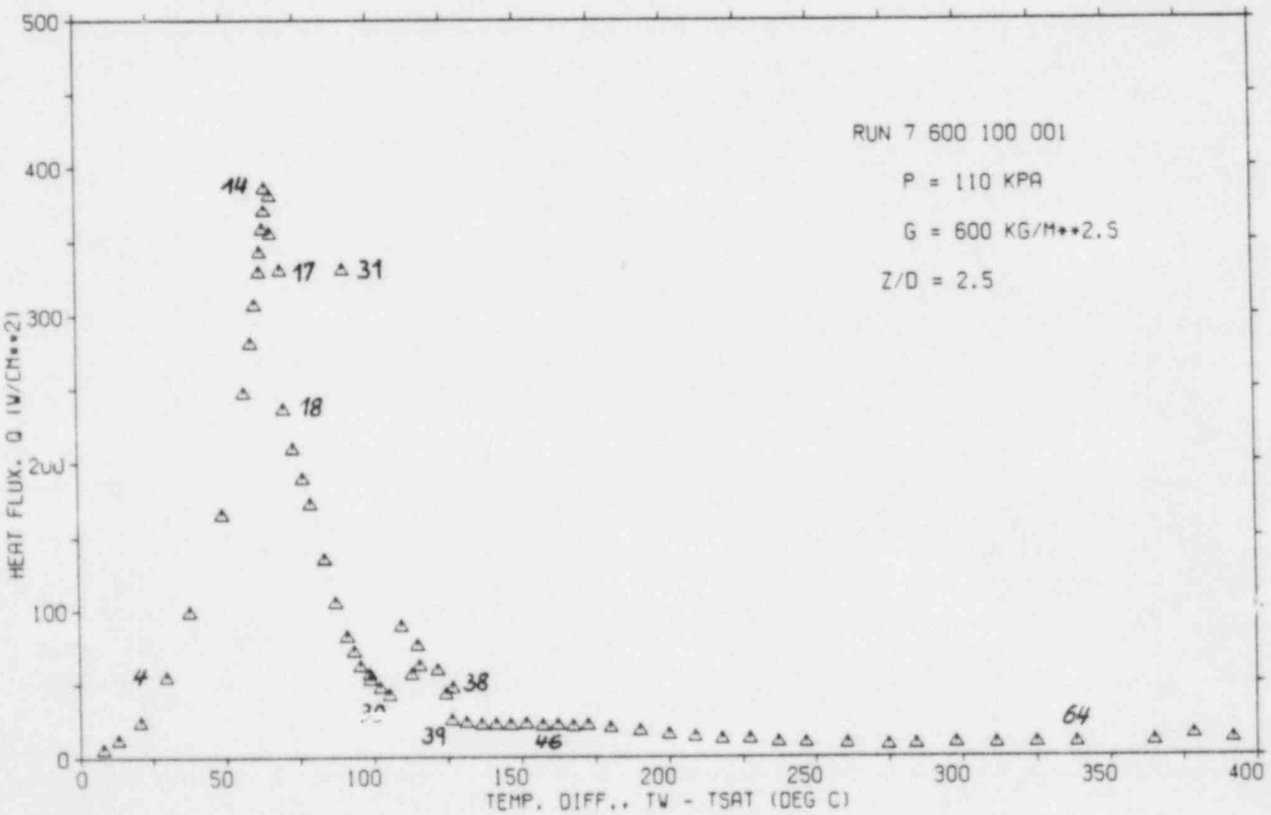

Fig. 7. Sample boiling curve at mid-plane of test section (ΔT_{SUB} = 2.5 ^{o}C)

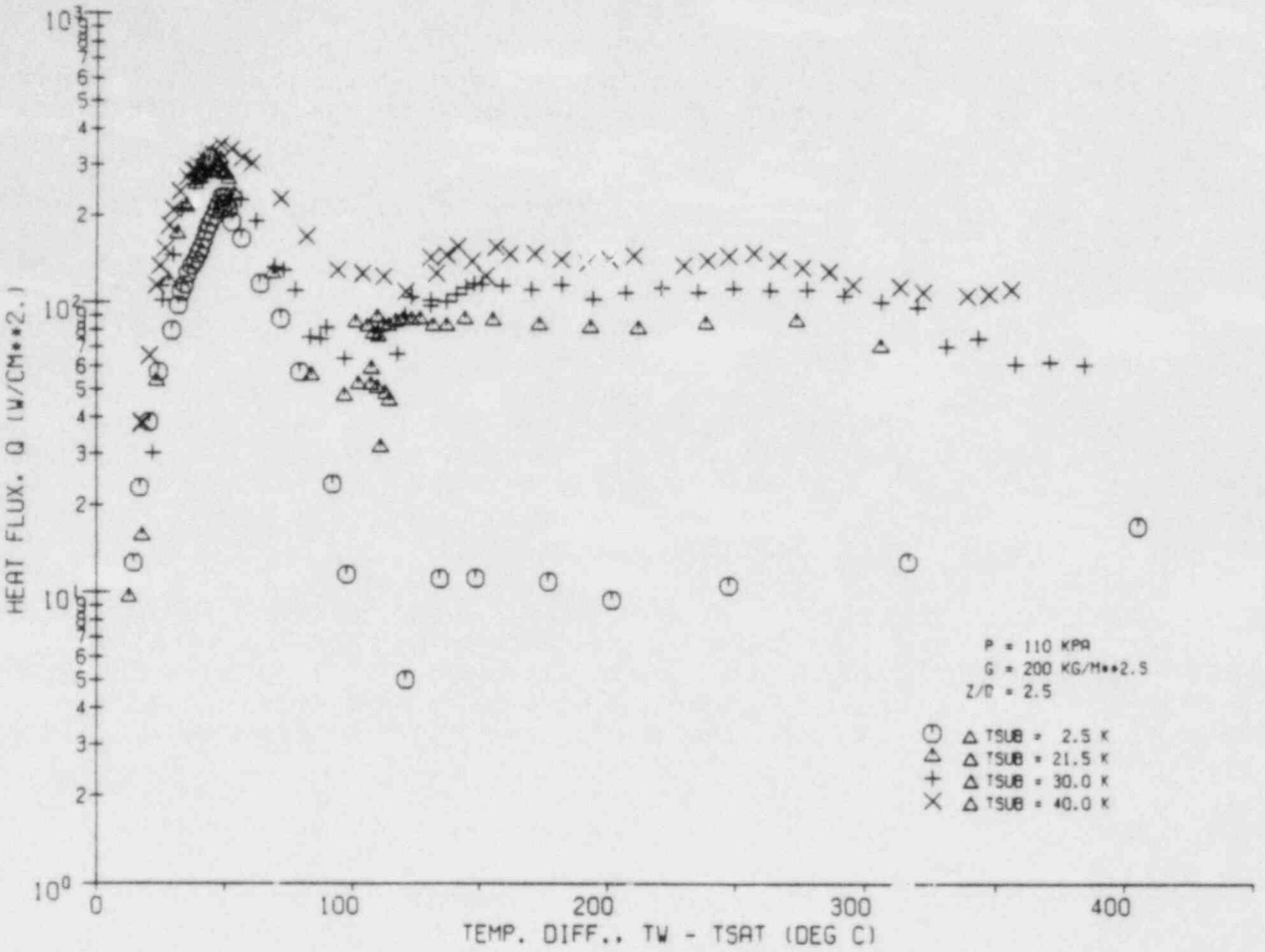

Fig. 8. Effect of inlet subcooling on boiling curve

as an intermediate mode of nucleate and film boiling heat transfer, mass flux is expected to have the opposite effect on CHF and transition boiling heat flux, for the favourable effects of improved convection on bubble removal at higher mass fluxes, vapor film heat transfer in film boiling, and more effective wall-liquid interaction. Fig. 9 appropriately exhibits this trend.

The post-CHF data for the lower mass flux show a minimum in heat flux at about 110 °C wall temperature above saturation, followed by an increase of heat flux with temperature difference and a relative maximum of heat flux at about 240 °C temperature difference. Then the heat flux again decreases. A similar, more pronounced anomaly seems to exist in the higher mass flux data at temperature differences between 215 and 280 °C, that disturbes the continuous trend delivered by the other data. As stable film boiling is approached, both data sets seem to merge. No satisfactory explanation of these peculiarities can be offered yet. At mass flux of 600 kg/m^{2}s, the minimum heat flux is reached at 400 °C wall temperature.

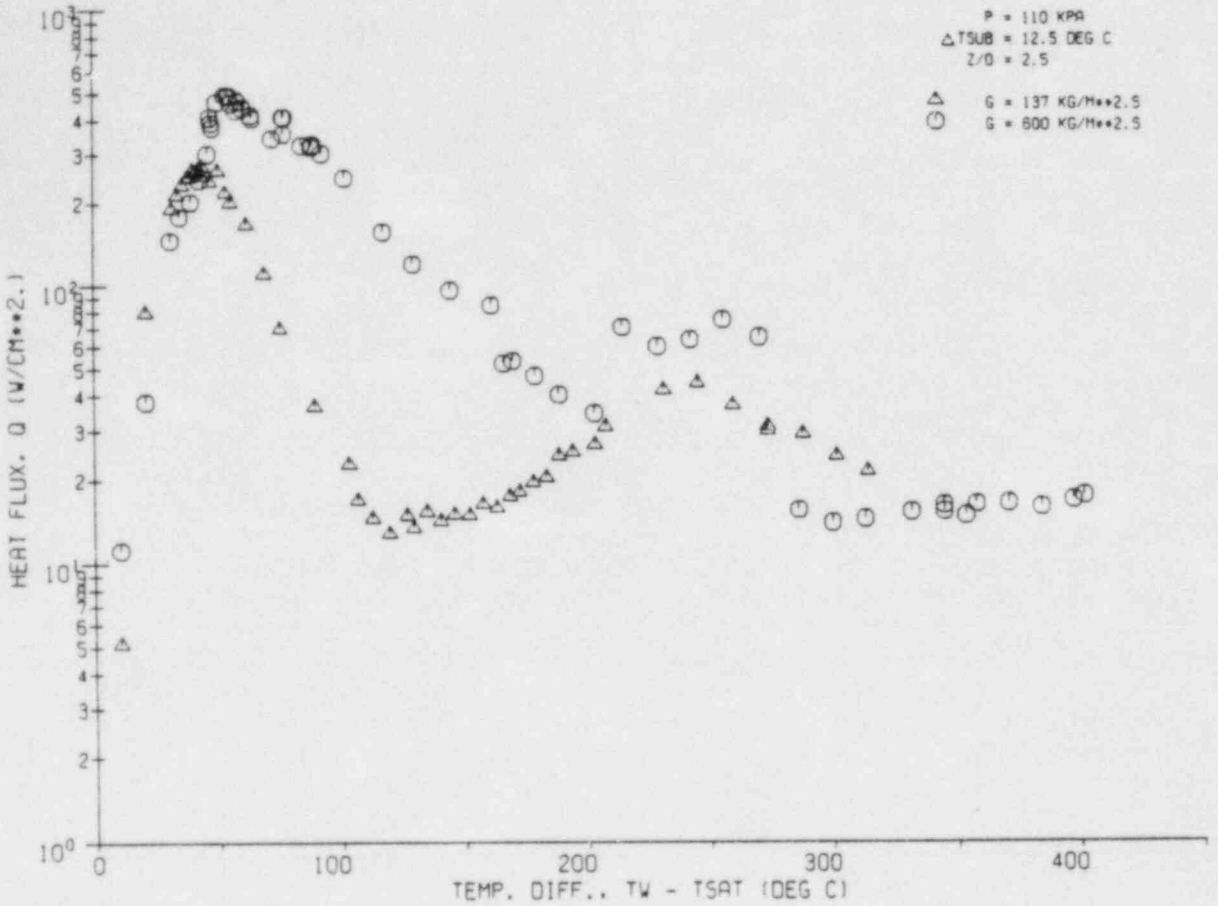

Fig. 9. Effect of mass flux on boiling curve

Effect of Distance from Inlet. This effect will be discussed in a later section in terms of variations of the local heat transfer coefficient.

3.5. CHF and Minimum Heat Flux

For a fixed inlet subcooling of 2.5 °C, maximum values of CHF regardless of axial location ranged from 232,5 W/cm^2 at a mass flux 200 kg/m^{2}s up to 716 W/cm^2 at a mass flux of 1000 kg/m^{2}s, thus demonstrating a strong mass flux effect. The effect of inlet subcooling was not found to be equally clear, though there seems to be a trend of an increase of CHF with inlet subcooling. More measurements at different mass fluxes are required to substantiate this finding.

CHF was found to depend on axial location at fixed inlet flow conditions. This length effect also depends on the axial wall temperature distribution, i.e., whether we consider the maximum heat flux occuring in a situation which is characterized by a temperature distribution shown in Figs. 4a, b, or c, respectively. At a rather

constant axial wall temperature as in Fig. 4a, CHF does not depend much on length in the present short test section (L/D = 5). When CHF occurs in a rewetting front as represented by Figs. 4b and c, CHF may vary rather strongly with position; then the temperature that CHF is associated with, may also change. For instance, at a mass flux of 200 kg/m^{2}s, absolute values of CHF have been found to be higher (by up to about 11 percent) in this situation only at the higher inlet subcoolings investigated (30 °C, 40 °C); at an inlet subcooling of 21.5 °C and less, the values were lower.

The effect of upstream history on CHF and the corresponding temperature is also exemplified in Fig. 10, which is for a mass flux of 600 kg/m^{2}s and an inlet subcooling of 2.5 °C. The triangle symbols indicate the heat flux versus wall temperature at the midplane of test section, z/D = 2.5, of the various experimental points as identically shown in Fig. 7. For the two experimental points no. 18 and 31, that are typical for an inverse and a regular rewetting front within the test section (cf. also Figs. 4b and 4c), respectively, there are also plotted curves of local heat flux vs. local wall temperature as occuring along the heat transfer surface within 0.8 and 4.2 cm distance from beginning of heated length. The arrows at the curves designate the direction that they are traversed downstream. These boiling curves are traversed in reverse at E.P. 18 and in flow direction at E.P. 31, respectively. Note that, due to the completely different upstream history of the flow, absolute values of CHF as well as transition boiling heat transfer differ remarkably in both cases. The minimum heat flux values are practically identical, though the temperatures at which they occur differ by about 30 °C. In the nucleate boiling region, upstream effects do not seem to play a major role. This example, though rather extreme, indicates that critical heat flux in low quality boiling quench fronts is not exclusively determined by the local flow conditions but may strongly depend on the upstream history of the flow.

The boiling curves presented in Figs. 8 and 9 as well as those measured by others at similar conditions /3/ do not exhibit the nice, unequivocal shape in the post-CHF region with one distinct minimum in heat flux as generally suggested in heat transfer textbooks. In Fig. 8, where boiling curves at the mid-plane of test section are shown, a minimum in heat flux can only be identified at the two lower values of subcooling. The corresponding wall temperature is around 220 °C and thus hardly identical with the minimum stable film boiling temperature which, according to the measurements of Fung /8, 13/, is expected to be around 400 °C. At the higher values of inlet subcooling (30 °C and 40 °C, respectively), minimum values of heat flux are found at 441 °C and 486 °C, respectively, which seems to be somewhat closer to be expected minimum stable film boiling temperature. This remarkable difference may be attributed to the fact that, in the first case, the minimum is experienced during an axial temperature distribution characteristic to a rewetting front (Fig. 4c), while in the latter case the minimum is found at the situation, where CHF is exceeded along the entire test section (cf. Fig. 4d). If we search in the data for the lowest value of local heat flux occuring just before this event takes place, the corresponding wall temperatures are found to be between 220 °C and 250 °C.

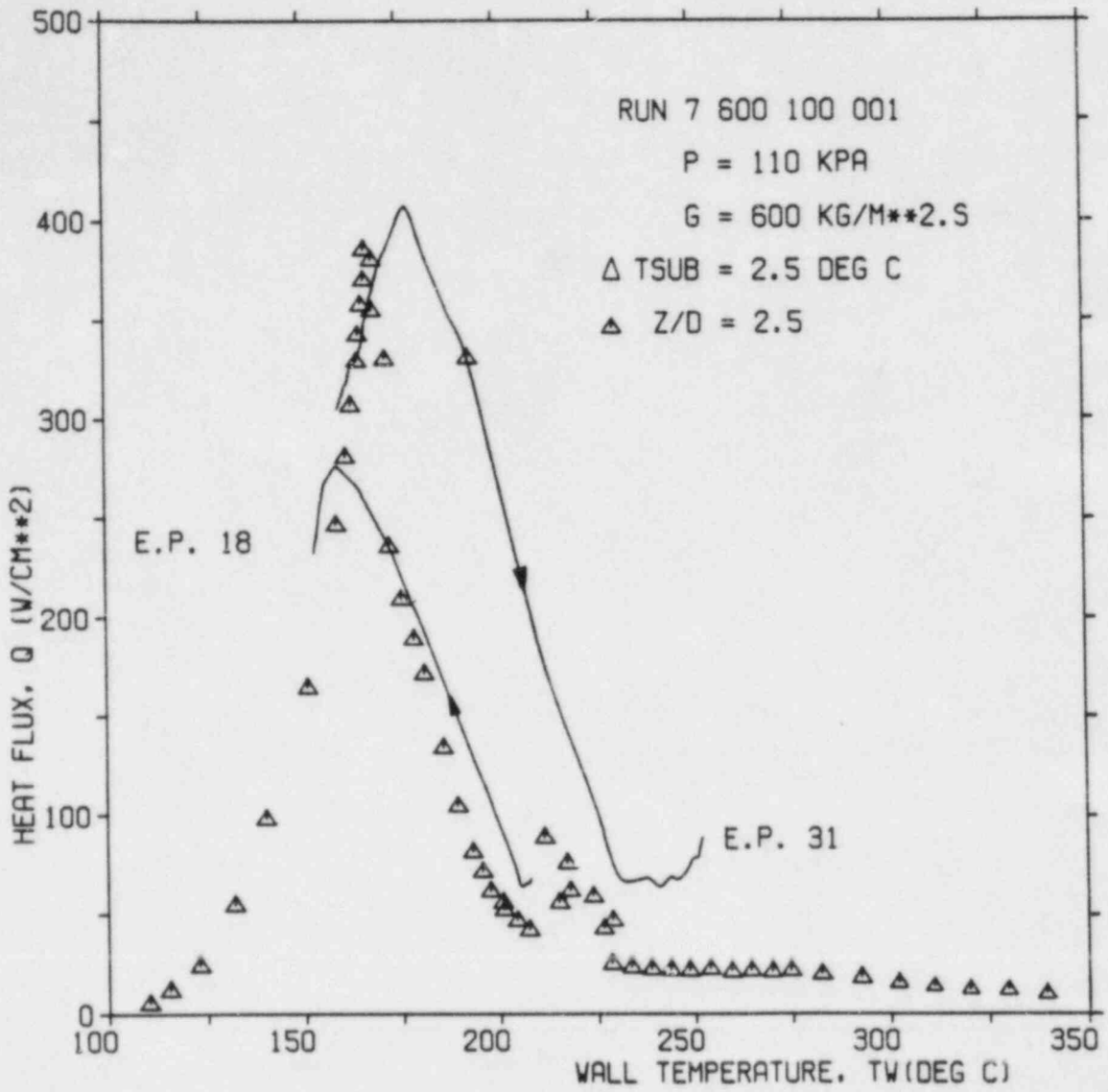

Fig. 10. Effect of axial distance on heat transfer in the transition boiling region

The absolute values of minimum heat flux increase the more the inlet subcooling is raised, regardless of axial location considered. The lowest absolute values found do not occur at the mid-plane but elsewhere along the test section; they may be more than fifty percent less than those at z/D = 2.5.

In conclusion, one may state that the occurence of relative and absolute minima of heat flux in the boiling curve as well as the associated wall temperatures obviously strongly depends on the different physical mechanisms that prevail in the specific situation. Further work is required to identify these various mechanisms.

3.6 Heat Transfer Coefficients

The local heat transfer coefficient is defined as the ratio of local wall heat flux and the associated difference between wall temperature and saturation temperature. In Fig. 11, this heat transfer coefficient is plotted versus wall temperature for the conditions which are identical to those already considered in Fig. 8 in terms of boiling curves. Again, it is seen that post-CHF heat transfer is

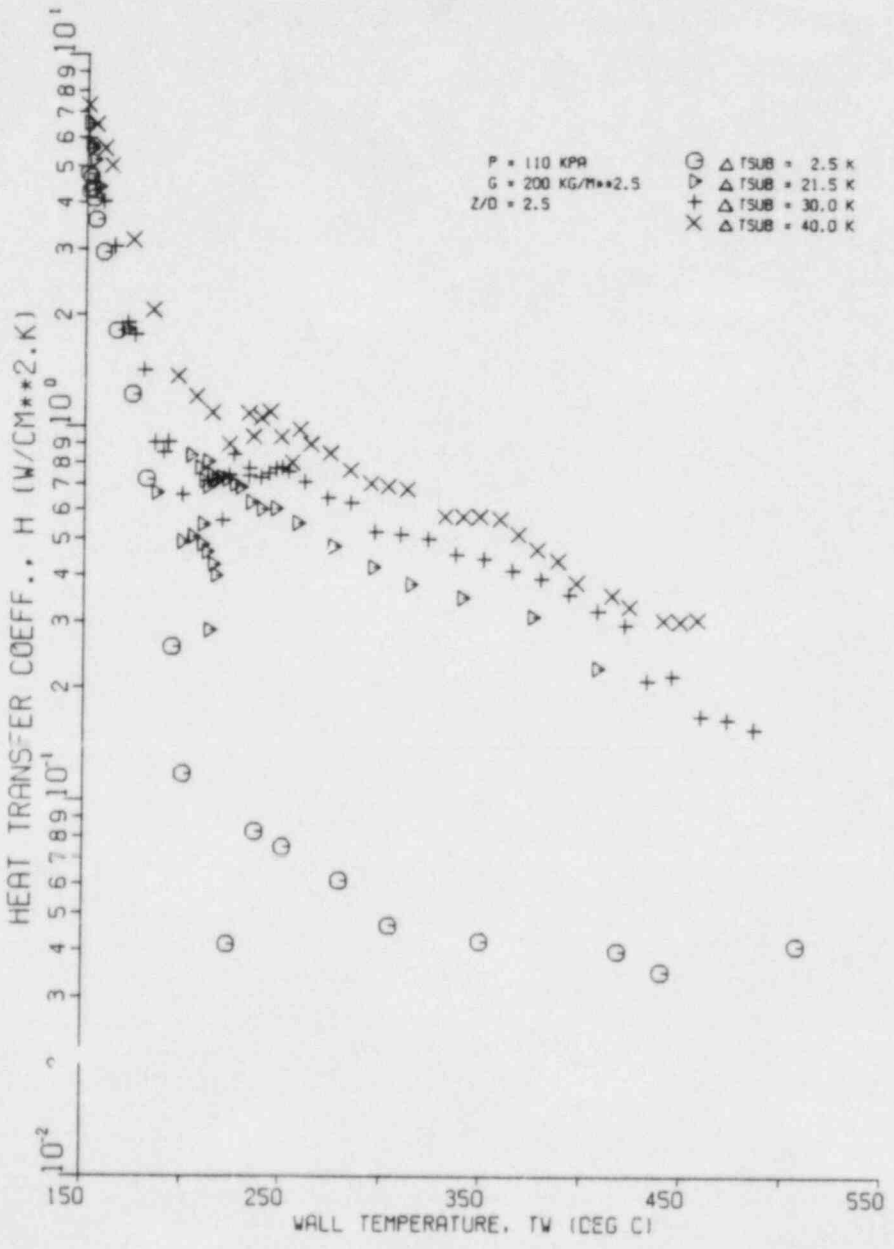

Fig. 11. Effect of subcooling on heat transfer coefficient in post-CHF region

improved by raising the inlet flow subcooling. It further may be noted that, at a wall temperature of roughly 220 °C, the gradient of a curve drawn through the data would strongly change, indicating a change in heat transfer mechanism, which obviously takes place once CHF has also been exceeded at the inlet of test section.

This behavior may more clearly be seen in Fig. 12, where, for a fixed set of parameters, values of the heat transfer coefficient are

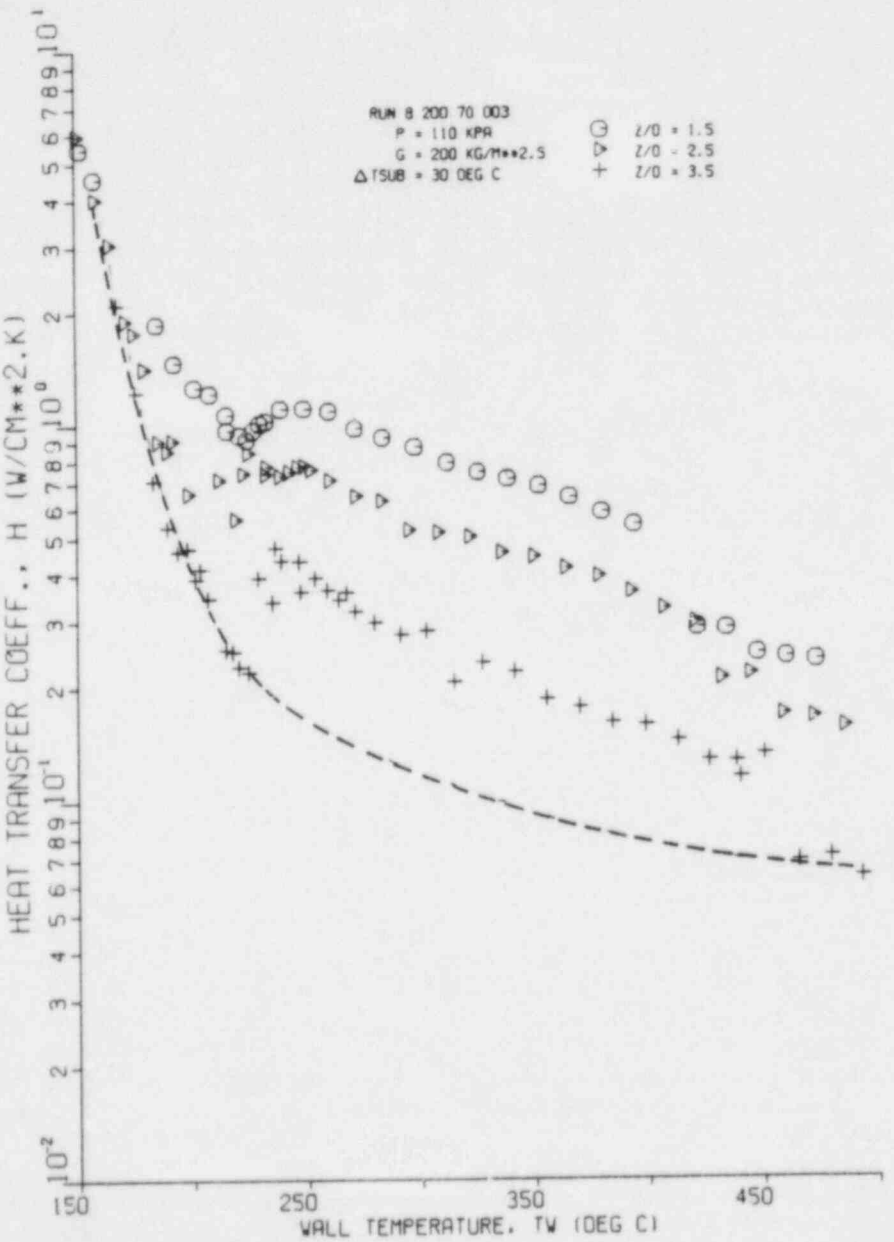

Fig. 12. Effect of axial distance from inlet on heat transfer coefficient in post-CHF region

plotted for three different axial locations. A dashed line has deliberately been drawn through the set of data for z/D = 3.5. It seems that, at wall temperatures between roughly 220 °C and 440 °C, an intermediate rather efficient heat transfer process prevails which is quite different from that within a rewetting front and that in the neighborhood of minimum stable film temperature. No conclusive explanation on the nature of this process can be offered yet. We are inclined to suspect, that in this intermediate region essentially film boiling exists where neither the interface of the liquid core nor entrained droplets within the vapor film get in close contact with the hot wall. There is some reason to believe in this hypothesis, since measured temperature fluctuations have been found to practically die out as soon as CHF is exceeded at the entrance of heated length /12/. Nevertheless, both the possibly wavy interface as well as entrained liquid droplets may have some effect in perturbing the vapor boundary layer near the wall when the liquid is subcooled. At wall temperatures around 400 °C, the laminar vapor sublayer cannot be affected anymore by occasionally penetrating liquid since, due to appreciable vapor superheat, liquid is vaporized before it approaches close enough. This reasoning would explain the obvious decrease in heat transfer rate which is in the expected range of minimum stable film boiling temperature. The length effect can be attributed to increasing vapor film thickness with axial distance from inlet.

The latter explanation may also be used to interpret the length effect on true transition boiling heat transfer: Considering transition boiling as an intermediate mode of nucleate and film boiling, a thicker vapor film will result in both a lower heat transfer rate during the time fraction of film boiling and in a lower probability of liquid-wall contacts, thus presumably also reducing the time fraction, during which the surface experiences very effective nucleate boiling.

4. CONCLUSIONS

Post-CHF heat transfer of water in vertical upflow has been investigated experimentally throughout the complete transition region at low mass qualities via a short, temperature controlled test-section. The general effects of inlet subcooling and mass flux on flow transition boiling heat transfer known from other experiments at similar conditions have been substantiated. In the experiments, CHF and minimum wall heat flux have been found to considerably depend on the situation prevailing upstream of location considered. Hence, care should be exercised when constructing or applying heat transfer correlations of transition boiling that involve expressions for CHF and minimum heat flux which are based on axially constant surface conditions. The present tests indicate that two different heat transfer mechanisms are present between CHF and minimum stable film boiling temperature. The change in the mechanisms occurs when CHF is also exceeded at the test section inlet. Further experiments are required to identify the nature of the process in the latter case. In further studying the minimum stable film temperature, tests might prove helpful where the boiling curve is traversed in both directions up to

wall temperatures of about 600 ^{o} C. The effect of wall temperature control deserves also due future attention.

ACKNOWLEDGEMENTS

The financial support of the German Research Foundation is gratefully acknowledged. The authors would further like to express their appreciation to M. Strangalies and H. Weihs and his coworkers for their invaluable help and excellent performance in preparing the experimental facilities. Thanks are also due to F. Bodemann for performing the computer calculations and graphs and to Mrs. U. Krause for typing the manuscript.

REFERENCES

1. Groeneveld, D.C., "Prediction Methods for Post-CHF Heat Transfer and Superheated Steam Cooling Suitable for Reactor Accident Analysis", Centre d'Etude Nucléaires de Grenoble, report TT/SETRE/82-4-E/DCGr, 1982.

2. Cheng, S.C., Ng, W.W.L., and Heng, K.T., "Measurements of Boiling Curves of Subcooled Water under Forced Convective Conditions", Int. J. Heat Mass Transf., 1978, Vol. 21, pp. 1385 - 1392.

3. Ragheb, H.S. and Cheng, S.C. and Groeneveld, D.C. "Observations in Transition Boiling of Subcooled Water under Forced Convective Conditions", Int. J. Heat Mass Transf., 1981, Vol. 24, pp. 1127 - 1137.

4. Ramu, K., and Weismann, J., "Transition Flow Boiling Heat Transfer to Water in a Vertical Annulus", Nucl. Engng. Design, 1977, Vol. 40, pp. 285 - 295.

5. Weismann, J., Kao, Y.K., and Rahrooh, G., "Transition Boiling Heat Transfer in a Vertical Tube", Amer. Soc. Mech. Engrs. paper no. 79-HT-47, 1979.

6. Wang, S., Kao, Y.K., and Weismann, J., "Studies of Transition Boiling Heat Transfer with Saturated Water at 1 - 4 bar", Nucl. Engng. Design, 1982, Vol. 70, pp. 223 - 243.

7. Fung, K.K., Gardiner, S.R.M., and Groeneveld, D.C., "Subcooled and Low Quality Flow Film Boiling of Water at Atmospheric Pressure", Nucl. Engng. Design, 1979, Vol. 55, pp. 51 - 57.

8. Fung, K.K., "Subcooled and Low Quality Film Boiling of Water in Vertical Flow at Atmospheric Pressure", Argonne National Laboratory, Argonne, Il., Report No. ANL 81 - 78 (= NUREG/CR-2461), 1981.

9. Stewart, J.C., and Groeneveld D.C. "Low Quality and Subcooled Film Boiling of Water at Elevated Pressures", Nucl. Engng. Design, 1981, Vol. 67, pp. 259 - 272.

10. Groeneveld, D.C., and Gardiner, S.R.M. "A Method for Obtaining Flow Film Boiling Data for Subcooled Water", Int. J. Heat Mass Transf., 1978, Vol. 21, pp. 664 - 665.

11. Kleen, U., and Johannsén, K., "Measurement of Transition Boiling Data of Subcooled Water at Forced Convective Conditions and Atmospheric Pressure via a Steady-State Process", Jahrestagung Kerntechnik '82 (Dt. Atomforum, ed.), Mannheim, 1982, pp. 105 - 108.

12. Johannsen, K., and Kleen, U., "Steady-State Measurement of Forced Convection Surface Boiling of Subcooled Water at and beyond Maximum Heat Flux via Indirect Joule Heating of a Test Section of High Thermal Conductance", Paper presented at the 3rd Multi-Phase FLow and Heat Transfer Symposium-Workshop, Miami Beach, Florida, U.S.A., 18 - 20 April 1983.

13. Groeneveld, D.C., and Stewart, J.C., "The Minimum Film Boiling Temperature for Water During Film Boiling Collapse", Proc. Seventh International Heat Transfer Conf., 1982, Vol. 4, pp. 393 - 398.

Summary of Discussion in the Low-Void Heat Transfer

Y. Murao

Japan Atomic Energy Research Institute

Tokai-Mura

Ibaraki-ken, 319-11 Japan

Summary of low-void heat transfer session

Yoshio Murao

Japan Atomic Energy Research Institute
Tokai-mura, Ibaraki-ken, 319-11, Japan

In this session, the following five poster session papers are presented:

(1) "Inverted Annular Film Boiling and the Bromley Model" by M.K. Denham,

(2) "A Correlation of Low Flow, Low Pressure, and Low-to-Moderate Quality Post-CHF Data" by C.D. Morgan and J.C. Chen,

(3) "Post-CHF Low-Void Heat Transfer of Water: Measurments in the Complete Transition Boiling Region at Atomospheric Pressure" by K. Johannsen and W. Meinen, and

(4) "Transition Boiling on Surfaces of Different Surface Energy" by S.K. Roy Chowdhury and R.H.S. Winterton.

Papers (1) and (2) are related to the film and dispersed flow boiling. Paper (1) is treating the heat transfer for the inverted annnular film boiling in a single tube, especially mainly subcooled film boiling and discussing the breakdown of the inverted annular core. Paper (2) is intending to modify the CSO (Chen-Sundaram-Uzkaynak) correlation developed at Lehigh University in order to correlate the heat transfer for dispersed flow in a single tube.

On the other hand, Papers (3) and (4) are related to the transition boiling. Paper (3) is treating the boiling curve for the transition boiling by means of a feed-back control of electric power for heating a test section. Paper (4) is investigating the influence of the surface energy of the heating surface on the transition boiling by changing the surface treating condition.

In Paper (1), modification of Bromley's model was made by allowing the heat transfer into the subcooled liquid core through the vapor film. The heat transfer into the core was estimated by using the transient heat conduction solusion for a circular cylinder of the liquid core.

In the model developed by Murao [1], the constant heat flux was assumed to solve analytically the equation derived by Bromley's method. In Paper (1), however, the above assumption was not used and the equation was numerically solved. The model was checked with the data from the REFLEX single tube test rig at Winfrith. Results shows good agreement between the measured and the calculated for the Weber number less than 20. The auther explained that the inverted annular flow was breakdown at the location of Weber number of 20. Additionally the auther concluded that the modified Bromley correlation is more less successful which used the representative lengh derived from the consideration of the interface instability. The comments for this paper are: (1) It is unreasonable that the density of the liquid column is the quality-weighted average density instead of the void-fraction-weighted average density. (2) The discrepancy shown in Fig. 2 of Paper (1) may be caused by the overestimation of the radiation term. (3) It is necessary to consider the hydraulic disturbance induced at the quench front. (4) It is necessary to consider the steam penetration from the vapor film to the liquid core and to consider the resultant two-phase core. (5) The flow pattern in the single tube is different from that in the bundle of the nuclear fuel.

In Paper (2), modification of the CSO correlation developed at Lehigh University was performed by considering the entry length effect, liquid droplet sink effect and wall heat flux effect, since the existing correlations listed in Table 2 in Paper (2) were found to be of questionable reliability for the B & W data of low flow rates and low-to-moderated qualities. Addition to the usual thermal entry length effect, hypothesized was the heat transfer enhancement due to heat sinks provided by evaporation of liquid droplets in the vapor. The axial length is defined as a distance from the CHF location in order to describe the entry length effect. The heat sink effect was assumed to be described as a function of liquid volume fraction (i.e. $1 - \alpha$), where α is void fraction and calculated using homogeneous flow theory. For wall heat flux effect, the Boiling number was used. For practical use, a correlation was derived by using the vapor quality instead of the vapor fraction in accounting for the presence of droplets.

The comments for this paper are: (1) The void fraction calculated

using homogeneous flow is different from the real value. (2) The limitation of the applicability to the heat transfer in the fuel bundle should be considered for the correlation developed using the data from the single tube tests.

In Paper (3), a copper hollow cylinder of high heat capacity was heated by electric heaters whose power was controlled to obtain the desired average temperature. Since average temperature evaluated by three thermocouples was used, a degree of the freedom of the temperature distribution existed in the test section. The coolant was introduced into the central hole of the cylinder positioned in vertical direction. By changing the inlet subcooling and the mass flux of the coolant (water), boiling curves and axial wall temperature distributions were measured. The comments for this paper is: It should be noted that the obtained results may be depend on the test apparatus, since the transition boiling may be explained as co-existance of the nucleate boiling and the film boiling and the average temperature is obtained from the temperatures at three points determined arbitrarily where the heat transfer mode depend on the test apparatus.

In Paper (4), the effect of the surface energy on the transition boiling was investigated by immersing the hot metal cylinder with verious degree of surface finish into the quenching fluid. It was found that the higher energy surface yields higher minimum film boiling temperature where the higher energy surface is more easily wetted with the fluid. The film boiling based on the hydrodynamic instability seems to occur in lower possibility on the higher energy surface. The comments for this paper are: (1) It should be carefully examined that the data evaluation method is reasonable or not, where the heat flux was evaluated by thermally lumped analysis assuming that the heat flux is equal over the whole surface. (2) The results may be dependent on the test apparatus.

In the discussion, summarized are:

(1) Excellent two papers of low-void heat transfer for the pool and flow film boiling are presented. One developed a Bromley type correlation and another developed a convective heat transfer type correlation.

(2) They are investigating the parameter effects of the subcooling, void fraction and distance from the quench front or CHF point.

(3) The hydrodynamic condition in the test section should be considered in the modeling for heat transfer, since the void fractions in the tube and the bundle are different from each other and the void fraction is not calculated with homogenous flow assumption and the droplet size and the droplet velocity is dependent on the configuration of the test apparatus.

(4) In the modeling of the heat transfer, to be additionally considered are: (i) vapor penetration from the vapor film to the inverted annular core or the inverted two-phase core, (ii) change of the flow pattern like the breakdown of the inverted annular core, (iii) disturbance yielded at the quench front or CHF point and (iv) treatment of the radiative heat transfer for verious flow conditions.

(5) The flow velocity effect on the film boiling heat transfer should be modeled by considering (i) heat transfer from vapor film to liquid, (ii) momentum balance governed by frictional force between two-phases, flow acceleration at the quench front or the CHF point and gravity force related to the void fraction.

(6) Excellent two papers of the transition boiling are presented. Both are investigating the boiling curve for transition boiling. One used steady-state temperature control method and another used a transient quenching method.

(7) They are investigating the parameter effects of the inlet subcooling, mass flux of the coolant and the surface energy.

(8) Though their results seem to be dependent on the test apparatus, since the transition boiling may be explained to be coexistance of the nucleate and the film boiling, they are qualitatively valid.

(9) The information of the surface energy effect on the transition boiling is useful to investigate the transition boiling itself and the film boiling caused by the hydrodynamic instability of the vapor-liquid interface.

Reference

[1] Murao, Y. and Sugimoto, J.: Correlation of heat transfer coefficient for saturated film boiling during reflood phase prior to quenching, J. Nucl. Sci. Technol., 18 [4], pp. 275 ~ 284, (1981).

IV. Dispersed-Flow Heat Transfer

A Simple-To-Use Post Dryout Heat Transfer Model Accounting for Thermal Non-Equilibrium

D. Hein, W. Köhler

Kraftwerk Union AG, Erlangen, FRG

Abstract

On the basis of own experiments with 6 m long inside cooled tubes in the pressure range 50 to 250 bar and data from the literature a post dryout heat transfer model was developed. It is based on the existence of a representative thermal non-equilibrium. The vapour superheat can be calculated from an energy balance. The only unknown quantities are the heat transfer coefficient α between the droplets and the steam and the surface area F of all the droplets. To avoid that the size distribution of the droplets and the slip has to be known for all parameter combinations of interest - which is unpractical for use in design calculations - the product of (αF) was looked at. It was found that the value (αF) is nearly constant with changing steam quality in the post dryout region. (αF) was determined from experimental data as a function of the mass flow rate and the Laplace-constant. Using the so calculated vapour superheat one of the well known single phase heat transfer correlations can be used for determindation of the wall temperature. Comparisons of measured wall temperatures with calculated ones showed good agreement over the pressure range 50 bar up to the critical pressure.

1. Introduction

In once-through boilers all flow patterns from single-phase water flow to dry-steam flow can be found. Similarly, all heat transfer regions including post-dryout with reduced heat transfer is present. In oder to design the boiler tubes correctly the maximum temperatures which could occur during operation should be known as accurately as possible. Another field in which heat transfer in the post-dryout region plays an important role is the loss of coolant accident in water cooled nuclear reactors. In this particular case the maximum fuel rod temperatures are of interest as they determine the possible extent of damage caused to the core.

Three different paths were taken in the development of computer codes for calculating heat transfer in the post-dryout region:

- purely empirical correlations based on single-phase heat transfer /1, 2, 3/. Their coefficients and exponents were determined with the help of regression analysis from a large amount of experimental data,

- predominantly theoretical models describing in detail transport phenomena which influence heat transfer /4, 5/,

- models taking into account the essential physical phenomena by means of empirical quantities /6, 7/.

The purely empirical correlations did not stand the test: here, the danger lies in the fact that slightly altered conditions could lead to disproportionately large errors. The other extreme - the effort to describe all physical phenomena on microscope scale proved only partically successful. This method assumes that the user has the knowledge of, among other things, the drop size distribution at all pressures and for low as well as high mass flow rates. This is obviously unrealistic.

Therefore a middle-of-the road solution suggests itself, namely a method that combines the advantages of both approaches described above: largely theoretical description of the dominant physical phenomena - in the case of post-dryout heat transfer it is the thermal non-equilibrium in the flow - and empirical determination of thermodynamic quantities i.e. there are no assumptions about physical details left to the user. This approach was chosen for the development of a simple-to-use heat transfer model in the post-dryout region.

2. Experimental Details

The test on whose results the model was based were carried out in the BENSON test rig /8/ shown in Fig. 1.

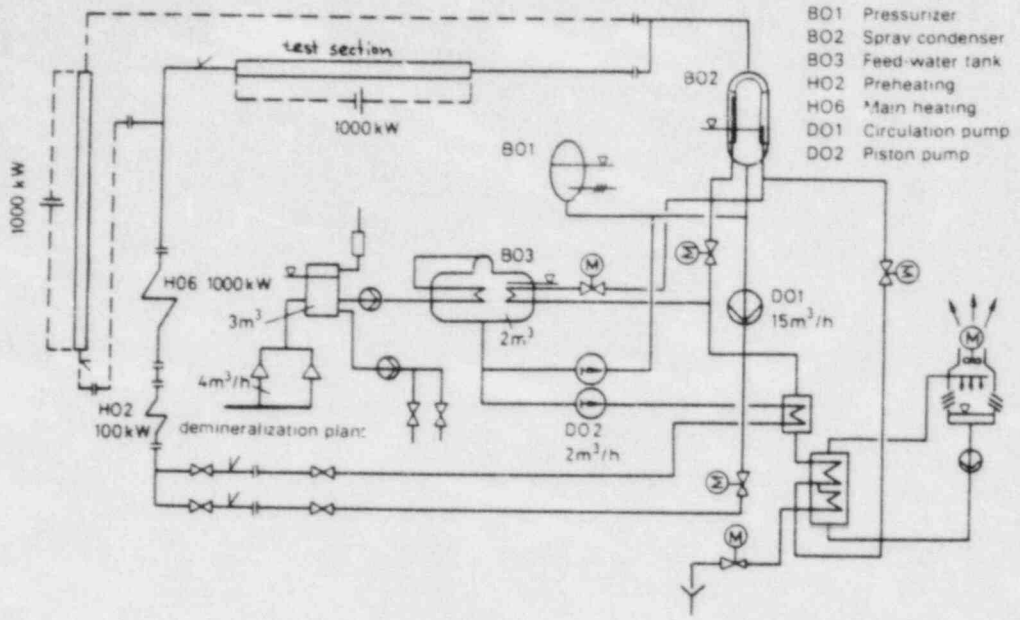

Fig. 1: BENSON-Test Rig

The experimental plant essentially consists of a high pressure loop, 1000 kW D.C. power supply unit, cooling tower and a water treatment plant. The rig is suitable for conducting tests with water, steam or two-phase mixture, its capability extends to supercritical pressures up to 330 bar.

The investigation of heat transfer in the post-dryout region was carried out using internally cooled 6 m long tubes. In order to achieve high flow stability the rig was operated in once-through mode.

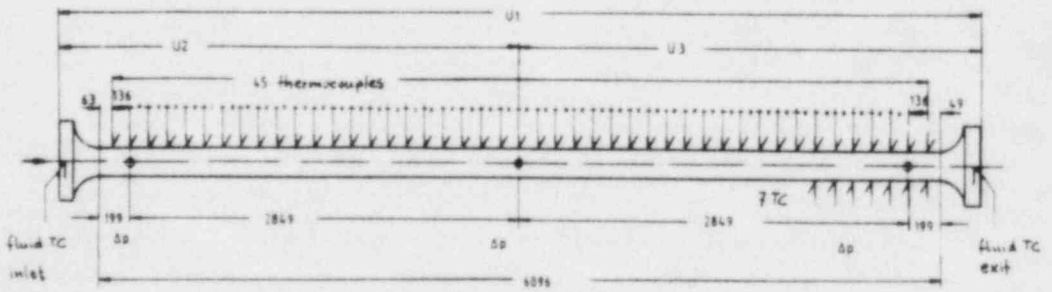

Fig. 2: Instrumentation of test section

Fig. 2 snows an instrumented test section. By soldering 45 thermocouples along the entire legth of the tube the temperature and hence the heat transfer could be determined.

A typical example of a temperature distribution is shown in Fig. 3 With constant heat input along the longitudinal axis the enthalpy of the fluid rises linearly.

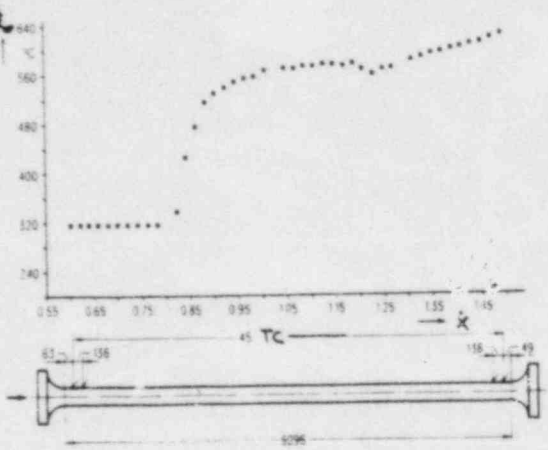

Fig. 3: Temperature distribution along heated pipe

The test matrix in post-dryout experiments comprised altogether 500 tests which covered the following parameters:

Pipe diameter:		12.5, 14.0, 24.3	mm
Pressure	:	50 - 250	bar
Mass flux	:	300 - 2500	kg/m²-s
Heat flux	:	up to 600	kW/m²

3. Model Description

At the position of the boiling crisis both phases - water and steam - of the two-phase mixture have the same temperature. Downstream the vapour can be superheated while the water droplets remain at saturation temperature. A thermal non-equilibrium between the two phases builds up. At a certain distance the process stabilizes i.e. developed thermal non-equilibrium exists. With increasing steam quality resulting in higher velocity and increased turbulence of the two-phase mixture the thermal non-equilibrium can be reduced again. Therfore the heat transfer increases more than the increase due to higher convection (caused by higher velocity) alone.

However, the highest surface temperatures in the post-dryout region occur just as developed thermal non-equilibrium is reached. If it were possible to calculate these temperatures with sufficient accuracy it would mean that the deviations upstream and downstream of this region were only of secondary importance leading to a significantly simplified prediction of heat transfer in boiler tubes. When taking this approach the assumption is made that for all parameter combinations a value of developed thermal non-equilibrium exists by which the behaviour of the surface temperature is determined.

The degree of the developed thermal non-equilibrium can be determined from an energy balance, Fig. 4. Making the simplifying assumption that the specific steam enthalpy alongthe pipe section does not change we can put $h_{D1} = h_{D2}$. The added heat input is used only for evaporation and superheating of the newly formed steam.

inlet enthalpy flux + heat input = exit enthalpy flux

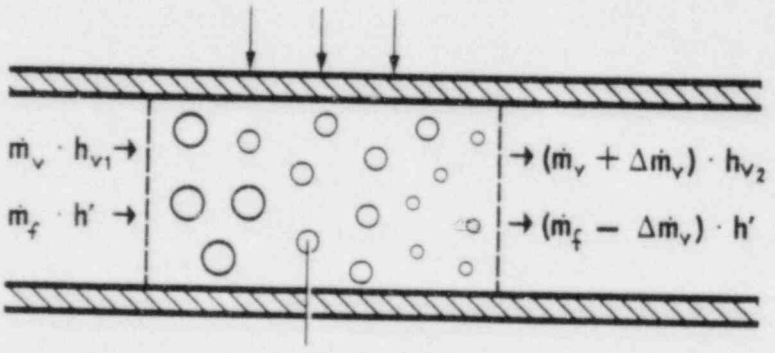

Fig 4: Determiantion of thermal non-equilibrium from energy balance

With these assumptions the steam superheat can be expressed as

$$\Delta\vartheta_{sup} = \vartheta_v - \vartheta_S = \frac{\Delta h_{fg}}{2 \cdot c_v}\left[\sqrt{1 + \frac{4 \cdot c_v \cdot \dot{q}}{\Delta h_{fg}(\alpha \cdot F)_{dr}}} - 1\right]$$

Here, only the product (α F) of which α being the heat transfer coefficient between the water droplets and steam, F the surface area of all the evaporating droplets, is unknwon. The water droplets surface area is related to unit area of the heated pipe wall.

In the literature the attempt is made to determine the value of (α F) using heat transfer correlations for flow in contact with spheres. This approach requires however, the knowledge of representative droplet diameter, droplet distribution function and the

relative velocity between the droplets and steam along the evaporation path of the droplets. This information is not available as yet.

If we assume that for every combination of system parameters there exists a value for the developed thermal non-equilibrium then we do not require the detailed calculation of heat transfer between droplets and steam .

To every parameter combination a value of (α F) can be attributed. This value is independent of local steam quality and therefore it is constant along the flow path.

An empirical correlation for heat transfer coefficients and heat exchanging area between the steam and water phase was developed from experimental data:

$$(\alpha \cdot F)_{dr} = \begin{cases} 1{,}473 \cdot 10^{-7} \cdot (\dot{m}/A)^{1{,}33} & \text{for } \dot{m}/A \leq 1767 \cdot 10^{3} \\ 3{,}078 \cdot 10^{-24} \cdot (\dot{m}/A)^{4} & \text{for } \dot{m}/A > 1767 \cdot 10^{3} \end{cases}$$

where $\mathring{m}$ is the mass flux and A the Laplace constant

$$A = \sqrt{\frac{\sigma}{g(\varrho_f - \varrho_v)}}$$

The actual steam quality can be found from energy balance

$$\dot{x}_{act.} = \frac{h - h'}{\Delta h_{fg} + c_v \cdot \Delta \vartheta_{sup}}$$

where h is the enthalpy of the fluid which can be determined on the basis of mass flow and heat input. When the steam is not superheated the above equation reduces to the usual definition of steam quality namely to

$$\dot{x}_{equ.} = \frac{h - h'}{\Delta h_{fg}}$$

The thermal non-equilibrium factor $\dot{\omega}$ is often employed to quantify ther thermal non-equilibrium. $\dot{\omega}$ is the ratio of the actual steam quality to that arrived through the energy balance equation:

$$\dot{\omega} = \frac{\dot{x}_{actual}}{\dot{x}_{equilibrium}}$$

Using the above equation we obtain

$$\omega = 2/(\sqrt{1 + (4\, c_v\, \dot{q})/[\Delta h_{fg}(\alpha\, F)_{dr}]} + 1)$$

Fig. 5 shows, for pressure between 50 and 210 bar, mass flux from 500 to 350 kg/m²s and heat flux up to 1000 kW/m², the calculated thermal non-equilibrium factor $\dot{\omega}$. The relationship between $\dot{\omega}$ and steam superheat is established in Fig. 6.

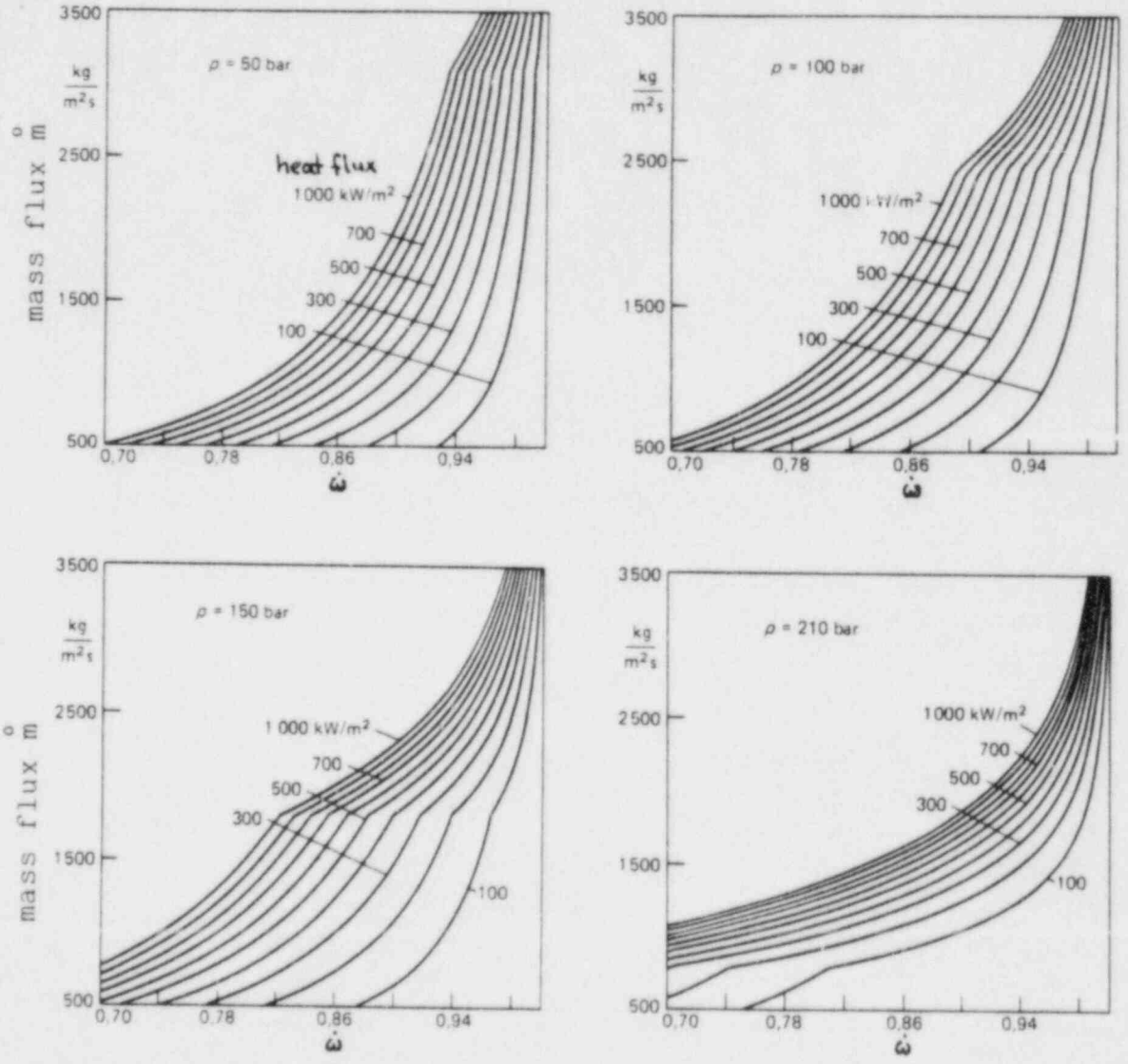

Fig. 5: Determination of non-equilibrium factor $\dot{\omega}$

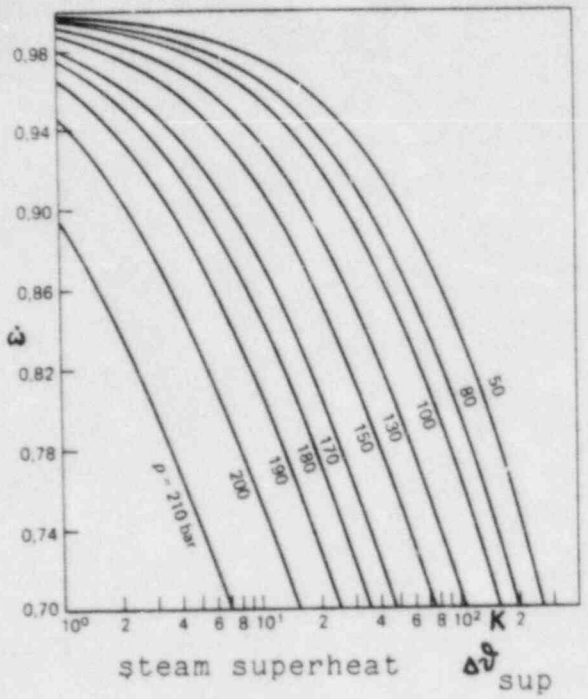

Fig. 6: Determination of steam superheat

To determine the wall temperature it is only necessary to find the heat transfer coefficient between the steam flow and pipe wall. To this purpose the proven correlation for single phase flow by GNIELINSKI /9/ can be employed:

$$Nu = \frac{(\xi/8)\cdot(Re - 1000)\cdot Pr}{1 + 12{,}7\cdot\sqrt{\xi/8}\cdot(Pr^{2/3} - 1)}$$

$$\xi = (1{,}82\cdot\log_{10} Re - 1{,}64)^{-2}$$

The Reynolds number is determined using the average velocity of the two-phase flow. Assuming no slip in the post-dryout region the two-phase flow Reynolds number is

$$Re = \frac{\dot{m}\cdot d}{\eta_v}\left[\dot{x}_{actual} + (1 - \dot{x}_{act.})\,(\rho_v/\rho_f)\right]$$

The above assumption of no slip (made for the post-dryout region) implies that the water droplets travel "passively" within the flow and that neither momentum nor heat exchange between the droplets and the heated surface take place.

To determine the value of fluid properties the average boundary layer temperature is used; it is formed from the arithmetic mean of steam and wall temperatures.

Finally, the wall temperature is obtained from the sum of saturation temperatures ϑ_{SAT}, superheated steam temperature $\Delta\vartheta_{SUP}$ and excess wall temperature $\dot{q}/\alpha_v$.

$$\vartheta_W = \vartheta_S + \Delta\vartheta_{sup} + \dot{q}/\alpha_v$$

Up to the point of heat transfer crisis ($\overset{o}{x}_{D0}$), two-phase flow is practically in thermal quilibrium since even the wall temperature is only a few degrees above saturation.
Thermal non-equilibrium begins to form downstream of the location where heat transfer crisis first occurs and is not fully developed until the point of minimum heat transfer ($\overset{o}{x}_{\alpha\,min}$) is reached.

In order to obtain a reference value for the development of thermal non-equilibrium it is assumed, that, from the onset of the heat transfer crisis, the entire heat input is used to superheat the steam already generated up to that point. With this assumption, the value $\overset{o}{x}_{min}$, at which the steam reaches that superheat temperature which corresponds to fully developed thermal non-equilibrium, can be determined with the help of an energy balance.

$$\dot{x}_{\alpha\,min} = \dot{x}_{cr} + \frac{\dot{x}_{cr}\, c_v\, \Delta\vartheta_{sup}}{\Delta h_{fg}}$$

In the region between $\overset{o}{x}_{D0}$ and $\overset{o}{x}_{\alpha\,min}$ we assume a linear increase of wall temperature. We believe that the development of thermal non-equilibrium is the explanation for the gradual decrease in the heat transfer coefficient in the region following the dryout point.

The transition to single-phase steam flow is simulated in the calculation model by keeping the wall temperature constand above a certain steam quality $\overset{o}{x}_{lim}$ until all droplets have evaporated. This steam quality is a function of pressure:

$$\dot{x}_{lim} = 0{,}7 + 0{,}002 \cdot p$$

4. Model Verification

The model was verified by 368 reference calculations using data from heat transfer tests carried out by HERKENRATH /10/ and own test data. The model is being tested further by employing data by BECKER /11/ and CHOJNOWSKI /12/. Fig. 7 and 8 show typical comparison between calculated and measured values.

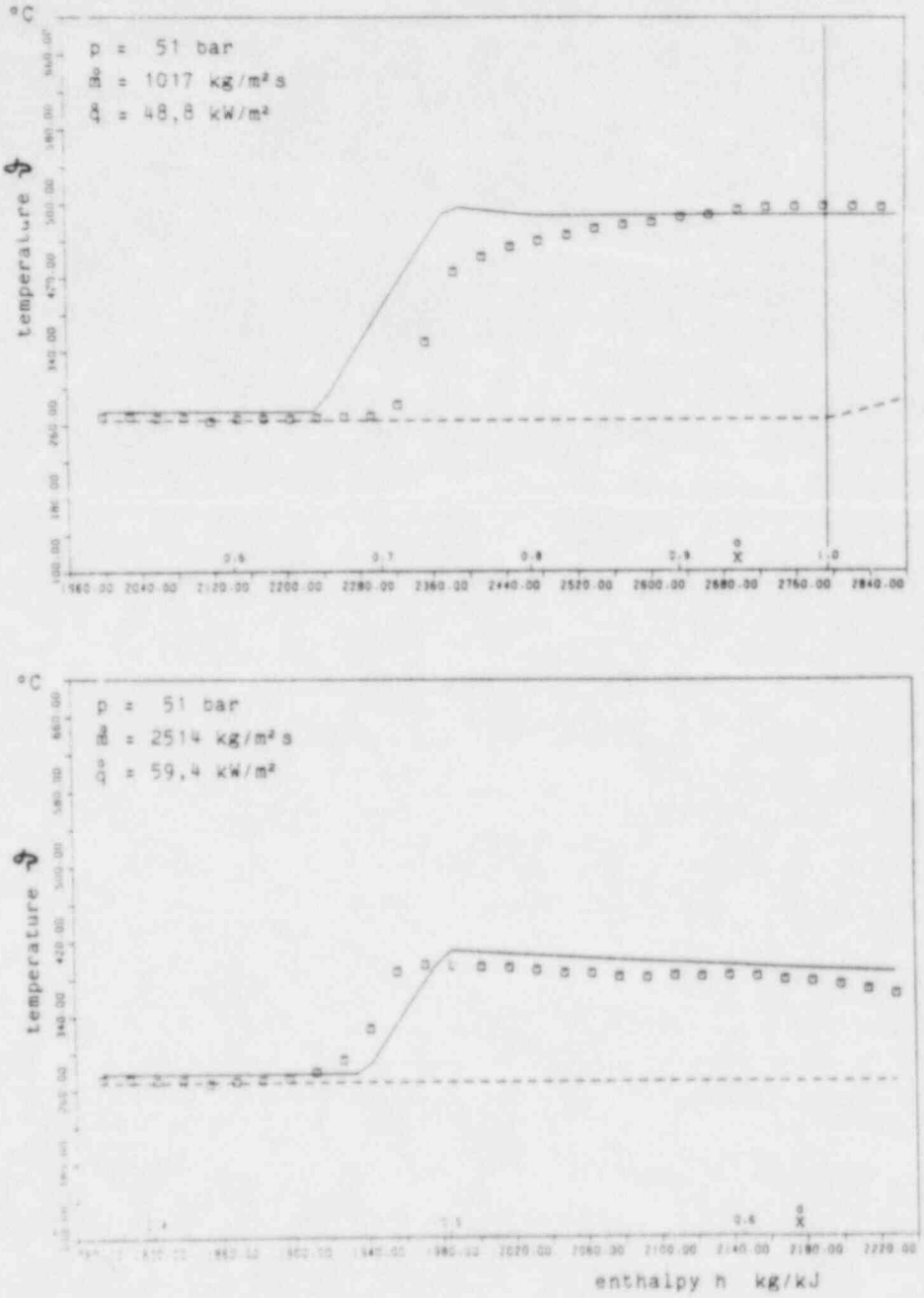

Fig. 7: Calculated and measured wall temperature distribution (d = 12,5 mm)

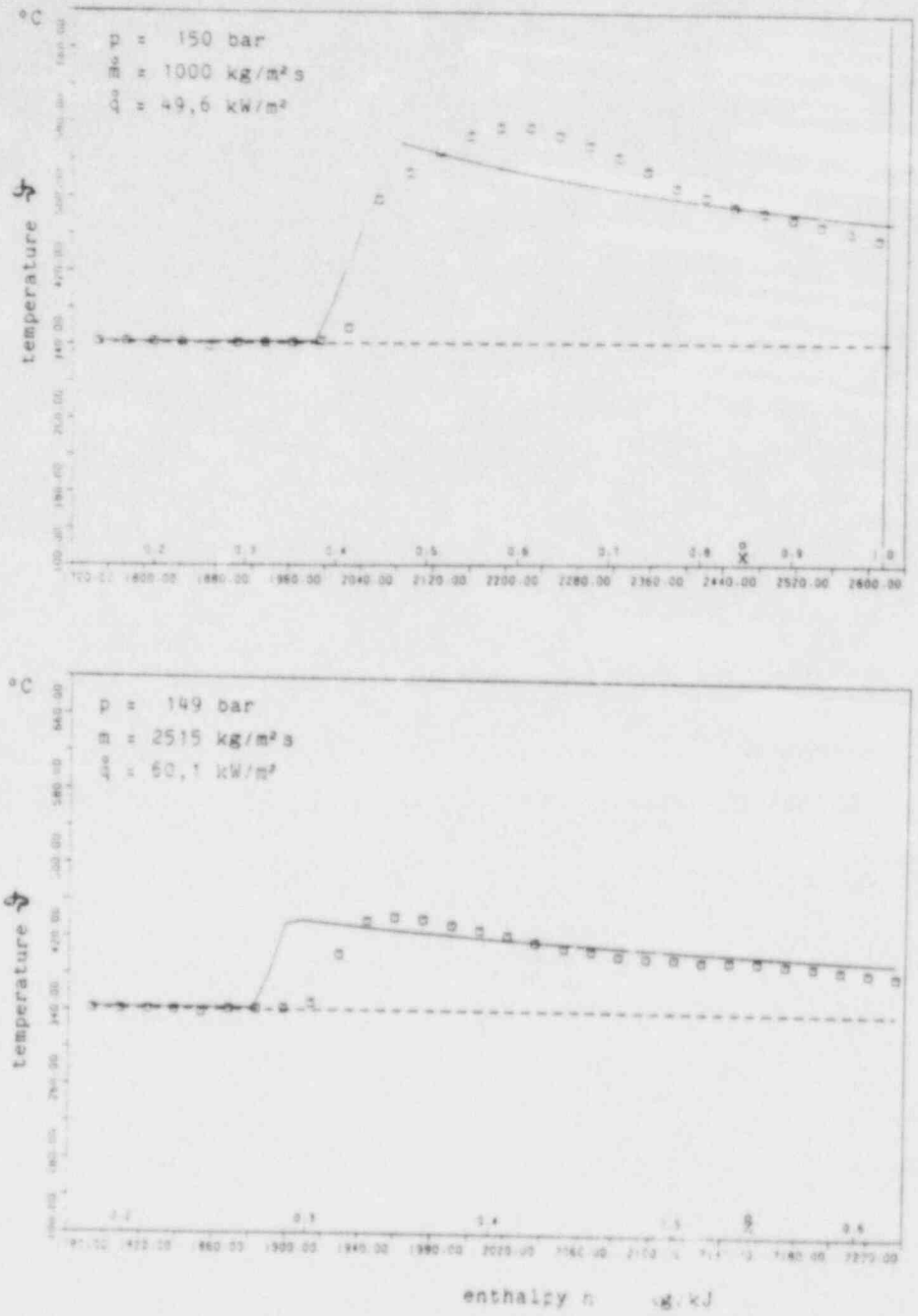

Fig. 8: Calculated and measured wall temperature distributions (d = 12,5 mm)

Comparison of low and high mass flux is shown in the upper and lower diagrams respectively. The figures show also that the formation of thermal non-equilibrium from the point of boiling crisis up to the location of minimum heat transfer coefficient is predicted with sufficient accuracy by the model. The largest deviations between model and measurement are caused by errors in predicting the location of the boiling crisis and are therefore independent of the heat transfer model used in the post-dryout region. However the above kind of comparison was chosen in order to point out

As far as wall temperatures are concerned 88 % of all dryout tests were predicted within ± 40 K. The mean square deviation between the measured and calculated maximum temperatures is 5.8 K, the standard deviation and RMS error are 26 K and 27 K respectively.

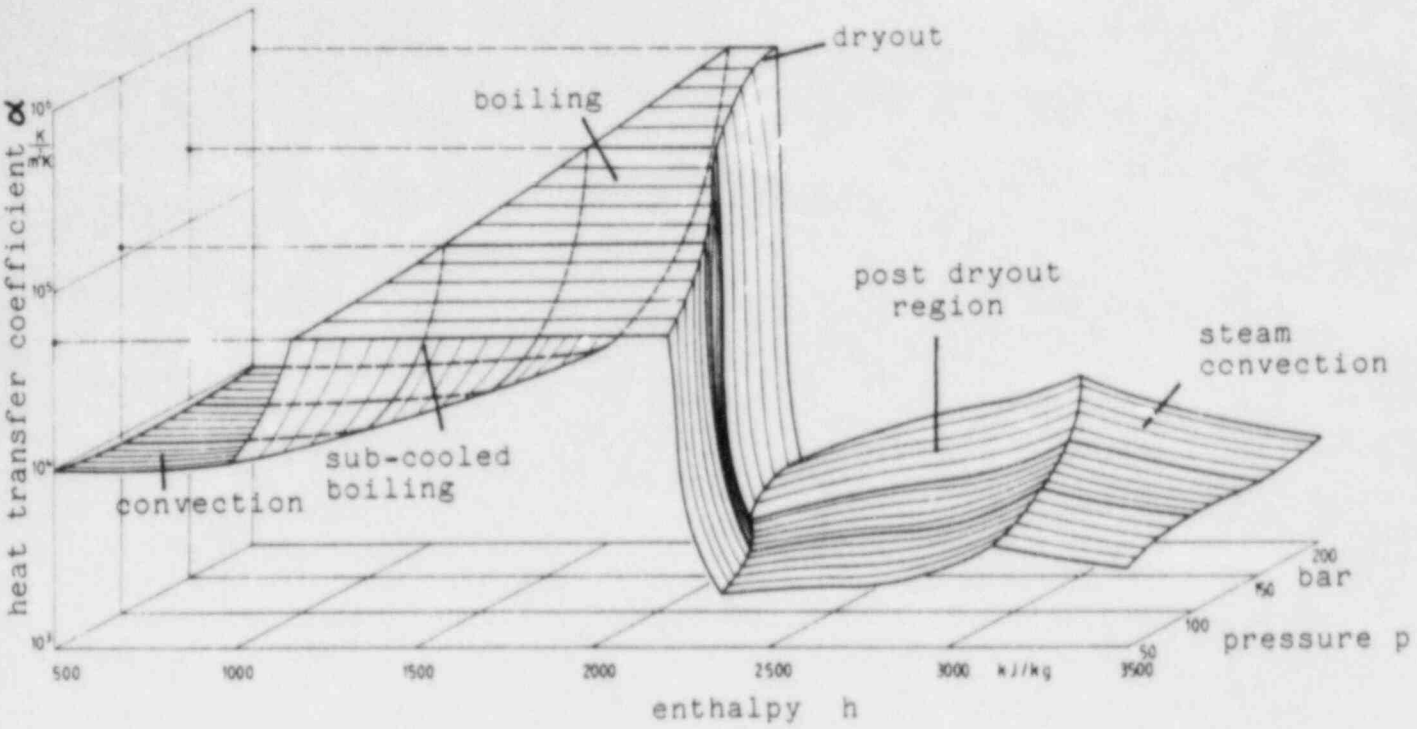

Fig. 10: 3-dimensional representation of heat transfer for forced flow conditions in pipes

Fig. 10 depicts in a three dimensional view the calculated heat transfer coefficient as a function of the enthalpy of the fluid and pressure. In the region of fully developed nucleate boiling the heat transfer coefficient was calculated according to JENS and LOTTES /13/, in single-phase flow GNIELINSKI's correlation /9/ was used.

that models for heat transfer in the post-dryout region are only as good as the model which predicts the boiling crisis.

In order to get "a feeling" for the accuracy obtainable with this model, the difference between the maximum measured and calculated wall temperatures in the post-dryout region are shown in Fig. 9.

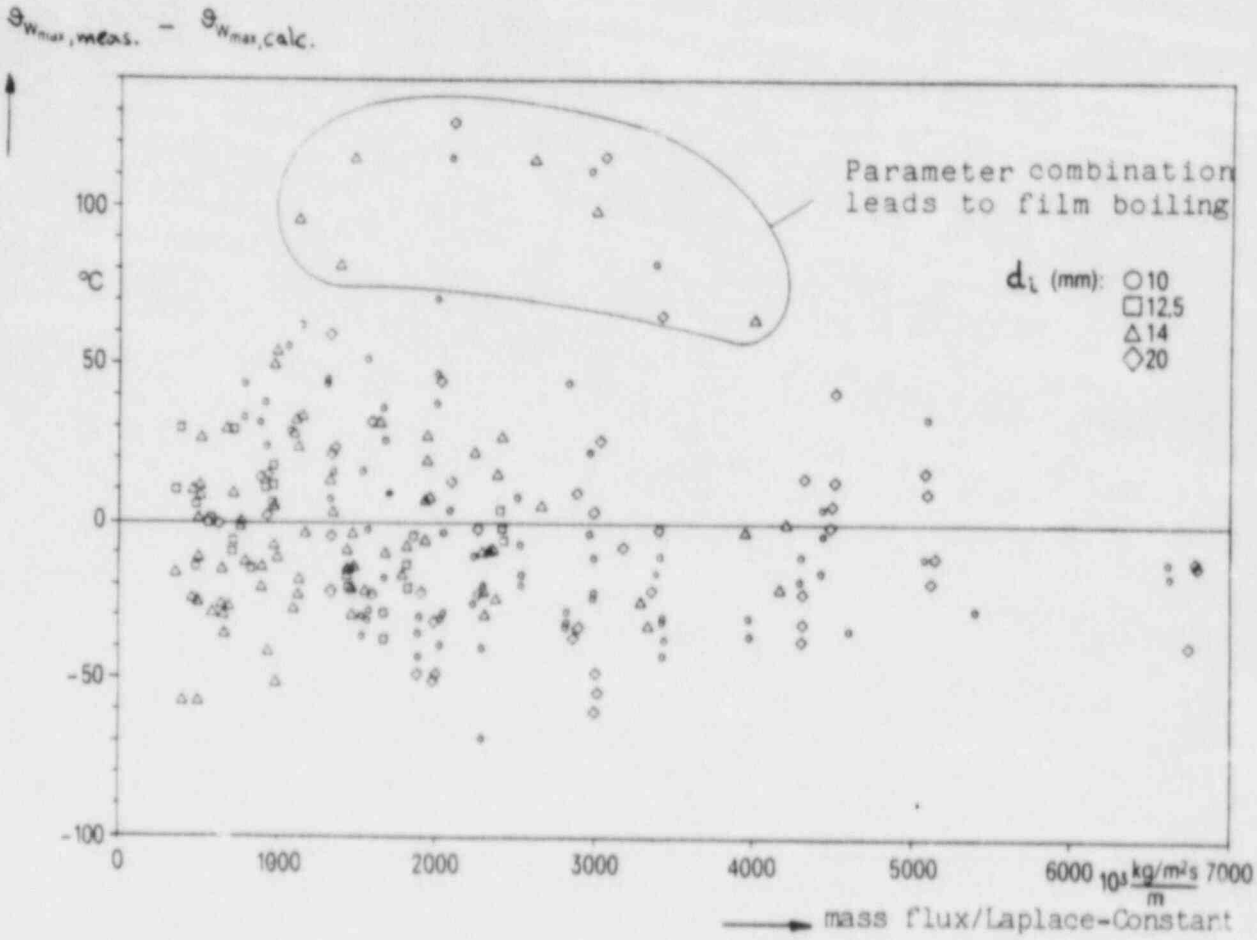

Fig. 9: Comparison between calculated and measured maximum wall temperature in post-dryout region

The ratio of mass flux and the Laplace constant, this being a measure of heat transfer between the steam and water phase in this model, is plotted along the abscissa. In this way the empirical correlation for heat transfer between steam and water in a large pressure and mass flux region was checked. The values in Fig. 9 confirm that the model gives good results for the range of examined pipe diameters between 10 and 24 mm. Larger deviations originate almost completely from tests in which film boiling (DNB instead of dryout) occured. In these cases the boiling crisis location shifts towards low or even negative steam qualities (obtained from an energy balance).

5. Conclusions

The proposed model uses a single-phase steam correlation to calculate the heat transfer in the post-dryout region while taking into account the thermal non-equilibrium between the water and steam phase. Thus it can be classified as two-step model as introduced by /14/. The empirically determined quantity (αF) was identified to be a function of mass flux and through the Laplace constant a function of pressure. This leads, apart from the obvious advantage of being easy to use, to a wide range of parameters over which results with good accuracy can be achieved.

References

/1/ Groeneveld, D.C.,
An investigation of heat transfer in the liquid deficient region
AECL-Report 3281, 1969

/2/ Mattson, R.J., Condie, K.G., Bengtson, S.J., Obenchain, C.F.
Regression analysis of post-CHF flow boiling data.
Proceedings Fifth Intern. Heat Transfer Conference, Tokio, Sept. 1974

/3/ Slaughterbeck, D.C., Mattson, R.J., Ybarrondo, L.Y., Condie, K.G.,
ASME-Paper 73-HT-20, 1973

/4/ Iloeje, O.C., Plummer, D.N., Rohsenow, W.M. Griffith, P.,
A study of wall rewett and heat transfer in dispersed vertical flow.
MIT Dept. of Mech. Engng., Report 72718-92, Sept. 1974

/5/ van Koppen et. al.
A non-uniform post dryout flow and heat transfer model
Report WPS3-81-06.R317 Eindhoven Univesity of Technology

/6/ Groeneveld, D.C., Delorme, G.G.J.
Prediction of thermal non-Equilibrium in the post-dryout regime
Nuclear Engineering and Design 36, pp. 17 - 26, (1976)

/7/ Chen, J.C., Sundaram, R.K., Ozkaynak, F.T.
A phenomenological correlation for post-CHF heat transfer.
UREG-Report 0237, 1977

/8/ Hein, D., Keil, H., Köhler, W.
The BENSON test rig
VGB-Kraftwerkstechnik, 57th Annual Series, No. 6, June 1977

/9/ Gnielinski, V.
Neue Gleichungen für den Wärme- und den Stoffübergang in turbulent durchströmten Rohren und Kanälen
Forsch. Ing.-Wes. 41, Nr. 1 (1975)

/10/ Herkenrath, H., Mörk-Mörkenstein, P. et. al.
Wärmeübergang an Wasser bei erzwungener Strömung im Druckbereich von 140 bis 250 bar
EUR 3658 d - EURATOM Ispra (1967)

/11/ Becker, K.M., Ling, C.H., Hedberg, S., Strand, G.
An experimental investigation of post-dryout heat transfer
KTH-NEL-33, Department of Nuclear Engineering, Royal Institute of Technology, Stockholm, Sweden, May 1983

/12/ Scruton, B., Chojnowski, B.
Post-dryout heat transfer for steam/water flowing in vertical tubes at high pressure
European Two-Phase Flow Group Meeting, Strathclyde University 3rd-6th June, 1980

/13/ Jens, W.H., Lottes, P.A.
Analysis of heat transfer, burnout, pressure drop and density data for high pressure water
USAEC Report ANL-4627 (1951)

/14/ Bennett, A.W., Hweitt, G.F., Kearsey, H.A., Keeys, R.K.F.
Heat transfer to steam water mixtures flowing in uniformly heated tubes in which the critical heat flux has been exceeded.
AERE-R-5373, 1967

DROPLET DYNAMICS AND HEAT TRANSFER IN DISPERSED TWO-PHASE FLOW

A.J. Clare and S.A. Fairbairn

Central Electricity Generating Board
Berkeley Nuclear Laboratories,
Berkeley,
Gloucestershire,
UK.

ABSTRACT

A mechanistic model of heat transfer in a dispersed steam and droplet flow has been compared with experimental data from a multi-rod facility designed to allow detailed measurements of droplet size and velocity distributions. For the conditions analysed the droplet field was adequately described by a single drop equation of motion, and the steam desuperheating effect of the drops was well predicted by use of the Lee-Ryley steam-drop heat transfer correlation. It was found that enhancement of steam convective cooling by droplet-induced turbulence can be significant and modelling refinements in this area are needed.

1. INTRODUCTION

Heat transfer in dispersed flow film boiling conditions is of importance for cooling a PWR core during the reflood phase of a postulated LOCA. Some advanced reflood codes incorporate mechanistic models in which the dynamics and heat transfer for each phase are considered separately. In order to obtain information to aid the development of such models, experiments have been undertaken in a heated multi-rod cluster of PWR type geometry, with flow visualisation, in which water droplets can be injected into an established steady steam flow. The resulting rod cooling rates and measured droplet size and velocity spectra are being used in developing an analytical model in which the droplet dynamics and the contribution of droplets to the overall heat transfer are represented in detail. Here we describe the relevant experiments and present a selection of data. The main features of the model are described and predictions compared with experimental data. Uncertainties in the modelling of steam-droplet heat transfer and of drop-induced enhancement of steam convective cooling are examined, and requirements for further modelling refinements are identified.

2. THE EXPERIMENTAL DATA

2.1 Objectives

The experimental data is taken from the Multipin Cluster Rig at Berkeley Laboratories. This test facility, described below, is aimed at studying the effects of local blockage upon reflood emergency core cooling. This paper is however limited to consideration of data obtained below the blockage elevation and in the undistorted blockage bypass region. Thermohydraulic effects are measured separately as far as possible. Two types of test are considered here, viz:-

1) Steam flow tests which can be used to assess steady state single phase heat transfer.

2) Steam and droplet tests in which the cooling rates observed upon injecting a steady flow of water drops into a co-current steam flow enable investigation of dispersed flow two phase effects with well characterised test section inlet conditions.

Reflood and air flow distribution tests are also performed and are described elsewhere, e.g. Fairbairn and Piggott (3).

Unblocked bundle single phase data and blocked bundle steam and droplet data corresponding to unblocked subchannels are described below after the following outline of the test facility.

2.2 Description of Test Facility

The test section is shown schematically in Figure 1. The 44 heater rods are held in the vertical on a square pitch (pitch to diamter ratio of 1.33) inside a transparent cylindrical silica shroud. Each rod has a maximum power of 2 kw and a 1 metre heated length. Some heater rods contain 6 thermocouples whose junctions are spot-welded to the inner surface of their Inconel sheaths at certain prescribed positions. In order to preserve the correct value of flow area per rod within the circular perimeter of the silica shroud 8 unheated dummy pins have been included between the top and bottom grids. A spacer grid is installed at an elevation near the centre of the heated length of the rods. This extra spacer grid was made by spot-welding together lengths of 0.72 mm diameter Nichrome wire. It causes a 32.4% blockage of the subchannels between the rods.

Steam or water flows can be introduced into the lower plenum where they pass along the unheated section of the rods (~ 400 mm long) prior to passing over the bottom grid to flow along the heated section (~ 1000 mm long) of the rods within the silica shroud. An air flow can be introduced into the test section using the water supply inlet port. It is also possible to inject water droplets directly into each subchannel through capillary tubes which are terminated just above the bottom grid.

The silica shroud can be surrounded by a thin walled metal reflector used to minimise bundle radial temperature gradients. Vertical slots ~ 3 pin pitches wide were left at opposite ends of a diameter of the reflector to enable photography of droplets inside the silica shroud under conditions of back-lighting.

All tests are performed at atmospheric pressure.

2.3 Steam Heat Transfer Tests

This work is an essential precursor to the two phase tests because it permits estimation of rig specific details like thermal entry and grid effects. Single phase data are necessary for model development as steam convection is a dominant part (~ 80%) of total rod heat transfer in a dispersed flow (see later). Effort has been concentrated on the transition flows, between laminar and fully developed turbulent conditions, which are in the relevant range for dispersed flows in the FLECHT experiments (1).

Steam generated in an electrode boiler can be passed up the rods at a rate of up to ~ 6 kgm m^{-2} s^{-1}. Heat transfer tests are performed at a steady state with rod powers adjusted to give a steady temperature across the whole rod bundle at an axial elevation (the control elevation) of ~ 18 equivalent diameters from the start of the heated length. Typical results for an unblocked bundle are shown in Figure 2 in the form of Nusselt numbers calculated using the local subchannel

hydraulic diameter and the local steam temperature (calculated from a heat balance). They represent convective heat transfer only since rod thermal radiation losses are calculated separately, by considering each rod to be surrounded by a cylindrical surface of mean temperature and area determined as a function of elevation from the temperatures and perimeters of surrounding rods. Radiative absorption by the steam is described in terms of a mean beam length (taken to be 0.85 of a subchannel hydraulic diameter) and an attenuation coefficient which treats the steam as an optically thin medium. Axial radiative heat transfer is ignored, as is axial thermal conduction which is usually ~ 1% of radial heat transfer. Overall uncertainty in the Nusselt number is mostly ~ 15%. Thermal entry effects at the start of the heated length and heat transfer enhancement at the Nichrome spacer grid are obvious. Reynolds numbers from this test vary from ~ 6000 at inlet to ~ 4000 at the end of the heated length - this variation accentuates the entry effects.

The variation of Nusselt number with Reynolds number is shown in figure 3 for an elevation near the end of the heated length where the entry and grid effects have largely decayed away. The data show a transition between the laminar flow prediction of Kim (2) and the standard Dittus-Boelter relationship. A least squares fit gives the Nusselt number varying as $Re^{0.45 \pm 0.10}$. This power law has been used, together with an axial variation described by a polynomial fit to the data (shown as the dashed line in figure 2), to represent steam phase heat transfer in the model of dispersed flow presented later. This approach enables attention to be focussed on the behaviour of the droplets where the greatest uncertainties lie.

2.4 Steam and Droplet Tests

In these tests saturated water droplets are injected through capillary tubes into the steam flow at the subchannel centres near the start of the heated length. most of the drops created by the break-up of the water jets issuing from these tubes are of ~ 1.2 mm diameter. The rod powers are low ($\lesssim$ 0.36 kW m^{-1}) but sufficient to maintain an initial steady temperature.

The steam boiler takes about 100 seconds to stabilize out at its maximum output and this characteristic has been exploited to obtain data on rod temperatures and cooling rates at two steam flows. Figure 4 shows inlet and outlet steam flowrates during an experiment used below for comparison with model predictions. In such an experiment it is not possible to achieve steady state conditions so the experimental data are plotted in the form of cooling rates which have been taken as the slopes of least squares linear fits to the data taken over 10 second time intervals (21 data points). Uncertainties in the slopes are generally $\lesssim$ 6%. The droplet injection rate (1.35 gm s^{-1} per subchannel), equivalent to a reflood rate of ~ 10 mm s^{-1}, was constant throughout this experiment. The axial variations in rod temperature and cooling rate for centre and peripheral rods for the two steam flows chosen are shown in figures 12 to 15. Apart from blockage effects which are described elsewhere by Fairbairn and Piggott (3), there is an obvious enhancement in heat transfer above the spacer grid, particularly at the earlier time point when the rod temperatures are higher.

Photographic studies have been carried out for tests with water injection into only one subchannel in order to simplify analysis of the films. Figures 5 to 8 show droplet velocities taken from high speed movies of tests with a steam flow of ~ 6.5 kg m^{-2} s^{-1} (or 57 gm s^{-1} - i.e. similar to conditions at time B in figure 5) and a constant single injector flow of 0.675 gm s^{-1}. The initial jet velocity is 2.50 ms^{-1} so that the relative velocity between the steam and the drops is near the droplet terminal velocity. The drops are therefore accelerated slowly up to

the grid elevation and few drop interactions are observed. The mean velocities, $\bar{u}$, shown on the figures are momentum averages such that

$$\bar{u} = \frac{\sum_i m_i u_i}{\sum_i m_i}$$

where m_i and u_i are the individual drop masses and axial velocities for a sample of 100 consecutive drops. Drop size histograms are presented in figure 9 which show that the sauter mean diameter increases somewhat, presumably due to drop coalescence, up to an elevation just below the spacer grid. Above the grid there is a marked increase in the number of small drops due to drop breakup at the grid. Some 70% of the drops are observed to hit the grid. The effect of the grid on drop velocities is shown in figure 7 where we show velocities for a typical subset of the data of figure 6 (elevation 12 mm below the grid) plotted along with the sizes and velocities of those same drops and a selection of the fragments produced from them at an elevation 12 mm above the grid. It is clear from the movies that most of the mass of each drop usually carries on at much the same velocity after hitting the grid and that a number of small, slower moving, fragments tends to be left trailing back to the point of impact. Some droplets are entrained from water deposited on the grid. Figure 8 (elevation 39 mm above the grid) shows that the small fragments are accelerated rapidly. The mean velocity is not strongly affected by the grid as shown in figure 11.

3. DISPERSED FLOW HEAT TRANSFER MODEL

3.1 Introduction

In order to predict the cooling rates measured in the steam and droplet tests described above a detailed model is being developed which attempts a mechanistic representation of the heat transfer processes. In its present, early, stage of development the model calculates the cooling rate of a single unballooned pin given the inlet fluid conditions and the axial temperature profiles of the central, intermediate and outer groups of rods. The time rates of change of all parameters in the tests analysed are sufficiently low to permit quasi-steady state equations to be employed. The spatial variations are treated by a marching method which proceeds stepwise from inlet to outlet.

The control region of the model, shown in figure 10, is centred on the rod whose cooling rate is to be calculated and includes the fluid of the surrounding four subchannels and the facing elements of the neighbouring pins.

All the droplets are assumed to have the same size and velocity. Their initial velocity is derived from the inlet liquid mass flow rate and the injector internal diameter (d_j). The initial drop size (d_o) is calculated from the wavelength of maximum instability of a capillary jet given by Chandrasekhar (4) as

$$\lambda = \frac{\pi d_j}{0.697},$$

giving $$d_o = \left(\frac{3}{2} d_j^2 \lambda\right)^{1/3} = 1.891\, d_j. \qquad (1)$$

Droplet interactions are not modelled so that changes is drop size result only from evaporation.

3.2 Basic Equations

The basic conservation equations solved are:

(i) mass conservation,

$$W_L + W_V = \text{constant}; \tag{2}$$

(ii) momentum conservation for each phase,

$$\frac{1}{A}\frac{d}{dz}(W_L u_L) = -(1-\alpha)\frac{dP}{dz} + F_D - F_{GL} - (1-\alpha)\rho_L g \tag{3}$$

and

$$\frac{1}{A}\frac{d}{dz}(W_V u_V) = -\alpha\frac{dP}{dz} - F_D - F_W - F_{GV} - \alpha\rho_V g, \tag{4}$$

where W_L, W_V are the subchannel mass flow rates of the liquid and vapour phases and where the F_i (described below) are forces per unit volume of the channel accounting for interphase drag (F_D), wall friction (F_W) and momentum losses at the grid (F_{FL}, F_{GV}) where they occur;

(iii) energy conservation,

$$\frac{d}{dz}\left[W_L(h_L + {}^1/_2 u_L^2) + W_V\,(h_V + {}^1/_2 u_V^2)\right] = Q_f, \tag{5}$$

where Q_f is the total heat transferred to the fluid per unit length of channel. An equation for the evaporation rate,

$$\frac{dW_V}{dz} = Q_L/h_{fg} \tag{6}$$

where Q_L is the heat transferred to the (saturated) droplets per unit length of channel, completes the set of basic equations. At each space step solutions to these equations are obtained by an implicit numerical scheme.

3.3 The Momentum Terms

Interphase Drag

The drag force on a single droplet in the vapour stream is

$$f_D = C_D \frac{\pi d^2}{4}\ {}^1/_2\rho_V(u_V - u_L)\left|u_V - u_L\right|, \tag{7}$$

and since there are

$$N_d = \frac{6(1-\alpha)}{\pi d^3} \tag{8}$$

droplets per unit volume, the drag force per unit volume is

$$F_D = N_d f_D = C_D \frac{3}{4}\frac{1-\alpha}{d}\rho_V(u_V - u_L)\left|u_V - u_L\right|. \tag{9}$$

The drag coefficient C_D is computed as a function of the droplet Reynolds number

$$Re_d = \frac{\rho_V \, d}{\mu_V} \left| u_V - u_L \right| \tag{10}$$

according to empirical results for smooth spheres.

Grid Model

The grid at 481 mm elevation is a simple wire mesh of small axial extent; it introduces a form loss into the vapour momentum equation,

$$F_{GV} = K_G \, {}^1/_2 \rho_V u_V^2 \tag{11}$$

where the coefficient $K_G = 0.53$ is obtained from the grid pressure drop measured in air flow tests. The momentum loss of the liquid phase is given by

$$F_{GL} = f_{imp} \cdot x_{mom} \cdot W_L u_L, \tag{12}$$

where f_{imp} is the probability of a drop impacting on the grid wire, calculated as a function of grid geometry and incident drop size, and x_{mom} is the mean fractional momentum loss of a droplet as a result of impact. It is assumed that for a given impacting drop the fraction of the incident axial momentum which is normal to the surface of the grid wire at each point is destroyed. The momentum loss is averaged over all displacements, relative to the grid, of impacting drops, and the mean fractional momentum loss of a drop is found to be

$$x_{mom} = \frac{2 \, d_g}{3(d_g + d)}, \tag{13}$$

where d_g is the diameter of the spacer grid wire.

3.4 Heat Transfer

Wall/Steam Convection

Since the main objective of analysing the steam and droplet tests was to assess the modelling of the droplet contribution to the overall heat transfer it was necessary to minimize errors in calculating the steam cooling contribution. Therefore, the functional dependence of the steam convective heat transfer coefficient used in the model was that derived from measurements in steam cooling tests, and shown in figures 2 and 3. This procedure effectively bypasses the difficulties of predicting the facility - dependent entry and grid effects, and minimises the uncertainties associated with transition region Reynolds number dependence.

Droplet-induced Enhancement

The presence of drops in the steam flow provides a source of turbulence additional to that generated by wall shear, and this will enhance the steam convective heat transfer as deduced from steam only experiments. The calculation of this enhancement is problematic, and since the steam convective heat transfer component is usually dominant this uncertainty could become very significant if the droplet number density were high.

If the steam flow is fully turbulent the convective heat transfer is determined within a thin boundary layer at the wall. In this case, since the

boundary layer will be considerably smaller than the mean drop size, the boundary layer wil be mainly affected by drop-induced turbulence in the free stream, rather than by submergence of the drops in the boundary layer. Blair (5) has investigated experimentally the effect of free stream turbulence intensity on convective heat transfer and has expressed the results in the following modification of Reynolds analogy:

$$St = \frac{f_w}{2} (1.18+1.3\ T), \tag{14}$$

where T ($= \sqrt{u'^2}/u$) is the turbulence intensity of the free stream. Similarly Simonich and Bradshaw (6) report an enhancement of the skin friction coefficient with increasing turbulence intensity in the form

$$f_w = f_{w_o} (1+a\ T) \tag{15}$$

where a is length scale dependent and has a value a = 2 if the length scale is comparable with the boundary layer thickness.

The prediction of turbulence intensities in two-phase dispersed flows has been treated by Theofanous and Sullivan (7) who propose that the familiar relationship between turbulence velocity, shear velocity and shear stress

$$u' = u_w^* = \sqrt{\frac{\tau_w}{\rho}}$$

remains valid if τ_w is replaced by the total shear stress on the continuous phase. Theofanous and Sullivan introduced a turbulence energy distribution parameter δ, and found that a value δ=2 resulted in predicted turbulence intensities in good agreement with measured values in both dispersed bubble and dispersed particle flow experiments. Their analysis for mechanical equilibrium flows has been adapted for the conditions of interest here, where droplets may not be travelling at their terminal velocity, to give

$$T^2 = \frac{f_w}{2} (\alpha+\delta(1-\alpha))+\delta \frac{F_D\ d_h}{2\ \rho_v u_v^2} \tag{16}$$

Equations (14), (15) and (16) are used, together with equation (9), in the standard form of the model to calculate an enhanced steam convective heat transfer coefficient. For single phase conditions the values of f_w required for agreement with the measured heat transfer coefficient are in excellent agreement with values derived from air flow tests, and this gives some confidence in the validity of the approach. It is anticipated that at lower flows, when conditions may not be fully turbulent, and the boundary layer may occupy a significant fraction of the subchannel area, this model will increasingly underestimate the enhancement since the direct interaction of droplets with the boundary layer will no longer be negligible.

A simple alternative model which can be expected generally to overestimate the heat transfer enhancement in the transition region treats the interphase drag as a direct augmentation of the wall shear stress. In this case an effective friction factor is obtained from the total shear stress on the gas phase:

$$f = \frac{d_h\ (F_w+F_D)}{2\ \rho_v u_v^2} . \tag{17}$$

The effect of the drops is treated as an effective increase in wall roughness with a "rough wall" friction factor given by equation (17). Kays (8) has suggested that the reported heat transfer effect of rough walls is well represented by the relationship

$$\frac{h}{h_{smooth}} \propto \sqrt{\frac{f}{f_{smooth}}}, \tag{18}$$

rather than the normal Reynolds analogy. Equations (17) and (18) provide a simple, "rough wall" model of the droplet enhancement of steam convective cooling.

Steam/Droplet Convective Heat Transfer

The convective heat transfer between the phases, per unit volume, is given by

$$q_{VLC} = h_{VLC} \frac{6(1-\alpha)}{d} (T_V - T_{sat}). \tag{19}$$

A number of correlations of steam/droplet heat transfer coefficient have been reported, of which two have been used in the model to examine the sensitivity to this parameter. These are the Lee-Ryley (9) correlation

$$Nu_{VLC} = 2 + 0.74\ Re_d^{0.5}\ Pr_V^{0.33} \tag{20}$$

evaluated using free stream properties, and the Yuen-Chen (10) correlation

$$Nu_{VLC}\ (1+B) = 2 + 0.6\ Re_d^{0.5}\ Pr_V^{0.33}, \tag{21}$$

where

$$B = (h_V - h_g)/h_{fg},$$

and where properties are evaluated at film conditions with the exception of the density in Re_d which is the free stream density. The Lee-Ryley correlation is used in the standard form of the model.

Radiation

Radiative heat transfer is calculated in the manner described earlier with the addition of the liquid component represented as an optically thin medium with an attenuation coefficient given by

$$a_L = \alpha_{eff} \cdot \frac{\pi d^2}{4} \cdot N_d \tag{22}$$

where N_d is given by equation (8) and the effective absorptance of the drops ($\alpha_{eff} = 0.9$) is taken from Harpole (11).

3.5 Flow Diversion

In the axial region of the blockage the flow in the peripheral unblocked part of the rod bundle is enhanced by diversion of flow from the central blocked region. In the present model this is represented by a step increase in the peripheral steam flow at the elevation where the blockage begins, and a step decrease at the end of the blockage. The magnitude of the diversion is calculated

on the basis of the flow areas in the blocked and peripheral regions, and is applied to the steam component only. This approximation is a good one for the peripheral region since the blockage flow area is a small proportion of the total, but the analysis of blockage throat conditions requires a proper calculation of the flow diversion. Such a calculation is currently under-development.

4. COMPARISON OF MODEL WITH EXPERIMENT

4.1 Droplet Dynamics

The model has been used to calculate fluid conditions upstream of the blockage in the central subchannel for comparison with droplet dynamics data from the high speed films. Measured and calculated mean droplet velocities are shown in figure 11 where it can be seen that the droplets are calculated to accelerate a little more rapidly than observed. This can be attributed to the lack of droplet coalescence in the model. The initial drop size is in good agreement with data (1.09 mm calculated c.f. 0.93 mm measured), whereas that just below the grid is too small (1.085 mm calculated c.f. 1.58 mm measured at 469 mm). The errors of small drop size and large drop velocity partially outweigh each other in the calculation of convective heat transfer to the drops, but the drop size effect is the more powerful.

It is also apparent from figure 11 that the calculated droplet momentum loss at the grid is large compared with the small loss indicated by the measurements. In spite of these discrepancies the calculated droplet velocities are within ± 15% of measured values and this is encouraging in view of the simplifications of single drop size and no interactions made in the model.

4.2 Heat Transfer

Pin cooling rates and steam temperatures calculated by the standard form of the model are compared with experimental data in figures 12 and 13 for low steam flow, and in figures 14 and 15 for high steam flow. Additional calculations are presented in figure 16 to illustrate the sensitivity to droplet heat transfer modelling, and in figure 17 to show the sensitivity to turbulence enhancement modelling.

It can be seen that the standard model prediction of rod cooling rate and steam temperature is generally good, particularly for the centre rod calculations. For these cases, where uncertainties in steam convective cooling and radiation cooling are small, the good agreement between calculated and measured steam temperatures implies that droplet evaporation is well predicted. For the peripheral rods in the region upstream of the blockage, the calculated cooling rates at both times are high by up to 25%. It is apparent from the 'no drops' result in figure 16 that the error is mainly in the steam cooling and/or radiation heat loss calculations. The source of the error is not certain, but the radiative heat losses for peripheral rods are considerable in the low flow test (figure 12) and are possibly not well modelled. Bundle steam velocity non-uniformities are also neglected.

It is clear from figure 16 that the droplet contribution to rod cooling is small at low elevations but becomes very considerable in the upper half of the bundle. In part this arises from the decreasing importance of bundle entry effects on steam convective cooling (see figure 2), but it also reflects the progressive increases in steam temperature and phase velocity difference which lead to a corresponding increase in droplet evaporation. The comparison in figure 16 of different droplet heat transfer models shows differences of rod cooling rate

comparable with the experimental scatter, though the outlet steam temperature is better predicted by the Lee-Ryley correlation used in the standard form of the model.

Figure 17 shows that the effect of drop-induced enhancement of convective rod cooling is small but not negligible. For the droplet flow of this experiment (1.35 gm s^{-1} per subchannel) the enhancement of the convective component lies in the range 10 - 20% depending on the model used. Discrimination between the models considered here would require data from experiments with considerably greater droplet flows.

The droplet and steam flows in the experiment described above are typical of PWR reflood simulation experiments and the model results presented here indicate that for these conditions the modelling uncertainties associated wtih droplet related heat transfer are not large in the unblocked part of the bundle. However, it is expected that in the blocked region droplet concentrations will rise by up to a factor 10 since only the smallest droplets will be diverted into peripheral subchannels. In these conditions the modelling uncertainties both of droplet heat transfer and droplet induced turbulence enhancement will be very significant and prediction of rod cooling in the blockage throat is expected to be considerably more difficult as a result.

5. CONCLUSIONS

Comparison of predictions of a detailed droplet dispersed flow heat transfer model with measured rod cooling rates and droplet behaviour in a rod bundle has led to the following conclusions:

(i) A droplet equation of motion representing non-interacting drops of uniform size has calculated drop velocities correct to within 15% of measured values. Future improvements should include a refinement of the model of momentum losses at grids, and representation of observed droplet coalescence and breakup processes.

(ii) Rod cooling rates were well modelled in the centre of the cluster and steam temperatures were well predicted. This indicates that the Lee-Ryley correlation used for steam-drop heat transfer provides an adequate prediction of the desuperheating effect of the drops. Residual errors in predicted cooling rates for peripheral rods are probably accounted for by neglect of bundle radial steam velocity profiles and inadequate modelling of radiative losses.

(iii) Enhancement of steam convective cooling by droplet-induced turbulence was found to be small but significant at the low droplet flux of these tests. Currently proposed models differ by a factor 2 in predicting the effect, but discrimination between them requires experimental data for higher liquid fractions.

ACKNOWLEDGMENT

This paper is published by permission of the Central Electricity Generating B Board.

REFERENCES

(1) Lee, N., Wong, S., Yeh, H.C. and Hochreiter, L.E., 1981, PWR FLECHT-SEASET Unblocked bundle forced and gravity reflood task data evaluation and analysis report. WCAP-9891.

(2) Kim, J.H., 1979, "Heat transfer in longitudinal laminar flow along circular cylinders in square array", from "Fluid Flow and Heat Transfer over Rod or Tube Bundles", presented at Winter Annual Meeting of ASME, New York, Dec. 2-7.

(3) Fairbairn, S.A. and Piggot, B.D.G., 1983, Progress Report No. 6 - CEC Contract SR004 UK-N, "Studies on the Effects of Blockage upon LWR Emergency Core Cooling Systems".

(4) Chandrasekhar, S., 1961, "Hydrodynamic and Hydromagnetic Stability", Oxford University Press.

(5) Blair, M.F., 1983, "Influence of free-stream turbulence on turbulent boundary layer heat transfer and mean profile development, part II - Analysis of Results", Trans ASME J Heat Transfer, vol. 105, pp 41-47.

(6) Simonich, J.C. and Bradshaw, P., 1978, "Effect of free stream turbulence on heat transfer through a turbulent boundary layer", ASME Journal of Heat Transfer, vol 100, No. 4, pp 671-677.

(7) Theofanous, T.G. and Sullivan, J., 1982, "Turbulence in two-phase dispersed flows", J. Fluid Mech. vol. 116, pp 343-362.

(8) Kays, W.M., 1966, "Convective Heat and Mass Transfer", McGraw Hill.

(9) Lee, K. and Ryley, D.J., 1968, "The evaporation of water droplets in superheated steam", Trans, ASME J. of Heat Transfer, Nov. 1968, pp 445-451.

(10) Yuen, M.C. and Chen, L.W., 1978, "Heat Transfer Measurements of Evaporating Liquid Droplets", Int. J. Heat Mass Transfer, Vol 21, pp 537-542.

(11) Harpole, G.M., 1980, "Radiative absorption by evaporating droplets", Int. J. Heat and Mass Transfer, Vol 23, No. 1, pp 17-26.

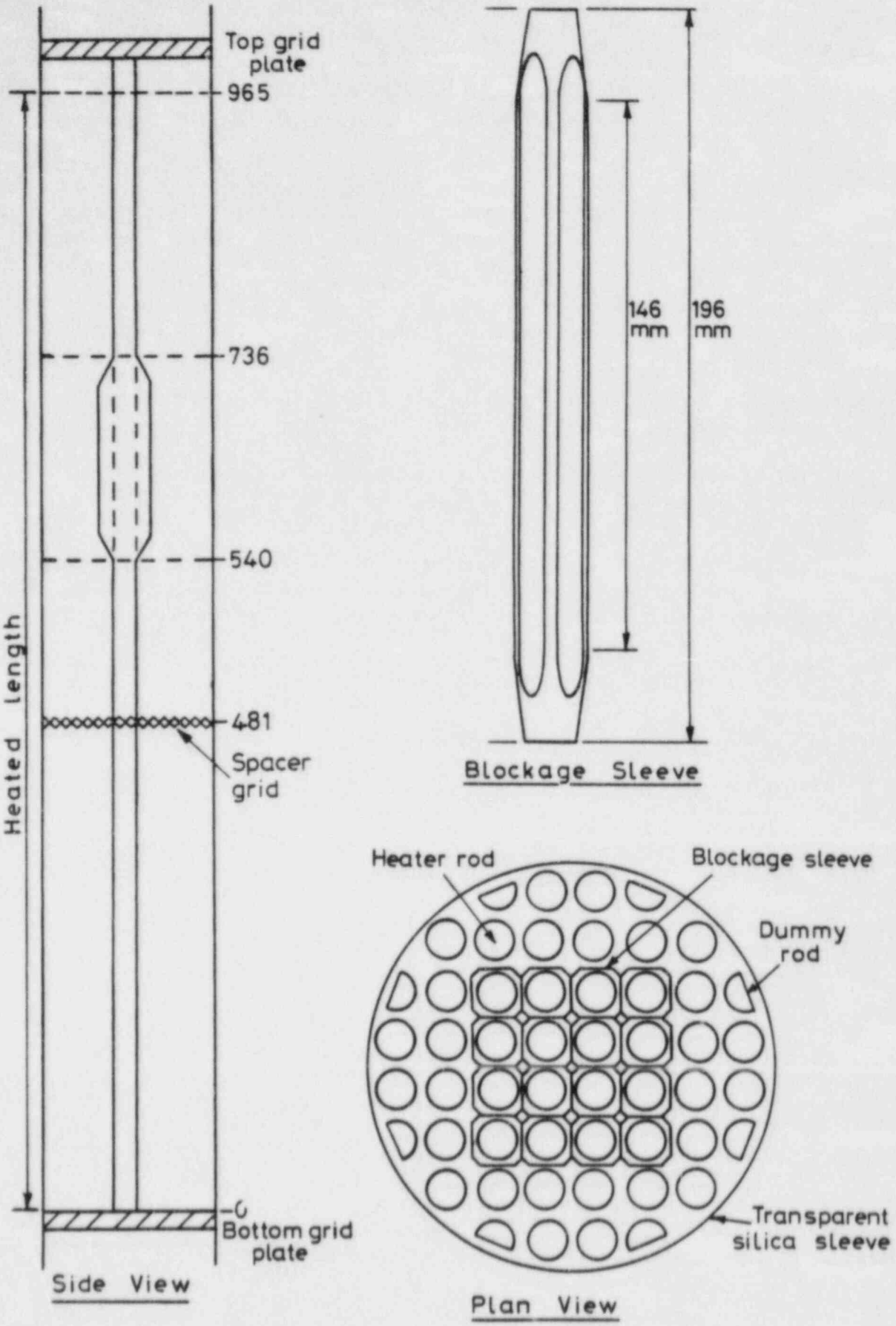

FIG.1. Details of Two Sections and Blockage Sleeves.

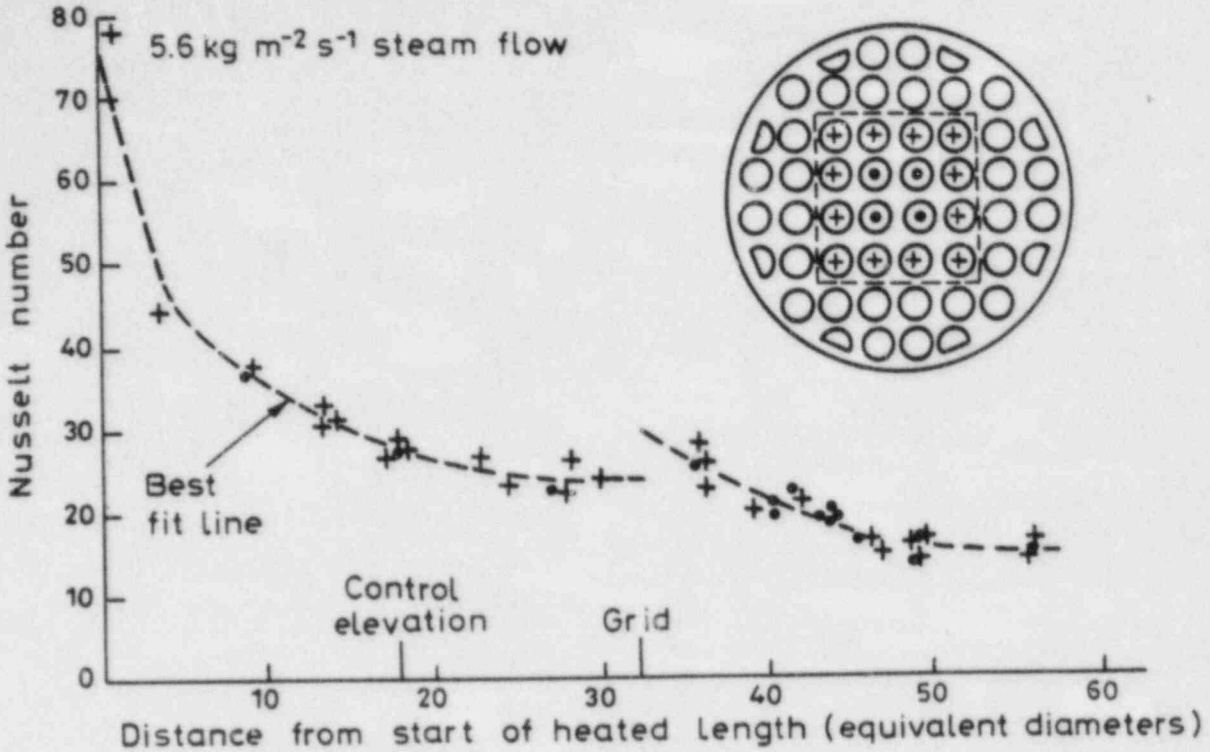

FIG. 2. Axial Variation of Steam Convective Heat Transfer in an Unblocked Pin Bundle.

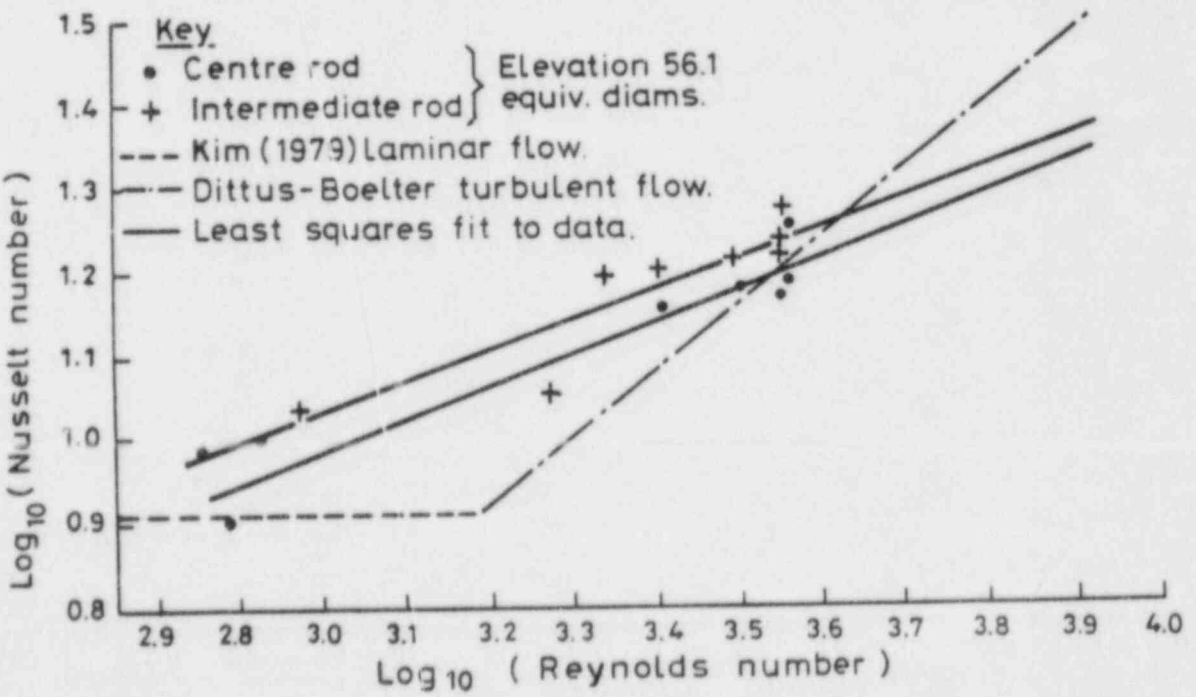

FIG. 3. Variation of Steam Convective Heat Transfer with Reynolds Number.

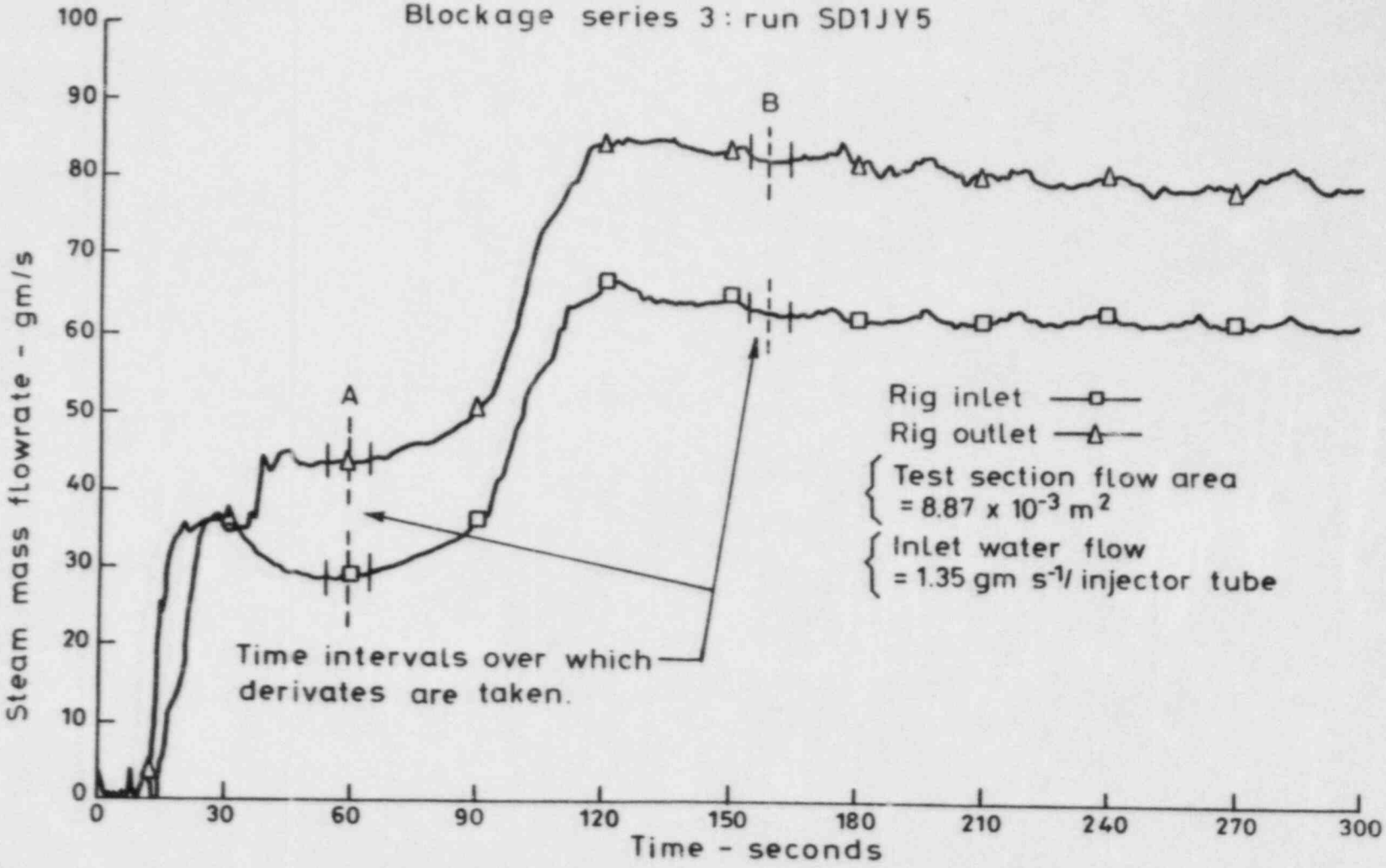

FIG. 4. Test Section Steam Flows during a High Temperature Steam and Droplet Test.

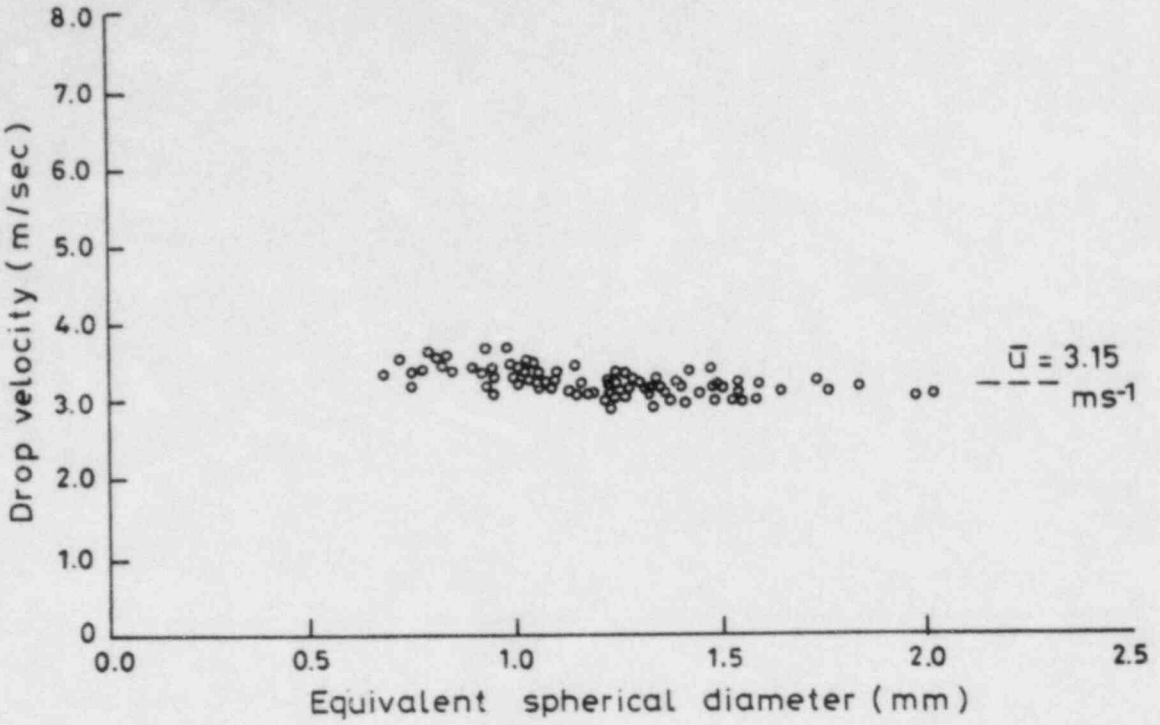

FIG.5. Drop Sizes and Velocities at 290 mm Elevation.

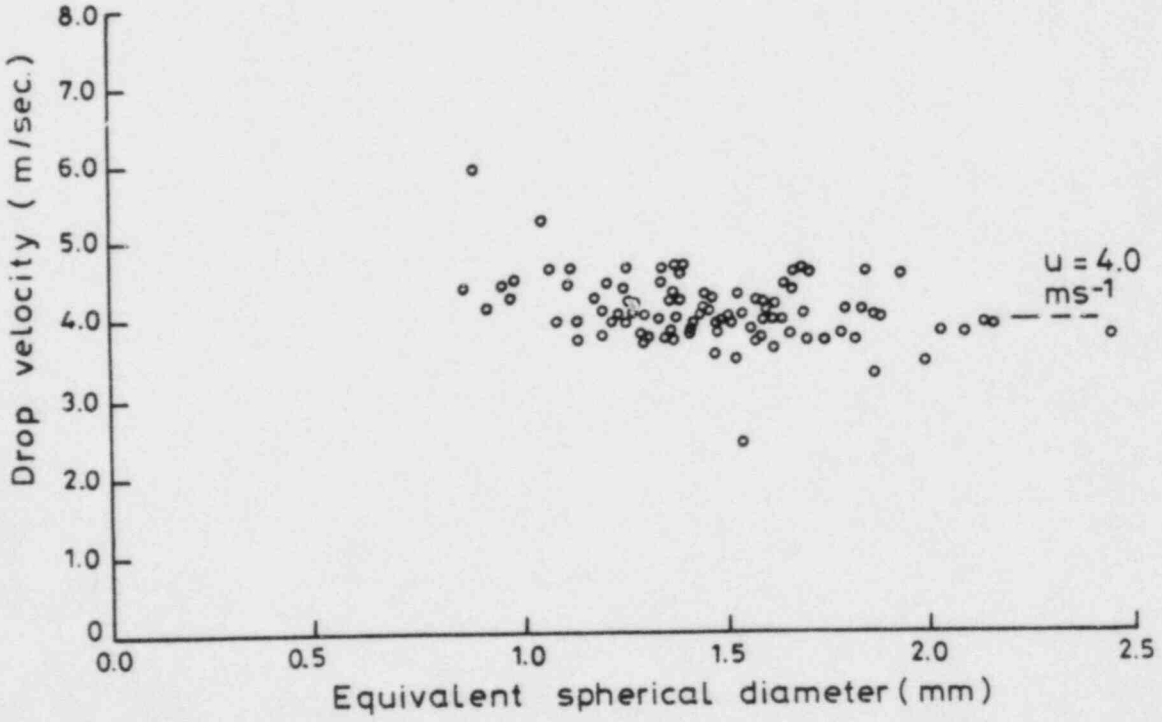

FIG.6. Drop Sizes and Velocities at 469 mm Elevation.

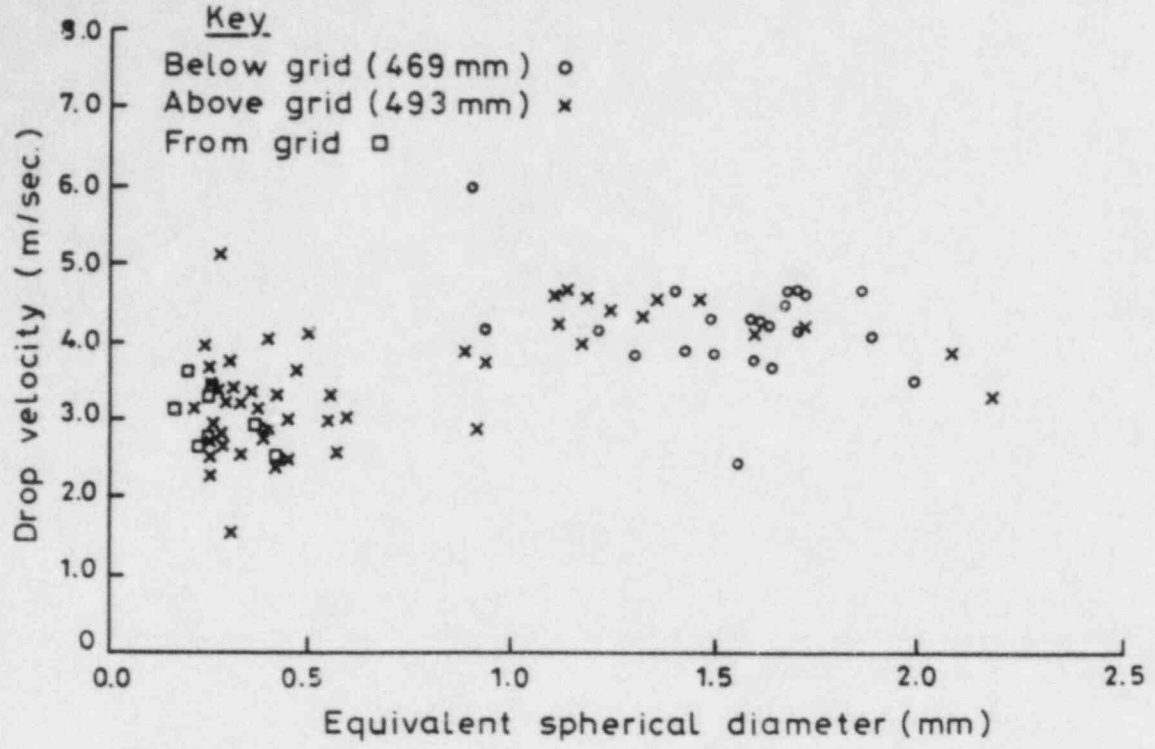

FIG.7. Effect of Grid on Drop Behaviour.

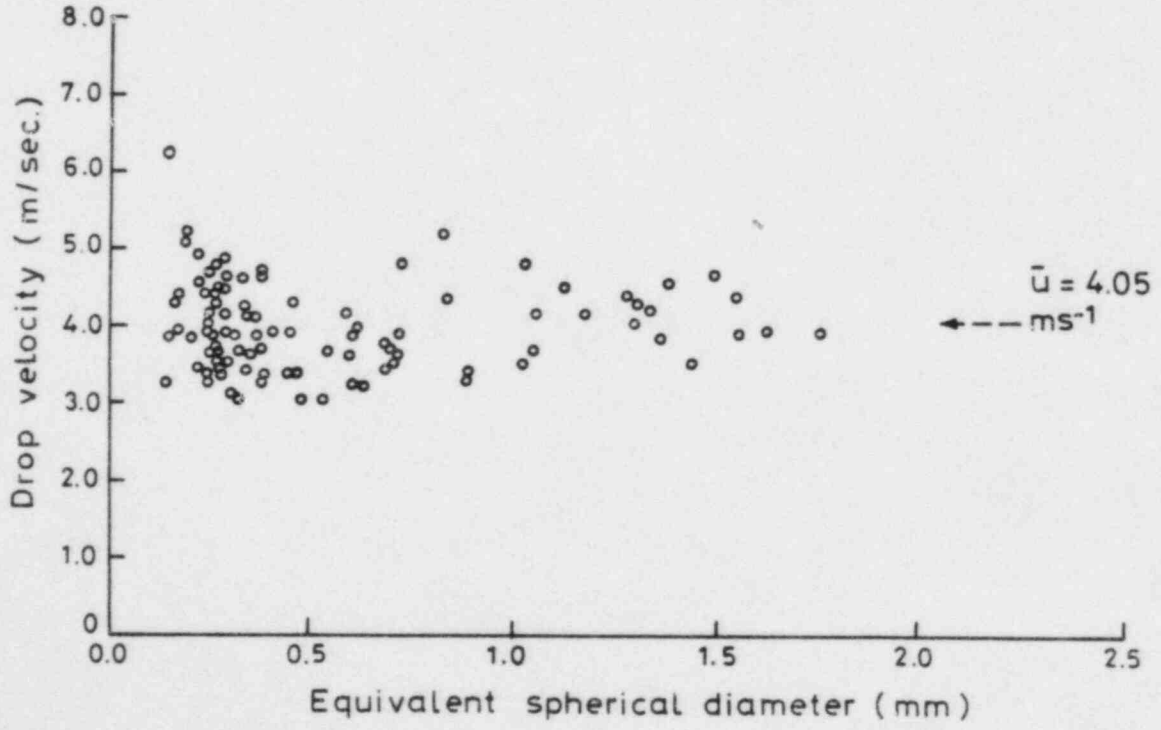

FIG.8. Drop Sizes and Velocities at 520 mm Elevation.

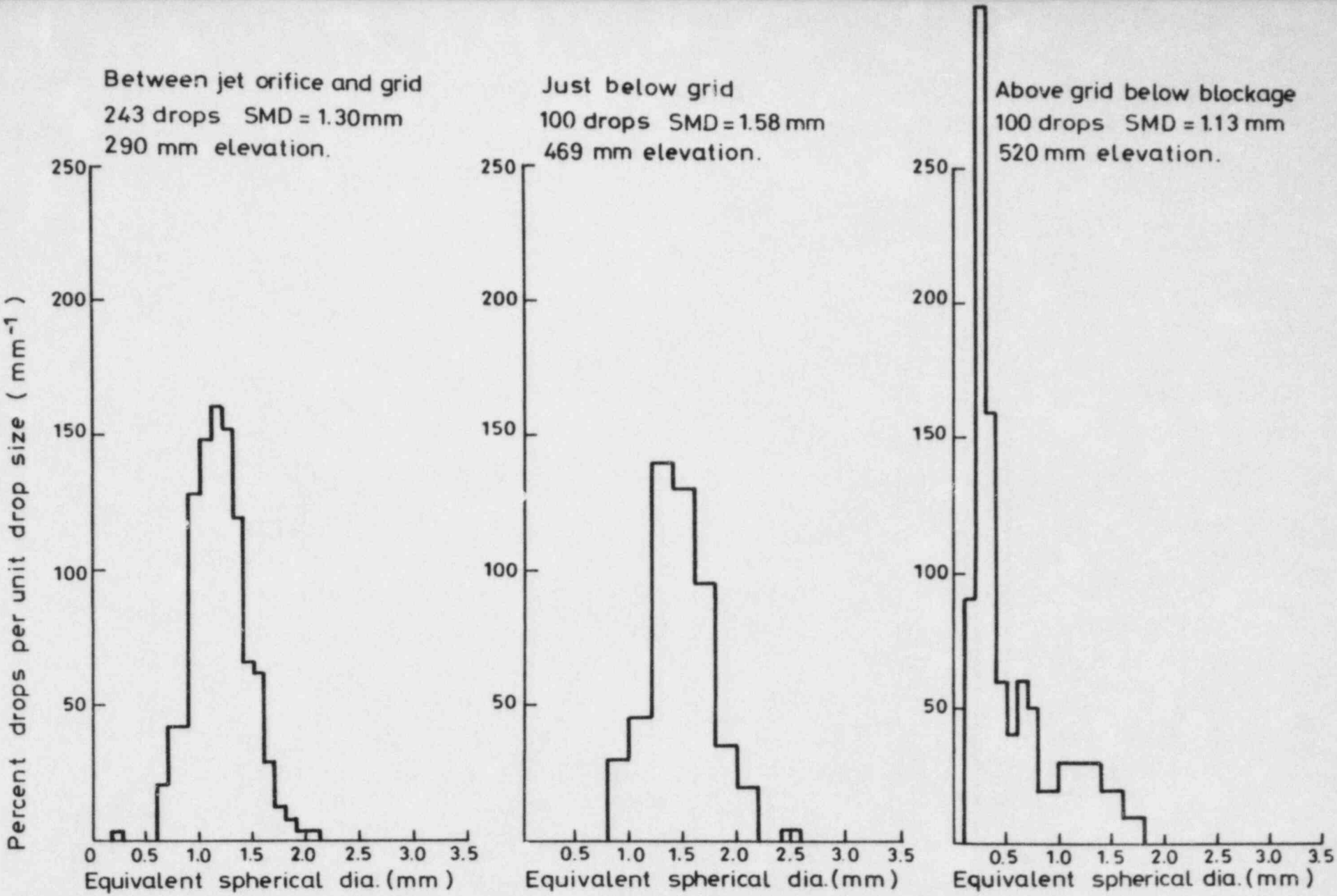

FIG.9. Drop Sizes from High Speed Movies of 800°C Steam and Drop Tests.

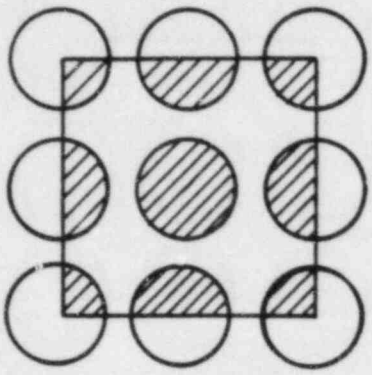

FIG.10. Control Region used in the Model.

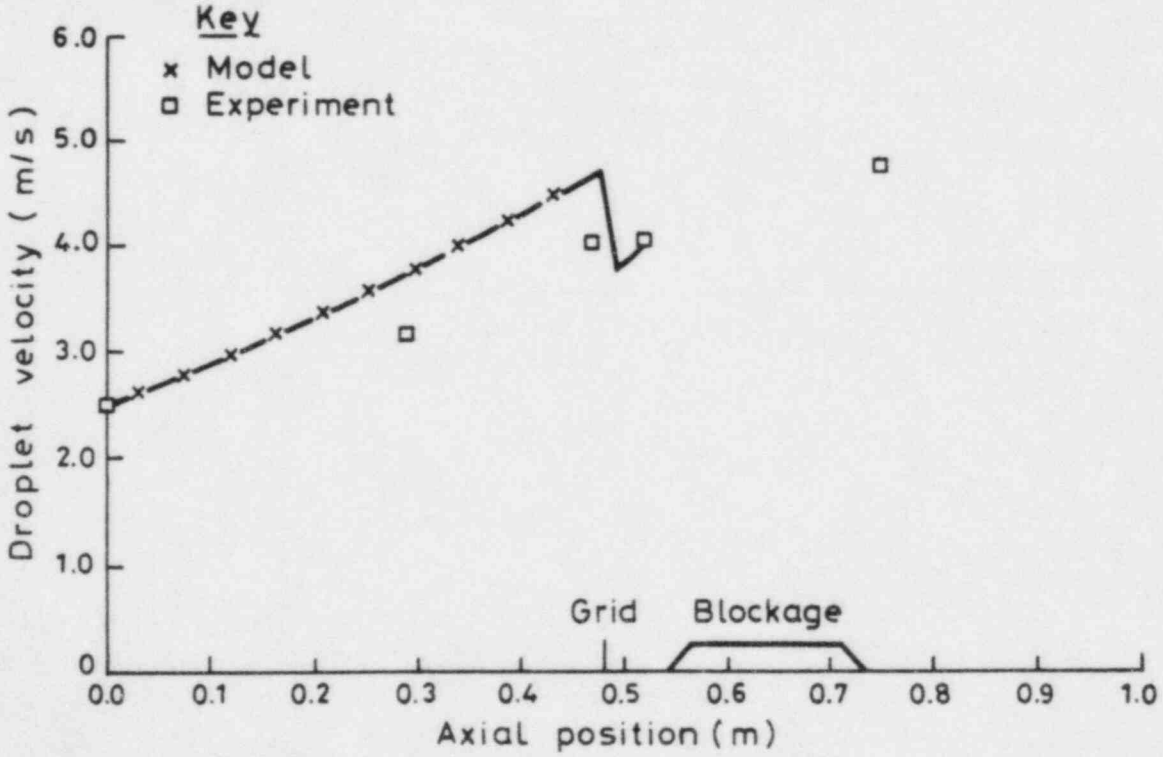

FIG.11. Comparison of Measured and Calculated Mean Droplet Velocities.

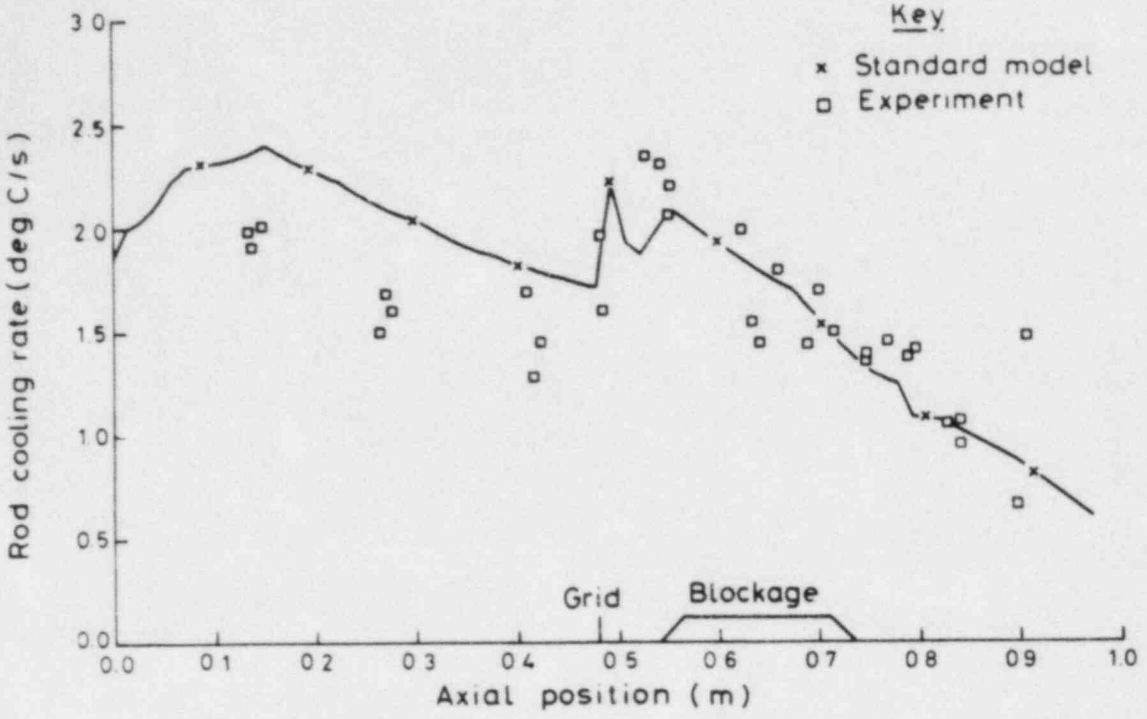

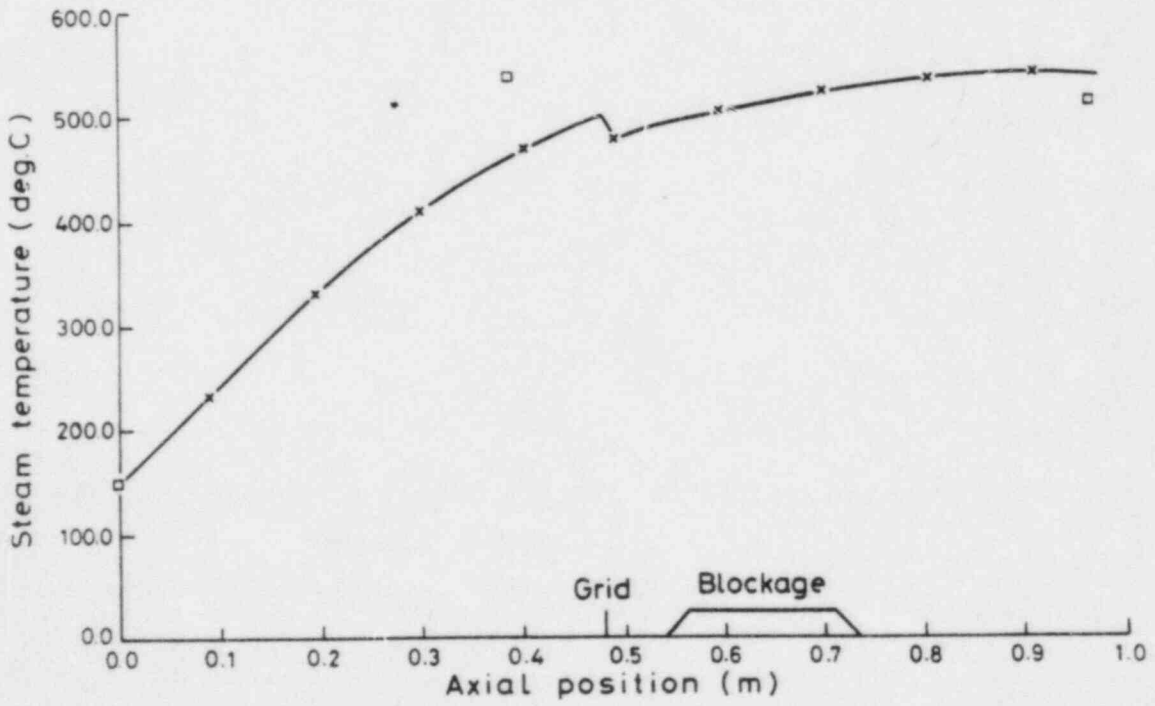

FIG.12. Model vs. Experiment, Peripheral Rod, t = 60 sec.

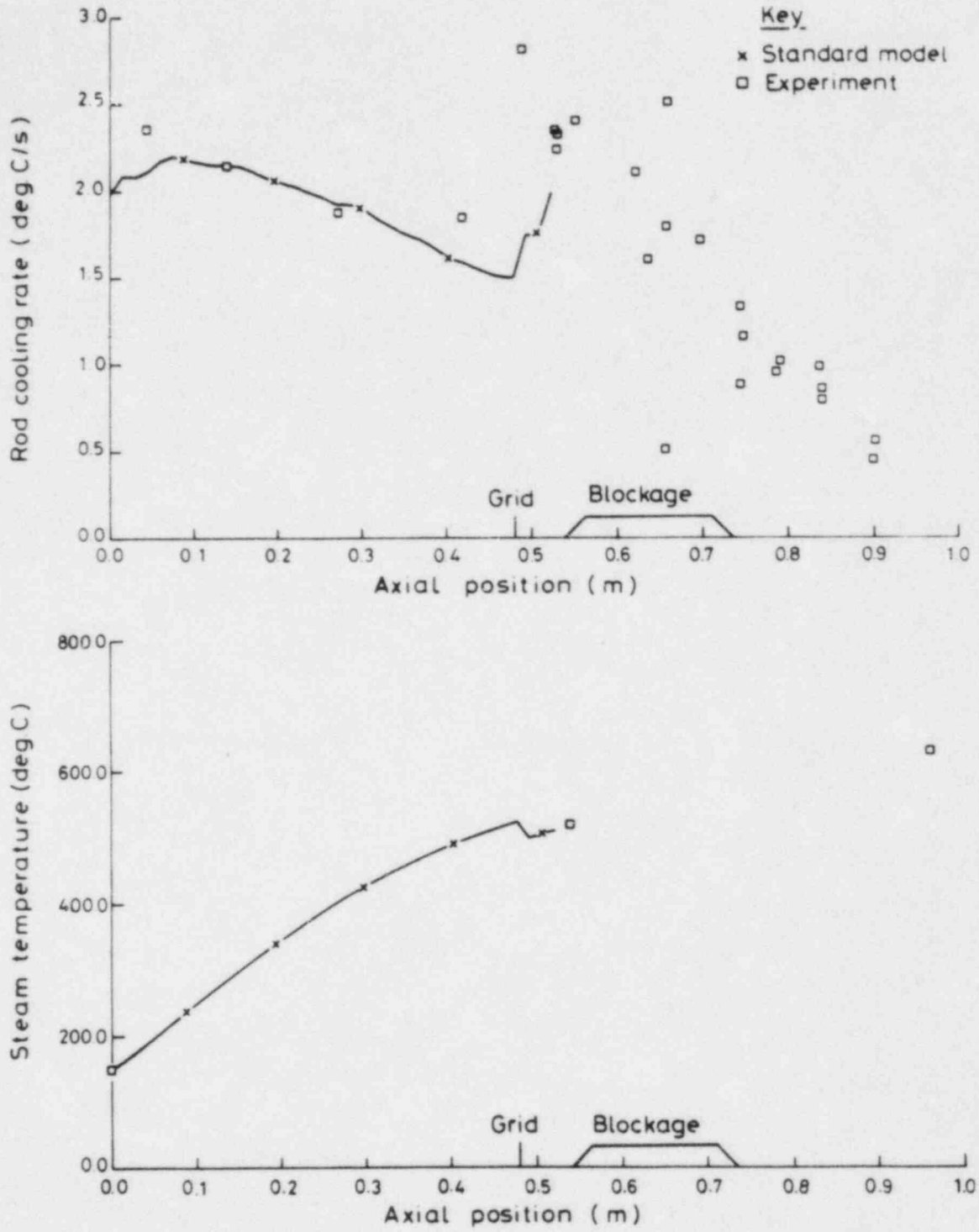

FIG.13. Model vs. Experiment, Central Rod, t = 60 sec.

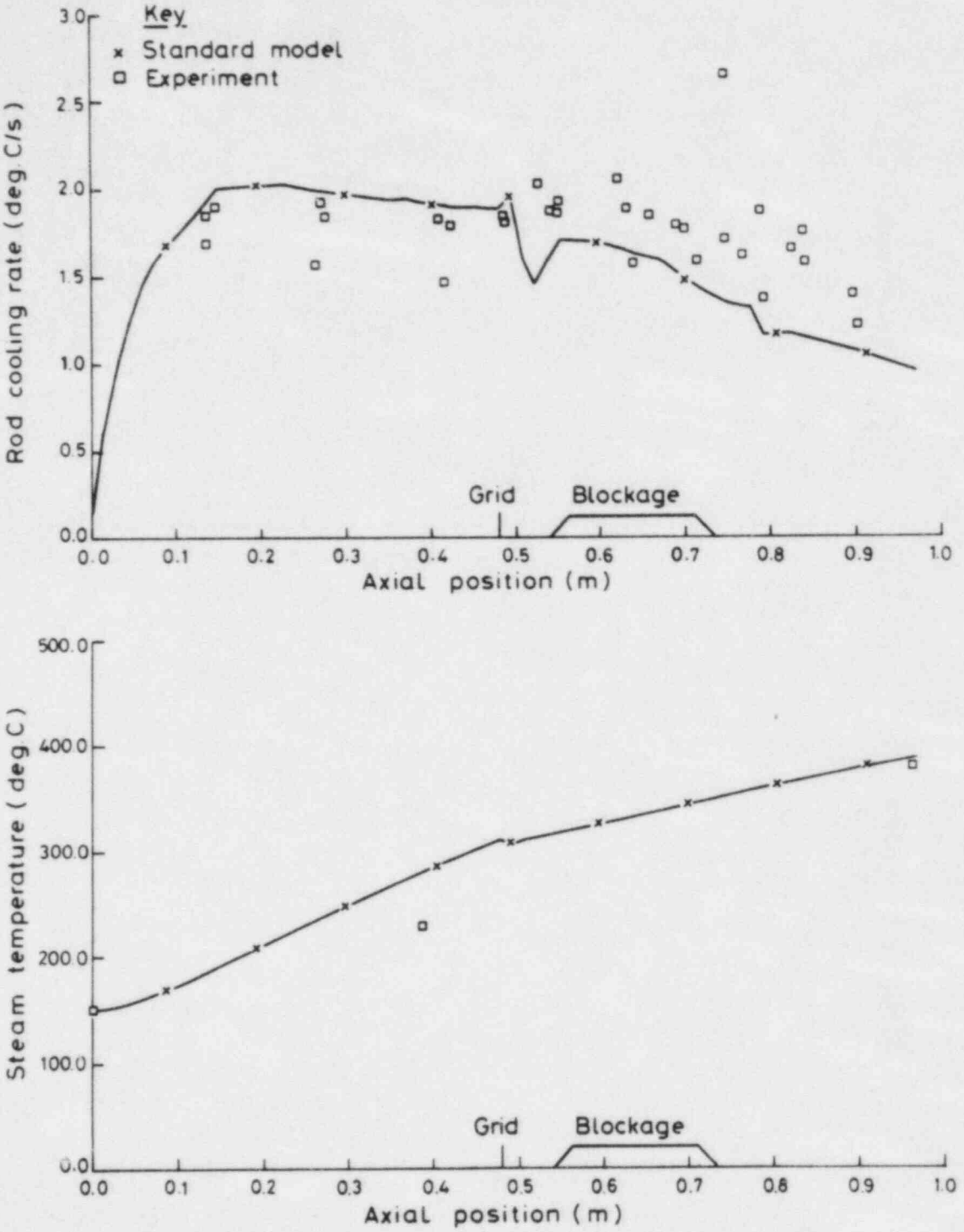

FIG. 14. Model vs. Experiment, Peripheral Rod, t = 160 sec.

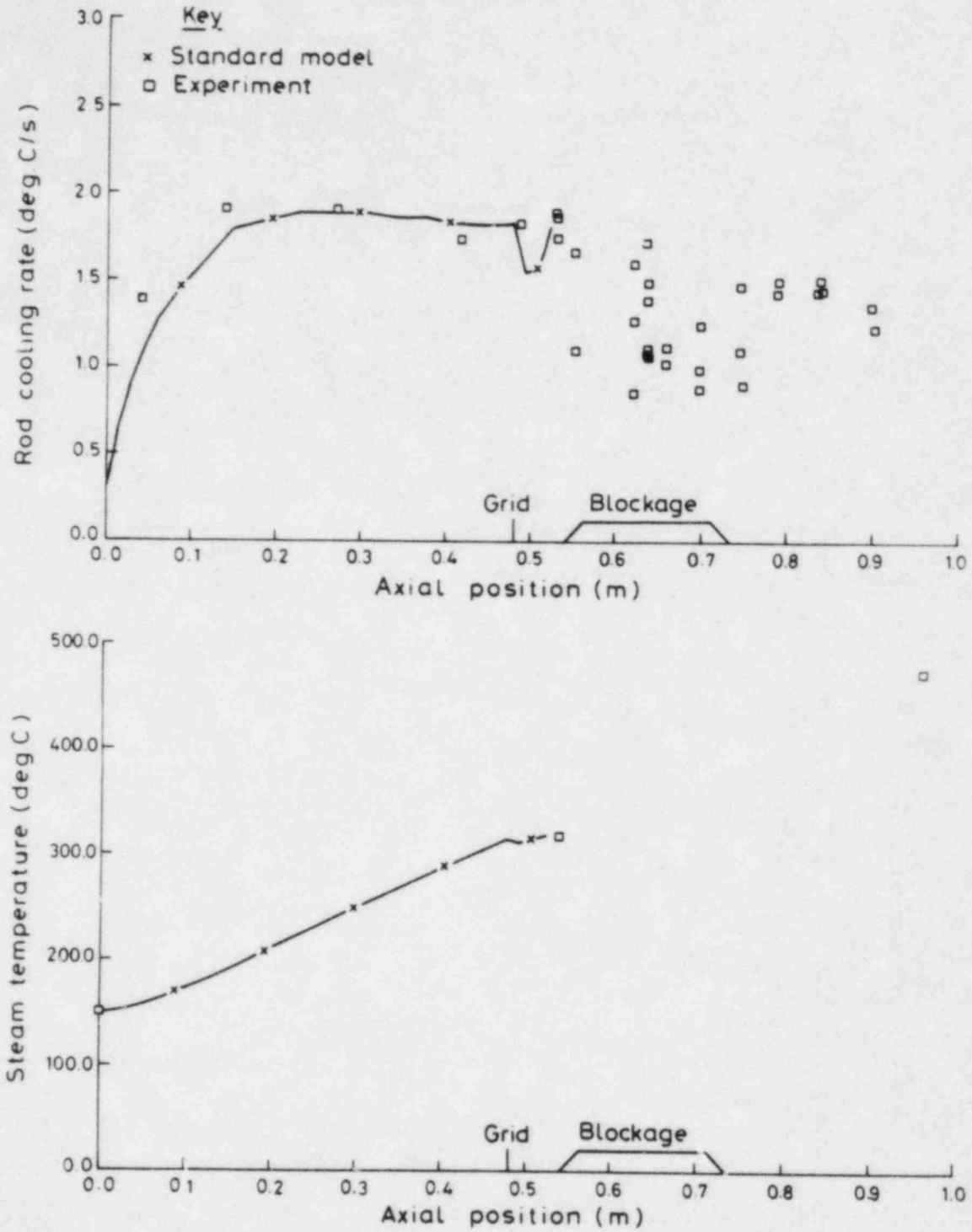

FIG.15. Model vs. Experiment, Central Rod, t = 160 sec.

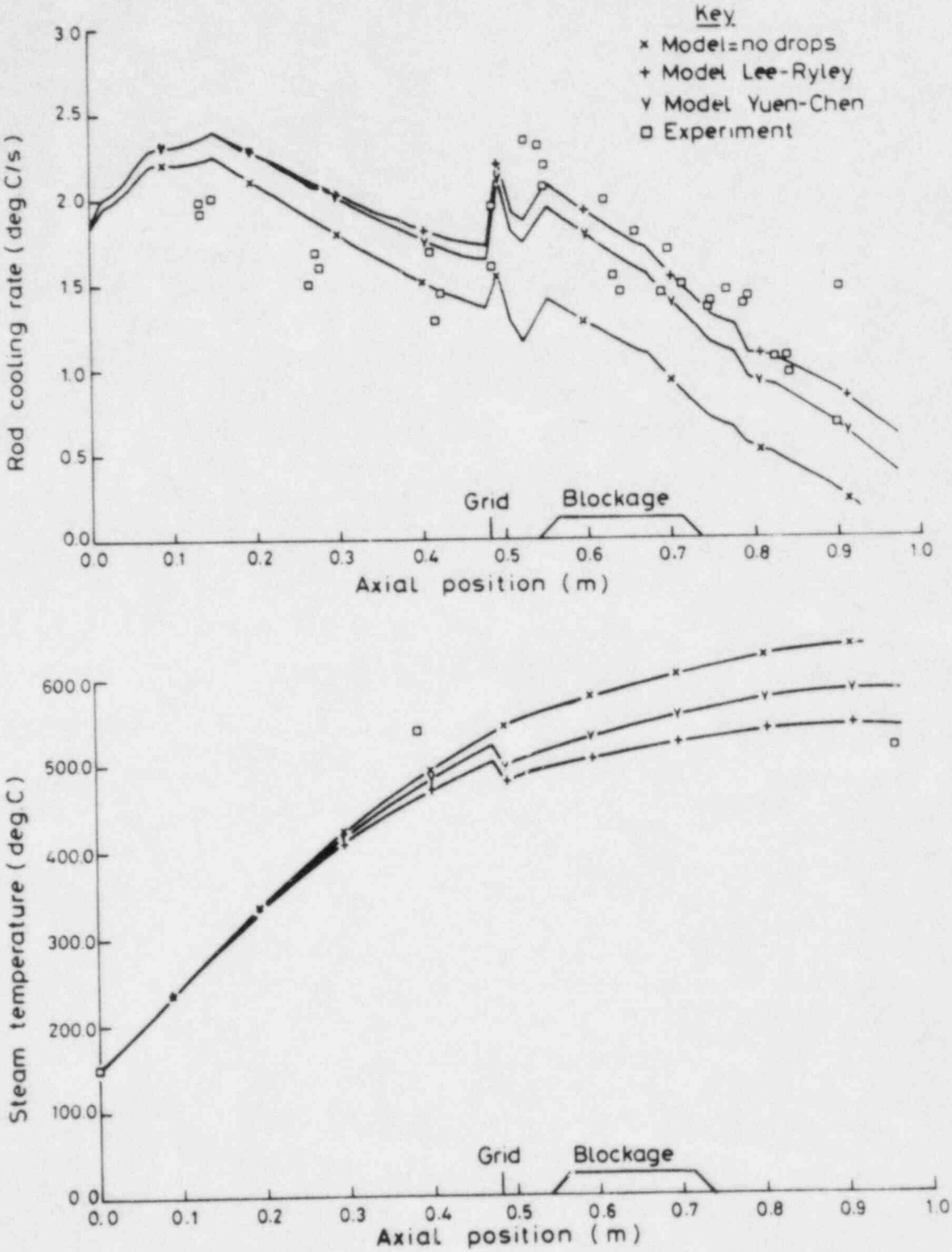

FIG.16. Sensitivity to Droplet Heat Transfer Modelling.

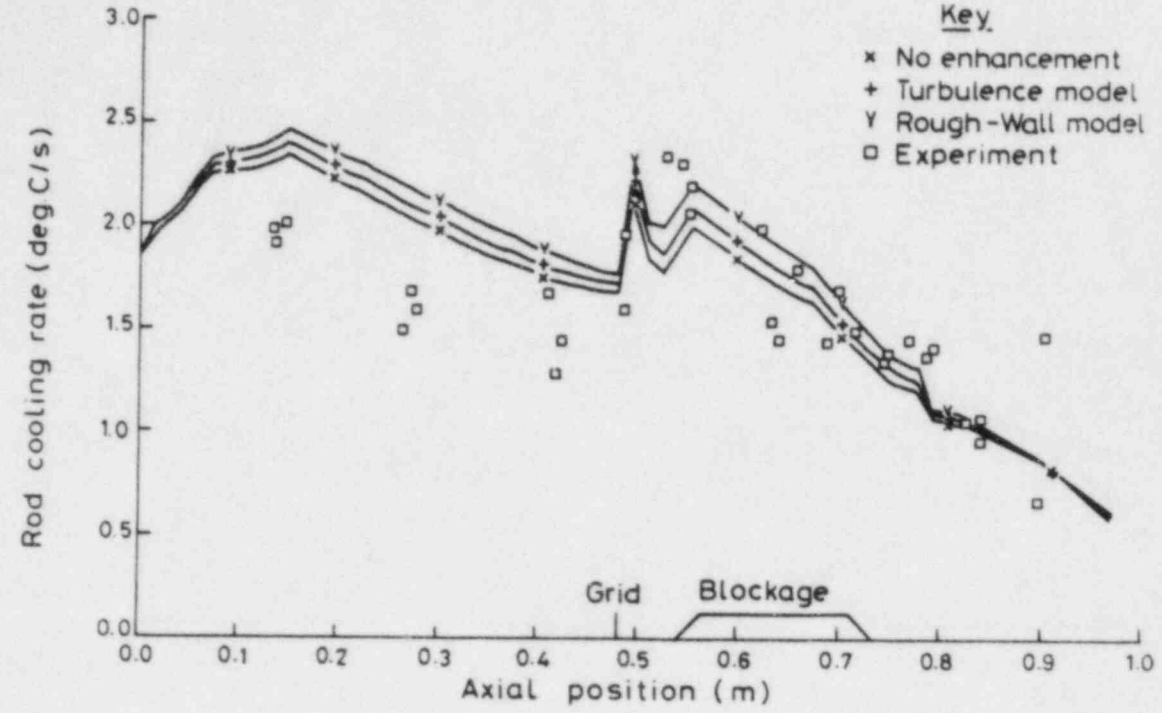

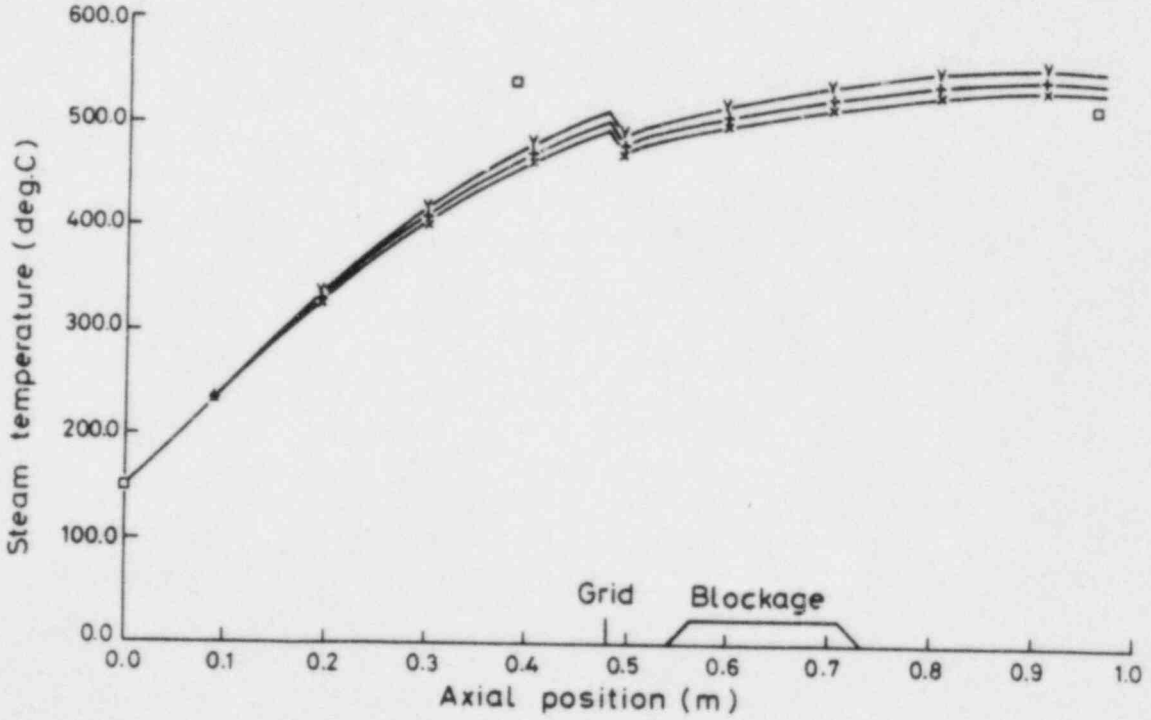

FIG.17 Sensitivity to Drop-Induced Turbulence Modelling.

AN EXPERIMENTAL STUDY OF HEAT TRANSFER ENHANCEMENT IN DISPERSE FLOW IN ROD BUNDLES†

by

H. Kianjah, V.K. Dhir and A. Singh*
School of Engineering and Applied Science
University of California, Los Angeles

ABSTRACT

In this work experiments have been carried out to study the effect of the presence of a discontinuous phase on heat transfer in rod bundles. The test-section is a four rod bundle with rod diameter and pitch of typical PWR fuel elements and is housed in a plexi-glass tube. The rod bundle is 184 cm tall and heated electrically. In the experiments glass particles with a mean diameter of 30 μm and 100 μm are entrained in air. The data for the heat transfer coefficient are obtained for mass flow rate ratio of particles to air varying from 0 to 8.6 or the volume fraction, β, of particles to air varying from 0 to 3×10^{-3}.

The results of the experiments show that in the presence of the particles the heat transfer coefficients are significantly increased. The enhancement increases with mass flow rate ratio of particles to air but decrease with the flow Reynolds number. An enhancement of as much as 200% is observed with 30 μm particles at a Reynolds number of 14500. However the enhancement with bigger particles is much smaller, the maximum being about 30%.

INTRODUCTION

During reflood phase of a loss of coolant accident in light water reactors, entrained flow conditions exist over a large extent of rod bundles downstream of the quench front. The maximum temperature attained by the rods prior to complete cooling significantly depends on the heat transfer rate under entrained flow conditions. The purpose of this work is to determine experimentally under simulated conditions the enhancement in heat transfer resulting from agitation or turbulence created by the presence of droplets in steam flow.

Several studies [e.g. 1-6] documenting the two phase gas-liquid heat transfer coefficients have been reported in the literature. These studies unequivocally show that the presence of small amounts of gas in a flowing liquid can significantly enhance the heat transfer from the wall. It is found that the magnitude of the ratio of two phase to single phase heat transfer coefficient for bubbly and slug flow increases with the cross-sectionally averaged void fraction. The enhancement in heat transfer

† This work was supported by the Electric Power Research Institute

* Safety and Analysis Department, EPRI.

coefficient however decreases with an increase in the liquid Reynolds number.

Two phase heat transfer is largely dominated by its turbulent nature. In an attempt to better understand this, Serizawa et al [7,8] have made a detailed study of the structure of turbulence in air-water bubbly flows. From their results it was noted that in fully developed turbulent flows generally all of the turbulent parameters were uniform across the central portion of the tube. Serizawa et al found that the relative turbulent intensity was minimum at the tube center and generally increased towards the tube wall. However, it must be noted that measurements were not taken for $|r/R| > 0.9$. They also observed that for a constant liquid velocity the turbulent intensity first decreased with an increase in gas flow rate and then as the gas flow rate was further increased the turbulent intensity increased also. Finally, Serizawa et al concluded that in the turbulent transport process it is the turbulent velocity components of the liquid-phase which are the most important. Contrary to these observations, Theofanous and Sullivan [9] have found that there is a strong dependence of the turbulent intensity on the flow rate of the discontinuous phase. Theofanous et al have experimentally studied turbulent intensity in two phase bubbly flow in pipes and have modeled the effect of turbulence on wall shear stress. Use of Reynold's analogy to their wall shear stress model, as has been shown by Drucker et al [10], results in an expression for the ratio of two phase to single phase heat transfer coefficients as

$$\psi \equiv \frac{Nu_{tp}}{Nu_{sp}} = (1-\alpha^2) + 300\,(1-\alpha)\,\frac{\alpha Gr}{Re^2} \qquad (1)$$

Arguing that the increase in wall shear stress in the presence of a discontinuous phase results from the interaction of the two phases and that the velocity characterizing this interaction can be assumed to be proportional to the slip velocity between the two phases, Drucker et al correlated most of the two phase flow heat transfer data available in the literature as

$$\psi = 1 + C_1 \left(\frac{\alpha Gr}{Re^2}\right)^{\frac{1}{2}} \qquad (2)$$

The constant C_1 was found to be 2.5 for flow in tubes and 3.25 for flow over a four rod bundle [10]. Drucker et al proposed that similar enhancement mechanism and a correlation similar to equation (2) should be valid when solid particles are entrained in a gas. Theofanous and Sullivan also made the same observation.

Several studies of heat transfer in flowing solid-gas mixtures have also been reported in the literature. The earliest quantitative study out of these is that of Farbar and Morley [11]. In their experiments Farbar and Morley entrained alumina-silica catalyst particles in air and passed the mixture through a 17.5 mm I.D. tube with its wall maintained at a nearly constant temperature. They observed that the heat transfer coefficient

increased with the ratio of mass flow rate of solids and air and with the flow velocity. However for turbulent flow of air, the enhancement in heat transfer was found to decrease with flow Reynolds number. For mixtures of particles lying in the size range 20-210 μm, they correlated their data as

$$Nu_{tp} = 0.14\ Re^{0.6} \left(\frac{Ws}{Wa}\right)^{0.45} \qquad (3)$$

Subsequently Farbar and Depew [12] conducted experiments on nearly uniform particle sizes of 30, 70, 140 and 200 μm. In these experiments they observed that the smallest particles resulted in highest enhancement in heat transfer whereas the largest size particles had no appreciable effect. The thermal entry length was found to increase with particles and Depew and Farbar [13] report, it could be three times higher than that for flow with no particles.

Danziger [14] correlated a variety of heat transfer data obtained with solid-gas flows. These data covered a range of Reynold's number from 178-25400 solid loading ratio from 2 to 446 and tube diameter from 17.5 to 38.5 mm. From these data it was concluded that the two phase heat transfer coefficient increases with loading ratio in the same way as given by equatior (3).

An attempt at developing a mechanistic model for heat transfer in solid-gas flows has been made by Briller and Peskin [15]. They proposed that shrinkage of the laminar sublayer as a result of penetration by solid particles is the main reason of enhancement of heat transfer. By incorporating quantities such as laminar sublayer thickness, number density of particles and penetration depth, they have obtained an explicit expression for the two phase heat transfer coefficient. Their expression gives a dependence of $(Ws/Wa)^{0.4}$ with loading ratio which is about the same as given by equation (3). However their expression has a limited range of application. At very high Reynold's numbers they conclude from their data that it is the thermal capacity of the flow which enhances the heat transfer rather than the thinning of the laminar sublayer. This conclusion is consistent with the observation made by Tien and Quan [16] from their experiments with lead and glass particles. The enhancement was smaller with lead particles which had lower thermal capacity.

The presence of particles in a gas stream is also found to enhance heat transfer during cross flow over tubes [17]. A very comprehensive review of heat transfer in solid-gas flows has been presented by Kramer [18].

The purpose of this study is to quantify the enhancement in heat transfer as would occur in disperse flow regime due to the turbulence generated by the droplets. During reflood phase of the LOCA the droplets continue to evaporate as a result of heat transfer from the wall and from the steam. The continuous evaporation coupled with different modes in which heat can be transferred to the droplets, makes it difficult to discern in a real system the role the droplets play in improving the heat transfer from the wall. Thus in this study experiments are conducted by entraining glass particles in air. The density ratio of glass to air is about the same as of water to steam at expected system pressure during a LOCA.

EXPERIMENTAL APPARATUS AND PROCEDURE

The test apparatus was designed so that entrained flow heat transfer experiments without phase change could be performed on a 4 rod bundle with rod size and spacing typical of that of PWR fuel elements. The flow parameters and the loading ratio of the particles were chosen so as to cover the range of these parameters in typical reflood conditions.

Apparatus: The main components of the test apparatus are: the test section, a mixing chamber, variable area nozzle for metering flow of particles and a filtering system. Figure 1 shows a schematic diagram of the apparatus. The glass particles are stored in the feeder tank which is placed on a weighing machine. The variable area nozzle connects the feeder tank to a horizontal plexiglas tube which acts as a mixing chamber. One end of the mixing chamber is connected to utility air supply via a rotameter. The other end is connected to a flow establishing section preceding the test section. The flow establishing section is 77 cm long and is a 5.08 cm I.D. plexiglas tube. To re-establish the flow soon after it leaves the mixing chamber, a secondary air supply line is connected to the flow reestablishing section at the bottom. After passing through the test section, the mixture of particles and air is fed into a dust collector. A series of filters and a vacuum cleaner are used to collect particles entrained in the air leaving the dust collector.

The test section consists of 4 rods arranged in a square grid and housed in a 5.08 cm I.D. plexiglas tube. The rods are 1.1 cm O.D. stainless steel tubes with a wall thickness of 0.84 mm and a length of 184.2 cm. The rods are held together with spot welding at discrete locations wire wraps made out of 0.6 mm diameter stainless steel wire. Two of the four rods are instrumented with 30 gage chromel-alumel thermocouples. The thermocouples are spotwelded on the inner wall of the stainless stell tubes. Figure 2 shows the location of these thermocouples and a cross-sectional view of the test section. Copper flanges which act as grid plates as well as electrodes are silver soldered at both ends of the rods. During soldering, the rods are positioned such that the thermocouples on one of the instrumented rods face the inner channel while those on the outer rod face the outer channel. The rod thermocouples and the thermocouple placed at the inlet of the test section to measure the incoming fluid temperature are connected to a data logger. The electrodes are connected to A.C. power supply through a variac.

Procedure: Prior to initiation of experiments with a new rod bundle, the thermocouples mounted on the rods are caliberated with respect to the thermocouple placed at inlet of the test section. During caliberation room temperature air is passed over the rod bundle in the absence of any heating. After equilibrium conditions are attained the difference in temperatures given by the rod thermocouples and the inlet thermocouple are noted. Thereafter the flow rate of air is adjusted to a desired value and the electrical heating of the rods is initiated by maintaining a constant AC voltage across the rod bundle. The voltage is adjusted with the help of a variac and current and voltage are noted with a multimeter. During initial heating period and after steady state conditions are achieved, the data are scanned every fifteen seconds from all the thermocouples. To allow for any variation in the inlet temperature of air, an average of three sets of steady state data is used for calculations.

The solid particles are then entrained by opening the valve connecting the mixing chamber with the feeder tank. The choice of a particular nozzle is made

apriori depending on the desired flow rate of the particles. The reduction in the weight of the feeder tank is recorded every ten minutes. In a manner similar to the single phase experiments, the thermocouple output is continuously recorded on the data logger. Because of the fluctuations in wall temperature due to the turbulence created by the particles, the instability of the flow and the electrostatic charge developing between glass particle, an average of 6 to 12 data sets is taken.

Data Reduction: The thermocouple output recorded in millivolts was converted into temperature by using appropriate conversion factor. The evaluation of heat transfer coefficient requires outer wall temperature rather than the inner wall temperature as noted from the thermocouple output. Therefore assuming axial symmetry, no axial conduction and insulated inner wall, the steady state one dimensional conduction equation with heat generation was solved. For the highest heating rates employed in the present experiments, the maximum temperature difference between inner and outer wall was found to be 0.01K. This difference is extremely small in comparison to the temperature difference between the wall and the fluid. Thus the thermocouples can be considered to give the outer surface temperature.

Knowing the current, the voltage, the inlet temperature of the mixture, the total length of the rods and the mass flow rate of solid and air, the bulk mixture temperature at any axial location was calculated as

$$T_b(z) = Ti + \frac{EI}{(Wa c_{pa} + Ws c_{ps})} \frac{z}{L} \qquad (4)$$

In writing equation (4), it is assumed that the fluid and the particles are at the same temperature. This is a realistic assumption as has been shown in reference [19]. Knowing at a given location the wall temperature and the fluid temperature from equation (4), the local heat transfer coefficient is calculated as

$$h = \frac{EI}{4[T_w(z) - T_b(z)]\ As} \qquad (5)$$

While developing the correlation for enhancement in heat transfer, the volumetric fraction of particles rather than ratio of mass flow rate of solids to air is used. With the assumption that the particles attain their terminal velocity very quickly and that Stoke's drag law is valid, a relation between mass flow rate ratio and volumetric fraction of solids was found. A derivation of this is given in the Appendix.

RESULTS AND DISCUSSION

The single and two phase entrained flow experiments for heat transfer from a four rod bundle were conducted with Reynolds number varying from 14,500 to 21,000. In the experiments particles of 30 μm and 100 μm nominal size were used with mass flow rate ratio of particles to air varying from 0 to 8.6. These mass flow rate ratios resulted in the variation of solid volume fraction, β from 0 to 3×10^{-3}. Most of the results presented here pertain to the inner channel of the rod bundle however in one instance the heat transfer results for the outer channel are plotted in order to compare the behavior of the two channels.

Single Phase Heat Transfer: Single phase heat transfer coefficient data formed a subset of the two phase heat transfer data. In Figure 3, the Nusselt number based on heat transfer coefficient data for fully developed flow conditions is plotted as a function of Reynolds number. In defining the Nusselt number and the Reynolds number, the hydraulic diameter of the test section is used. The solid symbols represent the Nusselt number for the outer channel while the open are for the inner channel. It is noted that the turbulent flow data compare quite well with the correlation developed earlier in reference [10] for a similar test section and with water as the test liquid. The data also compare well with the Dittus Boelter correlation. However the data tend to be about 15-20% lower than the correlation of Weisman [20]. For Reynolds numbers in the laminar range, the Nusselt number as expected is independent of the Reynold's number. In the laminar range the Nusselt number has a value of about 5.5. This value is significantly lower than that obtained by Drucker et al [10] with water. One plausible reason for the large difference between air and water results is that for very low thermal conductivity fluid such as air, the bulk temperatures in the inner and outer channel are different. At the same axial location, the fluid in the inner channel is hotter than that in the outer channel. In calculating the Nusselt number, plotted in Fig. 3 however, an average bulk temperature has been used. For air, the circumferential conduction in the tube may also influence the tube wall temperature in the inner and outer channels.

Two Phase Heat Transfer: The Nusselt numbers obtained with various ratios of mass flow rates of 30 μm particles and air and for flow Reynolds number of 20,500 are plotted in Figure 4 as a function of number of hydraulic diameters from inlet. The plotted data are for the inner channel. The arrows on the abscissa indicate the location of wire wraps. With increase in mass flow rate of solids the heat transfer coefficient is seen to increase all along the rod bundle. At higher mass loadings of particles a sudden increase in heat transfer coefficient is observed downstream of the wire wraps. This is probably due to separation and re-attachment of the flow. In the presense of the particles the distance from inlet at which the flow fully develops thermally is observed to increase somewhat. Figure 5 shows the dependence of Nusselt number on axial distance from inlet for 100 μm particles. Again with increase in the ratio of mass flow rate of particles to air, the Nusselt number is found to increase. In comparison to the data plotted in Figure 4 for 30 μm particles, the enhancement for the same Re and Ws/Wa, is found to be smaller with 100 μm particles. Also with bigger particles no significant increase in heat transfer just downstream of the wire-wraps is observed.

The relative enhancement in heat transfer as a result of presence of 30 μm is plotted in Figures 6 as a function of axial distance from inlet. The plotted data are for the mid region of the rod bundle and for Re = 14,500 and 20,500. The data show little or no dependence of the enhancement on the axial distance from inlet. This observation is in contradiction to the conclusion drawn by Depew and Farbar from their data [13] in which they found enhancement to die down with distance from inlet. The data also show that for the same Ws/Wa, the relative enhancement decreases with increase in Reynolds number.

The relative enhancement in heat transfer with 100 μm particles is plotted in Figure 7 as a function of Z/D_h for flow Reynolds numbers of 16,900, 18,000 and 20,700. Again as was the case with 30 μm particles, no dependence of the enhancement on axial distance is observed. Also, with increase in Re the enhancement decreases. The maximum enhancement with 100 μm particles is found to be only about 35%.

The number of hydraulic diameters at which the flow is nearly fully developed with 30 μm particles entrained in air is plotted in Figure 8 as a function of the ratio of mass flow rate of particles to that of air. Because of some scatter in data as well as sudden increase in heat transfer just down stream of the wire wraps, it was difficult to ascertain accurately the location at which the flow became fully developed in the presence of the particles. Thus the location at which the slope of the curve representing the best fit through the Nu vs Z/D_h data had a value of 0.05 was termed as the fully developed length. The data of Figure 8 show that with particles the flow becomes fully developed at about 50 hydraulic diameters downstream of inlet. In the present test section the flow with air alone became fully developed at about 40-45 hydraulic diameters. This is in contrast to 10-15 diameters at which the flow becomes fully developed in tubes. The observed increase in the distance at which flow becomes fully developed with particles is consistent with the observation of Depew and Farbar [13].

The Nusselt number for the outer channel is plotted in Figure 9 as a function of number of hydraulic diameters from inlet. The plotted data were obtained with 30 μm particles and at a flow Reynolds number of 14,500. These data show the same behavior as seen in the inner channel data plotted in Figure 3. For the same Ws/Wa and Re, the relative enhancement in inner and outer channel is found to be about the same. This indicates that the mass ratio of particles to air remains about the same in the inner and the outer channel.

Correlation of Two Phase Heat Transfer Data: The ratio, ψ, of two phase to single phase Nusselt numbers for 30 μm particles is plotted in Figure 10 as a function of Ws/Wa. At a fixed Reynolds number, the ratio, ψ, is observed to increase as $(Ws/Wa)^{0.42}$. This functional dependence is about the same as found by Farbar and Morley [11] and Danziger [14].

In the work of Drucker, Dhir and Duffey [10] it was proposed that the enhancement in heat transfer in the presence of particles should depend on a dimensionless group $\beta Gr/Re^2$. Here β is the volume fraction of the solids, Gr is

the Grashof number based on the density difference between particles and fluid and hydraulic diameter of the test section; and Re is the Reynolds number based on the average fluid velocity through the test section. The volume fraction β can be easily related to the mass flow rate of particles if the particle velocity relative to the fluid is known. In the present work the value of β is evaluated by assuming that the particles attain their terminal velocity very quickly. Details of the derivation are given in the Appendix. For the range of the Re studied in this work, it is found that for 100 μm particles

$$\beta \cong 0.558 \times 10^{-3} \left(\frac{Ws}{Wa} - 1.3\right) + 7.19 \times 10^{-4} \tag{6}$$

and for 30 μm particles

$$\beta \cong 0.538 \times 10^{-3} \left(\frac{Ws}{Wa} - 2.8\right) + 1.51 \times 10^{-3} \tag{7}$$

In Figure 11 the relative enhancement obtained with 30 μm particles is plotted as a function of $\beta Gr/Re^2$. It is found that the data covering more than an order of magnitude variation in $\beta Gr/Re^2$ are correlated within ± 40% as

$$\psi = 1 + 71.5 \, (\beta Gr/Re^2)^{0.85} \tag{8}$$

The large variability of the data with respect to the best fit through the data results from the large uncertainty associated with the data for which the enhancement is only 10-15%. The 30 μm data show a much stronger dependence on $\beta Gr/Re^2$ in comparison to the bubbly flow data of Drucker et al [10]. However the data are closer to the prediction made from an extension [10] of Theofanous and Sullivan's model [9].

The enhancement observed with 100 μm diameter particles is plotted in Figure 12. The large particle data covering a relatively smaller range of $\beta Gr/Re^2$ are correlated as

$$\psi = 1 + 2.6 \, (\beta Gr/Re^2)^{0.5} \tag{9}$$

The correlation (9) shows a similar dependence of relative enhancement on $\beta Gr/Re^2$ as was obtained in reference [10] with bubbly flow. However the relative enhancement obtained with bigger particles is about 25% lower than that found in the bubbly flow. In Figure 12 the symbol, solid square represents one set of data obtained with a mixture of 30 μm and 100 μm particles having a weight fraction of 0.17 and 0.83 respectively. The symbol on the left represents the data if β is based on the loading ratio of the smaller particles only while the symbol on the right is for β corresponding to the larger particles only. Although the smaller particles have a five times lower weight fraction, their number density is about seven times higher than the bigger particle and as such the enhancment obtained with the mixture is more representative of presence of smaller particles.

From the data plotted in Figures 11 and 12 it can be concluded that not only the size of the particles but probably the number density of particles also plays a role in enhancing the wall heat transfer. In bubbly flow no such dependence on bubble size and number density of bubbles was observed.

The presence of droplets in the steam region far downstream of the quench front during reflooding will thus definitely enhance heat transfer. The smaller particles in the size range of about 30 μm will mainly contribute to this enhancement. Though the mass fraction of the smaller particles under entrained flow conditions during reflooding may be small, the number density of these particles can be easily larger. As observed in FLECHT SEASET [21] experiments, an enhancement of 70-80% above the single phase flow conditions is easily possible. In order to precisely quantify the enhancement more data with different distributions of particles are needed. It should also be pointed out that the effect of evaporation of droplets on the local temperature profile need to be included when using the correlation developed with the particles.

CONCLUSIONS

1. Presence of particles leads to enhancement in heat transfer. At about 40 t 50 hydraulic diameters from inlet the enhancement is found to be independen of the axial distance.

2. The presence of particles results in a small increase in the thermal entry length.

3. With 30 μm particles, an enhancement of about 200% has been observed for solid fraction of 3×10^{-3}. The maximum enhancement observed with 100 μm particles is only about 30%.

4. The enhancement is correlated with dimensionless group $\beta Gr/Re^2$. However the functional dependence of the enhancement on $\beta Gr/Re^2$ is found to depend on particle size.

REFERENCES

1. Collier, J.G., Convective Boiling and Condensation, McGraw Hill, London, 1972.

2. Michiyoshi, I., "Two-Phase Two-Component Heat Transfer", Proceedings Sixth International Heat Transfer Conference, Toronto, Vol. 6, 1978, pp. 219-233.

3. Verschoor, H., and S. Stemerding, "Heat Transfer in Two-Phase Flow", Proceedings General Discussion on Heat Transfer, Institute of Mechanical Engineers, Sept. 1951, pp. 201-204.

4. Kudirka, A.A., "Two-Phase Heat Transfer with Gas Injection Through a Porous Boundary Surface", ANL-6862, 1964.

5. Kudirka, A.A., R.J. Grosh, and P.W. McFadden, "Heat Transfer in Two-Phase Flow of Gas-Liquid Mixtures", I&EC Fundamentals, Vol. 4, No. 3, 1965, pp. 339-344.

6. Fedotkin, I.M., and L.P. Zarudnev, "Correlation of Experimental Data On Local Heat Transfer in Heating of Air-Liquid Mixtures in Pipes", Heat Transfer--Soviet Research, Vol. 2, No. 1, 1970, pp. 175-181.

7. Serizawa, A., I. Kataoka, and I. Michiyoshi, "Turbulence Structure of Air-Water Bubbly Flow -- II. Local Properties", International Journal of Multiphase Flow, Vol. 2, 1975, pp. 235-246.

8. Serizawa, A., I. Kataoka, and I. Michiyoshi, "Turbulence Structure of Air-Water Bubbly Flow -- III. Transport Properties", International Journal of Multiphase Flow, Vol. 2, 1975, pp. 247-259.

9. Theofanous, T.G., and J. Sullivan, "Turbulence in Two-Phase Dispersed Flows", Journal of Fluid Mechanics, Vol. 116, 1982, pp. 343-362.

10. Drucker, M.I., Dhir, V.K. and Duffey, R.B., "Two Phase Heat Transfer for Flow in Tubes and Over Rod Bundles with Blockages", presented at Winter ASME meeting Nov. 1982, and to be published in Journal of Heat Transfer.

11. Farbar, L., and M.J. Morley, "Heat Transfer to Flowing Gas-Solids Mixtures in a Circular Tube", Industrial and Engineering Chemistry, Vol. 49, No. 7, 1957, pp. 1143-1150.

12. Farbar, L., and C.A. Depew", Heat Transfer Effects to Gas-Solids Mixtures Using Solid Spherical Particles of Uniform Size", Industrial and Engineering Chemistry, Vol. 2, No. 2, 1963, pp. 130-135.

13. Depew, C.A., and L. Farbar, "Heat Transfer to Pneumatically Conveyed Glass Particles of Fixed Size", Journal of Heat Transfer, Vol. 85, 1963, pp. 164-172.

14. Danziger, W.J., "Heat Transfer to Fluidized Gas-Solids Mixtures in Vertical Transport", I&EC Process Design and Development, Vol. 2, No. 4, 1963, pp. 269-276.

15. Briller, P., R.L. Peskin, "A Mechanistic Approach to Gas-Solid Suspension Heat Transfer and Friction Factors", "Augmentation of Convective Heat Transfer" (A.E. Bergles and R.L. Webb, eds.), p. 124, ASME, New York, 1970.

16. Tien, C.L., and V. Quan, "Local Heat Transfer Characteristics of Air Glass and Air Lead Mixtures in Turbulent Pipe Flow", ASME paper 62-HT-15, 1962.

17. Gol'dshleger, U.I., and V.V. Barzykin, "Investigation of Heat Transfer in Transverse Flow of a High-Temperature Dust-Gas Past a Cylinder", Journal Of Engineering Physics, Vol. 18, No. 3, 1973, pp. 267-271.

18. Depew, C.A. and T.J. Kramer, "Heat Transfer to Flow Gas Solid Mixtures", Advances in Heat Transfer, Vol. 9, 1979.

19. Kianjah, H. and V.K. Dhir, "An Experimental Study of Enhancement of Heat Transfer in the Presence of a Discontinuous Phase". Report to be submitted to EPRI, 1984.

20. Weisman, J., "Heat Transfer to Fluid Flowing Parallel to Tube Bundles", Nuc. Sci. & Engr., Vol. 6, No. 1, 1959.

21. Personal Communication with L.E. Hochreiter, Washington Electric Corporation, Pittsburgh, March, 1982.

NOMENCLATURE

A	flow cross-sectional area
A_s	surface area of one of the rods
B	buoyancy force as defined in equation (A.2)
C_1, C_2	empirical constants
C_D	drag coefficient as defined in equation (A.4)
c_{pa}	specific heat of air
c_{ps}	specific heat of solids
D	drag as defined in equation (A.1)
D_h	hydraulic diameter of the test section
D_s	particle diameter
E	voltage
Gr	Grashof number, $\frac{\rho_a(\rho_s-\rho_a)\, g\, D_h^3}{\mu_a^2}$
g	gravitational acceleration
h	heat transfer coefficient
I	current
k_a	thermal conductivity of air
L	length of the rod bundle
Nu	Nusselt number , hD_h/k_a
Re	flow Reynolds number
Re_s	Reynolds number based on relative velocity of particles
T_b	bulk temperature
T_w	wall temperature
V_a	average superficial velocity of air
V_t	average terminal velocity of particles

Wa	mass flow rate of air
Ws	mass flow rate of particles
Z	vertical distance measured from inlet

Greek Symbols

α	void fraction
β	volume fraction of the solids
μ	viscosity of air
ρ_a	density of air
ρ_s	density of solids
ψ	ratio of two phase to single phase Nusselt numbers, Nu_{tp}/Nu_{sp}

Subscripts

sp	single phase
tp	two phase

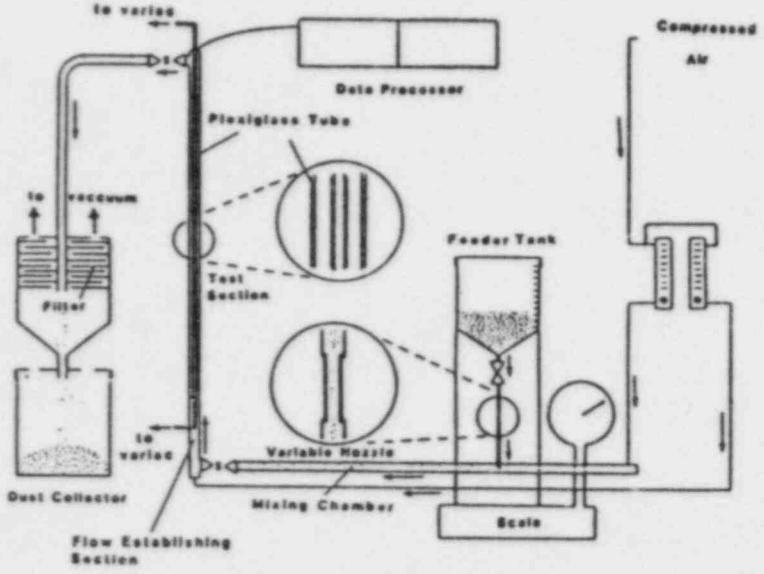

Figure 1 Schematic Diagram of the Experimental Setup

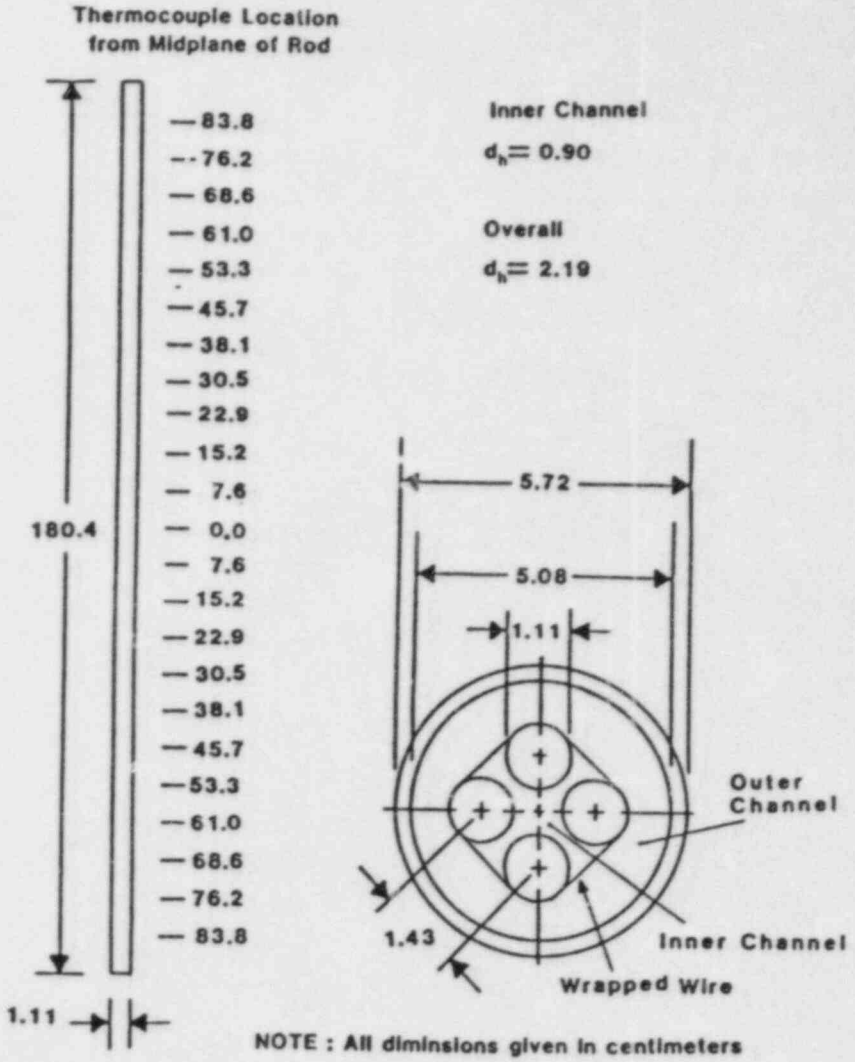

Figure 2 Details of the Test Section Cross-Section and Thermocouple Locations

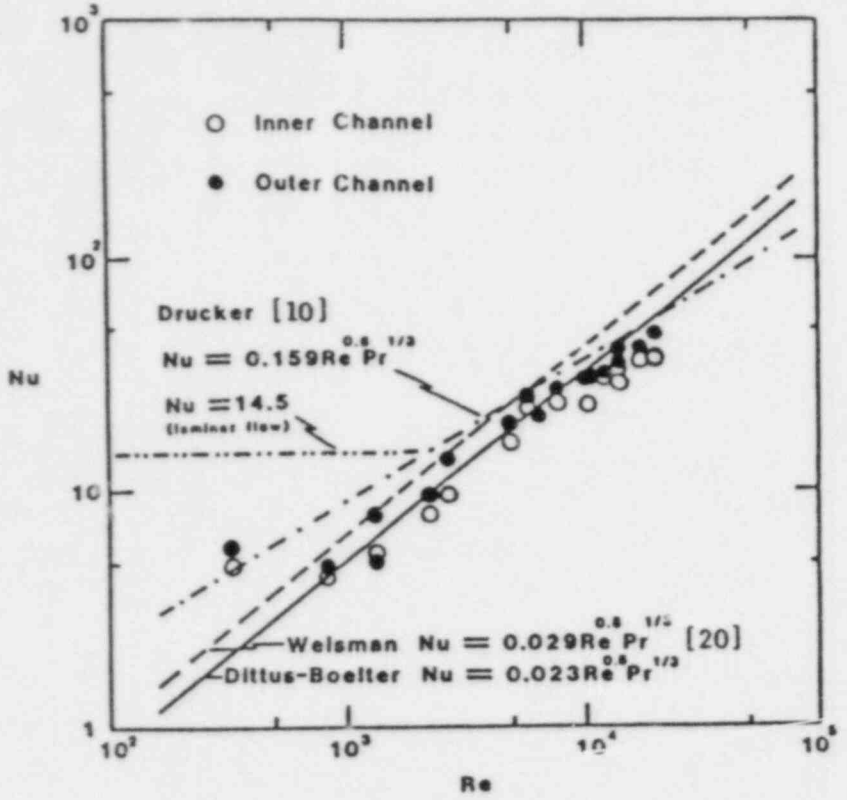

Figure 3 Dependence of Nusselt Number on Reynolds Number for Fully Developed Flow of Air Only

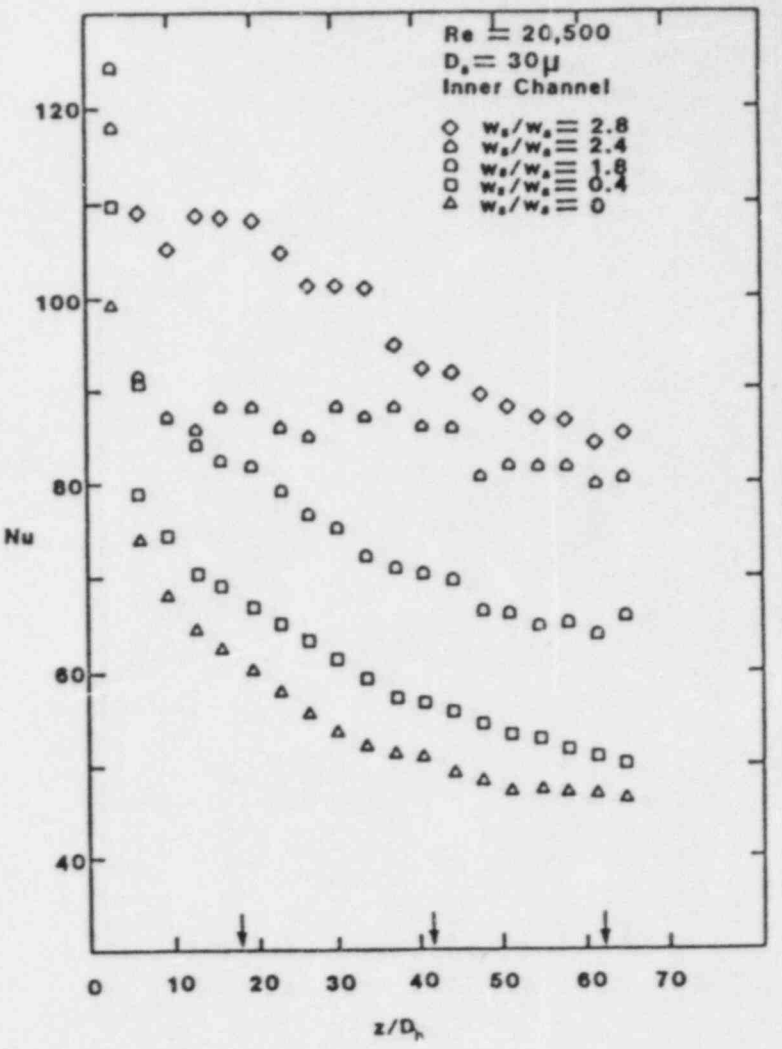

Figure 4 Variation with Axial Distance of the Inner Channel Two Phase Nusselt Number with 30 μm Particles

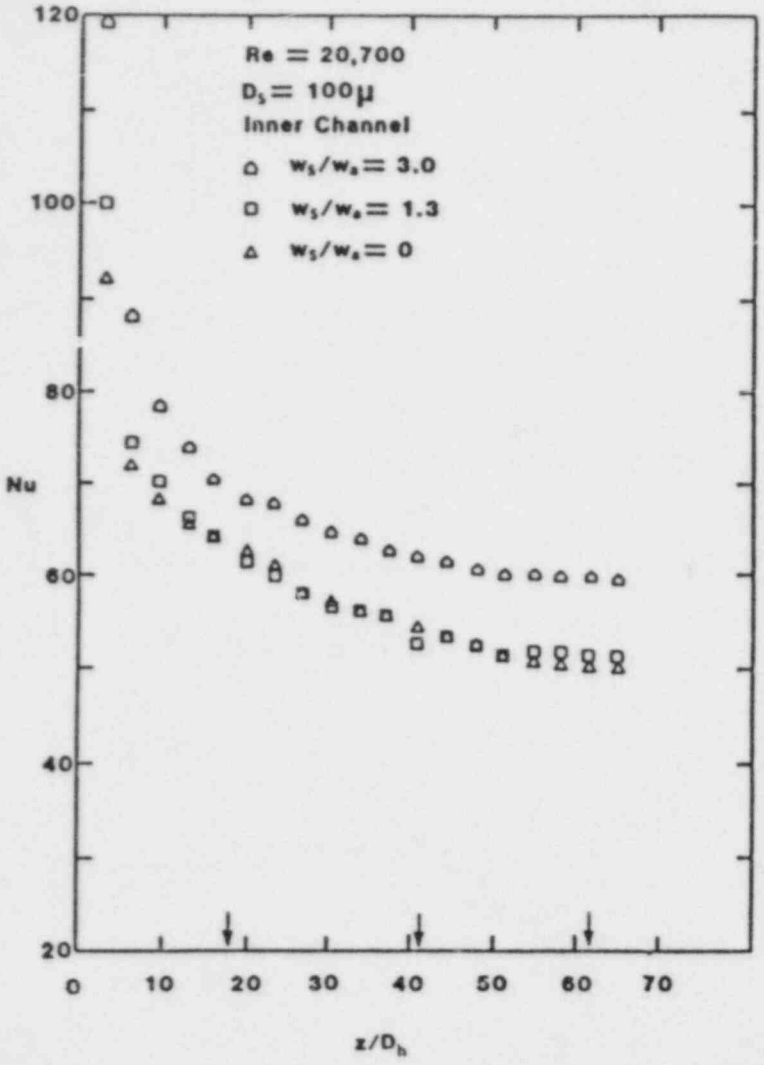

Figure 5 Variation with Axial Distance of the Inner Channel Two Phase Nusselt Number with 100 μm Particles

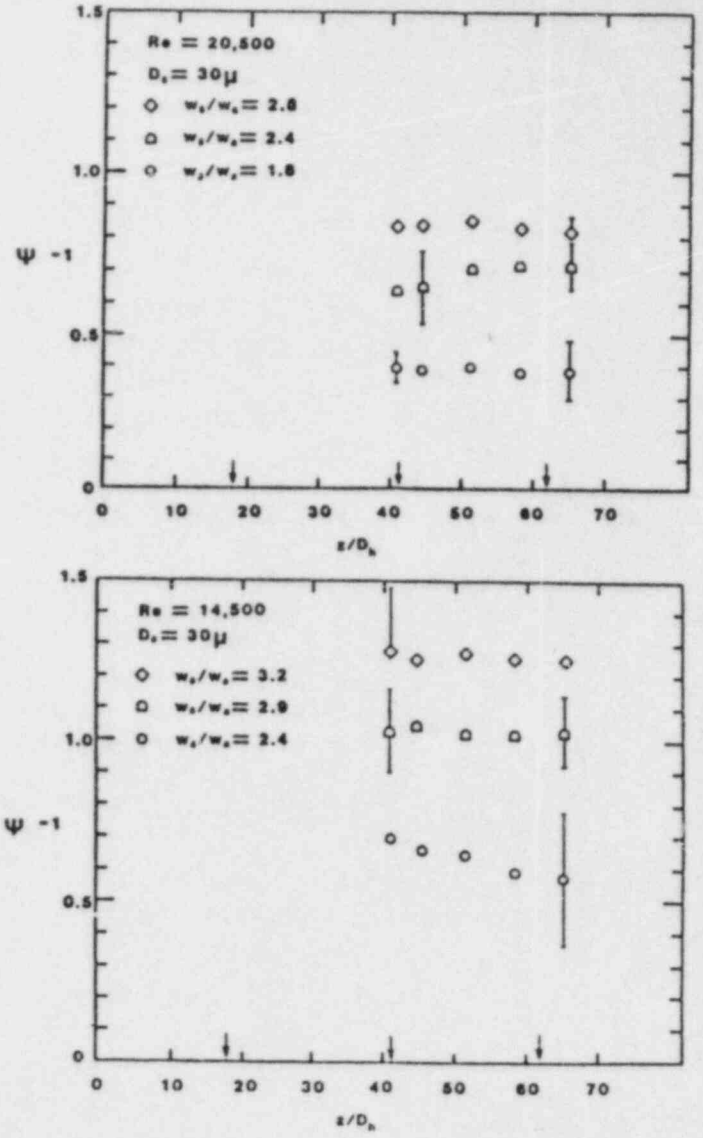

Figure 6 The Dependence of Relative Enhancement on the Axial Distance obtained with 30 μm Particles

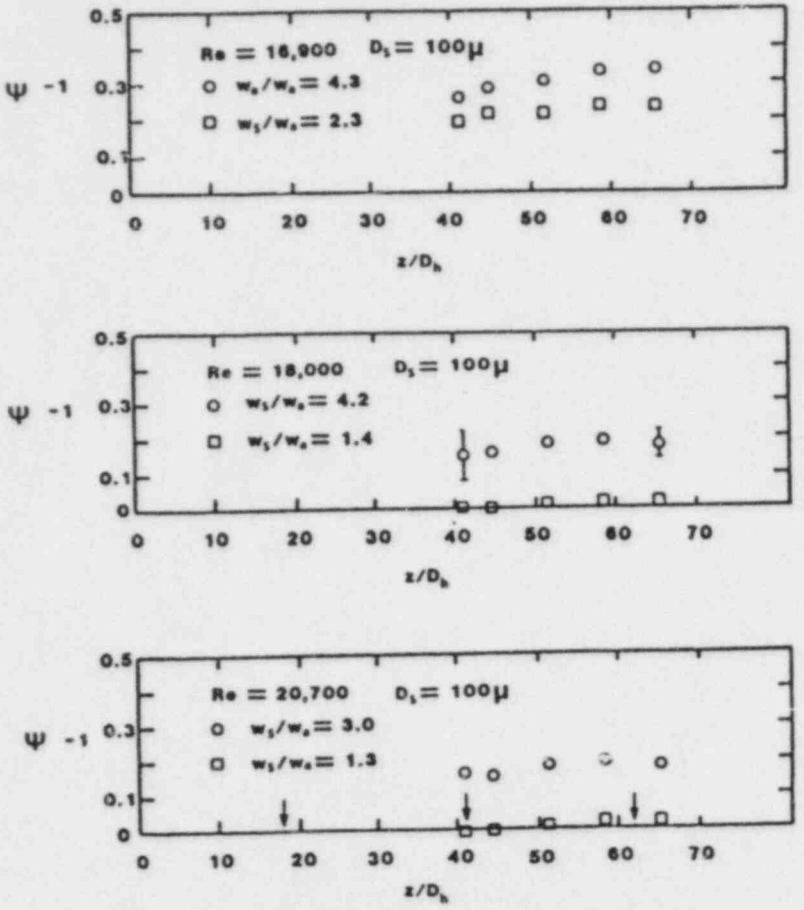

Figure 7 The Dependence of Relative Enhancement on the Axial Distance obtained with 100 μm Particles

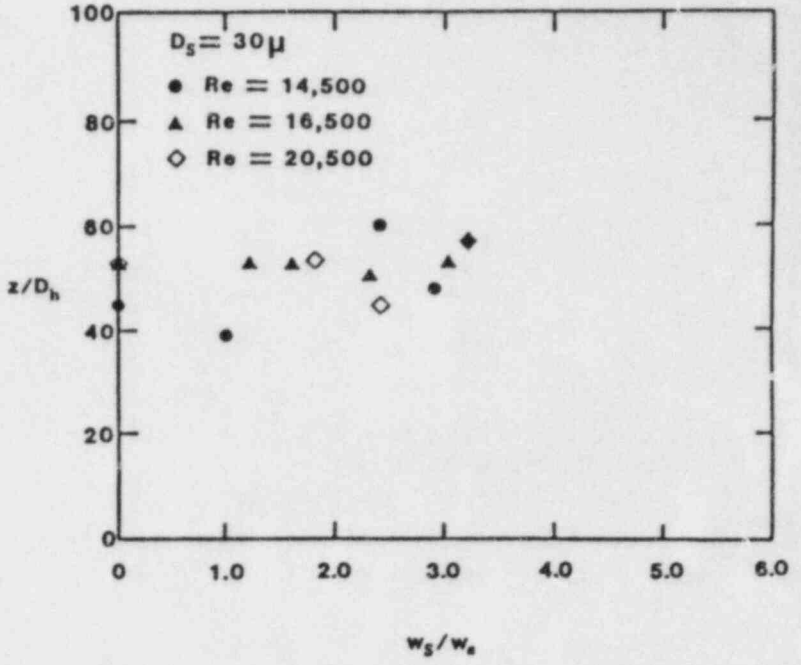

Figure 8 Variation with Loading Ratio of the Distance at which the Flow becomes Fully Developed

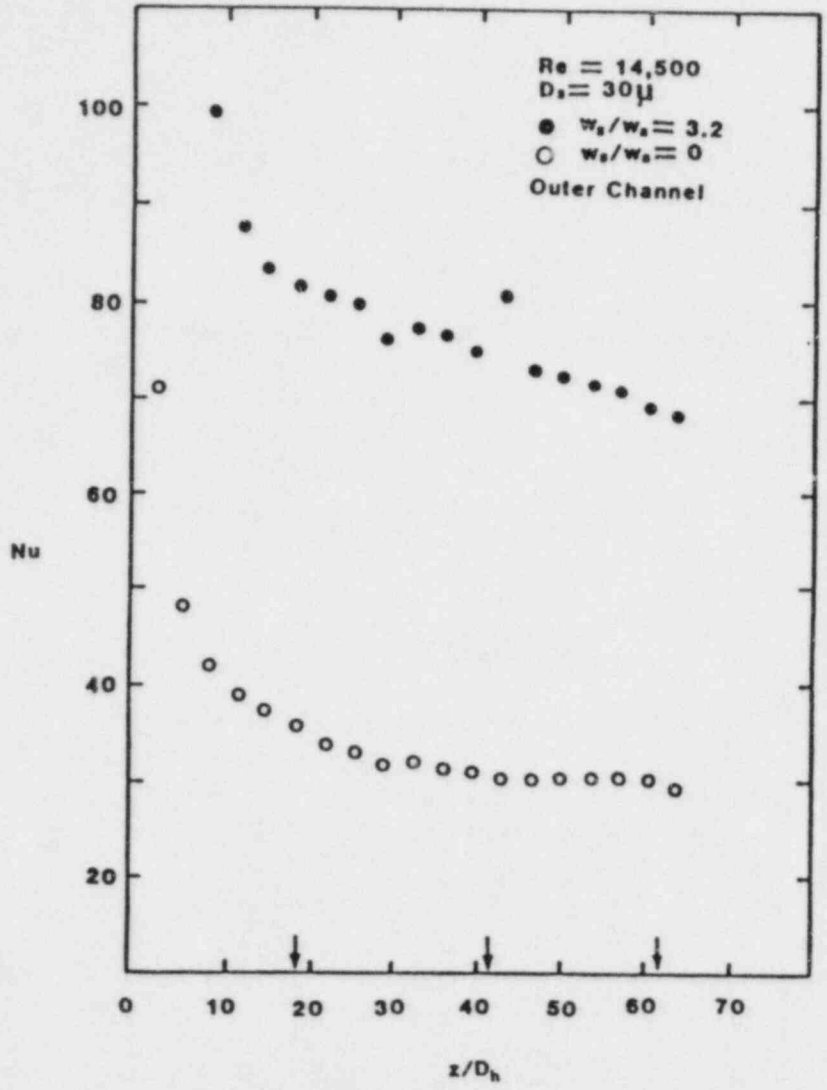

Figure 9 Variation with Axial Distance of the Outer Channel Two Phase Nusselt Number with 30 μm Particles

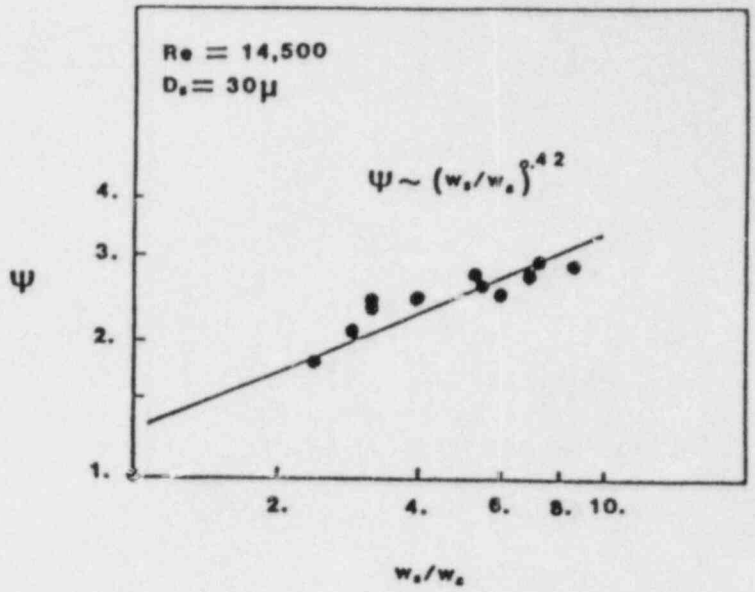

Figure 10 Correlation of Ratio of Two Phase to Single Phase Nusselt Number with Loading Ratio

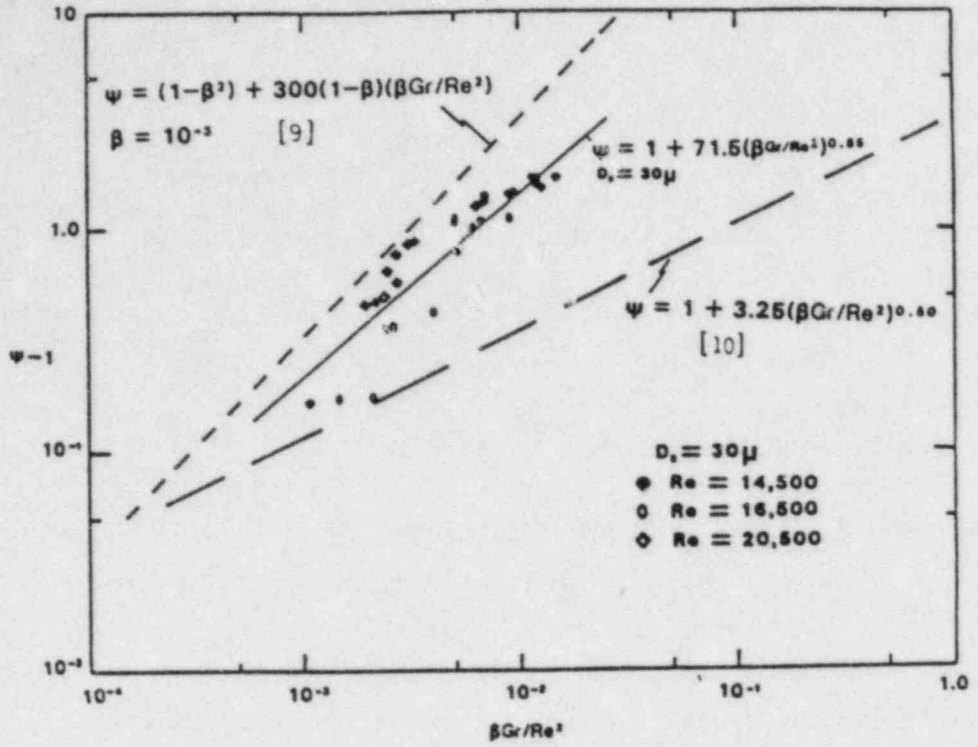

Figure 11 Correlation of ψ-1 with $\beta Gr/Re^2$ for 30 μm Particles

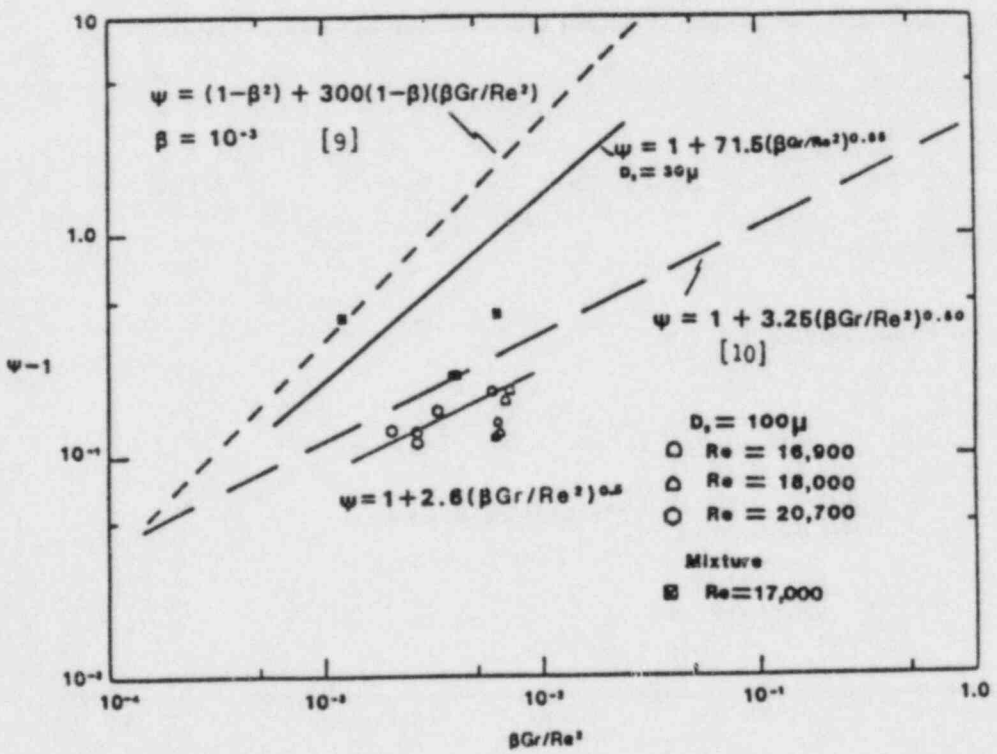

Figure 12 Correlation of ψ-1 with $\beta Gr/Re^2$ for 100 μm Particles

APPENDIX

Assuming that the particles attain their terminal velocity very quickly, the terminal velocity of the particles can be obtained by balancing the drag and buoyancy forces acting on the particles. The expressions for these forces are written as

$$D = C_D \rho_a \left(|V_t - V_a|\right)^2 \pi D_s^{\,2}/8 \tag{A.1}$$

$$B = (\rho_s - \rho_a)\, g\, \pi D_s^{\,3}/6 \tag{A.2}$$

Equating equations (A.1) and (A.2) an expression for $V_t - V_a$ is obtained as

$$|V_t - V_a| = \left[\frac{4\, D_s g\, (\rho_s - \rho_a)}{3\, C_D \rho_a}\right]^{\frac{1}{2}} \tag{A.3}$$

In equation (A.3) C_D is the drag coefficient which using Stokes law is written as

$$C_D = \frac{C_2}{Re_s} \equiv \frac{C_2\, \mu_a}{\rho_a\, |V_t - V_a|\, D_s} \tag{A.4}$$

Substitution of C_D from equation (A.4) into (A.3) yields

$$V_t = V_a \pm \frac{4\, (\rho_s - \rho_a)\, g\, D_s^{\,2}}{3\, C_1 \mu_a} \tag{A.5}$$

In equation (A.5) the + sign is for downflow and - is for upflow. Now if β is defined as the ratio of the volume of the solids to the total flow volume, it can be written as

$$\beta = \frac{W_s}{\rho_s\, V_t\, A} = \frac{Ws}{Wa} \cdot \frac{\rho_a}{\rho_s} \cdot \frac{V_a}{V_t} \tag{A.6}$$

Knowing V_t from equation (A.5), β can be calculated.

FORCED CONVECTIVE, NONEQUILIBRIUM POST-CHF HEAT TRANSFER EXPERIMENT: DESCRIPTION, DATA ANALYSIS AND CORRELATION COMPARISON

K. G. Condie,[1] R. C. Gottula,[1] S. Neti,[2] R. K. Sundaram,[3] J. C. Chen[2] and R. A. Nelson[1]

1. EG&G Idaho, Inc., P. O. Box 1625, Idaho Falls, ID 83415.

2. Lehigh University, Bethlehem, Pennsylvania 18015.

3. Yankee Atomic, 20 Turnpike Rd, Westborough, MA 01581.

ABSTRACT

Forced convective, nonequilibrium post-CHF heat transfer data (766 points) have been obtained at high pressure and low mass flux ranges not previously tested. The data are unique in that the superheated vapor temperature was measured at multiple elevations allowing the direct calculation of vapor generation rates. The data are useful for verification or development of nonequilibrium heat and mass transfer models.

Statistical analyses of the data indicated the importance of flow rate represented by the vapor Reynolds number to the .8 power. Three additional parameters; a nonequilibrium term, the quench front quality and the distance from the quench front were shown to be statistically significant in fitting the data. The Prandtl number was also included in the fit but was the least significant parameter.

Current film boiling heat transfer correlations do not predict the data well. The Dougall-Rohsenow equilibrium correlation is the only one investigated that reasonably predicts the measured wall heat fluxes. Current vapor generation rate models do not adequately predict the measured vapor generation rates.

ACKNOWLEDGMENT

Funding for this experiment was provided by the U.S. Nuclear Regulatory Commission, Office of Nuclear Regulatory Research and the Japan Atomic Energy Research institute, under DOE Contract No. DE-AC07-76ID01570.

NOMENCLATURE

C_p	heat capacity (kJ/kg-K)
D	test section diameter (m)
DZQF	distance from quench front
G	mass flux (kg/m^2-s)
h_{fg}	heat of vaporization (kJ/kg)
h	enthalpy (kJ/kg) or heat transfer coefficient (W/m^2-K)
k	thermal conductivity (W/m-K)
P	pressure (MPa)
Pr	Prandtl number
q"	heat flux (kW/m^2)
Re	Reynolds number
T	temperature (K)
x	quality
z	axial position in test section measured from the test section inlet (m)
α	void fraction
ρ	density (kg/m^3)
σ	surface tension (N/m) or Stefan-Boltzmann constant (W/m^2-K^4)
ϵ	emissivity
Γ	volumetric vapor generation rate (kg/m^3-s)
μ	viscosity (kg/m-sec)

Subscripts

a	actual
chf	critical heat flux
e	equilibrium
f	saturated liquid

g	saturated vapor
h	homogeneous
ℓ	liquid
s	saturation
v	vapor
w	wall

INTRODUCTION

Best estimate predictions of various nuclear reactor transients, and their associated fuel rod temperature responses require an accurate prediction of post-critical-heat-flux (CHF), thermal nonequilibrium, and quenching phenomena. These post-CHF heat transfer mechanisms significantly affect the rod cladding temperature response, vapor superheat, core thermal excursion, and quenching during a hypothetical loss-of-coolant accident (LOCA) and severe accident conditions in a nuclear reactor. The purpose of this paper is to present new nonequilibrium post-CHF data, the analysis of the data including comparisons with current heat and mass transfer correlations used in best estimate predictions and to demonstrate the need for further model development.

A phenomenological understanding of these mechanisms is important for an understanding of early quenches such as those experienced during the blowdown phase of a LOCA, as shown by the Loss-Of-Fluid Test (LOFT) Experiments L2-2 and L2-3 (1,2)[a] (cold leg offset shear break transients), where early core quenching occurred at pressures as high as 6.9 MPa. The mechanisms are also important in the reflood phase of a LOCA as shown in the FLECHT (3) results. In addition, recent studies in the Severe Accident Sequence Analysis (SASA) program (4,5) at the Idaho National Engineering Laboratory (INEL) indicate that low flow rate (2-150 kg/s-m^2), low to high quality, post-CHF nonequilibrium exists at high pressure during both pressurized water reactor station blackout accident sequences and boiling water reactor anticipated transient without scram (ATWS) accident sequences. The predicted timing and extent of core damage, as well as the magnitude and timing of hydrogen generation and the fission product source term, depend on an accurate prediction of cladding temperature and rupture, where the oxidation layer of the cladding and cladding rupture are dependent on the predicted cladding temperature and time at temperature. In the event of fission product release from the rod,

---

a. Numbers in parentheses refer to references at end of paper.

an important concern is the effect of fission product decay heat and vapor superheating on the transport of the fission products. It is believed that much of the transport of the important compounds CsI and CsOH is caused by condensation of these species on Ag-In-Cd aerosols from the control rods. A key unresolved question is the distribution of the condensates between aerosol surfaces and immobile wall surfaces. The distribution is a function of the difference between the aerosol and wall temperatures. Both of these temperatures are dependent upon the degree of vapor superheating occurring in the core. Since as much as 30% of the decay heat may be associated with material released from fuel assemblies (6), detailed heat and mass transfer correlations will be required to understand the transport of fission products from reactor cores during hypothetical severe fuel damage accidents. The first step required in this modeling of fission product transport is the determination of vapor superheat. The mechanisms may be important during other pressurized water reactor (PWR) or boiling water reactor (BWR) operational or severe accident transients, where the reactor may operate in the post-CHF regime.

Advanced computer codes such as RELAP5 (7) and TRAC (8,9) attempt to describe the post-CHF phenomena through the use of numerous heat and mass transfer models. These models incorporate methods to represent both wall and interfacial considerations and allow for unequal velocities between the phases as well as thermal nonequilibrium.

Thermal nonequilibrium between the phases was first suggested by Parker and Grosh (10) and measured in tubes by Mueller (11), Polomik (12), and more recently by Nijhawan (13,14), and Evans, Webb and Chen (15). The nonequilibrium data of Mueller and Polomik were obtained in the high quality region, while that of Nijhawan and Evans, Webb and Chen covers a wide range of qualities at low pressures. The data represent a measurement at a single point (elevation) and are limited in both number and parametric ranges. Only the data of Nijhawan and Evans, Webb and Chen are well documented. Measurements of vapor superheat in a rod bundle have been made by Rosal (16) under reflood conditions. The definition of the local conditions that occur in a rod bundle are however not as well determined as those in the single-tube experiments.

Thus, extensive additional nonequilibrium post-CHF data are required in order to provide an understanding of the post-CHF heat transfer mechanisms and to develop or verify the heat and mass transfer models in the post-CHF regime important to fuel rod quenching and vapor superheating. In particular, data are needed under low-flow, low quality, and high pressure conditions (up to 7 MPa) such as occurred during the LOFT L2-2 and L2-3 blowdown quenches and for the low-flow, high quality, high pressure conditions that occur during severe accidents.

To obtain nonequilibrium film boiling data at low flow rates, low quality, and high pressure, a post-CHF experiment (17) extending the work of Nijhawan was developed at the INEL in conjunction with Lehigh University. The objectives of the experiment were to (a) provide nonequilibrium data at pressures up to 7 MPa, over a range of flow rates and fluid qualities, to extend the existing nonequilibrium data base, (b) verify existing film boiling heat transfer correlations, and (c) verify existing vapor generation rate models. To verify vapor generation rate models, the rate of change of vapor superheat with respect to length was obtained by measuring the vapor superheat at different axial levels in the test section simultaneously. The experiment objectives were met by conducting steady state and quasi-steady-state (slowly moving quench front) experiments over a range of flow rates, qualities, and pressures.

Included in this paper is a description of the test facility, the test section, experimental measurements, and experimental procedure. A statistical analysis of the data is presented to show which parameters are important to the correlation of the data. Comparisons are made between measured and predicted heat transfer coefficients and vapor generation rates. Conclusions are stated based upon these comparisons.

TEST FACILITY DESCRIPTION

The post-CHF experiments were conducted in the Blowdown Loop of the Thermal-Hydraulics Experimental Facility at the INEL. The main loop, consisting of a pressure vessel, a coolant pump, a warmup heater vessel, and associated valves and piping, provided a high temperature, high

pressure water supply to the test section. A feed and bleed system maintained the main loop in a liquid hard, constant pressure condition so that a constant supply of fluid could be provided to the test section in a once-through manner. The supply fluid was maintained in a subcooled condition so that the flow rate to the test section could be accurately measured through an orifice. The main loop was capable of supplying fluid at temperatures up to 619 K and pressures up to 16.2 MPa. This fluid was then flashed across a flow control valve downstream of the flow measuring orifice which resulted in fluid qualities at the inlet to the lower hot patch of up to 47% at a test section pressure of 0.4 MPa. The outlet of the test section was connected to a surge tank to provide a constant back pressure during a test run. A nitrogen supply was connected to the surge tank to provide the initial test section pressure. A schematic of the experiment loop is shown in Figure 1.

Test loop process measurements and controls were accomplished using a microprocessor controller. Process and experimental measurements were displayed on a CRT terminal that allowed operator monitoring and on-line setpoint modifications at any time prior to the actual period of experiment sequencing and data acquisition. Thus, test section pressure and wall temperature could be controlled automatically. The operators could also manually control test section power and flow rate.

TEST SECTION DESCRIPTION

The test section shown in Figure 2 consisted of a vertical Inconel-625 tube with a 15.39 mm ID and 1.83 mm wall thickness. The heated length of the test section was 2.134 m. The hot patch technique, developed by Groeneveld and Gardiner (18) was utilized in this experiment to prevent a quench front from entering the test section for the steady state experiments. Copper hot patches 152.4 mm in diameter were brazed to the inlet and outlet of the Inconel test section. Cartridge heaters in the inlet (lower) hot patch were capable of delivering 7 kW of power, while those in the outlet (upper) hot patch were capable of providing 5 kW. The

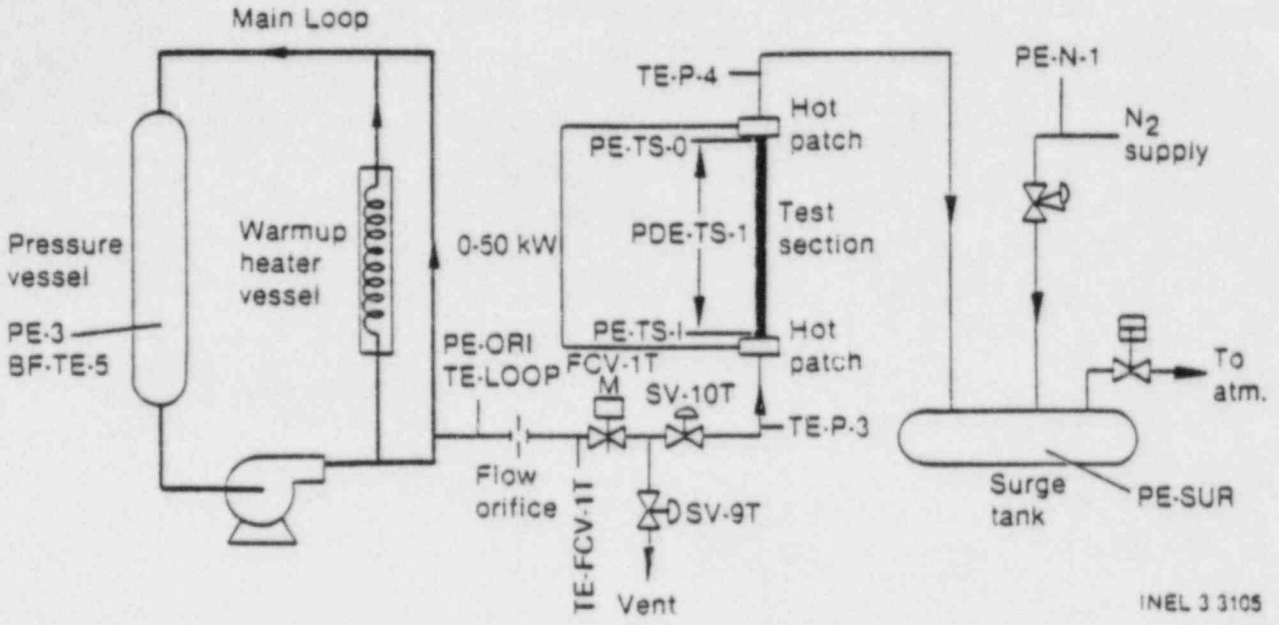

Figure 1. Experiment loop and instrumentation diagram.

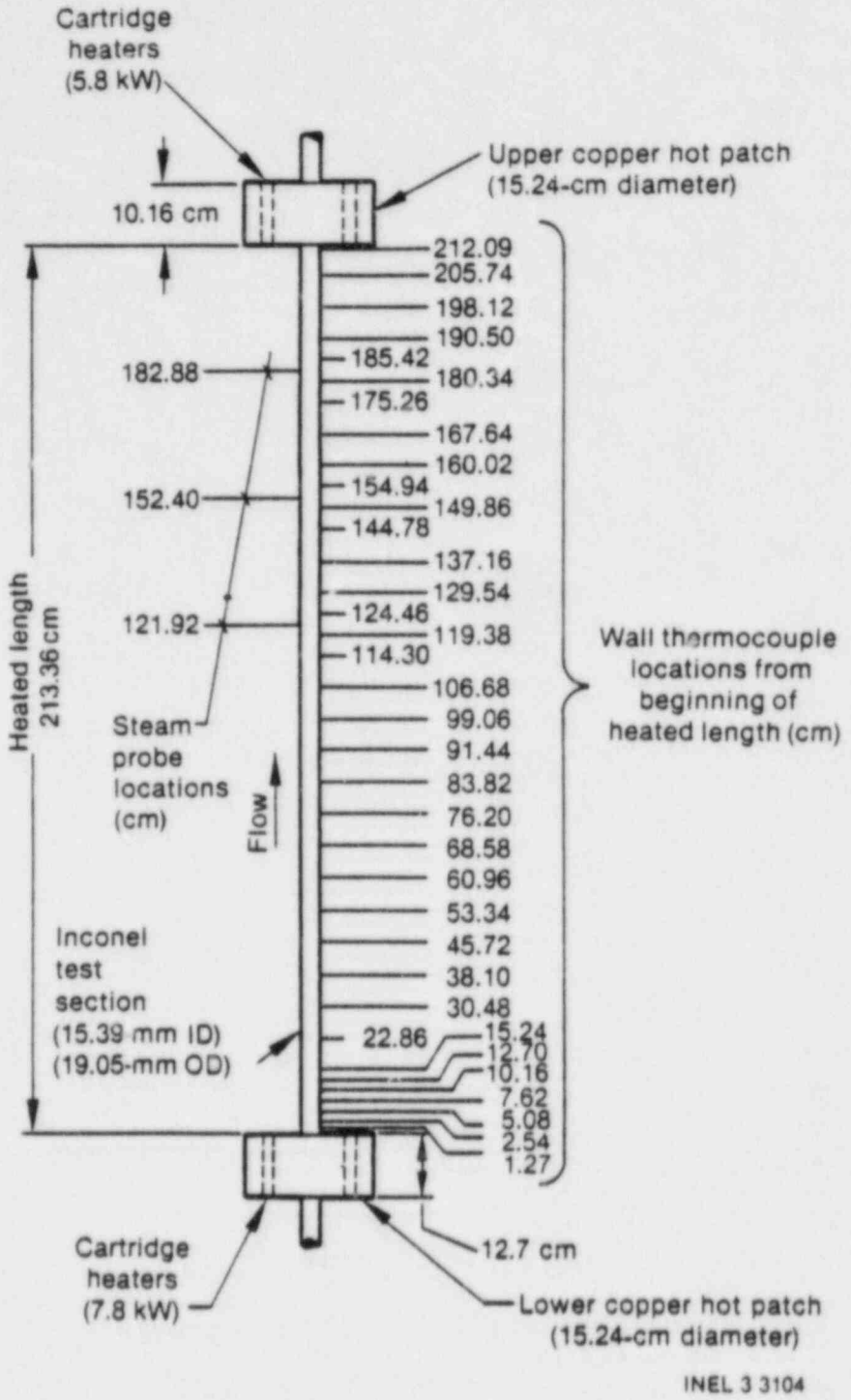

Figure 2. Test section geometry and instrument locations.

hot patches also functioned as the electrical connectors to the test section. A 75 kW dc power supply was used to provide joule heating of the test section.

Heater tape, located on the inlet line from the inlet flow control valve to the test section, maintained the inlet line at the saturation temperature corresponding to the test pressure.

EXPERIMENTAL MEASUREMENTS

Principle experimental measurements include 38 ungrounded 1.02 mm outside diameter Type K thermocouples to measure the wall superheat. The thermocouples were laser welded to the test section at the various axial elevations shown in Figure 2. Vapor superheat measurement stations were located at the 1.229 m, 1.524 m, and 1.829 m elevations in the test section, and measurements were made using a double aspirated steam probe as developed by Nijhawan (14). The vapor probe design utilized (a) inertial separation of liquid droplets from the vapor sample, (b) differential aspiration of the separated phases to minimize probe quench by liquid, and (c) multiple radiation shielding of the thermocouple junction to minimize radiation heat transfer from the neighboring hot walls. Fluid temperature measurements were made using a resistance thermemeter for the main loop temperature, a grounded type K thermocouple upstream of the flow orifice and a type K exposed junction thermocouple at the flow control valve.

Absolute pressure measurements were made in the main loop and at the inlet and outlet to the test section. The test section flowrate was determined by measuring the subcooled fluid pressure drop across an orifice upstream of the test section inlet flow control valve. Total test section power was determined from measurements of test section voltage and current.

Experimental and process measurements were monitored and recorded by a MODCOMP II/45 computer, at a rate of 50 samples per second. Data plots were made immediately following each experiment.

EXPERIMENTAL PROCEDURES

To initiate a steady state film boiling experiment, the main loop was first heated to a temperature that provided fluid at the desired test section inlet quality when flashed across the inlet flow control valve at a given test section pressure. The surge tank and test section were pressurized with nitrogen to the desired pressure. The test section was heated to the desired temperature for the experiment based on a thermocouple measurement at the 1.803 m axial level. The lower and upper hot patches were heated to their desired temperature for the given experiment.

Flow to the test section was then initiated and adjusted using the inlet flow control valve until the desired flow rate was obtained. The test section pressure was held constant during the experiment by using a flow control valve to vent nitrogen and steam from the surge tank to atmosphere. Power to the hot patches and the test section was controlled automatically by the microprocessor to maintain the preset temperatures.

Selected test section wall thermocouples were monitored on strip charts to determine when the temperature profile on the test section had stabilized. The steam probe aspirating valves were open and adjusted to provide measurement of the vapor temperature. For high-quality low flow inlet conditions typical of the steady state experiments, infrequent rewets were observed on the steam probe thermocouples (17).

When all parameters were stable, data were recorded for a period of several minutes. The process of lowering the test section temperature and taking data was repeated until the test section inlet quenched; each temperature being counted as a test run. Following quench, a backflow of nitrogen from the surge tank was initiated and low test section power applied to dry out the test section. Conditions were then reset for the next series of experiments.

The operating procedure for the quasi-steady state experiments was similar to that for the steady state experiments, with the following

exceptions. The lower hot patch was heated to the saturation temperature at the corresponding test section pressure for a given test run. This process eliminated (a) heat transfer between the hot patch and the incoming fluid to simplify determination of the test section inlet fluid quality and (b) heat losses from the hot patch to the environment.

For the quasi-steady-state test runs, the amount of nonequilibrium at each vapor probe decreased as the quench front moved up the test section. The vapor probes encountered more frequent rewets and recoveries as the quench front approached, and generally quenched permanently when the quench front was within about 150 to 300 mm of the probe (17). However, at higher flow rates and lower inlet qualities, many rewets typical of those discussed in References 14 and 17 were observed. A typical steam probe response experiencing several rewets is shown in Figure 3. When all of the vapor probes had encountered permanent quenches, the test was terminated.

RESULTS

The original test matrix called for steady state film boiling experiments over a broad range of test conditions including a pressure range of 0.4 to 7 MPa. However, steady state film boiling could not be obtained over that range of conditions, due to inadequate performance of the inlet hot patch. For this reason, steady state experiments were limited to the following ranges of conditions: pressures of 0.21, 0.4, 0.7 MPa; mass fluxes of 12 to 24 kg/m^2-s; test section inlet equilibrium qualities of 32 to 58%, heat fluxes from 7.7 to 27.5 kW/m^2 and distances from the quench front of 1.32, 1.63, and 1.93 m. Eighty three steady state data points were obtained. In addition, 683 quasi-steady state data points were obtained over the following ranges: pressures of 0.4 to 7 MPa, mass fluxes of 12 to 70 kg/m^2-s with some data up to 100 kg/m^2-s, test section inlet qualities of -7 to 47%, heat fluxes of 8 to 225 kW/m^2, and the distance from quench front from 0.06 to 1.94 m. Depending on test pressure, the steam probes tended to quench and remain quenched at mass fluxes ranging from 50 to 110 kg/m^2-s, thus limiting the mass flux range of data.

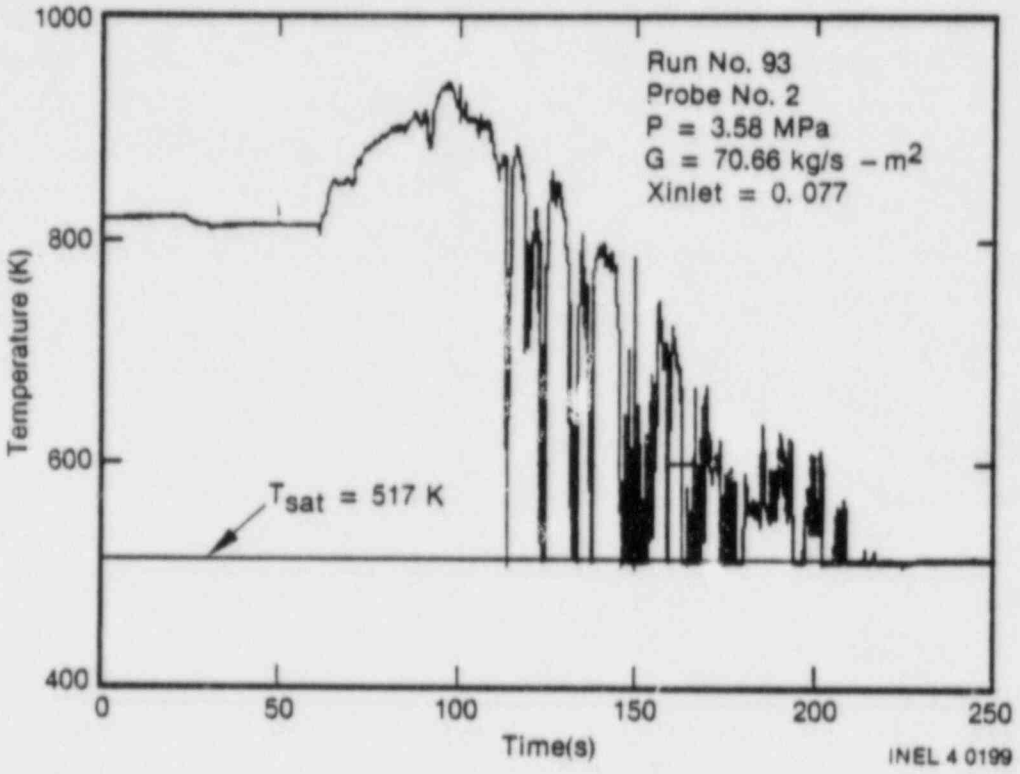

Figure 3. Vapor temperature measurement for probe 2, run 93.

The low pressure data are in good agreement (17,19) with earlier data taken by Nijhawan at Lehigh University (19). A comparison of the low pressure steady state data has also been made to the vapor generation models (19). The data base provides valuable wall heat transfer and vapor generation information to develop or assess the heat transfer and vapor generation models used in the advanced two-phase nonequilibrium thermal hydraulic computer codes. The initial step taken by the analysis was to determine the key parameters statistically important to the data. This step was followed by the comparison of the data to the current models and provided a means for understanding their agreement with the data.

Statistical Analysis of Wall Heat Transfer Data

A statistical fit of the data was performed using linear regression analysis techniques. The primary tool for this analysis was the STEPWISE linear regression code (20). It is not intended that this statistical fit of the data provide a new correlation for the film boiling region, but rather that it provide (a) insight into the data trends from this experiment and (b) a means to determine important parameters for the heat transfer process.

The terms used in the statistical fit were selected on the basis of the following criteria:

1. Parameters thought to be important to the mechanism involved.

2. Appropriate dimensionless parameters. The variables in the dimensionless parameters may be evaluated at more than one set of conditions.

3. Parameters suggested by their use in other correlations.

On the basis of the above criteria and initial results from the regression analysis, key parameters for the heat transfer coefficient of the phenomena were obtained. These were found to be: (a) the vapor Reynolds number, Re_v, reflecting the influence of vapor flow rate on the

process; (b) the vapor Prandtl number, Pr_v, accounting for the physical properties of the superheated vapor; (c) an (x_e/x_a) term, representing nonequilibrium effects [its presence indicates that heat flux is not a true linear function of (T_w-T_v)]; and (d) the two remaining terms, x_{chf} and (1-DZQF/D), representing the influence of the quench front hydraulics and distance from the quench front. The tube diameter was included to maintain nondimensionality in the correlating parameters.

The Reynolds and Prandtl numbers are standard parameters included in many correlations. Nonequilibrium effects have been included by several investigators, indicating their influence on post-CHF heat transfer. Andersen (21) included a term for the vapor superheat of the vapor enthalpy for an inverted annular flow model. Within the data base obtained in this program, it is probable that the inverted annular flow regime existed near the quench front for the higher pressures and lower inlet qualities. Chen, Sundaram, and Chen (22) included a nonequilibrium term attributed to an increased sink effect of the liquid drops in dispersed flow. The effects of distance from the quench have also been included by several post-CHF researchers. Andersen's inverted annular flow film boiling model (21) with a laminar vapor film yielded a heat transfer coefficient proportional to $DZQF^{(-1/4)}$. Similar models, requiring a numerical solution, have been obtained by Chan and Yadigaroglu (23) and Denham (24). Chen, Sundarum, and Chen (22) also included an entrance region effect in their dispersed flow, post-CHF correlation, which was written in terms of the distance from the quench front, DZQF. This entrance region was determined to exist for length-to-diameter ratios of 100 or less. For the 15.39-mm tube tested here, the entrance region effect for dispersed flow should be considered for DZQF < 1.539 m which is a significant portion of the data.

The effect of quality at CHF has also been shown to have an influence on inverted annular flow by Yu and Yadiagaroglu (25). They included the effect in the quality rise at the quench front due to its passage, and the differences between the subcooled inlet and saturated coolant at the quench front. They also correlated a heat transfer coefficient exponentially

decaying with respect to distance from the quench front. No models are known which have included the effects of CHF quality in the dispersed flow regime.

It is important to realize that these parameters [(x_e/x_a), x_{chf}, and (1-DZQF/D)] represent effects which were found to be significant but which may not be formatted in terms of the physical variables truly influencing the phenomena. For example, distance from the quench front may, in reality, be only the best parameter available to reflect the effects of slip between the phases. However, since slip was not measured, it cannot be included in the analysis.

The correlation obtained for the vapor Nusselt number from the regression analysis yielded the exponents shown in column 2 below.

Term	Exponent	t Value	Exponent[b]	t Value[b]
Re_v	0.80272	41.8	0.8	--
Pr_v	1.0487	6.6	1.0	--
x_e/x_a	2.6557	21.8	2.6314	24.9
x_{chf}	-0.28479	-19.0[a]	-0.28459	-19.8[a]
[1 + DZQF/D]	-0.43605	-19.9[a]	-0.44031	-25.3[a]

a. Negative t-values accompany negative exponents.

b. Obtained by fixing exponents of Re_v at .8 and Pr_v at 1.0.

The importance of each term is reflected by the absolute value of the t-value (third column) relative to the others. It is interesting to note that the vapor Reynolds (Re_v) number correlates with an exponent of approximately 0.8, as it should. To simplify the correlation, the exponents of Re_v and Pr_v were then set to 0.8 and 1.0, respectively, and a final statistical fit was made. The exponents and t-values from the final fit are given listed in the two right-hand columns above. This final statistical fit of the 766 data points is given by

$$h = \frac{0.073454\ Re_v^{0.8}\ Pr_v\ (x_e/x_a)^{2.6314}}{x_{chf}^{0.28459}\ (1.0 + \frac{DZQF}{D})^{0.44031}}\ \frac{k_v}{D}\ .$$

Where the heat transfer coefficient is defined as $h = Q_{total}/(T_w-T_v)$. As can be seen above, the t-values (right-hand column) for the remaining quanitities change little for the case where the Re_v and Pr_v are fixed.

Figure 4 shows a plot of measured heat flux versus predicted heat flux using the above regression fit, where the calculated heat flux is defined as $h(T_w-T_v)$. The regression fit has a standard deviation of about 24% with respect to the data used for its development.

As noted earlier, it is not intended that the results of this regression analysis provide a new film boiling correlation, even though a 24% standard deviation does indicate a respectable fit. The problem is that such a statistically based correlation cannot be used with any confidence outside its data base. The data for each individual parameter are fairly uniform over their quoted range, however, all possible combinations of parameters are not necessarily represented by the data. It is also questionable whether a single mechanism is controlling the entire data base, as a single correlation implies. This is particularly true of the high pressure, low quality data compared to the low pressure, high quality data. Also, the vapor Reynolds number spans the range of 2000 to 25,000, indicating that both laminar and turbulent data exist in the data base. Therefore, the modeling of a data base this broad may require the use of an additive-type correlation to incorporate several mechanisms.

Data Comparison with Existing Wall Heat Transfer Correlations

This section presents comparisons of the data base with six correlations and a correlation package which are currently in use throughout the nuclear safety industry. The correlations are given in the appendix.

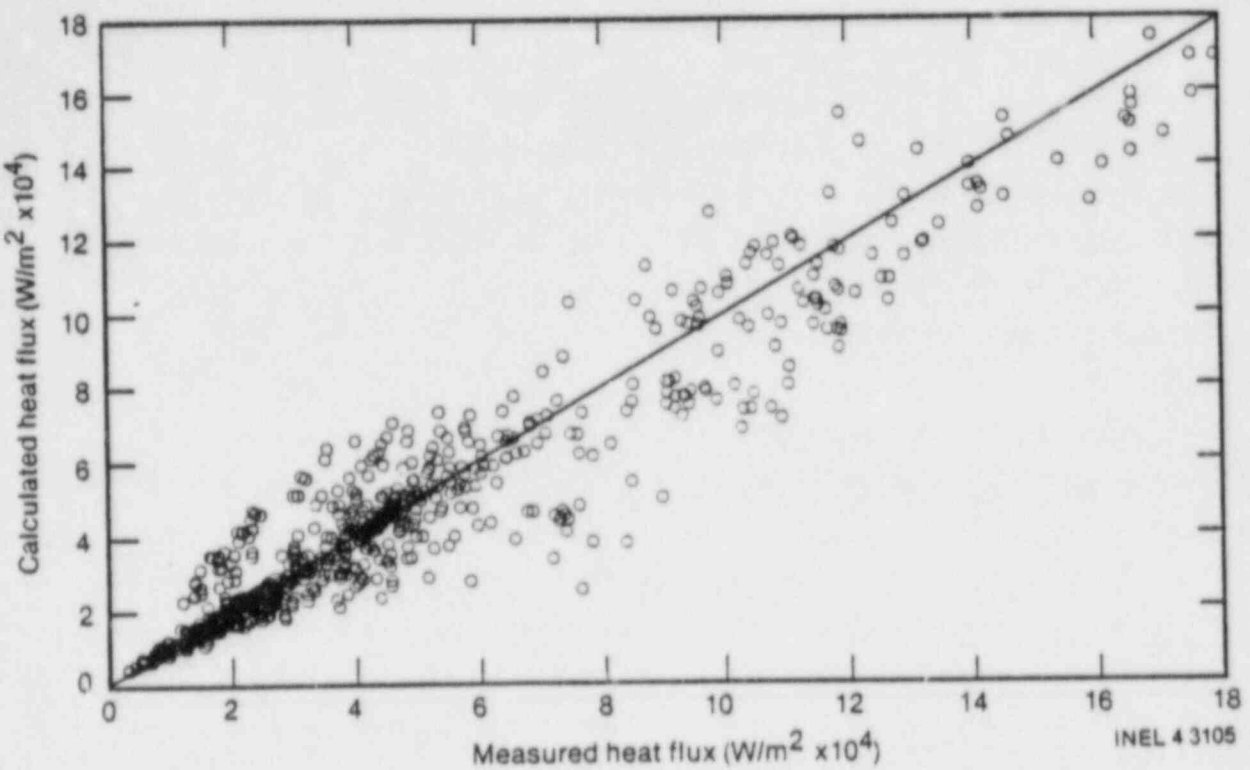

Figure 4. Calculated vs. measured heat flux for statistical data fit.

Three of the correlations used in the data comparisons were developed and are commonly applied, assuming saturation conditions for both the liquid and the vapor. The comparisons for these correlations--which include the Dougall-Rohsenow (26), the Groeneveld 5.7 (27), and the Condie-Bernston IV (28) correlations--were made on the basis of heat flux, with the calculated flux defined as $h(T_w-T_s)$.

The Dougall-Rohsenow correlation, when applied in this manner, produced the best overall fit of the data of all the correlations, as shown in Figure 5.

The Groeneveld 5.7 and the Condie-Bengston IV are both statistical-based correlations and were developed from similar data sets. As a result, the two correlations are similar. The Groeneveld 5.7 correlation generally overpredicts the data, whereas the Condie-Benston IV correlation falls somewhere in the middle. The scatter is very large for both correlations, as shown in Figures 6 and 7.

The Dittus-Boelter (29) and Dougall-Rohsenow (26) correlations were developed without consideration of nonequilibrium effects. They have since been applied in nonequilibrium situations by evaluating the properties at the superheated conditions and using a temperature potential of (T_w-T_v). Comparisons of the nonequilibrium correlations were made on the basis of heat transfer coefficient. Comparison to the data shows similar results for both correlations, which underpredict most of the data, as shown in Figures 8 and 9, with the Dougall-Rohsenow correlation calculating somewhat smaller heat transfer coefficients than the Dittus-Boelter Correlation.

The Chen-Sundaram-ozkaynak (CSO) (30) correlation was developed as a mechanistic, nonequilibrium correlation, using mostly tube film boiling data in which the vapor temperatures were inferred. Figure 10 shows the calculated heat transfer coefficient vs the measured value. The response is very similar to the Dittus-Boelter and Dougall-Rohsenow correlations in that it underpredicts the majority of the data.

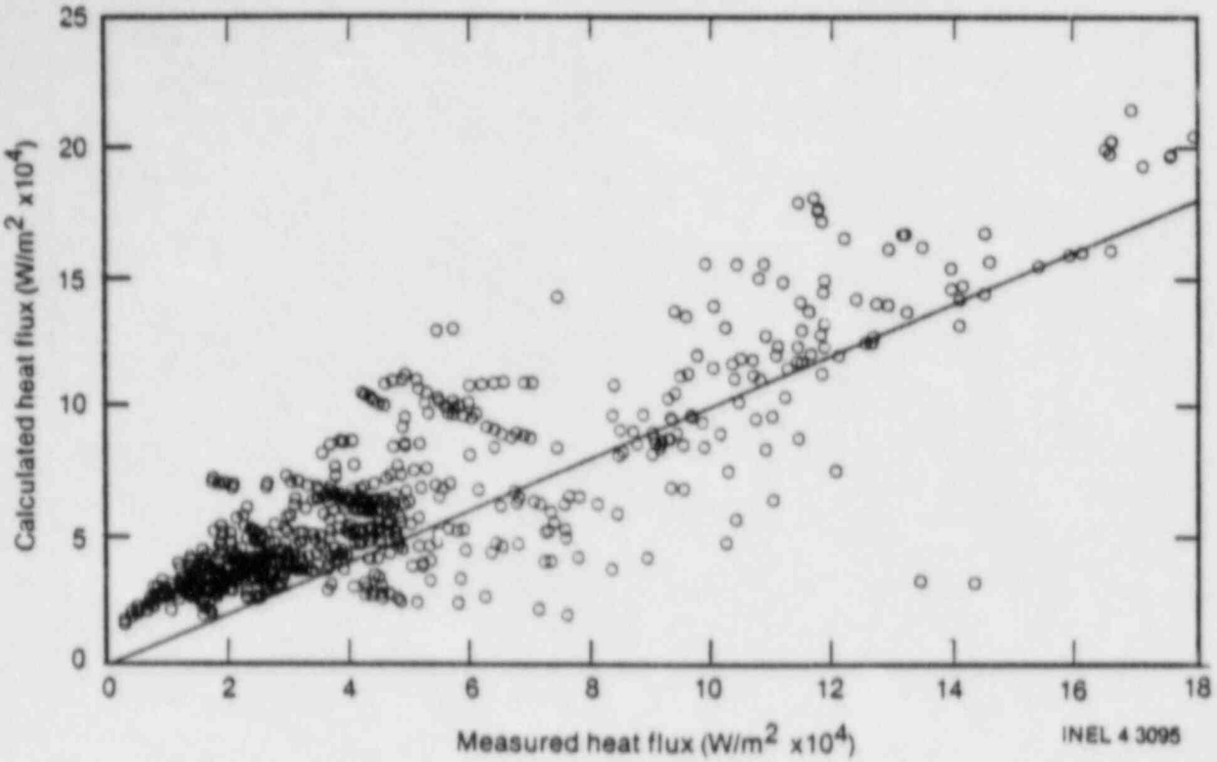

Figure 5. Calculated vs. measured heat flux for Dougall-Rohsenow saturated correlation.

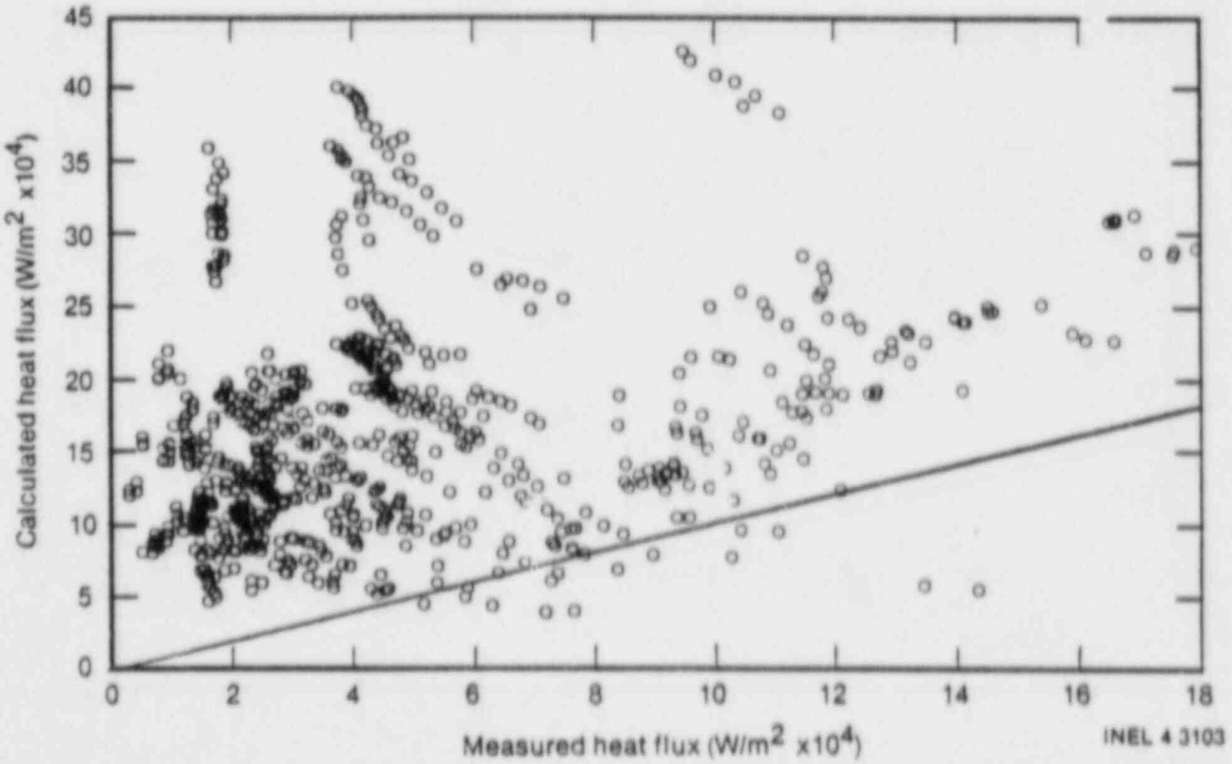

Figure 6. Calculated vs. measured heat flux for Groeneveld 5.7 correlation.

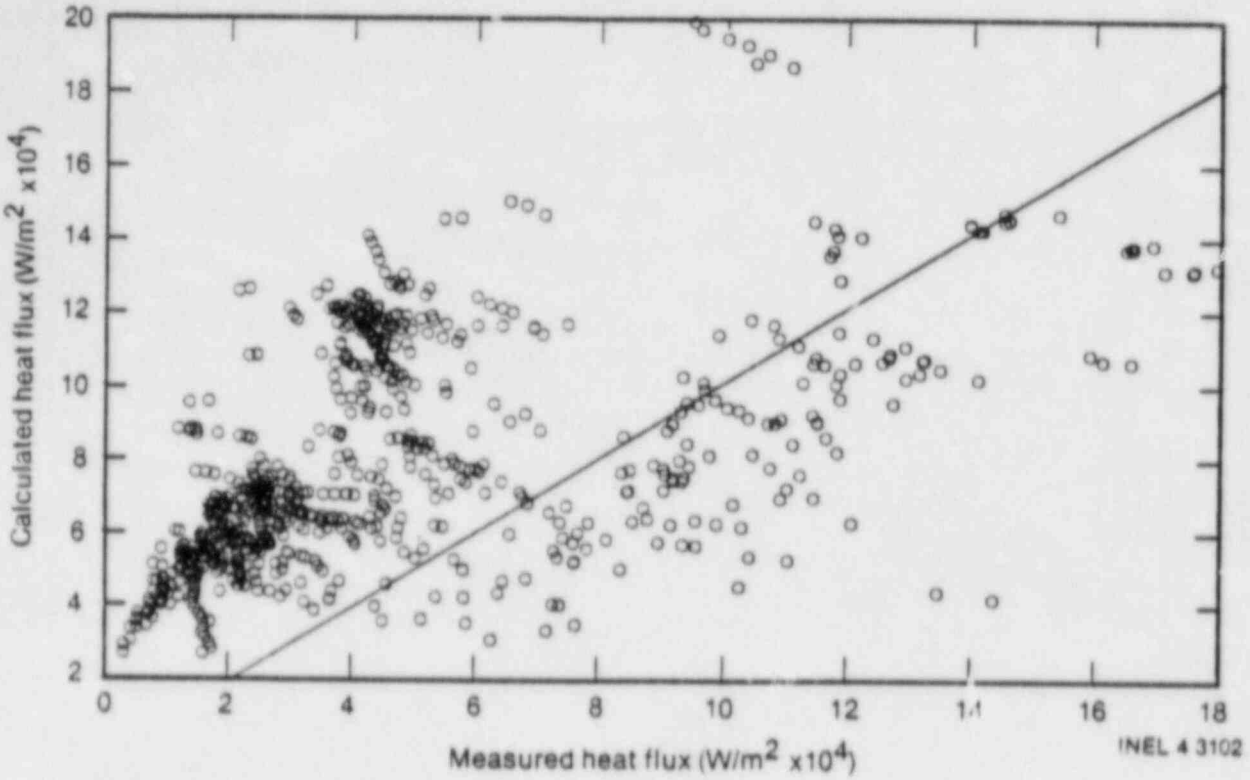

Figure 7. Calculated vs. measured heat flux for Condie-Bengston IV correlation.

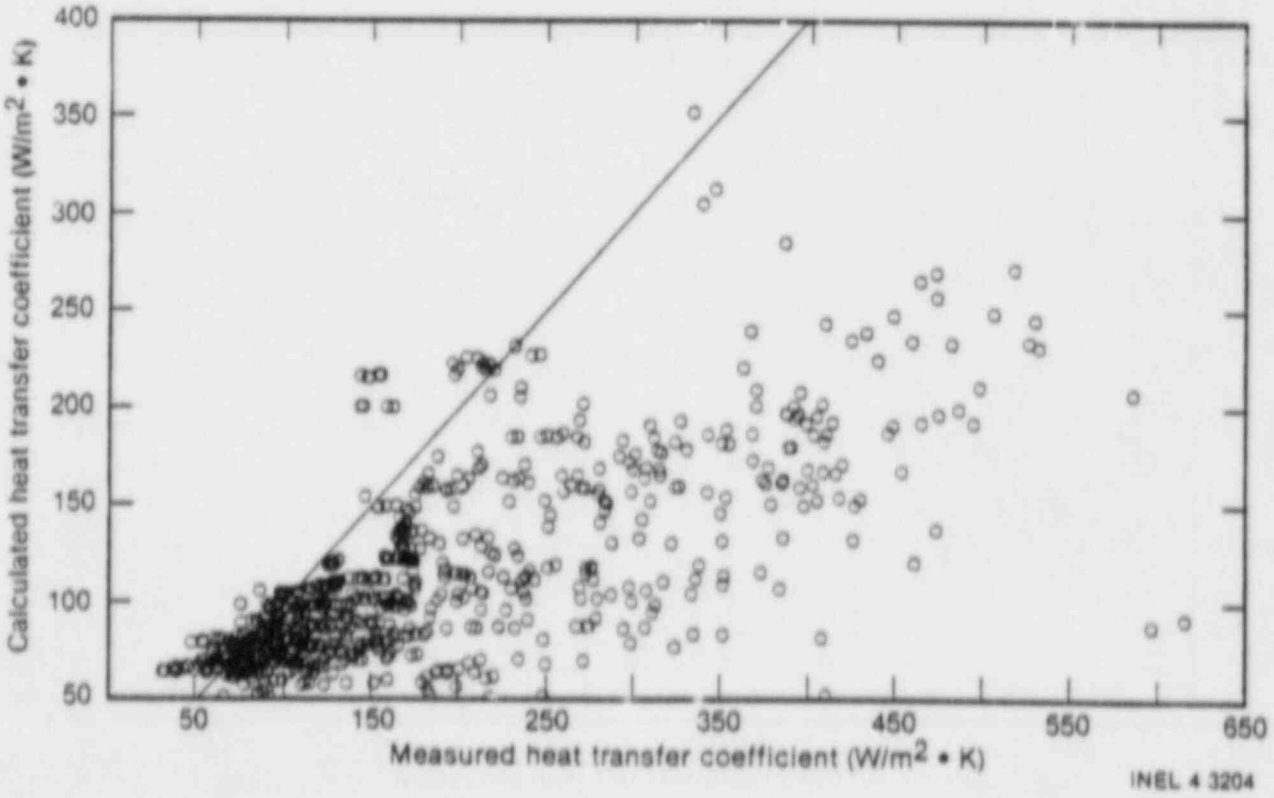

Figure 8. Calculated vs. measured heat transfer coefficient for Dittus-Boelter correlation using superheated properties.

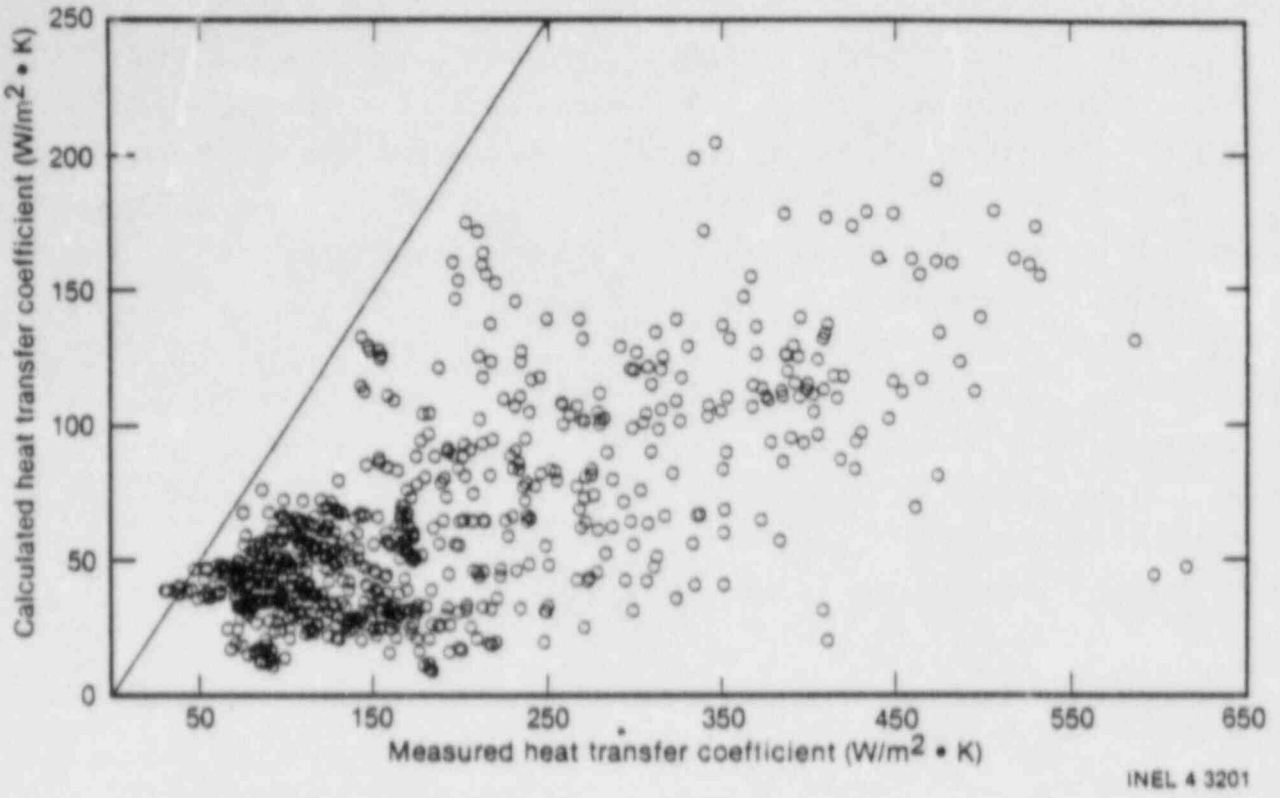

Figure 9. Calculated vs. measured heat transfer coefficient for Dougall-Rohsenow correlation using superheated properties.

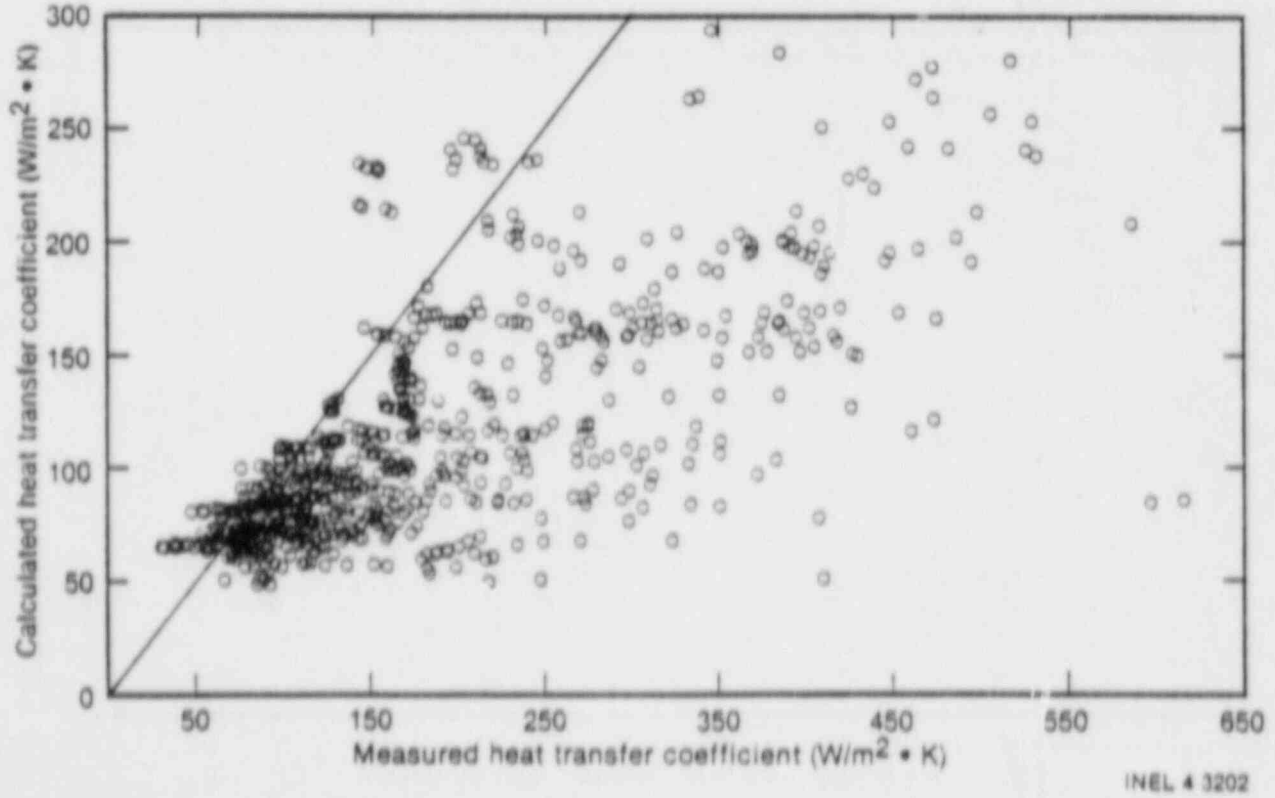

Figure 10. Calculated vs. measured heat transfer coefficient for CSO correlation.

1. e TRAC heat transfer package (31) is made up of several correlations representing individual heat transfer mechanisms. The package calculates the heat transfer from the wall to the liquid and from the wall to the vapor, nd then sums to define the total. The comparison shown in Figure 11 is based on heat transfer coefficient, where the calculated heat transfer coefficient is defined as $h = (q"_{\ell} + q"_{v})/(T_w - T_v)$. The correlation package significantly overpredicts all of tne data, except for two points. As noted in the description of the package in the appendix, the vapor heat transfer is taken as the maximum of the Bromley, Dougall-Rohsenow, and natural circulation correlations. For the range of these data, the Bromley correlation is the maximum in each case and dominates the calculated heat transfer, causing the noted overprediction.

During the reduction of the data, no attempt was made to separate the wall heat flux into radiation and convection components, because the radiation was assumed small relative to the convection. For the same reason, no special attempt was made to include a radiation term in the correlations. The TRAC heat transfer package includes a radiation term in the liquid heat transfer, which was negligible for these data ranges. The Groeneveld 5.7 and the Condie-Bengston IV correlations are statistical fits of data, which were also reduced originally without separating the radiation term. Consequently, the radiation effect is inherent in these correlations.

Vapor Generation Rate Comparisons

From the vapor continuity equation, the volumetric vapor generation rate, Γ, is given by

$$\Gamma = G \frac{dx_a}{dz} \quad . \tag{1}$$

where, from an energy balance,

$$x_a = \frac{x_e h_{fg}}{h_v(P,T_v) - h_{\ell}(P,T_s)} \quad . \tag{2}$$

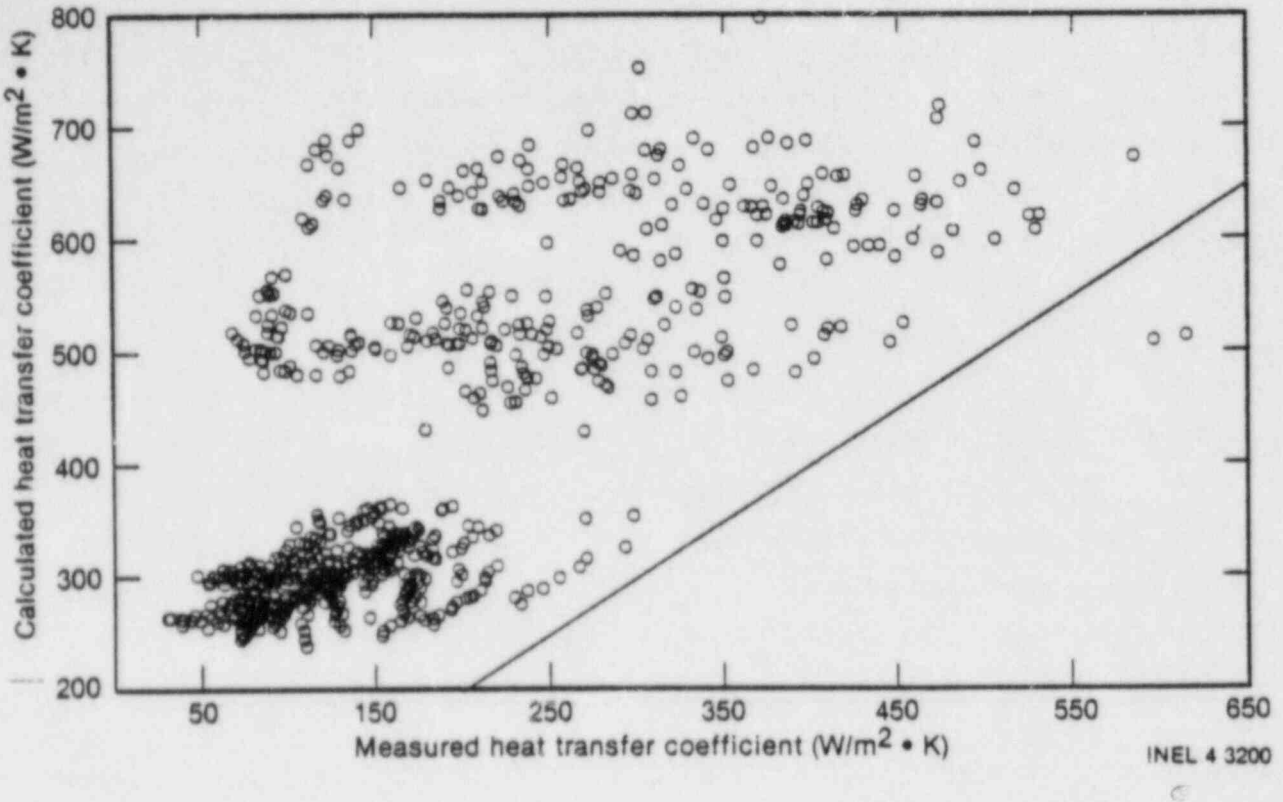

Figure 11. Calculated vs. measured heat transfer coefficient for TRAC heat transfer package.

Thus, the rate of change of actual flowing quality with respect to length must be known in order to evaluate the vapor generation rate. Reference 19 provided an early comparison of the steady state results for fixed quench front data. The vapor generation rate has two bounding cases. The thermodynamic equilibrium model implies that the vapor temperature is always equal to the saturation temperature. No vapor superheating occurs and all of the energy from the heated walls goes directly into evaporation of the liquid droplets. The other bounding case is the frozen droplet model. This model implies that the flow quality is frozen at a fixed quality with none of the energy from the heated walls going into evaporation of the liquid droplets.

Previously (11,12,13,14), the rate of change of actual quality with respect to length has not been measured. Earlier work (32) to verify vapor generation rate correlations (32,33,34) compared the predicted vapor temperature using various correlations with an experimentally measured vapor temperature at a single point with a fixed quench front. Agreement between the measured and predicted vapor temperature inferred that the vapor generation rate model was correct but could not assure it since the rate of change of actual flowing quality with respect to length required in Eq. (1) was not known. The vapor superheat measurements at multiple axial positions in the test section provide the necessary information to evaluate the rate of change of actual flowing quality with respect to length and therefore the vapor generation rate for either fixed or moving quench front. One hundred sixty two vapor generation rate measurements were obtained from the data.

Figure 12 shows the change in equilibrium quality with the change in actual quality for each data point. The quality change was from either probe 1 to probe 2 or from probe 2 to probe 3 consistant with the location where the data point was obtained. The diagonal line represents the thermal equilibrium condition while the abscissa represents the frozen droplet condition. As indicated in Figure 12 the data are fairly evenly scattered between the two bounding conditions. Some of the data indicate very little heat transfer between the vapor and liquid droplets and

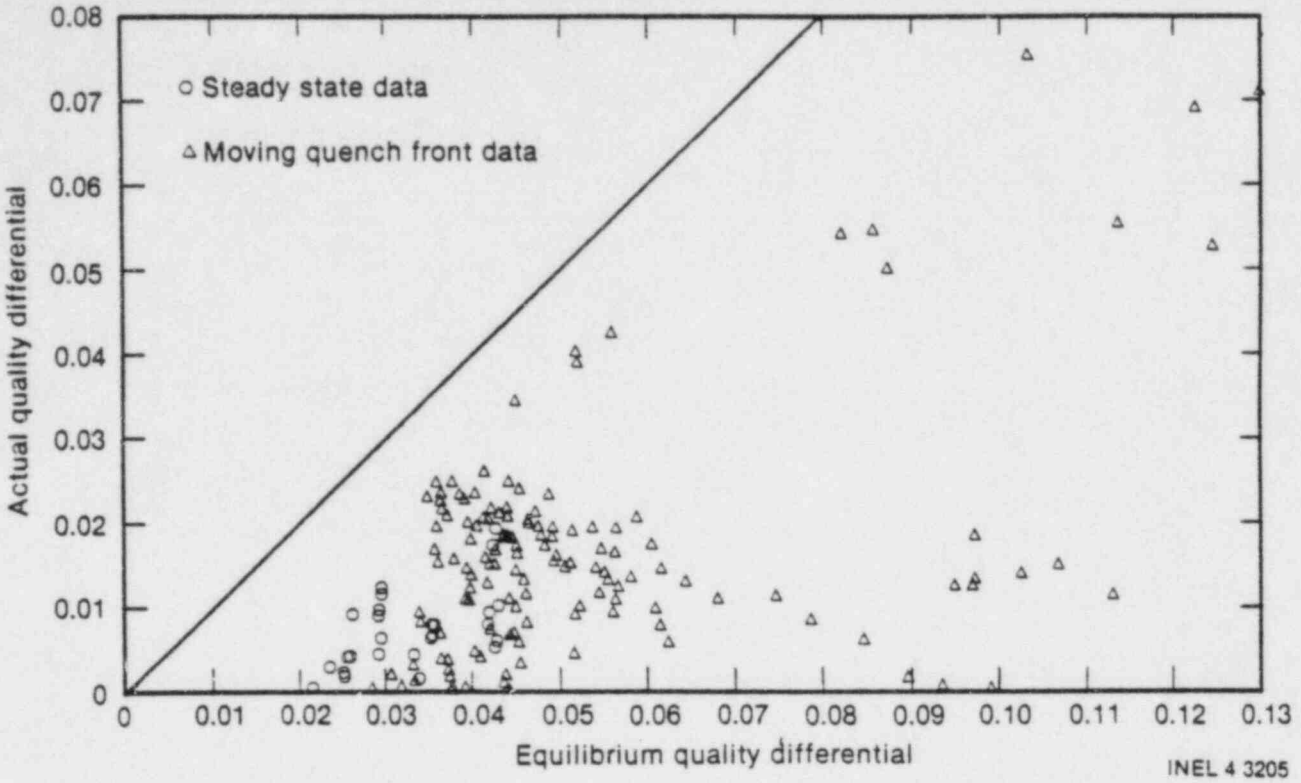

Figure 12. Actual quality change vs. equilibrium quality change for INEL data.

approach the frozen droplet model, while other data have significant heat transfer between the vapor and liquid droplets and lie between the frozen droplet and thermodynamic equilibrium models.

In comparing the THEF data with existing vapor generation rate correlations, significant differences were found. Figure 13 presents the comparison with the vapor generation correlation developed by Webb(32,33), and given by

$$\Gamma = 1.32 \left(\frac{P}{P_c}\right)^{-1.1} \left(\frac{Gx_a}{\alpha_h}\right)^2 \frac{(1 - \alpha_h)^{2/3} (T_v - T_s) k_v}{\rho_v \sigma h_{fg} D} \quad . \tag{3}$$

Figure 14 presents the comparison with the modified Saha correlation (33) given by

$$\Gamma = 6300 \left(1 - \frac{P}{P_c}\right)^2 \left[\left(\frac{Gx_a}{\alpha_h}\right)^2 \frac{D}{\rho_v \sigma}\right]^{0.5} \frac{k_v (1 - \alpha_h) (T_v - T_s)}{D^2 h_{fg}} \quad , \tag{4}$$

where

$$\alpha_h = \left[1 + \frac{(1 - x_a)}{x_a} \frac{\rho_v}{\rho_\ell}\right]^{-1}$$

The Webb correlation passes through the data with a large scatter in the data. The correlation overpredicts all of the steady state data as shown by the circles in Figure 13. The steady state data is primarily low flow, high void data. The modified Saha correlation significantly overpredicts all of the THEF data as noted in Figure 14.

The Webb correlation was based on only low-pressure data (0.4 MPa or less) with only a single vapor temperature measurement available while the modified Saha correlation was based on data having only vapor temperatures inferred from an assumed heat transfer coefficient. The above comparisons

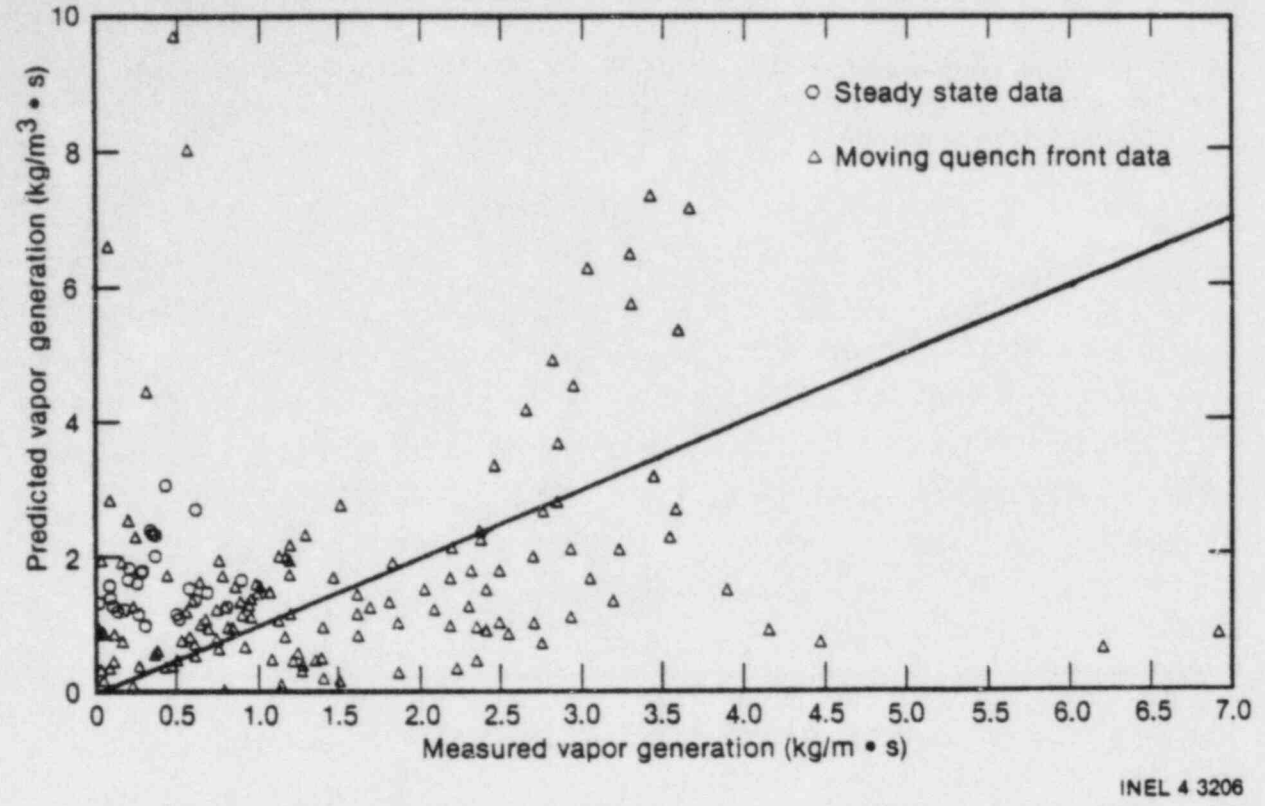

Figure 13. Calculated vs. measured vapor generation rate for Webb correlation.

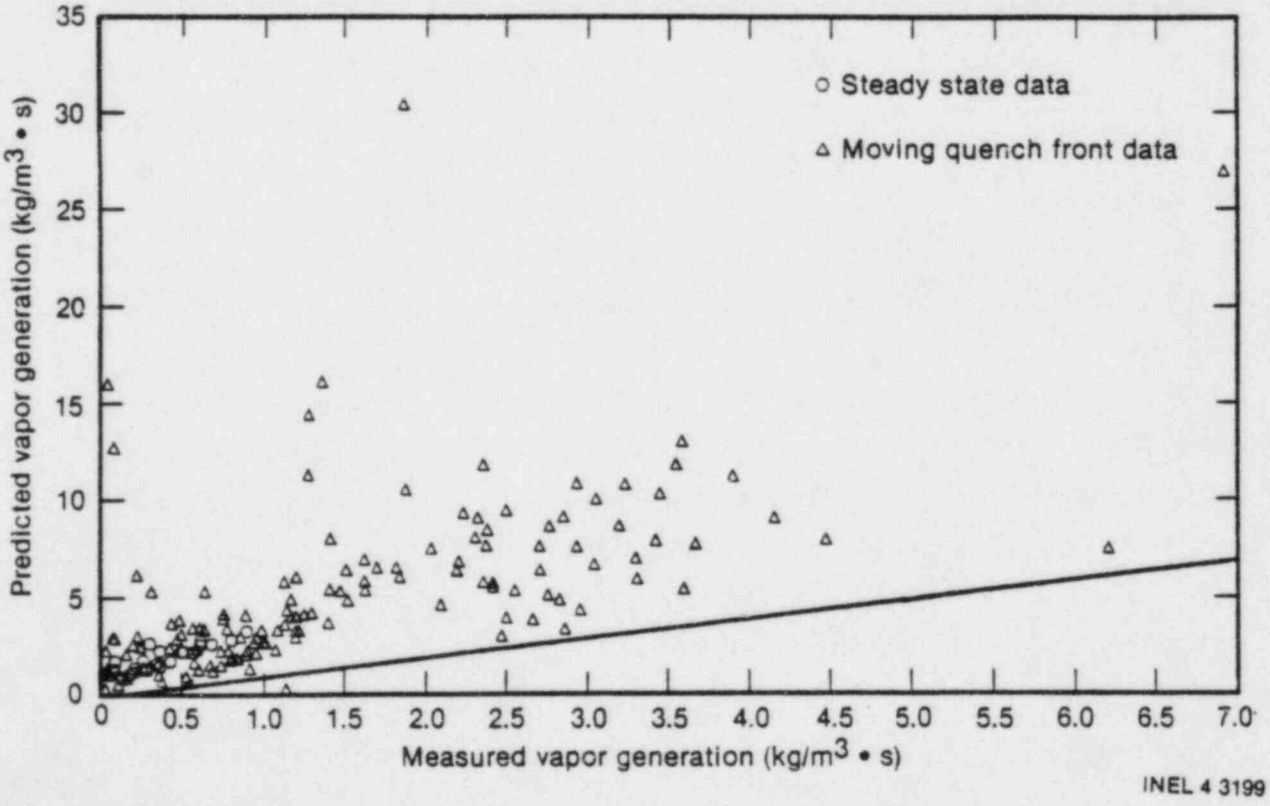

Figure 14. Calculated vs. measured vapor generation rate for modified Saha correlation.

should not be unexpected and the factors influencing the nonequilibrium vapor generation are believed to be similar to those previously discussed for the wall heat transfer, i.e., quench front quality, distance from quench front and degree of nonequilibrium.

CONCLUSIONS

Forced convective, nonequilibrium, post-critical-heat-flux (post-CHF) heat transfer experiments have been conducted at the INEL for water flowing up within a vertical tube. Steady state (fixed quench front) experiments were conducted at pressures of 0.2 to 0.7 MPa, mass fluxes of 12 to 24 kg/m^2-s, test section inlet qualities of 38 to 64%, and heat fluxes of 7.7 to 27.5 kW/m^2. Quasi-steady-state (slow moving quench front) experiments were conducted at pressures of 0.4 to 7 MPa, mass fluxes predominantly in the range of 12 to 70 kg/m^2•s with some data up to 100 kg/m^2-s, test section inlet qualities of -7 to 47%, and heat fluxes of 8 to 225 kW/m^2. Eighty three steady state and 683 quasi-steady-state data points were obtained.

A regression analysis to obtain a nonequilibrium wall heat transfer correlation yielded four important parameters. The most significant was the flow effect represented by the vapor Reynolds number. The effects of nonequilibrium, (x_e/x_a) quench front quality, x_{chf}, and distance from the quench front, (1 - DZQF/D), were all of approximately equal importance behind the Reynolds number. Prandtl number was also included but was not as significant as any of the other parameters.

The data have been compared with current heat and mass transfer correlations used in state-of-the-art computer codes such as RELAP5 and TRAC. Film boiling correlations considered were Dougall-Rohsenow, Dittus-Boelter, Groeneveld 5.7, Condie-Bengston IV, Chen-Sundaram-Ozkaynak (CSO), and the TRAC heat transfer package. The Dougall-Rohsenow, Dittus-Boelter, and CSO correlations when based on nonequilibrium conditions underpredict most of the data while the Groeneveld 5.7 and TRAC correlations overpredict most of the data. The Condie-Bengston IV correlation shows a large amount of scatter. The original saturated

Dougall-Rohsenow correlation is the only one that gives a reasonable prediction of wall heat flux even though it does not account for the correct physics.

The measured vapor generation rates have been compared with those predicted by the Webb and modified Saha correlations. The Webb correlation correctly predicts some of the data but there is a large scatter whereas the modified Saha correlation significantly overpredicts the measured data.

The results of this study indicate that additional nonequilibrium post-CHF data are needed and that heat and mass transfer model development work is needed in order to assure accurate predictions of cladding temperature and vapor superheating during reactor severe accident transients and LOCA transients.

REFERENCES

1. McCormick-Barger, M., Experimental Data Report for LOFT Power Ascension Test L2-2, NUREG/CR-0492, TREE-1322, February 1979.

2. Prussions, P. G., Galusha, B. M., and Engelman, D. B., Experimental Data Report for LOFT Power Ascension Experiment L2-3, NUREG/CR-0792, TREE-1326, July 1979.

3. Rosal, E. R., Hochreiter, L. E., McGuire, M. F., and Krepinevich, M. C., FLECHT Low Flooding Rate Cosine Test Series Data Report, WCAP-8651, December 1985.

4. Dobbe, C. A., "Pressurized Water Reactor Severe Accident Sequence Analysis (SASA)", 11th Water Reactor Safety Research Information Meeting October 24-28, 1983.

5. Jouse, W. C., "INEL BWR Severe Accident ATWS Study," 11th Water Reactor Safety Research Information Meeting October 24-28, 1983.

6. Schnitzler, B. G. Fission Product Decay Heat Modeling for Disrupted Fuel Regions (FDECAY), EGG-PHYS-5698 (December, 1981).

7. Ransom, V. H., et. al., RELAP5/MOD1 Code Manual, NUREG/CR-1826, EGG-2070, March 1982.

8. "TRAC-PD2: An Advanced Best-Estimate Computer Program for Pressurized Water Reactor Loss-of-Coolant Accident Analysis," LA-8709-MS, February 1981, Los Alamos Scientific Laboratory.

9. Spore, J. W.,et at., TRAC-BD1. An advanced Best Estimate Computer Program for Boiling Water Reactor Loss-of-Coolant Accident Analysis, NUREG/CR-2178, EGG-2109, October 1981.

10. Parker, J. D. and Grosh, R. J., Heat Transfer to a Mist Flow, ANL-6291, 1962.

11. Mueller, R. E., Film Boiling Heat Transfer Measurements in Tubular Test Section, EURAEC-1971 GEAP-5423, October 1967.

12. Polomik, E. E, Transition Boiling Heat Transfer Program--Final Summary Report for Feb/63--Oct/67, GEAP-5563, October 1967.

13. Nijhawan, S. M., Experimental Investigation of Thermal Non-Equilibrium in Post-Dryout Steam-Water Flow, Ph.D. Dissertation, Lehigh University, 1980.

14. Nijhawan, S. M., Chen, J. C., Sundaram, R. K., and London, E. J., "Measurement of Vapor Superheat in Post-Critical-heat Flux Boiling," Journal of Heat Transfer, 102, 1980, pp. 465-470.

15. Evans, D. G., Webb, S. W., and Chen, J. C., "Measurement of Finally Varying Nonequilibrium in Post-Critical-Heat-Flux Boiling in a Vertical Tube," NUREG/CR-3363, TS-831-1, Vols 1 and 2, June 1983.

16. Rosal, E. R., Conway, C. E., and Krepinevich, M. C., FLECHT Low Flooding Rate Skewed Test Series Data Report, WCAP-9108, 1977.

17. Gottula, R. C., Condie, K. G., Sundaram, R. K., Neti, S., Chen, J. C., and Nelson, R. A., Forced Convective, Nonequilibrium, Post-CHF Heat Transfer Experiment Data and Analysis Report, DRAFT NUREG/CR-3193, January 1984.

18. Groeneveld, D. C. and Gardiner, L. R. M., "A Method of Obtaining Flow Film Boiling Data For Subcooled Water," International Journal Heat Mass Transfer, 21, 1978, pp. 665-665.

19. Gottula, R. C., Nelson, R. A., Chen, J. C., Neti, S., and Sundaram, R. K, "Forced convective Nonequilibrium Post-CHF Heat Transfer Experiments in a Vertical Tube", ASME-JSME Joint Conference on Two-Phase Flow and Boiling Heat Transfer, Honolulu, Hawaii, March 20-24, 1983.

20. Matthews, S. D. and Smith N. C., "STAPP, A Statistical Analysis and Plotting Package," EGG-EA-5495, September 1981.

21. Andersen, J. G. M., "Low Flow Film Boiling Heat Transfer on Vertical Surfaces. Part 1: Theroetical Model," AIChE Symp. Series, 73 (No. 164), 1977, pp. 2-6.

22. Chen, J. C., Sundaram, R. K. and Chen, K. L., "Analysis of Babcock and Wilcox Data on Film Boiling Heat Transfer," Institute of Thermo-Fluid Engineering to Science, Report TS-811, Lehigh University, 1981.

23. Chan, K. C. and Yadigaroglu, G., "Calculations of Film Boiling Heat Transfer Above the Quench Front During Reflood," presented at 19th National Heat Transfer Conference, Orlando, 1980.

24. Denham, M. K., Inverted Annular Film Boiling and the Bromley Model," AEEW-R 1590, 1983.

25. Yu, K. P, and yadigaroglu, G., "Heat Transfer Immediately Downstream of the Quench Front During Reflooding," 1979 ASME Annular Winter Meeting, 79-HT-48.

26. Dougall, R. L. and Rohsenow, W. M., Film-Boiling on the Inside of Vertical Tubes with Upward Flow of the Fluid at Low Qualities, MIT-TR-9079-26, 1963.

27. Groeneveld, D. C., An Investigation of Heat Transfer in the Liquid Deficient Regime, AECL-3281 (Rev.), August 1969.

28. Condie, K. G., Bengston, S. J. and Richlen, S. L., Post-CHF Heat Transfer DAta Analysis, Comparison, and Correlation, unpublished INEL report.

29. Dittus, F. W. and Boelter, L. M. K., "Heat Transfer in Automobile Radiators of the Tubular Type," University of California Publications, 2, pp 443-461, 1930.

30. Chen, J. C., Sundaram, R. K. and Ozkaynak, F. T., A Phenomenological Correlation for Post-CHF Heat Transfer, NUREG-0237, 1977.

31. TRAC-PD2, An Advanced Best-Estimate Computer Program for Pressurized Water Reactor Loss-of-Coolant Accident Analysis, DRAFT, Los Alamos National Laboratory.

32. Webb, S. W. and Chen, J. C., Vapor Generation Rate in Nonequilibrium Convective Film Boiling, Report No. TS-820, Institute of Thermo-Fluid Eng. and Science, Lehigh University, December 1981.

33. Webb, S. W. and Chen, J. C., and Sundaram, R. K., "Vapor Generation Rate in Nonequilibrium Convective Film Boiling," Vol. 4, Paper FB45, 7th International Heat Transfer Conference, Munich, Germany, September 1982.

34. Saha, P., Shiralkar, B. S., and Dix, G. E., "A Post-Dryout Heat Transfer Model Based on Actual Vapor Generation Rate in Dispersed Droplet Regime," ASME Paper 77-HT-80.

Appendix A

This appendix defines the film boiling heat transfer coefficients used in this paper.

1. Dougall-Rohsenow (for saturated conditions) (A-1)

$$h = 0.023 \frac{k_g}{D} \left\{ Re_g \left[x_e + \frac{\rho_g}{\rho_f} (1 - x_e) \right] \right\}^{0.8} Pr_g^{0.4} ,$$

where

$$Re_g = D\, G/\mu_g$$

$$Pr_g = \frac{\mu_g C_{p_g}}{k_g} .$$

The heat flux q" is defined as

$$q" = h (T_w - T_s) .$$

2. Dittus Boelter (A-2)

$$h = 0.023 \frac{k_v}{D} Re_v^{0.8} Pr_v^{0.4}$$

where

$$Re_v = \frac{G\, x_a\, D}{\mu_v} ,$$

and

$$Pr_v = \frac{u_v C_{p_v}}{k_v} \quad .$$

The heat flux q" is defined as

$$q" = h\,(T_w - T_v) \quad .$$

3. Groeneveld 5.7 (A-3)

$$h = 0.0520 \frac{k_g}{D} R^{0.688}\, Pr_g^{1.26}\, Y^{(-1.06)} \quad ,$$

where

$$R = \frac{DG}{u_g} \left[x_e + \frac{\rho_g}{\rho_f} (1 - xe)\right]$$

$$Pr_g = \frac{u_g C_{p_g}}{k_g}$$

$$Y = 1.0 - 0.1 \left(\frac{\rho_\ell}{\rho_g} - 1.0\right)^{0.4} (1 - x_e)^{0.4} \quad .$$

The heat flux q" is defined as

$$q" = h(T_w - T_s) \quad .$$

4. Condie-Bengston IV (A-4)

$$h = \frac{0.05245\, k_g^{0.4593}\, Pr_w^{2.2598}}{D^{0.8095}\, (x_e + 1)^{2.0514}}\, R \quad ,$$

where

$$R = \frac{DG}{\mu_g}\left[0.6249 + 0.2043 \ln (x_e + 1) \right]$$

The heat flux q" is defined as

$$q" = h (T_w - T_s) \quad .$$

5. Chen, Sundaram, Ozkaynak (A-5)

$$h = 0.5 F G_v C_{p_{vf}} Pr_{vf}^{-2/3}$$

where

$$F = 0.037 RE^{(-0.17)}$$

$$RE = \frac{D \rho_v V_{pt}}{\mu_v}$$

$$V_{pt} = \frac{G x_a}{\rho_v} + \frac{G (1 - x_a)}{\rho_\ell}$$

$$G_v = G x_a$$

$C_{p_{vf}}$ = Specific heat evaluated at $\frac{(T_w + T_v)}{2}$

Pr_{vf} = Prandtl no. evaluated at $\frac{(T_w + T_v)}{2}$

The heat flux q" is defined as

$$q" = h(T_w - T_v) \quad .$$

6. TRACPD2/MOD1 Heat Transfer Logic (A-6)

The liquid heat transfer coefficient is given by

$$h_\ell = h_r \left(\frac{T_w - T_s}{T_w - T_\ell} \right) + h_{df} \quad ,$$

where

$$h_r = (1 - \alpha)\, \sigma\varepsilon \left(\frac{T_w^4 - T_s^4}{T_w - T_s} \right) \quad ,$$

and σ is the Stefan-Boltzmann constant and ε is the wall emissivity. The liquid absorptivity is 1.0.

The dispersed flow heat transfer coefficient, h_{df}, uses the Forslund and Rohsenow (A-7) equation modified by multiplying $(1 - \alpha)$ by the fraction of liquid entrained, E,

$$h_{df} = 0.2\, c_1\, (1 - \alpha) E^{0.6667}\, BRAC^{0.25} \left(\frac{T_w - T_s}{T_w - T_\ell} \right) \quad ,$$

where c_1 is a constant equal to 1.2760 and

$$BRAC = \frac{g \rho_\ell \rho_g h'_{\ell g} k^3}{(T_w - T_s)\, \mu_g\, d_{drop}} \quad .$$

The dispersed flow HTC is set equal to zero if $(1 - \alpha)E > 0.05$

$$d_{drop} = \frac{We\ \sigma}{\rho_g (v_g - v_\ell)^2} \quad , \text{ and } We = 4.0 \quad .$$

The droplet diameter is restricted to the range

$$1.0 \times 10^{-4} \leq d_{drop} \leq 3.0 \times 10^{-3}$$

The fraction of liquid entrained is found in the following manner,

$$E = 0, \qquad \text{if } |V_g| \leq V_E \quad ,$$

or

$$E = 1.0 - \exp 0.23 \left[-\left(|V_g| - V_E\right)\right] \quad , \qquad \text{if } |V_g| > V_E \quad ,$$

where the entrainment velocity is

$$V_E = 3.65 \left[\frac{(\rho_\ell - \rho_g)}{\rho_g^2}\right]^{1/4}$$

and E is restricted to values between 0.07 and 1.0.

The vapor heat transfer coefficient is given by

$$h_g = \max (h_{fbb}, h_{nc}, h_{DR}) \quad .$$

The Bromley film boiling heat transfer coefficient (A-8), h_{fbb}, is given by

$$h_{fbb} = 0.62 \left[\frac{\rho_g k^3 (\rho_\ell - \rho_g)\ g h'_{\ell g}}{\mu_g (T_w - T_s)^g}\right]^{1/4} \quad ,$$

where the characteristic length, λ, is

$$\lambda = 2\pi\left[\frac{\sigma}{g\,(\rho_\ell - \rho_g)}\right]^{1/2} .$$

The latent heat of vaporization is modified as suggested in Reference A-9

$$h'_{\ell g} = h_{\ell g} + 0.5\,(c_p)_g\,(T_w - T_s) .$$

The turbulent natural convection equation used in this heat-transfer regime is

$$h_{nc} = 0.13\,k_g\left(\frac{\rho_g^2 g\,|T_w - T_g|}{u^2 T_g}\right)^{0.333} Pr_g^{0.333} .$$

The forced convection equation is based on Dougall and Rohsenow's modification to the Dittus-Boelter equation

$$h_{fc} = 0.023\,\frac{k_g}{D_h}\left\{\frac{\rho_g\left[\alpha|V_g| + (1-\alpha)|V_\ell|\right]D_h}{u_g}\right\}^{0.8}\left[\frac{u_g(c_p)_g}{k_g}\right]^{0.4} ,$$

where the Reynolds number is modified to reflect the volumetric flow rate of the two-phase mixture.

As in the previous heat-transfer regimes, linear interpolation is used $\alpha > \alpha_c$.

The total heat flux q" is given by

$$q'' = h_\ell\,(T_w - T_s) + h_g\,(T_w - T_v) .$$

References

A-1. Dougall, R. L. and Rohsenow, W. M., Film-Boiling on the Inside of Vertical Tubes with Upward Flow of the Fluid at Low Qualities, MIT-TR-9079-26, 1963.

A-2. Dittus, F. W. and Boelter, L. M. K., "Heat Transfer in Automobile Radiators of the Tubular Type," University of California Publications, 2, pp 443-461, 1930.

A-3. Groeneveld, D. C., An Investigation of Heat Transfer in the Liquid Deficient Regime, AECL-3281 (Rev.), August 1969.

A-4. Condie, K. G., Bengston, S. J. and Richlen, S. L., Post-CHF Heat Transfer Data Analysis, Comparison, and Correlation, unpublished INEL report.

A-5. Chen, J. C., Sundaram, R. K. and Ozkaynak, F. T., A Phenomenological Correlation for Post-CHF Heat Transfer, NUREG-0237, 1977.

A-6. TRAC-PD2, An Advanced Best-Estimate Computer Program for Pressurized Water Reactor Loss-of-Coolant Accident Analysis, Draft, Los Alamos National Laboratory.

A-7. R. P. Forslund and W. M. Rohsenow, "Dispersed Flow Film Boiling," Journal of Heat Transfer, 90, November 1968, pp. 399-407.

A-8. L. A. Bromley, "Heat Transfer in Stable Film Boiling," Chemical Engineering Progress, 46, May 1950, pp. 221-227.

A-9. S. S. Kutateladze, "Heat Transfer During Film Boiling," in Heat Transfer in Condensation and Boiling, Atomic Energy Commission Report AEC-TR-3770, 1952.

POST DRYOUT HEAT TRANSFER PREDICTION

by

Anthony F. Varone, Jr.
Warren M. Rohsenow
Massachusetts Institute of Technology
Cambridge, Massachusetts 02139 U.S.A.

ABSTRACT

A mechanistic model of post dryout heat transfer has been developed involving momentum and energy equations for both vapor and liquid, average drop diameter at the dryout location, and using heat transfer correlations for vapor-to-drop, wall-to-drop, and wall-to-vapor. This involves a computer calculation stepwise down the tube from dryout.

This calculation was simplified making possible the heat transfer prediction at any position down the tube without the stepwise solution.

The two solutions agree well with each other. To make the predictions agree with data it was found necessary to multiply the wall-to-vapor heat transfer coefficient by a factor ranging from around 0.7 to about 2. At present this factor is found to be a function of bulk to wall viscosity ratio and quality. It may also be a function of liquid and vapor densities, tube and particle diameters and Reynolds number.

A similar effect of wall-to-gas heat transfer is found in solid particle-gas flowing mixtures. The detailed explanation is as yet unknown, but appears to be due to turbulence suppression and enhancement resulting from particle motion.

NOMENCLATURE

English Symbols

Ac	acceleration group
C_D	drag coefficient
c_p	specific heat
c_v	volumetric concentration
D	diameter
$\overline{D}$	mass weighted average drop diameter
f	drop diameter function
G	mass flux
g	gravitational acceleration
h	heat transfer coefficient
h_{fg}	latent heat of vaporization
I_1	constant
I_2	constant
K	non-equilibrium parameter
k	thermal conductivity
Nu	Nusselt number
$\dot{n}$	droplet flux
Pr	Prandtl number
q''	heat flux
$\overline{R}$	average drop extension radius
R_{max}	maximum drop extension radius
R_{Nu}	ratio of the two phase Nusselt number to the single phase Nusselt number

Re	Reynolds number
r	radius of curvature
S	free stream slip ratio
S_f	film slip ratio
T	temperature
$\underline{V}$	velocity
$\underline{v}_r$	radial component of turbulent fluctuations
v_z	axial component of turbulent fluctuations
W_g	gas mass flow rate
W_s	solid mass flow rate
x	quality
y	distance from tube wall
y_f^*	universal law of the wall coordinate
z	axial position along tube

Greek Symbols

α	void fraction
β_1	coefficient
β_2	coefficient
δ	drop-wall separation distance
ε	drop effectiveness
λ	deposition parameter
σ	surface tension
ϕ	drop diameter function
ρ	density
μ	dynamic viscosity

Subscripts

A	in Eqs. (5) and (6)
a	actual
b	referenced to bulk temperature
c	critical
do	dryout
e	equilibrium
ℓ	liquid
ℓf	liquid film
$\perp$	perpendicular to tube wall
s	saturation
T	tube
v	vapor
v-d	vapor to drop
w	wall
w-d	wall to drop
w-v	wall to vapor

INTRODUCTION

Dispersed flow heat transfer is heat transfer to a fluid consisting of a primary vapor phase with a fine dispersion of entrained liquid droplets. It is usually preceeded by an annular flow in which a liquid film is present on the channel wall with a flowing vapor core. High relative velocities exist between the vapor and liquid film, which cause liquid to be torn from the film and entrained in the vapor. Evaporation of the liquid film along with the liquid entrainment cause the film to disappear.

This point is known as the dryout point and is where the dispersed flow regime begins. Vapor now contacts the wall and the wall heat transfer coefficient is reduced due to a lower thermal conductivity of the vapor relative to the liquid. This results in lower heat transfer in constant wall temperature applications and a sharp rise in wall temperatures in constant heat flux applications. Temperatures can be high enough to physically destroy the heating surface, a phenomenon termed burnout.

Droplet evaporation takes place by heat transfer from the vapor and during direct drop-wall collisions. Wall temperatures are usually too high for liquid to wet the wall, making the drop-wall heat transfer usually less than 5% of the total. A finite heat transfer resistance exists between the vapor and liquid, resulting in the vapor becoming superheated. Since all of the energy does not go into evaporating the liquid, the actual quality will not equal the equilibrium quality. The vapor travels at a higher velocity than the liquid drops, whose diameters are typically on the order of 30 - 300 μm. Because of large density differences between the phases (except near the critical point), vapor void fractions are usually 80 - 100%.

ANALYSIS

This analysis has been restricted to

1) vertical upflow in a circular tube
2) uniform wall heat flux
3) steady state conditions

Yoder [1] developed a stepwise computer solution which predicts tube wall temperatures as a function of axial position beyond dryout. It is a physical model based on continuity, momentum, and energy equations and uses empirical correlations where necessary. The major assumptions of this model are

1) equilibrium quality exists at dryout
2) both liquid and vapor are at saturation temperature at dryout
3) drop size distribution can be characterized by one average drop size
4) liquid temperature remains at the saturation temperature

AVERAGE DROP DIAMETER AT DRYOUT

It is necessary to calculate the average drop size at dryout. Assuming annular flow preceeds dryout, drops are formed at all points along the tube before dryout. Drops are formed by Helmholtz instabilities in the liquid film and by liquid being thrown into the vapor core during vigorous boiling in the liquid film. It has been assumed that the latter mechanism is the dominant drop sizing mechanism of drops being formed from the liquid film. Once the drops enter the vapor core, further droplet breakup can occur due to free stream slip between the liquid and vapor. Yoder arrived at expressions needed to calculate the mass weighted average drop diameter at dryout $\overline{D}$, which are presented in Table 1.

To calculate the mass weighted average droplet diameter, the following procedure is used:

1) Iterate over Eqs. (1), (2), (3), and (28)(for C_D) to calculate D_{do}, α, and S_{do} ($D = D_{do}$ in Eq. (3)).
2) Calculate S_f using Eq. (4).
3) Calculate x_A from Eq. (5). If $x_A < 0.1$, then set $x_A = 0.1$.
4) Calcuate $\bar{D}$ using Eq. (6).
5) Recalculate α and S_{do} by iterating over Eqs. (2) and (3) with $D = \bar{D}$.

HEAT TRANSFER MODEL

The following heat transfer mechanisms have been considered important

1) heat transfer directly from the tube wall to the vapor
2) heat transfer directly from the tube wall to the drops during drop-wall collisions
3) heat transfer from the vapor to the entrained droplets.

Radiation effects are considered negligible. Yoder included axial conduction in the tube wall, which he found to have a negligible effect on predicted wall temperatures. Table 2 summarizes the equations used to calculate the tube wall temperature. Table 3 lists the equations needed to calculate the drop effectiveness, defined as the ratio of the actual drop-wall heat transfer to that completely required to evaporate drops colliding with the wall,

$$\varepsilon = \frac{q''_{w\text{-}d}}{\dot{n}_p \frac{\pi}{6} D^3 \rho_\ell h_{fg}}$$

Table 4 summarizes the empirical correlations used to calculate heat transfer coefficients, the drop deposition velocity and droplet drag coefficient. Wall heat transfer coefficients were calculated assuming the vapor behaves as a single phase flowing in the tube at the vapor velocity.

The known quantities for the computer model are the mass velocity G, wall heat flux q''_w, tube diameter D_T, dryout quality x_{do}, and fluid properties. The following is an outline of the computer model.

1) Input G, q''_w, $\bar{D}_T$, x_{do}, and fluid properties.
2) Calculate $\bar{D}$, S_{do}, and α from the equations in Table 1.
3) Calculate V_v, and V_ℓ from Eqs. (8) and (9) with $S = S_{do}$.
4) With $T_w = T_s + 1°$, initially, calculate ε, β_1, and β_2 from the equations in Table 3 and $h_{v\text{-}d}$ (Eq. (27)), V_p (Eq. (30)), and $h_{w\text{-}v}$ (Eq. (31)).
5) Determine T_w from Eq. (16).
6) Calculate the derivatives $\frac{d V_\ell}{dz}$ (Eq. (12)), $\frac{dD}{dz}$ (Eq. (13)), $\frac{d x_a}{dz}$ (Eq. (14)), and $\frac{d T_v}{dz}$ (Eq. (15)).
7) Assume a Δz for a new $z_{n+1} = z_n + \Delta z$. Integrate to calculate new values of V_ℓ, D, x_a, and T_v at this next axial position (a fourth order Runge- Kutta routine was used for the integration).
8) Calculate new values of S, α, V_v using Eqs. (10), (11), and (9).
9) Repeat steps 4 - 8 to calculate the axial temperature profile.

TABLE 1 - Summary of Equations Used to Calculate the Mass Weighted Average Drop Diameter $\overline{D}$, (Yoder [1]).

$$\frac{D_{do}}{D_T} = \frac{\rho_v \sigma}{G^2 D_T} \frac{We_c}{(S_{do} - 1)^2 \left(\frac{\rho_v}{\rho_\ell} + \left(\frac{1}{S_{do}} - \frac{\rho_v}{\rho_\ell}\right) x_{do}\right)^2} \tag{1}$$

$$\alpha = \frac{1}{\frac{\rho_v}{\rho_\ell} S_{do} \frac{1 - x_{do}}{x_{do}} + 1} \tag{2}$$

$$S_{do} = \frac{1 + \sqrt{1 - \left(1 - \frac{4}{3} \frac{\rho_\ell \rho_v g \left(1 - \frac{\rho_v}{\rho_\ell}\right)}{G^2 C_D} D \frac{\alpha^2}{x_{do}^2}\right)\left(1 - \frac{16}{3} \frac{q''_w}{G h_{fg}} \frac{D}{D_T} \frac{\rho_\ell}{\rho_v} \frac{1}{x_{do}}\right)}}{\left(1 - \frac{4}{3} \frac{\rho_\ell \rho_v g \left(1 - \frac{\rho_v}{\rho_\ell}\right)}{G^2 C_D} D \frac{\alpha^2}{x_{do}^2}\right)} \tag{3}$$

$$S_f = \frac{V_v}{V_{\ell f}} = \left(\frac{\rho_\ell}{\rho_v}\right)^{0.205} \left(\frac{G D_T}{\mu_\ell}\right)^{-0.016} \quad \text{(Ahmad [2])}, \tag{4}$$

$$x_A = \left(\frac{S_{do} - 1}{S_f - 1}\right) \frac{\frac{\rho_v}{\rho_\ell} + \left(\frac{1}{S_{do}} - \frac{\rho_v}{\rho_\ell}\right) x_{do}}{\frac{\rho_v}{\rho_\ell} + \left(\frac{1}{S_f} - \frac{\rho_v}{\rho_\ell}\right)} \tag{5}$$

$$\frac{\overline{D}}{D_T} = \frac{1}{x_{do} - 0.1} \left\{ \frac{D_{do}}{D_T} (x_A - .1) + \left(\frac{\rho_\ell}{\rho_v}\right)^2 \frac{We_c}{(S_f - 1)^2} \frac{\rho_v \sigma}{G^2 D_T} \right. \tag{6}$$

$$\left. \frac{1}{\left(\frac{\rho_\ell}{\rho_v} \frac{1}{S_f} - 1\right)} \left[\frac{1}{1 + x_A \left(\frac{\rho_\ell}{\rho_v} \frac{1}{S_f} - 1\right)} - \frac{1}{1 + x_{do} \left(\frac{\rho_\ell}{\rho_v} \frac{1}{S_f} - 1\right)} \right] \right\}$$

$$We_c = 6.5 \tag{7}$$

properties evaluated at the saturation temperature, T_s

TABLE 2 - Summary of Equations in Numerical Model, (Yoder [1])

$$V_v = \frac{G\, x_a}{\rho_v \alpha} \tag{8}$$

$$V_\ell = \frac{V_v}{S} \tag{9}$$

$$S = \frac{\dfrac{G x_a}{\rho_v}}{\left[V_\ell - \dfrac{G(1 - x_a)}{\rho_\ell}\right]} \tag{10}$$

$$\alpha = \frac{1}{\left[\dfrac{1 - x_a}{x_a}\dfrac{\rho_v}{\rho_\ell} S + 1\right]} \tag{11}$$

Liquid Velocity Gradient

$$\frac{dV_\ell}{dz} = \frac{-g}{V_\ell}\left(1 - \frac{\rho_v}{\rho_\ell}\right) + \frac{3}{4} C_D \frac{\rho_v}{\rho_\ell} V_\ell (S - 1)^2 \frac{1}{D} \tag{12}$$

Droplet Diameter Gradient

$$\frac{dD}{dz} = -2\left[\frac{h_{v\text{-}d}(T_v - T_s)}{V_\ell \rho_\ell h_{fg}} + \frac{1}{3}\frac{D}{D_T}\frac{V_p}{V_\ell}\varepsilon\right] \tag{13}$$

Actual Quality Gradient

$$\frac{dx_a}{dz} = -3\frac{(1 - x_a)}{D}\frac{dD}{dz} \tag{14}$$

Vapor Temperature Gradient

$$\frac{dT_v}{dz} = \frac{4 q_w''}{D_T G x_a c_{pv}} - \left[(T_v - T_s) + \frac{h_{fg}}{c_{pv}}\right]\frac{1}{x_a}\frac{dx_a}{dz} \tag{15}$$

Wall Energy Balance

$$T_w - T_v = \frac{q_w''}{h_{w\text{-}v}\alpha} - \frac{1}{2}\frac{(1 - \alpha)h_{fg} V_p \rho_\ell}{h_{w\text{-}v}\alpha}\frac{\beta_1}{\beta_2}\varepsilon \tag{16}$$

Vapor properties evaluated at the bulk vapor temperature, T_v.

TABLE 3 - Summary of Equations Use to Calculate the Effectiveness ε, (Kendall (McCarthy) [3])

$$\varepsilon = 2.6 \left(\frac{\rho_v}{\rho_\ell}\right)^{1/2} \left(\frac{\overline{R}}{D}\right)\left(\frac{\rho_\ell V_p^2 D}{\sigma}\right)^{1/8} \left(\frac{\beta_2 k_v (T_w - T_s)}{h_{fg}(\rho_v \sigma D)^{1/2}}\right)^{1/2} \left(I_2 \frac{\mu_v h_{fg}}{\beta_2 k_v (T_w - T_s)} + I_1\right)^{-1/4} \tag{17}$$

$$I_1 = 0.225 \qquad I_2 = 1.5 \tag{18}$$

$$\overline{R} = (R_{max} + 0.43\ D)/2 \tag{19}$$

$$\frac{R_{max}^2}{D^2} = \frac{2}{3}\left(1 + \frac{We_p}{12}\right) \cos^2 \left\{\frac{1}{3}\left[\arccos\left(\frac{-1.225}{\left(1 + \frac{We_p}{12}\right)^{3/2}}\right)\right]\right\} \tag{20}$$

$$We_p = \frac{\rho_\ell V_p^2 D}{\sigma} \tag{21}$$

if $We_p < 1.74$ then $R_{max} = 0.43\ D$ (22)

$$\beta_1 = \left(1 + 0.43 \frac{c_{pv}(T_w - T_s)}{h_{fg}}\right) \Big/ \left(1 + 0.3 \frac{c_{pv}(T_w - T_s)}{h_{fg}}\right) \tag{23}$$

$$\beta_2 = \frac{1}{1 + 0.3 \frac{c_{pv}(T_w - T_s)}{h_{fg}}} \tag{24}$$

$$\delta^4 = 0.45\ \pi\ \overline{R}^4 \left(\frac{1}{We_p}\right)^{1/2} \left[\frac{\beta_2 k_v \mu_v (T_w - T_s)}{\rho_v h_{fg} \sigma D}\right]\left[I_2 + \frac{\beta_2 k_v\ (T_w - T_s)}{\mu_v h_{fg}}\ I_1\right] \tag{25}$$

$$\frac{\delta_c}{D_T} = \frac{\beta_1}{Nu_w}\left[\frac{T_w - T_s}{T_w - T_v}\right] \tag{26}$$

if $\delta > \delta_c$ drop wall interaction is not included in the wall energy balance

if $\delta < \delta_c$ drop wall interaction is included in the wall energy balance

vapor properties evaluated at the temperature $T_f = \frac{(T_v + T_s)}{2}$

TABLE 4 - Summary of Empirical Correlations Used in Numerical Model

Droplet Heat Transfer Coefficient, (Yuen [4]).

$$\frac{h_{v\text{-}d}D}{k_v} = \frac{[2 + 0.6\ Re^{1/2} Pr_v^{1/3}]}{[1 + \frac{c_{pv}(T_v - T_s)}{h_{fg}}]} \tag{27}$$

$Re = \frac{(V_v - V_\ell)\rho_v D}{\mu_v}$, properties evaluated at the temperature $T = \frac{T_v + T_s}{2}$

Droplet Drag Coefficient

$$C_D = \frac{27}{Re^{0.84}} \qquad \text{(Ingebo [5])} \tag{28}$$

$Re < 150$

$$C_D = 0.4 \qquad \text{(Groeneveld [6])} \tag{29}$$

$Re \geq 150$

$Re = \frac{(V_v - V_\ell)\rho_v D}{\mu_v}$, properties evaluated at the bulk vapor temperature, T_v

Drop Deposition Velocity (Liu and Ilori [7])

$$\frac{V_p}{V_v} = \frac{0.023}{Re^{0.1}} \tag{30}$$

$Re = \frac{V_v \rho_v D_T}{\mu_v}$, properties evaluated at the bulk temperature, T_v

Single Phase Heat Transfer Coefficient (Hadaller [8])

$$h_{w\text{-}v} = 0.008348 \frac{k_v}{D_T} Re^{0.8774}\ Pr_v^{0.6112} \tag{31}$$

$Re = \frac{G x_a D_T}{\mu_v \alpha}$, properties evaluated at the film temperature $T_f = \frac{(T_v + T_w)}{2}$

RESULTS OF COMPUTER MODEL

Figures 1- 3 show some typical results of the computer model for three fluids and four investigators. Errors in $T_w - T_s$ ranged from -30 to 60% with errors in temperature of -85 to 140°C. Notice the similarity between the Cumo [9] data and the Era [10] data and how similar the predicted curves deviate from the data. In both cases the data has a sharp peak and a smooth, rapid decrease in wall temperatures downstream. The predicted curve cannot follow the rapid changes in the data. It predicts no sharp peaks and no large decreases in wall temperatures downstream. The model does a better job predicting Bennett's [11] data in Figures 2a through 3a, but is still in error by as much as 50°C. Hynek's [12] nitrogen data is predicted fairly well downstream in Fig. 3b, but is underpredicted by 55°C in the region just after dryout.

MODIFICATION OF THE WALL TO VAPOR HEAT TRANSFER COEFFICIENT

Figures 1 - 3 present comparisons of predicted and actual wall temperatures. Only a few cases are shown as they are typical of the many data sets which were used. The primary concern of these comparisons is not so much the magnitude of the error in the predicted wall temperatures, but the shape of the axial temperature profiles. The predicted profiles do not resemble the actual ones, especially in the cases of Cumo and Era. It was felt that some aspect of dispersed flow was not modeled accurately to give such differences in the predicted and actual wall temperatures.

The procedure to attempt to discover what might be causing the discrepancies in the actual and predicted wall temperatures was one of trial and error. Dryout drop diameters, slip ratios, vapor to drop heat transfer coefficients, and droplet breakup criterion were varied. These variations resulted in changes in the predicted wall temperatures, but in no way changed the shape of the axial temperature profiles. It was thought that turbulent fluctuations might begin to influence the flow downstream, increasing simultaneously the vapor to drop heat transfer and droplet breakup. However, for the length of tube considered in a given data set, the Reynolds number changes at most by a factor of three. This should not alter radically the basic structure of the turbulence. (Note that for all data sets $2 \times 10^4 \leq Re \leq 10^6$). Direct drop wall heat transfer was reconsidered, but the wall temperature data for all cases are well above the critical temperature for each fluid. It is possible, but very doubtful, that the drops could be wetting the tube wall downstream resulting in the shape of the data of Cumo and Era. It was then decided that the flaw might lie in the assumption that the wall-vapor heat transfer coefficient can be accurately calculated from single phase correlations. What must be emphasized here is that while only one wall heat transfer coefficient correlation was used in the model, other correlations only change the magnitude of the predicted wall temperatures. They do not radically change the shape of the axial temperature profile.

Equation (31) was rewritten as

$$h_{w-v} = 0.008348\ R_{Nu}\ \frac{k_v}{D_T}\ Re^{0.8774}\ Pr_v^{0.6112} \tag{32}$$

where R_{Nu} is the ratio of Nusselt number with droplets present to that without droplets. The computer model was used to determine the value of R_{Nu} required to make the calculated wall temperature equal the measured wall temperature of the data.

It was postulated that

$$R_{Nu} = R_{Nu}\left(\frac{\mu_b}{\mu_w}, x_a, \frac{\rho_v}{\rho_\ell}, \frac{D}{D_T}, Re_b\right) \quad (33)$$

In Fig. 4 the Nusselt number ratio R_{Nu} is plotted against the actual quality x_a for fixed values of the bulk to wall viscosity ratio, μ_b/μ_w. Values of R_{Nu} range from about 0.7 to 2 (although not shown, some values were as high as 10). For each viscosity ratio value the points fall on a curve, creating a family of curves of R_{Nu} vs. x_a as shown in Figs. 5 and 6. As x_a decreases from 1 an increase in R_{Nu} is observed until a maximum occurs at about $x_a = 0.9$. As x_a decreases further R_{Nu} decreases until $0.4 \leq x_a \leq 0.6$, where R_{Nu} is a minimum. Then R_{Nu} begins to increase slowly and all the curves merge as x_a is reduced further. The magnitude of R_{Nu} read from Fig. 6 should be used in the computer model to predict the wall temperature.

Figures 1 - 3 also show the wall temperatures predicted using values of R_{Nu} read from Fig. 6. Now the predicted temperatures virtually coincide with the data, which is not surprising, since this data is part of the data base used to generate the curves of Fig. 6. The corrected model overpredicts the data in the region just after dryout for the data of Cumo and Hynek, but recovers to accurately predict the data downstream. In Fig. 1a the corrected model stops at an equilibrium quality of 1.1 because values of μ_b/μ_w were too large to be read from Fig. 6. Only a few points had values of $\mu_b/\mu_w > 0.825$, so accurate curves could not be drawn to fit the points. The corrected model predicts the data of Era and Bennett almost perfectly.

Figure 7 shows R_{Nu} vs. μ_b/μ_w for fixed quality. Generally, as μ_b/μ_w increases, increases with μ_b/μ_w having the greatest influence at higher actual qualities. As the quality decreases the effect of viscosity ratio becomes less important, until R_{Nu} vs. μ_b/μ_w is constant for $x_a = 0.25$.

OTHER POSSIBLE EFFECTS ON R_{Nu}

Thus far any effect of remaining variables on R_{Nu} has not been found. This will be investigated later.

COMPARISON TO SOLID PARTICLE-GAS MIXTURE DATA

Figure 8 presents data of R_{Nu} vs. quality for solid particle-gas flowing mixtures of several investigators. The shapes of the curves are similar to those of the dispersed flow data. In most cases R_{Nu} decreases as particles are added, reaching a minimum, then increases as x decreases further. In some data of Depew [13] R_{Nu} increases greater than 1.0 as particles are added with R_{Nu} decreasing and reaching a minimum as x is decreased further. The majority of the solid particle data falls in the range of $0.7 \leq R_{Nu} \leq 2$, as does the dispersed flow data.

EXPLANATION

A possible explanation for this behavior is that the liquid droplets and solid particles affect the turbulence in the flow, making the gas not behave as a single phase. Fig. 9 presents turbulence data of Zisselmar [16] for 50 μm glass particles flowing in methylbenzoate (properties like that of water) at a Re of 10^5. Solid volumetric concentrations c_v, ranged from 0 - 6%, which would correspond to vapor void fractions in dispersed flow of 94 to 100%. Values of the axial and radial turbulent fluctuations were measured throughout the core and close to the wall. In the core, both fluctuations were steadily reduced from the single phase value as c_v was increased. The axial component was reduced by 14% and the radial component by 50% for a c_v of 5.6%. Near the wall axial fluctuations were increased by about 10% for c_v = 3%, then were

reduced by about 20% as c_v was increased to 5.6%. The radial component of turbulent fluctuations increased steadily as c_v was increased, until it reached twice the single phase value at c_v = 5.6%.

The following is an attempt to explain the behavior of R_{Nu} vs. x_a and R_{Nu} vs. μ_b/μ_w.

1) R_{Nu} vs. x_a

a) R_{Nu} is 1.0 for single phase vapor (x_a = 1.0).
b) When some droplets are present, turbulence is produced near the wall. There are not enough droplets to affect significantly the turbulence in the core. A net increase in heat transfer and R_{Nu} results. This could result in the temperature distribution shown by the dotted curve in Fig. 10 for x = 0.85 with a lower wall temperature, $R_{Nu} > 1$.
c) When more droplets are present, more turbulence is produced at the wall, but turbulence is damped in the core. These effects tend to offset each other resulting in a higher wall temperature, as for the dash-dot curve for x = 0.5 in Fig. 10, $R_{Nu} < 1$.
d) As the amount of droplets are further increased, turbulence at the wall is increased more than the decrease in the core. This results in R_{Nu} increasing from the minimum as x_a decreases.

2) R_{Nu} vs. μ_b/μ_w

a) For given flow conditions and bulk fluid temperature the droplets damp the turbulence in the core, reducing the fluid mixing.
b) Droplets increase the turbulence near the wall when wall temperatures are close to the bulk temperature. This results in more fluid mixing and increased heat transfer due to the presence of the droplets; so $R_{Nu} > 1$.
c) As the wall temperature is increased, the viscosity of the vapor near the wall increases, decreasing μ_b/μ_w. This results in less generation of turbulence near the wall, making the reduction of turbulence in the core of more relative importance; thus R_{Nu} decreases.

The single phase heat transfer coefficient equation uses a viscosity based on the average of the bulk vapor and tube wall temperatures. If μ_b/μ_w is close to 1.0, the effect of particles increasing turbulence near the wall and decreasing turbulence in the core could result in the lower dashed curve of Fig. 11, producing a higher heat transfer coefficient at the wall, $R_{Nu} > 1$.

For large temperature differences ($\mu_b/\mu_w << 1$) the vapor viscosity at the wall is significantly greater than the viscosity used in the prediction equation for h_{w-v}, thus reducing the turbulence near the wall. This could result in the upper dotted temperature distribution in Fig. 11 and a reduced h_{w-v}, $R_{Nu} < 1$.

CONCLUSION

The effects of liquid droplets on wall heat transfer coefficients are presented. The ratio of Nusselt number for dispersed flow to that of single phase flow ranges from about 0.7 to 2, and is a function of bulk to wall viscosity ratio and quality. Similar effects are observed in solid particle-gas flowing mixtures. Nusselt number ratios vary from about 0.25 to 2.0 and show a similar dependence on quality as does the dispersed flow data.

A possible explanation for this behavior is that the drops and particles in the flow affect the basic turbulent structure of the flow. Evidence was presented that particles in the flow damp out the turbulence in the core and produce turbulence near

the wall. The combination of these effects probably produces the observed differences in Nusselt numbers from single phase values.

ACKNOWLEDGEMENTS

The authors gratefully acknowledge the support of the National Science Foundation for the pursuit of this work.

APPENDIX A

Local Conditions Solution

The computer solution requires a complicated stepwise solution starting at the dryout point and proceeding down the tube. Later, Yoder [1] found simplifications that permit the prediction of wall and vapor temperatures at any location downstream of the drycut point without a stepwise calculation or computer. This is called the "Local Conditions Solution".

He simplified the various equations to obtain the following relation:

$$\frac{K\, x_a^{3/4}\, x_e}{(1 - x_a)^{7/12}} \frac{dx_a}{dx_e} = x_e - x_a \tag{A-1}$$

where K remained essentially constant along the tube. Hill [17] developed the following relation for K:

$$K = 0.013 \frac{f\phi Pr_v^{2/3}\left(\sqrt{\frac{\rho_\ell}{\rho_v}}\, x_{do} + 1\right)^{5/2} \left(\frac{\mu_v}{\mu_\ell}\right)^{5/6} Ac^{3/4}\, Re_{do}^{4/3}}{(1 - x_{do})^{5/12}\, x_{do}^{7/4} \left(\frac{\rho_\ell}{\rho_v}\right)^{1/12} We_{do}^{5/4}} \tag{A-2}$$

where

$$Ac \equiv \frac{q_w''}{G h_{fg}} \tag{A-3}$$

$$Re_{do} = \frac{GD_T}{\mu_v}\left[x_{do} + \frac{\rho_v}{\rho_\ell}(1 - x_{do})\right] \tag{A-4}$$

$$We_{do} \equiv \frac{G^2 x_{do}^2 D_T}{\rho_v \sigma} \tag{A-5}$$

The quantities f and ϕ are read from Figs. A-1 and A-2 where

$$\lambda x_{do} = \frac{0.0338\, x_{do}}{Re_{do}^{1/8} Ac} \tag{A-6}$$

Equation (A-1) is shown in Fig. A-3 as x_a vs. x_e for various magnitudes of the non-equilibrium parameter K for $x_{do} = 0.1$. A family of such graphs may be constructed for various magnitudes of x_{do}. However, Fig. A-3 may be used for any $x_a = x_e = x_{do}$ by making a simple construction. It is noted that since at x_{do}, $x_a = x_e = x_{do}$, Eq. (A-1) shows $dx_a/dx_e = 0$. If Eq. (A-1) is differentiated once, the radius of curvature of a constant K curve at x_{do} is:

$$\frac{1}{d^2x_a/dx_e^2} \equiv r_{do} = \frac{K\, x_{do}^{7/4}}{(1 - x_{do})^{11/12}} \qquad \text{(A-7)}$$

Figure A-3 shows the construction to be made to obtain the constant K curve for any $x_{do} > 0.1$. Shown in Fig. A-3 is the construction to obtain a good approximation to the x_a vs. x_e curve for $K = 0.4$ and $x_{do} = 0.5$. Calculate r_{do} from Eq. (A-7). This is in units of x. Draw an arc of radius r_{do} as shown at $x_{do} = 0.5$. Then draw the dashed line tangent to the arc and to the solid curve labelled $K = 0.4$. The total line consisting of the arc, dashed line joining the solid curve represent the x_a vs. x_e curve for $x_{do} = 0.5$ and $K = 0.4$. The same construction is made for any $x_{do} > 0.1$ and any K.

The calculation procedure is as follows. The known quantities are G, D_T, z_{do}, x_{do}, q_w'' and all fluid properties. To determine the wall temperature T_w at any $z > z_{do}$:

1) Calculate Ac, Re_{do} and K from Eqs. (A-2 to A-4) where f and ϕ are read from Figs. A-1 and A-2 with λx_{do} calculated from Eq. (A-6)
2) Calculate x_e from $(x_e - x_{do}) = 4q_w''(z - z_{do})/D_T G h_{fg}$ (A-8)
3) Calculate r_{do} from Eq. (A-7) and make the construction on Fig. A-3 for the appropriate K and x_{do}. Read x_a from Fig. A-3.
4) Calculate T_v from Eq. (A-9)

$$\frac{c_{pv}(T_v - T_s)}{h_{fg}} = \frac{x_e - x_a}{x_a} \qquad \text{(A-9)}$$

5) Calculate h from

$$\frac{hD_T}{k_v} = 0.008348\, R_{Nu} \left(\frac{Gx_a D_T}{\mu_v \alpha}\right)^{0.8774} Pr_v^{0.6112} \quad \left(\text{properties evaluated at } T_f = \frac{T_w + T_v}{2}\right) \qquad \text{(A-10)}$$

where R_{Nu} is read from Fig. 6 for an assumed μ_b/μ_w, and

$$\frac{1}{\alpha} = 1 + \frac{1 - x_a}{x_a}\,\frac{\rho_v}{\rho_\ell} \qquad \text{(A-11)}$$

The assumed magnitude of μ_b/μ_w will be verified after T_w is calculated.

6) Calculate $T_w = T_v + q''/h$.

This calculation for T_w may be made at any $z > z_{do}$ without integration from z_{do}.

The results of this simplified Local Conditions Solution agree very well with those of the detailed stepwise computer solution.

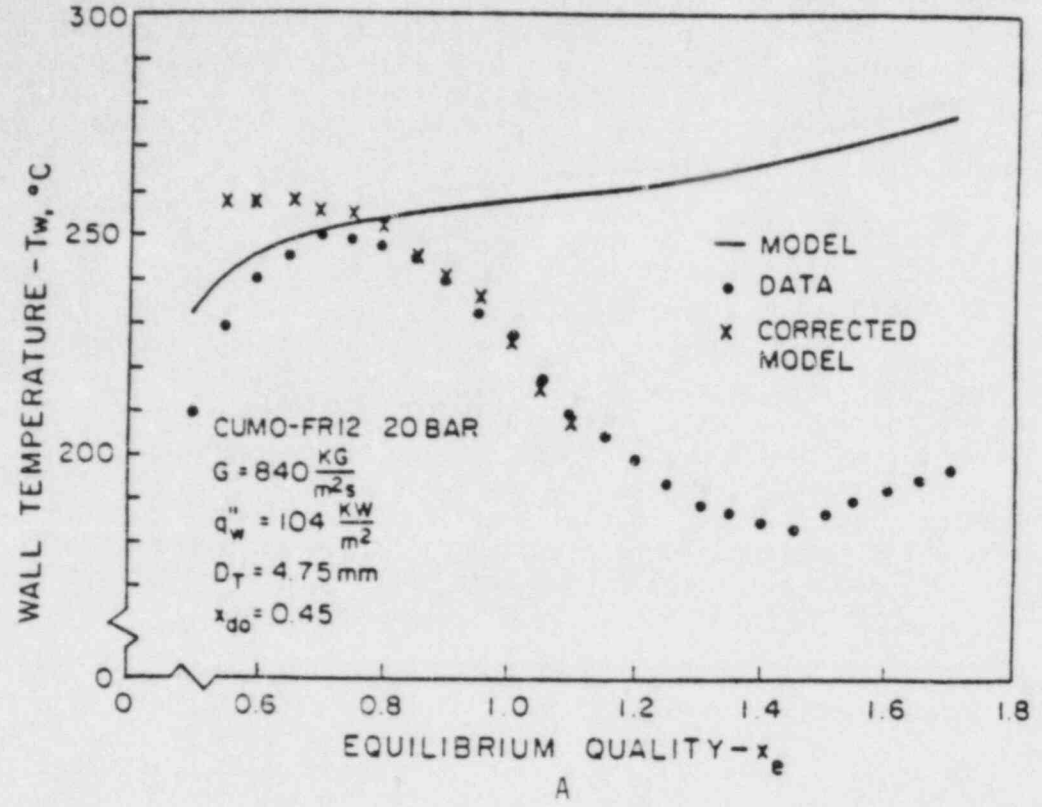

A

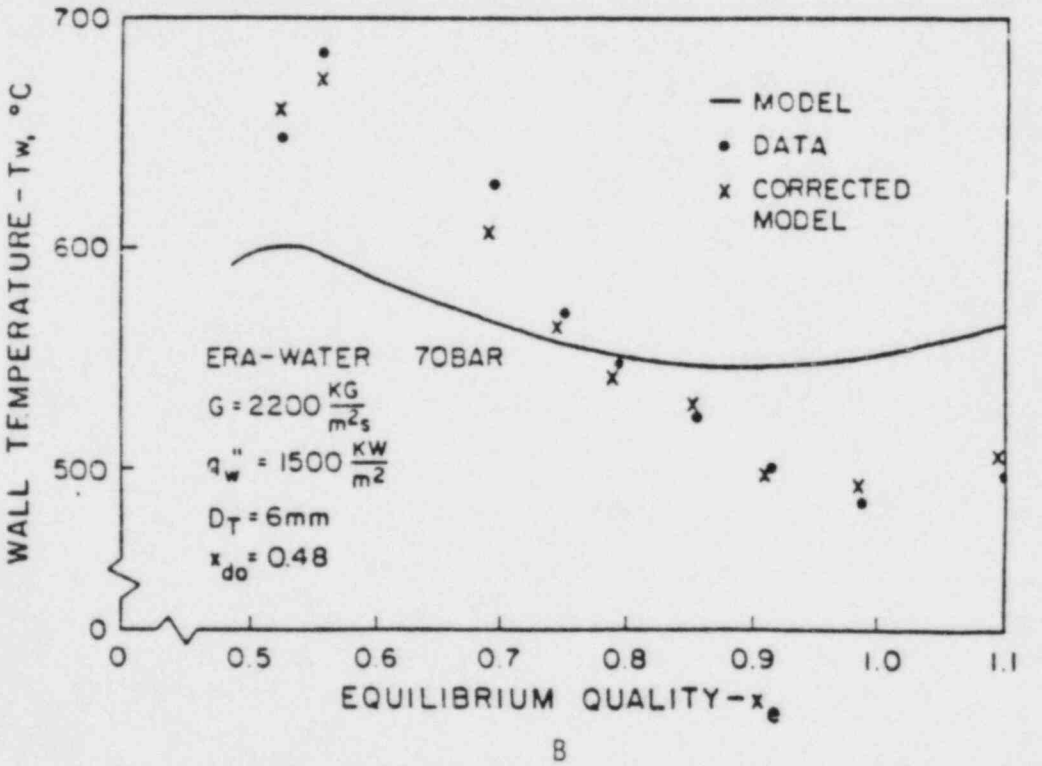

B

Fig. 1 - Tube Wall Temperature vs. Equilibrium Quality, [9], [10].

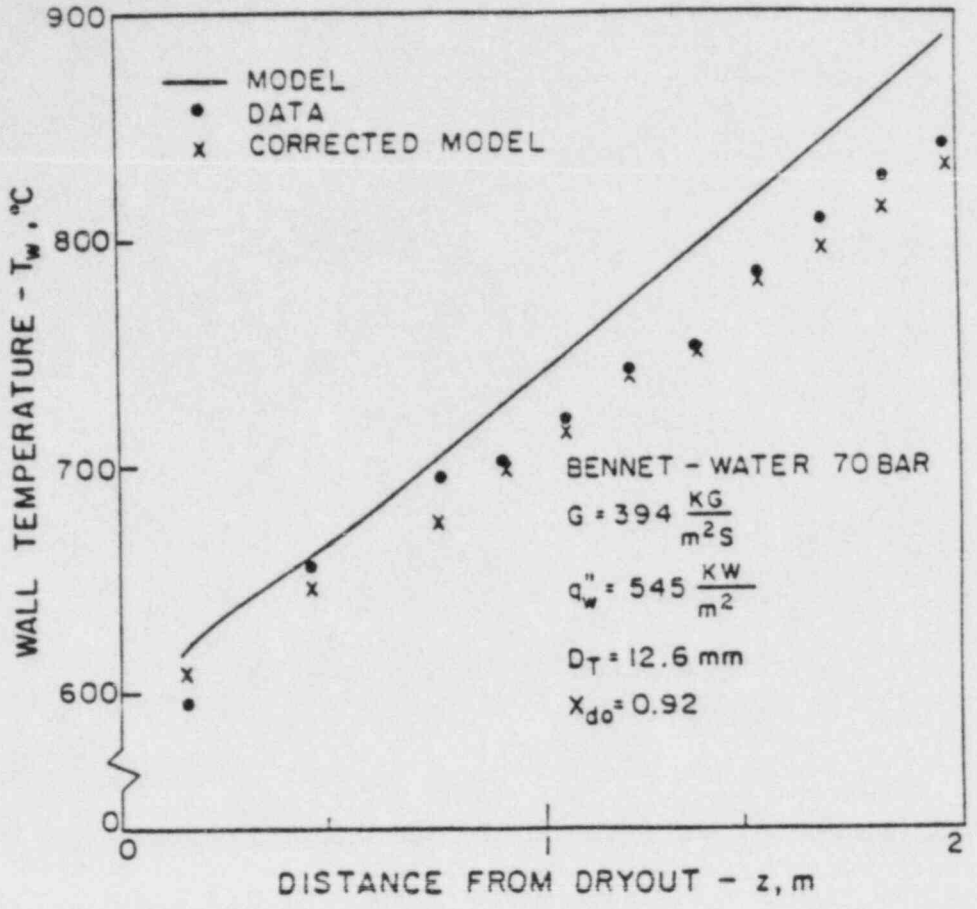

A

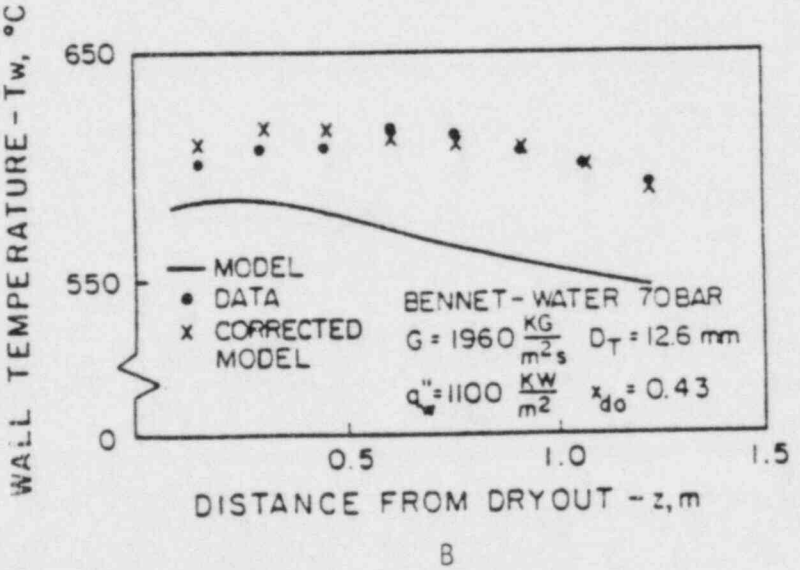

B

Fig. 2 - Tube Wall Temperature vs. Axial Position Beyond Dryout, [11].

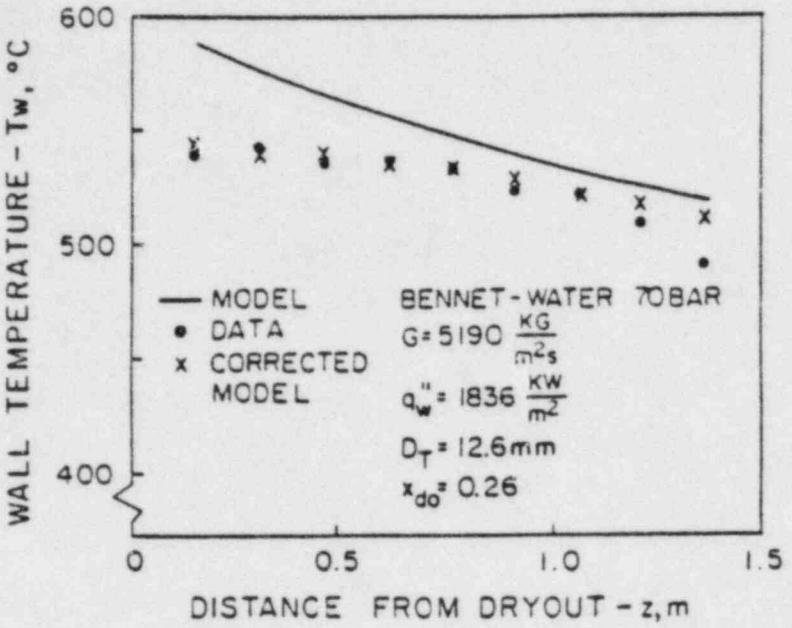

A

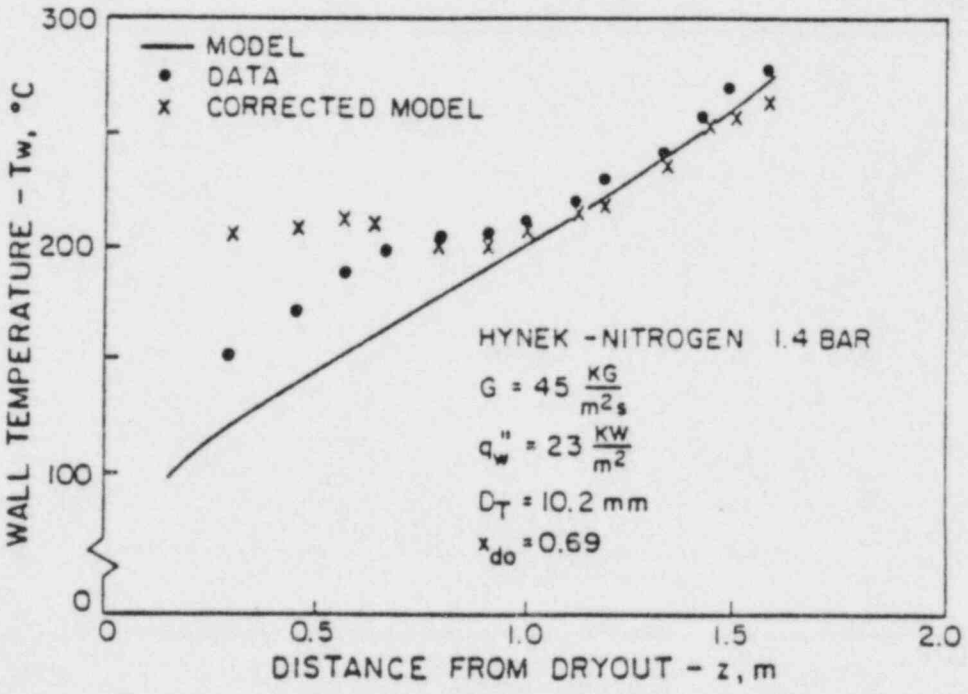

B

Fig. 3 - Tube Wall Temperature vs. Axial Position Beyond Dryout, [11], [12].

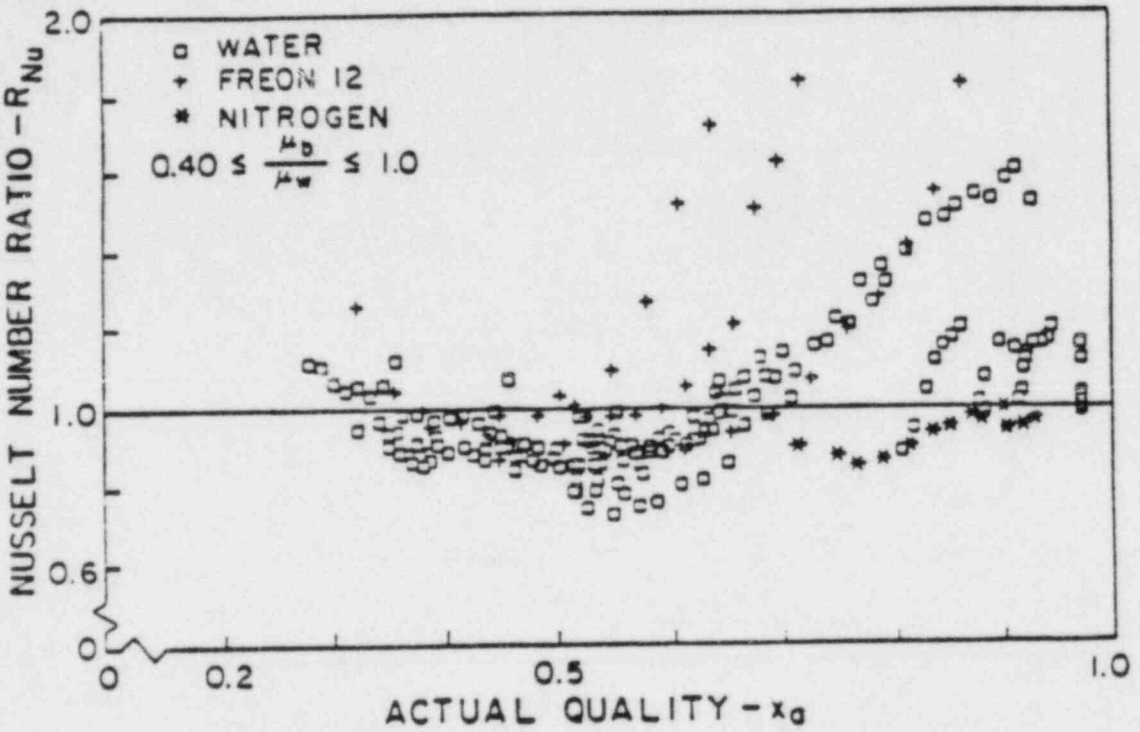

Fig. 4 - Nusselt Number Ratio vs. Actual Quality Calculated from Computer Model.

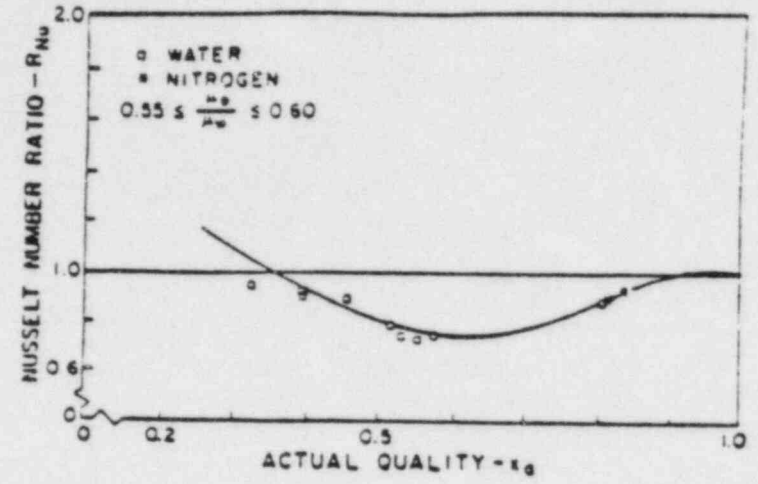

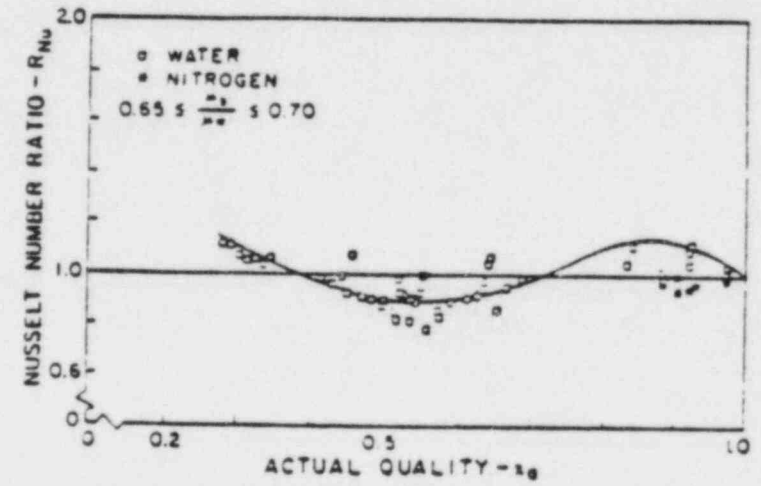

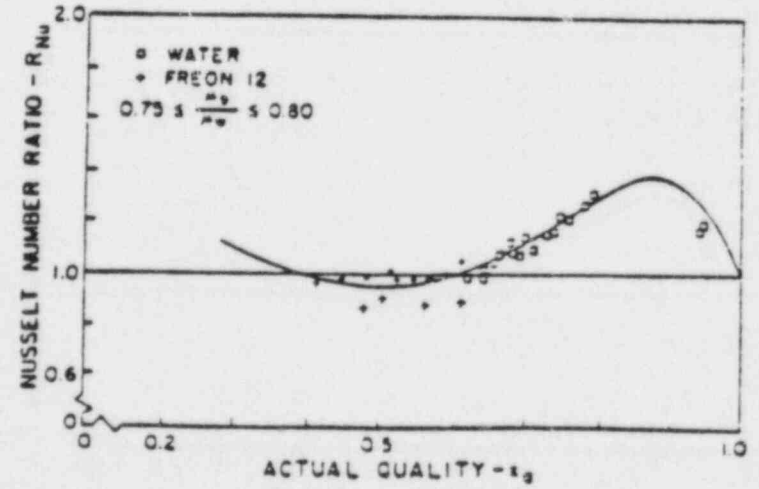

Fig. 5 - Nusselt Number Ratio vs. Quality With Constant Viscosity Ratios.

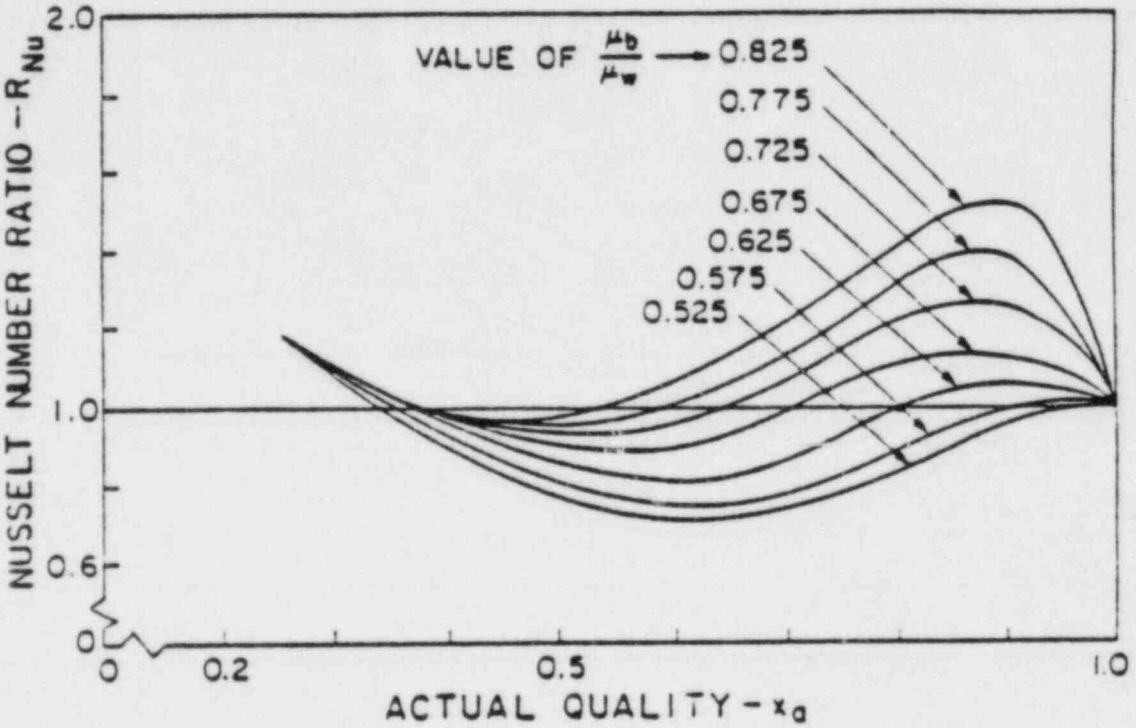

Fig. 6 - Family of Curves of Nusselt Number Ratio vs. Actual Quality With Constant Viscosity Ratios.

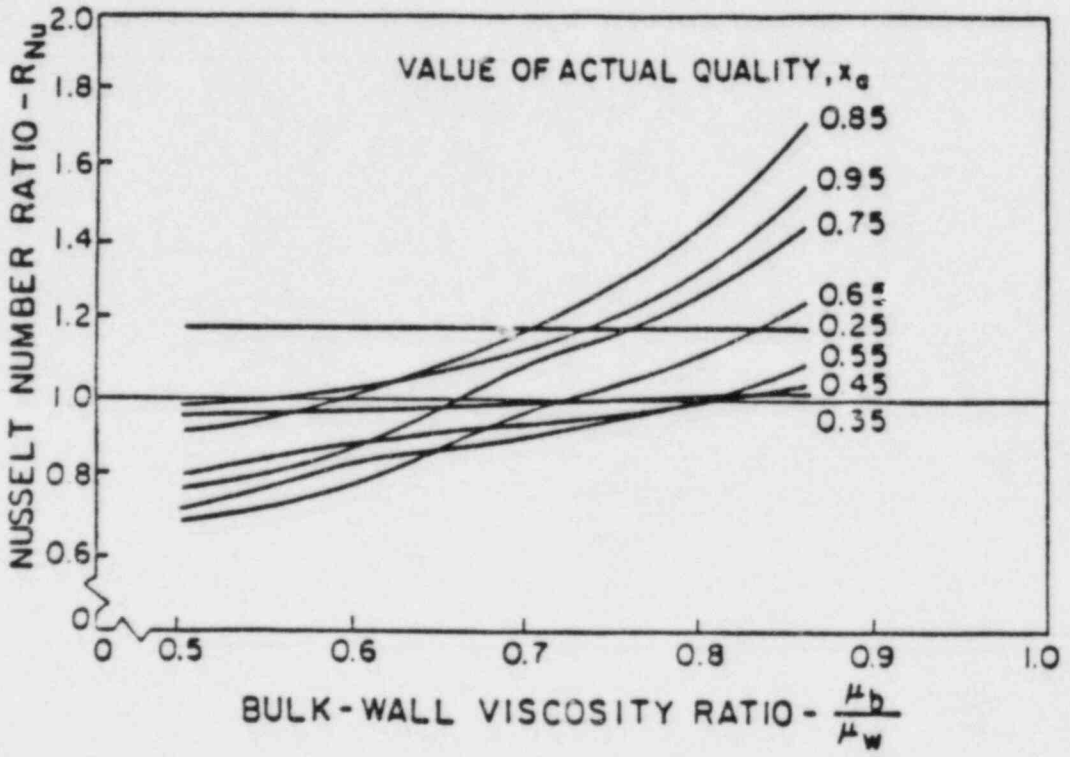

Fig. 7 - Family of Curves of Nusselt Number Ratio vs. Viscosity Ratio for Constant Actual Quality.

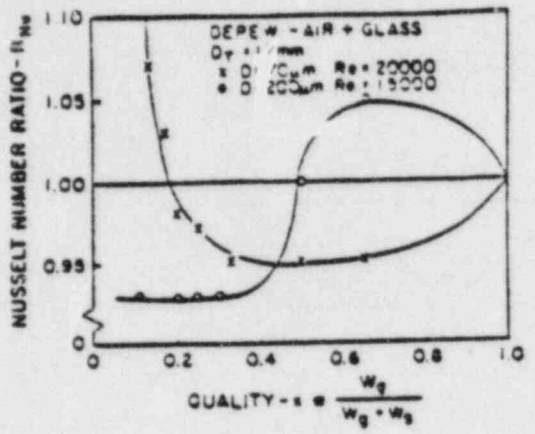

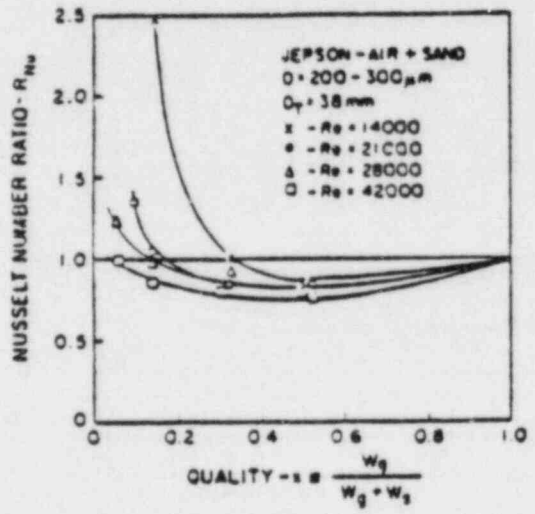

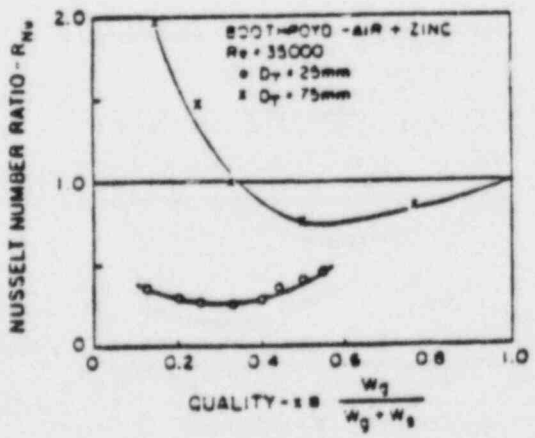

Fig. 8 - Nusselt Number Ratios vs. Quality for Solid Particle-Gas Flowing Mixtures, [13], [14], [15].

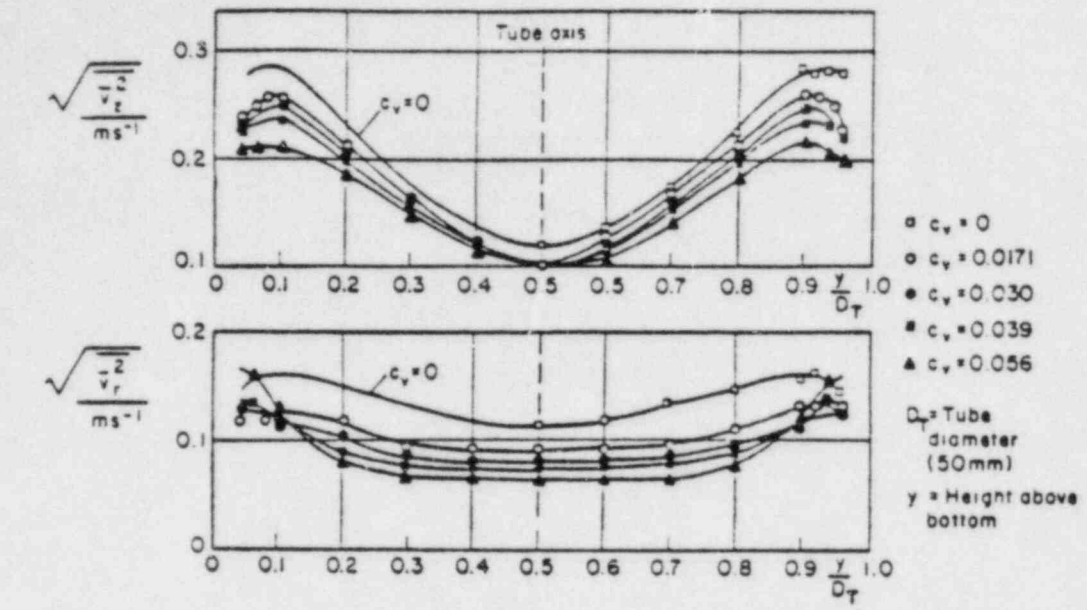

A - Core Region

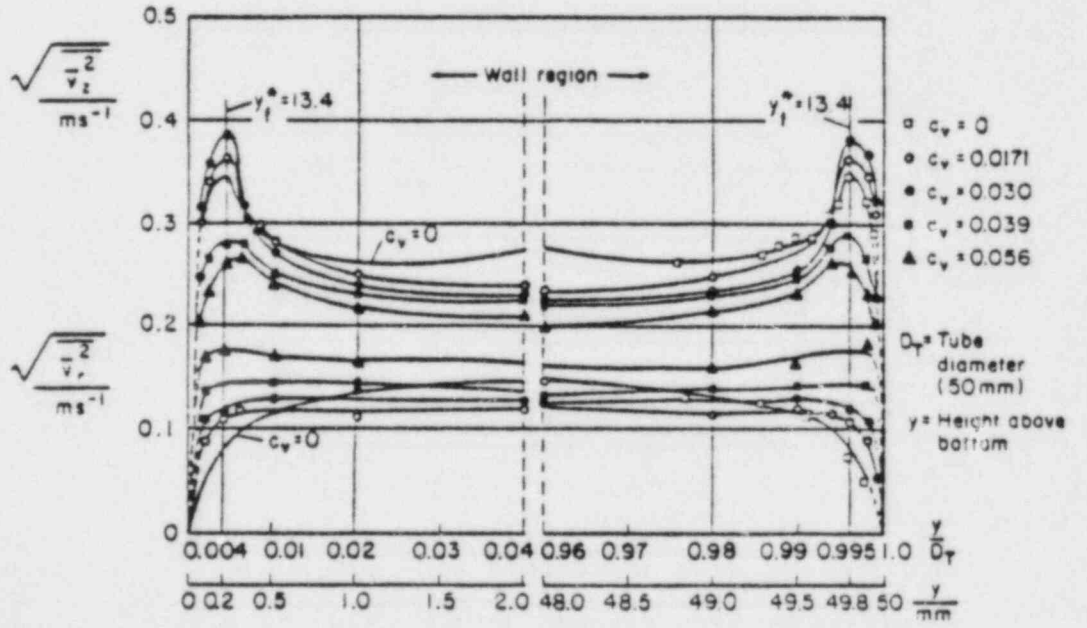

B - Wall Region

Fig. 9 - Axial and Radial Turbulent Fluctuating Velocities vs. Radial Position for a Solid Particle - Methylbenzoate Mixture in the Core Region (A) and Wall Region (B), [16].

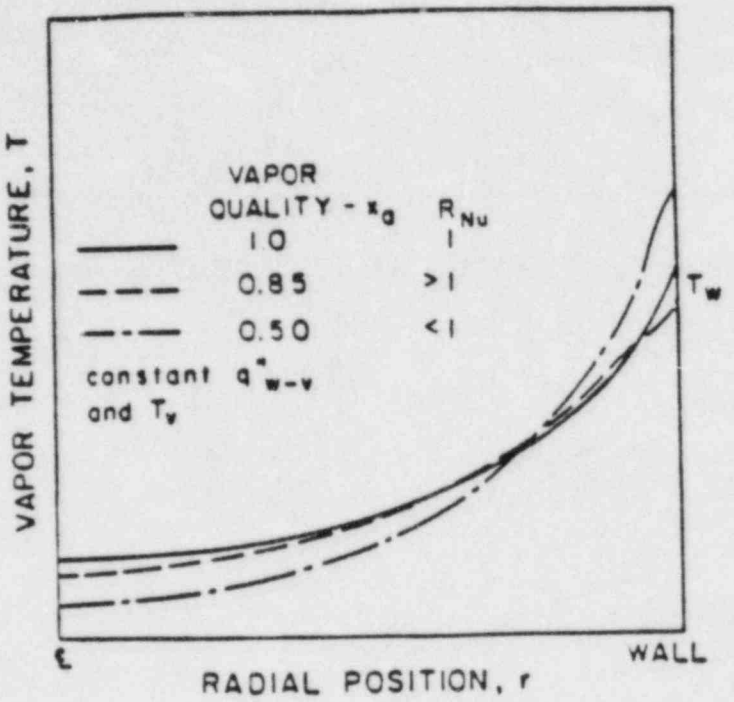

Fig. 10 - Effect of Quality on Vapor Radial Temperature Profile.

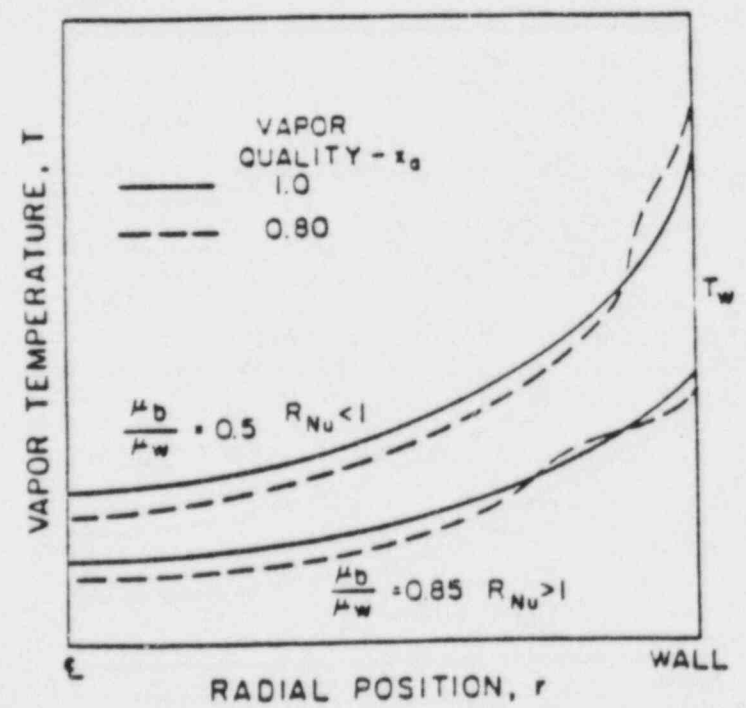

Fig. 11 - Effect of Viscosity Ratio on Vapor Radial Temperature Profile.

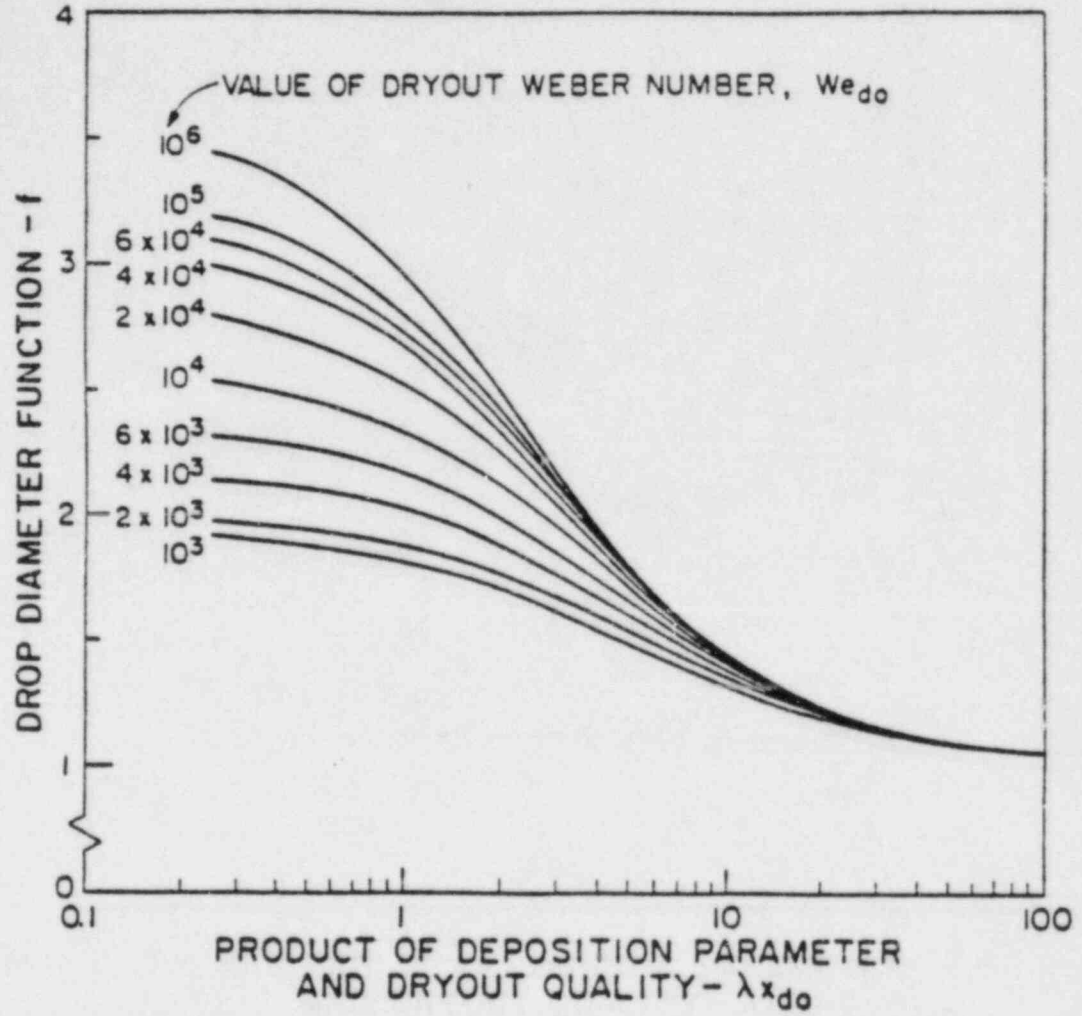

Fig. A1 - Drop Diameter Function vs. Product of the Deposition Parameter and Dryout Quality with Constant Dryout Weber Numbers and $x_{do} = 0.2$.

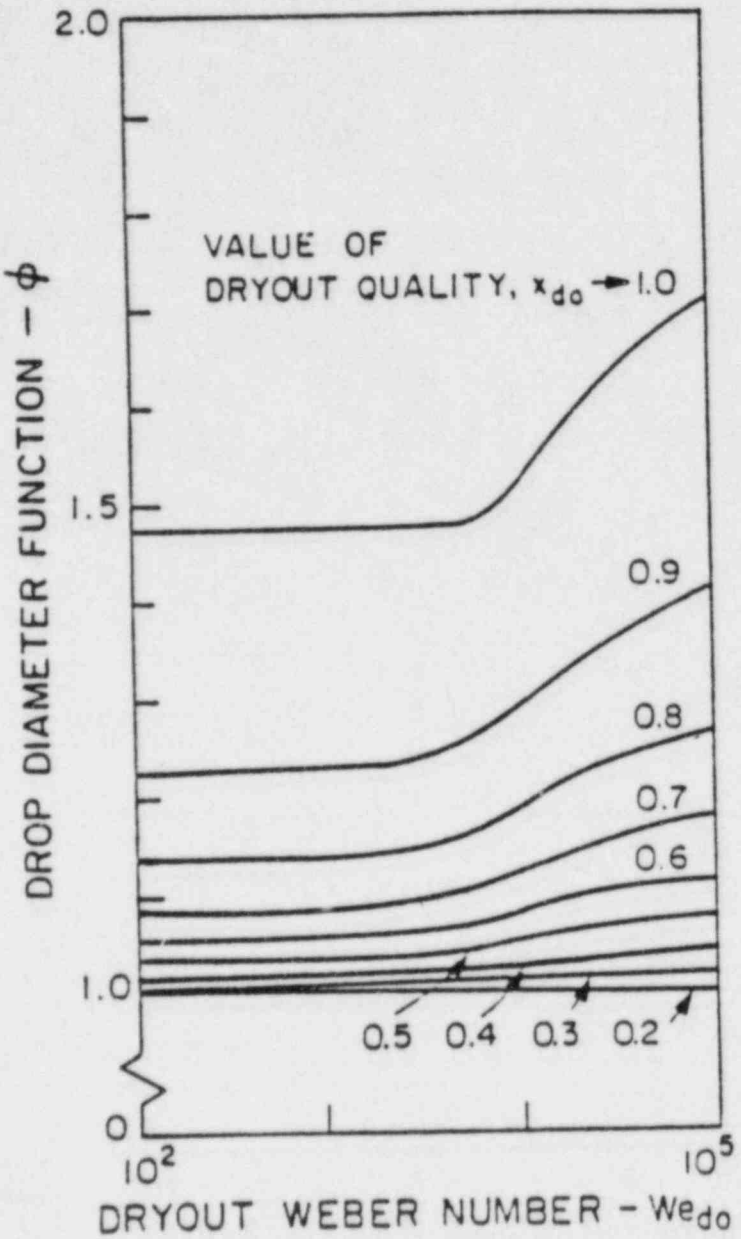

Fig. A2 - Plot of Drop Diameter Function vs. Dryout Weber Number with Constant Dryout Quality.

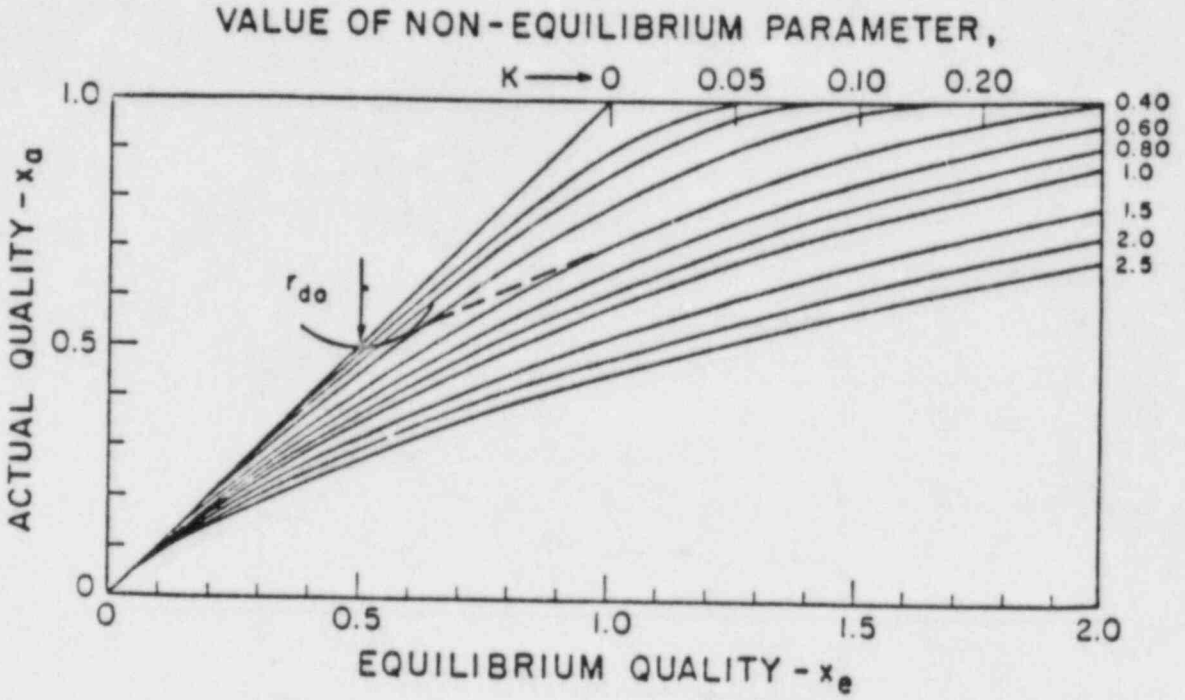

Fig. A-3 - Actual Quality vs. Equilibrium Quality with Constant Values of the Non-Equilibrium Parameter.

REFERENCES

1. Yoder, G.L., Rohsenow, W.M., "Dispersed Flow Film Boiling", MIT Heat Transfer Laboratory Report No. 85694-103, March 1980. Also Journal of Heat Transfer, 105, 1, pp. 10-17, Feb. 1983.

2. Ahmad, S.Y., "Axial Distribution of Bulk Temperature and Void Fraction in a Heated Channel with Inlet Subcooling", Journal of Heat Transfer, pp. 595-609, Nov. 1970.

3. Kendall (McCarthy) G.E., Rohsenow, W.M., "Heat Transfer to Impacting Drops and Post Critical Heat Flux Dispersed Flow", MIT Heat Transfer Laboratory Report No. 85694-100, March 1978.

4. Yuen, M.C., Chen, L.W., "Heat Transfer Measurements of Evaporating Liquid Droplets", Int. Journal of Heat and Mass Transfer, 21, pp. 537-542, 1978.

5. Ingebo, R.D., "Drag Coefficients for Droplets and Solid Spheres in Clouds Accelerating in Airstreams", NACA Technical Note - 3762, Sept. 1956.

6. Groeneveld, D.C., "The Thermal Behavior of a Heated Surface at and Beyond Dryout", AECL - 4309, 1972.

7. Liu, Y.H., Ilori, J.A., "Aerosol Deposition in Turbulent Pipe Flow", Environmental Science and Technology, 8, pp. 351-356, April 1974.

8. Hadaller, G., Banerjee, S., "Heat Transfer to Superheated Steam in Round Tubes, AECL unpublished Report, 1969.

9. Cumo, M., Farello, G.E., Ferrari, G., "The Influence of Curvature in Post Dryout Heat Transfer", Report of the XXVI Nat. ATI Annual Meeting, L'Aquila, Sept. 1971.

10. Era, A., Gaspari, G.P., Hassid, A., Milani, A., and Zavattarelli, R., "Heat Transfer Data in the Liquid Deficient Region for Steam-Water Mixtures at 70 kg/cm^2 Flowing in Tubular and Annular Conduits", CISE-R-184, 1966.

11. Bennett, A.W., Hewitt, G.F., Kearsey, H.A., and Keeys, R.F.K., "Heat Transfer to Steam-Water Mixtures in Uniformly Heated Tubes in which the Critical Heat Flux has been Exceeded", AERE-R573.

12. Hynek, S.J., "Forced Convection Dispersed Flow Film Boiling", Ph.D. Thesis, M.I.T., 1969.

13. Depew, C.A., "Heat Transfer to Flowing Gas-Solids in a Vertical Duct", SM Thesis, U. of California, 1957 (UCRL-9280).

14. Jepson, G., Poll, A., Smith, W., "Heat Transfer from Gas to Wall in a Gas-Solids Transport Line", Institution of Chemical Engineers Transactions, 41, pp. 207-211, 1963.

15. Boothroyd, R.G., Haque, H., "Fully Developed Heat Transfer to a Gaseous Suspension of Particles Flowing Turbulently in Ducts of Different Size", Journal of Mechanical Engineering Science, 12, 4, pp. 191-200, 1970.

16. Zisselmar, R., Molerus, O., "Investigation of Solid-Liquid Pipe Flow with Regard to Turbulence Modification", Two-Phase Momentum, Heat, and Mass

Transfer in Chemical Process, and Energy Engineering Systems, Seminar of the Int. Center for Heat and Mass Transfer, Sept. 4-9, 1978, 1, pp. 119-132, Hemisphere Publishing Co., Wash., D.C., 1979.

17. Hill, W.S., Rohsenow, W.M., "Dryout Droplet Distribution and Dispersed Flow Film Boiling", MIT Heat Transfer Laboratory Report No. 85694-105, Aug. 1982.

SAND84-1040C

International Workshop on Fundamental Aspects
of Post-Dryout Heat Transfer
Salt Lake City, Utah
April 1-4, 1984

A TWO-REGION VAPOR GENERATION RATE MODEL FOR CONVECTIVE FILM BOILING

by

S. W. Webb

Thermal/Hydraulic Analysis Division 6444
Sandia National Laboratories
Albuquerque, NM

and

J. C. Chen

Institute of Thermo-fluid Engineering and Science
Lehigh University
Bethlehem, PA

Abstract

A convective film boiling heat transfer model has been developed based on the recently obtained Lehigh University and INEL nonequilibrium data. A two-region vapor generation rate model is proposed including a near-field region and a far-field region. The heat transfer in convective film boiling has also been correlated in terms of enhancement of single-phase values due to the entrained liquid. Comparison of this new model with the data shows significant improvement in the prediction of thermodynamic nonequilibrium and wall heat flux over existing models.

I. INTRODUCTION

Convective film boiling, or post-CHF heat transfer, is encountered in a number of applications such as in postulated nuclear reactor accidents. In many cases, the flowing two-phase mixture may exist such that the vapor is superheated even in the presence of entrained liquid. Under these conditions, thermodynamic nonequilibrium exists, and the actual mass quality is not equal to the equilibrium value but is related to it by

$$\frac{X_a}{X_e} = \frac{i_{fg}}{i_v(P,T_v)-i_{\ell s}} \tag{1}$$

In the analysis of these conditions, axial history models can be formulated in terms of a vapor generation source function, defined as the mass of liquid evaporated per unit mixture volume per unit time. The steady-state one-dimensional continuity and energy equations can then be written as

$$GdX_a = \Gamma dz \tag{2}$$

$$q''_w \quad P_H \, dz = GAi_{fg}dX_e \tag{3}$$

where Γ is the vapor generation source function.

A few preliminary models for the vapor generation source function have been proposed, including those of Saha[1] and of Webb and Chen[2]. In addition, Webb and Chen[3] proposed a modification of the Saha correlation, using the homogeneous void fraction, to alleviate problems encountered with the Saha model at low mass fluxes. Other models which do not directly specify Γ have also been proposed to characterize the thermodynamic nonequilibrium conditions including those by Yoder and Rohsenow[4], Chen, Sundaram, and Ozkaynak[5], and Groeneveld and Delorme[6]. The assessment of these models has been hampered by the lack of experimental data on the thermodynamic nonequilibrium.

A number of experiments in convective film boiling have been conducted over the past twenty years. However, in most of these tests, the vapor superheat, or degree of thermodynamic nonequilibrium, was not determined due to the difficulty of the measurement. Until recently, the data of Nijhawan[7] were the most complete and the best documented experiment to date. In that work, however, the vapor superheat was only measured at one distance downstream of the quench front, so the axial behavior of the nonequilibrium was unknown.

Recently, two series of tests have been conducted at Lehigh University and at Idaho National Engineering Laboratory (INEL) to acquire the desired data. These tests used a fixed quench front technique (hot patch) as well as the moving quench front method to evaluate the axial variation of nonequilibrium downstream of the quench front. In the tests at Lehigh University, Evans, Webb, and Chen[8] used a single vapor probe to evaluate the nonequilibrium conditions resulting in the acquisition of over 500 sets of data at low pressure, low mass flux conditions. At INEL, Gottula, et al.[9] used multiple vapor probes over a wide pressure range (up to 7000 kPa) to obtain over 700 sets of data for low mass flux conditions. The parametric ranges of each data set are summarized in Table 1. With the addition of these data to the nonequilibrium data base, existing convective film boiling models can be better evaluated.

TABLE 1

DATA PARAMETRIC RANGES

	LEHIGH	INEL
Pressure (kPa)	240 - 539	200 - 7000
Mass Flux(kg/m2-s)	14 - 78	12 - 100
CHF Quality	0. - 0.99	.01 - 0.66
Wall Heat Flux(W/cm2)	1.3 - 7.2	0.8 - 22.5

Some typical vapor superheat data from the tests conducted by Evans, Webb, and Chen are shown in Figure 1. From this information, the vapor generation rate can be seen to be high near the quench front and to decrease further downstream. Existing models postulate that the vapor generation rate is directly proportional to the local vapor superheat. Therefore, these models would predict a low vapor generation rate near the quench front and a higher value further downstream in direct conflict with these new data. Data-model comparisons have been performed by Webb and Chen[10] for the Lehigh data and by Condie, et al.[11], for the INEL data. As expected, no present model is able to adequately predict the data. Therefore, a new vapor generation rate model has been developed from this new data base. In addition, a heat transfer coefficient model is proposed to account for the heat sink effect of the entrained liquid in the superheated steam. This total model will be developed in the next section.

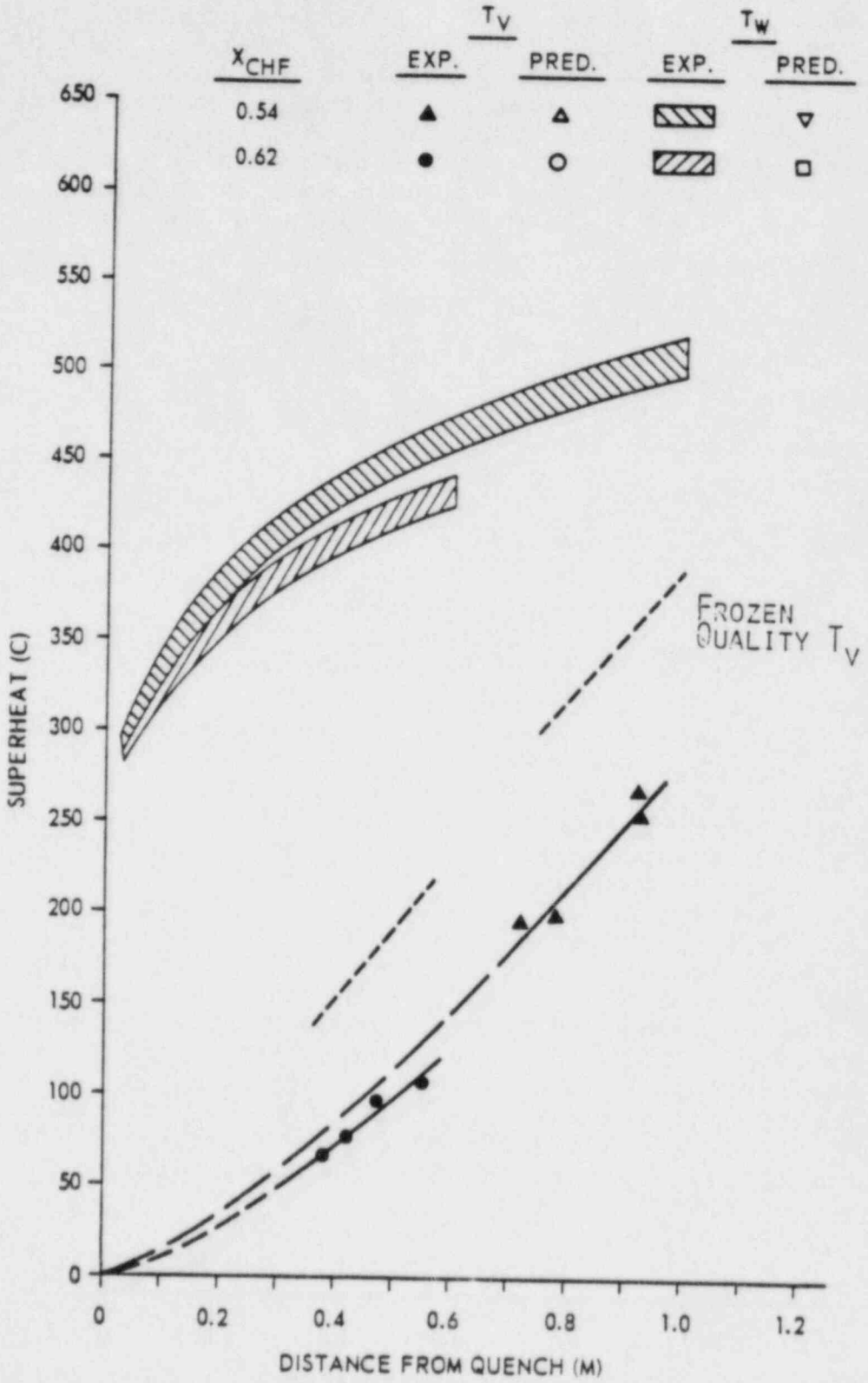

FIGURE 1. AXIAL VAPOR SUPERHEAT DATA

II. MODEL DEVELOPMENT

A. Vapor Generation Rate

As indicated by the new data, which includes reliable axial information for the first time, the vapor generation rate is high near the quench front and decreases dramatically further downstream. This behavior can be separated into a near-field region where the vapor generation rate is relatively high, and a far-field region where the vapor generation rate is much lower. Different mechanisms are postulated in each region.

Near-Field Region

In the region near the CHF location, the vapor generation rate is high even though the vapor superheat is low, as exemplified by the data shown in Figure 1. Conventional convective film boiling models assume that the vapor generation is due to evaporation of entrained drops, so that the rate is directly proportional to the local vapor superheat. These models would therefore predict a low vapor generation rate in the near-field, in direct conflict with the data.

In order to account for this new experimentally observed trend, a near-field vapor generation mechanism due to liquid-wall contact is postulated. At the quench front location, the liquid which was on the wall as a liquid film before the CHF location is violently driven off the wall. It is hypothesized that this sputtering action may induce direct wall to liquid contact in this region. This near-field vapor generation rate is postulated to vary with the following parameters:

1. Wall Superheat (Θ_w)

   As the wall superheat increases, reduced vapor generation is expected due to repulsive evaporative forces on the liquid.

2. Distance (L/D)

   As the distance from the quench front increases, the near-field vapor generation rate should decrease.

3. Liquid Mass ($G(1.-X_a)$)

   As the liquid mass flux increases, the vapor generation rate should also increase.

As a first approximation, the near-field vapor generation rate is postulated to be of the form

$$\Gamma_{NF} \propto \exp(-c \frac{\Theta_w L/D}{G(1-X_a)}) \quad (4)$$

The proportionality constant can be evaluated by recognizing that the magnitude of the near-field vapor generation rate should be continuous with the upstream conditions before CHF. Before the quench front, in the nucleate boiling region, the vapor superheat is negligible, and the vapor generation rate must be such that the equilibrium quality is maintained,

$$\Gamma_{NF} = \Gamma_{eq} = \frac{4q''_w}{Di_{fg}} \quad (5)$$

At the quench front, the near-field rate should be equal to this value. This condition results in the following form for the near-field vapor generation rate

$$\Gamma_{NF} = \Gamma_{eq} \exp(-c \frac{\Theta_w L/D}{G(1-X_a)}) \quad (6)$$

where, at the quench front, the L/D term is equal to zero, and the vapor generation rate is equal to the equilibrium value. Note that Γ_{eq} is the local value of the vapor generation rate which may be different than the value at the CHF location. After the quench front, the rate decreases rapidly due to increased values of the wall superheat, distance, and actual quality. This behavior is qualitatively depicted in Figure 2.

The Lehigh University and INEL data have been used to assess the above near-field vapor generation rate model. From comparison of the model to data, the value of the empirical constant c was determined to be

$$C = 0.0016 \frac{Kg}{m^2\text{-}s\text{-}^oc}$$

This constant was found to be independent of pressure. The same value is applicable to the low pressure (250-800 kPa) data as well as the high pressure (7000 kPa) data. Thus, the expression for the near-field vapor generation rate is

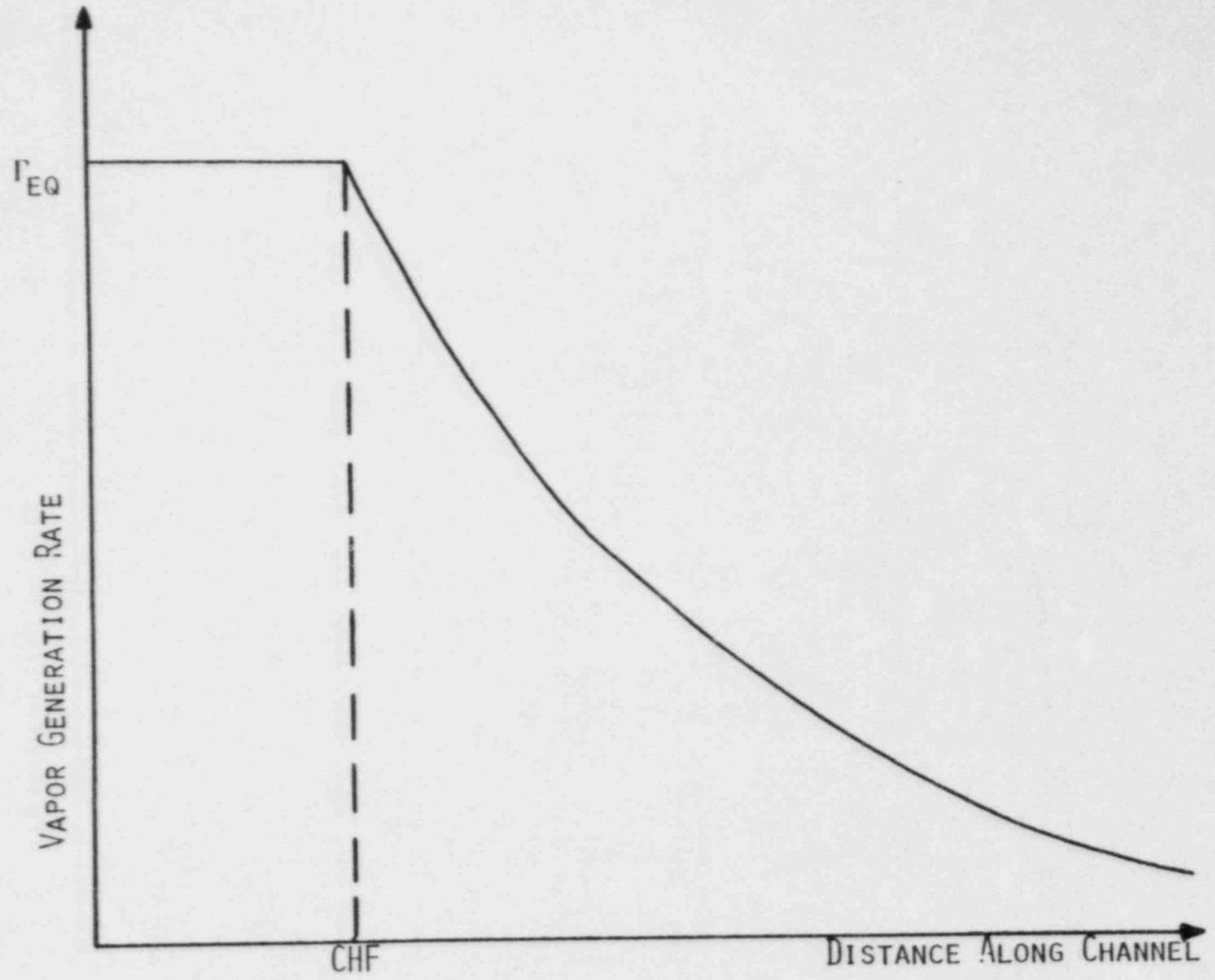

FIGURE 2. NEAR-FIELD VAPOR GENERATION RATE BEHAVIOR

$$\Gamma_{NF} = \Gamma_{eq} \exp(-0.0016 \frac{\Theta_w L/D}{G(1-X_a)}) \quad (7)$$

where Θ_w and G are in ^oC and kg/m2-s, respectively.

Far-Field Region

In the far-field region, direct liquid-wall contact is postulated to become negligible, and the vapor generation occurs by droplet evaporation, with the rate dependent on the local vapor superheat. This behavior is consistent with earlier vapor generation rate models for dispersed post-CHF flow.

The multiple vapor probe INEL data indicate the axial variation of vapor superheat and thus allow calculation of the vapor generation rate for a given CHF quality. Most of the data reported with multiple vapor probes are sufficiently far from the quench front that the near-field effect is small. Therefore, these data can be used to directly evaluate the far-field region.

The vapor generation rate in the far-field is postulated to be directly proportional to the vapor superheat consistent with existing post-CHF models. Gottula, et al.[12] have evaluated the Webb-Chen[2] vapor generation model as well as the modified Saha correlation suggested by Webb and Chen[3] with the INEL data. Both models significantly overpredict the measured vapor generation rates. These models were originally developed to predict the vapor generation rate based on the local vapor superheat starting from the CHF point. In view of the recent finding that the vapor generation is enhanced in the near-field region, it is not surprising that these models overestimate local vapor generation rates in the far-field region.

In this work, the INEL data have been used to modify the original Webb-Chen correlation in an attempt to account for the two-region behavior. Multiple vapor probe data are available up to a pressure of 7000 kPa. Therefore, these data can also be used to directly evaluate the pressure effect.

The original Webb-Chen correlation is

$$\Gamma = K \left(\frac{GX_a}{\alpha_h}\right)^2 \frac{(1-\alpha_h)^{2/3} \Theta_v k_v}{\rho_v \sigma i_{fg} D} \quad (8)$$

where

$$K = \frac{h}{k_v} \frac{\sigma}{\rho_v V_v^2} \frac{(1-\alpha_{CHF})^{1/3}}{(1-\alpha_{CHF}^{1/2})} - 1.32(P/Pc)^{-1.1} \quad (9)$$

Evaluation of the experimental data showed that the pressure dependence in K can be mainly attributed to the variation of the thermodynamic properties. In addition, it was determined that the vapor mass flux - void fraction term should be replaced by the total mass flux. Thus, the revised Webb-Chen correlation for the far-field vapor generation rate becomes

$$\Gamma_{FF} = c \frac{\sigma}{\rho_v k_v} G^2 \frac{(1-\alpha_h)^{2/3} \theta_v k_v}{\sigma \rho_v i_{fg} D} \quad (10)$$

and c is equal to 0.02 kJ-s/m4-C. Some of the various terms can be combined, and the above expression can be rewritten as

$$\Gamma_{FF} = 0.02 \frac{G^2}{\rho_v^2} \frac{(1-\alpha_h)^{2/3} \theta_v}{i_{fg} D} \quad (11)$$

where the units on the constant are kJ-s/m4-C.

Total Vapor Generation Rate

The total vapor generation rate is simply the sum of the near-field and the far-field contributions,

$$\Gamma = \Gamma_{NF} + \Gamma_{FF} \quad (12)$$

In order to assess this correlation, the model was used to evaluate the integrated vapor generation rate for the Lehigh University and INEL data. The integrated vapor generation rate between the CHF location and the vapor probe is simply the total mass flux times the increase in actual quality, or

$$\int_{z_{CHF}}^{z_{vp}} \Gamma dz = G\,(x_{a_{vp}} - x_{CHF}) \qquad (13)$$

Using the measured wall temperatures and heat flux values, and knowing the thermal-hydraulic conditions at CHF, local vapor generation rates were calculated by equation (12). These local values were numerically integrated from the CHF location to the vapor probe elevation. These values were then compared to the experimental data. Figure 3 shows the data-model comparison for the Lehigh University data while Figure 4 gives the results for the INEL data. It is seen that the present two-region vapor generation model is able to predict the experimental values for both sets of data with reasonable agreement.

B. Heat Transfer Coefficient

In addition to the vapor generation function (Γ), one also needs to estimate the convective heat transfer coefficient at the heated wall. As has been discussed by Webb and Chen[13], the use of a single-phase heat transfer coefficient to predict the wall-vapor temperature difference in convective film boiling is questionable, especially at low mass flux conditions. The heat transfer coefficient is found to be consistently underpredicted by this approach. With the expanded nonequilibrium data base, a heat transfer correlation can be developed for convective film boiling conditions.

Comparison of the experimentally observed heat transfer coefficient with the value calculated by the modified CSO correlation[13] is shown in Figure 5 for the Lehigh University and INEL data. The modified CSO correlation is given in the Appendix. Significant higher values of the heat transfer coefficient are observed in the experimental data compared to the calculated values. A possible explanation of this apparent improved heat transfer is that the entrained liquid acts as distributed heat sinks in the vapor, leading to enhanced wall heat transfer in dispersed flow.

This enhancement concept was first hypothesized by Chen, Sundaram, and Chen[14], who suggested that the improvement in heat transfer can be correlated by the addition of a sink function to account for the effect of the entrained liquid droplets:

$$h_{2\phi} = h_{1\phi}\,(1+F_s) \qquad (14)$$

where F_s is the sink function. Thus, when no liquid is present, the sink function vanishes, and one obtains the single-phase heat transfer correlation.

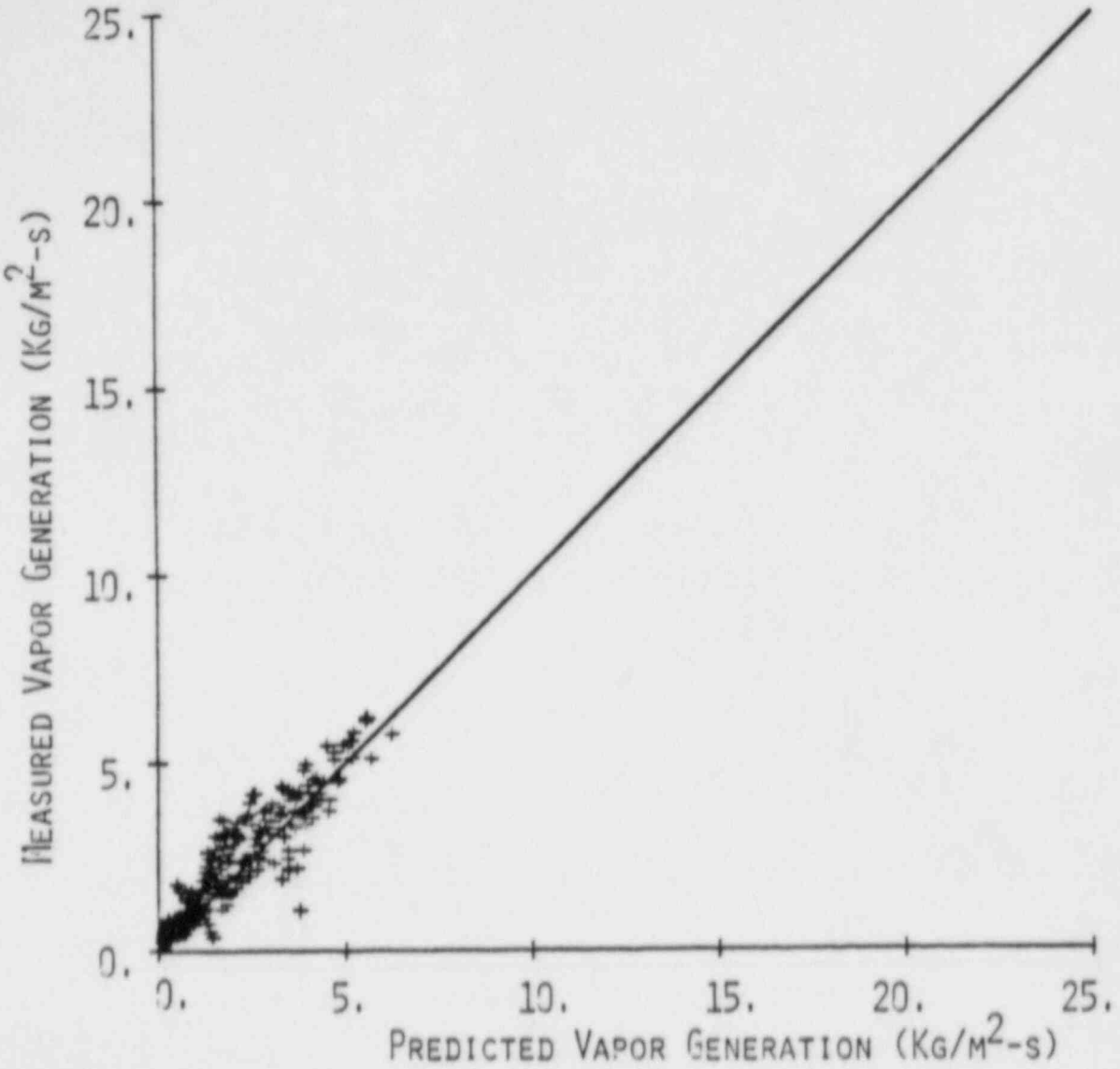

FIGURE 3. VAPOR GENERATION DATA-MODEL COMPARISON FOR LEHIGH DATA

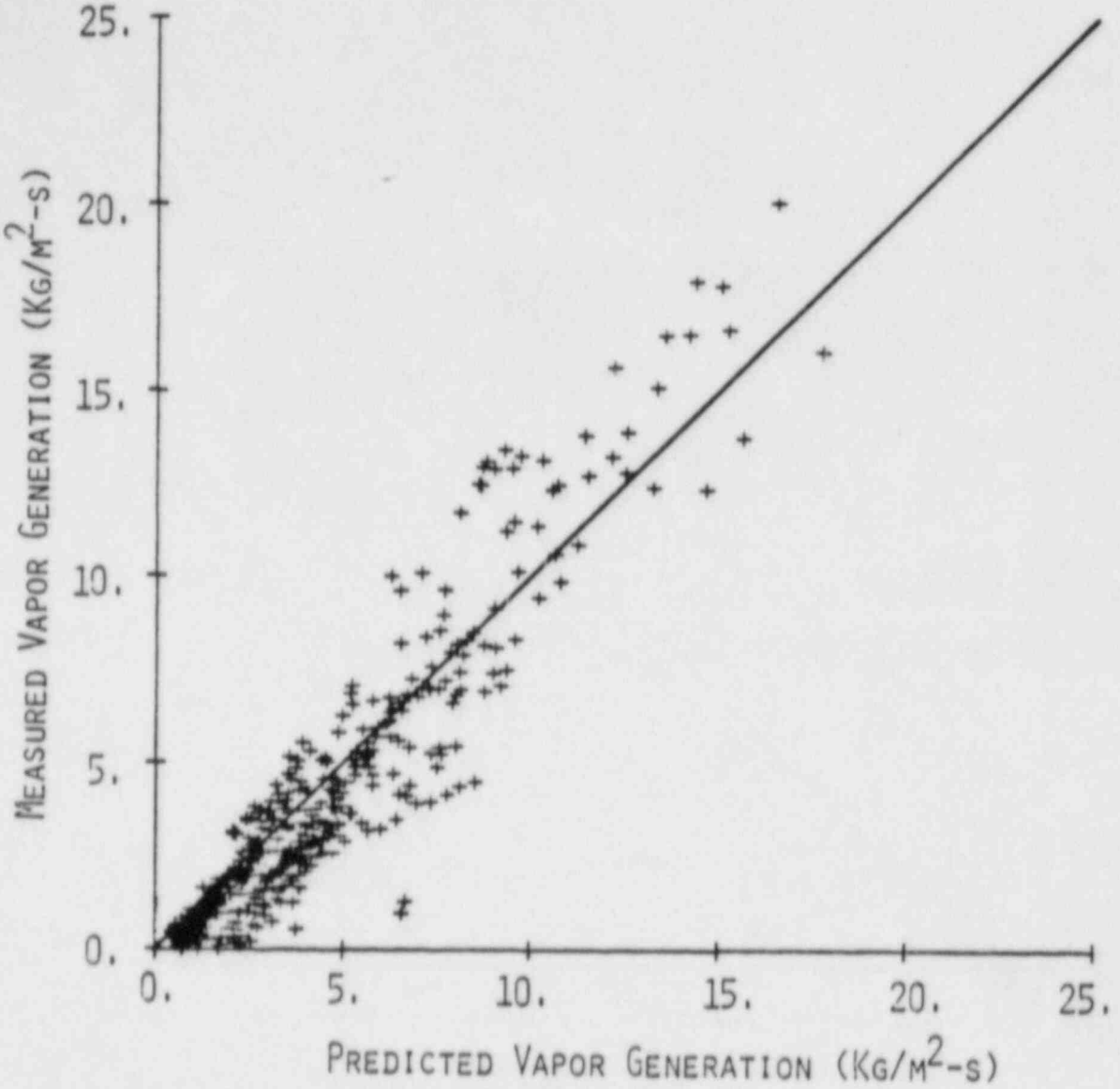

FIGURE 4. VAPOR GENERATION DATA-MODEL COMPARISON FOR INEL DATA

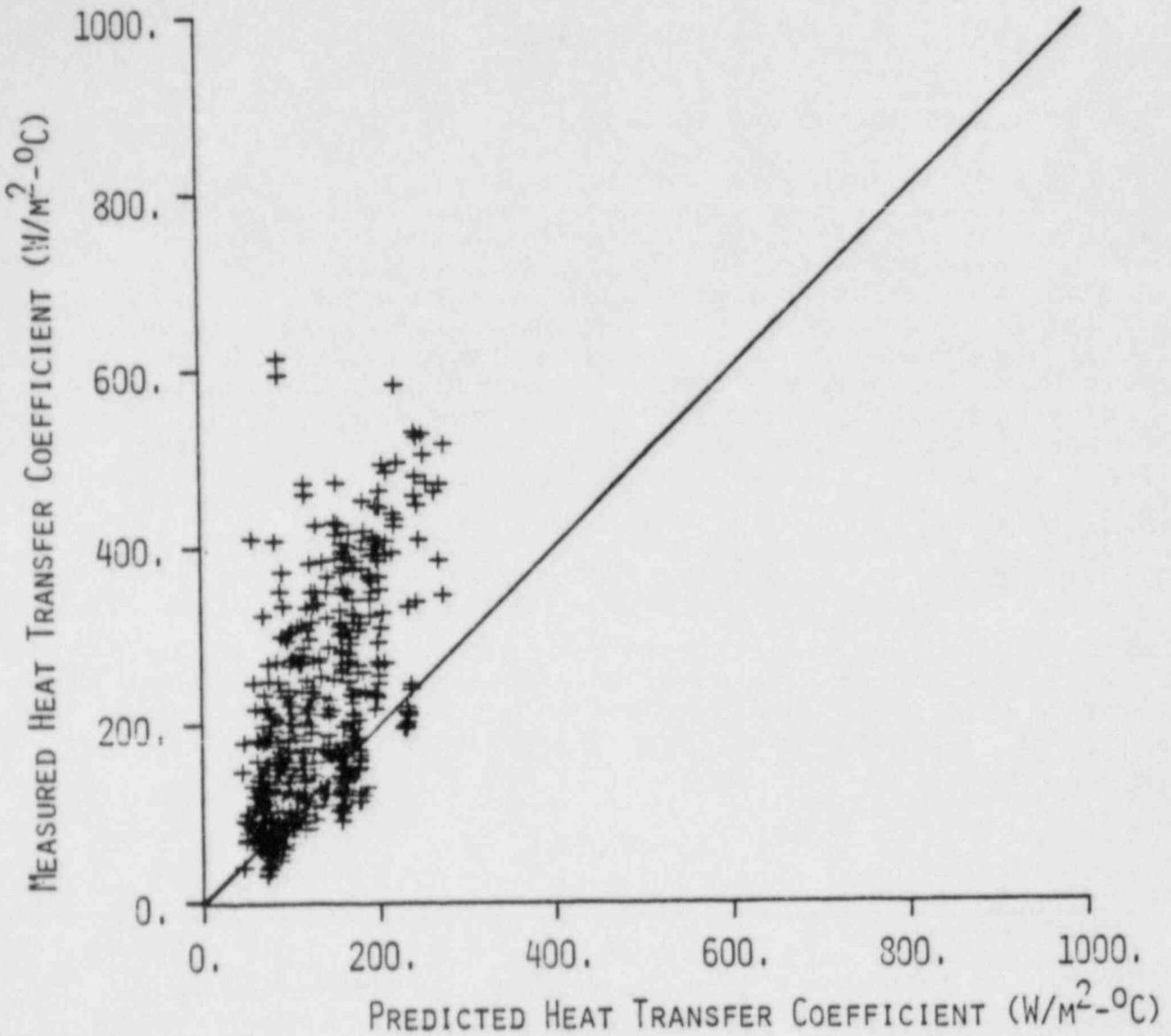

FIGURE 5. SINGLE-PHASE HEAT TRANSFER COEFFICIENT DATA-MODEL COMPARISON FOR LEHIGH AND INEL DATA

These authors also suggested that an entrance-region factor is required in order to account for the thermal boundary layer development at the hot wall. The entrance region factor presented by Yoder and Rohsenow[4] has been used for this purpose. The revised correlation then becomes

$$h_{2\phi} = h_{1\phi} (1+F_s) (1+0.8(L/D)^{-1}) \quad (15)$$

where L is measured from the CHF location.

In the present work, the sink function was re-correlated with the same variables used by Chen, Sundaram, and Chen[14] in their original model. In addition, however, a term involving the reduced pressure has been introduced. The original model was based on data with a relatively small pressure range (170-510 kPa). The new Lehigh University and INEL data cover a much wider pressure range (250-7000 kPa), allowing a more definitive correlation of the pressure term. The modified CSO correlation was used as the single-phase model. By regression analysis, the following sink function was determined

$$F_s = 250(P/Pc)^{0.69} \left(\frac{1-Xa}{Xa}\right)^{0.49} Re_v^{-0.55} \quad (16)$$

The exponents on the various terms are in reasonable agreement with the correlation presented by Cokmez[15] in a re-evaluation of the data used by Chen, Sundaram, and Chen. The convective film boiling heat transfer coefficient is given by

$$h_{2\phi} = h_{\text{mod CSO}} (1+F_s) (1+0.8(L/D)^{-1}) \quad (17)$$

where F_s is defined above.

Comparison of this correlation with the data is shown in Figure 6. This new model represents a significant improvement compared to the single-phase modified CSO correlation without the sink factor.

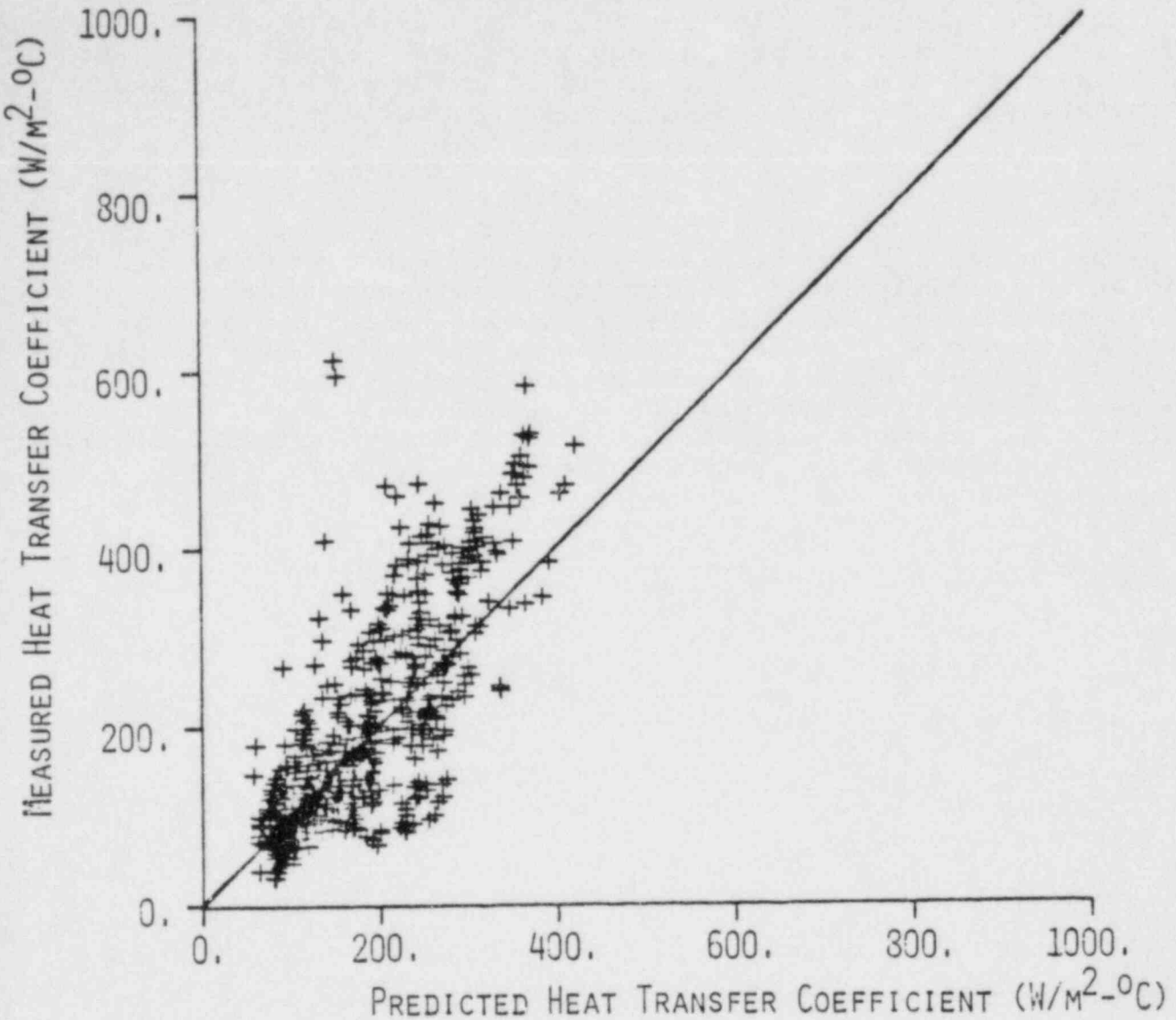

FIGURE 6. MODIFIED HEAT TRANSFER COEFFICIENT DATA-MODEL COMPARISON FOR LEHIGH AND INEL DATA

III. RESULTS

With the development of the vapor generation source function and the heat transfer coefficient expression, a complete convective film boiling model has been developed. Comparisons to the Lehigh University and INEL data are shown in Figures 7 and 8. In this evaluation, the model matched the experimental wall temperature values and predicted the vapor superheat and wall heat flux values. The statistical information is summarized in Tables 2 and 3 including the results from a number of other correlations. A significant improvement in the agreement between predicted and measured vapor superheats and heat flux values is noted.

IV. SUMMARY

A new model for convective film boiling has been developed to predict the nonequilibrium conditions. The vapor generation source function approach has been used with near-field and far-field contributions. A revised heat transfer coefficient model has also been correlated to account for the heat sink effect of the entrained liquid droplets in the superheated steam. The overall model shows comsiderable improvement over existing models for the new Lehigh University and INEL nonequilibrium data.

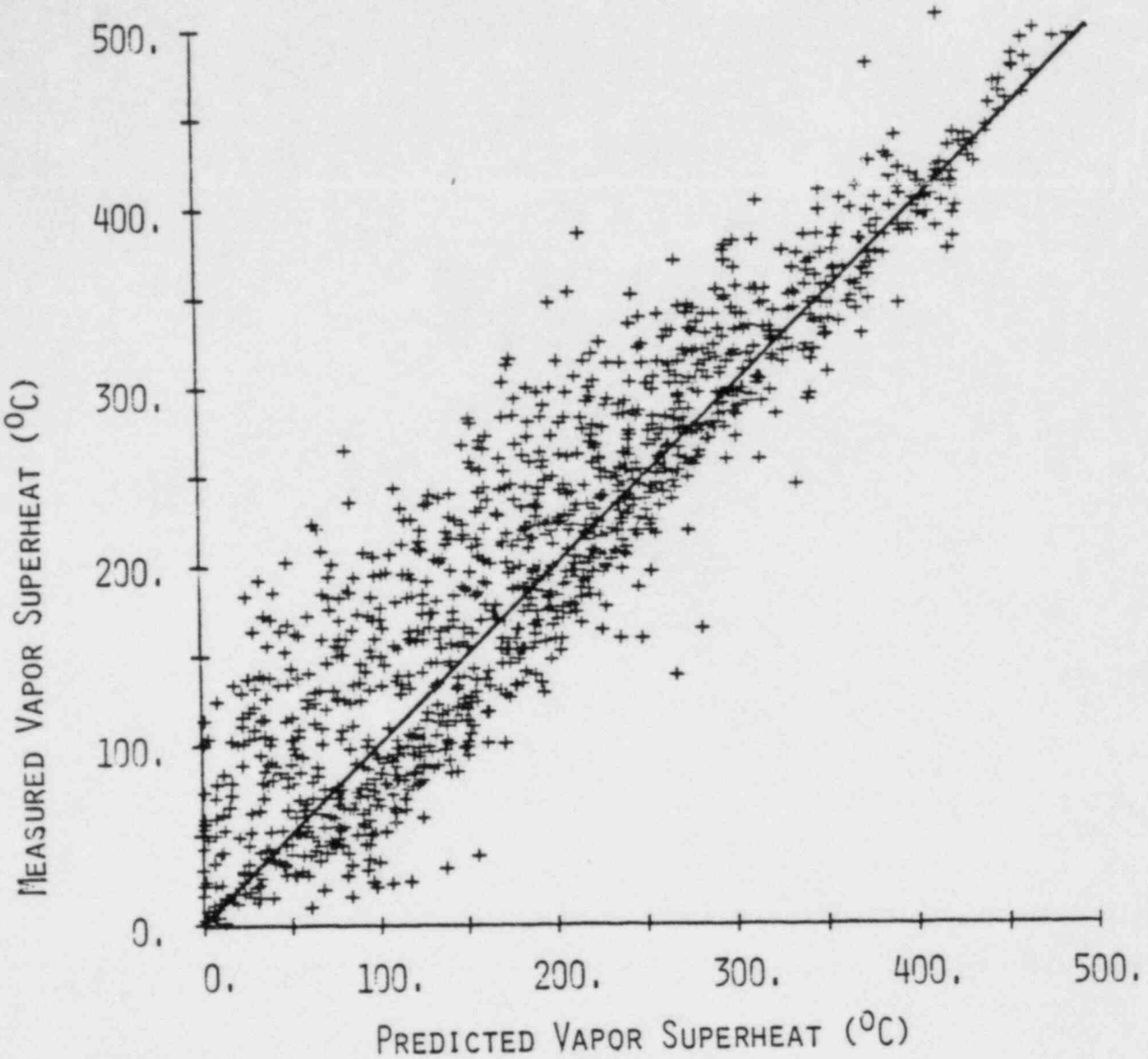

FIGURE 7. VAPOR SUPERHEAT DATA-MODEL COMPARISON FOR LEHIGH AND INEL DATA

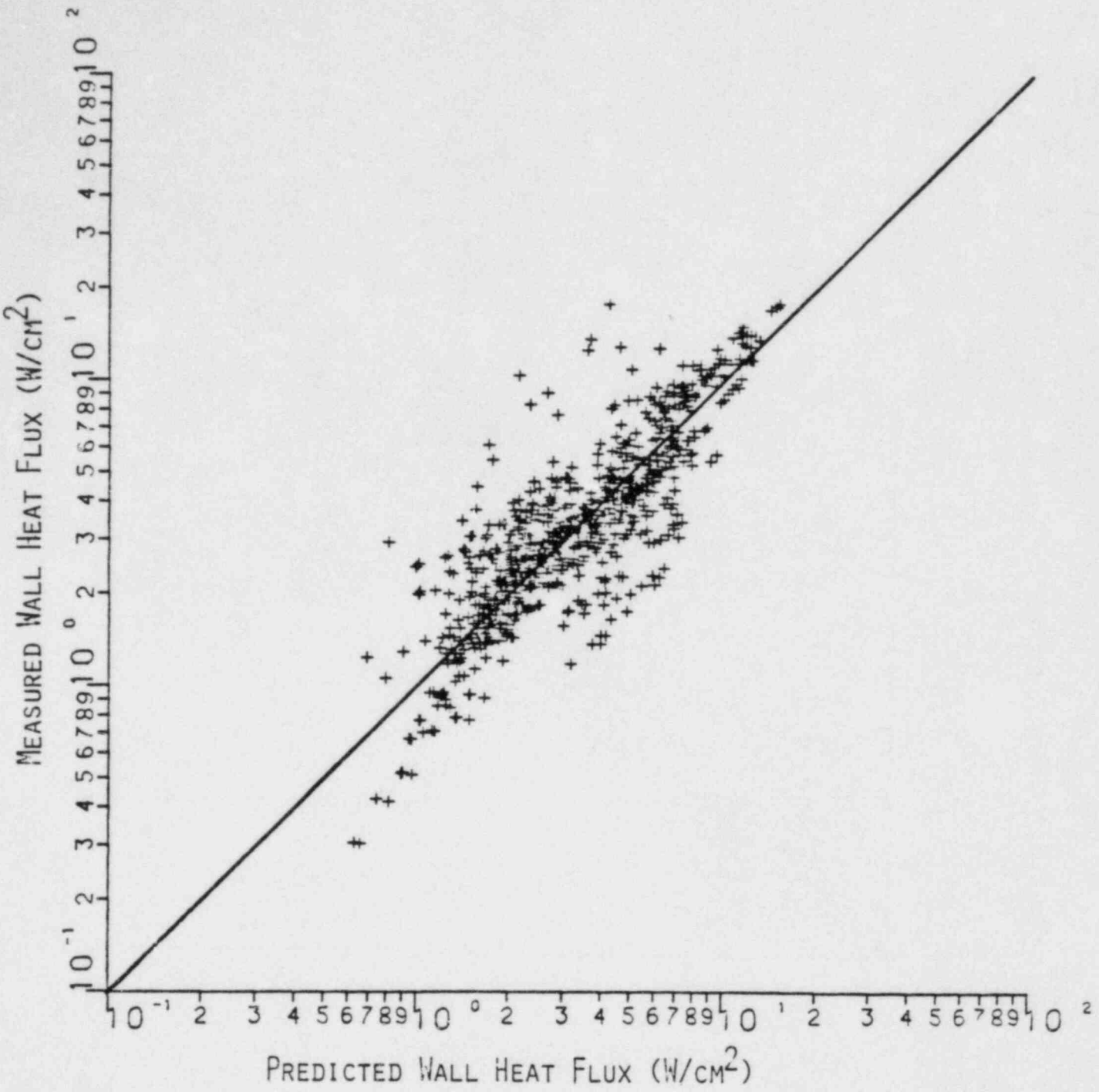

FIGURE 8. WALL HEAT FLUX DATA-MODEL COMPARISON FOR LEHIGH AND INEL DATA

TABLE 2

STATISTICAL RESULTS
FOR LEHIGH AND INEL DATA

Vapor Superheat

	LEHIGH DATA		INEL DATA	
Correlation	Ave Dev	Std Dev	Ave Dev	Std Dev
New Model	34.	65.	23.	35.
Webb-Chen[2]	75.	132.	21.	63.
Saha[1]*	64.	123.	33.	37.
Saha-Mod[3]	54.	107.	41.	52.
CSO[5]	75.	154.	43.	137.
Groeneveld-Delorme[6]	250.	690.	69.	282.

Wall Heat Flux

	LEHIGH		INEL	
Correlation	Ave Dev	Std Dev	Ave Dev	Std Dev
New Model	14.	21.	28.	41.
Webb-Chen[2]	26.	36.	38.	47.
Saha[1]*	16.	17.	16.	22.
Saha-Mod[3]	31.	37.	32.	40.
CSO[5]	19.	25.	45.	67.
Groeneveld-Delorme[6]	91.	91.	87.	87.

* Able to calculate only 61% of the Lehigh data and only 14% of the INEL data.

TABLE 3
STATISTICAL RESULTS
FOR ALL THE DATA

	Vapor Superheat		Wall Heat Flux	
Correlation	Ave Dev	Std Dev	Ave Dev	Std Dev
New Model	28.	50.	22.	34.
Webb-Chen[2]	43.	97.	26.	43.
Saha[1]*	57.	108.	16.	18.
Saha-Mod[3]	46.	79.	32.	38.
CSO[5]	56.	144.	34.	54.
Groeneveld-Delorme[6]	140.	490.	89.	89.

* Able to calculate only 33% of the data.

Nomenclature

A	flow area
D	hydraulic diameter
F_s	sink factor
G	mass flux
h	heat transfer coefficient
i	enthalpy
j	volumetric flux
k	thermal conductivity
L	distance from quench front
P	pressure
P_H	heated perimeter
q''_w	wall heat flux
Re	Reynolds number based on j
T	temperature
V	velocity
X	quality
z	axial coordinate

Greek

α	void fraction
ρ	density
σ	surface tension
Γ	vapor generation source function
θ	superheat, $T - T_s$

Subscripts

a	actual
c	critical
CHF	critical heat flux
e,eq	equilibrium
FF	far-field
fg	latent heat
h	homogeneous
l	liquid
mod CSO	modified CSO correlation
NF	near-field
s	saturation
v	vapor
VP	vapor probe
w	wall
1ϕ	single-phase
2ϕ	two-phase

References

1. P. Saha, B. S. Shiralkar, and G. E. Dix, "A Post-dryout Heat Transfer Model Based on Actual Vapor Generation Rate in Dispersed Droplet Regime," ASME Paper 77-HT-80, 1977.

2. S. W. Webb, J. C. Chen, and R. K. Sundaram, "Vapor Generation Rate in Nonequilibrium Convective Film Boiling," 7th International Heat Transfer Conference, Munich, 1982.

3. S. W. Webb and J. C. Chen, "Vapor Generation Rate in Nonequilibrium Convective Film Boiling," Report TS-820, Institute of Thermo-Fluid Engineering and Science, Lehigh University, December 1981.

4. G. L. Yoder, Jr., and W. M. Rohsenow, "A Solution for Dispersed Flow Heat Transfer Using Equilibrium Fluid Conditions," Journal of Heat Transfer, Trans. ASME, Vol. 105, No. 1, pp. 10-17, 1983.

5. J. C. Chen, R. K. Sundaram, and F. T. Ozkaynak, "A Phenomenological Correlation for Post-CHF Heat Transfer," NUREG-0237, June 1977.

6. D. C. Groeneveld and G. G. J. Delorme, "Prediction of Thermal Non-Equilibrium in the Post-dryout Regime," Nuc. Eng. and Des., Vol. 36, No. 1, pp. 17-26, 1976.

7. S. Nijhawan, "Experimental Investigation of Thermal Non-Equilibrium in Post-Dryout Steam-Water Flow," Ph.D. Dissertation, Lehigh University, 1980.

8. D. G. Evans, S. W. Webb, and J. C. Chen, "Measurement of Axially Varying Nonequilibrium in Post-Critical-Heat-Flux Boiling in a Vertical Tube," NUREG/CR-3363, Vols. 1 and 2, June 1983.

9. R. C. Gottula, K. G. Condie, R. K. Sundaram, S. Neti, J. C. Chen, and R. A. Nelson, "Forced Convective, Nonequilibrium, Post-CHF Heat Transfer Experiment Data and Correlation Comparison Report," NUREG/CR-3193, EGG-2245 DRAFT, January 1984.

10. S. W. Webb and J. C. Chen, "Post-CHF Model Assessment With Lehigh Nonequilibrium Data," to be presented at 1984 ANS Meeting, New Orleans.

11. K. G. Condie, R. C. Gottula, S. Neti, R. K. Sundaram, J. C. Chen, and R. A. Nelson, "Comparison of Heat and Mass Transfer Correlations With Forced Convective Nonequilibrium Post-CHF Experimental Data," to be presented at 1984 National Heat Transfer Conference, Niagara Falls, New York.

12. R. C. Gottula, R. A. Nelson, J. C. Chen, S. Neti, and R. K. Sundaram, "Forced Convective Nonequilibrium Post-CHF Heat Transfer Experiments in a Vertical Tube," ASME-JSME Thermal Engineering Joint Conference, Honolulu, March 20-24, 1983.

13. S. W. Webb and J. C. Chen, "Inferring Nonequilibrium Vapor Conditions in Convective Film Boiling," Second International Topical Meeting on Reactor Thermal-Hydraulics, Santa Barbara, CA, January 11-14, 1983.

14. J. C. Chen, R. Sundaram, and K. L. Chen, "Analysis of Babcock and Wilcox Data on Film Boiling Heat Transfer," Report TS-811, Institute of Thermo-Fluid Engineering and Science, Lehigh University, March 1, 1981.

15. A. F. Cokmez, "Analysis of Transient Effects in Babcock and Wilcox Data on Film Boiling Heat Transfer," Report TS-825, Institute of Thermo-Fluid Engineering and Science, Lehigh University, August 1982.

Appendix

Modified CSO Heat Transfer Correlation

The modified CSO heat transfer correlation[13] is

$$h = \frac{f}{2} C_{p_{vf}} G X_a Pr_{vf}^{-2/3} \tag{A-1}$$

$$f = f_{cp} \left(\frac{T_w}{T_v}\right)^{-0.1} \tag{A-2}$$

$$\left(\frac{1}{f_{cp}}\right)^{1/2} = 3.48 - 4 \log_{10} \left(\frac{2\varepsilon}{D} + \frac{9.35}{Re_v (f_{cp})^{1/2}}\right) \tag{A-3}$$

$$\varepsilon = 1.5 \ \mu m \text{(drawn tubing)} \tag{A-4}$$

POST-DRYOUT HEAT TRANSFER IN A VERTICAL STRAIGHT TUBE OF A STEAM GENERATOR

K. Roko and M. Shiraha

Kawasaki Heavy Industries, Ltd. Hyogo, Japan

ABSTRACT

Post-dryout (dispersed flow) heat transfer coefficients of forced convective water flow in a vertical straight tube have been experimentally and analytically studied in order to evaluate the practical performance and design of a LMFBR steam generator. Experiments were carried out over the range of steam pressure 8.2 ∿ 14.3 Mpa and mass velocity 240 ∿ 550 kg/m^{2}s, using the sodium heated test tube.

Heat transfer characteristics in the post-dryout region have been analyzed on the view point that they are mainly influenced by a thermal nonequilibrium between steam and entrained droplets. A droplet diameter is treated as an experimental factor. Reynolds number which is defined by the droplet diameter and two-phase relative velocity at a dryout point, was experimentally correlated with the reduced pressure.

Next, two kinds of approximate solution by using equilibrium fluid conditions at a dryout point have been deduced by simplifing the above analysis.

These solutions were in good agreement with the data by our experiments under the non-uniform heat fluxes, and also by Bennett, et al. and Era, et al. under the uniform heat fluxes.

Also, the main parameter which indicates the degree of the thermal non-equilibrium, has been obtained in the course of deducing the approximate solution.

I. INTRODUCTION

In order to evaluate the practical performance and design of a LMFBR one-through steam generator, it is necessary to know the predicting method of a post-dryout heat transfer coefficient under the indirect (non-uniform) heating, on the conditions of middle or high pressure and low flow rate of steam-water mixtures.

Many correlations in the post-dryout region have been proposed[1]. However, since most of them are restricted in the region of high mass velocities, it may lead to major errors to extraporate them to low mass velocities in which thermal nonequilibrium becomes large.

On the other hand, many proposed theoretical analyses are complicated and also experiments on which these analyses have been based, do not cover over the high pressure region of steam-water mitures[2]∿[5]. Moreover these experiments have been carried out by using the direct (uniform) heating.

The purpose of this study is to establish the predicting method of the post-dryout (dispersed flow) heat transfer coefficient of a forced convective water flow in a vertical straight tube under non-uniform heat fluxes.

Experiments have been carried out over the range of steam pressure 8.2 ∿ 14.3 MPa and mass velocity 240 ∿ 550 kg/m^{2}s, using a sodium heated test tube.

First, the heat transfer correlations in the post-dryout region which were already proposed, have been compared with the measured data. Second, heat transfer characteristics have been analyzed under consideration of the thermal nonequilibrium between steam and entrained droplets. Moreover, two kinds of approximate solutions by using equilibrium fluid conditions have been deduced by simplifing the exact analysis. These solutions have been compared with experimental data under uniform and nonuniform heat fluxes.

II. STEAM GENERATOR TEST FACILITY AND EXPERIMENTAL CONDITIONS

The test loop is shown in Fig. 1. Sodium is circulated by an electromagnetic pump and heated up by an electric heater. High temperature sodium enters into the test steam generator giving heat to the water and goes out of it. Generated steam in the steam generator is led to an air cooled condenser. The condensate water is recirculated through a feed water pump.

The sodium heated test section is shown in Fig. 2. It consists of an inner tube of 10.8 mm i.d. and 15.9 mm o.d. enclosed by an outer tube (shell) of 32.9 mm i.d. Water enters into the bottom of the inner tube, flows upwards and is heated by high temperature sodium which flows downwards from the top of the shell.

Forty-six sheathed thermocouples (3.2 mm in sheath diameter) are mounted on the outer wall of the shell with distances of 200 ∿ 500 mm along the tube axis and eight sheathed thermocouples (1.0 mm in sheath diameter) on the outer wall

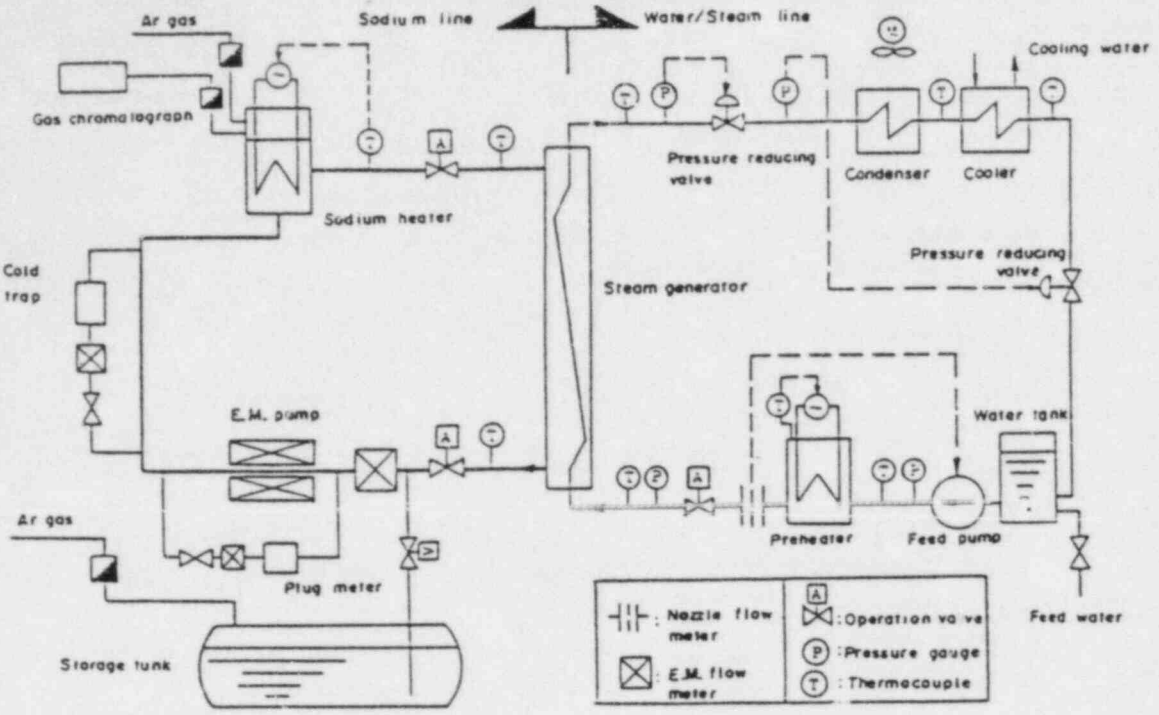

Fig. 1 Sodium heated test loop

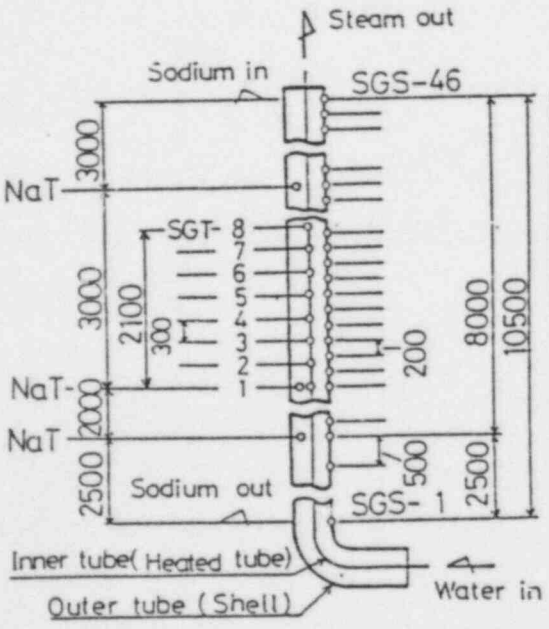

Fig. 2 Test tube

Table 1 Experimental conditions

Steam Pressure (P)	, MPa	8.2 ~ 14.3
Mass Velocity ($\dot{m}$)	, kg/m^2s	240 ~ 550
Mean Heat Flux ($\dot{q}m$)	, W/m^2	$(0.5 \sim 1.7) \times 10^5$
Max. Heat Flux / Min. Heat Flux		1.2 ~ 3.6
Dryout Quality (X_d)		0.46 ~ 0.93
Exit Quality (X_{ex})		1.07 ~ 1.40
Tube Inner Dia. (D_i)	, mm	10.8
Heated Length of Postdryout region	, m	1.8 ~ 7.6
Material of Tube		2¼Cr-1Mo
Heating Method		Sodium Heating

of the inner tube with distances of 300 mm as shown in Fig. 2.

As the outer surface of the shell is thermally insulated, temperatures on it are equal to the ones of the inner surface. Steam-water temperature at the inlet and the outlet of the test tube are measured by 3.2 mm sheathed thermocouples, steam pressure at the outlet measured by a strain type pressure gauge, water flow rate measured by an orifice flow meter and sodium flow rate measured by an electromagnetic flow meter.

The experimental conditions are shown in Table 1.

III. DATA REDUCTION

The sodium bulk temperature is determined from the shell wall temperature by the following Dwyer's equation[6].

$$\left.\begin{aligned} T_{nb} &= T_{ns} - \frac{(1-\zeta)}{\zeta}\,\frac{D_o}{D_i}\,\frac{\dot{q}}{\alpha_n} \\ \text{where}\quad \zeta &= \frac{y^4 \ell n(y)/(y^2-1) - (3y^2-1)/4}{y^2 \ell n(y) - (y^2-1)/2} \\ y &\equiv D_s/D_o \end{aligned}\right\} \qquad (1)$$

From the heat balance of a sodium and a steam-water mixture,

$$\dot{q} = -G_n\,\frac{1}{\pi D_i}\,\frac{d\,(c_{pn}\,T_{nb})}{dz} = G\,\frac{1}{\pi D_i}\,\frac{dh}{dz} \qquad (2)$$

The relation of the specific enthalpy and the equilibrium quality of a steam-water mixture is

$$h = h_\ell + h_{fg}\,x_e \qquad (3)$$

By using eqs. (1) ∿ (3) can be calculated the profiles of heat fluxes ($\dot{q}$), steam qualities (x_e), steam temperatures (T_e) and sodium bulk temperatures (T_{nb}).

The overall heat transfer rate (U) is

$$U = \dot{q} \,/\, (T_{nb} - T_e) \qquad (4)$$

The heat transfer coefficient of a steam-water mixture (α) is

$$1/\alpha = 1/U - (D_i/D_0) / \alpha_n - D_i / [2\lambda_M \ell_n (D_i/D_0)] \quad (5)$$

Then, the heat transfer coefficient of a sodium (α_n) can be calculated by Baker's equation[7] which has been correlated to a liquid metal flow in an annular conduit.

IV. ANALYSIS OF DISPERSED FLOW HEAT TRANSFER

The flow or the heat transfer regime in a post-dryout region becomes to a dispersed flow type after a transition one.

In a transition region, a wall temperature or a heat transfer coefficient oscillates because dry and wet on the heated surface alternate. However, because the length of a transition region is short[8] the heat transfer in this region gives less influence than in a dispersed flow region on estimating a heat transfer area of a steam generator[5][9].

In the dispersed flow region most of the heat added on the heated surface is transfered first to a steam. Next, a part of the heat vaporizes entrained droplets and the other part superheats a steam. So the thermal nonequilibrium exists between a superheated steam and saturated droplets.

This nonequilibrium plays a important role to a post-dryout (dispersed flow) heat transfer.

At the above view point, the heat transfer coefficient has been analysed under the following assumptions.

1. Assumptions

(1) The heat transfer by the direct contact of liquid (Leidenfrost heat transfer) can be neglected.

(2) The radiant heat transfer can be neglected.

(3) Steam is assumed to be saturated at a dryout point and liquid is everywhere saturated.

(4) The droplet diameters are assumed to be the same across a transversed section. The breack-up and the combination of droplets can be neglected.

2. Analysis

(1) Equations of a heat balance and a heat transfer

(i) Relation of a heat flux and an equilibrium quality:

$$\pi D_i \dot{q}\, dz = \frac{\pi}{4} D_i^2 \dot{m} h_{fg}\, dx_e$$

$$\frac{dx_e}{dz} = \frac{4\dot{q}}{D_i h_{fg} \dot{m}} \tag{6}$$

(ii) Heat balance for a nonequilibrium quality along a tube axis:

$$\frac{\pi}{4} D_i^2 \dot{m} \{(1 - x_a) h_\ell + x_a h_v\} + \pi D_i \dot{q}\, dz$$

$$= \frac{\pi}{4} D_i^2 \dot{m} \left[\{(1 - x_a) - \frac{dx_a}{dz} dz\} h_\ell + (x_a + \frac{dx_a}{dz} dz)(h_v + \frac{dh_v}{dz} dz)\right]$$

$$\frac{4}{D_i} \frac{\dot{q}}{\dot{m}} = \frac{d}{dz} \{x_a (h_v - h_\ell)\}$$

The relation of a nonequilibrium quality and an equilibrium one is deduced by the above equation and eq. (6), as follows

$$\frac{d}{dz} \{x_a (h_v - h_\ell)\} = h_{fg} \frac{dx_e}{dz}$$

at $z = 0$, $x_e = x_a = x_d$, $h_v = h_{s,v}$ and $h_\ell = h_{s,v} - h_{fg}$

so $\quad x_a(h_v - h_{s,v}) = h_{fg} (x_e - x_a)$ (7)

(iii) Heat transfer coefficient ($\alpha_{w,v}$) and heat flux ($\dot{q}$) from a tube inner surface to a superheated steam;

Bishop's equation[10] can be applied in a high pressure steam.

$$\alpha_{w,v} = 0.0073(\lambda_{fw}/D_i) (\dot{m} D_i/\eta_{fw})^{0.886} P_{r,fw}^{0.61}$$

$$\times \{x_a + (1 - x_a)(\rho_v/\rho_\ell) S\}^{0.886} \tag{8}$$

$$\dot{q} = \alpha_{w,v} (T_w - T_v) \tag{9}$$

(iv) Heat transfer coefficient ($\alpha_{\delta,v}$) and heat flux ($\dot{q}_\delta$) from a superheated steam to a droplet:

Frössling's correlation[11] can be used.

$$\alpha_{\delta,v} = \frac{\lambda_{f\delta}}{\delta} \left[2 + 0.552 \left\{ \frac{w_v - w_\ell}{\eta_{f\delta}} \rho_{f\delta} \cdot \delta \right\}^{1/2} P_{r,f\delta}^{1/3} \right] \tag{10}$$

$$\dot{q}_\delta = \alpha_{\delta,v} (T_v - T_s) \tag{11}$$

(v) Relation of a droplet diameter and a heat flux:

Heat supplied to a droplet is consumed to vaporize it.

$$- h_{fg} \frac{d}{dt} \left(\frac{\pi}{6} \delta^3 \rho_\ell \right) = \pi \delta^2 \dot{q}_\delta$$

where $\frac{d}{dt} = w_\ell \frac{d}{dz}$, and so

$$\frac{d\delta}{dz} = - \frac{2}{h_{fg} \rho_\ell w_\ell} \dot{q}_\delta \tag{12}$$

(vi) Post-dryout heat transfer coefficient:

It is defined by a temperature difference between a tube inner surface temperature and a thermal equilibrium one.

$$\alpha = \dot{q} / (T_w - T_e) \tag{13}$$

where, $x_e \leq 1.0$; $T_e = T_s$

$x_e \geq 1.0$; T_e = thermal equilibrium superheated steam temperature (14)

(2) Equations of a mass balance

(i) Relation of a droplet diameter and nonequilibrium quality:

All liquids are in the state of droplets in a dispersed flow region.

$$\dot{m} (1 - x_a) = n \frac{\pi}{6} \delta^3 \rho_\ell$$

As n is constant at every location along a tube axis and $x_a = x_d$, $\delta = \delta_0$ at a dryout point, the following equation is derived from the above one.

$$\frac{1 - x_a}{1 - x_d} = \left(\frac{\delta}{\delta_0}\right)^3 \tag{15}$$

(ii) Relations among liquid and steam velocities, slip ratio and non-equilibrium quality:

$$W_\ell = \dot{m} \{x_a + (1 - x_a)\rho_v/\rho_\ell \cdot S\} / (\rho_v S) \tag{16}$$

$$W_v = \dot{m} \{x_a + (1 - x_a)\rho_v/\rho_\ell \quad S\} / \rho_v \tag{17}$$

(iii) Slip ratio:

Ahmad's correlation[12] can be used.

$$S = (\rho_\ell/\rho_v)^{0.205} \ (\dot{m}D_i/\eta_\ell)^{-0.016} \tag{18}$$

(3) Dryout quality

It can be predicted by the correlation proposed in the author's previous paper[8].

$$\frac{1 - x_d}{x_d} = (12.01\ p_r^2 - 5.628\ p_r + 0.8623)\left(\frac{\dot{m}}{1000}\right)^{1.2} \tag{19}$$

(4) Boundary conditions

$$Z = 0\ ;\ x_a = x_e = x_d\ ,\ T_v = T_e = T_s\ ,\ \delta = \delta_0 \tag{20}$$

By using eqs. (6) ∿ (20), local heat transfer coefficients can be predicted under operating conditions such as a flow rate, pressure and a profile of heat fluxes along a tube axis, if the initial droplet diameter (δ_0) is known.

V. EXPERIMENTAL AND ANALYTICAL RESULTS

1. Comparisons of Experimental Data and Existing Correlations

Fig. 3 (a) ∿ (f) show comparisons of the experimental data and the existing correlations. In these figures the experimental heat transfer coefficients are shown in black symbols, the profiles of heat fluxes in dashed lines and each predicted heat transfer coefficients by Dougal - Rohsenow's[13], Tong's[14], Miropolsky's[15], Bishop's[16], Groenevelt's[13] and Remizov's[14] correlation in chain lines. The heat transfer coefficient (α_{ne}), assumed no evaporation of droplets, is the lowest limit and can be predicted by the following equation.

$$\left.\begin{aligned} x_e \leq 1.0 \;;\; \frac{1}{\alpha_{ne}} &= \frac{1}{\alpha_d} + \frac{h_{fg}}{C_{pv}} \cdot \frac{1}{\dot{q}} \cdot \frac{x_e - x_d}{x_d} \\ x_e > 1.0 \;;\; \frac{1}{\alpha_{ne}} &= \frac{1}{\alpha_d} + \frac{h_{fg}}{C_{pv}} \cdot \frac{1}{\dot{q}} \left\{ \frac{x_e - x_d}{x_d} + \frac{C_{pv}}{C_{pm}} (1 - x_e) \right\} \end{aligned}\right\} \quad (21)$$

where $C_{pm} \equiv (h_v - h_{sv})/(x_e - x_d)$

It is shown in Fig. 3 that heat transfer coefficients predicted by every correlations except by the Remizov's one are considerably higher than experimental data. These inconsistency increases with decreasing pressure and a flow rate. On the other hand, predicted values by the Remizov's correlation are relatively consistent with experimental data around a dryout point, but become inconsistent in the distance from a dryout point.

2. Initial Droplet Diameter (δ_0)

The initial droplet diameters (δ_0) are so decided with each cases as the calculated heat transfer coefficients by eqs. (6) ∿ (20) are most consistent with the experimental data.

Reynolds number ($R_{e,\delta}$) which is defined by the droplet diameter and the two-phase relative velocity at a dryout point is correlated with the reduced pressure (p_r).

$$R_{e,\delta} \equiv (\dot{m}\, \delta_0/\eta_g)\, x_d\, (S_d - 1)/S_d \quad (22)$$

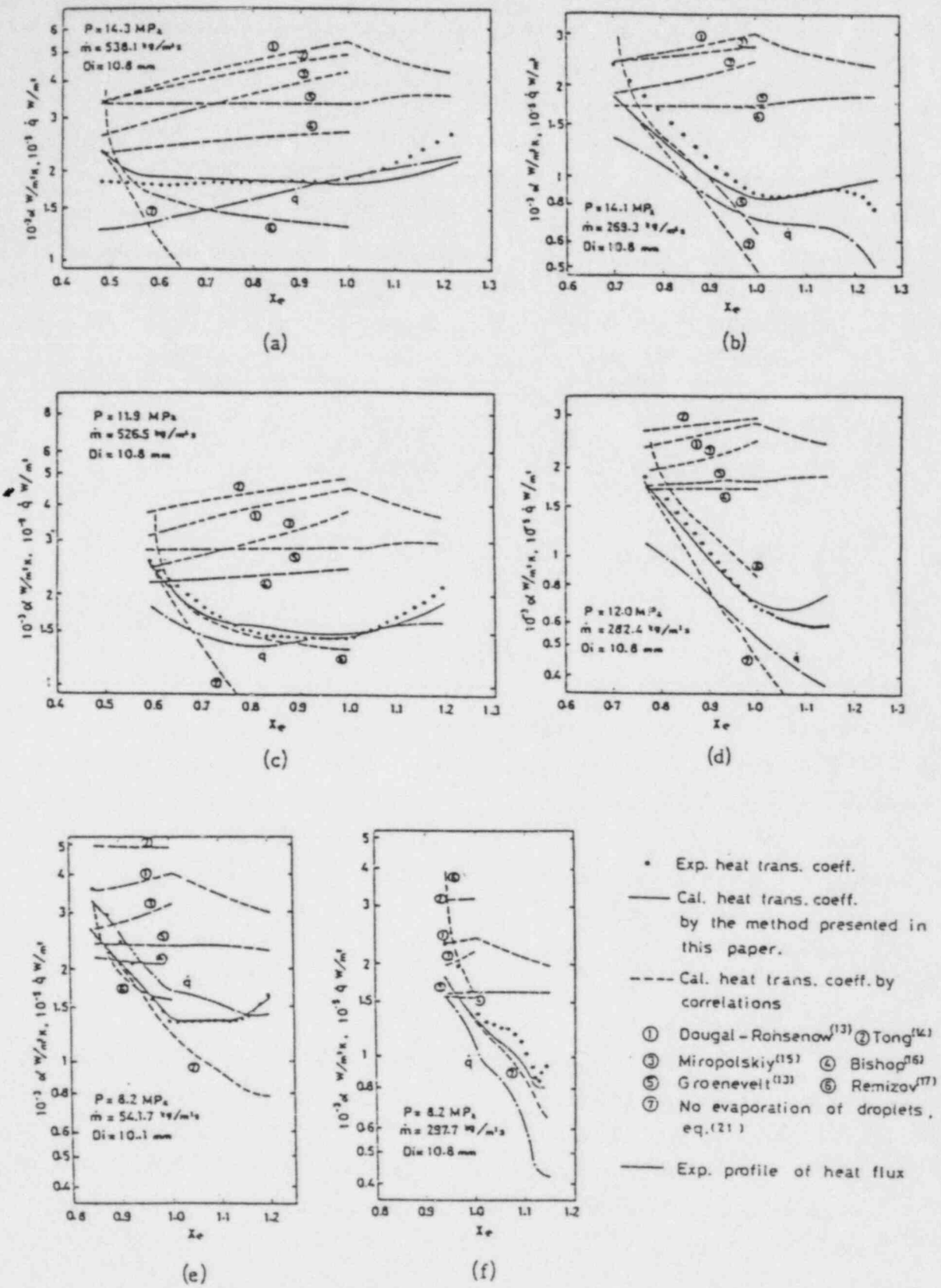

Fig. 3 Comparisons of existing corretions and exact numerical solution to experimental data

$R_{e,\delta}$ versus $(1 - p_r)$ is shown in Fig. 4 as a parameter of mass velocity. It is shown in Fig. 4 that relation of $R_{e,\delta}$ and $(1 - p_r)$ is linear on the logalismic scales and is hardly influenced by mass velocity. So the following correlation can be obtained.

$$R_{e,\delta} = 1.209 \times 10^{4} \ (1 - p_r)^{1.482} \tag{23}$$

Because the slip ratio (S_d) and the dryout quality (x_d) are calculated by eqs. (18) and (19) respectively, the initial droplet diameter (δ_0) can be predicted by eqs. (22) and (23).

3. Comparisons of Experimental and Analytical Results

The analytical results of local heat transfer coefficients are shown in solid lines of Fig. 3 (a) ∿ (f). The analytical results are in good agreement with the experimental data. The R.M.S. errors between them are 0.02 ∿ 0.13 over the range of experimental conditions shown in Table 1.

Figs.5 and 6 show the comparisons of the above analysis and the experimental data by Bennett, et. al. and Ena, et al. under uniform heat fluxes.

In Fig. 7 the analytical average heat transfer coefficients from a dryout point to a tube exit are compared with the experimental data by authors, Bennett, et al. and Ena, et al. respectively. The analytical values consist with these experimental data within the deviation of ± 10%.

VI. APPROXIMATE ANALYSIS

It has been shown that local heat transfer coefficients can be predicted by the use of eqs. (6) ∿ (20), (22), (23). But as the analysis is slightly complex, it is convenient to simplify the one for a performance evaluation and a design of a steam generator.

In this section, two kinds of approximate equations are deduced by simplifing the above analysis. Also the main parameter which defines a relation of an actual quality and a thermal equilibrium one, has been obtained in the course of deducing the approximate equation.

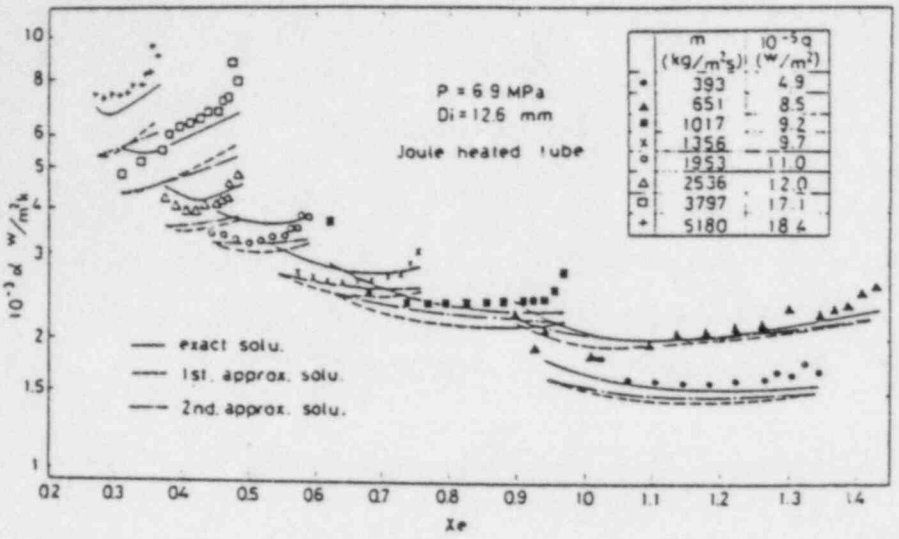

	m (kg/m²s)	10⁻³q (w/m²)
•	393	4.9
▲	651	8.5
■	1017	9.2
x	1356	9.7
○	1953	11.0
△	2536	12.0
□	3797	17.1
+	5180	18.4

Fig. 5 Comparisons of three kinds of numerical solution to Bennett's data

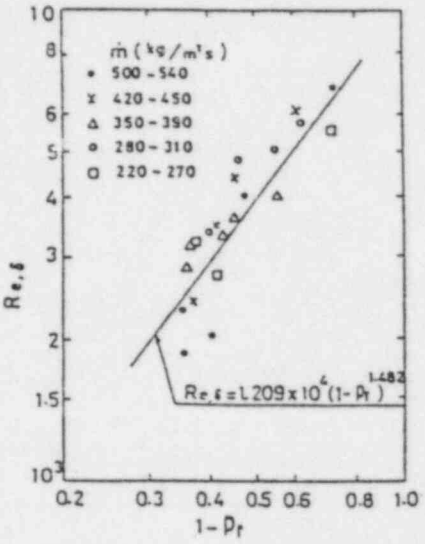

Fig. 4 $Re,_{\delta}$ versus $(1-p_r)$

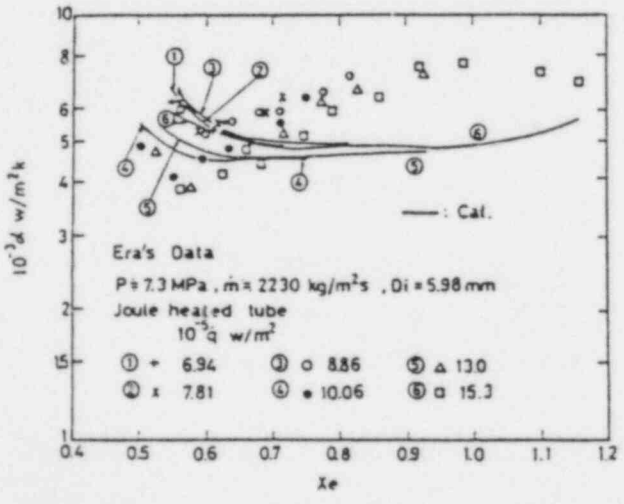

Fig. 6 Comparison of exact numerical solution to Era's data

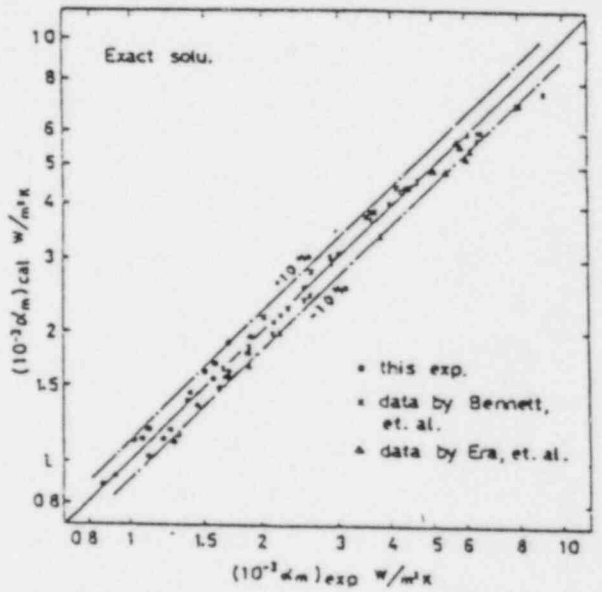

Fig. 7 Comparison of experimental and analytical average heat transfer coefficient

1. Relations of an Actual Quality and a Thermal Equilibrium One (First Approximate Equation)

The equations in section IV are approximated as below. In eqs. (16) and (17)

$$x_a + (1 - x_a)\,(\rho_v/\rho_\ell)S \doteqdot x_a \tag{24}$$

The enthalpy in eq. (7) is expressed by a temperature and a specific heat capacity.

$$\left.\begin{aligned} T_v - T_s &= h_{fg}\,(x_e - x_a) \,/\, (C_{pv}\,x_a) \\ C_{pv} &\equiv (h_v - h_{sv}) \,/\, (T_v - T_s) \end{aligned}\right\} \tag{7'}$$

From eqs. (6), (7'), (10) ∿ (12), (15) ∿ (17) and (24), the relation of an actual quality (x_a) and a thermal equilibrium one (x_e) is deduced as following equations.

$$\frac{dx_a}{dx_e} = F\frac{1}{\dot{q}^*}\left(\frac{1 - x_a}{x_a}\right)^{1/2}\frac{1}{x_a} + F'\frac{(1 - x_a)^{1/3}}{x_a^2}(x_e - x_a) \tag{25}$$

where F and F' are defined as follows.

$$F \equiv 0.828\,K\left(\frac{\rho_{sv}}{\rho_\ell}\frac{h_{fg}\,\lambda_{sv}}{C_{p,sv}}\right) P_{r,sv}^{1/3}\,R_{e\delta}^{1/2}\,S_d\left(\frac{1 - x_d}{x_d}\right)^{1/2}\frac{D_i}{\delta_0^2\,\dot{q}_m} \tag{26}$$

$$F' \equiv 3.62\,K'\,P_{r,sv}^{1/3}\,R_{e\delta}^{-1/2}\,x_d^{1/2}\,(1 - x_d)^{1/6} \tag{27}$$

$$K \equiv \left(\frac{\rho_v}{\rho_{sv}}\cdot\frac{\lambda_{f\delta}}{\lambda_{sv}}\cdot\frac{C_{p,sv}}{C_{pv}}\right)\left(\frac{\eta_{sv}}{\eta_{f\delta}}\right)^{1/2}\left(\frac{S - 1}{S_d - 1}\,\frac{S}{S_d}\right)^{1/2}\left(\frac{P_{r,f\delta}}{P_{r,sv}}\right)^{1/3} \tag{28}$$

$$K' \equiv \left(\frac{\eta_{f\delta}}{\eta_{sv}}\right)^{1/2}\left(\frac{P_{r,sv}}{P_{r,f\delta}}\right)^{1/3}\left(\frac{S_d - 1}{S - 1}\right)^{1/2}\left(\frac{S}{S_d}\right)^{1/2} \tag{29}$$

In eqs. (25) and (26), $\dot{q}_m$ is the average heat flux from a dryout point to a perfect evaporation point or a tube exit, and $\dot{q}^*$ is a normalized local heat flux ($\dot{q}^* \equiv \dot{q}/\dot{q}_m$). In the case of an uniform heat flux, $\dot{q}^*$ is equal to unity. F is in the range of 1.6 ∿ 20.4 and F' is 0.016 ∿ 0.038 under the conditions by authors, Benett, et al. and Era, et al.

Physical properties included in F and F' are the ones under the sutu-rated condition. Changes of properties to temperature are modified by K and K'. As the second term in eq. (25) is less than 10% of the first term, it is simplified as follows.

$$\frac{dx_a}{dx_e} = F \frac{1}{\dot{q}^*} \left(\frac{1 - x_a}{x_a}\right)^{1/2} \frac{x_e - x_a}{x_a} \tag{30}$$

where $x_e = x_d$; $x_a = x_d$

Eq. (30) relates an actual quality with a thermal equilibrium one, and is named the first approximate equation. R_{e_δ}, δ_0, S_d and x_d included in the parameter F are expressed by eqs. (22), (23), (18) and (19), respectively. Therefore F can be calculated if K is known.

Strictly discussing, K is dependent upon every thermal equilibrium qualities along a tube axis with which the thermal nonequilibrium temperature varies. But in the following discussion K is treated as an experimental constant.

(1) Experimental constant K

In Fig. 8 (a), (b) the actual qualities calculated by eqs. (26) and (30), assuming K = 1.05, are compared with the ones by the exact analysis mentioned in sections IV and V. In these figures, the solid lines show the solutions by the exact analysis, the dashed lines by the first approximate one and the chain lines by the second approximate one mentioned later (VI - 2).

It is shown in Fig. 8 that the first approximate solution when K = 1.05 agrees with the exact one. Moreover, little difference has been recognized between the solution considering the heat flux profile and the one assuming the uniform heat flux ($\dot{q}^* = 1.0$), over the experimental conditions shown in Table 1 ($\dot{q}^* = 0.4 \sim 2.1$).

(2) Parameter F

Parameter F can be calculated by eq. (26) when K is assumed 1.05. For a steam-water mixture, F is approximated as follows.

$$F = 2.08 \times 10^4 \, p_r^{1.6} \left(\frac{\dot{m}}{1000}\right)^{2.5} x_d^2 \frac{D_i}{(10^{-5} \dot{q}_m)} \tag{31}$$

where, $\dot{m}$ = kg/m^{2}s, D_i = m, $\dot{q}_m$ = w/m^2

Fig. 9 shows F versus reduced pressure (p_r) for a steam-water mixture as a parameter of mass velocity ($\dot{m}$). In this figure, the solid lines are by eq. (26) and the dashed lines are by eq. (31).

F is one of the basic parameters defining the relation of x_a and x_e, which is approximately predicted by the dryout quality (x_d) and the parameter F as shown in eq. (30). Fig. 10 shows the relation of $(x_e - x_a)$ and x_e as a function of x_d in case of F = 5. The relation of x_a and x_e is strongly influenced by x_d around a dryout point. However, in the distance from a dryout point, it becomes less affected by x_d and mainly depends upon F. Fig. 11 shows the relation of $(x_e - x_a)$ and x_e as a function of F in case of x_d = 0.6. As F is smaller, $(x_e - x_a)$ is greater.

This result is explained by eq. (30), in which the increasing rate of x_a to x_e, (dx_a/dx_e) decreases with decreasing F. F decreases with decreasing a flow rate and a tube diameter and with increasing a heat flux, as shown in Fig. 9. On the other hand the temperature defference between the thermal nonequilibrium temperature and the saturaled one, $(T_v - T_s)$ increases with increasing $(x_e - x_a)$ as shown in eq. (7'). Accordingly, the parameter F indicates the degree of the thermal nonequilibrium in the distance from a dryout point.

2. Second Approximate Equation

The relation of the actual quality and the thermal equilibrium one has been considerably simplified by eq. (30). In this section, the relation is more simplified than the differential equation (30).

The value of x_a equals x_d at a dryout point and unity at a point of complete evaporation. Assuming x_a is linear to x_e, the relation of x_a and x_e is

$$x_a = \{(1 - x_d)x_e + (x_0 - 1)x_d\} / (x_0 - x_d) \qquad (32)$$

where, x_0 is the thermal equilibrium quality at a point of a complete evaporation of droplets. Fig. 12 shows the relation of x_0 and F calculated by the exact analysis (by the method mentioned in sections IV and V). The value of x_0 is correlated only with F as follows.

$$x_0 = 1 + 1.09\ F^{-0.536} \tag{33}$$

Eqs. (32) and (33) are named the second approximate equation. It is reasonable that x_0 is correlated only with F, because the relation of x_a and x_e is defined only by F in the distance from a dryout point as mentioned before.

3. Simplification of Heat Transfer Coefficient

A heat transfer coefficient (α) is calculated by eqs. (7) ∿ (9), (13), (14) if x_a is predicted. In this section these equations are simplified.

In eq. (7') c_{pv} can be replaced by the specific heat capacity (c_{pe}) at the saturated temperature. The average specific heat capacity between the superheated and the saturated temperature can be replaced by c_{pe}.

$$\left.\begin{aligned} &x_e \leq 1.0\ ;\ T_e = T_s \\ &x_e > 1.0\ ;\ T_e \doteqdot T_s + h_{fg}\ (x_e - 1) / c_{pe} \end{aligned}\right\} \tag{14'}$$

In eq. (8), ρ_v/ρ_ℓ is neglected and physical properties are expressed at the average temperature of the thermal equilibrium and the heated surface. Therefore the following equations are deduced by eqs. (7') (8) (9) and (14').

$$\left.\begin{aligned} &x_e \leq 1\ ;\ \alpha/\alpha_{w,v} = \kappa \,/\, \{1 + \frac{\alpha_{w,v}}{q}\ \frac{h_{fg}}{c_{pe}}\ \frac{x_e - x_a}{x_a}\} \\ &x_e > 1\ ;\ \alpha/\alpha_{w,v} = \kappa \,/\, \{1 + \frac{\alpha_{w,v}}{q}\ \frac{h_{fg}}{c_{pe}}\ \frac{x_e(1 - x_a)}{x_a}\} \end{aligned}\right\} \tag{34}$$

$$\alpha_{w,v} = 0.0073\ (\lambda_f/D_i)\ (\dot{m}D_i/\eta_f)^{0.886} P_{rf}^{0.61}\ x_a^{0.886} \tag{8'}$$

In above equations a subscript f shows the value at the average temperature of the thermal equilibrium and the heated surface and κ is a modified factor. Predicted heat transfer coefficients agree with experimental ones over the range shown in Table 1, if $\kappa = 0.9$.

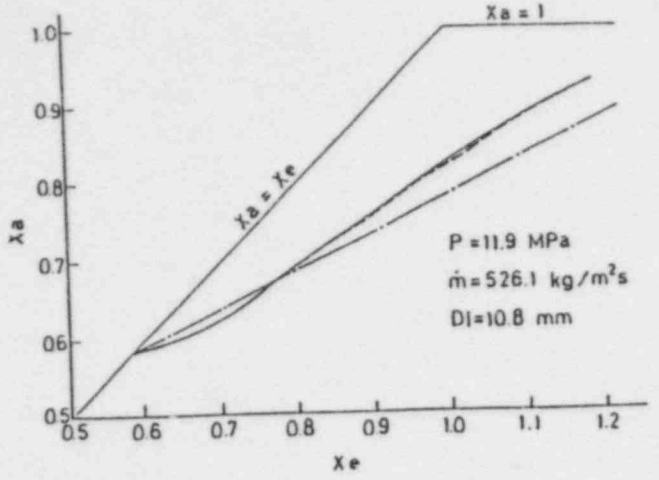

(a)

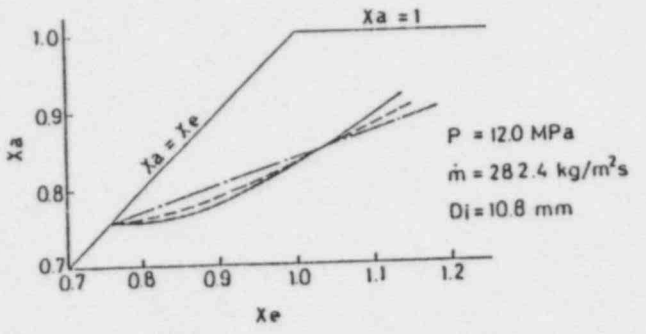

(b)

—— exact solu.
---- 1st. approx. solu.
—·—·— 2nd approx. solu.

Fig. 8 x_a versus x_e (exact solution, 1st. and 2nd. approximate solutions)

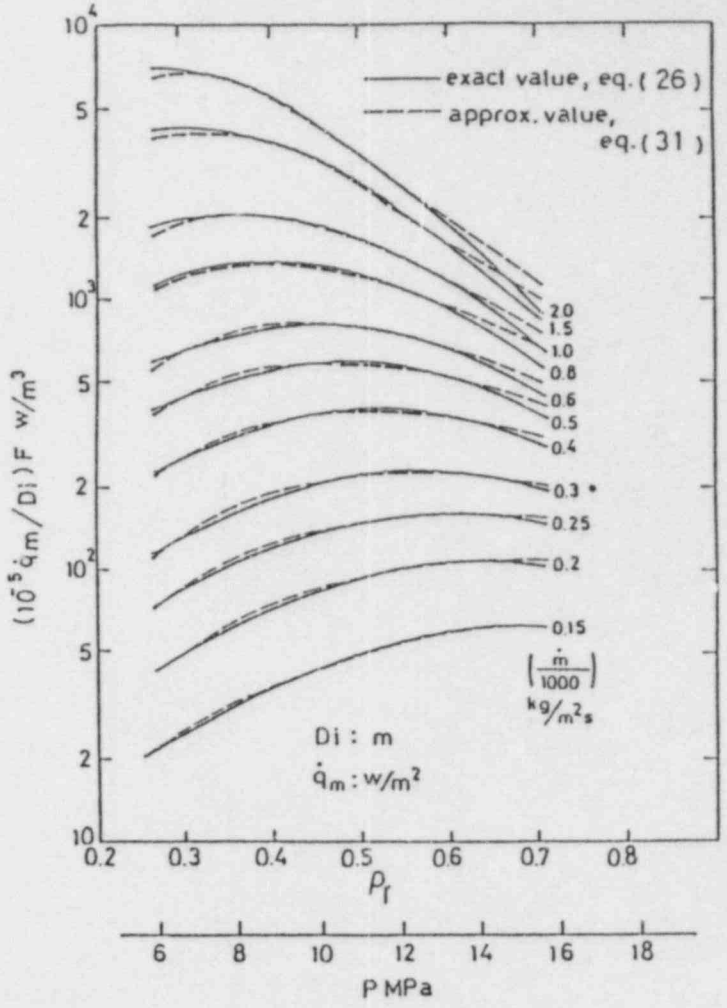

Fig. 9 Parameter F versus steam pressure as a function of mass velocity

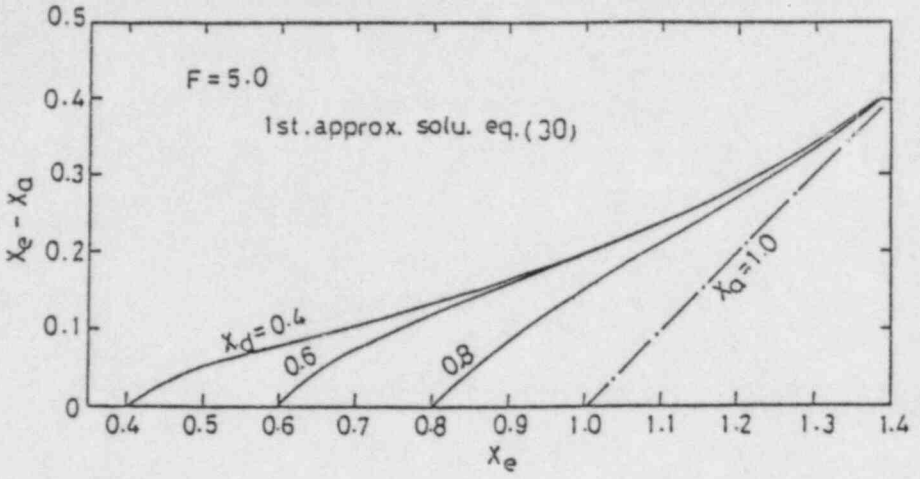

Fig. 10 $(x_e - x_a)$ versus x_e as a function of x_d

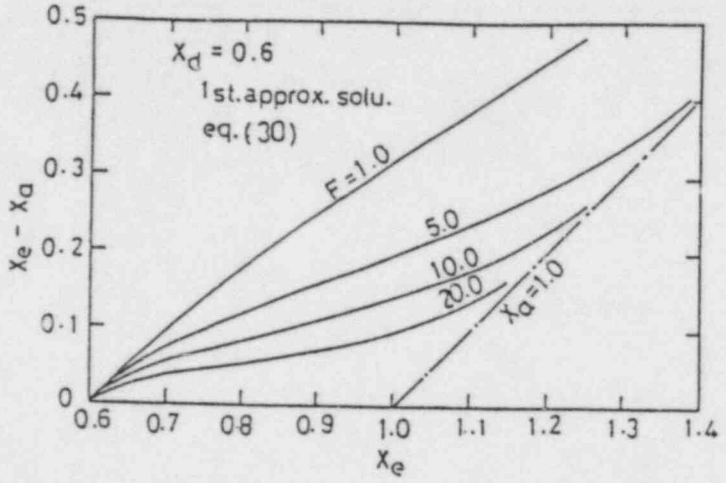

Fig. 11 $(x_e - x_a)$ versus x_e as a function of F

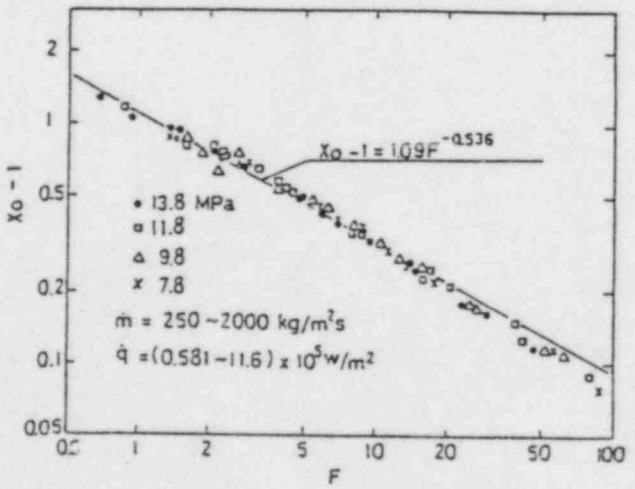

Fig. 12 x_o versus F

VII. COMPARISONS OF APPROXIMATE SOLUTIONS AND EXPERIMENTAL DATA

The first and second approximate solutions are compared in Fig. 13 with author's data and in Fig. 5 with ones by Bennett, et al. As a whole, both solutions are good agreement with experimental data except in a very high velocity region ($\dot{m} \geq 5000$ kg/m^{2}s). In this region, both solutions are 30% lower than the data by Bennett, et al. It is because the term $(1 - x_a)(\rho_v/\rho_\ell)S$, which is neglected in the course of simplification, becomes 20% of x_a for a low dryout quality and K is assumed 0.9 in eq. (34).

In section IV ∿ VII, three predicting methods for post-dryout heat transfer coefficients have been proposed. Comparisons of the experimental data and every solutions by these methods are summarized in Table 2. The solution by the exact analysis is naturally best agreement with the experimental data. The R.M.S. error of the second approximate solution is less than 15% in the average heat transfer coefficient and is almost the same as the one of the first approximate solution.

It should be noted that because a part of conditions by Bennett, et al. and Era, et al. is out of the range of the dryout equation (19), thier measured dryout data have been used in predicting every solutions.

VIII. CONCLUSIONS

1. The data of the post-dryout heat transfer coefficients in a vertical straight tube were obtained over the range of steam pressure 8.2 ∿ 14.3 MPa and mass velocity 240 ∿ 550 kg/m^{2}s, using the sodium heated test tube. These data were compared with the predicted values by Dougal-Rohsenow's, Tong's, Miroporsky's, Bishop's, Groeneveld's and Remizov's correlation. The predicted heat transfer coefficients except by Remizov's one were considerably higher than the experimental data. On the other hand, the predicted values by Remizov's correlation are relatively consistent with the experimental data around the dryout point, but become inconsistent in the distance from a dryout point.

2. Heat transfer characteristics in the post-dryout region have been analyzed on the view point that they are mainly influenced by the thermal non-equilibrium between a steam and entrained droplets. The droplet diameter

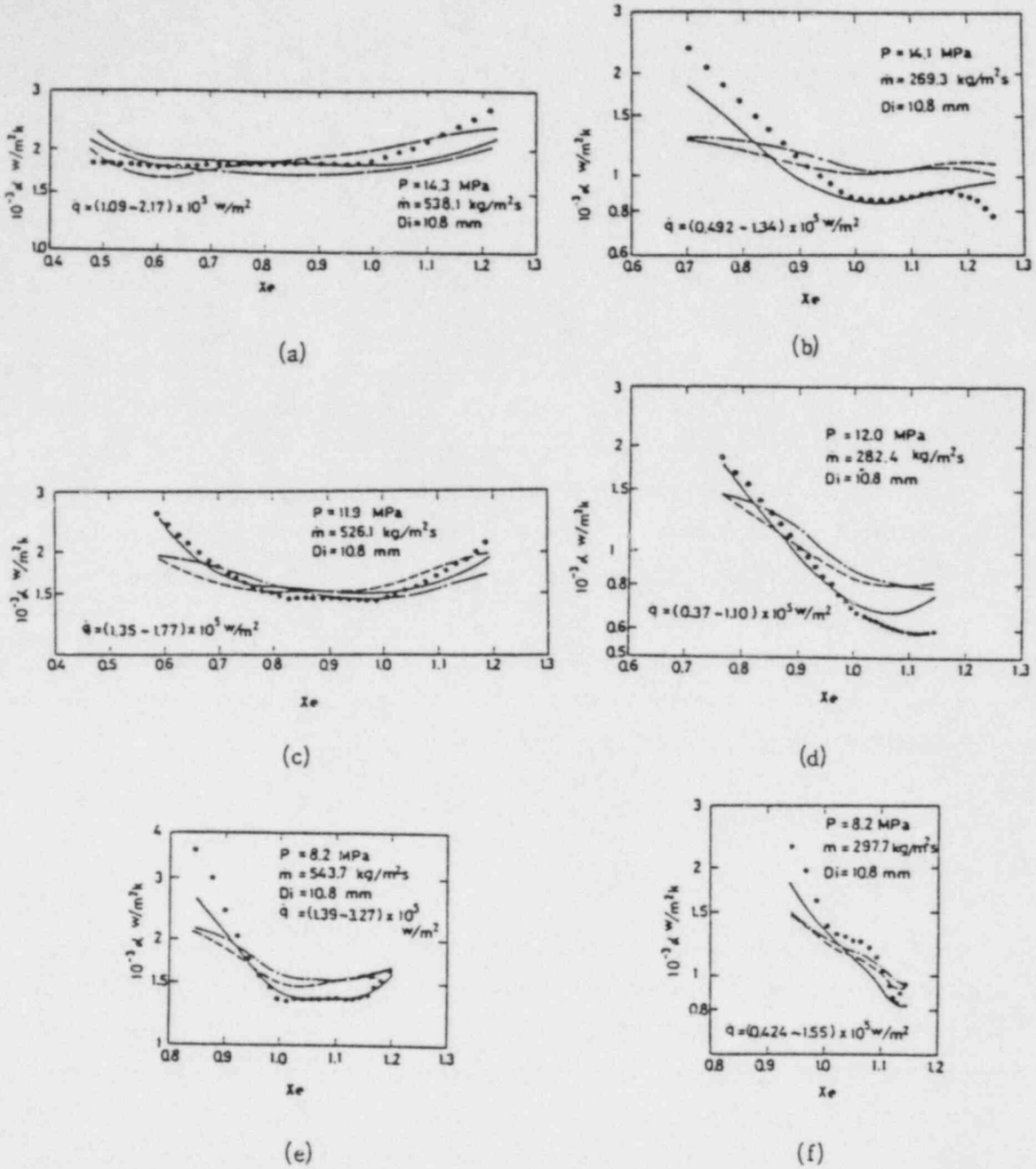

—— exact solu.

---- 1st. approx. solu. —·—·— 2nd approx. solu.

Fig. 13 Comparisons of three kinds of solution to experimental data

Table 2 R.M.S. errors of three kinds of numerical solution

		Data by this exp.	Data by Bennett, et al.	Data by Era, et al.
Heating method		Sodium heating	Joule heating	Joule heating
P	MPa	8.2 ∿ 14.3	6.9	7.3
$\dot{m}$	kg/m^2S	270 ∿ 540	390 ∿ 5200	2230
$\dot{q}_m$	W/m^2	$(0.5 \sim 1.7) \times 10^5$	$(4.1 \sim 18.4) \times 10^5$	$(6.9 \sim 15.3) \times 10^5$
D_i	mm	10.8	12.6	5.98
Nos. of data for local H.T.R.		645	304 (279)	38
Nos. of data for average H.T.R.		21	34 (31)	6
R.M.S. error				
Local H.T.R.	Exact solu.	0.0825	0.0740	0.213
	1st approx. solu.	0.180	0.220 (0.190)	0.232
	2nd approx. solu.	0.177	0.217 (0.184)	0.266
Average H.T.R.	Exact solu.	0.074	0.066	0.102
	1st approx. solu.	0.110	0.165 (0.141)	0.142
	2nd approx. solu.	0.124	0.154 (0.131)	0.137

( ) : $\dot{m} \leq 3800\ kg/m^2S$

was treated as an experimental factor. Reynolds number, which was related to the droplet diameter moderately fitted to the experimental heat transfer data, was correlated with the reduced pressure. The analytical heat transfer coefficients were in good agreement with the data by authors under non-uniform heat fluxes and also by Benett et al. and Era et al. under uniform heat fluxes.

3. Two kinds of approximate analysis using equilibrium fluid conditions at a dryout point have been deduced by simplifing the exact analysis. These solutions were in good agreement with the data by authors, Bennett, et al. and Era, et al.

4. The parameter F which indicates the degree of the thermal nonequilibrium, has been obtained in the course of deducing the approximate analysis.

NOMENCLATURE

c_p : specific heat capacity, J/kg K

D_i, D_o : inside and outside diameter of a test tube, m

D_s : inside diameter of a shell

F : parameter defined by eq. (26) or eq. (31)

G : flow rate, kg/h

h : enthalpy, J/kg

h_{fg} : latent heat, J/kg

K : experimental constant in eq. (26)

κ : experimental constant in eq. (34)

$\dot{m}$: mass velocity, kg/m^2s

n : number of droplets $1/m^2s$

P_r : Prandtl number

p, p_r: pressure (MPa) and reduced pressure

$\dot{q}$, $\dot{q}_m$: local and mean heat flux on a inner surface of a test tube, w/m^2

$\dot{q}^* = \dot{q} / \dot{q}_m$

R_e : Reynolds number

S : slip ratio

T : temperature

T_{nb}, T_{ns} : sodium bulk temperature and outer wall temperature of a shell, °C

U : overall heat transfer rate, w/m^2K

w : velocity, m/s

x_e, x_a : equilibrium and nonequilibrium (actual) quality

x_0 : quality at the perfect evaporating point

z : axial distance from a dryout point, m

α : heat transfer coefficient, w/m^2K

α_{ne} : heat transfer coefficient assuming no evaporating after a dryout, w/m^2K

δ, δ_0 : droplet diameter and initial one at a dryout point, m

η : viscosity, kg/ms

λ, λ_M: heat conductivity and one of a tube metal, w/mK

ρ : mass density, kg/m^3

Subscript

d : dryout point

e : thermal equilibrium

f : average temperature of a tube inner surface and equilibrium fluid

fw : average temperature of a tube inner surface and nonequilibrium superheated steam

fδ : average temperature of saturated water and nonequilibrium superheated steam

ℓ : saturated liquid

m : mean from a dryout point to a tube outlet

n : sodium

s : saturated

sv : saturated steam

v : nonequilibrium superheated steam

w, v : from a tube inner surface to superheated steam

δ : droplet

δ, v : from superheated steam to a droplet

REFERENCES

(1) Groenevelt, D.C., Nucl. Engng. & Des., 32 (1975-3), 283.

(2) Forslund, R.P. and Rohsenow, W.M., Trans. ASME, Ser. C, 90 - 4 (1968 - 11), 399.

(3) Ganic, E.N. and Rohsenow, W.M., Int. J. Heat & Mass Transf., 20 (1977), 855.

(4) Bennett, A.W., Hewitt, G.F., Kearsey, H.A. and Keeys, R.K.F., AERE-R, 5373 (1967 - 10).

(5) Koizumi, Y., Ueda, T. and Tanaka, H., Int. J. Heat & Mass Transf., 22 (1979), 669.

(6) Dwyer, O.E., Nucl. Sci. & Engng., 17 (1963), 336.

(7) Baker, R.A. and Sesonske, A., Nucl. Sci. & Engng., 13 (1962), 283.

(8) Roko, K., Takitani, K., Yoshizaki, A. and Shiraha, M., Proc. 6th. Int. Heat Transf. Conf., Toronto (1978 - 8), 429.

(9) Mayinger, F. and Langner, H., Proc. 6th. Int. Heat Transf. Conf., Toronto (1978 - 8), 181.

(10) Bishop, A.A., WCAP - 2056, Pt. 3A, (1964 - 7)

(11) Frössling, Gerlands Beitr. Geophys., 52 (1938).

(12) Ahmad, S.Y., Trans. ASME, Ser. C, 92 - 4 (1970 -11), 595.

(13) Groenevelt, D.C. and Delorme, G.G.J., Nucl. Engng. & Des., 36 (1976-3) 17.

(14) Tong, L.S., Boiling Heat Transfer & Two Phase Flow, (1965), John-Wiley & Sons.

(15) Miropolskiy, Z.L., Teploenergetika, 1015 (1963), 49.

(16) Bishop, A. A., Sandberg, R.O., Tong, L.S., ASME Paper, No. 65-HT-31 (1965 - 9).

(17) Remizov, O.B., Teploenergetika, (1978 - 1), 16.

APPENDIX

1. Initial Droplet Diameter

Figs. A1 and A2 show the effect of an initial droplet diameter on an average and a local heat transfer coefficient, respectively. The heat transfer coefficient increases with decreasing the initial droplet diameter. The effect is more significant in high pressure than in low pressure. Table A1 shows the comparison of the droplet diameter calculated by existing correlations. Each calculated diameter decreases with increasing mass velocity and steam pressure, except by Ueda's correlation. But these values are largely different with each other. The calculated values by eqs. (22) and (23) are relatively large and close to the ones by Forslund - Rohsenow's, modified Nukiyama - Tanazawa's and Hinge's correlation.

2. Slip Ratio

The effect of slip ratio estimation on the predicted heat transfer coefficient is discussed below.

Force balance on droplets in the upward dispersed flow can be written as follows.

$$\frac{d\,w_\ell}{dt} = w_\ell \frac{d\,w_\ell}{dz} = \frac{3\,C_D \rho_v}{4\rho_\ell \delta} (w_v - w_\ell)^2 - g \qquad (A1)$$

where, C_D is a drag coefficient of droplets in steam and g is a gravitational constant.

Assuming that the acceleration of steam by evaporation of droplets is neglected, the correlation to a solid sphere can be used.

$$\begin{aligned} &0 < R_e \leq 2 \quad ; \quad C_D = 24 / R_e \\ &2 < R_e \leq 500 \; ; \quad C_D = 18.5 / Re^{0.6} \\ &R_e > 500 \quad ; \quad C_D = 0.44 \end{aligned} \qquad (A2)$$

where $R_e = (w_v - w_\ell)\, \rho_v \delta / \eta_v$

On the other hand, considering the acceleration of steam, Ingebo's correlation can be used.

$$C_D = 27 / R_e^{0.84} \tag{A3}$$

Fig. A3 and Table A2 show the effect of slip ratios on the local and the average heat transfer coefficients, respectively. Slip ratios have been estimated by using the equation of motion (eq. (A1)), Ahmad's correlation (eq. (18)) and nonslip assumption (S=1). Ingebo's correlation and the one for a solid sphere are used as the drag coefficient (C_D) in eq. (A1).

Slip ratio estimation gives a large influence on the predicted heat transfer coefficients. The difference among the predicted values increase with increasing steam pressure and mass velocity. The heat transfer coefficient predicted by using Ahmad's correlation as the slip ratio estimation lies between the ones by the equation of motion (eq. (A1)) using eq. (A2) and eq. (A3) as the drag coefficient.

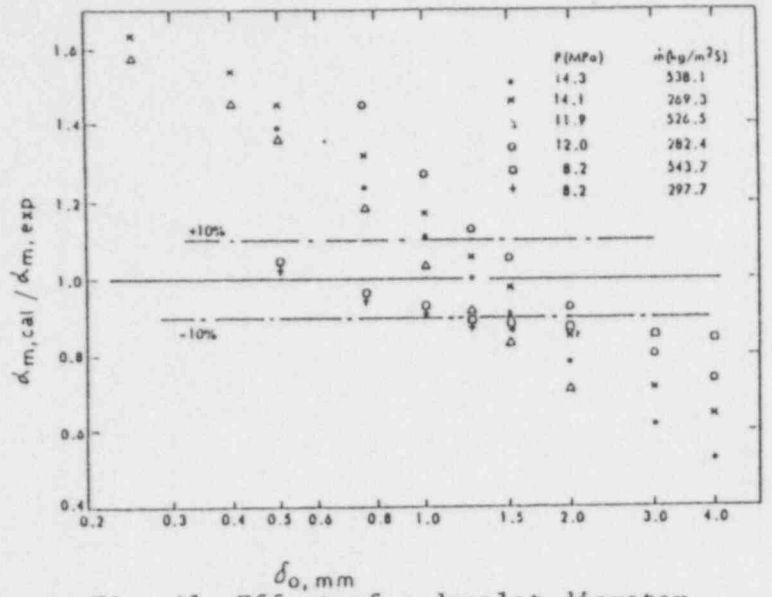

Fig. A1 Effect of a droplet diameter on an average heat transfer coefficient

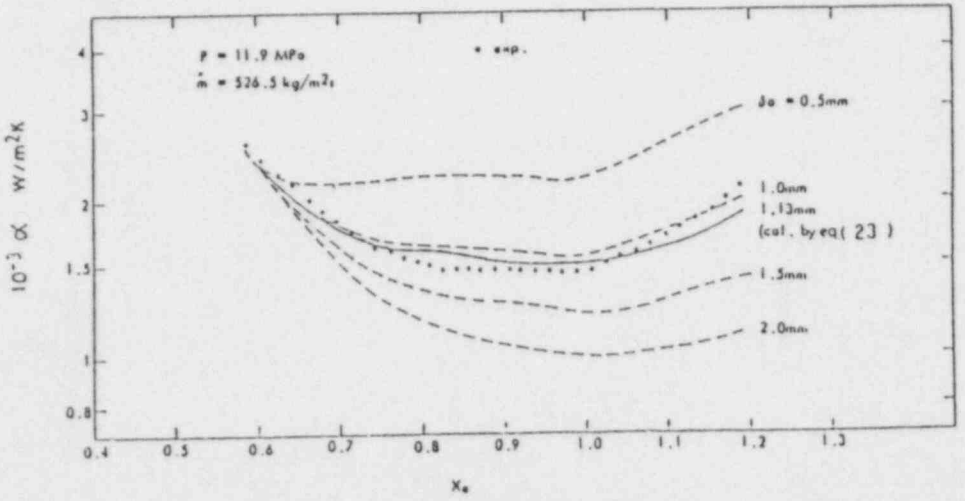

Fig. A2 Effect of a droplet diameter on a local heat transfer coefficient

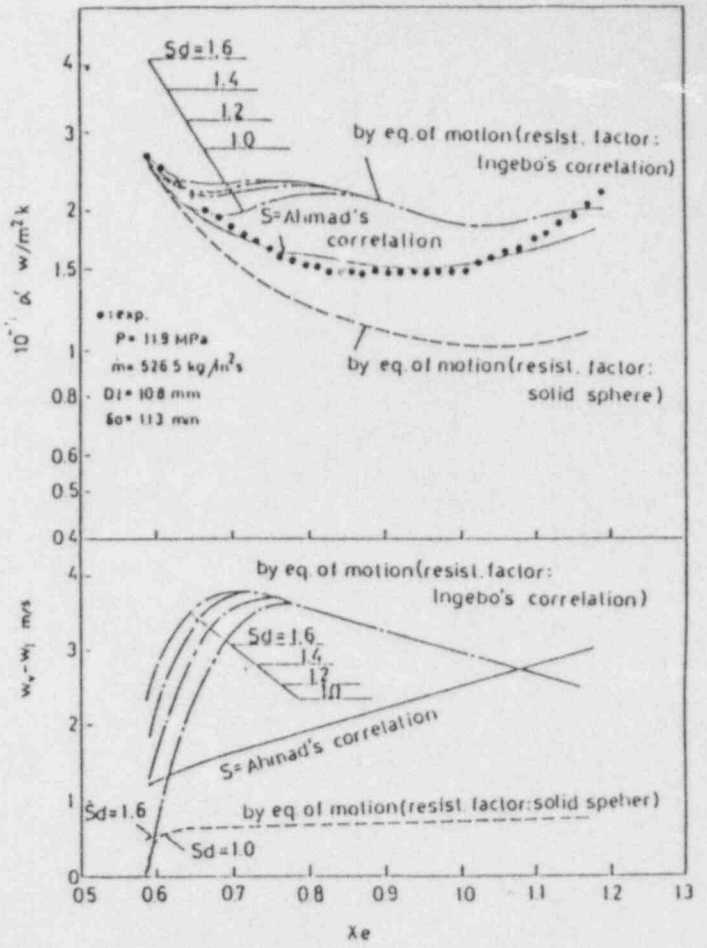

Fig. A3 Effect of slip ratio on a local heat transfer coefficient

Table A1 Comparison of droplet diameters calculated by existing correlations

Researchers	droplet dia. δ mm				References
	G = 250 kg/m^{2}S		500 kg/m^{2}S		
	p=7.8 bar	137 bar	7.8 bar	137 bar	
Calculated by eqs.(22)and(23)	1.54	1.74	0.85	1.23	This paper
Forslund & Rohsenow	0.727	2.25	0.220	0.998	(2)
Simp. Nukiyama & Tanazawa by Ganic & Rohsenow	1.38	3.72	0.757	2.48	(3)
Saha, et. al.	0.602	0.880	0.260	0.491	ASME paper, 77-HT-80(1978-8)
Cumo, et. al.	0.042	0.038	0.023	0.025	ASME paper, 73-HT-18(1978-8)
Ueda	0.045	0.0405	0.037	0.036	Bull. JSME, 22-171 (1979)
Tatterson, et al. (vol. mean)	0.121	0.137	0.070	0.097	A.I. Ch. E.J., 23-1 (1977)
ibid (length mean)	0.018	0.021	0.011	0.015	ibid
Modified Tatterson by Ueda	0.0997	0.139	0.081	0.121	Bull. JSME, 22-171 (1979)
Hinze (for Sudden acc.)	1.26	3.89	0.381	1.73	A.I. Ch. E.J., 1,289 (1955)
ibid (for Gradual acc.)	2.13	6.60	0.645	2.93	ibid
Bennett, et al.	P = 6.9 bar δ = 0.3 mm				(4)

Table A2 Effect of slip ratio on an average heat transfer coefficient

P bar	$\dot{m}$ kg/m^{2}s	$\alpha_{m,cal}/\alpha_{m,exp}$			
				by eq. of motion	
		S = Ahmad	S = 1.0	resist. fact. =solid sphere	resist. fact. =Ingebo
14.3	538.1	1.00	0.288	0.833	1.53
14.1	269.3	0.943	0.490	0.862	1.44
11.9	526.5	0.990	0.297	0.735	1.21
12.0	282.4	1.04	0.625	0.917	—
8.2	543.7	0.962	0.694	0.794	0.917
8.2	297.7	0.885	0.806	0.833	0.909

NUMERICAL FLUID DYNAMICS CALCULATIONS OF NONEQUILIBRIUM STEAM-WATER FLOWS WITH ENTRAINED DROPLETS*

by

K. A. Williams
Deputy Group Leader
Thermal Hydraulics Group

Energy Division
Los Alamos National Laboratory

ABSTRACT

An improved thermal-hydraulic modeling capability for the engineering analysis of nonequilibrium steam-water flows with entrained droplets has been developed. An efficient numerical fluid dynamics method was formulated that solves the conservation equations of a four-field model consisting of a vapor field, a continuous liquid field, and two dispersed droplet fields, (e.g., an annular flow situation with droplets being entrained from the liquid film). The numerical method advances a two-field (vapor/liquid) formulation for two-phase flows such that the additional field equations are efficiently solved without increasing the size of the matrix problem. Conservation equations for mass and momentum are included for two additional liquid fields to represent dispersed droplets of two different sizes. The thermal characteristics of the liquid phases are represented with a single energy equation; however, the interfacial heat transfer between the vapor and the three liquid fields is evaluated separately for each field based on its own surface area and heat transfer coefficient.

Also, interfacial surface area transport equations were solved for each droplet field resulting in an accurate calculation of the interfacial surface area as drops move through the Eulerian computational mesh.

Assessment of the present work concentrated on predicting the thermal-hydraulics of steam-water-droplet flows in a post-critical-heat-flux experimental test section with superheated walls. This work was shown to be in good agreement with experimental measurements of significant thermal nonequilibrium between the vapor and dispersed droplets. The tests analyzed covered a range of mass fluxes and wall heating rates but were all at low pressures where nonequilibrium effects are most pronounced. The present work predicted the vapor superheating in all tests to within an error range of -6.1% to +7.4%.

*Work performed under the auspices of the United States Nuclear Regulatory Commission.

NUMERICAL FLUID DYNAMICS CALCULATIONS OF NONEQUILIBRIUM STEAM-WATER FLOWS WITH ENTRAINED DROPLETS*

by

K. A. Williams
Deputy Group Leader
Thermal Hydraulics Group

Energy Division
Los Alamos National Laboratory

INTRODUCTION

Over the past decade there has been remarkable progress in the development and application of advanced numerical fluid dynamics methods for nuclear reactor safety issues. These so-called "advanced computer codes" model the two-phase thermal-hydraulic phenomena in a mechanistic manner accounting for nonequilibrium effects between the liquid and vapor phases.

In the context of the present work the term "nonequilibrium" implies that the vapor phase and the liquid phase may not be in thermal equilibrium with each other or with the local saturation temperature, and furthermore that relative motion may exist between these phases. For example, a boiling two-phase mixture in a heated channel may exist with the vapor significantly superheated while moving relative to saturated liquid droplets. Recent experimental results have demonstrated that vapor superheats of over 311^{o}C can exist even in highly dispersed droplet flows with low qualities [1].

*This work was performed under the auspices of the United States Nuclear Regulatory Commission.

The present work is concerned with the numerical fluid dynamics of such nonequilibrium steam-water flows with entrained droplets. Modeling a vapor field flowing with three liquid fields consisting of a continuous liquid film or pool and droplets of two different sizes is of primary concern. A method for extending a state-of-the-art numerical technique [2] to this objective is developed and assessed against experimental measurements of thermal nonequilibrium effects in a post-critical-heat-flux test facility [3,4,5].

PREVIOUS WORK

Previous work on modeling steam-water flows in which nonequilibrium effects are important can be grouped into two separate classes: numerical fluid dynamics codes and correlations.

Over the last decade there has been remarkable progress made in numerical modeling of two-phase flow. One of the early, and most significant, numerical techniques capable of describing the solution of fluid flow problems in which several fields interact with one another was the implicit, multifield (IMF) solution method of Harlow and Amsden [6]. Improvements to the IMF technique were made by Rivard and Torry [7]. An overview of multifluid flow calcuational methods has been conducted by Stewart [8]. He concluded that the semi-implicit method developed by Liles and Reed [2] is "the most coherent numerical technique for smooth two-phase flows". The overall philosophy behind the method is closely tied to the physics of flows. That is, during the iteration all the conservation equations for both phases are simultaneously updated, and both the thermal and caloric equations of state have already been included into the iteration. The present work extends this method from a two-field representation to a four-field model. However, this procedure results in the final matrix problem to be solved for the new time unknowns having the same size as in the two-field model. Therefore, the additional computational costs associated with the improved physics in the more detailed fluid dynamics are minimized.

A three-field model for general reactor safety analysis has been developed by Thurgood, et al. [9]. This approach is an extension of the method of Liles and Reed and considers a single droplet field.

Various workers have developed models that are specific to the case of dispersed droplet flows. These models have attempted to represent in a mechanistic way the thermal nonequilibrium of vapor-droplet flows. That is, they have accounted for the various paths of heat flow that can result in the superheating of the vapor phase. One of the earliest models was due to Laverty and Rohsenow who experimented with film boiling of liquid nitrogen [10]. Forslund and Rohsenow extended this work by including the effect of direct wall to droplet heat transfer [11]: a similar model was developed independently by Bennett, et al [12].

An early attempt to apply such nonequilibrium models to the prediction of heat transfer in nuclear fuel rods is due to Sun, Gonzalez-Santalo and Tien [13]. Their model included the combined effects of radiation and convective heat transfer to investigate the influence of droplet sizes on the calculated vapor superheating. Improvements to this approach were made by Wong and Hochrieter [14] for application to reflood heat transfer in pressurized water reactors.

To date the most complete model for dispersed droplet nonequilibrium flows is due to Moose and Ganic [15]. Their model is applicable to high vapor fraction dryout in vertical upflows. A single representative drop size was chosen to represent the effects of a detailed consideration to the droplet size distribution. The calculated results were compared to data for high pressure steam-water, nitrogen and Freon-12.

Several researchers have attempted to develop correlations capable of predicting the vapor superheat (or nonequilibrium quality) as a function of the initial and boundary conditions for a given system. The two most important efforts have been due to Groenveld and Delorme [16] and to Chen, Sundaram and Ozkaynak [5]. The empirical correlation of Grovenveld and Delorme is applicable only in the dry-wall region but has the correct asymptotic trends and may be extrapolated outside the range of data on which it is based. The correlation of Chen, et al. is more phenomenological in that it was developed on the basis of additive vapor and liquid heat transfer

mechanisms at the hot wall. A detailed model was considered for the heat transfer between the wall and liquid that represents liquid superheating, bubble nucleation and growth, and evaporation of the residual liquid film. These correlations predict heat flux, actual quality, and vapor temperature using known values of pressure, mass flow rate, equilibrium quality and wall temperature. However, Nijhawan, et al. show that such correlations cannot predict the wall heat flux to within an order of magnitude under some situations [3].

PRESENT WORK

The objective of the present work was to develop an improved thermal-hydraulic modeling capability for the engineering analysis of nonequilibrium steam-water flows with entrained droplets. An efficient numerical fluid dynamics method was formulated that solves the conservation equations for a four-field model consisting of a vapor field, a continuous liquid field, and two dispersed droplet fields, (e.g., an annular flow situation with droplets being entrained from the liquid film). Conservation equations for mass and momentum are included for two additional liquid fields to represent dispersed droplets of two different sizes. The philosophy is that the important thermal and hydraulic effects of a spectrum of drop sizes in a spray can be represented with two droplet groups. This is reasonable because most of the interfacial surface area is contained within the smaller diameter droplet group, and most of the mass is contained within the larger diameter droplet group. Within any computational mesh cell all three liquid fields exist at the same temperature and pressure. Thus, the thermal characteristics of the liquid phases can be represented with a single liquid energy equation; however, the interfacial heat transfer between the vapor and the three liquid fields is evaluated separately for each field based on its own surface area and heat transfer coefficient. The details of all aspects of the development and assessment of the present work are given in Ref. 17.

FIELD EQUATIONS AND MODELS

The field equations representing the conservation of mass, momentum, and energy in the present four-field model are the following:

Conservation of Mass

Vapor Field

$$\frac{\partial}{\partial t}(\alpha_v \rho_v) + \vec{\nabla}\cdot(\alpha_v \rho_v \vec{V}_v) = \Gamma \tag{1}$$

Continuous Liquid Field

$$\frac{\partial}{\partial t}(\alpha_\ell \rho_\ell) + \vec{\nabla}\cdot(\alpha_\ell \rho_\ell \vec{V}_\ell) = -(1-\eta_1-\eta_2)\Gamma - S \tag{2}$$

Droplet Field 1

$$\frac{\partial}{\partial t}(\alpha_{d1} \rho_\ell) + \vec{\nabla}\cdot(\alpha_{d1} \rho_\ell \vec{V}_{d1}) = -\eta_1\Gamma + S_1 \tag{3}$$

Droplet Field 2

$$\frac{\partial}{\partial t}(\alpha_{d2} \rho_\ell) + \vec{\nabla}\cdot(\alpha_{d2} \rho_\ell \vec{V}_{d2}) = -\eta_2\Gamma + S_2 \tag{4}$$

Conservation of Momentum

Vapor Field

$$\alpha_v \rho_v \frac{\partial \vec{V}_v}{\partial t} + \alpha_v \rho_v \vec{V}_v \cdot \vec{\nabla} \vec{V}_v = - \alpha_v \vec{\nabla} P - \vec{F}_{wv} - \vec{F}_{i,v\ell} - \vec{F}_{i,vd1} - \vec{F}_{i,vd2} + [\Gamma \vec{V}] + \alpha_v \rho_v \vec{g} \quad (5)$$

Continuous Liquid Field

$$\alpha_\ell \rho_\ell \frac{\partial \vec{V}_\ell}{\partial t} + \alpha_\ell \rho_\ell \vec{V}_\ell \cdot \vec{\nabla} \vec{V}_\ell = - \alpha_\ell \vec{\nabla} P - \vec{F}_{w\ell} - \vec{F}_{i,\ell v} - [\Gamma_\ell \vec{V}] - [S \vec{V}] + \alpha_\ell \rho_\ell \vec{g} \quad (6)$$

Droplet Liquid Field 1

$$\alpha_{d1} \rho_\ell \frac{\partial \vec{V}_{d1}}{\partial t} + \alpha_{d1} \rho_\ell \vec{V}_{d1} \cdot \vec{\nabla} \vec{V}_{d1} = - \alpha_{d1} \vec{\nabla} P - \vec{F}_{wd1} - \vec{F}_{i,d1v} - [\Gamma_{d1} \vec{V}] + [S_1 \vec{V}] + \alpha_{d1} \rho_\ell \vec{g} \quad (7)$$

Droplet Liquid Field 2

$$\alpha_{d2} \rho_\ell \frac{\partial \vec{V}_{d2}}{\partial t} + \alpha_{d2} \rho_\ell \vec{V}_{d2} \cdot \vec{\nabla} \vec{V}_{d2} = - \alpha_{d2} \vec{\nabla} P - \vec{F}_{wd2} - \vec{F}_{i,d2v} - [\Gamma_{d2} \vec{V}] + [S_{d2} \vec{V}] + \alpha_{d2} \rho_\ell \vec{g} \quad (8)$$

Conservation of Energy

Vapor Field

$$\frac{\partial}{\partial t}(\alpha_v \rho_v e_v) + \vec{\nabla}\cdot(\alpha_v \rho_v e_v \vec{V}_v) + P\vec{\nabla}\cdot(\alpha_v \vec{V}_v)$$

$$+ P\frac{\partial \alpha_v}{\partial t} = \dot{Q}_{wv} + \dot{Q}_{i,\ell v} + \dot{Q}_{i,d1v} + \dot{Q}_{i,d2v} + \Gamma h_{sat,v} \tag{9}$$

Total Liquid Fields

$$\frac{\partial}{\partial t}[(1-\alpha_v)\rho_\ell e_\ell] + \vec{\nabla}\cdot(\alpha_\ell \rho_\ell e_\ell \vec{V}_\ell) + \vec{\nabla}\cdot(\alpha_{d1}\rho_\ell e_\ell \vec{V}_{d1})$$

$$+ \vec{\nabla}\cdot(\alpha_{d2}\rho_\ell e_\ell \vec{V}_{d2}) + P\vec{\nabla}\cdot[\alpha_\ell \vec{V}_\ell + \alpha_{d1}\vec{V}_{d1} + \rho_{d2}\vec{V}_{d2}] \tag{10}$$

$$+ P\frac{\partial}{\partial t}(1-\alpha_v) = \dot{Q}_{w\ell} + \dot{Q}_{i,v\ell} + \dot{Q}_{i,vd1} + \dot{Q}_{i,vd2} - \Gamma h_{sat,\ell}$$

The above field equations describe only the conservation principles and do not describe the thermodynamic properties of the materials involved or the interfacial area transport. For the analysis to apply to a specific fluid it is necessary to specify the equations of state. It is assumed that there are general thermal and caloric equations of state of the form.

$$\rho_\ell = \rho_\ell(P, T_\ell) \tag{11}$$

$$\rho_v = \rho_v(P, T_v) \tag{12}$$

$$e_\ell = e_\ell(P, T_\ell) \tag{13}$$

$$e_v = e_v(P, T_v) \tag{14}$$

We also have the continuity consideration that the volume fractions of all phases must sum to unity.

$$\alpha_v + \alpha_\ell + \alpha_{d1} + \alpha_{d2} = 1 \tag{15}$$

$$(1-\alpha_v) = \text{total liquid volume fraction} \tag{16}$$

Accurately modeling the thermal and hydraulic characteristics of a size distribution of droplets was an important consideration in the present work. Therefore, the following interfacial surface area transport equations were solved for each droplet field.

$$\frac{\partial A_{i,d1}}{\partial t} + \vec{\nabla}\cdot(A_{i,d1}\vec{V}_{d1}) = \frac{6S_1}{\rho_\ell D_{d1}} - S_{T,d1} \tag{17}$$

(18)

$$\frac{\partial A_{i,d2}}{\partial t} + \vec{\nabla}\cdot(A_{i,d2}\vec{V}_{d2}) = \frac{6S_2}{\rho_\ell D_{d2}} - S_{T,d2}$$

This modeling approach results in an accurate calculation of the interfacial surface area as drops move through the Eulerian computational mesh. Models for the droplet volume mean diameter, upper-log-normal size distribution function, and entrainment rates developed by Ishii, et al. from air-water data were adapted to the present work [18,19]. The droplet size distribution was correlated in terms of the volume fraction oversize (Δ), defined as the volume fraction of the droplets having a diameter larger than D. Their correlation is,

$$\frac{d\Delta}{dy} = -\frac{0.884}{\sqrt{\pi}} e^{-0.781y^2} \tag{19}$$

with

$$y = \ln\left(\frac{2.13D}{D_{max}-D}\right) \tag{20}$$

The authors also developed a correlation for the volume mean diameter, D_{vm}, of the spray. At a diameter of D_{vm} there are an equal volume of droplets at diameters above and below D_{vm}. That is, D_{vm} is the droplet diameter corresponding to a volume fraction oversize of 0.5. Their correlation for the volume mean diameter in terms of the flow properties is,

$$D_{vm} = 0.0099\frac{\sigma}{\rho_g j_g^2} R_{e_g}^{2/3}\left(\frac{\rho_g}{\rho_\ell}\right)^{-1/3}\left(\frac{\mu_g}{\mu_\ell}\right)^{2/3} \tag{21}$$

where j_g is the gas volumetric flux (superficial velocity). With the above distribution it can be shown that,

$$\frac{D_{max}}{D_{vm}} = 3.13 \tag{22}$$

The interfacial drag between the vapor and the two droplet fields uses a C_D type drag relationship for a solid sphere with the Reynolds number based on the relative velocity between the vapor and each droplet. The interfacial drag between the vapor and continuous liquid for annular flow is given by Wallis' model [20].

The interfacial heat transfer coefficient is based on a Nusselt type correlation for steam-water flows due to Lee and Riley [21],

$$h_{iv} = \frac{k_v}{D_d} Nu_v = \frac{k_v}{D_d} [2 + 0.74 R_e^{0.5} P_r^{1/3}] \tag{23}$$

The Reynolds number is based on the relative velocity between the vapor and each droplet phase. The interfacial area per unit volume A_i comes directly from the interfacial area transport equations. For spherical droplets the following relationship must hold at any point,

$$A_i = \frac{6\alpha_d}{D_d} \tag{24}$$

In dispersed flows with heated walls the surface temperature is normally above the minimum stable film boiling temperature. However, some heat transfer directly from the wall to the droplets can occur due to collisions between the drops and the wall. The heat transfer in this regime is very difficult to model and has been the subject of numerous investigations. The model of Forslund and Rohsenow is used in the present work [22].

The field equations and constitutive models of the present work have now been presented. The finite-different representation of these equations and the numerical solution procedure is given in Ref. 17. The numerics are a direct extension of the method of Liles and Reed [2]. The algebraic

difference equations are first-order accurate in space and time and are differenced over a staggered mesh. The resulting set of nonlinear equations are solved at each time step by a Newton iteration procedure. The important result here is that the number of linearized equations to be solved at each iteration are the same in the present four-field model as in a two-field formulation. At each computational mesh cell we obtained a set of four linearized equations involving the four unknowns P, α, T_ℓ and T_v of that mesh cell and the pressures of the six adjacent cells. These equations can be written in matrix from as,

$$\begin{bmatrix} x & x & x & x \\ x & x & x & x \\ x & x & x & x \\ x & x & x & x \end{bmatrix} \begin{bmatrix} P \\ \alpha \\ T_v \\ T_\ell \end{bmatrix} + \begin{bmatrix} x & x & x & x & x & x \\ x & x & x & x & x & x \\ x & x & x & x & x & x \\ x & x & x & x & x & x \end{bmatrix} \begin{bmatrix} P_1 \\ P_2 \\ P_3 \\ P_4 \\ P_5 \\ P_6 \end{bmatrix} = \begin{bmatrix} x \\ x \\ x \\ x \end{bmatrix} \qquad (25)$$

where the subscripts 1-6 designate the six surrounding cells in three dimensions. This system can be put into a reduced form by multiplying through by the triangular decomposition of the 4 x 4 matrix. Then the first equation will involve only the cell pressure and its' six neighbors pressure. The remaining three equations then relate the vapor fraction and temperatures to the pressures. The full set of pressure equations for all mesh cells constitute a seven-striped linear algebraic system of equations for the pressure in all mesh cells. An important property of this reduced pressure formulation is its diagonal dominance. All coupling between the mesh cells is expressed in the pressure equations matrix. It is emphasized that the above process can be carried out in one mesh cell at a time, storing only the 28 quantities per mesh cell that appear as X's in the 4 x 6 matrix and the right

hand side of Eq. 25. These coefficients must be retained so that T_ℓ, T_v, and α can be found from a back-substitution after the pressures have been determined from the pressure iteration.

The size of the matrix problem in a four-field model does not increase because of two reasons. First, although there are now four velocities, the momentum equations are used to eliminate new-time velocities in favor of new-time pressures. Secondly, all three liquid fields exist at the same temperature and pressure at any location and a single liquid energy equation can be used. The two additional mass conservation equations can be solved for the new-time droplet volume fractions at the end of an iteration since all unknowns in these equations have been determined. Thus, any additional computational costs associated with doubling the number of fields has been minimized. Computer timing studies show that the present four-field model requires only a 15-17 percent increase over the two-field model in computation time per mesh cell per time step.

ASSESSMENT

Assessment of the present work concentrated on predicting the thermal-hydraulics of steam-water-droplet flows in a post-critical-heat-flux experimental test section with superheated walls. Until recently such data have been particularly lacking for post-CHF flows at low pressures, low flow rates and low qualities where nonequilibirum effects are most pronounced. This is because measurement of the vapor temperature in dispersed droplet flows is extremely difficult. Any temperature sensor will tend to be quenched by the entrained liquid droplets which are near the local saturation temperature, therefore preventing detection of vapor superheating. Also, radiation heat transfer from the high temperature walls can introduce measurement errors.

Such experimental measurements have recently been taken at Lehigh University [3,4,5] in a forced convection boiling two-phase experimental test facility shown in Fig. 1. The test section for post-CHF flows consists of a vertical heated channel of Inconel-600 that is 150 cm in length with a 1.41 cm inside

diameter tube. The test section is located above a "hot patch" designed to ensure post-CHF flow conditions. Wall temperature measurements are provided at 7.5 cm intervals along the test section. Joule heating of the tube is supplied by direct current through the walls using a variable d-c power supply of 30 kW. The vapor superheat probe is located 130 cm above the inlet to the copper hot patch.

The tests performed at Lehigh University covered a range of operating conditions. Three specific tests were selected for assessment of the present work. These tests were chosen in concert with the experimenters to cover important operating ranges in which there was very reliable data [23]. The experimental tests are,

Test 138: High inlet quality, intermediate mass flux, intermediate power.

Test 134: High inlet quality, intermediate mass flux, high power.

Test 50: Low inlet quality, low mass flux, low power.

The operating conditions for these three experiments are summarized in Table I. In all tests there is the substantial nonequilibrium effect of vapor superheating by roughly 280°C-350°C. This nonequilibirum effect can be clearly seen by comparing the change in equilibrium quality to the change in actual quality. For test 138 the actual change in quality was only 0.064 while the equilibrium value was 0.233. The ratio of the two quality changes is termed by Chen as the "heat-partition ratio" (R_Q) and measures the fraction of total wall heat transfer that went into evaporating the liquid phase. Thus, R_Q varies from zero for complete lack of thermodynamic equilibrium to one for complete equilibrium. In test 138 the R_Q is 0.27, in test 134 the R_Q is 0.32 and in test 50 the R_Q is 0.62.

Test 134 is a parametric variation on wall heat flux relative to test 138. The total power was increased by 31 percent, however the vapor superheating only increased by 12 percent. The vapor velocity in the test section for these two tests is quite high producing significant entrainment. The thermal-hydraulic conditions of test 50 are much different from those of test 138 and 134. The low inlet quality, mass flux and power result in very low vapor velocities producing much less entrainment.

A one-dimensional input model of the Lehigh Univesity facility used in the present numerical calculations is shown in Fig. 2. There are a total of twelve (12) computational mesh cells over a total length of 1.806 meters. The flow area is 1.5617×10^{-4} m^2 with a hydraulic diameter of 1.41 centimeters. Boundary conditions are supplied at the first and last mesh cells. Inlet mass flux and steam-water volume fractions are specified at cell number 1, the inlet plenum. Test section pressure is imposed at cell number 12, the outlet plenum. The heated test section extends from mesh cells 2 through 11 for a total length of 1.456 meters. Cell 2 represents the high thermal inertia hot patch. As shown in Fig. 2, the experimental location of zero (0.0 m) elevation corresponds to the beginning of cell 2 which in the model has an absolute elevation of 0.20 meters. Vapor probe data from the experiment are to be compared with computed parameters of mesh cell 10: this corresponds to a heated length above the inlet of 1.306 meters.

The calculated vapor temperature as a function of heated length in test 138 is shown in Fig. 3. On all such figures the test section inlet (bottom of hot patch) corresponds to 0.2 m, as discussed above. The vapor probes experimental result of 692 K is seen to be in satisfactory agreement with the calculated value of 657 K. Experimentally this corresponds to a nonequilibrium superheated state of 279°C. The calculated vapor superheat is 262°C, for a relative error of -6.1 percent.

In Fig. 4 experimental wall temperature mesurements (chained line) along the heated test section are compared to the calculated wall surface temperatures (solid line). The wall temperature drops about 75°C just downstream of the hot patch in both the data and the calculation due to a reduction in the linear heating rate in the test section. Along the test section the wall temperatures vary from about 650 K to 900 K. The calculated surface temperature is in close agreement with the data along the first half of the test section and then begins to exceed the data by roughly 75°C for the last half. However, it is very important to note that the axial variation of power being input to the steam-water flow in the calculations is in exact agreement with the expermental boundary conditions. That is, the total wall heat flux into the mixture is correct at all elevations. Any deviation in

wall temperature between the data and calculation arises from errors in the heat transfer coefficients and/or fluid conditions and not from the heat flux boundary conditions.

Calculated vapor volume fraction as a function of height is shown in Fig. 5 to increase rapdily downstream of the hot patch due to entrainent and boiling of the liquid film. Droplet field 1 (larger diameter drops) volume fraction and droplet field 2 (smaller diameter drops) are compared in Fig. 6. Both droplet fields have a rapidly increasing volume fraction near the hot patch due to entrainment of the liquid film; the droplet volume fractions then decrease as a result of evaporation and acceleration with the vapor flow.

The calculated vapor axial velocity profile is shown in Fig. 7 to increase from 11 m/s at the inlet to almost 20 m/s at the outlet. The vapor velocity is continuously increasing due to a relatively constant vapor generation rate from the evaporation of the liquid droplets and from heating of the vapor. Droplet velocities are compared in Fig. 8. At the test section exit the smaller drops are moving at 8 m/s while the larger drops have a velocity of 4.5 m/s; thus there is a substantial relative velocity between the vapor field and the droplets even at the end of the heated length.

The relative partitioning of heat flow from the wall into the four fields can be evaluated from the numerical calculation. The product of interfacial heat transfer coefficient and surface area (hA) for both droplet groups is shown in Fig. 9. From this figure it can be seen that the smaller droplet field contributes almost three times the interfacial heat flow as does the larger drop field. This effect was not unexpected and is part of the original motivation for having two droplet fields. The heat flow paths from the wall into the vapor and liquid fields at the elevation of the vapor probe are shown in Fig. 10. It can be seen that three-fourths of the wall heat flux is delivered directly to the vapor phase. One-fourth of the energy flow is absorbed directly by the droplets as a result of collisions with the wall. However, this wall-to-droplet energy transport mechansim is responsible for the majority of the evaporation of the liquid phase since the interfacial flow of energy from the superheated vapor is very small. Even with the vapor superheated by 244^{o}C the interfacial heat transfer amounts to only 8 percent of the wall heat flux.

This surprising finding of poor interfacial heat transfer between the superheated vapor and saturated droplets is responsible for the large nonequilibrium effects in these post-CHF experiments. To better understand why this occurs it is necessary to analyze the interfacial surface areaconcentrations of the droplets; these are shown in Fig. 11 to vary from 2 to 20 m^2/m^3. The "area concentration of the wall" is a useful comparison to obtain an appreciation of the magnitude of these numbers.

$$A_{i,wall} = \frac{\pi D \cdot L}{\frac{\pi D^2}{4} \cdot L} = 4/D \qquad (26)$$

For this test section with a hydraulic diameter of 1.41 cm the wall surface area concentration is 284 m^2/m^3. Thus, the effective surface area of the droplets along the heated length is an order of magnitude less that the wall itself. This then is the reason for the low interphase heat transfer that produces the high nonequilibrium state.

Test number 134 was performed at conditions very near those of test 138 with the exception of the wall heating rate (total power). This test is therefore useful for assessing the ability of the present work to correctly predict the parametric effects of varying only the wall heat flux. The power input to the mixture was increased 31 percent from test 138 to test 134; however, the vapor superheat only increased by 12 percent. The calculated vapor temperature as a function of heated length is shown in Fig. 12. It can be seen that the calculated and measured vapor superheats at the probe elevation are in very good agreement. The experimental vapor temperature is superheated by 312°C while the present work predicts 321°C for a relative error of +2.9 percent.

The operating conditions of test number 50 make it completely different in a thermal-hydraulic standpoint from tests 134 and 138. The major difference is that the inlet quality is very low at 6.6 percent corresponding to an inlet vapor volume fraction of 96.98 percent. Thus the liquid volume fraction has been increased by a factor of 20 from the high quality tests 138 and 134. Additionally, the mass flux and power have both been reduced which produces an inlet vapor velocity almost an order of magnitude lower than the other two tests. Indeed the vapor velocity of only 2-3 m/s is not sufficient to entrain the liquid film in a continuous manner.

The calculated vapor temperature profile is shown in Fig. 13. The experimental vapor probe measured a vapor superheat of 350°C and the present work predicted a value of 375°C for a relative error of +7.4 percent. However, the high superheating in this test has arisen from a very low entrainment at its' operating conditions and not from a low interfacial heat transfer as in tests 134/138.

The numerical calculations of tests 134, 138, and 50 discussed above were all performed using exactly the same code. The assessment study would not be complete however without conducting a sensitivity study. The two items of primary concern are the nodalization of the input model and the choice of the "free parameter" D/D_{vm} serving as the dividing point between the two droplet fields.

Nodalization sensitivity is addressed by modifying the input model so that the length of cells downstream of the hot patch were doubled from the base value of 15 to 30 centimeters. The high quality, high power test 134 was recalculated using this coarse node input model. The calculated vapor superheat was then 322°C as compared to the base case value of 321°C. Thus the computed results for this test are essentially unchanged by the choice of a different nodalization for the input model.

The free parameter of the present four-field model is the selection of D/D_{vm} that is used to partition surface area and mass between the two droplet fields. In the above calculations this parameter was set at 1.0 for a base value. This produces a 50-50 distribution of mass into the two droplet fields, but 77 percent of the total surface area is associated with the smaller droplet field. A value of $D/D_{vm} = 0.4$ was chosen for the sensitivity study. This choice results in only 7 percent of the entrained mass going to the smaller droplets but this field still contains 22 percent of the total droplet interfacial surface area. Test number 134 was recalculated with only this change. A vapor superheat of 323°C was now obtained which is only slightly different from the 321°C obtained in the base case calculation. The model is therefore relatively insensitive to the free parameter choice of D/D_{vm} for this case in which all of the liquid film has been entrained. A greater sensitivity may occur under conditions of lower vapor velocity where only the small droplets are entrained.

SUMMARY

The present work has developed a computational fluid dynamics formulation that efficiently solves the conservation laws for a vapor field, a continuous liquid field, and two dispersed droplet fields. The thermal-hydraulic effects resulting from the exchange of mass, momentum and energy between the vapor and the dispersed droplet phases has been accurately modeled. This work is an advancement of the state-of-the-art for engineering analyses of nonequilibrium steam-water-droplet flows in heated channels. It is particularly applicable for boiling steam-water flows in which it is important to represent the effects of significant thermal nonequilibrium between the vapor and the liquid phase. This work was shown to be in good agreement with unique experimental measurements of significant thermal nonequilibrium between the vapor and dispersed droplets. The tests analyzed covered a range of mass fluxes and wall heating rates, and were all at low pressures where nonequilibrium effects are most pronounced.

REFERENCES

1. Nijhawan, S., Chen, J. C., Sundaram, R. K., and London, E. J., "Measurement of Vapor Superheat in Post-Critical-Heat-Flux Boiling," J. Heat Transfer, Vol. 102, August (1980).

2. Liles, D. R., and Reed, Wm. H., "A Semi-Implicit Method for Two-Phase Fluid Dynamics," J. Computational Physics 26, pp 390-407 (1978).

3. Nijhawan, S., Chen, J. C., and Sundaram, R. K., "Parametric Effects on Vapor Nonequilibrium in Post-Dryout Heat Transfer," ASME Paper 80-WA/HT-50, July (1980).

4. Evans, D., Webb, S., Chen, J. C., and Neti, S., "Experimental Data for Nonequilibrium Post-CHF Heat Transfer in a Vertical Tube," Tenth Water Reactor Safety Research Information Meeting, NUREG/CP-0041, Vol. 1, October (1982).

5. Chen, J. C., Sundaram, R. K., and Ozkaynak, F. T., "A Phenomenological Correlation for Post-CHF Heat Transfer," USNRC Report NUREG-0237, June (1977).

6. Amsden, A. A., and Harlow, F. H., "KACHINA: An Eulerian Computer Program for Multifield Fluid Flows," Los Alamos Scientific Laboratory Report LA-5680, Los Alamos, NM (1974).

7. Rivard, W. C., and Torrey, M. D., "K-FIX: A Computer Program for Transient Two-Dimensional, Two-Fluid Flow," Los Alamos Scientific Laboratory report LA-NUREG-6623, Los Alamos, NM (1976).

8. Stewart, H. Bruce, "Overview of Multifluid Flow Calculation Methods," presented at Army Research Office Workshop on Multiphase Flow, Aberdeen Proving Ground, Maryland, February 2-4, (1981).

9. Thurgood, M. J., Kelly, J. M., Basehore, K. L., and George, T. L., "COBRA-TF: A Three-Field Two-Fluid Model for Reactor Safety Analysis," 19th National Heat Transfer Conference, Orlando, Florida, July 27-30, (1980).

10. Laverty, W. F. and Rohsenow, W. M., "Film Boiling of Saturated Liquid Nitrogen Flowing in a Vertical Tube," J. Heat Trans. 89, pp 90-98 (1964).

11. Forslund, R. P. and Rohsenow, W. M., "Dispersed Flow Film Boiling," ASME Paper No. 68-HT-44 (1968).

12. Bennett, A. W., Hewitt, G. F., Kearsey, H. A., and Keeys, R. K. F., "Heat Transfer to Steam Water Mixtures Flowing in Uniformly Heated Tubes in which the Critical Heat Flux has been Exceeded," Report No. AERE-R 5373 Harwell Laboratory (1967).

13. Sun, K. H., Gonzalez-Santalo, J. M., and Tien, C. L., "Calculations of Combined Radiation and Convective Heat Transfer in Rod Bundles Under Emergency Cooling Condtions," J. Heat Transfer, pp. 414-420, August (1976).

14. Wong, S. and Hochreiter, L. E., "A Model for Dispersed Flow Heat Transfer During Reflood," 19th Nat. Heat Transfer Conference, Orlando, FL, July 27-30 (1980).

15. Moose, R. A. and Ganic, E. N., "On the Calculation of Wall Temperatures in the Post Dryout Heat Transfer Regime," Int. J. Multiphase Flow, 8, No., pp. 525-542 (1982).

16. Groeneveld, D. C. and Delorme, G. G. J., "Prediction of Thermal Nonequilibrium in the Post-dryout Regime," Nuclear Engineering and Design, 36, pp. 17-26 (1976).

17. Williams, K. A., "Numerical Fluid Dynamics of Nonequilibrium Steam-Water Flows with Droplets," Ph.D. Dissertation, The University of New Mexico. May 1983.

18. Ishii, M. and Mishima, K., "Correlation for Liquid Entrainment in Annular Two-Phase Flow of Low Viscous Fluid," Argonne National Laboratory Report ANL/RAS/LWR 81-2 March (1981). Also published as NUREG/CR-2885.

19. Kataoka, I., Ishii, M., and Mishima, K., "Generation and Size Distribution of Droplets in Gas-Liquid Annular Two-Phase Flow," Argonne National Laboratory Report ANL/NAS/LWR 81-3 September (1981).

20. Wallis, G. B., One-Dimensional Two-Phase Flow, McGraw-Hill, New York (1969).

21. Lee, K. and Riley, D. J., "The Evaporation of Water Droplets in Superheated Steam," J. Heat Transfer, November (1966).

22. Forslund, R. P. and Rohsenow, W. M., "Dispersed Flow Film Boiling." J. Heat Transfer, Vol. 90, No. 6 (1968).

23. Private Communications, Professor J. Chen, Lehigh University.

NOMENCLATURE

Symbols

A_i	interfacial surface area per unit volume.
C_D	drag coefficient
D	diameter
D_H	hydraulic diameters.
e	specific internal energy.
$\vec{F}$	momentum drag vector.
$\vec{g}$	gravity field.
h	heat transfer coefficient.
$\hbar$	fluid enthalpy.
j	superficial velocity
k	thermal conductivity.
Nu	Nusselt number.
p	pressure.
Pr	Prandtl number
$\dot{Q}$	total rate of heat transfer.
Re	Reynolds number
S	total mass transfer rate due to liquid film entrainment.
S_1, S_2	mass transfer rate due entrainment of droplet field 1, field 2.
S_Γ	rate of interfacial surface area concentration (A_i) due to phase change.
t	time.
T	temperature.
x	quality
μ	fluid viscosity
Δ	droplet volume fraction oversize.
σ	surface tension.
ρ	density.
α_k	volume fraction of phase k.
Γ	total vapor generation rate from phase change
η_1, η_2	fraction of total phase change produced by droplet field 1, field 2.

Symbols and Operators

$\nabla\cdot$	divergence operator.
∇	gradient operator.

Subscript and Superscript

d,D,d1,d2	drop phase.
i	interface.
r	relative
s	saturation
v	vapor phase
w	wall
ℓ	liquid phase.

Table I. Summary of Lehigh University Post-CHF Tests

Test Number	P (bar)	G (kg/s-m²)	Q (kw/m²)	$x_{e,o}$ (%)	$x_{e,L}$ (%)	$x_{e,a}$ (%)	$\frac{\Delta x_a}{\Delta x_e}$	Tv,data (K)	Tv,calculation (K)
138	3.6	37.33	49.32	55.8	79.1	62.2	0.27	692	657
134	3.5	37.35	64.73	57.4	87.1	66.8	0.32	725	734
50	3.8	29.94	23.39	6.6	19.4	14.5	0.62	764	785

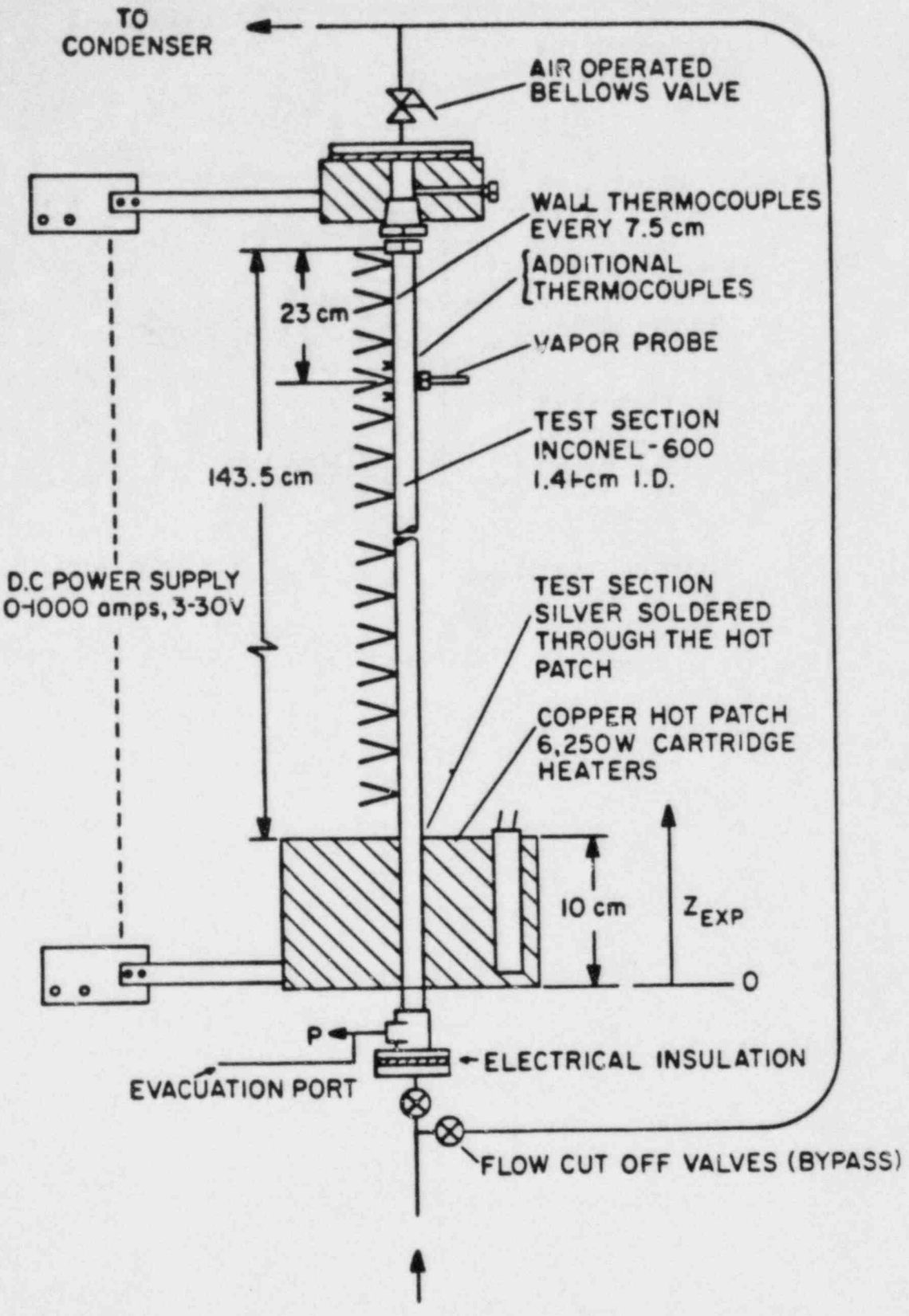

Fig. 1. Lehigh University experimental test facility for post-CHF heat transfer.

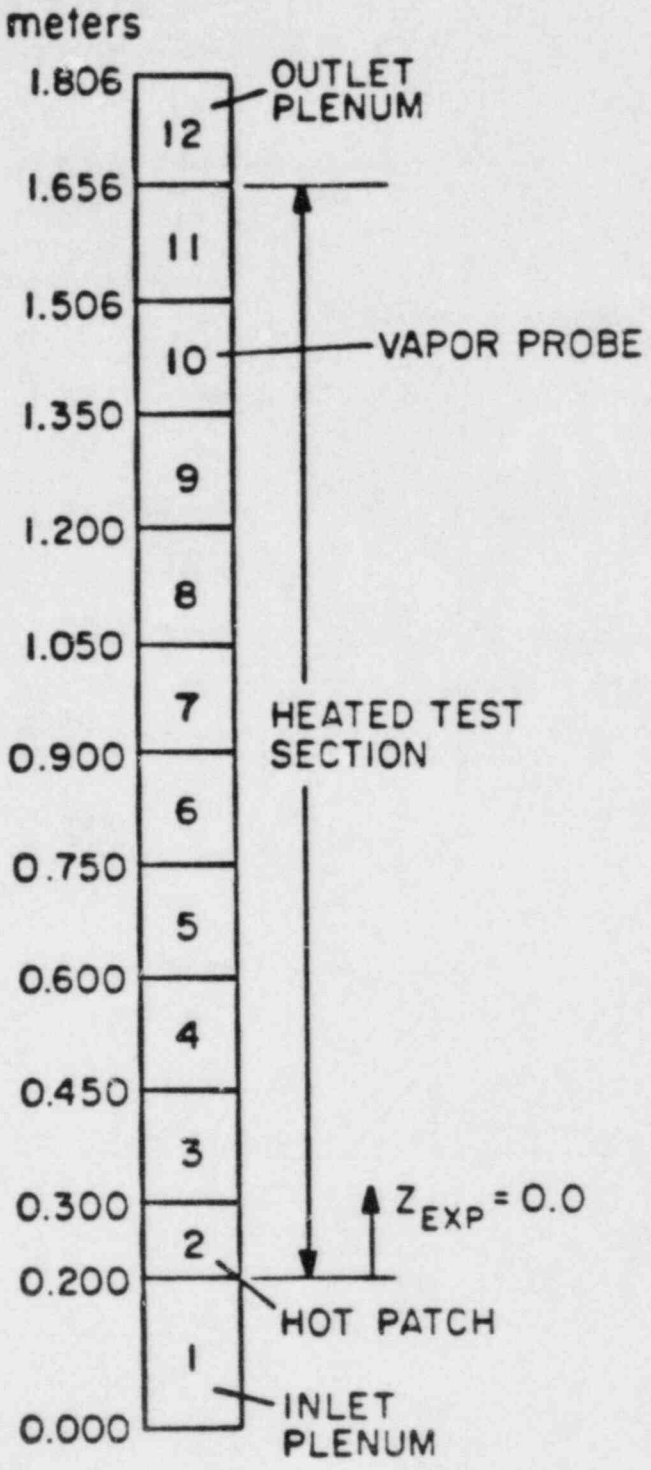

Fig. 2. Input model of the Lehigh University experimental test facility.

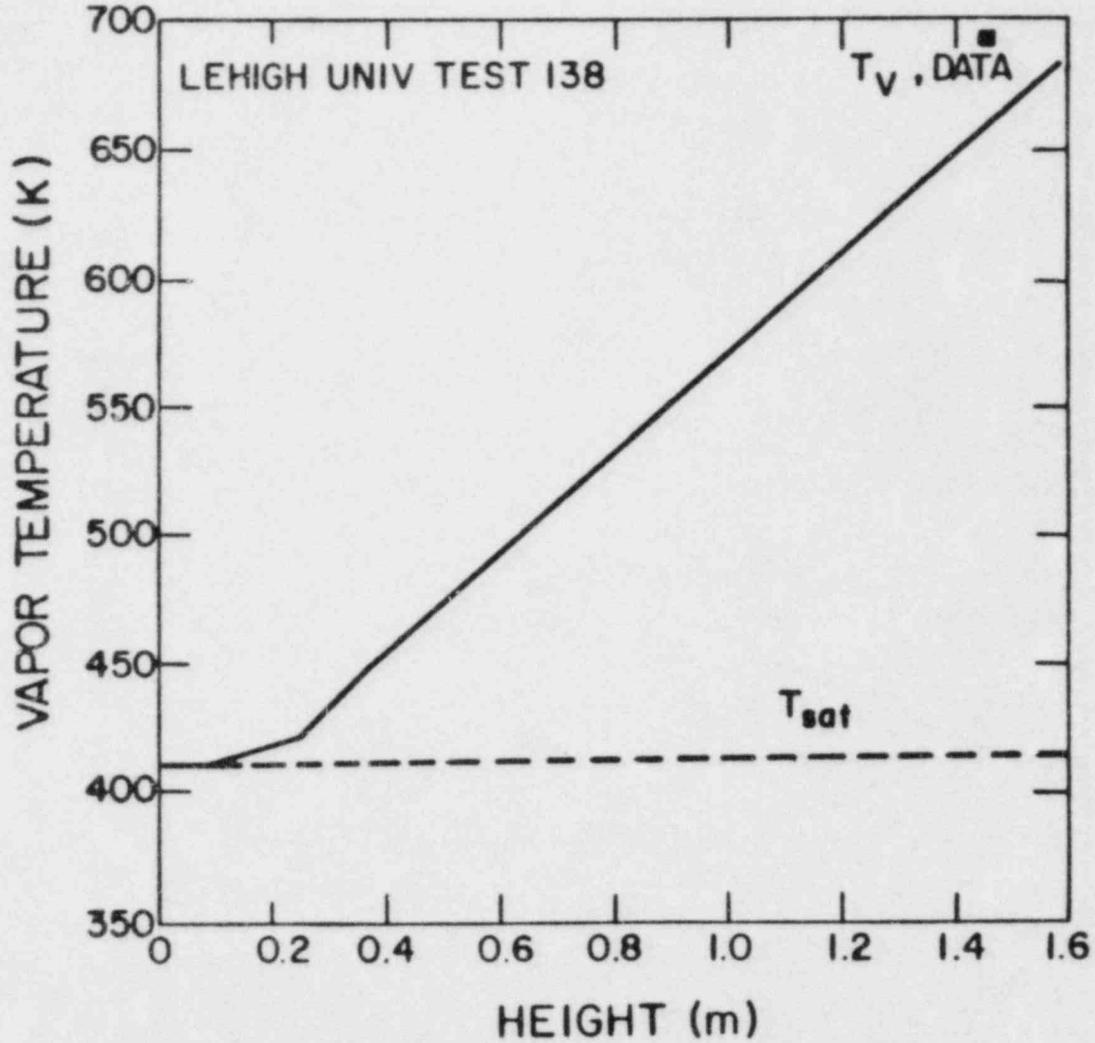

Fig. 3. Comparison between calculated and measured vapor temperature for test 138.

Fig. 4. Comparison between calculated and measured wall temperature for test 138.

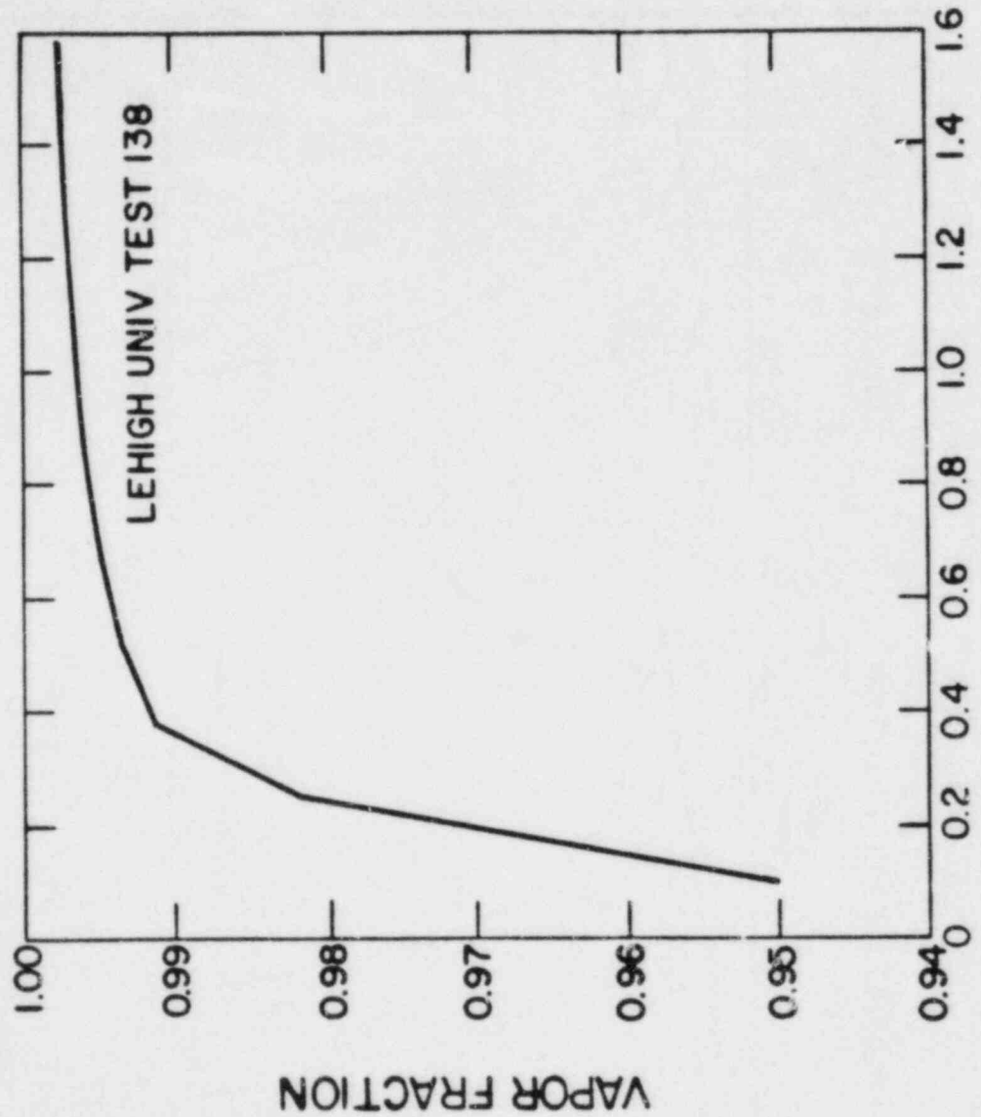

Fig. 5. Calculated vapor volume fraction versus heated length for test 138.

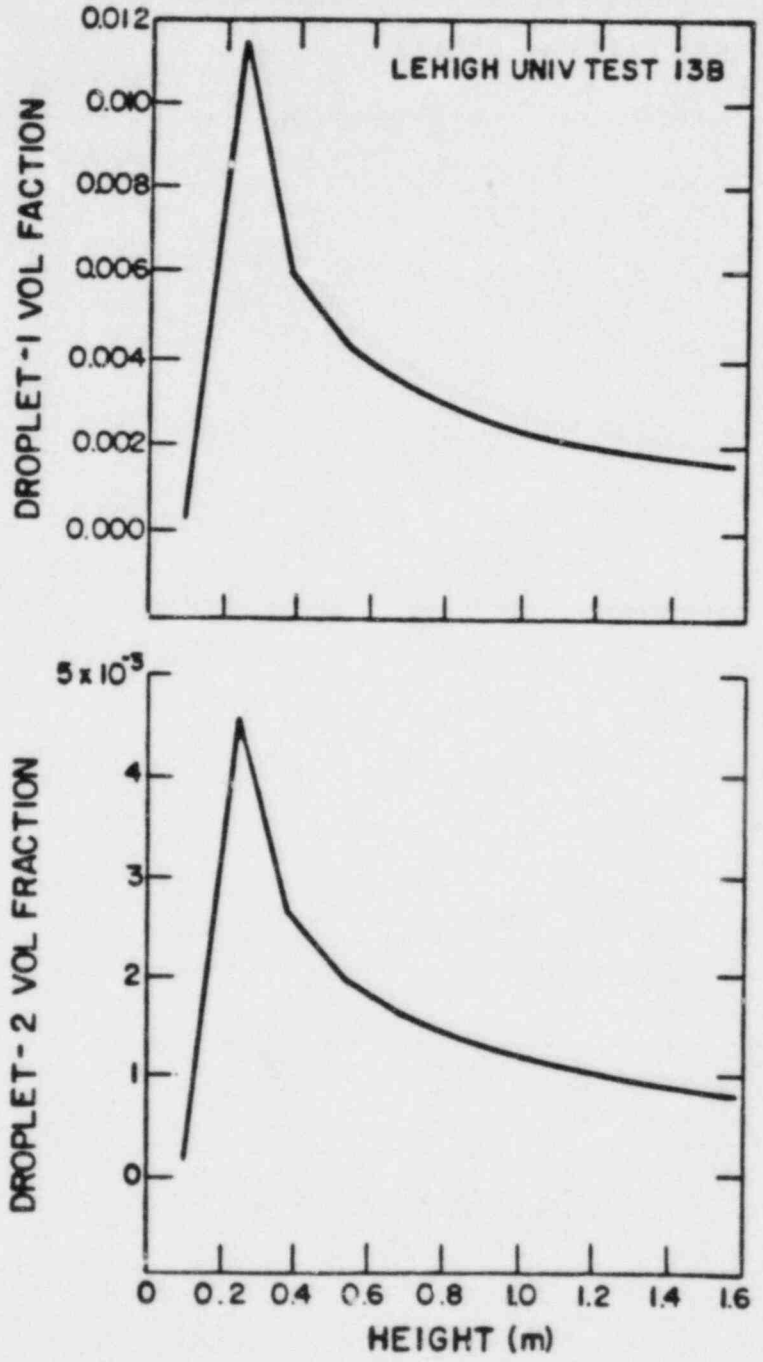

Fig. 6. Calculated droplet fields volume fraction versus heated length for test 138.

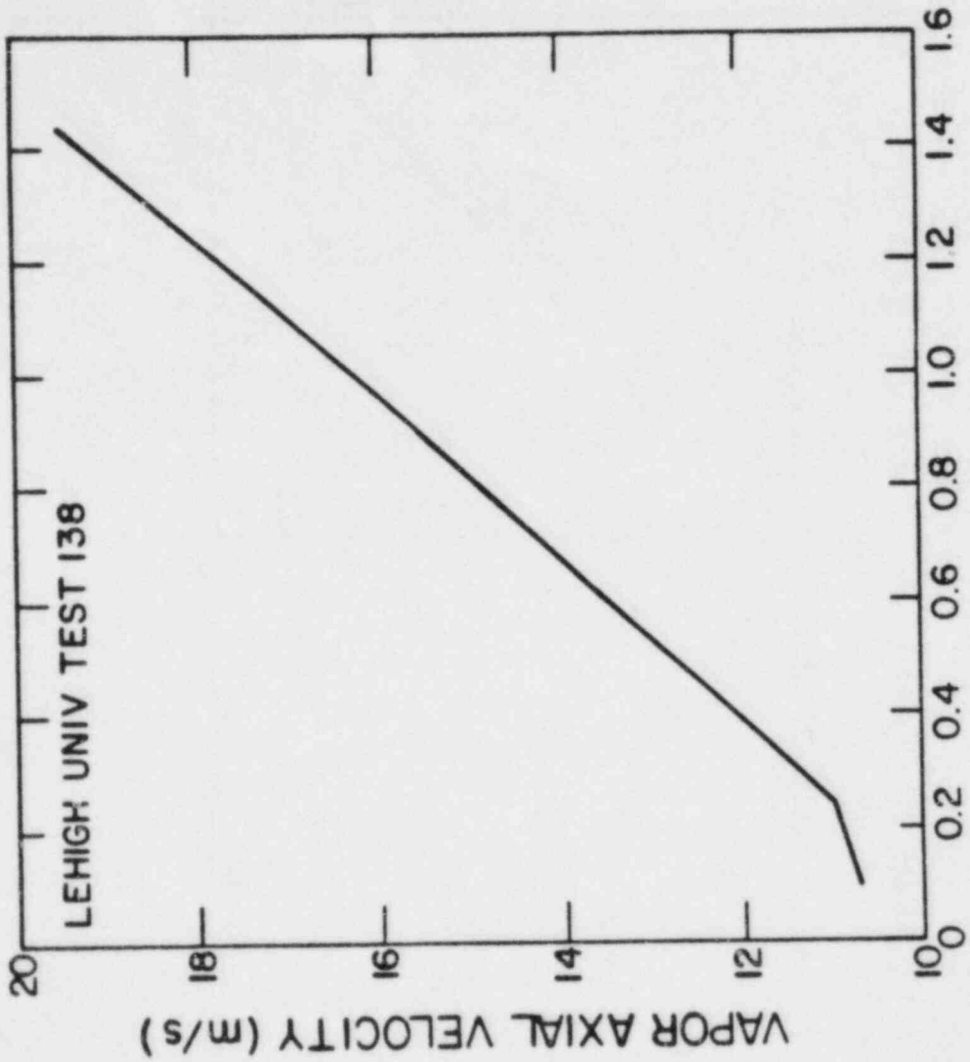

Fig. 7. Calculated vapor velocity versus heated length for test 138.

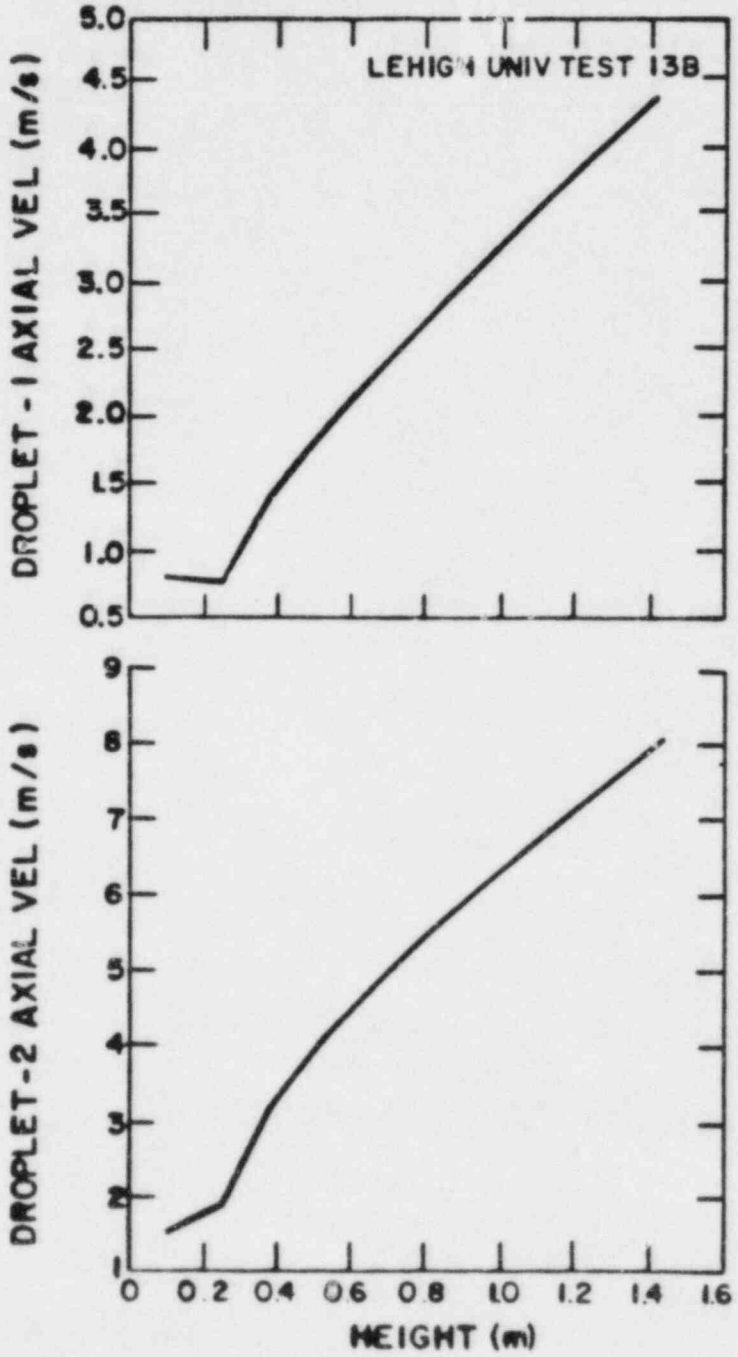

Fig. 8. Calculated droplet velocities versus heated length for test 138.

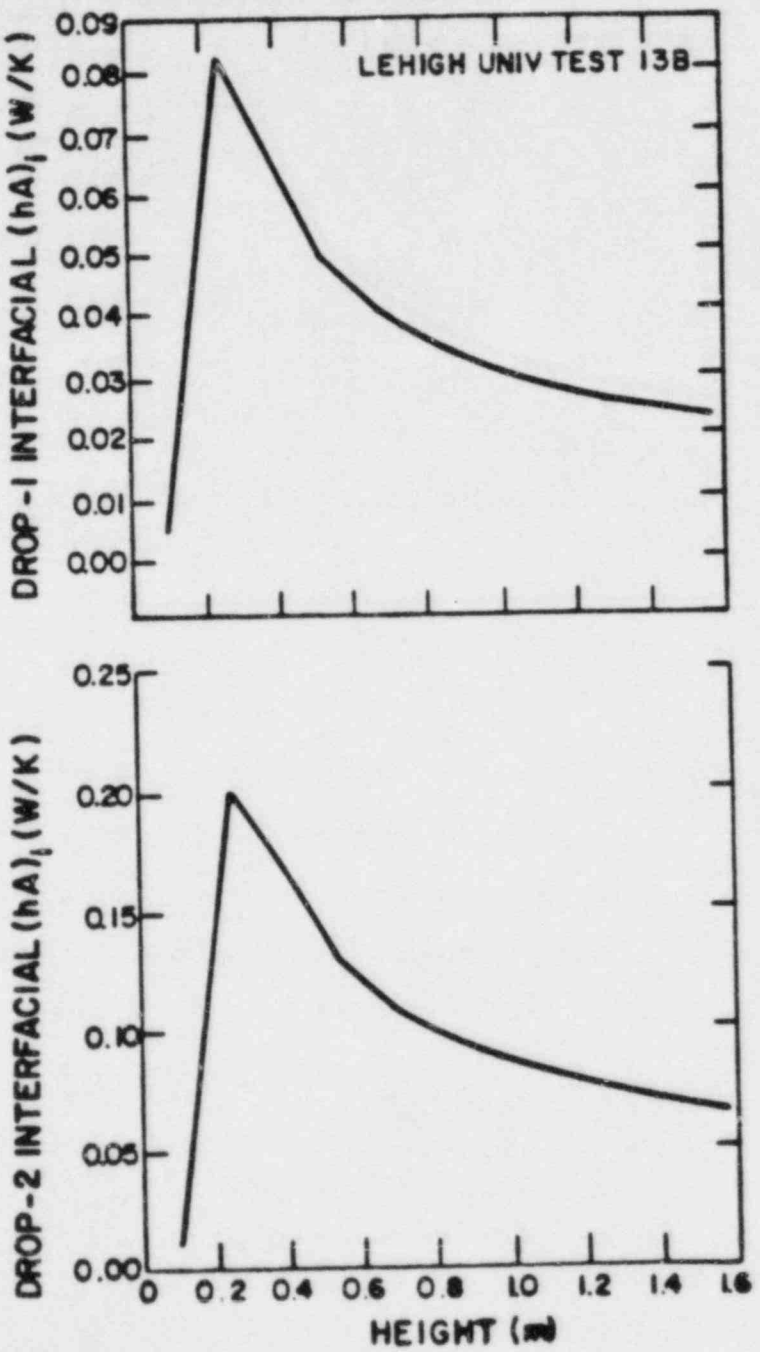

Fig. 9. Calculated interfacial heat transfer coefficient versus heated length for test 138.

Test 138

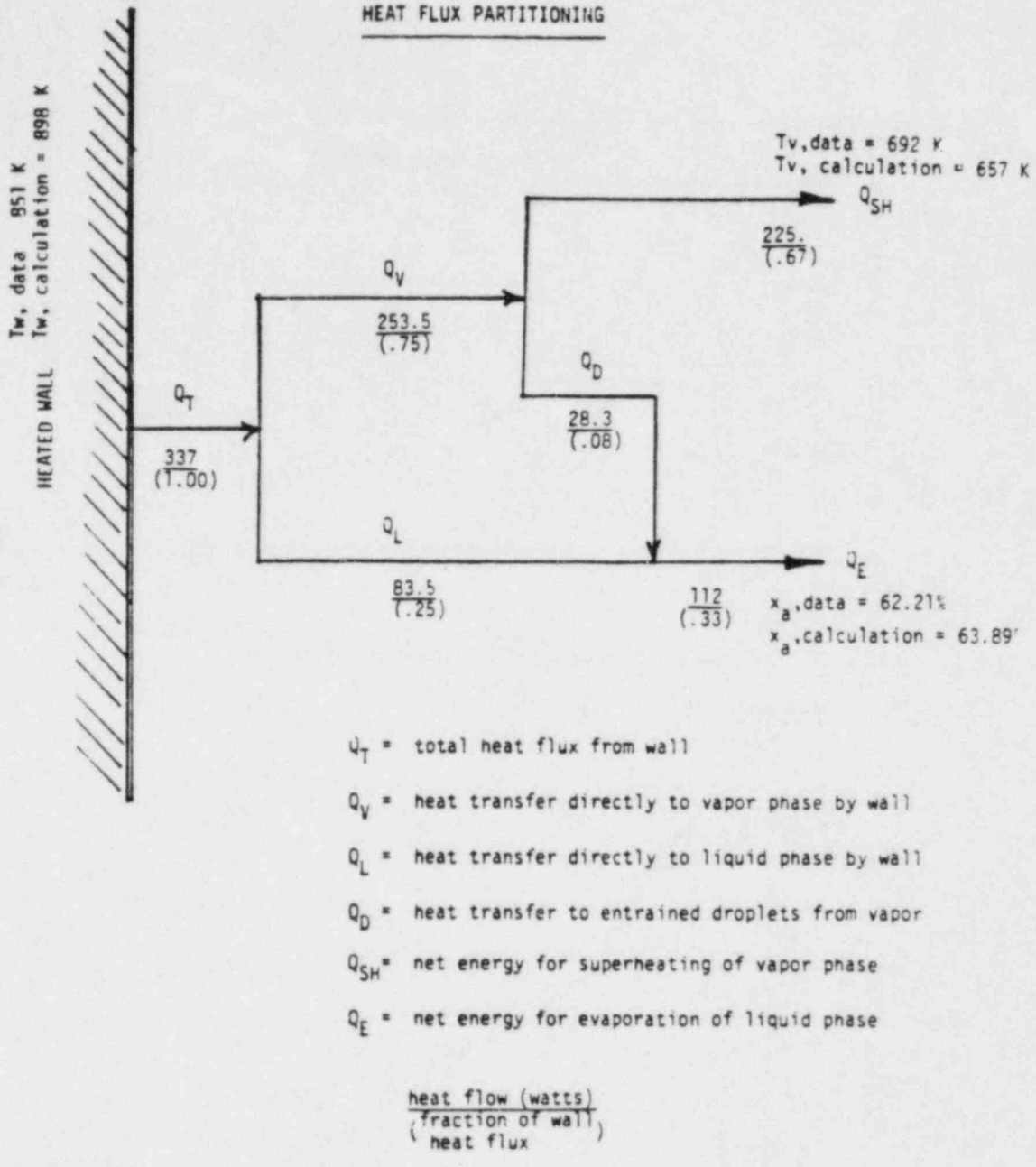

Fig. 10. Calculated heat flow to the vapor and liquid fields at the vapor probe elevation.

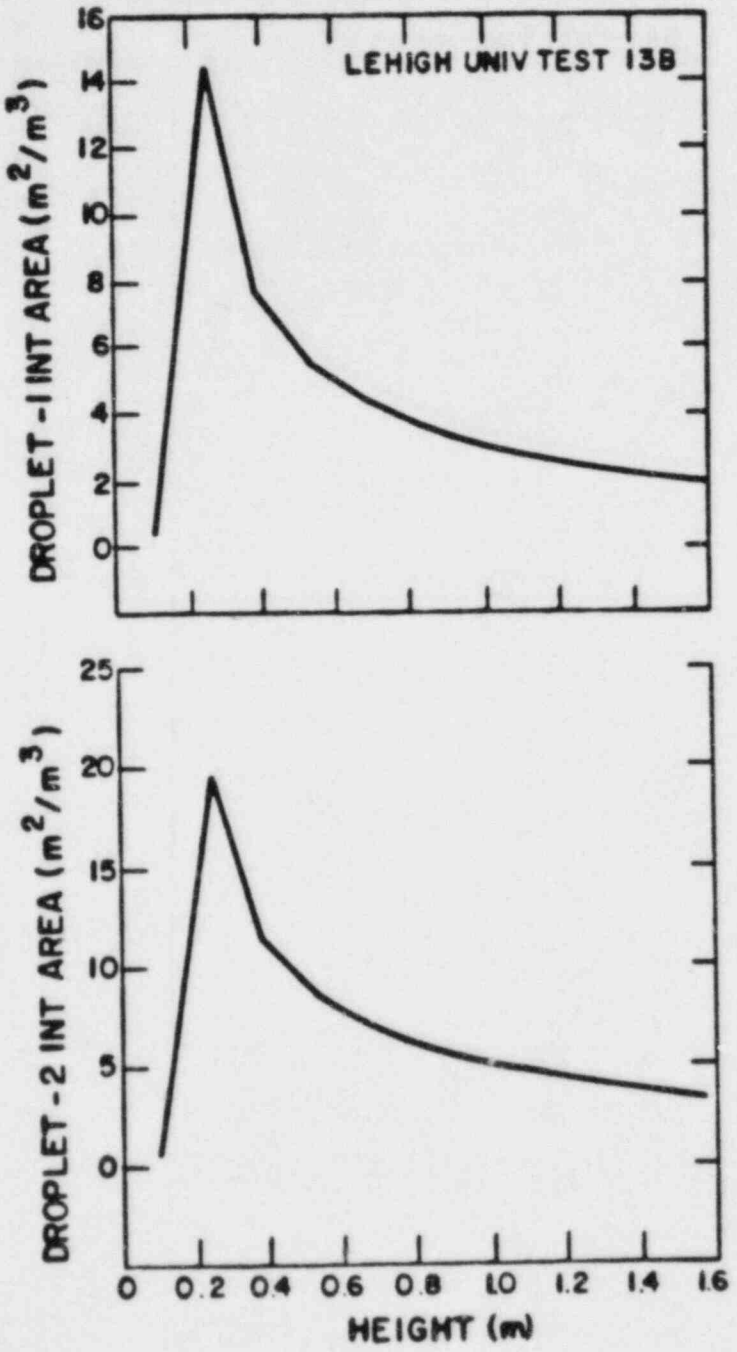

Fig. 11. Calculated droplet interfacial area concentration versus heated length for test 138.

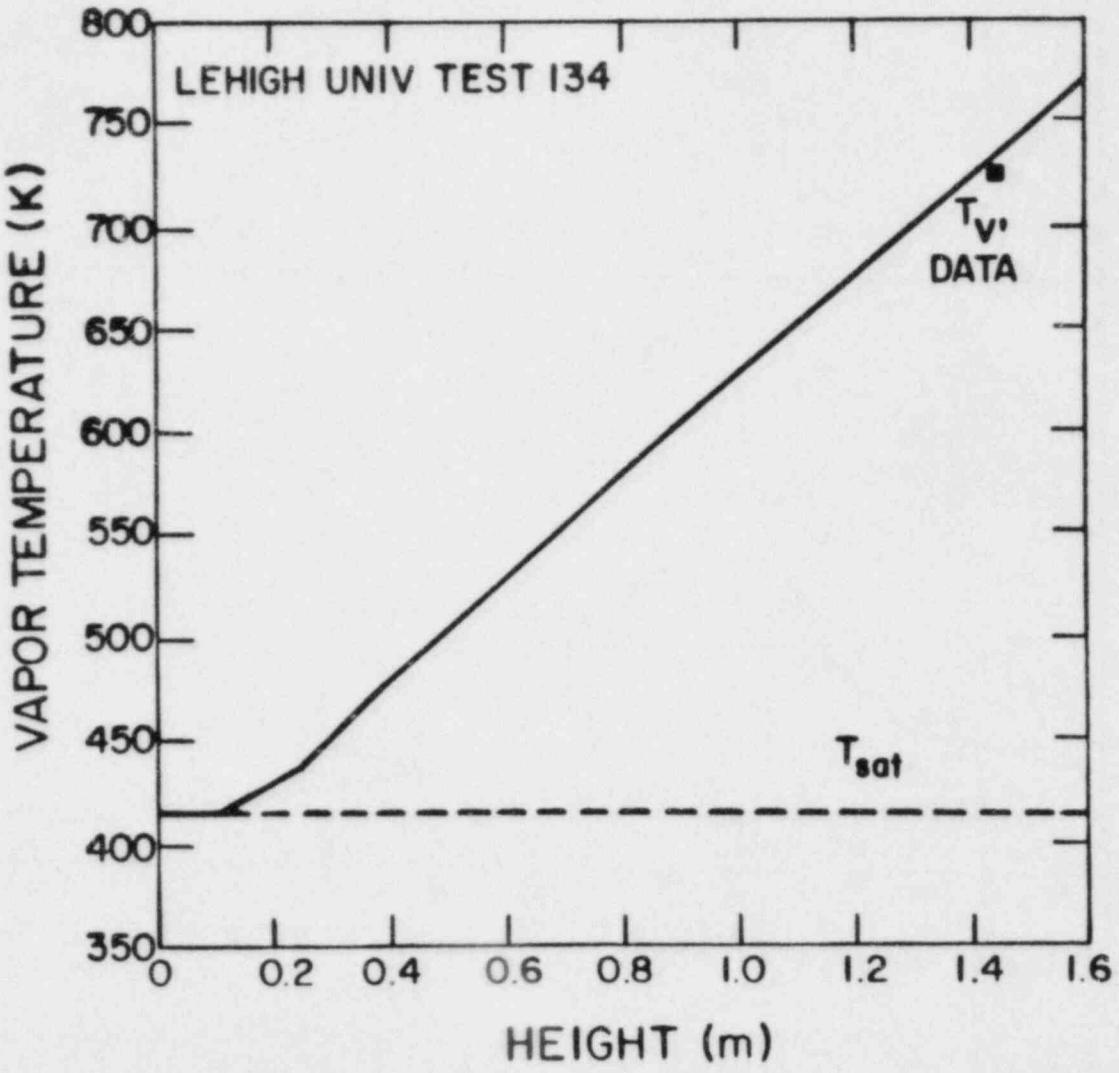

Fig. 12. Comparison between calculated and measured vapor temperature for test 134.

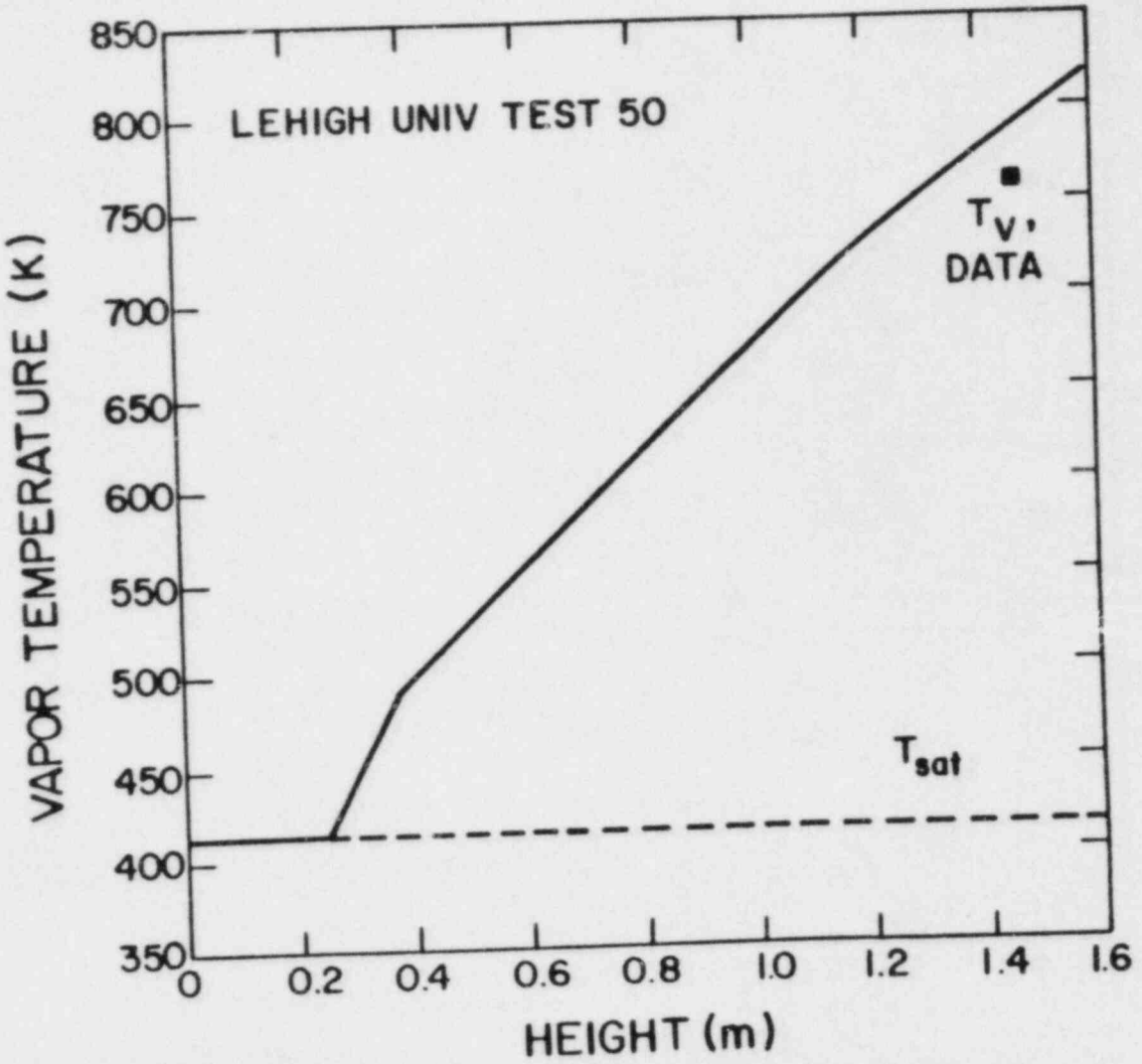

Fig. 13. Comparison between calculated and measured vapor temperature for test 50.

Dispersed Flow Reflood Heat Transfer in Rod Bundles of Different Fuel Rod Simulator Design

P. Ihle, K. Rust, F. Erbacher

Kernforschungszentrum Karlsruhe
Institut für Reaktorbauelemente
Postfach 36 40, 7500 Karlsruhe
Federal Republic of Germany

Abstract

Reflood experiments performed with a 5 x 5 rod bundle of fuel rod simulators with Zircaloy claddings and a helium filled gap between cladding and the Al_2O_3 pellets (REBEKA) provide data (SEFLEX) to be compared with existing data. The range of the reflood parameters selected is mostly the same as that for the existing data base (FEBA) used. The only difference between the SEFLEX tests and the FEBA tests is the design of the internals of the rods and their claddings. The FEBA rod consisted of a relatively thick stainless steel cladding swaged down to the MgO insulation of the internal heating coil.

The comparison of the results obtained from both the bundles show that the reflood transient is faster for fuel rod simulators with Zircaloy claddings and a gap. The cooling in the unwetted portion of such rod bundles is better as well. The dispersed flow heat transfer is increased due to the faster progression of the quench front and the increased heat removal in the film boiling regime downstream of it.

Introduction

The investigation deals with the influence, the radial thermal heat resistance of different fuel rod simulators exerts - as compared with nuclear fuel rods - on the dispersed flow reflood heat transfer during a LOCA of a PWR.

Most of the thermal-hydraulic reflood experiments were performed using electrically heated fuel rod simulators. The heating element is usually embedded in MgO or BN surrounded by a cladding tube. A close thermal contact between cladding and electrical insulation is achieved by swaging down the heater rods. That procedure leads to a minimization of the temperature difference between the outer surface exposed to the coolant and the internal heating element ("gapless" fuel rod simulators). Nuclear fuel rods are characterized by heat generating fuel pellets stacked in a tube with a specified radial gap of e.g. 0.05 mm between the cladding tube and the pellets. The gap is filled with pressurized helium to improve - among others - the heat transfer across the gap. During burn up fission gas released from the fuel is mixed to the Helium reducing the gap heat transfer. For steady state heat generating and cooling conditions, the temperatures at the outer surface of the different rods are identical.

However, they are different, e.g. for transient cooling conditions. The heat capacity of the individual rods, and especially, the heat resistance between the heat source and the outer surface of the individual rods influence the temperature transients of the claddings.

The objective of this investigation is to quantify the effects of fuel rod simulator design on dispersed flow reflood heat transfer and to understand the most important phenomena.

Experiments

The experimental data from tests performed with "gapless" fuel rod simulators are taken from the FEBA program /1, 2/. A cross section of a FEBA rod is shown in Fig. 1. The fuel rod simulators of the REBEKA program /3/ had been developed for ballooning tests. They are characterized by a Zircaloy cladding of 0.72 mm wall thickness surrounding Al_2O_3 pellets. An electrically heated rod of 6 mm diameter is placed in the center of the pellets (see Fig. 2). Heated length, axial power distribution and power steps are the same as those of the FEBA rods.

A 5 x 5 rod bundle consisting of REBEKA fuel rod simulators was installed in the FEBA test facility to minimize the influence of the boundary conditions of different installations.

For the performance of the SEFLEX program (Fuel Rod Simulator Effects in Flooding Experiments) flooding parameters have been selected in the same range as for the FEBA program. For the first set of SEFLEX tests using helium filled rods, the system pressure was 2 and 4 bar, the flooding velocity 3.8 and 5.8 cm/s. The initial bundle power of 200 kW for a heated length of 3.90 m followed later on the 120 % ANS decay heat transient for both types of rod bundles.

Results

The results confirm quantitatively the trend expected: The reflood transient is faster for fuel rod simulators with gap between heat source and cladding for all of the reflood conditions mentioned above. The influence of heater rod design on the quench front progression is shown in Figs. 3 through 6 for the flooding velocities and system pressures indicated. The quench front location versus reflood time allows the determination of the local quench front velocities within the different bundles and for the different reflood conditions, respectively.

A general finding can be summarized comparing the data plotted in Figs. 3 through 6: The overall quench time of a REBEKA rod bundle with helium in the gap is approximately 20 % shorter than that of a FEBA rod bundle for a system pressure of 4 bar and flooding velocities of 3.8 as well as 5.8 cm/s. For the system pressure of 2 bar the overall quench time is about 30 % shorter in SEFLEX than in FEBA.

The SEFLEX results were obtained with helium in the gaps of the rods with a pressure of 1 bar above the corresponding system pressures. For reduced gap conductance, i.e. increased gap width and/or filling gases of lower heat conductivity the gap effect increases leading to again shorter quench times.

The cooling conditions in the unwetted portions of the different bundles are different as well. Figure 7 shows cladding and housing temperatures measured in the upper portion of the bundles at the axial levels indicated. The maximum cladding temperature at that elevation is about 90 K lower in SEFLEX than in FEBA (p = 2 bar, v = 3.8 cm/s). The REBEKA rods have a slightly smaller heat capacity - about 10 % less - than the FEBA rods. The faster decrease of the cladding temperature in the SEFLEX test could be caused by

the lower amount of stored heat to be removed from that bundle. However, the heat stored in the housing - identical for both test runs - is the same at initiation of reflood. The transients of the housing temperatures indicate faster heat removal from the housing for the SEFLEX test run. This proves that the precursory cooling in a REBEKA rod bundle is increased compared with that of a FEBA rod bundle. The lower amount of heat stored in the bundle at initiation of reflood is not the only explanation for the faster reflood transient for bundles of REBEKA rods. However, the better heat removal is more pronounced for the film boiling regime and less for the dispersed flow regime.

Figure 8 shows cladding, housing and fluid temperatures of a FEBA test performed with a system pressure of 4 bar. In Fig. 9 data are plotted measured at the same locations of a SEFLEX test performed with the same flooding conditions as the FEBA test. The fluid temperature transients of the different tests are more or less the same. From these measurements no significant differences of the dispersed flow regimes in the different bundles can be found. Therefore, the dispersed flow heat transfer conditions are to be investigated by evaluation of data measured as well as calculated.

For analysis of the dispersed flow heat transfer, the transient surface heat flux and the heat stored in the different rods have been calculated from experimental data.

Figure 10 shows the corresponding transients from the set of tests performed with a system pressure of 2 bar. At initiation of reflood the cladding temperatures are the same for both tests. They diverge like shown and discussed above (see Fig. 7). The stored heat of the REBEKA rod at the axial level mentioned is somewhat lower than that of the FEBA rod. The difference at initiation of reflood increases during the dispersed flow cooling indicating that more heat per unit of time is removed from the REBEKA rods. The surface heat flux transients plotted show the quantitative amount for the reflood conditions mentioned.

In Fig. 11 the data are plotted obtained from the second set of tests (p = 4 bar). The trends remain the same. The surface heat flux - almost the same in these two tests - still is higher during the important time span at beginning of reflood. It had been shown already that for increasing system pressure the difference of the behavior of the two types of rods decreases. However, the dispersed flow heat transfer remains higher for rods with gap, and the temperatures of the Zircaloy claddings are significantly lower even in the dispersed flow regime.

For comparison of the behavior of gapless rods with that of nuclear fuel rods by calculation, the following assumptions sometimes are made: Same transient heat transfer coefficient and same quench front velocity for both types of rods. The usually smaller heat capacity of nuclear fuel rods leads with the assumptions mentioned to faster rise and to higher cladding temperatures calculated for the early portion of reflood. Again, due to the smaller heat capacity, the calculated cooling down after the turn around point is increased leading to somewhat earlier quenching. However, the evaluation of the experimental data presented proves that the assumptions mentioned do not describe adequately the real conditions: The reflood heat transfer in rod bundles with fuel rod simulators, simulating nuclear fuel rods more adequately, is higher - including the dispersed flow regime - than that in bundles of gapless rods. The quench front velocity is faster as well. Therefore, the cladding temperatures are always lower for rods with gap under the

conditions mentioned. Calculations as well as screening tests show that for increasing heat resistance in the gap the cladding temperatures decrease pogressively and the reflood phase is shortened again.

Conclusions

The design of fuel rod simulators influences the dispersed flow reflood heat transfer significantly.

In rod bundles consisting of fuel rod simulators with Zircaloy claddings and a helium filled gap between the cladding and the heat source, maximum cladding temperatures are significantly lower (40 K up to 90 K) than in bundles of gapless simulators.

The helium filling in the nominal gap of 0.05 mm represents the most conservative situation. For increasing gap width and/or smaller heat conductivity of the gas mixture in the gap maximum cladding temperatures as well as the quench times decrease progressively. Due to the faster progression of the quench front more heat stored in the bundle is removed per unit of time leading to increased dispersed flow cooling for fuel rod simulators with gap.

References

/1/ Ihle, P.; Rust, K.:
"FEBA - Flooding Experiments with Blocked Arrays, Evaluation Report"
KfK 3657, March 1984

/2/ Ihle, P.; Rust, K.:
"FEBA - Flooding Experiments with Blocked Arrays, Data Report 1, Test Series I through IV"
KfK 3658, March 1984

/3/ Erbacher, F.J.; Neitzel, H.J.; Wiehr, K.:
"Effects of Thermohydraulics on Clad Ballooning, Flow Blockage and Coolability in a LOCA"
OECD-NEA-CSNI/IAEA Specialists' Meeting on Water Reactor Fuel Safety and Fission Product Release in Off-Normal and Accident Conditions, Risø National Laboratory, Denmark, May 16-20, 1983

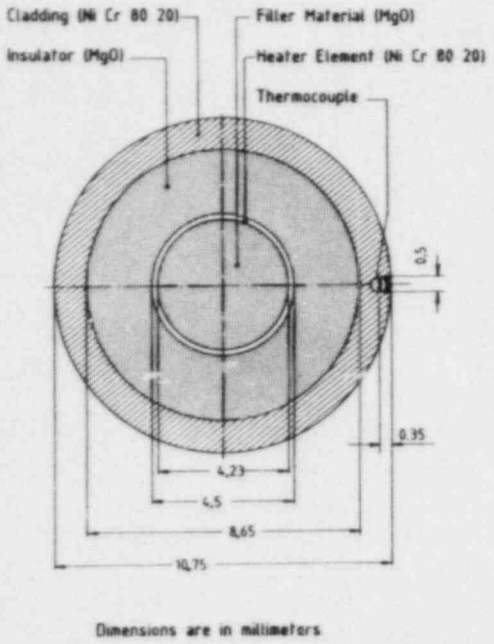

Fig. 1 FEBA fuel rod simulator

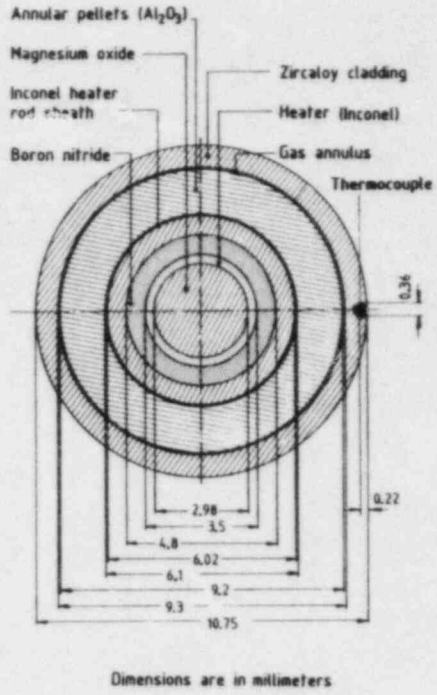

Fig. 2 REBEKA fuel rod simulator used for SEFLEX tests

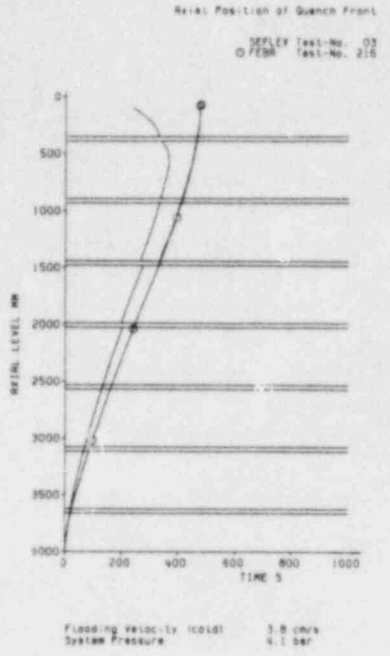

Fig. 3 Influence of heater rod design on quench front progression

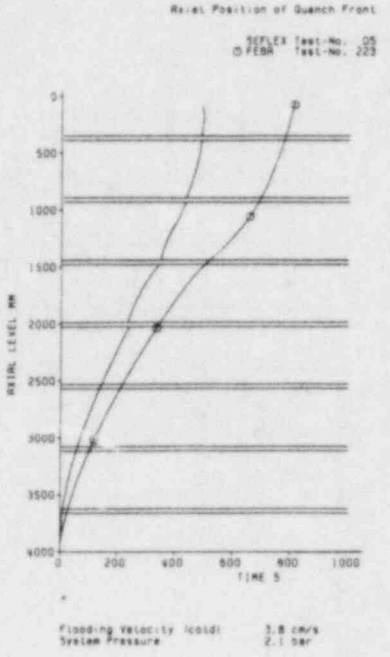

Fig. 4 Influence of heater rod design on quench front progression

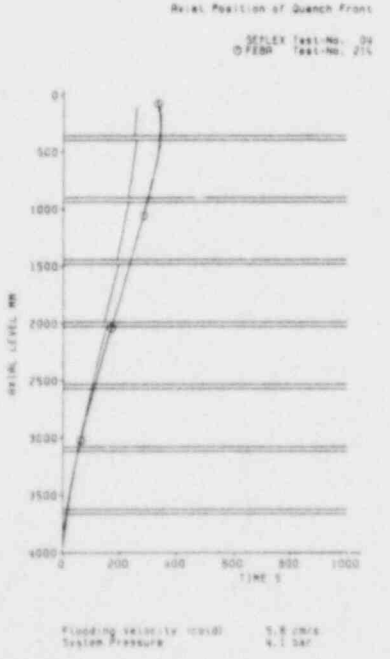

Fig. 5 Influence of heater rod design on quench front progression

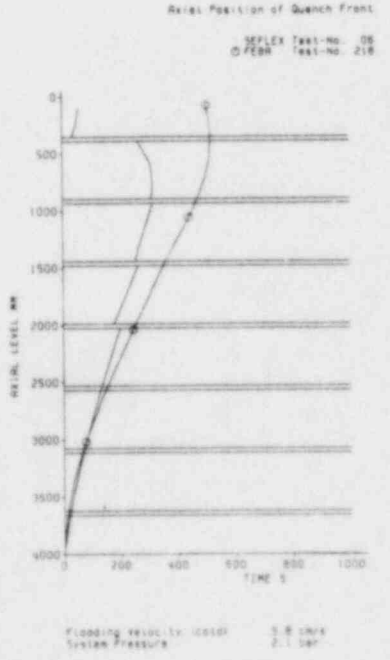

Fig. 6 Influence of heater rod design on quench front progression

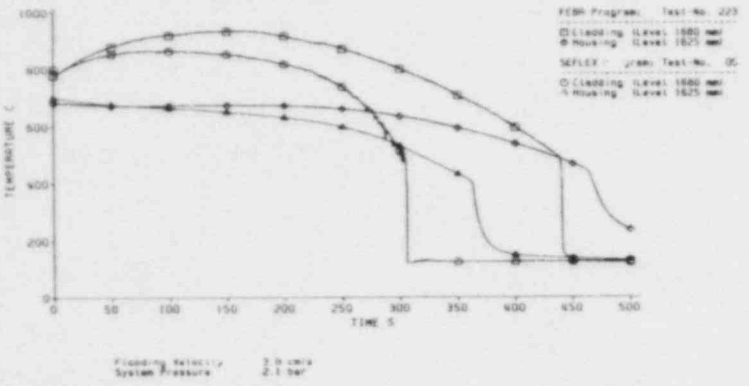

Fig. 7a Cladding and housing temperatures

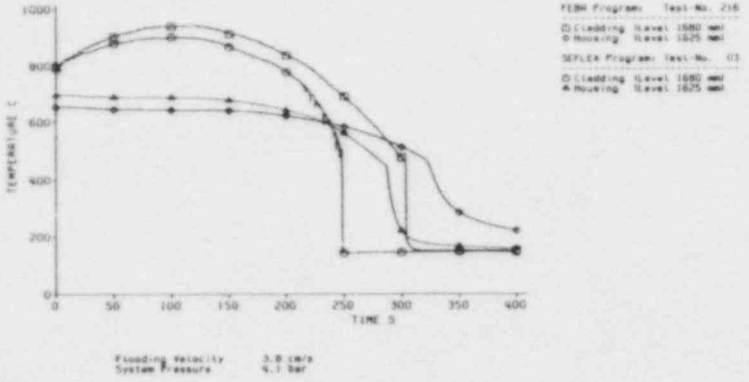

Fig. 7b Cladding and housing temperatures

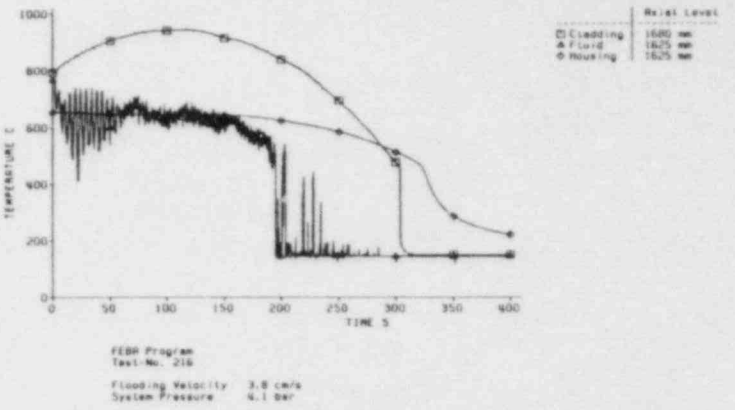

Fig. 8 Cladding, fluid and housing temperatures

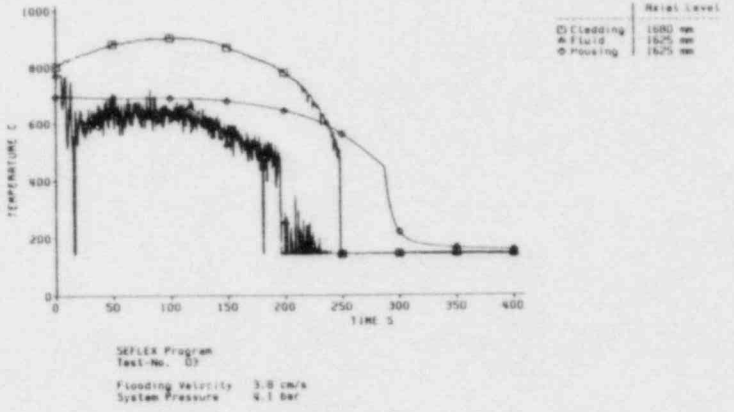

Fig. 9 Cladding, fluid and housing temperatures

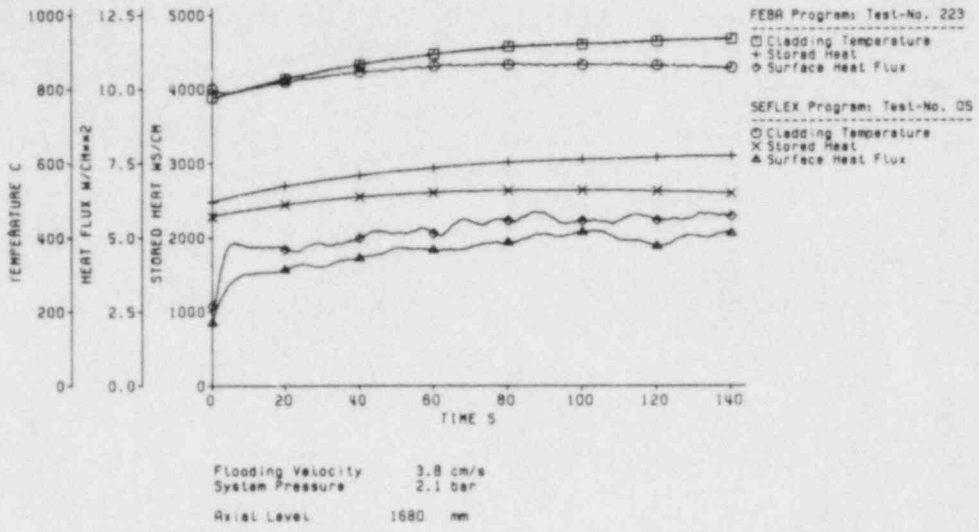

Fig. 10 Cladding temperature, stored heat, heat flux

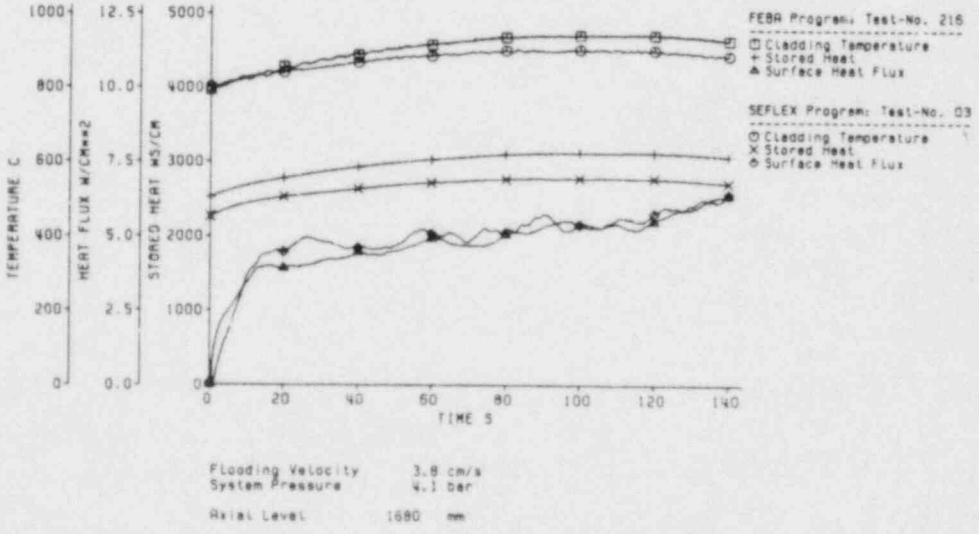

Fig. 11 Cladding temperature, stored heat, heat flux

Summary of Discussion in the Dispersed-Flow Heat Transfer

G.E. Hewitt

Building 392-7

Engineering Science Division

AERE Harwell

Oxfordshire, England

OX11 ORA

INTERNATIONAL WORKSHOP OF FUNDAMENTAL ASPECTS OF POST-DRYOUT HEAT TRANSFER

SALT LAKE CITY APRIL 2ND-4TH 1984

DISPERSED FLOW HEAT TRANSFER

Session Chairman's Summary

by
G F Hewitt, Harwell Laboratory, England

INTRODUCTION

The number of papers submitted for this Session reflects the importance and interest in post-dryout heat transfer in the dispersed flow region. In addition to new data and new empirical correlations, the work presented included models at various levels of sophistication, studies of detailed effects and studies of fuel element behaviour in dispersed flows.

NEW EXPERIMENTAL DATA (SINGLE TUBES)

New data for dispersed flow heat transfer was presented by ROKO and SHIRAHA, HEIN and KOHLER and CONDIE et al. In experiments carried out by ROKO and SHIRAHA a vertical sodium-heated channel was employed and experimental data obtained in the pressure range 8-14 MPa with dryout qualities in the range 0.46-0.93. Results with sodium heating are of particular interest since the heat flux falls when the post dryout region is entered. This gives a particularly severe test of the correlations for this region. In the tests by HEIN and KOHLER, a horizontal electrically heated tube was employed and in the work by CONDIE et al., a similar technique was employed with the addition of hot patches at the inlet and outlet of the test section. In this latter work, two types of tests were carried out

(1) "Steady state" tests in which the rewetting front was held at the test section inlet by pre-heating a copper hot patch at that point.

(2) Transient rewett tests in which the rewetting front proceeded up the tube.

In the CONDIE et al. experiments, pressures up to 7 MPa were employed and an important feature of the measurements was that of steam temperature determination using an aspirated probe. Again, steam temperature measurements provided a sensitive test of models for this heat transfer region.

EMPIRICAL CORRELATIONS

As was stated above, sodium heated experiments provide a particularly severe test for the correlations for post-dryout heat transfer and the comparisons reported by ROKO and SHIRAHA certainly demonstrated the deficiencies in the present correlations. The main reason for the discrepancy is probably the poor representation of the non-uniform flux effects by these correlations, as was demonstrated sometime ago in

Harwell tests using cosine flux shapes. Detailed comparisons with correlations were also carried out by CONDIE et al. and also showed that the fit to the data was rather poor. A new empirical correlation for heat transfer coefficient, giving a somewhat better fit, was reported by CONDIE et al. but this was not claimed to have a very general basis.

INTERMEDIATE MODELS

The processes occurring in dispered flow post-dryout heat transfer are highly complex and the rather poor performance of empirical correlations is perhaps not very surprising. However, exact modelling of the processes is extremely difficult and it is obviously desirable to try to develop models of intermediate complexity which can be used readily in design and assessment calculations. Models of this type were reported in the Session by ROKO and SHIRAHA and by HEIN and KOHLER. In the ROKO and SHIRAHA model, it was assumed that drop-to-wall heat transfer and radial heat transfer were negligible, that the slip between the drops and the vapour could be calculated using a standard correlation and that there was a single dropsize. Heat transfer from the wall to the superheated vapour was modelled using the Bishop correlation and that between the steam and the drops by the Frössling correlation. Reasonable fit was obtained to the data obtained in the sodium-heated experiments and also to earlier post-dryout data.

In the model by HEIN and KOHLER, it was assumed that there were essentially three regions beyond the dryout point:

(1) A region in which all the heat goes into superheating the vapour.

(2) An "equilibrium superheat" region in which the vapour superheat remains constant, and

(3) A steam heat transfer region in which it is assumed that all the droplets have been evaporated.

A simple correlation was produced for equilibrium vapour superheat and reasonable agreement with data was obtained except in conditions where film boiling rather than dispersed flow heat transfer was taking place.

MORE COMPLEX MODELS

There have been many attempts to actually model the detailed heat transfer and flow processes occurring. Droplet field equations are included in some advanced computer codes, for instance the TRAC code. Comparisons with the TRAC heat transfer model were made in the paper by CONDIE et al. and showed very poor agreement with calculated heat transfer coefficients being much higher than those actually measured. A modified version of the TRAC code was developed by WILLIAMS in which two droplet fields (one of large diameter dominated the mass transport and one of small diameter dominating the surface area) together with a vapour field were used for the post-dryout region. Reasonable agreement was obtained between the calculations and data obtained in the tests at Lehigh University. An interesting result from the calculations was that typically, 75% of the heat released from the wall was transferred to the vapour (the other 25% being transferred directly to the liquid droplets) but that only 8% of the heat released from the wall went ultimately into

evaporating the droplets. WILLIAMS made the interesting point that the wall surface area was one or two orders of magnitude greater per unit length of channel than that of the droplets.

For many years, a series of models have been developed (with increasing complexity) including wall-to-vapour, wall-to-drop and vapour-to-drop heat transfer. These models fitted much of the data, but systematic errors were observed in some of the comparisons. These models are reviewed in the paper by VARONE and ROHSENOW who suggest that some of the dicrepancies may be due to to the effect of the dispersed phase on vapour turbulence (see below).

CLARE and FAIRBAIRN also describe a more complex model which includes the effects of grids in fuel elements; they too claim the existence of significant effects on vapour phase turbulence due to the presence of the droplets.

DETAILED EFFECTS: DROP-TURBULENCE INTERACTION

The presence of the droplets in the vapour in a dispersed flow region gives rise to two competing effects:

(1) The drop-turbulence interaction in the core of the flow suppresses turbulence and this will lead to a decrease in the heat transfer coefficient.

(2) The drops may generate additional turbulence in the boundary layer as they approach the wall and this may lead to an enhancement of the heat transfer coefficient. Detailed measurements of heat transfer in rod bundles reported by CLARE and FAIRBAIRN indicated that there was indeed turbulent enhancement in the grid region, though this was small. VARONE and ROHSENOW showed that the discrepancies between the more classical models (mentioned above) and the data could be explained if it were postulated that the presence of the droplets enhanced heat transfer at low droplet concentration (high quality) and suppressed it at high concentrations (low quality). A competing effect at low quality was that of direct droplet-to-wall heat transfer. They postulated a simple model to take account of these effects and this gave general agreement with the available data.

More direct evidence for the influence of entrained particles on heat transfer was obtained in the experiments of KIANJAH, DHIR and SINGH who measured heat transfer enhancement in the flow of air and glass beads through a four-rod bundle. Very different behaviour was observed for 30 micron and for 100 micron particles respectively; this presumably reflects the different response between the particles and the gas phase turbulence.

DETAILED EFFECTS: VAPOUR GENERATION RATE

From the new experimental data by CONDIE et al. it is possible to estimate the vapour generation rate. Comparisons between the predicted and calculated rates indicated the very poor performance of the existing correlations for vapour generation rate and a phoenomenon of particular importance was the very high vapour generation rate observed near the quench front. A new expression for vapour generation rate was reported

by WEBB and CHEN; they postulated the existence of a "near field" region near the quench front and a "far field" rate further downstream. They were able to develop empirical expressions for these two regions which gave much better agreement with the Lehigh University and INEL data.

FUEL ELEMENT BEHAVIOUR

IHLE et al. reported detailed comparisons of the behaviour of two types of fuel rod simulators in reflood. The first had no gas gap, with the outer sheath being in direct contact with the internal insulator. The second type had a gas gap which could be filled with helium or argon. The simulators with no gas gap quenched much less rapidly than those with a helium filled gap which in turn quenched less rapidly than those with an argon filled gap. The importance of proper simulation of fuel elements was therefore very well established.

CLARE and FAIRBAIRN reported data of heat transfer in the dispersed region in blocked fuel elements. They used photographic methods to study the breakup of dispersed droplet in passing through the fuel element grids. Droplet sizes were in the range 0.5-2 mm and there was surprisingly little spread in the droplet velocity as a function of size. Droplets formed from the grid itself were less than 0.5 mm in diameter. Reasonable predictions of rod cooling rate and steam temperature were made using the detailed model mentioned above.

OVERVIEW

The main conclusions arising from this Session seemed to be as follows:

(1) The widely-used empirical equations for dispersed flow heat transfer have been shown to be inadequate in predicting data over a wide range, especially for non-uniform heat flux.

(2) Models for predicting dispersed flow heat transfer are becoming increasingly complex to allow prediction of a wider range of effects. However, the more complex the model the more difficult it is to incorporate into safety prediction codes and this may present a major difficulty in the application of advanced modelling.

(3) New phenomena (e.g. drop/turbulence interaction) continue to be discovered which need additional modelling techniques.

(4) There is a need for much more detailed measurements and advanced measurement techniques. Measurements of such parameters as dropsize, drop velocity, steam temperature are already giving benefits in testing and developing improved models.

Notwithstanding the advances reported at this Workshop, there remain still much to be done in the study of this heat transfer region.

15th May 1984

V. Effects of Grids and Blockage

International Workshop on Fundamental Aspects
of Post-Dryout Heat Transfer

DROPLET BREAKUP AND ENTRAINMENT AT P.W.R. SPACER GRIDS

- by -

J.E. Adams and A.J. Clare

Central Electricity Generating Board
Berkeley Nuclear Laboratories
Berkeley,
Gloucestershire, U.K.

ABSTRACT

A detailed photographic study of droplet grid interactions has been carried out to provide a basis for improvements in the modelling of heat transfer in the vicinity of a grid in dispersed flows characteristic of P.W.R. reflood. The fragmentation associated with impact of drops onto the leading edge of a grid has been studied and an understanding of the mechanisms governing the resulting drop size gained. Additionally for a wet grid the process of entrainment of drops from the trailing edge of the grid has been investigated, and the dependence of entrained droplet size on the flow conditions has been established.

The results indicate that adequate modelling of the droplet breakup due to impact is important in the calculation of heat transfer at a dry grid and may be significant in the modelling of grid rewetting. At a wet grid modifications to the droplet phase are shown to be of less significance since steam desuperheating is dominated by film evaporation.

1. INTRODUCTION

During the core reflood stage of a PWR design basis LOCA fuel pin cooling above the quench front relies on the flow of steam and water droplets produced at and beneath the quench front. Current analysis indicates that in the most highly rated region the clad temperatures could remain at levels at which the zircaloy clad is ductile for sufficiently long to allow clad ballooning to occur. The resulting local reduction in coolant flow area could perhaps reach about 80%. The heat transfer penalty introduced by such a blockage depends on its length. The balloon axial profile is determined by the clad axial temperature gradient which is found experimentally (Ihle et al, 1982) to be strongly influenced by a local enhancement of heat transfer occurring downstream of each spacer grid. The modelling of grid heat transfer in dispersed flows is at present inhibited by a lack of understanding of the interaction of a grid with the droplets.

This note presents the findings of a series of simple experiments which have led to a better understanding of the physical processes occurring when drops interact with grids. Section 2 below describes an investigation of the initial impact of single drops on the end of the grids. Section 3 considers the subsequent interactions of the liquid with grids and fuel pins within the depth of the grid. Section 4 outlines the results obtained from a small experimental apparatus designed to investigate liquid entrainment from a wetted grid. Drop size and velocity distributions are presented together with a flow regime map which establishes the criteria for the occurrence of different flow regimes. Additionally in Section 5 the implication of the results are discussed in the context of heat transfer for both wet and dry grids.

2. FRAGMENTATION AT FIRST IMPACT

When a single drop impacts on to a grid it divides initially into two fragments which may then undergo further breakup. To gain an understanding of the fragmentation process a detailed photographic study of water drops impacting on to the end of grids has been made.

Water drops of diameter ~5 mm were produced from a glass capillary tube, gravity fed from a reservoir, and fitted with a tap that enabled control of the drip rate. The drops were allowed to fall from various heights on to one of four stainless steel grids of different thickness, viz: 3.31, 1.63, 0.94, 0.47 mm. The other dimensions of the grids were 38 mm deep and 50 mm wide. The velocity of drop impact was controlled by altering the height $\bar{z}$ of the dripper above the grid and was calculated using the solution

$$U_i^2 = \frac{g}{K}\left(1 - e^{-2K\bar{z}}\right) \qquad (1)$$

of the equation of motion including drag. In equation (1)

$$K = \frac{3\, C_D\, \rho}{4\, D\, \rho_\ell}$$

where D is the drop diameter. A drag coefficient of $C_D = .7$ was used as it gave good agreement with measured velocities. Impact Weber numbers, We_i,

were defined from the impact velocity according to equation (2),

$$We_i = \frac{\rho_\ell U_i^2 D}{\sigma} \quad . \qquad (2)$$

The symmetry of the impact of the drop on the grid was also varied. This is described here in terms of the relative displacement, L, of the drop centre from the grid centre. Still photographs were obtained by illuminating the grid, predominantly from behind, with two flash units of $\sim 3\ \mu s$ flash duration. The flash units were triggered, with a variable time delay, when the falling drop intercepted a light beam directed at a photo diode. The camera used was an M.P.P. 5 x 4 plate camera with bellows extensions allowing magnifications up to $\sim$1.5 to be achieved. High speed films were also taken at a rate of 4,000 p.p.s. using a John Hadland 'HYSPEED' camera with a constant bright source of illumination.

2.2 The Initial Drop Partition

Photographs along the edge of the grid show that after impact the drop splits into two fragments. These leave the grid, as shown in Fig. 1 with masses M_α and M_β and centre-of-mass trajectories inclined at angles α and β to the grid. There is also some motion of the liquid along the grid which results in the fragments spreading along the grid edge in the y direction. Subsequent to leaving the grid further breakup may occur. The magnitude of M_α, M_β, α, β and the degree of fragmentation depend on the impact conditions.

Quantitative measurements of the angles α and β and the centre-of-mass velocities were obtained for approximately symmetrical impact (L=0) by plotting the trajectories observed in high speed films taken viewing along the edge of the grid. The results are shown in Figures 2A and B for impact velocities $\sim 3 \rightarrow 4\ ms^{-1}$. Also shown in the figures are the predictions of two different models which have been developed to describe the impact. The models differ in that Model 1 is a two-dimensional analysis in which motion is restricted to a vertical (x, z) plane perpendicular to the plane of the grid, whilst Model 2 is a three-dimensional analysis allowing components of motion in the y direction. Both models assume inviscid flow and employ conservation of mass, momentum and kinetic energy. Surface energy is neglected since its increase during the initial partition of the drops is negligible compared with the kinetic energy of impact in these experiments.

In Model 1 the conservation of kinetic energy requires that the centres of mass of the two fragments move at the impact velocity U_i. The angles α and β and masses M_α and M_β are then calculated from the conservation of the horizontal and vertical components of momentum.

Model 2 assumes that liquid impinging within the cross-section of the grid flows radially from a stagnation point. This results in a reduced total component of horizontal momentum in the plane perpendicular to the grid, as compared with Model 1, so angles α and β are smaller (see Fig. 2A). The centre-of-mass velocity in this plane is also reduced (see Fig. 2B) since there is now a component of motion parallel to the grid. Both models predict angles α and β to be independent of impact velocity. Comparison with experimental results indicate that this is approximately correct for the range

of conditions studied and that predictions of α and β by Model 2 for d/D up to about 0.5 are fairly good. The models could be used to provide upper and lower bound estimates of the centre of mass velocities.

2.3 Degree of Fragmentation

After the initial drop division on impact with a grid the two fragments may undergo further breakup. The extent to which this occurs under different impact conditions has been examined experimentally for symmetric impacts. Water drops of mean diameter 4.76 mm were dropped on to grids of thickness 3.3 mm, 1.6 mm and 0.94 mm. The impact Weber number was varied up to a maximum of ∿1400. Single shot photographs were obtained, using the same experimental arrangements as described in Section 2.1 with the flash units triggered at a time sufficiently delayed after the impact to ensure that the breakup was complete. Typical results obtained with the three grids and impact Weber numbers of about 500 are shown in Figure 3. With each of the thinner grids there is little breakup; two or three large fragments (1-3 mm diam.) are produced on each side of the grid in each case. In the case of the thinnest grid these are accompanied by one or two much smaller droplets ($\lesssim$ 0.3 mm diam.) whilst with the middle grid a larger number (∿ 12) of these smaller droplets are visible. At this Weber number the thick grid produces considerable fragmentation; about 70 drops ranging in size up to ∿ 1 mm diameter are produced.

From similar photographs taken over a range of Weber numbers the number of fragments produced by a single symmetric impact on to each of the three different grids has been plotted as a function of We_i in Figure 4A. It should be noted that though the depth of field of the photographs is large some drops with a large component of velocity in the y direction may pass out of the field of view. This may lead to an underestimation of the number of drops produced, more especially for large d/D and high impact velocities. The figure shows clear differences between the different grids except at low Weber numbers of ∿ 100 where the number of fragments is < 10 in all cases. For the thinnest grid ($d/D = 0.197$) the breakup increases slowly with We_i and appears to level off at $We_i \sim 1400$. The 1.60 mm grid ($d/D = 0.336$) produces a slowly increasing breakup for $100 < We_i < 600$, but the number of fragments increases more sharply for $We_i > 600$. For the thickest grid ($d/D = 0.693$) the number of fragments produced increases steeply with We_i from the lowest values showing no threshold.

Additionally for the second thickest grid ($d/D = .336$) drop size distributions have been measured for three impact Weber numbers. These are shown in Figure 5. From these results the Sauter mean diameter,

$$d_{sa} = \frac{\sum_i N_i d_i^3}{\sum_i N_i d_i^2},$$

has been calculated and is indicated on the histograms.

A further set of experiments was carried out using 2 mm diameter drops of Freon 113 impacting on an electrically heated grid of 0.47 mm thickness. Freon 113 was used primarily because a modest grid temperature of ∿ 200°C was sufficient to prevent quenching with this liquid. The results are shown

in Figure 4b in terms of fragmentation as a function of We_i. It is apparent that notwithstanding the different drop-size, liquid properties (ρ = 1.563 gm cm^{-3}, $\sigma \simeq$ 23 dyne/cm) and grid temperature, these results are fully in accord with those obtained with water drops when correlated in terms of the impact Weber number.

This consistency provides grounds for supposing that a further reduction in drop size to the $\sim$ 1 mm diameter relevant to reflood conditions would not significantly alter the results, although this requires confirmation.

Observation of asymmetric impacts have also been made. In this case the centre of mass trajectories of the fragments and the degree of fragmentation either side of the grid are different. This may be explained in terms of the shift in the position of the stagnation point away from the centre of the grid which is necessary to conserve horizontal momentum. The result of the shift is that the effective d/D becomes different on each side of the grid.

2.4 Mechanism of Breakup

To understand the mechanism by which the two fragments, formed by the initial impact, breakup a number of still photographs were taken with the camera's optical axis normal to the plane in which the breakup occurs. The drop spreads along the axis of the grid and the two fragments form expanding sheets, the lateral spread and sheet thickness being dependent on impact conditions. The dynamics of the impact are illustrated in Figure 6. The figure shows a series of photographs at increasing times following the impact of a drop of $We_i \sim 1020$ on to a relatively thick grid ($d/D \sim 0.69$). The photographs show the production of an expanding sheet. As the sheet expands a thickened cylindrical rim is formed by the free edge rolling up as a result of surface tension. The cylindrical rim is observed to be a source of small droplets. The sheet detaches from the grid and the edges roll together; when they meet breakup of the liquid fragment is complete. For a lower impact Weber number or smaller value of d/D the sheet expands laterally to a smaller extent and is thus thicker. The cylindrical rim formed is therefore also thicker, more stable, and produces a smaller number of larger drops. For a very thick rim no droplets are observed until the edges collide. This results in a small number of large drops or recoalescence of the fragment.

The production of drops from a liquid sheet has been discussed by Taylor (1959) and Dombrowski and Hooper (1964). Taylor describes in detail the production of a cylindrical rim at the free edge of a stationary parallel sided liquid sheet. By using a force balance between the change in momentum and surface tension forces he derives the equation of motion of the edge. This is then extended to a radially expanding sheet. Also discussed is the position at which the edge disintegrates for a constant liquid supply rate, such as occurs in a swirl atomiser. However, the mechanism of rim breakup is not discussed. Dombrowski describes the breakup of sheets which can occur, under some conditions, as a result of instability induced by rapidly growing hydrodynamic waves. These cause the edge of the sheet to break away and form ligaments, which then break up through capillary instability. The work of Dombrowski et al (1964) was directly principally at the liquid sheets produced as a result of the impact of two jets. He concluded that there was a critical

Weber number below which hydrodynamic fragmentation did not occur. Our photographs for impact velocities $\lesssim 5\ ms^{-1}$ show no indication of the rim detaching from the sheet though there is evidence of surface waves. For impact conditions of interest here capillary breakup of the undetached rim will generally occur.

Chandrasekhar (1961) has derived a criterion for capillary instability of liquid cylinders. The analysis he presents shows that a liquid cylinder is unstable to symmetric varicose deformations of wavelength exceeding the circumference of the cylinder. The most rapidly growing wavelength is given by

$$\lambda = \frac{2\pi R}{0.697} \tag{4}$$

where R is the cylinder radius. Dombrowski and Fraser (1954) have obtained experimental agreement with this prediction.

The characteristic breakup time τ is given by

$$\tau = \frac{1}{0.3433} \sqrt{\frac{R^3\rho}{\sigma}} . \tag{5}$$

As the cylinder thickens so τ increases and the cylinder becomes more stable. This accords with the experimental observation that the sheets with thicker cylindrical rims are less likely to be a source of small droplets. Rim thickness is determined by the sheet expansion, this will depend on the magnitude of the component of horizontal momenum along the grid edge. This is large for high We_i and large a/D. As noted earlier these are the experimental conditions which result in the greatest sheet expansion, and the largest degree of fragmentation (Figure 4A).

3. INTERACTIONS WITHIN THE GRID DEPTH

Following the first impact of a drop on the end of a grid, the resulting fragments or sheets will generally move at some angle across the steam flow and approach a pin wall. In cases where the initial impact is asymmetric the larger fraction of the drop may run along the grid face, providing some grid cooling by film boiling if the grid is nonwetted, or forming a liquid film if it is wetted.

In this section we consider the effects of collisions with pin and grid walls on the droplet size distribution at the grid outlet. Wachters and Westerling (1966) reported experiments showing that for drops colliding with a flat surface, too hot for quenching to occur, the drop would disintegrate if the Weber number based on the normal velocity component of the drop exceeded about 80. At lower Weber numbers $30 \lesssim We_i < 80$ one or two small droplets may be produced from the fluid stem formed as the bouncing drop leaves the surface. For $We_i < 30$ the impinging drop remains intact.

From Section 2 it is apparent that the liquid impinging on the hot pin walls may be in the form of small droplets or in the form of a liquid sheet which has not completely fragmented or recoalesced. The Wachters and Westerling (1966) criterion may be used to judge whether the impingement of the droplets on the pin walls will lead to further disintegration. However

most of the liquid is likely to be in the form of thin or thick sheets and the behaviour of these when impinging on a hot surface at some angle is not clear.

In order to examine sheet impact on a surface a small number of simple experiments have been performed using drops of Freon 113. The drops fall on to a first grid which splits the drops and generates the characteristic sheets. A neighbouring parallel grid is heated electrically to a temperature of $\sim 200^{\circ}C$ which is above the quenching temperature for Freon 113. The arrangement can be seen in the photographs of Figure 7.

The figure shows photographs illustrating the bounce for drops of high impact Weber number. The grid thickness is 0.47 mm and initial drop diameter is 2 mm. The drops impinge on the outer grid at a velocity of 3.2 ms^{-1} (We_i = 1336). Successive photographs are of different individual drops at advancing times in events with nominally identical initial conditions. There are, however, small variations in the symmetry of initial impact which result in differences in details such as angular dispersion and mean fraction of the component either side of the grid.

In Figure 7 the high We_i initial impact produces an unstable sheet either side of the grid which can be seen to break up into a cloud of small droplets on the free side. The normal velocity component of impact on the hot pin surface is roughly 0.9 m/s. It is not clear what dimension to use in a Weber number.

However, it is clear from the figure that the whole sheet bounces off the hot surface producing a distribution of drop sizes similar to that on the free side. The implication of this is that the mechanism of sheet breakup (discussed in Section 2) is not greatly affected by the bounce in this particular case. It might be expected that the impact with a hot surface could perturb a relatively stable (thicker) sheet and enhance breakup, but this has not been observed in the small number of experiments performed. Drops of low impact Weber number were also used and the bounce photographed. In these cases there were also no discernible effect of the bounce on the breakup behaviour.

Further experiments have been performed in which the'wall' surface was unheated. In all cases, whatever the form the impinging fragments where in, it was observed that they stuck to the surface forming a wet patch too small to run down the wall. In no case were small droplets seen to be ejected into the gap during this impact.

The above observations suggest that in general drop size distributions are not significantly modified by impingement on surfaces above the quench temperature, but that all liquid impinging on a surface below the quench temperature adheres to it.

4. ENTRAINMENT FROM WETTED GRIDS

In the case of the wetted grid droplets that have "bounced" off the hot pins impinge on the grid face and adhere to it, as described in Section 3. Because of the high steam velocities (5 - 20 ms^{-1}) along the fuel subchannels, between the grids and pins, it is anticipated that this liquid may be re-entrained from the downstream end of the grids.

This section describes results obtained from a small experimental apparatus designed for determining the conditions required for entrainment. The apparatus, shown schematically in Figure 8, is built of perspex to enable visual observation of the flow patterns. The dimensions were chosen such that a is approximately equal to the hydraulic diameter of the reactor subchannels, b was chosen comparatively large to minimise the effect of the end walls and enable a clearer view of the central region of the grid face. The grid depth and thickness of 38 mm and 0.33 mm are approximately those of a spacer grid in the core. A compressed air line supplied air of volumetric flow 0 - 1600 litres/min which in the test section yielded air velocities between 0 - 40 ms^{-1}. These air velocities cover the range of interest for reflood conditions. Water of constant variable flow rate between 0 - 9 cc sec^{-1} was supplied to the grid face by the injector as shown in Figure 8B. The apparatus was illuminated either behind the grid or along the grid axis by two flash units triggered either repeatedly at a selected rate for visual observation, or at a chosen instant to obtain photographs. Figure 9 shows a diagram of the different flow regimes observed to occur. In regime A the air flow is insufficient to drive the injected water to the top of the grid face. The water was seen to circulate between the grid face and the walls, being expelled at intervals from the top of the apparatus in surges or slugs. Expulsion of liquid in this manner continues, though to a lesser extent, in regions B and C. In region B however some liquid now reaches the top edge of the grid and some intermittent end entrainment occurs. In C liquid is continuously entrained from the end. In region D the air flow is sufficient to drive all the liquid up the grid face so all the injected water is entrained. A small number of drops were noticed coming from below the top edge but it is unclear whether these were due to film entrainment or came directly from the injector, however these represent a negligible proportion of the entrained liquid mass.

Drop size distribution were obtained from photographic prints giving a resolution of better than .05 mm. The Sauter Mean diameter, defined earlier, was calculated from the drop size distributions, and is shown as a function of air velocity in figure 10A. As can be seen d_{sa} decreases rapidly with increasing air velocity but appears to be relatively insensitive to changes in water injection rates.

Using high speed photography drops were filmed leaving the end of the grid at framing rates of 4,000 and 6,000 p.p.s. From these films the distance downstream of the grid within which all breakup was complete - the breakup length - was recorded and is shown as a function of air velocity in Figure 10B. The breakup length shows a strong dependence on both air velocity, with which it decreases, and water injection rate, with which it increases.

The photographs and high speed films allowed identification of the mechanism of droplet production by entrainment from the grid end. There were two mechanisms: a) the production of liquid sheets which are blown by the air into bags which burst, and b) thinning liquid filaments which break up by capillary instability. The initiation of both of these mechanisms is the drag force from the air flow acting on domes of liquid which form along the top edge of the grid. They can be seen occurring in Figure 11 together with the resulting drop size distributions. For low water injection rates and low air velocities these domes tend to be discrete and ligament breakup predominates.

As either the water injection rate or air velocity are increased, the domes form a more continuous liquid layer along the grid edge. This leads to an increase in the production of liquid bags, until this mechanism is dominant. The bag bursting mechanism produces drops in two size ranges. The larger, which is consistent with the drop size resulting from ligament breakup, arises from the disintegration of the cylindrical rims which form by surface tension at the edges of the liquid sheet. The smaller drops are produced from the central region of the liquid bag where it bursts.

Figures 12a, b, c, d, show velocity as a function of drop size for a range of water injection rates and air velocities. Examination of the figures show that there is a large amount of scatter in the distribution of velocity with drop size, though a general trend of decreasing velocity with increasing drop size is apparent. The drop velocities are recorded at the position where all breakup is observed to be complete, but the drops may have been formed at any position between here and the top edge of the grid. Drops will therefore have been accelerated over different distances and as initial acceleration is very rapid this could account for the scatter. Figure 12a and b show the velocity distribution arising from a water injection rate of 1.49 cc s^{-1} and air velocities of 15.3 and 20.4 ms^{-1} respectively. The breakup length and shape of the distribution are similar in both cases with the lower air velocity producing lower droplet velocities. Figures 2c and d show velocity distributions for an air velocity of 20.4 ms^{-1} and water injection rates of 4.4 and 6.75 cc s^{-1}. Figures 12 b and c are very similar having approximately the same breakup length as well as the same shape distributions. For the high water injection rate, shown in Figure12d, the velocity distribution is different. In this case it is apparent from the high speed films that sheets and ligaments are formed which detach from the grid edge before breakup is complete. For this reason the breakup length is much longer.

5. HEAT TRANSFER EFFECTS

5.1 Non-wetted grids

The experiments described above suggest that for non-wetted grids the drop size will depend on fragmentation at initial impact. In experiments designed to simulate reactor reflood (Lee, et al, 1981) typical drop sizes $\sim$ 1 mm have been measured at several axial positions in the cluster. For a P.W.R. spacer grid of thickness 0.33 mm this yields a value of $d/D = 0.33$. Steam velocities are typically 5 - 15 ms^{-1} for which the range of terminal velocities of a 1 mm drop is $\sim$ 1 - 11 ms^{-1} corresponding to maximum Weber numbers of 14 - 1700. This covers the entire range of our fragmentation studies and indicates that the number of fragments produced per impacting drop could range from $<$ 10 to $\sim$ 200, depending on impact velocity. The effect of such fragmentation as occurs will be diluted since $\sim$ 63% of 1 mm drops will miss the grid. These considerations suggest that close to the quench front unquenched grids will have little influence on drop size, but that far above the quench front where steam and drop velocities are higher unwetted grids are likely to introduce a population of smaller drops into the flow.

In addition to changes in size, the droplets suffer momentum loss due to collision with a grid. For a square edged grid the average fractional loss of axial momentum for all drops impacting on the leading edge is $d/(D+d)$. The

resulting lower droplet velocities will cause a local increase in droplet number density, and therefore of droplet surface area for heat transfer. The increase in phase velocity difference will also enhance steam-droplet heat transfer. In order to incorporate all of these factors in a mechanistic droplet heat transfer model, such as described by Clare and Fairbairn (1984), a model for calculating a mean resulting drop size from given impact parameters is required. Such a model, providing a basis for scaling the present results, is currently under development.

Observations of droplet breakup at a grid also have implications for the modelling of grid rewetting. It is probable that the leading edge of a grid will become wetted at an early stage in reflood due to droplet impact at the leading edge. The progression of the wetting front will depend, in part, on the amount of cooling that occurs in the unquenched region of the grid. This in turn is dependent on the relative magnitudes of the different heat fluxes i.e. radiation, steam convection and droplet impingment on the grid face. The first two of these are fairly well understood and correlated. The third is a function of the efficiency of a drop to cool a hot surface, which has been addressed in the literature (Hall (1975), Wachters and Westerling (1966)), and the flux of drops arriving at the grid walls. Our results give an indication of the droplet flux arising from breakup and angular dispersion at impact on the leading edge and subsequent bouncing from the hot pin walls. This is likely to yield a higher droplet flux than would be associated with side deposition from a turbulent parallel gas stream such as that considered by Ganic and Rohsenow (1977). Thus a successful grid rewetting model is likely to require adequate modelling of the drop breakup dynamics at the leading edge of the grid.

5.2 Wetted grids

For wetted grids fragments produced at initial impact are expected finally to stick to the grid face and the drop size will be determined by entrainment from the top edge of the grid. For low steam velocities, $< 6\ ms^{-1}$, such as occur in the wake of a blockage or close to the quench front, it is anticipated that entrainment will not occur and the liquid will drain down the grid. For steam velocities grater than $10\ ms^{-1}$ all the liquid adhering to the grid will be entrained by the steam flow. For steam flows up to $15 \rightarrow 20\ ms^{-1}$, the highest likely to occur during reflood, the entrained droplets will have Sauter mean diameter ~ 1 mm. Thus from our experiments entrainment of liquid from the wetted grids does not appear to reduce the drop size sufficiently to make a significant contribution to enhanced steam desuperheating, although the lower initial velocities of entrained drops will have some effect.

Adams (1984) has studied the problem of modelling heat transfer in the vicinity of a wetted grid using experimental data from the THETIS facility (Pearson et al, 1983), and has shown that the main contribution to vapour desuperheating arises from the evaporation of the liquid film from the grid surface. Droplet evaporation represents only $\sim 15\%$ of the initial evaporative heat flux in the immediate environment of the grid. Adams showed that the chief modelling problems are associated with the steam convective heat transfer to the liquid film and that a proper model must take account of the development of the boundary layer in the steam flow and also the wavy nature of the film. There are significant uncertainties

in such calculations, but figure 13 shows a comparison of model results with measured vapour temperatures above and below a wetted grid in a THETIS test. Convective heat transfer to the film is modelled using a developing boundary layer solution appropriate to flow over a flat plate in an infinite channel, modified to include the effect of the close proximity of the fuel pin walls. The heat transfer coefficient is further enhanced by a factor

$$\sqrt{\frac{f_w}{f}}$$

where f_w = wavy film friction factor

f = Blasius friction factor.

This treats the wavy film effectively as a rough wall, whose roughness is of the same order as the film thickness, and follows Kay's (1966) recommendation for rough wall heat transfer coefficients. The agreement with measured steam desuperheating is good.

CONCLUSIONS

The experiments described above indicate that drop/grid interactions will be different for grids above and below the quench temperature.

1. For grids above the quench temperature the impact of drops on the leading edge of the grid initially forms two liquid fragments which breakup through surface instabilities. The degree of breakup depends on the impact conditions. The drop dynamics at the leading edge, in addition to being important for modelling of droplet heat transfer, affect the estimate of the side deposition flux which may be important in the modelling of grid rewetting.

2. For wetted grids the modification to the droplet size and velocity spectra arises from entrainment at the trailing edge of the grid of the liquid film on the grid surface. The observed entrained drop size, $d_{sa} \sim 1$ mm, appropriate to reflood conditions is not sufficiently altered to account for observed heat transfer enhancement and the dominant steam desuperheating mechanism is evaporation of the liquid film.

ACKNOWLEDGMENTS

This paper is published by permission of the Central Electricity Generating Board. The authors also wish to thank Mr. B. Dorey for valuable assistance with much of the experimental work.

REFERENCES

Adams, J.E., 1984, To be published.

Chandrasekhar, S., 1961, "Hydrodynamic and Hydromagnetic Stability", Oxford University Press.

Clare, A.J. and Fairbairn, S.A., 1984, Droplet Dynamics and Heat Transfer in Dispersed Two-Phase Flow, Paper presented at this Workshop.

Dombrowski, N. and Fraser, R.P., 1954, "A Photographic Investigation into the Disintegration of Liquid Sheets", Phil. Trans A, Vol 247, pp 13-130.

Dombrowski, N. and Hooper, P.C., 1964, "A Study of the Sprays Formed by Impinging Jets in Laminar and Turbulent Flow", J. Fluid Mech. Vol 18, pp 392-400.

Ganic, E.N. and Rohsenow, W.M., 1976, "Dispersed Flow Heat Transfer", Inc. J. Heat Mass Transfer, Vol 20, pp 855-866.

Hall, P.C., 1975, "The Cooling of Hot Surfaces by Water Sprays", C.E.G.B. Report RD/B/N3361.

Ihle, P., Rust, K. and Lee, S.L., 1982, "Experimental Investigation of Reflood Heat Transfer in the Wake of Grid Spacers". Joint N.R.C./A.N.S. Meeting on Basic Thermal Hydraulic Mechanisms in L.W.R. Analysis, Bethesda, Maryland, U.S.A.

Kays, W.M., 1966, "Convective Heat and Mass Transfer", Mc Graw-Hill, New York.

Lee, N. et al, 1981, "PWR FLECHT SEASET Unblocked Bundle, Forced and Gravity Reflood Task Data Evaluation and Analysis" Nureg/CR-2256 WCAP-9891.

Taylor, G., 1959, "The Dynamics of Thin Sheets of Fluid", Proc. Roy. Soc. A, Vol 253, pp 289-321.

Wachters, L.H.J. and Westerling, N.A.Y., 1966, "The Heat Transfer from a Hot Wall to Impinging Water Drops in the Spheroidal State", Chemical Engineering Science, Vol 2, pp 1047-1056.

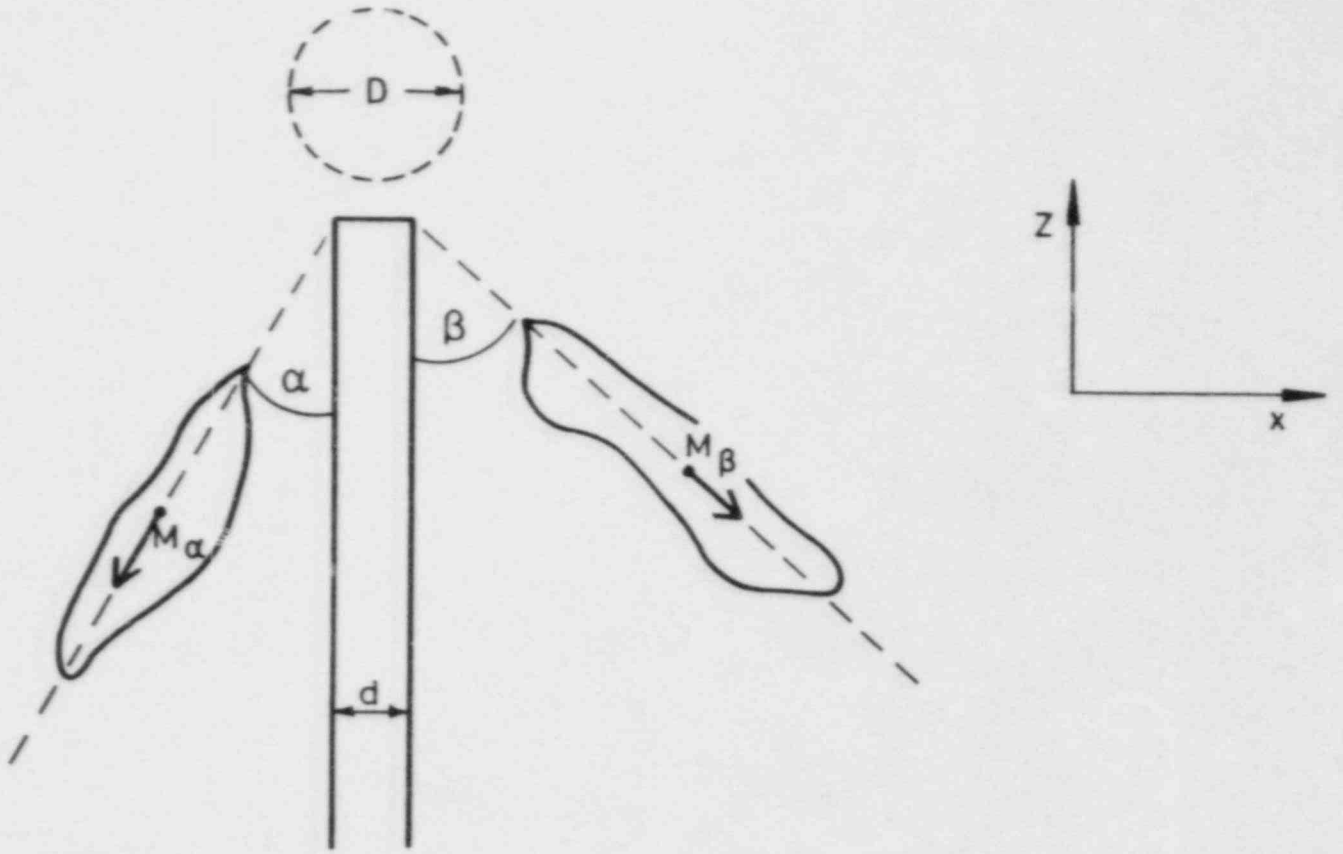

FIG. 1. Trajectories of Fragments After First Impact.

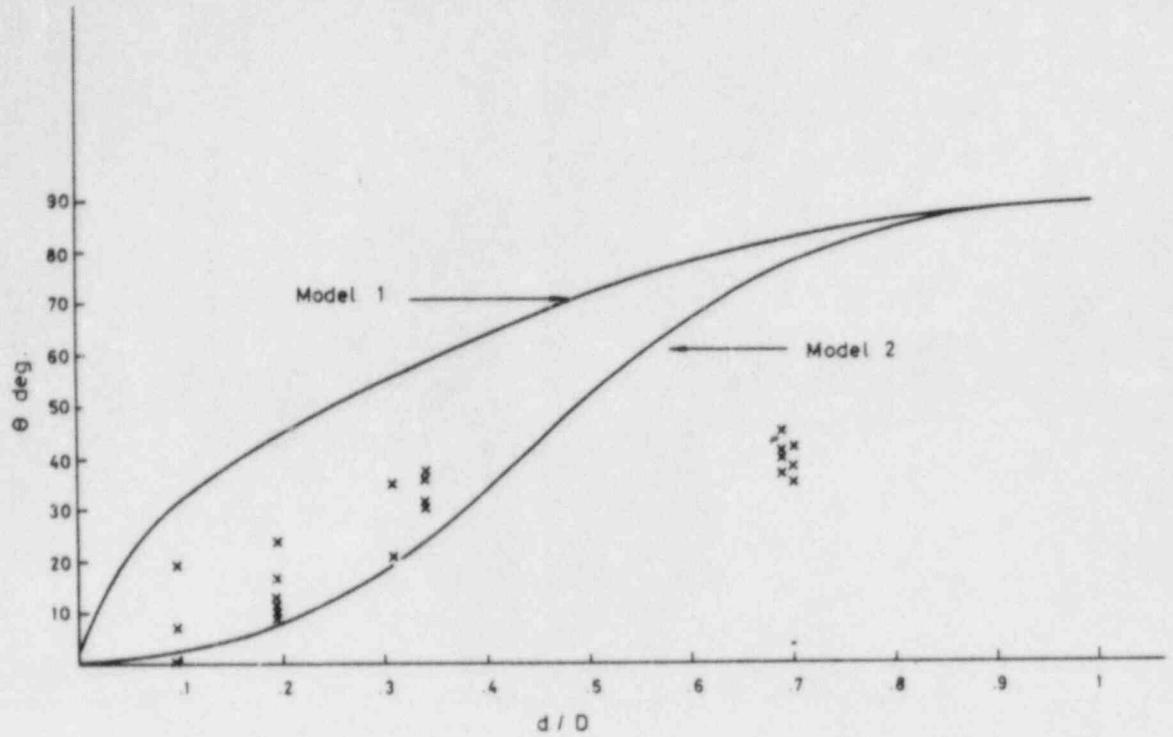

FIG. 2A. Variation of Angular Split with Grid Thickness.

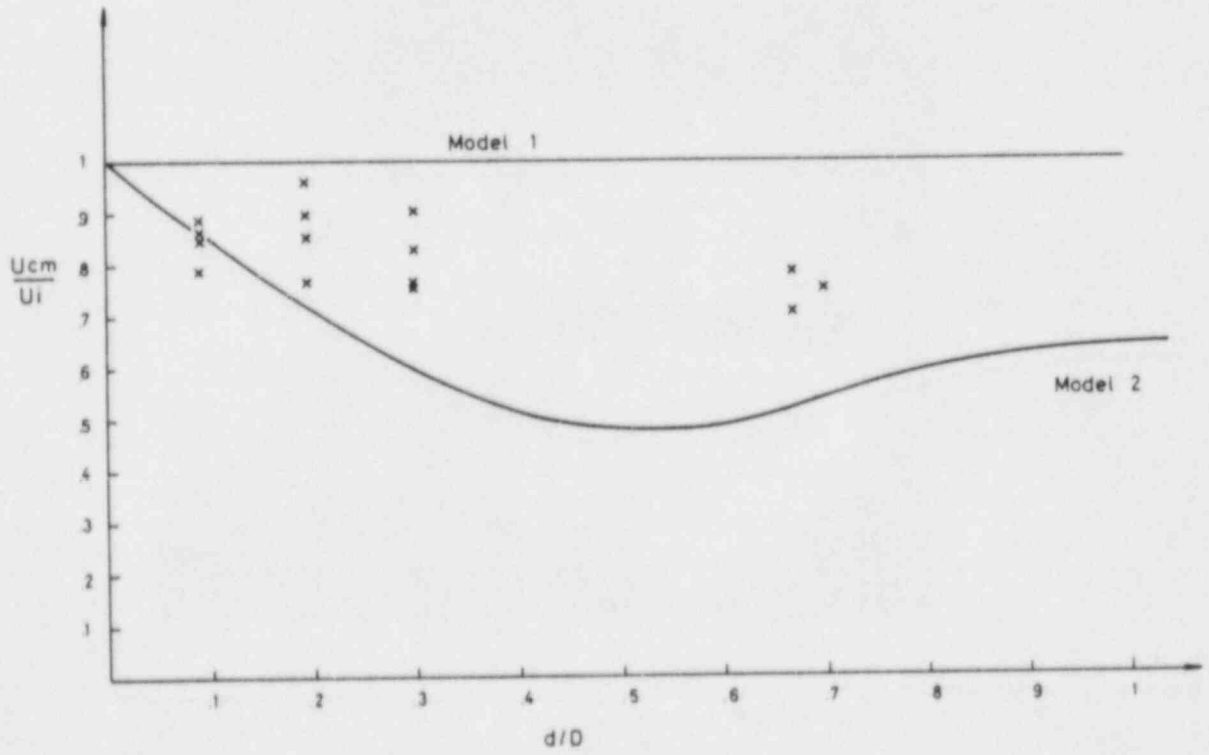

FIG. 2B. Centre of Mass Velocities for Different Grid Thicknesses.

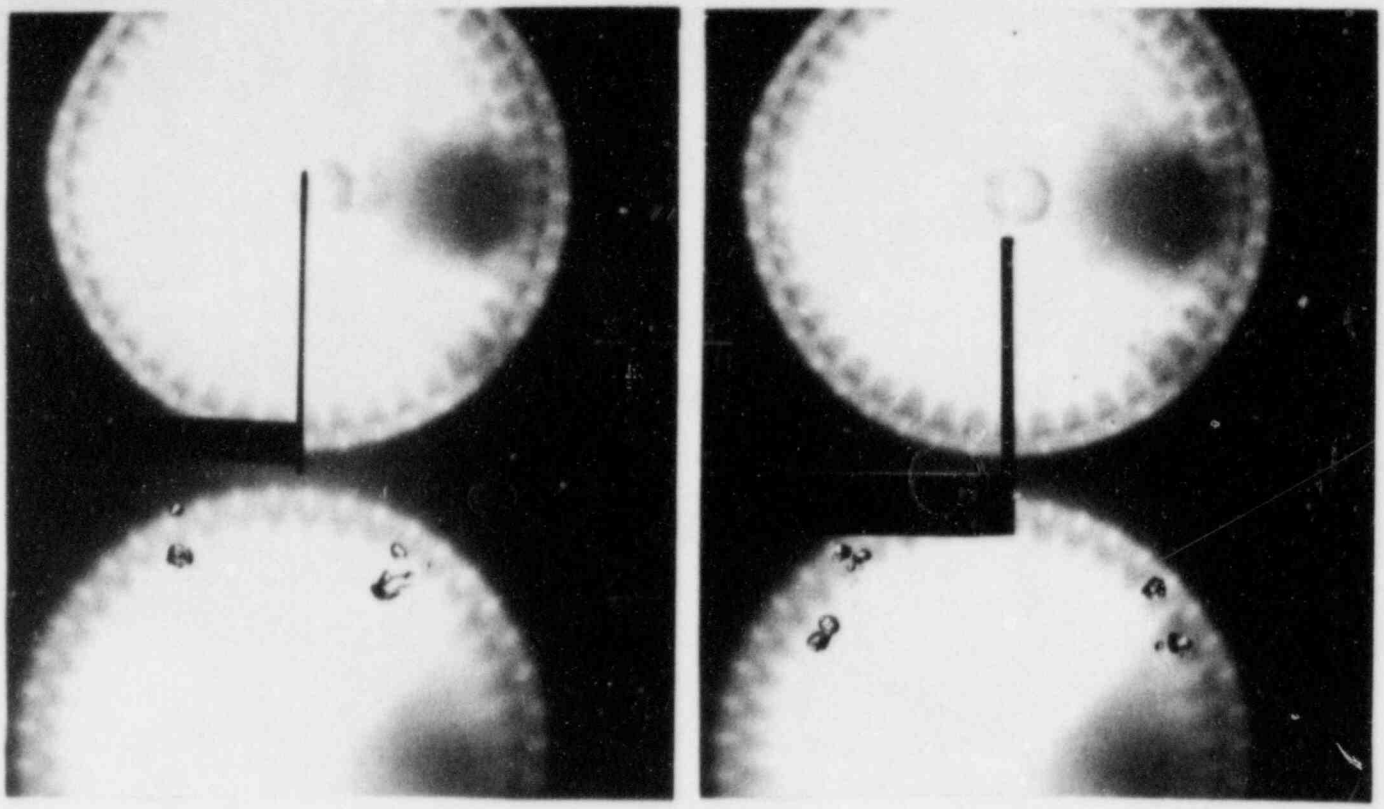

$d/D = 0.197$ $d/D = 0.336$

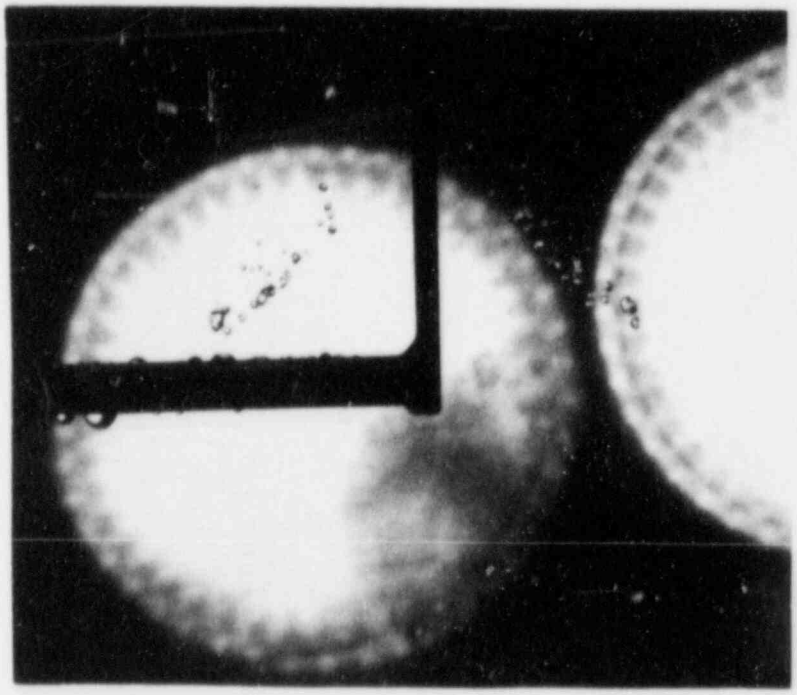

$d/D = 0.693$

FIG. 3. Breakup at $We_i \simeq 450 - 500$.

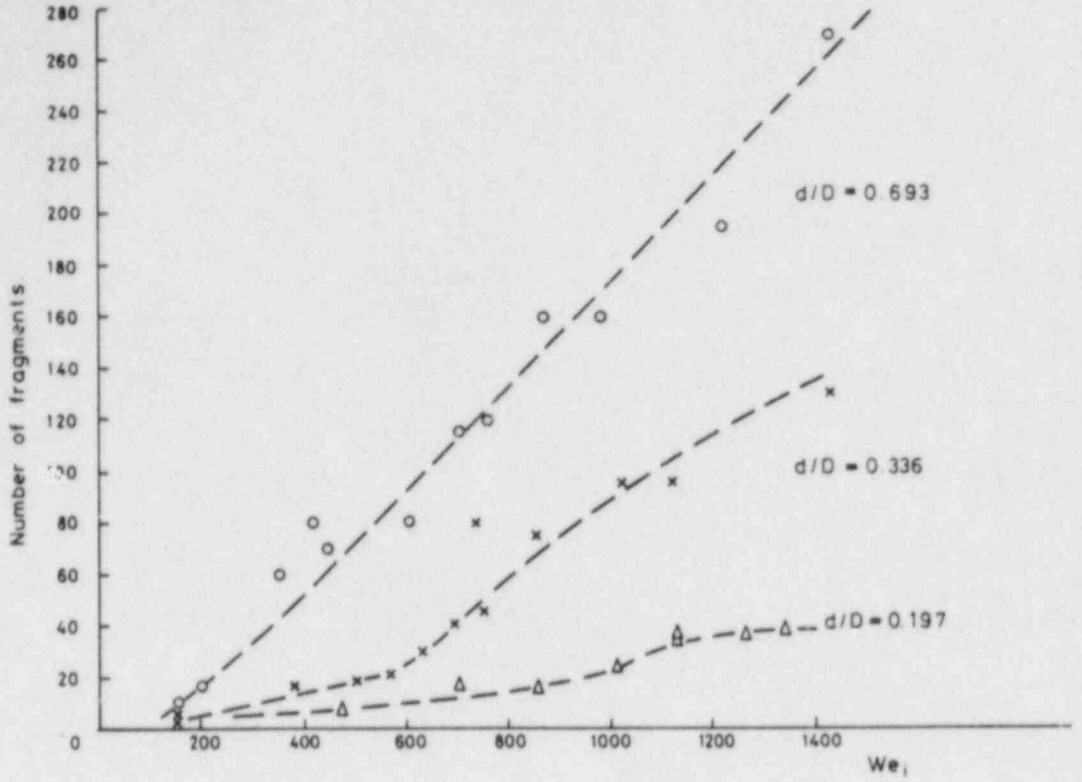

FIG. 4A. Degree of Breakup for 4.76 mm Water Drops on Cold Grids.

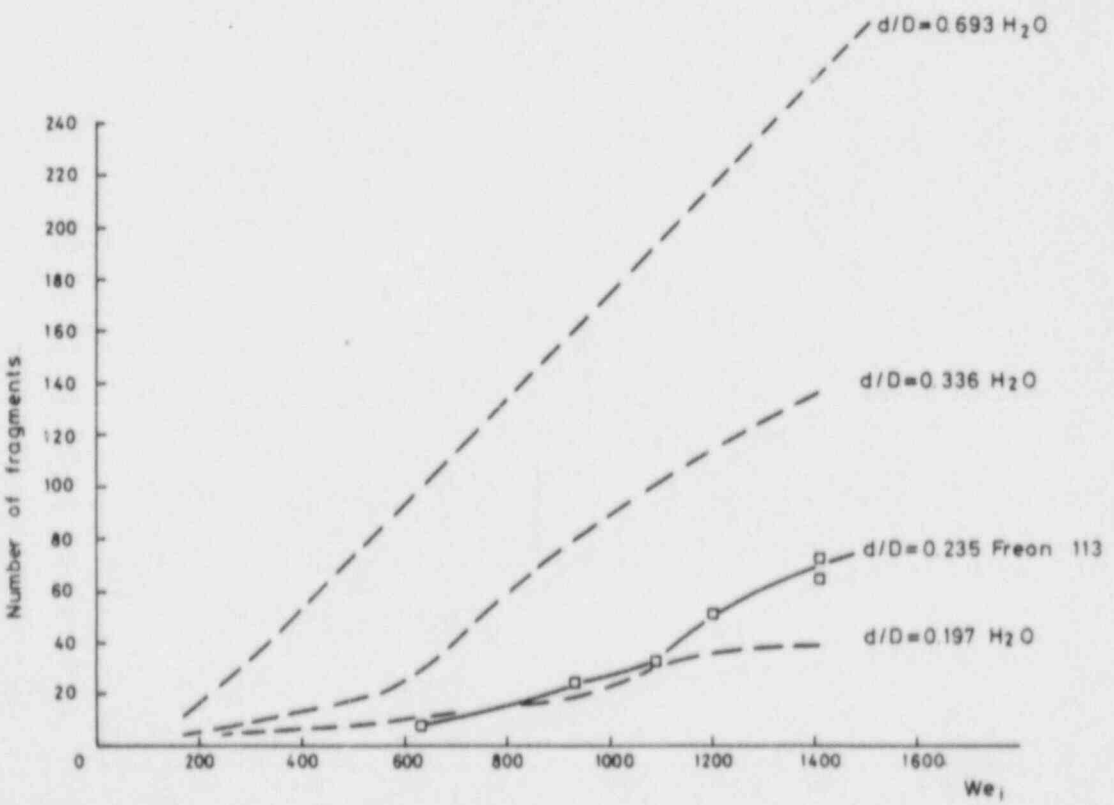

FIG. 4B. Degree of Breakup for 2 mm Freon 113 Drops on Hot Grid.

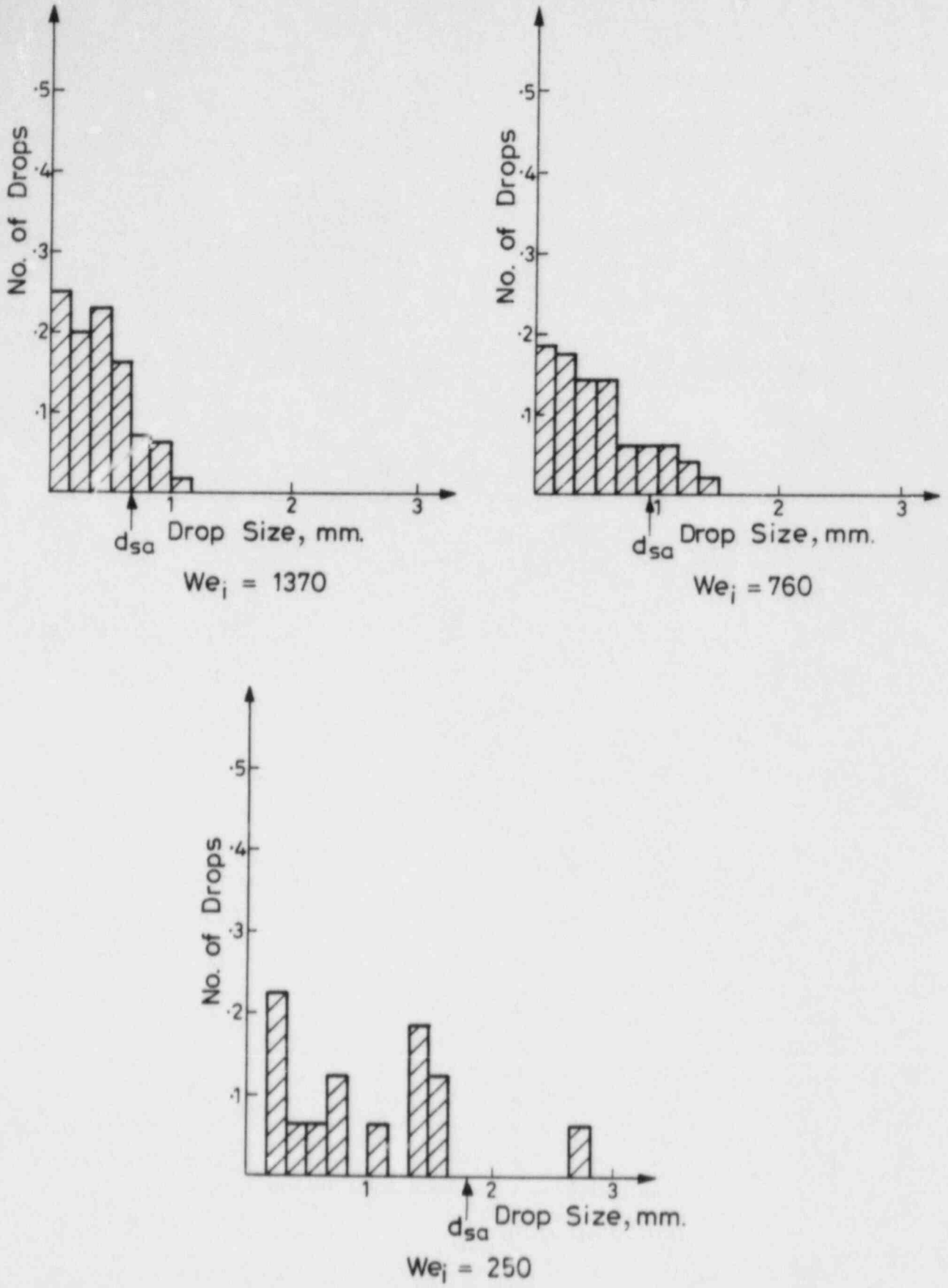

FIG. 5. Drop Size Distributions Arising from the Impact of a Single Drop Onto a Grid $d/D = \cdot 336$.

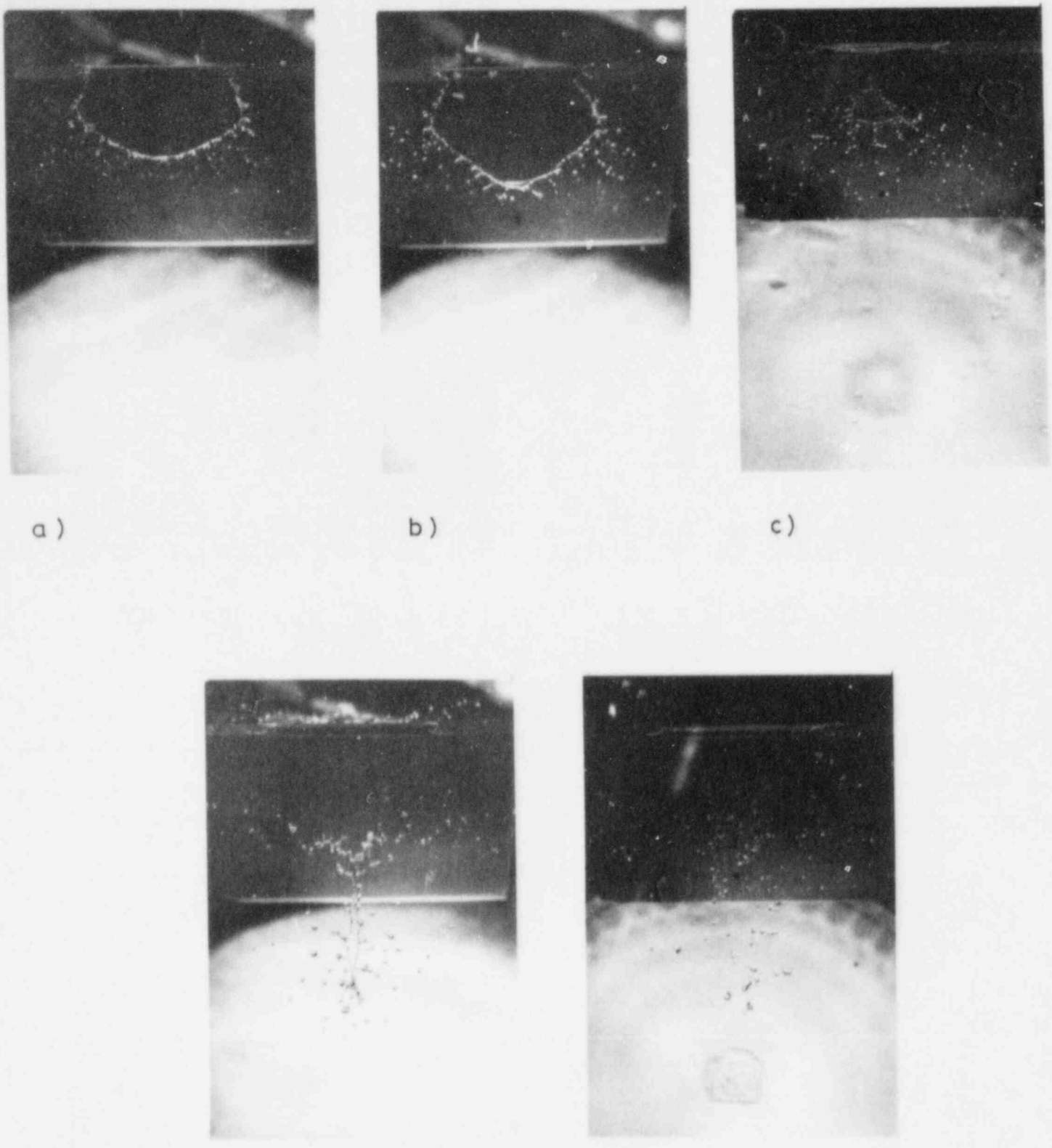

FIG. 6. The Impact of a Drop We_i = 1020 onto a Grid d/D = 0.695.

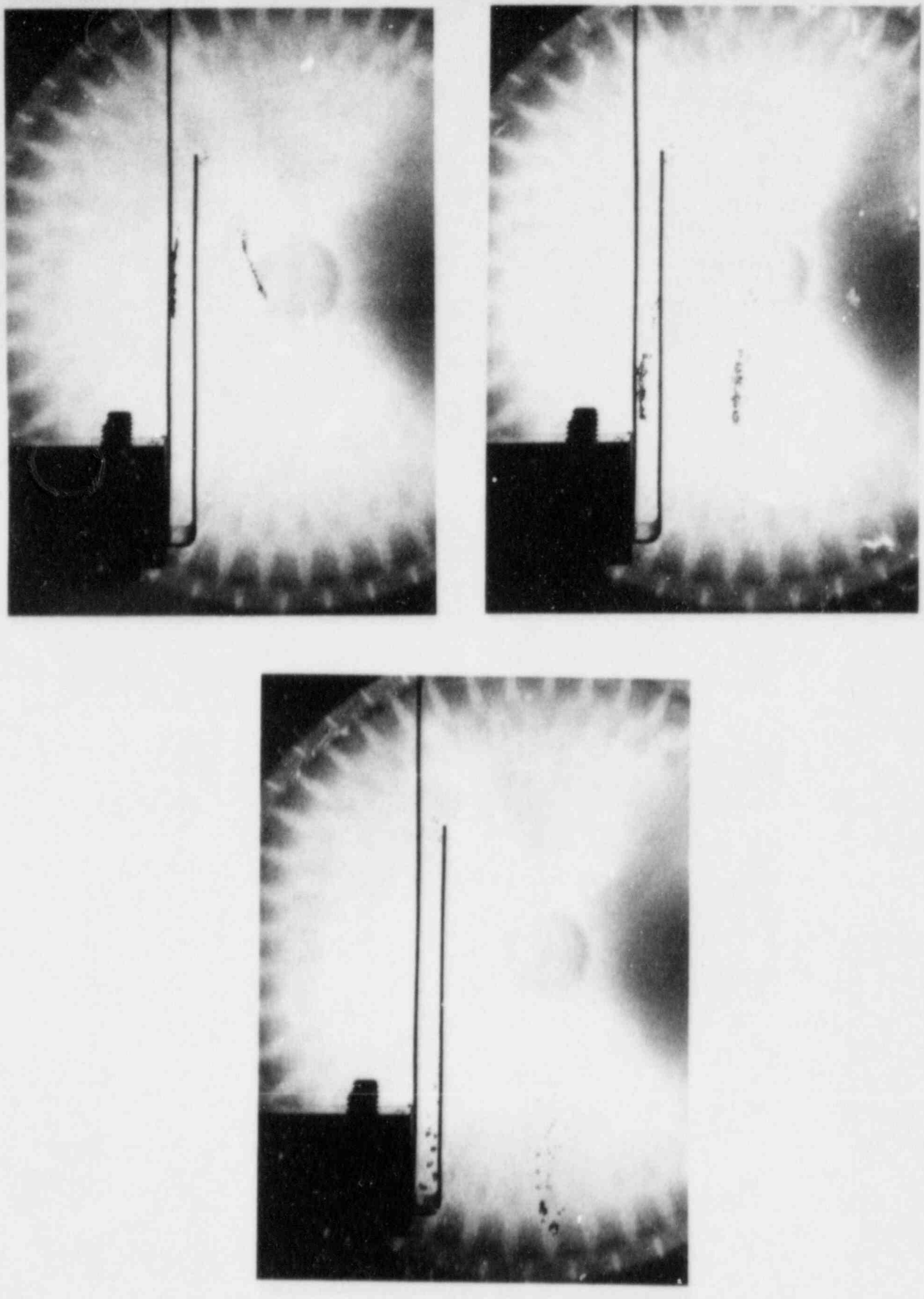

FIG. 7. Photographs of the Bounce Occurring for High Impact Weber Numbers.

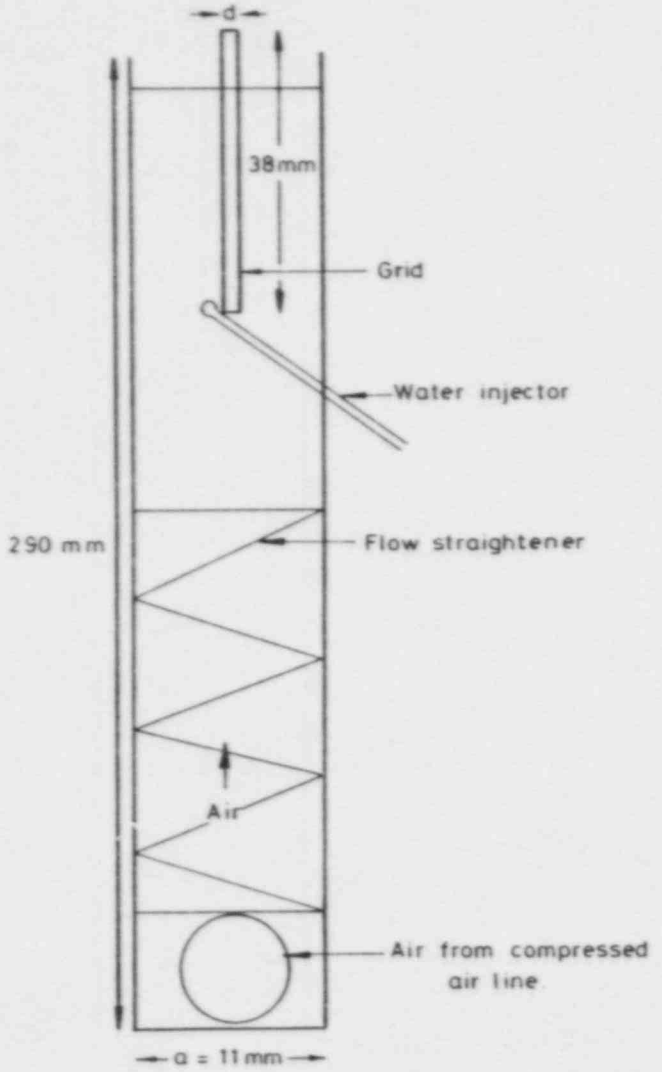

FIG. 8A. Apparatus used to Investigate Effect of Liquid Entrainment - Side View.

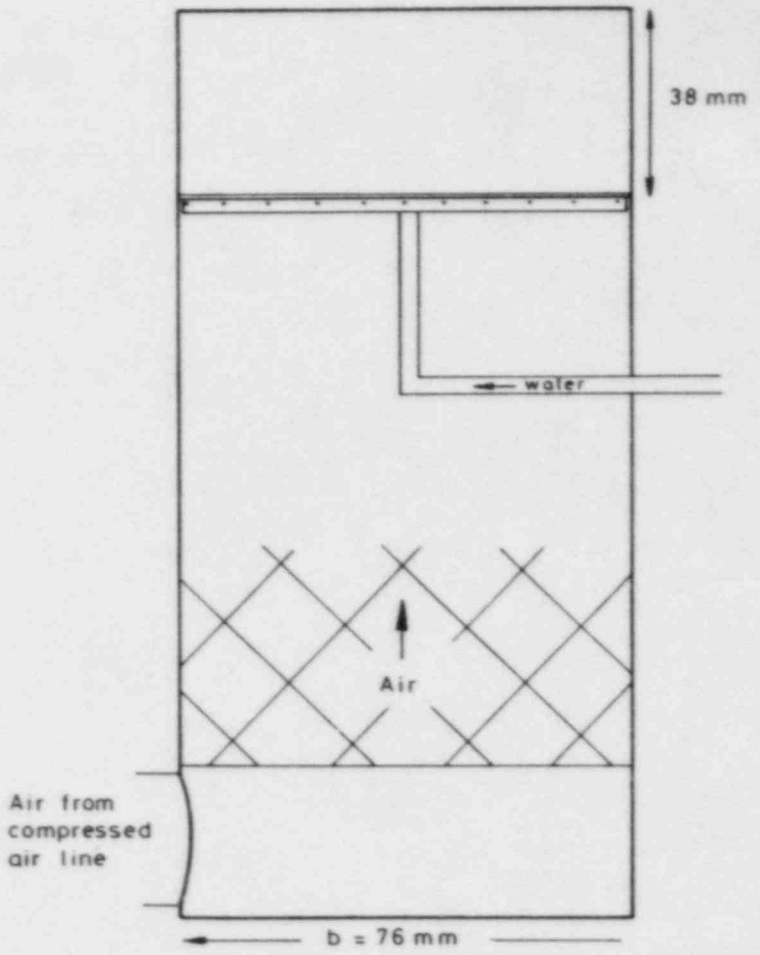

FIG. 8B. Entrainment Apparatus - Front View.

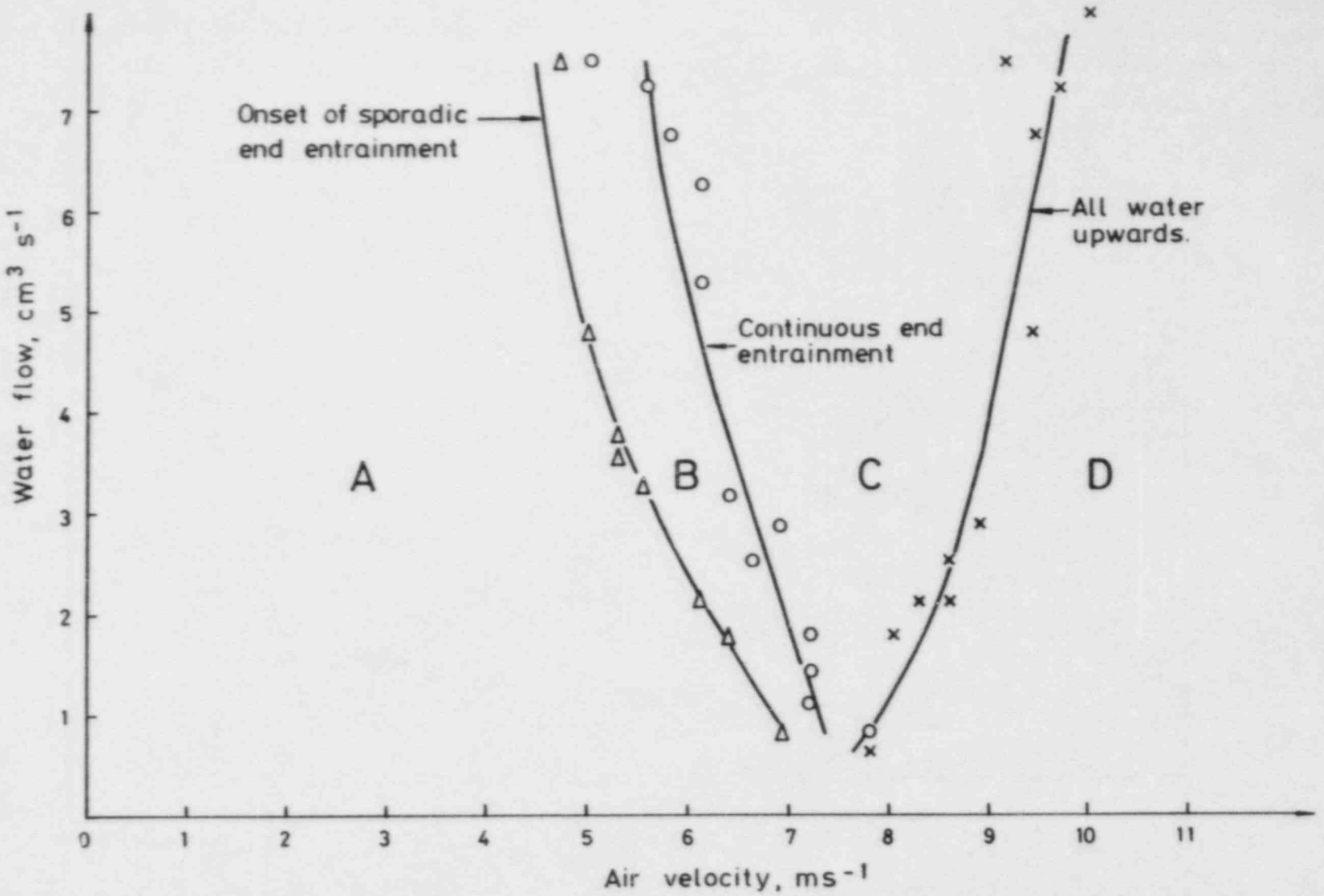

FIG. 9. Flow Regime Transition Map.

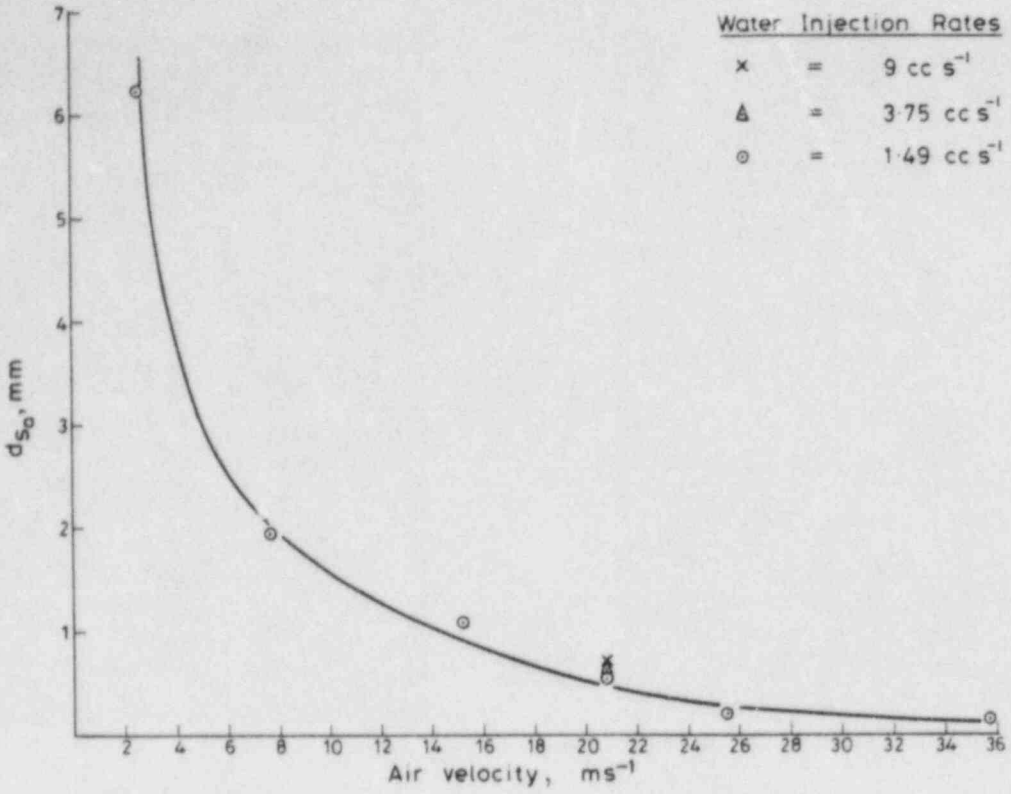

FIG. 10A. Sauter Mean Diameter as a Function of Air Velocity.

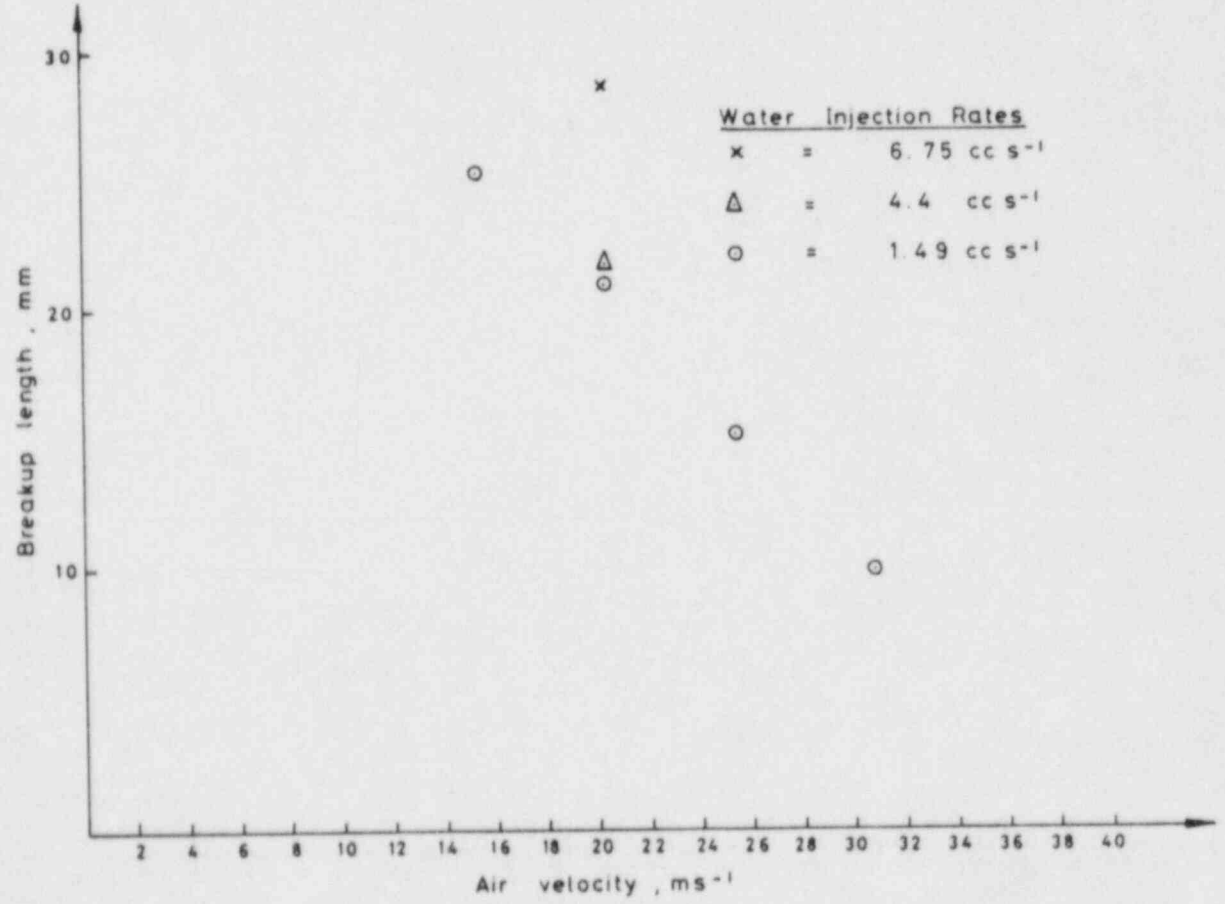

FIG. 10B. Breakup Length as a Function of Air Velocity and Water Flow Rate.

(a)

(b)

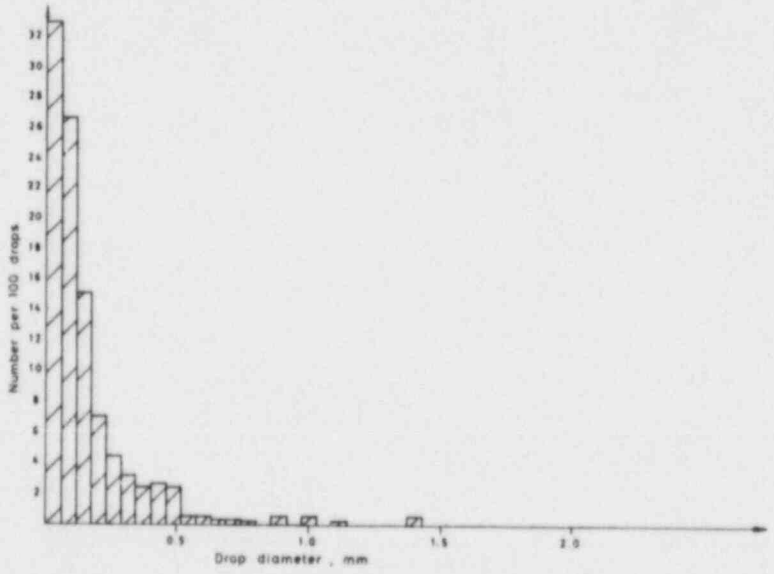

(c)

FIG.11. Drop Size Distribution Water Injection Rate $= 9\,cc\,s^{-1}$ Air Velocity $= 20.4\,ms^{-1}$.

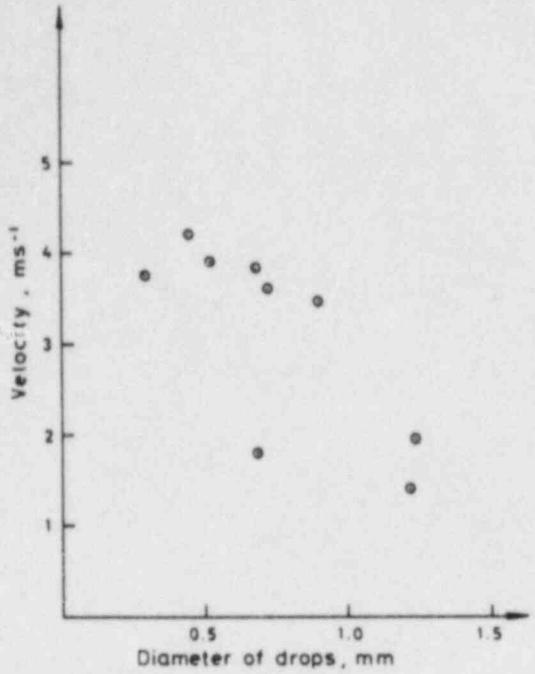

a) Air velocity = 15.3 ms^{-1}
Water injection rate = 1.49 cc s^{-1}
Breakup length = 24.4 mm

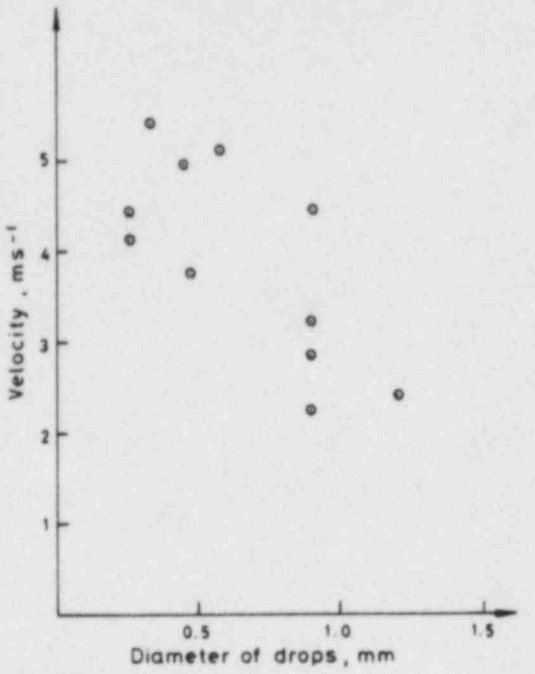

b) Air velocity = 20.4 ms^{-1}
Water injection rate = 1.49 cc s^{-1}
Breakup length = 20.7 mm

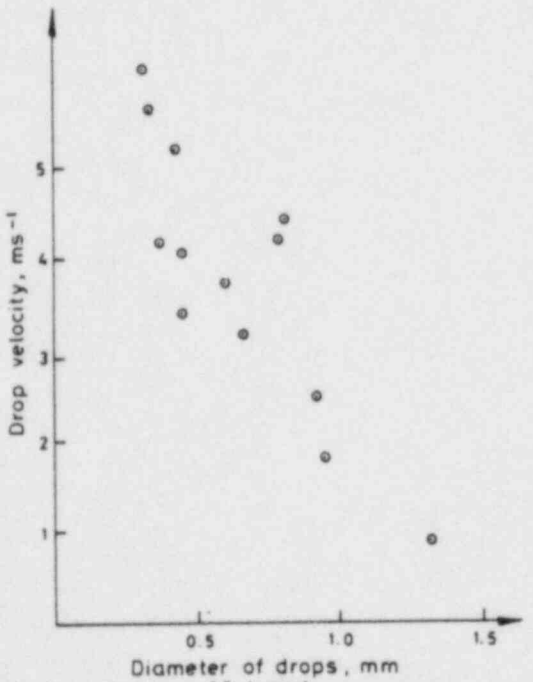

c) Air velocity = 20.4 ms^{-1}
Water injection rate = 4.4 cc s^{-1}
Breakup length = 21.9 mm

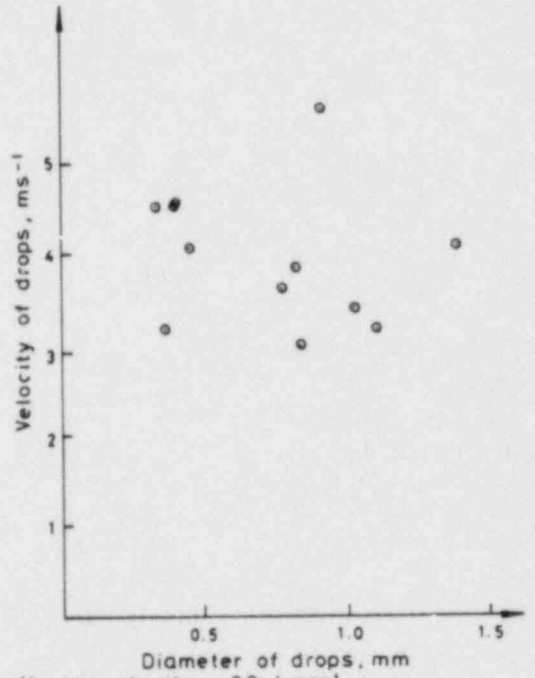

d) Air velocity = 20.4 ms^{-1}
Water injection rate = 6.75 cc s^{-1}
Breakup length = 28.7 mm.

FIG.12. Distribution of Drop Velocities with Drop Size.

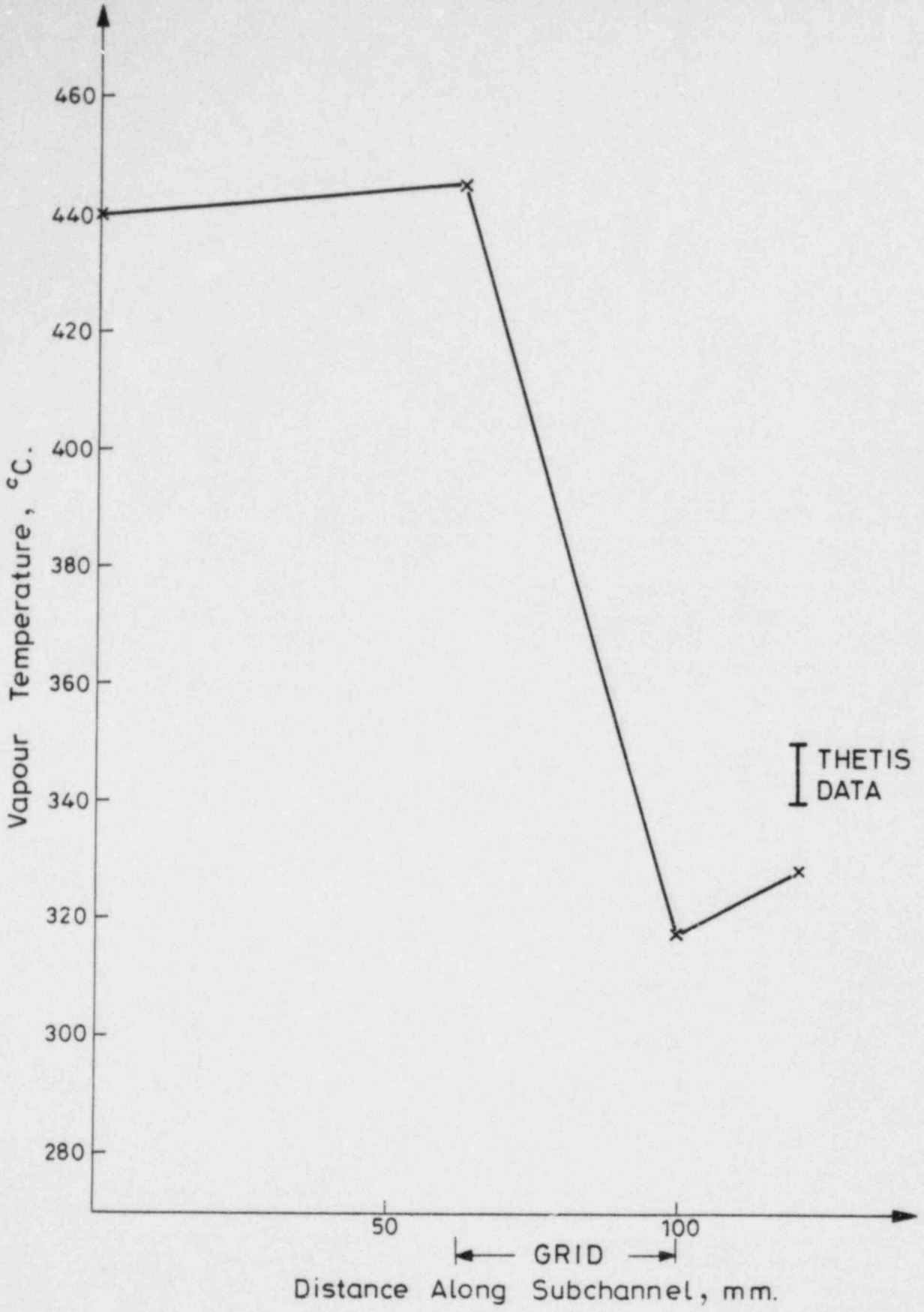

FIG. 13. Comparison of Theoretical Prediction of Vapour Temperature with Experimental Data.

PREMATURE QUENCHING BY BALLOONED AND BURST FUEL ROD CLADDINGS IN A LOCA

F. Erbacher, K. Wiehr
Kernforschungszentrum Karlsruhe
Institut für Reaktorbauelemente
Projekt Nukleare Sicherheit
Postfach 3640, 7500 Karlsruhe 1
Federal Republic of Germany

ABSTRACT

In a loss-of-coolant accident (LOCA) of a pressurized water reactor (PWR) some Zircaloy fuel rod claddings reach temperatures which cause them to burst due to internal overpressure. The coolability of burst fuel rod bundles has been investigated in the past by specific thermohydraulic experiments, in which the bursts were simulated by sleeves mounted on solid electric heater rods.

In contrast, in the REBEKA program which used electrically heated fuel rod simulators with pressurized Zircaloy claddings and a gap between the cladding and the pellets the coolability of burst claddings has been investigated in more detail. It has been shown that premature local quench fronts are generated at the bursts long before the regular quench front had reached these axial elevations. Such local quench fronts propagate in the axial and lateral directions and cause a fast quenching of the hot fuel rod bundle regions around burst claddings.

These favorable effects can not be expected to appear in tests which use sleeves to simulate burst claddings. Such phenomena are not modeled in existing computer codes but prove a higher safety margin of coolability in a LOCA of a PWR.

INTRODUCTION

In a LOCA of a PWR fuel rod claddings may reach temperatures at which they ballon and burst under the impact of internal overpressure. Thermohydraulic experiments, e.g. FEBA, FLECHT, SCTF, THETIS served to study the temperature and quenching behavior on electric heater rods. Ballooned claddings were simulated by sleeves mounted on these heater rods.

It was demonstrated in the REBEKA and HALDEN experiments [1, 2] that REBEKA-type fuel rod simulators and non-deformed fuel rods undergo earlier quenching as compared to heater rods. It will be shown in the following paragraphs that burst Zircaloy cladding tubes quench even earlier than non-deformed cladding tubes.

FUEL ROD BEHAVIOR

During the refill phase in a LOCA non-deformed and deformed non-ruptured cladding tubes exhibit nearly identical temperatures. However, in case the cladding tube bursts, gaping burst lips extend into the cooling channels and helium and fission gases escape from the rod. Steam with its much poorer thermal conductivity enters the fuel rod via the burst opening and causes decoupling of the cladding from its heat source. Now the two-phase mixture of the flooding phase is capable of cooling down the cladding at the point of burst very quickly. A new secondary quench front starts to propagate from the burst point. At that point of time the regular quench front in the non-deformed geometry may still be at a much lower level.

This process is shown schematically in Fig. 1. At the time t_2 the quench front has attained the axial point x_A and at the point x_B the cladding tube will burst. Two new secondary quench fronts will emanate from the axial position x_B, one of them proceeding upwards, the other downwards opposed to the direction of flow. At the time t_4 the quench front propagating downward meets the primary quenchfront rising in regular mode from the lower rod end. The secondary quench front attains the upper end of the rod at the time t_5 already. The most important effect of the appearance of the secondary quench front consists in the premature cooling within the range of maximum cladding tube temperatures.

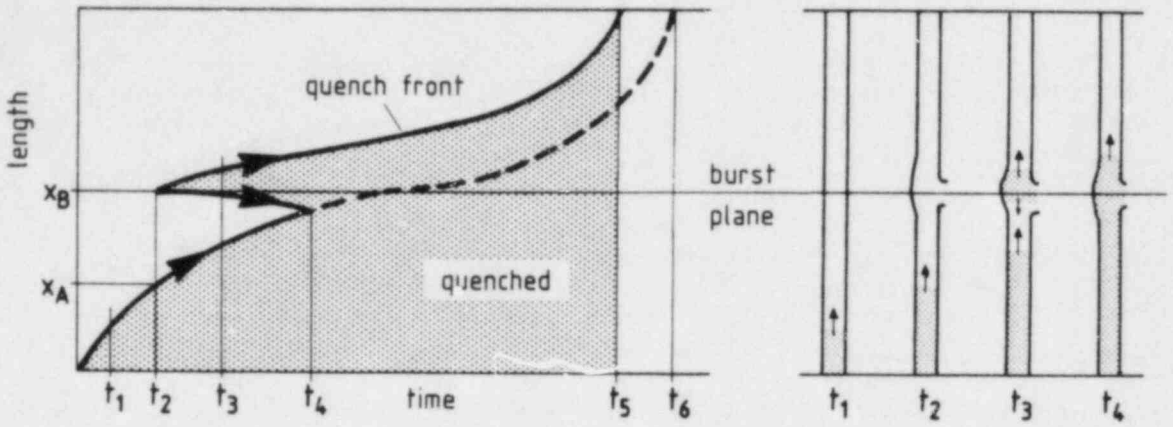

Fig. 1 Premature quenching of burst claddings (schematic)

TEST RESULTS

The REBEKA program on the fuel rod behavior during the refill and reflooding phase in a LOCA was devoted to studing the deformation behavior of Zircaloy cladding tubes in rod bundles as well as the coolability of blockages formed in the cooling channel. Since indirectly heated fuel rod simulators with a gas gap between the pressurized Zircaloy cladding tube and the pellets were used in these experiments, it was possible to simulate and record the generation and propagation of new quench fronts on burst cladding tubes.

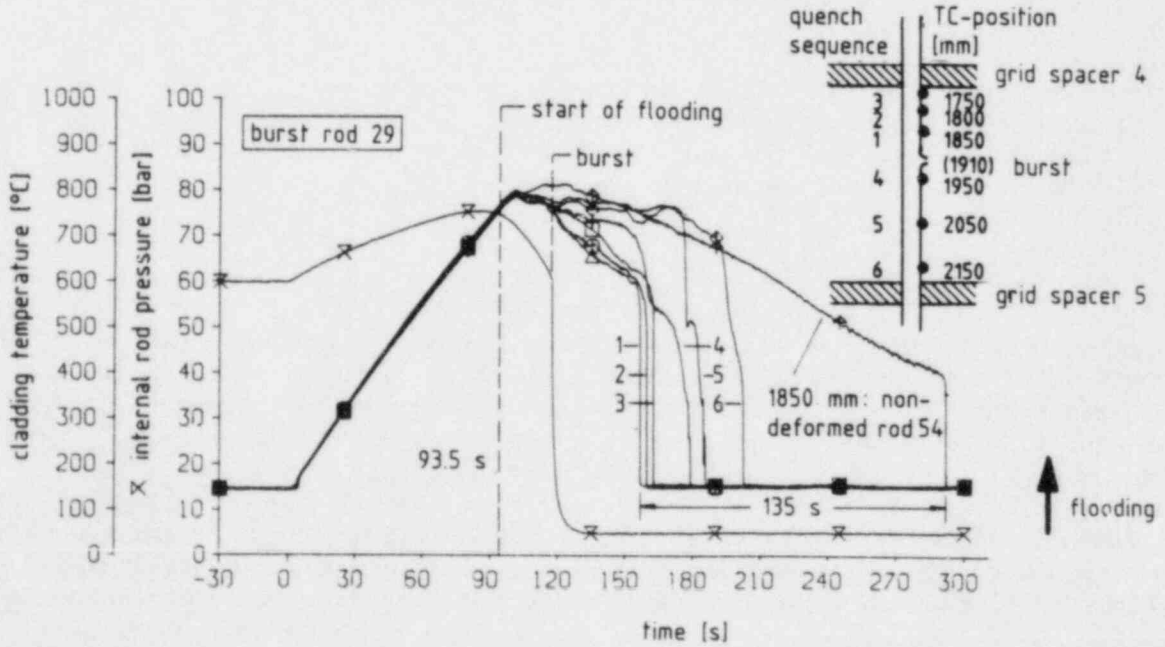

Fig. 2 Temperature- and quenching behavior of a burst cladding (REBEKA 6).

Fig. 2 shows among other things the plot of measured cladding tube temperature of the non-deformed cladding of rod 54 at an axial level of 1850 mm. This rod is not influenced by premature quenching of neighbored burst rods. Also shown is the temperature and pressure history of the deformed and burst rod 29 at various axial positions between the two central spacer grids. Two effects can be seen:

- 135 s earlier quenching of the burst rod at 1850 mm,
- a secondary quench front starting from the burst lips and propagating more quickly in the flow direction than opposed to it.

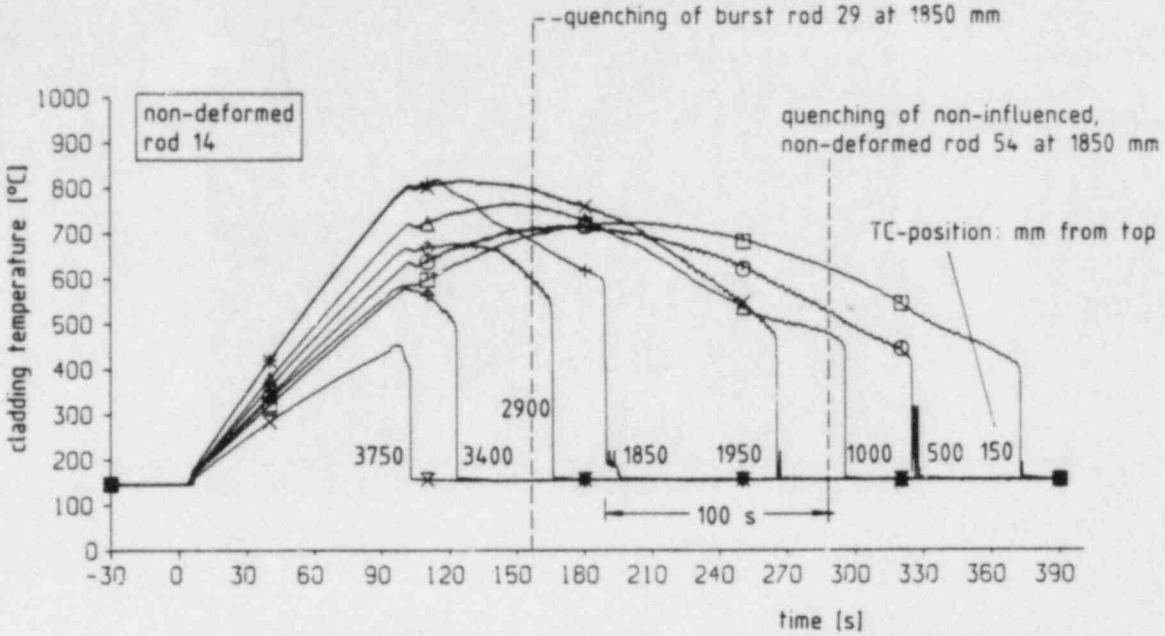

Fig. 3 Temperature- and quenching behavior of a non-deformed cladding (REBEKA 6)

Fig. 3 shows the plots of measured cladding tubes temperatures of the non-deformed rod 14 over an extended axial length. Three effects can be seen:

- At the time of quenching of rod 29 at 1850 mm the quench front of the non-deformed rod reaches an axial level of about 3000 mm, i.e. the regular quench front is at the same time at an more than 1000 mm lower level than the secondary quench front.

- Comparing the time of quenching of two non-deformed claddings of the rods 54 and 14 at the same axial level it can be noticed that the rod 14 quenches about 100 s earlier.

- The axial position at 1850 mm quenches about 75 s earlier than the axial position 1950 mm on the same cladding of rod 14.

The reason for the premature quenching of the axial position 1850 mm of the non-deformed cladding tube of rod 14 is a radial rod to rod interaction. The premature quenching of the burst neighboring rod 36 initiates a secondary quench front even on the non-deformed cladding of rod 14 (see Fig. 4).

These findings underline that burst cladding tubes do not only give rise to a generation and propagation of new secondary quench fronts in the axial direction but also to a propagation in the radial direction within the bundle.

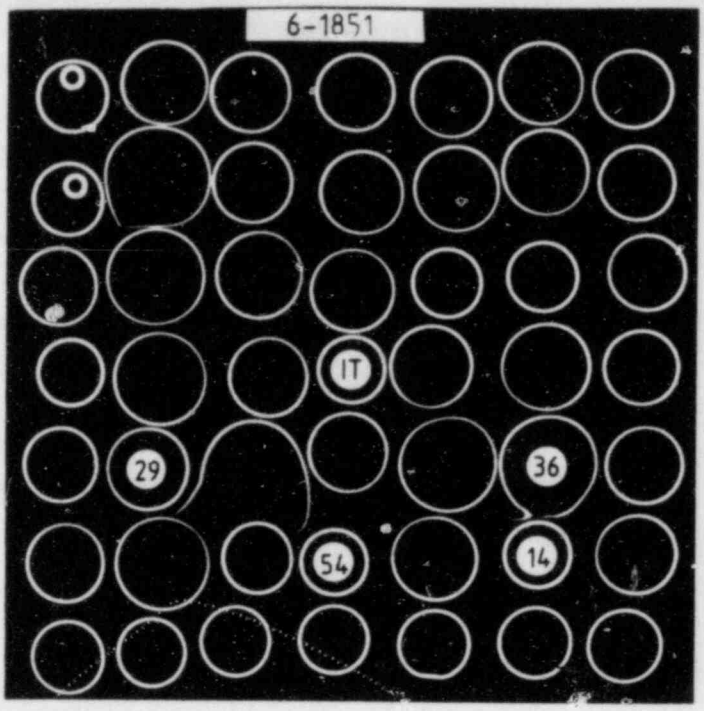

IT: instrument tube
54, 14: unpressurized, non-deformed

Fig. 4 Bundle cross-section at axial level 1851 mm (REBEKA 6)

SUMMARY

A secondary quench front at a burst of a cladding tube will be initiated if the locally increased heat transfer and a higher thermal resistance between the cladding and the heat source lead to a premature cooling and quenching of the burst lips of a cladding tube. This may occur long before the regular quench front has reached this axial point in the bundle. The secondary quench front may propagate to neighbored rods as well. Consequently the hot zones in the bundle containing burst claddings are cooled down quickly.

These favorable effects can not be expected from experiments involving sleeves for simulating burst cladding tubes. They have not been modeled in existing computer codes although they suggest a higher safety margin in assessing the coolability in a LOCA in a PWR.

REFERENCES

[1] Jahresbericht 1980, Projekt Nukleare Sicherheit, KfK 2950, pp. 4200-155, August 1981.

[2] Erbacher, F.J., Neitzel, H.J., Wiehr, K.: Effects of Thermohydraulics on Clad Ballooning, Flow Blockage and Coolability in a LOCA. OECD-NEA/IAEA Specialists' Meeting on Water Reactor Fuel Safety and Fission Product Release in Off-Normal and Accident Conditions. Risø National Laboratory, Denmark, May 1983.

MEASUREMENT OF DROPLET DYNAMICS ACROSS GRID SPACER IN MIST COOLING OF SUBCHANNEL OF PWR

S. L. Lee, H. J. Sheen, S. K. Cho and I. Issapour

Department of Mechanical Engineering
State University of New York at Stony Brook
Stony Brook, New York 11794

(Contract No. NRC-G-04-81-014)

ABSTRACT

An experiment was conducted of the dynamics and heat transfer of a droplet-vapor mist flow across a test grid spacer in a flow channel of 2x2 electrically heated simulation fuel rods. Embedded thermocouples were used to measure the rod cladding temperature and an unshielded Chromel-Alumel thermocouple was transversed in the center of the subchannel to measure the temperature of the water and steam coolant phases at various axial locations. Thermocouples were also embedded in the test grid spacer. Optical measurements of the size and velocity distributions of droplets and the velocity distribution of the superheated steam were made by special laser-Doppler anemometry techniques through quartz glass windows immediately upstream and downstream of the test grid spacer. Experiments over a range of steam and injected water flow rates and rod heat flux have been performed and some representative results and discussions are presented.

INTRODUCTION

The enhanced mist cooling downstream of grid spacers in fuel rod bundles has been recently suggested as an important heat transfer mechanism for the development of cladding temperature transient during reflood emergency cooling for LOCA in PWR [1,2,3]. Figure 1 shows three sketches of cladding temperature for 30, 90 and 150 seconds after the onset of flooding respectively in a 5x5 array of electrically heated rods simulating a full-length PWR fuel rod bundle. In each of these sketches, there are two axial profiles of the cladding temperature between three grid spacers, one for each of the two cases with and without the grid spacer at the midplane. It is clear that there is a substantial drop in the cladding temperature downstream of the grid spacer which cannot be possibly explained by the convective cooling of the superheated steam. The measured carry-over of liquid water at the top end of the rod bundle suggests the presence of large water droplets in the flow beginning at the onset of reflooding. It is conceivable that some of these thermally relatively inactive large droplets may interact with the grid spacers, which are distributed along the whole length of the bundle, to generate large population of small droplets in the flow. Due to their very large surface to mass ratios, these small droplets can serve as extremely efficient heat sinks for the region of the cladding downstream of the grid spacer. The purely fluid mechanical part of the phenomenom of the breaking up of large

droplet across a grid spacer was established from the measurement of a room-temperature water droplet-air mist flow [4]. A direct verification of the cooling effect of this phenomenom in a water droplet-vapor mist flow in a rod bundle at elevated temperatures is thus in order.

EXPERIMENTAL ARRANGEMENT

The flow channel consists of a simulated 1.60m-long pressurized water reactor fuel rod bundle of 2x2 electrically heated rods of 1.10m heated length with heating elements embedded in MgO filling inside the 1mm thick NiCr cladding of the rods which are 10.75mm in outside diameter and 14.30mm in pitch. Embedded thermocouples are used to measure the rod cladding temperature at various axial levels and an unshielded Chromel-Alumel thermocouple sheathed by an Inconel tube of 0.25mm outside diameter is transversed in the center of the subchannel to measure the temperature of the water and steam coolant phases at various axial levels. The channel with 7.94mm thick Inconel walls has an outside dimension of 36mm x 36mm and is connected at its upper and lower ends respectively to the upper and lower stainless steel settling chambers. The upper ends of the rods are tightly held by graphite seals and the lower ends by O-rings which are cooled by a water cooling jacket. A thin stainless steel water nozzle is placed 37mm below the test grid spacer in the center of the subchannel to supply the water droplets. An ensemble of electrically heated strip heaters is wrapped around the outside of the channel to heat up the walls.

The general flow arrangement is shown in the sketch of Figure 2. Steam coming from the steam supply passes through a ball valve, the steam separator and the electrically heated steam superheater to the test channel. Power for the simulated fuel rods, the strip heaters and the steam superheater is supplied from a bank of variable transformers. The whole flow system is wrapped with a heavy blanket of packed ceramic fiber insulation to reduce heat loss.

INSTRUMENTATION

The test grid spacer, 0.5mm thick and 38mm long and placed at the mid-section of the channel, has one of its central plates instrumented with the thermocouple as shown in the sketch of Figure 3. The elevation of the thermocouples embedded in the rod cladding as well as in the channel walls are shown in the sketch of Figure 4.

Two pairs of quartz glass windows at elevations respectively just before and after the test grid spacer are provided for *in situ* laser-Doppler anemometry measurement of droplet dynamics across the grid spacer in the subchannel. Two optical measurement scheme, one for large droplets (>240μm)[5] and one for small droplets (<240μm) [6], were alternately applied with an identical optical arrangement, a sketch of which is shown in Figure 5.

The optical measurement scheme for large droplets combines the conventional technique of optical gating for particle sizing and laser-Doppler anemometry for velocity measurement [5]. The optical gating is done by observing the blocking of the stationary scattering beam by the moving particle and the velocity Doppler signal is generated by scattering from the backward scattering point on the surface of

the droplet as shown in the sketch of Figure 6. In this arrangement, the location of the scattering point on the surface of the particle for velocity measurement coincides with the location corresponding to the ending of the blocking period for size measurement. Figure 7 presents respectively the oscilloscope traces of the photo-diode output showing the blocking and the photomultiplier output showing the same blocking together with a Doppler signal at the end.

The optical measurement scheme for small droplets makes use of the discrimination on the amplitude as well as the residence time and frequency of the individual Doppler signals to isolate the central core region of the optical measuring volume where the illumination is more uniform for droplet sizing [6] as shown in the sketches of Figures 8a, 8b and 8c.

Figure 9 shows the instrumentation blcok diagram. For the storage, processing and analysis of data, a PDP-11/34 minicomputer was used. Custom-designed computer interfaces (TSI Models 1998-D-1, 1998-S and 1998-Y) were used to interface the electronic circuits to the PDP-11/34 computer interface (DR-11B). Another custom-built electronic circuit was used to validate the signals. These data were stored in the memory of a hard disc (RK-05). The data acquisition system had been so automated that it was possible to collect as many data points as required under software control.

EXPERIMENTAL RESULTS AND DISCUSSIONS

Two series of tests were conducted under the following conditions:

Test Series I: Rod power: 1.14 kW/m
Inlet steam temperature: 175°C
Steam mass flux: 24.3 and 30.0 kg/hr

Test Series II: Rod power: 102.2 W/m
Inlet steam temperature: 225°C
Steam mass flux: 13.7 kg/hr.

Figures 10 and 11 show a plot of grid spacer temperature versus water injection rate for Test Series I and II respectively. It is observed that at low water injection rates the grid spacer remains dry, while at high water injection rates the grid spacer becomes wet due to quenching. Since the mechanism of reentrainment of small droplets from a dry grid spacer is different from that of a wet grid spacer, the enhanced mist cooling downstream of a grid spacer therefore is expected to vary according to whether the grid spacer is dry or wet.

In Test Series I, two water injection rates, namely 10.5 cm^3/min (dry grid spacer) and 32.0 cm^3/min (wet grid spacer), were selected for detailed measurements. For each of these water injection rates, two steam mass fluxes, namely 24.3 kg/hr (low steam mass flux) and 30.0 kg/hr (high steam mass flux), were selected. Figures 12 and 13 show, for low and high steam fluxes respectively, the axial temperature profiles for both the rod cladding and the steam in the subchannel for

no water injection and water injection rates 10.5 cm^3/min and 32.0 cm^3/min. In Test Series II, two water injection rates, namely 5.0 cm^3/min (dry grid spacer) and 13.5 cm^3/min (wet grid spacer), at a steam mass flux of 13.7 kg/hr were selected for detailed measurements. Figures 14 and 15 show the axial temperature profiles for both the rod cladding and the steam in the subchannel for no water injection and water injection rates 5.0 cm^3/min and 13.5 cm^3/min respectively.

In general, the grid spacer serves as a cooling fin for the rods with or without water injection. Water injection promotes significant cooling enhancement downstream. This effect is more pronounced in the case of wet grid spacer than in the case of dry grid spacer. At high steam mass flux for the case of wet grid spacer, the cooling enhancement region extends far beyond 500mm downstream (typically the distance between two successive grid spacers in an actual rod bundle).

Laser-Doppler anemometry measurements for the mist flow before and after the grid spacer for the selected mass flux and water injection rate conditions were made for both Test Series I and II.

Tables 1 and 2 give a sample summary of the optical droplet measurement across the dry and wet grid spacers for Test Series I respectively. It is shown that there is a significant increase in the small droplet population in the mist flow across the grid spacer. Furthermore, this increase in the small droplet population is directly related to the measured enhanced cooling of the rod cladding downstream of the grid spacer.

The following correlations for the size of the small droplets downstream of the grid spacer have been formulated:

Dry grid spacer

$$d_{D,S}/d_{U,L} = 13.6\ We^{-0.593} \qquad (1)$$

where $d_{D,S}$ = Sauter mean diameter of small droplets downstream of grid spacer

$d_{U,L}$ = Sauter mean diameter of large droplets upstream of grid spacer

We = $\rho_\ell V_{d_{U,L}}{}^2 d_{U,L}/\sigma$, the Weber number

ρ_ℓ = Density of liquid

$V_{d_{U,L}}$ = Mean velocity of large droplets upstream of grid spacer

σ = Surface tension

Wet grid spacer

$$\left(d_{D,S}\,\rho_\ell\sigma/\,\mu_\ell^2\right)\,We^{-0.49} = 1.8\times10^3 \qquad (2)$$

where μ_ℓ = Dynamic viscosity of liquid.

Figures 16 and 17 show the correlation for the size of small droplets downstream of a dry and wet grid spacer respectively.

ACKNOWLEDGEMENTS

The authors would like to express their gratitudes to the U.S. Nuclear Regulatory Commission for its support which made this investigation possible and to the Institut für Reaktorbauelemente of Kerforschungszentrum Karlsruhe, West Germany, for its generous supply of the grid spacers, the instrumented simulation heater rods and the flow thermocouples. They also wish to thank Mr. P. Ihle of KfK and R. L. Hochreiter of Westinghouse for the many useful discussions and suggestions on flow arrangement and instrumentations, to Mr. M. McGuire of Westinghouse for the preparation of the instrumented test grid spacer, and to Mr. H. Honigman for his enormous contribution to the fabrication of the test flow channel.

REFERENCES

1. Ihle, P., Rust, K. and Lee, S. L., "Experimental Investigation of Reflood Heat Transfer in the Wake of Spacer Grids," Proc. Joint NRC/ANS Mt. on Basic Thermal Hydraulic Mechanisms in LWR Analysis, Bethesda, Md., pp.417-443, 1982.

2. Ihle, P., Rust, K. and Lee, S. L., "Mist Core Cooling During the Reflood Phase of PWR-LOCA," Proc. int. Mt. on Thermal Nuclear Reacor Safety, Chicago, Ill., pp. 1801-1809, 1982.

3. Lee, S. L., Ihle, P. and Rust, K., "On the Importance of Grid Spacer Induced Mist Cooling on the Suppression of Core Peak Cladding Temperature During Reflood of PWR," Proc. ASME-JSME Thermal Eng. Joint Conf., 1983, Honolulu, Hawaii, Vol. 3, pp. 381-385, 1983.

4. Lee, S. L., Rob, K. and Cho, S. K., "LDA Measurement of Mist Flow Across Grid Spacer Plate Important in Loss of Coolant Accident Reflood of Pressurized Water Reactor," Proc. Int. Symp. on Appl. of Laser-Doppler Anemometry to Fluid Mech., Lisbon, pp. 5.3.1 to 5.3.7, 1982.

5. Lee, S. L. and Srinivasan, J., "A LDA Technique for In Situ Simultaneous Velocity and Size Measurement of Large Spherical Particles in a Two-Phase Suspension Flow," Int. J. of Multiphase Flow, Vol. 8, pp. 47-57, 1982.

6. Lee, S. L. and Srinivasan, J., "A Laser-Doppler Velocimetry Technique for In-Situ Local Measurement of Dilute Two-Phase Suspension Flows," Eng. Appl. of Laser Velocimetry, (H.W. Coleman, Ed.), ASME, New York, pp.117-125, 1982.

Table 1. Summary of droplet size and velocity measurement for dry grid spacer in Test Series I

Steam Mass Flux (kg/hr)	Water Inject. Rate (cm^3/min)	Size Meas. Scheme	Measurement Position	Sauter Mean Dia. (μm)	Date Rate (No./sec)	Mean Droplet Velocity (m/sec)
30.0 (High)	10.5 (Dry Grid Spacer)	Large	Upstream	2233.1	1.65	13.44
		Small	Upstream	179.36	9.85	15.34
		Large	Downstream	1749.97	1.13	12.84
		Small	Downstream	163.88	68.1	15.30
24.3 (Low)	10.5 (Dry Grid Spacer)	Large	Upstream	1566.48	4.17	11.14
		Small	Upstream	179.34	3.99	13.21
		Large	Downstream	1307.78	3.16	11.30
		Small	Downstream	177.95	90.7	11.01

Table 2. Summary of droplet size and velocity measurement for wet grid spacer in Test Series I

Steam Mass Flux (kg/hr)	Water Inject. Rate (cm^3/min)	Size Meas. Scheme	Measurement Position	Sauter Mean Dia. (μm)	Date Rate (No./sec)	Mean Droplet Velocity (m/sec)
30.0 (High)	32.0 (Wet Grid Spacer)	Large	Upstream	2615.59	5.70	12.64
		Small	Upstream	168.76	11.85	18.19
		Large	Downstream	2446.65	78.65	12.76
		Small	Downstream	175.55	670.1	15.90
24.3 (Low)	32.0 (Wet Grid Spacer)	Large	Upstream	1657.58	22.4	11.37
		Small	Upstream	175.68	57.4	11.23
		Large	Downstream	1558.05	83.0	9.65
		Small	Downstream	177.83	630.0	10.40

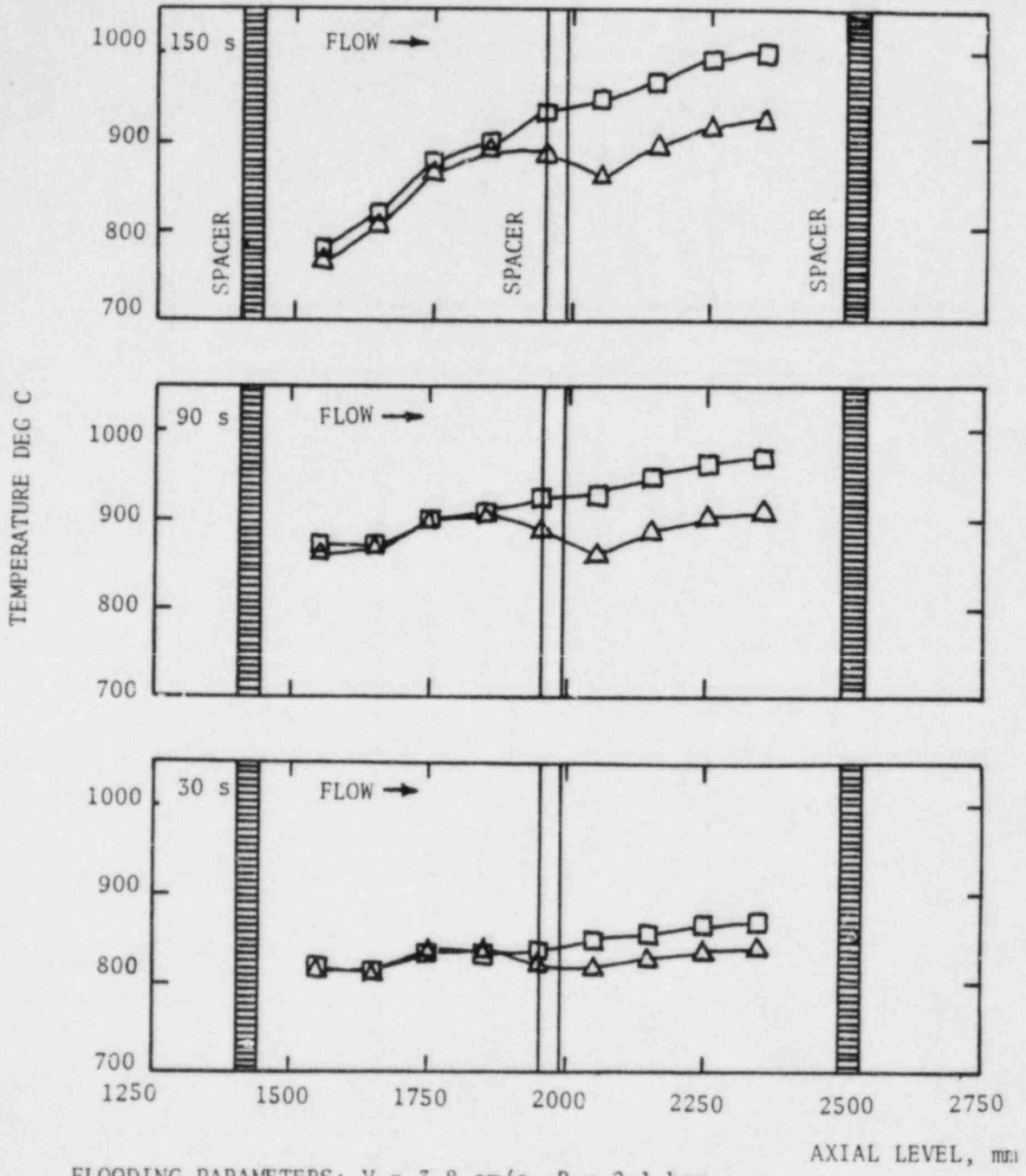

FLOODING PARAMETERS: V = 3.8 cm/s P = 2.1 bar

TEST NO. 223, (WITH SPACER AT BUNDLE MIDPLANE) ——△

TEST NO. 234, (WITHOUT SPACER AT BUNDLE MIDPLANE) ——□

Figure 1. Influence of a grid spacer on the axial temperature profile [1].

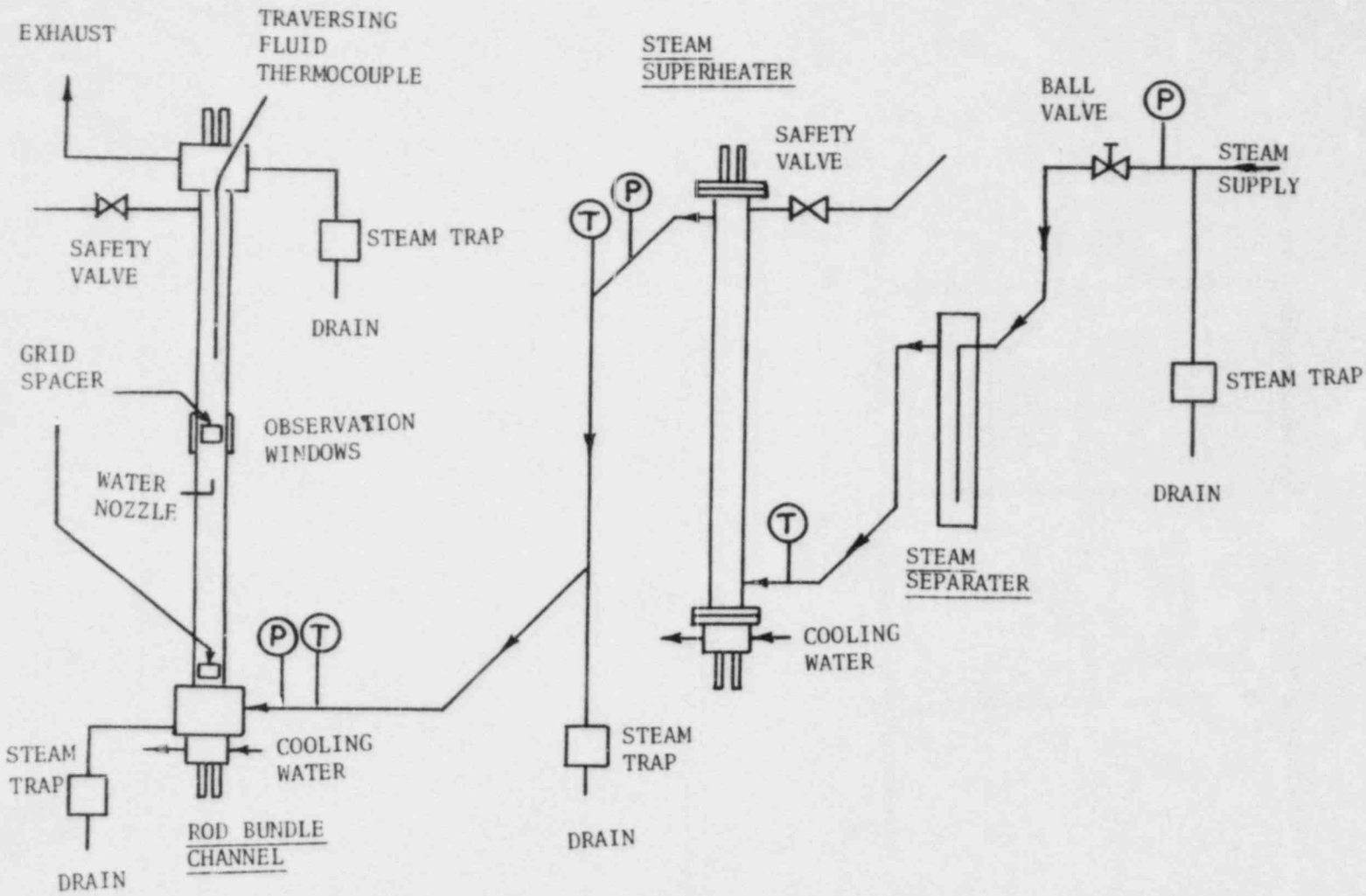

Figure 2. Flow arrangement.

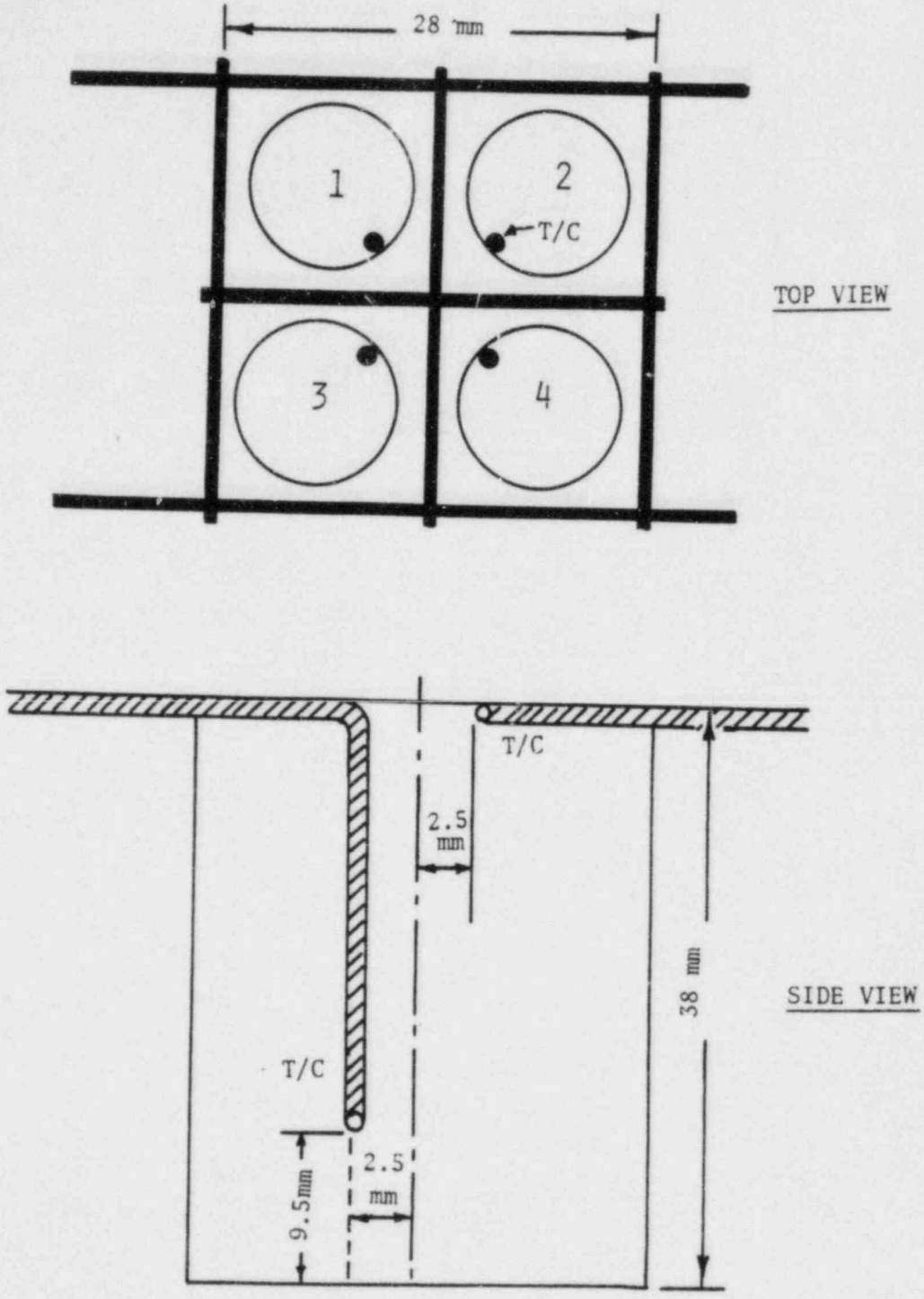

Figure 3. Instrumented grid spacer.

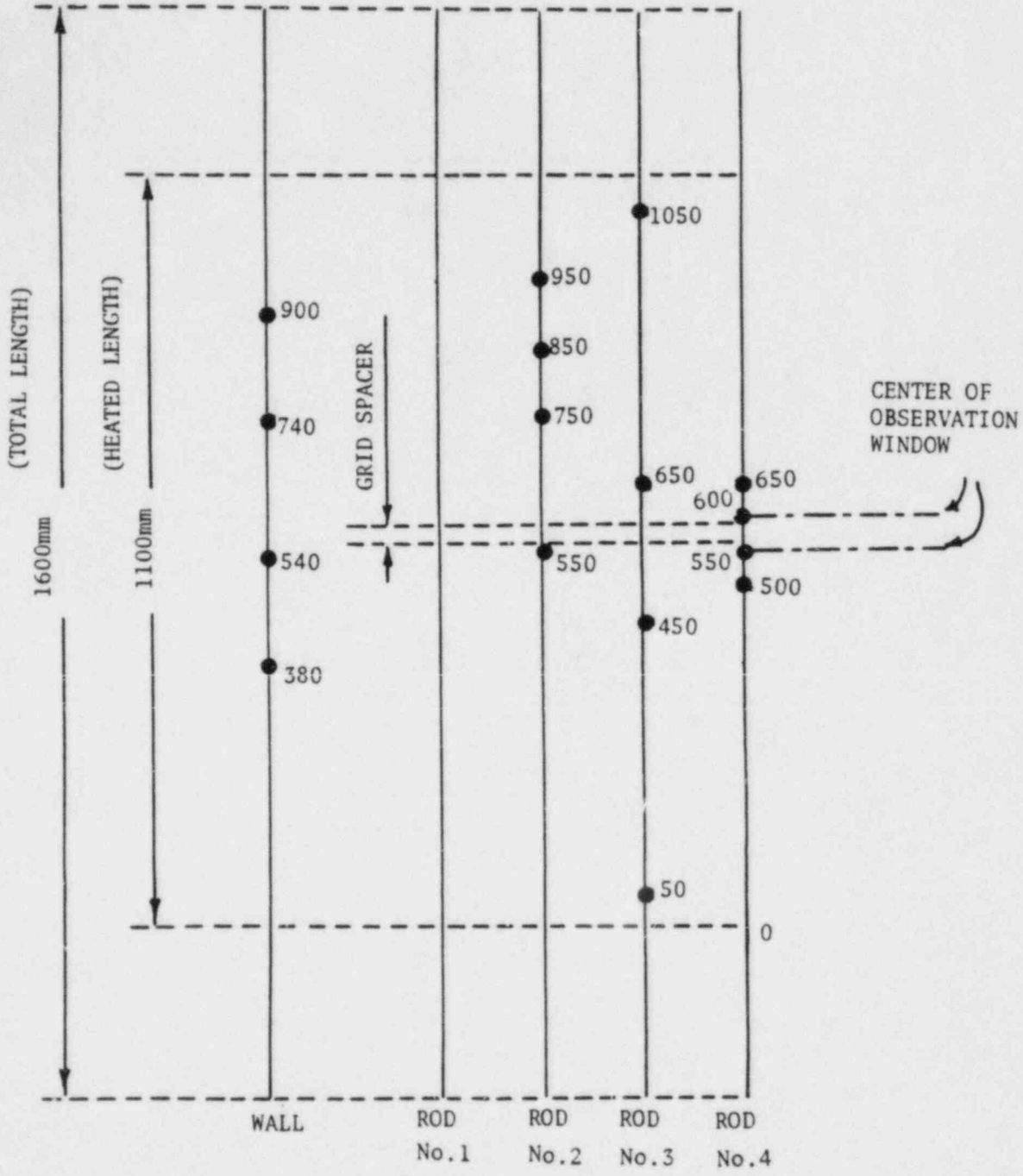

Figure 4. Thermocouple arrangement.

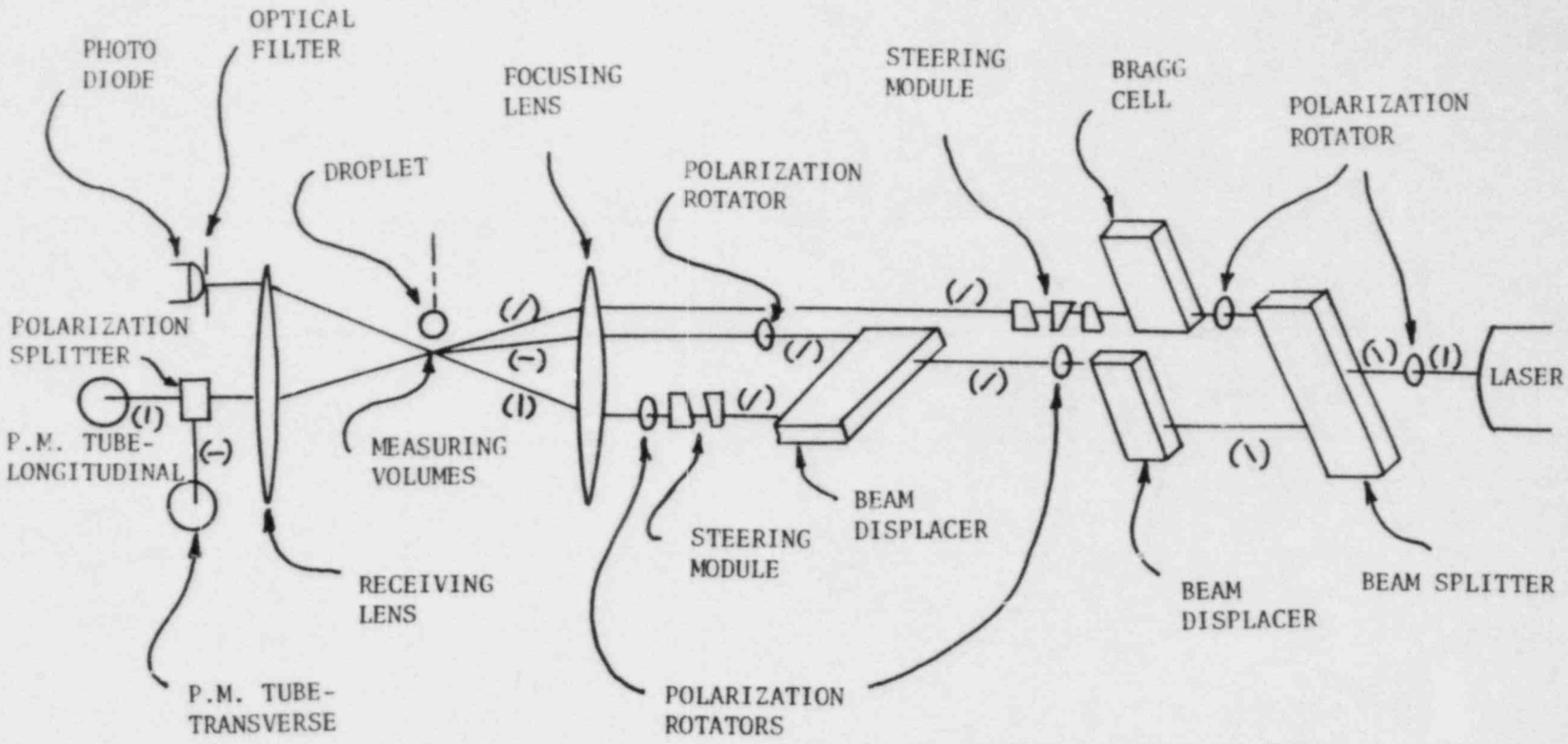

Figure 5. Optical arrangement (polarity orientation indicated in parenthesis).

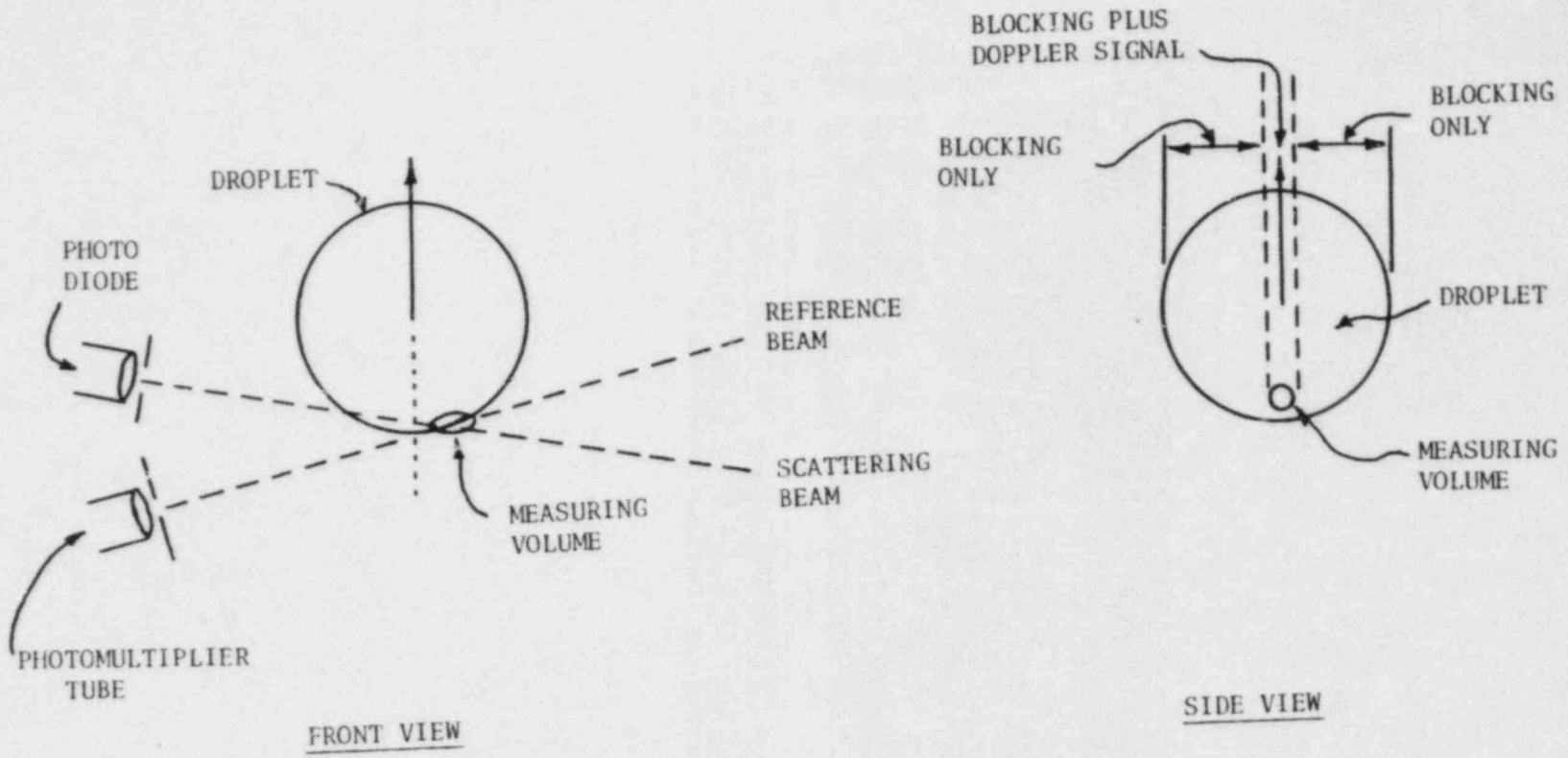

Figure 6. Laser-Doppler anemometry scheme developed for large-size droplet measurement.

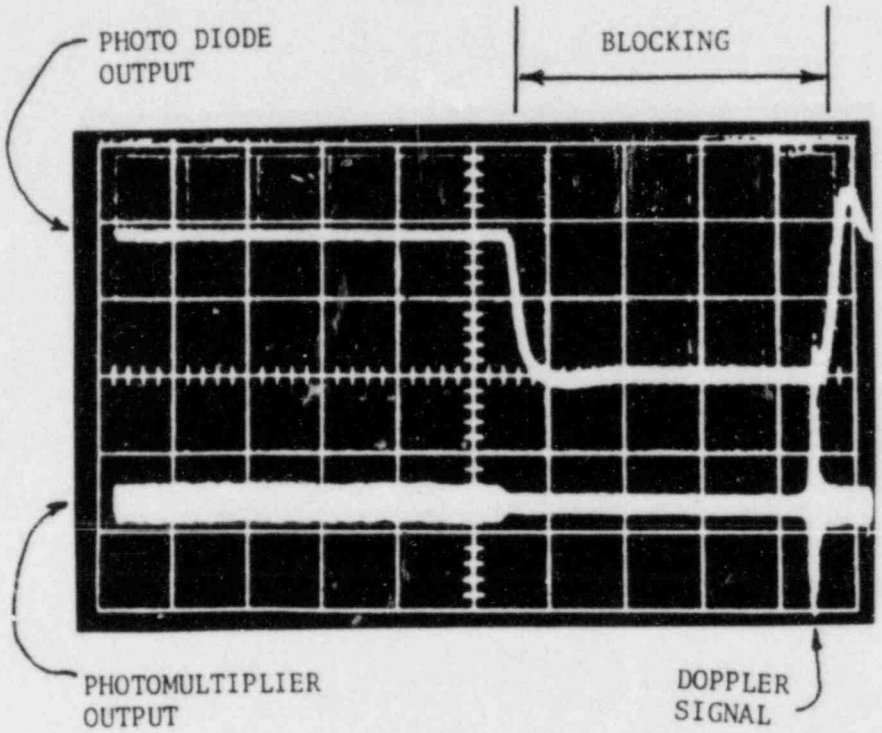

Figure 7. Oscilloscope traces of photo-diode and photomultiplier outputs.

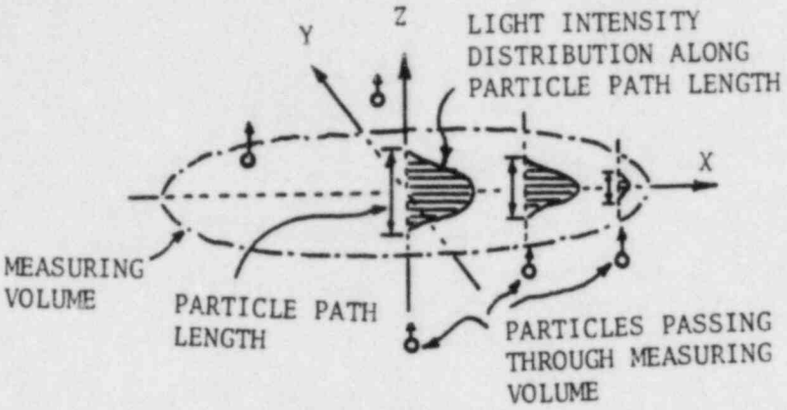

Figure 8a. Sketch of optical measuring volume.

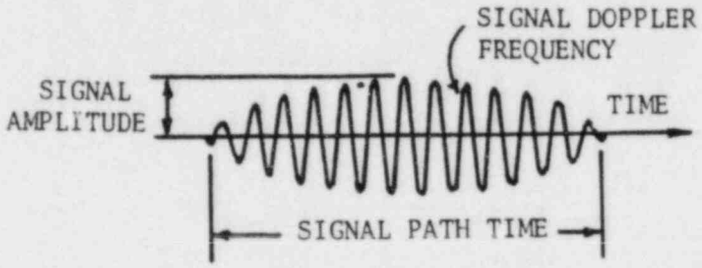

Figure 8b. Sketch of particle Doppler signal.

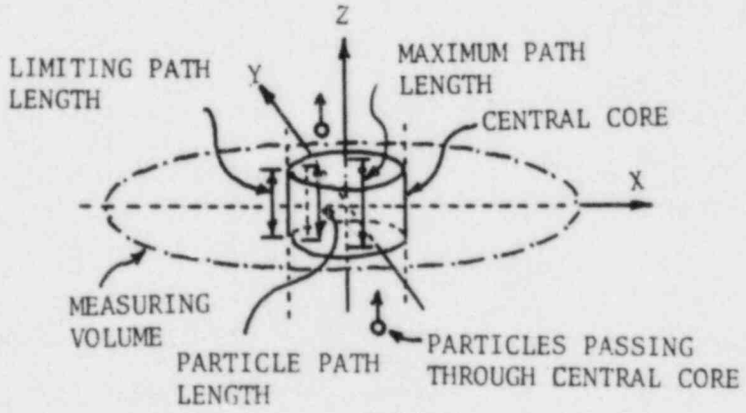

Figure 8c. Sketch of electronically isolated central core of measuring volume

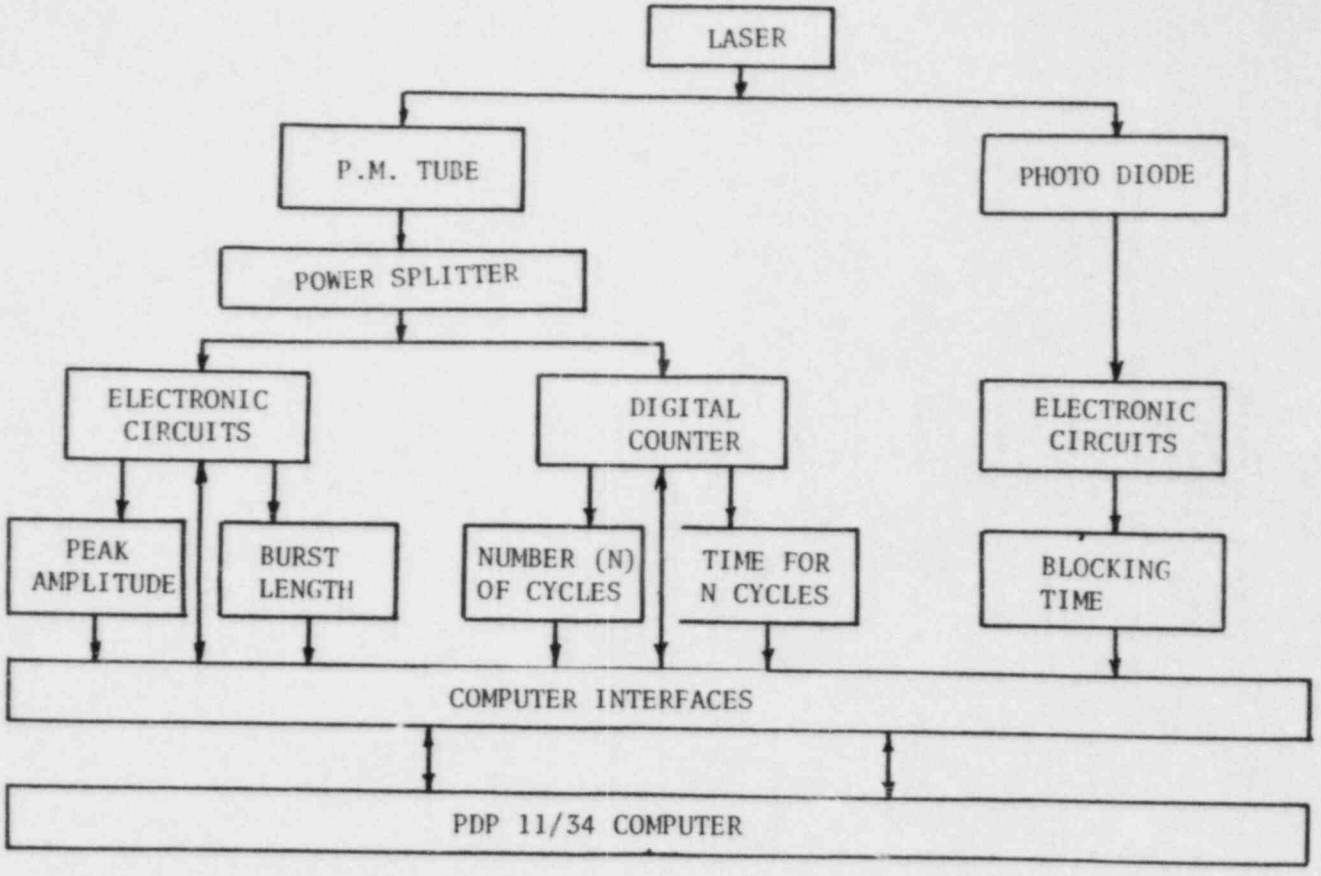

Figure 9. Instrumentation block diagram.

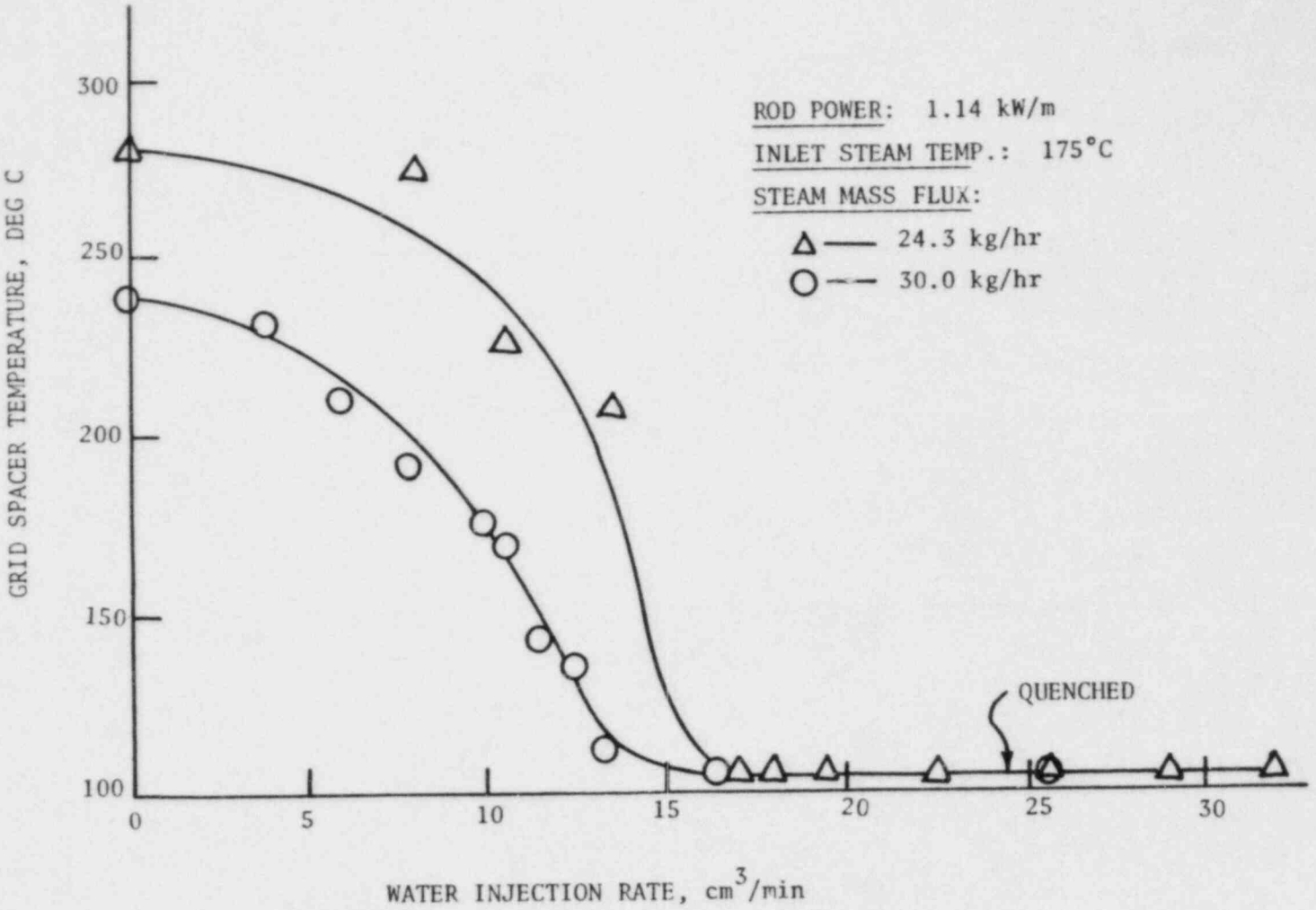

Figure 10. Quenching of grid spacer (Test Series I)

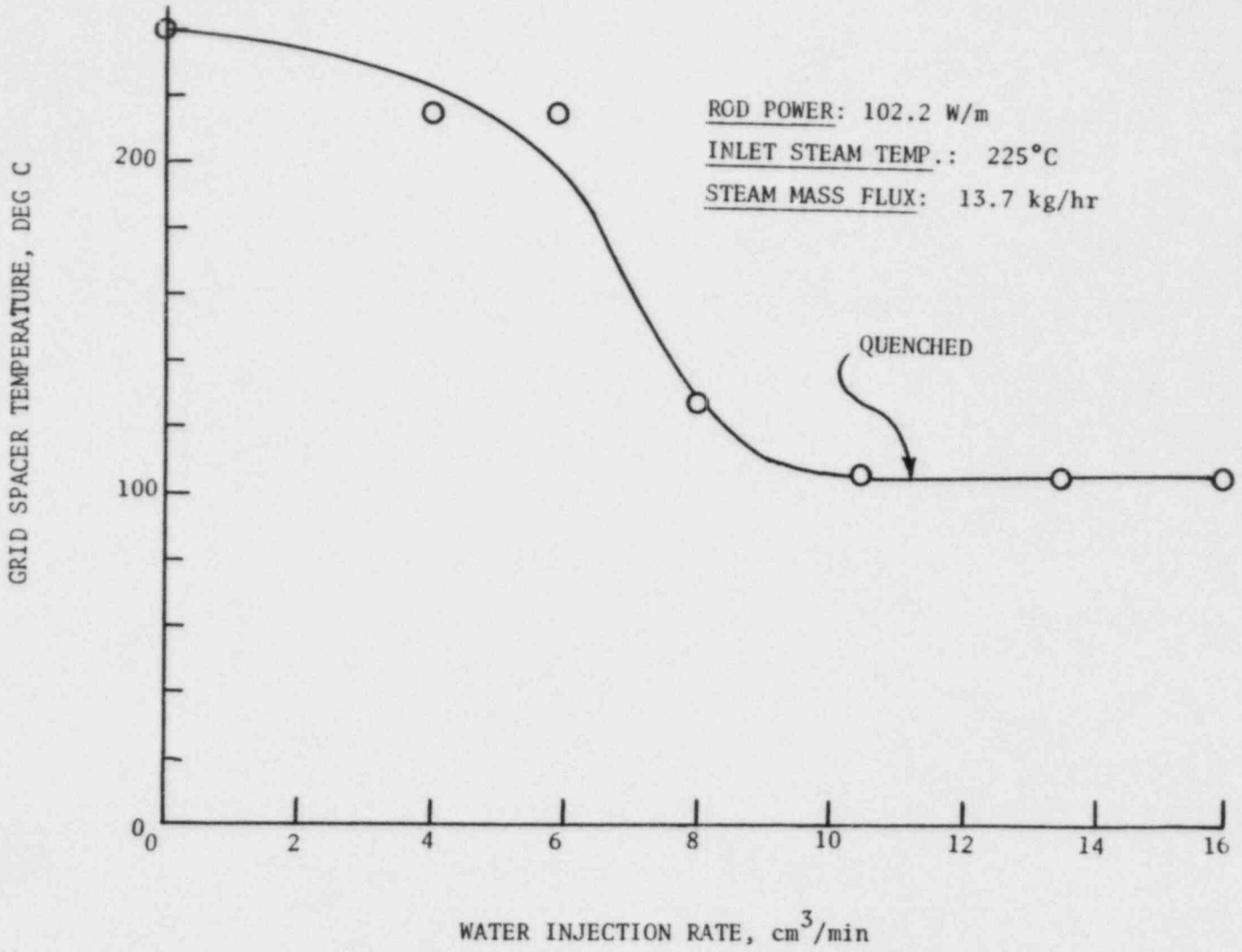

Figure 11. Quenching of grid spacer (Test Series II).

Figure 12. Axial temperature profiles (low steam mass flux). (Test Series I)

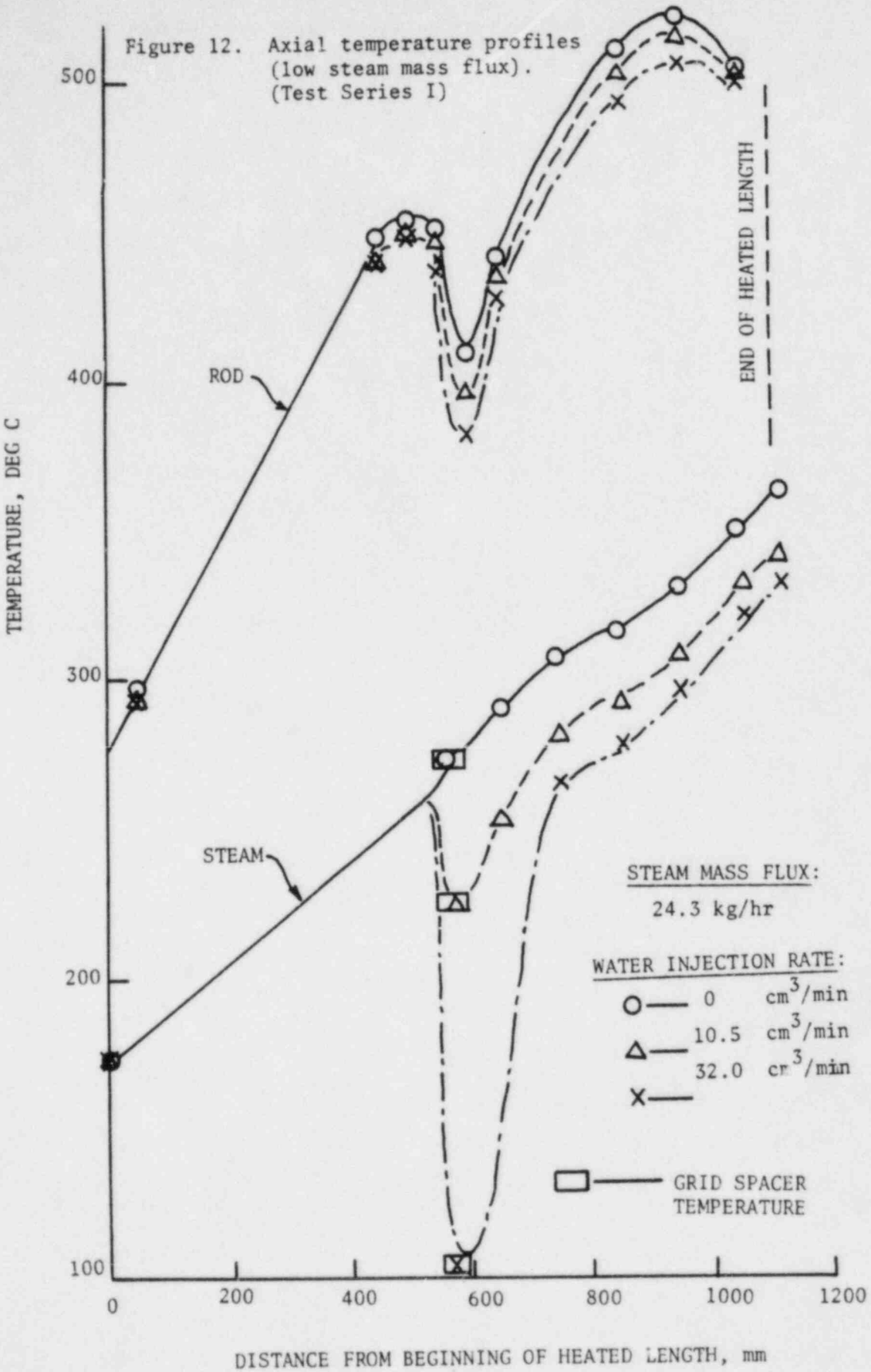

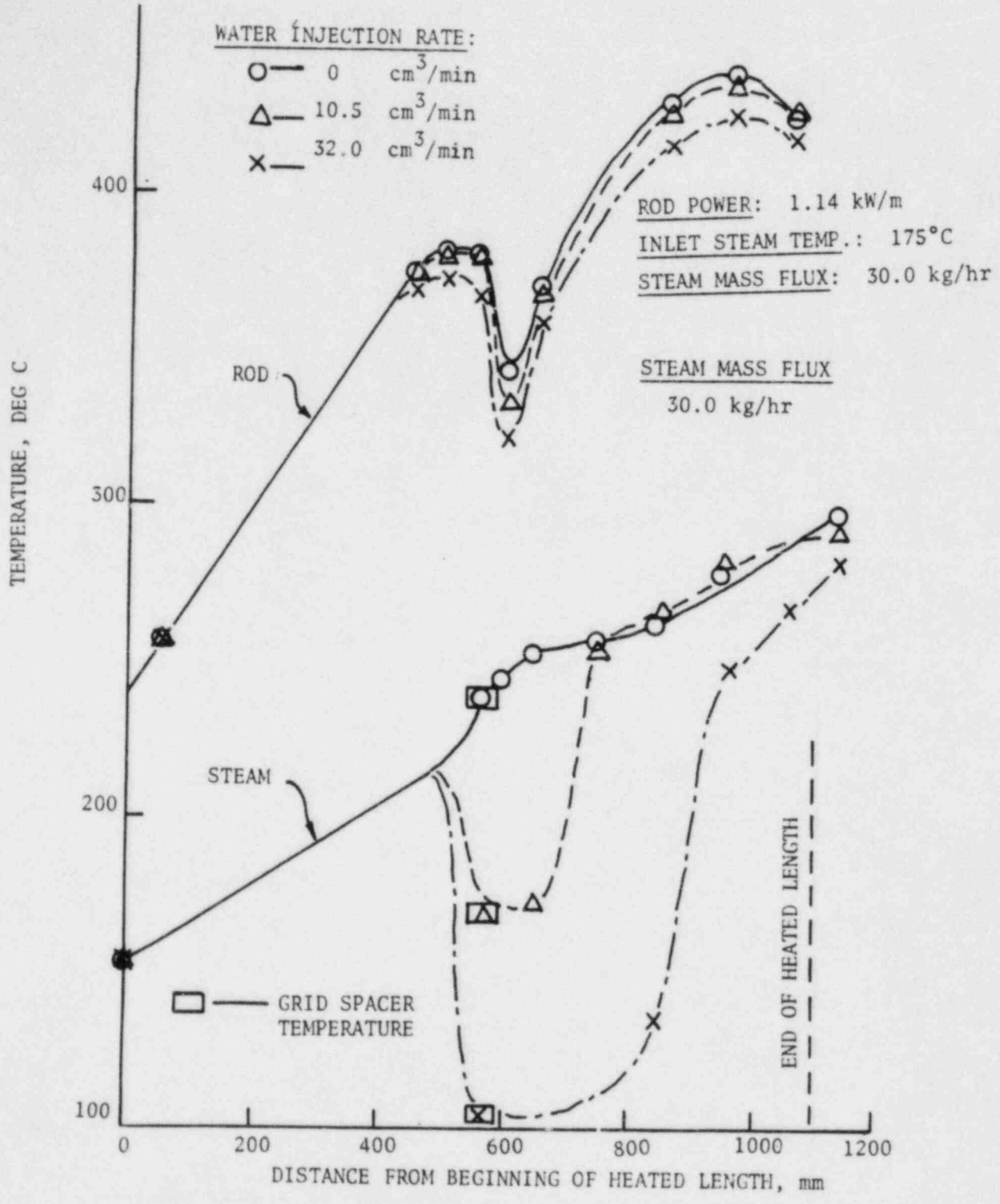

Figure 13. Axial temperature profiles (high steam mass flux) (Test Series II)

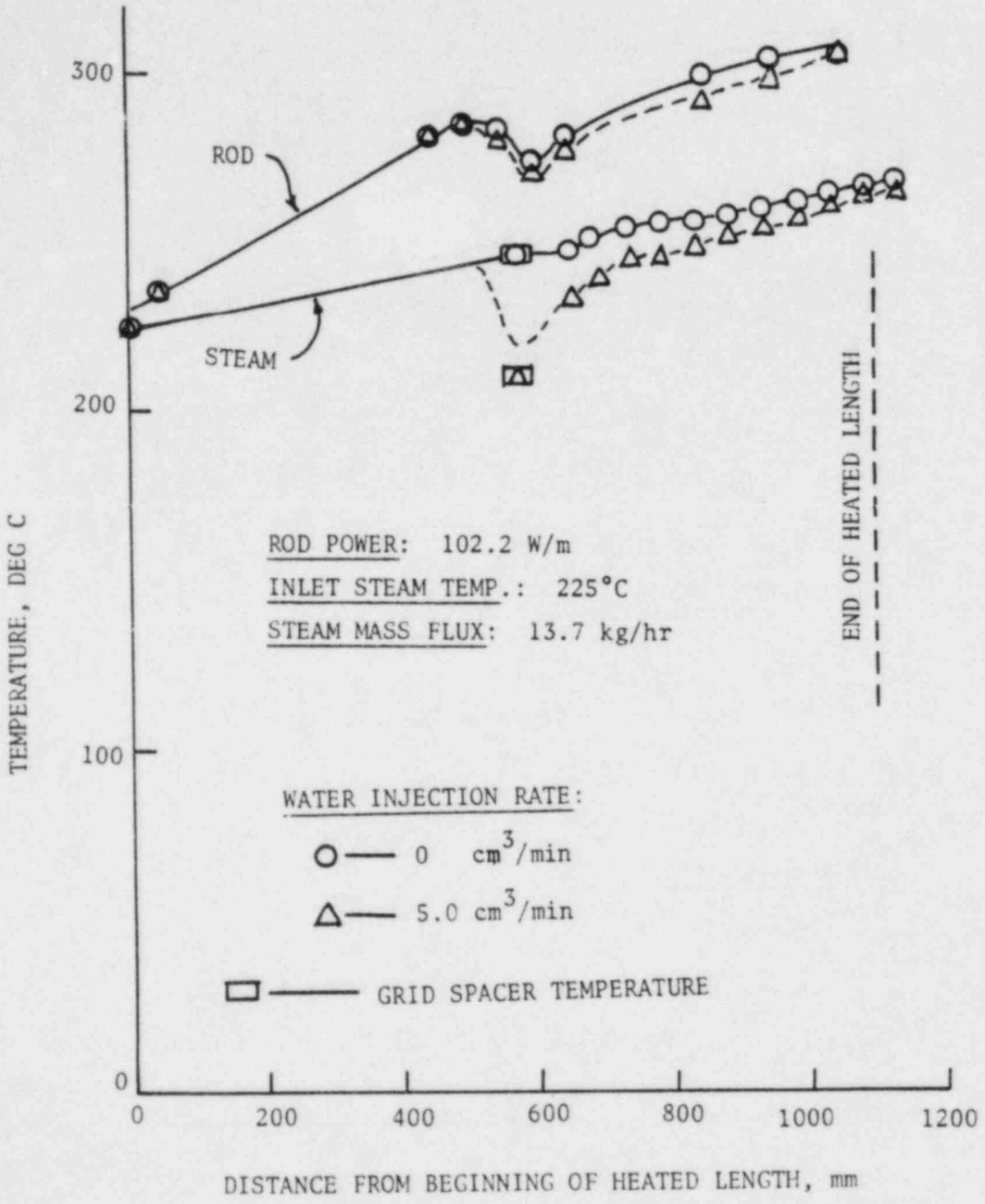

Figure 14. Axial temperature profile (dry grid spacer). (Test Series II)

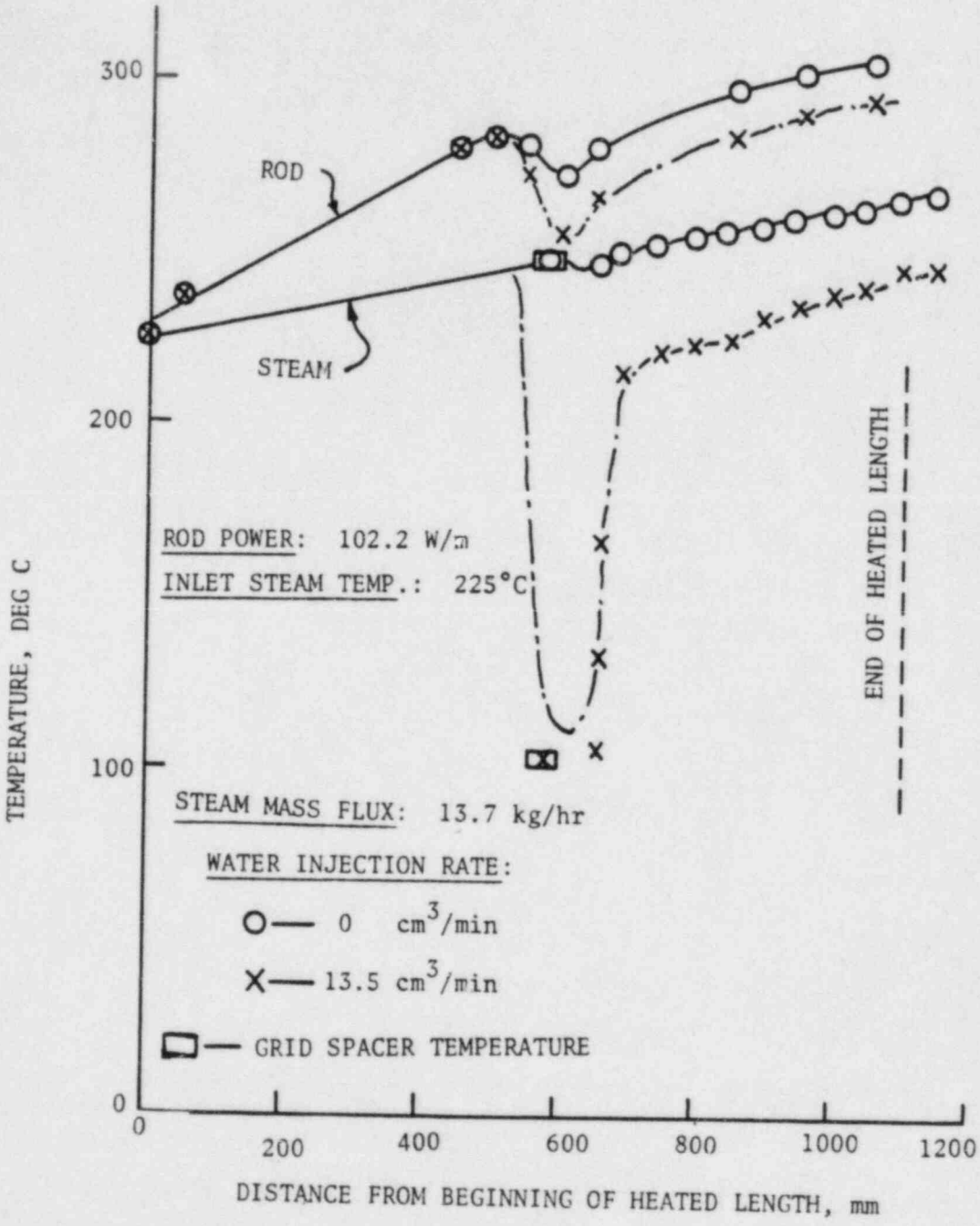

Figure 15. Axial temperature profile (wet grid spacer). (Test Series II)

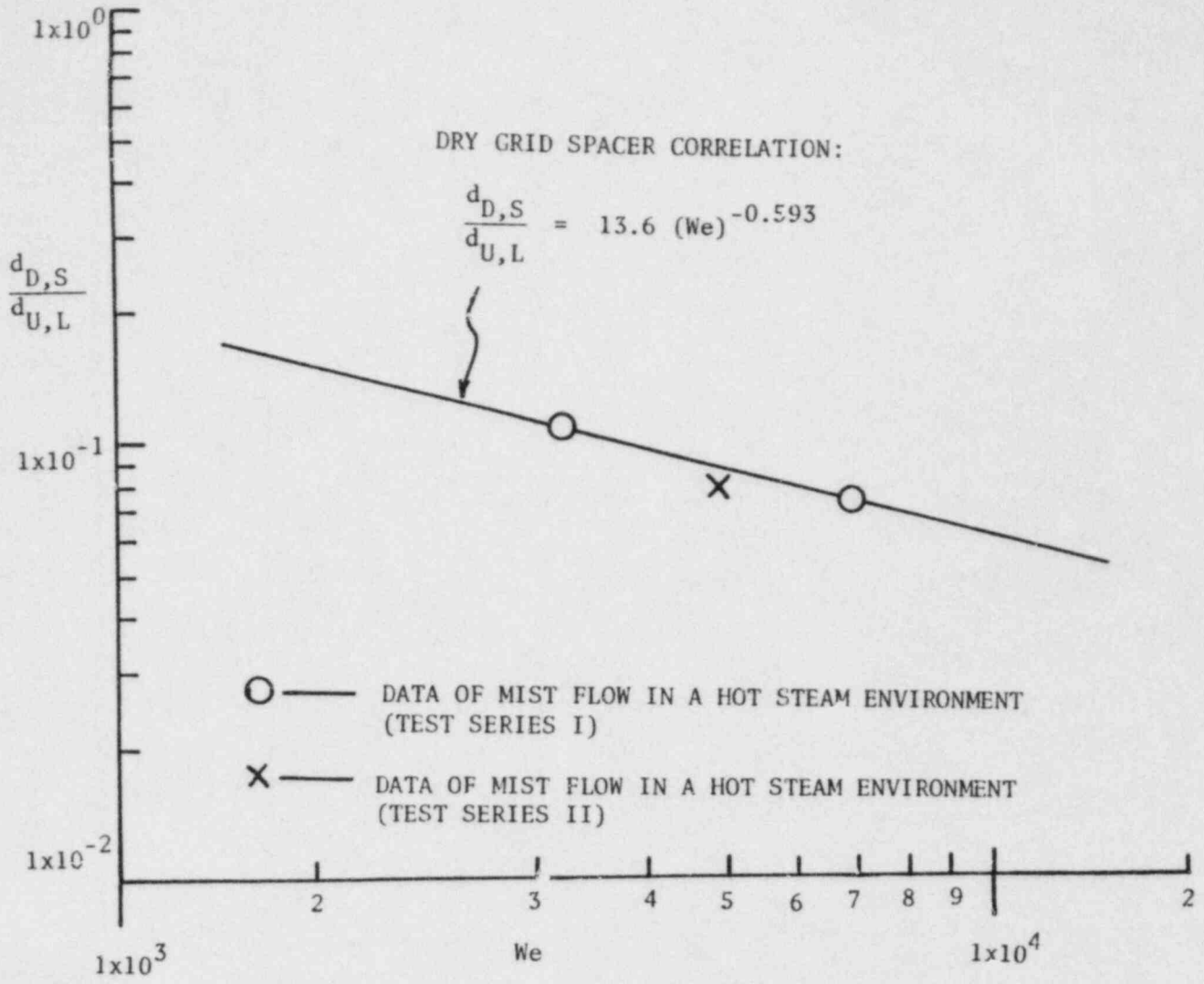

Figure 16. Correlation of size of small droplets downstream of dry grid spacer.

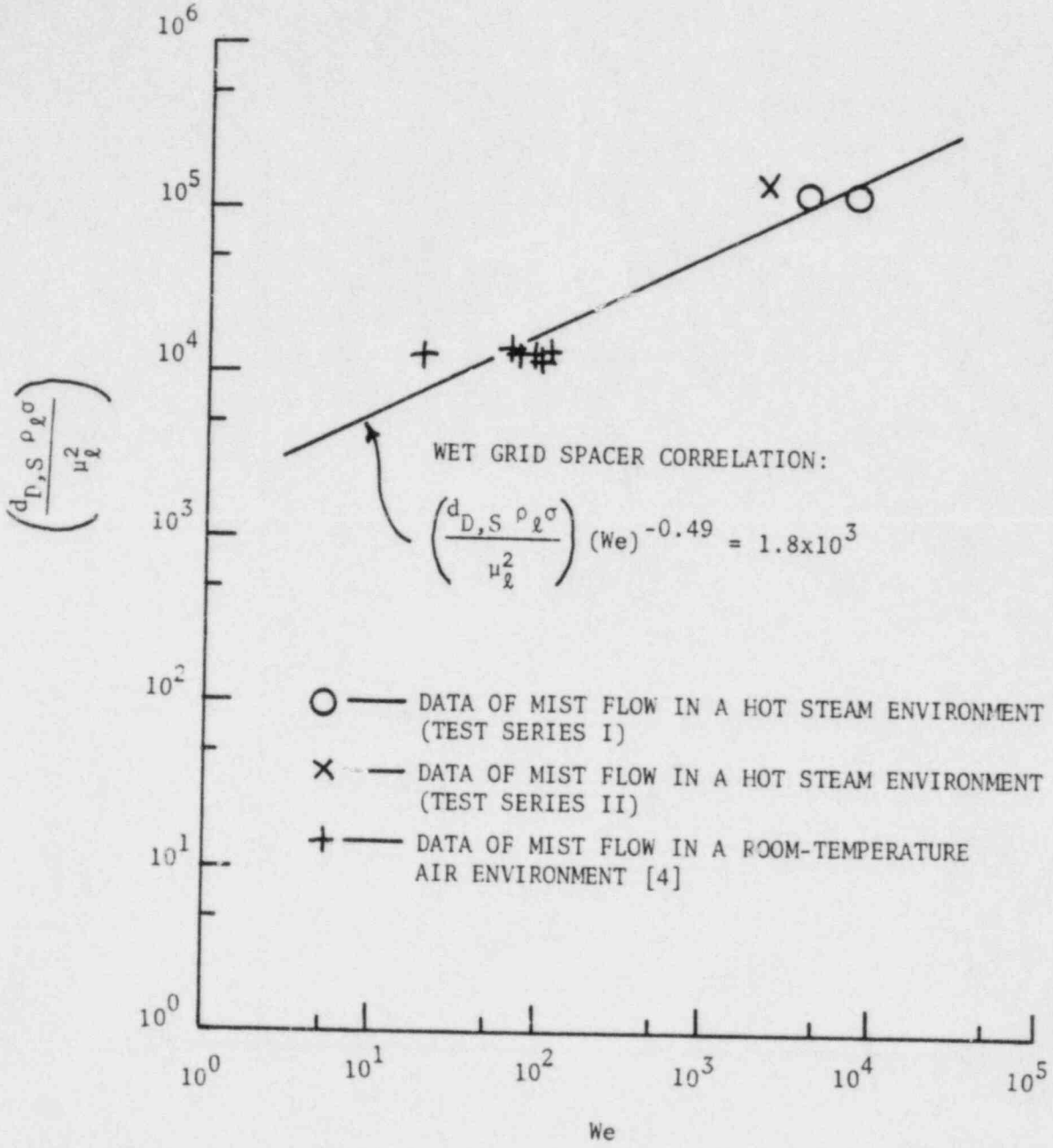

Figure 17. Correlation of size of small droplets downstream of wet grid spacer.

REFLOOD HEAT TRANSFER IN SEVERELY BLOCKED FUEL ASSEMBLIES

K G PEARSON*

C A COOPER*

ABSTRACT

In the event of a large break loss-of-coolant accident in a PWR the normal coolant would be lost. Cooling would be restored by reflooding the dry overheated reactor core from below. Heat transfer in the dried out core is crucial in limiting the temperature which the fuel reaches before the rising rewetting front covers it. A particular problem is that the fuel rods are pressurised internally, so that should the reactor depressurise and the fuel overheat the weakened fuel cladding could swell to partially block the coolant passages.

Experimental results are presented for the reflooding of fuel clusters containing severe partial blockages. These show that in the early stages of reflood cooling is good, but that it deteriorates later. This causes a temperature penalty at the lower reflooding rates.

A model of heat transfer in the dry region is also presented. It includes a film boiling and a dispersed flow region and explicitly represents the effect of spacer grids. In parallel channel mode it can calculate the effect of partial flow blockage. Predictions of the model are compared with experimental data and show good agreement in both blocked and unblocked configurations.

The experimental observations and the modelling work are then used to infer the nature of the heat transport processes within such severe blockages.

* UKAEA, AEE Winfrith, Dorchester, Dorset.

INTRODUCTION

The fuel rods in a Pressurised Water Reactor (PWR) are pressurised with helium during manufacture to improve the thermal conductance at the pellet-cladding interface and to reduce mechanical interaction between the pellet and cladding during service. In the event of a large break loss-of-coolant accident (LOCA) the primary circuit will depressurise rapidly and at the same time the cooling of the fuel may be seriously impaired. In such circumstances a large differential pressure tending to expand the cladding may build up while the cladding is weakening as its temperature rises. On the basis of conservative assumptions this combination of conditions may lead to significant swelling of the cladding occurring before the reactor core is eventually quenched.

The thermal-hydraulic conditions during the LOCA could cause these swellings to form as elongated coplanar groups. The flow in this partially blocked region could be significantly reduced giving poor heat removal from the fuel pins in the blockage. The magnitude of the two-phase heat transfer in the blockage would then be one of the most important parameters in determining the consequences of the LOCA.

In order to investigate the heat transfer in fuel rod arrays containing blockages two series of reflooding experiments on full-length electrically-heated simulations of PWR fuel assemblies containing severe partial blockages have been carried out in the THETIS rig at Winfrith. In this paper we briefly describe the experimental configurations tested and then discuss the most important findings from the reflooding experiments on the two test assemblies. We then describe a simple, but physically based, model of the reflood process which can treat such blockages and compare its predictions with some of the experimental data. Finally, from the experimental observations and the modelling work, we draw conclusions about the nature of the heat transport processes within severe blockages.

THE THETIS BLOCKED CLUSTER TEST ASSEMBLIES

Both THETIS blocked cluster test assemblies consisted of a 7 x 7 array of full length (3.58 m) fuel rod simulators mounted in a square shroud tube. The 7 x 7 array included an off-centre 4 x 4 array of simulators to which preformed simulated swellings had been attached (Figure 1). This geometrical arrangement gave a substantial bypass flow path around the blockage and no direct radial heat conduction path from the blockage to the shroud. Since the fuel rod simulators had a diameter of 12.2 mm, 28% larger than the diameter of a PWR fuel rod, the pitch of the rod array in the THETIS experiments was chosen to be 16.2 mm to give the same pitch-to-diameter ratio as in the PWR.

In the THETIS experiments the blockage was formed by fitting thin metal shells over the centre section of the fuel rod simulators. The preformed swellings gave a good simulation of radial thickness and could be filled with helium or nitrogen to simulate different PWR fuel rod gas gap compositions. These features ensured that radial heat conduction effects in the blockage were well modelled. The detailed axial shape of the swellings for both series of experiments was derived from the German REBEKA (1) tests but with the maximum cladding strains increased. The swellings occupied a central region between two grids and consisted of a 200 mm long parallel section with upstream and downstream conical tapers of 200 mm and 50 mm respectively (Figure 2). Along the parallel section the subchannel flow area was reduced by 90% for the first series of experiments and by 80% in the second series.

The grids used in the THETIS experiments were of a cellular box structure and were not equipped with mixing vanes. The grid pitch was 523 mm.

The test assemblies were comprehensively instrumented and the computerised data acquisition system recorded data from 800 inputs, including 588 from thermocouples embedded in the fuel rod simulators and 48 on the surfaces of the swellings, at intervals of 0.5 seconds.

A full description of the test assembly and instrumentation used in the 90% blocked cluster experiment is given in Reference 2.

SOME RESULTS OF FORCED REFLOODING EXPERIMENTS

Reflooding of the fuel rod array was usually initiated when the peak temperature in the bypass region around the blockage was 650°C. As the reflooding progressed rewetting fronts moved smoothly up the fuel rods. As Figure 3 shows the axial variation of temperature above the rewetting fronts was strongly influenced by the presence of the spacer grids. We shall now briefly discuss the rewetting of the fuel rods and the effects of the spacer grids on heat transfer before considering the more complex issue of blockage heat transfer. A full discussion of these issues is given in Reference 2.

Rewetting

Figure 4 shows the progress of the rewetting front along the bypass region for Run T1R065 in which the 90% blocked cluster test assembly was reflooded under conditions of pressure 2 bar, reflood rate 2 cm/s, inlet water temperature 90°C and cluster power of 100 kw. The rewetting front progresses smoothly upwards

with its speed initially at the reflood rate of 2 cm/s. Soon, however, it begins to decelerate and this continues until the rewetting front reaches mid-height in the bundle. Thereafter the rewetting becomes progressively more rapid, particularly near grids. Slightly premature rewetting is observed in the top grid interval. The gradual deceleration of the rewetting front over the first 300 seconds occurs because increasingly large amounts of energy, both stored heat and electrical power, have to be removed from the fuel rod per unit length of travel as the rewetting front approaches the peak of the axial power profile near mid-height. This effect is reinforced by the gradual loss of subcooling in the water reaching the quench front which has been shown (3) to reduce the effectiveness of the rewetting process. Above the cluster mid-height progressively less energy has to be removed per unit travel so the rewetting front travels more quickly. The particularly good heat transfer at and just downsteam of the spacer grids produces local minima in temperature which result in local accelerations of the rewetting front in these regions.

The axial variation of quench temperature in the bypass region for Run T1R065 is shown in Figure 5. The quench temperature is the temperature below which heat transfer suddenly increases at the rewetting front. Over most of the cluster height it is between 300 and 400°C, the lower value applying just above a grid and the higher value being reached at the top of the grid interval, before the next grid. Over the top metre of the heated length the quench temperature falls to about 200°C. These effects are believed to be due to changes in vapour temperature and liquid fraction which are influenced by the grids and the distance from the rewetting front. It can thus be seen that, contrary to current practice in advanced thermal hydraulic codes such as TRAC (4), it is necessary to take account of both the enhanced cooling downstream of grids and the decrease of minimum film boiling temperature with distance from the rising rewetting front, if rewetting is to be modelled properly.

In all of the experiments with the 90% blocked cluster test assembly the fuel rods in the blockage rewetted at almost the same time as the bypass rods. In the experiments with the 80% blocked cluster the rewetting of the blockage invariably preceded the rewetting of the bypass. Under conditions most relevant to reactor accident analysis the difference in rewetting times was small, that is less than 10% of the quench time at the height of the blockage, but under conditions of high flooding rates or low pressures very early rewetting of two or three rods in the blockage occurred. Examination of the results suggests that this effect may have been caused by the passage of a plug of water within the blockage. The fact that, in both experiments, the blockage did not rewet later than the bypass sets an important limitation on the maximum temperature rise in the blockage.

As observed previously in reflooding experiments (eg 3) the time to rewet the cluster was reduced if the pressure or the reflood rate were increased or the inlet water temperature or the cluster power were reduced.

Effects of Spacer Grids on Reflood Heat Transfer

The THETIS experiments confirm previous findings that the grids have a significant effect on reflood, causing heat transfer enhancements in both single phase and two phase flow. For two phase flow the enhancement is very much larger if the grid is wet. The effects of the spacer grids on the temperature distribution for bypass rods is shown in Figure 3.

When the grids are dry their most important effect is to enhance heat transfer by increasing turbulence in the flow. Figure 6 shows the increase in Nusselt number due to local grid effects for single phase conditions at different Reynolds numbers and also compares the results with the correlation of Yao, Hochreiter and Leech (5). The local increase in heat transfer can be as high as 80% and persist for 100 to 200 mm downstream of the grid.

When the grids are wet they are very effective at desuperheating the steam passing through them. Figure 7, which shows steam temperatures just above and below a grid, demonstrates this effect. While the grid is dry the steam temperature hardly changes on passing through the grid, but after the grid rewets, at about 90 seconds, the steam desuperheats by about 150°C as it passes through the wet grid. Figure 8 compares rod temperatures just below and just above the same grid. There is negligible cooling until about 15 s, when liquid starts to be entrained into the coolant flow. Then the downstream location is better cooled, presumably as a result of turbulence enhancement similar to that shown in Figure 6. After 90 s, when the grid rewets, there is a further increase in cooling, presumably due to the additional effect of steam desuperheating. In spite of the better cooling the downstream location rewets in sequence, but from a lower temperature.

Heat Transfer in the Blockages

Figure 9 shows the variation with time of the swelling surface temperatures along the 200 mm, 90% restricted part of the central blockage subchannel in run T1R065. Once entrainment of droplets into the steam flow has begun at about 15 seconds a period of good cooling is present all along the blockage throat. After this the balloon temperatures generally rise until about 90 seconds when a second period of good cooling occurs. Thereafter temperatures again rise until at 200 seconds an axial temperature gradient of 140°C is present. Cooling then sets in at the lower levels, at an increasing rate until rewetting occurs sequentially

from the bottom. However, the top of the blockage stays hot until shortly before the rewetting front arrives.

In Figure 10 we compare swelling surface temperatures at the top of the 90% blockage with corresponding bypass temperatures for run T1R065. It can be seen that during the early part of the reflood heat transfer in the blockage is comparable to that in the bypass. However later the cladding temperatures start to exceed those in the bypass and the blockage heat transfer deteriorates until the arrival of the rewetting front.

Figures 11 and 12 present the corresponding results for run T2R020, performed under nominally the same conditions but with the 80% blocked cluster. A similar overall pattern emerges but the erratic behaviour of the temperatures towards the top of the blockage, observed in the early stages of reflood with the 90% blockage, are much less in evidence. As soon as liquid entrainment begins there is an axial temperature gradient along the blockage, which increases with time. Surprisingly overall cooling is slightly worse at the top of the 80% blockage than at the top of the 90% blockage. It does not show the early periods of exceptionally good cooling exhibited by the 90% blockage. Later it is somewhat better cooled, but not enough to make up for the earlier period of worse cooling. The peak blockage temperature is 50°C higher than the earlier peak in the bypass. For the 90% blockage it was 40°C higher than the bypass.

The small temperature penalty associated with the blockages in these two experiments does not mean that there is no cooling problem, because the power used was rather low. Figure 13 compares the maximum temperature in the 80% blockage with that in the bypass for the same conditions as the earlier figures except that the power decays with time, but has been approximately doubled and the starting temperature has been reduced (run T2R043). Much higher temperatures result in both the blockage and the bypass. The blockage temperature peaks 110°C higher than the earlier peak in the bypass.

Figure 14 compares the maximum temperatures in the 80% blockage with that in the bypass for run T2R037. The test conditions were the same as for run T2R043 except that the reflood rate was increased to 3 cm/s. This has had the effect of reducing the maximum bypass temperature by 60°C and reducing the maximum blockage temperature by 140°C. The blockage temperature now peaks only 30°C higher than the bypass.

Looking at the results of both experimental programmes the following points emerge.

1 The blockages were comparatively well cooled early in the reflood but badly cooled later.

2 The 80% blockage was frequently worse cooled than the 90% blockage. Exceptions are high reflood rates, when the 80% blockage tended to rewet early while its temperature was still rising, and at very low reflood rates of around 1 cm/s.

3 The peak blockage temperature exceeded the peak bypass temperature, which occurred earlier in the reflood, when the reflood rate was below about 3 cm/s. The temperature penalty associated with the blockage increased as the reflood rate was reduced below this value.

In order to help understand the heat transport phenomena in these severe blockages and to explain the above rather surprising observations, a mechanistic model of the thermal hydraulic processes involved has been developed. This model is called BERTHA, which is an acronym for 'Blockage Experiments: Reflood Thermal Hydraulic Analysis' We shall now briefly describe the model and present comparisons of predictions with experimental results.

THE BERTHA MODEL

The BERTHA model only considers the region above the rewetting front. Since the transit time of coolant through this region is short a quasi steady state formulation is employed. At any time the known boundary conditions are the axial variation of fuel rod surface temperature, the flow conditions at the rewetting front and the system pressure. Immediately above the rewetting front is a film boiling region, represented by the Denham/Bromley model (6). The mass flow rate entering this region is equal to the flow entering the bottom of the assembly, less that accumulating below the moving rewetting front if the thermodynamic quality there is negative (3). This region terminates when the liquid core Weber number exceeds 20, when the coolant is rearranged into a dispersed flow of liquid drops in vapour. The vapour temperature returns to saturation by heating and evaporating an outer layer from the drops, but the interior of the drops may still be subcooled. At the start of the dispersed flow region the drops travel at their terminal velocity relative to the vapour. The equations of energy, mass and momentum for both vapour and liquid phases are integrated axially to yield the mass flow rates and speeds of the two phases and the vapour temperature. When spacer grids are encountered their effect on heat transfer and pressure drop are taken into account. When a blockage is encountered, typical blocked and unblocked sub-channels are considered in parallel and vapour is interchanged between them to achieve equality of overall axial pressure drop. The resulting cross flow of vapour is used to predict the diversion of liquid using a lateral force balance.

The Film Boiling Region

Denham's model is essentially an extension of Bromley's original model to include the effects of flow rate and quality (Figure 15). The central liquid core is insulated from the hot surface by a vapour film in which the flow is assumed to be laminar. Heat is transferred across this film by conduction and radiation. Some of the heat is transported into the liquid core and the remainder evaporates liquid to increase the vapour flow in the film. The pressure drop along the vapour film balances the hydrostatic pressure drop along the liquid column. This governs the thickness of the film and hence the heat transfer across it. The film grows steadily in thickness with increasing distance from the rewetting front and the heat transfer coefficient falls accordingly. The effects of flow rate and subcooling arise because increasing either causes more heat to be transported into the liquid core. This reduces the amount available for vapour generation, leading to a thinner vapour film and better heat transfer. For positive quality the core is assumed to be a homogeneous mixture of liquid and vapour. The presence of the vapour phase in the core reduces its density and hence the hydrostatic pressure drop along it. This increases the thickness of the vapour film and reduces heat transfer.

The Dispersed Flow Region

The dispersed flow region is illustrated in Figure 16. Heat is interchanged between the vapour and liquid phases and the surface. Heat transfer between the surface and the vapour is purely convective and is represented by the expressions of Kim (7) for Reynolds numbers below 1000, Dittus-Boelter (8) for Reynolds numbers above 4000 and logarithmic interpolation for intermediate Reynolds numbers. Heat transfer between the surface and the liquid drops is entirely radiative, using the model of Sun, Gonzales and Tien (9). Heat transfer between the vapour and the liquid is convective using the correlation of Yuen and Chen (10). The initial diameter of the drops is taken as 1 mm. Evaporation reduces the drop diameter, not the flux of drops. The speeds of the two phases are obtained by integrating the axial acceleration of the drops, whose drag coefficient is 1.0 (11). It is important to note that the heat flux to the liquid phase is proportional to the concentration of liquid drops, which is inversely proportional to the drop speed. The axial variation of pressure, which is important in the vicinity of blockages, takes into account surface friction, drop drag, gravity and acceleration, as well as grid losses where appropriate.

Transition Region

In reality the film boiling region does not break down instantaneously into a dispersed flow. The transition is a gradual process, with the liquid core first breaking into chunks

which then further break down into drops. The present model goes some way to representing this by treating the liquid drops which have been created at the termination of the film boiling region proper as a dispersed liquid core. Drops near the edge of this core are in close contact with the hot surface and can receive heat by direct conduction through the vapour just as does the liquid core in the film boiling region. Because the core is dispersed, its effective surface area is reduced by a factor (1 - void fraction), so as the void fraction tends to unity with increasing distance into the dispersed flow region this effect disappears.

At low void fractions, also, the validity of the equations for heat transfer between the vapour and the liquid become suspect since they are appropriate to isolated drops. To allow for the proximity of other evaporating drops surrounded by saturated vapour this heat flux term is reduced by multiplying it by the void fraction.

Treatment of Spacer Grids

Spacer grids improve reflood heat transfer in at least three ways. First they increase convective heat transfer between the surface and the vapour by introducing turbulence. Second, when the grids are wet the liquid film on the grids cools the vapour in the dispersed flow and absorbs thermal radiation from the surface. Third, they may modify the size and speed distribution of the liquid phase by drop shattering and, when wet, by capturing drops which are then reentrained from the grid trailing edge. In the present model only the first two effects are represented.

A correlation for single phase turbulent enhancement at grids by Yao, Hochreiter and Leech (5) is compared with experimental data from our own THETIS facility in Figure 6. For reflood modelling the THETIS enhancement is assumed to apply to the heat transfer between the rod surface and the vapour phase, unaffected by the presence of the liquid phase.

The vapour cooling effect of wet grids is modelled as heat transfer through a developing vapour boundary layer (12) to the liquid on the grid. The liquid film is expected to be in a disturbed state, being continually struck by drops from the flow which create turbulence and increase its effective surface area. Therefore a turbulent boundary layer is assumed and the effective surface area of the film is considered to be greater than the surface area of the grid by an appropriate factor. A value of 4 is currently used. The virtual complete absorption of thermal radiation on the liquid film (13) is satisfied by setting the liquid phase absorptivity to unity at wet grids.

Blockage Modelling

In the vicinity of a blockage two subchannels are modelled, one typical of the blocked region and the other typical of the bypass region. The fuel assembly as a whole is considered to comprise specified numbers of these typical blockage and bypass subchannels. The swellings formed by clad ballooning tend to be smooth, with gentle tapers, and when adjacent swellings come into contact they isolate the blocked subchannels from each other and from the bypass region. To model the diversion of the vapour phase it is assumed that the pressures in the blockage and bypass subchannels begin to diverge at the start of the swelling. The cross flow between the two subchannels is calculated using elements of the HAMBO model (14), taking into account the pressure difference and gap size. So cross flow ceases where the swellings come into contact and restarts further downstream where the gaps open again. The axial variation of pressure along each subchannel is calculated taking into account surface friction, drop drag, gravity and acceleration. Because of the gently tapered shape of the swellings, form drag is not included.

The deceleration of flow in the entrance to the blockage causes the blockage subchannel pressure to rise, while the acceleration in the bypass due to receipt of the diverted flow causes the pressure there to fall more rapidly. The pressure difference thus created drives vapour out of the blockage entry region. When the gaps close cross flow ceases and the pressure falls faster along the blockage subchannels than along the bypass, so that by the point when the gaps open again the pressure difference has reversed. This causes flow to return to the blockage subchannels in the wake of the blockage. If the amount of upstream vapour diversion has been correctly calculated the pressures in the two subchannels should come together again downstream of the blockage. Because the cross flow model is applied to two groups of subchannels rather than a pair of directly connected subchannels, the cross flow coefficient is uncertain. It is therefore used as an adjustable parameter to produce the correct amount of flow diversion to obtain equality of pressure drop along the blockage and bypass subchannels. This is done by an iterative procedure, and when convergence is achieved the resulting pressure profile is as illustrated in Figure 17.

As well as causing a blockage, swelling of the clad alters the subchannel shape. The effect of this on the friction factor and heat transer coefficient within the blockage is taken into account.

Diversion of the liquid phase is calculated explicitly by integrating the lateral acceleration of liquid drops in the vicinity of the exit passages connecting the blockage region with the bypass region. The lateral component of vapour velocity in

these exits is known from the calculated vapour cross flow and the gap size. The flow back of liquid into the wake of the blockage is calculated in the same way. In implementing this part of the model it was found necessary to use a high value of 4 for the lateral drag coefficient. With a lower value too little liquid was diverted so that evaporation within the blockage created too high a pressure drop for a pressure balance to be achieved.

RESULTS OF BERTHA CALCULATIONS

Results are first presented for the bypass region to show the axial variation of the important flow parameters. Then predicted heat flux variations are compared with experimental data for the bypass region over a range of reflood rates and pressures. Finally the behaviour within the blockage is presented and compared with experimental data.

Bypass Region

Figures 18 to 21 show the variation of important flow parameters with reflood rate 2 cm/s, pressure 2 bar and inlet temperature 90°C. They portray a point in time when the rewetting front has reached an elevation of 0.73 m. The letters W and D indicate whether a grid is wet or dry. The film boiling region extends for 0.13 m so the dispersed flow region starts at 0.86 m. Figure 18 shows the predicted vapour temperature together with the experimental rod surface temperature and the vapour temperature measured by instream thermocouples. The latter have been corrected downwards to account for the effect of thermal radiation, but are still much higher than the calculated values except near the top of the assembly. However, the strong cooling effect of wet grids is apparent both in the experimental data and the calculation. Figure 19 shows the axial variation of vapour mass flow rate per subchannel. There is a rapid initial rise when the void fraction is low, but the rate of evaporation decreases as the drops accelerate, increasing the void fraction. Wet grids produce significant local increases in vapour flow from evaporation of the liquid film on their surface. Figure 20 shows the vapour and liquid speeds along the assembly. At the start of the dispersed flow region the drops are travelling slowly and at their terminal velocity relative to the vapour. The speed of both phases increases slowly at first because any small increase in drop speed simply increases the void fraction leaving more room for the vapour. So the vapour speed cannot increase until the void fraction approaches unity. Then the vapour speed increases rapidly as a result of its increasing temperature and mass flow rate, and the drops accelerate in turn. There is a local increase in vapour speed alongside the blockage, between 1.6 and 2.0 m, and sudden reductions in vapour speed at wet grids due to vapour cooling. The drops continue to accelerate to the

top of the assembly. Figure 21 compares the calculated heat flux with experimental data. There is a discontinuity when the flow regime changes from film boiling to dispersed flow. The agreement with experiment is good, with the overall level, the reduction between grids and the abrupt increase at wet grids being well predicted.

Figures 22 to 25 compare the predicted heat flux with experiment for four other test conditions, covering reflood rates from 1 to 4 cm/s and pressures from 1.3 to 4 bar. In each case the rewetting front is at an elevation of about 0.7 m. Increasing the reflood rate from 1 to 4 cm/s produces a number of effects. The rewetting front travels faster, the film boiling region becomes somewhat longer and the spacer grids rewet much earlier. At the start of the dispersed flow region the liquid mass flow rate is greatly increased, but the vapour mass flow rate is slightly reduced. However, evaporation soon increases the vapour flow rate so that it too is higher at the highest reflood rate along most of the assembly. The higher vapour flow and the better cooling of the vapour by the liquid phase and the wet grids produces a substantial improvement in heat flux. The predictions for both 1 and 4 cm/s agree well with the data.

Increasing the pressure from 1.3 to 4 bar makes the rewetting front travel faster. The more rapid release of energy at the rewetting front creates more vapour at the start of the film boiling region but, because mass is being stored at a greater rate below the advancing rewetting front, the total coolant flow above the rewetting front is reduced and there is less liquid in the flow. Because of the higher vapour density both vapour and liquid speeds are lower. The lower liquid speed tends to increase the liquid phase concentration which more than offsets the reduction in liquid flow rate, so that one might expect vapour temperatures to be lower at higher pressures and heat fluxes to be higher. However, another effect of the reduced liquid speed is that the spacer grids rewet at a later stage at high pressure. The loss of this important heat sink actually causes the vapour temperature to be higher in the upper part of the assembly at higher pressures. So the expected improvement does not occur and, at the top of the assembly, heat fluxes are actually negative at the highest pressure. The predictions for both 1.3 and 4 bar agree well with the data. Thus from Figures 21 to 25 it appears that the model predicts bypass heat flux well over the range of reflood rate and pressure tested.

Blockage Region

Figures 26 to 29 illustrate calculated conditions within a long 80% blockage, located as in Figure 17, at an early stage of reflood for a reflood rate of 2 cm/s and a pressure of 2 bar. Figure 26 shows that almost 90% of the vapour arriving at the blockage is diverted into the bypass, taking with it about 50% of

the liquid. In the closed-off part of the blockage liquid evaporation increases the vapour flow. Both vapour and liquid flow back into the wake of the blockage but this flow is temporarily suppressed at a spacer grid. Figure 27 shows how the axial variation of vapour flow and flow area create minima in vapour speed at the elevations where the gaps between swellings close and then open again. The vapour speed increases along the parallel part of the blockage because of liquid evaporation, and its average value is comparable to that at the start of the blockage. The liquid drops decelerate while passing through the upstream minimum so that their speed within the blockage is significantly reduced. Figure 28 shows that the reduction in vapour flow in the blockage entry causes the vapour temperature to rise steeply, but within the blockage throat the low liquid speed increases the concentration of liquid phase enough to offset the loss in liquid flow rate. As a consequence further superheating of the vapour is suppressed. The net results on heat flux is shown in Figure 29. In the entry to the blockage there is a rapid fall due to the rapid superheating of the vapour, but within the blockage the fall is arrested. Along the bypass there is a steady fall in heat flux. There is good agreement between the predicted heat fluxes and the experimental data.

DISCUSSION

The simple BERTHA model presented here is capable of good predictions of reflood heat transfer in both unblocked and blocked fuel assemblies. The influences of reflood rate and pressure are well predicted as well as the important effects of spacer grids. Vapour temperatures appear to be significantly underpredicted for some distance downstream of the rewetting front, probably due to the lack of a proper transition to dispersed flow following the start of break up of the film boiling region. The fact that the predicted heat fluxes are so good in spite of this error suggests that the convective heat transfer correlation used is too conservative. It appears probable that it should be enhanced to take account of turbulence caused by the liquid phase.

In spite of these shortcomings it does appear that the important thermal hydraulic phenomenon are reasonably well modelled, so the predictions of the model should help to explain the experimental observations. The explanation which they do provide is as follows.

Until shortly before the blockage rewets the heat transfer regime is dispersed flow, with a continuum of superheated vapour flowing upwards carrying with it a suspension of liquid drops as in Figure 16. Most of the heat flux from the balloon surface is by convection to the vapour in this flow. A lesser amount is by

radiation, principally to the liquid drops. Because of the high surface temperature there is little heat transfer to the drops by direct contact with the surface.

There is also convective heat transfer and a small amount of radiative heat transfer from the superheated vapour to the liquid drops, whose surfaces are at about saturation temperature. This does not directly cool the blockage, but tends to reduce the superheat of the vapour and to generate more vapour. This improves convective heat transfer from the surface further downstream.

The rate of change of vapour temperature with distance along a subchannel is given by

$$\frac{\partial T_v}{\partial z} = \frac{q_{sv} - q_{v\ell} - \frac{h_v - h_g}{h_g - h_f}(q_{v\ell} + q_{s\ell})}{m_v\, c_{pv}} \qquad (1)$$

Typically the heat transfer terms in this expression are in the ratio

$$q_{sv} : q_{v\ell} : q_{s\ell} = 10 : 3 : 1$$

while $\dfrac{h_v - h_g}{h_g - h_f} \approx 0.5$

So the numerator is generally positive and the vapour superheat increases along the subchannel.

As the upflowing vapour approaches the blockage much of it is diverted into the bypass so that the mass flow rate of vapour through the blockage subchannels is reduced. For long blockages such as those used in the THETIS experiments it can be shown that the vapour speed in the blockage subchannels is comparable to that in the bypass region. Thus since the flow area is greatly reduced the vapour mass flow rate is also greatly reduced in proportion. Reference 15 presents results of single phase flow tests done on a model of the THETIS 90% blockage geometry. At Reynolds numbers above about 10^4 the mass flow rate in the central subchannel is reduced to about 15% of the original unblocked flow rate while that in the other 8 subchannels is reduced to about 11% of the original unblocked flow rate. At lower Reynolds numbers the reduction is greater and all the blocked subchannels pass only about 6% of the unblocked flow at a Reynolds number of 10^3. This comes about because the flow becomes laminar earlier in the blocked subchannels, because of their much smaller hydraulic diameter, giving larger friction coefficients.

Since the vapour is the principal agent for removing heat from the surface it would appear that this very great reduction in vapour flow through the blockage would drastically impair the heat transfer there. However, it should be noted that the heat transfer coefficient between the surface and the vapour may not be greatly reduced by the flow diversion. This comes about as a result of three effects:-

1 In most situations of interest the flow in the bypass region will be turbulent, but within the blockage it will generally be laminar due to the relatively low vapour mass flow rate and the small hydraulic diameter. For a typical Reynolds number in the bypass of 4000 and for laminar flow in the blockage the ratio of blockage Nusselt number to bypass Nusselt number is found from established correlations to be 0.45. However, for an 80% blockage the hydraulic diameter is only 0.22 of that in the bypass. So the heat transfer coefficient between the clad surface and the vapour is actually greater in the blockage than in the bypass by a factor of 2 (ie 0.45/0.22).

2 The above argument ignores the fact that the shape of the blocked subchannel is less effective for heat transfer because parts of it are in poor contact with the main flow. An indication of the reduction in Nusselt number can be had from the reduction in friction factor produced by the same effect. Compared with the bypass region the laminar friction factor at a given Reynolds number is reduced by a factor of 0.45 (ie 6.5/14.5). Although Reynolds analogy does not apply in laminar flow this factor can be taken as a guide to the reduction in Nusselt number to be expected.

3 Finally the surface area within the blockage available for heat transfer may differ from that in the bypass. However, for an idealised 80% blockage the heat transfer perimeter is virtually unchanged compared with the bypass.

So for an 80% blockage the net effect is to only change the heat transfer per unit length per unit temperature difference in the ratio of about 0.9 (ie 2 x 0.45 x 1).

It is an interesting fact that for any other blockage severe enough for laminar flow to occur within it, precisely the same ratio is obtained. This is because all such blockages have the same subchannel shape, and any difference in subchannel size has opposite and cancelling effects on items 1 and 3 above. So the heat transfer per unit length per unit temperature difference in a 90% blockage will be the same as in an 80% blockage; and not much less than for an unblocked cluster.

Thus the main parameter controlling the heat removal in the blockage, and any difference there might be between and 80% and a 90% blockage, is the vapour superheat.

From equation 1 it appears that the rate of superheating would be very high through a severe blockage because, as we have seen, the vapour mass flow rate is so greatly reduced. The more severe the blockage the more rapid the superheating would appear to become. But we have also to consider the effect of the blockage on the numerator of equation 1. This is a difference of terms which are not too dissimilar in magnitude so changes in the relative magnitudes of the three heat transfer terms can have a large effect. Taking the typical relative magnitudes quoted above as an example, if the relative importance of the terms involving the liquid phase were doubled the numerator in equation 1 would change from "5" to zero. This would suppress the superheating completely irrespective of any change in the vapour mass flow rate. Further emphasis on heat transfer to the liquid phase would actually cool the vapour as it passed through the blockage. In such circumstances the rate of cooling would be greater the lower the vapour mass flow, that is the more severe the blockage.

So it does not follow that the reduction in vapour mass flow rate caused by the blockage necessarily results in an increased rate of superheating. The vapour temperature depends just as much on how the blockage influences the behaviour of the liquid phase. But it is true that the more severe the blockage the more erratically will the rate of superheating vary if the liquid phase behaviour is modified.

Let us then consider the behaviour of the liquid phase within the blockage. The liquid drops are entrained into the vapour flow in the vicinity of the rewetting front. They are accelerated in the upward flowing vapour, and gain speed as they move further from the rewetting front. So early in the reflood, when the rewetting front is far from the blockage, the speed of the drops as they reach the blockage is relatively high. But the speed at which the drops arrive at the blockage decreases with time as the rewetting front comes closer.

Within the blockage a large fraction of the vapour flow is diverted out of the blockage subchannels along the entry taper, where the available flow area is steadily reducing. However, vapour diversion ceases when the swollen clad comes into contact and closes the gaps between the blocked subchannels. In an idealised geometry this occurs at a strain of 32% and a blockage of 61%. If the blockage is more than 61% a further reduction in flow area occurs along the subchannel while the vapour flow is not further diminished. Indeed it increases somewhat due to evaporation from the liquid phase. So the vapour speed must increase beyond the point where the gaps close. But we have seen

that within the blockage throat the vapour speed is comparable to that in the unblocked part of the assembly. Therefore there must exist a minimum in vapour speed at the point where the gaps close. Figure 27 shows the calculated axial variation of vapour speed along an 80% blockage. The minimum where the gaps between the subchannels close is very pronounced. The vapour speed in the blockage throat is comparable with that before the blockage, but it increases along the throat because of evaporation from the liquid phase. There is a second minimum downstream of the throat because the subchannel flow area increases before the gaps between the cans open again to permit vapour to flow back into the wake of the blockage.

Figure 27 also shows the calculated speed of a typical liquid drop of 1 mm diameter as it passes through the blockage. This represents an early stage in the reflood when such drops are arriving at the blockage at the relatively high speed of about 2 m/s. If no blockage had been encountered this drop would have continued to accelerate in the accelerating vapour flow. But on passing through the region of low vapour speed in the blockage entry taper its speed actually falls to about 1 m/s. Then it accelerates again as it encounters the higher vapour speeds in the blockage throat. Not all the drops arriving at the blockage actually pass through it. The lateral flow of vapour in the entry up to the point where the gaps close sweeps some of them into the bypass. But at this early stage the drops arrive with sufficient momentum that most of them are able to enter the blockage without being swept aside in this way.

The heat flux to the liquid phase is proportional to the flow of drops but inversely proportional to their speed, because the lower the speed the longer they reside in the blockage. At this early stage in the reflood there is not too much liquid diversion so the flow of drops through the blockage is not greatly reduced. But the speed is reduced significantly so there can be an overall increase in heat transfer to the liquid. This can have the effect of reducing the numerator in equation 1, offsetting the reduction in the denominator. So the rate of superheating can be much less than the reduction in vapour flow would at first suggest.

However, as the reflood proceeds, drops arrive at the blockage with progressively lower speeds. They spend more time in the blockage entry allowing gravity to slow them further and the lateral vapour flow to sweep them aside into the bypass. The flow of liquid through the blockage falls even lower and the heat flux to the liquid phase decreases. Without the moderating influence of the liquid phase heat transfer terms in the numerator of equation 1, the reduction in vapour mass flow begins to take full effect and the rate of superheating rises steadily.

This appears to explain the observed behaviour in the THETIS 80% blockage where superheating along the blockage was slight at first but increased steadily with time.

In the THETIS 90% blockage the minimum in vapour speed in the entry to the blockage would be much more pronounced, causing the drops to slow even more on passing through the blockage. In the early stages of reflood, when there is not much liquid diversion, this could increase the heat transfer to the liquid phase even more than in the 80% blockage. This appears to have been the case because negative axial temperature gradients did occur over certain periods in the 90% blockage, implying that the sign of equation 1 had become negative. The erratic behaviour of the axial temperature gradient in the early stages of reflood is also consistent with the numerator of equation 1 being the difference of two similar but varying quantities while the denominator is small. However, later in the reflood, as in the 80% blockage, the flow of liquid through the blockage is greatly reduced and its moderating influence diminishes. Then the vapour superheats on passing through the blockage at an even greater rate than in the 80% blockage, because of the lower vapour mass flow rate.

So the fact that early in the reflood the 90% blockage was better cooled than the 80% blockage is seen as a consequence of the liquid drops passing more slowly through the blockage, increasing their cooling effect by more than enough to offset the lower vapour mass flow rate. And the reason that later in the reflood the 80% blockage is better cooled than the 90% blockage is because little liquid passes through the blockage anyway, so the higher vapour mass flow rate in the 80% blockage dominates the issue.

As the reflood rate is reduced the amount of liquid entrained in the coolant flow decreases. The heat transport to the liquid phase become less important and vapour superheating becomes more pronounced and more dependent on the vapour flow rate, even in the early stages of reflood. This explains why the blockage temperature penalty increases as the reflood rate decreases and also explains the observation in the THETIS experiments that, while the 90% blockage was generally somewhat better cooled than the 80% blockage, the reverse was true at a low reflood rate of 1 cm/s.

CONCLUSIONS

The THETIS experiments and the interpretation of the results using the BERTHA model have led to the following view of the heat transport processes which occur within long severe blockages during reflood.

1 The vapour flow through the blockage is greatly reduced. However, because of the small hydraulic diameter of the blocked subchannels the heat transfer coefficient within the blockage is hardly changed, and is virtually independent of the blockage severity.

2 Heat transfer in these blockages depends largely on the superheating of the vapour which does pass through the blockage. This in turn depends on the behaviour of the liquid in the two phase flow.

3 Liquid entering the blockage slows down in the entry region and so spends more time in the blockage to remove heat from the vapour. In the early stages of reflood this limits the superheating of the vapour giving good cooling throughout the blockage. Cooling may even be better for more severe blockages because they slow the liquid more.

4 As the rewetting front approaches the blockage the speed at which liquid arrives at the blockage decreases. This allows progressively more liquid to be swept aside into the bypass. As less liquid penetrates the blockage its desuperheating effect diminishes, allowing the vapour to superheat more and more. This causes a late peak in blockage temperature, with the highest temperature occurring at the top of the blockage.

5 The lower the reflood rate the less liquid is entrained in the coolant flow, so the mitigating effect of the liquid decreases. Superheating of the vapour within the blockage becomes more exclusively dependent on the amount of vapour passing through the blockage This is less the more severe the blockage. So as the reflood rate is reduced a blockage temperature penalty develops, which becomes greater as the reflood rate decreases or the severity of the blockage increases.

Other important findings of the THETIS programme are:

Rewetting

The blockage region rewets generally no later and sometimes rather earlier than the corresponding bypass region. Quench temperatures vary markedly with axial position and are strongly influenced by the presence of spacer grids.

Spacer Grids

Spacer grids significantly enhance both single and two-phase heat transfer. The passage of hot steam through wet grids gives considerable desuperheating.

ACKNOWLEDGEMENT

We would like to thank the Commission of the European Communities for its partial financial support of the THETIS 80% blocked cluster experiments and the BERTHA model development.

NOMENCLATURE

cp_v	Specific heat of vapour	kJ/kg°C
h_f	Specific enthalpy of saturated liquid	kJ/kg
h_g	Specific enthalpy of saturated vapour	kJ/kg
h_v	Specific enthalpy of superheated vapour	kJ/kg
m_v	Mass flow rate of vapour	kg/s
q_{sv}	Heat transfer from surface to vapour	kW/m
$q_{s\ell}$	Heat transfer from surface to liquid	kW/m
$q_{v\ell}$	Heat transfer from vapour to liquid	kW/m
T_v	Temperature of vapour	°C
z	Elevation	m

REFERENCES

1 ERBACHER, F. J., NEITZEL, H. J. AND WIEHR, K. 5th International Conference of Zirconium in the Nuclear Industry. 4-7 August 1980, Boston, USA.

2 PEARSON, K. G., COOPER, C. A., JOWITT, D. and KINNEIR, J. H. AEEW - R 1591.

3 DENHAM, M. K., ELLIOTT, D. F. and SHAWYER, K. J. AEEW - R 1353.

4 "TRAC-PD2" An Advanced Best-Estimate Computer Program for Pressurised Water Reactor Loss-of-Coolant Accidnet Analysis". Los Alamos Scientific Laboratory LA-8709-MS, April 1981.

5 YAO, S. C., HOCHREITER, L. E. and LEECH, J. J. J. of Heat Transfer, Vol 104, pp 76-81, (1982).

6 DENHAM, M. K. AEEW - R 1590 (1983).

7 KIM, J. H. ASME Conference on Fluid Flow and Heat Transfer over Rod or Tube Bundles, pp 155-161 (1979).

8 DITTUS, F. W. and BOELTER, L. M. K. University California, Eng 2 pp 443-461 (1930).

9 SUN, K. H., GONZALES, J. M. and TIEN, C. L. J. Heat Transfer, Vol 98, pp 414-420 (1976).

10 YUEN, M. C. and CHEN, L. W. Int J. Heat Mass Transfer, Vol 21, pp 537-542 (1978).

11 ARDRON, K. H. and HALL, P. C. CEGB Report RD/B/5007N81 (1981).

12 BENNETT, C. O. and MYERS, J. E. 'Momentum, Heat and Mass Transfer', McGraw-Hill (1962).

13 PEARSON, K. G. and ELLIOTT, D. F. AEEW - R 1098 (1977).

14 BOWRING, R. W. AEEW - R 524 (1967).

15 AYTEKIN, A. NNC Report No PWR/R625.

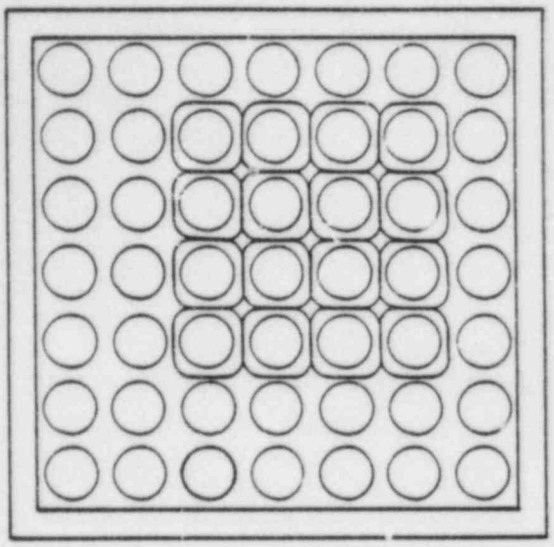

FIG.1 THETIS 7×7 BLOCKED CLUSTER WITH 4×4 BLOCKAGE

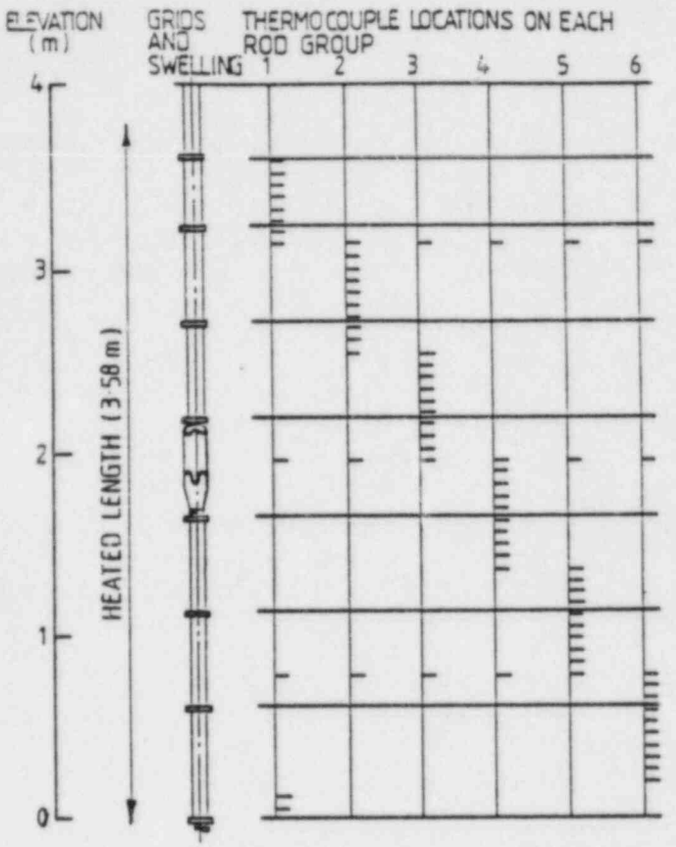

FIG.2 RELATIVE LOCATIONS OF THERMO-COUPLES TO GRIDS SWELLING AND HEATED LENGTH

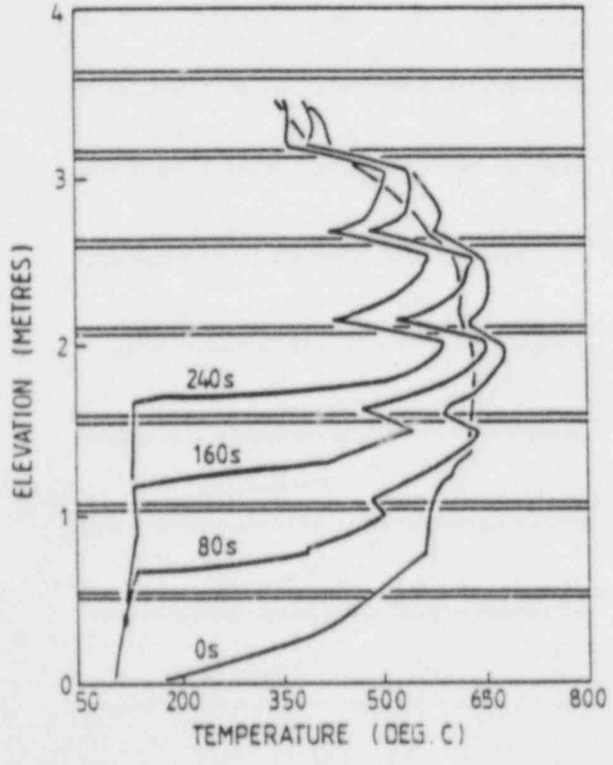

FIG.3 RUN T1R065 - BYPASS TEMPERATURES AT VARIOUS TIMES DURING REFLOOD

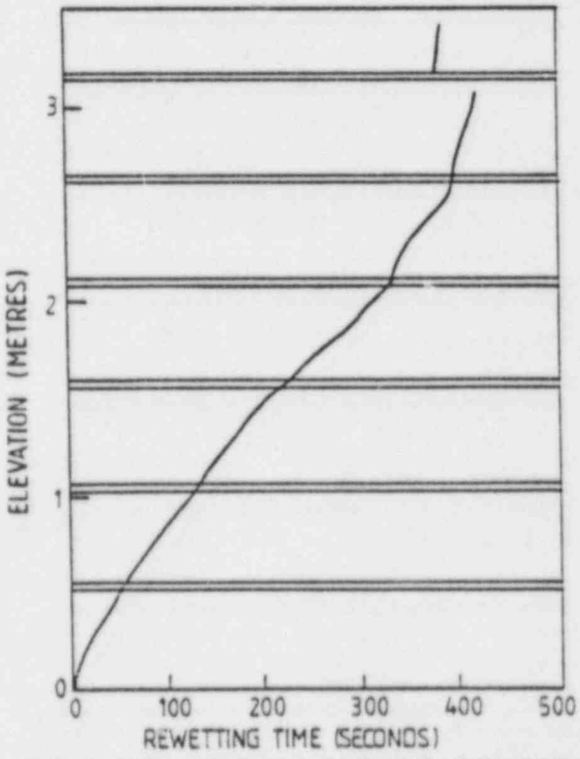

FIG.4 RUN T1R065 - BYPASS REWETTING TIMES.

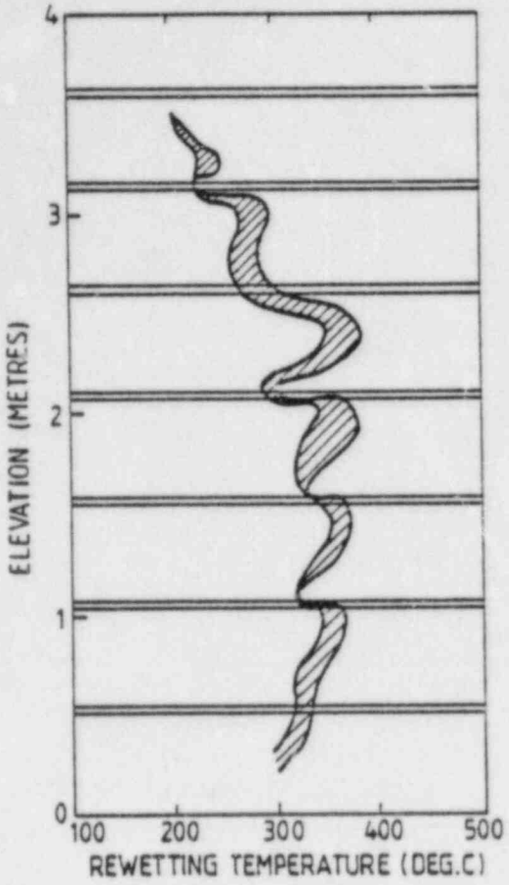

FIG.5 RUN TIR065-BYPASS REWETTING TEMPERATURES

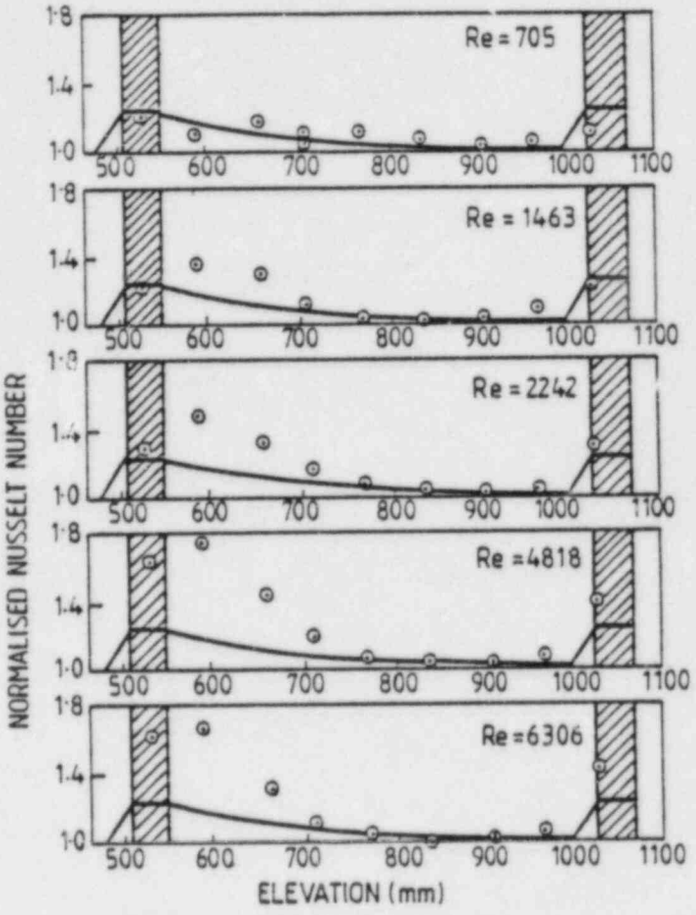

FIG.6 GRID ENHANCEMENT COMPARED WITH CORRELATION OF YAO, HOCHREITER AND LEECH.

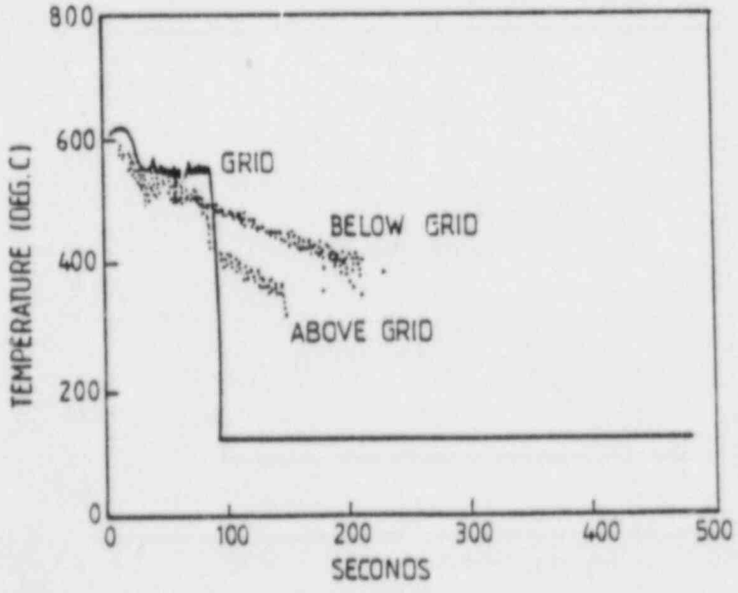

FIG. 7 STEAM DESUPERHEATING BY WET GRID

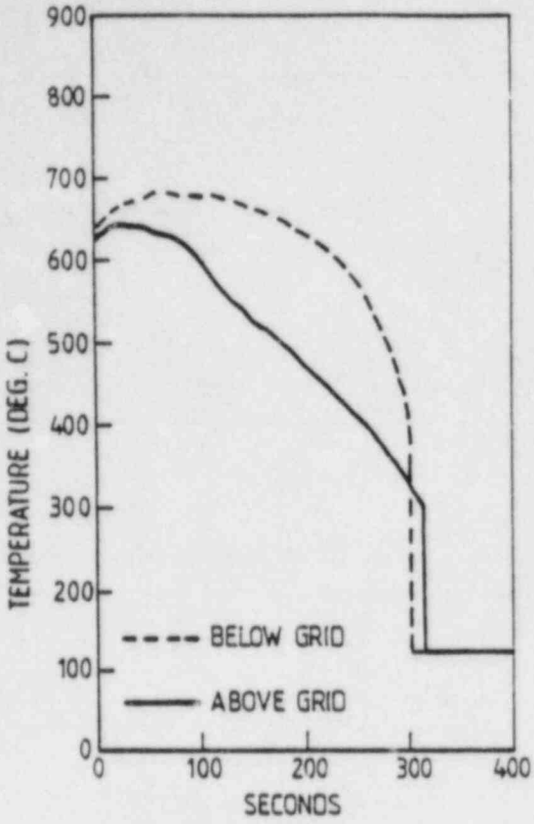

FIG.8 RUN T1R065-ROD TEMPERATURE HISTORIES ABOVE AND BELOW GRID

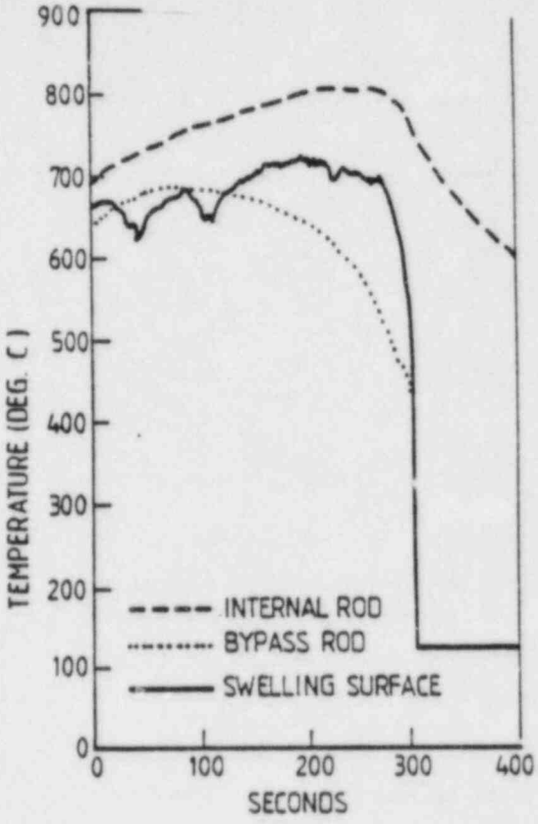

FIG.10 RUN T1R065-MAXIMUM BLOCKAGE AND BYPASS TEMPERATURES.

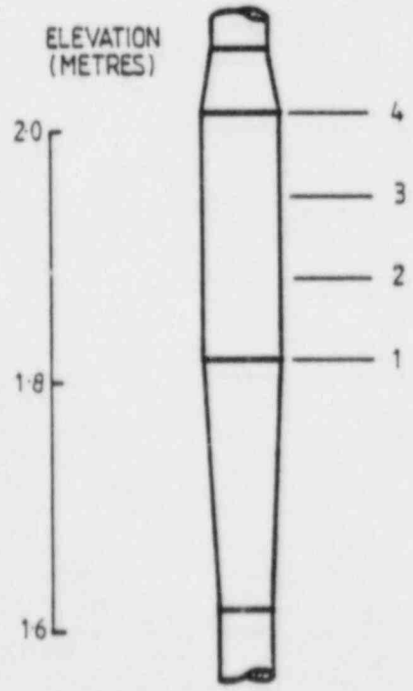

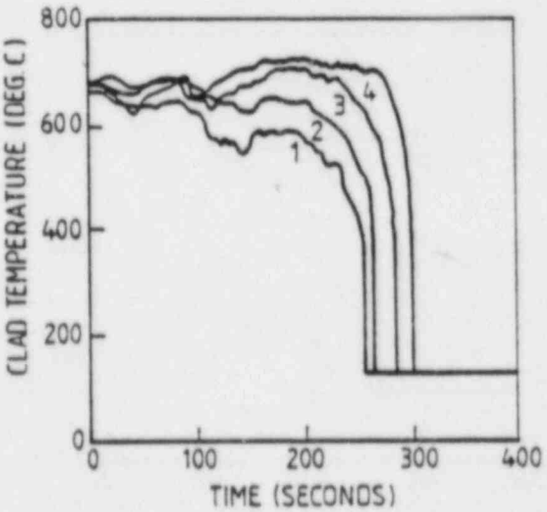

FIG.9 TEMPERATURES MEASURED IN 90% BLOCKAGE DURING RUN T1R065

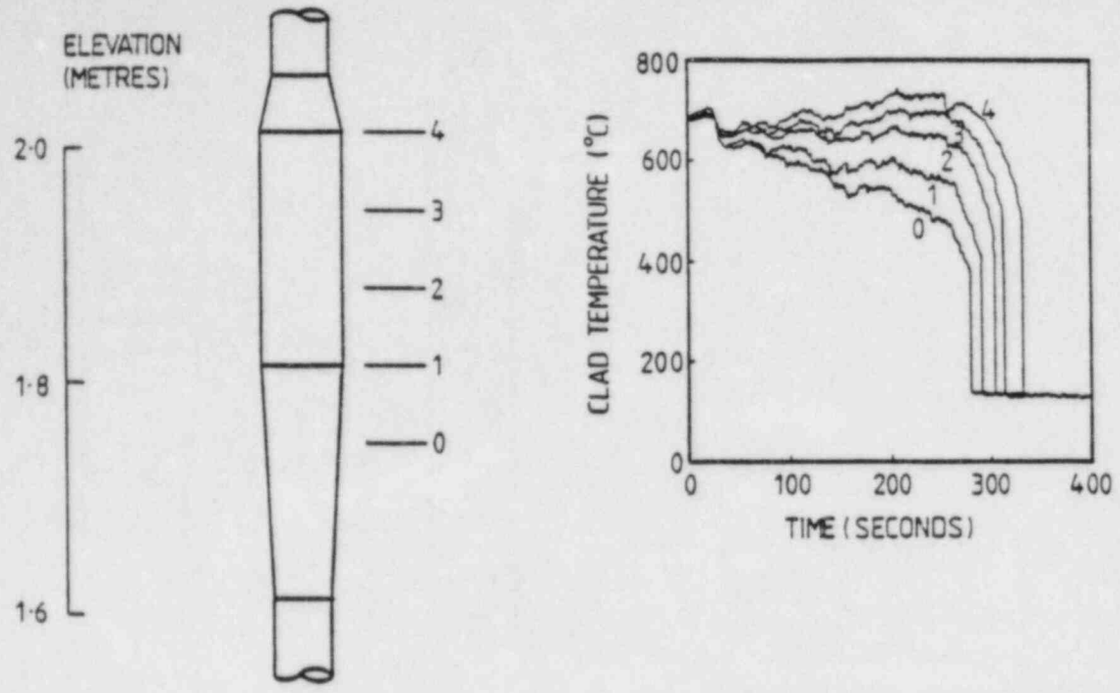

FIG. 11 TEMPERATURES MEASURED IN 80% BLOCKAGE DURING RUN T2R020

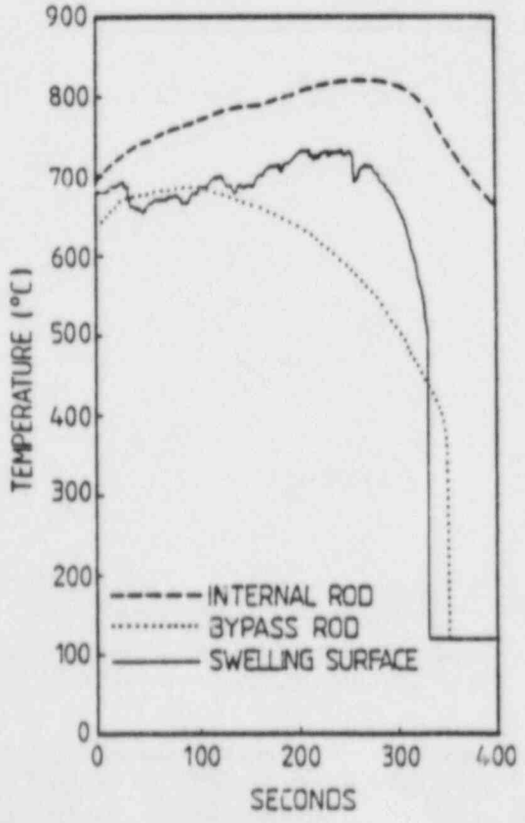

FIG. 12 RUN T2R020 - MAXIMUM BLOCKAGE AND BYPASS TEMPERATURES

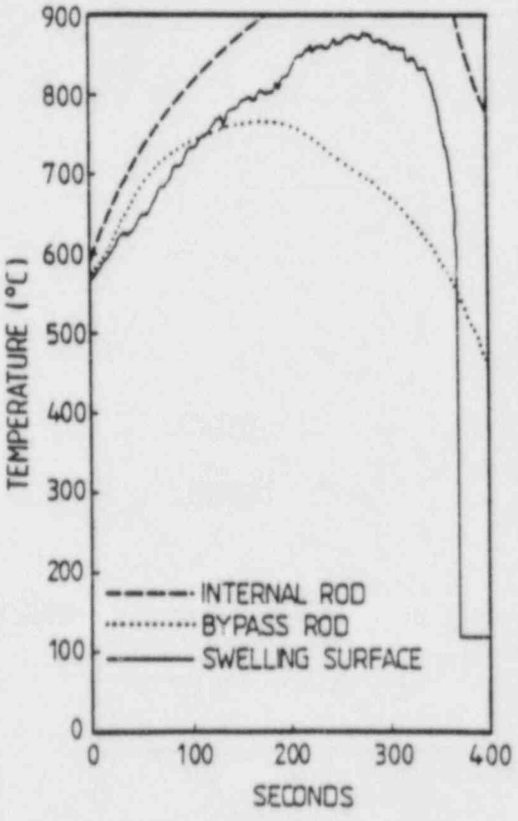

FIG. 13 RUN T2R043 - MAXIMUM BLOCKAGE AND BYPASS TEMPERATURES

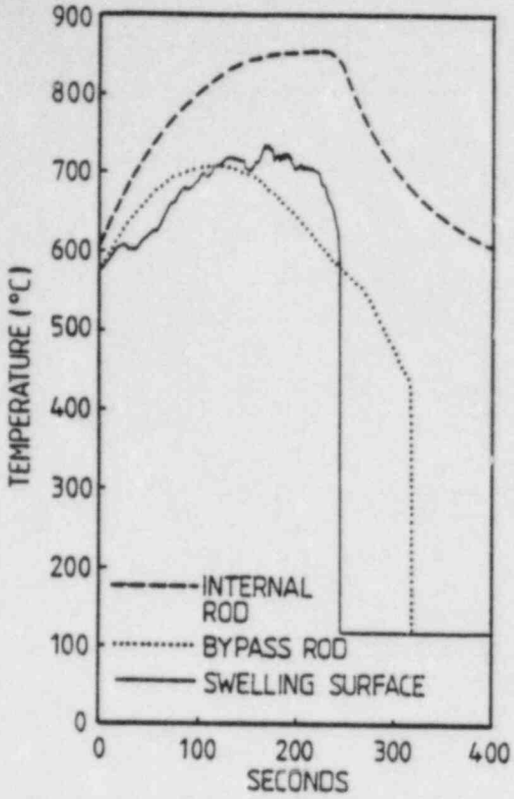

FIG. 14 RUN T2R037 - MAXIMUM BLOCKAGE AND BYPASS TEMPERATURES

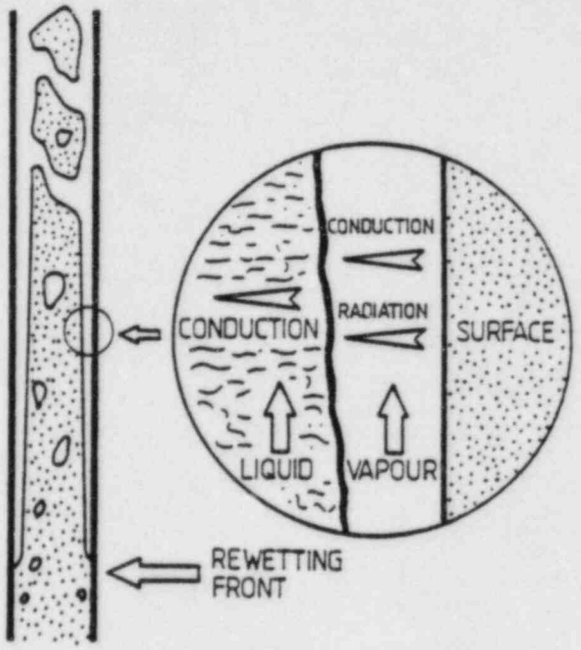

FIG. 15 FILM BOILING REGION

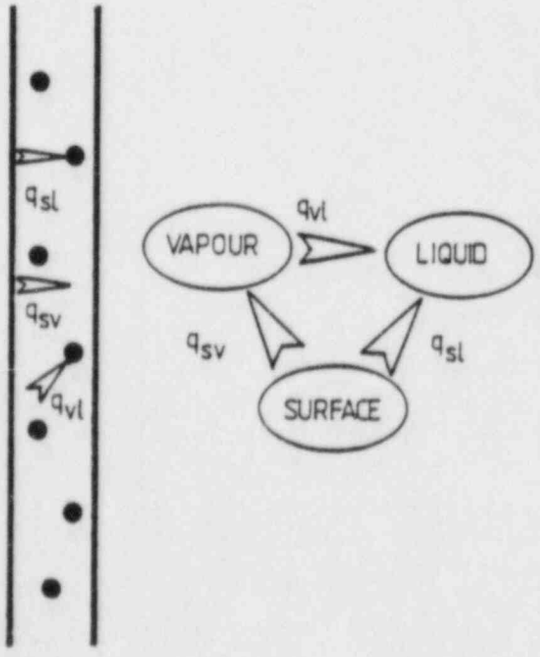

FIG. 16 DISPERSED FLOW REGION

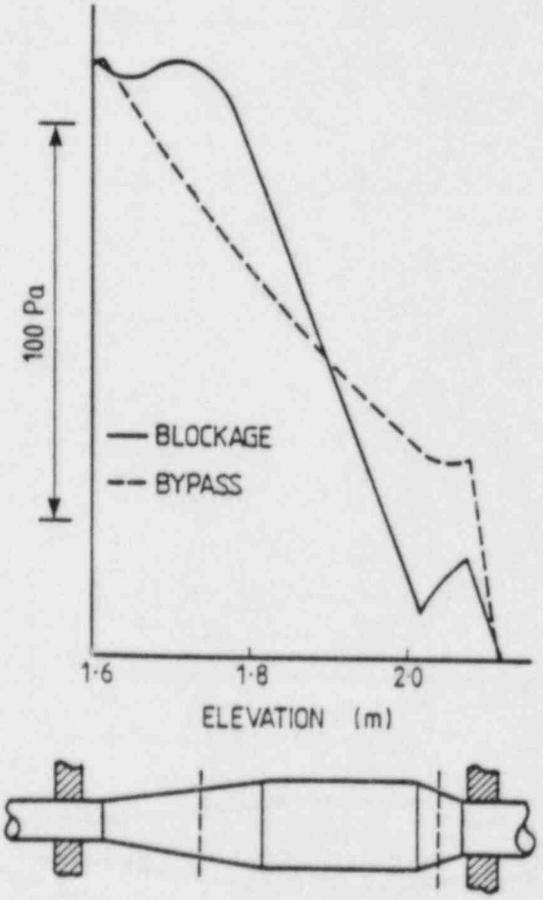

FIG. 17 AXIAL PRESSURE VARIATION

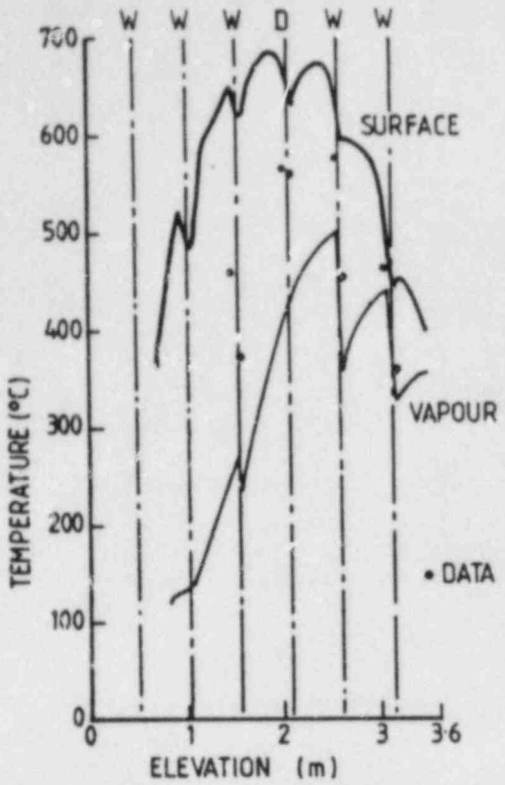

FIG.18 BYPASS VAPOUR TEMPERATURE

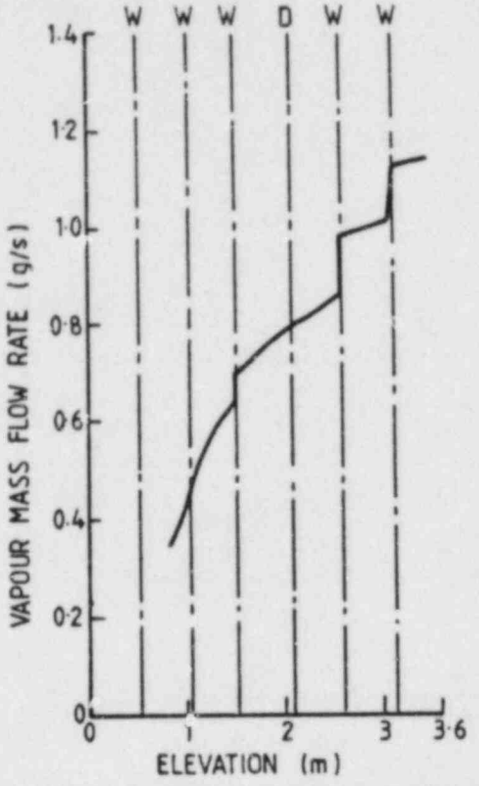

FIG.19 BYPASS VAPOUR FLOW RATE

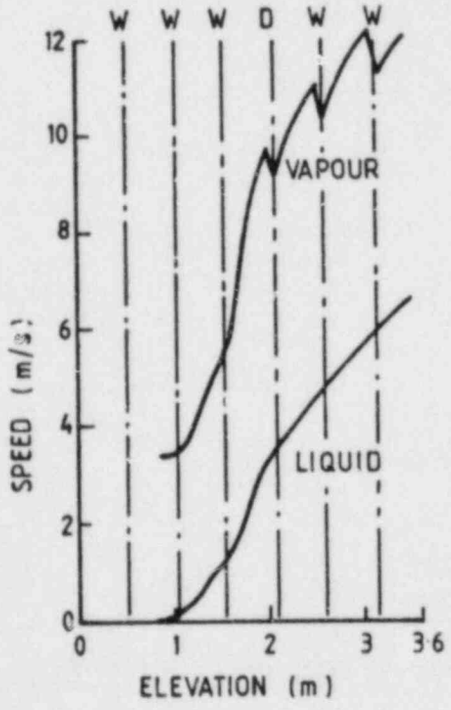

FIG.20 BYPASS VAPOUR AND LIQUID SPEEDS.

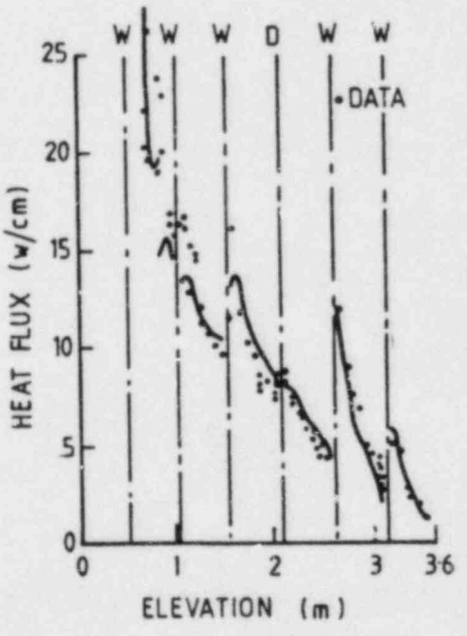

FIG.21 BYPASS HEAT FLUX

REFLOOD RATE 2 cm/s
PRESSURE 2 bar

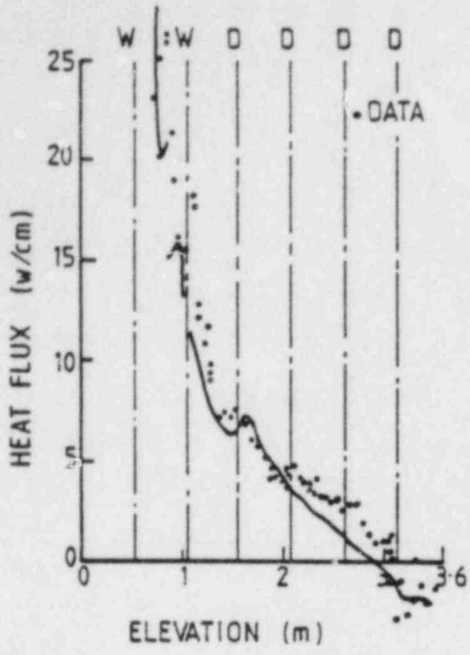

FIG.22 BYPASS HEAT FLUX
REFLOOD RATE 1 cm/s
PRESSURE 2 bar

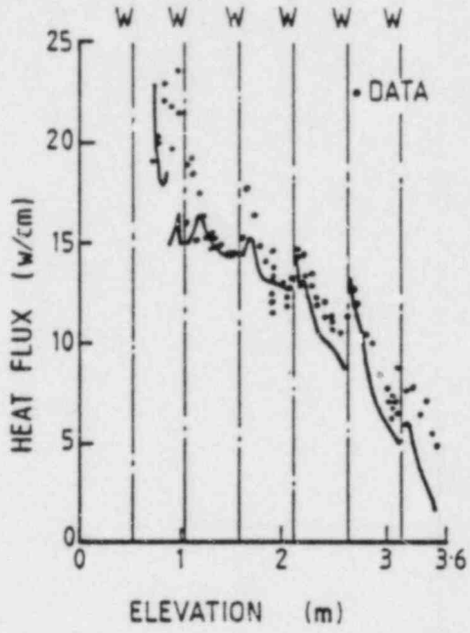

FIG.23 BYPASS HEAT FLUX
REFLOOD RATE 4 cm/s
PRESSURE 2 bar

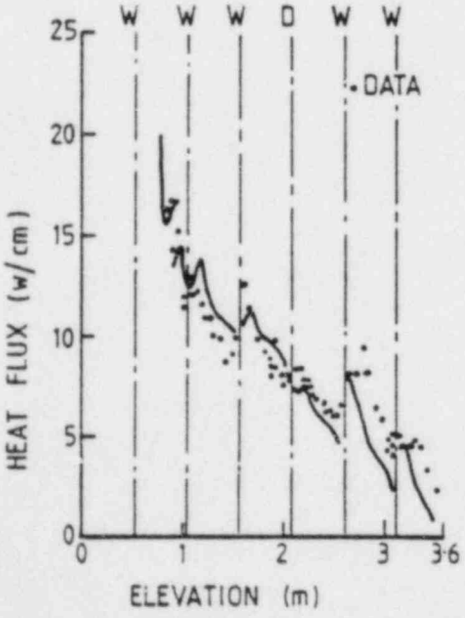

FIG.24 BYPASS HEAT FLUX
REFLOOD RATE 2 cm/s
PRESSURE 1·3 bar

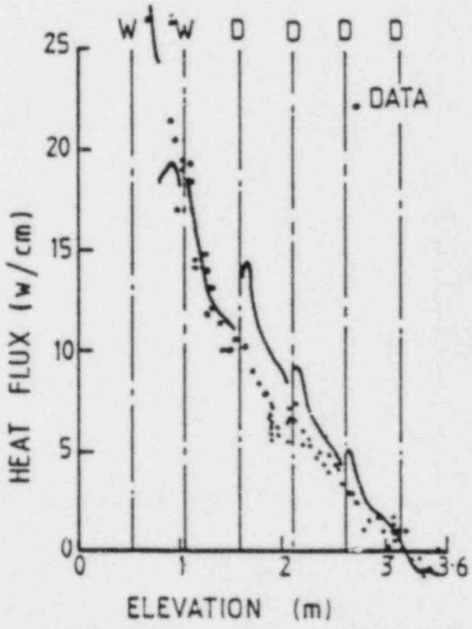

FIG.25 BYPASS HEAT FLUX
REFLOOD RATE 2 cm/s
PRESSURE 4 bar

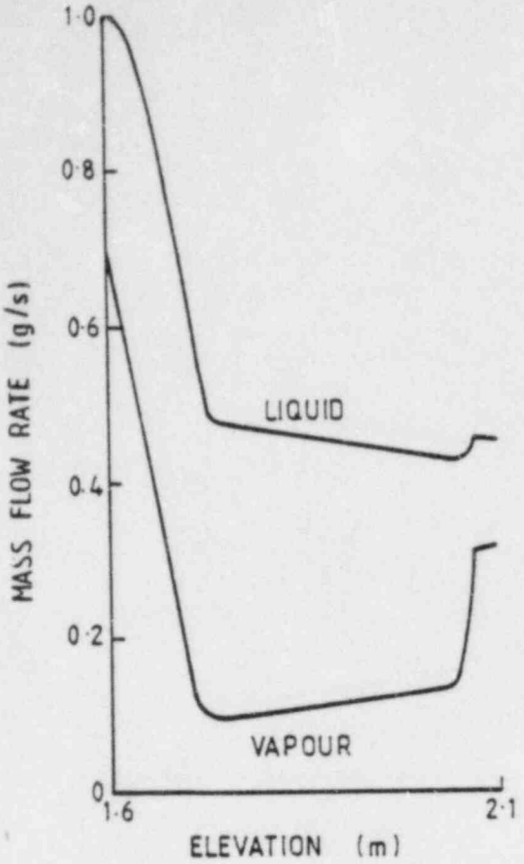

FIG. 26 MASS FLOW RATES IN BLOCKAGE

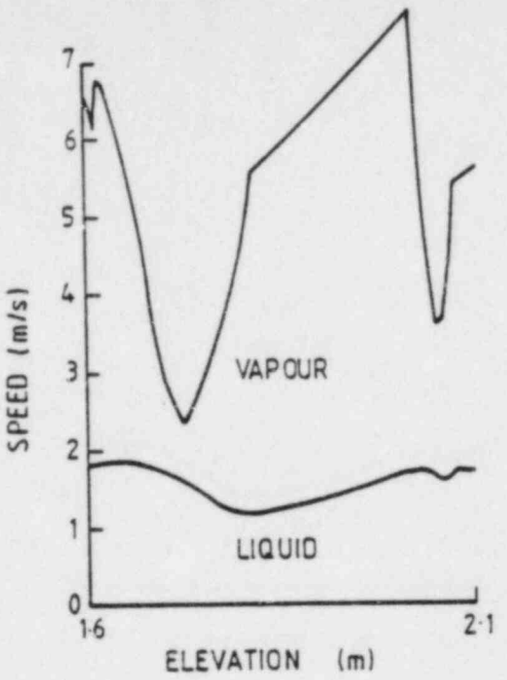

FIG. 27 SPEEDS IN BLOCKAGE

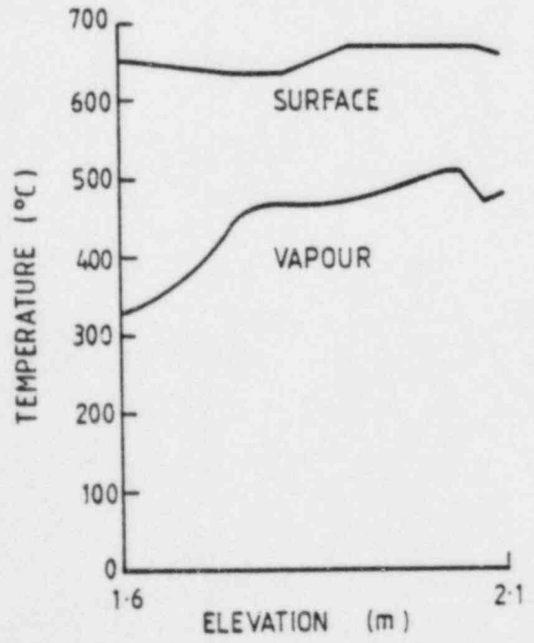

FIG. 28 TEMPERATURES IN BLOCKAGE.

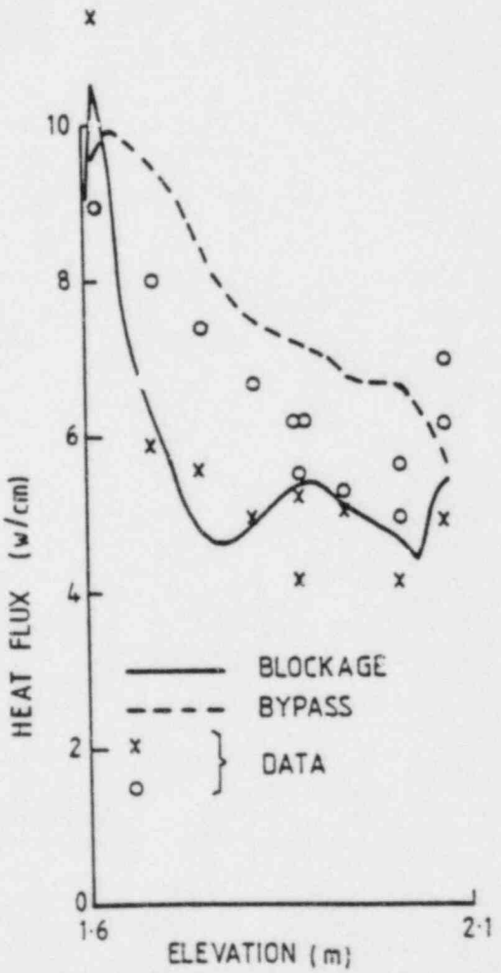

FIG. 29 HEAT FLUXES IN BLOCKAGE AND BYPASS.

Grid Spacer Effects in Reflooding Experiments Using Rod Bundles of Different Fuel Rod Simulator Design

P. Ihle, K. Rust, F. Erbacher

Kernforschungszentrum Karlsruhe
Institut für Reaktorbauelemente
Postfach 3640, 7500 Karlsruhe
Federal Republic of Germany

Abstract

A comparison of the grid spacer effects, investigated previously in the frame of the FEBA program, with those obtained from tests using fuel rod simulators with Zircaloy claddings and helium filled gaps (REBEKA-rods) is made. For such rods, simulating more adequately nuclear fuel rods than "gapless" heater rods (e.g. FEBA), the variation of the axial temperature profile due to grid spacers is more pronounced during the reflood phase. In a 5x5 bundle of REBEKA rods, tested in the FEBA facility, the cladding temperatures were about 20 K up to 100 K lower downstream of the midplane grid spacer than in corresponding FEBA tests. The grid spacers are hot and dry for most time of the dispersed flow regime.

Introduction

The objective of this investigation is to study the effect of grid spacers on the reflood temperature transients measured in full length rod bundles simulating fuel rod clusters of PWR geometry.

The grid spacer effects analyzed in the FEBA program /1, 2/ were obtained from 5x5 rod bundles consisting of electrically heated "gapless" fuel rod simulators usually used for thermal-hydraulic reflood experiments. Nuclear fuel rods as well as electrically heated simulators with Zircaloy claddings and a gap between the cladding and the internals of the rods show lower cladding temperatures and shorter quench times than gapless fuel rod simulators /3/. Are such rods more sensitive to grid spacer effects as well?

Experiments

In the SEFLEX program (Fuel Rod Simulator Effects in Flooding Experiments) cladding as well as grid spacer temperatures were measured in a 5x5 rod bundle consisting of fuel rod simulators with Zircaloy claddings. The data are to be compared with those obtained from corresponding FEBA tests. A cross section of a FEBA rod is shown in Fig. 1. The heater rod is characterized by a relatively thick stainless steel cladding with a close thermal contact to the MgO insulation. The REBEKA rods used for the SEFLEX tests have the same outer dimensions including the axial power distribution. However, the internal electrical heating element is surrounded by Al_2O_3 pellets simulating UO_2 (see Fig. 2). A nominal gap of 0.05 mm width is provided between the cladding and the pellets. For the first SEFLEX test series the gap was filled with Helium. The tests are reflood experiments with 5x5 rod bundles of REBEKA rods placed in the FEBA facility to minimize the influence of different test installations and operational procedures. Prior to reflood the bundle is preheated in stagnant steam to the desired initial cladding temperature, using a small rod power. The test housing - identical to FEBA - is in the meantime being heated up passively to the desired initial temperature by radiation

from the rods. Initial axial temperature profiles and bundle power (200 kW) at initiation of reflood, decay heat transient, axial power distribution as well as power steps along the rods were the same for the FEBA and the SEFLEX test series. The design and the arrangement of the grid spacers - without mixing vanes - were the same as well.

Results

The overall reflood behavior of the REBEKA rod bundle is different from that of the FEBA rod bundle. Figure 3 shows nine cladding temperature transients. The measurement locations were at the bundle midplane (axial level 2025) and four each upstream and downstream of it with axial distances of 100 mm from each other. In the upper portion of Fig. 3, FEBA data are plotted from a test performed with 2 bar and a flooding velocity of 3.8 cm/s (FEBA 223). The SEFLEX data obtained from the REBEKA rod bundle under the same reflood conditions (SEFLEX 05) are shown in the lower portion of the figure. Quench times and turn around times are significantly shorter in the SEFLEX test. Maximum temperatures are lower. For the axial length of 800 mm (2425-1625) shown, in the FEBA test the quench front needs 210 s to rewet the measuring positions taken into consideration. Following the equidistant measuring positions and the roughly equidistant quench times the quench front has about constant velocity (3.8 mm) along the bundle axis of this bundle section. The quench front is nearly unaffected by the grid spacer under these flooding conditions. In SEFLEX, the quench front passes the bundle section shown with an overall velocity of about 5.7 mm/s, and it is not constant. It is slightly delayed upstream of the leading edge of the grid spacer, and accelerated downstream of the trailing edge.

The cladding, housing and grid spacer temperature transients at the bundle midplane for two different reflood conditions are shon in Fig. 4. In the upper portion of the figure FEBA 223 and SELFEX 05 are compared with each other. In the test FEBA 223, there was no grid spacer instrumentation. Therefore, only SEFLEX data were plotted. Prior to initiation of reflood, the grid spacer temperatures are high in these tests because of the long preheating phase of the operational procedure applied. After initiation of reflood, entraining by the steam water droplets and the radiation from the rods control the temperatures of the grid spacers. After the sudden drop of the temperature of the midplane grid from more than 700 ^{o}C down to about 550 ^{o}C during the first few seconds of SEFLEX 05, a temperature increase was observed up to about 700 ^{o}C for the leading edge and up to about 630 ^{o}C for the trailing edge of the grid spacer. This heating up is mainly due to heat convection from the superheated steam. For tests performed with short preheating (ramp tests), it leads to dryout too.

Quenching of the grid is initiated at the trailing edge at about one quarter of the quench time of the rod cladding at the same elevation. Quenching of the leading edge occurs later significantly. It has to be mentioned that leading and trailing edges of the grid spacer were instrumented in two different subchannels. Since across the bundle slightly different cooling conditions are probable, the magnitude of the differences between leading and trailing edges may be exaggerated in this case. However, the trend is confirmed. The grid spacer is quenching in the time span between 70 s and 105 s of the SEFLEX test. The lowest cladding temperature at that time interval is measured downstream of the trailing edge of the grid spacer. The data plotted in the lower portion of Fig. 4 are obtained from identical measurement positions as above. The test was carried out under the same flooding velocity,

but with a system pressure of 4 bar (SEFLEX 03) instead of 2 bar (SEFLEX 05). The grid spacer temperatures show similar trends as before. However, for increasing system pressure the quench time of the grid spacer related to the quench time of the rod cladding is delayed. The grid spacer is quenching at about 2/3 of the quench time of the rod claddings.

The cladding temperature transients 100 mm upstream through about 200 mm downstream of the gridspacer are shown in Figs. 5 and 6. The grid spacer of a height of 38 mm is placed between the axial levels 2025 mm (leading edge) and 1987 mm (trailing edge). At the axial level 19 5 mm, i.e. 12 mm downstream of the trailing edge, the cladding is quenching at about the same time as upstream at the axial level 2025 mm in the SEFLEX test No. 05 performed with a system pressure of 2 bar (see Fig. 5). In the SEFLEX test No. 03 (4 bar) quenching of the cladding downstream of the grid occurs about 3 s earlier than upstream of the grid (see Fig. 6). For the whole time span of the recording windows plotted in both the figures, the grid spacer was wet.

Investigations published /1, 2, 4/ showed that a grid spacer improves the heat transfer downstream of it mainly during the dispersed flow regime. From the SEFLEX tests, it can be concluded that for most of the flooding conditions investigated, the grid spacer is hot and dry for about 50 % up to 100 % of the time span of the dispersed flow regime during reflood. Some FEBA tests performed with instrumented grid spacers confirm this finding. The FEBA grid spacer temperatures were rather higher and quenching occured rather later - due to the higher FEBA cladding temperatures - than those shown for SEFLEX.

The grid spacer effects on the axial temperature distribution of the rod claddings is more pronounced for fuel rod simulators with gap than for gapless rods. Figure 7 shows a comparison of axial cladding temperature profiles evolved in FEBA and SEFLEX tests under identical reflood conditions (compare Fig. 3). The axial temperature profiles are recorded 30, 90 and 150 s after initiation of reflood. After 30 s, the temperature drop at and downstream of the grid spacer amounts to about 30 K more for REBEKA rods than for gapless FEBA rods. Upstream of the grid spacer the cladding temperatures of both the bundles are still at the same temperature level. Measurements taken from the axial level 1975 mm in the SEFLEX test (see Fig. 5 and 6) are not considered in Fig. 7, since, they are not existant for the FEBA tests.

After 90 and 150 s, respectively, the overall difference between both the temperature profiles increases. This is due to the faster overall reflood transient during the SEFLEX test. However, at and downstream of the grid spacer the difference is pronounced more significantly indicating enhanced grid spacer effects in SEFLEX compared with FEBA.

For increased system pressure the difference between the axial profiles of the cladding temperatures downstream of the grid spacer decreases because the grid spacer effects decrease in general /1/. However, it remain more pronounced for REBEKA rods than for gapless FEBA rods.

The reason for this is mainly the higher heat resistance between cladding and internals of the REBEKA rod as well as the lower heat capacity of the Zircaloy cladding compared with the characteristics of the FEBA rod. For given cooling conditions at the outer surface of the claddings the temperature of the thin Zircaloy cladding approaches faster the fluid temperature leading to an increase of the temperature difference across the gap between cladding and pellets as compared with the FEBA rod.

Conclusions

The comparison of grid spacer effects observed in a 5x5 bundle of gapless FEBA rods and those observed in an identical bundle of REBEKA rods with Zircaloy claddings and Helium filling in the gap between cladding and Al_2O_3 pellets shows the following trends:

- The grid spacer effect is more pronounced for REBEKA rods simulating more adequately nuclear fuel rods.
- The cladding temperatures are 20 K up to 100 K lower downstream of the grid spacer at the bundle midplane.
- The grid spacers are hot and dry for most of the dispersed flow time span. The temperature transients follow roughly the fluid temperatures measured.

References

/1/ Ihle, P.; Rust, K.:
"FEBA - Flooding Experiments with Blocked Arrays, Evaluation Report"
KfK 3657, March 1984

/2/ Ihle, P.; Rust, K.:
"FEBA - Flooding Experiments with Blocked Arrays, Data Report 1, Test Series I through IV"
KfK 3658, March 1984

/3/ Erbacher, F.J.; Neitzel, H.J.; Wiehr, K.:
"Effects of Thermohydraulics on Clad Ballooning, Flow Blockage and Coolability in a LOCA"
OECD-NEA-CSNI/IAEA Specialists' Meeting on Water Reactor Fuel Safety and Fission Product Release in Off-Normal and Accident Conditions, Risø National Laboratory, Denmark, May 16-20, 1983

/4/ Loftus, M.J.; Hochreiter, L.E.; Utton, D.B.; Young, M.Y.:
"Spacer Grid Heat Transfer Effects During Reflood"
NUREG/CP-0043, April 1983, pp. 445-475

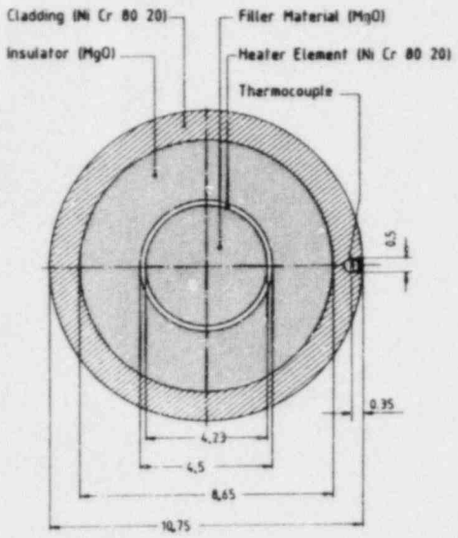

Fig. 1 FEBA fuel rod simulator

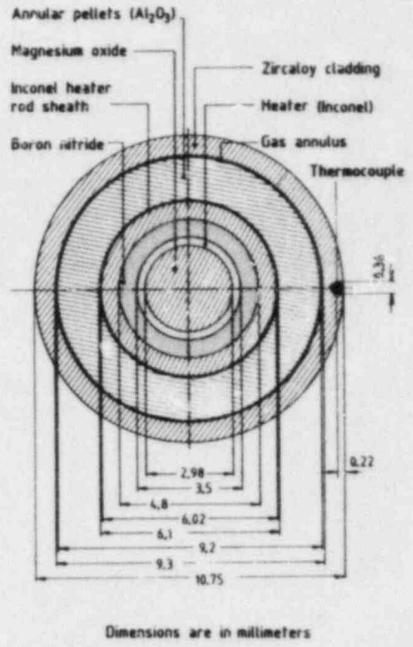

Fig. 2 REBEKA fuel rod simulator used for SEFLEX tests

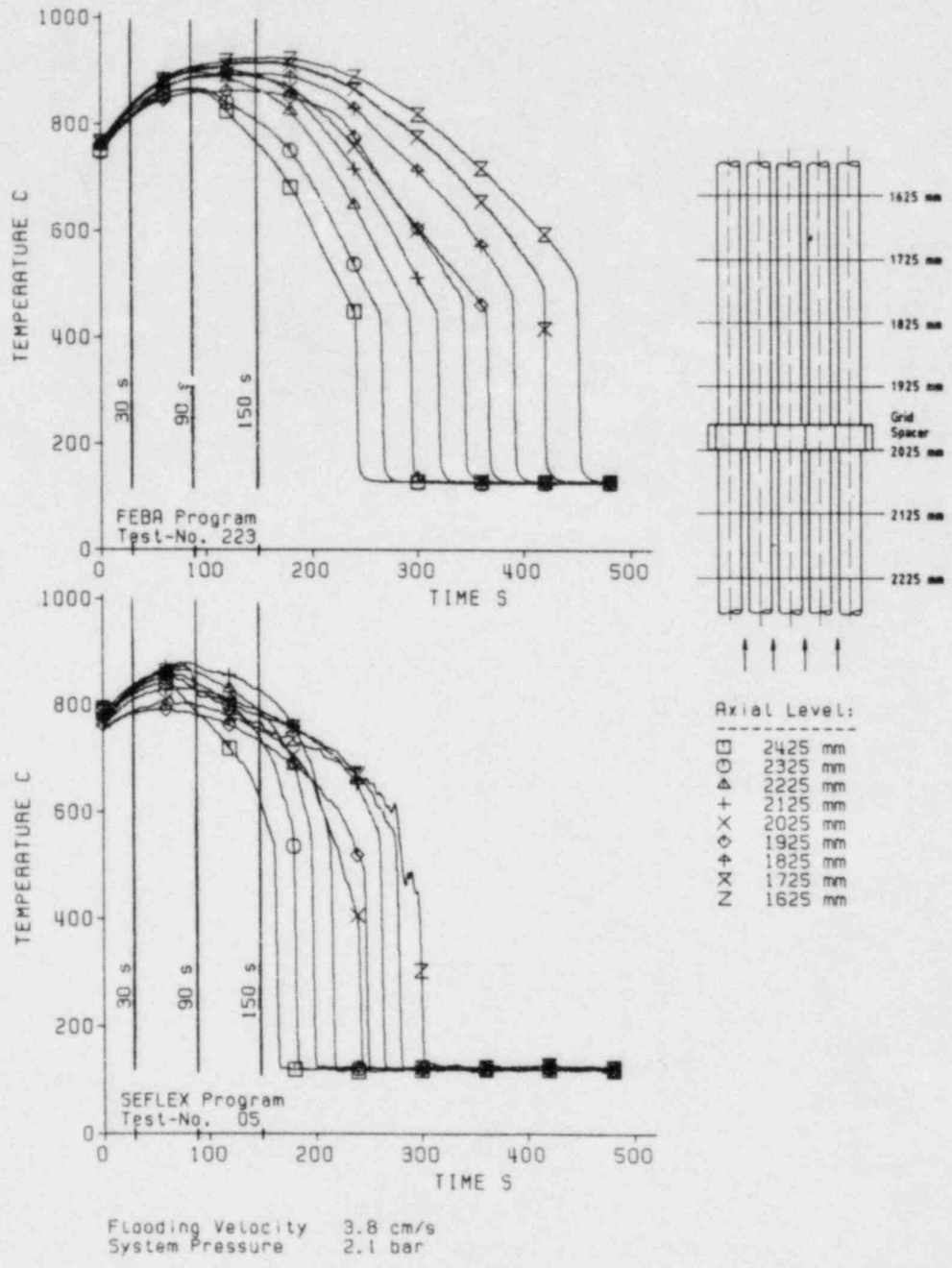

Fig. 3 Influence of heater rod design on the transient cladding temperatures at the bundle midplane

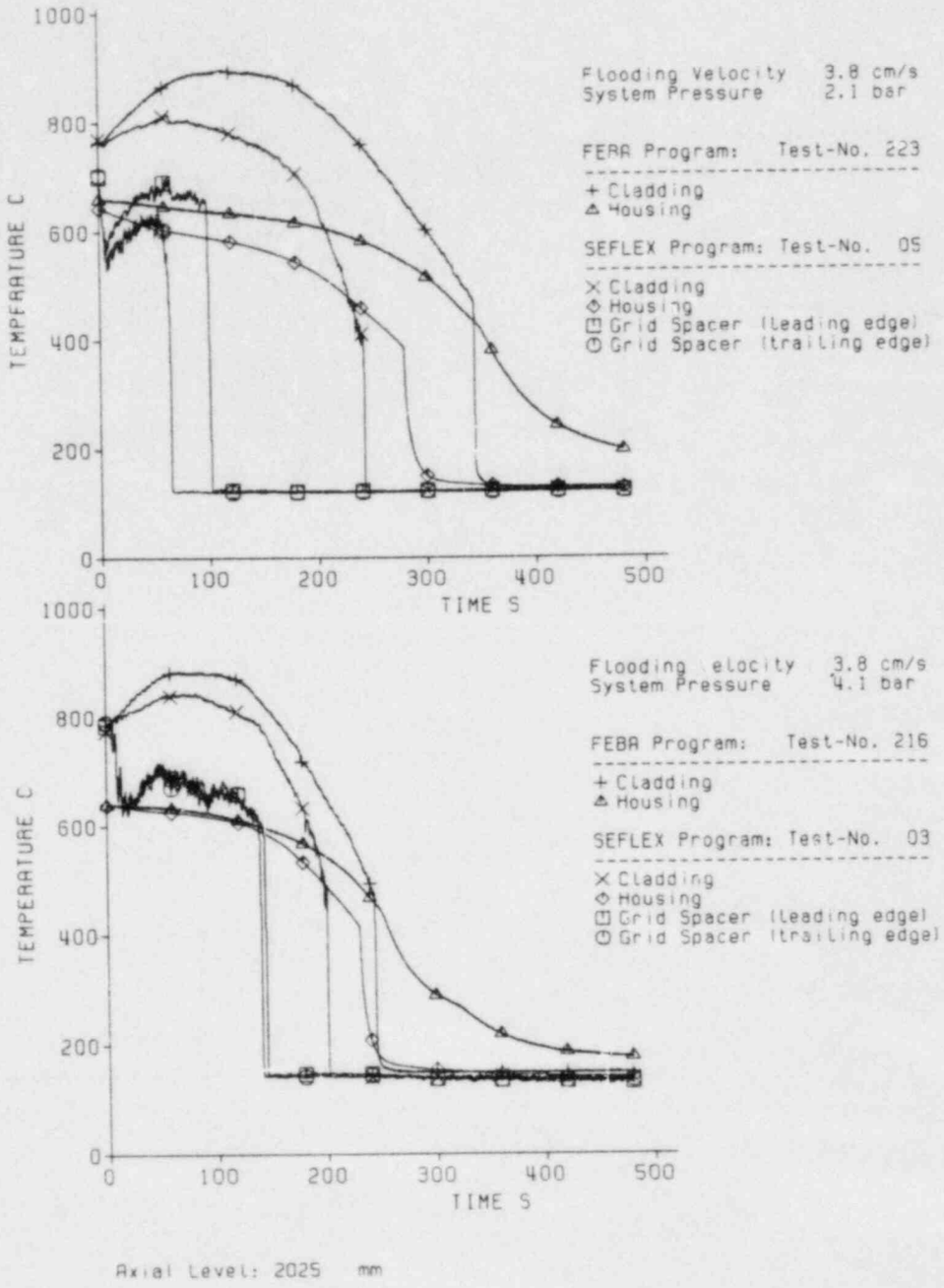

Fig. 4 Influence of heater rod design on cladding, housing, and grid spacer temperatures at the bundle midplane

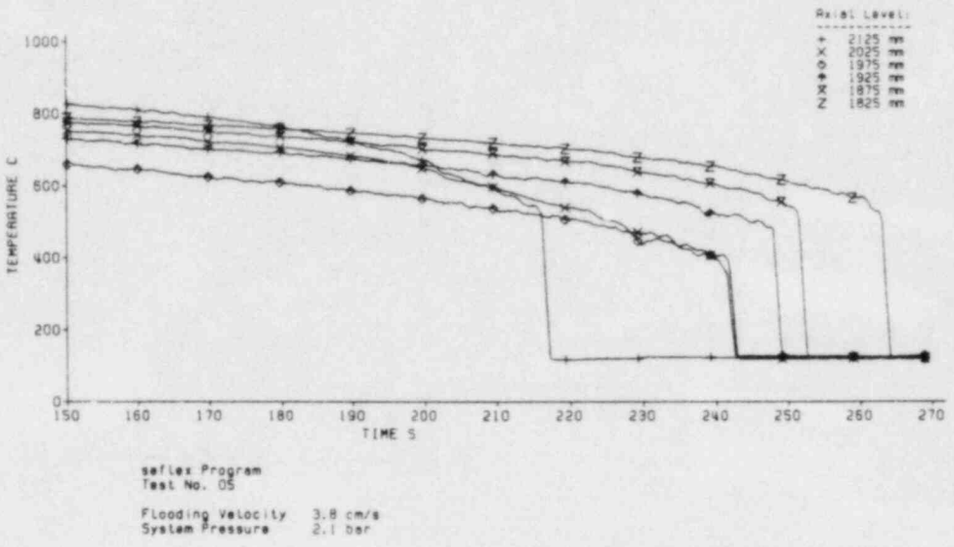

Fig. 5 Cladding temperatures close to midplane grid spacer

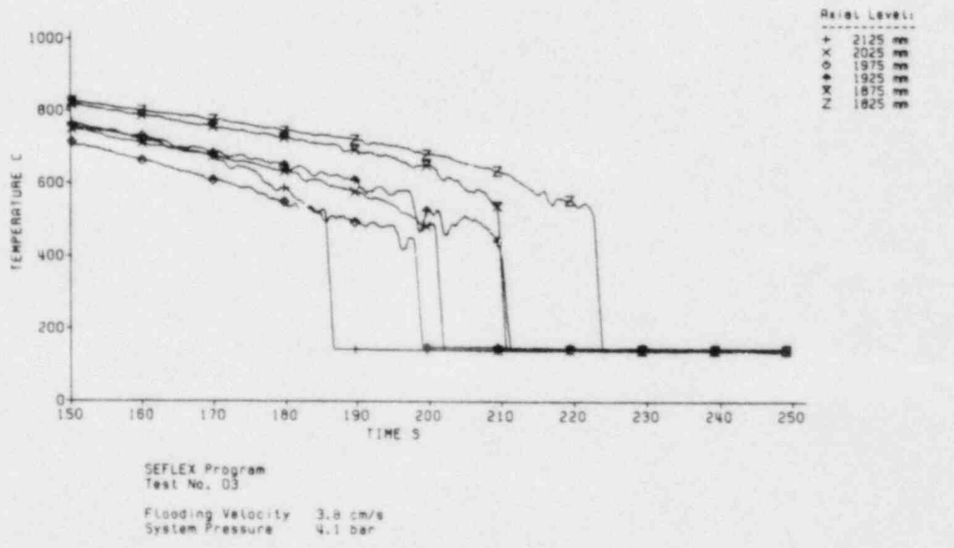

Fig. 6 Cladding temperatures close to midplane grid spacer

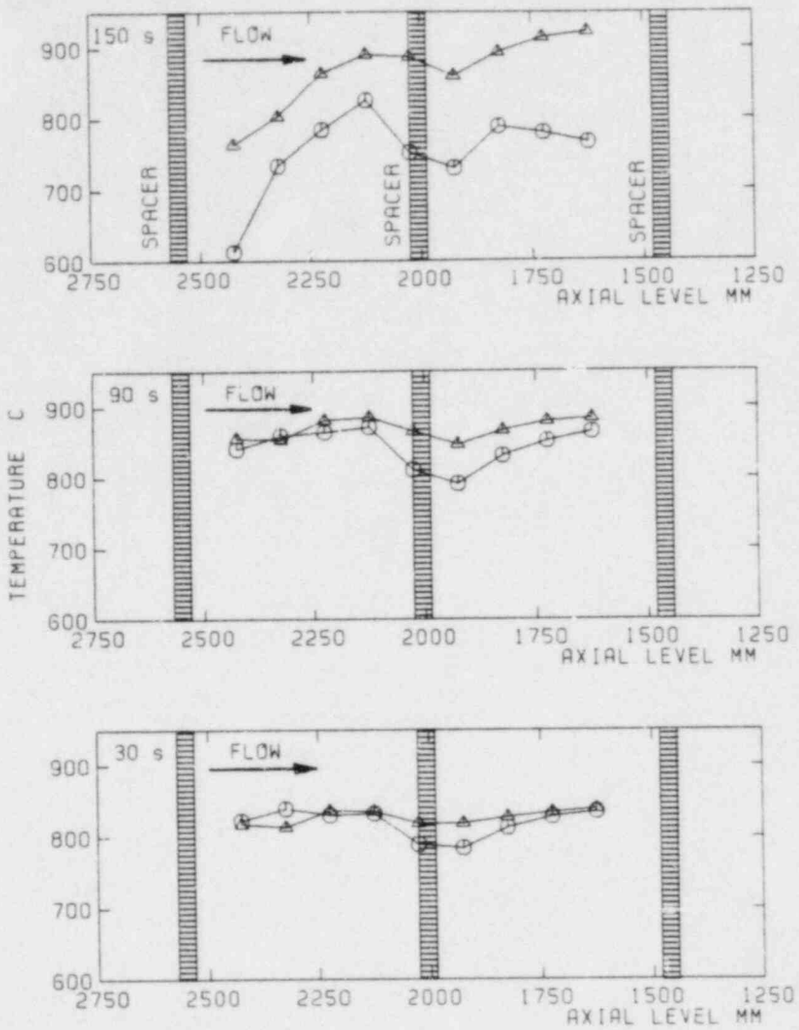

Flooding Velocity 3.8 cm/s
System Pressure 2.1 bar

△ FEBA Program
Test No. 223
Heater Rod: NiCr-Cladding, No Gap

Ⓣ SEFLEX Program
Test No. 05
Heater Rod: Zr-Cladding, He Filled Gap of 0.050 mm Width

Fig. 7 Influence of heater rod design on axial temperature profile at bundle midplane

Summary of Discussion in the Effects of Grids and Blockage Session

Y.Y. Hsu

Dept. of Chemical and Nuclear Engineering

University of Maryland

College Park, Maryland 2074

The discussions in this session were very diversed. However, they can be grouped in several major areas:

1. Blockage/grid effect

   In general, the blockage/grid do give beneficial effect to cooling heat transfer. But the blockage does cause detrimental effects through flow diversion, although the diversion effect is not serious in the downstream of blockage. According to Japanese test results, early quenching was observed for runs with high flood rate, but delayed quenching was observed for low flooding cases. So for the low flooding rate cases, blockage may not be beneficial.

2. Droplet sizes

   In the SUNY study, the entrainment droplet size increases with the flow rate while in the study by Adam and Clare, the drop size decreases with increasing velocity. However, it was noted that the range of drop size and velocity of thses two studies were different (see summary of each paper) and the initial conditions were different. Thus more paramety study is needed.

   In addition, people should be aware that with photographical studies, only drops of visible range have been analyzed. Those very small droplets not visible on photo film can still be detected by laser and these drops could account for significant fraction of interfacial area.

3. Water accumulation above grids

   Water has been observed to accumulate above the grids, in both Japanese and German tests. This phenomenon has

not been factored into the codes yet.

4. Codes

People are concerned about the expenses and inaccessibility of advanced codes for practical application, fast running and cheaper codes are needed.

Summary of Scopes & Subjects
Covered by the Papers in this session

Grid/Blockage Effects	Adams & Clure	Lee et al	Erbader & Wiehr	Ihle et al	Pearson & Cooper
Hydraulics					
Enhanced Convection					Model
Grid/blockage rewetting					Model
Droplet Breakup (dry grids)	mode & drop size	Drop Size			
Droplet Entrainment (wet grids)	Drop size	Drop Size			
Flow diversion (blockage only)					Model
Heat Transfer					
Temperature profiles			Data	Data	Data
Quenching envelops					Data
Heat Transfer coeff.					Data

Adam & Clare (CEGB)

Droplets Breakup and Entrainment at PWR Spacer grids

1. Objectives

   Photographic study of droplet fragmentation on dry grid & entrainment from wet grids.

2. Approach

   Simple exp't to show the drop-grid interaction

   a. Drop fragmentation - impact of falling drops on the edge of thin plate
   b. Bouncing of drops - fragmented drops bouncing on and off between heated parallel plates
   c. Droplet entrainment - droplet spray wetting the plate and re-entrained.

3. Results

   a. Dry-grid: fragmentation increases with increasing We (Fig. 4)
   b. Drop impingement do not significantly affect drop size distribution
   c. Wet-grid entrainment - entrainment drop size decreases with increasing We (Fig. 10A)

   (Note: For wet-grid entrainment, the trend is opposite from SUNY-SB result. However the range of drop size and velocity are different and difficult to make direct comparison. D 100∿500μm)
   u 0∿30 m/sec

Lee et al, SUNY-SB

Measurement of Droplet Dynamics across the grid spacer in Mist Cooling and subchannel

1. Objective
   Measurement of drop size and velocity in steam-water flow acrosss the grid spacer.
2. Approach
   Laser optical measurements of flow in a 2x2 rod bundle with dry and wet grids.
3. Results
   a. Cooling effect across the grid (Fig. 14, 15 of the paper)
   b. Droplet size:
      (1) Dry grid (fragmentation) - drop size decreases with increasing Weber number (Fig. 16).
      (2) We grid (entrainment) - drop size increases with increasing We. (Fig. 17)

(Ncte: wet grid drops $d_{mea.} \approx 100\mu m$)
$u \approx 10$ m/sec.

Erbacher and Wiehr, KfK

Premature Quenching by Ballooned and Burst Fuel Rods Cladding in a LOCA

1. Objective
   To verify the early quenching of burst cladding
2. Approach
   Tests were conducted on simulated rods with Zr-cladding under pressure. The rod burst during test and initiated secondary quench front at burst.
3. Results
   The burst Lips stick out into the flow (Fig. 1 of the paper). The 2nd quench front spreads up and down to give complete quenching of rod earlier than that for the non-deformed rod. (Fig. 2 and 3 of the paper).

Ihle, Rust and Ebacher, KfK

1. Objective

   To determine the grid-spacer effect on rods simulating fuel rods (with pressurized cladding and He-filled gap).

2. Approach

   Reflood behavior of pressurized-cladding rod simulated was compared against that in FEBA tests with gapless rods under identical hydraulic conditions. (Fig. 4 of the paper)

3. Results

   Grid effect is more pronounced with SEFLEX rods. Clad temp. may be lowered by 20-100°K downstream of grids. (Fig. 7 of the paper)

Pearson & Cooper, AEE Winfrith

Reflood Heat Transfer in Severely Blocked Fuel Assemblies

1. Objective

   To study the effects of grid and blockage on heat transfer for bundles with 80% and 90% blockage.

2. Approach

   *Heat transfer measurement on 7x7 blocked cluster with 4x4 blockage. Measurements include temp. profile, quench elevation envelop in both the blocked region and by-pass region.

   *Model was postulated to explain expt'l findings.

3. Results

   a. Improved heat transfer and early quenching downstream of grids (Fig. 5 of the paper)

   b. In the early stage of reflood, 90% blockage cools better than 80% blockage (due to more liquid in the blocked zone) (Fig. 12 & 13).

   c. In the later stage of reflood, 90% blockage shows poorer cooling than 80% blockage (Fig. 12 & 13) (loss of coolant by diverting the by-pass zone).

   d. Blockage region rewetting is no later and may even be earlier than the by-pass region.

VI. Appendix - Attendence List

Attendance List for the International Heat Transfer
Workshop on Fundamental Aspects of Post-Dryout
Salt Lake City, Utah, U.S.A.
April 2-4, 1984

Name	Address
1. Nick Newman	LOFT Program EG&G Idaho, Inc. P. O. Box 1625 Idaho Falls, ID 83415
2. Don Utton	N.N.C. Whetstone Leicester, U.K.
3. Andrew Clare	C.E.G.B. Berkeley Nuclear Labs Berkeley, Gloucestershire U.K.
4. Klaus Johannsen	Institut für Kerntechnik Technische Universitat Berlin Marchstrabe 18, 1000 Berlin 10 Federal Republic of Germany
5. Kemal Tuzla	Chemical Engineering Dept. Lehigh University Whitaker Lab., Bldg. 5 Bethlehem, PA 18018
6. Anastassioi Katsaounis	Guss-Forschungszentrum Geesthacht 2054 Geesthacht Federal Republic of Germany
7. Salih Guntay	LOFT Program EG&G Idaho, Inc. P. O. Box 1625 Idaho Falls, ID 83415
8. Ju-Chuan Lin	EG&G Idaho, Inc. P. O. Box 1625 Idaho Falls, ID 83415
9. John C. Chen	Chemical Engineering Lehigh University Whitaker Lab., Bldg. 5 Bethlehem, PA 18015

10. F. J. Erbacher
Kernforschungszentrum Karlsruhe
Postfach 3640
75 Karlsruhe
Federal Republic of Germany

11. George Costigan
Engineering Science Division
AERE Harwell
Oxfordshire, England OX11 ORA

12. Warren M. Rohsenow
Rm. 3-158
Massachusetts Institute of Technology
Cambridge, MA 02139

13. Dé Groeneveld
AECL
Chalk River Nuclear Lab.
Chalk River, Ontario Canada KOJ 1J0

14. R. Winterton
Mechanical Engineering Dept.
Birmingham University
P. O. Box 363
Birmingham 15
England

15. J. Birchley
LOFT Program
EG&G Idaho, Inc.
P. O. Box 1625
Idaho Falls, ID 83415

16. Kurt Becker
Department of Reactor Technology
Royal Institute of Technology
10044 Stockholm FO
Sweden

17. Ian Brittain
Atomic Energy Establishment, Winfrith
Dorchester, Dorset
England DT2 8DH

18. Ken Pearson
Atomic Energy Establishment, Winfrith
Dorchester, Dorset
England DT2 8DH

19. Mike Denham
Atomic Energy Establishment, Winfrith
Dorchester, Dorset
England DT2 8DH

20. Harold Sullivan

MS-K552, P.O. Box 1663
Los Alamos National Lab.
Los Alamos, New Mexico 87545

21. Roger Deruaz

French Atomic Energy Committee
Heat Transfer Department
85X 38041 Grenoble CEDEX
France

22. Didier Juhel

French Atomic Energy Committee
Heat Transfer Department
85X 38041 Grenoble CEDEX
France

23. Rudy Pauls

Ontario Hydro
Nuclear Studies & SAF Dept
700 University Ave.
Canada Toronto, Ontario

24. Yoshio Murao

Japan Atomic Energy Research Institute
Tokai-mura
Ibaraki-ken, 319-11 Japan

25. Stephen W. Webb

Thermal/Hydraulic Analysis, Division
P.O. Box 5800
Sandia National Lab.
Albuquerque, New Mexico 87185

26. Keith G. Condie

EG&G Idaho
P.O. Box 1625
Idaho Falls, Idaho 83415

27. Romney B. Duffey

EPRI
3412 Hillvriew Avenue
Palo Alto, CA 94303

28. S. Nusret Aksan

Swiss Federal Institute
For Reactor Research (EIR)
5303 Wuerenlingen
Switzerland

29. George Yadigarogly

Swiss Federal Inst. of Technology
ETH-Zentrum
CH-8092 Zurich, Switzerland

30. Ulrich Muller

Kernforschungszentrum (FRB)
75 Karlsruhe Leopoldshafen
BRD Germany

31. Mamora Ishii

RAS 208
Argonne Nat. Lab.
9700 South Cass Ave.
Argonne, IL 6043930.

32. Richard S. L. Lee
Dept. of Mechanical Engineering
State Univ. of New York at Stony Brook
Stony Brook, NY 11794

33. Cheng-Chih Tsai
EG&G Idaho, Inc.
P. O. Box 1625
Idaho Falls, ID 83415

34. I. Vojtek
MS K555, P. O. Box 1663
Los Alamos Nat. Lab.
Los Alamos, NM 87545

35. Bernhard Brand
Dep. R573
Kraftwerk Union AG
D8520 Erlangen
Federal Republic of Germany

36. Geoff F. Hewitt
Building 392-7
Engineering Science Division
AERE Harwell
Oxfordshire, OX11 ORA

37. Shigefumi Nishio
Institute of Industrial Science
Univ. of Tokyo
22-1 7 Chome, Roppongi
Minato-ku, Tokyo
Japan

38. Rex W. Shumway
EG&G Idaho, Inc.
Box 1625
Idaho Falls, ID 83415

39. J. Weisman
Dept. of Chem. & Nuc. Engineering
Univ. of Cincinnati
Cincinnati, OH 45221

40. Ramu Sundaram
Yankee Atomic Electric Co.
1671 Worcester Rd.
Framingham, MA 01701

41. Harry Tovmassian
Mail Stop 1130SS
U. S. NRC
Washington, DC 20555

42. Mike Young
Mail Stop 1130SS
U. S. NRC
Washington, DC 20555

43. Vijay K. Dhir
5532 Boelter Hall
UCLA
Los Angeles, CA 90024

44.	Joseph M. Kelly	Battelle Pacific Northwest Lab. P. O. Box 999 Richand, WA 99352
45.	Hans Herkenrath	J.R.C. ISPRA I-21020 Centro Euratom Varese, Italy
46.	Yih-yun Hsu	Dept. of Chem. & Nuc. Eng. University of Maryland College Park, MD 20742
47.	Kenneth A. Williams	MS-K555, P. O. Box 1663 Los Alamos National Lab. Los Alamos, NM 87545
48.	Novak Zuber	Mail Stop 1130SS U. S. NRC Washington DC 20555
49.	Jose N. Reyes, Jr.	Mail Stop 1130SS U.S. NRC Washington, DC 20555
50.	Fuat Odar	Mail Stop 1130SS U. NRC Washington, DC 20555
51.	Richard Lee	Mail Stop 1130SS U.S. NRC Washington, DC 20555
52.	Keith H. Ardron	Thermalhydraulic Research Branch Whiteshell-AECL Pinawa, Manitoba Canada ROE 1LO
53.	Marvin J. Thurgood	Battelle Pacific Northwest Lab Box 999 Richand, WA 99352
54.	Chick-Bong So	Thermalhydraulic Research Branch Whiteshell-AECL Pinawa, Manitoba Canada ROE 1LO
55.	Ralph A. Nelson	MS K553, P. O. Box 1663 Los Alamos National Lab. Los Alamos, NM 87545

56. Charles D. Morgan
Utility Power Generation Div.
Babcock & Wilcox
P. O. Box 1260
Lynchburg, VA 24503

57. Dennis Liles
MS-K553, P. O. Box 1663
Los Alamos National Lab.
Los Alamos, NM 87545

58. L. E. Hockreiter
Westinghouse Electric Corp.
P. O. Box 355
Pittsburg, PA 15230

59. Zia Rouhani
EG&G Idaho, Inc.
P. O. Box 1625
Idaho Falls, ID 83415

NRC FORM 335 (7-77)

U.S. NUCLEAR REGULATORY COMMISSION

BIBLIOGRAPHIC DATA SHEET

1. REPORT NUMBER (Assigned by DDC)
NUREG/CP-0060

4. TITLE AND SUBTITLE (Add Volume No., if appropriate)
The First International Workshop on Fundamental Aspects of Post-Dryout Heat Transfer

2. (Leave blank)

3. RECIPIENT'S ACCESSION NO.

7. AUTHOR(S)
Compiled by R. Lee

5. DATE REPORT COMPLETED
MONTH: November YEAR: 1984

9. PERFORMING ORGANIZATION NAME AND MAILING ADDRESS (Include Zip Code)
Division of Accident Evaluation
Office of Nuclear Regulatory Research
U. S. Nuclear Regulatory Commission
Washington, D. C. 20555

DATE REPORT ISSUED
MONTH: December YEAR: 1984

6. (Leave blank)

8. (Leave blank)

12. SPONSORING ORGANIZATION NAME AND MAILING ADDRESS (Include Zip Code)
Same as Item 9 above

10. PROJECT/TASK/WORK UNIT NO.

11. CONTRACT NO.

13. TYPE OF REPORT
Workshop proceedings

PERIOD COVERED (Inclusive dates)
April 2-4, 1984

15. SUPPLEMENTARY NOTES

14. (Leave blank)

16. ABSTRACT (200 words or less)

This report contains papers presented at the First International Workshop on Fundamental Aspects of Post-Dryout Heat Transfer that was held in Salt Lake City on April 2-4, 1984. The purpose of the workshop is to review recent development and the state-of-art in the field of post-dryout heat transfer. It centered on interchanging ideas, reviewing current research results, and defining future research needs. The five sessions dealing with the fundamental aspects of post-dryout heat transfer were: computer code modeling and flow phenomena, quenching phenomena, low-void heat transfer, dispersed-flow heat transfer and effects of grids and blockages.

17. KEY WORDS AND DOCUMENT ANALYSIS

17a. DESCRIPTORS

Post-Dryout Heat Transfer
Computer Code Modeling and Flow Phenomena
Quenching Phenomena
Low-Void Heat Transfer
Dispersed-Flow Heat Transfer
Effects of Grids and Blockages on Heat Transfer

17b. IDENTIFIERS/OPEN-ENDED TERMS

18. AVAILABILITY STATEMENT
Unlimited

19. SECURITY CLASS (This report)
Unclassified

21. NO. OF PAGES

20. SECURITY CLASS (This page)
Unclassified

22. PRICE
$

UNITED STATES
NUCLEAR REGULATORY COMMISSION
WASHINGTON, D.C. 20555